NOVA SCHOOL OF SCIENCE & TECHNOLOGY

DEPARTMENT OF CHEMISTRY

ADVANCED WATER-SOLUBLE SOFT NANO-MATERIALS ENCAPSULATING LUMINES-CENT INORGANIC AND ORGANIC EMIT-TERS AND HYDROPHOBIC DRUGS AS NOVEL NANOCARRIERS:

FROM BIOIMAGING TO DRUG DELIVERY AND ENVIRONMENTAL APPLICATIONS

FREDERICO GONÇALO DO VALE DUARTE

Master in Bioorganic Chemistry

DOCTORATE IN SUSTAINABLE CHEMISTRY

NOVA University of Lisbon

January, 2026

NOVA SCHOOL OF SCIENCE & TECHNOLOGY

DEPARTMENT OF CHEMISTRY

ADVANCED WATER-SOLUBLE SOFT NANOMATERIALS ENCAPSULATING LUMINESCENT INORGANIC AND ORGANIC EMITTERS AND HYDROPHOBIC DRUGS AS NOVEL NANOCARRIERS:

FROM BIOIMAGING TO DRUG DELIVERY AND ENVIRONMENTAL APPLICATIONS

FREDERICO GONÇALO DO VALE DUARTE

Master in Bioorganic Chemistry

Adviser: Carlos Lodeiro Y Espiño
Full Professor, NOVA University Lisbon, Portugal

Co-advisers: Elisabete de Jesús Oliveira Marques
Assistant Professor, NOVA University Lisbon, Portugal

Cristián Cuerva de Alaíz
Assistant Professor, Complutense University of Madrid, Spain

Examination Committee:

Chair: João Carlos Pereira de Lima,
Full Professor, NOVA University Lisbon, Portugal

Rapporteurs: Amparo Navarro Rascón,
Associate Professor with Habilitation, University of Jaen, Spain

Maria do Amparo Ferreira Faustino,
Associate Professor, University of Aveiro, Portugal

Adviser: Carlos Lodeiro Y Espiño,
Full Professor, NOVA University Lisbon, Portugal

Members: Margarita Parra Alvarez,
Full Professor, University of Valencia, Spain

Nuno Miguel Jesuíno Basílio,
Assistant Professor, NOVA University Lisbon, Portugal

Hugo Miguel Baptista Carreira dos Santos,
Assistant Researcher, NOVA University Lisbon, Portugal

DOCTORATE IN SUSTAINABLE CHEMISTRY

NOVA University of Lisbon
January, 2026

Advanced water-soluble soft nanomaterials encapsulating luminescent inorganic and organic emitters and hydrophobic drugs as novel nanocarriers: from bioimaging to drug delivery and environmental applications

Copyright © Frederico Gonçalo do Vale Duarte, NOVA School of Science and Technology, NOVA University Lisbon.

The NOVA School of Science and Technology and the NOVA University Lisbon have the right, perpetual and without geographical boundaries, to file and publish this dissertation through printed copies reproduced on paper or on digital form, or by any other means known or that may be invented, and to disseminate through scientific repositories and admit its copying and distribution for non-commercial, educational or research purposes, as long as credit is given to the author and editor.

To tiPaula and toinoZé.

ACKNOWLEDGMENTS

My PhD journey has been marked by ups and downs, but I cherish everything I've learned along the way, especially the lessons gained outside of academia, which in many ways helped me endure the sacrifices required to complete this phase of my life. I trust that, in time, everything will fall into its rightful place, and I remain hopeful that the future will be bright. May my curiosity and contrarian thinking never dim.

First of all, I would like to express my gratitude towards my main PhD supervisor, Professor Lodeiro, who paved the way for this work to be accomplished, who also instilled in me a sense of independence for future endeavors and for pushing me beyond my limits. I believe in his impact and vision, which in many ways echo the famous words Fernando Pessoa *"Deus quer, o homem sonha, a obra nasce".* I hope that you still think you bet on the right horse.

I also want to extend my thanks to my co-supervisor Dr. Cristián Cuerva, who was my first point of contact in the lab when I was a candidate for my bachelor's degree and who has continued to follow my journey from afar. His support, though at a distance, has been truly appreciated, as has his warm reception during my productive visit to the Complutense University of Madrid, enabling me to advance this thesis. To my co-supervisor, Dr. Elizabete Oliveira, who I admire for her strength and tenderness, a special thanks for the help and advice during this thesis and the related projects.

A profound acknowledgment is extended to Dr. Atanas Kurutos and Dr. Georgi Dobrikov from the Bulgarian Academy of Sciences, whose long-standing collaboration has greatly supported this thesis, with the hope that it continues indefinitely. This gratitude also embraces the warm welcome I received in Bulgaria, which provided the opportunity to present some of the work accomplished so far.

In addition, I am beholden to the BIOSCOPE Research Group. A heartfelt thanks to Professor Capelo, whose spirit I may not always fully agree with but deeply understand, and whose

standards and intentions I aspire to follow. I extend these words to the exceptional current lab and group colleagues, Dr. Hugo Santos, Dr. Javier Lodeiro, André Figueiredo, Joana Galhano, Inês Domingos, Filipe Morais, Gonçalo Pedro, João Montes and Raquel Fonseca. I also wish to acknowledge the former members of the BIOSCOPE Group, who were part of my daily work life, Dr. Luis Carvalho, Dr. Adrián Lodeiro, and Dr. Silvia Nuti.

A sincere thanks to Dr. Clément Cabanetos for the warm welcome to his group at the University of Angers, France, the result of another enduring collaboration. His distinction and goodwill made the experience particularly memorable. I am also grateful for the support provided during my stay in France, which enabled me to advance and complete some of the work abroad. Furthermore, I wish to acknowledge the significant contribution of the CAMPUS FRANCE agency, whose grant facilitated this visit and helped foster this valuable collaboration.

I am grateful to all the individuals who contributed results from their respective areas of expertise: Dr. Hugo Santos for the high-resolution mass spectrometry data; Dr. Elisabete Oliveira and Joana Galhano for their work on bacterial studies; Dr. Javier Lodeiro, for his valuable insights into nanoparticle synthesis and related characterization; Dr. Luísa Maia for the electron paramagnetic resonance spectroscopy data; Dr. Carla Gomes for the single-crystal X-ray diffraction data; Oleksandr Bondarchuk for the X-ray photoelectron spectroscopy data; and the *Laboratório de Análises* of LAQV Requimte specially to Carla Rodrigues.

A special thanks to Inês Gomes, Igor Lourenço, and Diogo Torres, with whom I had the pleasure of sharing my knowledge during their bachelor's projects and who contributed to some of the work presented in this thesis.

I would like to acknowledge Dr. Beatriz Cugnasca, Dr. Carla Santos, and José Celorico for their invaluable collaborations and daily contributions to our work.

I am incredibly grateful to the PROTEOMASS Scientific Society for the trust and continuous financial support; to Fundação para a Ciência e a Tecnologia for the PhD grant (2021.05161.BD) and financial support as well.

To my close friend, Ruben Costa, whose friendship has kept the memory of my past alive. To my close friends, Gonçalo Pedro, Igor Lourenço and Inês Gomes who shared their journey with me in the lab, thanks for the support, laughs and continuous help during these years, and may you each find everything you are seeking.

Para a minha família, por quem sinto a responsabilidade e a necessidade de ser bem-sucedido. À minha mãe, "tiPaula", e ao meu pai, "toinoZé", a quem o tempo nem sempre terá sido benevolente, espero que este esforço vos traga algum conforto pelos vossos sacrifícios e preocupações. Que chegue o momento em que possamos sentir-nos em paz. Por isso me empenho, ainda que nem sempre seja visível. Desejo-vos eternidade.

To my mini mini, I will never forget when you brought me a lamp while I was in the dark, may God keep our distance at bay.

" The society that separates its scholars from its warriors will have its thinking done by cowards and its fighting by fools."

(Thucydides)

THESIS CONTRIBUTION SUMMARY

Journal articles

1. Frederico Duarte, Georgi Dobrikov, Atanas Kurutos, Hugo M. Santos, Javier Fernández-Lodeiro, Jose Luis Capelo-Martinez, Elisabete Oliveira, Carlos Lodeiro. "**Enhancing water sensing via aggregation-induced emission (AIE) and solvatofluorochromic studies using two new dansyl derivatives containing a disulfide bound: Pollutant metal ions detection and preparation of water-soluble fluorescent polymeric particles**". *Dyes and Pigments* 218 (2023): 111428. https://doi.org/10.1016/j.dyepig.2023.111428.
2. Frederico Duarte, Georgi Dobrikov, Atanas Kurutos, Jose Luis Capelo-Martinez, Hugo M. Santos, Elisabete Oliveira, Carlos Lodeiro. " **Development of fluorochromic polymer doped materials as platforms for temperature sensing using three dansyl derivatives bearing a sulfur bridge** ". *Journal of Photochemistry and Photobiology, A: Chemistry* 445 (2023): 115033. https://doi.org/10.1016/j.jphotochem.2023.115033.
3. Frederico Duarte, Inês Pereira-Gomes, Georgi M. Dobrikov, Joana Galhano, Clara S. B. Gomes, Atanas Kurutos, Hugo M. Santos, Elisabete Oliveira, Maria Paula Duarte, José Luis Capelo-Martinez, Carlos Lodeiro. "**Antimicrobial profile and Turn-On sensing of cyanide and water traces using a dual chromophoric Dansyl-Acridine conjugate as multifunctional system**". *Microchemical Journal* 205 (2024): 111237. https://doi.org/10.1016/j.microc.2024.111237.
4. Igor Lourenço, Frederico Duarte, Georgi M. Dobrikov, Atanas Kurutos, Ivaylo Slavchev, José Luis Capelo-Martínez, Hugo M. Santos, Carlos Lodeiro. "**Design and evaluation of dansyl-derived chemosensors for disulfide-cleavage-triggered detection: photophysical, metal sensing, and thermometric applications**". *Journal of Materials Chemistry C* 13 (2025): 6708. https://doi.org/ 10.1039/d4tc04750h
5. Inês Pereira-Gomes, Frederico Duarte, Georgi M. Dobrikov, Ivaylo Slavchev, Atanas Kurutos, Jose Luis Capelo-Martinez, Hugo M. Santos, Carlos Lodeiro. "**Tetra**

dansylamides substituted cyclen and cyclam macrocycles as fluorescent sensing probes for metal ions and temperature-responsive materials in dopped polymers". *Dyes and Pygments* 232 (2025): 112461. https://doi.org/10.1016/j.dyepig.2024.112461

6. Frederico Duarte, Diogo Torres, Georgi M. Dobrikov, Atanas Kurutos, Luisa B. Maia, Oleksandr Bondarchuk, Ivaylo Slavchev, Jose Luis Capelo-Martínez, Hugo M. Santos, Carlos Lodeiro. "**A dual-responsive Dansyl–Naphthalimide system for Hg(II) CHEF detection and ligand-mediated Cu(II) reduction with catalytic relevance**". *Dyes and Pigments* 243 (2025): 113088. https://doi.org/10.1016/j.dyepig.2025.113088
7. Frederico Duarte, Cristián Cuerva, Georgi M. Dobrikov, Atanas Kurutos, Nikolay G. Vassilev, Javier Fernández-Lodeiro, José Luis Capelo-Martinez, Hugo M. Santos, Carlos Lodeiro. "**Engineering multifunctional Cyclen fluorophores for metal ion sensing, self-assembly and Nanocolloid applications**". *Spectrochim. Acta A Mol. Biomol. Spectrosc.* 349 (2026): 127285. https://doi.org/10.1016/j.saa.2025.127285

Book Chapter

1. Frederico Duarte *et al.*, "**Recent Advances in Dansyl-Based Probes for Chemical and Biological Sensing**". In Understanding Metals in the Environment and Human Health - Taylor & Francis Group, LLC / CRC Press 2026. In press.

Oral Communications

1. Oral Communication (15min) at XVIII International Workshop on Sensors and Molecular Recognition (2025) "**Harnessing Valence Tautomerism and CHEF Effect for Distinctive Sensing of Hg(II) and Cu(II) Using Dyad Fluorophores**" València, Spain – 19th to 20th June 2025.
2. Oral Communication (15min) at Institute of Organic Chemistry with Centre of Phytochemistry Bulgarian Academy of Sciences (IOCCP-BAS) (2024). **"The success between NOVA-FCT and the Institute of Organic Chemistry with Centre of Phytochemistry around luminescent materials"** Sofia, Bulgaria – 15th October 2024.
3. Oral Communication (5min) at University of Chemical Technology and Metallurgy (UCTM-Sofia) (2024). **"The success between NOVA-FCT and the Institute of Organic Chemistry with Centre of Phytochemistry around luminescent materials"** Sofia, Bulgaria – 16th October 2024.

4. Oral Communication (5min) at 5th International Caparica Christmas Conference on Translational Chemistry (2024). "**Highly Selective and Sensitive CHEF-Based Fluorescent and Colorimetric Detection of Hg(II) and Cu(II) Ions Using Naphthalimide-Dansyl Conjugates**" Caparica, Portugal – 08th to 12th December 2024.
5. Oral Communication (5min) at 5th International Caparica Christmas Conference on Translational Chemistry (2024). "**Fluorescent Tetra-Substituted Dansylamides with macrocyclic design: Solvatochromic systems, AIE behaviour and Enhanced Thermal Stability in Polymers**" Caparica, Portugal – 08th to 12th December 2024.
6. Oral Communication (5min) at 6th International Caparica Conference on Chromogenic and Emissive Materials (2024). "**Novel Acridine Conjugates with DMF and Dansyl Amide Multifaceted Applications in Anion Sensing, Temperature Monitoring, and Antimicrobial Studies**" Caparica, Portugal – 07th to 11th July 2024.
7. Oral Communication (5min) at 6th International Caparica Conference on Chromogenic and Emissive Materials (2024). "**Advanced fluorescent tetra substituted dansylamides: macrocycle integration for metal ion detection and thermal stability in polymers.**" Caparica, Portugal – 07th to 11th July 2024.
8. Oral Communication (5min) at 6th International Caparica Conference on Chromogenic and Emissive Materials (2024). "**Design and Functionality of Bis-Dansyl Amide Pincer Compounds with S and S-S Bridging Units for Enhanced Metal Sensing in Solids, Solutions, and Polymers.**" Caparica, Portugal – 07th to 11th July 2024.
9. Oral Communication (5min) at 6th International Caparica Conference on Chromogenic and Emissive Materials (2024). "**Combining dansyl and naphthalimide unique solvatofluorochromic properties for enhanced thermometry and pollutant metal ions sensing.**" Caparica, Portugal – 07th to 11th July 2024.
10. Oral Communication (5min) at 5th International Caparica Conference on Chromogenic and Emissive Materials (2022). "**Dansyl-based compounds containing a S-S bond as molecular sensors for Metal ions detection.**" Caparica, Portugal – 04th to 07th July 2022.

Poster communications

1. Poster presentation at 6th International Caparica Conference on Pollutant Toxic Ions & Molecules (2025). "**Exploiting Valence Tautomerism and CHEF Effect in Dyad Fluorophores for Selective Recognition of Cu (II) and Hg(II)**" Caparica, Portugal – 02nd to 06th November 2025.
2. Poster presentation at 5th International Caparica Christmas Conference on Translational Chemistry (2024). "**Fluorescence Enhancement via Sodium Dithionite Reduction,**

Aggregation-Induced Emission, and Metal Ion Sensing in Two Novel Dansyl-Based Chemosensors with S and S-S Bridging Units" Caparica, Portugal – 08th to 12th December 2024.

3. Poster presentation at XI International Congress on Analytical Nanoscience and Nanotechnology (2024). "**Water-soluble soft nanomaterials encapsulating luminescent Eu(III) and B(III) complexes and organic emitters as novel nanocarriers**" Santiago de Compostela, Spain – 03rd to 06th September 2024.
4. Poster presentation at 14th Inorganic & Bioinorganic Chemistry Conference (2024). "**Two new tetrasubstituted macrocycles with dansyl dyes as fluorescent and solvatochromic systems for metal ion detection**" Lisboa, Portugal – 16th to 18th May 2024.
5. Poster presentation at 14th Inorganic & Bioinorganic Chemistry Conference (2024). "**Sensing copper(II) and mercury(II) ions by a solvent modulated emission sulfur bridged dansyl dyes as molecular probes**" Lisboa, Portugal – 16th to 18th May 2024.
6. Poster presentation at 5th International Caparica Conference on Pollutant Toxic Ions and Molecules (2023). "**Exploring a new molecular chemosensors based on naphthalimide: from chemical to environmental potential applications.**" Caparica, Portugal – 06th to 09th November 2023.
7. Poster presentation at 5th International Caparica Conference on Pollutant Toxic Ions and Molecules (2023). "**Metal Ion Sensing and Reversible Acid-Induced Emission Modulation of 9-Aminoacridine Derivative and polymer-supported applications. Advancing Water Detection in Organic Solvents**" Caparica, Portugal – 06th to 09th November 2023.
8. Poster presentation at XXVIII Encontro Nacional da SPQ (2023). "**Studying a novel fluorescent molecular probe containing a naphthalimide unit as a temperature and toxic metal ions sensor**" Aveiro, Portugal – 24th to 26th July 2023.
9. Poster presentation at XVI International Workshop on Sensors and Molecular Recognition (2023). "**Aggregation-induced emission and acidic effects on novel dansyl-based emissive molecular probes entrapped in polymers sheets and microparticles**" València, Spain – 06th to 07th July 2023.
10. Poster presentation at 8th EuChemS Chemistry Congress (2022). "**From Blue to Green: Solvent effects on novel emissive molecular probes of dansyl-based dyes**" Lisboa, Portugal – 28th August to 01st September 2022.

Scholarships and Awards

1. PhD Scholarship provided by *Fundação para a Ciência e a Tecnologia* (ref. 2021.05161.BD), from 1st January 2022 to 31st December 2025.
2. Scholarship of International mobility provided by CAMPUS FRANCE (Ministry of Foreign Affairs - French Government, ref. 179886U), from 3rd September 2025 to 5th November 2025.
3. Shotgun poster communication prize presented in the 5th International Caparica Conference on Chromogenic and Emissive Materials 2022 held in Caparica- Portugal, 3rd-7th July 2022.

Abstract

Fluorescent molecular probes have become indispensable tools across chemical, environmental, and biomedical sciences, yet current sensing technologies often lack the sensitivity, multifunctionality, and adaptability required to address today's analytical challenges. With increasing concerns regarding environmental pollutants, toxic metal exposure, and real-time diagnostics, there is a growing demand for highly responsive, cost-effective, and versatile fluorescent systems capable of reliable performance across diverse settings.

This doctoral thesis addresses this need by developing innovative molecular platforms that combine advanced photophysical design with practical sensing capabilities. It presents the conception, synthesis, and application of next-generation multifunctional fluorophores, showing how strategic chromophore engineering can improve detection accuracy, environmental responsiveness, and functional versatility.

Central to this research is the construction of eighteen dansyl-based fluorophores integrating tailored receptor architectures, macrocyclic frameworks, and dual-chromophoric assemblies to enhance optical responses and enable finely tuned sensing pathways. Key advancements include (i) the development of solvatochromic and aggregation-induced emission (AIE) systems capable of reporting subtle changes in microenvironmental polarity and water content; (ii) the design of single-chromophore and dyads that exploit ICT, PET, and CHEF mechanisms for selective detection of toxic ions such as Hg^{2+}, Cu^{2+}, and cyanide; (iii) the incorporation of disulfide (S–S) and thiol (–S–) functionalities that induce fluorescence quenching with emission restored upon cleavage and serve as recognition sites for soft-soft selective Hg^{2+} detection; (iv) the design of macrocycle-based dansyl platforms that enhance light absorption and fluorescence intensity while alkyl side chains promote mesomorphic organization, improving stability in aggregated environments; (v) the fabrication of polymeric particles and films providing water stability, temperature-responsive sensing by incorporating the fluorophores which

can also act as stabilizers during metallic nanoparticle synthesis; and (vi) the discovery of fluorophores exhibiting intrinsic antimicrobial activity, demonstrating multifunctionality beyond sensing.

Overall, this thesis shows how multifunctional dansyl-based fluorophores can be rationally designed to combine tunable photophysics, selective sensing, material fabrication, and biological activity. These findings provide a versatile framework for developing next-generation fluorescent materials with applications in environmental monitoring, analytical chemistry, and biomedical diagnostics.

Keywords: Dansyl, Metal Ion Sensing, Solvatochromism, Aggregation Induced Emission, Polymers, Microparticles, Antimicrobial Activity.

Resumo

As sondas fluorescentes moleculares tornaram-se ferramentas indispensáveis nas áreas química, ambiental e biomédica, contudo, as tecnologias de deteção atuais carecem frequentemente da sensibilidade, multifuncionalidade e adaptabilidade necessárias para enfrentar os desafios analíticos contemporâneos. Com o aumento das preocupações relativas a poluentes ambientais, exposição a metais tóxicos e à necessidade de diagnósticos em tempo real, cresce a procura por sistemas fluorescentes altamente responsivos, económicos e versáteis, capazes de apresentar desempenho fiável em diferentes contextos.

Esta tese de doutoramento responde a esta necessidade, desenvolvendo plataformas moleculares inovadoras que combinam design fotofísico avançado com capacidades práticas de deteção. Apresenta a concepção, síntese e aplicação de fluoróforos multifuncionais de última geração, demonstrando como *design* estratégico de cromóforos pode melhorar a precisão na deteção, a resposta ambiental e a versatilidade funcional.

O cerne desta investigação é a construção de dezoito fluoróforos à base de dansilo, integrando arquiteturas de recetores à medida, estruturas macrocíclicas e montagens duplo-cromóforos para potenciar respostas ópticas e possibilitar vias de deteção finamente ajustadas. Os principais avanços incluem: (i) o desenvolvimento de sistemas solvatocrómicos e de emissão induzida por agregação (AIE), capazes de reportar alterações subtis na polaridade do microambiente e no teor de água; (ii) o desenho de sistemas monocromóforos e díades que exploram mecanismos ICT, PET e CHEF para deteção seletiva de iões tóxicos como Hg^{2+}, Cu^{2+} e CN^{-}; (iii) a incorporação de funcionalidades dissulfeto (S–S) e tiol (–S–) que induzem supressão da fluorescência com restauração da emissão após clivagem, servindo também como sítios de reconhecimento para deteção seletiva de Hg^{2+} via interações soft–soft; (iv) o design de plataformas à base de dansilo macrocíclicas que aumentam a absorção de luz e a intensidade da fluorescência, enquanto cadeias laterais alquílicas promovem organização mesomórfica, melhorando a estabilidade em ambientes agregados; (v) a fabricação de partículas e filmes

poliméricos incorporando os fluoróforos, proporcionando estabilidade em água, deteção responsiva à temperatura e que atuam como estabilizadores durante a síntese de nanopartículas metálicas; e (vi) a descoberta de fluoróforos com atividade antimicrobiana intrínseca, demonstrando que a multifuncionalidade pode ir além da deteção.

De forma geral, esta tese demonstra como fluoróforos multifuncionais à base de dansilo podem ser racionalmente projetados, combinando fotofísica ajustável, deteção seletiva, fabrico de materiais e atividade biológica. Estes resultados fornecem uma estrutura versátil para o desenvolvimento de materiais fluorescentes de próxima geração, com aplicações em monitorização ambiental, química analítica e diagnósticos biomédicos.

Palavras-chave: Dansilo, Deteção de iões metálicos, Solvatocromismo, Emissão induzida por agregação, Polímeros, Micropartículas, Atividade Antimicrobiana.

In the present work, generative artificial intelligence tools, namely ChatGPT v5.1, were used for grammatical revision and to improve the clarity of the text. This tool was employed under the author's supervision, and all generated content was carefully verified for accuracy. The authorship and validation of the content remain entirely the responsibility of the author, and the use of artificial intelligence complies with institutional standards of academic integrity.

CONTENTS

1 INTRODUCTION 1
1.1 Luminescence 1
1.1.1 Fluorescence 1
1.2 Fluorescent molecular sensors 3
1.2.1 Recognition mechanisms 4
1.2.2 Fluorophores 9
1.2.3 Dansyl chloride 10
1.2.4 Dansyl-based Fluorescent Probes for Detection of Metal Ions 11
1.2.5 Dansyl-based Fluorescent Probes for Detection of Anions 40
1.2.6 Dansyl-based Fluorescent Probes for Detection of Small Molecules 45
1.2.7 Dansyl-based Dyad Systems 61
1.2.8 Future Dansyl Perspectives 74
1.3 References 76
2 OBJECTIVES 95
3 ANTIMICROBIAL PROFILE AND TURN-ON SENSING OF CYANIDE AND WATER TRACES USING A DUAL CHROMOPHORIC DANSYL-ACRIDINE CONJUGATE AS MULTIFUNCTIONAL SYSTEM 99
3.1 Abstract 100
3.2 Introduction 100
3.3 Experimental Section 102
3.3.1 Materials 102

3.3.2 Instrumentation 102
3.3.3 Synthetic procedures 104
3.3.4 Spectrophotometric and spectrofluorometric measurments 105
3.3.5 Determination of the detection and quantification limits (LOD and LOQ) 106
3.3.6 Preparation of the polymer Dye-Doped thin films 106
3.3.7 Synthesis of polymeric microparticles 107
3.3.8 Antimicrobial assays 107
3.4 Results and Discussion 108
3.4.1 Synthesis 108
3.4.2 Photophysical characterization 109
3.4.3 Sensing of water molecules 110
3.4.4 Acidochromic behaviour 112
3.4.5 Acid-base anion sensing 114
3.4.6 Polymeric particles 116
3.4.7 Antimicrobial Assay 117
3.5 Conclusions 121
3.6 Supplementary material 122
3.7 Contributions & Aknowledgements 143
3.7.1 Author Contributions 143
3.7.2 Acknowledgments 143
3.8 References 144
4 A DUAL-RESPONSIVE DANSYL–NAPHTHALIMIDE SYSTEM FOR HG(II) CHEF DETECTION AND LIGAND-MEDIATED CU(II) REDUCTION WITH CATALYTIC RELEVANCE 151
4.1 Abstract 152
4.2 Introduction 152
4.3 Experimental Section 154
4.3.1 Materials 154

4.3.2 Instrumentation 155
4.3.3 Synthetic procedures 156
4.3.4 Spectrophotometric and spectrofluorimetric measurements 163
4.3.5 Determination of the detection and quantification limits (LOD and LOQ) 164
4.4 Results & Discussion 164
4.4.1 Synthesis 164
4.4.2 Photophysical characterization 167
4.4.3 Metal Ion sensing 170
4.4.4 Anti-Interference performance in Hg^{2+} detection 175
4.4.5 Determination of association constants and sensing limit parameters 176
4.4.6 Characterization of L1 and L3 complexes with Hg^{2+} and Cu^{2+} 177
4.4.7 Interaction mechanism study of L1 with Cu^{2+} 178
4.5 Conclusions 182
4.6 Supplementary material 183
4.7 Contributions & Aknowledgements 236
4.7.1 Author Contributions 236
4.7.2 Acknowledgments 236
4.8 References 237

5 ENHANCING WATER SENSING VIA AGGREGATION-INDUCED EMISSION (AIE) AND SOLVATOFLUOROCHROMIC STUDIES USING TWO NEW DANSYL DERIVATIVES CONTAINING A DISULFIDE BOUND: POLLUTANT METAL IONS DETECTION AND PREPARATION OF WATER-SOLUBLE FLUORESCENT POLYMERIC PARTICLES 247

5.1 Abstract 248
5.2 Introduction 248
5.3 Experimental Section 250
5.3.1 Materials 250
5.3.2 Instrumentation 250
5.3.3 Synthetic procedures 251

5.3.4 Spectrophotometric and spectroflurimetric measurements 253
5.3.5 Synthesis of polymeric microparticles 254
5.3.6 Determination of the detection and quantification limits (LOD and LOQ) 255
5.4 Results & Discussion 255
5.4.1 Synthesis 255
5.4.2 Photophysical characterization 256
5.4.3 Metal Ion sensing 259
5.4.4 Exploring dansyl derivatives behaviour in aqueous media 262
5.4.5 L1 doped SBS polymeric microparticles 265
5.5 Conclusions 266
5.6 Supplementary material 268
5.6.1 Supplementary figures 268
5.7 Contributions & Aknowledgements 282
5.7.1 Author Contributions 282
5.7.2 Acknowledgments 282
5.8 References 283
6 DEVELOPMENT OF FLUOROCHROMIC POLYMER DOPED MATERIALS AS PLATFORMS FOR TEMPERATURE SENSING USING THREE DANSYL DERIVATIVES BEARING A SULFUR BRIDGE. 289
6.1 Abstract 290
6.2 Introduction 290
6.3 Experimental Section 293
6.3.1 Materials 293
6.3.2 Instrumentation 293
6.3.3 Synthetic procedures 294
6.3.4 Spectrophotometric and spectrofluorimetric measurements 296
6.3.5 Determination of the detection and quantification limits (LOD and LOQ) 297
6.3.6 Preparation of polymer Dye-Doped thin films 298

6.4 Results & Discussion 298
6.4.1 Synthesis 298
6.4.2 Photophysical characterization 300
6.4.3 Metal Ion sensing 302
6.4.4 Studies using solid support compound L1 306
6.4.5 Tuning the emission of dansyl derivatives towards temperature smart materials 306
6.5 Conclusions 310
6.6 Supplementary material 312
6.6.1 Supplementary figures & tables 312
6.7 Contributions & Aknowledgements 327
6.7.1 Author contributions 327
6.7.2 Acknowledgements 327
6.8 References 328
7 DESIGN AND EVALUATION OF DANSYL-DERIVED CHEMOSENSORS FOR DISULFIDE-CLEAVAGE-TRIGGERED DETECTION: PHOTOPHYSICAL, METAL SENSING, AND THERMOMETRIC APPLICATIONS 335
7.1 Abstract 336
7.2 Introduction 336
7.3 Experimental Section 338
7.3.1 Materials 338
7.3.2 Instrumentation 338
7.3.3 Synthetic procedures 339
7.3.4 Spectrophotometric and spectrofluorimetric measurements 341
7.3.5 Determination of the detection and quantification limits (LOD and LOQ) 342
7.3.6 Procedure of polymeric thin films doped with L1 343
7.4 Results & Discussion 343
7.4.1 Synthesis 343

7.4.2 Photophysical characterization 344
7.4.3 Aggregation induced emission behaviour in water 347
7.4.4 Metal Ions Sensing 348
7.4.5 Sensing of sodium dithionite 351
7.4.6 NMR titrations of the free ligands 352
7.4.7 Temperature dependent emission of polymer doped films 355
7.5 Conclusions 357
7.6 Supplementary material 359
7.6.1 Determination of the limit of detection and quantification (LOD and LOQ) 359
7.6.2 Supplementary figures & tables 360
7.7 Contributions & Aknowledgements 395
7.7.1 Author Contributions 395
7.7.2 Acknowledgments 395
7.8 References 396
8 TETRA DANSYLAMIDES SUBSTITUTED CYCLEN AND CYCLAM MACROCYCLES AS FLUORESCENT SENSING PROBES FOR METAL IONS AND TEMPERATURE-RESPONSIVE MATERIALS IN DOPPED POLYMERS 401
8.1 Abstract 402
8.2 Introduction 402
8.3 Experimental Section 404
8.3.1 Materials 404
8.3.2 Instrumentation 404
8.3.3 Synthetic procedures 405
8.3.4 Spectrophotometric and spectroflurimetric measurements 406
8.3.5 Determination of the detection and quantification limits (LOD and LOQ) 407
8.3.6 Preparation of the polymer dye-doped thin films 408
8.4 Results & Discussion 408
8.4.1 Synthesis 408

8.4.2 Photophysical characterization 409
8.4.3 Exploring the behavior in aqueous media 412
8.4.4 Metal ion sensing 413
8.4.5 Designing temperature-responsive materials using dansyl derivative emission 417
8.5 Conclusions 421
8.6 Supplementary material 422
8.6.1 Supplementary figures & tables 422
8.7 Contributions & Aknowledgements 433
8.7.1 Author Contributions 433
8.7.2 Acknowledgments 433
8.8 References 434
9 ENGINEERING MULTIFUNCTIONAL CYCLEN FLUOROPHORES: BRIDGING METAL ION DETECTION, SELF-ASSEMBLY AND NANOCOLLOID APPLICATIONS 441
9.1 Abstract 442
9.2 Introduction 442
9.3 Experimental Section 444
9.3.1 Materials 444
9.3.2 Instrumentation 444
9.3.3 Synthetic procedures 446
9.3.4 Spectrophotometric and spectrofluorimetric measurements 449
9.3.5 Determination of the detection and quantification limits (LOD and LOQ) 450
9.3.6 DFT calculations 450
9.3.7 Colloidal synthesis of platinum nanoparticles 450
9.4 Results & Discussion 451
9.4.1 Conformational Analysis and Molecular Geometry 451
9.4.2 Mesomorphic behavior 453

9.4.3 Photophysical characterization 454
9.4.4 Modulation of aggregation induced emission in water 457
9.4.5 Metal ion detection 459
9.4.6 Colloidal synthesis of platinum nanoparticles 461
9.5 Conclusions 462
9.6 Supplementary material 463
9.6.1 Supplementary figures & tables 463
9.7 Contributions & Aknowledgements 497
9.7.1 Author Contributions 497
9.7.2 Acknowledgments 497
9.8 References 499
10 GENERAL CONCLUSIONS 503
11 FUTURE PERSPECTIVES 505

LIST OF FIGURES

Figure 1–1. Perrin-Jablonski diagram adapted from ref. [1] and characteristic times for each process obtained from ref. [2]. 2

Figure 1–2. Generic representation of the interaction between a fluorescent molecular sensor and an analyte resulting in a recognition signal..... 3

Figure 1–3. Arrangement of the fluorophore and receptor HOMO/LUMO levels that enables the a) acceptor-type PET and b) donor-type PET mechanism in the probe. c) Schematic representation of the overall sensing process mediated by a PET-based fluorescent probe. Adapted from ref. [5]..... 5

Figure 1–4. Representation of ICT-based sensing showing donor–acceptor interactions and analyte binding. Adapted from ref. [5] 6

Figure 1–5. a) Energy diagram of the FRET process. b) Turn-on FRET system. c) Turn-off FRET system. Adapted from refs. [5,11] 7

Figure 1–6. ESIPT-driven sensing pathway with a visual representation of the enol and keto states of an ESIPT fluorophore. Adapted from ref. [5,11] 8

Figure 1–7. Visualization of the fluorescence turn-on of an AIE fluorophore. Adapted from ref. [13a] 9

Figure 1–8. Molecular structures of the common fluorophores are used as fluorescent molecular sensors..... 10

Figure 1–9. Structures of compounds **1**-**7** and proposed detection mechanisms for Cu^{2+}. a) Confocal Laser Scanning Microscopy (CLSM) images of HepG2 cells: (a1-a3) Cells incubated with **1**; (b1-b3) Cells incubated with **1** and then with Cu^{2+}; (c1-c3) Cells incubated with **1** and then with Cu^{2+} and subsequently treated with Na_2EDTA. (a1, b1, c1): Merged images; (a2, b2, c2): Bright-field images; (a3, b3, c3): Fluorescent images. Adapted from ref.[61] copyright 2021, Elsevier. 14

Figure 1–10. Structures of compounds **8**-**19** and proposed detection mechanisms for Hg^{2+}. a) Fluorescence spectra of **9** with excitation wavelength of 330 nm upon addition of increasing concentrations of Hg^{2+} in HEPES buffer at pH 7.4. Inset picture is the variation of color excited at 365 nm. Adapted from ref.[78] copyright 2024, Elsevier. 20
Figure 1–11. Structures of compounds **20**-**24** and proposed detection mechanisms for Zn^{2+}. a) Fluorescence emission spectra of **22** following addition of various metal ions in HEPES buffer (pH 7.4) solutions. (left) Excitation wavelength: 280 nm, (right) Excitation wavelength: 320 nm. Fluorescence emission changes under UV lamp (365 nm) of **22** upon addition of various metal ions. Adapted from ref.[95] copyright 2021, Elsevier. 26
Figure 1–12. Structures of compounds **25**-**28** and proposed detection mechanisms for Cd^{2+}. a) Confocal images of zebrafish larvae treated with **26** for 1 h (A1-A2) and further treated with 2.5 μM (B1-B2), 5 μM (C1-C2) and 10 μM (D1-D2) of Cd^{2+} for 1 h. Adapted from ref.[102] copyright 2024, Elsevier. 29
Figure 1–13. Structures of compounds **29**-**31** and proposed detection mechanisms for several metal ions. 32
Figure 1–14. Structures of compounds **32**-**38** for the dual detection for several metal ions. a) Smartphone-assisted RGB responses for the recognition of Ag^{+} and Hg^{2+}. Adapted from ref.[124] copyright 2025, Elsevier. 34
Figure 1–15. Structures of compounds **39**-**50** for the dual detection of Cu^{2+} and Hg^{2+}. a) Spectrophotometric and spectrofluorimetric titrations of compounds **46** and **47** with increased additions of Cu^{2+} and Hg^{2+} in acetonitrile. The inset represents the emission as a function of the number of equivalents of metal. Adapted from ref.[130] copyright 2024, Elsevier. 38
Figure 1–16. Structures of compounds **51**-**60** for the detection of F^{-} and CN^{-}. 41
Figure 1–17. Structures of compounds **61**-**64** and proposed detection mechanisms for HSO_3^{-} /SO_3^{2-}. 44
Figure 1–18. Structures of compounds **65**-**67** and proposed detection mechanisms for H_2S.. 46
Figure 1–19. Structures of compounds **68**-**70** and proposed detection mechanisms for NO and HNO. 49
Figure 1–20. Structure of compound **71** and proposed mechanism for the detection of HOCl. a) Fluorescence images of RAW264.7. First row: RAW264.7 cells were treated with **71** for 1 h; second row: RAW264.7 cells were incubated with LPS then with **71** for 1 h. Adapted from ref.[158] copyright 2017, Elsevier. 52
Figure 1–21. Structures of compounds **72**-**75** for the detection of nitroaromatic compounds. 53

Figure 1–22. Structures of compounds **76**-**79b** proposed detection mechanisms of aminoacids. a) Photographed colorimetric (365nm) changes of **78** in the presence of various competing analytes. Adapted from ref.[171] copyright 2018, Elsevier. 58
Figure 1–23. Structures of dansyl-naphthalimide dyads **80**-**87**. a) UV–Vis and luminescent titration of compound **86** (left) upon continuous additions of Hg^{2+}. The inset represents the emission of [Hg2+]/[L1] at 515 nm (left) and the time-resolved fluorescence decay profile of 86 before and after the titration with Hg^{2+}ions (right). UV–vis time continuous spectra of L1 (left) after the addition of 7 eq. of Cu^{2+}. The inset represents the images under natural light and UV light (left) and the time-dependent response of the absorbance at 500 nm (right). Adapted from ref.[176] copyright 2025, Elsevier. 63
Figure 1–24. Structures of dansyl-rhodamine dyads **88**-**91**. 68
Figure 1–25. Structures of dansyl-pyrene dyads **92**-**94**. 71
Figure 1–26. Structures of examples of emerging dansyl dyads **95** and **96**. a) Normalized emission intensity of **96** after addition of CN^-, F^-, Br^-, Cl^- in chloroform and inset image under UV light after the addition of CN^- ions in a solution of chloroform (left) and THF (right) of **96**. UV–Vis and luminescent titrations of compounds **96** upon continuous addition of CN^-, in chloroform. Inset: Emission as a function of $[CN^-]$/[L2] at 476 nm. Adapted from ref. [190] copyright 2024, Elsevier. 74
Figure 2–1. Integration of the doctoral thesis objectives across the chemical structures presented in the different chapters of the thesis. 97
Figure 3–1. Graphical abstract. 99
Figure 3–2. (a) Absorption, (b) emission spectra and (c) images of L1 in acetonitrile with different water fraction (f_w = 0%, 17%, 33%, 55%, 67%, 83%) at natural light (up) and under UV light (down, 365 nm). (d) Emission spectra (λ_{excL1}= 395 nm) and (e) plot of the normalized emission intensities at 490 nm of L1 in acetonitrile with increasing amounts water aliquots (0%-0.067%, v/v) with the corresponding linear regressions. [L]= 10 μM, T = 298K. 111
Figure 3–3. (a) Absorption and emission spectra of **L1** in acetonitrile after addition of 1.4 eq. of H^+ followed by 1.6 eq. of OH^- ($[H^+]$ = $[OH^-]$= 0.6 mM) and (b) the emission as a function of ($[H^+]$+$[OH^-]$/[**L1**]) at 487 nm. (c) Spectrophotometric and spectrofluorimetric titrations of compounds **L1** with increased additions of 10 μl of trifluoroacetic acid ([TFA] = 0.15 mM) in chloroform and (d) the emission as a function of $[H^+]$/[**L1**] at 487 nm. Inset images of the solution of **L1** in chloroform prior (left) and after (right) the titration under UV light (365 nm). Acidochromic behaviour of **L1-PMMA**. (e) Normalised emission spectra recorded after treatment with HCl solution (12 M) followed by immersion in a NH_3 solution (25% in water), (f)

normalized emission intensity maximum at 474 nm after successive cycles of HCl/NH_3 treatments by immersion in the corresponding aqueous solutions. (g) Images of the reversible acidochromic behaviour of **L1-PMMA** taken with the naked eye (left) and under UV light (right). 113

Figure 3–4. (a) Normalized emission intensity of **L2** after addition of CN^-, F^-, Br^-, Cl^- in successive proportions of 1, 5, and 10 equivalents in chloroform and inset image under UV light after the addition of 10 eq. of CN^- ions in a solution of chloroform (left) and THF (right) of **L2** ([**L2**] = 10 μM, $\lambda_{em\mathbf{L2}}$ = 476 nm, T = 298K). (b) UV-Vis and luminescent titrations of compounds **L2** upon continuous addition of 10 mL of CN^- ([CN^-] = 0.3 mM; [**L2**] = 10 μM), in chloroform. Inset: Emission as a function of [CN^-]/[**L2**] at 476 nm. For clarity of the reader the red spectra correspond to the initial spectrum and the blue to the endpoint of the titration. 115

Figure 3–5. Bacterial growth profile against Gram-negative and Gram-positive bacteria of compounds **L1**, **L2** and **CAA** (9-aminoacridine:control). 118

Figure 3–6. (**a**) Results of antibacterial assays of PVA:PVP and Irogran® polymers (*color diffusion to the media), and (**b**) Bacterial growth profile against Gram-negative and Gram-positive bacteria of free and **L1** doped Irogran® nanoparticles. 120

Figure 3–7. (a) Molecular structure of 9-aminoacridine derived compounds **L1** and **L2**. Photophysical characterization of compound **L1** (b) in acetonitrile and **L2** (c) in chloroform ([**L1**] = [**L2**] = 5 μM)..... 122

Figure 3–8. Photophysical characterization of derivative **L1** in a) ethanol and b) chloroform ([**L1**] = 5 μM). c) Photophysical characterization of derivative **L2** in THF ([**L2**] = 5 μM). 123

Figure 3–9. Spectrophotometric and spectrofluorimetric titrations of compounds **L1** (a) with increased additions of 5 μl of hydrochloric acid ([H^+]=0.6 mM) followed by (b) successive additions of 5 μl of sodium hydroxide ([OH^-]=0.6 mM) in acetonitrile. 124

Figure 3–10. Acidochromic behaviour of **L1-PMMA**. Normalized emission spectra recorded after treatment with HCl solution (A) 10 M, (B) 8 M and (C) 6 M..... 125

Figure 3–11. Acidochromic behaviour of **L1-PMMA**. Normalised emission spectra recorded after treatment with HCl vapours (12 M)..... 126

Figure 3–12. (a) UV-Vis and luminescent titrations of compounds **L2** upon continuous addition of 10 mL of CN^- ([CN^-] = 0.3 mM; [**L2**] = 10 μM), in THF. (b) Emission as a function of [CN^-]/[**L2**] at 479 nm..... 126

Figure 3–13. Comparison of the absorption spectra of (a) **L1** in the protonated form and **L2** recorded initially and (b) **L1** without addition of any analyte and **L2** at the endpoint of the

titration with cyanide. (c) Emission spectra of **L1** of the unprotonated form and **L2** at the endpoint of the titration with cyanide..... 127
Figure 3–14. Transmission electron microscopy (TEM) images of (a,b) @Nano and (c-f) **L1**@Nano..... 128
Figure 3–15. ESI-HRMS spectrum of compound **L1** without TFA..... 129
Figure 3–16. ESI-HRMS spectrum of compound **L1** with TFA..... 130
Figure 3–17. ESI-HRMS spectrum of compound **L2**..... 131
Figure 3–18. Mercury representation of the molecular structure of compounds **L1HCl** (a) and **L1HOTf** (b). In **L1HCl**, a $CHCl_3$co-crystallized solvent molecule was omitted for clarity..... 134
Figure 3–19. Representation of the intermolecular interactions responsible for the supramolecular arrangement in (a) **L1HCl** and (b) **L1HOTf**. Classical and non-classical hydrogen bonds, halogen and π…π interactions are depicted as dashed lines [N–H…Cl, magenta; C–H…Cl, blue; Cl…Cl, orange; π…π, light blue; C–H…F, green; C–H…O, light green; and N–H…O, fuchsia]. 135
Figure 3–20. ^{1}H-NMR spectrum of compound **L1** in chloroform..... 136
Figure 3–21. ^{13}C-NMR spectrum of compound **L1** in chloroform (details)..... 136
Figure 3–22. COSY-NMR spectrum of compound **L1** in chloroform..... 137
Figure 3–23. HSQC-NMR spectrum of compound **L1** in chloroform..... 137
Figure 3–24. HMBC-NMR spectrum of compound **L1** in chloroform..... 138
Figure 3–25. NOESY-NMR spectrum of compound **L1** in chloroform..... 138
Figure 3–26. ^{1}H-NMR spectrum of compound **L2** in DMSO..... 139
Figure 3–27. ^{13}C-NMR spectrum of compound **L2** in DMSO..... 139
Figure 3–28. DEPT-NMR spectrum of compound **L2** in DMSO..... 140
Figure 3–29. COSY-NMR spectrum of compound **L2** in DMSO..... 140
Figure 3–30. HSQC-NMR spectrum of compound **L2** in DMSO..... 141
Figure 3–31. HMBC-NMR spectrum of compound **L2** in DMSO..... 141
Figure 3–32. NOESY-NMR spectrum of compound **L2** in DMSO..... 142
Figure 4–1. Graphical abstract..... 151
Figure 4–2. (a) Molecular structure of dual dansyl-naphthalimide and naphthalimide derived compounds **L1** to **L4**. Photophysical characterization of compounds **L1** to **L4** ((b) to (e)) in acetonitrile ([**L1**] to [**L4**] = 5 μM). Images under natural light (left) and irradiated under UV light (right) for (f) **L1** and (g) **L4** in different solvents, as representative example..... 168

Figure 4–3. Normalized emission intensity of **L1** (a) and **L4** (b) upon addition of 1, 5, and 10 equivalents of Ca^{2+}, Co^{2+}, Ni^{2+}, Cu^{+}, Cu^{2+}, Zn^{2+}, Ag^{+}, Cd^{2+}, Hg^{+}, Hg^{2+} and Pb^{2+} metal ions. ([**L1**] = [**L4**] = 10μM, $\lambda_{em\mathbf{L1}}$ = 515 nm, $\lambda_{em\mathbf{L4}}$ = 513 nm, T = 298K). 171

Figure 4–4. UV-Vis and luminescent titration of compound **L1** (a) upon continuous 10 mL additions of Hg^{2+} ([**L1**] = 10 μM; [Hg^{2+}] = 0.225 mM). The inset represents the emission of [Hg^{2+}]/[**L1**] at 515 nm (left) and the time-resolved fluorescence decay profile of **L1** before and after the titration with Hg^{2+} ions (right). UV-vis time continuous spectra of **L1** (b) after the addition of 7 eq. of Cu^{2+} ([**L1**] = 10 μM). The inlet represents the images under natural light and UV light (left) and the time-dependent response of the absorbance at l = 500 nm (right). UV-Vis and luminescent titration of compound **L4** (c) upon continuous 10 mL additions of Hg^{2+} ([**L4**] = 5 μM; [Hg^{2+}] 0.15 mM). The inlet represents the emission of [Hg^{2+}]/[**L4**] at 513 nm (left) and the time-resolved fluorescence decay profile of **L4** before and after the titration with Hg^{2+} ions (right). UV-Vis and luminescent titration of compound **L4** (d) upon continuous 10 mL additions of Cu^{2+} ions ([**L4**] = 10 μM; [Cu^{2+}] = 1.5 mM). The inlet represents the emission of [Cu^{2+}]/[**L4**] at 514 nm. For clarity of the reader the red spectrum represents the initial spectrum and the blue at the end point of the titration while the black curves in the fluorescent decay profile represent the fitting obtained. 172

Figure 4–5. General representation of the interaction mechanism after complexation with Cu^{2+} and Hg^{2+} metal ions for (a) **L1** and **L3**, (b) **L2** and (c) **L4**. 175

Figure 4–6. Normalized emission response of **L1** in the presence of 5 equivalents Hg^{2+} and upon the addition of metal ions in acetonitrile. ([**L1**] = 10μM, $\lambda_{em\mathbf{L1}}$ = 515 nm, T = 298K). 176

Figure 4–7. (a) EPR spectra at 77K of L1:Cu^{2+} 1:4 (0.5mM:2.0mM) in MeCN, at time zero (green line) and after 45s (brown), 5 min (dark red), 15 min (red), 25 min (orange) and 75 min (light orange). (b) Cu^{2+} reduction as a function of time, upon mixing L1 and Cu^{2+} at 1:4 (0.5:2.0 mM; light blue line), 1:7 (0.5:3.5 mM; blue) and 1:10 (0.5:5.0 mM; dark blue) ratios. Cu^{2+} concentration values (in arbitrary units, au) were determined from the respective EPR spectra intensity (double spectrum integration). 179

Figure 4–8. Cu2p XPS spectra (a) after the addition of **L1** and Cu^{2+} in proportion 1:4 as prepared and 4h later while (b) exhibits the spectra of the [Cu(II)**L1**]$^{2+}$ complex and in proportion 1:1 (L:M). 181

Figure 4–9. ESI-HRMS spectrum of compound **L1**. 183

Figure 4–10. ESI-HRMS spectrum of compound **L2**. 184

Figure 4–11. ESI-HRMS spectrum of compound **L3**. 185

Figure 4–12. ESI-HRMS spectrum of compound **L4**. 186

Figure 4–13. Photophysical characterization of **L1** in (a) chloroform, (b) THF, (c) ethanol and (d) DMSO..... 187
Figure 4–14. Photophysical characterization of **L2** in (a) chloroform, (b) THF and (c) DMSO.188
Figure 4–15. Photophysical characterization of **L3** in (a) chloroform, (b) THF, (c) ethanol and (d) DMSO..... 189
Figure 4–16. Photophysical characterization of **L4** in (a) chloroform, (b) THF, (c) ethanol and (d) DMSO..... 190
Figure 4–17. Emission spectra after the addition of 10 eq. of each metal for **L1** (a), **L2** (b), **L3** (c) and **L4** (d). For clarity of the reader the red spectrum corresponds to the initial fluorescence. 191
Figure 4–18. Normalized emission intensity of **L2** (a) and **L3** (b) upon addition of 1, 5, and 10 equivalents of Ca^{2+}, Co^{2+}, Ni^{2+}, Cu^{+}, Cu^{2+}, Zn^{2+}, Ag^{+}, Cd^{2+}, Hg^{+}, Hg^{2+} and Pb^{2+} metal ions. ([**L2**] = [**L3**] = 10μM). Emission spectra after the addition of 10 eq. of each metal for **L1** (c) and **L3** (d). For clarity of the reader the red spectrum corresponds to the initial fluorescence..... 192
Figure 4–19. UV-Vis and luminescent titration of compound **L2** (a) upon continuous 4.8 μL additions of Hg^{2+} ([**L2**] = 10 μM; [Hg^{2+}] = 1.54 mM). The inset represents the emission of [Hg^{2+}]/[**L2**] at 513 nm. UV-Vis and luminescent titration of compound **L2** (b) upon continuous 20 μL additions of Cu^{2+} ions ([**L2**] = 10 μM; [Cu^{2+}] = 0.3 mM). The inset represents the emission of [Cu^{2+}]/[**L2**] at 513 nm. UV-Vis and luminescent titration of compound **L3** (c) upon continuous 10 μL additions of Hg^{2+} ([**L3**] = 10 μM; [Hg^{2+}] = 0.3 mM). The inset represents the emission of [Hg^{2+}]/[**L3**] at 508 nm (left) and the time-resolved fluorescence decay profile of **L3** before and after the titration with Hg^{2+} ions (right). UV-vis time continuous spectra of **L3** (d) after the addition of 8 eq. of Cu^{2+} ([**L3**] = 10 μM). The inset represents the time-dependent response of the absorbance at l = 500 nm (right). For clarity of the reader the red spectrum represents the initial spectrum and the blue at the end point of the titration while the black curves in the fluorescent decay profile represent the fitting obtained. 193
Figure 4–20. ESI-HRMS spectrum of compound **L1** after the addition of Hg^{2+}..... 194
Figure 4–21. ESI-HRMS spectrum of compound **L3** after the addition of Hg^{2+}..... 195
Figure 4–22. Absorption (a, c) and emission (b, d) spectra of the batch titrations recorded 24 hours after the incremental addition of 0.5 eq. of Cu^{2+} to a solution of (a, b) **L1** and (c, d) **L3** until it reached 7 and 8 eq., respectively ([**L1**] = [**L3**] = 10μM). Image of the batch titration of **L1**. 196
Figure 4–23. ESI-HRMS spectrum of compound **L1** after the addition of Cu^{2+}. 197
Figure 4–24. ESI-HRMS spectrum of compound **L3** after the addition of Cu^{2+}. 198

Figure 4–25. ESI-HRMS spectrum of compound **L2** after the addition of Hg^{2+}..... 199
Figure 4–26. ESI-HRMS spectrum of compound **L2** after the addition of Cu^{2+}..... 200
Figure 4–27. ESI-HRMS spectrum of compound **L4** after the addition of Hg^{2+}..... 201
Figure 4–28. ESI-HRMS spectrum of compound **L4** after the addition of Cu^{2+}..... 202
Figure 4–29. UV-Vis and luminescent titration of compound **L1** (a) and **L3** (b) upon continuous 10 µL additions of H^+ ([**L3**] = 10 µM; [H^+] = 0.3 mM). The inset represents the time-resolved fluorescence decay profile of **L1** and **L3** before and after the titration with H^+ ions. 203
Figure 4–30. Normalized emission response of **L3** (a) in the presence of 5 equivalents Hg^{2+} and additional metal ions in acetonitrile. ([**L3**] = 10µM, T = 298K)..... 203
Figure 4–31. Infrared spectrum of compound **L1**..... 204
Figure 4–32. Infrared spectrum of $[Hg(II)\mathbf{L1}_2]^{2+}$..... 204
Figure 4–33. Infrared spectrum of $[Cu(II)\mathbf{L1}_2]^{2+}$..... 205
Figure 4–34. Infrared spectrum of compound **L3**..... 205
Figure 4–35. Infrared spectrum of $[Hg(II)\mathbf{L3}_2]^{2+}$..... 206
Figure 4–36. Infrared spectrum of $[Cu(II)\mathbf{L3}_2]^{2+}$..... 206
Figure 4–37. ESI-HRMS spectrum of $[Hg(II)\mathbf{L1}_2]^{2+}$..... 207
Figure 4–38. ESI-HRMS spectrum of $[Cu(II)\mathbf{L1}_2]^{2+}$..... 208
Figure 4–39. ESI-HRMS spectrum of $[Hg(II)\mathbf{L3}_2]^{2+}$..... 209
Figure 4–40. ESI-HRMS spectrum of $[Cu(II)\mathbf{L3}_2]^{2+}$..... 210
Figure 4–41. ^{1}H-NMR spectrum of compound **3** in DMSO. 211
Figure 4–42. ^{13}C-NMR spectrum of compound **3** in DMSO. 211
Figure 4–43. COSY-NMR spectrum of compound **3** in DMSO..... 212
Figure 4–44. HSQC-NMR spectrum of compound **3** in DMSO. 212
Figure 4–45. HMBC-NMR spectrum of compound **3** in DMSO. 213
Figure 4–46. ^{1}H-NMR spectrum of compound **5** in DMSO. 213
Figure 4–47. ^{13}C-NMR spectrum of compound **5** in DMSO..... 214
Figure 4–48. COSY-NMR spectrum of compound **5** in DMSO. 214
Figure 4–49. HSQC-NMR spectrum of compound **5** in DMSO..... 215
Figure 4–50. HMBC-NMR spectrum of compound **5** in DMSO. 215
Figure 4–51. ^{1}H-NMR spectrum of compound **7** in DMSO..... 216
Figure 4–52. ^{13}C-NMR spectrum of compound **7** in DMSO..... 216
Figure 4–53. COSY-NMR spectrum of compound **7** in DMSO. 217
Figure 4–54. HSQC-NMR spectrum of compound **7** in DMSO. 217
Figure 4–55. HMBC-NMR spectrum of compound **7** in DMSO..... 218

Figure 4–56. ^{1}H-NMR spectrum of compound **9** in chloroform. 218
Figure 4–57. ^{1}H-NMR spectrum of compound **10** in DMSO. 219
Figure 4–58. ^{13}C-NMR spectrum of compound **10** in DMSO. 219
Figure 4–59. DEPT135-NMR spectrum of compound **10** in DMSO. 220
Figure 4–60. COSY-NMR spectrum of compound **10** in DMSO. 220
Figure 4–61. HSQC-NMR spectrum of compound **10** in DMSO. 221
Figure 4–62. HMBC-NMR spectrum of compound **10** in DMSO. 221
Figure 4–63. ^{1}H-NMR spectrum of compound **13** in DMSO. 222
Figure 4–64. ^{13}C-NMR spectrum of compound **13** in DMSO. 222
Figure 4–65. DEPT135-NMR spectrum of compound **13** in DMSO. 223
Figure 4–66. COSY-NMR spectrum of compound **13** in DMSO. 223
Figure 4–67. ^{1}H-NMR spectrum of compound **L1** in DMSO. 224
Figure 4–68. ^{13}C-NMR spectrum of compound **L1** in DMSO. 224
Figure 4–69. COSY-NMR spectrum of compound **L1** in DMSO. 225
Figure 4–70. HSQC-NMR spectrum of compound **L1** in DMSO. 225
Figure 4–71. HMBC-NMR spectrum of compound **L1** in DMSO. 226
Figure 4–72. ^{1}H-NMR spectrum of compound **L2** in DMSO. 226
Figure 4–73. ^{13}C-NMR spectrum of compound **L2** in DMSO. 227
Figure 4–74. DEPT135-NMR spectrum of compound **L2** in DMSO. 227
Figure 4–75. COSY-NMR spectrum of compound **L2** in DMSO. 228
Figure 4–76. HSQC-NMR spectrum of compound **L2** in DMSO. 228
Figure 4–77. HMBC-NMR spectrum of compound **L2** in DMSO. 229
Figure 4–78. ^{1}H-NMR spectrum of compound **L3** in DMSO. 229
Figure 4–79. ^{13}C-NMR spectrum of compound **L3** in DMSO. 230
Figure 4–80. DEPT135-NMR spectrum of compound **L3** in DMSO. 230
Figure 4–81. COSY-NMR spectrum of compound **L3** in DMSO. 231
Figure 4–82. HSQC-NMR spectrum of compound **L3** in DMSO. 231
Figure 4–83. HMBC-NMR spectrum of compound **L3** in DMSO. 232
Figure 4–84. ^{1}H-NMR spectrum of compound **L4** in DMSO. 232
Figure 4–85. ^{13}C-NMR spectrum of compound **L4** in DMSO. 233
Figure 4–86. DEPT135-NMR spectrum of compound **L4** in DMSO. 233
Figure 4–87. COSY-NMR spectrum of compound **L4** in DMSO. 234
Figure 4–88. HSQC-NMR spectrum of compound **L4** in DMSO. 234
Figure 4–89. HMBC-NMR spectrum of compound **L4** in DMSO. 235

Figure 5–1. Graphical abstract. 247
Figure 5–2. (A) Chemical structure of dansyl derivatives **L1** and **L2**. Absorption, excitation, emission and solid-state emission spectra for **L1** (B) and **L2** (C) in CH_3CN ([**L1**]=[**L2**]= 6 μM). 257
Figure 5–3. (Top) Images of **L1** and **L2** under a UV light lamp. Polarity decreases from 1 to 6 (1 – DMSO; 2 – CH_3CN; 3 – EtOH; 4 – THF; 5 – $CHCl_3$; 6 – toluene). (Down) υ_0, a, b and p-values, in cm^{-1}, slope and correlation coefficients obtained from Kamlet–Taft multiparametric fitting of the emission data. 259
Figure 5–4. Maximum emission intensities of **L1** (A) and **L2** (B) upon the addition of 1, 5 and 10 equivalents of Ca^{2+}, Co^{2+}, Ni^{2+}, Cu^{2+}, Zn^{2+}, Ag^{+}, Cd^{2+}, Hg^{2+} and Pb^{2+} metal ions. ([**L1**] =[**L2**] = 20μM, λ_{emL1} = 527 nm, λ_{emL2} = 518 nm, T = 298K). 260
Figure 5–5. Spectrophotometric and spectrofluorimetric titrations of compounds **L1** (A, B) and **L2** (C, D) with increased additions of Cu^{2+} (A, C), and Hg^{2+} (B, D) in CH_3CN. The inset represents the emission (A-D) as a function of [Cu^{2+}]/[**L1**] at 527 nm (A), of [Cu^{2+}]/[**L2**] at 518 nm (C), of [Hg^{2+}]/[**L1**] at 527 nm (B) and of [Hg^{2+}]/[**L2**] at 518 nm (D). [**L1**] = [**L2**] = 20 μM, λ_{excL1}=332 nm, λ_{excL2}=340 nm,T = 298 K). 261
Figure 5–6. Absorption (A, C) and emission spectra (B, D) of **L1** (A,B) and **L2** (C,D) in CH_3CN with different water fraction f_w(0%, 17%, 33%, 55%, 67%, 83%). [**L1**]=[**L2**] = 10 μM, T = 298K. 263
Figure 5–7. (Top) Images of **L1** and **L2** in CH_3CN with different water fraction f_w(0%, 17%, 33%, 55%, 67%, 83%). [**L1**]=[**L2**] = 10 μM, T = 298K. Size according to number, volume, and intensity distributions of a solution of CH_3CN/water solution of **L1** (A) and **L2** (B) with f_w = 83%. 264
Figure 5–8. (A) Image of **L1**@SBS particles under UV-lamp; (B, C) TEM images of the **L1**@SBS particles, (D, E and F) Emission spectrum, zeta potential and hydrodynamic size of **L1**@SBS particles. 266
Figure 5–9. Emission, excitation and solid-state emission spectra of compound **L1** in 1) acetonitrile, 2) ethanol and 3) DMSO ([**L1**] = 6 μM). 268
Figure 5–10. Emission, excitation, and solid-state emission spectra of compound **L1** in 4) chloroform, 5) toluene and 6) THF ([**L1**] = 6 μM). 268
Figure 5–11. Emission, excitation and solid-state emission spectra of compound **L2** in1) acetonitrile, 2) ethanol and 3) DMSO ([**L2**] = 6 μM). 269
Figure 5–12. Emission, excitation, and solid-state emission spectra of compound **L2** in 4) chloroform, 5) toluene and 6) THF ([**L2**] = 6 μM). 269
Figure 5–13. Absorption (A) and emission spectra (B) of **L1** in CH_3CN with water fraction f_w (83%) in different concentrations, T = 298K. 270

Figure 5–14. Size histogram of L1@SBS nanoparticles. 270
Figure 5–15. ESI-HRMS spectrum of compound **L1**. 271
Figure 5–16. ESI-HRMS spectrum of compound **L2**. 272
Figure 5–17. ^{1}H-NMR spectrum of compound **3**. 273
Figure 5–18. ^{13}C-NMR spectrum of compound **3**. 273
Figure 5–19. DEPT135-NMR spectrum of compound **3**. 274
Figure 5–20. COSY-NMR spectrum of compound **3**. 274
Figure 5–21. ^{1}H-NMR spectrum of compound **L1**. 275
Figure 5–22. ^{13}C-NMR spectrum of compound **L1**. 275
Figure 5–23. DEPT135-NMR spectrum of compound **L1**. 276
Figure 5–24. COSY-NMR spectrum of compound **L1**. 276
Figure 5–25. HSQC-NMR spectrum of compound **L1** (details). 277
Figure 5–26. HSQC-NMR spectrum of compound **L1** (details). 277
Figure 5–27. HSQC-NMR spectrum of compound **L1** (details). 278
Figure 5–28. HMBC-NMR spectrum of compound **L1** (details). 278
Figure 5–29. ^{1}H-NMR spectrum of compound **L2**. 279
Figure 5–30. ^{13}C-NMR spectrum of compound **L2**. 279
Figure 5–31. DEPT135-NMR spectrum of compound **L2**. 280
Figure 5–32. COSY-NMR spectrum of compound **L2**. 280
Figure 5–33. HSQC-NMR spectrum of compound **L2** (details). 281
Figure 5–34. HSQC-NMR spectrum of compound **L2** (details). 281
Figure 6–1. Graphical Abstract. 289
Figure 6–2. (A) Molecular structure of dansyl based compounds **L1**, **L2** and **L3**. Photophysical characterization of derivatives **L1** (B), **L2** (C) in acetonitrile and **L3** (D) in DMSO ([**L1**]=[**L2**]=[**L3**]= 6 μM). 300
Figure 6–3. Images of **L1** (1-6), **L2** (7-12) and **L3** (13-15) in different organic solvents [Toluene (1,7); THF (2, 8, 13); Chloroform (3, 9); Acetonitrile (4, 10); Ethanol (5, 11); DMF (14); DMSO (6, 12, 15)] under a UV lamp. 302
Figure 6–4. Normalized emission intensity of **L1** (A), **L2** (B) and **L3** (C) after addition of Ca^{2+}, Co^{2+}, Ni^{2+}, Cu^{2+}, Zn^{2+}, Ag^{+}, Cd^{2+}, Hg^{2+} and Pb^{2+} metal ions in successive proportions of 1, 5, and 10 equivalents in acetonitrile for **L1** and **L2** while in DMSO for **L3**. ([**L1**] = [**L2**] = [**L3**] = 20μM, λ_{em}**L1** = 524 nm, λ_{em}**L2** = 518 nm, λ_{em}**L3** = 532 nm, T = 298K). 304
Figure 6–5. UV-Vis and luminescent titrations of compounds **L1** (A, B) and **L2** (C, D) upon continuous addition of 10 mL of Cu^{2+} (A, C; [Cu^{2+}] = 0.9 mM), and Hg^{2+} (B, D; [Hg^{2+}] = 0.3 mM)

in acetonitrile. The inset represents the emission (A-D) as a function of [Cu^{2+}]/[**L1**] at 524 nm (A), of [Cu^{2+}]/[**L2**] at 518 nm (C), of [Hg^{2+}]/[**L1**] at 524 nm (B) and of [Hg^{2+}]/[**L2**] at 518 nm (D). [**L1**] = [**L2**] = 20 μM, $\lambda_{exc\mathbf{L1}}$=330 nm, $\lambda_{exc\mathbf{L2}}$=340 nm, T = 298 K). 305

Figure 6–6. Visual changes in Blank Discs (*Liofilchem*) containing compound **L1** (10 mM) after immersion in water solutions containing increasing concentrations of Hg^{2+} metal ion (0-400 ppm). 306

Figure 6–7. Temperature-dependent emission spectra of **L3** in the solid state (A) collected through a warming cycle between 30ºC to 170ºC. $I_{norm.}$ vs. T plot recorded in the emission maximum at 472 nm upon heating (B) [30 to 129 ºC (Y= 1.2243 + 0.0077612x), yielding R=0.99663]. Temperature-dependent emission spectra of **L3** (C) collected through a cooling cycle between 31ºC to 149ºC. $I_{norm.}$ vs. T plot recorded in the emission maximum at 472 nm upon cooling (D) [31 to 149 ºC (Y= 1.2571 + 0.0072628x), yielding R=0.99502]. 307

Figure 6–8. Comparison between the emission spectra of the different polymer thin films doped with (A) **L1**, (B) **L2** and (C) **L3** and the respective emission spectrum in the solid state. Images of the different polymer doped films and in the solid state under UV-light and under natural light (*) (D). 308

Figure 6–9. Temperature-dependent emission spectra of **L2** doped in (A) PMMA during heating cycle [Inset: $I_{norm.}$ vs. T plot at 467 nm upon heating: 120 to 218 ºC (Y= 1.0919 - 0.004465x), yielding R=0.9948]; (B) PMMA during cooling cycle [Inset: $I_{norm.}$ vs. T plot at 467 nm upon cooling: 51 to 218 ºC (Y= 1.0787 - 0.0042258x), yielding R=0.99644]; (C) SBS during heating cycle [Inset: $I_{norm.}$ vs. T plot at 471 nm upon heating: 70 to 189 ºC (Y= 1.2484 - 0.0060553x), yielding R=0.99652]; (D) PVA/PVP during heating cycle [Inset: $I_{norm.}$ vs. T plot at 472 nm upon heating: 110 to 199 ºC (Y= 1.1712 - 0.0055656x), yielding R=0.99736]; (E) TPU during heating cycle [Inset: $I_{norm.}$ vs. T plot at 487 nm upon heating: 70 to 158 ºC (Y= 0.99593 - 0.00411x), yielding R=0.99574]. Temperature-dependent emission spectra of **L3** doped in (F) TPU during heating cycle [Inset: $I_{norm.}$ vs. T plot at 491 nm upon heating: 80 to 159 ºC (Y= 1.611 - 0.0096602x), yielding R=0.99758]. 309

Figure 6–10. Emission, excitation and solid-state emission spectra of compound **L1** in: 1) acetonitrile, 2) ethanol and 3) DMSO ([**L**] = 6 μM). 312

Figure 6–11. Emission, excitation, and solid-state emission spectra of compound **L1** in: 4) chloroform, 5) toluene and 6) THF ([**L**] = 6 μM) 312

Figure 6–12. Emission, excitation and solid-state emission spectra of compound **L2** in: 1) acetonitrile, 2) ethanol and 3) DMSO ([**L**] = 10 μM). 313

Figure 6–13. Emission, excitation, and solid-state emission of compound **L2** in: 4) chloroform, 5) toluene ([**L**] = 10 mM) and 6) THF ([**L**] = 6 mM) 313
Figure 6–14. Emission, excitation, and solid-state emission of compound **L3** in: 1) DMSO, 2) THF and 3) DMF ([L] = 6 mM) 314
Figure 6–15. Temperature-dependent emission spectra of **L1** in the solid state (A) [Inset: I_{norm}. vs. T plot at 507 nm upon heating: 30 to 70ºC (Y=1.0825-0.0026806x), yielding R=0.9957]. Temperature-dependent emission spectra of **L1** (B) collected through a cooling cycle between 33ºC to 110ºC. 314
Figure 6–16. Temperature-dependent emission spectra of **L2** in the solid state (A) and (B) collected through a cooling cycle. 315
Figure 6–17. Temperature-dependent emission spectra of **L1** doped in (A) PMMA during heating cycle [Inset: I_{norm}. vs. T plot at 472 nm upon heating: 98 to 228ºC (Y=1.6211-0.0061283x), yielding R=0.9959]; (B) PMMA during cooling cycle [Inset: I_{norm}. vs. T plot at 472 nm upon cooling: 110 to 189ºC (Y= 1.5489 - 0.0057221x), yielding R=0.9949]. 315
Figure 6–18. Temperature-dependent emission spectra of **L1** doped in (A) SBS during heating cycle [Inset: I_{norm}. vs. T plot at 506 nm upon heating: 70 to 188ºC (Y=1.5151-0.0074734x), yielding R=0.996]; (B) SBS during cooling cycle. 316
Figure 6–19. Temperature-dependent emission spectra of **L1** doped in (A) PVA/PVP during heating cycle [Inset: I_{norm}. vs. T plot at 499 nm upon heating: 70 to 160ºC (Y=0.82272-0.0035002x), yielding R=0.9971]; (B) PVA/PVP during cooling cycle. 316
Figure 6–20. Temperature-dependent emission spectra of **L1** doped in (A) PVA/PVP during heating cycle [Inset: I_{norm}. vs. T plot at 493 nm upon heating: 79 to 139ºC (Y=1.5036-0.0078832x), yielding R=0.9972]; (B) PVA/PVP during cooling cycle [Inset: I_{norm}. vs. T plot at 493 nm upon heating: 33 to 170ºC (Y=0.33868-0.0016254x), yielding R=0.999] 317
Figure 6–21. Temperature-dependent emission spectra of **L2** doped in (A) SBS (B) PVA/PVP and (C) TPU during cooling cycle [Inset: I_{norm}. vs. T plot at 487 nm upon cooling: 34 to 170ºC (Y=0.26991-0.0010004x), yielding R=0.9968]. 317
Figure 6–22. Temperature-dependent emission spectra of **L3** doped in TBU during heating cycle [Inset: I_{norm}. vs. T plot at 491 nm upon heating: 33 to 148ºC (Y=0.51427-0.0028025x), yielding R=0.9969]. 318
Figure 6–23. ESI-HRMS spectrum of compound **L1**. 319
Figure 6–24. ESI-HRMS spectrum of compound **L2**. 320
Figure 6–25. ESI-HRMS spectrum of compound **L3**. 321
Figure 6–26. ^{1}H-NMR spectrum of compound **3**. 322

Figure 6–27. ^{13}C-NMR spectrum of compound **3**..... 322
Figure 6–28. ^{1}H-NMR spectrum of compound **L1**..... 323
Figure 6–29. ^{13}C-NMR spectrum of compound **L1**. 323
Figure 6–30. ^{1}H-NMR spectrum of compound **6**..... 324
Figure 6–31. ^{13}C-NMR spectrum of compound **6**..... 324
Figure 6–32. ^{1}H-NMR spectrum of compound **L2**..... 325
Figure 6–33. ^{13}C-NMR spectrum of compound **L2**. 325
Figure 6–34. ^{1}H-NMR spectrum of compound **L3**..... 326
Figure 6–35. ^{13}C-NMR spectrum of compound **L3**. 326
Figure 7–1. Graphical abstract. 335
Figure 7–2. (a) Molecular structure of the dansyl derived compounds **L1** and **L2** bearing single sulfur and disulfide bridges. Photophysical characterization of derivatives **L1** (b) and **L2** (c) in acetonitrile ([**L1**] = [**L2**] = 10 μM). Images under UV light (365 nm) for (d) **L1** (left) and **L2** (right) in different solvents varying polarity..... 344
Figure 7–3. Absorption (a,d) and emission spectra (b,e) of **L1** in THF (a,b) and in acetonitrile (d,e) with different water fractions f_w (0%, 17%, 33%, 55%, 67%, 83%), [**L1**]= 10 μM. Images of **L1** in (c) THF and (f) acetonitrile with different water fractions under UV light (365 nm). Hydrodinamic diameter of **L1** aggregates in THF (g) and acetonitrile (h) according to number, volume, and intensity distributions and zeta potential (i) of the solutions of 83% water fractions. 348
Figure 7–4. Maximum emission intensities of **L1** (a) after the addition of 0.5, 1, and 5 equivalents of Co^{2+}, Cu^{+}, Cu^{2+}, Zn^{2+}, Ag^{+}, Cd^{2+}, Hg^{+}, Hg^{2+} and Pb^{2+} metal ions in acetonitrile. Spectrophotometric and spectrofluorometric titrations of compound **L1** with increased additions of Cu^{2+} ([**L1**] = 16.8 μM) (b) and Hg^{2+} ([**L1**] = 20 μM) (c) in acetonitrile. The inset represents the emission as a function of [Cu^{2+}]/[**L1**] at 534 nm (b), of [Hg^{2+}]/[**L1**] at 534 nm (c). 349
Figure 7–5. UV-vis (a) and emission (b) spectra response after the addition of up to 9 equivalents of sodium dithionite to **L2** solution in acetonitrile. Image under the UV-light (365 nm) (c) of the initial solution (left) and after addition of 5 equivalents (right). 351
Figure 7–6. Comparison between the emission spectra of the different polymer thin films doped with (a) **L1** and (b) images under natural (up) and UV light (down) of TPU (left) and PMMA (right)..... 355
Figure 7–7. Temperature-dependent emission spectra of **L1** doped in (a) TPU during heating cycle [Inset: $I_{norm.}$ vs. T plot at 496 nm upon heating: 32 to 149ºC (Y= 1.1685 - 0.0050481x),

yielding R=0.9902]; (b) TPU during cooling cycle [Inset: I_{norm}. vs. T plot at 496 nm upon cooling: 30 to 182ºC (Y= 0.10949 - 0.0050184x), yielding R=0.9933]; (c) PMMA during heating cycle [Inset: I_{norm}. vs. T plot at 481 nm upon heating: 100 to 220ºC (Y= 1.481 - 0.0062098x), yielding R=0.9963]; (d) PMMA during cooling cycle [Inset: I_{norm}. vs. T plot at 481 nm upon cooling: 51 to 227ºC (Y= 1.1278 - 0.0044644x), yielding R=0.9925]. 356

Figure 7–8. Ptophysical characterization of L1 in a) chloroform, b) THF, c) ethanol and d) DMSO. 360

Figure 7–9. Photophysical characterization of L2 in a) chloroform, b) THF, c) ethanol and d) DMSO. 361

Figure 7–10. ESI-HRMS spectrum of compound L1. 362

Figure 7–11. ESI-HRMS spectrum of compound L2. 363

Figure 7–12. Emission spectra after the addition of 1 eq. of each metal. For clarity of the reader the red spectrum corresponds L1. 364

Figure 7–13. Reversible changes of fluorescence intensity at 533 nm of L1 upon addition of a) Cu_{2+} and b) Hg_{2+} with Na_2EDTA alternately. 364

Figure 7–14. ESI-HRMS spectrum of compound L1+Cu^{2+} complex. 365

Figure 7–15. ESI-HRMS spectrum of compound L1+Hg^{2+} complex. 366

Figure 7–16. UV-vis (a) and emission (performed in JASCO FP-8350) (b) spectra response after the addition of up to 9 equivalents of sodium dithionite. 367

Figure 7–17. ESI-HRMS spectrum of compound L2 after the addition of $Na_2S_2O_4$. 368

Figure 7–18. ^{1}H-NMR spectrum of compound **L1** in chloroform. 369

Figure 7–19. ^{13}C-NMR spectrum of compound **L1** in chloroform. 369

Figure 7–20. COSY-NMR spectrum of compound **L1** in chloroform. 370

Figure 7–21. HSQC-NMR spectrum of compound **L1** in chloroform. 370

Figure 7–22. HMBC-NMR spectrum of compound **L1** in chloroform. 371

Figure 7–23. ^{1}H-NMR spectrum of compound **L1** in acetonitrile. 371

Figure 7–24. ^{13}C-NMR spectrum of compound **L1** in acetonitrile. 372

Figure 7–25. DEPT135-NMR spectrum of compound L1 in acetonitrile. 372

Figure 7–26. COSY-NMR spectrum of compound **L1** in acetonitrile. 373

Figure 7–27. HSQC-NMR spectrum of compound **L1** in acetonitrile. 373

Figure 7–28. HMBC-NMR spectrum of compound **L1** in acetonitrile. 374

Figure 7–29. ^{1}H-NMR spectrum of compound **L1** in DMSO. 374

Figure 7–30. ^{13}C-NMR spectrum of compound **L1** in DMSO. 375

Figure 7–31. DEPT135-NMR spectrum of compound L1 in DMSO. 375

Figure 7–32. COSY-NMR spectrum of compound L1 in DMSO. 376
Figure 7–33. HSQC-NMR spectrum of compound **L1** in DMSO. 376
Figure 7–34. HMBC-NMR spectrum of compound L1 in DMSO. 377
Figure 7–35. ^{1}H-NMR spectrum of compound **L2** in chloroform. 377
Figure 7–36. ^{13}C-NMR spectrum of compound **L2** in chloroform. 378
Figure 7–37. COSY-NMR spectrum of compound **L2** in chloroform. 378
Figure 7–38. HSQC-NMR spectrum of compound **L2** in chloroform. 379
Figure 7–39. HMBC-NMR spectrum of compound **L2** in chloroform. 379
Figure 7–40. ^{1}H-NMR spectrum of compound **L2** in acetonitrile. 380
Figure 7–41. ^{13}C-NMR spectrum of compound **L2** in acetonitrile. 380
Figure 7–42. DEPT135-NMR spectrum of compound L1 in acetonitrile. 381
Figure 7–43. COSY-NMR spectrum of compound **L2** in acetonitrile. 381
Figure 7–44. HSQC-NMR spectrum of compound **L2** in acetonitrile. 382
Figure 7–45. HMBC-NMR spectrum of compound **L2** in acetonitrile. 382
Figure 7–46. ^{1}H-NMR spectrum of compound **L2** in DMSO. 383
Figure 7–47. ^{13}C-NMR spectrum of compound **L2** in DMSO. 383
Figure 7–48. DEPT135-NMR spectrum of compound L2 in DMSO. 384
Figure 7–49. COSY-NMR spectrum of compound L2 in DMSO. 384
Figure 7–50. HSQC-NMR spectrum of compound **L2** in DMSO. 385
Figure 7–51. HMBC-NMR spectrum of compound L1 in DMSO. 385
Figure 7–52. Comparison between ^{1}H-NMR spectra of compound L1 in acetonitrile before and after the addition of 1 eq. of Cu^{2+}. 386
Figure 7–53. Comparison between ^{13}C-NMR spectra of compound **L1** in acetonitrile before and after the addition of 1 eq. of Cu^{2+}. 387
Figure 7–54. Comparison between ^{1}H-NMR spectra of compound **L1** in acetonitrile before and after the addition of 1 eq. of Hg^{2+}. 387
Figure 7–55. Comparison between ^{13}C-NMR spectra of compound **L1** in acetonitrile before and after the addition of 1 eq. of Hg^{2+}. 388
Figure 7–56. Comparison between ^{1}H-NMR spectra of compound **L1** in DMSO before and after the addition of 1 eq. of Cu^{2+}. 388
Figure 7–57. Comparison between ^{13}C-NMR spectra of compound **L1** in DMSO before and after the addition of 1 eq. of Cu^{2+}. 389
Figure 7–58. Comparison between ^{1}H-NMR spectra of compound **L1** in DMSO before and after the addition of 1 eq. of Hg^{2+} at different timepoints. 389

Figure 7–59. Comparison between ^{1}H-NMR spectra of compound **L2** in acetonitrile before and after the addition of 1 eq. of Cu^{2+} 390
Figure 7–60. Comparison between ^{13}C-NMR spectra of compound **L2** in acetonitrile before and after the addition of 1 eq. of Cu^{2+} 390
Figure 7–61. Comparison between ^{1}H-NMR spectra of compound **L2** in acetonitrile before and after the addition of 1 eq. of Hg^{2+} at different timepoints. 391
Figure 7–62. Comparison between ^{1}H-NMR spectra of compound **L2** in DMSO before and after the addition of 1 eq. of Cu^{2+}. 391
Figure 7–63. Comparison between ^{13}C-NMR spectra of compound **L2** in DMSO before and after the addition of 1 eq. of Cu^{2+}. 392
Figure 7–64. Comparison between ^{1}H-NMR spectra of compound **L2** in DMSO before and after the addition of 1 eq. of Hg^{2+}. 392
Figure 7–65. Comparison between ^{13}C-NMR spectra of compound **L2** in DMSO before and after the addition of 1 eq. of Hg^{2+}. 393
Figure 7–66. Comparison between ^{1}H-NMR spectra of compound **L2** in acetonitrile before and after the addition of 1 eq. of $Na_2S_2O_4$ at different timepoints. 393
Figure 7–67. Comparison between ^{1}H-NMR spectra of compound **L2** in DMSO before and after the addition of 1 eq. of $Na_2S_2O_4$ at different timepoints. 394
Figure 7–68. Comparison between ^{13}C-NMR spectra of compound **L2** in acetonitrile before and after the addition of 1 eq. of $Na_2S_2O_4$. 394
Figure 7–69. Comparison between ^{13}C-NMR spectra of compound **L2** in DMSO before and after the addition of 1 eq. of $Na_2S_2O_4$. 395
Figure 8–1. Graphical abstract. 401
Figure 8–2. The method of synthesis of a) KURARITY L44285 and b) IROGRAN 4 92 P 4637 films. 408
Figure 8–3. (a) Molecular structure of tetradansylated cyclen and cyclam derived compounds **L1** and **L2**. Photophysical characterization of derivatives **L1** (b) and **L2** (c) in chloroform ([**L1**] = [**L2**] = 5 μM). Images under UV light for (d) **L1** (left) and **L2** (right) in different solvents. 410
Figure 8–4. Absorption (a,d) and emission spectra (b,e) of **L1** (a,b) and **L2** (d,e) in THF with different water fractions f_w (0%, 17%, 33%, 55%, 67%, 83%), [**L1**]=[**L2**]= 10 μM. Images of **L1** (c) and **L2** (f) in THF with different water fractions. Hydrodynamic diameter of **L1** (g) and **L2** (h) aggregates according to number, volume, and intensity distributions and zeta potential (i) of a solution of THF/water with f_w = 83%. 413

Figure 8–5. Normalized emission intensity of **L1** (a) and **L2** (b) upon addition of 1, 5, and 10 equivalents of Ca^{2+}, Co^{2+}, Ni^{2+}, Cu^{2+}, Zn^{2+}, Ag^{+}, Cd^{2+}, and Hg^{2+} metal ions in acetonitrile. ([**L1**] = [**L2**] = 5 μM, T = 298K). 414

Figure 8–6. Spectrophotometric and spectrofluorimetric titrations of compounds **L1** (a, b) and **L2** (c, d) with increased additions of Cu^{2+} (a, c), and Hg^{2+} (b, d) in CH_3CN. The inset represents the emission (a-d) as a function of $[Cu^{2+}]/[$**L1**$]$ at 530 nm (a), of $[Cu^{2+}]/[$**L2**$]$ at 525 nm (c), of $[Hg^{2+}]/[$**L1**$]$ at 525 nm (b) and of $[Hg^{2+}]/[$**L2**$]$ at 523 nm (d). [**L1**] = [**L2**] = 5 μM, T = 298 K)... 415

Figure 8–7. General representation of the chelation enhanced quenching effect after complexation with Cu^{2+} and Hg^{2+} metal ions. 416

Figure 8–8. Temperature-dependent emission spectra of **L1** in the solid state (a) collected through a warming cycle between 25ºC to 200ºC. $I_{norm.}$ vs. T plot recorded in the emission maximum at 504 nm upon heating (b) [40 to 110 ºC (Y= 1.0529 - 0.0016231x), yielding R=0.99139]. Temperature-dependent emission spectra of **L2** (d) collected through a warming cycle between 24ºC to 200ºC. $I_{norm.}$ vs. T plot recorded in the emission maximum at 487 nm upon heating (d). 418

Figure 8–9. Comparison between the emission spectra of the different polymer thin films doped with (a) L1 and (b) L2 and the respective emission spectrum in the solid state. 419

Figure 8–10. Temperature-dependent emission spectra of **L1** doped in (a) Kurarity during heating cycle [Inset: $I_{norm.}$ vs. T plot at 480 nm upon heating: 40 to 200 ºC (Y= 1.151 - 0.004844x), yielding R=0.9975]; (b) Kurarity during cooling cycle [Inset: $I_{norm.}$ vs. T plot at 480 nm upon cooling]; (c) Irogran during heating cycle [Inset: $I_{norm.}$ vs. T plot at 503 nm upon heating: 60 to 120 ºC (Y= 1.099 - 0.00251x), yielding R=0.9916]; (d) Irogran during cooling cycle [Inset: $I_{norm.}$ vs. T plot at 503 nm upon cooling: 30 to 200 ºC (Y= 0.2527 - 0.0009083x), yielding R=0.9989]; 420

Figure 8–11. Photophysical characterization of L1 in (a) THF, (b) Acetonitrile and (c) DMSO. 422

Figure 8–12. Photophysical characterization of L2 in (a) THF, (b) Acetonitrile and (c) DMSO. 423

Figure 8–13. Temperature-dependent emission spectra of (a) L1 and (b) L2 in the solid state collected through a cooling cycle between 25ºC to 200ºC. $I_{norm.}$ vs. T plot recorded in the emission maximum at 504 nm and 487 nm upon cooling for L1 and L2, respectively. 423

Figure 8–14. Temperature-dependent emission spectra of L2 doped in (a) Kurarity during heating cycle [Inset: Inorm. vs. T plot at 480 nm upon heating: 25 to 200 ºC (Y= 1.1452 - 0.0044x), yielding R=0.9938]; (b) Kurarity during cooling cycle [Inset: Inorm. vs. T plot at 480

nm upon cooling 60 to 160 ºC (Y= 1.1035 - 0.0038x), yielding R=0.9948]; (c) Irogram during heating cycle [Inset: Inorm. vs. T plot at 498 nm upon heating: 28 to 159 ºC (Y= 1.1402 - 0.0048x), yielding R=0.9959]; (d) Irogram during cooling cycle [Inset: Inorm. vs. T plot at 498 nm upon cooling: 80 to 180 ºC (Y= 0.28 - 0.0009x), yielding R=0.9979]. 424
Figure 8–15. L1 and L2 in solid-state (left and right, respectively) and at polymer films, L1 in IROGRAN and L2 in KURARITY (left and right, respectively) under an UV light before heating and after cooling 425
Figure 8–16. ESI-HRMS spectrum of compound L1. 426
Figure 8–17. ESI-HRMS spectrum of compound L1. 427
Figure 8–18. ^{1}H-NMR spectrum of compound **L1** 428
Figure 8–19. ^{13}C-NMR spectrum of compound **L1**. 428
Figure 8–20. DEPT135-NMR spectrum of compound **L1** 429
Figure 8–21. COSY-NMR spectrum of compound **L1**. 429
Figure 8–22. HSQC-NMR spectrum of compound **L1** 430
Figure 8–23. ^{1}H-NMR spectrum of compound **L1** 430
Figure 8–24. ^{13}C-NMR spectrum of compound **L2**. 431
Figure 8–25. DEPT135-NMR spectrum of compound **L2**. 431
Figure 8–26. COSY-NMR spectrum of compound **L2**. 432
Figure 8–27. HSQC-NMR spectrum of compound **L2**. 432
Figure 9–1. Graphical abstract. 441
Figure 9–2. Cube vertices representing the eight conformations of model compound and the edges mapping out the exchange pathways. The nomenclature of all conformations is presented in Table 9-2 452
Figure 9–3. (a,b) Textures of the mesophases observed by POM for (a) **L2** and (b) **L3**, at 43 and 68 ºC, respectively, in the first heating cycle. (c,d) DSC thermograms registered in the first heating and cooling cycles. 454
Figure 9–4. Photoluminescent characterization of compound **L1** in THF (a) and acetonitrile (b). Image (c) under UV light (365 nm) of **L1** dissolved in various solvents. 455
Figure 9–5. Absorption (a-c) and emission (d-e) spectra of **L1** (a,d), **L2** (b,e) and **L3** (c,f) in different mixtures THF and water fractions f_w (0%, 17%, 33%, 55%, 67%, 83%). Images of **L1** (g), **L2** (h) and **L3** (i) with different water fractions under UV light (365 nm). The images are displayed in increasing water fraction order. 458
Figure 9–6. Maximum emission intensities of **L1** in acetonitrile (a) after the addition of 1, 5, and 10 equivalents of Ca^{2+}, Co^{2+}, Ni^{2+}, Cu^{+}, Cu^{2+}, Zn^{2+}, Ag^{+}, Cd^{2+} and Hg^{2+} in acetonitrile while Hg^{+}

and Pb^{2+} metal ions were in aqueous solution. Spectrophotometric and spectrofluorometric titrations of compound **L1** with increased additions of Cu^{2+} (b) and Hg^{2+} (c) in acetonitrile. The inset represents the emission as a function of [Cu^{2+}]/[**L1**] at 530 nm (b), of [Hg^{2+}]/[**L1**] at 530 nm (c). 460
Figure 9–7. ^{1}H NMR spectrum of compound **L1** in TCE-d_2 at 393 K. 464
Figure 9–8. ^{13}C NMR spectrum of compound **L1** in TCE-d_2 at 393 K. 464
Figure 9–9. COSY NMR spectrum of compound **L1** in TCE-d_2 at 393 K. 465
Figure 9–10. HSQC NMR spectrum of compound **L1** in TCE-d_2 at 393 K. 465
Figure 9–11. HMBC NMR spectrum of compound **L1** in TCE-d_2 at 393 K. 466
Figure 9–12. Stack plot of ^{1}H NMR spectra of compound **L1** in TCE-d_2 at 243, 273, 298, 333, 353, 373 and 393 K. 466
Figure 9–13. ^{1}H NMR spectrum of compound **L2** in TCE-d_2 at 393 K. 467
Figure 9–14. ^{13}C NMR spectrum of compound **L2** in TCE-d_2 at 393 K. 468
Figure 9–15. 2D COSY NMR spectrum of compound **L2** in TCE-d_2 at 393 K. 468
Figure 9–16. 2D HSQC NMR spectrum of compound **L2** in TCE-d_2 at 393 K. 469
Figure 9–17. 2D HMBC NMR spectrum of compound **L2** in TCE-d_2 at 393 K. 469
Figure 9–18. Stack plot of ^{1}H NMR spectra of compound **L2** in TCE-d_2 at 243, 273, 298, 333, 353, 373 and 393 K. 470
Figure 9–19. ^{1}H NMR spectrum of compound **L3** in TCE-d_2 at 393 K. 471
Figure 9–20. ^{13}C NMR spectrum of compound **L3** in TCE-d_2 at 393 K. 471
Figure 9–21. COSY NMR spectrum of compound **L3** in TCE-d_2 at 393 K. 472
Figure 9–22. HSQC NMR spectrum of compound **L3** in TCE-d_2 at 393 K. 472
Figure 9–23. HMBC NMR spectrum of compound **L3** in TCE-d_2 at 393 K. 473
Figure 9–24. Stack plot of ^{1}H NMR spectra of compound **L3** in TCE-d_2 at 243, 273, 298, 333, 353, 373 and 393 K. 473
Figure 9–25. ESI-HRMS spectrum of compound **L1**. 474
Figure 9–26. ESI-HRMS spectrum of compound **L2**. 475
Figure 9–27. ESI-HRMS spectrum of compound **L3**. 476
Figure 9–28. Photophysical characterization of **L1** in a) chloroform, b) ethanol and d) DMSO. 477
Figure 9–29. Photophysical characterization of **L2** in a) chloroform and b) THF. 478
Figure 9–30. Photophysical characterization of **L3** in a) chloroform and b) THF. 478
Figure 9–31. UV-vis spectra of Pt@1:5 and Pt@1:10. 479
Figure 9–32. Transmission electron microscopy (TEM) images of Pt@1:5. 479

Figure 9–33. Transmission electron microscopy (TEM) images of Pt@1:10..... 480

List of Tables

Table 1-1. Comparison of dansyl-based compounds composed of peptide moieties for the detection of Cu^{2+}. 16
Table 1-2. Comparison of dansyl-based compounds composed of peptide moieties for the detection of Hg^{2+}. 21
Table 1-3. Comparison of dansyl-based compounds reported by us for the detection of Cu^{2+} and Hg^{2+} in acetonitrile. 39
Table 1-4. Comparison of dansyl-based compounds previously discussed in this work for the detection of Cu^{2+} and Hg^{2+} that further applied for the sensing of H_2S. 48
Table 1-5. Comparison of dansyl-based compounds previously discussed in this work for the detection of Cu^{2+}, Hg^{2+} and Cd^{2+} that further applied for the sensing of amino acids. 61
Table 3-1. Absorption maximum wavelength in solution (λ_{abs}), emission maximum wavelength in solution (λ_{em}), molar absorption coefficients (ε), Stokes shift ($\Delta\lambda$), emission maximum in the solid state (λ_{em}^{Solid}), fluorescence quantum yields (ϕ), fluorescence lifetimes (τ) for compound **L1** and **L2** in different solvents. 110
Table 3-2. HypSpec's calculated association constants for the probe **L2** towards CN^- ions, fluorescence quantum yields (ϕ), and fluorescence lifetimes (τ) for compound **L2** after addition of CN^- ions in different solvents. 115
Table 3-3. Dynamic light scattering data for the obtained particles. 116
Table 3-4. Crystallographic experimental data and structure refinement parameters. 132
Table 3-5. Selected bond distances (Å) and angles (º) for compounds **L1HCl** (a) and **L1HOTf**. 133
Table 4-1. Spectroscopic polarity parameters, physical properties of the different solvents. ε_r : relative permittivity; η: refractive index; α: the solvent's HBD acidity; β: the solvent´s HBA basicity; π^*: the solvent´s dipolarity/polarizability 164

Table 4-2. Absorption maximum wavelength in solution (λ_{abs}), emission maximum wavelength in solution (λ_{em}), molar absorption coefficients (ε), Stokes shift ($\Delta\lambda$), fluorescence quantum yields (ϕ), emission maximum in the solid state (λ_{em}^{Solid}), fluorescence lifetimes (τ) for compounds **L1** to **L4** in various solvents. 169
Table 4-3. Independent fluorescence wavenumber ($\upsilon 0$), solvent polarity (*p*), HBD (*a*), HBA (*b*), slope and coefficient (R^2) of the linear fitting plot $\upsilon_{exp.}$ versus $\upsilon_{calc.}$ 170
Table 4-4. Association constants evaluated employing HypSpec software for compounds **L1** to **L4** towards Hg^{2+} and Cu^{2+} ions with included stoichiometry in acetonitrile. Respective values for the detection limit (LOD) and quantification limit (LOQ) amounts (μM). 176
Table 5-1. Spectroscopic polarity parameters, physical properties of the different solvents. ε_r : relative permittivity; η: refractive index; α: the solvent's HBD acidity; β: the solvent´s HBA basicity; π^*: the solvent´s dipolarity/polarizability..... 254
Table 5-2. Photophysical data of the dansyl derivatives **L1** and **L2** evaluated in organic solvents. 257
Table 5-3. Stability association constants and stoichiometry for the complexes formed **L1** and **L2** with Cu^{2+} and Hg^{2+} ions, in CH_3CN. Minimal detectable (LOD) and quantified (LOQ) amounts (μM) of Cu^{2+} and Hg^{2+} metal ions (M) **L1** and **L2.** LOD and LOQ were measured by emission at 527 nm and 518 nm for **L1** and **L2**, respectively. 261
Table 6-1. Spectroscopic polarity parameters, physical properties of the different solvents. ε_r : relative permittivity; η: refractive index; α: the solvent's HBD acidity; β: the solvent´s HBA basicity; π^*: the solvent´s dipolarity/polarizability..... 297
Table 6-2. Absorption maximum wavelength in solution (λ_{abs}), emission maximum wavelength in solution (λ_{em}), molar absorption coefficients (ε), Stokes shift ($\Delta\lambda$), emission maximum in the solid state (λ_{em}^{Solid}), fluorescence quantum yields (ϕ), brightness ($\varepsilon x\phi$), fluorescence lifetimes (τ) for compounds **L1** to **L3** performed in different organic solvents..... 301
Table 6-3. Independent fluorescence wavenumber ($\upsilon 0$), solvent polarity (*p*), HBD (*a*), HBA (*b*), slope and coefficient (R^2) of the linear fitting plot $\upsilon_{exp.}$ versus $\upsilon_{calc.}$ 302
Table 6-4. HypSpec's calculated association constants and stoichiometry for the probes **L1** and **L2** towards Cu^{2+} and Hg^{2+} ions, in CH_3CN alongside the respective values for the Minimal detectable (LOD) and quantified (LOQ) amounts (μM). LOD and LOQ were measured by the emission at 524 and 518 nm for **L1** and **L2**, respectively..... 305
Table 6-5. Emission maximum in the solid state (λ_{em}^{Solid}), emission maximum of PMMA thin films (λ_{em}^{PMMA}), emission maximum of SBS thin films (λ_{em}^{SBS}), emission maximum of PVA/PVP thin films ($\lambda_{em}^{PVA/PVP}$), emission maximum of TPU thin films (λ_{em}^{TPU})..... 308

Table 7-1. Spectroscopic polarity parameters, physical properties of the different solvents. ε_r : relative permittivity; η: refractive index; α: the solvent's HBD acidity; β: the solvent´s HBA basicity; π^*: the solvent´s dipolarity/polarizability..... 342
Table 7-2. Absorption maximum wavelength in solution (λ_{abs}), emission maximum wavelength in solution (λ_{em}), molar absorption coefficients (ε), Stokes shift ($\Delta\lambda$), fluorescence quantum yields (ϕ), emission maximum in the solid state (λ_{em}^{Solid}), fluorescence lifetimes (τ) for compounds **L1** and **L2** in various solvents..... 345
Table 7-3. Independent fluorescence wavenumber ($\upsilon 0$), solvent polarity (*p*), HBD (*a*), HBA (*b*), slope and coefficient (R^2) of the linear fitting plot $\upsilon_{exp.}$ versus $\upsilon_{calc.}$..... 346
Table 7-4. Association constants using HypSpec software for compounds **L1** towards Hg^{2+} and Cu^{2+} ions with included stoichiometry in acetonitrile. Respective values for the detection limit (LOD) and quantification limit (LOQ) amounts (μM) were measured following the emission at 534 nm..... 351
Table 8-1. Spectroscopic polarity parameters, physical properties of the different solvents. ε_r: relative permittivity; η: refractive index; α: the solvent's HBD acidity; β: the solvent´s HBA basicity; π^*: the solvent´s dipolarity/polarizability..... 407
Table 8-2. Absorption maximum wavelength in solution (λ_{abs}), emission maximum wavelength in solution (λ_{em}), molar absorption coefficients (ε), Stokes shift ($\Delta\lambda$), fluorescence quantum yields (ϕ), emission maximum in the solid state (λ_{em}^{Solid}), brightness (ε x ϕ), fluorescence lifetimes (τ) for compounds **L1** and **L2** in various solvents..... 411
Table 8-3. Independent fluorescence wavenumber ($\upsilon 0$), solvent polarity (*p*), HBD (*a*), HBA (*b*), slope and coefficient (R^2) of the linear fitting plot $\upsilon_{exp.}$ versus $\upsilon_{calc.}$..... 412
Table 8-4. Association constants using HypSpec software for compounds **L1** and **L2** towards Hg^{2+} and Cu^{2+} ions with included stoichiometry in acetonitrile. Respective values for the detection limit (LOD) and quantification limit (LOQ) amounts (μM) were measured following the emission maximum wavelength..... 416
Table 9-1. Spectroscopic polarity parameters, physical properties of the different solvents. ε_r: relative permitivity; η: refractive index; α: the solvent's HBD acidity; β: the solvent´s HBA basicity; π^*: the solvent´s dipolarity/polarizability..... 449
Table 9-2. B3LYP/6-31+G(d,p) calculated thermodynamic parameters for stereoisomers at 298 K..... 453
Table 9-3. Phase behavior of **L2** and **L3** established by DSC..... 454
Table 9-4. Absorption maximum wavelength in solution (λ_{abs}), emission maximum wavelength in solution (λ_{em}), molar absorption coefficients (ε), Stokes shift ($\Delta\lambda$), emission maximum in the

solid state (λ_{em}^{Solid}), fluorescence quantum yields (ϕ), fluorescence lifetimes (τ) for compounds **L1** to **L3** in different solvents. 456
Table 9-5. Independent fluorescence wavenumber ($\upsilon 0$), solvent polarity (p), HBD (a), HBA (b), slope and coefficient (R^2) of the linear fitting plot $\upsilon_{exp.}$ versus $\upsilon_{calc.}$ 456
Table 9-6. Dynamic light scattering data, quantum yield and lifetime measurements of each compound in different mixtures of THF and water. 459
Table 9-7. Association constants and stoichiometry for compound **L1** in the sensing of Hg^{2+} and Cu^{2+} ions in acetonitrile, determined using HypSpec software. Detection limit (LOD) and quantification limit (LOQ) values (in μM) were calculated based on emission intensity at 530 nm. 461
Table 9-8. Dynamic light scattering data for the obtained particles. 462
Table 9-9. DFT calculated ground state (GS) conformations of model compound 480
Table 9-10. B3LYP/6-31+G(d,p) calculated activation parameters for the exchange processes of the studied model compound. 495

GLOSSARY

Dyad	A dyad is a molecular system composed of two distinct chromophores covalently linked within a single structure.
HypSpec	Computational software used for fitting spectroscopic titration data and determining binding constants.
Kamlet–Taft equation	Empirical model correlating solvent-dependent spectral shifts to H-bond acidity (α), basicity (β), and dipolarity/polarizability (π*).
Limit of Detection (LOD)	Lowest concentration of an analyte that can be reliably distinguished from the blank (noise).
Limit of Quantification (LOQ)	Lowest analyte concentration that can be accurately quantified.
Molecular Thermometer	A molecule or molecular system whose fluorescence intensity, emission wavelength, lifetime, or phosphorescence is sensitive to temperature.
Temperature-Dependent Emission	The variation in the intensity, wavelength, or lifetime of light emitted by a material as a function of temperature.
Polydispersity index (PDI)	A dimensionless number that describes the uniformity of molecular size distribution in a sample, lower values indicate more uniform sizes.

Acronyms

Abs	Absorbance
Acp	Aminocaproic acid residue
ACN	Acetonitrile
ACQ	Aggregation-Caused Quenching
AIE	Aggregation-Induced Emission
AIEE	Aggregation-Induced Enhanced Emission
Ala	Alanine
APP	Smartphone application
Arg	Arginine
Asn	Asparagine
Asp	Aspartate
BODIPY	Boron-Dipyrromethene
CAA	9-aminoacridine
CD	Circular Dichroism
CHEF	Chelation-Enhanced Fluorescence
CIE	Commission Internationale de l'Éclairage
CLSM	Confocal Laser Scanning Microscopy
CMC	Critical Micelle Concentration

CopC	Copper-resistance protein
CPL	Circularly Polarized Luminescence
COSY	Correlation Spectroscopy
Cys	Cysteine
Cyclam	1,4,8,11-Tetraazacyclotetradecane
Cyclen	1,4,7,10-Tetraazacyclododecane
d	Doublet
dd	Doublet of doublets
dt	Doublet of triplets
DanC4A	Dansyl-functionalized calix[4]arene
D-A	Donor–Acceptor
DCM	Dichloromethane
DEPT-135	Distortionless Enhancement by Polarization Transfer
DCP	Diethyl chlorophosphate
DDVP	Dichlorvos
DFT / TDDFT	Density Functional Theory / Time-Dependent Density Functional Theory
DsCl / DNS-Cl	Dansyl chloride
Ds-cyclen	Dansylated cyclen
DLS	Dynamic Light Scattering
DMF	*N,N*-Dimethylformamide
DMSO	Dimethyl sulfoxide
DNT	2,4-Dinitrotoluene
DIPEA	*N,N*-Diisopropylethylamine
DSC	Differential Scanning Calorimetry
DNA	Deoxyribonucleic Acid
EA	Elemental Analysis

EDTA	Ethylenediaminetetraacetic acid
EPA	Environmental Protection Agency
EPR	Electron Paramagnetic Resonance
ESI-MS / ESI-HRMS	Electrospray Ionization Mass Spectrometry / High-Resolution MS
ESIPT	Excited-State Intramolecular Proton Transfer
EtOH	Ethanol
Eq.	Equivalents
FRET	Förster Resonance Energy Transfer
f_w	Fraction of water (v/v) in solvent mixtures
QY	Quantum yield
Glu	Glutamic acid
Gln	Glutamine
Gly	Glycine
GSH	Glutathione
GS / TS	Ground State / Transition State
GYY4137	Hydrogen sulfide donor
HBA	Hydrogen Bond Acceptor
HBD	Hydrogen Bond Donor
HEPES	4-(2-hydroxyethyl)piperazine-1-ethanesulfonic acid buffer
HEPPS	4-(2-Hydroxyethyl)piperazine-1-propanesulfonic acid buffer
HeLa	Human cervical cancer cells
HepG2	Liver carcinoma cells
His	Histidine
Hcy	Homocysteine
Hz	Hertz

HNO	Nitroxyl
HMBC	Heteronuclear Multiple Bond Correlation
HSQC	Heteronuclear Single Quantum Coherence
HOMO	Highest occupied molecular orbital
HMBC	Heteronuclear Multiple Bond Correlation
HUVEC	Human Umbilical Vein Endothelial Cells
ICP-MS	Inductively Coupled Plasma Mass Spectrometry
ICT	Intramolecular Charge Transfer
ISC	Intersystem crossing
IR	Infrared Spectroscopy
Leu	Leucine
LOD	Limit of Detection
LOQ	Limit of Quantification
LLC	Lung carcinoma cell line
LNCaP	Human prostate cancer cells
LPS	Lipopolysaccharide
LUMO	Lowest Unoccupied Molecular Orbital
Lys	Lysine
m	Multiplet
MCF-7	Breast cancer cells
MOF	Metal-Organic Framework
MTBE	Methyl-tert-butyl ether
MTT	Cell-viability assay
MHA	Mueller-Hinton Agar
MHB	Mueller-Hinton Broth
m/z	Mass-to-charge ratio

NMR	Nuclear Magnetic Resonance
^{1}H-NMR	Proton NMR
^{13}C-NMR	Carbon-13 NMR
^{31}P-NMR	Phosphorus-31 Nuclear Magnetic Resonance
^{77}Se NMR	Selenium-77 Nuclear Magnetic Resonance
NO	Nitric oxide
NMP	N-Methylpyrrolidone
NEM	N-ethylmaleimide
PBS	Phosphate-buffered saline
PET / a-PET / d-PET	Photoinduced Electron Transfer
PEG	Polyethylene glycol
POM	Polarized Optical Microscopy
PPi	Pyrophosphate
Pro	Proline
Py	Pyridine
PMMA	Poly(methylmethacrylate)
PVP	Polyvinylpyrrolidone
PVA	Polyvinyl alcohol
TPU-A92 (Irogran®)	Thermoplastic polyurethane
PFA	Perfluoroalkoxy
PDI	Polydispersity Index
PyY	Pyronine Y
q	Quartet
QY	Quantum Yield

RGB	Red-Green-Blue color model
RSS	Reactive sulfur species
ROS	Reactive oxygen species
RNS	Reactive nitrogen species
s	Singlet
SBD	Sulfonyl-benzoxadiazole
SBS	Styrene-Butadiene-Styrene
SDS	Sodium dodecyl sulfate
Sec	Selenocysteine
Ser	Serine
SPPS	Solid-Phase Peptide Synthesis
t	Triplet
TBTU	2-(1H-Benzotriazole-1-yl)-1,1,3,3-tetramethylaminium tetrafluoroborate
TMCM	2-(3,5,5-trimethylcyclohex-2-en-1-ylidene)malononitrile
td	Triplet of doublets
TEM	Transmission Electron Microscopy
THF	Tetrahydrofuran
Thr	Threonine
TLC	Thin-Layer Chromatography
TMS	Tetramethylsilane
TNT	2,4,6-trinitrotoluene
TNP	2,4,6-Trinitrophenol
Tris	Tris(hydroxymethyl)aminomethane
T_g	Glass transition temperature
UV / UV-Vis	Ultraviolet spectroscopy
VX	Nerve agent

XPS	X-ray Photoelectron Spectroscopy
WHO	World Health Organization

1

INTRODUCTION

1.1 Luminescence

Luminescence is the emission of photons either in the ultraviolet, visible or infrared region of a species which is in an electronically excited state. *Luminescenz* as it was first introduced by Eilhardt Wiedemann in 1888 would describe the phenomena of light which were not uniquely conditioned by temperature. To this end, luminescence (*cold light*) was described in opposition to incandescence (*hot light*). Depending on the excitation mode, luminescence can be further classified as radioluminescence (ionizing radiation); electroluminescence (electric field); sonoluminescence (ultrasounds) and photoluminescence (absorption of photons), to name a few.[1] In the case of photoluminescence, fluorescence and phosphorescence can occur since the absorbing species tend to de-excite and the emission of photons is one possible pathway to return to the ground state. Since the Middle Ages, the term *phosphor* ("which bears light") has referred to substances that glow in the dark after light exposure. In contrast, the term *fluorescence* would only be coined in 1852 by Sir George Gabriel Stokes throughout his experiments with a solution of quinine sulfate. In the end, the difference between the two phenomena, as described in the nineteenth century, is that for fluorescence the emission of light vanishes when excitation ends while for phosphorescence the emission persists with the end of the excitation.[1]

1.1.1 Fluorescence

Over the last two decades, fluorescence has become widely used across biological sciences. It was comprised as a research method in biochemistry and biophysics, however, it has evolved and eventually became essential in many applied fields such as biotechnological applications, cellular sorting techniques, clinical diagnostic procedures, sequencing of genetic

material, forensic investigations, and the study of genetic information.[1] Its popularity comes from its high sensitivity and the fact that it replaces the need for radioactive tracers. Fluorescence has also become important in cellular and molecular imaging, allowing scientists to visualize where molecules are located inside cells.[1]

In order to delve into the intricacies of the processes that manifest from the absorption and emission of light, one should consider the Jablonski diagram as a starting point (Figure 1–1).[1] Named after Professor Alexander Jablonski, a typical Jablonski diagram shows the singlet electronic states of a molecule as S_0, S_1, and S_2, each with several vibrational levels. Light absorption is shown as a vertical transition because it happens extremely fast, too quickly for the nuclei to move, which reflects the Franck-Condon principle. At room temperature, only the lowest vibrational levels are significantly populated, and light is needed to reach the excited electronic states. When a fluorophore absorbs light, it is first excited to a higher vibrational level of S_1 or S_2. It then rapidly relaxes to the lowest vibrational level of S_1 through internal conversion, a process that happens much faster than fluorescence emission. Therefore, fluorescence usually originates from this lowest vibrational level. The emitted light typically returns the molecule to a higher vibrational level of S_0, which then quickly relaxes. This explains the vibrational structure seen in emission spectra and why emission and absorption spectra often appear as mirror images. Molecules in S_1 can also undergo intersystem crossing to the triplet state T_1. Emission from T_1 is called phosphorescence, which occurs at longer wavelengths and much slower rates because the transition back to the ground state is forbidden. Molecules with heavy atoms like bromine or iodine show stronger phosphorescence because these atoms promote intersystem crossing.

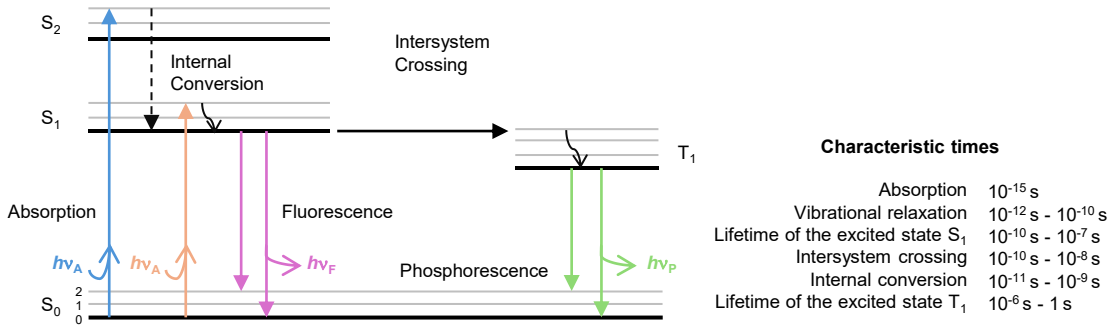


Figure 1–1. Perrin-Jablonski diagram adapted from ref. [1] and characteristic times for each process obtained from ref. [2].

Fluorescence is a photophysical phenomenon that exhibits several general characteristics, with only occasional exceptions. Fluorescent emission has less energy than the light that was originally absorbed, so the emitted light appears at longer wavelengths. This energy

difference between absorption and emission is referred to as the Stokes shift.[1] The Stokes shift arises from the energy losses during excitation and emission through the decay to the lowest vibrational level of the excited state and ground state, excess vibrational energy is dissipated as heat. Beyond these intrinsic molecular processes, additional contributions to the Stokes shift can result from interactions with the solvent, chemical reactions in the excited state, formation of molecular complexes, or energy transfer between molecules.[1]

Two other important parameters that help characterize a fluorophore's behavior are its fluorescence quantum yield and fluorescence lifetime.[1] The quantum yield is defined as the ratio of the number of photons emitted to the number of photons absorbed. Fluorophores with high quantum yields are very efficient at converting absorbed light into emitted light and, therefore, exhibit bright fluorescence. The fluorescence lifetime corresponds to the average time a molecule remains in the excited state before returning to the ground state by all possible deactivation pathways, including photon emission. This parameter is important because it reflects the competition between radiative and non-radiative processes and can provide information about the local environment surrounding the fluorophore.[1]

1.2 Fluorescent molecular sensors

Fluorescent molecular sensors is a (supra)-molecular moiety that can undergo an interaction with analyte which causes a change in their own photophysical properties, effectively transforming that interaction into a measurable signal (Figure 1–2). Among various applications, fluorescent molecular sensors can be used in the detection of cations, anions, neutral molecules and gases.[2,3] These systems allow non-destructive and real-time visual detection of the analyte with high sensitivity, low cost and experimental simplicity.[1] The fluorophore can be distinguished in three classes: the first and the second classes differ if the interaction is through collision or binding with the analyte while the third class requires special attention to its design since the receptor may or may not be linked to the fluorophore by a spacer.[2]

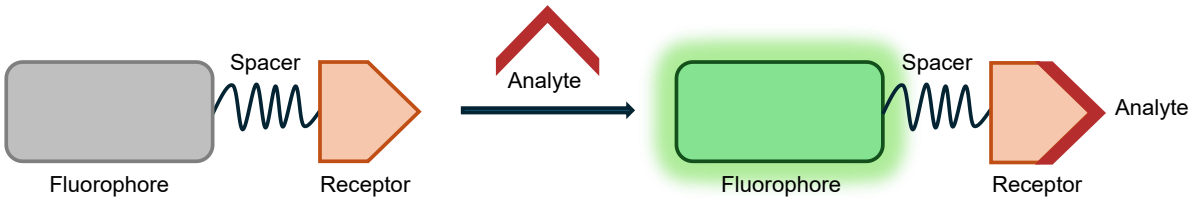


Figure 1–2. Generic representation of the interaction between a fluorescent molecular sensor and an analyte resulting in a recognition signal.

1.2.1 Recognition mechanisms

Several recognition mechanisms come forth depending on the interaction between the fluorophore and the target analyte being divided into five types, namely, photo-induced electron transfer (PET), intramolecular charge transfer (ICT), fluorescence resonance energy transfer (FRET), excited state intramolecular proton transfer (ESIPT), aggregation induced emission (AIE) and C=N/C=C isomerization.[4,5]

1.2.1.1 Photo-induced electron transfer (PET)

Fluorescent sensors that operate through PET often rely on the three integrated components: a fluorophore, which can function as either an electron donor or acceptor, the recognition unit, and a spacer that keeps these two elements at an appropriate electronic distance. In the absence of analyte, excitation of the fluorophore promotes electronic communication with the receptor, enabling PET.[4–8] This electron-transfer process causes the suppression of emission, giving the probe a weak or complete "off" fluorescence background. Once the analyte binds to the receptor, PET becomes energetically or kinetically unfavorable, allowing the fluorophore to regain its emissive pathway. The resulting fluorescence enhancement provides a clear signal for analyte detection.

PET processes can occur in two directions, giving rise to a-PET and d-PET modes (Figure 1–3).[4–8] In a-PET systems, the receptor possesses a higher-energy highest occupied molecular orbital (HOMO) than the fluorophore. Upon excitation of the fluorophore, its HOMO becomes singly occupied, providing the opportunity for an electron from the receptor's HOMO to transfer into this position. This transfer blocks radiative relaxation and quenches fluorescence. In d-PET systems, the receptor's lowest unoccupied molecular orbital (LUMO) lies between the HOMO and LUMO of the fluorophore. Upon excitation, the electron promoted to the fluorophore's LUMO is diverted into the lower-lying LUMO of the receptor, again disabling emission. Binding of the target analyte alters the electronic structure of the receptor in a way that prevents PET, restoring the fluorophore's radiative decay pathway. This produces a strong turn-on response, which forms the basis for analyte recognition.

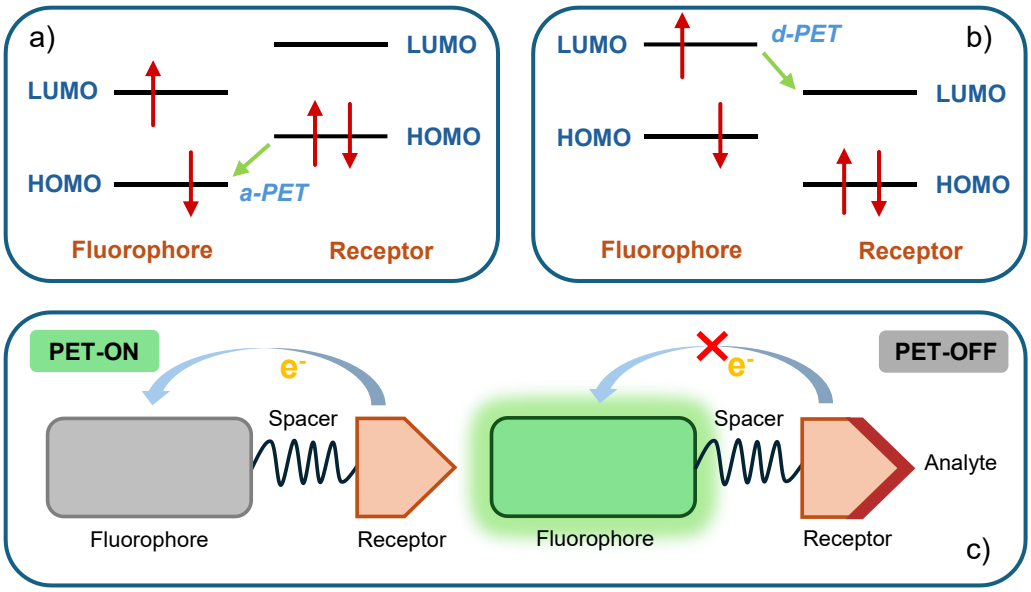


Figure 1–3. Arrangement of the fluorophore and receptor HOMO/LUMO levels that enables the a) acceptor-type PET and b) donor-type PET mechanism in the probe. c) Schematic representation of the overall sensing process mediated by a PET-based fluorescent probe. Adapted from ref. [5]

1.2.1.2 Intramolecular charge transfer (ICT)

Considering a donor-acceptor molecular system, where there is integration of an electron-donating group which is conjugated to an electron-withdrawing group, there is a driving force to display intramolecular charge-transfer (ICT) behavior.[4,5] In these systems, the donor contributes most of the HOMO electron density, while the acceptor dominates the LUMO. When the molecule absorbs light, electrons are promoted in a way that induces charge toward the acceptor, leading to a noticeable ICT excited state. Given that this process is highly influenced by changes in electronical distribution, an analyte that might interact with the donor or the acceptor site can alter the HOMO-LUMO energies (Figure 1–4). This results in the shift of the ICT strength alongside its photophysical response which typically appears as changes in the emission wavelength (red or blue shifts) and fluorescence quantum yield. These optical modulations form the basis for detecting analytes with D-A type sensors.[4,5] If an analyte coordinates to the acceptor site of an ICT probe, it lowers the energy of the acceptor-centered LUMO, causing the emission band to shift to longer wavelengths. In contrast, if an analyte interacts with the donor portion, it stabilizes the HOMO, usually leading to a blue shift in the fluorescence. When these spectral changes are sufficiently large, the intensities at the emission maxima of the free and bound probe can be quantitatively compared, enabling precise determination of analyte concentration.

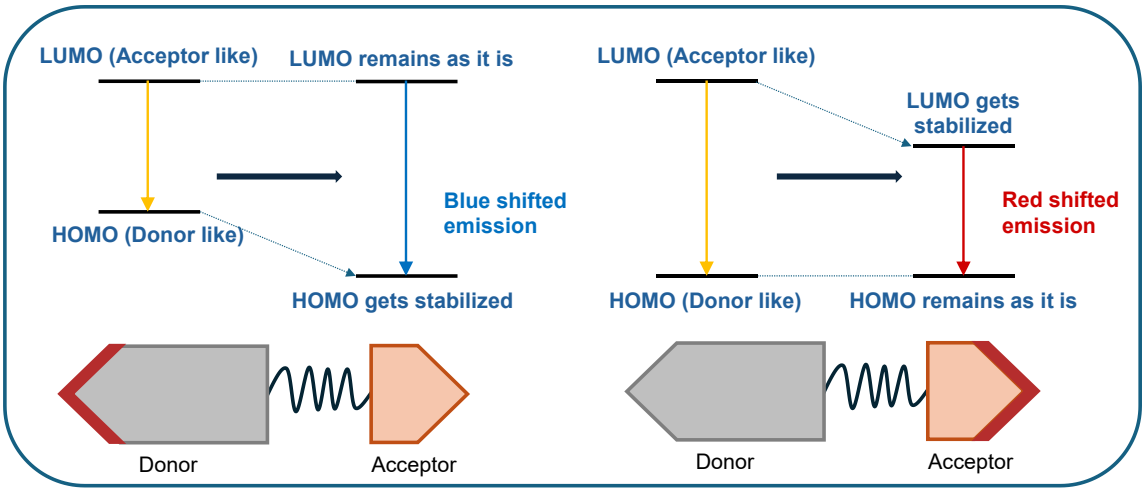


Figure 1–4. Representation of ICT-based sensing showing donor–acceptor interactions and analyte binding. Adapted from ref. [5]

1.2.1.3 Föster resonance energy transfer (FRET)

In systems where their design involves the presence of two separate chromophores within the same molecule, these units can exchange energy through a nonradiative pathway (Figure 1–5). In these cases, the excited-state energy of one unit (the donor) is transferred to another unit (the acceptor) through long-range dipole–dipole interactions. This mechanism is known as Förster resonance energy transfer (FRET).[4,5,9–11] The effectiveness of FRET depends essentially on three factors: the distance between the donor and acceptor, the overlap between the donor's emission spectrum and the acceptor's absorption band, and the relative orientation of their transition dipoles. FRET-based sensors typically employ fluorescent donor and acceptor units so that both the emission coming from the donor and the emission resulting in the sensitization of the acceptor can be monitored. These dual signals allow ratiometric detection, improving accuracy in analyte measurement. In such sensors, the analyte may bind to either the donor or the acceptor site of the probe. This binding event alters the probe's structure, which in turn changes either the spacing between the two chromophores or the way their dipoles are oriented. Because these structural changes directly influence the efficiency of FRET, the resulting variation in the optical output provides a reliable method for identifying and quantifying the analyte.[4,5,9–11]

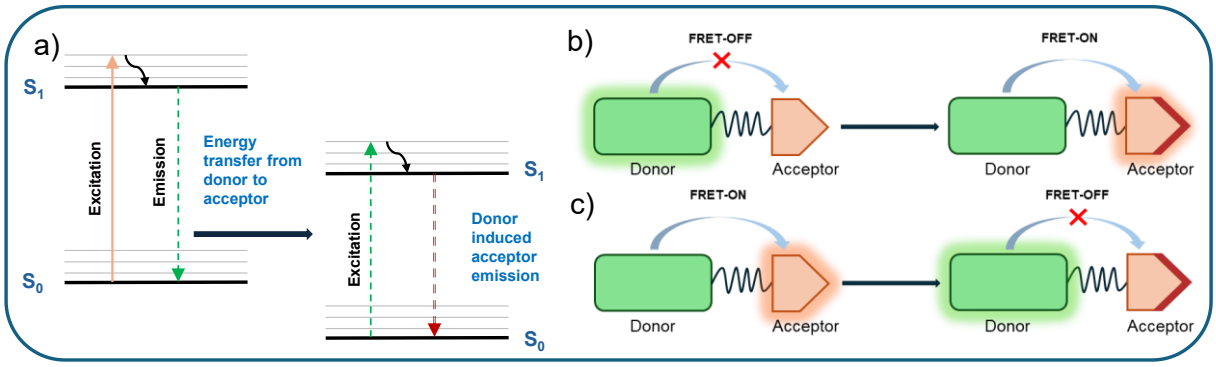


Figure 1–5. a) Energy diagram of the FRET process. b) Turn-on FRET system. c) Turn-off FRET system. Adapted from refs. [5,11]

1.2.1.4 Excited state intramolecular proton transfer (ESIPT)

Several fluorescent probes contain structural features that allow a proton to transition internally from one part of the molecule to another, similar to what occurs in keto-enol tautomerism. These systems can undergo excited-state intramolecular proton transfer (ESIPT), a process that relies in a proton moving from a donor site to an acceptor site only after the molecule has been promoted to its excited state (Figure 1–6).[4,5,12] In most ESIPT-active molecules, the enol form dominates in the ground state, usually because it is stabilized by intramolecular hydrogen bonding. Upon excitation, the acidity and basicity of the donor and acceptor groups change significantly, allowing rapid conversion of the enol form to the keto form via ESIPT. The resulting keto tautomer emits at a significantly longer wavelength than the enol form, producing a characteristic dual-band emission profile. When an analyte binds to an ESIPT-capable chromophore, it can disrupt or weaken the proton-transfer pathway in the excited state. This suppression of ESIPT leads to enhanced wavelength emission from the enol form and a corresponding decrease in the wavelength emission from the keto form. Because these two emission bands respond in opposite directions, ESIPT-based probes are well suited for ratiometric sensing. They are particularly powerful for detecting small analytes by comparing the relative intensities of the enol and keto emissions.[4,5,12]

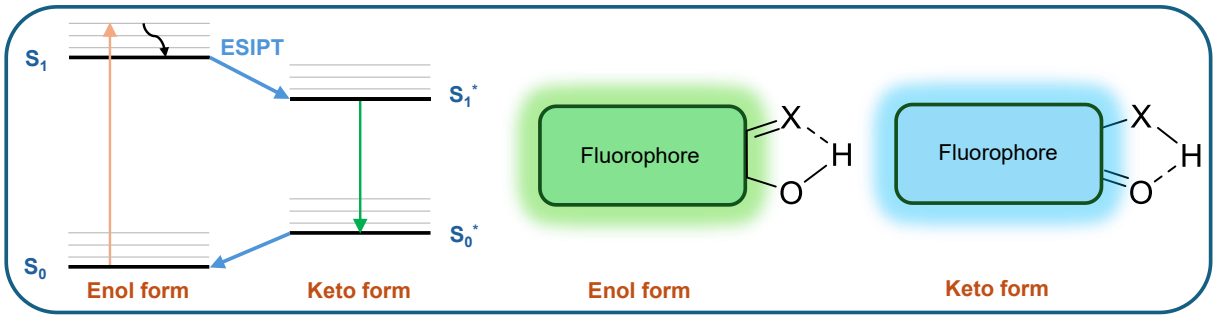


Figure 1–6. ESIPT-driven sensing pathway with a visual representation of the enol and keto states of an ESIPT fluorophore. Adapted from ref. [5,11]

1.2.1.5 Aggregation induced emission (AIE)

Since Tang and colleagues first reported aggregation-induced emission (AIE) in 2001,[13] this photophysical phenomenon has become highly dominant in fluorescence-based analyte sensing. AIE molecules are typically faint or non-emissive as isolated molecules because of their flexible structure or freely rotating, propeller-like substituents enable efficient non-radiative relaxation of their excited states.[4,5] When these molecules begin to group, whether due to increased concentration or solvent-driven factors such as polarity, viscosity, or electrostatic attraction to oppositely charged hosts, they switch to strong fluorescence (Figure 1–7). Aggregation restricts internal motions and limits conformational freedom, reducing non-radiative decay and directing excited-state energy into radiative emission, which substantially enhances fluorescence. This is the opposite of what is observed for traditional fluorophores which are bright in dilute solutions but lose emission efficiency as they aggregate, a process known as aggregation-caused quenching (ACQ). ACQ often hinders their utility in sensing, where relatively high dye concentrations are commonly needed. AIE-active probes avoid this drawback entirely since instead of being quenched, they become strongly emissive upon aggregation. For this reason, AIE molecules have become powerful tools in sensing, as the AIE effect naturally counters the limitations imposed by ACQ.[4,5]

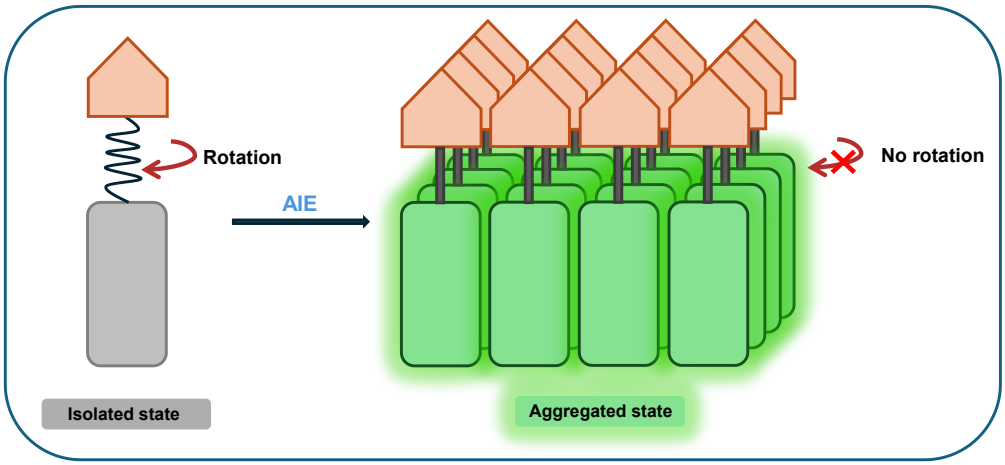


Figure 1–7. Visualization of the fluorescence turn-on of an AIE fluorophore. Adapted from ref. [13a]

1.2.1.6 C=N and C=C isomerization

Chromophores containing unbridged C=N or C=C double bonds often experience *cis-trans* isomerization upon photoexcitation, a process that opens efficient nonradiative decay pathways and typically reduces these molecules to only exhibit weakly fluorescent in their free state. For dyes bearing unbridged C=N groups, coordination to bio-analytes, particularly metal ions, commonly involves the nitrogen lone pairs.[5] Binding at these sites restricts isomerization around the C=N bond, suppressing the associated nonradiative pathway and producing a pronounced enhancement in emission.[14] The strong fluorescence modulation resulting from this coordination provides a reliable basis for quantitative analyte detection. Although investigated to a lesser extent, chromophores with unbridged C=C units can operate through a similar mechanism.[5] Interaction of an analyte with appropriately positioned anchoring groups in the probe restricts the *cis-trans* motion around the C=C bond, thereby increasing radiative decay efficiency and leading to significant fluorescence enhancement. The deliberate design of such systems, combining unbridged double bonds with tailored binding moieties, holds considerable promise for improving emission responsiveness and advancing the development of sensitive fluorescence probes.

1.2.2 Fluorophores

Fluorophores can generally be divided into three categories: organic fluorophores, nanoparticle-based fluorophores, and biological fluorophores. Nanoparticle fluorophores such as quantum dots are recognized for their brightness and photostability, although some concerns about biocompatibility and long-term toxicity can be raised.[15] Biological fluorophores, including fluorescent proteins, are useful for tracking within living systems. At the same time,

they often offer limited spectral range and responsiveness.[16] Organic fluorophores, by contrast, are very versatile since their chemical structures can be designed to cover a wide spectral range, achieve high quantum yields, and respond sensitively to environmental changes.[17]

Within this category lies a notable diversity of molecular families: fluorescein, rhodamine, coumarin, cyanine, BODIPY, and dansyl among others, each provide distinct photophysical behaviors that can specifically be tuned for an application (Figure 1–8).[18–20] For example, fluorescein derivatives are known for their brightness and reversible pH sensitivity, rhodamines for their stability and sharp signal changes through spirolactam ring-opening, coumarins for their strong donor properties in energy transfer systems, and cyanines for extending detection into the near-infrared region.[18] Among these examples, Dansyl chloride (DNS-Cl) stands out as a widely used and consistent fluorophore due to its accessible conjugation, predictable photophysical properties, environmental sensitivity, and compatibility with a broad range of biochemical applications.[1,21] Due to these reasons, this family of compounds was chosen as central piece in this work.

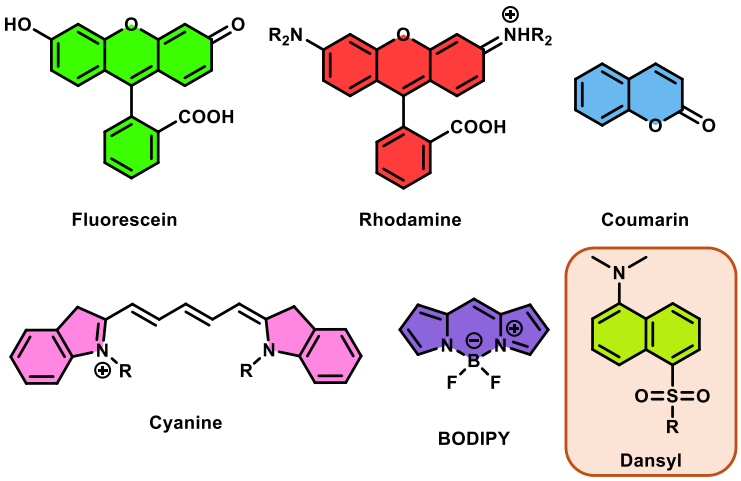


Figure 1–8. Molecular structures of the common fluorophores are used as fluorescent molecular sensors.

1.2.3 Dansyl chloride

Dansyl chloride is one of the earliest and most influential fluorophores introduced into biochemical research, recognized for its sensitivity to microenvironmental changes and its strong reactivity toward soft metal centers.[1,21] First described by Weber in 1952, [22] DNS-Cl was initially employed to generate fluorescent conjugates of albumin, and this work established its broad applicability in protein chemistry. Since then, DNS-Cl has been widely used as a versatile reagent for labeling terminal amino groups, particularly in studies where fluorescence polarization measurements are required. Its widespread adoption was favored by its

photophysical characteristics, including a fluorescence lifetime of approximately 10 ns, which is well suited for time-dependent fluorescence techniques.[1,21]

DNS-derived fluorophores exhibit distinct absorption behavior in the 275-360 nm region, corresponding to n–π* and π–π* transitions of the DNS group. They can be efficiently excited around 350 nm, a wavelength range where proteins typically do not absorb, allowing selective monitoring of the dansyl label without interference from intrinsic protein fluorescence.[1,21] The emission of the dansyl moiety is strongly influenced by solvent polarity, yielding significant Stokes shifts and notable changes in quantum yield as microenvironmental conditions vary. These properties make DNS-based fluorophores exceptionally sensitive reporters of local environmental changes.[1,21]

The historical development of DNS-Cl represents a major conceptual shift in fluorescence spectroscopy. Weber's work emphasized the importance of the molecular probe in determining the quality and interpretability of fluorescence data.[1] His contributions laid the foundation for modern fluorescence methods, demonstrating that fluorophores such as DNS-Cl could be used to extract important information about the behavior of proteins and their interactions. His insistence that effective fluorescence spectroscopy depends foremost on the choice and design of suitable probes continues to guide contemporary research.

1.2.4 Dansyl-based Fluorescent Probes for Detection of Metal Ions

Heavy metal ions are a significant environmental and public health concern due to their toxicity, persistence, and bioaccumulative nature. Safe and accessible water is essential for human health, however, contamination with metal ions remains prevalent, occurring from both natural processes and anthropogenic activities such as industrial discharge, mining, and inappropriate wastewater treatment.[21,23,24] While certain metals, including iron, zinc, copper, and cobalt, are essential trace elements for biological processes, their excess or deficiency can lead to severe physiological disorders.[21,25,26] In contrast, non-essential heavy metals such as mercury, lead, and cadmium pose serious threats to ecosystems and human health even at low concentrations.[21,23,26] Monitoring and detecting metal ions in environmental and biological systems are therefore of utmost importance.

Traditional analytical techniques such as atomic absorption spectroscopy, inductively coupled plasma mass spectrometry, and electrochemical methods offer high sensitivity but are often costly, time-consuming, and require specialized equipment and expertise.[27–29] In contrast, fluorescent probes have surfaced as powerful tools for metal ion detection, offering advantages such as high sensitivity, rapid response, simplicity, and the potential for *in situ* and

real-time monitoring.[26,30,31] Fluorescent sensors use the mechanisms discussed previously to generate measurable optical signals upon binding to metal ions.[26,31] Their application is particularly important for mercury and copper ions due to the severe environmental and health consequences associated with these metals.

Copper is an essential trace element, playing critical roles in enzymatic catalysis, mitochondrial respiration, melanin synthesis, neurotransmitter production, and antioxidant defense.[25,28] However, excessive Cu^{2+} exposure can occur due to contaminated water, industrial waste, or soil leaching, leading to oxidative stress, gastrointestinal disturbances, liver and kidney toxicity, and neurodegenerative diseases such as Wilson's and Alzheimer's disease.[25,28] This dual nature, essential at low concentrations but toxic at higher levels, requires careful monitoring of copper in environmental and biological systems. The choice of ligands or functional groups is important to ensure strong and specific coordination with Cu^{2+} ions, which induces measurable changes in fluorescence or absorption.[25,28] Furthermore, fluorescent probes enable real-time monitoring of Cu^{2+} in complex matrices such as drinking water, biological fluids, and environmental samples, making them highly valuable for environmental protection and biomedical applications.[25,28]

Mercury is a highly toxic, nonessential metal that presents severe risks to both human health and ecosystems. It exists in various chemical forms, including elemental mercury, inorganic mercury salts, and organic mercury compounds such as methylmercury, which is particularly toxic due to its lipophilicity and ability to cross biological barriers such as the blood-brain barrier.[21,24,29,30,32] Mercury is released into the environment primarily through coal combustion, battery production, electronic waste, and other industrial activities, ultimately accumulating in water systems and the food chain.[21,24,32] Prolonged exposure to Hg^{2+} can lead to neurological disorders, kidney damage, endocrine disruption, reproductive toxicity, and developmental defects, as exemplified by historical incidents such as Minamata disease in Japan.[21,24,29,30,32]

Fluorescent probes have become an essential tool for detecting Hg^{2+} due to their high sensitivity, rapid response, and suitability for *in situ* monitoring. These probes rely on selective interactions with Hg^{2+}, often exploiting the strong affinity of Hg^{2+} for sulfur- or nitrogen-containing functional groups, such as thiols, amines, or sulfonyl groups.[21,30] Strategies include "turn-on" sensors that become fluorescent upon Hg^{2+} binding, quenching-based systems, and multifunctional materials that allow simultaneous detection and removal of Hg^{2+} from aqueous media.[21,29,30] The integration of fluorescent detection with adsorption offers the dual

advantage of monitoring and mitigating mercury pollution, a critical requirement given the global scale of contamination.[24,32]

Overall, fluorescent probes offer a versatile and effective approach for the detection of heavy metal ions, addressing the limitations of traditional analytical methods. The development of probes that combine high sensitivity, selectivity, and rapid response remains a critical area of research. This literature review focuses on strategies, mechanisms and applications of dansyl-based probes from 2016 onward for a variety of analytes. Although, an acknowledgment should be given to key pre-2016 studies for the detection of metal ions,[33–47], anions,[48–50] small molecules,[51,52] amino acids[53] and the use of dyad approaches[54–56] for the detection of the mentioned analytes.

1.2.4.1 Fluorescent Probes for Cu^{2+} Detection

Copper is prevalent both in plants and animals occupying the third position as the most plentiful element in the human body usually in the form of divalent copper (Cu^{2+}).[57] Its presence is crucial for the normal functioning of the central nervous system; it is also tied as catalyst cofactor for electron transport being also able to act as a catalyst for protein production and the production of reactive oxygen species (ROS) essential for programmed cell death.[58] Excess concentrations of this metal ion leads to an overflow production of these reactive species that degrade biomacromolecules and is considered the basis process in which grave diseases emerge, such as neurodegenerative syndromes.[59,60] The World Health Organization (WHO) and the U.S. Environmental Protection Agency (US EPA) bodies have stipulated 31.5 mM an acceptable limit of Cu^{2+} ion in drinking water and its presence in human blood should range between 15.7-23.6 mM.[60]

As a contribution towards the detection of Cu^{2+}, Liu *et al.* designed a new dansyl-based compound **1** (Figure 1–9) composed of a dipeptide, i.e. glycyl-L-tyrosine, with the intention of render water solubility and the presence of multiple N and O atoms enabling coordination with metal ions.[61] The assessment of **1** sensitivity towards metal ions was implemented in HEPES buffer solution at pH 7.4 against a variety of metal ions. The strong emission observed at 558 nm is only influenced significantly when Cu^{2+} is present, promoting a 90% fluorescence quenching with an associated decrease of the fluorescence quantum yield from 4.70% to 0.08% after the addition of 5.0 equiv. Cu^{2+}. Moreover, the assigned absorption band with a peak at 337 nm gradually blue-shifts and broadens after the addition of Cu^{2+}, indicative of complexation and selective responsiveness given that no obvious shifts in absorbance were found for the other metal ions. The fluorescence titration allowed the determination of the detection

limit (0.69 mM) which enables its potential applicability in real samples since it is far below the value suggested by the US EPA. Job's plot experiment and ESI-MS analysis concluded a 1:1 biding ratio of **1** and Cu^{2+} with an association constant value of 6.47 x 10^4 M^{-1} in the aqueous solution. Anti-interference studies showed no significant influence of other metals on compound **1** ability to selectively sense Cu^{2+}, although, when tested in the presence of several amino acids L-His and L-Glu showed competitive coordination. The influence of the pH demonstrated that this system can be applied in a pH range of 6 to 12. Finally, compound **1** has been used successfully to detect Cu^{2+} in HepG2 cells with low toxicity in the range of 5 mM to 100 mM and the use of Na_2EDTA demonstrated recovery of fluorescence (Figure 1–9a).

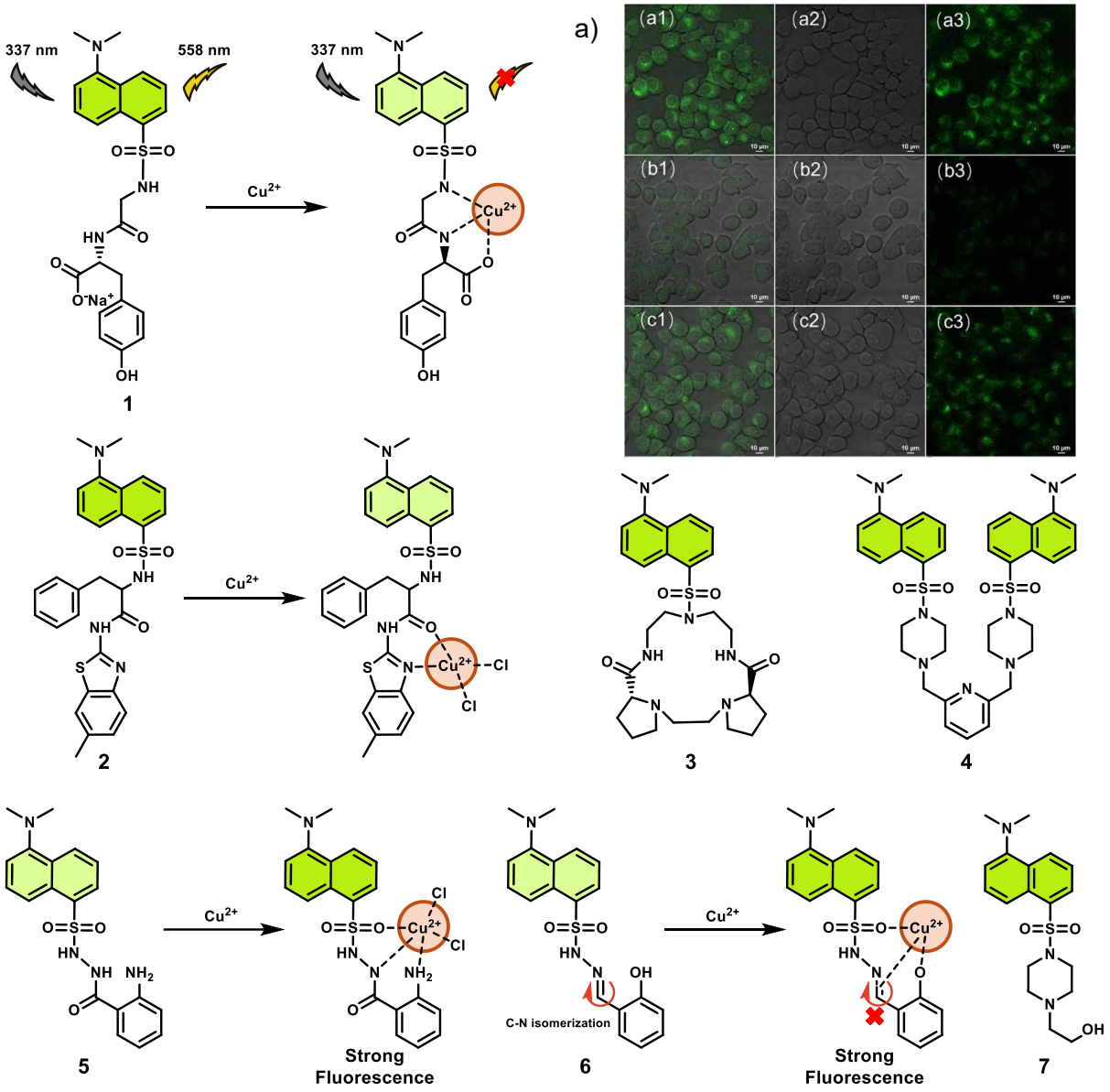


Figure 1–9. Structures of compounds **1**-**7** and proposed detection mechanisms for Cu^{2+}. a) Confocal Laser Scanning Microscopy (CLSM) images of HepG2 cells: (a1-a3) Cells incubated with **1**; (b1-b3) Cells incubated with **1** and then

with Cu^{2+}; (c1-c3) Cells incubated with **1** and then with Cu^{2+} and subsequently treated with Na_2EDTA. (a1, b1, c1): Merged images; (a2, b2, c2): Bright-field images; (a3, b3, c3): Fluorescent images. Adapted from ref.[61] copyright 2021, Elsevier.

On top of the findings previously discussed and the lack of theoretical calculations, Li *et al.* decided to perform time-dependent density functional theory (TDDFT) to provide a better understanding of the fundamental principles and mechanisms that rule in ion recognition.[57] Comparison between compound **1** and its copper(II) complex showed that the oscillator strength of the maximum emission peak of the fluorescence mechanism is large for **1** while a contrast is observed for the complex, reaching nearly zero. Thus, the predicted radiative rate k_r of **1** was several orders of magnitude larger, yet the predicted internal conversion rate k_{ic} was similar for both. Furthermore, due to the heavy atom effect, the simulated ISC rate k_{isc} of the complex was considerably higher than that of **1**. This information allowed them to obtain a calculated fluorescence quantum yield of 0.16% for **1** and 10^{-6}% for the complex. The hole-electron pair analysis of the complex showed that the $S_0 \rightarrow S_1$ is attributed to metal-to-ligand charge transfer. The density-of-state diagram shows that the HOMO includes contributions from the copper atom's s orbital. This s orbital mixing lowers the energy of the frontier orbital and reduces the degree of overlap between the HOMO and the LUMO.

Lee's group have fabricated an unnatural benzothiazole conjugated phenylalanine bearing dansyl moiety **2** (Figure 1–9).[58] The sensing capabilities of compound **2** were tested against 16 alkali, alkali-earth, and transition metal ions in DMSO:water (1:1, v/v, pH 7.4). The selective Cu^{2+} detection was marked by a change from light green to light brown color at the naked eye due to the coordination between the ligand and the metal ion. The absorption profile when Cu^{2+} is added is characterized by a small bathochromic shift and increased intensity of the 307 nm maximum absorbance value attributed to the $n \rightarrow p^*$ transition, while the fluorescence response is associated with a 95% quenching that suffers a hypsochromic shift from 539 to 534 nm when titrated. The interference studies revealed that the fluorescence remained strong in the presence of various metal ions but was completely quenched upon the addition of Cu^{2+}, indicating a strong affinity for this ion and suggesting its selective discrimination even in the presence of competing metals. The fluorescence lifetime measurements showed that **2** is subject to dynamic quenching since the increasing concentration of Cu^{2+} was associated with a consistent decrease in its value. The ^1H NMR titration revealed that the NH protons were not involved in the binding of Cu^{2+}, while the IR spectrum analysis demonstrated the presence of metal-oxygen and metal-nitrogen bonds. Finally, given that the limit of detection was found

to be 3.0 mM, compound **2** was applied for the determination of Cu^{2+} in ordinary water samples being able to recover up to 99.92% of the spiked Cu^{2+} ion.

Wang and co-workers developed compound **3** (Figure 1–9), a novel L-proline-based heterocyclic ligand functionalized with a dansyl fluorophore for copper detection.[62] In an aqueous solution (DMSO:H_2O = 9:1, HEPES buffer, pH 7.4), the free ligand exhibits strong fluorescence, but the addition of one equivalent of Cu^{2+} quenches the emission to just 11.4% of its original intensity. Other biologically relevant metal ions, including Zn^{2+}, Ni^{2+}, and Pb^{2+}, cause negligible quenching, with only Fe^{3+} producing a minor decrease. High-resolution ESI mass spectrometry confirmed the formation of a 1:1 ligand-Cu^{2+} complex, and the binding constant was determined to be 1.32×10^4 M^{-1}. The detection limit of 1.39 μM is well below the WHO guideline. Importantly, the sensor was successfully applied in living HeLa cells, where intracellular fluorescence was efficiently quenched upon Cu^{2+} exposure, demonstrating its promise for bioimaging applications.

Further examples of the design of dansyl-based compounds incorporating peptides moieties and associated detection parameters for Cu^{2+} are summarized in Table 1-1. Alongside simpler examples such as DGly and GG-Dns[63,64], Wang's group developed compounds DNH to DP5 (Table 1-1) through solid-phase peptide synthesis (SPPS) technology.[65–71] All compounds presented solubility in water and were found to exhibit a "turn off" of the fluorescence in the presence of Cu^{2+}.

Table 1-1. Comparison of dansyl-based compounds composed of peptide moieties for the detection of Cu^{2+}.

Compound	Peptide composition	Recognition unit	LOD (nM)	pH range	Ref
DGly	(Gly)	-NH and carbonyl groups	1.32×10^3	6-8	[63]
GG-Dns	(Gly-Gly)	-NH and -OH groups	290	6-13	[64]
DNH	(Asn-His-NH_2)	-NH group	19.6	7-12	[65]
DAH	(Ala-His-NH_2)	-NH group	18.0	6-11	[66]
DSD	(Ser-Asp- NH_2)	-NH and carbonyl groups	2.4	7-8	[67]
DAHK	(Ala-His-Lys-NH_2)	-NH and carbonyl groups	38.9	4-12	[68]
DGGH	(Gly-Gly-His-NH_2)	-NH group	37.9	6-12	[69]
L	(Ala-Ser-Arg-His-NH_2)	-NH and -OH groups	12.04	6-12	[70]
DP5	(Ser-Pro-Gly-His-Gly-NH_2)	-NH and -OH groups	23.5	6-12	[71]
P	(Asp–Asp–Gly–Gly–$(Glu)_2$)	-OH groups	47	7-12	[72]

Compounds DNH, DAH, DAHK and DP5 (Table 1-1) also showed some level of quenching towards Hg^{2+} but not to the full extent observed for Cu^{2+}. Aside from compound L (Table 1-1), the remaining fluorophores were successfully used for bioimaging applications including different cell lines and zebrafish larvae demonstrating negligible biological toxicity. Furthermore, as a way of improving user-friendliness and portability, compounds DNH, DAH, DAHK and L were embedded in test trips showing the absence of emission only when submerged in Cu^{2+} solution while DNH and DAH were further explored for the semi-quantitative detection of Cu^{2+} in solution using a color recognition app on the smartphone to obtain RGB values. The linear equations were fitted as R/B= -0.1358X + 0.9539 (R^2 = 0.9749) and G/B = -0.0603X + 1.1361 (R^2 = 0.9888) with associated limits of detection of 0.49 mM and 0.25 mM for DNH and DAH, respectively. Finally compound P (Table 1-1) incorporating six amino acids into the dansyl unit was reported by Hu *et al.* that recognizes Cu^{2+} without interference of Hg^{2+} and other metal ions which showed good biocompatibility and low biotoxicity for the imaging of HeLa cells and zebrafish.

Beyond peptide-appended dansyl probes, Zhou *et al.* designed compound **4** (Figure 1–9) through the nucleophilic substitution of 2,6-bis(bromomethyl)pyridine and N-dimethyl-5-(piperazin-1 ylsulfonyl)naphthalen-1-amine, a five-step synthetic route resulting in a 49% overall yield.[60] HEPPS buffer system was used to evaluate the selectivity of sensor **4** in physiological pH window. Although some slight changes in fluorescence were observed for most of the metal ions tested, only Cu^{2+} was able to considerably attenuate the emission at the peak of 540 nm leading to a 40-fold decrease in fluorescence being hardly affected when performed in competition experiments. This system was found to be functional between pH 5-14 with a detection limit of 0.25 mM and formed a 1:1 complex formation with Cu^{2+}. Furthermore, the successful bioimaging application, supported by living-cell experiments, demonstrated that **4** possesses high cell-membrane permeability and strong capability for Cu^{2+} detection.

Sahoo's group reported compound **5** (Figure 1–9) through a simple one pot reaction between dansyl chloride and 2-aminobenzohydrazide in the presence of a base.[73] Compound **5** has a fluorescence maximum wavelength at 438 nm when excited at 335 nm in DMSO:H_2O (1:1, v/v). Upon testing with several metal ions, only Cu^{2+} was able to enhance, and blue shift its original emission to 474 nm with also the appearance of a new shoulder at 411 nm. The 1:1 biding stoichiometry was supported by HRMS data, and the limit of detection was estimated to be 0.98 μM. Probe **5** was used for the determination of Cu^{2+} concentration in water samples from tap and river being able to measure the concentration of spiked Cu^{2+} between the range of 92-112%. A similar compound (**6**, Figure 1–9) with a quantum yield of 0.51

was obtained by Nasomphan *et al.* that exhibited also a "turn-on" fluorescence response towards Cu^{2+} with an associated blue shift from 547 to 479 nm.[74] In this case, Hg^{2+} and Fe^{2+} would cause significant degree of fluorescence quenching. A limit of detection of 0.5 μM was achieved at the physiological pH 7.2 while exciting at 366 nm. The proposed mechanism suggests that the rigid chelation inhibits the non-radiative pathway for a C=N isomerization. Given the absence of cytotoxicity **6** was applied for the detection Cu^{2+} in Vero cells.

A simple probe **7** (Figure 1–9) was constructed by Jiang *et al.* using 2-(piperazin-1yl)ethanol moiety as receptor unit and its photophysical properties were evaluated in CH_3CN-H_2O (95:5, v/v).[75] The emission would suffer a red-shift from 540 to 557 nm only in the presence of Cu^{2+}. The Job's plot confirmed the formation of 1:1 stoichiometry and further supported by DFT calculations which suggest that Cu^{2+} coordinates with the O atom of the sulfonyl group and the N atom of the sulfur. The detection limit falls below the value that is present in the US EPA guidelines being 0.11 μM. This compound was applied to two-photon confocal fluorescence imaging for A549 cells, a technique that uses two photons of lower energy that provide advantages regarding lower autofluorescence levels, low damage induced by light and higher tissue penetration depth.

Considering more sophisticated systems, Zhao *et al.* prepared a new biosensor by covalently link DNS-Cl with amine groups of the Copper resistance operon coded protein C (CopC) and FRET behavior was implemented by exciting the DNS-Cl through the emission of the tryptophan residue (Trp83) on CopC.[76] The selectivity was performed in 30 mM Na_2CO_3/$NaHCO_3$ buffer solution (pH 9.3) and no metal ion studied aside from Cu^{2+} was able to quench the emission with no obvious interference when in the presence of other metal ions and amino acids. The mechanism involves the excitation at 280 nm of the Trp83 of CopC that in turn fluoresces at 320 nm. This emission overlaps with the absorption band of DNS-Cl, enabling efficient FRET and producing a strong secondary emission at 505 nm. The detection mechanism arises when copper ions coordinate with specific residues of CopC (His1, His91, Glu27, and Asp89). These processes quench the tryptophan fluorescence at 320 nm, thereby reducing the excitation of DNS-Cl and leading to a marked decrease in the 505 nm emission. Sensitivity tests showed a linear response over the range of 0.04 to 11 μM, with a detection limit of 6.81 ± 0.07 nM. Finally, the biosensor was successfully applied to real-world samples, including tap water and industrial wastewater, with results in agreement with ICP-MS measurements.

Biswas' group reported the synthesis of a dansyl anchored hafnium based fluorescent metal-organic framework (MOF) that demonstrated high stability in the pH range of 4 to 10.[77] The sensing of Cu^{2+} was achieved in 10 Mm HEPES buffer at pH 7.4 reveling strong

emission at 428 nm with gradual decrease in emission. This system maintained a quenching efficiency of Cu^{2+} between 78 to 84% given the absence of interference from other metals when they are present with a limit of detection of 229 nM. The MOF was applied for the detection of Cu^{2+} in different water specimens (tap water, river water, distilled water and lake water) with its recovery percentage found to fall between 96.3 and 103.9%. Time-resolved photoluminescent measurements confirmed that the fluorescence lifetime of the probe remained unchanged in the presence of Cu^{2+}, indicating static quenching while powder X-ray diffraction patterns showed no structural changes after Cu^{2+} treatment, ruling out trans-metalation with the Hf(IV) ions of the framework. Instead, Cu^{2+} engages in weak complexometric interactions with oxygen and nitrogen atoms of the linker, as evidenced by XPS, which revealed shifts in O 1s and N 1s binding energies while signals for Hf, C, and S remained unchanged. Selectivity arises because Cu^{2+}, with its high charge density and smaller ionic radius, exhibits stronger complexation than other competing ions, while only minimal interference was observed from paramagnetic species like $Fe^{2+}$and Cr^{3+}.

1.2.4.2 Fluorescent Probes for Hg^{2+} Detection

Mercury (Hg) represents one of the most hazardous heavy metals and an impactful global pollutant due to its extreme toxicity, persistence, and ability to bioaccumulate in living organisms.[21,78,79] Mercury released into aquatic systems can be transformed by microorganisms into highly toxic organic forms, which bioaccumulate in fish and other organisms and pose serious risks to humans through dietary exposure. Owing to the extreme toxicity of Hg^{2+}, the US EPA has defined a maximum contaminant level of 10.0 nM (2.0 ppb) in drinking water.[21,80]

Wang's group reported probe **8** (Figure 1–10) based on dansyl and tyrosine using SPPS.[81] The metal ion selectivity experiment was carried out in HEPES buffer solution at pH 7.4 displaying a "turn-on" response to Hg^{2+} with no relevant effect upon exposure to the remaining metal ions. The presence of 5 equiv. of coexisting metal ions did not display the inability for Hg^{2+} to maintain the increase of the fluorescence with an associated blue shift from 545 to 515 nm. Job's plot suggests a 2:1 (L:M) stoichiometric complexation which promotes the presence of monomer-excimer mechanism causing the 30 nm shift in emission. The NMR experiments revealed the strong contribution of the sulfonamide group and the phenol moiety on the binding with Hg^{2+}. This system showed a detection limit of 22.65 nM and its reversibility was demonstrated with EDTA. pH was found to limit the detection of Hg^{2+} between 7 to 10 for

maximum enhancement of emission. Finally, cell viability was maintained at 90% when using 8 to 100 mM and was able to serve as a fluorescent probe for Hg^{2+} in HeLa cells and HK2.

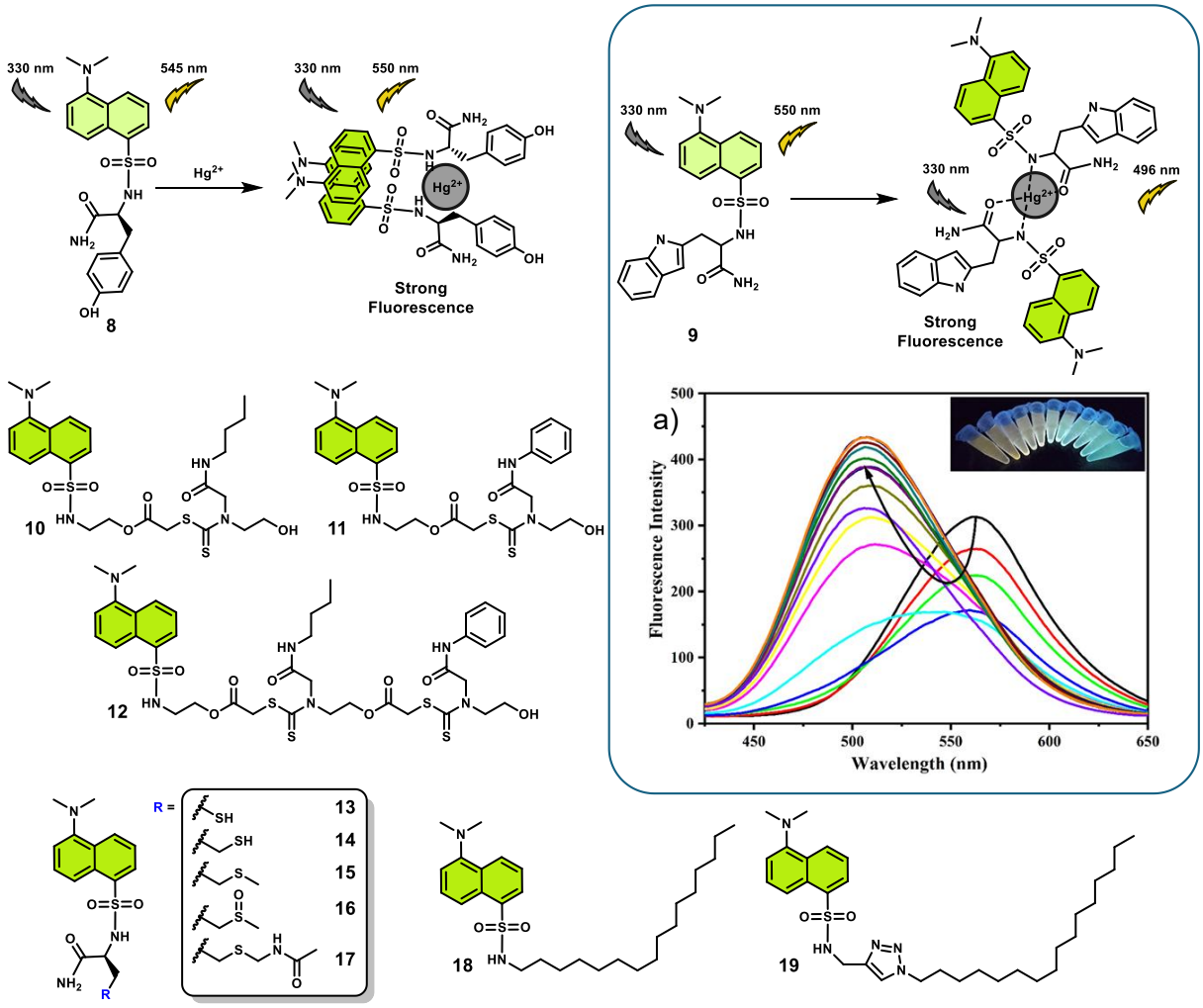


Figure 1–10. Structures of compounds **8**-**19** and proposed detection mechanisms for Hg^{2+}. a) Fluorescence spectra of **9** with excitation wavelength of 330 nm upon addition of increasing concentrations of Hg^{2+} in HEPES buffer at pH 7.4. Inset picture is the variation of color excited at 365 nm. Adapted from ref.[78] copyright 2024, Elsevier.

Contribution of Zhang *et al.* involved the synthesis of a dansylated tryptophan **9** (Figure 1–10) through SPPS.[78] Among different metal ions tested in HEPES buffer (pH 7.4), only Hg^{2+} was able to cause any meaningful change in the emission causing an enhancement of fluorescence accompanied by a 54 nm blue shift from 550 to 496 nm and no interference was detected by other metals (Figure 1–10a). The CHEF effect was elucidated through fluorescence lifetime since an increase from 3.17 to 5.91 ns was observed with a related increase of the quantum yield from 6.31 to 10.41%. The detection limit was found to be as low as 6.53 nM and was functional between pH 7 to 12. A 2:1 complexation with Hg^{2+} was proposed and evidence suggested the involvement of the sulfonamide and the amide groups in the interaction with

Hg^{2+}. The portability aspect of detecting Hg^{2+} was demonstrated through a smartphone color recognition APP showing good linearity in the range of 10 to 70 mM with a corresponding linear regression equation of R/B = -0.0171X + 1.3832 (R^2 = 0.9969). Finally, the potential monitoring of Hg^{2+} was tested in real water samples and presented good recoveries in the range of 6 to 10 mM when spiked.

Implementation of three or more aminoacids as the backbone of the design of dansyl based compounds are gathered in Table 1-2.

Xue *et. al* reported compound L (Table 1-2) that integrated two dansyl units into a lysine backbone using a serine aminoacid.[82] The chemosensor would adopt a 2:1 stoichiometry with Hg^{2+} causing a quenching of the emission in aqueous solution. The MTT assay showed low cytotoxicity in HK2 normal cells when tested until 80 mM, which promoted monitoring of Hg^{2+} ions in living LNCap cells.

The dansyl-peptide probe DGRK (Table 1-2) was synthesized via SPPS for selective Hg^{2+} detection in water and displayed strong fluorescence at 560 nm.[83] Upon Hg^{2+} binding, DGRK formed a 1:1 non-fluorescent complex. Fluorescence titration revealed a linear response up to 1 μM Hg^{2+} with a detection limit of 33.6 nM. In live-cell assays (RKO and GES-1), DGRK showed low cytotoxicity (>90% viability at 80 μM) and efficient cell permeability, enabling imaging of intracellular Hg^{2+}. For portable detection, paper-based test strips gave clear fluorescence quenching with Hg^{2+} under 365 nm UV light, and smartphone-assisted RGB analysis allowed semi-quantitative detection (R/B = -0.1609 X + 1.98, R^2 = 0.9773) with an LOD of 0.23 μM.

Table 1-2. Comparison of dansyl-based compounds composed of peptide moieties for the detection of Hg^{2+}.

Compound	Peptide composition	Recognition unit	LOD (nM)	pH range	Ref
L	(DNS-Ser-Lys-Ser-DNS)	-OH groups	7.59	6-12	[82]
DGRK	(DNS-Gly-Arg-Lys-NH_2)	-NH groups	33.6	6-12	[83]
DKA	(DNS-Ala-Lys-Ala-DNS)	Carbonyl groups	13.4	5-10	[79]
DWPH	(DNS-Trp-Pro-His-NH_2)	-NH and carbonyl groups	24.6	7-11	[80]
D-P4	(DNS-Glu-Cys-Glu-Trp-NH_2)	-NH and -SH groups	23.0	8-11	[84]
D-P4'	(DNS-His-Pro-Gly-Asp-NH_2)	-Sulfonamide and imidazole	61.0	7-12	[85]
KEEP	((Dansyl-Glu-Glu)$_2$-Lys-NH_2)	-NH and carbonyl groups	40.0	7-11	[86]

Closely related to the previous work, Wang's group also designed compounds DKA and DWPH (Table 1-2) that this time a "turn-on" with an associated blue shift of the emission was

noticed.[79,80] For both compounds the initial emission observed at 560 nm would weaken while at 510 nm an increase was observed only in the presence of Hg^{2+}. DKA showed very low cytotoxicity to Hacat cells up to 80 mM and its ability to measure Hg^{2+} levels in live cells was demonstrated. The use of a smartphone APP that reads RGB values was used for the semi-quantitative analysis of Hg^{2+} providing good linearity (R/G =-0.0439 X + 0.7249, R^2 =0.9799) with a detection limit of 2.5 mM. In turn, DWPH was found to be under a PET phenomenon from the lone pair electrons of the imidazole that would quench the emission and could only be restored through a CHEF mechanism initiated by Hg^{2+}. HGC-27 cells were used to assess the cytotoxicity which had a survival rate above 90% when incubated up to 80 mM of DWPH. The monitoring of Hg^{2+} in zebrafish larvae was validated. The use of the smartphone APP revealed good linearity (R/G = 0.6412X + 1.1330 (R^2 =0.9855)) with a detection limit of 0.45 mM.

Pang *et. al* developed D-P4 (Table 1-2) that manifested a turn on response towards Hg^{2+} in HEPES solution (pH 7.1).[84] While excited at 330 nm, the band located at 550 nm would blue shift 45 nm to 505 nm and an increase of fluorescence intensity was observed, clear evidence of CHEF effect. The presence of Trp residue allowed the monitoring of the emission of D-P4 using the 295 nm wavelength which evidenced a fluorescence emission peak at 337 nm and 550 nm. With the addition of Hg^{2+} the band at 337 nm decreased due to the folding of D-P4 that would shorten the distance between the Trp residue (donor) and the dansyl unit (acceptor). This translated in an increase of the fluorescence intensity at 505 nm suggesting a FRET effect and another pathway for the sensing of Hg^{2+}. Fluorescence lifetime decay profiles suggest a decrease from 2.80 ms to 2.77 ms at 337 nm emission when exciting at 295 nm while the fluorescence lifetime at 505 nm emission peak increased from 7.43 to 11.18 ms. Furthermore, D-P4 was found to recover Hg^{2+} in the range of 0.1 to 1.5 mM from river water while the visual detection was assessed in agarose gel flakes and test paper.

Compound KEEP (Table 1-2) was designed by Li *et. al* as a fluorescent probe capable of producing distinct fluorescence responses depending on the mercury form.[86] When binding Hg^{2+}, the probe undergoes fluorescence quenching, giving a clear "turn-off" signal. Conversely, interaction with organic mercury compounds (CH_2Hg^{2+} and $PhHg^{+}$) enhances fluorescence emission, generating a "turn-on" response. Quantitative studies revealed high sensitivity, with a detection limit as low as 40 nM for Hg^{2+}, and micromolar detection limits for CH_3Hg^{+} (5.32 μM) and $PhHg^{+}$ (0.79 μM). This enhancement is attributed to steric hindrance introduced by the organic groups, which restricts non-radiative relaxation pathways and thus strengthens fluorescence. Among them, $PhHg^{+}$ produces a stronger enhancement than CH_3Hg^{+} due to greater steric effects.

Anna Jose and co-workers have designed three water soluble sequence-defined oligo-dithiocarbamate dansyl derivatives **10** to **12** (Figure 1–10) for the detection of Hg^{2+}.[87] Compound **10** was used as model compound showing in aqueous medium an absorption and emission maxima of 330 and 560 nm with an associated quantum yield of 0.138. A blue shift of 60 nm was observed when Hg^{2+} is present and no interference from other metal ions were detected. This sensor adopts a 1:1 binding stoichiometry and has a LOD of 9.3 nM. Comparable LOD value (8.1 nM) was demonstrated by substitution of the butyl moiety with the phenyl ring (**11**). The possibility of increasing the receptor units for Hg^{2+} was accomplished by increasing the chain length. Sensor **12** that incorporates two dithiocarbamate units yielded an LOD of 60 pM. Visual detection of Hg^{2+} was made possible through paper strips and fluorescence microscopy which was validated in MCF-7 and HeLa cancer cell lines.

Guided by the principles demonstrated in earlier studies on the dansyl-methionine chemosensor, Andrea Cusano's group developed new dansyl-amino acids incorporating methionine and cysteine (cys) derivatives for Hg^{2+} ion recognition in aqueous buffer (**13** to **17**, Figure 1–10).[88] Sensors containing only a thioether moiety, **15** and **17**, exhibited a turn-on fluorescence response to Hg^{2+} in the 0–120 μM range. In contrast, chemosensors containing oxidized methionine or free cysteine/homocysteine showed a turn-off response under the same conditions. The most sensitive probe **15** had a limit of detection of 140 nM, which exceeds the EPA limits for drinking water. To enhance sensitivity, a portable optical fiber-based experimental setup was tested, improving the LOD by ~100-fold to approximately 5 nM, well below safe human exposure limits. However, the sensors are not suitable for detecting Hg^{2+} in marine water due to interference from high chloride concentrations.

The self-assembly properties originated from the reaction between dansyl chloride and hexadecyl amine enabled Gadiyaram *et al.* to integrate the compound **18** (Figure 1–10) into sphere-like phospholipid nanovesicles with an average particle size of 102.9 nm at biological pH.[89] The positioning of the dansyl unit on the vesicle surface motivated studies on its interaction with metal ions. In the presence of Hg^{2+}, the emission at 525 nm was significantly quenched, corresponding to a limit of detection of 6.41 μM. Fluorescence lifetime measurements supported this observation, showing a decrease from the initial 13.24 ns, which was attributed to Hg^{2+}-induced aggregation of the vesicles, further confirmed by scanning electron microscopy (SEM) imaging.

A similar approach was taken by Kim's group who fused the dansyl unit with a cetyl chain bridged by a triazole (**19**, Figure 1–10).[90] Probe **19** was found to emit strongly in the green region with an emission maximum at 500 nm in aqueous solution containing 0.5% DMSO.

Addition of Hg^{2+} would lead to a shift of the emission to 476 nm at its peak with an associated quenching. A five-membered ring between the Hg^{2+} center and the N donors of the sulfonamide and the triazole in a 1:1 stoichiometry was the proposed recognition site. The sensing of Hg^{2+} was associated with the initial induced self-aggregation of the probe, since dynamic light scattering (DLS) data revealed the presence of nanoaggregates with 120 nm average diameter while transmission electron microscopy (TEM) showed diameters between 20-50 nm in the solid state. The critical aggregation concentration (CMC) was 7.86 μM and presented a sensing response between pH 4 to 11. MTT assay demonstrated 90% cell viability until 40 μM for 24h in HepG-2 liver cancer cells with further studies supported the fluorescence imaging of intracellular Hg^{2+} using this probe.

Uttam and co-workers reported a lower rim dansyl-functionalized calix[4]arene (DanC4A) as a selective fluorescent probe for mercury ions (Hg^{2+}) in solution, solid state, and living cells.[91] DanC4A exhibited strong emission at 510 nm in THF, which was quenched by nearly 80% upon Hg^{2+} addition, with a detection limit of 0.56 μM and a 1:1 binding stoichiometry confirmed by Job's plot. XPS studies revealed that both sulfur atoms from thiophene and nitrogen atoms from tertiary amines participated in Hg^{2+} coordination. DanC4A was biocompatible in HeLa cells (>70% viability up to 100 μg/mL) and intracellular fluorescence imaging confirmed quenching upon Hg^{2+} uptake. To address solubility and reusability issues, DanC4A was encapsulated into ZIF-8, forming DanC4A@ZIF-8 hybrid MOFs, maintaining its fluorescence. These hybrid materials not only enabled confocal Hg^{2+} sensing but also achieved up to 95% removal of Hg^{2+} from aqueous solutions. In contrast, Oguz *et al.*[92] designed water-soluble sulfonated dansyl-calixarenes for live-cell Hg^{2+} imaging in SW-620 cells, achieving non-toxicity up to 200 μM and PET-based fluorescence quenching with detection limits in the 10^{-5} M range, thereby emphasizing biological compatibility rather than environmental remediation.

1.2.4.3 Fluorescent Probes for Zn^{2+} Detection

Zinc (Zn) is an essential trace element and the second most abundant transition metal ion in the human body, following iron. It is widely distributed in living organisms and plays indispensable roles in a wide range of biological processes, including cell proliferation, protein and nucleic acid synthesis, enzyme catalysis, carbohydrate and lipid metabolism, and immune system regulation.[93,94] Beyond these functions, Zn^{2+} is critical for neural development, reproductive processes, and multivitamin metabolism, thereby supporting growth and immune defense. Structurally, zinc stabilizes zinc-finger proteins through coordination with histidine and cysteine residues, which are crucial for gene regulation, protein folding, and DNA binding.

More than 200 zinc-containing enzymes have been identified to date, highlighting the central role of zinc in maintaining normal cellular function.[93–96] Physiological levels of Zn^{2+} are essential for sustaining life, but imbalances in zinc homeostasis are associated with numerous pathological conditions.[97,98] Zinc deficiency has been linked to growth retardation, immune deficiency, neurological dysfunction, ischemic injury, epilepsy, and neurodegenerative diseases such as Alzheimer's and Parkinson's. Conversely, excessive zinc accumulation is toxic and can lead to oxidative stress, metabolic disturbances, and environmental contamination. In agriculture and food systems, zinc pollution reduces soil microbial activity and causes phytotoxic effects, thereby posing risks to both ecological balance and human health.[93–96]

Motivated by the critical role of Zn^{2+} in health and the environment, Wang's group have synthesized compounds **20** to **22** (Figure 1–11) that manifest a "turn-on" response towards Zn^{2+}.[93–95] Probe **20** is a dipeptide conjugated with dansyl unit (DNS-Ser-His-NH_2).[93] The selective detection of metal ions in HEPES buffer solution resulted in a pronounced blue shift of the emission maximum from 545 nm to 515 nm, accompanied by an enhanced fluorescence intensity and an increase in quantum yield from 0.079 to 0.169. Job's plot suggests a 2:1 (2(**20**):Zn^{2+}) detection system and the detection limit was estimated to be 11.2 nM in pH range from 7 to 10. Cytotoxicity tests in H2K cells revealed cellular viability above 80% until concentrations up to 80 μM of **20**. H2K cells alongside SV-HUC-1 cells were used to validate the detection of Zn^{2+} in living cells.

The synthesis of **21** (Figure 1–11) was accomplished by conjugating the dansyl group with a tetrapeptide using SPPS (DNS-Glu-Pro-Gly-His-NH_2).[94] The selective detection of Zn^{2+} was demonstrated in aqueous solution without interference from other metals, especially Cd^{2+} and Hg^{2+}. Its fluorescence emission with a maximum at 545 nm is increased in the presence of Zn^{2+} promoting a rise in the quantum yield from 9.46% to 17.97%. A PeT phenomenon from the lone pair electrons of the imidazole group to the dansyl unit was the cause of the initial quenching. The formation of a 2:1 stoichiometry of **21** and Zn^{2+} was evidenced by Job's plot being the two oxygen atoms of the Glu groups and the N atoms of the His groups responsible for the coordination. The detection of Zn^{2+} could be achieved in the pH range of 7 to 12 and has a limit of detection of 18 nM. HeLa cells were used to assess the cell survival rate that maintained above 90% up to concentrations of **21** below 200 μM and was successfully utilized for fluorescence imaging of Zn^{2+}.

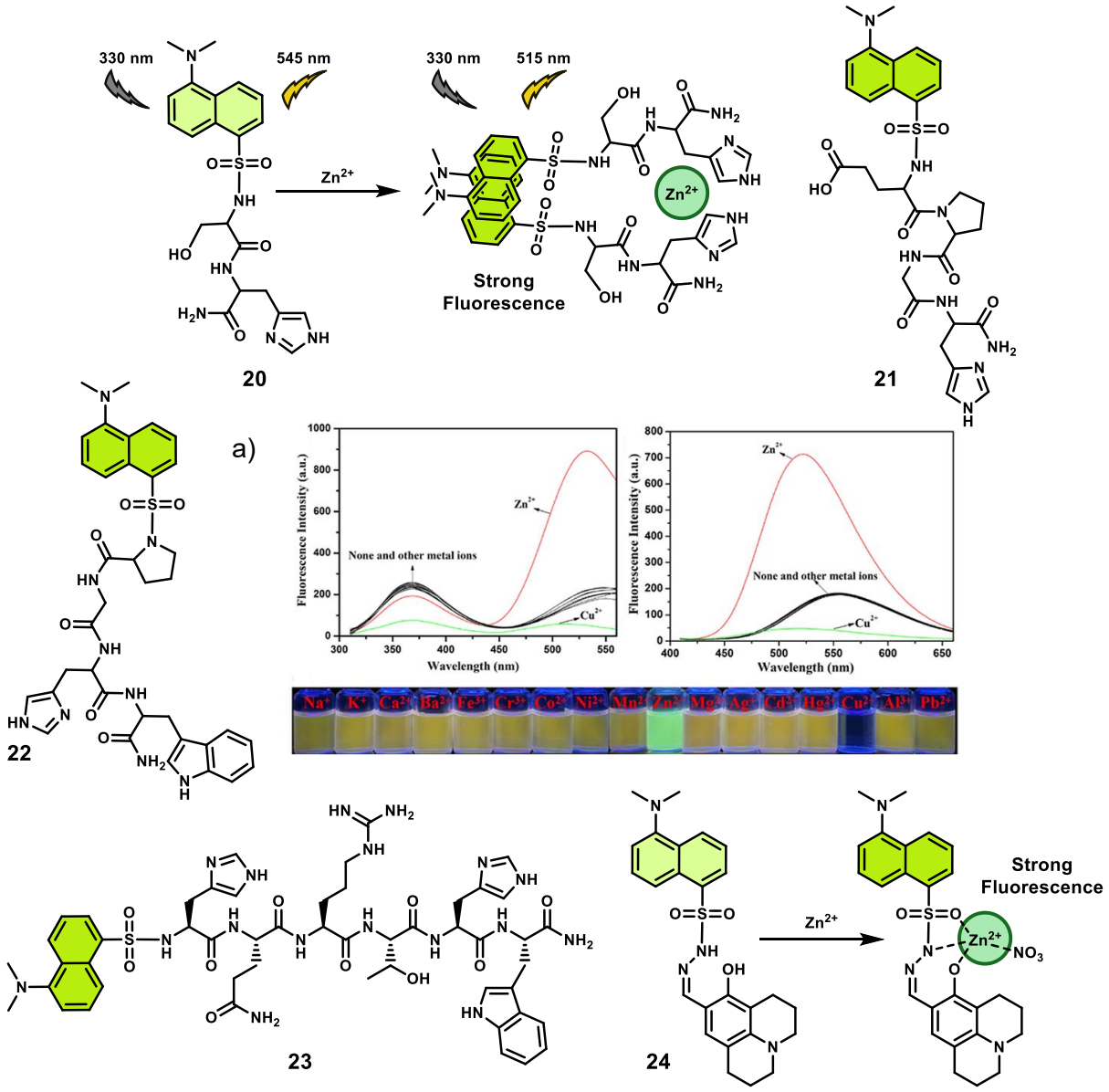


Figure 1–11. Structures of compounds **20**-**24** and proposed detection mechanisms for Zn^{2+}. a) Fluorescence emission spectra of **22** following addition of various metal ions in HEPES buffer (pH 7.4) solutions. (left) Excitation wavelength: 280 nm, (right) Excitation wavelength: 320 nm. Fluorescence emission changes under UV lamp (365 nm) of **22** upon addition of various metal ions. Adapted from ref.[95] copyright 2021, Elsevier.

The probe **22** (Figure 1–11), synthesized via SPPS, consists of a tetrapeptide scaffold (Pro-Gly-His-Trp-NH_2) functionalized with a dansyl fluorophore. Histidine coordinates Zn^{2+} through its imidazole group, while tryptophan acts as a fluorescence donor and dansyl as an acceptor.[95] At 280 nm excitation, **22** shows in aqueous solution a ratiometric FRET response, and at 320 nm, a turn-on PeT response given the increase in emission associated with a blue shift from 555 to 525 nm with the addition of Zn^{2+} (interference only to Cu^{2+}, (Figure 1–11a)). Spectroscopic and ESI-MS analyses revealed a 2:1 binding stoichiometry (**22**:Zn^{2+}) coordinating

through amide and imidazole groups. The limit of detection was calculated to be 5.43 nM. Compound **22** remained effective across pH 5-12 and showed low cytotoxicity (>90% cell viability at 80 μM, SV-HUC-1 cells). Confocal imaging demonstrated bright green fluorescence upon Zn^{2+} binding, confirming applicability in live-cell Zn^{2+} imaging.

Yu and co-workers designed compound **23** (Figure 1–11), a six-amino acid labeled with a dansyl unit (DNS-His-Gln-Arg-Thr-His-Trp-NH_2) based on a zinc finger peptide motif of CP1.[96] Excitation in HEPES buffer solution at 295 nm revealed two emission peaks at 519 and 362 nm corresponding to the dansyl group and Trp, respectively. The addition of Zn^{2+} promoted the decrease of the 362 nm peak and the opposite effect at 519 nm being an indication that **23** produces a FRET effect. Lifetime measurements follow this tendency with an increase of the fluorescence lifetime at 519 nm from 4.78 ns to 12.44 ns and an associated increase of the quantum yield from 0.06 to 0.17. The calculated limit of detection was found to be 33 nM and a 2:1 complex model **23**:Zn^{2+} was proposed with imidazole groups acting as chelating groups. The optimal pH conditions for Zn^{2+} sensing were between 7 and 9 with Cu^{2+} exerting some interference. MTT assay using HeLa cells confirmed low toxicity until 160 μM and confocal microscopy validated the intracellular detection of Zn^{2+}.

A Schiff base **24** (Figure 1–11) combining julolidine aldehyde and dansyl hydrazine was reported by Ahamed and co-workers which showed high selectivity towards Zn^{2+} in DMSO/H_2O (8/2, v/v, pH 7.2 buffer).[99] Upon excitation at 380 nm the weak fluorescence emission at 554 nm was enhanced after the addition of Zn^{2+}. This is attributed to the inhibition of the PeT mechanism and C=N isomerization due to complexation. Job's plot analysis suggests a 1:1 stoichiometry and the limit of detect was calculated to be 15 nM in optimal pH range of 4 to 8. Coordination with the Zn^{2+} occurs via the imine N atom, phenolic OH group, and sulfonyl oxygen. Probe **24** was applied for real water sample analysis in samples of double-distilled water and tap water reaching recovery values from 95.0% to 98.7%. Cost-effective detection of Zn^{2+} was performed in test strips for on-site applications.

Recent developments have extended the use of dansyl fluorophores beyond small-molecule probes toward hybrid and nanostructured systems. In the Fe_3O_4@SiO_2-PEG-DNS nanosystem reported by Pourfallah and Lou,[100] a magnetic silica core was functionalized with dansyl units via a PEG ($M_n \approx 3000$) linker, producing spherical particles of 33 ± 6 nm. The PEG spacer doubled surface fluorophore density (6.7×10^{-6} vs. 3.1×10^{-6} mmol·mg^{-1} without PEG) and boosted quantum yield from 0.28 to 0.39 compared with 0.07 for free dansyl chloride. These enhancements were attributed to reduced core-fluorophore quenching and an intensified "push-pull" electronic effect through the sulfonate-oxygen linkage. Upon Zn^{2+} addition,

fluorescence was selectively quenched by 12.5-fold, with a detection limit of 6.25 nM and a 2:1 ligand-to-metal stoichiometry. Quenching originated from Zn^{2+} coordination to the dimethylamino group, disrupting electron transfer responsible for emission. Other cations, including Cd^{2+}, showed negligible interference. The sensor's signal was fully recoverable with EDTA, retaining 98% fluorescence and ~76% of mass after five reuse cycles.

1.2.4.4 Fluorescent Probes for Cd^{2+} Detection

Cadmium (Cd) is a naturally occurring metallic element mainly found as cadmium sulfide and cadmium carbonate. It is widely applied in metallurgy, electroplating, pigments, phosphate fertilizers, nickel–cadmium batteries, semiconductors, and other industrial fields. However, Cd^{2+} is a highly toxic and bioaccumulative heavy metal that poses serious threats to the environment and human health. Anthropogenic activities such as metal smelting, sewage discharge, fertilizer use, and industrial waste disposal have led to the long-term accumulation of cadmium in soil and water, from where it enters the food chain and accumulates in organisms.[101–104]

In the human body, Cd^{2+} binds to proteins containing sulfhydryl and hydroxyl groups, forming cadmium-thionein complexes that accumulate mainly in the liver and kidneys. It disrupts cellular processes by damaging membranes, inhibiting enzymes, altering DNA, and generating reactive oxygen species (ROS), leading to oxidative stress. Acute exposure can cause gastrointestinal symptoms, while chronic exposure is associated with kidney, liver, and bone damage, as well as cancers such as lung, prostate, and bladder cancer.[105–107] Recognized as one of the most dangerous global pollutants, cadmium's maximum contaminant levels in drinking water are limited to 5.0 ppb (EPA) and 3.0 ppb (WHO). Owing to its chemical similarity to Zn^{2+}, achieving selective and sensitive detection of Cd^{2+} in environmental and biological systems remains an important research priority.[101–104]

Notably, Peng Wang's group have developed methods for cadmium detection using dansyl chromophores.[101–104] **Figure 1–12** gathers probes **25** to **28** synthesized by SPPS technology. Compound **25**, a dipeptide conjugated with a dansyl group (DNS-Ser-Cys-NH_2), exhibits a fluorescence 'turn-on' response at 545 nm upon addition of Cd^{2+}, with the quantum yield increasing from 0.068 to 0.154 in aqueous solution.[101] Binding studies demonstrate that **25** coordinates in a 2:1 stoichiometry with Cd^{2+} by the sulfhydryl group with an associated limit of detection of 13.8 nM. The sensing mechanism involves a PeT process from the sulfhydryl group of cysteine to dansyl unit quenching the initial emission that is restored upon addition of Cd^{2+} exhibiting some interference only to Cu^{2+}. Given that the optimal response to Cd^{2+} was observed between pH 7 to 10, cytotoxicity experiments were carried out using living H2K

cells revealing no toxicity until 80 μM of **25**. The same cell line helps validate the usefulness of **25** on the detection of Cd^{2+} in biological applications.

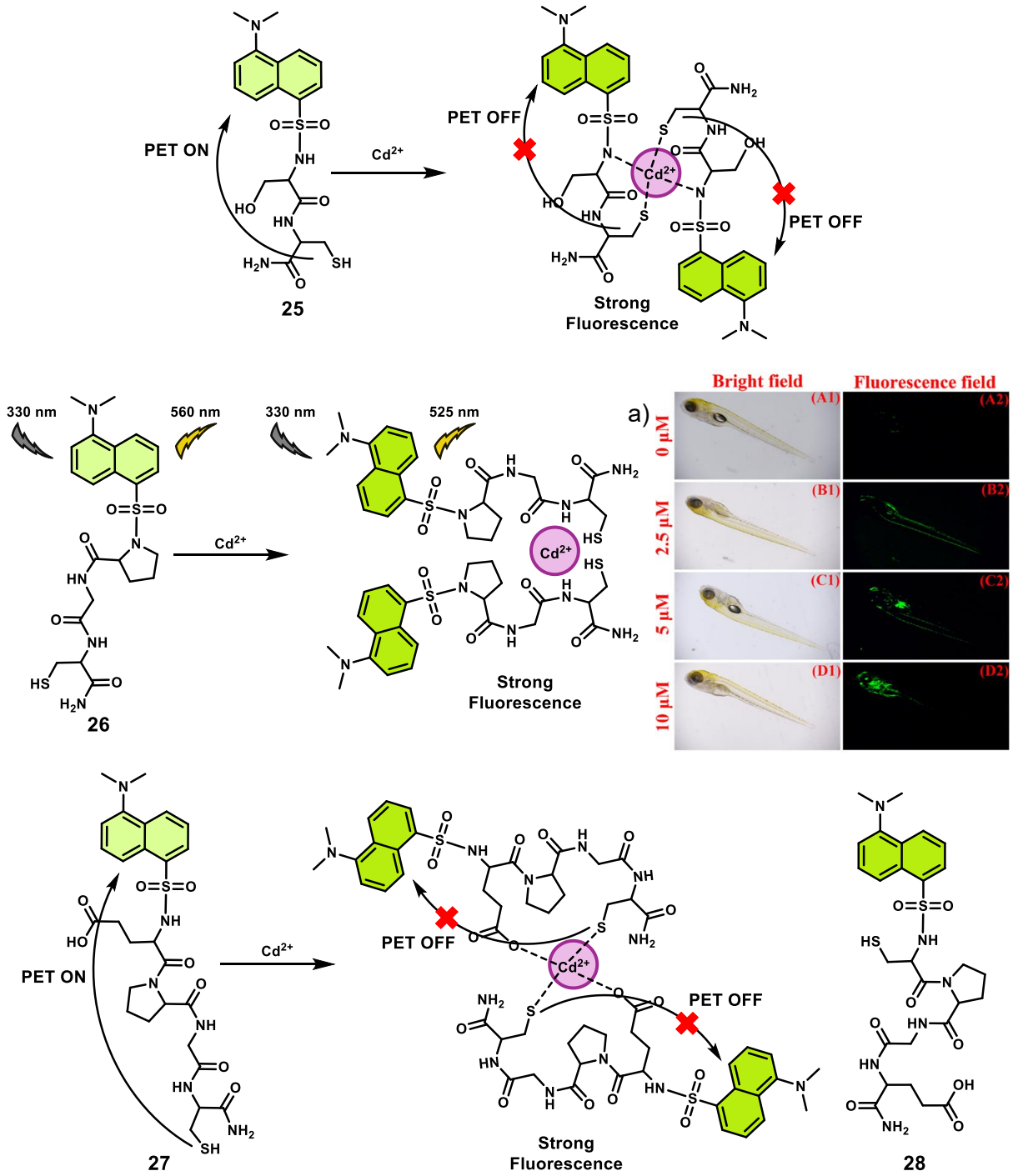


Figure 1–12. Structures of compounds **25**-**28** and proposed detection mechanisms for Cd^{2+}. a) Confocal images of zebrafish larvae treated with **26** for 1 h (A1-A2) and further treated with 2.5 μM (B1-B2), 5 μM (C1-C2) and 10 μM (D1-D2) of Cd^{2+} for 1 h. Adapted from ref.[102] copyright 2024, Elsevier.

Probe **26** (**Figure 1–12**) is a dansyl labelled tripeptide (DNS-Pro-Gly-Cys-NH_2) that shows a fluorescence peak at 560 nm in aqueous solution that is blue shifted to 525 nm with a 22-fold increase upon exposure to Cd^{2+}.[102] Adopting a 2:1 (L:M) stoichiometry through coordination of the sulfur atom in the sulfhydryl group, the probe exhibited a calculated detection limit of 12.4 nM for Cd^{2+}. Fluorescence decay curves suggest an increase from 2.095 ns to 18.724 ns when Cd^{2+} is present allied with an increase of the quantum yield from 6.14% to 51.35%. Moreover, the optimal pH for the detection of Cd^{2+} was found to be between 7 and 11. Cadmium(II) detection using **26** (>95% cell viability at 80 μM, SW620 cells) in living cells was demonstrated using SW620 cells showing the increase of intracellular fluorescence which was also evident in zebrafish models (**Figure 1–12**a). The use of **26** for recovery of Cd^{2+} in diverse water samples reach values from 95.3% to 108.0%. Finally, using a Colour Picket App it was possible to validate a smartphone-assisted sensing system showing excellent linear relationship between G and B value (G/B = 0.2430X + 0.6452, R^2 =0.9792) achieving a detection limit of 0.29 μM of Cd^{2+}.

The dansyl-conjugated tetrapeptide **27** (DNS-Glu-Pro-Gly-Cys, **Figure 1–12**) exhibited a 5-fold enhancement in fluorescence intensity upon interaction with Cd^{2+} ions in aqueous solution, accompanied by an increase in quantum yield from 0.0857 to 0.1769.[103] Notably, the probe demonstrated high selectivity toward Cd^{2+}, showing minimal interference from other metal ions. Experimental studies suggest that **27** adopt a 2:1 stoichiometry with Cd^{2+} through the O atom of Glu and the S atom of Cys which prevents the initial PeT process from the sulfhydryl group to the dansyl unit. Fluorescence lifetime measurements revealed an increase from 9.32 ns to 17.36 ns in the presence of Cd^{2+}. Moreover, the calculated limit of detection was demonstrated to reach 45 nM in optimal pH values between 7 to 10. MTT assays revealed a survival rate above 90% to 200 μM of **27** in HeLa cells which were used to validate the imaging of endogenous Cd^{2+} ions.

A similar response towards Cd^{2+} was found for compound **28** (DNS-Cys-Pro-Gly-Glu-NH_2, **Figure 1–12**) which adopts a 2:1 (L:M) stoichiometry with the initial quenching caused by PeT process being reverted after complexation.[104] The limit of detection for this system was found to be 93 nM. Moreover, the coordination process occurred through the O atoms of the Glu and sulfhydryl of Cys which induced a change in the fluorescence lifetime from 9.86 ns to 18.78 ns after complexation. Cytotoxicity experiments were conducted using HeLa cells (>90% cell viability at 200 μM) and an additional cell line (H2K) was used to demonstrate the usefulness of **28** as a probe for detecting Cd^{2+} in living cells.

1.2.4.5 Fluorescent Probes for Fe^{2+}, Ag^{+}, Pb^{2+} and Pr^{3+} Detection

In addition to the extensively studied metal ions discussed above, several other metals have also been explored to a lesser extent using dansyl-based sensors. Although the number of reports is comparatively limited, these studies highlight the versatility of the dansyl fluorophore and its ability to respond to a diverse range of metal ions. The following section summarizes the reported examples involving these less commonly studied metals, outlining their sensing behaviors and detection characteristics.

Iron is the most abundant transition metal on Earth being involved in a variety of biological processes namely oxygen transport, maintenance of hematopoietic activity, and the synthesis of various coenzymes and DNA.[108–110] The redox pair of Fe^{2+} and Fe^{3+} represents the most important oxidation states of active iron in biological systems, with the ferrous form (Fe^{2+}) being the predominant species under physiological conditions.[111] Gao and colleagues have synthesized compound **29** (Figure 1–13) which contains a dansyl unit and a Fe^{2+} reduction functional group (N-oxide).[111] The initial weak emission at 489 nm (Tris-DMSO 4:1, pH = 7.4, v/v) would undergo a substantial increase in the presence of Fe^{2+} that was not affected by other metal ions. However, the detection could only be performed between pH 4 and 7 with a limit of detection of 18 nM given the formation of other complexes in alkaline conditions. The mechanism involved the initial suppression of emission due to the p-conjugation effect of the N-oxide group that would be cleaved by Fe(II)-induced deoxygenation leading to the reinstate of ICT. Probe **29** was also implemented for the detection of Fe^{2+} in physiological saline, demonstrating also a detection limit of 18 nM. Cytotoxicity assay (CKK-8 assay) and bioimaging application of **29** were performed in living Kyse180 cell lines, which demonstrated good biocompatibility and effective fluorescence imaging of Fe^{2+}.

The increased use of silver and related compounds by modern industry induced serious environmental pollution and potentially can harm living organisms.[112] In biological systems, Ag^{+} has a strong affinity for sulfhydryl and amino groups. It forms harmful complexes with amino acids, nucleic acids, and other biomolecules in the body.[113] Excessive exposure to Ag^{+} can cause various health problems, including argyria (silver poisoning), growth retardation, cardiac enlargement, urinary silver excretion, and liver damage. Prolonged ingestion of Ag^{+} may also lead to skin disorders or ocular damage due to the accumulation of insoluble silver deposits.[113] US EPA has set a permissible level of silver in drinking water of 0.93 mM.[114]

To address the lack of fluorescent probes with good biocompatibility and water solubility for Ag^{+} detection, Cheng's group devised a dansyl unit bearing a biomolecular peptide **30** (DNS-Leu-Leu-Cys-Acp-Asp-OH, Figure 1–13) that showed a "turn on" effect in the presence

of Ag^+ in HEPES buffer solution.[113] The coexistence of other metal ions did not enable any variations on the detection Ag^+ which was found optimal in the pH range of 5 to 10 with an associated limit of detection of 61.7 nM. Moreover, investigation into the binding mode revealed the formation of a 2:1 (L:M) complex through the S atom. Fluorescence lifetime measurements revealed an increase from 5.86 ns to 14.6 ns in tandem with the quantum yield that saw an increment from 23.64% to 49.54% by interaction with Ag^+. Cytotoxicity and intracellular detection of Ag^+ was performed using HeLa cells (>90% cell viability at 50 μM) demonstrating the usefulness of **30** in cell imaging.

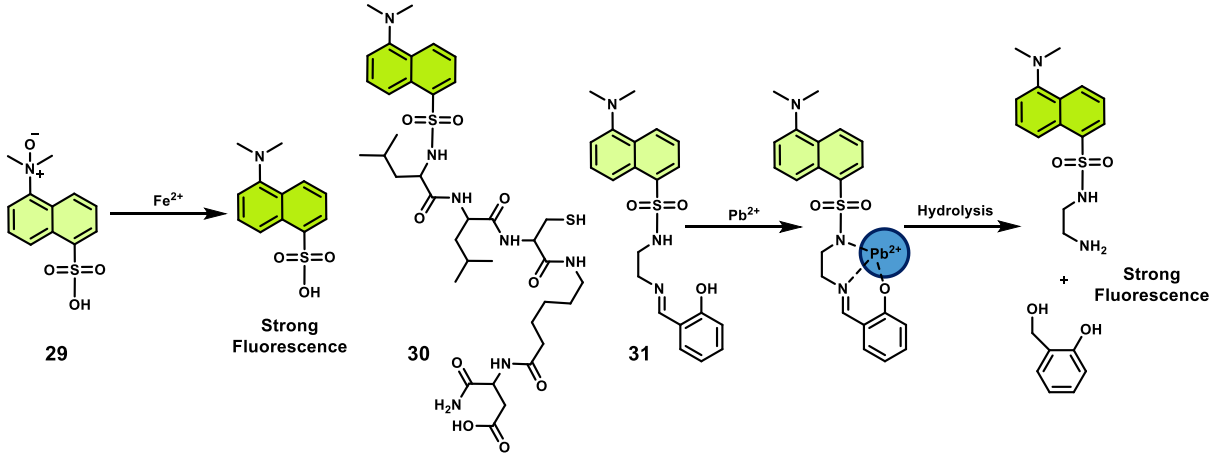


Figure 1–13. Structures of compounds **29**-**31** and proposed detection mechanisms for several metal ions.

Lead(II) is among the most toxic heavy metal ions causing cardiovascular, reproductive and developmental disorders when accumulated in the body.[115] To address the lack of chemosensors directly targeted towards Pb^{2+} sensing, Wu's group covalently linked dansyl unit with 2-hydroxybenzaldehyde resulting in **31** (Figure 1–13).[115] In acetonitrile, **31** shows some changes to the absorption spectra upon the addition of Fe^{3+}, Fe^{2+}, Cu^{2+}, Hg^{2+} and Al^{3+} indicating a partial interaction with **31**. However, only with Pb^{2+} was observed a prominent fluorescence increase inducing a change in the quantum yield from 0.05 to 0.07 after complexation. A 1:1 stoichiometric complexation with Pb^{2+} was proposed based on the Job's plot and mass spectrometry. The detection limit for the detection of Pb^{2+} was 23.2 ppb. The mechanism of detection involves the hydrolysis of the imine bond promoted by Pb^{2+}. Finally, **31** was applied to the determination of Pb^{2+} in real water samples reaching recoveries in the range of 100.8-117.1%.

Praseodymium (Pr^{3+}) belongs to the lanthanide series with a wide range of uses in everyday technology and industry. It helps create the bright colors seen on televisions, powers fluorescent and energy-saving lamps, and improves the quality of certain types of glass. In the film industry, praseodymium is an important material in carbon arc lights used for projection.

It also plays a key role in fiber optic cables, where it enhances signal strength and transmission. The yellow pigments produced from its compounds are commonly used in ceramic glazes and enamels. However, activities such as industrial manufacturing, petroleum processing, and the disposal of electronic devices can release praseodymium into the environment.[116] Over time, it can build up in soil and water, eventually finding its way into plants, animals, and humans. To address this issue, Soni *et al.* have reported a calix[4]arene bearing hydrazine carbonyl spacers linked to dansyl unit.[116] In acetonitrile, the selective quenching in the presence of Pr^{3+} has been demonstrated against several other lanthanide ions due to the presence of a PeT process. ESI-MS and Job's plot experiments elucidate a 1:1 stoichiometry ratio. Moreover, the minimum detection limit was 3.571 nM for Pr^{3+} with the theoretical limit of detection being 0.214 nM. Fabrication of wax printed paper devices demonstrated the on-site detection of Pr^{3+}.

1.2.4.6 Fluorescent Probes for Dual Metal Ion Detection

While most dansyl-based probes have been developed for the selective detection of individual metal ions, several systems have shown the ability to recognize two different metal ions simultaneously. These dual-responsive sensors often display distinct optical or fluorescence changes depending on the ion present, enabling differential or even sequential detection within the same molecular framework. This unique behavior typically comes from multiple coordination sites or flexible binding modes associated with the fluorophore.[117–119] The versatility of such systems not only broadens the sensing scope of dansyl-based probes but also provides valuable insights into their underlying recognition mechanisms. The following section summarizes representative examples of these dual-metal sensing systems and their characteristic fluorescence responses.

A notable contribution to this area was made by Wang's group, who developed the dual-responsive dansyl probes **32** to **36** for metal ion detection (Figure 1–14).[120–124] Compound **32** is a dansyl-appended dipeptide (DNS-Gly-Cys-NH_2) that in HEPES buffer solution displays a "turn on" response to Cd^{2+} with a change in the emission peak from 560 to 515 nm, while Cu^{2+} detection is characterized by "turn off" effect.[120] For both metal ions, the binding modes would originate a 2:1 complex (L:M) and the calculated detection limits were 14.5 and 26.3 nM for Cd^{2+} and Cu^{2+}, respectively. The proposed mechanism involves a monomer-excimer mechanism in aqueous solution upon complexation. Since the optimal sensing conditions were between pH 7 to 12, cell viability was performed in H2K cells (>90% cell viability at 80 μM) while fluorescence imaging was carried out in LNCaP cancer cells demonstrating the successful implementation of **32** for sensing Cd^{2+} and Cu^{2+} in living cells.

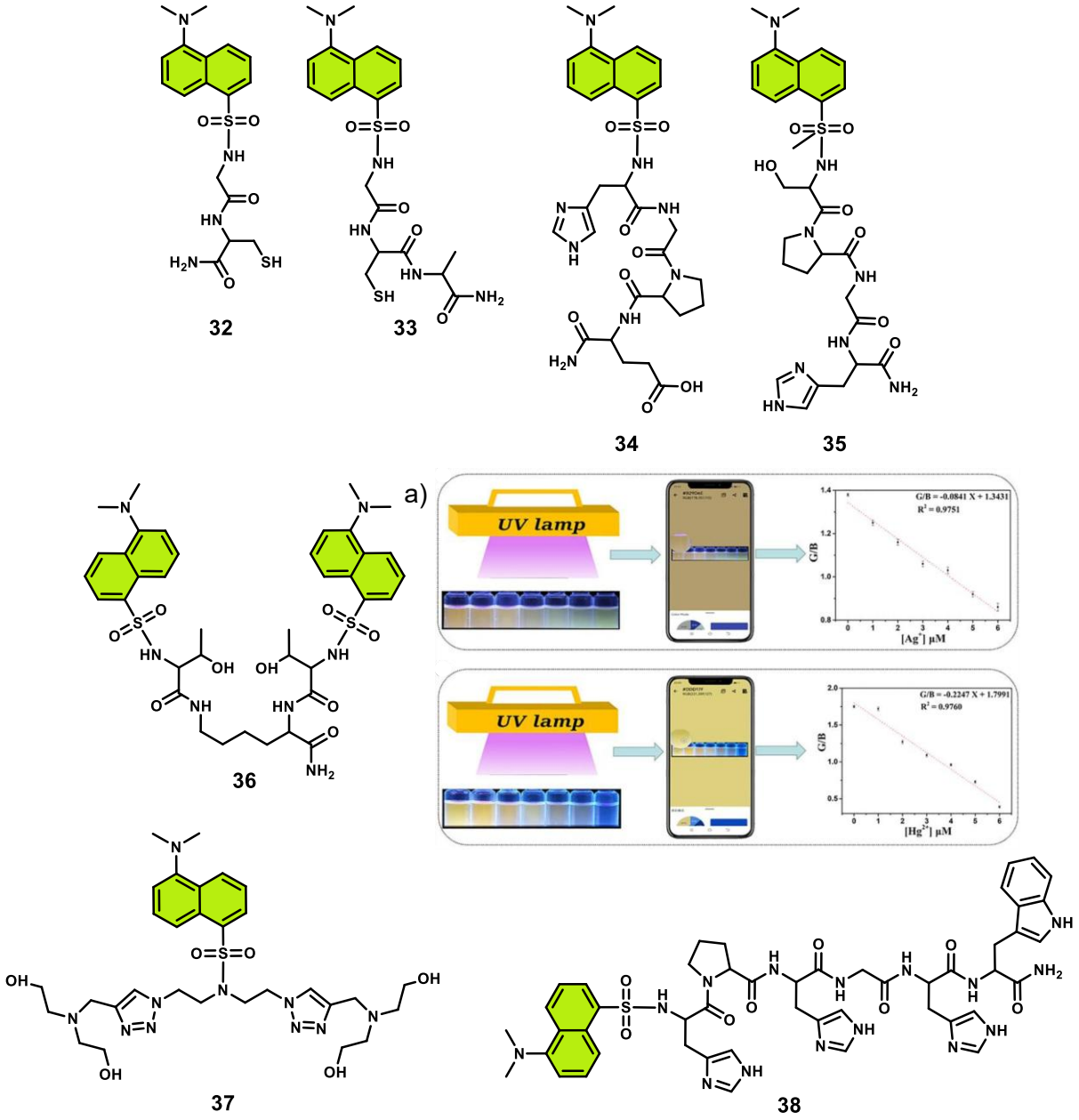


Figure 1–14. Structures of compounds **32**-**38** for the dual detection for several metal ions. a) Smartphone-assisted RGB responses for the recognition of Ag^{+} and Hg^{2+}. Adapted from ref.[124] copyright 2025, Elsevier.

The dansyl unit modified tripeptide **33** (DNS-Gly-Cys-Ala-NH_2, Figure 1–14) acts as a dual sensor exhibiting a fluorescence enhancement by Ag^{+} and fluorescence quenching by Cu^{2+} in HEPES buffer solution (pH 7.4).[121] With an emission maximum at 560 nm, a 6.38-fold enhancement was observed upon addition of Ag^{+} revealing also a blue shift to 520 nm. Compound **33** showed good anti-interference for both metals which assemble in a 1:1 stoichiometric ratio through one -NH of sulfonamide, the -SH group and two O atoms. The optimized detection of Ag^{+} and Cu^{2+} could be done in pH 5 to 11 and 7 to 12 with associated LODs of 7.4 nM and 5.9 nM, respectively. Lifetime measurements revealed an increase from 2.8 ns to

6.9 ns upon complexation with Ag^+ and a static quenching was elucidated for Cu^{2+} giving the almost unchanged fluorescence lifetime upon its addition. Quantum yield experiments demonstrated an increase from 5.98% to 14.80% with the addition of Ag^+. Given these results a logic gate was built where the ON state was present only with Ag^+ input alone. Cytotoxicity studies were carried out with **33** through the MTT assay in SW620 cells (>90% cell viability at 80 μM) while confocal fluorescence images support the capacity of **33** to detect both metals in living cells and zebrafish larvae. Compound **33** was further used for recovery experiments in three real water samples (91.6% to 107.9%), three tea samples (94.5% to 109.5%) and real food samples (92.3% to 107.7%). Finally, semi-quantitative detection of each metal was carried out using a smartphone through color recognition software which provided good linear relationships for Ag^+ (G/B = 0.0357X + 0.9864, R^2 = 0.9944) and Cu^{2+} (G/B = −0.0284 X + 0.9783, R^2 = 0.9954) with accompanying LODs of 0.92 and 1.37 μM.

Probe **34** is assembled by conjugating the dansyl unit with a tetrapeptide (DNS-His-Pro-Gly-Glu-NH_2, Figure 1–14) which manifest a fluorescent "turn on" response to Zn^{2+} and a fluorescence quenching to Cu^{2+} in aqueous solution.[122] In both cases, a blue shift was observed from 545 to 515 nm, with Zn^{2+} inducing an increase of the quantum yield from 0.115 to 0.168, while other metal ions did not induce any meaningful interference. A 2:1 (L:M) stoichiometric ratio was found for both metal ions coordinating by the O atom of Glu and the N atom of His while LOD calculations demonstrated values of 4.9 nM and 15 nM to Zn^{2+} and Cu^{2+}, respectively. The proposed mechanism relates to the initial PeT process arising from the electron-donating ability of the imidazole groups to the dansyl unit, which is suppressed upon coordination with Zn^{2+}. Since the optimal pH values for the detection of both metals were between 7 to 12, intracellular fluorescence imaging began with cytotoxicity experiments in HeLa cells demonstrating a survival rate above 95% up to 160 μM of **34** with confocal microscopy supporting its use for the detection of Zn^{2+} and Cu^{2+} in living cells.

Similar results have been obtained for the dansyl-based tetrapeptide **35** (DNS-Ser-Pro-Gly-His-NH_2, Figure 1–14) which also revealed a "turn-on" behavior Zn^{2+} and a fluorescence quenching for Cu^{2+} in HEPES buffer solution.[123] The increase of fluorescence was associated with a blue shift from 560 to 530 nm due to the blocking of the PeT process initially imposed between the imidazole and the dansyl unit. The 2:1 (L:M) stoichiometry was proposed for both metal ions through the coordination of the hydroxyl group from Ser and imidazole group of His. Both metals could be detected in the pH range of 6 to 12 with the LOD values being 13.2 nM and 4.1 nM for Zn^{2+} and Cu^{2+}, respectively. Cell viability was evaluated through the MTT assay in HK2 cells (88.145% cell viability at 80 μM), HeLa cells (>90% cell viability at 80 μM) and

LNCaP cells (>90% cell viability at 80 μM) while the detection of Zn^{2+} and Cu^{2} by fluorescence imaging was carried out using LNCaP cells suggesting positive results.

Probe **36** integrates two dansyl units into a tripeptide backbone (DNS-Thr-Lys-Thr-DNS, Figure 1–14) which can detect Ag^{+} in a "turn on" manner and Hg^{2+} through fluorescence quenching in aqueous solution.[124] The detection of Ag^{+} is associated with a blue shift in emission from 553 to 531 nm translating into an increase of the quantum yield from 12.25% to 19.94% while the fluorescence lifetime decay saw an increase from 3.67 to 9.12 ns. A static quenching was assigned to Hg^{2+} given the small change in the lifetime of **36** after complexation tested as 3.26 ns. ESI-HRMS and Job's plot suggest a 2:1 (L:M) stoichiometry for both metals through four O atoms of Thr. The underlying LOD values were determined to be 37.1 nM and 26.7 nM for Ag^{+} and Hg^{2+}, respectively. pH dependent studies revealed that **36** has an optimal detection of Ag^{+} between 7 to 12 and 5 to 10 for Hg^{2+}. MTT assays showed biocompatibility of **36** to LLC cells (>80% cell viability at 80 μM) while fluorescence imaging in the same cell line and zebrafish larvae provided the results to demonstrate the detection of Ag^{+} and Hg^{2+} in biological systems. Probe **36** was further used for the recovery detection in water samples (lake, purified and tap water) ranging from 97.6% and 107.6% and four food samples (green, black and jasmine tea and watermelon juice) which saw recoveries from 90.6% to 106.8%. Lastly, with the aid of a Color Recognizer application good linear relationships were obtained (Figure 1–14a) regarding the concentration of Ag^{+} (G/B= 0.0841X + 1.3431, R^{2}=0.9751) and Hg^{2+} (G/B= 0.2247X + 1.7991, R^{2}=0.9760) achieving LOD values of 0.37 μM and 0.21 μM, respectively.

Anand *et al.* reported probe **37** (Figure 1–14), a dansyl-based molecule with four hydroxy groups and two triazole units with a versatile tertiary amine center.[125] In aqueous solution, compound **37**, with a quantum yield of 0.3182, displayed a fluorescence quenching at 510 nm for Ag^{+} and Pb^{2+}. Additionally, the introduction of Ag^{+} causes a colorimetric response to the naked eye from clear to brownish-yellow color accompanied by the emergence of a peak at 448 nm. The LOD values were found to be 38.5 nM and 57.7 nM for Ag^{+} and Pb^{2+}, respectively, within the optimal range of pH 4 to 7. Lifetime measurements revealed that the addition of both metals did not cause the average lifetime (13 ns) to change, signifying that the binding mechanism is of static nature. Finally, compound **37** was successfully implemented in Whatman filter paper strips and for the detection of both metals in real water samples reaching a removal capacity of 98.40% and 76.20% for Ag^{+} and Pb^{2+}, respectively.

Notomista's group synthesized the peptide DNS-His-Pro-His-Gly-His-Trp-NH_2 (**38**, Figure 1–14) that exhibited a "turn-on" effect to Zn^{2+} and a strong quenching for Cu^{2+}.[126] Excitation at 295 nm revealed two peaks at 370 nm and 527 nm attributed to the indole ring and

the dansyl unit. Upon the addition of Zn^{2+} the peak at 370 nm decreased while the peak at 527 nm increased and shifted to 515 nm, suggesting a FRET effect. It was found that the peptide binds to Zn^{2+} in a 2:1 stoichiometry promoting an increase in the quantum yield from 0.04983 to 0.1933. Interference studies revealed that Ni^{2+} and Co^{2+} were able to displace Zn^{2+} to some degree with Cu^{2+} totally quenching the emission indicating a higher affinity for dH3w. In this case Cu^{2+} promotes a 1:1 stoichiometric ratio. The determined LOD values were 5.2 nM and 5.5 nM for Zn^{2+} and Cu^{2+}, respectively, within the optimal pH of 7. Finally, peptide **38** was used for the staining of HeLa cells which did not show negative effects in cell viability up to 50 μM.

Our contribution to the detection of metal ions and the design of new applications using dansyl compounds was accomplished through compounds **39** to **50** (Figure 1–15).[127–131] Compounds **39** to **45** were designed to compare the influence of a disulfide group versus a single sulfur bridge on metal ion detection, while also examining the effect of different spacers or direct linkage, as seen in compounds **39** and **40**, as well as the presence of a more complex system, such as the thiophene-based compound **45**. Compounds **46** and **47** are examples of tetradansylated compounds bearing cyclen and cyclam cores which provide higher molar absorptivity and signal (Figure 1–15a) while the implementation of different alkyl side chains may modulate physical properties seen in compounds **48** to **50**.

The photophysical properties of each compound were studied in a diverse set of solvents to elucidate the solvatochromic behavior using the Kamlet-Taft equation to quantitatively characterize the solute-solvent interactions. Given the low solubility in water, aggregation studies were performed using THF or acetonitrile with different water fractions providing insights into the modulation of the emission culminating in the presence of AIE in high water content. The presence of aggregates was supported by DLS measurements and the enhanced emission properties were subject to quantum yield and fluorescence lifetime experiments. Except for compound **39**, which was non-emissive due to a disulfide bridge directly attached to the dansyl unit, and compound **45**, whose high structural rigidity precluded its use as a sensor, all derivatives reliably detected Cu^{2+} and Hg^{2+} through a "turn off" response in acetonitrile. Table 1-3 gathers the association constants considering the 1:1 stoichiometry alongside the limit of detection for comparison of compounds **40** to **48**.

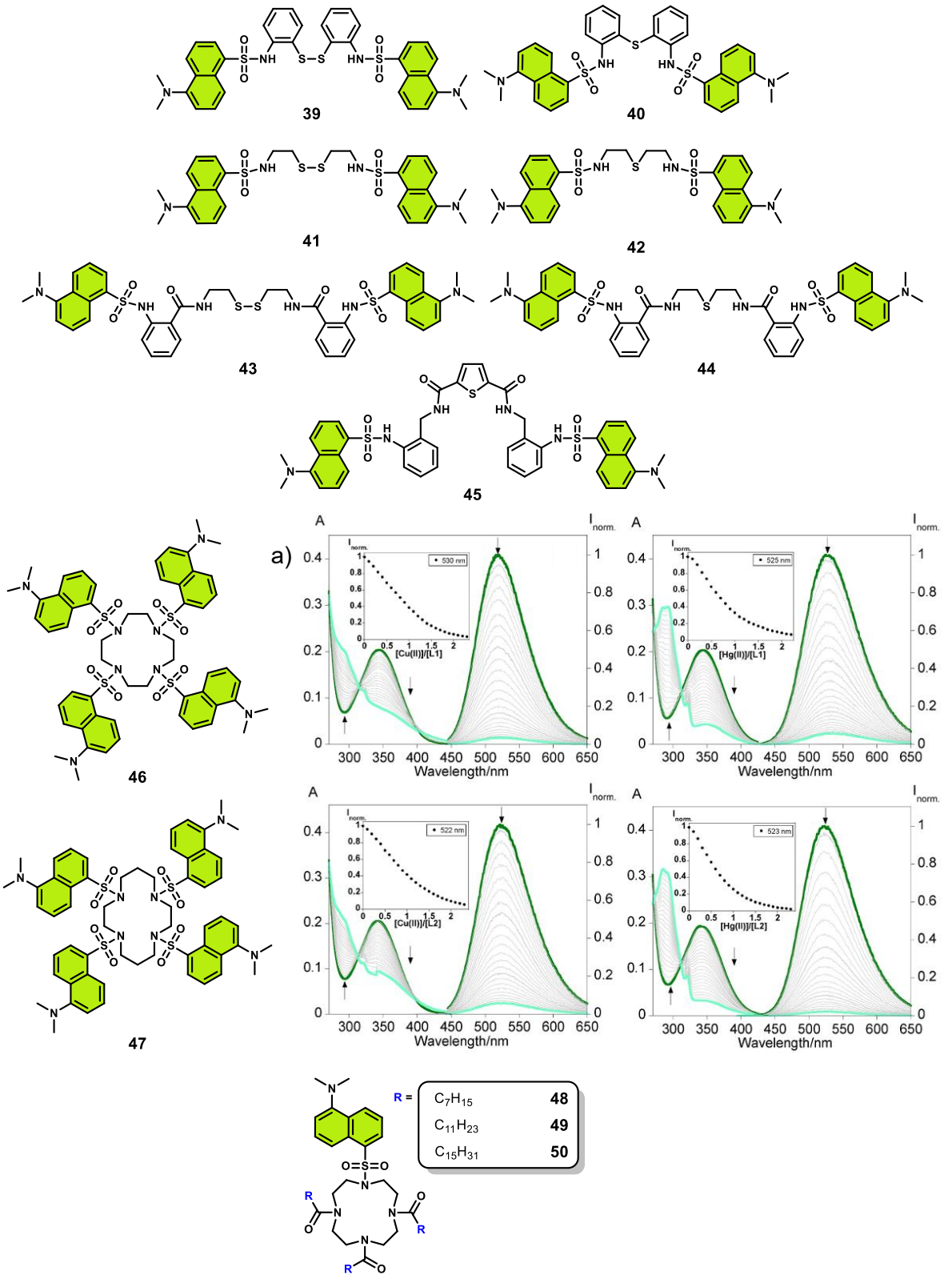


Figure 1–15. Structures of compounds **39**-**50** for the dual detection of Cu^{2+} and Hg^{2+}. a) Spectrophotometric and spectrofluorimetric titrations of compounds **46** and **47** with increased additions of Cu^{2+} and Hg^{2+} in acetonitrile. The inset represents the emission as a function of the number of equivalents of metal. Adapted from ref.[130] copyright 2024, Elsevier.

Table 1-3. Comparison of dansyl-based compounds reported by us for the detection of Cu^{2+} and Hg^{2+} in acetonitrile.

Compound	Metal ion	$LogK_{ass}$	LOD (nM)	Ref
40	Cu^{2+}	5.73 ± 0.01	4.0	[127]
	Hg^{2+}	5.80 ± 0.02	2.0	
41	Cu^{2+}	4.59 ± 0.01	6.0	[128]
	Hg^{2+}	6.38 ± 0.06	2.5	
42	Cu^{2+}	5.00 ± 0.04	6.0	[129]
	Hg^{2+}	6.38 ± 0.02	4.0	
43	Cu^{2+}	5.11 ± 0.06	7.5	[128]
	Hg^{2+}	5.00 ± 0.01	8.0	
44	Cu^{2+}	4.82 ± 0.03	6.0	[129]
	Hg^{2+}	5.29 ± 0.06	7.0	
46	Cu^{2+}	5.613 ± 0.002	2.9	[130]
	Hg^{2+}	5.104 ± 0.002	3.5	
47	Cu^{2+}	5.870 ± 0.003	2.8	[130]
	Hg^{2+}	5.047 ± 0.002	2.0	
48	Cu^{2+}	4.73 ± 0.01	2.0	[131]
	Hg^{2+}	3.10 ± 0.01	40	

Furthermore, integration of these compounds in polymeric thin films revealed the possibility to construct materials with tunable emission since depending on the polymer used the resulting thin film would acquire a different emission peak. The obtained materials were then applied for the development of temperature smart materials exhibiting good linearity in a wide range of temperatures. Finally, compound **43** was used for the synthesis of polymeric microparticles using styrene-butadiene-styrene polymer through an oil-in-water approach as a method to avoid solubility restrictions while **50** was found useful to stabilize platinum microparticles employing ethanol as the reducing agent.

1.2.5 Dansyl-based Fluorescent Probes for Detection of Anions

1.2.5.1 Fluorescent Probes for F^- and CN^- Detection

Fluoride is an essential anion that contributes significantly to both human health and environmental systems. It is widely recognized for its role in preventing dental cavities and reinforcing tooth enamel, and it has also been used in the treatment of bone-related conditions such as osteoporosis.[132,133] Nevertheless, an excess of fluoride in the body can lead to serious health issues, including dental and skeletal fluorosis. Beyond human health, fluoride contamination in natural water sources is a growing environmental concern, as it can accumulate through the food chain and threaten ecosystem stability. To safeguard public health, the WHO has set a maximum allowable concentration of 1.5 mg L^{-1} fluoride in drinking water.[132,133]

Cyanide is another anion of critical environmental and biological importance, but unlike fluoride, it is highly toxic even at trace levels. Cyanide binds strongly to the iron center in cytochrome oxidase, a key enzyme in cellular respiration, leading to severe disruption of metabolic processes and often resulting in fatal outcomes.[134,135] The lethal dose for humans is reported to be around 0.5–3.5 mg per kilogram of body weight, and its concentration in drinking water is recommended by WHO to remain below 2 μM (42 ppb).[134,135] Despite these hazards, cyanide continues to be used extensively in various industrial applications such as electroplating, metal extraction, and the synthesis of organic compounds and polymers.

Although fluoride and cyanide differ greatly in their biological effects, they share similar chemical characteristics, including high basicity and strong affinity for Lewis acidic centers.[136,137] This section focuses on recent progress in the use of dansyl derivatives for the detection of fluoride and cyanide ions, summarizing key design strategies, sensing mechanisms, and analytical performance reported in the literature.

Ajay Jayaprakash *et al.* have reported a mono and bidentate dansyl-triazine ligands **51** and **52** (Figure 1–16) for fluoride sensing.[132] In DMSO, when excited at 326 nm, an emission peak was observed for **51** at 481 nm with a quantum yield of 0.4 and at 462 nm for **52** with a quantum yield of 0.22. The screening of various anions revealed a fluorescence enhancement in the presence of fluoride while no interference was detected from the other anions. The calculated limit of detection sets a difference between **51** (1.31 μM) and **52** (293.6 nM) due to the presence of two sulfonamide groups in **52**. Lifetime measurements showed that the initial lifetime of **51** (3.56 ns) remained the same after addition of fluoride while for **52** an increase from 1.65 ns to 6.23 ns was registered. These differences were explained by DFT calculations which concluded that the charge densities of the HOMO and LUMO in **51** were on the dansyl while

for **52** the LUMO was in the triazine moiety, an indication of an intra-molecular charge transfer. Both compounds were tested in deionized water while **52** was further tested in lake, pond and tap water due to the superior enhancement of fluorescence in comparison with **51**. Finally, a simple optical detection using Whatman filter paper was performed to illustrate the potential use of these compounds towards fluoride sensing.

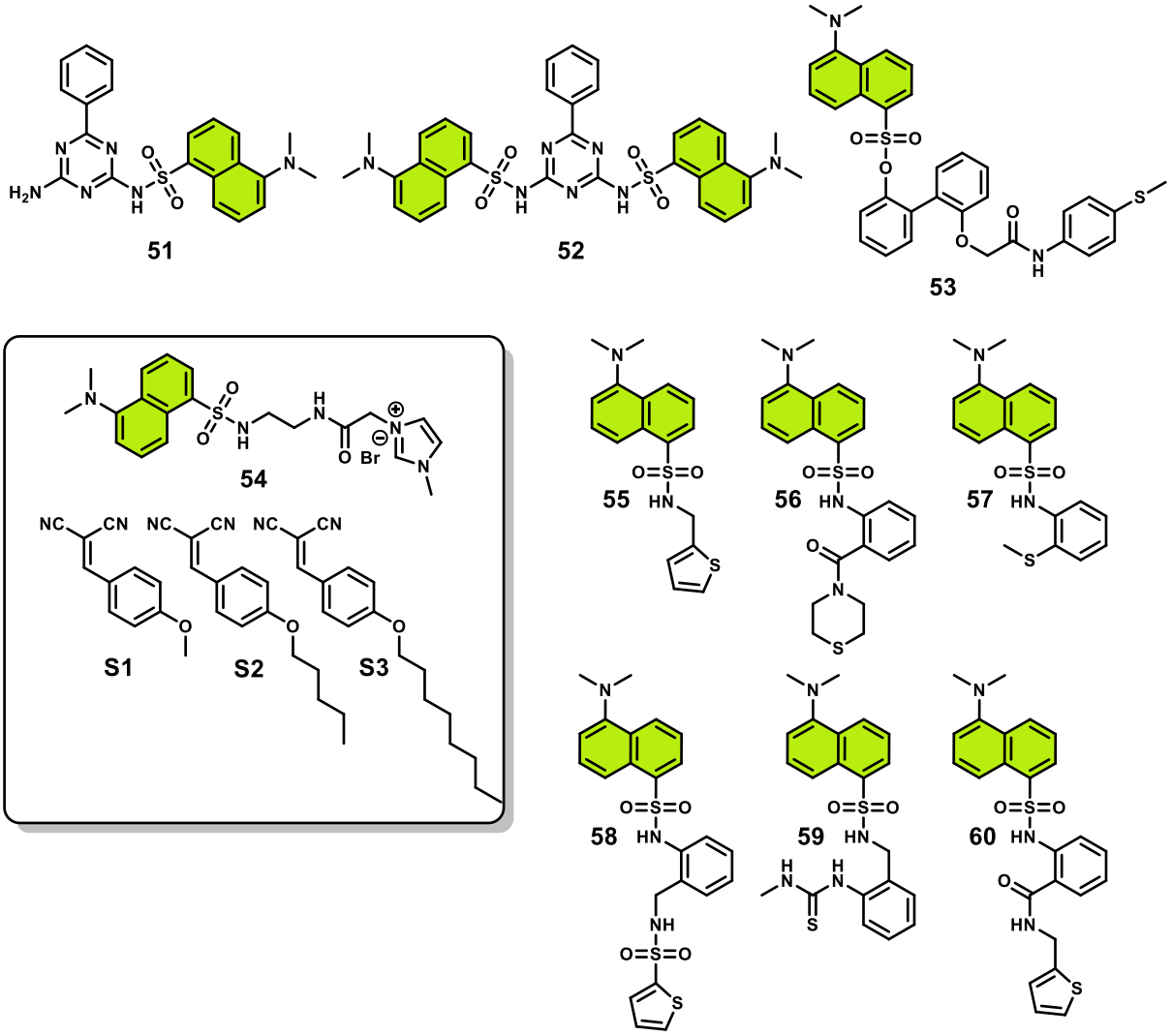


Figure 1–16. Structures of compounds **51**-**60** for the detection of F^- and CN^-.

Wannalerse's group designed compound **53** (Figure 1–16), a biphenolic-dansyl derivative for the specific detection of fluoride in DMSO.[133] The initial absorbance at 360 nm is decreased while a new peak at 300 nm emerges upon addition of fluoride with no relevant changes when other anions are introduced. This selective response toward fluoride was also evident from a distinct color change from yellow to colorless. The fluorescence response saw an increase of the 434 nm band accompanied by a decrease of the band located at 564 nm with a change of color from orange-yellow to blue. The detection limit for **53** was found to be

18 μM. Finally, a rapid detection of fluoride was demonstrated by emerging **53** in TLC plate and filter paper providing a colorimetric response at 0.05 M of fluoride.

Jeong *et al.* report an imidazolium-bearing, methyl-imidazolium-linked dansyl probe **54** (Figure 1–16) paired with three para-alkoxy benzylidene-malononitrile substrates (S1-S3) to form binary ensembles (**54**S1-**54**S3) for selective "turn-on" fluorescence detection of cyanide.[135] Under optimized conditions (HEPES:DMSO 2:8, pH 7.4, probe 1 = 5 μM, substrate = 300 μM, excitation 350 nm), the **54** ensembles exhibit large CN^--triggered emission at 525 nm with excellent selectivity over a panel of anions showing negligible interference. Mechanistically, CN^- undergoes rapid nucleophilic 1,4-addition to the dicyano-vinyl substrates to give anionic amphiphiles that electrostatically associate with the cationic dansyl probe and drive supramolecular self-assembly. The incorporation of the dansyl unit into the hydrophobic assembly interior causes the emission "turn-on." Dynamic light scattering and TEM confirm assembly growth from small species (3-10 nm) to aggregates of a few $\times 10^2$ nm after CN^- addition, consistent with the assembly-driven emission increase. Quantitatively, the octyl-bearing ensemble **54**S1 shows the highest sensitivity and affinity and the lowest limit of detection (200 nM) reaches fluorescence saturation at 120 μM of CN^-. Shorter alkyl chains lower the performance; **54**S2 (pentyl) LOD: 1 μM (saturation 190 μM); **54**S3 (methyl); LOD: 2 μM (saturation 350 μM). Quantum yields rise dramatically upon CN^- addition (**54**S1 from 0.093 to 0.54; **54**S2 0.035 to 0.51; **54**S3 0.043 to 0.71), illustrating the large photophysical gain driven by assembly and hydrophobic sequestration of the dansyl fluorophore. The authors stress the importance of long lipophilic pendants in lowering the critical assembly concentration of the anionic adduct and thereby improving sensitivity and that the **54**S1 LOD (0.2 μM) is an order of magnitude below the WHO drinking-water guideline (2 μM).

Our group reported six structurally diverse dansyl-derived fluorescent probes (**55** to **60**, Figure 1–16) for the optical recognition of hazardous cyanide and fluoride ions in organic media via a deprotonation-driven sensing mechanism.[134] The ligands were synthesized and characterized previously in multiple solvents for the detection of Cu^{2+} and Hg^{2+}.[138] All six derivatives exhibited a selective fluorescence "turn-off" response upon exposure to CN^- and/or F^-, with no response to Br^- or Cl^-. The most responsive compound, **58** displayed the lowest limits of detection of 2 μM (CN^-) and 4 μM (F^-). All complexes exhibited a 1:1 ligand–anion stoichiometry, confirmed by both spectroscopic and mass-spectrometric data. Among the six ligands, **55** responded exclusively to F^-, attributed to a single N-H donor site, while **58** to **60**, possessing two or more NH groups and flexible methylene linkers, exhibited higher affinities due to enhanced hydrogen-bonding and base-induced deprotonation. Collectively, the series

demonstrated sensing behavior through a fluorescence turn-off mechanism based on proton abstraction rather than covalent modification.

1.2.5.2 Fluorescent Probes for HSO_3^-/SO_3^{2-} Detection

Sulfur dioxide (SO_2) is one of the main atmospheric pollutants and exists in aqueous environments as sulfite (SO_3^{2-}) and bisulfite (HSO_3^-) ions.[139,140] Inside living systems, SO_2 can also be formed enzymatically in the cytosol and mitochondria during the breakdown of sulfur-containing amino acids. Similar to nitric oxide, it has been identified as a gaseous messenger involved in the control of vascular tone and blood pressure.[139] Although SO_2 may act as an antioxidant, its precise biological roles are still not clearly defined, largely because of the difficulty in detecting it at the cellular level. In addition to its biological relevance, SO_2 derivatives are commonly used as preservatives in foods and beverages.[141,142] While effective in preventing oxidation and microbial growth, an excessive amount of these species can cause respiratory problems, hypotension, allergic reactions, and neurological effects.[141,142] For these reasons, reliable and straightforward methods to monitor bisulfite and sulfite ions are needed in both biological and environmental samples.

In order to further improve the detection methods towards sulfur dioxide derivatives, Zhao's group developed compounds **61** to **64** (Figure 1–17) based on a FRET mechanism.[139,141–143] Compound **61** incorporates a dansyl fluorophore as the energy donor and a hemicyanine chromophore as the acceptor.[139] Notably, the donor's emission band exhibits complete spectral overlap with the acceptor's absorption band, facilitating efficient energy transfer. The response towards HSO_3^-/SO_3^{2-} was investigated in PBS (pH = 7.4, containing 30% DMF) that upon addition of $NaHSO_3$ the initial red solution with an emission peak at 582 nm changed to a green emission at 530 nm. The optimal pH range was found to be between 6 and 8.3 while the calculated limit of detection was 0.1 μM. Furthermore, HRMS suggest the formation of 1:1 product through 1,4-addition confirmed by NMR. The calculated 95% efficiency of the energy transfer from the dansyl to the hemicyanine would be interrupted by the addition of $NaHSO_3$ leading to the recovery of emission of the dansyl unit. Compound **61** was implemented in cell imaging using HeLa cells which showed low cytotoxicity in the range 1-10 μM and a 0.94 colocalization coefficient (Pearson's coefficient) between **61** Mito Tracker Deep Red in mitochondria. Finally, **61** was used to detect endogenous bisulfite in HepG2 cells (human liver cancer cells) and L-02 cells (human normal liver cells) being able to differentiate between the two cell lines based on the different endogenous bisulfite levels.

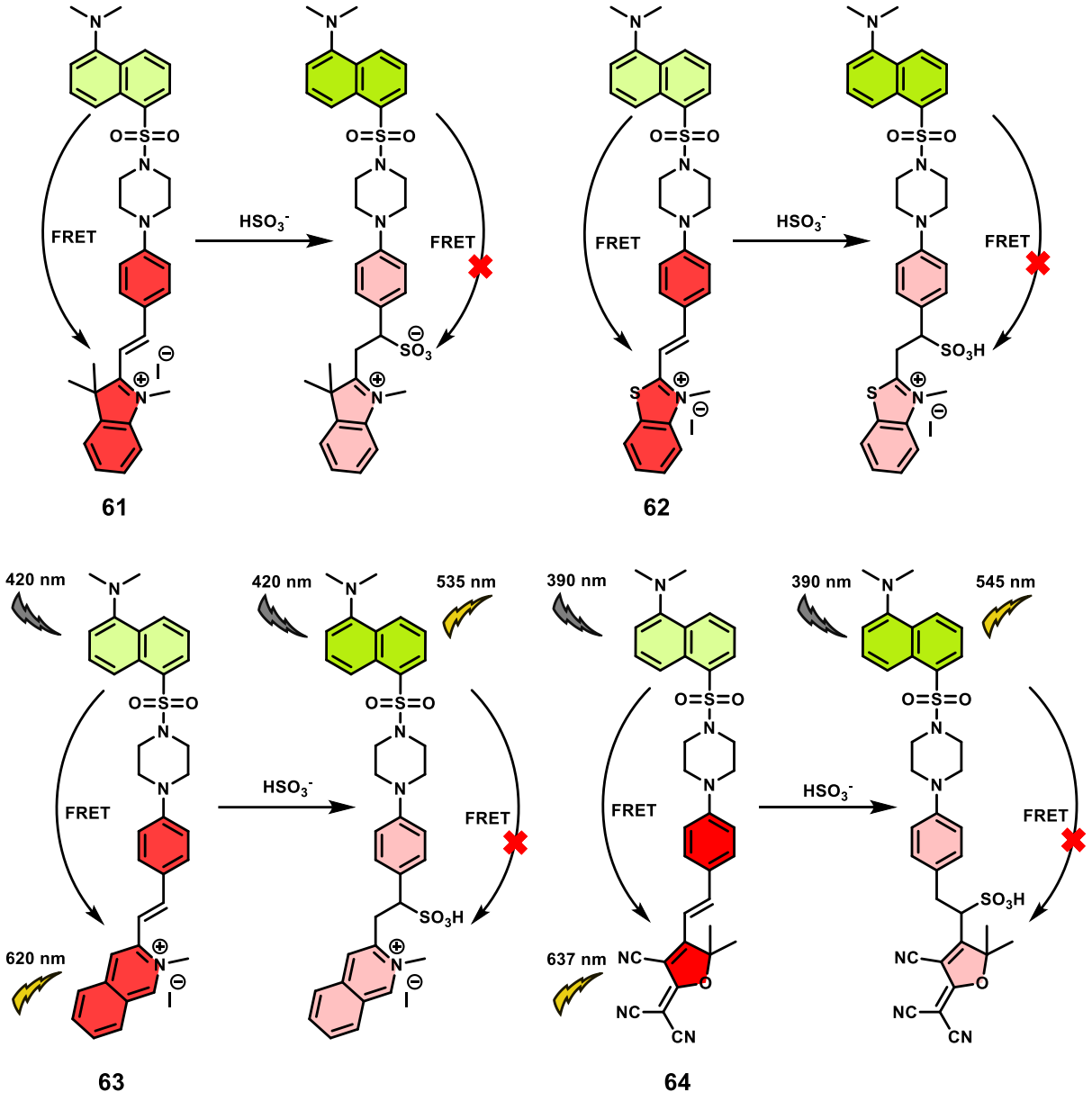


Figure 1–17. Structures of compounds **61**-**64** and proposed detection mechanisms for HSO_3^-/SO_3^{2-}.

The dansyl-piperazine-benzothiazolium conjugate **62** (Figure 1–17) was investigated in DMSO and PBS (5:5) although it keeps stable detection towards bisulfite in the pH range of 5 to 11.[141] The initial emission at 590 nm while exciting at 390 nm, would be interrupted upon addition of bisulfite restoring the dansyl's emission at 540 nm with an isosbestic point at 565 nm. Given the presence of FRET mechanism efforts revealed an intramolecular energy transfer efficiency of 74.3%. Additionally, the calculated limit of detection was found to be 69 nM towards bisulfite being unaffected by other biological relevant analytes. Implementation of **62** in test strips saw the gradual change of the fluorescence from orange to blue with increasing concentrations of bisulfite. Furthermore, realistic samples were tested such as tap water and

dry white wine showing comparable results as with PBS buffer system. Cytotoxicity tests in HeLa cells showed low toxicity until 10 μM of **62** while a co-localization assay using Mito Tracker Deep Red revealed a coefficient of 0.91. Probe **62** was also able to differentiate HepG2 cells from L-02 cells based on bisulfite levels.

Introduction of a quinolinium moiety yielded compound **63** (Figure 1–17) which displays red fluorescence with an emission peak at 620 nm.[143] The addition of bisulfite gradually displaces the emission revealing a new peak at 535 nm disrupting the FRET pathway due to the Michael addition reaction of bisulfite and conjugated carbon double bond. The calculated detection limit was determined as 5.15 μM in the optimal pH range of 6 to 9. Additionally, the intramolecular energy efficiency was found to be 83% between the dansyl and the quinolinium moiety. Application of **63** for the determination of bisulfite in tap and spring water spiked samples yielded a recovery between 90.86% to 110.20%. Moreover, the cytotoxicity of **63** was evaluated in HUVEC and HepG2 cells suggesting biocompatibility while the induced production of endogenous bisulfite in HUVEC cells confirmed the ability of compound **63** to detect bisulfite in living cells. In contrast with previous examples this compound lacked the ability to localize organelles.

Probe **64** (Figure 1–17) was designed by covalently linking the dansyl unit with trimethyl furan-ylidene malononitrile and its ability to sense bisulfite was evaluated in EtOH-PBS (5:5, pH 6.5).[142] The addition of bisulfite causes the emission peak at 637 nm to decrease and gives rise to a new band with a peak at 545 nm. In the absorption spectrum, the peak at 557 nm continuously decreases, while the band at 334 nm increases. The detection limit was determined to be 66 nM, and the FRET process was calculated to have an efficiency of 0.91. Compound **64** was used towards cell imaging with experiments revealing negligible cytotoxicity up to 10 μM in HeLa cells. Colocalization assay showed a 0.93 coefficient with the neutral lipid dye Invitrogen indicating that **64** could target lipid droplets. Finally, the detection of endogenous bisulfite was validated in HepG2 cells.

1.2.6 Dansyl-based Fluorescent Probes for Detection of Small Molecules

1.2.6.1 Fluorescent Probes for H_2S Detection

Hydrogen sulfide (H_2S) is a highly toxic gas that originates from numerous industrial sources, including the manufacture of sulfuric acid, dyes, and cosmetics, as well as from microbial degradation of sulfur-containing materials.[144–146] Extended exposure to this compound can cause serious health problems such as respiratory paralysis and lasting brain

damage.[146] Beyond its toxic nature, H_2S functions as an endogenous signaling molecule involved in the regulation of the cardiovascular, nervous, and immune systems.[68,71,146] Abnormal fluctuations in its concentration have been associated with several disorders, including diabetes, Alzheimer's disease, and Down syndrome.[68,146] Both hydrogen sulfide and its ionic form (S^{2-}) play significant biological and environmental roles, yet elevated levels of these species can pose serious risks to living organisms and ecological systems.[62,66,68] In addition, H_2S is one of the main volatile compounds released during food spoilage, serving as an indicator of food freshness.[66,71] Considering its dual nature as a vital biomolecule and a harmful pollutant, the ability to detect H_2S with high selectivity, sensitivity, and speed is essential for applications in environmental monitoring, biological research, and food quality assessment.[62,66,68,71,146]

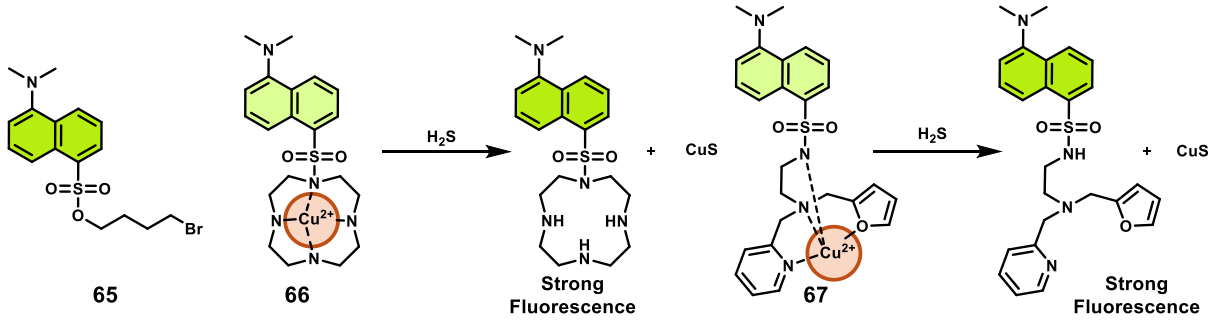


Figure 1–18. Structures of compounds **65**-**67** and proposed detection mechanisms for H_2S.

Fan and co-workers designed a FRET-based ratiometric sensor composed of a dansyl derivative (**65**, donor) and pyronine Y (PyY, acceptor) within CTAB micelles (Figure 1–18).[147] Upon excitation at 345 nm, **65** emitted at 528 nm and PyY at 569 nm. Introduction of H_2S in PBS disrupted the FRET process through nucleophilic reaction with PyY, leading to decreased PyY emission and enhanced **65**'s emission, accompanied by a visible color change from orange to blue-green. The limit of detection calculated for this system is 110 nM while the energy transfer efficiency was determined to be 23%. The sensor demonstrated high selectivity while analytes such as Cys, Hcy, and GSH caused a decrease of fluorescence enhancement. Finally, the system has been applied for the detection of H_2S in biofluids such as serum where in spiked samples saw a recovery between 98.9% and 102%.

Kim and co-workers synthesized a dansyl based Cu(II) complex **66** (Figure 1–18) bearing cyclen designed to detect hydrogen sulfide in hypoxic environments.[148] The fluorescence of **66** (excitation at 319 nm, emission at 491 nm) was quenched by Cu^{2+} and recovered in the presence of H_2S through CuS precipitation. The system exhibited a limit of detection of 4.07 μM and a fluorescence enhancement factor of approximately 60-fold. The probe showed

negligible response towards different bioanalytes except H_2S. The fluorescence quantum yield increased from 0.04 to 0.52 after H_2S treatment. The optimal response occurred at pH 7 to 9. MTT assays (HeLa and EMT6 cells) revealed cell viability above 80% after 24 h incubation with up to 25 μM of the probe. Fluorescence imaging confirmed the ability for the probe to detect exogenous/endogenous H_2S under pathophysiological or hypoxic conditions.

Yan *et al.* prepared a dansyl-Cu(II) complex **67** (Figure 1–18) acting as a "turn-on" fluorescent probe for H_2S detection based on Cu-S displacement.[146] Probe **67** complex exhibited a weak baseline emission at 534 nm, which intensified significantly upon reaction with S^{2-} to release the fluorescent dansyl ligand. The emission intensity increased linearly over 0.125–1.375 mM Na_2S, with a calculated LOD of 11 nM and showing no interference from other anions. The reusability of **67** for the alternate detection of S^{2-} and Cu^{2+} over four cycles promoted the construction of an optical logic gate. The probe successfully quantified H_2S in real water samples (lake and mineral water) with recoveries ranging from 98.2% to 102.3% and relative errors below 5%. The probe was also integrated into portable detector vials, producing a visible fluorescence switch under UV light at 365 nm upon exposure to H_2S gas concentrations as low as 0.5 ppm.

Several of the previously discussed dansyl-based systems originally developed for metal ion sensing, particularly Cu^{2+} and Hg^{2+}, have also been employed for hydrogen sulfide detection. In these cases, H_2S recognition was achieved through metal-sulfide interactions, where the formation of insoluble metal sulfides or metal displacement reactions led to distinct fluorescence changes. To illustrate this dual functionality, these studies have been summarized in Table 1-4, emphasizing their limits of detection, sensing mechanisms, and demonstrated applications across environmental and biological matrices.

Table 1-4. Comparison of dansyl-based compounds previously discussed in this work for the detection of Cu^{2+} and Hg^{2+} that further applied for the sensing of H_2S.

Compound	LOD (nM)	pH range	Fluorescence response	Application	Ref
3-Cu^{2+}	6.1 x 10^3	N. A.	Turn on	Bioimaging (HeLa cells)	[62]
DAH-Cu^{2+}	72.6	6-11	Turn on	Test strips; Bioimaging (RM-1 cells and zebrafish larvae); Real water samples (lake, purified, tap water); Pork and chicken meat samples; Visual detection via smartphone app (LOD = 0.62 nM)	[66]
DAHK-Cu^{2+}	47.3	4-12	Turn on	Test strips; Bioimaging (RKO cells); Real water samples (lake, tap water);	[68]
DGGH-Cu^{2+}	13.7	6-12	Turn on	Bioimaging (LNcap cells)	[69]
DP5-Cu^{2+}	17.2	6-12	Turn on	Bioimaging (H2K and Bladder cancer cells)	[71]
P-Cu^{2+}	57	5-12	Turn on	Bioimaging (HeLa cells and zebrafish larvae)	[72]
DKA-Hg^{2+}	12.9	5-10	Turn off	Bioimaging (Hacat cells); Visual detection via smartphone app (LOD = 0.98 μM)	[79]
DWPH-Hg^{2+}	23.3	7-11	Turn off	Bioimaging (HGC-27 cells and zebrafish larvae); Visual detection via smartphone app (LOD = 0.32 μM)	[80]
DGRK-Hg^{2+}	60.9	6-12	Turn on	Test strips; Bioimaging (RKO and GES-1 cells); Visual detection via smartphone app (LOD = 0.23 μM)	[83]
KEEP- Hg^{2+}	87	6-12	Turn on	Bioimaging (HeLa cells)	[86]
2**(30)**-Ag^{+}	74.0	5-10	Turn off	Bioimaging (HeLa cells)	[113]

1.2.6.2 Fluorescent Probes for NO and HNO Detection

Nitroxyl (HNO), the one-electron reduced and protonated analogue of nitric oxide (NO), exhibits unique chemical and biological behaviors distinct from NO.[149,150] While NO plays vital roles in vascular regulation, neurotransmission, and immune response[151–153], HNO demonstrates promising pharmacological effects such as vasoprotection and enhanced cardiac contractility.[149,154] However, its instability and rapid dimerization make detection in biological systems challenging.[150] Fluorescence-based sensing, particularly with transition metal–based probes, offers high sensitivity and selectivity for reactive nitrogen species.[151] Among these, Cu(II)-centered systems show fluorescence enhancement through reductive nitrosylation, enabling potential differentiation between NO and HNO.[149,151]

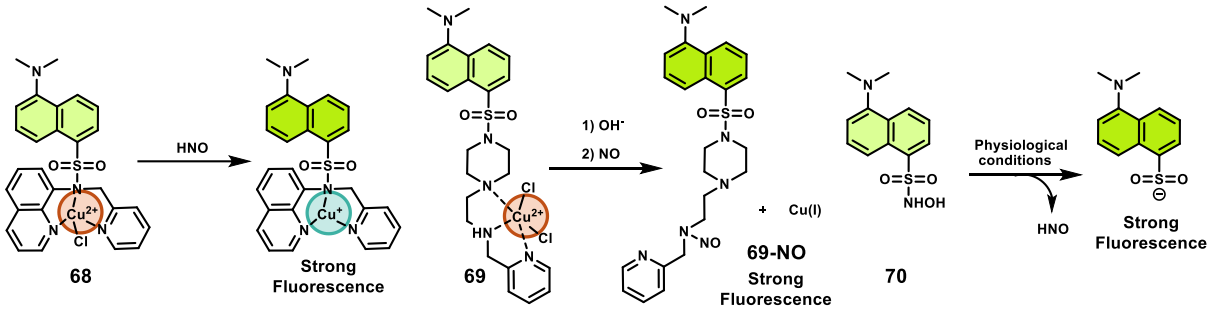


Figure 1–19. Structures of compounds **68**-**70** and proposed detection mechanisms for NO and HNO.

Debjani Maiti *et al.* reported a dansyl Cu(II) complex (**68,** Figure 1–19) bearing 8-amino-quinoline and methyl pyridine as a selective fluorescent probe for HNO detection.[149] The ligand has a limit of detection towards Cu^{2+} of 0.091 μM, which after complexation has an absorption at 370 nm and quenched fluorescence near 543 nm due to PET from the dansyl fluorophore to the paramagnetic Cu^{2+} center. In MeCN/HEPES buffer (8:2, v/v), the complex was screened against reactive oxygen, nitrogen and sulphur species being only HNO able to induce an increase in fluorescence setting a contrast against its related biological species NO. Upon reaction with HNO, delivered via Angeli's salt, the complex undergoes Cu^{2+} to Cu^{+} reduction, suppressing PET and generating a strong fluorescence "turn-on" response with an associated detection limit of 0.41 μM between pH 4 to 10. The sensing mechanism was supported by EPR spectroscopy, which showed attenuation of the Cu^{2+} signal upon HNO treatment, and ESI-MS, which detected the corresponding Cu^{+} species. The system was applied for cell imaging showing more than 80% cell viability at 10 μM in HepG2 cells and the sensing of HNO was validated in the same cell line.

Muthusamy and colleagues reported a Cu(II) complex (**69**, Figure 1–19) based on a N3-tridentate ligand bearing a dansyl fluorophore, designed for selective NO detection via a pH-gated reductive nitrosylation mechanism.[151] The free ligand is strongly fluorescent (f = 59 %) but upon coordination with Cu^{2+}, fluorescence is quenched by over 96 %, consistent with PET process. In neutral or acidic buffers, **69** shows no significant response to NO, but under alkaline conditions (pH ≥ 9), NO triggers reductive nitrosylation: Cu^{2+} is reduced to Cu^{+}, and the ligand undergoes nitrosylation (**69** to **69**-NO). These changes suppress quenching and restore dansyl emission, producing a clear fluorescence "turn-on" response. Under these optimized conditions (methanol and CHES-H_2O buffer at pH ≥ 9), the probe exhibits a limit of detection of 1 nM and high selectivity over other reactive nitrogen/oxygen species. To probe mechanistic details, a secund complex not bearing the dansyl unit was prepared bearing two distinct -NH. After the addition of NO under pH ≥ 9, the secund complex undergoes

mono-N-nitrosylation of the amine coordinated to Cu, resulting in Cu^{2+} to Cu^{+} reduction, thereby confirming the importance of the secondary amine site and the base-catalyzed nitrosylation pathway in achieving the fluorescent response.

Guo *et al.* reported probe **70** (Figure 1–19), a novel HNO donor integrating a dansyl fluorophore within a Piloty's acid framework.[150] Compound **70** represents the first fluorescence HNO donor that simultaneously generates a bright fluorescence turn-on response upon HNO release. Under physiological conditions (0.10 M phosphate buffer, pH 7.4, 95:5 v/v H_2O/MeCN, 37 °C), **70** decomposed with isosbestic points at 243, 276, and 331 nm, following first-order kinetics (k_{obs} = 3.49 × 10^{-2} min^{-1}, $t_{½}$= 19.86 min). At 25 °C, the decomposition slowed significantly (k_{obs} = 6.12 × 10^{-3} min^{-1}, $t_{½}$ = 113 min), and pH-dependent studies gave a pK_a = 9.21, indicating that it can easily deprotonate near physiological pH. HNO release was confirmed via two independent assays. Reaction of **70** with hydroxycobalamin produced nitroxylcobalamin with a characteristic color change and isosbestic points at 338, 371, and 498 nm. The conversion followed first-order kinetics (k_{obs} = 2.54 × 10^{-1} min^{-1}, $t_{½}$ = 2.73 min) and demonstrated a 1:1 stoichiometry. A complementary ^{31}P NMR experiment employing methyl-2-diphenyl phosphinoterephthalate confirmed stoichiometric HNO formation, yielding phosphine oxide and phosphine amide in an approximate 1:1 ratio. Fluorescence monitoring revealed that intact **70** exhibited weak emission, which increased 88-fold upon complete decomposition, producing a bright blue fluorescence centered at 491 nm. The fluorescent quantum yield of the decomposed product was 0.83. Fluorescence intensity correlated linearly allowing quantitative estimation of HNO concentrations with a detection limit of 0.55 μM. HNO release rates were pH dependent, with the response time decreasing from 56.2 seconds at pH 7.4 to 1.4 seconds above pH 10, while the fluorescence output remained pH independent. Fluorescence imaging in HD11 macrophages demonstrated the biological applicability of **70**. Cells treated with **70** (50 μM, 12 h, 37 °C) displayed strong intracellular blue fluorescence, while untreated controls showed negligible emission, confirming that **70** is cell-permeable and capable of releasing HNO in living systems. Unlike traditional HNO probes, which detect pre-existing HNO, this system self-reports the kinetics release, integrating donor function and fluorescence readout. It shifts the goal from passive detection to active, real-time monitoring of HNO generation, providing unique insights into HNO dynamics in biological environments

1.2.6.3 Fluorescent Probes for HOCl detection

HOCl (hypochlorous acid) is widely known as a bleaching and disinfectant agent and, biologically, as one of the major reactive oxygen species produced in living systems.[155–157]

In organisms, endogenous HOCl is generated through the myeloperoxidase-catalyzed reaction of chloride ions with hydrogen peroxide.[158] It acts as a dominant microbicidal mediator in the human immune system, efficiently killing invading pathogens and bacteria. Maintaining a normal level of HOCl is essential for immune defense and cellular homeostasis, but abnormal overproduction has been associated with several pathological conditions, including cardiovascular and inflammatory diseases, neurodegenerative disorders, asthma, rheumatoid arthritis, and cancer.[158]

In this context, Xi *et al.* developed the ratiometric fluorescent probe **71** (Figure 1–20) that was constructed using a FRET system composed of a dansyl fluorophore as the donor and 2-(3,5,5-trimethylcyclohex-2-en-1-ylidene)malononitrile (TMCM) as the near-infrared acceptor for HOCl detection.[158] Spectroscopic evaluation was performed in a DMF/PBS (1:1, v/v, pH 7.4) system at an excitation wavelength of 370 nm. Before exposure to HOCl, **71** exhibited strong emission from the TMCM acceptor centered at 670 nm and weak emission from the dansyl donor at 550 nm, indicating efficient energy transfer. Upon gradual addition of HOCl, the emission intensity at 670 nm sharply decreased while the 550 nm band increased, with a distinct isosbestic point at 620 nm with an associated detection limit of 0.19 μM. The energy transfer efficiency between dansyl and TMCM was calculated to be 93.59%, confirming the complementarity between donor emission and acceptor absorption. UV-vis absorption spectra supported this behavior, showing a progressive decrease in the absorption band at 472 nm as HOCl concentration increased, consistent with disruption of the FRET pathway. Selectivity experiments were carried out by testing the fluorescence response of **71** toward various reactive oxygen and nitrogen species with HOCl being the only analyte to cause a significant ratiometric change in emission intensity. The probe maintained a stable fluorescence ratio in the pH range 3 to 10, and after HOCl addition, the fluorescence enhancement remained constant across this interval. Mechanistic analysis confirmed that HOCl oxidatively cleaves the C=C double bond of the TMCM moiety, leading to formation of two oxidation products which correspond to aldehyde-containing fragments and account for the interruption of FRET and the switch in emission from NIR to visible light. Biological imaging experiments demonstrated the probe's excellent performance in living cells. In A549 human lung carcinoma cells, incubation with **71** (10 μM) for 1 h produced bright red fluorescence, confirming cell membrane permeability. Upon subsequent treatment with HOCl, the red emission decreased while green emission intensified, giving a pronounced increase in the ratiometric fluorescence signal. Cytotoxicity evaluation using a cell viability assay showed no significant decrease in survival up to 10 μM probe concentration for 12 h, confirming low toxicity. Photostability tests under continuous irradiation

(0-240 s) revealed negligible fluorescence loss. The probe was also applied to RAW264.7 macrophages, which endogenously generate HOCl via lipopolysaccharide (LPS) catalysis (Figure 1–20a). Cells incubated with the probe alone displayed dominant red emission, while LPS-treated cells (2 μg/mL for 12 h) exhibited enhanced green fluorescence and a decreased red signal, consistent with intracellular HOCl formation. The green/red fluorescence intensity ratio increased significantly, demonstrating the probe's capability to visualize endogenous HOCl generation.

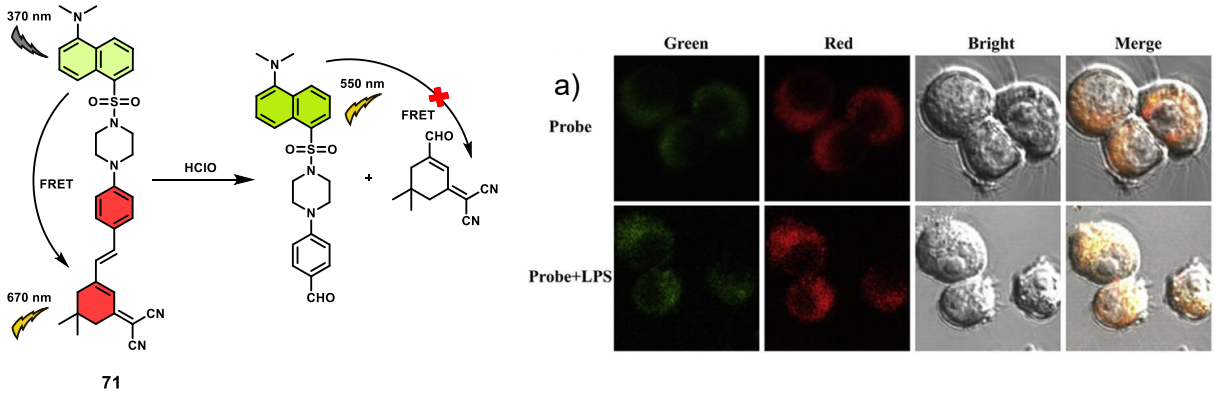


Figure 1–20. Structure of compound **71** and proposed mechanism for the detection of HOCl. a) Fluorescence images of RAW264.7. First row: RAW264.7 cells were treated with **71** for 1 h; second row: RAW264.7 cells were incubated with LPS then with **71** for 1 h. Adapted from ref.[158] copyright 2017, Elsevier.

1.2.6.4 Fluorescent Probes for nitro-containing Compounds

Nitro-containing compounds, commonly found in explosives and industrial chemicals, present serious environmental and security challenges.[159] This section explores recent progress in detecting these compounds using dansyl-based fluorescent probes, focusing on their enhanced sensitivity, selectivity, and potential for real-world sensing applications.

Secondary explosives such as 2,4-dinitrotoluene (DNT), 2,4,6-trinitrotoluene (TNT), and 2,4,6-trinitrophenol (TNP) are of particular concern due to their widespread use in defense and industry. Highly soluble compounds like TNP can contaminate surface waters, posing risks to human health through skin absorption or inhalation. Prolonged exposure to these nitroaromatics has been linked to blood and liver disorders, and some are classified as possible carcinogens. Their nitro groups are also chemically reactive, undergoing reduction to amino derivatives under suitable redox or pH conditions, an aspect central to their detection and sensing mechanisms.[160]

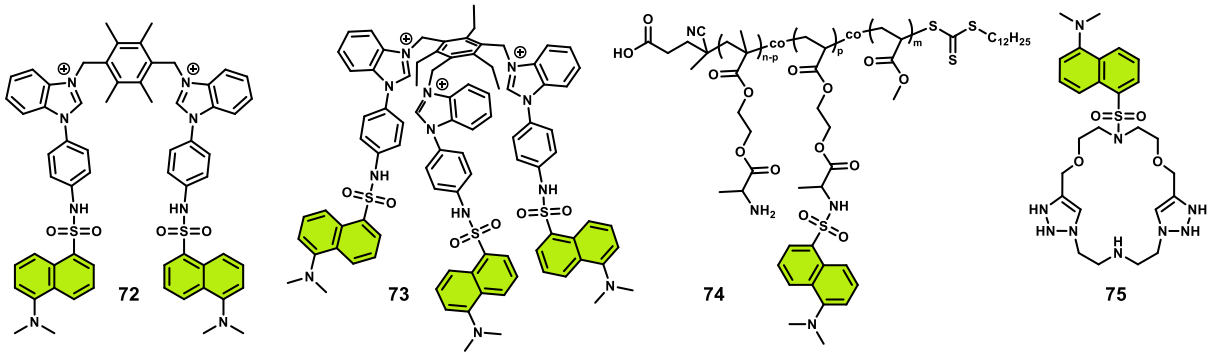


Figure 1–21. Structures of compounds **72**-**75** for the detection of nitroaromatic compounds.

To meet this need, Tripathi and co-workers developed a dansyl conjugated benzimidazolium based dipodal and tripodal systems **72** and **73** (Figure 1–21) capable of detecting TNP.[161] The emission of both compounds was examined in binary DMSO-water mixtures. For probe **73**, increasing the water fraction to 50% caused a red shift from 494 to 540 nm and a sharp enhancement of the emission up to 99.9% water due to aggregation, accompanied by a rise in quantum yield from 6.2% to 68%. DLS and TEM confirmed aggregate sizes around 231 nm. In contrast, probe **72** showed a blue shift from 534 to 520 nm and ACQ. The detection of TNP was achieved in H_2O-DMSO (98:2) which caused a 70% quenching after the addition of 0.5 equivalents while other nitroaromatic compounds did not exert any meaningful change. The titration revealed the non-linear relationship between the concentration of TNP and fluorescence intensity causing it to decrease exponentially. Additionally, the calculated limit of detection was 10 pM and the probe maintained its fluorescence stability between pH 4 to 6. DLS data suggest that the aggregates do not alter their morphology after the addition of TNP showing an average size of 174 nm. In less aqueous media (H_2O–DMSO 1:1), detection efficiency decreased, highlighting the key role of aggregation. Probe **72** was less selective and sensitive, with a detection limit of 1 nM. Mechanistic studies suggested that TNP interacts within the cavity of **73**, aligning its aniline and aromatic rings to facilitate ground-state energy transfer from the HOMO of TNP to the LUMO of **73**, supported by DFT calculations. Lifetime measurements confirmed static quenching (8.7 ns constant lifetime). Finally, paper test strips enabled visual TNP detection under UV light, with a minimum detectable mass of 13.7 × 10^{-18}g/cm^2 under UV light irradiation.

Kumar *et al.* introduced a highly emissive dansyl-tagged copolymer, P(MMA-co-Dansyl-Ala-HEMA) (**74**, Figure 1–21), synthesized via RAFT polymerization for the detection of nitroaromatic explosives such as DNT, TNT, and TNP.[162] The copolymer exhibited excellent photophysical properties (f = 77%) and strong fluorescence quenching in the presence of nitroaromatics, with detection limits of 10.1 µM (DNT), 9.1 µM (TNT), and 3.7 µM (TNP).

Following their earlier development of **74**, Kumar and co-workers advanced the concept by integrating FRET into the sensing mechanism.[160] In this system, a tryptophan-based donor copolymer, P[DMA-co-(Boc-Trp-EMA)] (RP), and the previously reported **74** were synthesized using RAFT copolymerization. The donor (RP) exhibits blue fluorescence at 330 nm, while the acceptor **74** emits in the green region around 505 nm. The strong spectral overlap between the donor's emission and the acceptor's absorption bands provided ideal conditions for non-radiative energy transfer. The FRET interaction between RP and **74** was quantified through time-resolved fluorescence spectroscopy, revealing a high energy transfer efficiency of 63%. The sensing mechanism relies on the synergistic action of FRET and PeT, which requires proximity between the sensor's fluorophores and the analytes. Among the studied nitroaromatic compounds, TNP exhibits the highest sensitivity due to its strong acidity (pKa = 0.38), which facilitates deprotonation in polar solvents like THF. The resulting anionic TNP molecules strongly interact with the cationic amine groups of the RP-**74** pair, promoting efficient charge and energy transfer and leading to pronounced fluorescence quenching. In contrast, TNT and DNT show weaker interactions and correspondingly lower quenching efficiency. The sensor demonstrates excellent performance, with limits of detection of 0.4 μM, 2.3 μM, and 5.4 μM for TNP, TNT, and DNT, respectively. Finally, the system was applied for the visual detection of nitroaromatic compounds using test strips.

A recent study by Thurakkal *et al.* reported a dansyl-triazole-based macrocycle (**75**, Figure 1–21) designed for the selective detection of nitro-containing antibiotics and heteroaromatics.[163] The macrocycle was obtained via a Cu(I)-catalyzed azide–alkyne cycloaddition between a dialkyne and diazide precursor, with dansyl appended to the alkyne fragment. Photophysical characterization in water with 0.2% DMSO revealed an absorption maximum at 330 nm and emission at 560 nm. Fluorescence titrations against a panel of pharmaceuticals demonstrated high selectivity for nitro-antibiotics, specifically dimetridazole, nitrofurantoin, and nitrofurazone exhibiting detection limits of 100 nM, 500 nM, and 1 μM, respectively. Importantly, the selectivity was retained in the presence of competing drugs, salts, and metabolites, and extended to other nitro-heteroaromatics such as nitrobenzothiazoles and nitroisoquinoline. Neither nitrobenzene nor imidazole induced quenching, confirming that both the nitro group and heteroaromatic framework are required for interaction. The sensing platform was further validated in real matrices, including lake and tap water, milk, and human serum albumin. A paper-strip format was also demonstrated, enabling naked-eye detection under UV light with stability exceeding ten days. Mechanistically, quenching was attributed to disruption of the

dansyl ICT process by electron-deficient nitro groups, assisted by π-π stacking and hydrogen bonding interactions mediated by the triazole and NH functionalities of the macrocycle.

1.2.6.5 Fluorescent Probes for organophosphorus compounds

Detection of organophosphorus compounds is of vital importance due to their widespread application as agricultural pesticides and their potential use as toxic chemical agents. These compounds act as potent inhibitors of acetylcholinesterase, leading to the accumulation of acetylcholine in the nervous system, which can cause neurotoxicity, paralysis, and even death in severe cases. Therefore, rapid and reliable detection of organophosphorus residues is essential for ensuring environmental safety, protecting human health, and monitoring food contamination.[164]

Glyphosate is one of the most widely used organophosphate herbicides due to its broad-spectrum activity, non-selectivity, and low cost.[70,165] Its extensive use, especially with glyphosate-resistant transgenic crops, has led to accumulation in soil, water, and food, raising concerns for human health and ecosystems.[70,165] Exposure has been associated with neurological, reproductive, and developmental effects, and glyphosate is classified as a probable carcinogen (Group 2A) by the IARC.[70] Regulatory limits, such as 0.7 μg/mL in drinking water (US EPA) and 0.1 to 0.5 μg/g in crops (EU), emphasize the need for sensitive detection methods to ensure environmental and food safety.[70,165]

Deng *et al.* developed a fluorescent probe, DSG-Cu^{2+}, for glyphosate detection. DSG was synthesized by reacting dansyl chloride with glycine under basic conditions.[165] The probe was prepared by dissolving DSG and Cu^{2+} ions in an ethanol–water mixture (3:2, v/v), forming the DSG-Cu^{2+} complex. Spectral measurements showed that DSG absorbs at 335 nm and emits at 514 nm when excited at 350 nm. Upon binding with Cu^{2+}, the emission shifted to 533 nm with quenching of intensity. Job's plot analysis indicated a 1:1 stoichiometry, confirmed by HR-MS. Glyphosate, containing glycine and phosphate groups, displaced Cu^{2+} from DSG-Cu^{2+}, restoring fluorescence. Calibration curves constructed with glyphosate concentrations from 0 to 8 μM provided the determination of the detection limit as 35 nM. Selectivity was tested against other pesticides (carbaryl, thiram, mesotrione, oxyfluorfen, trichlorfon, imidacloprid, nicosulfuron), amino acids, glucose, and ions producing negligible changes, while glyphosate consistently restored fluorescence. Application to real samples included tap water, soil extracts, cabbage, and celery. Spiked samples at 2.00 and 4.00 μM glyphosate yielded recoveries between 95.2% and 104.5%, with relative standard deviations between 0.64% and 1.39%. For example, celery root spiked at 4.00 μM gave 4.16 μM detected (104.5% recovery), while

cabbage spiked at 2.00 μM gave 1.91 μM detected (95.2% recovery). Test strips were prepared by immersing filter paper in DSG-Cu^{2+} solution and drying. Under 365 nm UV light, strips exposed to glyphosate solutions (0–50 μM) showed fluorescence recovery, with color changing from gray-black to yellow. Fluorescence intensity increased proportionally with glyphosate concentration, confirming the strips' suitability for semi-quantitative on-site monitoring.

The previously mentioned compound L (Table 1-1) was further used for glyphosate detection, the L-Cu^{2+} ensemble exhibited a specific "off-on" response accompanied by a fluorescence intensity increase at 560 nm with glyphosate concentration and reached a plateau near 1.5 equivalents.[70] The calibration was linear from 5.0 to 13.0 μM and the LOD was 12.59 nM. Selectivity experiments in HEPES showed negligible change with common anions and pesticides (DDVP, malathion, parathion-methyl, parathion, dimethoate), while glyphosate consistently restored fluorescence. Reversibility studies between Cu^{2+} and glyphosate maintained its signal over five cycles. pH studies showed effective detection within pH 6-12, with experiments performed at pH 7.4. Applications in real samples included tap, lake, and purified water, as well as food matrices (milk, watermelon juice, soda water). Standard additions from 0 to 10.0 μM yielded recoveries of 91.1-118.9% in water and 99.7-110.4% in food. Representative values include tap water recoveries of 98.9-106.7% across 0-5 spikes, lake water 101.9–118.9%, and purified water 91.2-116.1%, supporting quantitative detection under aqueous buffer conditions. Under 365 nm UV light, strips exposed to analytes showed a visible change only for glyphosate reversing the color to yellow while other anions and pesticides did not produce observable changes. For field use, smartphone-based imaging under 365 nm UV extracted RGB values, and the G/B ratio provided a linear response to glyphosate concentration ($G/B = 0.0239X + 0.2613$, $R^2 = 0.9939$) with an LOD of 0.42 μM, enabling semi-quantitative analysis in situ.

Nerve agents represent a highly toxic class of organophosphorus compounds designed to disrupt the nervous system through inhibition of acetylcholinesterase. The main families of these agents include the G-series, such as sarin, soman, and tabun, and the V-series, such as VX. They are typically colorless, volatile liquids with high potency even at trace levels, and their potential misuse in warfare or terrorism has made the development of rapid and reliable detection methods a major research priority.[166]

In this context, Chen and co-workers reported a dansyl-based fluorescent probe for the rapid and visual detection of nerve agent mimics in both solution and vapor phases.[166] The probe was synthesized in a single step by coupling *o*-phenylenediamine with dansyl chloride. The sensing target was diethyl chlorophosphate (DCP), a commonly used mimic for highly toxic

organophosphorus agents. The probe operates through a nucleophilic substitution between the amine group of the o-phenylenediamine unit and the phosphorus center of DCP, forming a phosphate ester. This reaction suppresses photoinduced electron transfer from the donor to the dansyl fluorophore, resulting in a strong turn-on fluorescence response. In DMF solution, the absorption maximum of the probe at 320 nm shifts to 345 nm upon DCP addition, with emission centered at 515 nm. The fluorescence intensity increases up to 18-fold within two minutes, accompanied by a visible color change from colorless to green under 365 nm UV light. Quantitative titration experiments established a linear relationship between emission intensity and DCP concentration from 0 to 90 μM and a detection limit of 0.082 μM. Selectivity studies against common interferents such as triethyl phosphate, tributyl phosphate, acetic acid, diethyl cyanophosphate, and diethyl cyanomethyl phosphate demonstrated minimal cross-reactivity, confirming specificity toward DCP. For practical use, the authors prepared test papers coated with the probe, which exhibited visible fluorescence enhancement when exposed to DCP vapor at concentrations around 40 ppm, with detectable responses appearing within minutes. Mechanistic studies using ^{1}H NMR revealed the disappearance of the amine proton signal near 9.6 ppm and the emergence of new ethyl signals at 3.92 and 2.91 ppm, consistent with phosphorylation. Mass spectrometry and DFT calculations supported the formation of a phosphorus ester intermediate responsible for fluorescence activation.

1.2.6.6 Fluorescent Probes for amino acids

Amino acids are the building blocks of proteins and key intermediates in metabolism. They are essential for growth, development, and physiological balance. Certain amino acids, including arginine, glutamine, glycine, proline, and branched-chain types, influence blood flow, metabolism, and immune function. Accurate qualitative and quantitative analysis of amino acids in biological fluids is therefore important for reliable assessment of physiological and metabolic states.[167–169]

Among the various amino acids, aspartic acid (Asp) and glutamic acid (Glu) are of particular interest due to their critical roles in neural signaling and brain function. Imbalances in their concentrations are closely associated with neurological and psychiatric disorders, underscoring the need for precise analytical tools.[170] In this sense, Zhang *et al.* designed a supramolecular fluorescent sensor composed of a cationic imidazolium-dansyl derivative (**76**, Figure 1–22) and sodium dodecyl sulfate micelles for the selective recognition of aspartic acid (Asp) and glutamic acid (Glu) in water.[170] The supramolecular sensor emitted strongly at 537 nm, with fluorescence intensity decreasing significantly upon addition of Asp and Glu while

remaining nearly unaffected by the other 11 tested amino acids. In optimized conditions the detection limits were 0.6 mM for Asp and 2.1 mM for Glu. Fluorescence lifetime measurements confirmed static quenching given the slight changes of the lifetime upon titration of the amino acids which suggest a complex formation between the probe and the analyte. UV–vis spectra exhibited isosbestic points at 273 and 313 nm and the appearance of a new band near 291 nm, consistent with protonation of the dansyl amine. Similar fluorescence suppression by HCl and full recovery upon NaOH addition demonstrated reversible proton-driven response. SDS micelles were essential for sensitivity, as the probe alone showed negligible response in pure water. The negatively charged micellar interface promoted enhanced proton access and stabilized the quenched complex.

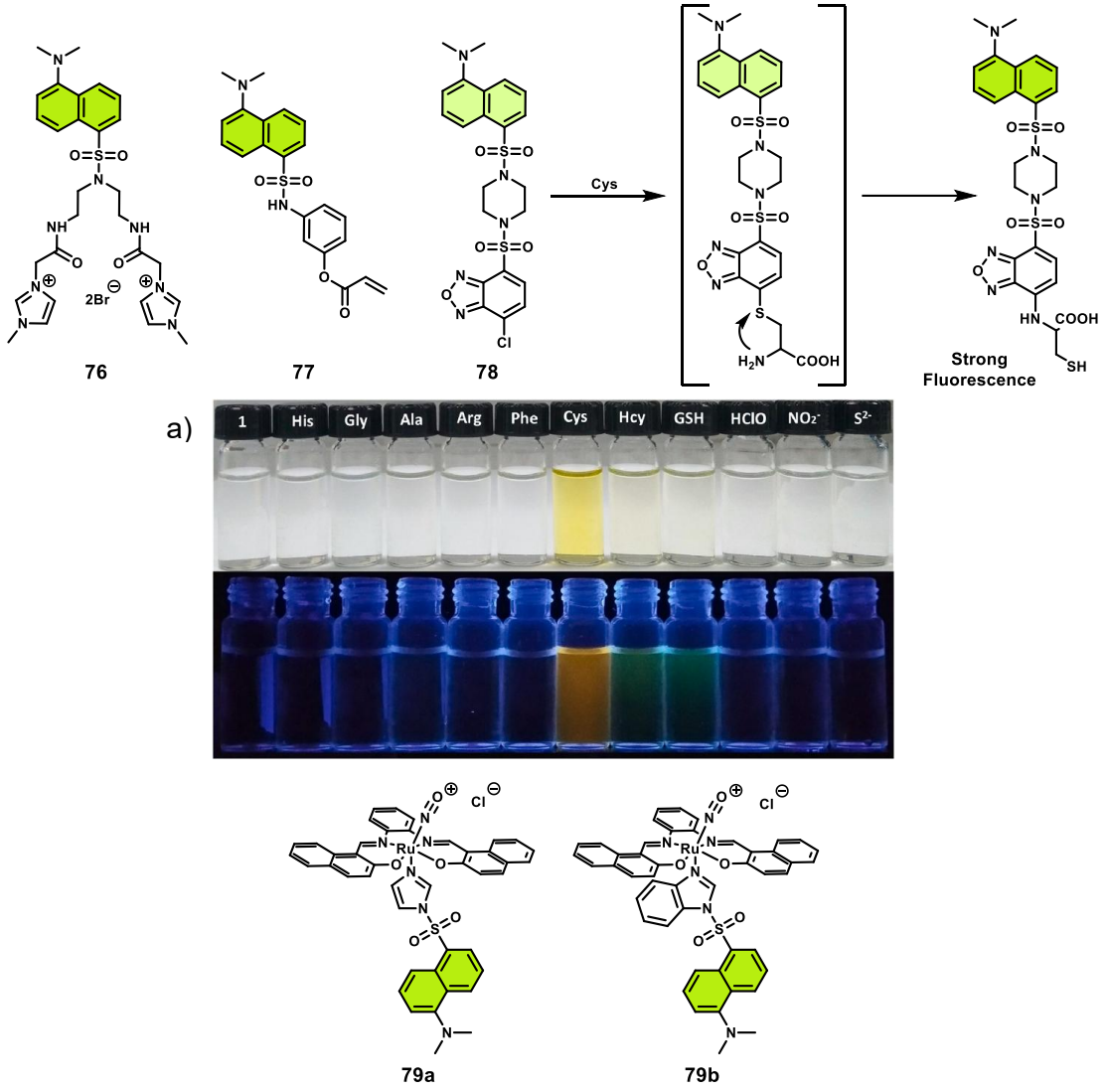


Figure 1–22. Structures of compounds **76**-**79b** proposed detection mechanisms of aminoacids. a) Photographed colorimetric (365nm) changes of **78** in the presence of various competing analytes. Adapted from ref.[171] copyright 2018, Elsevier.

Biothiols, including cysteine, homocysteine (Hcy), and glutathione (GSH), have received considerable attention due to their biological and physiological roles in redox processes.[171] Among them, Cys is an essential amino acid involved in protein synthesis, detoxification, metal binding, post-translational modifications, and metabolism.[171] It also serves as a precursor for glutathione, and both can be obtained from the diet or formed metabolically from homocysteine.[172] Abnormal levels of Cys are associated with various syndromes, such as slowed growth, lethargy, skin lesions, liver damage, and loss of muscle and fat.[172] The critical roles of Cys in cellular function have driven ongoing efforts to develop efficient methods for its selective detection and quantification under physiological conditions.[171,172]

Jiang's group reported a new fluorescent probe (**77**, Figure 1–22) based on a dansyl fluorophore linked to an acryloyl group.[172] The acryloyl unit serves as a reactive site for cysteine and functions as an electron-accepting moiety in a donor-excited photoinduced electron transfer mechanism. In its unreacted state, **77** shows weak fluorescence because the excited dansyl unit transfers an electron to the acryloyl acceptor, quenching the emission. Upon reaction with Cys, the acryloyl group is cleaved (via conjugate addition and intramolecular cyclization) such that the d-PeT process is disrupted and the dansyl fluorophore recovers strong fluorescence. Spectroscopic studies revealed that this "turn-on" fluorescence response is both sensitive and selective: addition of Cys resulted in nearly a 28-fold increase in emission intensity at 545 nm in a CH_3CN/PBS (50:50, v/v, pH 7.4) mixture with a detection limit of 13 nM. The selectivity of **77** was demonstrated by testing against glutathione, homocysteine, and common amino acids which none of these caused a significant fluorescence enhancement under the same conditions. Finally, **77** was demonstrated to be cell-permeable and could image intracellular Cys in living human breast duct carcinoma (T-47D) cells. Pre-treatment with a thiol-trapping reagent (N-ethylmaleimide) suppressed fluorescence, confirming that the observed fluorescence signals were due to endogenous thiols (specifically Cys) interacting with the probe.

Li *et al.* synthesized the dual-channel probe **78** (Figure 1–22) for the selective recognition of Cys through colorimetric and "turn on" fluorescence responses.[171] The probe is built by linking a benzoxadiazole (SBD) fluorophore to a dansyl group via a piperazine bridge. The chloride substituent at the 4-position of the SBD group serves as the reactive site toward thiols. In PBS buffer (pH 7.4, 10% DMF), **78** exhibited an absorption maximum at 330 nm. After addition of Cys, this band disappeared, a transient peak appeared at 400 nm, and subsequently an increase was observed at 435 nm. This sequential change indicated the formation of a reaction product corresponding to a substitution and rearrangement process. When homocysteine or glutathione were added, only a single transition from 330 nm to 400 nm was recorded, and no

subsequent shift to 435 nm occurred (Figure 1–22a). The fluorescence spectra showed that upon addition of Cys, a new band at 575 nm appeared, producing bright yellow fluorescence. The limit of detection was calculated to be 12.21 ± 0.04 nM. In contrast, the addition of Hcy and GSH under the same conditions resulted in almost no fluorescence. A visible color change of the solution from colorless to yellow was observed only in the presence of Cys under 365 nm UV light, while no visible change occurred with Hcy or GSH. The probe remained spectrally stable up to pH 11, showing measurable fluorescence response to Cys in the pH 6 to 12 range, with the most pronounced signal near pH 8. Cell-based imaging experiments were carried out with MCF-7 cells incubated with 10 μM probe for 30 min at 37 °C. Strong intracellular yellow fluorescence was detected. Pretreatment with 0.5 mM N-ethylmaleimide (NEM) eliminated fluorescence. Cells pretreated with NEM and then exposed to 0.5 mM Cys, Hcy, or GSH displayed fluorescence only in the Cys-treated group, while Hcy and GSH groups showed no detectable emission. Cytotoxicity measurements by MTS assay after 72 h exposure to probe concentrations from 25–500 μM showed no significant decrease in cell viability.

Bazany-Rodríguez *et al.* reported the first fluorescent chemodosimetric mechanism for the selective recognition of selenocysteine (Sec) using dansyl-appended ruthenium nitrosyl complexes (**79a** and **79b**, Figure 1–22).[173] The reaction of Sec with these complexes in aqueous media under physiological pH promotes fluorescence enhancement accompanied by nitric oxide ($NO^{\bullet}$) release, confirmed through fluorimetric titrations, UV–vis, IR, EPR, MS, and ^{77}Se NMR studies. The mechanism involves nucleophilic attack of Sec's selenolate on the electrophilic nitrosonium (NO^{+}) ligand, yielding aqua–ruthenium(II) complexes and selenocystine (Sec_2). Both chemodosimeters exhibit high selectivity for Sec over biothiols (Cys, Hcy, GSH), attributed to Sec's lower pKa (≈5.24) and stronger nucleophilicity. Detection occurs within 5 minutes at physiological pH (7.4) with low detection limits of 0.31 μM for **79a** and 0.12 μM for **79b**. Electronic and theoretical DFT analyses show that the π-extended tetradentate ligand and conjugated dansyl units enhance the Ru–NO^{+} susceptibility to nucleophilic attack, facilitating $NO^{\bullet}$ release and fluorescence recovery. Confocal microscopy demonstrates successful visualization of Sec in live *Saccharomyces cerevisiae* cells, confirming biocompatibility and cellular applicability.

As similarly seen for the detection of H_2S, some previously discussed dansyl-based systems originally developed for metal ion sensing were also used as probes for the detection of amino acids. These studies have been summarized in Table 1-5, emphasizing their limits of detection, sensing mechanisms, and demonstrated applications across environmental and biological matrices.

Table 1-5. Comparison of dansyl-based compounds previously discussed in this work for the detection of Cu^{2+}, Hg^{2+} and Cd^{2+} that further applied for the sensing of amino acids.

Compound	Amino acid	LOD (nM)	pH range	Fluorescence response	Application	Ref
DNH-Cu^{2+}	L-His	22.8	7-11	Turn on	Test strips; Bioimaging (MLE-12 cells and zebrafish larvae); Visual detection via smartphone app (LOD = 0.63 μM)	[65]
5-Cu^{2+}	Cys	1.76 x10^3	N. A.	Turn off	N. A	[73]
D-P4-Hg^{2+}	Biothiols	52.0 (Cys)	N. A.	Turn on	Spiked human serum samples	[84]
D-P4'-Hg^{2+}	Biothiols	80.0 (Cys)	N. A.	Turn on	N. A.	[85]
19-Hg^{2+}	Biothiols	10.6 (Cys) 5.6 (GSH) 10.0 (Hcy)	N. A.	Turn on	Real lake water samples	[90]
28-Cd^{2+}	Biothiols	35 (Cys)	7-12	Turn off	Bioimaging (HeLa cells and HK2 cells)	[104]

1.2.7 Dansyl-based Dyad Systems

Small organic dyes are widely used in bioimaging, biosensing, medical diagnostics, and environmental monitoring due to their bright fluorescence and versatility. However, many suffer from narrow Stokes shifts, leading to self-quenching and interference from excitation light, and intensity-based measurements can be affected by environmental factors, probe localization, and optical path variations.[174] Ratiometric fluorescence, which measures emission at two wavelengths and calculates the intensity ratio, provides a more reliable approach. While single-fluorophore systems can achieve ratiometric responses via ICT, multi-fluorophore constructs transfer energy from a donor to an acceptor, generating larger pseudo-Stokes shifts and dual-emission signals with built-in correction for environmental effects.[174] Dansyl derivatives are particularly suited for these architectures, as their high quantum yields, environmental sensitivity, and easy modification allow them to act as donors. Conjugating dansyl with other chromophores can tune absorption and emission, enhance photostability, and improve energy transfer efficiency. Exploring these donor-acceptor strategies with dansyl derivatives thus holds significant promise for the search of robust and tunable fluorescent probes. This section examines the principles, strategies, and recent developments in conjugating dansyl with other chromophores, emphasizing how such designs expand the functionality and applicability of fluorescent probes in sensing, imaging, and molecular diagnostics.

1.2.7.1 Dansyl-Naphthalimide Systems

Das and co-workers reported the synthesis and application of **80** (Figure 1–23), a dansyl–naphthalimide sulfonamide chemodosimeter, for hydrogen sulfide detection.[175] Spectroscopic titrations in CH_3CN-H_2O (1:8 v/v, pH 7.2) showed a strong absorbance increase at 560 nm with an isosbestic point at 372 nm. The probe exhibited a detection limit of 0.18 μM, below the Occupational Safety and Health Administration permissible exposure limit. Only H_2S produced the characteristic purple coloration and absorbance increase in selectivity experiments against other analytes. NMR and mass spectrometry experiments revealed the formation of naphthalimide hydrazone responsible for the colorimetric behavior. Practical validation included biogas samples collected from rural digesters. Soaked paper strips with **80** exposed to these samples produced distinct purple color changes, corresponding to H_2S concentrations in the 2-75 ppm range. Tap water assays showed recovery rates above 97% for spiked H_2S concentrations, confirming quantitative accuracy.

Kong *et al.* reported the design and synthesis of **81** (Figure 1–23), a dansyl-naphthalimide fluorescent probe, developed for selective visualization of HNO in biological systems.[177] Compound **81** was synthesized via amidation of dansyl-piperazine and naphthalimide-propanoic acid, incorporating a benzeneboronic pinacol ester as the recognition site. Optical studies in PBS/DMSO solution (pH 7.4) showed that **81** exhibited a weak baseline fluorescence at 552 nm (f_f = 3.3%). Upon addition of Angeli's salt as an HNO donor, fluorescence intensity increased nearly 13-fold, with a strong emission at 555 nm (f_f = 32.5%). The detection limit was calculated at 0.44 μM. Selectivity assays against biologically relevant analytes showed negligible interference, with only slight signal reduction in the presence of thiols due to oxidation by HNO. Nitroaromatic compounds caused minor fluorescence attenuation through inner filtering effects but did not interfere under physiological conditions. The mechanism underlying the response of **81** to nitroxyl is based on the hydrolysis of the boronic pinacol ester recognition unit. The conversion changes the electronic structure of the probe, enabling ICT between the dansyl donor and the naphthalimide acceptor. Normalized absorption and emission spectra indicated that the fluorescence enhancement was further supported by FRET between the dansyl and naphthalimide units. Computational studies using DFT provided additional evidence, showing a donor-acceptor distance of 10.7 Å, which is within the range for efficient FRET. HOMO-LUMO distribution analysis confirmed that the electron density shifted from the dansyl donor to the naphthalimide acceptor upon HNO reaction, consistent with ICT. Biological validation included cytotoxicity assays in HepG-2 cells, showing survival rates above 85% at 100 μM **81**. Confocal imaging demonstrated that **81** permeated cell membranes and produced strong fluorescence

upon HNO generation with Angeli's salt. In vivo imaging in mice confirmed noninvasive detection, with **81** producing fluorescence only when co-injected with Angeli's salt.

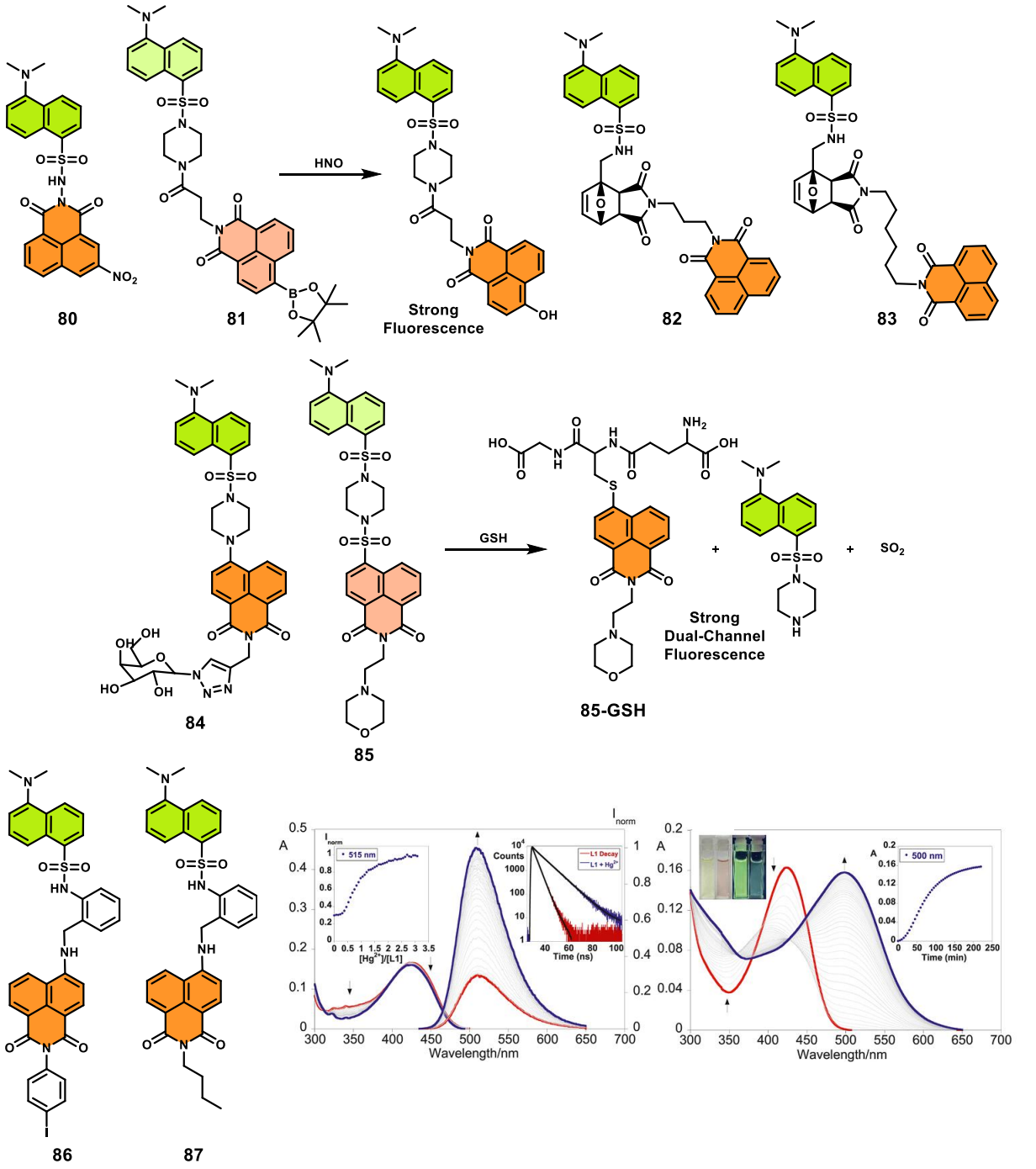


Figure 1–23. Structures of dansyl-naphthalimide dyads **80**-**87**. a) UV–Vis and luminescent titration of compound **86** (left) upon continuous additions of Hg^{2+}. The inset represents the emission of [Hg2+]/[L1] at 515 nm (left) and the time-resolved fluorescence decay profile of 86 before and after the titration with Hg^{2+}ions (right). UV–vis time continuous spectra of L1 (left) after the addition of 7 eq. of Cu^{2+}. The inset represents the images under natural light

and UV light (left) and the time-dependent response of the absorbance at 500 nm (right). Adapted from ref.[176] copyright 2025, Elsevier.

Gong's group reported the development of two donor-acceptor dyes synthesized through Diels-Alder click chemistry, linking a naphthalimide donor to a dansyl acceptor with spacers of different lengths (**82** and **83**, Figure 1–23). The synthetic pathway involved preparation of dansyl-furan acceptors and naphthalimide-maleimide donors, followed by cycloaddition. In dichloromethane, excitation of the donor at 310 nm produced dual emission, with donor peaks around 370-380 nm and acceptor emission centered at 505 nm. Excitation at 350 nm confirmed intramolecular FRET, as the acceptor emission remained visible. Fluorescence lifetime measurements revealed that the donor lifetime decreased from 3.6 ns to 0.7 ns in **82**, corresponding to an energy transfer efficiency of about 80%, while in **83** the donor lifetime decreased from 3.4 ns to 1.9 ns, giving an efficiency of about 43%. This difference directly reflected the longer donor-acceptor distance in **83**. Solvent polarity strongly influenced emission behavior. In nonpolar methylcyclohexane, the dansyl acceptor emitted in the blue-green region, while in polar methanol its emission shifted to the green-yellow region, with a bathochromic shift of nearly 70 nm. The donor emission remained relatively unchanged, consistent with intramolecular charge transfer. Density functional theory calculations supported this interpretation, showing HOMO localization on the dansyl acceptor and LUMO on the naphthalimide donor, which produced polarized excited states and solvatochromism. Dynamic luminescence control was demonstrated in water-methanol binary solvents. Increasing the water fraction quenched the acceptor's yellow-green emission while maintaining stable donor blue emission. At 60% water content, complementary donor and acceptor emissions combined to yield white light with CIE coordinates of (0.32, 0.33). Over time, bond cleavage shifted the emission coordinates toward blue, confirming the role of dynamic covalent bonds in controlling energy transfer. Thermal demonstrated that heating **83** at 85 °C in toluene triggered retro-Diels-Alder cleavage, spatially separating donor and acceptor and suppressing FRET, which shifted emission from white to blue. Cooling restored the covalent bond, re-establishing energy transfer and white-light emission.

Li and co-workers described the design and synthesis of a ratiometric fluorescent glycoprobe (**84**, Figure 1–23) for the selective detection of thiophenol in aqueous solution and environmental river water.[178] The probe was designed by coupling an alkynyl naphthalimide-dansyl dyad with an azido galactoside. The galactoside moiety enhanced water solubility, enabling direct operation in fully aqueous buffers. Spectroscopic measurements were performed in aqueous Tris-HCl buffer (20 mM, pH 7.3) at 25 °C. Upon excitation at 260 nm, the probe

exhibited an emission peak at 534 nm. Addition of thiophenol caused a sharp decrease in this peak and the simultaneous emergence of a blue-shifted peak at 414 nm, attributed to the release of a dansyl fragment. The limit of detection was calculated to be 3.8 nM, significantly lower than earlier probes. Selectivity tests showed that common thiols and nucleophiles did not interfere with the ratiometric response. Even in mixtures containing these competing species, **84** retained sensitivity to thiophenol. The probe did not show any response to *p*-nitro-thiophenol but responded to *p*-amino-thiophenol. The sensing ability was stable across a wide pH range (4-10). Environmental relevance was demonstrated by quantifying thiophenol in river water samples. Spiked concentrations ranging from 0.05 to 5 μM were accurately recovered using **84**, validating its applicability for trace detection in real water matrices. Cell viability assays in Hep-G2 and HEK293 lines indicated only slight cytotoxicity at concentrations up to 500 μM, suggesting biocompatibility for potential imaging applications.

Xu *et al.* reported the design and synthesis of a dual-emission fluorescent probe (**85**, Figure 1–23) that combines a naphthalimide donor with a dansyl-sulfonamide acceptor to selectively visualize glutathione (GSH) in lysosomes of living cells.[179] Spectroscopic characterization was performed in HEPES buffer (0.02 M, pH 7.4) containing 10% DMSO at 37 °C. The probe was non-fluorescent in its free state but exhibited strong dual emission upon reaction with GSH showing a green peak at 495 nm (excitation 370 nm) corresponding to the nucleophilic substitution product (**85**-GSH, Figure 1–23), and an orange peak at 595 nm (excitation 330 nm) attributed to the cleavage product dansyl. The detection limit was calculated to be 0.10 μM, with fluorescence intensity increasing linearly across 2-150 μM GSH. Kinetic studies showed rapid response, reaching a plateau within 3 h at 100 μM GSH, while homocysteine and cysteine induced negligible changes, confirming high selectivity. Cell imaging experiments were conducted in U-87MG human glioblastoma cells revealing that **85** permeated cells and produced distinct green and orange fluorescence channels within 30-90 minutes of incubation. Pretreatment with N-ethylmaleimide suppressed fluorescence, while subsequent addition of GSH restored dual emission, further validating specificity. Co-localization with LysoTracker Red confirmed lysosomal targeting, with overlap coefficients of 0.88 (green channel) and 0.87 (orange channel). Cytotoxicity assays indicated >90% cell viability at 20 μM probe concentration after 24 h, demonstrating biocompatibility. Mechanistic studies confirmed that GSH triggers both nucleophilic substitution and cleavage pathways, yielding **85**-GSH and dansyl fragments. Time-dependent density functional theory calculations supported the dual-emission design, showing distinct electronic transitions localized on the naphthalimide and dansyl units.

Our contribution to this field was introduced by the design of four naphthalimide-derived ligands, two of which are engineered as dansyl-naphthalimide dyads (**86** and **87**, Figure 1–23).[176] These dyads were designed to exploit intramolecular electron transfer processes, enabling dual responsiveness toward Hg^{2+} and Cu^{2+} ions. Photophysical characterization revealed that the dyads (**86** and **87**) display distinct dual-emission behavior compared to single naphthalimide analogues. In acetonitrile at 298 K, they absorb around 425 nm and emit at 515 nm, with quantum yields ranging from 7.5% to 33% depending on solvent. Solvatochromism was evident, with emission shifting from green to yellow as solvent polarity increased. Metal ion sensing highlighted the unique role of the dyads. Upon addition of Hg^{2+}, both **86** and **87** demonstrated CHEF, a rare "turn-on" response given mercury's heavy atom effect (Figure 1–23a). Quantum yields increased two- to threefold, and fluorescence lifetimes extended to ~9 ns. In contrast, Cu^{2+} induced quenching and a bathochromic shift of absorption bands, accompanied by visible color changes from yellow to pink (Figure 1–23a). Time-dependent studies revealed ligand-mediated reduction of Cu^{2+} to Cu^{+}, supported by EPR and XPS data, establishing the dyads as non-redox-innocent systems capable of electron transfer. Mechanistically, the dansyl unit in the dyads initiates PeT, which is suppressed upon Hg^{2+} coordination, restoring fluorescence. For Cu^{2+}, the dyads promote ligand-to-metal electron transfer, reducing Cu^{2+} to Cu^{+} and altering absorption profiles. This dual functionality, fluorescence "turn-on" for Hg^{2+} and colorimetric response for Cu^{2+}, distinguishes the dyads from single naphthalimide analogues, which generally show quenching behavior. Catalytic relevance was demonstrated by incorporating an iodophenyl moiety as a substrate probe. In **86**, Cu^{2+} reduction facilitated Ullmann-type amidation, highlighting the potential of these dyads as ancillary ligands in copper-catalyzed reactions. The dual responsiveness and catalytic activity underscore their versatility as both sensors and functional ligands.

1.2.7.2 Dansyl-Rhodamine Systems

Yang and co-workers reported compound **88** (Figure 1–24), a ratiometric fluorescent probe put together from a dansyl donor and a rhodamine acceptor, designed to detect trace amounts of water in organic solvents through a FRET-based mechanism.[180] Solvent composition was shown to influence the optical properties since in protic solvents such as ethanol, hydrogen bonding with the carbonyl group of the rhodamine promoted spirolactone ring opening, enabling efficient FRET and strong ratiometric emission. In aprotic solvents the probe displayed weaker donor emission and required water addition to trigger the FRET process. Spectral titrations in acetone, THF, DMF, and acetonitrile confirmed that increasing water

content produced a gradual decrease in donor emission at 520 nm and a corresponding increase in acceptor emission at 620 nm. Calibration curves showed linearity between the fluorescence intensity ratio and water fraction over the range 0-8%, with particularly high sensitivity in DMF. Even at trace levels between 0-0.3% water, the probe maintained a clear linear response. The limit of detection was calculated at 0.026 wt% in DMF. Reversibility was demonstrated by repeated cycles of water addition and removal using K_2CO_3 drying in acetone, with the fluorescence ratio returning to baseline at least during five cycles. Selectivity experiments showed that common cations and anions did not interfere with the probe's response to water. Practical application was demonstrated using test strips coated with **88**. When immersed in acetone containing increasing water fractions, the strips exhibited a visible color change under UV light from blue to red, consistent with the solution-phase response. This simple visual readout confirmed the probe's utility for rapid, on-site detection of water contamination in organic solvents.

Gao *et al.* reported the design of probe **89** (Figure 1–24), a reversible ratiometric fluorescent probe designed to monitor labile Fe^{3+} fluctuations in living cells undergoing ferroptosis.[181] The probe links spirolactam rhodamine and dansylamide through the Fe^{3+} chelator HEDTA, enabling a FRET-based sensing mechanism. Optical characterization showed that free **89** exhibited a dansylamide emission maximum at 483 nm upon excitation at 405 nm, with no rhodamine signal. Upon Fe^{3+} binding, spirolactam rhodamine was converted to rhodamine B, producing a new absorption band at 561 nm and a bathochromic emission shift to 576 nm. This ratiometric response was reversible, as demonstrated by alternating additions of Fe^{3+} and the chelator TPEN, which restored the original emission profile over multiple cycles. Spectral titrations confirmed a 1:1 binding stoichiometry between **89** and Fe^{3+}, with a detection limit of 0.13 μM in aqueous solution. The probe's emission ratio increased nearly 170-fold in the presence of Fe^{3+}, while other cations and transition metals produced negligible interference, except for minor effects from Cr^{3+} and Hg^{2+}. The probe maintained stable ratiometric behavior across a broad pH range (5.0 to 10.0). Biocompatibility was assessed by MTT assays in HeLa cells, where viability remained above 80% after 24 h exposure to probe concentrations up to 40 μM. Confocal microscopy confirmed efficient cellular uptake and subcellular localization primarily in the endoplasmic reticulum and lysosomes. Imaging experiments demonstrated that **89** could visualize both exogenous and endogenous Fe^{3+} fluctuations. In HeLa cells incubated with $FeCl_3$, the probe produced a strong red-channel signal at 576 nm and diminished green-channel emission at 483 nm. Endogenous Fe^{3+} changes during ferroptosis were also detected: treatment with erastin for 8 h elevated the emission ratio compared to controls, while co-incubation

with deferoxamine or ferrostatin-1 suppressed this increase. The probe was further applied to tissue imaging in fresh rat kidney slices. In untreated tissue, **89** produced strong green-channel emission and weak red-channel signals. Preincubation with ferric citrate resulted in a pronounced red-channel enhancement.

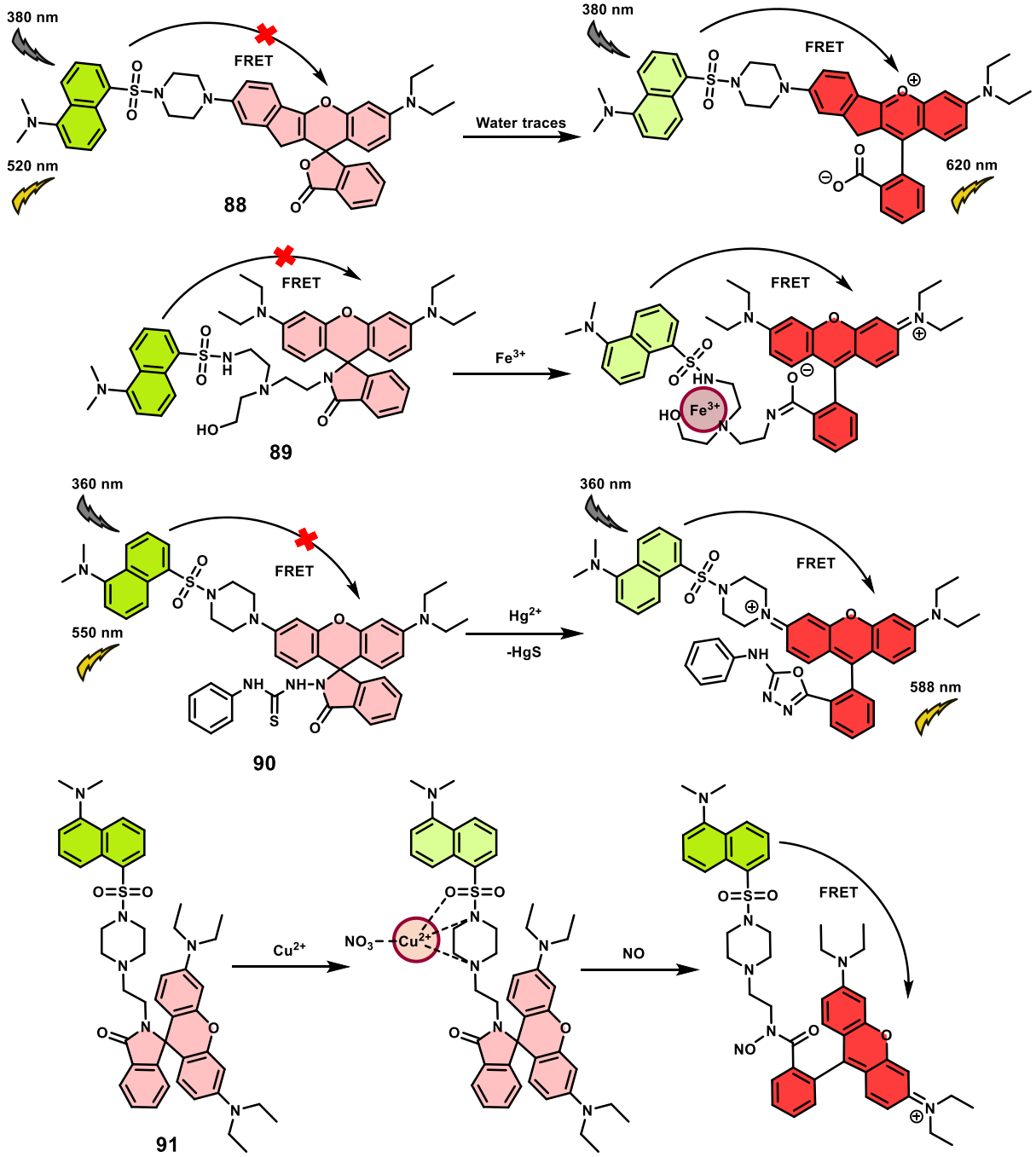


Figure 1–24. Structures of dansyl-rhodamine dyads **88**-**91**.

Silva's group introduced compound **90** (Figure 1–24), a dual-fluorophore FRET-based sensor designed for the selective detection of Hg^{2+} ions.[182] The sensor integrates a

rhodamine unit with a dansyl moiety through a thiosemicarbazide recognition site. The optical behavior of **90** was examined in mixed solvent systems of MOPS buffer and acetonitrile. Different solvent compositions showed that high acetonitrile fractions suppressed the detection mechanism, while mixtures containing around 30% acetonitrile provided the best compromise between signal intensity and sensitivity. The pH dependence demonstrated that **90** exhibited maximum fluorescence intensity at physiological pH near 7, while acidic conditions around pH 2 led to an 80% reduction in overall fluorescence. Spectral experiments revealed a two-stage response mechanism. At low Hg^{2+} concentrations, the dansyl emission at 550 nm was quenched through static interactions, forming a non-fluorescent complex. At higher concentrations, the rhodamine unit underwent ring opening, activating the donor-acceptor system and enabling efficient energy transfer from dansyl to rhodamine. This produced a new emission at 588 nm, accompanied by a visible color change from colorless to violet. The FRET efficiency was calculated at 77%. This hybrid mechanism expanded the linear detection range and was corroborated by time-resolved fluorescence and DFT calculations. In the quenching stage, the limit of detection was 0.15 ppm, while in the FRET stage it was 0.93 ppm. Selectivity experiments against competing ions showed that although Cu^{2+} interfered in the initial quenching stage, only Hg^{2+} was able to activate the donor-acceptor system, ensuring specificity in the second stage. Mechanistic investigations using NMR and HRMS confirmed that Hg^{2+} interaction led to desulfurization and cyclization of the thiosemicarbazide moiety into a 1,3,4-oxadiazole. Biological experiments demonstrated that **90** was cytocompatible, maintaining cell viability above 90% in L929 fibroblasts even at concentrations up to 64 μM. Confocal microscopy confirmed rapid cellular uptake within ten minutes and showed that the sensor retained its dual fluorescence response in vitro. Addition of Hg^{2+} led to the expected quenching of the dansyl channel and activation of the rhodamine channel, with increasing mercury concentrations producing progressively stronger rhodamine signals.

Srivastava and co-workers reported the development of a rhodamine-dansyl conjugate (**91**, Figure 1–24) designed as a FRET-based ratiometric probe for nitric oxide detection mediated by Cu^{2+} ions.[183] The optical behavior of the probe was examined in aqueous phosphate buffer (10 mM, pH 7.4) with acetonitrile as co-solvent. The system showed strong dependence on sequential chemical inputs since Cu^{2+} binding first quenched the dansyl emission at 481 nm, and subsequent addition of NO triggered ring opening of the rhodamine spirolactam, producing a new emission band at 580 nm. This sequence-dependent response was accompanied by visible color changes, from colorless to pink under ambient light and from pale green to orange under UV illumination, allowing naked-eye detection. Spectral studies confirmed that the

probe-Cu^{2+} complex exhibited high selectivity for NO over other reactive oxygen and nitrogen species. The detection limit for NO was determined to be approximately 1 nM, with a tenfold increase in quantum yield upon NO binding. FRET efficiency was calculated at 88%. The probe maintained stable performance across a biologically relevant pH range (6.5-9.0), confirming suitability for cellular applications. Metal ion interference experiments showed that **91** was selective for Cu^{2+} among a panel of cations. Binding stoichiometry was established as 1:1 by Job's plot analysis, with a binding constant of $4.36 \times 10^4\ M^{-1}$. Cyclic voltammetry confirmed the easily achieved reduction of Cu^{2+} to Cu^{+} at 0.201 V vs Ag/AgCl, consistent with the proposed mechanism in which NO coordinates to Cu^{2+} before inducing rhodamine ring opening. The probe was also evaluated as a molecular keypad lock device, where the correct input sequence, Cu^{2+} followed by NO, produced the "unlock" state with strong emission at 580 nm. Alternative sequences, such as NO before Cu^{2+} or Cu^{2+} followed by EDTA, resulted in no signal, demonstrating sequence-dependent logic gate behavior. Biological experiments confirmed low cytotoxicity in HeLa and MCF-7 cells, with viability maintained after 24 h exposure to probe concentrations up to 40 μM. Confocal microscopy showed efficient cellular uptake and dual-channel emission. In HeLa cells, the probe–Cu^{2+} complex alone produced weak green emission, while subsequent NO treatment generated strong signals in both green and red channels, consistent with the dual fluorophore activation mechanism.

1.2.7.3 Dansyl-Pyrene Systems

Paul *et al.* designed a pyrene-dansyl dyad (**92**, Figure 1–25) as a multi-channel probe for Cu^{2+} and CN^- ions, with additional responsiveness to aqueous environments.[184] The dyad links a dansyl donor to a pyrene acceptor through an imine bridge. Compound **92** shows weak emission when excited at 290 nm, displaying only faint blue emission around 450 nm. This low intensity arises from PET between the hydrazone nitrogen and the pyrene ring, as well as cis-trans isomerization of the imine bond, both of which act as non-radiative decay pathways. Upon addition of Cu^{2+} in aqueous acetonitrile, the emission is enhanced and shifted to green-cyan at around 490 nm. The mechanism involves chelation of Cu^{2+} by the azomethine nitrogen and sulfonyl oxygen, which blocks PET and stabilizes the excited state. At the same time, the dansyl emission overlaps with pyrene absorption, enabling FRET. The combined CHEF-FRET-isomerization suppression pathway produces a "turn-on" fluorescence response with a detection limit of 37.75 nM. Increasing addition of CN^- to **92** in acetonitrile exhibits a yellow color solution and cyan emission. The acidic -NH proton of the hydrazone establish hydrogen bonding with CN^-, which induces ICT and shifts the absorption band

bathochromically to ~395 nm. The emission is initially quenched by PET which is then suppressed resulting in an increase of intensity as the hydrogen bond is formed. The detection limit is 0.62 mM, with no interference from other common anions. As the proportion of water in acetonitrile increases up to 90%, **92** undergoes AIEE. Pyrene excimer formation and J-type aggregation produce a broad blue emission band, shifted relative to the monomer. Solid-state fluorescence is further red-shifted at around 515 nm compared to solution, consistent with intermolecular π–π stacking. Plant cells of Tecoma stans and Peperomia pellucida incubated with Cu^{2+} followed by addition **92** displayed bright green-cyan luminescence under UV excitation, confirming cell permeability and selective Cu^{2+} tracking. In fetal bovine serum, **92** detected copper at 0.28 ppm, a concentration relevant to the diagnostic window for Menke's disease, showing potential as a biomarker. DNA binding studies with calf thymus DNA revealed hypochromism in absorption spectra, consistent with intercalation. Competitive binding assays showed that **92**-Cu^{2+} could displace ethidium bromide, suggesting possible cytotoxic activity.

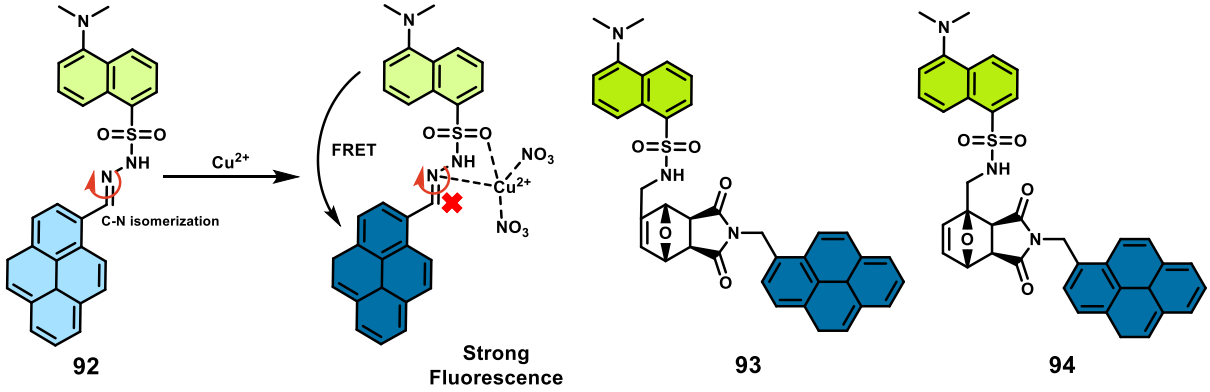


Figure 1–25. Structures of dansyl-pyrene dyads **92**-**94**.

Probe **92** was also reported by Wang *et al.* for water detection in organic solvents.[185] The probe was tested in a wide range of solvents purified by conventional distillation methods. In polar aprotic media such as DMF, DMSO, acetonitrile, and acetone, the ICT pathway was suppressed by solvent-solute interactions, where only pyrene emission was visible, typically as excimer bands around 425-465 nm. In contrast, in less polar or halogenated solvents like dichloromethane, chloroform, ethyl acetate, and toluene, FRET from pyrene to dansyl occurred, producing strong green emission near 510 nm. For water detection, the probe was tested with increasing additions of H_2O into organic solutions. In acetone, water induced a red-shift and intensity increased at 455 nm. In DMF, water produced a ratiometric change: pyrene bands at 376 and 396 nm increased while the 441 nm band diminished. In DMSO, reciprocal intensity changes at 396 nm provided the analytical signal. Detection limits were 0.0165% in acetone, 0.0012-0.0014% in DMF, and 0.294% in DMSO. In DMF, aggregation through π–π stacking

extended excited-state lifetimes and blocked ICT, explaining the dominance of pyrene emission. In halogenated solvents, spectral overlap between pyrene emission and dansyl absorption facilitated FRET, accounting for the green fluorescence.

Zhang's group reported the synthesis and characterization of two regioisomeric pyrene-dansyl conjugates (**93** and **94**, Figure 1–25) linked through dynamic Diels-Alder bonds, designed as intramolecular FRET probes with sensitivity to both temperature and solvent polarity.[186] The distinction between the two compounds concerns the substitution of the dansyl–furan acceptor since **93** incorporates the *β*-substituted furan, while **94** includes the *α*-substituted analogue. Both dyes exhibit strong absorption in the 277-345 nm region, dominated by the pyrene donor. In emission, the donor fluorescence is suppressed and a green band centered at 509 nm is noticed, with both expressing a quantum yield around 0.3. Heating solutions from 20 °C to 75 °C induces retro-Diels-Alder cleavage, decoupling donor and acceptor and reducing fluorescence intensity more than tenfold. Cooling reverses the process and restores emission with nearly twentyfold increases. Solvent polarity provides another dimension of sensitivity. Absorption spectra did not provide meaningful changes, but emission maxima shifted considerably, from 457 nm in nonpolar methylcyclohexane to 549 nm in polar methanol/water mixtures. Transfer efficiencies rise from 55.0% in methylcyclohexane to 95.3% in methanol/water, while donor lifetimes extend from ~20 ns to >100 ns. The authors extended the study of this FRET system by isolating the endo and exo forms of **94**, with the exo form being thermodynamically favored and more stable due to reduced steric hindrance, while the endo form was kinetically favored but unstable.[187] To achieve white-light emission, the authors introduced a dynamic furan moiety exchange. Heating the solution with furfuryl alcohol at 75 °C would separate the donor from the acceptor which in turn blocked the energy transfer pathway. As the exchange proceeded, green-yellow acceptor fluorescence decreased while violet donor fluorescence reappeared being this process reversible. The combination of complementary violet and green-yellow emissions produced white light, with CIE chromaticity coordinates (0.32, 0.33) close to pure white. Finally, by introducing a furan-dansyl moiety with a longer spacer into the pyrene, the authors demonstrated an achiral-to-chiral conversion by heating the new compound with a slight excess of chiral furan at 110 °C.[188] This exchange replaces the achiral dansyl furan moiety with the chiral furan derivative, effectively converting the dye into a chiral form. During this process, the efficient pyrene-to-dansyl energy transfer is suppressed, and donor emission is restored. The chiral nature of the newly formed compound does not display circular dichroism or circularly polarized luminescence, indicating that chirality does not transfer to the pyrene chromophore in solution. However, in solid state, clear CD and CPL signals

are noticed, with dissymmetry factors on the order of 1.6 x 10^{-3}. This demonstrates that chiral transfer from the non-chromophore moiety to the pyrene chromophore occurs in the aggregated solid, producing measurable chiral optical activity.

1.2.7.4 Emerging Dansyl–Chromophore system

Li *et al.* described the design of probe **95** (Figure 1–26), a polarity-sensitive fluorescent probe directed for lipid droplet imaging in live cells.[189] The molecule was synthesized by coupling a Nile Red derivative with dansyl chloride through a sulfonate ester linkage, providing a dyad that combines solvatochromic sensitivity with resistance to aggregation-caused quenching. Photophysical characterization was carried out in various solvents, including dioxane, dichloromethane, ethanol, methanol, and mixed aqueous systems. Under these conditions, **95** exhibited dual emission bands corresponding to dansyl fluorescence in the 450-500 nm range and Nile Red emission between 580-640 nm. Increasing solvent polarity produced red shifts of approximately 30 nm and a pronounced decrease in Nile Red intensity, while the dansyl signal remained detectable. Lifetime measurements confirmed faster decay in polar solvents, and DFT calculations demonstrated solvent-dependent dipole moment changes consistent with charge-transfer behavior. Biological evaluation was performed in HeLa cells showing viability above 80% at 30 μM of probe **95**, indicating low toxicity. Oleic acid incubation induced droplet proliferation, observed as a four-fold increase in red-channel fluorescence. Oxidative stress induced by hydrogen peroxide led to a decrease in droplet number, with red-channel fluorescence reduced by more than 60 %. Co-staining with commercial markers such as BODIPY 493/503 and Nile Red confirmed selective localization, with Pearson correlation values of 0.85 and 0.94, respectively. Compound **95** showed negligible interference from reactive oxygen and nitrogen species or amino acids, stable fluorescence across pH 1 to 12, and good photostability. Experiments in giant unilamellar vesicles composed of phospholipids, cholesterol, and sphingomyelin confirmed sensitivity to microenvironment polarity, supporting its relevance for biomembrane models.

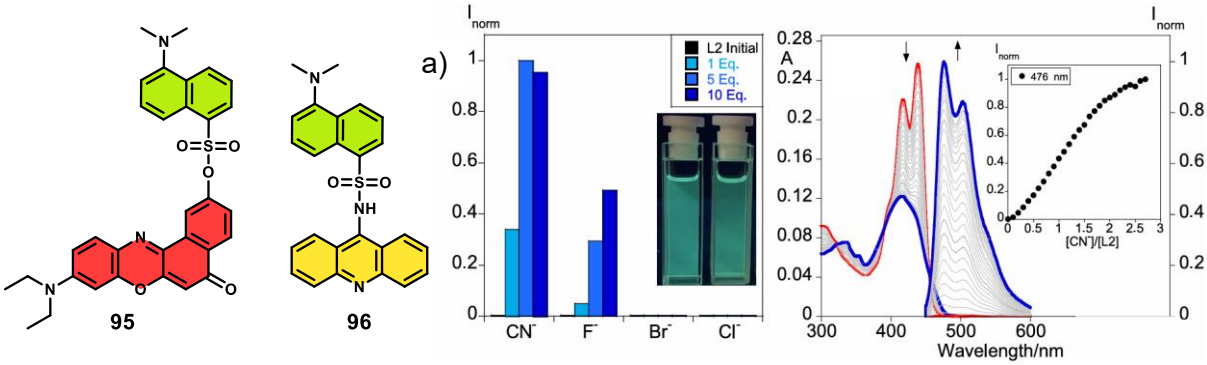


Figure 1–26. Structures of examples of emerging dansyl dyads **95** and **96**. a) Normalized emission intensity of **96** after addition of CN^-, F^-, Br^-, Cl^- in chloroform and inset image under UV light after the addition of CN^- ions in a solution of chloroform (left) and THF (right) of **96**. UV–Vis and luminescent titrations of compounds **96** upon continuous addition of CN^-, in chloroform. Inset: Emission as a function of $[CN^-]/[L2]$ at 476 nm. Adapted from ref. [190] copyright 2024, Elsevier.

With the intention to search new dyad systems we reported the preparation and study of the dansyl-acridine dyad **96**, obtained by reacting 9-aminoacridine with dansyl chloride for the detection of CN^- (Figure 1–26a).[190] In solution, **96** showed absorption maxima near 439 nm but emission was absent in chloroform and THF, however, solid samples displayed an emission at 587 nm. When titrated with anions in chloroform, only strongly basic species such as cyanide and fluoride produced a fluorescence turn-on, with cyanide being most effective. Progressive additions of cyanide reduced the absorption bands at 418 and 440 nm and generated new emission peaks at 476 and 505 nm, accompanied by a shoulder at 546 nm. The quantum yield increased to 29% in chloroform, and lifetime measurements revealed biexponential decay components of 1.2 and 3.9 ns.

Considering the versatility of functionalization offered by dansyl chromophores, together with the wide range of applications already reported for dansyl-based fluorescent sensors, this work aims to explore the design and study of new dansyl derivatives intended for applications in the detection of analytes of environmental interest. In this context, the present work includes both the synthetic development of new dansyl systems, their photophysical investigations and the implementation into supported matrixes such as nanoparticles and polymer thin films to evaluate their reactivity toward a variety of analytes, including cations, anions, among others.

1.2.8 Future Dansyl Perspectives

The studies discussed in this review highlight the broad potential of dansyl-based and related fluorophores as adaptable platforms for sensing and functional material development. Future advances in this field will benefit from a deeper understanding of structure-property

relationships, supported by systematic photophysical studies and complementary computational approaches. Such efforts are expected to enable more predictable control over solvatochromism, aggregation-induced emission, and intramolecular charge-transfer processes.

One of the most promising directions lies in advanced chemical and biological sensing. Dansyl fluorophores exhibit pronounced sensitivity to polarity, viscosity, pH, and microenvironmental changes, making them well suited for next-generation chemosensors and biosensors. Their integration into modular receptor architectures, including macrocycles, hydrogen-bonding motifs, and metal-binding units, may enable selective detection of ions, small molecules, and biologically relevant targets. In this context, ratiometric and lifetime-based sensing strategies are expected to gain increasing relevance, as they overcome the limitations of intensity-based measurements and allow more reliable analysis in complex matrices.

In parallel, dansyl derivatives are likely to continue evolving within biomedical imaging and diagnostic applications. Through molecular engineering, energy-transfer strategies, or incorporation into aggregation-induced emission systems, their optical properties may be further optimized for multichannel or functional imaging. Probes responsive to enzymatic activity, redox status, or local microviscosity may offer new opportunities for monitoring dynamic biological processes, particularly when combined with time-resolved fluorescence techniques.

The role of dansyl units in materials science is also expected to expand. Their incorporation into polymers, hydrogels, liquid-crystalline systems, and hybrid nanomaterials enables fluorescence-based reporting on molecular organization and environmental changes. Such systems hold promises for responsive materials, optical sensing platforms, and supramolecular assemblies, where dansyl fluorophores can serve as versatile reporters within self-organized architectures.

In environmental and food-related analysis, future developments may focus on portable and low-cost sensing platforms. The integration of dansyl-based probes into paper-based devices, microfluidic systems, or wearable formats could facilitate real-time monitoring of contaminants and pollutants, benefiting from the inherent sensitivity of the dansyl chromophore to subtle microenvironmental variations.

Finally, emerging opportunities lie at the intersection of translational and data-driven chemistry. The combination of dansyl fluorophores with machine learning, high-throughput screening, and advanced spectroscopic analysis may accelerate the discovery of new structure-property relationships and sensing concepts. Coupled with sustainable synthetic approaches, these efforts position dansyl-based compounds to evolve from classical fluorescent labels into multifunctional components across analytical, biomedical, and materials-oriented applications.

1.3 References

[1] B. Valeur, Molecular fluorescence: principles and applications, Wiley-VCH, Weinheim, 2002.

[2] J. R. Lakowicz, Principles of fluorescence spectroscopy, 3rd ed., Springer, New York, 2010.

[3] D. Wu, A. C. Sedgwick, T. Gunnlaugsson, E. U. Akkaya, J. Yoon and T. D. James, Fluorescent chemosensors: the past, present and future, *Chem. Soc. Rev.*, **46** (2017) 7105-7123. DOI: 10.1039/c7cs00240h.

[4] Y. Yang, F. Gao, Y. Wang, H. Li, J. Zhang, Z. Sun and Y. Jiang, Fluorescent Organic Small Molecule Probes for Bioimaging and Detection Applications, *Molecules* **27** (2022) 8421. DOI: 10.3390/molecules27238421.

[5] D. K. Mal, H. Pal and G. Chakraborty, A comprehensive review on recent advances in fluorescence-based bio-analytes sensing, *TrAC Trends in Analytical Chemistry*, **171** (2024) 117493. DOI: 10.1016/j.trac.2023.117493.

[6] H. Niu, J. Liu, H. M. O'Connor, T. Gunnlaugsson, T. D. James and H. Zhang, Photoinduced electron transfer (PeT) based fluorescent probes for cellular imaging and disease therapy, *Chem. Soc. Rev.*, **52** (2023) 2322-2357. DOI: 10.1039/d1cs01097b.

[7] L. Yang, J. Y. Niu, R. Sun, Y. J. Xu and J. F. Ge, The pH-influenced PET processes between pyronine and different heterocycles, *Org. Biomol. Chem.*, **15** (2017) 8402–8409. DOI: 10.1039/C7OB02247F.

[8] D. Escudero, Revising Intramolecular Photoinduced Electron Transfer (PET) from First-Principles, *Acc. Chem. Res.*, **49** (2016) 1816–1824. DOI: 10.1021/acs.accounts.6b00299.

[9] J. A. Broussard, B. Rappaz, D. J. Webb and C. M. Brown, Fluorescence resonance energy transfer microscopy as demonstrated by measuring the activation of the serine/threonine kinase Akt, *Nat. Protoc.,* **8** (2013) 265–281. DOI: 10.1038/nprot.2012.147.

[10] B. Zhang, G. Lyu, E. A. Kelly and R. C. Evans, Förster Resonance Energy Transfer in Luminescent Solar Concentrators, *Adv. Sci.,* **9** (2022) 2201160. DOI: 10.1002/advs.202201160.

[11] L. Wu, C. Huang, B. P. Emery, A. C. Sedgwick, S. D. Bull, X. P. He, H. Tian, J. Yoon, J. L. Sessler and T. D. James, Förster resonance energy transfer (FRET)-based small-molecule sensors and imaging agents, *Chem. Soc. Rev.*, **49** (2020) 5110-5139. DOI: 10.1039/c9cs00318e.

[12] D. Udhayakumari, P. Jerome, N. Vijay and T. Hwan Oh, ESIPT: An approach and future perspective for the detection of biologically important analytes, *J. Lumin.*, **267** (2024) 120350. DOI: 10.1016/j.jlumin.2023.120350.

[13] J. Luo, Z. Xie, Z. Xie, J. W. Y. Lam, L. Cheng, H. Chen, C. Qiu, H. S. Kwok, X. Zhan, Y. Liu, D. Zhu and B. Z. Tang, Aggregation-induced emission of 1-methyl-1,2,3,4,5-pentaphenylsilole, *Chem. Commun.*, (2001) 1740–1741. DOI: 10.1039/B105159H.

[13a] Tang, Y., & Tang, B. Z. (Eds.), Principles and applications of aggregation-induced emission. Springer International Publishing, New York, 2019. DOI: 10.1007/978-3-319-99037-8.

[14] M. K. Goshisht, G. K. Patra and N. Tripathi, Fluorescent Schiff base sensors as a versatile tool for metal ion detection: strategies, mechanistic insights, and applications, *Mater. Adv.*, **3** (2022) 2612-2669. DOI: 10.1039/d1ma01175h.

[15] J. Krämer, R. Kang, L. M. Grimm, L. De Cola, P. Picchetti and F. Biedermann, Molecular Probes, Chemosensors, and Nanosensors for Optical Detection of Biorelevant Molecules and Ions in Aqueous Media and Biofluids. *Chem. Rev.*, **122** (2022) 3459-3636. DOI: 10.1021/acs.chemrev.1c00746.

[16] N. W. Nkune, K. Moloudi, B. P. George and H. Abrahamse, An update on recent advances in fluorescent materials for fluorescence molecular imaging: a review, *RSC Adv.,* **15** (2025) 22267–22284. DOI: 10.1039/d5ra03102h.

[17] T. C. Lovell, B. P. Branchaud and R. Jasti, An Organic Chemist's Guide to Fluorophores – Understanding Common and Newer Non-Planar Fluorescent Molecules for Biological Applications, *Eur. J. Org. Chem.,* **27** (2024) e202301196. DOI: 10.1002/ejoc.202301196.

[18] R. Gui and H. Jin, Organic fluorophores-based molecular probes with dual-fluorescence ratiometric responses to in-vitro/in-vivo pH for biosensing, bioimaging and biotherapeutics applications, *Talanta,* **275** (2024) 126171. DOI: 10.1016/j.talanta.2024.126171.

[19] D. Ceballos-Ávila, I. Vázquez-Sandoval, F. Ferrusca-Martínez and A. Jiménez-Sánchez, Conceptually innovative fluorophores for functional bioimaging, *Biosens. Bioelectron.,* **264** (2024) 116638. DOI: 10.1016/j.bios.2024.116638.

[20] D. Udhayakumari, S. Ramasundaram, P. Jerome and T. H. Oh, A Review on Small Molecule Based Fluorescence Chemosensors for Bioimaging Applications, *J. Fluoresc.*, **35** (2025) 3763–3787. DOI: 10.1007/s10895-024-03826-2.

[21] I. Muhammad, T. Z. Ren, R. Han, X. Zhang, K. Dawood and A. Shahzad, Design Strategies and Analytical Performance of Dansyl Fluorophore-Based Fluorescent Sensors for Mercury Ion (Hg^{2+}) Detection in Water. *Crit. Rev. Anal. Chem.*, (2025) 1–15. DOI: 10.1080/10408347.2024.2449532.

[22] G. Weber, Polarization of the fluorescence of macromolecules. I. Theory and experimental method, *Biochem. J.*, **51** (1952) 145–155. DOI: 10.1042/bj0510145.

[23] Ritu, U. Narang and V. Kumar, Heavy Metal Detection with Organic Moiety-Based Sensors: Recent Advances and Future Directions, *ChemBioChem*, **25** (2024) e202400191. DOI: 10.1002/cbic.202400191.

[24] M. Li, Q. Shi, N. Song, Y. Xiao, L. Wang, Z. Chen and T. D. James, Current trends in the detection and removal of heavy metal ions using functional materials, *Chem. Soc. Rev.*, **52** (2023) 5827–5860. DOI: 10.1039/d2cs00683a.

[25] T. Chopra, S. Sasan, L. Devi, R. Parkesh and K. K. Kapoor, A comprehensive review on recent advances in copper sensors, *Coord. Chem. Rev.*, **470** (2022) 214704. DOI: 10.1016/j.ccr.2022.214704.

[26] D. T. Quang and J. S. Kim, Fluoro- and chromogenic chemodosimeters for heavy metal ion detection in solution and biospecimens, *Chem. Rev.*, **110** (2010) 6280–6301. DOI: 10.1021/cr100154p.

[27] S. Chowdhury, B. Rooj, A. Dutta and U. Mandal, Review on recent advances in metal ions sensing using different fluorescent probes, *J. Fluoresc.*, **28** (2018) 999–1021. DOI: 10.1007/s10895-018-2263-y.

[28] M. Saleem, M. Rafiq, M. Hanif, M. A. Shaheen and S. Y. Seo, A brief review on fluorescent copper sensor based on conjugated organic dyes, *J. Fluoresc.*, **28** (2018) 97–165. DOI: 10.1007/s10895-017-2178-z.

[29] Z. H. Yuan, Y. S. Yang, P. C. Lv and H. L. Zhu, Recent Progress in Small-Molecule Fluorescent Probes for Detecting Mercury Ions, *Crit. Rev. Anal. Chem.*, **52** (2022) 250–274. DOI: 10.1080/10408347.2020.1797466.

[30] Q. Li and Y. Zhou, Recent advances in fluorescent materials for mercury(II) ion detection, *RSC Adv.*, **13** (2023) 19429–19446. DOI: 10.1039/d3ra02410e.

[31] L. Li, J. Wang, S. Xu, C. Li and B. Dong, Recent Progress in Fluorescent Probes For Metal Ion Detection, *Front. Chem.*., **10** (2022) 875241. DOI: 10.3389/fchem.2022.875241.

[32] X. Cheng, T. Luo, F. Chu, B. Feng, S. Zhong, F. Chen, J. Dong and W. Zeng, Simultaneous detection and removal of mercury (II) using multifunctional fluorescent materials, *Sci. Total Environ.*, **905** (2023) 167070. DOI: 10.1016/j.scitotenv.2023.167070.

[33] P. Wang, L. Liu, P. Zhou, W. Wu, J. Wu, W. Liu and Y. Tang, A peptide-based fluorescent chemosensor for multianalyte detection, *Biosens. Bioelectron.*, **72** (2015) 80–86. DOI: 10.1016/j.bios.2015.04.094.

[34] J. Huang, M. Tang, M. Liu, M. Zhou, Z. Liu, Y. Cao, M. Zhu, S. Liu and W. Zeng, Development of a fast responsive and highly sensitive fluorescent probe for Cu^{2+} ion and imaging in living cells, *Dyes and Pigments*, **107** (2014) 1–8. DOI: 10.1016/j.dyepig.2014.02.022.

[35] P. Wang, J. Wu, P. Zhou, W. Liu and Y. Tang, A novel peptide-based fluorescent chemosensor for measuring zinc ions using different excitation wavelengths and application in live cell imaging, *J. Mater. Chem. B*, **3** (2015) 3617–3624. DOI: 10.1039/C5TB00142K

[36] P. Wang, J. Wu, P. Su, C. Xu, Y. Ge, D. Liu, W. Liu and Y. Tang, Fluorescence "on-off-on" peptide-based chemosensor for the selective detection of Cu^{2+} and S^{2-} and its application in living cell bioimaging, *Dalton Trans.*, **45** (2016) 16246–16254. DOI: 10.1039/C6DT03330J

[37] P. Wang, J. Wu, P. Su, C. Shan, P. Zhou, Y. Ge, D. Liu, W. Liu and Y. Tang, A novel peptide-based fluorescent probe for selective detection of Fe^{3+} and its application in living cells, *J. Mater. Chem. B*, **4** (2016) 4526–4533. DOI: 10.1039/C6TB00517B.

[38] Y. Bin Ruan, A. Depauw and I. Leray, Aggregation-induced emission enhancement upon Al^{3+} complexation with a tetrasulfonated calix[4]bisazacrown fluorescent molecular sensor, *Org. Biomol. Chem.*, **12** (2014) 4335–4341. DOI: 10.1039/C4OB00187G.

[39] K. H. Jung, E. T. Oh, H. J. Park and K. H. Lee, Development of new peptide-based receptor of fluorescent probe with femtomolar affinity for Cu^{+} and detection of Cu^{+} in Golgi apparatus, *Biosens. Bioelectron.*, **85** (2016) 437–444. DOI: 10.1016/j.bios.2016.04.101.

[40] S. Zhou, Z. Q. Zhou, X. X. Zhao, Y. H. Xiao, G. Xi, J. T. Liu and B. X. Zhao, A dansyl-based fluorescence chemosensor for Hg^{2+} and its application in complicated environment samples, *Spectrochim. Acta A Mol. Biomol. Spectrosc.*, **148** (2015) 348–354. DOI: 10.1016/j.saa.2015.03.126.

[41] M. G. Choi, J. Kim, J. M. Hong, I. J. Chang, S. Ahn and S. K. Chang, Cu^{2+}-selective ratiometric fluorescence signaling probe based on the hydrolysis of dansylhydrazine, *Tetrahedron Lett.*, **57** (2016) 975–978. DOI: 10.1016/j.tetlet.2016.01.052.

[42] L. N. Neupane and K. H. Lee, Selective and sensitive turn on detection of Hg^{2+} in aqueous solution using a thioether-appended dipeptide, *Tetrahedron Lett.*, **54** (2013) 5007–5010. DOI: 10.1016/j.tetlet.2013.07.003.

[43] P. Srivastava, R. Ali, S. S. Razi, M. Shahid, S. Patnaik and A. Misra, A simple blue fluorescent probe to detect Hg^{2+} in semiaqueous environment by intramolecular charge transfer mechanism, *Tetrahedron Lett.*, **54** (2013) 3688–3693. DOI: 10.1016/j.tetlet.2013.05.014.

[44] J. Isaad and A. El Achari, Azathia crown ether possessing a dansyl fluorophore moiety functionalized silica nanoparticles as hybrid material for mercury detection in aqueous medium, *Tetrahedron*, **69** (2013) 4866–4874. DOI: 10.1016/j.tet.2013.04.072.

[45] L. J. Ma, J. Liu, L. Deng, M. Zhao, Z. Deng, X. Li, J. Tang and L. Yang, Selective and sensitive fluorescence-shift probes based on two dansyl groups for mercury(II) ion detection, *Photochem. Photobiol. Sci.*, **13** (2014) 1521–1528. DOI: 10.1039/C4PP00094C.

[46] S. Zhang, T. Yu, M. Sun, H. Yu, Z. Zhang, S. Wang and H. Jiang, Highly sensitive and selective fluorescence detection of copper (II) ion based on multi-ligand metal chelation, *Talanta*, **126** (2014) 185–190. DOI: 10.1016/j.talanta.2014.03.076

[47] L. J. Ma, W. Cao, J. Liu, M. Zhang and L. Yang, Chromium (III) ion-selective "turn-on" and ratiometric probe based on the asparagine bearing dansyl group in aqueous solutions, *Sens. Actuators B Chem.*, **181** (2013) 782–786. DOI: 10.1016/j.snb.2013.01.095.

[48] G. N. Wei, J. L. Zhang, C. Jia, W. Z. Fan and L. R. Lin, Selective recognition of sulfate anions in a 95% ethanol solvent with a simple neutral salicylaldehyde dansyl hydrazine Schiff base tuned by Brønsted–Lowry acid–base reaction, *Spectrochim. Acta A Mol. Biomol. Spectrosc.*, **128** (2014) 168–175. DOI: 10.1016/j.saa.2014.02.088.

[49] Y. A. Jeong, I. J. Chang and S. K. Chang, Discriminative sensing of sulfide and azide ions in solution by a nitrobenzoxadiazole-dansyl dyad, *Sens. Actuators B Chem.*, **224** (2016) 73–80. DOI: 10.1016/j.snb.2015.10.013.

[50] S. Areti, S. Bandaru, D. S. Yarramala and C. P. Rao, Optimizing the electron-withdrawing character on benzenesulfonyl moiety attached to a glyco-conjugate to impart sensitive and selective sensing of cyanide in HEPES buffer and on cellulose paper and silica gel strips, *Anal. Chem.*, **87** (2015) 12396–12403. DOI: 10.1021/acs.analchem.5b04085.

[51] R. Alam, T. Mistri, P. Mondal, D. Das, S. K. Mandal, A. R. Khuda-Bukhsh and M. Ali, A novel copper(II) complex as a nitric oxide turn-on fluorosensor: intracellular applications and DFT calculation, *Dalton Trans.*, **43** (2014) 2566–2576. DOI: 10.1039/C3DT52521J.

[52] R. Qian, L. Ding, L. Yan and H. Ju, Fluorescence imaging for in situ detection of cell surface sialic acid by competitive binding of 3-(dansylamino)phenylboronic acid, *Anal. Chim. Acta*, **894** (2015) 189–198. DOI: 10.1016/j.aca.2015.08.054.

[53] S. Areti, S. K. Verma, J. Bellare and C. P. Rao, Selenocysteine vs Cysteine: Tuning the Derivatization on Benzenesulfonyl Moiety of a Triazole-Linked Dansyl Connected Glycoconjugate for Selective Recognition of Selenocysteine and the Applicability of the Conjugate in Buffer, in Serum, on Silica Gel, and in HepG2 Cells, *Anal. Chem.*, **88** (2016) 7259–7267. DOI: 10.1021/acs.analchem.6b01518.

[54] K. Kaur and S. Kumar, Dansyl-anthracene dyads for ratiometric fluorescence recognition of Cu^{2+}, *Dalton Trans.*, **40** (2011) 2451–2458. DOI: 10.1039/C0DT01016B.

[55] Z. Hu, J. Hu, Y. Cui, G. Wang, X. Zhang, K. Uvdal and H. W. Gao, A facile "click" reaction to fabricate a FRET-based ratiometric fluorescent Cu^{2+} probe, *J. Mater. Chem. B*, **2** (2014) 4467–4472. DOI: 10.1039/C4TB00441H

[56] H. J. Lee, M. J. Cho and S. K. Chang, Ratiometric signaling of hypochlorite by the oxidative cleavage of a sulfonhydrazide-based rhodamine-dansyl dyad, *Inorg. Chem.*, **54** (2015) 8644–8649. DOI: 10.1021/acs.inorgchem.5b01284.

[57] H. Li, X. Wang, K. Yuan, L. Lv, K. Liu and Z. Li, Fluorescent Mechanism of a Highly Selective Probe for Copper(II) Detection: A Theoretical Study, *ACS Omega*, **8** (2023) 17171–17180. DOI: 10.1021/acsomega.3c01528.

[58] R. Nagarajan, H. I. Ryoo, B. D. Vanjare, N. Gyu Choi and K. Hwan Lee, Novel phenylalanine derivative-based turn-off fluorescent chemosensor for selective Cu^{2+} detection in physiological pH, *J. Photochem. Photobiol. A Chem.*, **418** (2021) 113435. DOI: 10.1016/j.jphotochem.2021.113435.

[59] H. Xu, Y. Xiao, Y. Liu and W. Sun, Research Progress on Naphthalimide Fluorescent Probes, *Adv. Sens. Res.*, **3** (2023) 2300032. DOI: 10.1002/adsr.202300032.

[60] M. Zhou, X. Wang, K. Huang, Y. Huang, S. Hu and W. Zeng, A fast, highly selective and sensitive dansyl-based fluorescent sensor for Cu^{2+} ions and its imaging application in living cells, *Tetrahedron Lett.*, **58** (2017) 991–994. DOI: 10.1016/j.tetlet.2017.01.090.

[61] Y. Liu, B. Jiang, L. Zhao, L. Zhao, Q. Wang, C. Wang and B. Xu, A dansyl-based fluorescent probe for sensing Cu^{2+} in aqueous solution, *Spectrochim. Acta A Mol. Biomol. Spectrosc.*, **261** (2021) 120009. DOI: 10.1016/j.saa.2021.120009

[62] X. Wang, P. Xia and X. Huang, A dansyl-appended N-heterocycle for Cu^{2+} and S^{2-} recognition via a displacement mode, *Spectrochim. Acta A Mol. Biomol. Spectrosc.*, **210** (2019) 98–104. DOI: 10.1016/j.saa.2018.11.017.

[63] H. Cai, Y. Liang, L. Huang and J. Wang, elay detection of Cu^{2+} and bovine serum albumin by a dansyl derivative-based fluorescent probe, *Spectrochim. Acta A Mol. Biomol. Spectrosc.*, **277** (2022) 121281. DOI: 10.1016/j.saa.2022.121281.

[64] Y. Wang, J. Zhou, L. Zhao and B. Xu, A dual-responsive and highly sensitive fluorescent probe based on a dansyl derivative for Cu^{2+} and pH, *Dyes and Pigments*, **180** (2020) 108513. DOI: 10.1016/j.dyepig.2020.108513.

[65] P. Wang, X. Cao, S. Xue, Z. Wang, Y. Zhou and J. Wu, Peptide-based fluorescent probe with large Stokes shift for specific sequential detection of copper(II) ions and histidine, *Microchem. J.*, **207** (2024) 111728. DOI: 10.1016/j.microc.2024.111728.

[66] Y. Ren, M. Jia, S. Xiong, C. Pu, P. Wang and Y. An, Highly selective sequential detection of Cu^{2+} and S^{2-} using a large Stokes shift peptide-based fluorescent probe and its multi-application, *Microchem. J.*, **216** (2025) 114732. DOI: 10.1016/j.microc.2025.114732.

[67] Z. Guo, Q. Wang, D. Zhou, Y. An, P. Wang and F. Liao, A novel peptide-based fluorescent probe with a large Stokes shift for rapid and sequential detection of Cu^{2+} and CN^- in aqueous systems and live cells, *Spectrochim. Acta A Mol. Biomol. Spectrosc.*, **264** (2022) 120257. DOI: 10.1016/j.saa.2021.120257.

[68] P. Wei, L. Xiao, Y. Gou, F. He, D. Zhou, Y. Liu, B. Xu, P. Wang and Y. Zhou, Fluorescent "on–off–on" probe based on copper peptide backbone for specific detection of Cu^{2+} and H_2S in 100% aqueous medium and application in cell imaging, real water samples and test strips, *Microchem. J.*, **182** (2022) 107848. DOI: 10.1016/j.microc.2022.107848.

[69] Q. Wang, Z. Guo, D. Zhou, J. Wu, P. Wang, X. Yang and S. Wen, A novel fluorescent probe for highly selective and sensitive detection of sulfur ions in real samples and living cells based on the tripeptide-Cu^{2+} ensemble system, *Microchem. J.*, **169** (2021) 106612. DOI: 10.1016/j.microc.2021.106612.

[70] P. Wei, L. Xiao, P. Hou, Q. Wang and P. Wang, A novel Cu(II)-assisted peptide fluorescent probe for highly sensitive detection of glyphosate in real samples: real application in test strips and smartphone, *Anal. Bioanal. Chem.*, **415** (2023) 5985–5996. DOI: 10.1007/s00216-023-04869-3.

[71] Y. An, P. Wang and Z. Yue, A sequential and reversibility fluorescent pentapeptide probe for Cu(II) ions and hydrogen sulfide detections and its application in two different living cells imaging, *Spectrochim. Acta A Mol. Biomol. Spectrosc.*, **216** (2019) 319–327. DOI: 10.1016/j.saa.2019.03.065

[72] Y. Hu, S. Quan, C. Zhao, J. Li, X. Sun and J. Xiao, An "on–off–on" fluorescent peptide probe for the specific detection of Cu^{2+} and S^{2-} in living cells and zebrafish, *New J. Chem.*, **46** (2022) 7663–7668. DOI: 10.1039/D2NJ00408A.

[73] A. Thangaraj, V. Bhardwaj and S. K. Sahoo, A multi-analyte selective dansyl derivative for the fluorescence detection of Cu(ii) and cysteine, *Photochem. Photobiol. Sci.*, **18** (2019) 1533–1539. DOI: 10.1039/C9PP00080A.

[74] W. Nasomphan, P. Tangboriboonrat and S. Smanmoo, Dansyl Based "Turn-On" Fluorescent Sensor for Cu2+ Ion Detection and the Application to Living Cell Imaging, *J. Fluoresc.*, **27** (2017) 2201–2212. DOI: 10.1007/s10895-017-2161-8.

[75] H. Jiang, Z. Li, Y. Kang, L. Ding, S. Qiao, S. Jia, W. Luo and W. Liu, A two-photon fluorescent probe for Cu^{2+} based on dansyl moiety and its application in bioimaging, *Sens. Actuators B Chem.*, **242** (2017) 112–117. DOI: 10.1016/j.snb.2016.11.033.

[76] Y. Zhao, D. Chen, J. Yang and B. Yang, Visual and fast detection of trace copper ions using biosensor based on FRET, *Spectrochim. Acta A Mol. Biomol. Spectrosc.*, **217** (2019) 101–106. DOI: 10.1016/j.saa.2019.03.082.

[77] S. Mukherjee, K. Sarkar and S. Biswas, A fluorophore anchored MOF for fast and sensitive sensing of Cu(II) and 3-nitrotyrosine in a physiological medium, *Dalton Trans.*, **52** (2023) 5597–5605. DOI: 10.1039/D3DT00660C.

[78] L. Zhang, P. Zhao, S. Yu, J. Kong, L. Gao and L. Li, Dansyl-modified tryptophan fluorescence sensor for highly sensitive and selective detection of Hg^{2+} in aqueous solutions, *Microchem. J.*, **200** (2024) 110520. DOI: 10.1016/j.microc.2024.110520.

[79] W. Deng, S. Li, M. Zhou, M. Zheng, P. Wang and Y. An, Ratiometric peptide-based fluorescent probe with large Stokes shift for detection of Hg^{2+} and S^{2-} and its applications in cells imaging and smartphone-assisted recognition, *Spectrochim. Acta A Mol. Biomol. Spectrosc.*, **315** (2024) 124306. DOI: 10.1016/j.saa.2024.124306.

[80] M. Zhou, M. Zheng, P. Wang and Y. An, A novel ratiometric peptide-based fluorescent probe for sequential detection of Hg^{2+} and S^{2-} ions and its application in living cells and zebrafish imaging, *Spectrochim. Acta A Mol. Biomol. Spectrosc.*, **309** (2024) 123829. DOI: 10.1016/j.saa.2023.123829.

[81] P. Wang, Y. An and J. Wu, Highly sensitive turn-on detection of mercury(II) in aqueous solutions and live cells with a chemosensor based on tyrosine, *Spectrochim. Acta A Mol. Biomol. Spectrosc.*, **230** (2020) 118004. DOI: 10.1016/j.saa.2019.118004.

[82] S. Xue, P. Wang and K. Chen, A novel fluorescent chemosensor for detection of mercury(II) ions based on dansyl-peptide and its application in real water samples and living LNCaP cells, *Spectrochim. Acta A Mol. Biomol. Spectrosc.*, **226** (2020) 117616. DOI: 10.1016/j.saa.2019.117616.

[83] P. Wei, L. Xiao, Y. Gou, F. He, P. Wang and X. Yang, A novel peptide-based relay fluorescent probe with a large Stokes shift for detection of Hg^{2+} and S^{2-} in 100 % aqueous medium and living cells: Visual detection via test strips and smartphone, *Spectrochimica Acta Part A: Molecular and Biomolecular Spectroscopy*, **285** (2023) 121836. DOI: 10.1016/j.saa.2022.121836.

[84] X. Pang, J. Dong, L. Gao, L. Wang, S. Yu, J. Kong and L. Li, Dansyl-peptide dual-functional fluorescent chemosensor for Hg^{2+} and biothiols, *Dyes and Pigments*, **173** (2020) 107888. DOI: 10.1016/j.dyepig.2019.107888.

[85] S. Yu, L. Gao, R. Li, C. Fu, W. Meng, L. Wang and L. Li, Ultrasensitive mercury ion and biothiol detection based on dansyl-His-Pro-Gly-Asp-NH_2 fluorescent sensor, *Spectrochim. Acta A Mol. Biomol. Spectrosc.*, **250** (2020) 119246. DOI: 10.1016/j.saa.2020.119246.

[86] Y. Li, Z. Ren, Y. Ge, C. Di, J. Zhou, J. Wu and L. Jia, A novel peptide fluorescent probe based on different fluorescence responses for detection of mercury species and hydrogen sulfide, *Microchem. J.*, **184** (2023) 108160. DOI: 10.1016/j.microc.2022.108160.

[87] A. Jose, R. Sahadevan, M. Vijay, S. Sadhukhan and M. Porel, Dansyl-appended sequence-defined oligomers for selective ultrasensitive detection of Hg^{2+} in water, paper strips, living cells and its efficient removal, *Sens. Actuators B Chem.*, **380** (2023) 133335. DOI: 10.1016/j.snb.2023.133335.

[88] A. Aliberti, P. Vaiano, A. Caporale, M. Consales, M. Ruvo and A. Cusano, Fluorescent chemosensors for Hg^{2+} detection in aqueous environment, *Sens. Actuators B Chem.*, **247** (2017) 727–735. DOI: 10.1016/j.snb.2017.03.026.

[89] S. Gadiyaram, M. Aakshika Sree, N. Sharma and D. Amilan Jose, An amphiphilic dansyl-based multianalyte sensor for the detection of Hg^{2+}, PPi, and TNP: a three-in-one chemical sensor, *Methods*, **223** (2024) 45–55. DOI: 10.1016/j.ymeth.2024.01.007.

[90] L. He, H. Tao, S. Koo, G. Chen, A. Sharma, Y. Chen, I. T. Lim, Q. Y. Cao and J. S. Kim, Multifunctional fluorescent nanoprobe for sequential detections of Hg^{2+} ions and biothiols in live cells, *ACS Appl. Bio Mater.*, **1** (2018) 871–878. DOI: 10.1021/acsabm.8b00300.

[91] B. Uttam, S. Polepalli, S. Sinha, A. Majumder and C. P. Rao, Selective sensing and removal of mercury ions by encapsulating a dansyl-appended calix[4]arene conjugate in a zeolitic imidazolate framework as an organic–inorganic hybrid nanomaterial, *ACS Appl. Nano Mater.*, **5** (2022) 11371-11380. DOI: 10.1021/acsanm.2c02459.

[92] M. Oguz, A. A. Bhatti, S. Karakurt, M. Aktas and M. Yilmaz, New water soluble Hg^{2+} selective fluorescent calix[4]arenes: Synthesis and application in living cells imaging, *Spectrochim. Acta A Mol. Biomol. Spectrosc.*, **171** (2017) 340–345. DOI: 10.1016/j.saa.2016.08.042.

[93] P. Wang, J. Wu, Y. An and Y. Liao, A novel fluorescent chemosensor for detection of Zn(II) ions based on dansyl-appended dipeptide in two different living cells, *Spectrochim. Acta A Mol. Biomol. Spectrosc.*, **220** (2019) 117140. DOI: 10.1016/j.saa.2019.117140.

[94] P. Wang, D. Zhou and B. Chen, High selective and sensitive detection of Zn^{2+} using tetrapeptide-based dansyl fluorescent chemosensor and its application in cell imaging, *Spectrochim. Acta A Mol. Biomol. Spectrosc.*, **204** (2018) 735-742. DOI: 10.1016/j.saa.2018.07.001.

[95] P. Wang, Q. Wang, Z. Guo, S. Xue, B. Chen, Y. Liu, W. Ren, X. Yang and S. Wen, A bifunctional peptide-based fluorescent probe for ratiometric and turn-on detection of Zn(II) ions and its application in living cells, *Spectrochim. Acta A Mol. Biomol. Spectrosc.*, **268** (2022) 120653. DOI: 10.1016/j.saa.2021.120653.

[96] S. Yu, Y. Li, L. Gao, P. Zhao, L. Wang, L. Li and Y. W. Lin, A highly selective and sensitive Zn^{2+} fluorescent sensor based on zinc finger-like peptide and its application in cell imaging, *Spectrochim. Acta A Mol. Biomol. Spectrosc.*, **261** (2021) 120042. DOI: 10.1016/j.saa.2021.120042.

[97] J. Wen, Q. Hua, S. Ding, A. Sun and Y. Xia, Recent advances in fluorescent probes for zinc ions based on various response mechanisms, *Crit. Rev. Anal. Chem.*, **54** (2024) 3313–3344. DOI: 10.1080/10408347.2023.2238078.

[98] J. Yu, H. Yu, S. Wang and Y. Qi, Progress in research of zinc ion fluorescent probes for biological imaging, *J. Lumin.*, **266** (2024) 120318. DOI: 10.1016/j.jlumin.2023.120318.

[99] A. A. Ahamed, S. A. Alharbi and G. Venkatesan, A Julolidine Aldehyde Dansyl Hydrazine Schiff Base as Fluorescence Chemosensor for Zn^{2+} ions Recognition and its Application, *J. Fluoresc.*, **35** (2025) 4547–4557. DOI: 10.1007/s10895-024-03842-2.

[100] G. Pourfallah and X. Lou, A novel recyclable magnetic nanostructure for highly sensitive, selective and reversible detection of zinc ions in aqueous solutions, *Sens. Actuators B Chem.*, **233** (2016) 379–387. DOI: 10.1016/j.snb.2016.04.087.

[101] P. Wang, Y. An and Y. Liao, A novel peptide-based fluorescent chemosensor for Cd(II) ions and its applications in bioimaging, *Spectrochim. Acta A Mol. Biomol. Spectrosc.*, **216** (2019) 61–68. DOI: 10.1016/j.saa.2019.03.014.

[102] W. Deng, J. Liu, S. Zhao, Z. Liu, Y. Wang, P. Wang, Y. An and J. Wu, Highly selective peptide-based fluorescent turn-on probe with large Stokes shift for the detection of Cd^{2+} and its applications in bio-imaging and smartphone-assisted recognition, *J. Mol. Struct.*, **1321** (2024) 140146. DOI: 10.1016/j.molstruc.2024.140146.

[103] P. Wang, D. Zhou and B. Chen, A fluorescent dansyl-based peptide probe for highly selective and sensitive detect Cd^{2+} ions and its application in living cell imaging, *Spectrochim. Acta A Mol. Biomol. Spectrosc.*, **207** (2019) 276–283. DOI: 10.1016/j.saa.2018.09.029.

[104] P. Wang, L. Duan and Y. Liao, A retrievable and highly selective fluorescent probe for detection of Cd^{2+} and Cys in aqueous solutions and live cells, *Microchem. J.*, **146** (2019) 818–827. DOI: 10.1016/j.microc.2019.02.004.

[105] C. T. Shi, Z. Y. Huang, A. Bin Wu, Y. X. Hu, N. C. Wang, Y. Zhang, W. M. Shu and W. C. Yu, Recent progress in cadmium fluorescent and colorimetric probes, *RSC Adv.*, **11** (2021) 29632–29660. DOI: 10.1039/d1ra05048f.

[106] A. Akheel Ahmed, N. Mohan, U. Mithra, V. Vijayakumar and S. Sarveswari, Organic chemosensors: A comprehensive review of lead, cadmium, and arsenic ion detection strategies, *Results Chem.*, **18** (2025) 102823. DOI: 10.1016/j.rechem.2025.102823.

[107] W. Li, X. Zhang, X. Hu, Y. Shi, Z. Li, X. Huang, W. Zhang, D. Zhang, X. Zou and J. Shi, A smartphone-integrated ratiometric fluorescence sensor for visual detection of cadmium ions, *J. Hazard. Mater.*, **408** (2021) 124872. DOI: 10.1016/j.jhazmat.2020.124872.

[108] S. K. Sahoo and G. Crisponi, Recent advances on iron(III) selective fluorescent probes with possible applications in bioimaging, *Molecules*, **24** (2019) 3267. DOI: 10.3390/molecules24183267.

[109] S. K. Sahoo, D. Sharma, R. K. Ber, G. Crisponi and J. F. Callan, Iron(III) selective molecular and supramolecular fluorescent probes, *Chem. Soc. Rev.*, **41** (2012) 7195–7227. DOI: 10.1039/C2CS35152H.

[110] Z. Li, J. T. Hou, S. Wang, L. Zhu, X. He and J. Shen, Recent advances of luminescent sensors for iron and copper: Platforms, mechanisms, and bio-applications, *Coord. Chem. Rev.*, **469** (2022) 214695. DOI: 10.1016/j.ccr.2022.214695.

[111] G. Gao, X. Wang, Z. Wang, X. Jin, L. Ou, J. Zhou and P. Xie, A simple and effective dansyl acid based turn-on fluorescent probe for detecting labile ferrous iron in physiological saline and live cells, *Talanta*, **215** (2020) 120908. DOI: 10.1016/j.talanta.2020.120908.

[112] Y. Qi, H. Xu and H. Chen, Recent Progress in Silver-Ion-Selective Fluorescence Chemical Sensors, *ACS Omega*, **10** (2025) 11743–11754. DOI: 10.1021/acsomega.4c11607.

[113] P. Su, Z. Zhu, J. Wang, B. Cheng, W. Wu, K. Iqbal and Y. Tang, A biomolecule-based fluorescence chemosensor for sequential detection of Ag^+ and H_2S in 100% aqueous solution and living cells, *Sens. Actuators B Chem.*, **273** (2018) 93–100. DOI: 10.1016/j.snb.2018.06.037.

[114] H. M. Al-Saidi and S. Khan, A Review on Organic Fluorimetric and Colorimetric Chemosensors for the Detection of Ag(I) Ions, *Crit. Rev. Anal. Chem.*, **54** (2024) 1810–1836. DOI: 10.1080/10408347.2022.2133561.

[115] C. L. Li, P. hsuan Lu, S. Y. Lin and A. T. Wu, A turn-on dansyl-based fluorescent chemosensor for the recognition of Pb^{2+}, *J. Photochem. Photobiol. A: Chem.*, **385** (2019) 112088. DOI: 10.1016/j.jphotochem.2019.112088.

[116] H. Soni, S. A. Gandhi, A. Pandya and P. G. Sutariya, Dansyl driven fluorescence paper-based quencher probe for Pr^{3+} and I^- based on calix[4]arene, *J. Photochem. Photobiol. A: Chem.*, **431** (2022) 114012. DOI: 10.1016/j.jphotochem.2022.114012.

[117] L. Yu, S. Wang, K. Huang, Z. Liu, F. Gao and W. Zeng, Fluorescent probes for dual and multi-analyte detection, *Tetrahedron*, **71** (2015) 4679–4706. DOI: 10.1016/j.tet.2015.04.115.

[118] J. L. Kolanowski, F. Liu and E. J. New, Fluorescent probes for the simultaneous detection of multiple analytes in biology, *Chem. Soc. Rev.*, **47** (2018) 195–208. DOI: 10.1039/C7CS00528H.

[119] Y. Yue, F. Huo, F. Cheng, X. Zhu, T. Mafireyi, R. M. Strongin and C. Yin, Functional synthetic probes for selective targeting and multi-analyte detection and imaging, *Chem. Soc. Rev.*, **48** (2019) 4155–4177. DOI: 10.1039/C8CS01006D.

[120] P. Wang, J. Wu and C. Zhao, A water-soluble peptide fluorescent chemosensor for detection of Cd^{2+} and Cu^{2+} by two different response modes and its application in living LNcap cells, *Spectrochim. Acta A Mol. Biomol. Spectrosc.*, **226** (2020) 117600. DOI: 10.1016/j.saa.2019.117600.

[121] P. Wang, M. Jia and S. Xue, Rational design of a peptide-based fluorescent probe for selective recognition of Ag^{+} and Cu^{2+} ions and its multifunctional applications, *Luminescence*, **40** (2025) e70291. DOI: 10.1002/bio.70291.

[122] P. Wang and J. Wu, Highly selective and sensitive detection of Zn(II) and Cu(II) ions using a novel peptide fluorescent probe by two different mechanisms and its application in live cell imaging, *Spectrochim. Acta A Mol. Biomol. Spectrosc.*, **208** (2019) 140–149. DOI: 10.1016/j.saa.2018.09.054.

[123] P. Wang, S. Xue and X. Yang, A novel peptide-based fluorescent chemosensor for detection of Zn^{2+} and Cu^{2+} through differential response and application in logic-gate and bioimaging, *Microchem. J.*, **158** (2020) 105147. DOI: 10.1016/j.microc.2020.105147.

[124] C. Pu, S. Li, X. Cao, Y. Ren, R. Bai, F. You and P. Wang, A novel dual-function peptide-based fluorescent probe with large Stokes shift for the simultaneous detection and quantification of Ag(I) and Hg(II) ions, *Spectrochim. Acta A Mol. Biomol. Spectrosc.*, **336** (2025) 126032. DOI: 10.1016/j.saa.2025.126032.

[125] G. Anand and M. Porel, Hydroxy-terminated tunable triazole scaffolds for selective and discriminative Pb(II)/Ag(I) detection and their removal, and protein interaction profiling, *Talanta*, **297** (2026) 128643. DOI: 10.1016/j.talanta.2025.128643.

[126] G. Donadio, R. Di Martino, R. Oliva, L. Petraccone, P. Del Vecchio, B. Di Luccia, E. Ricca, R. Isticato, A. Di Donato and E. Notomista, A new peptide-based fluorescent probe selective for zinc(II) and copper(II), *J. Mater. Chem. B*, **4** (2016) 6979–6988. DOI: 10.1039/C6TB00671J.

[127] I. Lourenço, F. Duarte, G. M. Dobrikov, A. Kurutos, I. Slavchev, J. L. Capelo-Martínez, H. M. Santos and C. Lodeiro, Design and evaluation of dansyl-derived chemosensors for disulfide-cleavage-triggered detection: photophysical, metal sensing, and thermometric applications, *J. Mater. Chem. C*, **13** (2025) 6708–6719. DOI: 10.1039/D4TC04750H.

[128] F. Duarte, G. Dobrikov, A. Kurutos, H. M. Santos, J. Fernández-Lodeiro, J. L. Capelo-Martinez, E. Oliveira and C. Lodeiro, Enhancing water sensing via aggregation-induced emission (AIE) and solvatofluorochromic studies using two new dansyl derivatives containing a disulfide

bond: pollutant metal ions detection and preparation of water-soluble fluorescent polymeric particles, *Dyes and Pigments*, **218** (2023) 111428. DOI: 10.1016/j.dyepig.2023.111428.

[129] F. Duarte, G. Dobrikov, A. Kurutos, J. L. Capelo-Martinez, H. M. Santos, E. Oliveira and C. Lodeiro, Development of fluorochromic polymer-doped materials as platforms for temperature sensing using three dansyl derivatives bearing a sulfur bridge, *J. Photochem. Photobiol. A: Chem.*, **445** (2023) 115033. DOI: 10.1016/j.jphotochem.2023.115033.

[130] I. Pereira-Gomes, F. Duarte, G. M. Dobrikov, I. Slavchev, A. Kurutos, J. L. Capelo-Martinez, H. M. Santos and C. Lodeiro, Tetra dansylamides substituted cyclen and cyclam macrocycles as fluorescent sensing probes for metal ions and temperature-responsive materials in doped polymers, *Dyes Pigments*, **232** (2025) 112461. DOI: 10.1016/j.dyepig.2024.112461.

[131] F. Duarte, C. Cuerva, G. M. Dobrikov, A. Kurutos, N. G. Vassilev, J. Fernández-Lodeiro, J. L. Capelo-Martinez, H. M. Santos and C. Lodeiro, Engineering multifunctional Cyclen fluorophores for metal ion sensing, self-assembly and Nanocolloid applications, *Spectrochim. Acta A Mol. Biomol. Spectrosc.*, **349** (2026) 127285. DOI: 10.1016/j.saa.2025.127285.

[132] A. Jayaprakash, R. Mol K. M and M. Porel, Hybrid dansyl-triazine based mono and bidentate ligands for the selective sensing of fluoride anion through fluorescence enhancement, *RSC Adv.*, **15** (2025) 15801–15805. DOI: 10.1039/D5RA01092F.

[133] S. Mongkholkaew, A. Songsasen, W. Sirisaksoontorn and B. Wannalerse, A colorimetric and fluorescence sensor based on biphenolic-dansyl derivative for specific fluoride ion detection, *Supramol. Chem.*, **33** (2021) 151–159. DOI: 10.1080/10610278.2021.1950720

[134] G. Pedro, F. Duarte, I. Lourenço, G. M. Dobrikov, A. Kurutos, L. Fernandes, E. Gaspar, H. M. Santos, J. L. Capelo-Martinez, E. Oliveira and C. Lodeiro, Targeted identification of cyanide and fluoride ions utilizing dansyl-derived fluorescent probes: a deprotonation-driven sensing mechanism, *Inorg. Chem. Commun.*, **181** (2025) 115290.

[135] E. Jeong, S. Yoon, H. S. Lee, A. Kumar and P. S. Chae, TURN-ON fluorescence detection of cyanide using an ensemble system consisting of a dansyl-based cationic probe and dicyanovinyl derivative, *Dyes and Pigments*, **162** (2019) 348–357. DOI: 10.1016/j.dyepig.2018.10.033

[136] C. Immanuel David and H. il Lee, Cutting-edge advances in colorimetric and fluorescent chemosensors for detecting lethal cyanide ion: A comprehensive review, *Microchem. J.*, **200** (2024) 110359. DOI: 10.1016/j.microc.2024.110359.

[137] Y. Zhou, J. F. Zhang and J. Yoon, Fluorescence and colorimetric chemosensors for fluoride-ion detection, *Chem. Rev.*, **114** (2014) 5511–5571. DOI: 10.1021/cr400352m.

[138] G. Pedro, F. Duarte, G. M. Dobrikov, A. Kurutos, H. M. Santos, J. L. Capelo-Martínez, E. Oliveira and C. Lodeiro, Optical evaluation of dansyl derivatives and their implementation in

low-cost and flexible dye-doped PMMA platforms for efficient detection of hazardous chemical vapours, *Dyes and Pigments*, **224** (2024) 112042. DOI: 10.1016/j.dyepig.2024.112042.

[139] D. P. Li, Z. Y. Wang, X. J. Cao, J. Cui, X. Wang, H. Z. Cui, J. Y. Miao and B. X. Zhao, A mitochondria-targeted fluorescent probe for ratiometric detection of endogenous sulfur-dioxide derivatives in cancer cells, *Chem. Commun.*, **52** (2016) 2760–2763. DOI: 10.1039/C5CC09092J.

[140] B. Yang, J. Xu and H. L. Zhu, Recent progress in the small-molecule fluorescent probes for the detection of sulfur-dioxide derivatives (HSO_3^-/SO_3^{2-}), *Free Radic. Biol. Med.*, **145** (2019) 42–60. DOI: 10.1016/j.freeradbiomed.2019.09.007

[141] W. L. Wu, H. L. Ma, M. F. Huang, J. Y. Miao and B. X. Zhao, Mitochondria-targeted ratiometric fluorescent probe based on FRET for bisulfite, *Sens. Actuators B Chem.*, **241** (2017) 239–244. DOI: 10.1016/j.snb.2016.10.028

[142] M. F. Huang, L. N. Chen, J. Y. Ning, W. L. Wu, X. D. He, J. Y. Miao and B. X. Zhao, A new lipid droplets–targeted fluorescence probe for specific detection of SO_2 derivatives in living cells, *Sens. Actuators B Chem.*, **261** (2018) 196–202. DOI: 10.1016/j.snb.2018.01.139

[143] F. T. Liu, X. F. Liu, Z. Jin, B. X. Zhao and Z. M. Lin, A dansyl-quinolinium-based ratiometric fluorescent probe for detecting HSO_3^-/SO_3^{2-} in living cells, *Anal. Chim. Acta*, **1373** (2025) 344488. DOI: 10.1016/j.aca.2025.344488.

[144] Y. Li, N. M. Nouman, C. Yin and F. Huo, The development of near-infrared hydrogen sulfide probes and its application in the past ten years, *Dyes and Pigments*, **228** (2024) 112246. DOI: 10.1016/j.dyepig.2024.112246

[145] K. G. Fosnacht and M. D. Pluth, Activity-Based Fluorescent Probes for Hydrogen Sulfide and Related Reactive Sulfur Species, *Chem. Rev.*, **124** (2024) 4124–4257. DOI: 10.1021/acs.chemrev.3c00683.

[146] Y. Yan, L. Chen, R. Liu, Y. Zheng and S. Wang, A turn-on fluorescent probe with a dansyl fluorophore for hydrogen sulfide sensing, *RSC Adv.*, **9** (2019) 27652–27658. DOI: 10.1039/C9RA04790E

[147] J. Fan, E. Wu, J. Dong, R. Zhu, M. Li, J. Gao, H. Han and L. Ding, A minimalist ratiometric fluorescent sensor based on non-covalent ternary platform for sensing H_2S in aqueous solution and serum, *Colloids Surf. A Physicochem. Eng. Aspects*, **616** (2021) 126299. DOI: 10.1016/j.colsurfa.2021.126299

[148] J. Y. Kim, S. Sarkar, K. N. Bobba, P. T. Huynh, A. Bhise and J. Yoo, Development of dansyl based copper(II) complex to detect hydrogen sulfide in hypoxia, *Org. Biomol. Chem.*, **17** (2019) 7088–7094. DOI: 10.1039/C9OB00948E.

[149] D. Maiti, A. S. M. Islam, A. Dutta, M. Sasmal, C. Prodhan and M. Ali, Dansyl-appended Cu(II)-complex-based nitroxyl (HNO) sensing with living cell imaging application and DFT studies, *Dalton Trans.*, **48** (2019) 2760–2771. DOI: 10.1039/C8DT04564J

[150] Q. Guo, Y. Wu, L. Zhang, Y. Qin, J. Bao, Y. Feng, Y. Liu and Y. Zhou, Real-time visualization of efficient nitroxyl (HNO) releasing using fluorescence technique, *Sens. Actuators B Chem.*, **369** (2022) 132309. DOI: 10.1016/j.snb.2022.132309.

[151] S. Muthusamy, S. Mahato, P. Bhardwaj, R. D. Rao, K. S. Karumban and P. Kumar, pH-Responsive Fluorescence Turn-On Copper(II)-Probe for Nitric Oxide Detection: A Reductive Nitrosylation Approach, *Chem. Eur. J.*, **31** (2025) e01833. DOI: 10.1002/chem.202501833.

[152] Y. Chen, Recent developments of fluorescent probes for detection and bioimaging of nitric oxide, *Nitric Oxide*, **98** (2020) 1–19. DOI: 10.1016/j.niox.2020.02.002.

[153] G. Gan, T. Ma, G. Zhang, K. He and J. Hu, Luminescent probes for detecting and bioimaging of nitric oxide and carbon monoxide, *TrAC Trends Anal. Chem.*, **168** (2023) 117340. DOI: 10.1016/j.trac.2023.117340.

[154] R. Smulik-Izydorczyk, K. Dębowska, J. Pięta, R. Michalski, A. Marcinek and A. Sikora, Fluorescent probes for the detection of nitroxyl (HNO), *Free Radic. Biol. Med.*, **128** (2018) 69–83. DOI: 10.1016/j.freeradbiomed.2018.04.564.

[155] K. Satheeshkumar, P. Saravana Kumar, R. Shanmugapriya, C. Nandhini, K. N. Vennila and K. P. Elango, Ratiometric fluorescence sensing of hypochlorite ion by dansyl hydrazine – Spectroscopic and TD-DFT studies, *J. Mol. Struct.*, **1275** (2023) 134719. DOI: 10.1016/j.molstruc.2022.134719.

[156] Y. R. Zhang, Y. Liu, X. Feng and B. X. Zhao, Recent progress in the development of fluorescent probes for the detection of hypochlorous acid, *Sens. Actuators B Chem.*, **240** (2017) 18–36. DOI: 10.1016/j.snb.2016.08.066.

[157] A. H. Ashoka, F. Ali, R. Tiwari, R. Kumari, S. K. Pramanik and A. Das, Recent advances in fluorescent probes for detection of HOCl and HNO, *ACS Omega*, **5** (2020) 1730–1742. DOI: 10.1021/acsomega.9b03420.

[158] L. L. Xi, X. F. Guo, C. L. Wang, W. L. Wu, M. F. Huang, J. Y. Miao and B. X. Zhao, A near-infrared ratiometric fluorescent probe for rapid and selective detection of hypochlorous acid in aqueous solution and living cells, *Sens. Actuators B Chem.*, **255** (2018) 666–673. DOI: 10.1016/j.snb.2017.08.073.

[159] M. Basak and G. Das, Fluorescent probes for detection of environmental contaminants (NACs & VOCs): probe design from a supramolecular perspective, *ChemPlusChem*, **88** (2023) e202300179. DOI: 10.1002/cplu.202300179.

[160] V. Kumar, S. K. Saini, N. Choudhury, A. Kumar, B. Maiti, P. De, M. Kumar and S. Satapathi, Highly sensitive detection of nitro compounds using a fluorescent copolymer-based FRET system, *ACS Appl. Polym. Mater.*, **3** (2021) 4017–4026. DOI: 10.1021/acsapm.1c00540.

[161] N. Tripathi, S. Sandhu, P. Singh, A. Mahajan, M. Kaur and S. Kumar, Dansyl conjugated tripodal AIEEgen for highly selective detection of 2,4,6-trinitrophenol in water and solid state, *Sens. Actuators B Chem.*, **231** (2016) 79–87. DOI: 10.1016/j.snb.2016.03.008.

[162] V. Kumar, B. Maiti, M. K. Chini, P. De and S. Satapathi, Multimodal fluorescent polymer sensor for highly sensitive detection of nitroaromatics, *Sci. Rep.*, **9** (2019) 7269. DOI: 10.1038/s41598-019-43836-w.

[163] L. Thurakkal, R. Mol K. M. and M. Porel, Dansyl-triazole-based fluorescent macrocycle for selective detection of nitro-antibiotic drugs and protein interaction, *Chem. Commun.*, **59** (2023) 7399–7402. DOI: 10.1039/D3CC01769A.

[164] M. Bhattu, M. Verma and D. Kathuria, Recent advancements in the detection of organophosphate pesticides: a review, *Anal. Methods*, **13** (2021) 4390–4428. DOI: 10.1039/D1AY01186C.

[165] B. Deng, F. Zeng and S. Wu, A fluorescent probe for convenient visual detection of glyphosate contamination in water, soil, and vegetable samples, *Chem. Asian J.*, **20** (2025) e202500494. DOI: 10.1002/asia.202500494.

[166] Q. Chen, J. Liu, S. Liu, J. Zhang, L. He, R. Liu, H. Jiang, X. Han and K. Zhang, Visual and rapid detection of nerve agent mimics in gas and solution phase by a simple fluorescent probe, *Anal. Chem.*, **95** (2023) 4390–4394. DOI: 10.1021/acs.analchem.2c04891.

[167] M. Naik and A. Patil, Development of an ultra-sensitive laser stimulated fluorescence system for simultaneous detection of amino acids, *RSC Adv.*, **14** (2024) 34279–34287. DOI: 10.1039/D4RA04845H.

[168] F. Q. Zhang, Z. Y. Xu, Y. Li, Y. Y. Zhu and S. X. Gu, Chemoselective and enantioselective fluorescent recognition of basic amino acids: A review, *Dyes and Pigments*, **240** (2025) 112842. DOI: 10.1016/j.dyepig.2025.112842.

[169] Y. Zhou and J. Yoon, Recent progress in fluorescent and colorimetric chemosensors for detection of amino acids, *Chem. Soc. Rev.*, **41** (2012) 52–67. DOI: 10.1039/C1CS15159B.

[170] Y. Zhang, J. Cao and L. Ding, Fluorescent ensemble based on dansyl derivative/SDS assemblies as selective sensor for Asp and Glu in aqueous solution, *J. Photochem. Photobiol. A: Chem.*, **333** (2017) 56–62. DOI: 10.1016/j.jphotochem.2016.10.018.

[171] K. Bin Li, W. B. Qu, D. M. Han, S. Zhang, W. Shi, C. X. Chen and X. X. Liang, A colorimetric/fluorescence dual-channel probe for highly discriminating detection of cysteine, *Talanta*, **194** (2019) 803–808. DOI: 10.1016/j.talanta.2018.11.007.

[172] Y. Xiao, Y. Guo, R. Dang, X. Yan, P. Xu and P. Jiang, A dansyl-based fluorescent probe for the highly selective detection of cysteine based on a d-PeT switching mechanism, *RSC Adv.*, **7** (2017) 21050-21053. DOI: 10.1039/C7RA00212B.

[173] I. J. Bazany-Rodríguez, P. Thangarasu, M. L. Almada-Leyva, J. G. Hernández, D. Martínez-Otero, M. K. Salomón-Flores and A. Dorazco-González, New fluorescent chemodosimetric mechanism for selective recognition of selenocysteine by dansyl-appended ruthenium nitrosyl complexes, *Inorg. Chem.*, **64** (2025) 3989–4004. DOI: 10.1021/acs.inorgchem.4c05277

[174] J. Fan, M. Hu, P. Zhan and X. Peng, Energy transfer cassettes based on organic fluorophores: construction and applications in ratiometric sensing, *Chem. Soc. Rev.*, **42** (2013) 29–43. DOI: 10.1039/C2CS35273G.

[175] S. Das and P. Sahoo, A colorimetric sensor for hydrogen sulfide: Detection from biogas and quantitative estimation in water, *Sens. Actuators B Chem.*, **291** (2019) 287–292. DOI: 10.1016/j.snb.2019.04.089.

[176] F. Duarte, D. Torres, G. M. Dobrikov, A. Kurutos, L. B. Maia, O. Bondarchuk, I. Slavchev, J. L. Capelo-Martínez, H. M. Santos and C. Lodeiro, A dual-responsive Dansyl–Naphthalimide system for Hg(II) CHEF detection and ligand-mediated Cu(II) reduction with catalytic relevance, *Dyes and Pigments*, **243** (2025) 113088. DOI: 10.1016/j.dyepig.2025.113088

[177] Y. Kong, X. Wan, Z. Liu, F. Chen, F. Wu, G. Qin, D. Cao and Y. Cui, A novel dansyl-naphthalimide fluorescent probe for visualizing nitroxyl (HNO) in biological systems, *Sens. Actuators B Chem.*, **350** (2022) 130852. DOI: 10.1016/j.snb.2021.130852

[178] K. Bin Li, D. Zhou, X. P. He and G. R. Chen, Ratiometric glyco-probe for transient determination of thiophenol in full aqueous solution and river water, *Dyes and Pigments*, **116** (2015) 52–57. DOI: 10.1016/j.dyepig.2015.01.013.

[179] Z. Xu, M. X. Zhang, G. Li, X. Chen, S. H. Liu, H. Chen and J. Yin, Naphthalimide-sulfonamide fused dansyl-sulfonamide fluorescent probe for tracking glutathione of lysosome with a dual-emission manner, *Dyes and Pigments*, **171** (2019) 107685. DOI: 10.1016/j.dyepig.2019.107685.

[180] D. Yang, X. T. Wu, X. J. Cao and B. X. Zhao, A reversible ratiometric fluorescence probe for fast detection of trace water in different organic solvents, *Dyes and Pigments*, **170** (2019) 107558. DOI: 10.1016/j.dyepig.2019.107558

[181] J. Gao, Y. He, Y. Chen, D. Song, Y. Zhang, F. Qi, Z. Guo and W. He, Reversible FRET fluorescent probe for ratiometric tracking of endogenous Fe^{3+} in ferroptosis, *Inorg. Chem.*, **59** (2020) 10920-10927. DOI: 10.1021/acs.inorgchem.0c01412.

[182] F. Martins, A. Granja, S. Reis, P. Gameiro, G. Barone, M. G. P. M. S. Neves and A. M. G. Silva, Synthesis, fluorescence and theoretical insights into a novel FRET-based dansyl-rhodamine sensor for the in vitro detection of toxic bioaccumulated Hg(II) ions, *Spectrochim. Acta A Mol. Biomol. Spectrosc.*, **329** (2025) 125534. DOI: 10.1016/j.saa.2024.125534.

[183] P. Srivastava, M. Verma, S. Sivakumar and A. K. Patra, A smart FRET probe exhibiting a molecular keypad-lock device based on rapid detection of nitric oxide mediated by Cu^{2+} ion, *Sens. Actuators B Chem.*, **291** (2019) 478–484. DOI: 10.1016/j.snb.2019.04.093.

[184] S. Paul, S. Mukherjee, D. Kundu, S. Nag, S. Bhuyan, N. Chandra Murmu and P. Banerjee, AIEE activated Pyrene-Dansyl coupled FRET probe for discriminating detection of lethal Cu^{2+} and CN^{-}: Bio-Imaging, DNA binding studies and prompt prognosis of *Menke's disease*, *Spectrochim. Acta A Mol. Biomol. Spectrosc.*, **303** (2023) 123110. DOI: 10.1016/j.saa.2023.123110.

[185] J. Wang, X. Zhang and H. B. Liu, Highly sensitive pyrene–dansyl conjugate-based fluorescent sensor for discriminative detection of water in organic solvents, *Dyes Pigments*, **182** (2020) 108685. DOI: 10.1016/j.dyepig.2020.108685.

[186] Y. Zhang, B. Lei and X. Zhang, Intramolecular energy transfer dyes as temperature- and polarity-sensitive fluorescence probes, *Dyes and Pigments*, **205** (2022) 110492. DOI: 10.1016/j.dyepig.2022.110492.

[187] Y. Zhang, B. Lei and X. Zhang, Reversible, controllable white-light emission of dye systems by dynamic covalent furan moiety exchange, *Chem. Commun.*, **58** (2022) 5261–5264. DOI: 10.1039/D2CC01309F.

[188] M. Jia, H. Zheng, Y. Zhang and X. Zhang, Modulating energy transfer and light-emitting colors by chiral dye exchange and achiral-to-chiral dye conversion, *Chem. Eur. J.*, **29** (2023) e202300906. DOI: 10.1002/chem.202300906.

[189] N. Li, W. Qin, Y. Chen, K. Liu, S. Wang and F. Kong, Construction of a robust polarity-sensitive platform and its application for tracking lipid droplets under oxidative stress in live cells, *Sens. Actuators B Chem.*, **346** (2021) 130491. DOI: 10.1016/j.snb.2021.130491.

[190] F. Duarte, I. Pereira-Gomes, G. M. Dobrikov, J. Galhano, C. S. B. Gomes, A. Kurutos, H. M. Santos, E. Oliveira, M. Paula Duarte, J. Luis Capelo-Martinez and C. Lodeiro, Antimicrobial profile and turn-on sensing of cyanide and water traces using a dual-chromophoric

dansyl-acridine conjugate as multifunctional system, *Microchem. J.*, **205** (2024) 111237. DOI: 10.1016/j.microc.2024.111237.

2

Objectives

Fluorescent probes are powerful analytical tools, yet many existing systems lack the sensitivity, adaptability, and multifunctionality required for emerging challenges in environmental monitoring and biomedical diagnostics. This doctoral project integrates advanced synthetic design - carried out in collaboration with Dr. Atanas Kurutos and Dr. Georgi Dobrikov from the Bulgarian Academy of Sciences (Bulgaria) - with photophysical engineering, supramolecular chemistry, and materials science to develop a new generation of dansyl-based fluorophores capable of precise environmental reporting, selective ion recognition, and seamless incorporation into functional materials.

Figure 2–1 highlights chemical structures designed under this PhD project, displaying the diversity of molecular frameworks and the design principles employed to tailor their optical responses, recognition abilities, and compatibility with advanced material platforms.
Specifically, the project aims to:

i. Design and synthesize a family of eighteen compounds strongly related to the dansyl unit by integrating tailored receptor units.
ii. Exploit intramolecular interactions by constructing dyad systems.
iii. Implement sulfur containing functionalities that operate through quenching–recovery pathways and allow soft–soft selective sensing.
iv. Engineer macrocycle-based fluorophores architectures to ensure enhanced performance.
v. Develop dansyl-based compounds bearing liquid-crystalline properties through the introduction of mesogenic elements to promote ordered self-assembly and anisotropic behavior.

vi. Characterize the photophysical behavior of the synthesized fluorophores.
vii. Develop fluorophores capable of sensitive environmental reporting through solvatochromism and aggregation-induced emission, enabling detection of microenvironment polarity and water content.
viii. Search for applications of the new compounds as colorimetric and fluorescent sensors for the detection and quantification of different analytes namely metal ions, anions, and relevant molecules.
ix. Introduction of the dansyl compounds in different matrixes (paper and polymers) with the intention to develop applications in the solid state.
x. Embed the dansyl compounds in polymeric microparticles with the objective to develop applications in aqueous environments.
xi. Evaluate the intrinsic antimicrobial properties of selected dansyl fluorophores.
xii. Assess the capacity to mediate metallic nanoparticle formation through self-assembly.
xiii. Combine insights from design, photophysics, sensing, and material integration to evaluate how the fluorophores function as adaptable, multifunctional systems.

These objectives collectively aim to produce a coherent suite of multifunctional fluorescent materials. Beyond the fundamental scientific contributions, the knowledge generated by this research intends to:

(i) Advance environmental sensing technologies;

(ii) Contribute to the development of robust analytical tools that reduce the burden of environmental contaminants and support public health;

(iii) Enable new design principles for smart materials with combined sensing, structural, and active functions.

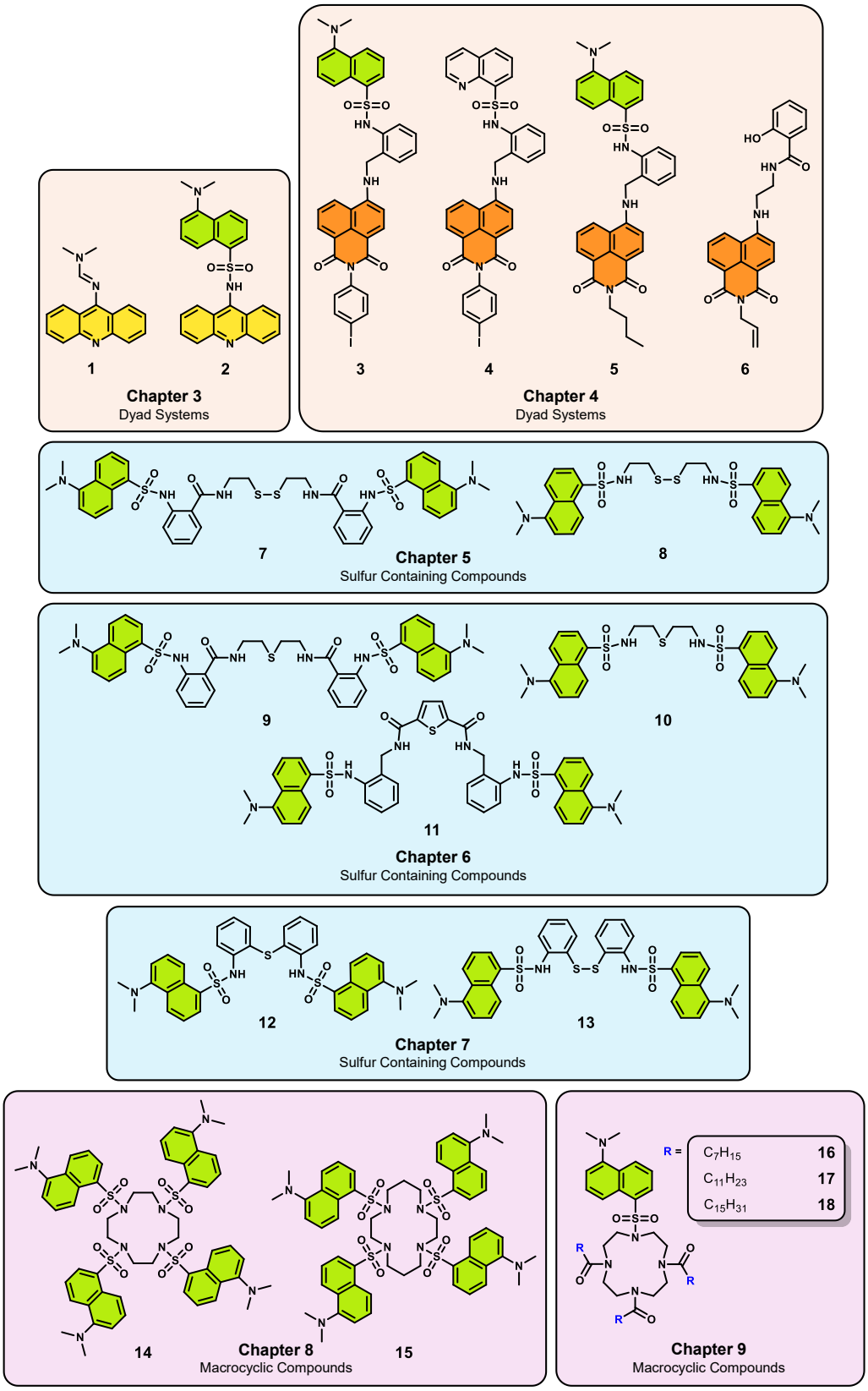


Figure 2–1. Integration of the doctoral thesis objectives across the chemical structures presented in the different chapters of the thesis.

3

ANTIMICROBIAL PROFILE AND TURN-ON SENSING OF CYANIDE AND WATER TRACES USING A DUAL CHROMOPHORIC DANSYL-ACRIDINE CONJUGATE AS MULTIFUNCTIONAL SYSTEM

Frederico Duarte, Inês Pereira-Gomes, Georgi M. Dobrikov, Joana Galhano, Clara S. B. Gomes, Atanas Kurutos, Hugo M. Santos, Elisabete Oliveira, Maria Paula Duarte, José Luis Capelo-Martinez, Carlos Lodeiro

Microchemical Journal 205 (2024) 111237 Doi: 10.1016/j.microc.2024.111237

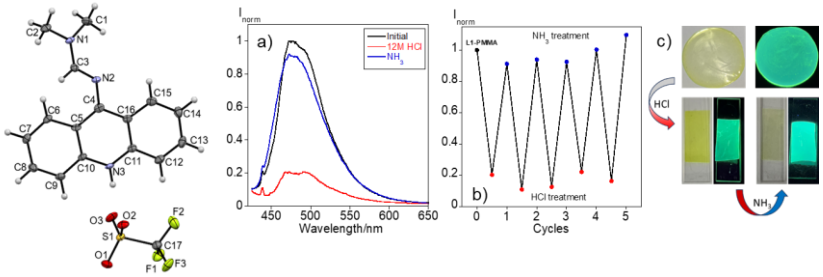
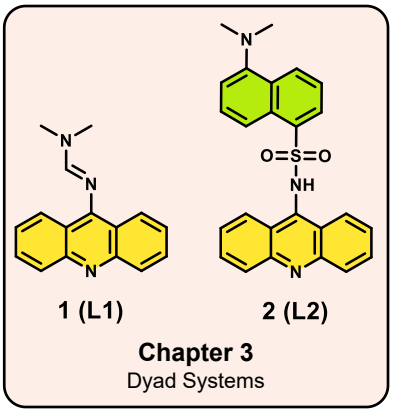


Figure 3–1. Graphical abstract.



Contribution to this work: Synthesis and crystal formation of L1; Photophysical characterization; Preparation of polymeric doped thin films and microparticles; Sensing experiments of water molecules, acidochromic behavior and anions; Writing original draft.

3.1 Abstract

9-aminocridine derivatives bearing a dimethylmethanimidamide, **L1**, and the dyad conjugate dansyl-acridine, **L2**, were synthesized and their ability to be used as multifunctional materials using different polymer matrixes was investigated. **L1** was found to modulate its emission in the presence of traces of water with a turn-on effect and to this end was used for the detection of water traces in organic solvents with a LOD and LOQ of 0.0028 and 0.0121 (V%) in acetonitrile, respectively. Due to the observed acidochromism for this compound and the different behavior in acetonitrile and chloroform due to different stabilization of the excited state a turn-off and turn-on effect was observed for respective solvents. PMMA polymer doped films aided on the elucidation for this compound to be used as a sensor of strong acids. Furthermore, compound **L2** was found fruitful for the detection of cyanide through an acid base anion sensing. Incorporation of these compounds in PVA:PVP polymer films and Irogran® microparticles were carried out to assess their antimicrobial profile.

3.2 Introduction

Fluorescent chemosensors have exhibited extraordinary optical qualities in various applications during the past decades due to their exceptional sensitivity, quickness, and non-invasive nature. As an example, the 1-(dimethylamino)-naphthalene-5-sulfonyl or dansyl derivatives which often present high fluorescence quantum yields, a significant Stokes Shift and the solvatochromism behaviour that provide the robustness necessary to be useful for the development of biosensors and biological imaging. [1-4]

One potential downside of these systems is that the fluorescence changes often occur in either a single emission or ratiometric response. Recently, several successful examples based on dual fluorescence probes bearing a dansyl unit have been reported which amplify the manners of fluorescence signals, improve the signal-to-noise ratio, and provide a wider region of emission. [5] Dithienylethene and diarylethene photoswitches [6,7], carbazole and triphenylamine-based energy donors [8], pyrene [9,10], naphthalimide [5,11], and rhodamine [12-14] are only a few examples.

In line with the premise of designing more versatile multifunctional dual fluorescent molecules, acridine and its derivatives become good candidates due to their sensing purposes. In the field of fluorescence sensors, different photophysical events might arise from a variety of chemical processes involving water such as hydrolysis, protonation and deprotonation

reactions and molecular aggregation. [15] It is also noteworthy to highlight the relevance of monitoring water as an analyte in several applications such as chemical production, petroleum-based fuel and food processing. [10,12,16-18]

Therefore, acridine derivatives become relevant since in aqueous solution it can adopt two prototropic forms (pKa ~5.3), namely the neutral and protonated forms. Each form has a characteristic fluorescence spectrum allowing acridine derivatives to be used as pH sensitive probes. [19,20]

In the realm of material science, there's a pressing demand for molecular sensors capable of detecting acidic species. Polymer materials emerge as ideal candidates that enable the detection of the targeted process, ensure the device's stability, and are cost-effective, and adaptable for production. With this in mind, Sandra Medel *et al.* have synthesized a hyperbranched polyeteramide functionalized with six acridine groups as a fluorescent acid sensor in solution as well as in solid polymer films exhibiting an increase in the fluorescence emission. [21] Due to the known contribution of acridine derivatives towards anti-cancer and antibacterial development fields [22-26], the authors have tested the synthesized polymer film against five bacteria (Gram positive and Gram negative) as well as two yeasts, exhibiting high antimicrobial activity. [21]

In this work, two compounds (**L1** and **L2**) based on the dyad dansyl-acridine have been synthesized with the intention to be used as multifunctional materials. Compound **L1** was found to be synthesized only in the presence of a sulfonyl chloride group while **L2** constitutes both chromophores. Their photophysical and sensorial recognition properties were investigated. The sensing of water traces as well as the acidochromism effect of **L1** was investigated in solution and polymer thin films of polymethylmethacrylate (PMMA). The turn-on effect of **L2** towards cyanide was demonstrated and the mechanism of interaction elucidated. The antimicrobial activity of both compounds was investigated in solution as well as in doped polymer films of polyvinyl alcohol and polyvinylpyrrolidone co-polymer (PVA:PVP) and the thermoplastic polyurethane TPU-A92 (Irogran®). Polymer doped particles of the latter polymer were also synthesized and characterized as proof of concept for antimicrobial purposes.

3.3 Experimental Section

3.3.1 Materials

All reagents and solvents employed for the synthesis and purification of the target compounds were purchased with purity >98% from Fluorochem Ltd (United Kingdom), Sigma-Aldrich (St Louis, Missouri, United States) or Tokyo Chemical Industry Co., Ltd (TCI). Photophysical experiments were carried out using spectroscopy grade solvents: ethanol (EtOH), acetonitrile (CH_3CN), chloroform ($CHCl_3$).

The synthesis and purification steps were accomplished using puriss p.a. grade solvents: dichloromethane (DCM), *N,N*-dimethylformamide (DMF), petroleum ether (PE), methanol (MeOH), methyl *tert*-butyl ether (MTBE).

Poly(methylmethacrylate), PMMA (MW ~ 350,000, T_g 105 °C), polyvinylpyrrolidone, PVP (MW ~40,000, T_g 170 °C), Polyvinyl alcohol (PVA, MW 27,000, T_g 85 °C) were purchased from Sigma-Aldrich (St. Louis, MO, USA) and the thermoplastic polyurethane TPU-A92 (Irogran®) was offered by Huntsman (Germany).

The perfluoroalkoxy (PFA) supports for the fabrication of polymer films were purchased to Bohlender, Gmbh, Germany. Mili-Q ultrapure water was used in all experiments.

3.3.2 Instrumentation

The chemical identities of the compounds under investigation were confirmed through the utilization of various analytical techniques, including ^{1}H-NMR, ^{13}C-NMR, DEPT-135, 2-D COSY, 2D-HSQC, and 2-D HMBC techniques. The ^{1}H-NMR and ^{13}C-NMR spectra were acquired on a Bruker Avance II+600 spectrometer and Bruker Avance Neo 400 (Institute of Organic Chemistry with Centre of Phytochemistry - Bulgarian Academy of Sciences / NMR Centre) using 5 mm tubes. The measurements were performed in $CDCl_3$ and DMSO-d_6 at 293 K, with operating frequencies of 600.13 MHz / 400.13 MHz and 150.92 MHz / 100.62 MHz for the ^{1}H and ^{13}C nuclei, respectively. The ^{1}H- and ^{13}C- nuclear magnetic resonance (NMR) spectra were standardized using the reference signal of tetramethylsilane (TMS) with a chemical shift value (δ) of 0.00. The precision of chemical changes is determined at a level of 0.01 ppm. The coupling constants (J) are displayed with a precision of 0.1 and denoted in units of hertz (Hz). The spin multiplicity observed in the ^{1}H nuclear magnetic resonance (NMR) spectroscopy was represented using the following abbreviations: s for singlet, d for doublet, t for triplet, q for quartet, dd for doublet of doublets, dt for doublet of triplets, td for triplet of doublets, and m for

multiplet. MestreNova v. 14.1.1 (Mestrelab Research S.L.) was used for processing the spectra. High-Resolution Mass Spectrometry analyses have been performed in the Laboratory for Biological Mass Spectrometry–Isabel Moura (PROTEOMASS Scientific Society Facility), using UHR ESI-Qq-TOF IMPACT HD (Bruker-Daltonics, Bremen, Germany). Samples of the corresponding compounds were prepared by dissolution in 50% (v/v) Acetonitrile containing 0.1% (v/v) aqueous formic acid to obtain a working solution of 0.1 µg/mL. Mass spectrometry analysis was carried out by the direct infusion of the compound solutions into the ESI source. MS data were acquired in positive polarity over the mass range of 80 – 1300 m/z. (Capillary voltage: 4500 V, End plate offset: -500 V, Charging voltage: 2000 V, Corona: 4000 nA, Nebulizer gas: 0.4 Bar, Dry Heater: 180 °C, Dry gas: 4.0 L/min).

Photophysical studies were performed at 293 K using a JASCO V-650 spectrophotometer to obtain the UV-Vis absorption spectra and a HORIBA Scientific FLUOROMAX-4 spectrofluorometer for recording fluorescence spectra, both instruments were from BIOSCOPE-PROTEOMASS facilities. Quartz cells with 10 mm optical path were used.

Crystals of compounds **L1HCl** and **L1HOTf** suitable for single-crystal X-ray analysis were selected, covered with Fomblin (polyfluoro ether oil) and mounted on a nylon loop. The data was collected at 110(2) K on a Bruker D8 Venture diffractometer equipped with a Photon II detector and an Oxford Cryostems Cooler, using graphite monochromated Mo-Kα radiation (λ= 0.71073 Å). The data was processed using the APEX4 suite software package, which includes integration and scaling (SAINT), absorption corrections (SADABS) [27] and space group determination (XPREP). Structure solution and refinement were done using direct methods with the programs SHELXT 2018/2 and SHELXL-2019/2 [28,29] inbuilt in APEX and WinGX-Version 2021.3 [30] software packages. All non-hydrogen atoms were refined anisotropically and, except for the N–H atom, all hydrogen atoms were inserted in idealized positions and allowed to refine riding on the parent carbon atom with C–H distances of 0.98 Å, 1.00 Å and 0.95 Å for methyl, methine and aromatic H atoms, respectively. The molecular diagrams were drawn with Mercury. [31] Crystal and structure refinement data are given in Table 3-4. The data was deposited in the CCDC under deposit numbers 2346365 for **L1HCl** and 2346366 for **L1HOTf**.

3.3.3 Synthetic procedures

3.3.3.1 Synthesis of L1

N'-(Acridin-9-yl)-*N,N*-dimethylformamidine:

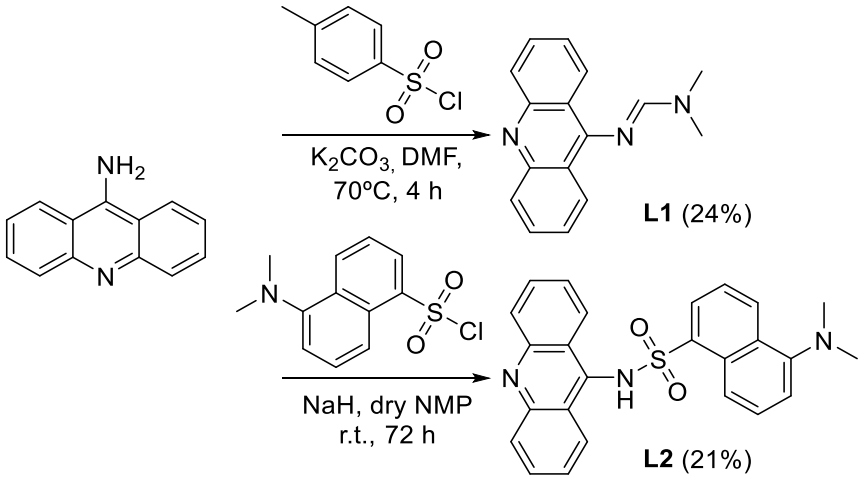
9-aminoacridine (300 mg, 1.54 mmol, 1.0 eq.) and K_2CO_3 (426 mg, 3.08 mmol, 2.0 eq.) were added consequently into a 50 mL flask containing 25 mL *N,N*-dimethylformamide and the resulting solution was stirred at room temperature for 10 min and then tosyl chloride (587 mg, 3.07 mmol, 2.0 eq.) was added. The formed heterogenous solution was further stirred at 70º C for 3 h. TLC of reaction mixture – mobile phase DCM:MeOH=10:1 (v/v). Workup: the solution was left to cool down to room temperature and filtrated to remove the K_2CO_3 and the excess of tosyl chloride, and the resulting clear solution was diluted with 120 mL of distilled water and decantated with 30 mL of $CHCl_3$ three times. The organic phase was concentrated *in vacuo* and diluted with 120 mL of water repeating the previous operation twice to remove the DMF. The concentrated mixture was then passed through a column using silica gel (70-230 mesh) as stationary phase and a mixture of DCM:MeOH=10:1 (v/v) as the eluent to give 95 mg (24%) of compound **L1** as an orange powder. M.p. 141-142°C. ^{1}H NMR (400 MHz, $CDCl_3$) δ 8.15 (*d*, *J* = 9.74 Hz, 4H), 7.71 (*ddd*, *J* = 8.43, 6.55, 1.31 Hz, 2H), 7.57 (*s*, 1H), 7.39 (*m*, 2H), 3.29 (*s*, 3H), 3.14 (*s*, 3H). ^{13}C NMR (101 MHz, $CDCl_3$) δ 156.46, 154.15, 149.25, 130.24, 128.75, 124.83, 123.77, 120.36, 40.34, 34.62. ESI-MS: $[M+H]^+$ without formic acid for $C_{16}H_{15}N_3$ = 250.1342 (-0.1 ppm) and $[M+H]^+$ with formic acid for $C_{16}H_{15}N_3$ = 250.1346 (-0.3 ppm)

3.3.3.2 Synthesis of L2

N-(acridin-9-yl)-5-(dimethylamino)naphthalene-1-sulfonamide:

Aminoacridine-base (327 mg, 1.68 mmol, 1.0 eq.) was suspended in 4 mL dry NMP (*N*-methylpyrrolidone) and NaH (65 mg, 1.68 mmol, 1.0 eq. – 65% disperse in mineral oil) was added. The mixture was stirred at room temperature for 15 min, until the formation of a brown solution. Then dansyl chloride (DsCl) (545 mg, 2.02 mmol, 1.2 eq.) was added and the resulting mixture was further stirred at room temperature for 72 h. Subsequently, 35 mL of distilled water was added, and the formed gray precipitate was filtered, washed with distilled water and PE (petroleum ether), then dried. The obtained gray powder was suspended in DCM and filtered through a silica gel pad (mobile phase DCM:MTBE=4:1 v/v). After evaporation under reduced pressure the product was recrystallized from 12 mL of 96% EtOH. The formed precipitate was decanted and further boiled with 5 mL of MTBE (methyl *tert*-butyl ether). After cooling down to room temperature, it was decanted and dried in *vaccuo* to furnish 153 mg (21%) of yellow

powder. M.p. 266°C. ^{1}H-NMR (400 MHz, DMSO) δ 12.92 (*s*, 1H), 8.63 (*dd*, *J* = 8.6, 1.0 Hz, 2H), 8.45 (*d*, *J* = 8.5 Hz, 1H), 8.34 (*d*, *J* = 8.7 Hz, 1H), 8.27 (*dd*, *J* = 7.3, 1.1 Hz, 1H), 7.84 (*ddd*, *J* = 8.3, 6.9, 1.3 Hz, 2H), 7.72 (*d*, *J* = 8.0 Hz, 2H), 7.64 (*dd*, *J* = 8.5, 7.3 Hz, 1H), 7.46 (*dd*, *J* = 8.6, 7.6 Hz, 1H), 7.31 (*ddd*, *J* = 8.3, 6.9, 1.1 Hz, 2H), 7.22 (*d*, *J* = 7.1 Hz, 1H), 2.86 (*s*, 6H).^{13}C-NMR (101 MHz, DMSO) δ 159.38, 151.12, 140.67, 140.00, 134.33, 129.25, 129.15, 128.53, 128.47, 127.13, 125.37, 123.55, 122.25, 120.23, 118.22, 117.75, 114.81, 45.11, 40.15, 39.94, 39.73, 39.52, 39.31, 39.10, 38.89. ESI-MS: $[M+H]^+$ for $C_{25}H_{21}N_3O_2S$ = 428.1421 (-1.4 ppm), calculated $[M+H]^+$ for $C^{25}H^{21}N^3O^2S$= 428.1427 m/z.



Scheme 3-1. Synthetic approach to the preparation of the acridine derivatives under investigation.

3.3.4 Spectrophotometric and spectrofluorometric measurments

3.3.4.1 Photophysical characterization and titrations

Spectroscopic studies were carried out in various organic solvents (EtOH, CH_3CN, THF, $CHCl_3$) by preparing a stock solution (ca. 10^{-3} M) through dissolution of an appropriate amount of the corresponding compound in a 10 mL volumetric flask. The photophysical analysis were performed by preparation of diluted working solutions with concentration ranging from 10^{-5} to 10^{-6} M.

Solid state and doped polymer thin films' emission spectra were obtained using a fiber-optics device connected to the spectrofluorometer by excitation of the samples choosing an appropriate wavelength.

3.3.4.2 Fluorescence quantum yield and Lifetime

Relative photoluminescence quantum yields were evaluated using 9-aminoacridine in absolute ethanol as a standard solution (ϕ_F = 0.99) and the relative QY formula was applied taking into consideration each spectra's area. [32] Lifetime measurements were performed on a Tempro Fluorescence Lifetime System equipped with a pulsed diode Nanoled controller from Horiba Jobin-Yvon from the BIOSCOPE-PROTEOMASS facilities.

3.3.5 Determination of the detection and quantification limits (LOD and LOQ)

Determination of the detection limit (LOD) and quantification limit (LOQ) began by collecting ten independent measurements of a solution containing the selected probe and no addition of any analyte (yblank). Final determination of the LOD and LOQ values followed the subsequent formulas: [33,34]

LOD = $y_{dl} = y_{blank} + 3std$, where y_{dl} = signal detection limit and std = standard deviation.

LOQ = $y_{dl} = y_{blank} + 10std$, where y_{dl} = signal detection limit and std = standard deviation. The final step involved the determination of the minimal detectable and quantified concentration of analyte by titration with the ligands.

3.3.6 Preparation of the polymer Dye-Doped thin films

PMMA doped thin films were prepared by weighting 100 mg of the polymer matrix and allowed to dissolve in $CHCl_3$ at a temperature of 50 ºC. After cooling down to room temperature, 0.5 mg of **L1** were added to the solution.

The synthesis of PVA/PVP polymers commenced by utilizing a solution comprising 0.5 mg of **L1** and **L2** was prepared in 3 mL of ethanol. Another solution containing 200 mg of PVA and 50 mg of PVP was prepared in 2 mL of milliQ water and 3 mL of ethanol. This mixture was stirred and heated over a hotplate at ca. 60 ºC until PVA and PVP were completely dissolved. The dye solution was then added to the polymer solution, and the mixture was kept on stirring and further placed under ultrasound.

TPU's solution was prepared by weighting 100 mg of this polymeric material and 0.5 mg of the compound in separate vials. The amount of TPU weighted was dissolved in 10 mL of THF over stirring at room temperature until it was totally dissolved. The dye solution was prepared in 1.5 mL of ethanol. This solution was after added to the Irogran® solution and sonicated on ultrasound.

All polymeric solutions were poured onto perfluoroalkoxy (PFA) supports of 5 cm diameter favouring solvent evaporation at room temperature over 24 h.

3.3.7 Synthesis of polymeric microparticles

A solution of polymer matrix thermoplastic polyurethane TPU-A92 (100 mg) in 10 mL of tetrahydrofuran (THF) was prepared and allowed to stir until complete solubilization was achieved. An aliquot of 0.6 mL of this solution was quickly added to **L1** and **L2** (0.5 mg) and transferred over 2.4 mL of deionized water, maintaining a magnetic stirring at 400 rpm for 5 min. For non-doped Irogran® particles the 0.6 mL aliquot was added directly to the 2.4 mL of deionized water. The resulting mixtures were stored at 20 ˚C in the dark for 24 h for oil-in-water droplets stabilization. The final particles were obtained after evaporation of THF at room temperature for 24 h. Before use, a filtration step using glass membranes with a pore size of 10–15 µm was performed to remove potential non-encapsulated **L1**, **L2** and polymer precipitates.

3.3.8 Antimicrobial assays

Four bacterial strains were chosen due to their relevance in antibiotic resistance in industrial and environmental fields: *Escherichia coli* (ATCC® 8739™), *Staphylococcus aureus* (ATCC® 6538™), *Enterococcus faecalis* (ATCC® 29212™) and *Salmonella enterica* subsp. *enterica* serovar *Choleraesuis* (ATCC® 10708™*).*

Bacterial stocks were maintained in appropriate broth containing 15% v/v glycerol at -70ºC. After thawing, the stocks were inoculated onto TSA plates and incubated for 24 hours at 35 ± 2°C. Bacterial suspensions with a density equivalent to 0.5 on the McFarland scale (determined using a DEN-1B McFarland Densitometer, Grant-bio) were prepared in a saline medium (0.85% m/v), resulting in a bacterial concentration of approximately 1.5×10^8 Colony Forming Units (CFU)/mL. The first stock solution was used for solid polymeric evaluation assays on an agar plate, while 1:10 dilutions of bacterial stocks were used for liquid assays.

Samples **L1**, **L2** and control 9-aminoacridine (**CAA**) were dissolved in DMSO to obtain a stock concentration of 1 mg/mL. Irogran® polymeric nanoparticles doped with **L1** were used as synthetized, with a concentration of **L1** inside the nanoparticles of 0.14 mg/mL. A 2-fold dilution series was prepared in 96-well plates using Mueller-Hinton broth (MHB), ranging from a maximum concentration of 100 µg/mL to a minimum concentration of 0.20 µg/mL for compounds and from 14 to 0.03 µg/mL for polymeric nanoparticles. Each well was then inoculated

with the bacterial stocks to achieve a bacterial concentration of approximately 10^6 CFU/mL for all tested bacterial strains. The plates were then incubated 24 h at 35±2ºC. The following day, the plates were collected, and the minimum inhibitory concentration (MIC) was accessed by optical density quantification at 600 nm in a CLARIOStar Spectrophotometer (BMG Labtech) at the PROTEOMASS Scientific Society Facility.

To evaluate the antimicrobial effect of the prepared doped polymers (**L1**@PVA:PVP, **L2**@PVA:PVP, **L1**@Irogran®, **L2**@Irogran®), 1 x1 cm pieces of each were placed into a Mueller-Hintor Agar (MHA) plates, which were previously inoculated with each bacterial strain. The plates were incubated at 35±2ºC for 24 hours. Control films (9-aminoacridine (**CAA**)-doped and non-doped PVA:PVP and Irogran®) were also evaluated. Bacterial growth was visually evaluated in MHA plates and inhibition zones were measured in squared centimeters (cm^2). Asepsis conditions were achieved in a VBH Laminar Flow Hood (Steril). All incubations were performed in a Mermmet Incubator B10 (Vikat Ekinox).

3.4 Results and Discussion

3.4.1 Synthesis

The synthesis of the target compound **L1** was achieved by utilizing the primary amine present on the commercially available 9-aminoacridine **1** (Scheme 3-1). The preparation of **L1** was accomplished by formation of an imine bond between **1** and dimethylformamide molecules also serving as the reaction solvent. It is noteworthy that this compound is only able to be formed in the presence of a sulfonyl group, in this case, tosyl chloride was used, instead of dansyl chloride for being an inexpensive reagent, also in the presence of potassium carbonate. No evidence was found for the formation of **L1** in the absence of tosyl chloride. This was favored due to the amine group's decreased reactivity as part of the aromatic system, as well as the delocalization of the nitrogen's lone pair of electrons within the ring. We suggest that the mechanism might involve the bond between the oxygen atom and the sulfur atom of the tosyl group aided by the nitrogen of the dimethyl group allowing the nitrogen of **1** to perform a nucleophilic attack to the aldehyde's carbon. The target compound was obtained in good yield after purification by column chromatography. NMR, MS, and melting point temperatures have been applied for the characterization of the compound. There is no indication that the imine bond decomposes in the presence of acidic or aqueous solutions, which will be examined subsequently. Acylation of 9-aminoacridine is a rather complicated procedure, due to tautomerism

of this compound and, respectively weak nucleophilicity of the amino group. There are only few such examples of acyl-aminoacridines which can be found in the literature. [35] The synthesis of the target compound **L2** was performed with preliminary activation of the free 9-aminoacridine by using of strong base (NaH in dry *N*-methylpyrrolidone), followed by addition of dansyl chloride. The yield of the target compound **L2** after purification is 21%.

Compound **L1** crystallized as pale-yellow crystals in the triclinic system, *P*-1 space group, in the form of acridinium cations with either chloride (**L1HCl**) or triflate (**L1HOTf**) as counterions. Their molecular structure is depicted in Figure 3–18, and selected bond lengths and angles are presented in Table 3-5.

L1HCl and **L1HOTf** have very similar crystal structures, with planar acridinium backbones, due to the aromatic nature of the fragment (Table 3-5) and an imine moiety, formed from the reaction of 9-aminoacridine with *N,N*-dimethylformamide. Both compounds have an *E* configuration and bond distances and angles within the reported values for similar compounds. [36] The main difference between these two derivatives, apart from the counterion, is the dihedral angle between the acridinium moiety and the imine fragment. In the case of **L1HCl**, this dihedral angle is slightly more pronounced with a value of 51.06(13) ° compared to 44.05(11) ° for **L1HOTf**. The supramolecular arrangement in these derivatives is generated from the formation of classical (N–H…O) and non-classical (C–H…O) hydrogen bonds, halogen (Cl…Cl, C–H…Cl, N–H…Cl and C–H…F) and π…π interactions (Figure 3–19).

3.4.2 Photophysical characterization

The 9-aminoacridine derived compounds exhibit luminescent properties both in solution and in the solid state. Both compounds have been synthesized with the intention of serving as multifunctional compounds and will be investigated in accordance with this principle. Figure 3–7 presents the chemical structures alongside the photophysical data performed at 298 K for compounds **L1** in acetonitrile and **L2** in chloroform as a representative example while Table 3-1 gathers all the photophysical data of the studied compounds.

The UV-Vis spectra exhibit notable disparities between the two compounds. In the case of **L1**, a band with a peak centered at 393 nm and a slight secondary peak allocated at 450 nm are detected, contributing to a faint pale green color visible to the human eye. Consequently, two sharp maximums centered around 415 and 440 nm in conjunction with a broader shoulder at 400 nm constitute the absorption fingerprint of **L2.**

Upon excitation at the appropriate wavelength, a blue-greenish light with a maximum at 486 nm can be observed for **L1** in all solvents. In turn, compound **L2** has not been found to be

emissive in solution and will be discussed further ahead. Regarding the solid-state emission, a red-shifted band from the one in solution is present with an emission maximum at 520 and 587 nm for **L1-L2**, respectively (Table 3-1). As quantum yield data is concerned, for **L1** a dependence according to the solvent is noticeable being in ethanol where the quantum yield is higher of around 29%. Life-time measurements, by instance, present single digit nanosecond times for **L1** that vary significantly with the solvent.

Table 3-1. Absorption maximum wavelength in solution (λ_{abs}), emission maximum wavelength in solution (λ_{em}), molar absorption coefficients (ε), Stokes shift ($\Delta\lambda$), emission maximum in the solid state (λ_{em}^{Solid}), fluorescence quantum yields (ϕ), fluorescence lifetimes (τ) for compound **L1** and **L2** in different solvents.

Cpd	Solvent	λ_{abs} [nm]	λ_{em} [nm]	ε [10^4 cm^{-1} M^{-1}]	Stokes shift [cm^{-1}]	ϕ (%)	τ[ns]	λ_{em}^{Solid} [nm]
L1	EtOH	393	486	1.01	4869	29	2.8	520
	CH_3CN	393	486	0.84		12	7.4	
	$CHCl_3$	393	486	1.35		17	9.2	
L2	$CHCl_3$	439	-	2.79	-	-	-	587
	THF	439	-	2.84	-	-	-	

3.4.3 Sensing of water molecules

Due to **L1**'s rather low solubility in water, various combinations were prepared using varied water fractions in acetonitrile. The final concentration of **L1** was kept constant throughout. Figure 3–2 displays the absorption and emission spectra of these mixtures where an interesting increase in the emission is perceived between 0% and 17% water fraction with minimal spectral variation regarding the one in pure acetonitrile. A yellow-greenish color begins to appear at the naked eye as the water content rises, and the absorption profile begins to develop, reaching a maximum at 430 nm with shoulders at 405 and 450 nm. When the water content is increased above 17%, the emission of the various solutions declines until 83% of the initial intensity is reached. When comparing the combination in pure acetonitrile, it was discovered that the fluorescence quantum yield for the most emissive mixture increased from 12% to 20%. This initial behaviour should be attributed to the different solvation sphere of **L1** possibly enabling hydrogen bridged between water molecules and the nitrogen of the aromatic ring.

Keeping in mind these results, efforts were made to establish if **L1** would be suitable for water detection in organic solvents. For this purpose, subsequent additions of small aliquots

of water have been added to a solution of **L1** in dried acetonitrile in order to determine a relation between the increase of the emission and the water content.

This experiment was performed through setting up a batch composed of several 3 mL solutions of **L1** and increasing total volumes in sums of 20 μl was added to each solution. As previously hypothesized, small quantities of water content can indeed increase the emission of **L1**. Figure 3–2a gathers the spectra in acetonitrile where an increase in the emission up to 60% in noticeable when added a total of 200 μl of water. The possibility for this system to be used as a sensor of water molecules in organic solvents is now supported by Figure 3–2b where two different linear regressions can be established, the first from its initial emission up to 100 μl of water added, and the second until 200 μl. To fully characterize the usefulness of **L1** towards water tracing, calculation of the detection and quantification limit parameters were found to be 0.0028 and 0.0121 (V%), respectively.

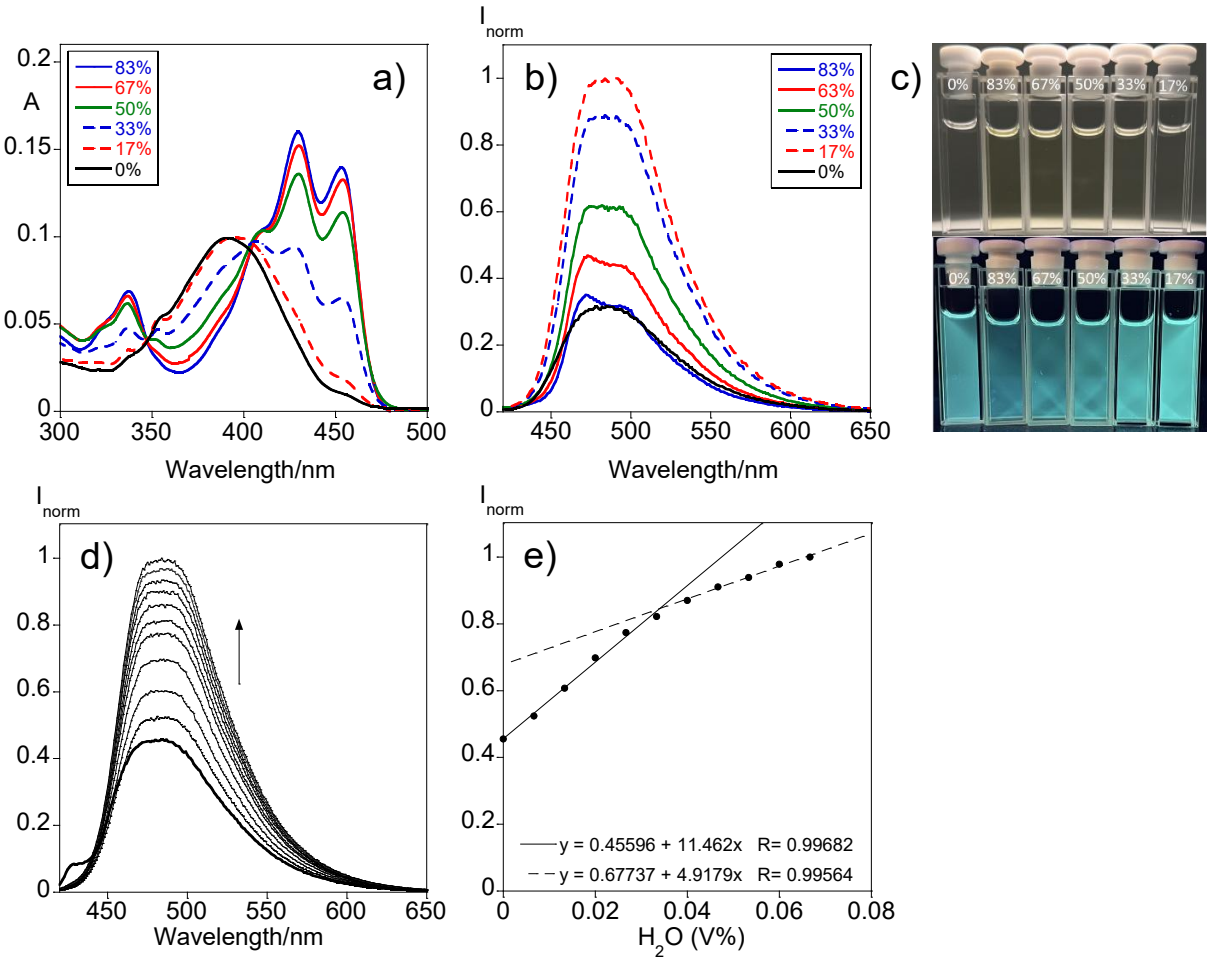


Figure 3–2. (a) Absorption, (b) emission spectra and (c) images of L1 in acetonitrile with different water fraction (f_w = 0%, 17%, 33%, 55%, 67%, 83%) at natural light (up) and under UV light (down, 365 nm). (d) Emission spectra

(λ_{excL1}= 395 nm) and (e) plot of the normalized emission intensities at 490 nm of L1 in acetonitrile with increasing amounts water aliquots (0%-0.067%, v/v) with the corresponding linear regressions. [L]= 10 μM, T = 298K.

3.4.4 Acidochromic behaviour

In line with the hypothesis that the nitrogen of the aromatic ring is capable of conduct hydrogen bonds with water molecules, we were interested in determining if **L1** would manifest acidochromism in solution and in solid supported thin films. For this, consecutive titrations of HCl and NaOH were performed to establish if also this behaviour would be reversible. Figure 3–3a gathers the absorption and emission spectra corresponding to each last addition of HCl and NaOH and the initial spectra are provided for better clarity while Figure 3–3b displays the emission of **L1** in relation to each addition in an equivalent manner. The complete titrations can be seen in Figure 3–9. The results obtained show that **L1** exhibits acidochromic behaviour in solution with the quenching of the emission as the concentration of HCl increases accompanied by a change in the absorption profile similarly seen previously. With the addition of NaOH the absorption returns to the initial maximum at 393 nm and the emission is recovered, suggesting that the imine bond is intact. The increase of the emission past the initial one could be attributed to the increasing deprotonation of **L1** alongside the increasing formation of hydrogen bonds with water molecules.

In order to gain a deeper understanding of this acidochromic behavior, other investigations have been conducted, including a titration with trifluoroacetic acid in chloroform. As in can be seen in Figure 3–3c, the absorption profile is similar to the titration in acetonitrile with the progressive increase of a redshifted band. However, in this case only the 430 nm maximum is well established. In a surprising manner, the emission in chloroform changes completely by increasing its emission with increments of the acid equivalents in contrast with what was observed in acetonitrile. Figure 3–3d offers a better understanding of this increase alongside the images under UV light. We suggest that the chloroform molecules stabilize differently the excited state of **L1** enabling the excited state proton transfer phenomenon, since the excitation spectra shown in Figure 3–8 is much similar to the absorption spectrum at the end point of the titration with TFA. [37]

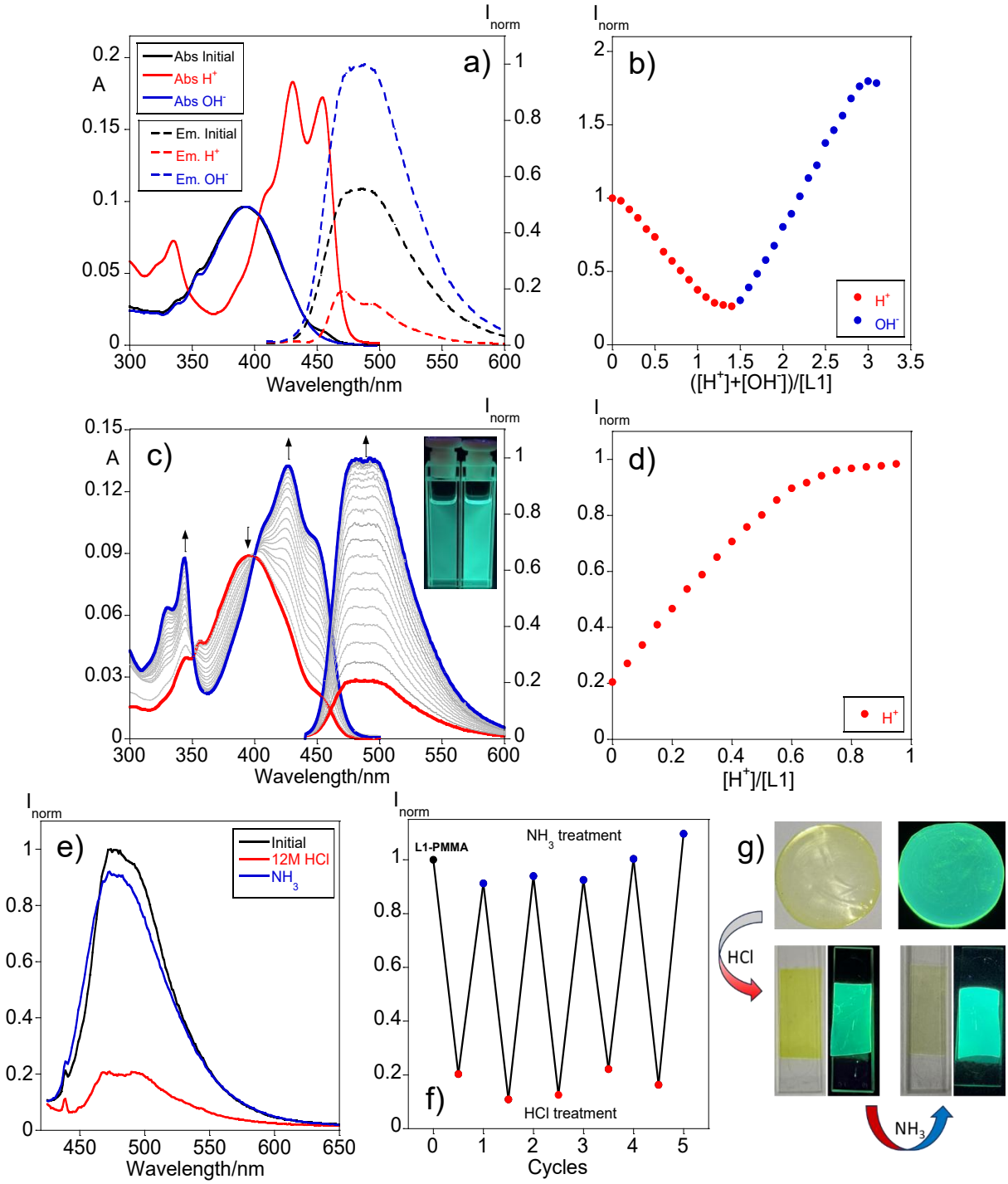


Figure 3–3. (a) Absorption and emission spectra of **L1** in acetonitrile after addition of 1.4 eq. of H^+ followed by 1.6 eq. of OH^- ($[H^+]$ = $[OH^-]$= 0.6 mM) and (b) the emission as a function of ($[H^+]$+$[OH^-]$/[**L1**]) at 487 nm. (c) Spectrophotometric and spectrofluorimetric titrations of compounds **L1** with increased additions of 10 µl of trifluoroacetic acid ([TFA] = 0.15 mM) in chloroform and (d) the emission as a function of $[H^+]$/[**L1**] at 487 nm. Inset images of the solution of **L1** in chloroform prior (left) and after (right) the titration under UV light (365 nm). Acidochromic behaviour of **L1-PMMA**. (e) Normalised emission spectra recorded after treatment with HCl solution (12 M) followed by immersion in a NH_3 solution (25% in water), (f) normalized emission intensity maximum at 474 nm after successive

cycles of HCl/NH_3 treatments by immersion in the corresponding aqueous solutions. (g) Images of the reversible acidochromic behaviour of **L1-PMMA** taken with the naked eye (left) and under UV light (right).

Since **L1** was able to manifest acidochromism in solution, the next step was to apply this behavior for the sensing of acidic solutions and environments. For this reason, PMMA polymer thin films were produced due to our previous experience with this polymer matrix. [38] For this purpose, an aqueous solution of HCl (12 M) was prepared and the polymer film doped with **L1** was submerged for 10 minutes. The prototype maintained its physical integrity, and we observed a color change from light green to yellow (Figure 3–3g). The emission of the film recorded before and after the treatment can be seen in Figure 3–3e where the polymer maintains its emission maximum around 485 nm, however, after treatment the emission is substantially quenched. In order to check if the polymer had any degree of reusability, the previously treated polymer thin film was submerged in an aqueous solution of NH_3, and in fact the emission is restored practically to the initial one (Figure 3–3e). To better assess the applicability of this material in the field of luminescent sensors, several cycles were performed and as it can be seen in Figure 3–3f, the quenching of the emission in contact with an acidic media and its recovery in direct contact with ammonia are maintained for at least five cycles. Further experiments were performed by introducing the doped material in HCl solutions at varying concentrations from 6 – 10 M, however the 10-minute mark for these solutions are not able to significantly alter the emission profile of the film (Figure 3–10). Studies performed by exposing this material to atmospheres of these gases also demonstrated difficulties to fully protonate and reverse the acidochromic behaviour to its initial emission (Figure 3–11).

3.4.5 Acid-base anion sensing

Taking into consideration that **L2** does not exhibit emission in solution, our first approach was to access if the compound was synthesized in the protonated form. Accompanied with several other examples in the literature of dansyl probes, [39,40,41,42,43] **L2** was used towards the sensing of anions, additions of 1, 5 and 10 equivalents of CN^-, F^-, Br^-, Cl^- in chloroform were performed. Figure 3–4 assembles the normalized emission intensities at 476 nm, upon addition of the aforementioned anions. Surprisingly, **L2** showed sensitivity towards CN^- and F^- ions evidenced by a turn on effect of the emission. Due to the more basic character of the cyanide anion, the turn on effect was accomplished before 5 equivalents while F^- ions were not able to reach the same intensities even at 10 equivalents.

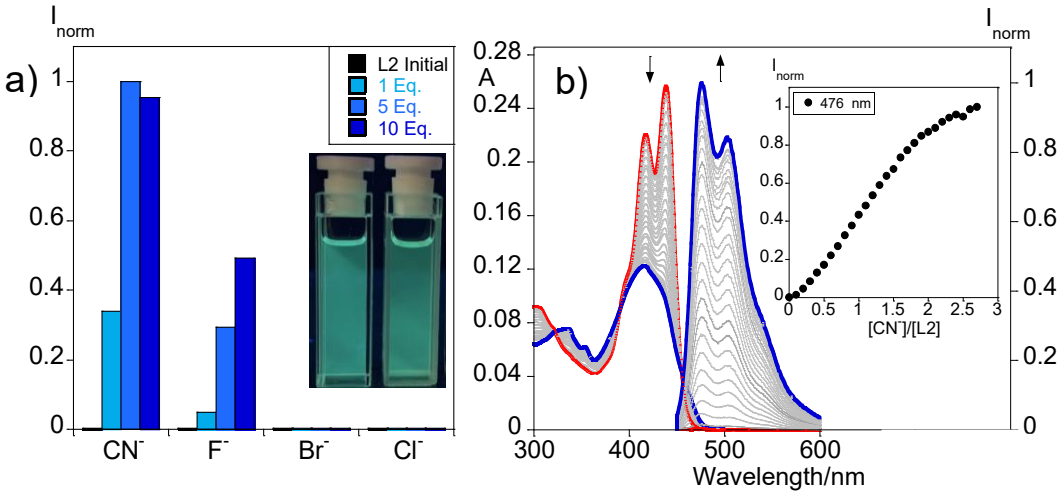


Figure 3–4. (a) Normalized emission intensity of **L2** after addition of CN^-, F^-, Br^-, Cl^- in successive proportions of 1, 5, and 10 equivalents in chloroform and inset image under UV light after the addition of 10 eq. of CN^- ions in a solution of chloroform (left) and THF (right) of **L2** ([**L2**] = 10 μM, $\lambda_{em\mathbf{L2}}$ = 476 nm, T = 298K). (b) UV-Vis and luminescent titrations of compounds **L2** upon continuous addition of 10 mL of CN^- ([CN^-] = 0.3 mM; [**L2**] = 10 μM), in chloroform. Inset: Emission as a function of [CN^-]/[**L2**] at 476 nm. For clarity of the reader the red spectra correspond to the initial spectrum and the blue to the endpoint of the titration.

In line with the previous results, Figure 3–4b gathers the UV-Vis and luminescent titrations towards increasing amounts of CN^- for **L2** in chloroform. Overall, the addition of the anion causes the continuous decrease of the absorbance maxima centered at 418 and 440 nm. In terms of the emission spectra, an enhancement of its intensity is observed with well-defined maxima at 476 nm and 505 nm with a shoulder at 546 nm. Similar behaviour was observed in THF (Figure 3–12). This progression with consequent additions of cyanide resembles the same behaviour of **L1** observed in acetonitrile when added OH^- ions with the loss of the characteristic absorption band and the increase in emission (Figure 3–13). In addition, the re-establish of the characteristic dansyl absorption band becomes evident at the endpoint of the titration.

Table 3-2. HypSpec's calculated association constants for the probe **L2** towards CN^- ions, fluorescence quantum yields (ϕ), and fluorescence lifetimes (τ) for compound **L2** after addition of CN^- ions in different solvents.

Cpd	Solvent	Association constants ($LogK_{ass.}$)	ϕ (%)	τ[ns]
L2	$CHCl_3$	4.23	29	T_1 = 1.2; T_2 = 3.9
	THF	3.62	16	T_1 = 1.1; T_2 = 2.7

To fully characterize the luminescence of the resultant species and the sensing ability towards CN^- the quantum yield alongside the lifetime measurement were obtained and the

stability constants was calculated with the aid of HypSpec software. [44] Table 3-2 reveals that **L2** has the largest constant in the presence of CN^- ions in chloroform with a constant value of $LogK_{ass.}$ = 4.23. Ligand **L2** was also found to exhibit a higher quantum yield of 29% in chloroform. Regarding lifetime measurements, a biexponential decay fitting was used for both solutions providing two distinct lifetimes due to the equilibrium of two species. Lifetime T_1 was found to contribute in one third and in half for chloroform and THF, respectively, with a value of 1.1 and 1.2 ns. By contrast, T_2 was the predominant lifetime of 3.9 and 2.7 ns as chloroform and THF are considered.

3.4.6 Polymeric particles

Considering our efforts on the development of systems that allow highly hydrophobic, and water quenched sensors to maintain their properties in water [4,45], Irogran® polymeric microparticles doped with **L1** were synthesized using the precipitation method as well as undoped particles. These polymeric particles were used in this case as an additional carrier for the assessment of the antimicrobial effect for **L1** as a proof of concept due to poor encapsulation of **L2** into the particles. The resulting Irogran® particles were characterized by dynamic light scattering (DLS) and transmission electron microscopy (TEM), the results showed that the particles present a spherical shape (Figure 3–14) while DLS data is included in Table 3-3.

Table 3-3. Dynamic light scattering data for the obtained particles.

Particles	Z-Average (nm)	PDI	ζ-Potential (mV)
@Nano	181±4	0.17±0.01	-39.6±0.7
L1@Nano	189±5	0.20±0.01	-39.9±1.1

Overall, DLS data suggest a smaller average size for the undoped Irogran® particles that increase considering the size of the compound introduced. Polydispersity index values suggest a mono distribution of size range and the zeta potential shows a negative surface charge indicative of good stability.

3.4.7 Antimicrobial Assay

The antibacterial activity of acridine derivatives **L1** and **L2** against Gram-negative (*E. coli*, *S. enterica*) and Gram-positive (*S. aureus*, *E. faecalis*) bacteria was evaluated by broth microdilution assays. The bacterial strains were incubated for 24 hours with a gradient concentration of each derivative from 100 to 0.20 µg/mL (see Figure 3–5).

Figure 3–5 summarizes the results obtained for the acridine derivatives **L1** and **L2**, as well as the control sample 9-aminoacridine (CAA). In general, the control CAA demonstrated antibacterial activity against all tested strains, with MIC_{50} values of 3.13 µg/mL for *E. coli*, 25 µg/mL for *S. aureus* and *E. faecalis*, and 12.5 µg/mL for *S. enterica*, indicating greater efficacy against Gram-negative bacteria. Compound **L1** exhibited MIC_{50} values of 12.5 µg/mL for *E. coli*,100 µg/mL for *S. aureus* and *S. enterica*, and 25 µg/mL for *E. faecalis*. On the other hand, **L2** showed an MIC_{50} value of 100 µg/mL for all tested strains.

The MIC_{50} values observed for the control compound CAA align with previously reported data in the literature, where 9-aminoacridine is known for its broad-spectrum antibacterial activity, particularly against Gram-negative bacteria. Typical MIC values for 9-aminoacridine compound are 8-32 µg/mL for *E. coli*, 32 µg/mL for *S. aureus* and 64 µg/mL for *E. faecalis*. [46]

For compound **L1**, the MIC_{50} values indicate more significant antibacterial activity than **L2**, particularly against *E. coli* and *E. faecalis*. Although the antibacterial activity is lower compared to CAA, these compounds may have several advantages, such as reduced toxicity, increased selectivity, versatility, and improved environmental impact. As acridine derivatives are known for their cytotoxicity, modifications in the chemical structure can lead to reduced toxicity, making them safer for environmental and industrial uses.

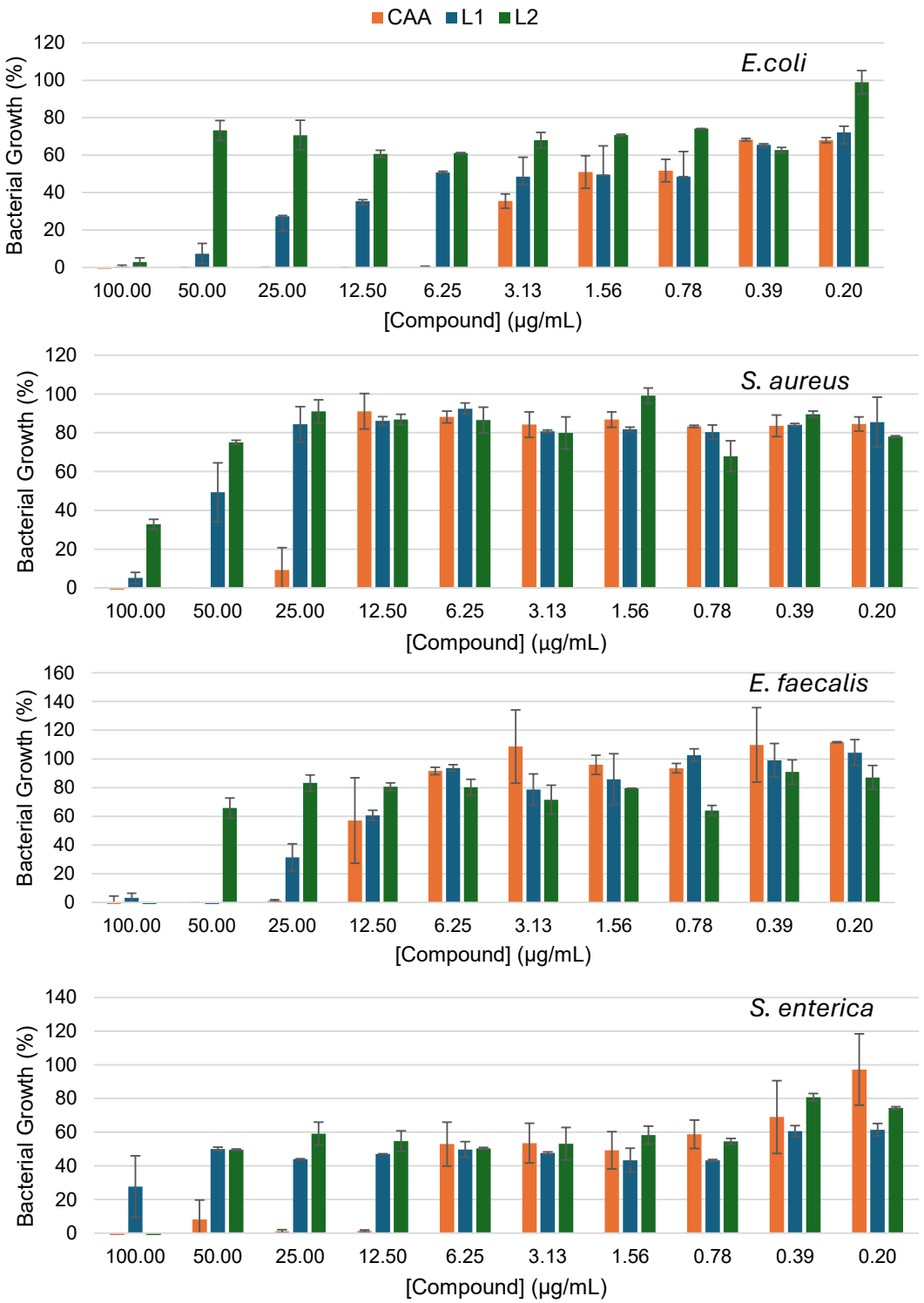


Figure 3–5. Bacterial growth profile against Gram-negative and Gram-positive bacteria of compounds **L1**, **L2** and **CAA** (9-aminoacridine:control).

To explore the versatility of **L1** and **L2**, they were integrated into polymer materials, such as PVA:PVP, and Irogran®, aiming to produce antibacterial coatings and films for diverse industrial applications. For these assays, the polymers were placed in contact with inoculated MHA plates and incubated for 24 hours to ensure bacterial growth. Non-doped polymers were used as controls. Additionally, based on the results obtained, Irogran® polymeric nanoparticles doped with **L1** were also synthesized, and their antibacterial activity was evaluated through a broth microdilution assay.

Figure 3–6 summarizes the results achieved for these assays. Firstly, no significant antibacterial activity was detected for the control non-doped PVA:PVP polymers, demonstrating once again their biocompatible profile. [47] A similar profile was obtained for PVA:PVP@**L2** polymers, with no inhibitory behavior observed for any bacterial strains tested.

Conversely, for PVA:PVP@**L1**, no bacterial growth was observed at the agar-polymer interface for *E. coli*, *S. aureus*, and *E. faecalis*, with a slight color diffusion in latter two, demonstrating some antibacterial properties.

Irogran® polymers exhibit intrinsic antibacterial properties, presenting no bacterial growth under the polymers in *E. faecalis* and *S. enterica,* as also previously reported in the literature. [48] The same behavior was verified for Irogran®@**L2** in *E. coli*, *E. faecalis* and *S. enterica* and for Irogran®@**L1** in all bacterial strains, with a halo formation of 9 cm^2 in *E. faecalis*, consistent with the release of some compound to the medium and their subsequent diffusion throughout. This increased inhibition zone observed with Irogran®@**L1** in *E. faecalis* suggests that combining Irogran® with **L1** may create a synergistic effect, enhancing the antibacterial efficacy.

Considering these results, Irogran® polymeric microparticles were thus synthesized with compound **L1** and tested against the same bacterial strains with undoped Irogran® microparicles, within a lower concentration range from 0.03 to 14 µg/mL. Surprisingly, the Irogran® microparticles doped with **L1** (**L1**@Nano) exhibit unprecedented selectivity, achieving an MIC_{50} value of 14 µg/mL for *E. faecalis*. This value is 2-fold lower than the obtained MIC_{50} of free **L1** in solution, indicating enhanced efficacy in the microparticle formulation and further validating the occurrence of possible synergistic mechanisms between the two.

a)

	PVA:PVP	PVA:PVP@L1	PVA:PVP@L2	PVA:PVP@CAA	Irogran	Irogran@L1	Irogran@L2	Irogran@CAA
E. coli	Growth	No growth No halo	Growth	No growth Halo: 3.7 cm^2	Growth	No growth No halo	No growth No halo	No growth Halo: 2.9 cm^2
S. aureus	Growth	No growth No halo*	Growth	No growth Halo: 2.2 cm^2	Growth	No growth No halo*	Growth	No growth Halo: 2.4 cm^2
E. faecalis	Growth	No growth No halo*	ND	No growth Halo: 2.4 cm^2	No growth No halo	No growth* Halo: 9.0 cm^2	No growth No halo	No growth Halo: 1.5 cm^2
S. enterica	Growth	Growth	Growth	No growth Halo: 3.3 cm^2	No growth No halo	No growth No halo*	No growth No halo	No growth Halo: 3.4 cm^2

b)

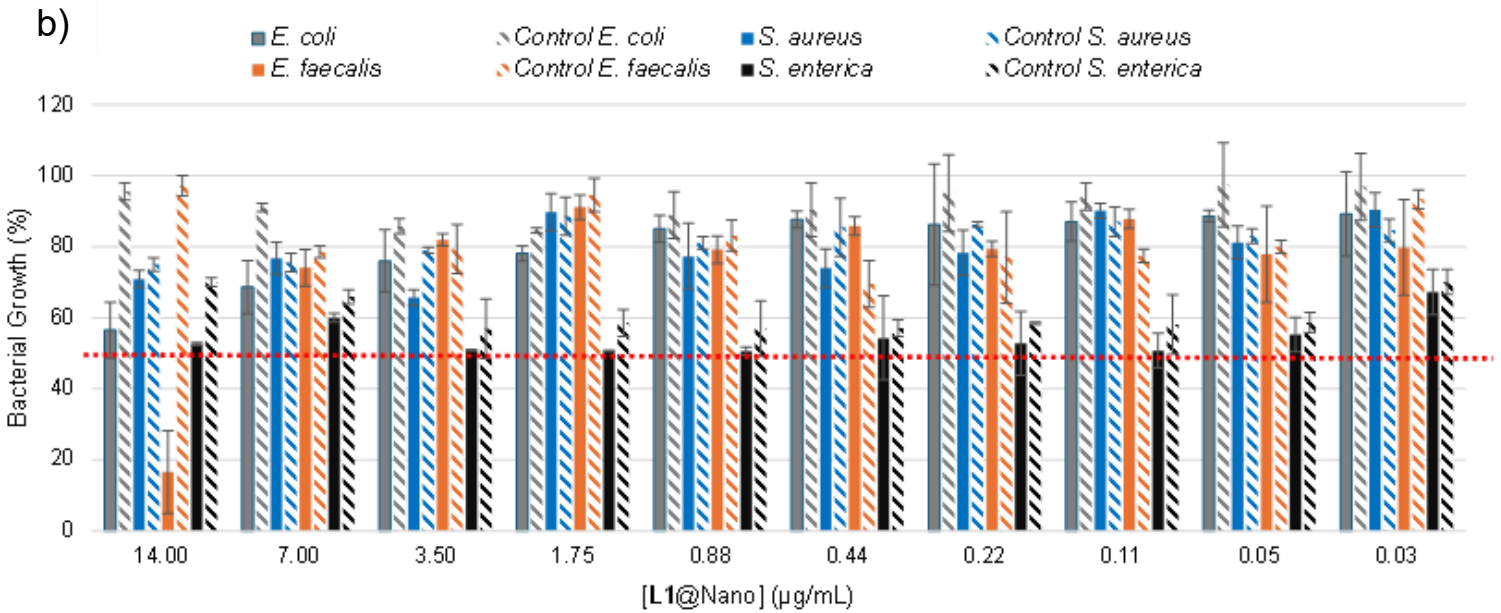


Figure 3–6. (**a**) Results of antibacterial assays of PVA:PVP and Irogran® polymers (*color diffusion to the media), and (**b**) Bacterial growth profile against Gram-negative and Gram-positive bacteria of free and **L1** doped Irogran® nanoparticles.

3.5 Conclusions

In this work, two 9-aminoacridine based fluorophores were synthesized with the intention to explore their photophysical properties using different polymer matrixes as multifunctional materials. **L1** was found to modulate its emission in the presence of trace amounts of water, exhibiting a turn-on effect. This property was utilized for detecting water traces in organic solvents, achieving a limit of detection (LOD) of 0.0028 V% and a limit of quantification (LOQ) of 0.0121 V% in acetonitrile. Additionally, **L1** displayed acidochromism and showed different behaviors in acetonitrile and chloroform due to the varying stabilization of the excited state, resulting in turn-off and turn-on effects in these respective solvents. PMMA polymer doped films were useful on the demonstration for this compound to be used as a sensor for strong acids and the reusability of this material has been elucidated through various cycles. Due to the photophysical similarities of the synthesized **L2** and the protonated **L1**, a proposed acid base anion sensing was carried out for cyanide. This led to a turn-on effect on the emission and a full characterization of the emission was performed resulting in an increment of the quantum yield to 29% and an association constant of $LogK_{ass.}$ = 4.23 in chloroform. Finally, the antibacterial profile of the newly synthesized compounds was performed through broth microdilution assay and integrated into polymer materials, such as PVA:PVP, and Irogran®, aiming to produce antibacterial coatings and films for diverse industrial applications. As a proof of concept, undoped and doped with **L1** Irogran® microparticles were synthesized using an oil-in-water method as an additional carrier for the assessment of the antimicrobial effect, achieving an MIC_{50} value of 14 µg/mL for *E. faecalis*.

3.6 Supplementary material

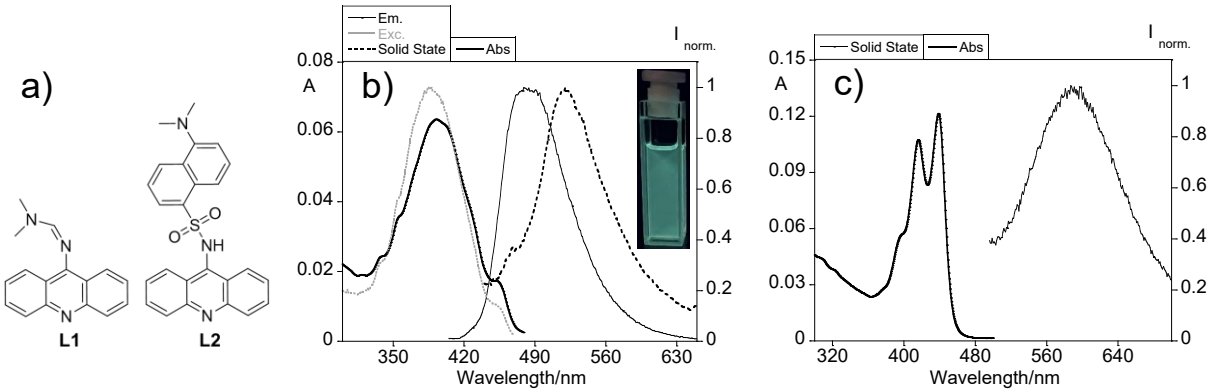


Figure 3–7. (a) Molecular structure of 9-aminoacridine derived compounds **L1** and **L2**. Photophysical characterization of compound **L1** (b) in acetonitrile and **L2** (c) in chloroform ([**L1**] = [**L2**] = 5 μM).

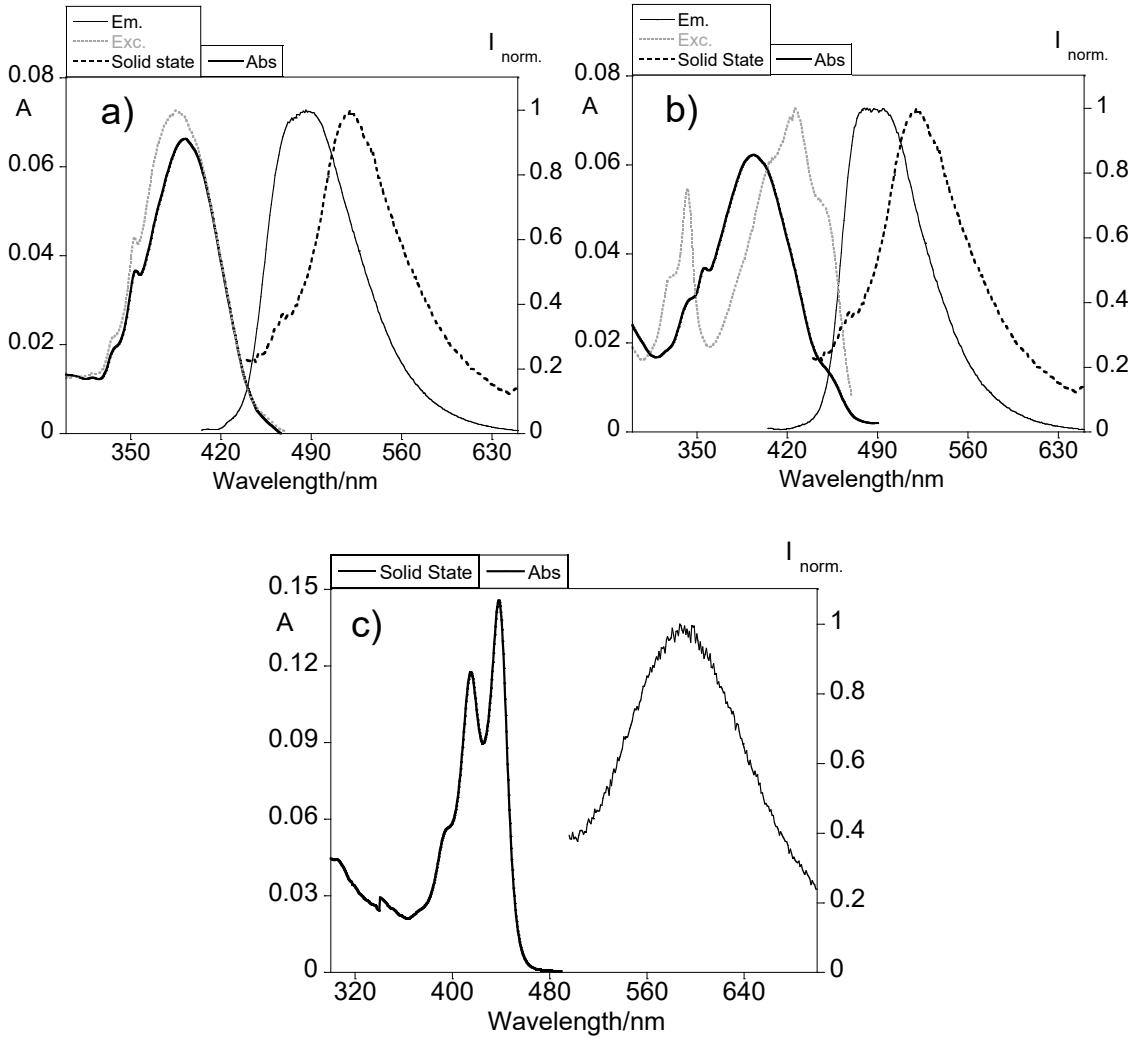


Figure 3–8. Photophysical characterization of derivative **L1** in a) ethanol and b) chloroform ([**L1**] = 5 μM). c) Photophysical characterization of derivative **L2** in THF ([**L2**] = 5 μM).

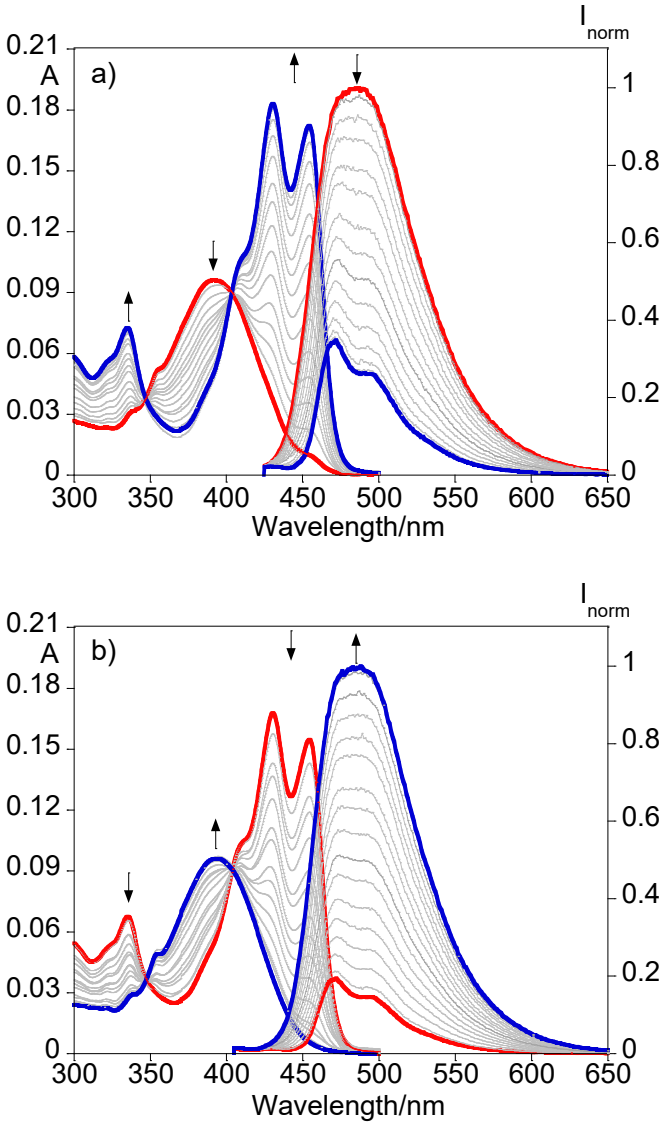


Figure 3–9. Spectrophotometric and spectrofluorimetric titrations of compounds **L1** (a) with increased additions of 5 µl of hydrochloric acid ([H^+]=0.6 mM) followed by (b) successive additions of 5 µl of sodium hydroxide ([OH^-]=0.6 mM) in acetonitrile.

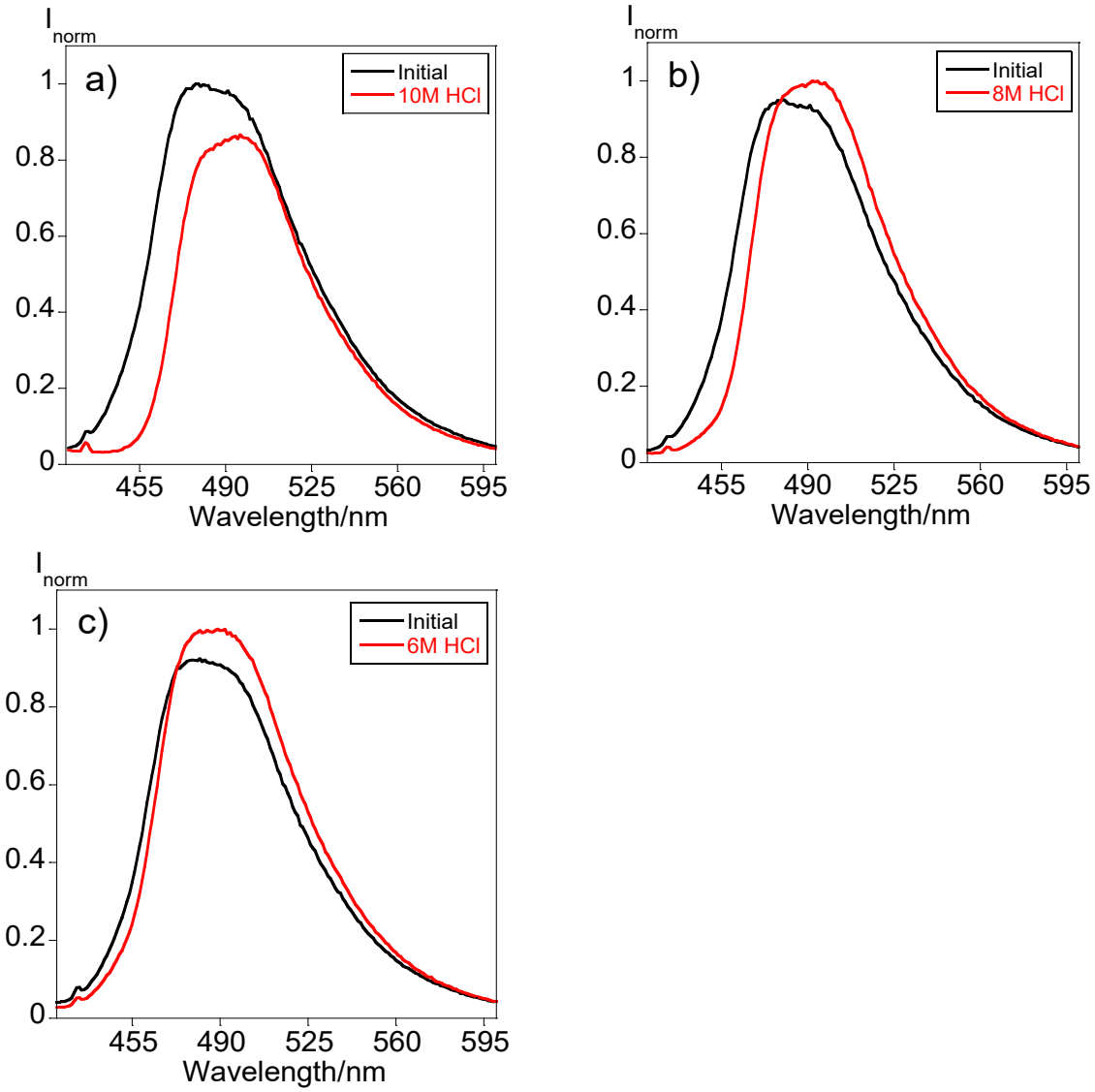


Figure 3–10. Acidochromic behaviour of **L1-PMMA**. Normalized emission spectra recorded after treatment with HCl solution (A) 10 M, (B) 8 M and (C) 6 M.

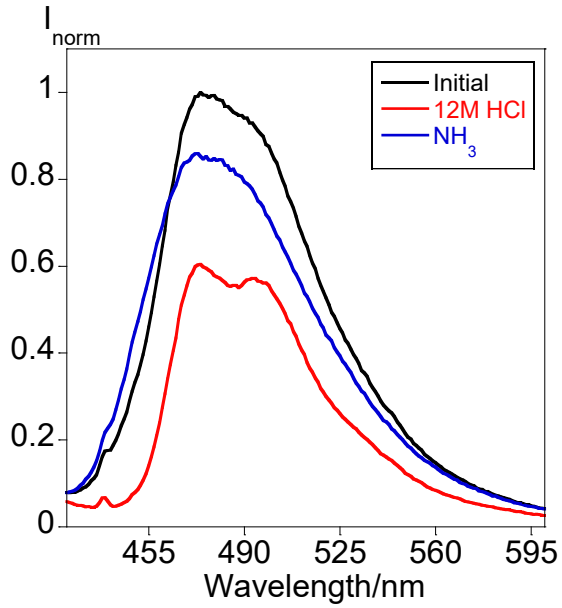


Figure 3–11. Acidochromic behaviour of **L1-PMMA**. Normalised emission spectra recorded after treatment with HCl vapours (12 M).

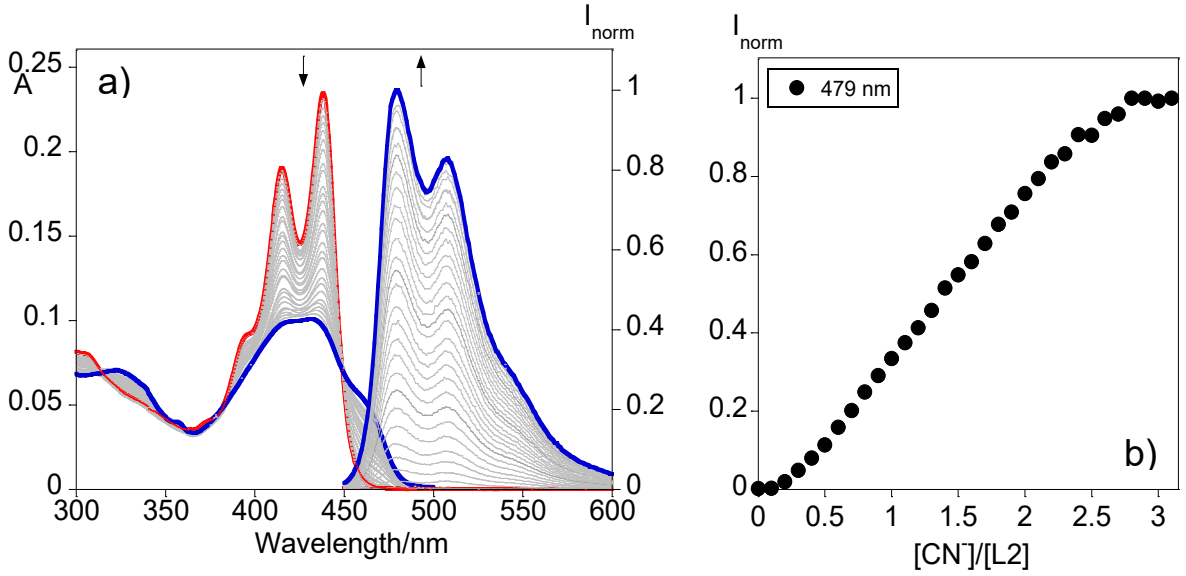


Figure 3–12. (a) UV-Vis and luminescent titrations of compounds **L2** upon continuous addition of 10 mL of CN^- ([CN^-] = 0.3 mM; [**L2**] = 10 μM), in THF. (b) Emission as a function of [CN^-]/[**L2**] at 479 nm.

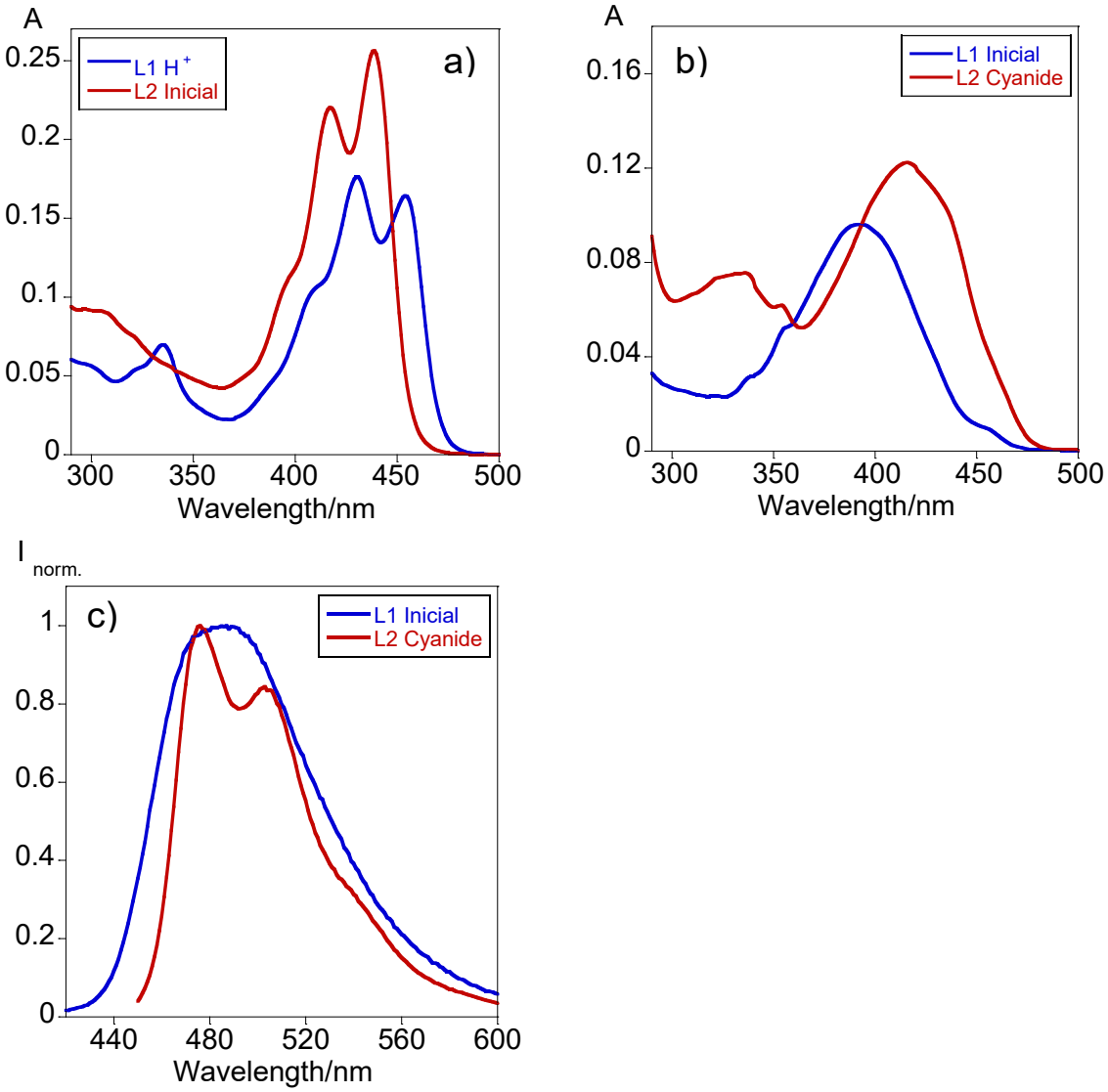


Figure 3–13. Comparison of the absorption spectra of (a) **L1** in the protonated form and **L2** recorded initially and (b) **L1** without addition of any analyte and **L2** at the endpoint of the titration with cyanide. (c) Emission spectra of **L1** of the unprotonated form and **L2** at the endpoint of the titration with cyanide.

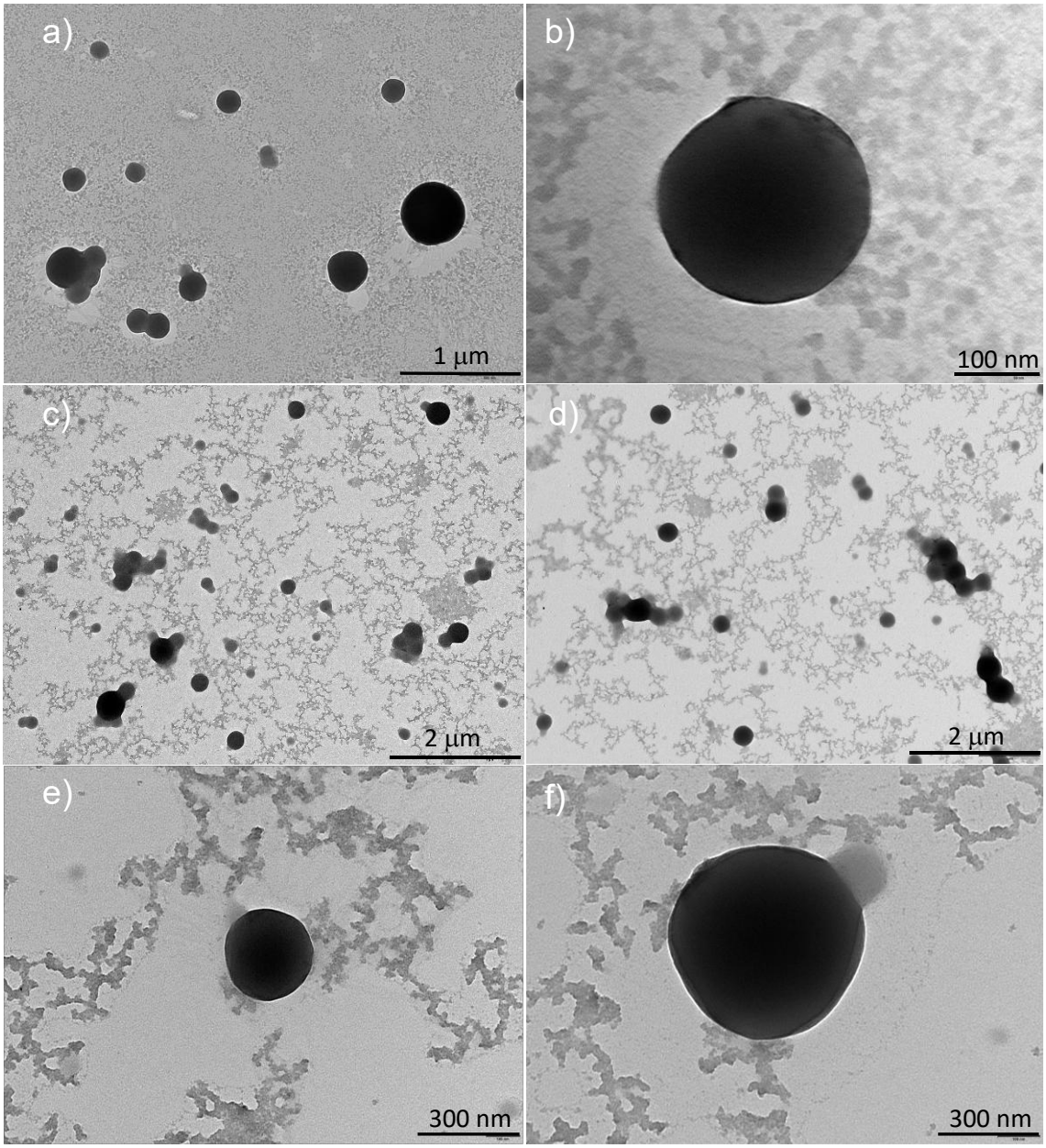


Figure 3–14. Transmission electron microscopy (TEM) images of (a,b) @Nano and (c-f) **L1**@Nano.

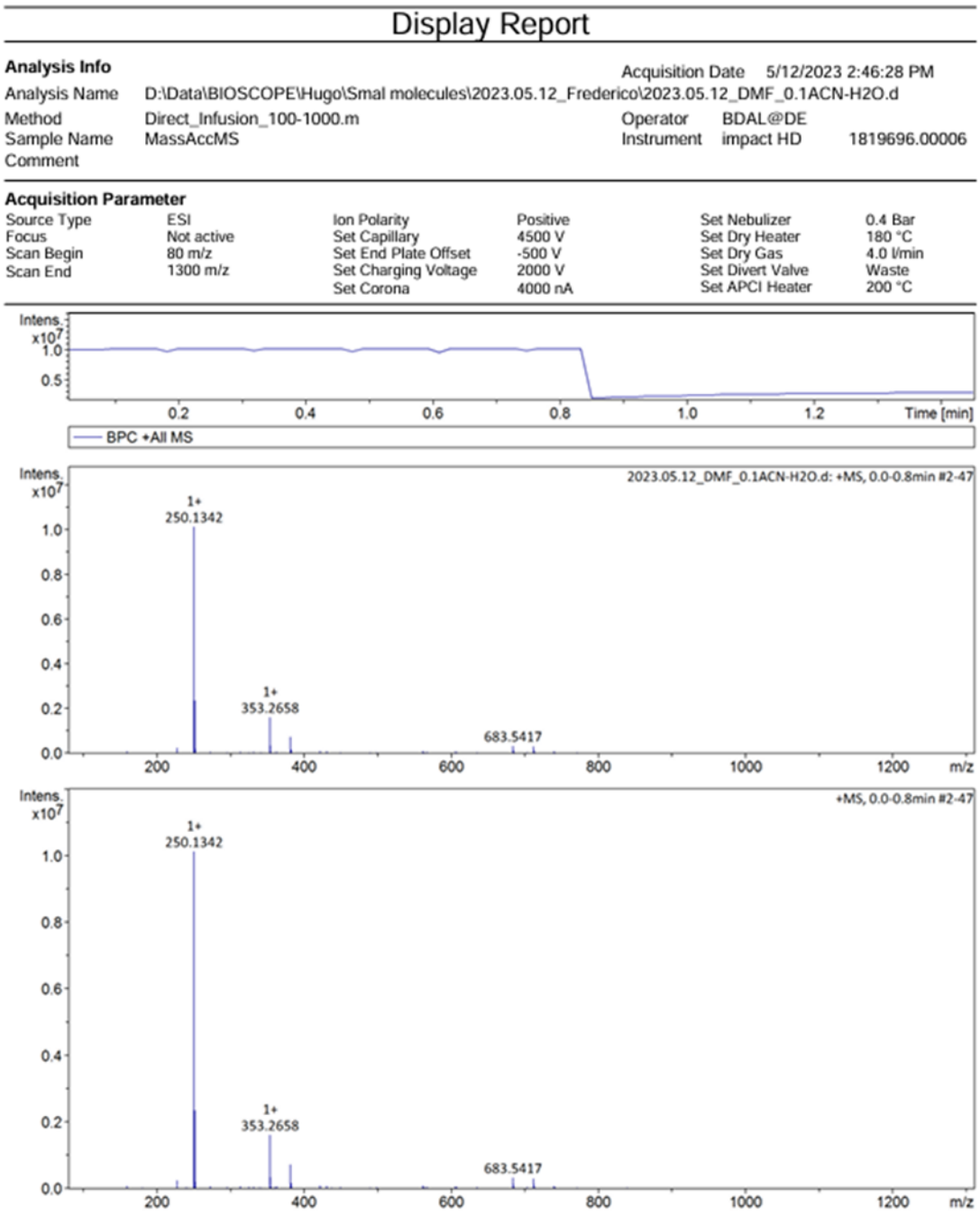


Figure 3–15. ESI-HRMS spectrum of compound **L1** without TFA.

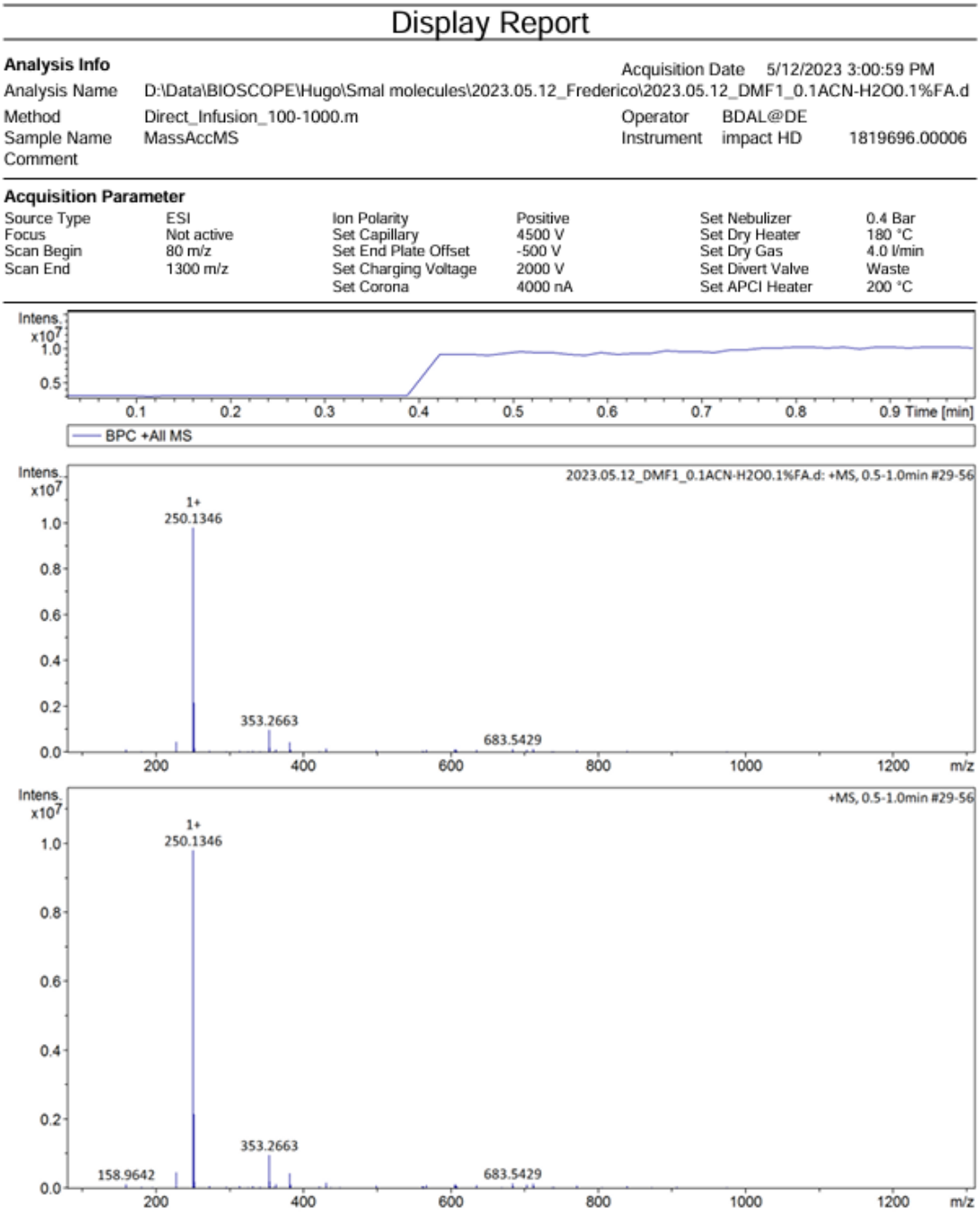


Figure 3–16. ESI-HRMS spectrum of compound **L1** with TFA.

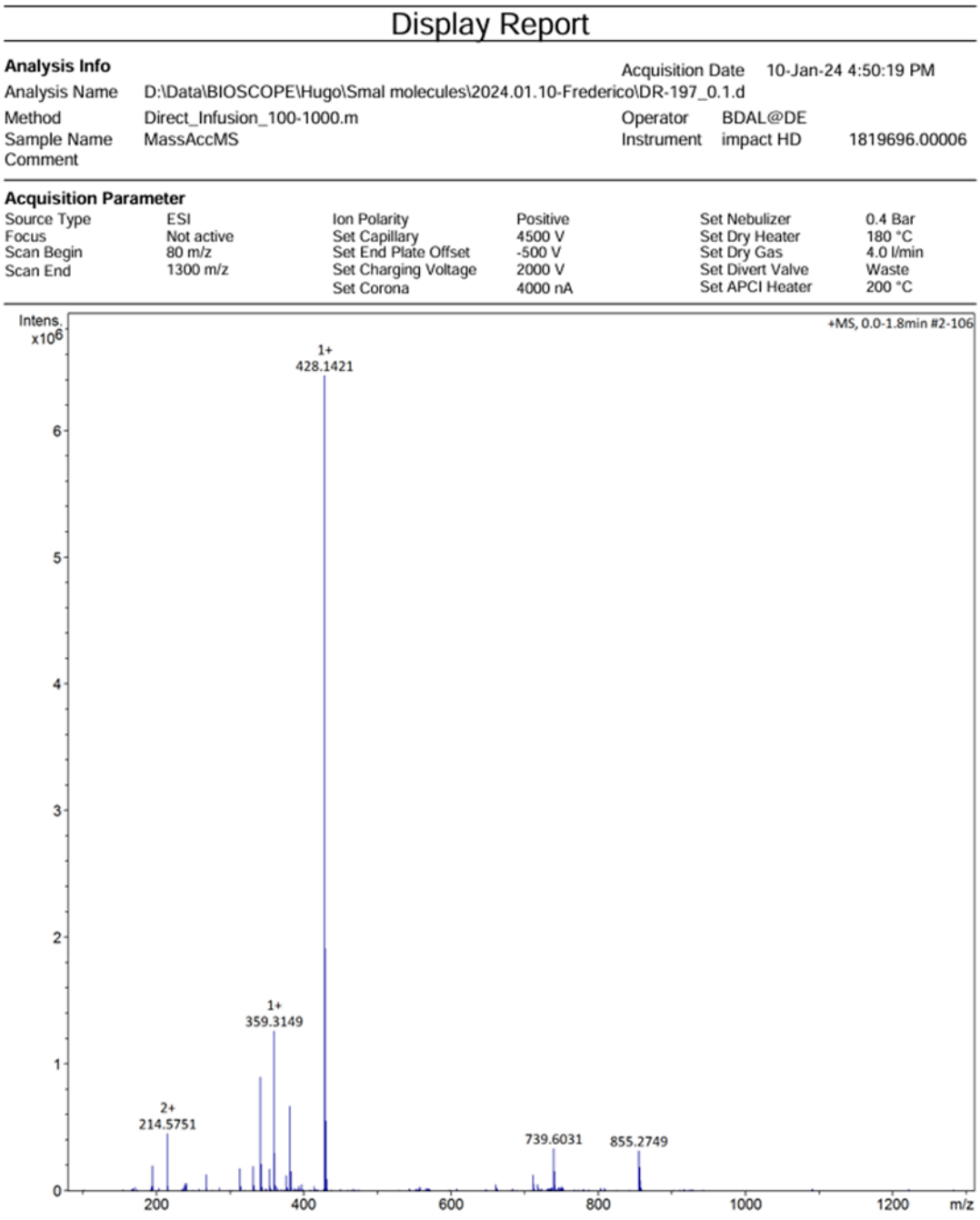


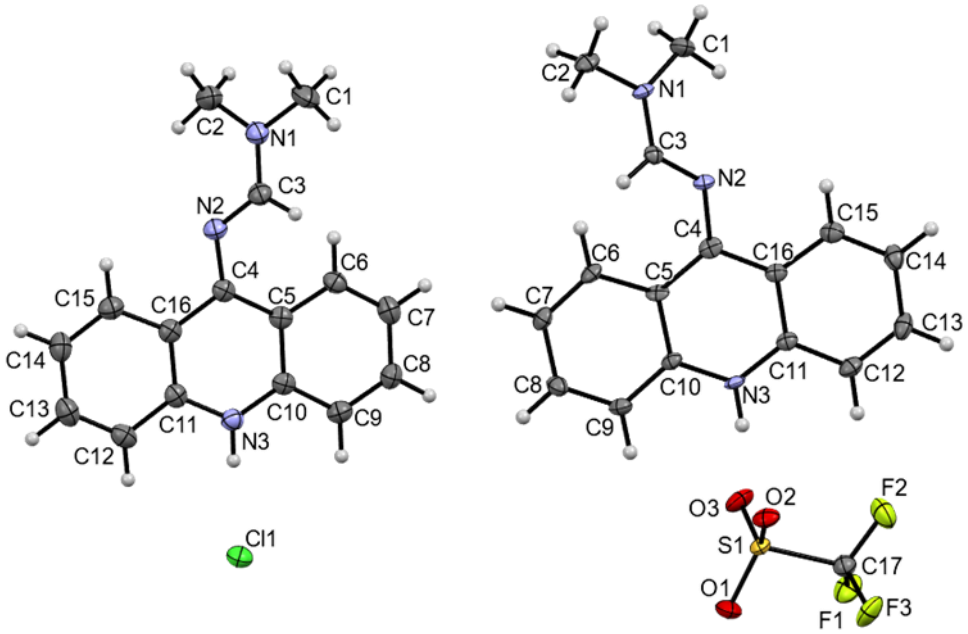
Figure 3–17. ESI-HRMS spectrum of compound **L2**.

Table 3-4. Crystallographic experimental data and structure refinement parameters.

	L1HCl	L1HOTf
Formula	$C_{16}H_{17}Cl_4N_3$	$C_{17}H_{16}F_3N_3O_3S$
M	405.13	399.39
λ (Å)	0.71073	0.71073
T (K)	110(2)	110(2)
crystal system	Triclinic	Triclinic
space group	P-1	P-1
Crystal description	Plate	Plate
Crystal color	Yellow	Yellow
Crystal Size	0.16 × 0.20 × 0.40	0.14 × 0.18 × 0.40
a (Å)	7.3075(11)	7.4616(8)
b (Å)	9.5061(16)	9.6779(11)
c (Å)	13.783(2)	12.0757(14)
α (deg)	81.728(6)	92.609(4)
β (deg)	83.727(5)	96.186(4)
γ (deg)	83.321(6)	94.778(4)
V (Å3)	936.9(3)	862.62(17)
Z	2	2
ρcalc (g cm-3)	1.436	1.538
μ (mm-1)	0.635	0.243
θmax (deg)	25.679	25.681
total data	42084	31922
unique data	3545	3261
Rint	0.1000	0.2574
R [I>3σ(I)]	0.0653	0.0661
wR2	0.1684	0.1483
Goodness of fit	1.040	1.064
ρ min	-0.678	-0.468
ρ max	1.191	0.411

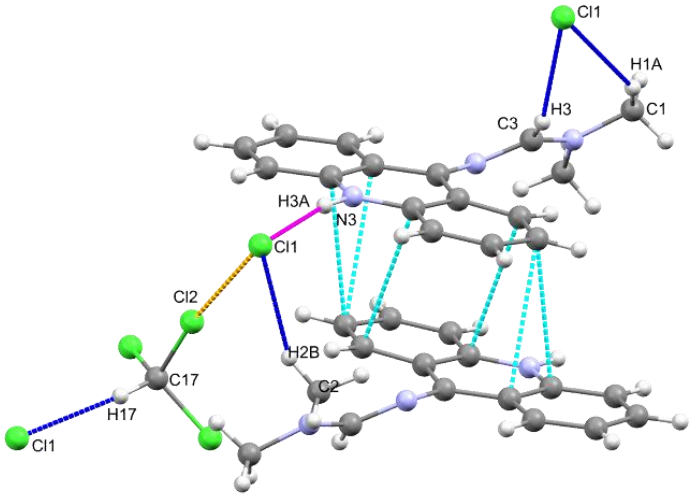
Table 3-5. Selected bond distances (Å) and angles (°) for compounds **L1HCl** (a) and **L1HOTf**.

	L1HCl	L1HOTf		L1HCl	L1HOTf
Bond distances			Bond angles		
C4–C5	1.432(5)	1.440(4)	C1–N1–C2	117.0(3)	116.9(3)
C16–C4	1.437(5)	1.426(4)	N1–C3–N2	122.6(3)	122.6(3)
C4–N2	1.348(5)	1.350(4)	C3–N2–C4	122.2(3)	123.1(3)
C3–N2	1.320(5)	1.316(4)	N2–C4–C5	124.5(3)	124.9(3)
C3–N1	1.307(5)	1.314(4)	C11–N3–C10	122.8(3)	123.0(3)
C2–N1	1.454(5)	1.458(4)	C3–N2–C4–C16	144.9(3)	-147.0(3)
C1–N1	1.457(5)	1.451(4)	C3–N2–C4–C5	-39.8(5)	36.4(5)
C10–N3	1.357(5)	1.358(4)			
C11–N3	1.362(5)	1.360(4)			

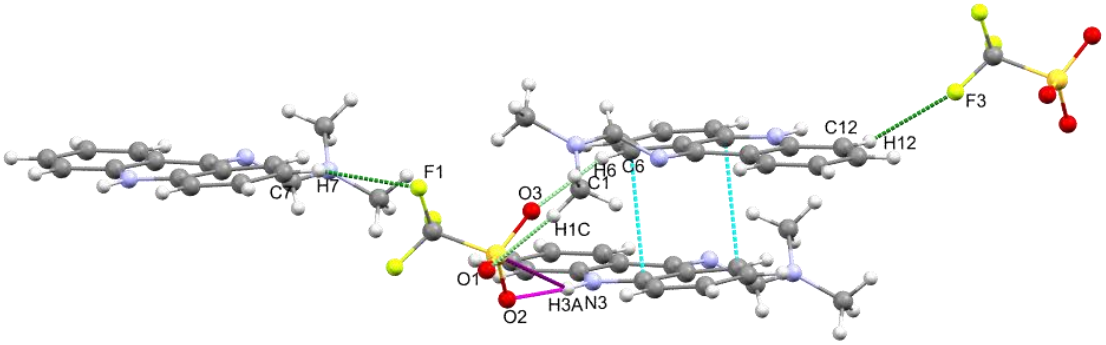


(a) (b)

Figure 3–18. Mercury representation of the molecular structure of compounds **L1HCl** (a) and **L1HOTf** (b). In **L1HCl**, a $CHCl_3$co-crystallized solvent molecule was omitted for clarity.



(a)



(b)

Figure 3–19. Representation of the intermolecular interactions responsible for the supramolecular arrangement in (a) **L1HCl** and (b) **L1HOTf**. Classical and non-classical hydrogen bonds, halogen and π…π interactions are depicted as dashed lines [N–H…Cl, magenta; C–H…Cl, blue; Cl…Cl, orange; π…π, light blue; C–H…F, green; C–H…O, light green; and N–H…O, fuchsia].

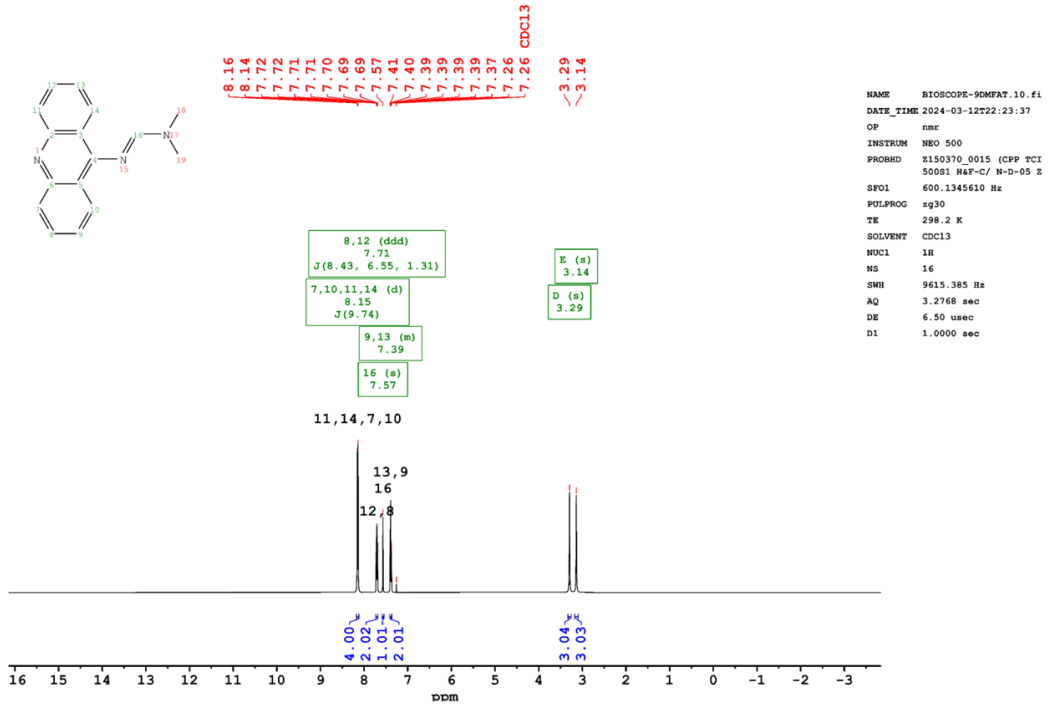


Figure 3–20. ^{1}H-NMR spectrum of compound **L1** in chloroform.

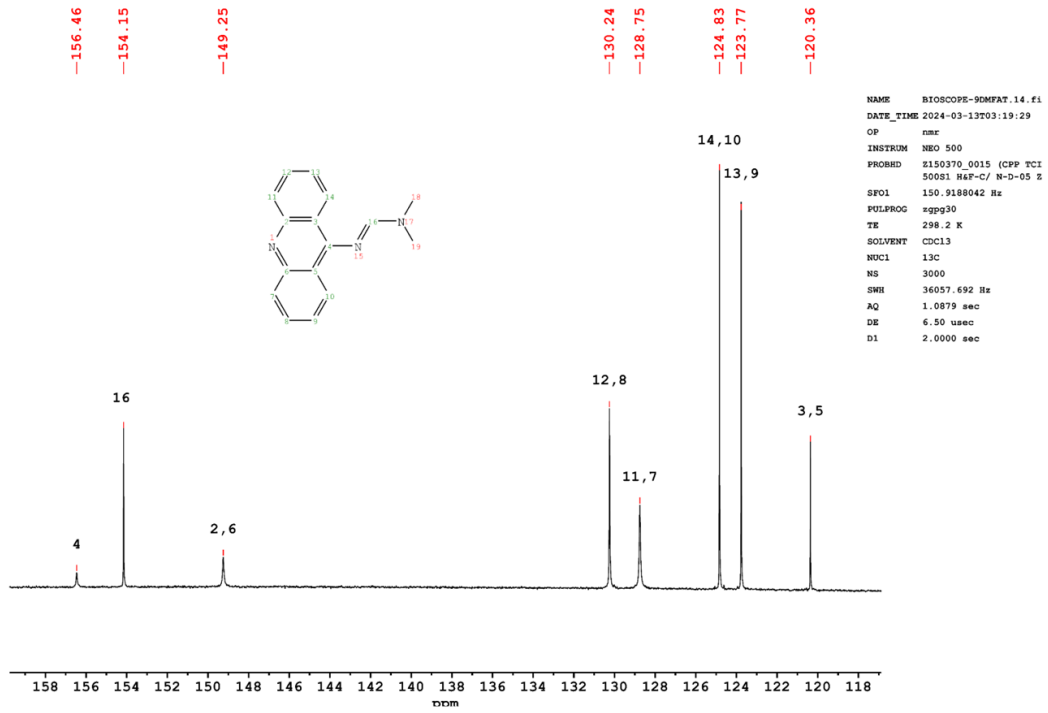


Figure 3–21. ^{13}C-NMR spectrum of compound **L1** in chloroform (details).

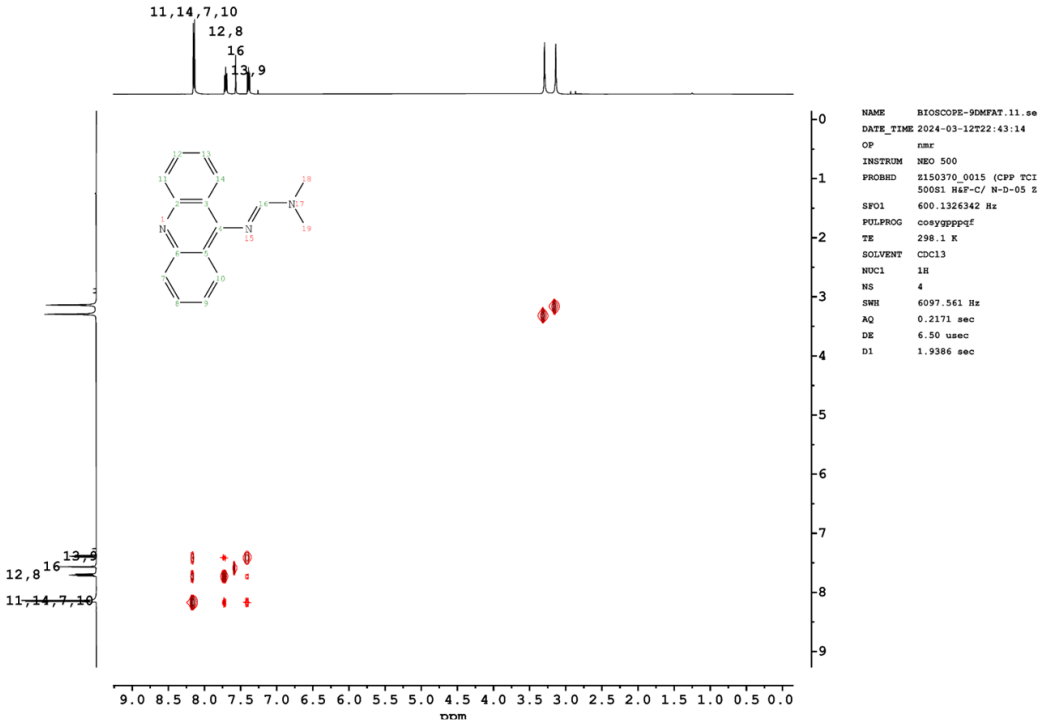


Figure 3–22. COSY-NMR spectrum of compound **L1** in chloroform.

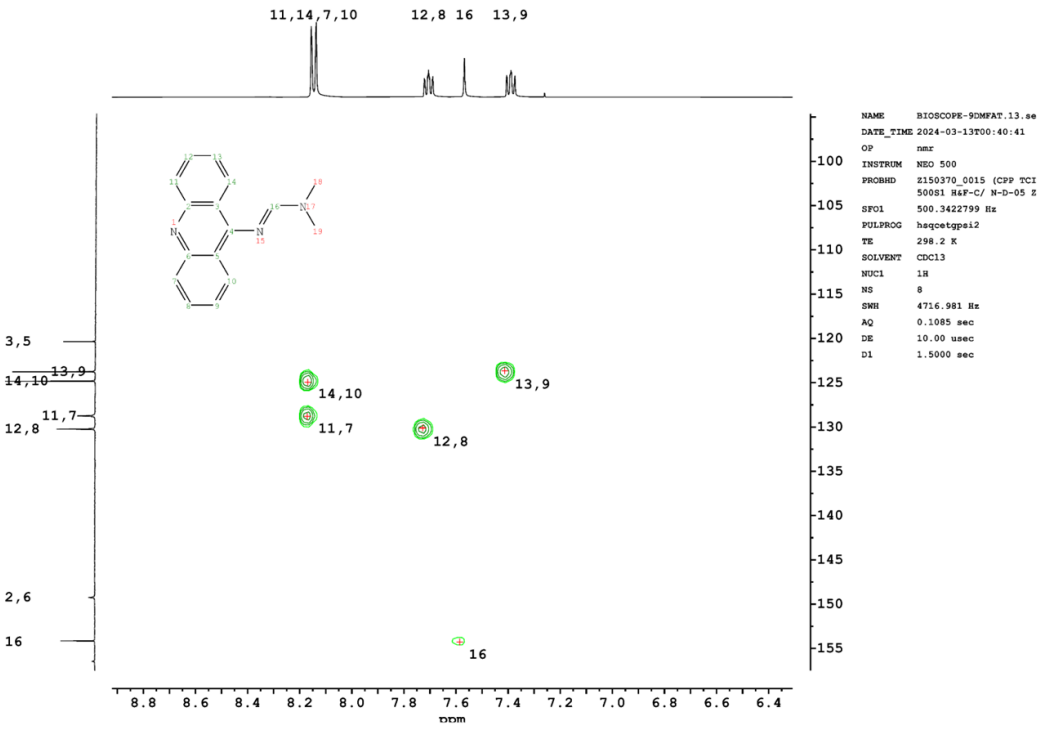


Figure 3–23. HSQC-NMR spectrum of compound **L1** in chloroform.

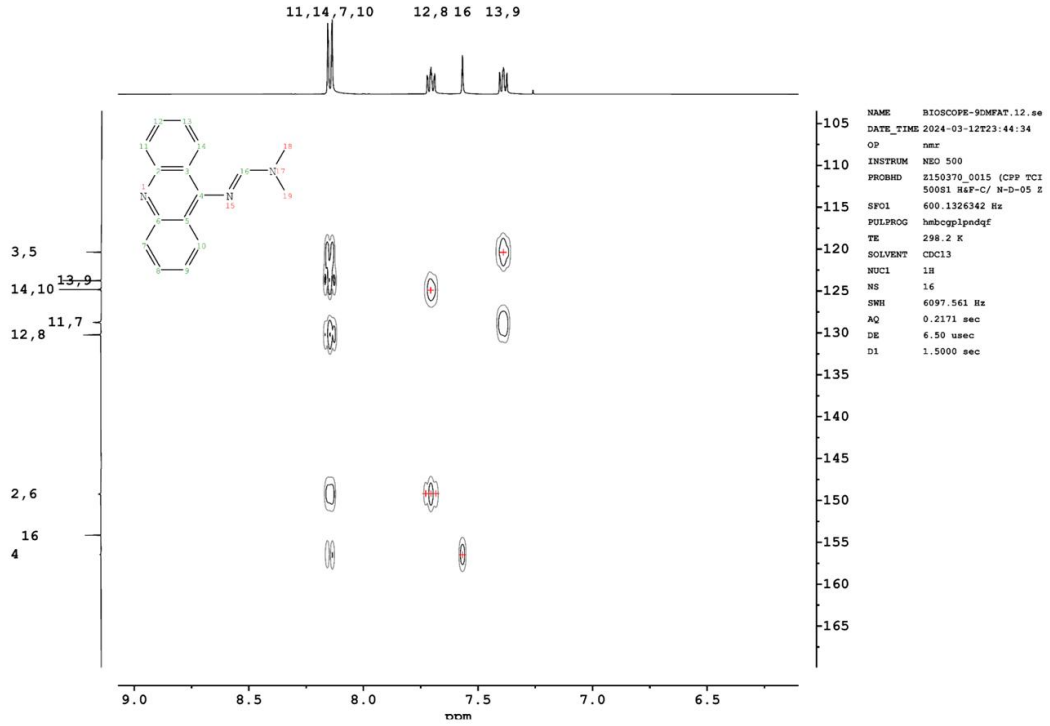


Figure 3–24. HMBC-NMR spectrum of compound **L1** in chloroform.

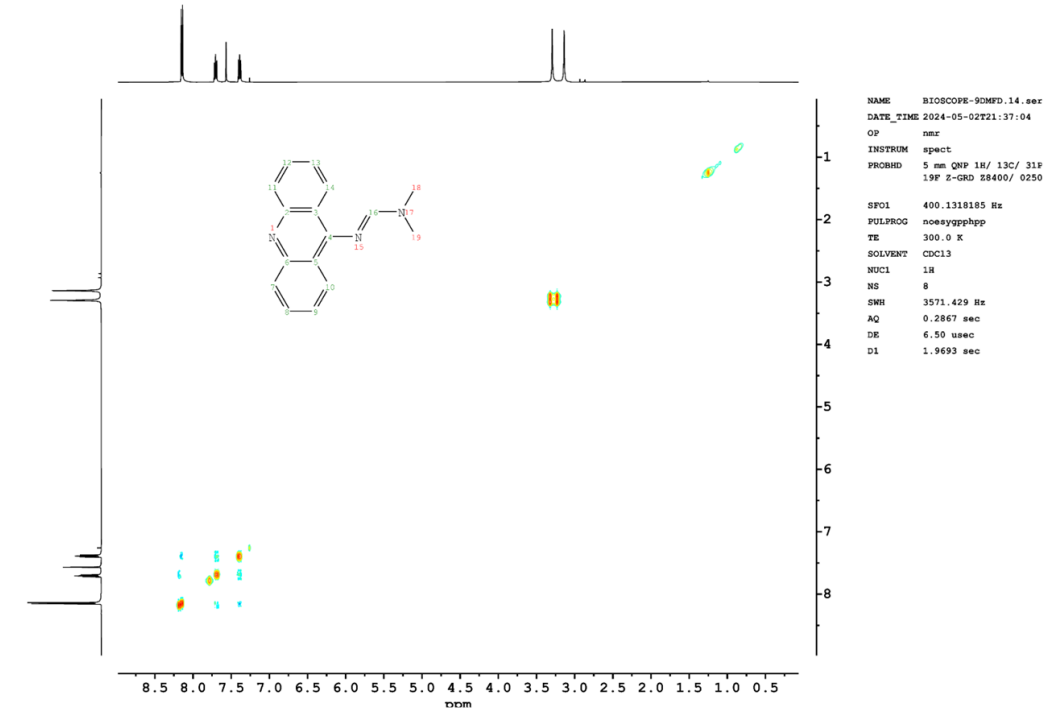


Figure 3–25. NOESY-NMR spectrum of compound **L1** in chloroform.

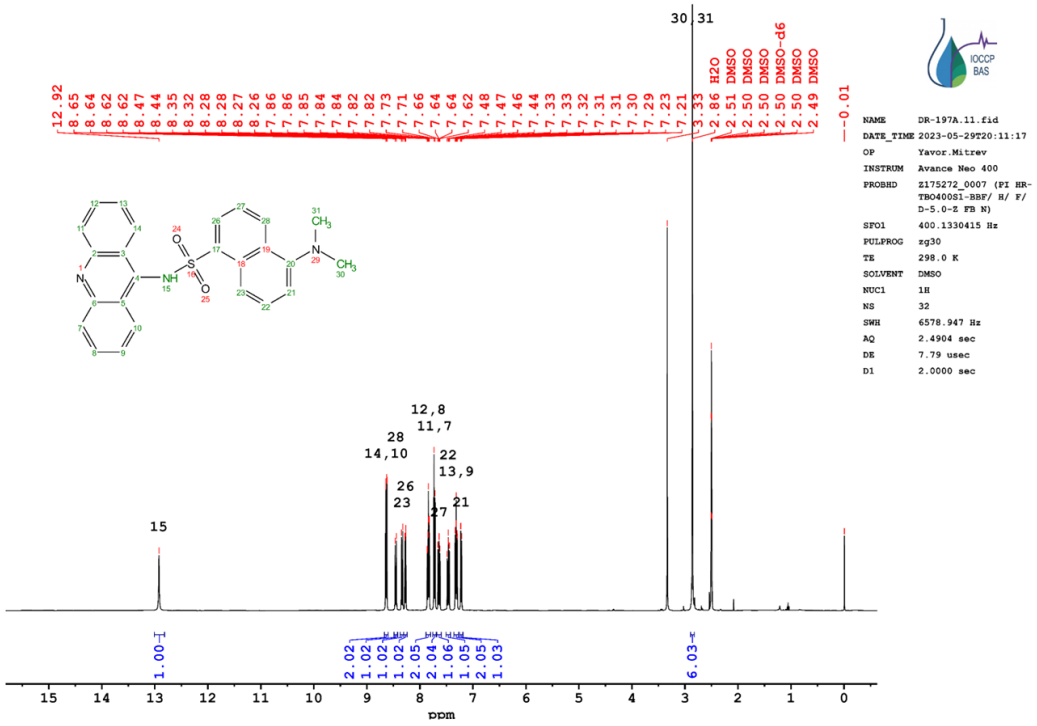


Figure 3–26. ^{1}H-NMR spectrum of compound **L2** in DMSO.

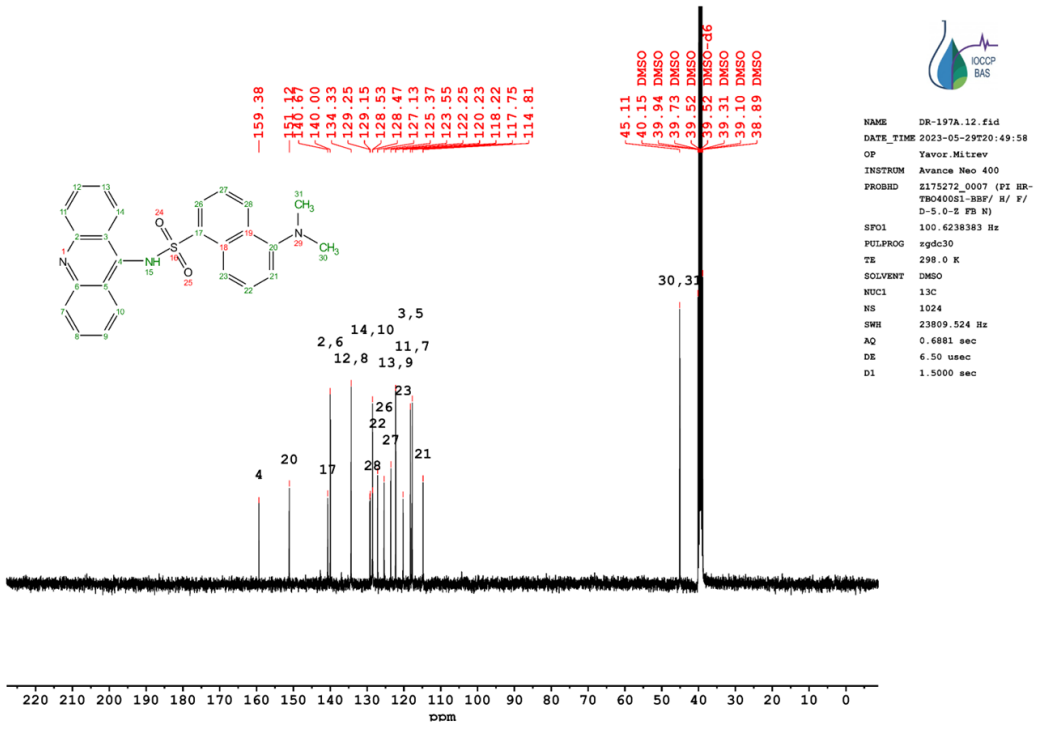


Figure 3–27. ^{13}C-NMR spectrum of compound **L2** in DMSO.

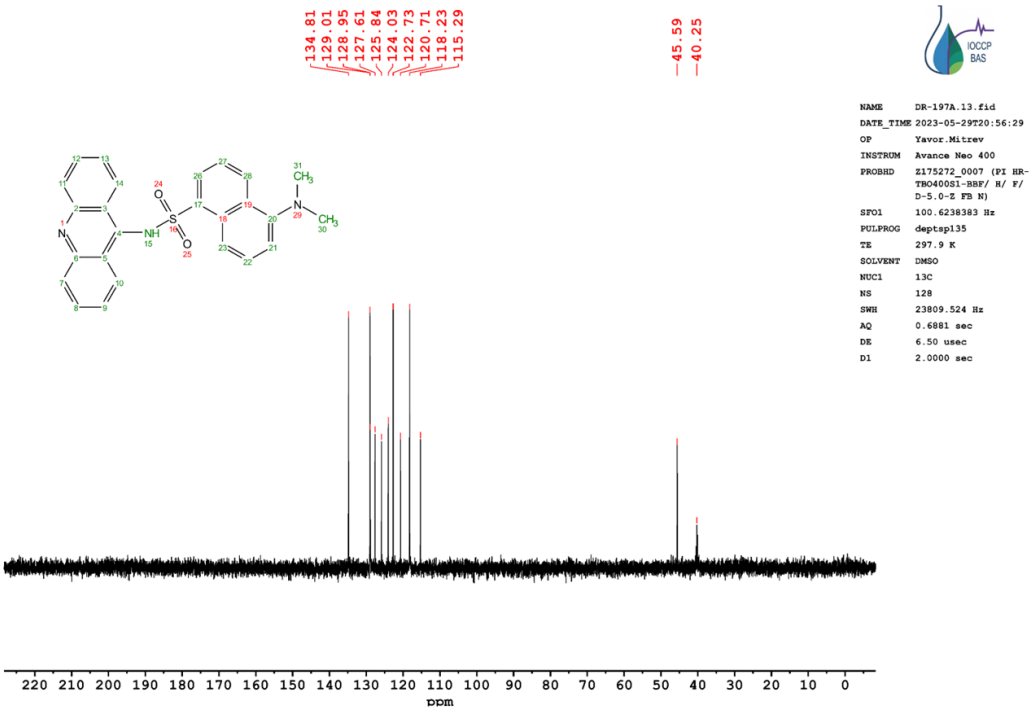


Figure 3–28. DEPT-NMR spectrum of compound **L2** in DMSO.

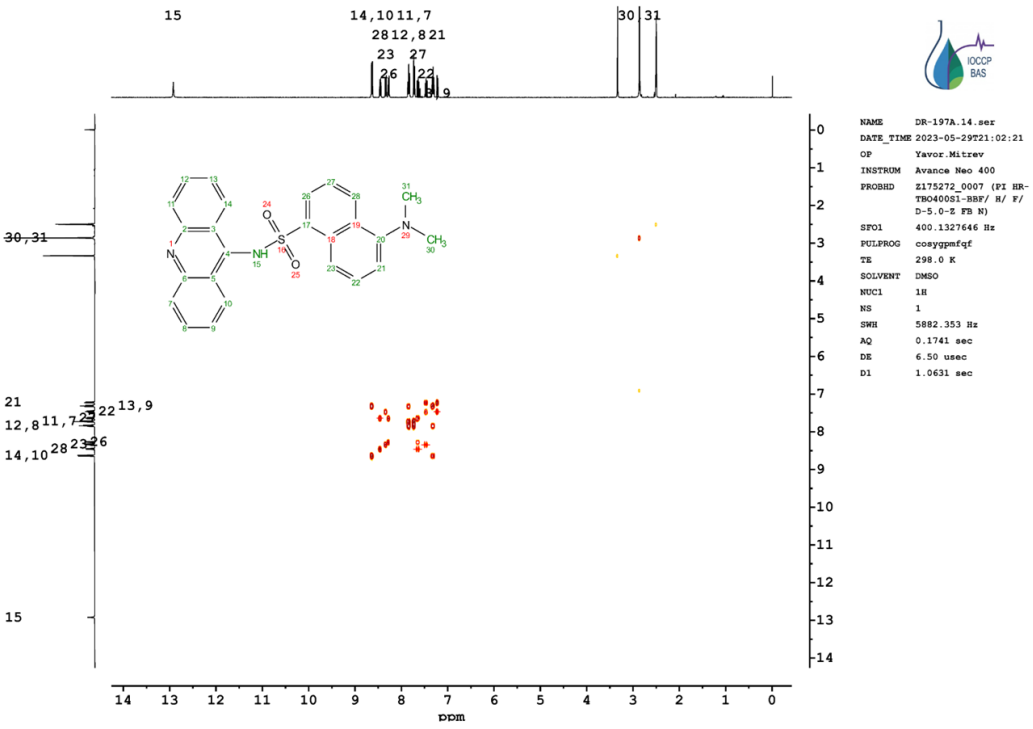


Figure 3–29. COSY-NMR spectrum of compound **L2** in DMSO.

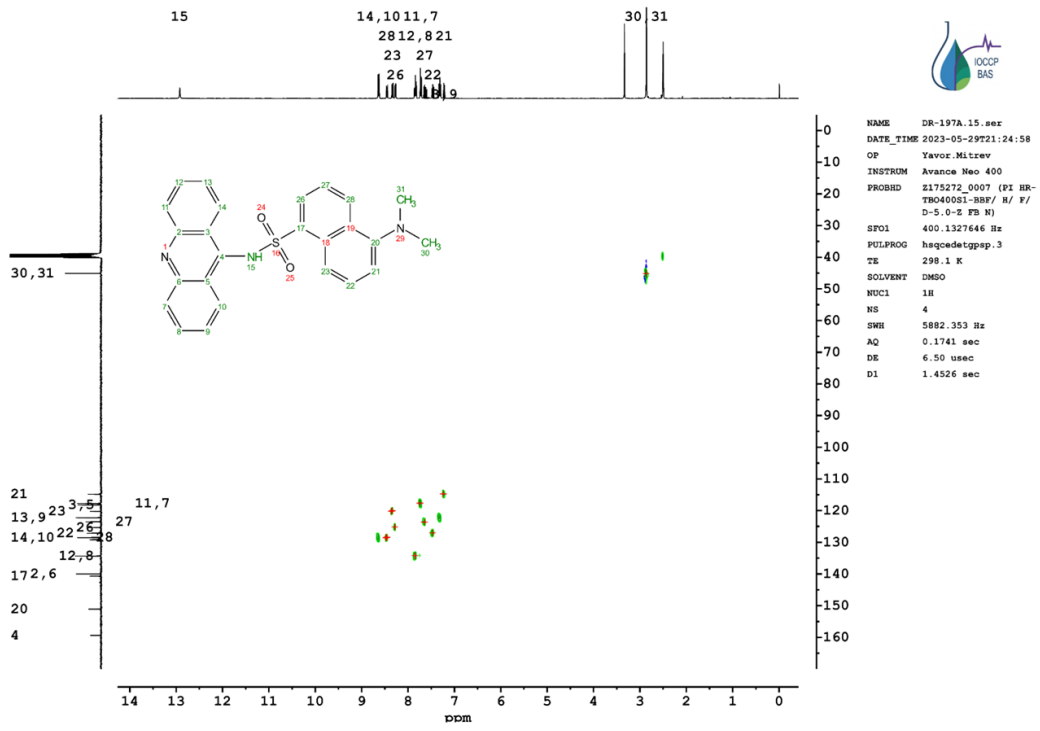


Figure 3–30. HSQC-NMR spectrum of compound **L2** in DMSO.

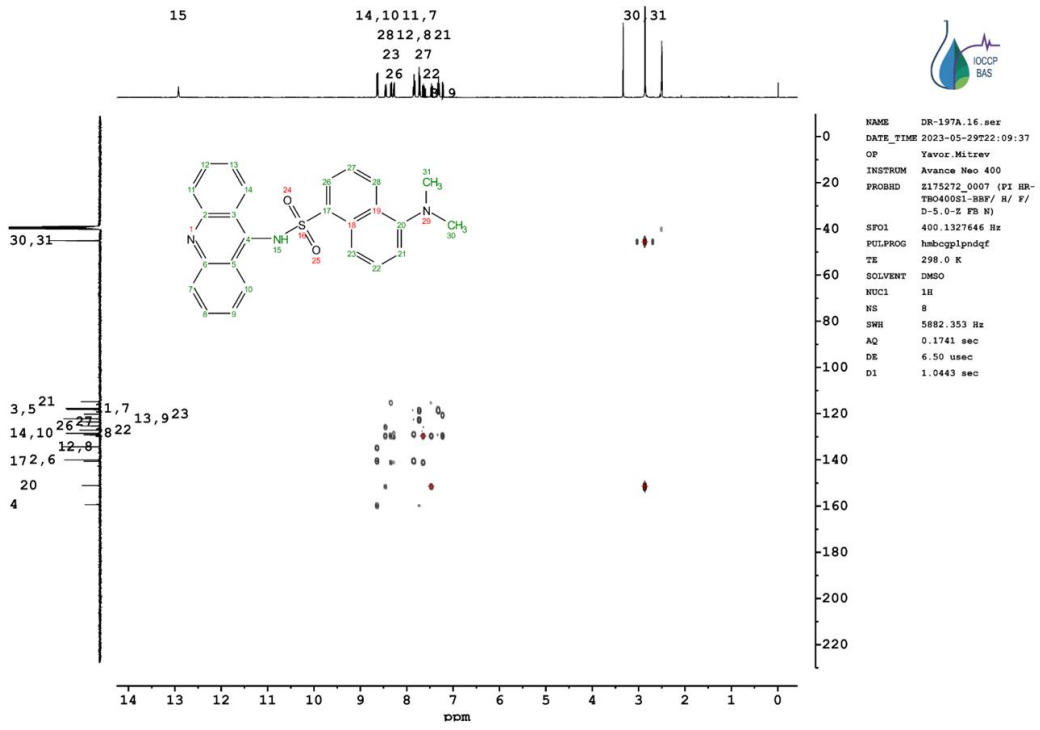


Figure 3–31. HMBC-NMR spectrum of compound **L2** in DMSO.

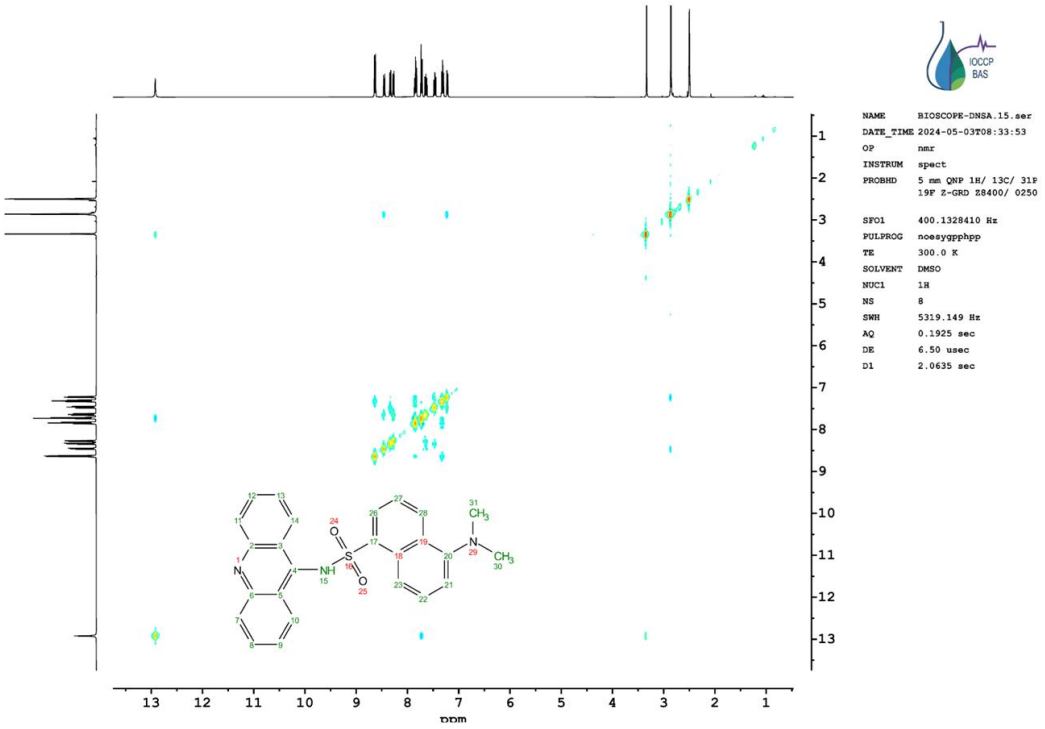


Figure 3–32. NOESY-NMR spectrum of compound **L2** in DMSO.

3.7 Contributions & Aknowledgements

3.7.1 Author Contributions

Frederico Duarte: Formal analysis, Investigation, Writing - Original Draft, Writing - Review & Editing, Visualization.

Inês Pereira-Gomes: Formal analysis, Investigation, Writing - Review & Editing, Visualization.

Georgi Dobrikov: Investigation, Validation, Methodology, Formal analysis, Conceptualization, Resources, Writing - Original Draft, Writing - Review & Editing, Funding acquisition.

Joana Galhano: Investigation, Formal analysis, Validation, Writing - Review & Editing.

Clara S. B. Gomes: Investigation, Formal analysis, Writing - Original Draft, Writing – Review & Editing.

Atanas Kurutos: Investigation, Validation, Methodology, Formal analysis, Conceptualization, Resources, Visualization, Writing - Original Draft, Writing - Review & Editing, Supervision, Funding acquisition.

Hugo M. Santos: Investigation, Resources, Validation, Writing - Review & Editing.

Elisabete Oliveira: Conceptualization, Methodology, Validation, Formal Analysis, Investigation, Resources, Writing - Original Draft, Writing - Review & Editing, Resources, Visualization, Supervision, Funding acquisition.

Maria Paula Duarte: Investigation, Resources, Writing - Review & Editing, Funding acquisition.

Jose Luis Capelo-Martinez: Resources, Writing - Review & Editing, Funding acquisition.

Carlos Lodeiro: Conceptualization, Methodology, Validation, Formal Analysis, Investigation, Resources, Writing - Review & Editing, Resources, Visualization, Supervision, Funding acquisition, Project administration

3.7.2 Acknowledgments

This work was supported by the Associate Laboratory for Green Chemistry LAQV which is financed by national funds from *Fundação para a Ciência e Tecnologia and Ministério da Ciência, Tecnologia e Ensino Superior* (FCT/MCTES) through the projects UIDB/50006/2020 (https://doi.org/10.54499/UIDB/50006/2020) and UIDP/50006/2020 (https://doi.org/10.54499/UIDP/50006/2020). PROTEOMASS Scientific Society (Portugal) is acknowledged by the funding provided through the General Funding Grants 2022-2023, and by the funding provided to the Laboratory for Biological Mass Spectrometry Isabel Moura (#PM001/2019 and #PM003/2016). F.D. and J.G. thank FCT/MCTES (Portugal) for their doctoral

grants 2021.05161.BD. and 2022.09495.BD., respectively. EO thanks FCT/MEC (Portugal) for the individual contract, CEECIND/05280/2022. H. M. S. and C. S. B. G. acknowledges the Associate Laboratory for Green Chemistry LAQV (LA/P/0008/2020 – https://doi.org/10.54499/LA/P/0008/2020) funded by FCT/MCTES for his research contract. This work is also developed and acknowledged by A.K. as part of contract BG-RRP-2.004-0002-C01, Laboratory of Organic Functional Materials (Project BiOrgaMCT), Procedure BG-RRP-2.004, Establishing of a network of research higher education institutions in Bulgaria", funded by BULGARIAN NATIONAL RECOVERY AND RESILIENCE PLAN". G. D. thanks to the European Regional Development Fund within the Operational Programme Science and Education for Smart Growth 2014 - 2020 under the Project Center of Excellence: National center of mechatronics and clean technologies - BG05M2OP001-1.001-0008 for the financial support. C. S. B. Gomes acknowledges the XTAL – Macromolecular Crystallography group (UCIBIO and i4HB) for granting access to the X-ray diffractometer. X-Ray infrastructure financed by FCT-MCTES through project RECI/BBBBEP/0124/2012.

3.8 References

[1] I. Pisagatti, D. Crisafulli, A. Pappalardo, G. Trusso Sfrazzetto, A. Notti, F. Nastasi, M. F. Parisi, N. Micali, G. Gattuso and V. Villari, Photoinduced electron transfer in host-guest interactions of a viologen derivative with a didansyl-pillar[5]arene, *Mater. Today Chem.* **24** (2022) 1000841. DOI: 10.1016/j.mtchem.2022.100841.

[2] E. O. Dare, V. Vendrell-Criado, M. C. Jiménez, R. Pérez-Ruiz and D. Díaz Díaz, Highly efficient latent fingerprint detection by eight-dansyl-functionalized octasilsesquioxane nanohybrids, *Dyes and Pigments* **184** (2021) 108841. DOI: 10.1016/j.dyepig.2020.108841.

[3] F. Duarte, G. Dobrikov, A. Kurutos, J. L. Capelo-Martinez, H. M. Santos, E. Oliveira and C. Lodeiro, Development of fluorochromic polymer doped materials as platforms for temperature sensing using three dansyl derivatives bearing a sulfur bridge, *J. Photochem. Photobiol. A Chem.* **445** (2023) 115033. DOI: 10.1016/j.jphotochem.2023.115033.

[4] F. Duarte, G. Dobrikov, A. Kurutos, H. M. Santos, J. Fernández-Lodeiro, J. L. Capelo-Martinez, E. Oliveira and C. Lodeiro, Enhancing water sensing via aggregation-induced emission (AIE) and solvatofluorochromic studies using two new dansyl derivatives containing a disulfide bound: Pollutant metal ions detection and preparation of water-soluble fluorescent polymeric particles, *Dyes and Pigments* **218** (2023) 111428. DOI: 10.1016/j.dyepig.2023.111428.

[5] Z. Xu, M. X. Zhang, G. Li, X. Chen, S. H. Liu, H. Chen and J. Yin, Naphthalimide-sulfonamide fused dansyl-sulfonamide fluorescent probe for tracking glutathione of lysosome with a dual-emission manner, *Dyes and Pigments* **171** (2019) 107685. DOI: 10.1016/j.dyepig.2019.107685.

[6] H. Cheng, P. Ma, Y. Wang, G. Hu, S. Fang, Y. Fang and Y. Lin, Photoswitchable and Water-Soluble Fluorescent Nano-Aggregates Based on a Diarylethene–Dansyl Dyad and Liposome, *Chem. Asian J.*, **12** (2017) 248–253. DOI: 10.1002/asia.201601501.

[7] Y. Pan, C. Zhang, S. H. Liu, Y. Tan and J. Yin, Fluorescent switch based on dithienylethene with dansulfonamide in multimedium, *Dyes and Pigments* **181** (2020) 108546. DOI: 10.1016/j.dyepig.2020.108546.

[8] Y. Cui, F. Li and X. Zhang, Controlling fluorescence resonance energy transfer of donor–acceptor dyes by Diels–Alder dynamic covalent bonds, *Chem. Commun.* **57** (2021) 3275–3278. DOI: 10.1039/d1cc00165e.

[9] Y. Zhang, B. Lei and X. Zhang, Reversible, controllable white-light emission of dye systems by dynamic covalent furan moiety exchange, *Chem. Commun.* **58** (2022) 5261–5264. DOI: 10.1039/d2cc01309f.

[10] J. Wang, X. Zhang and H. B. Liu, Highly sensitive pyrene–dansyl conjugate-based fluorescent sensor for discriminative detection of water in organic solvents, *Dyes and Pigments* **182** (2020) 108685. DOI: 10.1016/j.dyepig.2020.108685.

[11] S. Das and P. Sahoo, A colorimetric sensor for hydrogen sulfide: Detection from biogas and quantitative estimation in water, *Sens. Actuators B Chem.* **291** (2019) 287–292. DOI: 10.1016/j.snb.2019.04.089.

[12] D. Yang, X. T. Wu, X. J. Cao and B. X. Zhao, A reversible ratiometric fluorescence probe for fast detection of trace water in different organic solvents, *Dyes and Pigments* **170** (2019) 107558. DOI: 10.1016/j.dyepig.2019.107558.

[13] P. Srivastava, M. Verma, S. Sivakumar and A. K. Patra, A smart FRET probe exhibiting a molecular keypad lock device based on rapid detection of nitric oxide mediated by Cu^{2+} ion, *Sens. Actuators B Chem.* **291** (2019) 478–484. DOI: 10.1016/j.snb.2019.04.093.

[14] J. Gao, Y. He, Y. Chen, D. Song, Y. Zhang, F. Qi, Z. Guo and W. He, Reversible FRET Fluorescent Probe for Ratiometric Tracking of Endogenous Fe^{3+} in Ferroptosis, *Inorg. Chem.* **59** (2020) 10920–10927. DOI: 10.1021/acs.inorgchem.0c01412.

[15] P. P. Dash, A. K. Ghosh, P. Mohanty, R. Behura, S. Behera, B. R. Jali and S. K. Sahoo, Advances on fluorescence chemosensors for selective detection of water, *Talanta* **275** (2024) 126089. DOI: 10.1016/j.talanta.2024.126089.

[16] H. Sun, X. X. Tang, B. X. Miao, Y. Yang and Z. Ni, A new AIE and TICT-active tetraphenylethene-based thiazole compound: Synthesis, structure, photophysical properties and application for water detection in organic solvents, *Sens. Actuators B Chem.* **267** (2018) 448–456. DOI: 10.1016/j.snb.2018.04.022.

[17] H. Sun, X. X. Tang, R. Zhang, W. H. Sun, B. X. Miao, Y. Zhao and Z. H. Ni, Tetraphenylethene-substituted benzothiadiazoles: AIE and TICT properties, tunable intramolecular conjugation and application in detecting trace water in organic solvents, *Dyes and Pigments* **174** (2020) 108051. DOI: 10.1016/j.dyepig.2019.108051.

[18] L. Cai, X. Sun, W. He, R. Hu, B. Liu and J. Shen, A solvatochromic AIE tetrahydro[5]helicene derivative as fluorescent probes for water in organic solvents and highly sensitive sensors for glyceryl monostearate, *Talanta* **206** (2020) 120214. DOI: 10.1016/j.talanta.2019.120214.

[19] T. Yin, S. Zhang, M. Li, C. Redshaw and X. L. Ni, Macrocycle encapsulation triggered supramolecular pKa shift: A fluorescence indicator for detecting octreotide in aqueous solution, *Sens. Actuators B Chem.* **281** (2019) 568–573. DOI: 10.1016/j.snb.2018.10.136.

[20] H. Zhou, Y. Zhao, X. Chen and S. Zhang, Ultrafast spectroscopic studies of the pH responsive 9-acridinecarboxylic acid as a ratiometric and fluorescence lifetime pH indicator *Microchem. J.* **176** (2022) 107240. DOI: 10.1016/j.microc.2022.107240.

[21] S. Medel, E. Martínez-Campos, D. Acitores, E. Vassileva-Tonkova, I. Grabchev and P. Bosch, Synthesis and spectroscopic properties of a new fluorescent acridine hyperbranched polymer: Applications to acid sensing and as antimicrobial agent, *Eur. Polym. J.* **102** (2018) 19–29. DOI: 10.1016/j.eurpolymj.2018.03.008.

[22] J. Franco Pinto, A. Fillion, P. Duchambon, S. Bombard and A. Granzhan, Acridine–O^6-benzylguanine hybrids: Synthesis, DNA binding, MGMT inhibition and antiproliferative activity, *Eur. J. Med. Chem.* **227** (2022) 113909. DOI: 10.1016/j.ejmech.2021.113909.

[23] M. Vilková, M. Hudáčová, N. Palušeková, R. Jendželovský, M. Almáši, T. Béres, P. Fedoročko and M. Kožurková, Acridine Based N-Acylhydrazone Derivatives as Potential Anticancer Agents: Synthesis, Characterization and ctDNA/HSA Spectroscopic Binding Properties, *Molecules* **27** (2022) 2883. DOI:10.3390/molecules27092883.

[24] S. Zhang, H. Wu, C. S. Day and U. Bierbach, Platinum–Acridine Agents with High Activity in Cancers Expressing the Solute Carrier MATE1 (SLC47A1), *ACS Med. Chem. Lett.* **14** 2023 1122–1128. DOI: 10.1021/acsmedchemlett.3c00266.

[25] E. Abdelaziz, N. M. El-Deeb, M. F. Zayed, A. M. Hasanein, I. E. T. El Sayed, E. I. Elmongy and E. A. Kamoun, Synthesis and *in*-vitro anti-proliferative with antimicrobial activity of new

coumarin containing heterocycles hybrids, *Sci. Rep.* **13** (2023) 22791. DOI: 10.1038/s41598-023-50170-9.

[26] O. Sharhan, T. Heidelberg, N. M. Hashim, W. M. Al-Madhagi and H. M. Ali, Benzimidazolium-acridine-based silver N-heterocyclic carbene complexes as potential anti-bacterial and anti-cancer drug, *Inorganica Chim. Acta* **504** (2020) 119462. DOI: 10.1016/j.ica.2020.119462.

[27] L. Krause, R. Herbst-Irmer, G. M. Sheldrick and D. Stalke, Comparison of silver and molybdenum microfocus X-ray sources for single-crystal structure determination, *J. Appl. Cryst.* **48** (2015) 3–10. DOI: 10.1107/S1600576714022985.

[28] G. M. Sheldrick, Crystal structure refinement with SHELXL, *Acta. Cryst.* **C71** (2015) 3–8. DOI:10.1107/S2053229614024218.

[29] C. B. Hübschle, G. M. Sheldrick and B. Dittrich, ShelXle: a Qt graphical user interface for SHELXL, *J. Appl. Cryst.* **44** (2011) 1281–1284. DOI: 10.1107/S0021889811043202.

[30] L. J. Farrugia, WinGX and ORTEP for Windows: an update, *J. Appl. Cryst.* **45** (2012) 849–854. DOI: 10.1107/S0021889812029111.

[31] C. F. MacRae, I. Sovago, S. J. Cottrell, P. T. A. Galek, P. McCabe, E. Pidcock, M. Platings, G. P. Shields, J. S. Stevens, M. Towler and P. A. Wood, Mercury 4.0: from visualization to analysis, design and prediction, *J. Appl. Cryst.* **53** (2020) 226–235. DOI: 10.1107/S1600576719014092.

[32] S. J. Strickler and R. A. Berg, Relationship between Absorption Intensity and Fluorescence Lifetime of Molecules, *J. Chem. Phys.* **37** (1962) 814–822. DOI: 10.1063/1.1733166.

[33] D. Macdougall and W. B. Crummett, Guidelines for data acquisition and data quality evaluation in environmental chemistry, *Anal. Chem.* **52** (1980) 2242–2249. DOI: 10.1021/ac50064a004.

[34] G. L. Long and J. D. Winefordner, Limit of Detection A Closer Look at the IUPAC Definition, *Anal. Chem.* **55** (1983) 713A-724A, DOI: 10.1021/ac00258a724

[35] A. A. Taherpour, D. Kvaskoff, P. V. Bernhardt and C. Wentrup, 9-Azidoacridine and 9-acridinylnitrene, *J. Phys. Org. Chem.* **23** (2010) 382–389. DOI: 10.1002/poc.1657.

[36] C. R. Groom, I. J. Bruno, M. P. Lightfoot and S. C. Ward, The Cambridge Structural Database, *Acta Cryst.* **B72** (2016) 171–179. DOI: 10.1107/S2052520616003954.

[37] P. Zhou and K. Han, Unraveling the Detailed Mechanism of Excited-State Proton Transfer, *Acc. Chem. Res.* **51** (2018) 1681–1690. DOI: 10.1021/acs.accounts.8b00172

[38] G. Pedro, F. Duarte, G. M. Dobrikov, A. Kurutos, H. M. Santos, J. L. Capelo-Martínez, E. Oliveira and C. Lodeiro, Optical evaluation of dansyl derivatives and their implementation in low-cost and flexible dye-doped PMMA platforms for efficient detection of hazardous chemical vapours, *Dyes and Pigments* **224** (2024) 1112042. DOI: 10.1016/j.dyepig.2024.112042.

[39] E. Jeong, S. Yoon, H. S. Lee, A. Kumar and P. S. Chae, TURN-ON fluorescence detection of cyanide using an ensemble system consisting of a dansyl-based cationic probe and dicyanovinyl derivative, *Dyes and Pigments* **162** (2019) 348–357. DOI: 10.1016/j.dyepig.2018.10.033.

[40] F. Hu, M. Cao, J. Huang, Z. Chen, D. Wu, Z. Xu, S. H. Liu and J. Yin, Sulfonamide and urea-based anions chemosensors, *Dyes and Pigments* **119** (2015) 108–115. DOI: 10.1016/j.dyepig.2015.03.036.

[41] S. Areti, S. Bandaru, D. S. Yarramala and C. P. Rao, Optimizing the Electron-Withdrawing Character on Benzenesulfonyl Moiety Attached to a Glyco-Conjugate to Impart Sensitive and Selective Sensing of Cyanide in HEPES Buffer and on Cellulose Paper and Silica Gel Strips, *Anal. Chem.* **87** (2015) 12396–12403. DOI: 10.1021/acs.analchem.5b04085.

[42] L. L. Xi, X. F. Guo, C. L. Wang, W. L. Wu, M. F. Huang, J. Y. Miao and B. X. Zhao, A near-infrared ratiometric fluorescent probe for rapid and selective detection of hypochlorous acid in aqueous solution and living cells, *Sens. Actuators B Chem.* **255** (2018) 666–671. DOI: 10.1016/j.snb.2017.08.073.

[43] Z. Guo, Q. Wang, D. Zhou, Y. An, P. Wang and F. Liao, A novel peptide-based fluorescent probe with a large stokes shift for rapid and sequential detection of Cu^{2+} and CN^{-} in aqueous systems and live cells. *Spectrochim. Acta A Mol. Biomol. Spectrosc.* **264** (2022) 120257. DOI: 10.1016/j.saa.2021.120257.

[44] P. Gans, A. Sabatini and A. Vacca, Investigation of equilibria in solution. Determination of equilibrium constants with the HYPERQUAD suite of programs, *Talanta* **43** (1996) 1739–1753. DOI: 10.1016/0039-9140(96)01958-3.

[45] B. González-Tobío, F. Duarte, A. Arribas-Delgado, C. Fernández-Lodeiro, J. Fernández-Lodeiro, M. Cano, C. Lodeiro and C. Cuerva, Tuning and reviving the luminescence of a new class of pyridyl β-diketonate Eu(III) metallomesogens: From molecules to entrapment in polymer particles, *Dyes and Pigments* **204** (2022) 110440. DOI: 10.1016/j.dyepig.2022.110440.

[46] P. She, Y. Li, Z. Li, S. Liu, Y. Yang, L. Li, L. Zhou and Y. Wu, Repurposing 9-Aminoacridine as an Adjuvant Enhances the Antimicrobial Effects of Rifampin against Multidrug-Resistant Klebsiella pneumoniae, *Microbiol. Spectr.* 11:e04474-22. DOI: 10.1128/spectrum.04474-22.

[47] G. A. Marcelo, J. Galhano, M. P. Duarte, A. Kurutos, J. L. Capelo-Martínez, C. Lodeiro and E. Oliveira, Functional Cyanine-Based PVA:PVP Polymers as Antimicrobial Tools toward Food and Health-Care Bacterial Infections, *Macromol. Biosci.* **22** (2022) 2200244. DOI: 10.1002/mabi.202200244.

[48] S. Nuti, A. Fernández-Lodeiro, J. Galhano, E. Oliveira, M. P. Duarte, J. L. Capelo-Martínez, C. Lodeiro and J. Fernández-Lodeiro, Tailoring Mesoporous Silica-Coated Silver Nanoparticles

and Polyurethane-Doped Films for Enhanced Antimicrobial Applications, *Nanomaterials* **14** (2024) 462. DOI: 10.3390/nano14050462.

4

A Dual-Responsive Dansyl–Naphthalimide System for Hg(II) CHEF Detection and Ligand-Mediated Cu(II) Reduction with Catalytic Relevance

Frederico Duarte, Diogo Torres, Georgi M. Dobrikov, Atanas Kurutos, Luisa B. Maia, Oleksandr Bondarchuk, Ivaylo Slavchev, Jose Luis Capelo-Martínez, Hugo M. Santos, Carlos Lodeiro

Dyes and Pigments 243 (2025) 113088 Doi: 10.1016/j.dyepig.2025.113088

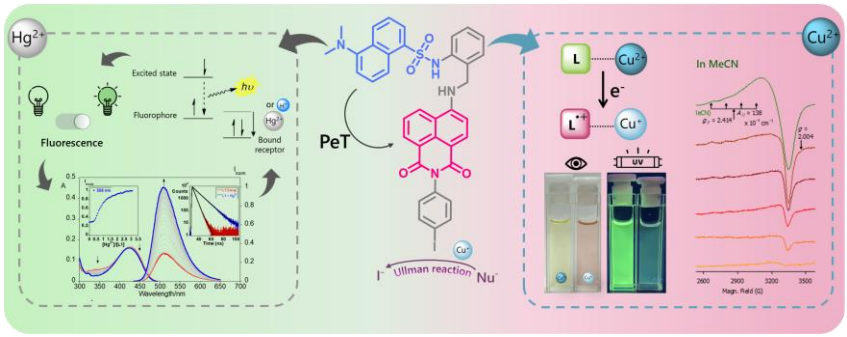
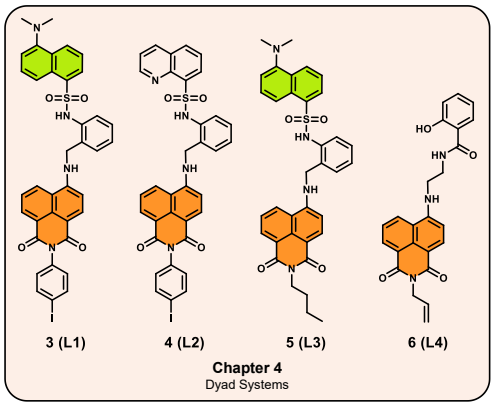


Figure 4–1. Graphical abstract.



Contribution to this work: Synthesis of the metal complexes; Photophysical characterization; Sensing experiments of metal ions; Writing original draft.

4.1 Abstract

We report a compelling structure–property relationship in a series of four naphthalimide-derived ligands, engineered for the selective and differential detection of Hg(II) and Cu(II) ions. By integrating a dansyl moiety, we induce intramolecular electron transfer that gives rise to two non-redox-innocent dyad systems. Notably, the detection of Hg(II) operates through a rare chelation-enhanced fluorescence (CHEF) mechanism, an unusual pathway considering the heavy atom effect typically associated with mercury. In contrast, the Cu(II) dyads reveal striking reduction of Cu(II) to Cu(I) in solution, driven by ligand-to-metal electron transfer, as conclusively demonstrated via EPR and XPS analysis. Furthermore, introducing a catalytic substrate probe highlights that this redox transformation is the bottleneck in catalytic efficiency. These findings provide deep mechanistic insights and position these ligands as versatile platforms for dual-mode ion sensing and redox-responsive catalysis.

4.2 Introduction

The design of luminescent probes for heavy and transition metal ions detection have gathered substantial attention due to their impact on environmental and biological assays. [1] Among these metal ions, divalent copper is known for being the third most abundant metal ion in the human body which are crucial in a wide range of biological processes and is linked to neurodegenerative illnesses. [2-4] In turn, high toxicity is the main reason why there is a constant demand for the monitorization of mercury in the environment in order to remediate the potential threat to public health. [1,5-7]

In light of the considerable progresses over the decades, dansyl and naphthalimide derivatives have been consistent fluorophores exhibiting strong biocompatibility and reliable photophysical properties. High fluorescence quantum yields, large Stokes shift and solvatochromic behavior are common characteristics related to dansyl derivatives while the tunable emission profiles of naphthalimide dyes by simple modification of the core offer the novelty and versatility as sensors towards heavy and transition metal ions. [1,8,9] Notably, the use of these dyes towards Cu(II) [10-25] and Hg(II) [6,7,26-33] are well entrenched in the literature. However, the main strategies employed for these systems often rely only on fluorescence changes in single-emission windows that may be hindered by environmental effects. Consequently, an increase in demand for the design of more efficient sensors that provide signal fidelity, dual-channel or ratiometric approaches have become more frequent to provide high

signal-to-noise ratio and mitigate environmental interference. [1,8] Dual fluorescence probes emerge as optimal choices providing a broader window of emission with enhanced fluorescence signal modalities. Some examples explore the utility of both dansyl and naphthalimide fluorophores as excited dye donors towards Föster resonance energy transfer (FRET) systems for metal ion sensing in conjunction with rhodamines [1,5,34-38] as well as other dyes across diverse applications. [8,39-42]

When considering the most desirable fluorescent sensor for metal ions, one may consider those that display chelation-enhanced fluorescence (CHEF) the best suited. However, the large spin-orbit coupling constant of Hg(II) and the paramagnetic nature of Cu(II) causes the majority of sensors towards these metals to be "turn-off" in nature. [43] Some of the aforementioned dyad systems avoid these hindrances due to the initial presence of a photoinduced electron-transfer (PeT) effect [1,5,35] that prevents an excited electron to relax radiatively to ground state since an electron from a lone pair that is higher in energy drops to the SOMO-H of the fluorophore. The coordination of the metal ion can stabilize the donor orbital lowering its energy below from the ground state restoring fluorescence with a few examples of this behavior applied in dansyl systems for the detection of Hg(II). [43-45] Furthermore, strategic multiple-ion-responsive sensors with built-in selective and differential detection are of upmost importance with several examples reported in the literature towards Cu(II) and Hg(II). [46-48]

Among the transition-metal compounds, in some cases, it is possible to observe reversible intramolecular electron-transfer between the metal and the ligand provided that the two electronic states are close-lying, energetically speaking. Valence tautomerism or redox isomerism rises from this notion when one or more non-redox-innocent ligand coordinates with a redox-active metal center and are capable of reversibly shift the electronic charge distribution. [49,50] However, electron delocalization must be avoided so that the two valence tautomers can be differentiated. Such processes of charge-distribution expand the scope and applicability since these systems are provided with unique physical properties and are found in nature in enzymatic processes. [51] The most known valence tautomeric systems are found for cobalt using dioxolane ligands accompanied with fewer examples of other metal complexes such as manganese, nickel, iron, ruthenium and others. [50,52-54] Copper can also form valence tautomerism since electronic and structural changes between Cu(I) and Cu(II) can create a barrier in energy sufficient enough to prevent charge delocalization so that they can be distinguishable. However, examples that fall outside of dioxolane and related structures are considered as rather rare. [49,51,55] Furthermore, copper shows some advantages over other metals in terms of catalysis since it is more cost-effective and has garnered industrial interest. For this reason,

copper-catalyzed cross coupling Ullmann type reactions have become a very useful process to build several types of bonds while ancillary chelating ligands have brought reliability and mildness to these systems. [56-58]

In this work, four new naphthalimide derived compounds (Scheme 4-2, **L1** to **L4**), from which two are dansyl-substituted dyad systems were successfully synthesized. Exploration of the interaction between dansyl and naphthalimide in dyad systems, to the best of our knowledge, is not well explored with only a handful works reported. [59-62] Bearing this in mind, efforts have been put forth to establish a structure/photophysical properties relation by intentional modification of the naphthalimide core and the presence or absence of the dansyl moiety. The complete characterization of the photophysical properties in a diverse array of solvents provided the foundation for the use of the Kamlet-Taft equation to assess the solvatochromism behavior of these systems. Due to the existence of well-defined coordination sites, these fluorophores have been tested for differential detection of metal ions owing to the occurrence of energy transfer processes in dual fluorescence probes. The determination of association constants and sensing limit parameters along with metal ion selectivity experiments were implemented. ESI-HRMS was employed to follow the complex formation in solution and to compare with the synthesized isolated complexes. Moreover, electron paramagnetic resonance spectroscopy (EPR) and X-ray Photoelectron Spectroscopy (XPS) were deemed beneficial for the elucidation of the ligand-mediated chemical reduction between the dyad systems and Cu^{2+} ions. Finally, the integration of iodophenyl moiety was found fruitful to establish the usefulness of these dyad compounds as ancillary chelating ligands for copper-catalyzed reactions.

4.3 Experimental Section

4.3.1 Materials

The fine chemicals for the synthesis of the target compounds (dansyl chloride, methyl salicylate, ethylenediamine, 4-bromo-1,8-naphthalic anhydride, 4-iodoaniline) were purchased from Sigma Aldrich, Tokyo Chemical Industry Co. Ltd., Acros Organics, Fluorochem Ltd and BLDPharm. Solvents (*N*-methylpyrrolidone, *N,N*-dimethylformamide (DMF), acetic acid, methanol, ethanol, dichloromethane (DCM), petroleum ether (PE), 2-methoxyethanol and acetone) for the synthesis and purification of compounds were with analytical grade (p. a.) and were acquired from Macron Fine Chemicals™ or Honeywell. Silica gel (high-purity grade, pore size 60 Å, 230-400 mesh particle size, 40-63 µm particle size, for flash chromatography) employed

for the column chromatography was purchased from Sigma Aldrich. Spectroscopy grade solvents, such as acetonitrile (CH_3CN), chloroform ($CHCl_3$), dimethyl sulfoxide (DMSO), ethanol (EtOH), and tetrahydrofuran (THF), were used for spectrophotometric and spectrofluorimetric measurements. Trifluoromethanesulfonate salts $Ca(OTf)_2$, $Co(OTf)_2$, $Ni(OTf)_2$, $Cu(OTf)_2$, $Zn(OTf)_2$, Ag(OTf) and $Cd(OTf)_2$, were provided from Solchemar, while $Cu(NCCH_3)_4(OTf)$ $Hg(OTf)_2$, $HgCl_2$ and $Pb(ClO_4)\cdot 3H_2O$ were purchased from Sigma Aldrich.

4.3.2 Instrumentation

The chemical identities of the compounds under investigation were confirmed through the utilization of various analytical techniques, including ^{1}H-NMR, ^{13}C-NMR, DEPT-135, 2-D COSY, 2D-HSQC, and 2-D HMBC techniques. The ^{1}H-NMR and ^{13}C-NMR spectra were acquired on a Bruker Avance II+600 spectrometer and Bruker Avance Neo 400 (Institute of Organic Chemistry with Centre of Phytochemistry - Bulgarian Academy of Sciences) using 5 mm tubes. The measurements were performed in $CDCl_3$ and DMSO-d_6 at 293K, with operating frequencies of 600.13 MHz/400.13 MHz and 150.92 MHz/100.62 MHz for the ^{1}H and ^{13}C nuclei, respectively. The precision of chemical changes is determined at a level of 0.01 ppm. The coupling constants (*J*) are displayed with a precision of 0.1 and denoted in units of hertz (Hz). The spin multiplicity observed in the ^{1}H nuclear magnetic resonance (NMR) spectroscopy was represented using the following abbreviations: s for singlet, d for doublet, t for triplet, q for quartet, dd for doublet of doublets, dt for doublet of triplets, td for triplet of doublets, and m for multiplet. MestreNova v. 14.1.1 (Mestrelab Research S.L.) was used for processing the spectra.

High-Resolution Mass Spectrometry analyses have been performed in the Laboratory for Biological Mass Spectrometry–Isabel Moura (PROTEOMASS Scientific Society Facility), using UHR ESI-Qq-TOF IMPACT HD (Bruker-Daltonics, Bremen, Germany). Samples of the corresponding compounds were prepared by dissolution in 50% (v/v) Acetonitrile containing 0.1% (v/v) aqueous formic acid to obtain a working solution of 0.1 µg/mL. Mass spectrometry analysis was carried out by the direct infusion of the compound solutions into the ESI source. MS data were acquired in positive polarity over the mass range of 80–1300 m/z. (Capillary voltage: 4500 V, End plate offset: -500 V, Charging voltage: 2000 V, Corona: 4000 nA, Nebulizer gas: 0.4 Bar, Dry Heater: 180°C, Dry gas: 4.0 L/min).

X-band EPR spectra were acquired using a Bruker EMX 6/1 spectrometer and a dual mode ER4116DM rectangular cavity (Bruker). The sample was cooled with liquid nitrogen using an Oxford Instruments ESR900 continuous-flow cryostat, fitted with a temperature controller. Spectra were acquired at 77K, with a modulation frequency of 100 kHz. Different modulation

amplitudes and microwave power values were tested to guarantee that the signal was not saturated and potential fine structure is observable. No other signals were observed between 100 and 6000G. The spectrum of Cu^{2+} in acetonitrile solution (without **L1**) does not change during the time periods studied. The Cu^{2+} concentration present in each sample was determined from the area beneath the integrated spectrum (double integration of the EPR spectrum), using 2mM Cu-EDTA as standard.

The XPS experiments were carried out in an ultra-high vacuum multi-chamber multi-technique system ESCALAB250Xi from Thermo Scientific with a base pressure below $5x10^{-10}$ mbar. The XPS spectra were generated using monochromated Al K_α source with excitation energy 1486.7 eV. High-resolution spectra were acquired using a 20 eV pass-energy with an energy step of 100 meV. The XPS spectra were analysed using the Avantage (Thermo Scientific) software package. The flood gun was deployed to compensate the sample charge. The spectra were fitted using the Lorentzian-Gaussian curve shapes and Shirley–type background. To estimate atomic concentration ratios the relative peak intensities were corrected using Scofield's sensitivity factors to account for subshell photoionization cross-sections at the relevant photon energies. The XPS peak intensities were calculated as the areas under the peaks corrected for the transmission functions of the deployed analysers as well as for the mean free pass for the corresponding kinetic energies of the collected photoelectrons. All the corrections were made by the spectral analysis software (Avantage).

UV-Vis absorption spectra were recorded on a JASCO V-650 spectrophotometer and a fluorescence emission spectrum on a HORIBA Scientific FLUOROMAX-4 spectrofluorometer from BIOSCOPE-PROTEOMASS facilities. Otherwise stated, all photophysical experiments were carried out at 293 K using a quartz cell with 10 mm of optical path.

4.3.3 Synthetic procedures

4.3.3.1 Synthesis of L1

Synthesis of intermediate 6-bromo-2-(4-iodophenyl)-1*H*-benzo[*de*]isoquinoline-1,3(2*H*)-dione (**5**):

A mixture of 4-bromo-1,8-naphthalic anhydride (5.00 g, 18.05 mmol) (**1**) and 3 equivalents of 4-iodoaniline (11.86 g, 54.14 mmol) (**4**) were refluxed in glacial acetic acid (80 mL) for 6 h under argon atmosphere. Upon cooling down to r.t. the mixture was poured into water, resulting in the appearance of a yellow precipitate. The product was filtered and recrystallized from acetic acid to yield 7.10 g (82%) of **5** as beige solid. m.p. 292-293°C. The product was used

for the synthesis of compound **7** without further purification. ^{1}H-NMR (600 MHz, DMSO) δ 8.62 (*dd*, *J* = 8.5, 1.0 Hz, 1H), 8.59 (*dd*, *J* = 7.3, 1.0 Hz, 1H), 8.35 (*d*, *J* = 7.8 Hz, 1H), 8.27 (*d*, *J* = 7.8 Hz, 1H), 8.04 (*dd*, *J* = 8.5, 7.3 Hz, 1H), 7.92 – 7.87 (*m*, 2H), 7.25 – 7.20 (*m*, 2H). ^{13}C-NMR (151 MHz, DMSO) δ 162.56, 162.50, 137.38, 135.28, 132.39, 131.22, 131.02, 130.99, 130.60, 129.77, 128.82, 128.55, 128.37, 123.01, 122.24, 93.63. EA Found C: 44.97; H: 1.76 and N: 2.92%. $C_{18}H_9BrINO_2$ requires 45.22; H: 1.90 and N: 2.93%.

Synthesis of intermediate 6-((2-aminobenzyl)amino)-2-(4-iodophenyl)-1*H*-benzo[*de*]isoquinoline-1,3(2*H*)-dione (**7**):

Intermediate **5** (1.000 g, 2.09 mmol) and 4 equivalents of diamine **6** (1.022 g, 8.37 mmol) were mixed with 2 mL dry *N*-methylpyrrolidone in a 50 mL round bottom flask. The formed thick slurry was flushed with argon and heated at 120°C for 3 h. After cooling down to room temperature, 50 mL of 1% aq. citric acid was added, and the resulting mixture was further stirred intensively for 1 h resulting in the formation of a yellow suspension. The solid was filtered, washed with water and dried *in vacuo*. The crude product was recrystallized from 18 mL ethanol:water(15:3 v/v). Upon cooling down to r.t. it was filtered, washed with 5 mL PE and dried *in vacuo* to furnish 0.970 g (89%) of compound **7** as an orange powder. m.p. >270°C. ^{1}H-NMR (400 MHz, DMSO) δ 8.81 (*d*, *J* = 8.3 Hz, 1H), 8.45 (*d*, *J* = 7.3 Hz, 1H), 8.37 (*t*, *J* = 5.6 Hz, 1H), 8.19 (*d*, *J* = 8.5 Hz, 1H), 7.85 (*d*, *J* = 8.5 Hz, 2H), 7.75 (*t*, *J* = 7.9 Hz, 1H), 7.14 (*d*, *J* = 8.5 Hz, 2H), 7.01 (*d*, *J* = 7.2 Hz, 1H), 6.96 (*t*, *J* = 7.6 Hz, 1H), 6.72 – 6.63 (*m*, 1H), 6.64 (*s*, 1H), 6.48 (*t*, *J* = 7.1 Hz, 1H), 5.13 (*s*, 2H), 4.48 (*d*, *J* = 5.5 Hz, 2H), ^{13}C-NMR (151 MHz, DMSO) δ 163.83, 162.93, 150.85, 146.14, 137.61, 136.44, 134.14, 131.67, 130.84, 129.90, 128.71, 127.59, 127.00, 124.50, 122.32, 120.35, 120.28, 115.99, 115.02, 108.08, 104.60, 93.99, 42.97. EA Found C: 58.75; H: 3.25 and N: 8.13%. $C_{25}H_{18}IN_3O_2$ requires 57.82; H: 3.49 and N: 8.09%.

Synthesis of 5-(dimethylamino)-*N*-(2-(((2-(4-iodophenyl)-1,3-dioxo-2,3-dihydro-1*H*-benzo[*de*]isoquinolin-6-yl)amino)methyl)phenyl)naphthalene-1-sulfonamide (**L1**):

Intermediate **7** (0.436 g, 0.84 mmol) was mixed with 3 mL dry pyridine in a 50 mL round bottomed flask. Subsequently, dansyl chloride (**11**) (0.408 g, 1.51 mmol) was added and the solution was heated at 60°C for 24 h. Workup: reaction cooled, diluted with excess of conc. aq. citric acid and extracted with DCM (2x60 mL). The organic phase was washed with aq. citric acid (x1), water (x1), and dried over anhydr. Na_2SO_4. TLC of crude product (DCM:acetone=100:1, developed x3). After evaporation to dryness the crude product was purified employing column chromatography (70 g silica gel; DCM:acetone=150:1 v/v). After column the product was additionally boiled with 3 mL PE, cooled down to r.t., decanted and dried *in vacuo* affording 0.341

g (54%) of compound **L1** as a yellow powder. m.p. 207-208°C. FTIR data (cm-1): 3380 ν(N-H), 3230 $\nu(C\text{-}H)_{arom.}$, 2950-2770 $\nu(C\text{-}H)_{aliph.}$ + ν(N-(CH3)2), 1685-1540 ν(C=O) + ν(C=C), 1350-1130 ν(S=O) + ν(C-N). ^{1}H-NMR (600 MHz, DMSO) δ 10.21 (*s*, 1H), 8.72 (*d*, *J* = 8.5 Hz, 1H), 8.49 (*d*, *J* = 8.5 Hz, 1H), 8.43 (*d*, *J* = 7.8 Hz, 2H), 8.28 (*t*, *J* = 5.9 Hz, 1H), 8.11 (*d*, *J* = 7.3 Hz, 1H), 7.85 (*dd*, *J* = 8.4, 3.9 Hz, 3H), 7.73 (*t*, *J* = 7.9 Hz, 1H), 7.59 (*dt*, *J* = 14.0, 8.1 Hz, 2H), 7.22 (*d*, *J* = 7.6 Hz, 1H), 7.12 (*d*, *J* = 8.5 Hz, 4H), 7.07 – 6.99 (*m*, 2H), 4.41 (*d*, *J* = 5.8 Hz, 2H), 2.79 (*s*, 6H). ^{13}C-NMR (151 MHz, DMSO) δ 163.75, 162.83, 151.56, 150.08, 137.63, 136.38, 135.75, 133.70, 133.46, 131.64, 130.86, 130.18, 129.72, 129.48, 129.07, 129.05, 128.60, 128.18, 127.46, 126.50, 126.12, 124.62, 123.62, 122.32, 120.24, 118.77, 115.19, 103.81, 94.01, 44.98, 42.11. ESI-HRMS: $[M+H]^+$ for $C_{37}H_{29}IN_4O_4S$= 753.1027 m/z (-0.01 ppm), calculated $[M+H]^+$ for $C_{37}H_{29}IN_4O_4S$= 753.10271 m/z.

4.3.3.2 Synthesis of L2

Synthesis of *N*-(2-(((2-(4-iodophenyl)-1,3-dioxo-2,3-dihydro-1*H*-benzo[*de*]isoquinolin-6-yl)amino)methyl)phenyl)quinoline-8-sulfonamide (**L2**):

Intermediate **7** (0.225 g, 0.0004332 mol, 1.0 eq.) was suspended in 3 mL dry pyridine. Then sulfochloride **15** (0.158 g, 0.0006931 mol, 1.6 eq.) was added at r.t. The resulting mixture turns spontaneously to clear orange solution. This solution was heated at 50°C for 20 h. Workup: the flask content was cooled down to room temperature and the pyridine was evaporated *in vacuo* to dryness. Then dissolved in 80 mL DCM and washed consequently with water, conc. aq. $NaHCO_3$ and again with water. The organic phase was dried over anhydr. Na_2SO_4 and evaporated to dryness (to remove any pyridine traces). The crude product was subjected to column chromatography on silica gel (mobile phase - DCM:MTBE=100:1v/v). After column, the product was boiled with 5 mL PE, cooled, decanted and dried i*n vacuo* to yield 0.236 g (77%) of **L2** as a bright yellow powder. m.p. 228-229°C. ^{1}H NMR (600 MHz, DMSO) δ 9.68 (*s*, 1H), 9.14 (*dd*, *J* = 4.2, 1.8 Hz, 1H), 8.73 (*dd*, *J* = 8.6, 0.9 Hz, 1H), 8.56 (*dd*, *J* = 8.4, 1.7 Hz, 1H), 8.44 (*dd*, *J* = 7.3, 1.0 Hz, 1H), 8.32 (*dd*, *J* = 8.2, 1.3 Hz, 2H), 8.29 (*dd*, *J* = 7.3, 1.4 Hz, 1H), 7.98 (*d*, *J* = 8.5 Hz, 1H), 7.88 – 7.82 (*m*, 2H), 7.77 – 7.70 (*m*, 3H), 7.17 – 7.11 (*m*, 3H), 7.03 (*pd*, *J* = 7.3, 1.7 Hz, 2H), 6.80 (*dd*, *J* = 7.7, 1.6 Hz, 1H), 6.06 (*d*, *J* = 8.7 Hz, 1H), 4.61 (*d*, *J* = 5.8 Hz, 2H). ^{13}C NMR (151 MHz, DMSO) δ 163.79, 162.90, 151.59, 150.23, 142.76, 137.61, 137.22, 136.40, 136.15, 134.77, 134.40, 134.18, 133.77, 131.67, 131.34, 130.87, 129.77, 128.67, 127.43, 126.79, 126.67, 126.21, 125.77, 124.60, 122.75, 122.33, 120.31, 108.40, 104.15, 94.01, 42.36. ESI-HRMS $[M+Na]^+$ for $C_{34}H_{23}IN_4O_4S$ = 733.0377 m/z (0.01 ppm). Calculated $[M+Na]^+$ $C_{34}H_{23}IN_4O_4S$ = 733.037695 m/z. $[2M+Na]^+$ for $C_{34}H_{23}IN_4O_4S$ = 1443.0862 m/z (0.02 ppm). Calculated $[2M+Na]^+$ $C_{34}H_{23}IN_4O_4S$ = 1443.086169 m/z.

4.3.3.3 Synthesis of L3

Synthesis of intermediate 6-bromo-2-butyl-1H-benzo[*de*]isoquinoline-1,3(2*H*)-dione (**9**):

Amine **8** (1.00 ml, 0.010 mol, 1.0 eq.) was dissolved in 60 ml 96% EtOH (in 100 ml flask). To this solution was added bromoanhydride **1** (2.77 g, 0.010 mol, 1.0 eq.). The formed suspension was stirred at r.t. for 30 min, then refluxed at 90°C for 20 h. After cooling down to room temperature the solvent evaporated to dryness. Purification by column chromatography on silica gel was performed (mobile phase PE:DCM=2:1) to afford 3.185 g (96%) of intermediate **9** as a pale-yellow powder. ^{1}H NMR (400 MHz, $CDCl_3$) δ 8.65 (*dd*, *J* = 7.3, 1.1 Hz, 1H), 8.56 (*dd*, *J* = 8.5, 1.2 Hz, 1H), 8.41 (*d*, *J* = 7.9 Hz, 1H), 8.03 (*d*, *J* = 7.9 Hz, 1H), 7.84 (*dd*, *J* = 8.5, 7.3 Hz, 1H), 4.20 – 4.14 (*m*, 2H), 1.77 – 1.67 (*m*, 2H), 1.45 (*dq*, *J* = 14.8, 7.4 Hz, 2H), 0.98 (*t*, *J* = 7.4 Hz, 3H). EA Found C: 57.54; H: 4.06 and N: 4.06%. $C_{16}H_{14}BrNO_2$ requires 57.85; H: 4.25 and N: 4.22%.

Synthesis of intermediate 6-((2-aminobenzyl)amino)-2-butyl-1*H*-benzo[*de*]isoquinoline-1,3(2*H*)-dione (**10**):

Bromonaphthalimide **9** (0.664 g, 0.0020 mol, 1.0 eq.) and diamine **6** (0.977 g, 0.0080 mol, 4.0 eq.) were mixed with 2 mL dry *N*-methylpyrrolidone in 50 mL flask. The formed thick slurry was flushed with argon and heated at 120°C for 2.5 h until the disappearance of the starting bromide by TLC (mobile phase - DCM). After cooling down to room temperature the reaction mixture was diluted with 100 mL 1% aq. citric acid and vigorously stirred for 1 h to furnish yellow suspension. This suspension was extracted with DCM (4x40 mL). The organic phase washed with water and dried over anhydr. Na_2SO_4. The solvent was evaporated, and the crude product was purified by column chromatography on silica gel (mobile phase DCM:MTBE=40:1 v/v). Intermediate **10** was obtained as 0.664 g (89%) bright yellow powder. m.p. 173-174 °C ^{1}H NMR (400 MHz, DMSO) δ 8.74 (*dd*, *J* = 8.6, 1.0 Hz, 1H), 8.43 (*dd*, *J* = 7.3, 1.0 Hz, 1H), 8.27 (*t*, *J* = 5.8 Hz, 1H), 8.18 (*d*, *J* = 8.5 Hz, 1H), 7.70 (*dd*, *J* = 8.4, 7.4 Hz, 1H), 7.02 (*dd*, *J* = 7.6, 1.3 Hz, 1H), 6.96 (*td*, *J* = 7.9, 1.5 Hz, 1H), 6.68 (*dd*, *J* = 8.0, 1.1 Hz, 1H), 6.61 (*d*, *J* = 8.6 Hz, 1H), 6.48 (*td*, *J* = 7.4, 1.2 Hz, 1H), 5.14 (*s*, 1H), 4.45 (*d*, *J* = 5.7 Hz, 2H), 4.07 – 3.95 (*m*, 2H), 1.57 (*p*, *J* = 7.4 Hz, 2H), 1.32 (*dq*, *J* = 14.5, 7.3 Hz, 2H), 0.90 (*t*, *J* = 7.4 Hz, 2H). ^{13}C NMR (101 MHz, DMSO) δ 163.70, 162.86, 150.60, 146.11, 133.99, 130.64, 129.33, 128.40, 127.58, 127.14, 124.43, 121.95, 116.00, 115.02, 107.96, 104.53, 42.99, 29.81, 19.81, 13.73. EA Found C: 72.77; H: 6.23 and N: 10.54%. $C_{23}H_{23}N_3O_2$ requires 73.97; H: 6.21 and N: 11.25%.

Synthesis of *N*-(2-(((2-butyl-1,3-dioxo-2,3-dihydro-1*H*-benzo[*de*]isoquinolin-6-yl)amino)methyl)phenyl)-5-(dimethylamino)naphthalene-1-sulfonamide (**L3**):

Intermediate **10** (0.614g, 1.64 mmol, 1 equiv.) was dissolved in 5 mL dry pyridine (in a 50 mL flask). Then dansyl chloride **14** (0.710 g, 2.63 mmol, 1.6 equiv.) was added and the formed clear dark-orange solution was heated at 40°C for 72 h. Workup: The solvent was evaporated almost to dryness, and the rest was dissolved in 100 mL DCM and washed with sat. aq. citric acid (x1) and water (x2). The organic phase was dried over anhydr. Na_2SO_4 and evaporated to dryness. The crude product was purified by column chromatography on silica gel (mobile phase - DCM:acetone=150:1 v/v) to afford **L3** as a yellow powder. Additional purification was achieved by filtering the product through a short silica pad (mobile phase DCM) and evaporated to dryness affording 0.225 g (23%) of **L3** as a bright yellow powder. m.p. 217-218°C. FTIR data (cm-1): 3435 ν(N-H), 3250 $\nu(C\text{-}H)_{arom.}$, 2915-2775 $\nu(C\text{-}H)_{aliph.}$ + ν(N-(CH3)2), 1680-1580 ν(C=O) + ν(C=C), 1350-1140 ν(S=O) + ν(C-N). ^{1}H NMR (400 MHz, DMSO) δ 10.20 (*s*, 1H), 8.65 (*d*, *J* = 8.3 Hz, 1H), 8.50 (*d*, *J* = 8.5 Hz, 1H), 8.43 (*t*, *J* = 7.6 Hz, 2H), 8.18 (*t*, *J* = 5.9 Hz, 1H), 8.13 – 8.04 (*m*, 1H), 7.84 (*d*, *J* = 8.5 Hz, 1H), 7.73 – 7.54 (*m*, 3H), 7.21 (*d*, *J* = 7.5 Hz, 1H), 7.14 – 6.98 (*m*, 4H), 5.44 (*d*, *J* = 8.6 Hz, 1H), 4.37 (*d*, *J* = 5.8 Hz, 2H), 4.03 – 3.95 (*m*, 2H), 3.07 (*s*, 1H), 2.78 (*s*, 6H), 1.56 (*p*, *J* = 7.4 Hz, 2H), 1.31 (*h*, *J* = 7.5 Hz, 2H), 0.90 (*t*, *J* = 7.3 Hz, 3H). ^{13}C NMR (101 MHz, DMSO) δ 163.63, 162.75, 151.57, 149.83, 135.70, 133.96, 133.57, 130.68, 130.19, 129.49, 129.15, 129.11, 129.02, 128.31, 128.19, 127.43, 126.59, 126.17, 124.57, 123.61, 121.94, 120.09, 118.77, 115.24, 108.17, 103.72, 48.71, 44.95, 42.09, 29.77, 19.78, 13.73. ESI-HRMS: $[M+Na]^+$ for $C_{35}H_{34}N_4O_4S$ = 629.2193 m/z (0.005 ppm). Calculated $[M+Na]^+$ for $C_{35}H_{34}N_4O_4S$ = 629.219297 m/z. $[M+H]^+$ for $C_{35}H_{34}N_4O_4S$ = 607.2374 m/z (0.08 ppm). Calculated $[M+H]^+$ for $C_{35}H_{34}N_4O_4S$ = 607.237353 m/z.

4.3.3.4 Synthesis of L4

Synthesis of intermediate 2-allyl-6-bromo-1*H*-benzo[*de*]isoquinoline-1,3(2*H*)-dione (**3**):

4-bromo-1,8-naphthalic anhydride (3.10 g, 11.19 mmol) (**1**) was suspended in 25 mL dry DMF, followed by the addition of 10% molar excess of allyl amine (0.70 g, 0.92 mL, 12.31 mmol) (**2**). The resulting reaction mixture was stirred at r.t. for 30 min., then at 50°C for additional 18 h. Workup: the reaction was cooled down to r.t. and diluted with 100 mL distilled water. The formed precipitate was filtered, washed with water and crystallized from 30 mL ethanol:water (25:5 v/v). After cooling down to r.t. the product was filtered and dried *in vacuo* affording 2.95 g (83%) of compounds **3** as an off-white powder. m.p. 138-139°C. ^{1}H-NMR (600 MHz, DMSO) δ 8.52 (*d*, *J* = 7.2 Hz, 1H), 8.50 (*d*, *J* = 8.4 Hz, 1H), 8.28 (*d*, *J* = 7.8 Hz, 1H), 8.18 (*d*, *J* = 7.8 Hz, 1H),

7.96 (*t*, *J* = 7.9 Hz, 1H), 5.93 (*ddt*, *J* = 15.7, 10.4, 5.2 Hz, 1H), 5.20 – 5.14 (*m*, 1H), 5.15 – 5.09 (*m*, 1H), 4.62 (*d*, *J* = 5.1 Hz, 2H). ^{13}C-NMR (151 MHz, DMSO) δ 162.60, 162.55, 132.75, 132.61, 131.70, 131.41, 131.08, 129.83, 129.29, 128.86, 128.35, 122.66, 121.88, 116.53, 41.92. EA Found C: 56.56; H: 3.03 and N: 4.25%. $C_{15}H_{10}BrNO_2$ requires 56.99; H: 3.19 and N: 4.43%.

Synthesis of intermediate *N*-(2-aminoethyl)-2-hydroxybenzamide (**13**):

Equimolar amounts of methyl salicylate (1.69 mL, 2.00 g, 13.15 mmol) (**11**) and ethylene diamine (0.88 mL, 0.790 g, 13.15 mmol) (**12**) were mixed together in a 50 mL flask and heated at 110°C for 6 h. The reaction outcome was monitored by TLC (DCM:MeOH=10:1 v/v). After cooling down to r.t. the crude product was purified by column chromatography (50 g silica; phase DCM:MeOH=10:1 v/v) to obtain compound **13** in 1.570 g (66%) as a colourless waxy solid. ^{1}H-NMR (600 MHz, DMSO) δ 7.78 (*dd*, *J* = 7.9, 1.7 Hz, 1H), 7.25 (*ddd*, *J* = 8.8, 7.1, 1.8 Hz, 1H), 6.78 (*dd*, *J* = 8.3, 1.0 Hz, 1H), 6.68 (*ddd*, *J* = 8.1, 7.2, 1.1 Hz, 1H), 3.35 (*t*, *J* = 6.4 Hz, 2H), 2.76 (*t*, *J* = 6.4 Hz, 2H). ^{13}C-NMR (151 MHz, DMSO) δ 169.37, 162.91, 133.51, 128.97, 118.83, 116.96, 116.75, 41.15, 40.99.

Synthesis of *N*-(2-((2-allyl-1,3-dioxo-2,3-dihydro-1*H*-benzo[*de*]isoquinolin-6-yl)amino)ethyl)-2-hydroxybenzamide (**L4**):

Intermediate **3** (1.312 g, 4.15 mmol) and excess of intermediate **13** (1.57 g, 8.71 mmol) were dissolved in 20 mL dry 2-methoxyethanol and the mixture was refluxed for 6 h. The reaction outcome was monitored by TLC (mobile phase = DCM). The crude product was purified by column chromatography on silica gel (mobile phase - DCM:acetone=20:1 v/v) resulting in 0.237 g (14%) of compound **L4** as a yellow powder. m.p. 105-106°C. ^{1}H-NMR (600 MHz, DMSO) δ 12.44 (*s*, 1H), 9.04 (*d*, *J* = 5.3 Hz, 1H), 8.65 (*dd*, *J* = 8.6, 1.0 Hz, 1H), 8.43 (*dd*, *J* = 7.3, 1.0 Hz, 1H), 8.27 (*d*, *J* = 8.5 Hz, 1H), 7.96 (*d*, *J* = 5.1 Hz, 1H), 7.82 (*dd*, *J* = 8.0, 1.6 Hz, 1H), 7.69 (*dd*, *J* = 8.4, 7.3 Hz, 1H), 7.40 (*ddd*, *J* = 8.4, 7.2, 1.6 Hz, 1H), 6.95 – 6.90 (*m*, 2H), 6.93 – 6.86 (*m*, 2H), 5.97 – 5.87 (*m*, 1H), 5.11 – 5.04 (*m*, 2H), 4.64 – 4.60 (*m*, 2H), 3.62 (*t*, *J* = 7.5 Hz, 4H). ^{13}C-NMR (151 MHz, DMSO) δ 169.32, 163.47, 162.60, 159.87, 150.69, 134.28, 133.78, 133.29, 130.84, 129.50, 128.62, 127.92, 124.46, 121.82, 120.26, 118.67, 117.39, 115.99, 115.38, 107.80, 103.87, 42.11, 41.35, 37.65. ESI-HRMS: $[M+Na]^+$ for $C_{24}H_{21}N_3O_4$ = 438.1424 m/z (-0.06 ppm). Calculated $[M+Na]^+$ for $C_{24}H_{21}N_3O_4$ = 438.142427 m/z.

4.3.3.5 Synthesis of Hg(II) and Cu(II) complexes with L1 and L3:

[Hg(II)**L1**$_2$]$^{2+}$:

L1 (19.7 mg, 0.0262 mmol, 1 equiv.) was dissolved in 15 mL of chloroform and an excess of $Hg(CF_3SO_3)_2$ (12.96 mg, 0.0259 mmol, 1 equiv.) dissolved in 5 mL of chloroform was slowly added at room temperature. The formation of precipitate was immediately noticed after the addition of the mercury salt and the reaction was allowed to continue for 10 minutes. The complex was precipitated under vacuum, washed with chloroform and with diethyl ether. The complex was dried at room temperature resulting in 19.68 mg (37.4%) orange powder. m.p. 243-244°C. FTIR data (cm^{-1}): 3370 ν(N-H), 3230 $\nu(C\text{-}H)_{arom.}$, 3055 $\nu(C\text{-}H)_{aliph.}$+ $\nu(N\text{-}(CH_3)_2)$, 1685-1575 ν(C=O)+ ν(C=C), 1360-1160 ν(S=O)+ ν(C-N). ESI-HRMS: $[M]^+$ for $C_{74}H_{58}HgI_2N_8O_8S_2$ = 1706.1622 m/z (0.1 ppm), calculated $[M]^+$ for $C_{74}H_{58}HgI_2N_8O_8S_2$ = 1706.162023 m/z. EA Found C: 45,51; H: 3.05 and N: 5.23%. $C_{76}H_{58}F_6HgI_2N_8O_{14}S_4$ requires C: 45,55; H: 2.92 and N: 5.59% corresponding to [Hg(**L1**)$_2$$(CF_3SO_3)_2$].

[Hg(II)**L3**]$^{2+}$:

L3 (10.24 mg, 0.0169 mmol, 1 equiv.) was dissolved in 15 mL of chloroform and $Hg(CF_3SO_3)_2$ (4.20 mg, 0.0084 mmol, 0.5 equiv.) dissolved in 5 mL of chloroform was slowly added and the mixture was stirred at room temperature for 1 h. The mixture evaporated to dryness resulting in 10.12 mg (70.2%) orange powder. m.p. 189-190°C °C. FTIR data (cm^{-1}): 3385 ν(N-H), 3150 $\nu(C\text{-}H)_{arom.}$, 2925-2845 $\nu(C\text{-}H)_{aliph.}$+ $\nu(N\text{-}(CH_3)_2)$, 1680-1580 ν(C=O)+ ν(C=C), 1390-1140 ν(S=O)+ ν(C-N). ESI-HRMS $[M+H]^+$ for $C_{35}H_{32}HgN_4O_4S$ = 807.1929 m/z (0.18 ppm). Calculated $[M+H]^+$ for $C_{35}H_{32}HgN_4O_4S$ = 807.192756 m/z.

[Cu(II)**L1**]$^{2+}$:

L1 (50 mg, 0.0664 mmol, 1 equiv.) was suspended in 10 mL dry acetonitrile and solid $Cu(CF_3SO_3)_2$ (24 mg, 0.0664 mmol, 1 equiv.) was added in one portion. The color of the reaction mixture spontaneously turns to deep yellow-orange and **L1** dissolves completely (see figure bellow). The solution was stirred for 4 h at ambient temperature without no further change in the appearance. The solvent was evaporated to dryness to obtain 73 mg (quantitative) of thick orange-brown oil, solidifying on stay. m.p. 173-174°C. FTIR data (cm^{-1}): 3370 ν(N-H), 3220-3065 $\nu(C\text{-}H)_{arom.}$, 2915-2850 $\nu(C\text{-}H)_{aliph.}$ + $\nu(N\text{-}(CH_3)_2)$, 1685-1575 ν(C=O) + ν(C=C), 1360-1140 ν(S=O) + ν(C-N). ESI-HRMS: $[M+H]^+$ for $C_{39}H_{33}CuN_5O_5S$= 747.1571 m/z (-0.02 ppm). Calculated $[M+H]^+$ for $C_{39}H_{33}CuN_5O_5S$ = 747.157114 m/z.



Ligand only; Ligand+Cu(II)triflate t=0 sec.; Ligand+Cu(II)triflate t=60 sec.

[Cu(II)**L3**]$^{2+}$:

L3 (9.36 mg, 0.0154 mmol, 1 equiv.) was dissolved in 15 mL of acetonitrile and $Cu(CF_3SO_3)_2$ (5.60 mg, 0.0155 mmol, 1 equiv.) dissolved in 5 mL of acetonitrile was slowly added and the mixture was stirred at room temperature for 3 h. The mixture evaporated to dryness resulting in 12.82 mg (52.46%) brown powder. m.p. 158-159°C. FTIR data (cm^{-1}): 3390 ν(N-H), 3225 $\nu(C\text{-}H)_{arom.}$, 2925-2835 $\nu(C\text{-}H)_{aliph.}$+ $\nu(N\text{-}(CH_3)_2)$, 1680-1580 ν(C=O)+ ν(C=C), 1390-1140 ν(S=O)+ ν(C-N). ESI-HRMS $[M+H]^+$ for $C_{70}H_{66}CuN_8O_8S_2$ = 1274.3817 m/z (0.25 ppm). $[M+H]^+$ for $C_{70}H_{66}CuN_8O_8S_2$ = 1274.381377 m/z.

4.3.4 Spectrophotometric and spectrofluorimetric measurements

4.3.4.1 Spectrophotometric and spectrofluorimetric measurements

Photophysical studies started with the preparation of stock solutions of compounds **L1** to **L4** (ca. 10^{-3} M) in different solvents (CH_3CN, EtOH, DMSO, $CHCl_3$, and THF), by dissolving each ligand in a 10 mL volumetric flask and diluting with the corresponding solvent. The studied solutions were then prepared by dilution of the stock solutions up to 10^{-5}–10^{-6} M.

Titrations of **L1** to **L4** were performed by successive additions of microliter aliquots of standard solutions of Ca^{2+}, Co^{2+}, Ni^{2+}, Cu^{+}, Cu^{2+}, Zn^{2+}, Ag^{+}, Cd^{2+} and Hg^{2+} ions prepared in acetonitrile while Hg^{+} and Pb^{2+} were prepared in water. A correction for the absorbed light was performed when necessary. Luminescence spectra of the compounds in the solid state and of doped polymer thin films were recorded using of a fiber-optics device connected to the spectrofluorometer while exciting the samples at appropriated wavelength.

Table 4-1. Spectroscopic polarity parameters, physical properties of the different solvents. ε_r : relative permittivity; η: refractive index; α: the solvent's HBD acidity; β: the solvent´s HBA basicity; π^*: the solvent´s dipolarity/polarizability.

Solvent	ε_r	α	β	π^*	η
DMSO	47.24	0	0.76	1.00	1.47
CH_3CN	35.94	0.19	0.40	0.66	1.34
EtOH	24.30	0.86	0.75	0.54	1.36
THF	7.58	0	0.55	0.58	1.40
$CHCl_3$	4.89	0.20	0.10	0.69	1.44

4.3.4.2 Fluorescence quantum yield and Lifetime

Relative photoluminescence quantum yields were measured using a solution of acridine yellow in absolute ethanol (ϕ_F=0.47) for quantifying the relative QY of **L1** to **L4** dissolved in all solvents [63]. Lifetime measurements were recorded at 293 K with a Tempro Fluorescence Lifetime System with a Horiba Jobin-Yvon NanoLed pulsed diode controller.

4.3.5 Determination of the detection and quantification limits (LOD and LOQ)

Determination of the detection limit (LOD) and quantification limit (LOQ) began by collecting ten independent measurements of a solution containing the selected probe and no addition of any metal ion (y_{blank}). Final determination of the LOD and LOQ values followed the subsequent formulas [64,65]:

LOD = y_{dl} = y_{blank} + 3std, where y_{dl} = signal detection limit and std = standard deviation.

LOQ = y_{dl} = y_{blank} + 10std, where y_{dl} = signal detection limit and std = standard deviation.

The final step involved the determination of the minimal detectable and quantified concentration of metal ion by titration with the ligands.

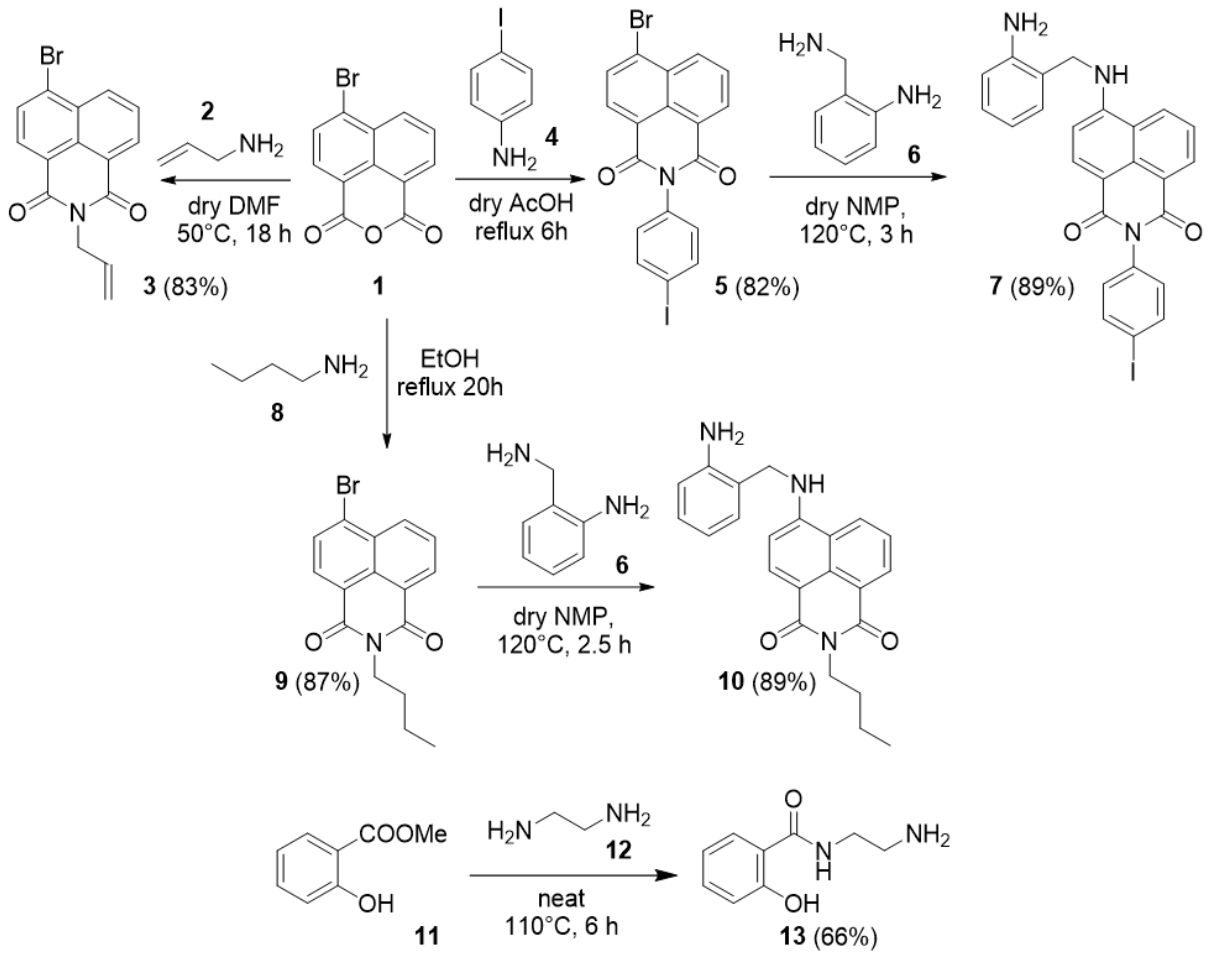
4.4 Results & Discussion

4.4.1 Synthesis

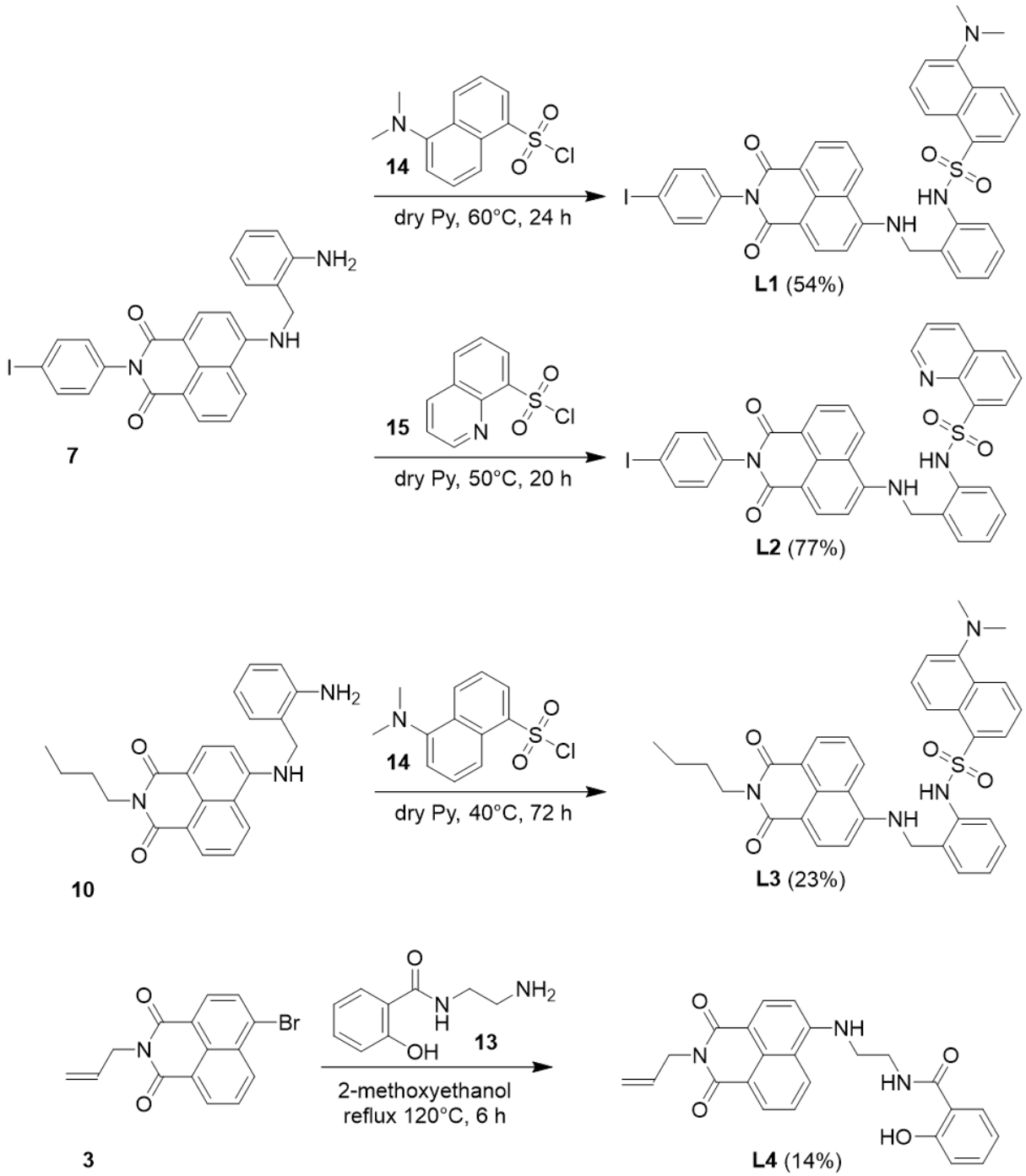
For the preparation of the target compounds (**L1**-**L4**), intermediates **3**, **5**, **7**, **9**, **10** and **13** were synthesized as shown in Scheme 4-1. Compound of **3** (83%) was synthesized starting from **1** and **2** in dry DMF according to a protocol reported in the literature. [66-68] The synthesis of

compound **5** was described by Benati *et al.* [69] and Chinapang *et al.* [70], however our attempt furnished **5** in increased yield (82% after crystallization). Naphthalimide **7** (89% after crystallization) is a new compound, though an analogue is described elsewhere. [71] Synthesis of bromide **9** from **1** and amine **8** was described in multiple studies, nevertheless we followed the procedure of Lim *et al.* [72] as the most suitable for our investigation (almost quantitative yield of **9**). Since **9** is well characterized, we performed only ^{1}H NMR spectra to confirm its chemical structure. Like compound **7**, intermediate **10** (89% after column chromatography) was prepared from **9** and the diamine **6** in dry *N*-methylpyrrolidone. As a new compound, it was fully characterized by various 1D and 2D NMR techniques (Figure 4–41 to Figure 4–89, Supplementary Material), melting point temperatures, and mass spectra. Although existing literature synthetic procedures report low yielded [73-75], amine **13** was readily prepared by heating of methyl salicylate (**11**) with ethylenediamine (**12**) under solvent free conditions. Compound **13** was purified by column chromatography and isolated in good yield (66%).

The target compounds **L1** and **L2** were prepared by heating the intermediate **7** in dry pyridine with sulfonyl chlorides **14** and **15**, respectively (Scheme 4-2). **L1** (54%) and **L2** (77%) were isolated after silica gel column chromatography. Ligand **L3** was prepared from **10** and dansyl chloride (**14**) by using the same procedure, as in case of **L1** and **L2**. However, the yield of compound **L3** (23%) was significantly decreased, due to the need of implementation of triple column chromatography. The synthetic approach to the preparation of **L4** (14%) involves the use of intermediates **3** and **13**. The reaction was performed in dry 2-methoxyethanol at 110°C (**Scheme 4-2**). The target compounds **L1**-**L4** as well as all new intermediate products were fully characterized by 1D and 2D NMR spectroscopic techniques (Figure 4–41 to Figure 4–89, Supplementary Material), HRMS and melting point temperatures.



Scheme 4-1. Synthesis of intermediates **3**, **5**, **7**, **9**, **10** and **13**.



Scheme 4-2. Synthetic approach to the preparation of the target compounds **L1**-**L4**.

4.4.2 Photophysical characterization

The conjugated dansyl-naphthalimide and single naphthalimide derived compounds manifest luminescent properties both in solution and in the solid state. Figure 4–2 complies the molecular structure accompanied by the photoluminescent data of all compounds in acetonitrile recorded at 298K as a representative example (Figure 4–13 to Figure 4–16) while Table

4-2 exhibits all the photophysical data of the compounds under investigation. The UV-Vis spectra in acetonitrile shows an absorption band maximum centered at 425 and 429 nm, contributing to the display of yellow solutions to the naked eye. Upon excitation at the appropriate wavelength, the samples emit a greenish yellow light with a maximum allocated around 515 nm resulting in a Stokes shift between 4150 and 3854 cm^{-1}. On a relatable note, significant disparities can be noted regarding the solid-state emission spectra since compounds **L1** to **L3** progressively display a red-shifted wide band centered at 528, 535 and 546 nm as in solution is concerned, while the opposite is found for **L4**, a clear, blue-shifted emission is observed with an emission maximum of 476 nm.

Overall, from a quantum yield perspective, higher values were obtained in the case of **L2** and **L4**, reaching values up to 69% in THF, while for **L1** and **L3** the presence of the dansyl unit translates a lower general trend of values, being the fluorescent mechanism most efficient in chloroform. Single digit nanosecond times were obtained from lifetime measurements for the majority of solvents being **L1** and **L3** the ones that present more variability as each solvent is considered while more prevalent values were found for **L2** and **L4**.

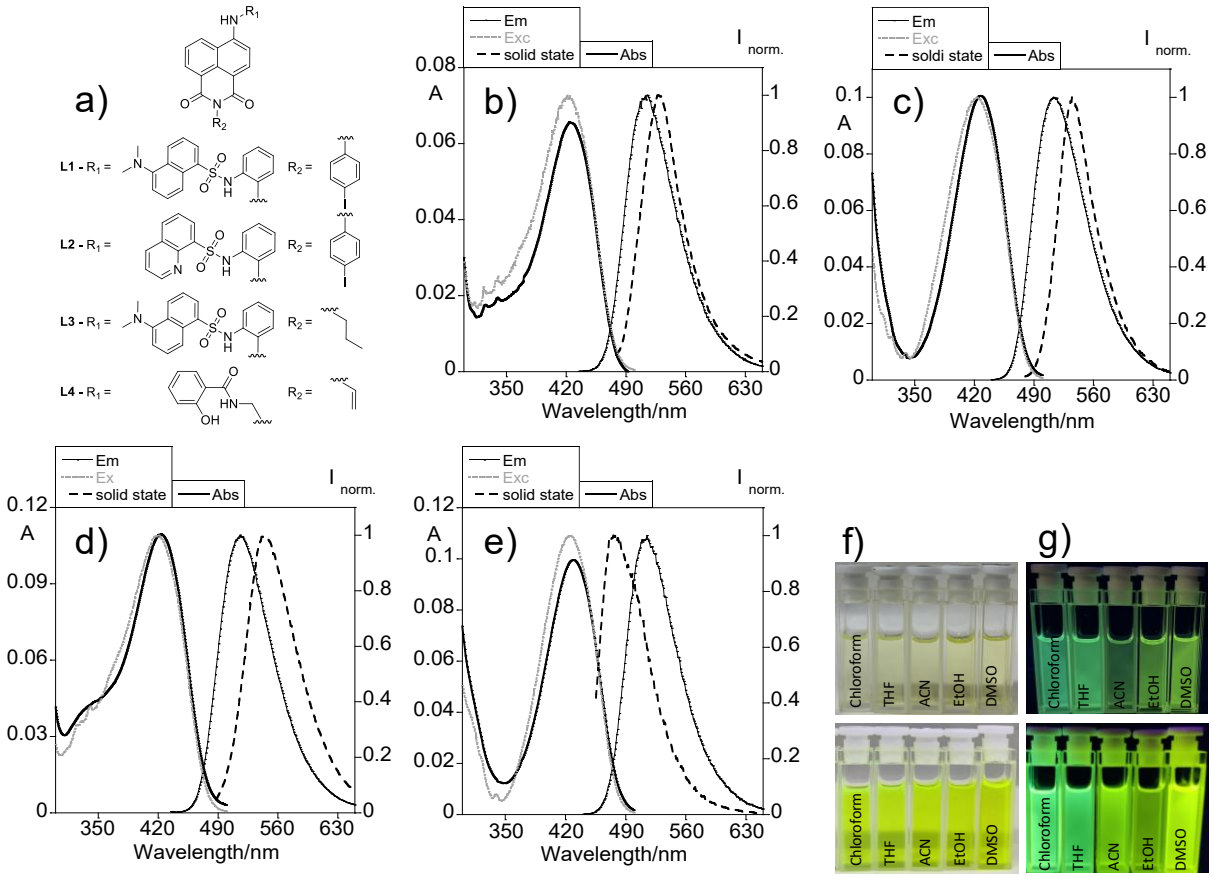


Figure 4–2. (a) Molecular structure of dual dansyl-naphthalimide and naphthalimide derived compounds **L1** to **L4**. Photophysical characterization of compounds **L1** to **L4** ((b) to (e)) in acetonitrile ([**L1**] to [**L4**] = 5 μM). Images under

natural light (left) and irradiated under UV light (right) for (f) **L1** and (g) **L4** in different solvents, as representative example.

Table 4-2. Absorption maximum wavelength in solution (λ_{abs}), emission maximum wavelength in solution (λ_{em}), molar absorption coefficients (ε), Stokes shift ($\Delta\lambda$), fluorescence quantum yields (ϕ), emission maximum in the solid state (λ_{em}^{Solid}), fluorescence lifetimes (τ) for compounds **L1** to **L4** in various solvents.

Cpd	Solv	λ_{abs} [nm]	λ_{em} [nm]	ε (10^4) [cm^{-1} M^{-1}]	Stokes shift [cm^{-1}]	ϕ(%)	λ_{em}^{Solid} [nm]	t[ns]
L1	DMSO	437	520	2.18	3652	15	528	5.9
	EtOH	439	521	1.99	3585	18		6.7
	CH_3CN	425	515	2.15	4111	7.5		3.3
	THF	425	497	1.70	3408	24		5.3
	$CHCl_3$	422	502	2.04	3776	33		7.1
L2	DMSO	438	521	2.09	3637	46	535	8.5
	CH_3CN	427	513	1.92	3926	35		7.5
	THF	427	498	1.74	3338	39		6.7
	$CHCl_3$	430	505	1.61	3453	53		8.0
L3	DMSO	448	516	2.17	2942	4.3	546	5.9
	EtOH	438	518	2.23	3526	20		7.1
	CH_3CN	425	516	2.16	4150	8.4		3.2
	THF	424	494	1.90	3342	26		5.6
	$CHCl_3$	418	499	1.51	3883	32		7.3
L4	DMSO	442	524	1.84	3540	43	476	10.3
	EtOH	438	523	1.61	3710	37		9.17
	CH_3CN	429	514	1.85	3854	44		10.4
	THF	426	497	1.81	3353	69		9.3
	$CHCl_3$	427	494	1.98	3176	42		9.1

Considering the well-documented solvatochromic behavior of dansyl and naphthalimide derivatives and given the visually detected solvent dependent color change under UV lamp (Figure 4–2f, g), compounds **L1** to **L4** manifest positive solvatochromism due to the change in color from green to yellow with increasing solvent polarity. In line with these observations, efforts have been made to fully characterize the occurring solvent-compound interactions, and for this, three solute-dependent parameters (υ_0, a, b and p) have been determined through the multiparametric fitting of the Kamlet-Taft equation (Equation 1).

$$\upsilon = \upsilon_0 + a\alpha + b\beta + p\pi^* \quad \text{(Equation 1)}$$

Where υ_0 represents the wavenumber value in a reference solvent; parameters a, b and p are obtained through multiple regression analysis that reflect the underlying sensitivity of the probes photophysical behavior to solvent polarity; α: hydrogen bond donor acidity (HBD); β: hydrogen bond acceptor basicity (HBA); π^*: stabilization of a charge or dipole without a specific dielectric interaction (Table 4-1). [76,77]

Table 4-3 summarizes the reference wavenumber value υ_0, the fitted parameters (a, b and p) alongside the slopes and correlation coefficients obtained through the fitting of a linear plot of $\upsilon_{exp.}$ versus υ_{calc}, by applying the Kamler-Taft model excluding acetonitrile.

Table 4-3. Independent fluorescence wavenumber ($\upsilon 0$), solvent polarity (p), HBD (a), HBA (b), slope and coefficient (R^2) of the linear fitting plot $\upsilon_{exp.}$ versus $\upsilon_{calc.}$

	υ0	a	b	p	Slope	R^2
L1	21474	-1053	-481	-1878	1.00	1.00
L2	21500	-2134	-753	-1733	1.00	1.00
L3	21556	-1066	-468	-1821	1.00	1.00
L4	21855	-979	-1167	-1884	1.00	1.00

Interestingly, all compounds present negative values of both a and b parameters, however, key inferences can be considered by comparing the dual and single chromophoric compounds. While the hydrogen bond donor sensitivity is roughly the same for **L1**, **L3** and **L4**, compound **L2** is 2-fold more susceptible to being influenced by protic solvents due to the quinoline group. Differences also rise in terms of sensitivity towards hydrogen bond acceptor interactions. Compound **L1** and **L3** are two-fold and three-fold less prone to be afflicted by the basic character of the solvent in regard to **L2** and **L3**, respectively. Finally, large negative p values indicate that the excited state of all compounds can be stabilized to the same degree by highly polarizable solvents.

4.4.3 Metal Ion sensing

Given the extensive literature on the application of dansyl and naphthalimide derivatives towards the sensing of metal ions and presence of well-defined coordination sites of the compounds in investigation, additions in acetonitrile of 1, 5 and 10 equivalents Ca^{2+}, Co^{2+}, Ni^{2+},

Cu^{+}, Cu^{2+}, Zn^{2+}, Ag^{+}, Cd^{2+}, Hg^{+}, Hg^{2+} and Pb^{2+} were performed. Figure 4–3 contains the normalized intensities at 515 and 513 nm of compounds **L1** and **L4** upon addition of each metal ion while **L2** and **L3** can be seen in Figure 4–18. All compounds show sensitivity towards Cu^{2+} and Hg^{2+} metal ions, however, it is noteworthy to highlight a chelation enhancement of fluorescence of **L1** and **L3** towards Hg^{2+} while the exact opposite was found in the case of compound **L2** and **L4**. It is noteworthy to highlight a shift of the emission band of **L4** to 493 nm towards the sensing of Hg^{2+} that can be seen in Figure 4–17 and will be discussed further ahead. In terms of Cu^{2+} a general quenching of the emission was observed across all compounds.

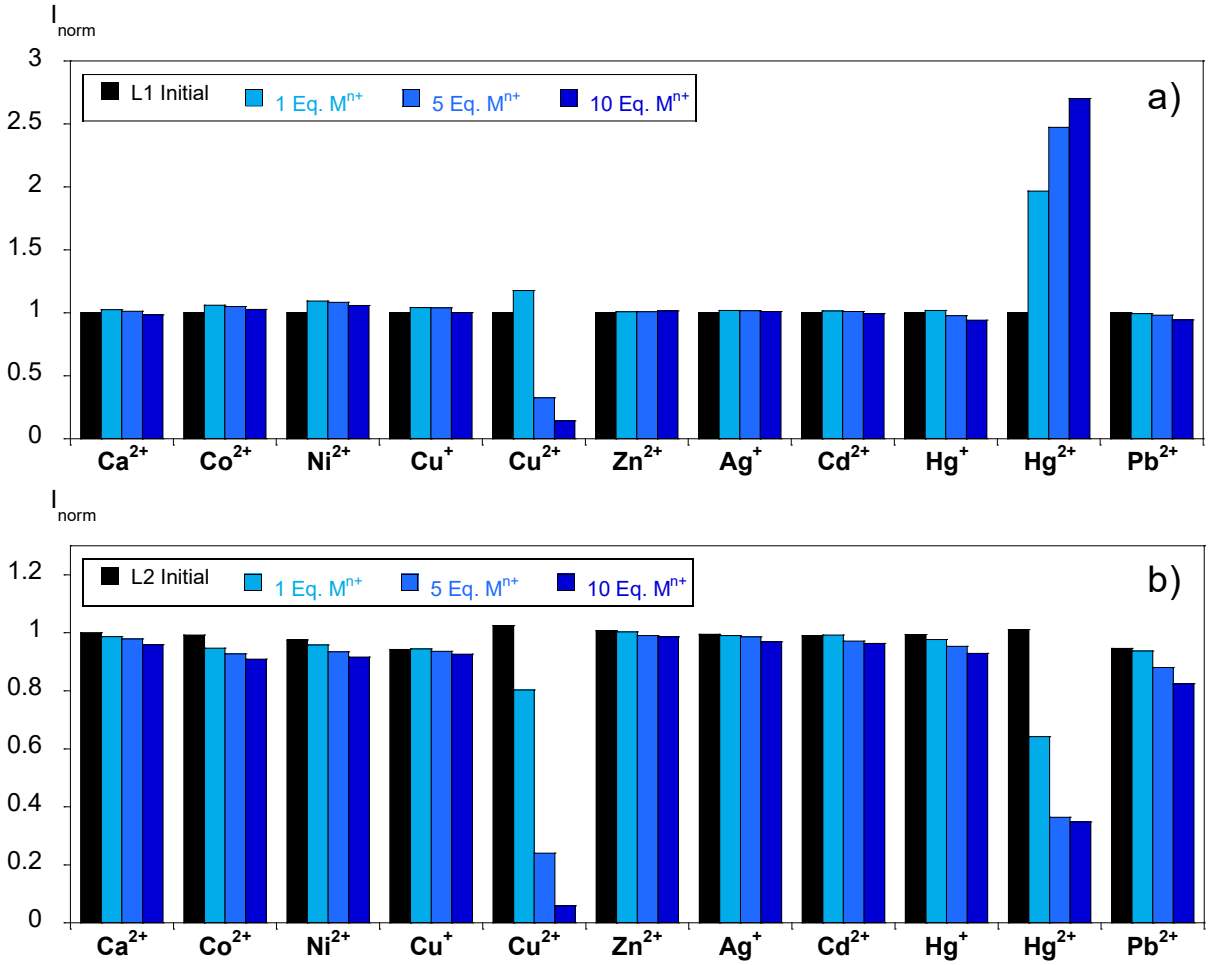


Figure 4–3. Normalized emission intensity of **L1** (a) and **L4** (b) upon addition of 1, 5, and 10 equivalents of Ca^{2+}, Co^{2+}, Ni^{2+}, Cu^{+}, Cu^{2+}, Zn^{2+}, Ag^{+}, Cd^{2+}, Hg^{+}, Hg^{2+} and Pb^{2+} metal ions. ([**L1**] = [**L4**] = 10μM, $\lambda_{em\mathbf{L1}}$ = 515 nm, $\lambda_{em\mathbf{L4}}$ = 513 nm, T = 298K).

In line with the previous results, Figure 4–4 exhibits the spectrophoto- and spectrofluorimetric titrations in response to increasing concentrations of Hg^{2+} and Cu^{2+} for **L1** and **L4**, and Figure 4–19 for **L2** and **L3**. Overall, consecutive additions of Hg^{2+} ions cause a relative no

change of the absorbance maxima centered at 425 nm for **L1** while simultaneously a gradual increase of the emission intensity is observed maintaining its maximum at around 515 nm. This change is associated with an increase in the quantum yield from 7.5% to 24.6% and a fluorescence decay of 9.36 ns representing an almost 2-fold increase (Figure 4–4a). A similar behavior was observed for **L3** with an increase in the quantum yield to 31.5% with the same 2-fold increase in fluorescence decay to 9.31 ns (Figure 4–19). ESI-HRMS elucidates the formation of 2:1 (L:M) complex for **L1** (Figure 4–20; $[M+H]^+$ for $C_{74}H_{56}HgI_2N_8O_8S_2$ = 1705.1542 m/z (0.002 ppm). Calculated $[M+H]^+$ for $C_{74}H_{56}HgI_2N_8O_8S_2$ = 1705.154197 m/z) while a 1:1 complex has been detected for **L3** (Figure 4–21; $[M+H]^+$ for $C_{35}H_{32}HgN_4O_4S$ = 807.1928 m/z (0.05 ppm). Calculated $[M+H]^+$ for $C_{35}H_{32}HgN_4O_4S$ = 807.192756 m/z)

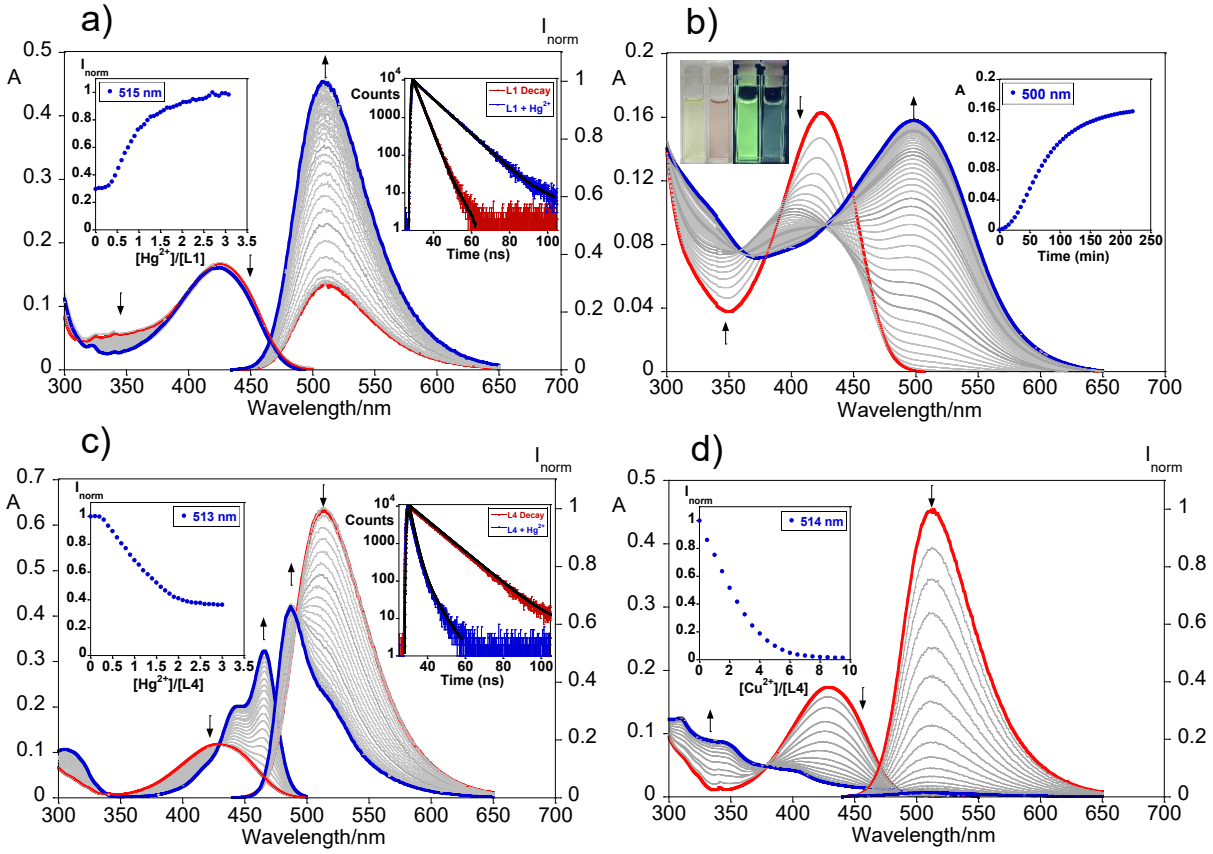


Figure 4–4. UV-Vis and luminescent titration of compound **L1** (a) upon continuous 10 mL additions of Hg^{2+} ([**L1**] = 10 μM; $[Hg^{2+}]$ = 0.225 mM). The inset represents the emission of $[Hg^{2+}]/[$**L1**$]$ at 515 nm (left) and the time-resolved fluorescence decay profile of **L1** before and after the titration with Hg^{2+} ions (right). UV-vis time continuous spectra of **L1** (b) after the addition of 7 eq. of Cu^{2+} ([**L1**] = 10 μM). The inlet represents the images under natural light and UV light (left) and the time-dependent response of the absorbance at l = 500 nm (right). UV-Vis and luminescent titration of compound **L4** (c) upon continuous 10 mL additions of Hg^{2+} ([**L4**] = 5 μM; $[Hg^{2+}]$ 0.15 mM). The inlet represents the emission of $[Hg^{2+}]/[$**L4**$]$ at 513 nm (left) and the time-resolved fluorescence decay profile of **L4** before and after the titration with Hg^{2+} ions (right). UV-Vis and luminescent titration of compound **L4** (d) upon continuous 10 mL additions of Cu^{2+} ions ([**L4**] = 10 μM; $[Cu^{2+}]$ = 1.5 mM). The inlet represents the emission of $[Cu^{2+}]/[$**L4**$]$ at 514

nm. For clarity of the reader the red spectrum represents the initial spectrum and the blue at the end point of the titration while the black curves in the fluorescent decay profile represent the fitting obtained.

The absorption response of **L1** and **L3** during the batch titration recorded 24 h after the addition increments of 0.5 eq. of Cu^{2+} until 7 eq. and 8 eq., respectively, showed the continuous decrease of the 425 nm band leading to the emergence of a band centered at 500 nm while a quenching of the emission was observed (Figure 4–22). When viewed by the unaided eye a progressive transition from yellow to pink solution was evident. To better characterize this behavior the progression of the absorption profile through time was recorded and is expressed in Figure 4–4b and Figure 4–19 for **L1** and **L3**, respectively. The results suggest the same general trend observed for the batch titration with a bathochromic shift of the absorption profile, which stabilizes around 220 minutes past the addition. Taking into consideration the time lapse, the formation of a complex with an inferior molecular weight than the original ligand has been found for **L1** (Figure 4–23; ESI-HRMS $[M+H]^+$ for $C_{39}H_{31}CuN_5O_5S$ = 745.1415 m/z (0.05 ppm). Calculated $[M+H]^+$ for $C_{39}H_{31}CuN_5O_5S$ = 745.141464 m/z) whereas for L3, the complex found shows no signs of ligand's cleavage at the same timepoint (Figure 4–24; ESI-HRMS $[M+Na]^+$ for $C_{35}H_{32}CuN_4O_4S$ = 690.1332 m/z (-0.07 ppm). Calculated $[M+Na]^+$ for $C_{35}H_{32}CuN_4O_4S$ = 690.133245 m/z) Although a better understanding of this phenomenon will be discussed and supported further ahead, early indications suggest that the iodophenyl moiety suffers changes in result of the complexation with Cu^{2+}. However, this has not demonstrated to be the limiting factor on the colorimetric response since in the absence of the iodophenyl moiety, **L3** showed the same behavior.

The introduction of the quinoline moiety in place of the dansyl unit in compound **L2** gives a stark contrast in the sensing mechanism of the aforementioned metal ions (Figure 4–19). In the case of Hg^{2+}, a generic quenching of the emission is observed with very few changes to the absorption profile. For Cu^{2+} an attenuation of the 427 nm absorption band and the formation of a band at around 370 nm in parallel with the quenching of the emission is observed. In this case, no changes in the resulting transparent solution of **L2** were detected in the upcoming hours after the experiment took place, highlighting the necessity for the presence of the dansyl moiety in both the turn-on effect and the colorimetric response. Complexation in 1:1 ratio has been found towards Hg^{2+} (Figure 4–25; ESI-HRMS $[M+H]^+$ for $C_{34}H_{21}HgIN_4O_4S$ = 911.0111 m/z (-0.03 ppm). Calculated $[M+H]^+$ $C_{34}H_{21}HgIN_4O_4S$ = 911.011127 m/z) and Cu^{2+} (Figure 4–26; ESI-HRMS $[M+H]^+$ for $C_{34}H_{21}CuIN_4O_4S$ = 771.9690 m/z (-0.9 ppm). Calculated $[M+H]^+$ $C_{34}H_{21}CuIN_4O_4S$ = 771.969698 m/z). Some attention should be given to the fact that,

in contrast to the case of **L1**, the iodophenyl moiety of **L2** maintained its integrity demonstrating a close association between the distinct properties of **L1** and Cu^{2+} ions.

Furthermore, the sensing abilities of compound **L4** towards Hg^{2+} ions are characterized by the progressive formation of a red-shifted band with a maximum centered at 465 nm accompanied by a shoulder at 445 nm. With respect to the emission spectra, a progressive quenching on its intensity is observed with the emergence of an emission maximum at 493 and a shoulder at 518 nm. Fluorescence decay curves set the initial emission with a lifetime of 10.4 ns that after addition of Hg^{2+} ions decreases to a lifetime value of 5.1 ns. The formation of a 1:1 complex towards Hg^{2+} has been detected using **L4** (Figure 4–27; ESI-HRMS $[M+H]^+$ for $C_{24}H_{19}HgN_3O_4$ = 616.1159 m/z (0.02 ppm). Calculated $[M+H]^+$ for $C_{24}H_{19}HgN_3O_4$ = 616.115890 m/z) The sensing capabilities of **L4** towards Cu^{2+} focus on the suppression of the absorption band and the rise of a new band centered at 350 nm while a continuous quenching of the emission is observed until the addition of 10 eq. of the metal ion. For this case, ESI-HRMS suggests a 2:1 complex (Figure 4–28; ESI-HRMS $[M+H]^+$ for $C_{48}H_{40}CuN_6O_8$ = 892.2277 m/z (0.07 ppm). Calculated $[M+H]^+$ for $C_{48}H_{40}CuN_6O_8$ = 892.227636 m/z).

Given the results observed for the dyad systems **L1** and **L3**, we propose that these compounds manifest a photoinduced electron transfer in solution, the coordinating Hg^{2+} metal ion subsequently stabilizes the donor orbital lowering its energy further below from the ground state preventing PeT and restoring fluorescence. Hyunjung Lee *et. al.* [43] highlighted this reasoning in modulating the fluorescence properties of Hg^{2+} complexes with also several examples reported in the literature of the turn-on sensing of Hg^{2+}. [78] In accordance with these observations and keeping in mind that PeT behavior can also be mitigated by protonation, several eq. additions of H^+ were performed for **L1** and **L3** demonstrating the same increase in fluorescence (Figure 4–29). Lifetime measurements help consolidate these findings with very similar increases of the decay's curves to 9.34 and 9.47 ns for **L1** and **L3**, respectively, a phenomenon much comparable as observed towards Hg^{2+} ions.

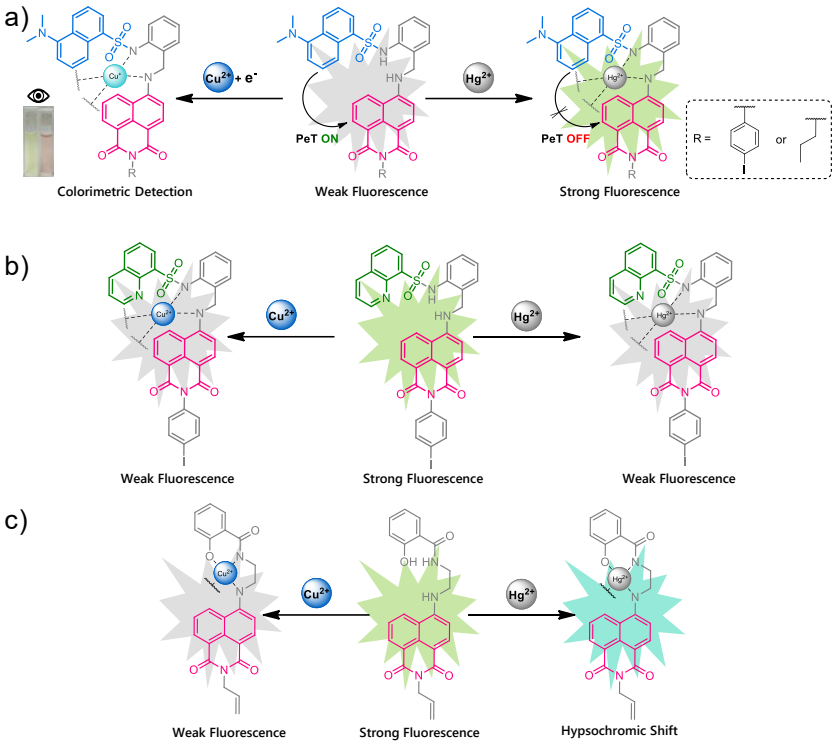


Figure 4–5. General representation of the interaction mechanism after complexation with Cu^{2+} and Hg^{2+} metal ions for (a) **L1** and **L3**, (b) **L2** and (c) **L4**.

These factors facilitate the comprehension of the highly coveted potential to detect both Hg^{2+} and Cu^{2+} in the same system without falling in the predicament of the "turn-off" behavior due to the large spin-orbit coupling constant of Hg^{2+} and the paramagnetic nature of Cu^{2+}. The incorporation of the dansyl unit enables dual-function sensing: a "turn-on" fluorescence response for Hg^{2+} detection and a distinct colorimetric response for Cu^{2+} with the overall detection mechanisms depicted in Figure 4–5. The colorimetric detection of Cu^{2+} will be discussed in more detail further ahead.

4.4.4 Anti-Interference performance in Hg^{2+} detection

The interference effect that metal ions might promote on the turn-on detection ability of **L1** and **L3** for Hg^{2+} has been investigated by the addition of 10 eq. of each metal to a solution of each compound already containing 5 eq. of Hg^{2+}. As shown in Figure 4–6 and Figure 4–30, the Hg^{2+} dependent fluorescence emission was not significantly altered by the presence of Ca^{2+} and the transition metal ions Co^{2+}, Ni^{2+}, Cu^{+}, Zn^{2+}, Ag^{+}, Cd^{2+}, Hg^{+}, and Pb^{2+} except for Cu^{2+} that causes a decrease in the enhanced fluorescent response towards Hg^{2+}. This behavior could be attributed to the paramagnetic nature of Cu^{2+} that may interact to different sites in the molecule or accept electrons from fluorophore's excited state. Furthermore, compound **L3**

was found susceptible to water molecules in which Hg^{+} and Pb^{2+} were dissolved, exhibiting interference on the interpretation of these metal ions.

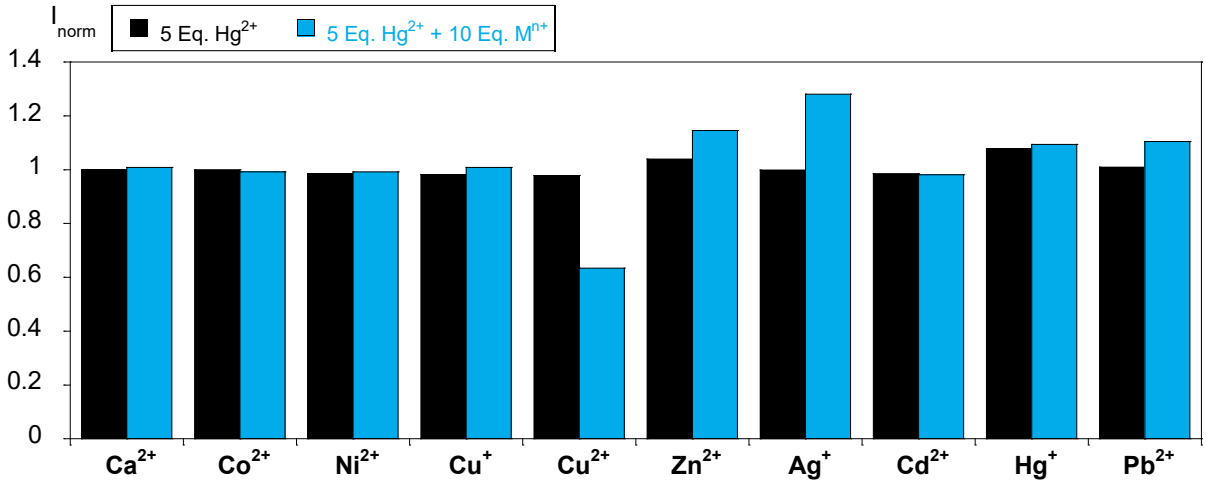


Figure 4–6. Normalized emission response of **L1** in the presence of 5 equivalents Hg^{2+} and upon the addition of metal ions in acetonitrile. ([**L1**] = 10μM, $\lambda_{em\mathbf{L1}}$ = 515 nm, T = 298K).

4.4.5 Determination of association constants and sensing limit parameters

In order to completely assess the sensing ability of all compounds towards Hg^{2+} and Cu^{2+}, the HypSpec software [79] was used for the evaluation of the stability constants. Also, the determination of the detection and the quantification limit parameters towards both metal ions has been fulfilled. The association constants, LOD and LOQ are summarized in Table 4-4.

Table 4-4. Association constants evaluated employing HypSpec software for compounds **L1** to **L4** towards Hg^{2+} and Cu^{2+} ions with included stoichiometry in acetonitrile. Respective values for the detection limit (LOD) and quantification limit (LOQ) amounts (μM).

Compounds	Metal (M)	Association constants ($LogK_{ass.}$), L:M	LOD (μM)	LOQ (μM)
L1	Hg^{2+}	9.39 ± 0.01 (2:1)	5.1	7.3
L2	Cu^{2+}	4.83 ± 0.03 (1:1)	8	12
	Hg^{2+}	5.54 ± 0.03 (1:1)	2.5	5
L3	Hg^{2+}	5.07 ± 0.04 (1:1)	1	2
L4	Cu^{2+}	9.37 ± 0.05 (2:1)	5	9.9
	Hg^{2+}	4.73 ± 0.04 (1:1)	3.9	7.1

Table 4-4 reveals the association constants considering the stoichiometry 2:1 and 1:1 (L:M) for Hg^{2+} and Cu^{2+} in accordance with the data obtained from mass spectrometry for complex formation is concerned. The constants that relate to the stoichiometry of 2:1 were found to be very similar using **L1** and **L4** for Hg^{2+} and Cu^{2+}, respectively. Among the remaining systems, stoichiometry 1:1 was prevalent, attributing to **L2** the highest association constant towards Hg^{2+} with an association constant of 5.54 ± 0.03. In terms of LOD and LOQ, values were found to range between 1 to 8 and 2 to 12 μM, respectively, attributing the lowest values for the sensing of Hg^{2+} using **L3**.

4.4.6 Characterization of L1 and L3 complexes with Hg^{2+} and Cu^{2+}

Given the extensive studies in solution that provided the complete framework for the differentiation towards the sensing of Hg^{2+} and Cu^{2+} using **L1** and **L3**, our interest shifted in the direction of obtaining the complexes in solid form. All complexes were successfully synthesized, and a complete description of the procedures can be found in the experimental section.

The structural characterization of the complexes was achieved by FTIR and the proposed formulations were also confirmed by HRMS. The solid-state FTIR spectra of **L1** and **L3** provided the expected bands for the dansyl and naphthalimide moieties (Figure 4–31 and Figure 4–34). Complexes of **L1** showed the broadening of the 3500 to 3000 cm^{-1} regions especially the band dedicated to the ν(N-H) with the unchanged profile of the dicarboximide group, between 1680 and 1575 cm^{-1}, suggesting the well stablished coordination site of the secondary amines spacer. Furthermore, the dedicated region for the ν(S=O) + ν(C-N) bands, between 1350 and 1130 cm^{-1}, showed an increase in strength due to the presence of the triflate counterion, consolidating this finding. Concerning the Cu^{2+} complex, the increase of the bands at 2915 and 2850 cm^{-1} suggests a change in the molecular structure. The ESI-HRMS spectrum suggests the formation of a 2:1 (L:M) Hg^{2+} complex with a m/z of 1706.1620 (Figure 4–37) in accordance with the findings in solution. In turn, a smaller ion than the ligand with a m/z of 747.1571 (Figure 4–38) was found for the Cu^{2+} complex similarly detected in solution, as mentioned previously which help illustrate the emergence of the band typically associated with aliphatic C-H stretches found in the FTIR spectrum. Thus, this demonstrates that iodine is no longer present in the molecular structure and will be discussed further ahead.

The complexation of Hg^{2+} and Cu^{2+} with compound **L3** shares the same changes in comparison to **L1**, broadening of the 3500 to 3000 cm^{-1} region while keeping the dicarboximide profile and the increase of the ν(S=O) + ν(C-N) bands suggesting the presence of triflate counterion. Both complexes were followed by ESI-HRMS giving insight of the formation of a 1:1

Hg^{2+} complex with an m/z of 807.1929 (**Figure 4–39**) as it was found in solution, whereas the Cu^{2+} complex would preferably adopt a 2:1 stoichiometry in the solid state with an m/z of 1274.3814 (Figure 4–40).

4.4.7 Interaction mechanism study of L1 with Cu^{2+}

To shed more light on the phenomenon underlying the **L1** and **L3** photophysical characteristics upon the introduction of Cu^{2+}, the time evolution of the L1:Cu^{2+} complex was studied by means of EPR and X-ray photoelectron spectroscopy.

At 1:4, the EPR of L1:Cu^{2+} displays a broad axial spectrum, characteristic of Cu^{2+} (Figure 4–7a, brown line), with $g_{//} > g_{\perp} > 2$, where only two of the expected copper four $g_{//}$ lines are visible. No super-hyperfine interactions were identified. Noteworthy, L1:Cu^{2+} displays the same key spectral features as Cu^{2+} (in acetonitrile solution, without L1; Figure 4–7a, green line), indicating that only copper not coordinated to L1 is being observed in the EPR spectrum of L1:Cu^{2+}. The spectrum likely arises from heterogeneous copper species coordinated by four oxygen atoms, as suggested by the $g_{//} \approx 2.414$ and $A_{//} \approx 138 \times 10^{-4} cm^{-1}$ values. [80]

The L1:Cu^{2+} 1:4 spectrum intensity decreases with time (Figure 4–7b, light blue line), clearly showing that Cu^{2+} is being reduced to the EPR silent Cu^{+}, and, after 75 minutes (Figure 4–7a, light orange line), almost all copper (2.0 mM) was reduced. For L1:Cu^{2+} 1:7 and 1:10, similar spectra were obtained and their intensity also decreased with time (Figure 4–7b, blue and dark blue lines, respectively). These results clearly demonstrate that L1 reduces copper. Moreover, because no spectral evidence of a L1:Cu^{2+} complex was observed, these results suggest that copper is reduced upon coordination/reaction with L1 (reduction would take place within 30-60s, the minimum time required to mix L1 and copper and freeze the solution, under our experimental conditions).

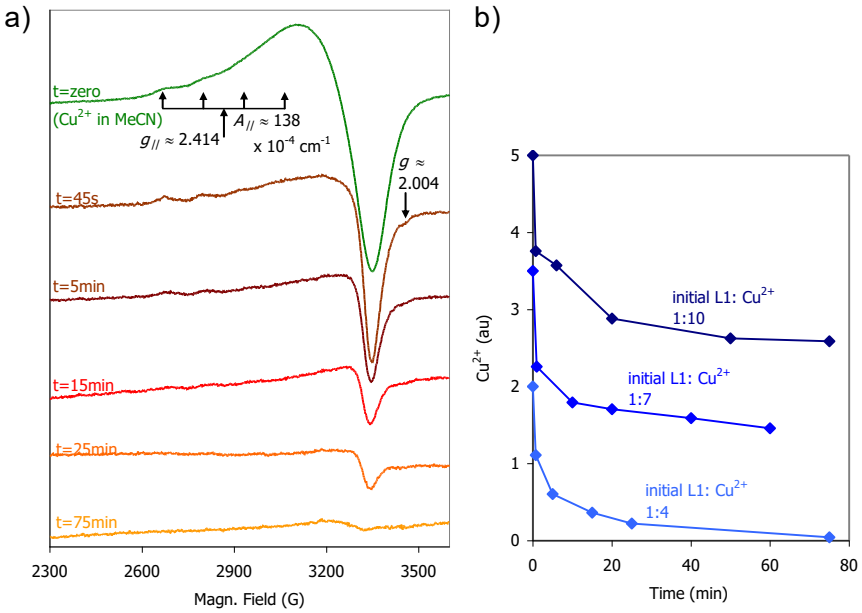


Figure 4–7. (a) EPR spectra at 77K of L1:Cu^{2+} 1:4 (0.5mM:2.0mM) in MeCN, at time zero (green line) and after 45s (brown), 5 min (dark red), 15 min (red), 25 min (orange) and 75 min (light orange). (b) Cu^{2+} reduction as a function of time, upon mixing L1 and Cu^{2+} at 1:4 (0.5:2.0 mM; light blue line), 1:7 (0.5:3.5 mM; blue) and 1:10 (0.5:5.0 mM; dark blue) ratios. Cu^{2+} concentration values (in arbitrary units, au) were determined from the respective EPR spectra intensity (double spectrum integration).

To be able to reduce copper, L1 needs to be oxidized by one electron, giving rise to an initial (transient) cation radical species, $L1^{\bullet+}$. The observation of such radical is dependent on its lifetime and, if the species is present in a low accumulated concentration, its EPR signal can be greatly obscured by the broad copper signal. In this context, the small feature at $g \approx 2.004$ observed in the 45 seconds spectra of L1:Cu^{2+} 1:4 (Figure 4–7a, brown line) can be taken as an evidence of a radical formation in very low amounts; for longer times, no such feature can be identified. Alternatively, L1 can be oxidized by two electrons to yield 2 Cu^{+}. After the initial (1 or 2-electron) oxidation, each L1 molecule ought to undergo additional oxidation events, involving a total of four electrons, to account for the complete copper reduction observed in L1:Cu^{2+} 1:4 after 75 minutes (Figure 4–7a, light orange line, and Figure 4–7b, light blue line). Noteworthy, when an excess of copper is used (L1:Cu^{2+} 1:7 and 1:10), the amount of Cu^{2+} reduced is approximately the same. For a L1:Cu^{2+} 1:4 (0.5:2.0 mM) ratio, (almost) no copper remains in the Cu^{2+} state; for 1:7 (0.5:3.5 mM) and 1:10 (0.5:5.0 mM) ratios, approximately 1.5 (3.5-2.0) and 3 (5.0-2.0) equivalents remain in the Cu^{2+} state, respectively (Figure 4–7b). These results give further support to the suggestion that L1 is able to promote a global 4-electron redox process with copper.

X-ray photoelectron spectroscopy was deployed to further gain insight into the oxidation states of Cu in the compounds under study after various treatments. Figure 7a presents Cu2p spectra for the L1:Cu^{2+} compound with a concentration ratio of 1:4 as prepared (black curve) and after 4 hours in a vacuum (red curve). Figure 7b presents Cu2p spectra for the L1:Cu^{2+} compound with a concentration ratio of 1:1 as prepared (green curve) and for the [Cu(II)**L1**]$^{2+}$ complex. All the Cu2p spectra have a complex multipeak structure, which includes doublets due to spin-orbit splitting (Cu2p3/2 and Cu2p1/2 peaks) and satellites in the binding energy range of ~938-948 eV. The complex structure of the Cu2p XPS spectra indicates a mixture of copper oxidation states. Strong satellites in the Cu2p spectra are an indication of the Cu^{2+} oxidation state. [81]

The Cu2p3/2 peaks in the spectra of the L1:Cu^{2+}=1:4 compound (Figure 4–8a) as prepared and after 4 hours, show a wide, asymmetric shape with peak positions shifted to 933-935 eV. In the case of the L1:Cu^{2+}=1:1 and [Cu(II)**L1**]$^{2+}$, the Cu2p3/2 peaks split into two components with maximum positions at ~933 and ~935 eV. Given the position of the main peak at ~933 eV and the presence of satellites, one can tentatively conclude that the L1:Cu^{2+}=1:1 and [Cu(II)**L1**]$^{2+}$ compounds contain a mixture of Cu^{1+} and Cu^{2+} species. An interesting observation is the splitting of the main Cu2p3/2 peak with an additional maximum at ~935 eV. The trivial explanation for this peak would be to assign it to an oxidation state higher than 2+. However, this peak splitting appears similar to that observed in the Ni2p spectra of NiO and is often mistakenly assigned to Ni^{3+}. It has been shown that the 2p peak splitting can be explained by the nonlocal screening of the core hole created during ionization of the 2p level by electrons donated by nearest and non-nearest ligands, while maintaining the 2+ oxidation state of Ni ions. [82]

It is noteworthy to analyze the relative intensity of the satellite peaks with respect to the intensity of the main Cu2p3/2 peaks. Figure 4–8a, shows that the relative intensity of the satellites substantially decreased after 4 hours. In the case of the L1:Cu^{2+}=1:1 compound, the relative satellite intensities are smaller than those in the L1:Cu^{2+}=1:4 compound. The decrease in satellites can indicate the reduction of Cu^{2+} species by mixing with the L1 substance. After 4 hours, Cu^{2+} species are still present in the L1:Cu^{2+}=1:4 compound as well as in the L1:Cu^{2+}=1:1 compound, as evidenced by the Cu2p XPS spectra. This could also be due to surface oxidation of the studied materials, which is detectable by the surface-sensitive XPS technique (information depth up to ~10 nm).

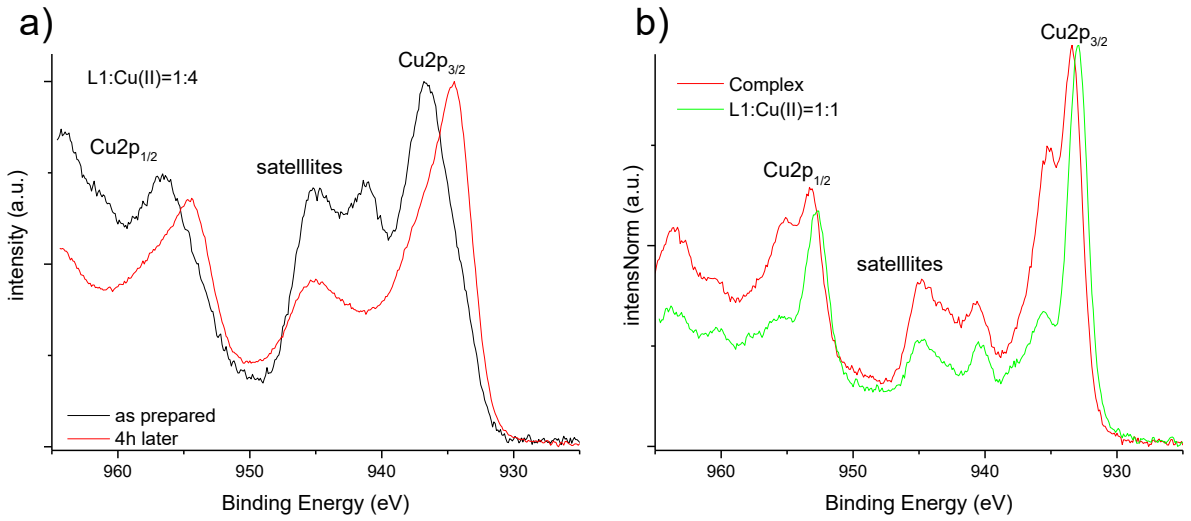


Figure 4–8. Cu2p XPS spectra (a) after the addition of **L1** and Cu^{2+} in proportion 1:4 as prepared and 4h later while (b) exhibits the spectra of the [Cu(II)**L1**]$^{2+}$ complex and in proportion 1:1 (L:M).

Provided the evidence that showed the copper reduction using **L1** and **L3** from EPR and XPS experiments and bearing in mind the PeT process that could be mitigated and applied for the sensing of Hg^{2+}, we propose that both compounds perform a ligand-mediated chemical reduction of Cu^{2+} to Cu^{+}. The presence of an intramolecular electron-transfer process leads to a shift of the electronic charge distribution and the identification of the Cu^{+} state, that can also be colorimetrically identified with a change in the absorption profile from yellow to pink. Given the absence of any indication of reversibility or equilibrium between Cu^{2+} and Cu^{+} states provided by EPR data, these systems cannot achieve valence tautomerism. Furthermore, the introduction of iodophenyl serves as a catalysis substrate probe, in which only **L1** was able to catalyze the cleavage of the carbon-iodine bond from within itself. This is mediated by the formation of the Cu^{+} complex evidenced by the formation of a complex with lower molecular weight. The reduction of copper was found the limiting factor since compound **L2**, that does not manifest intramolecular electron-transfer, would not catalyze the carbon-halogen bond given that does not reduce the copper ion. Thus, we propose that **L1** self-catalyzed an amidation of benzene through an Ullman-type reaction using acetonitrile as amino source demonstrating in this way the usefulness of these dyad systems for catalysis. [56-58]

4.5 Conclusions

In summary, we report the synthesis and characterization of four new naphthalimide derived ligands for the differential detection of Hg(II) and Cu(II) ions. Photophysical characterization in various solvents prompted us to characterize the solvent-compound interactions through the multiparametric fitting of the Kamlet-Taft equation and underlying solvatochromism. An understanding of the photophysical properties in dyad systems has been accomplished by comparison between the introduction of a quinoline or dansyl moiety to the naphthalimide core. Intramolecular electron transfer was possible in two compounds by introduction of a dansyl moiety constituting in two non-redox-innocent dyad systems. Application of these compounds to the sensing of metal ions, particularly of Hg(II) and Cu(II) ions, proved to be effective in avoiding the well-known suppression that these ions cause to fluorescent systems. A clear turn-on or CHEF effect of the emission was detected while sensing Hg(II) ions since it lowers the energy of the lone pair further from the ground state that would cause the initial quenching. A differential detection of Cu(II) ions was achieved by a colorimetric response accompanied by the intramolecular electron transfer. In this case, the two electronic states of the non-redox-innocent ligand and the redox-active metal center are close enough to observe ligand-mediated chemical reduction of Cu^{2+}. Application of EPR and XPS provided the evidences to establish a reduction of the copper(II) center to copper(I) promoted by the underlying close connection between the dansyl and naphthalimide units of the dyad. Finally, the resulting copper complexes were found the only suited compounds to be tested in the future for their catalysis properties since the cleavage of the carbon-halogen bond implemented as a probe was only mediated by prior reduction to copper(I).

4.6 Supplementary material

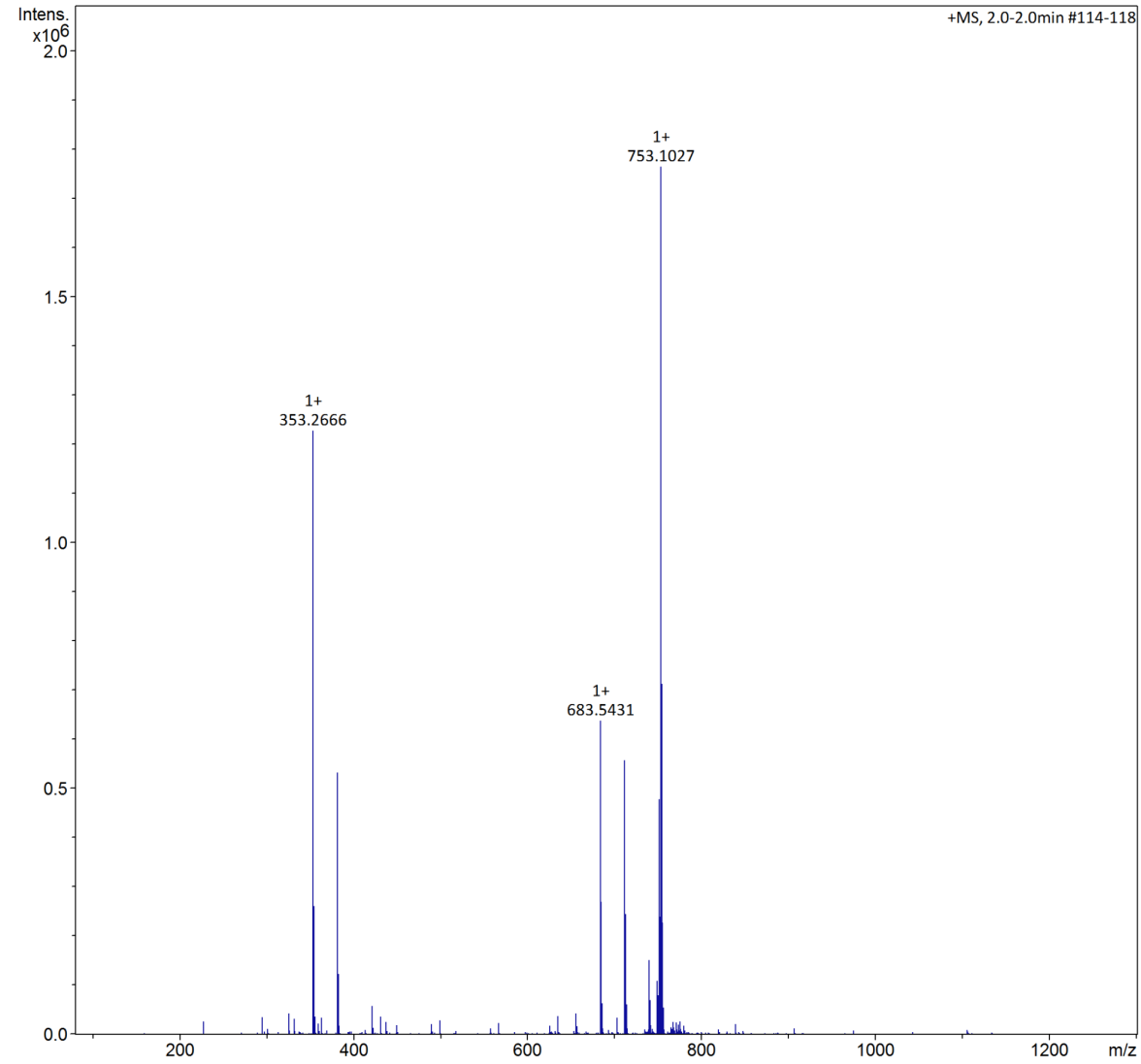
Display Report

Analysis Info

Analysis Name	D:\Data\BIOSCOPE\Hugo\Smal molecules\2024.04.17-Frederico\DR196.d	Acquisition Date	17-Apr-24 3:39:56 PM
Method	Direct_Infusion_100-1000.m	Operator	BDAL@DE
Sample Name	ACN	Instrument	impact HD 1819696.00006
Comment			

Acquisition Parameter

Source Type	ESI	Ion Polarity	Positive	Set Nebulizer	0.4 Bar
Focus	Not active	Set Capillary	4500 V	Set Dry Heater	180 °C
Scan Begin	80 m/z	Set End Plate Offset	-500 V	Set Dry Gas	4.0 l/min
Scan End	1300 m/z	Set Charging Voltage	2000 V	Set Divert Valve	Waste
		Set Corona	4000 nA	Set APCI Heater	200 °C



DR196.d
Bruker Compass DataAnalysis 4.2 printed: 05-Jun-24 10:47:44 AM by: BDAL@DE Page 1 of 1

Figure 4–9. ESI-HRMS spectrum of compound **L1**.

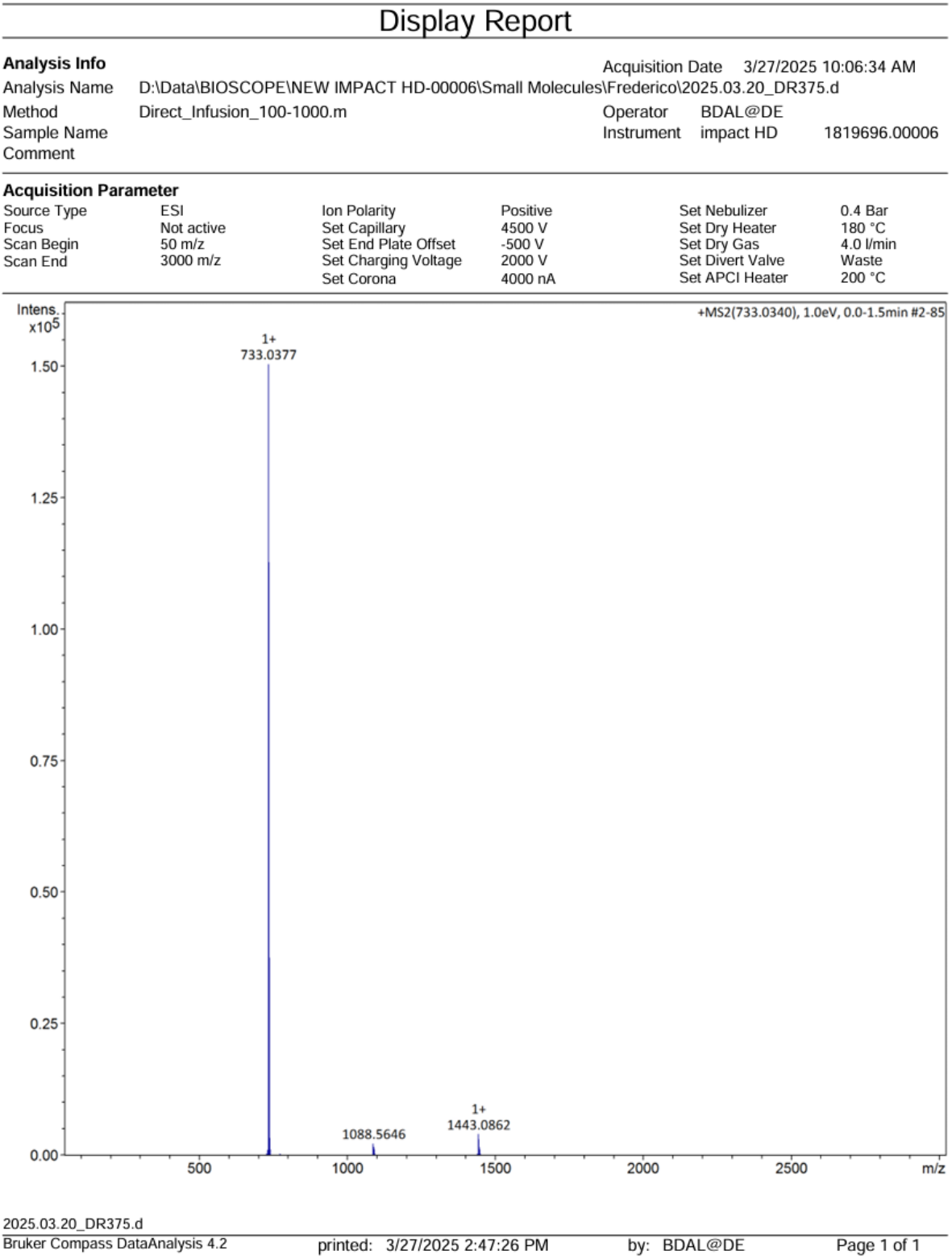


Figure 4–10. ESI-HRMS spectrum of compound **L2**.

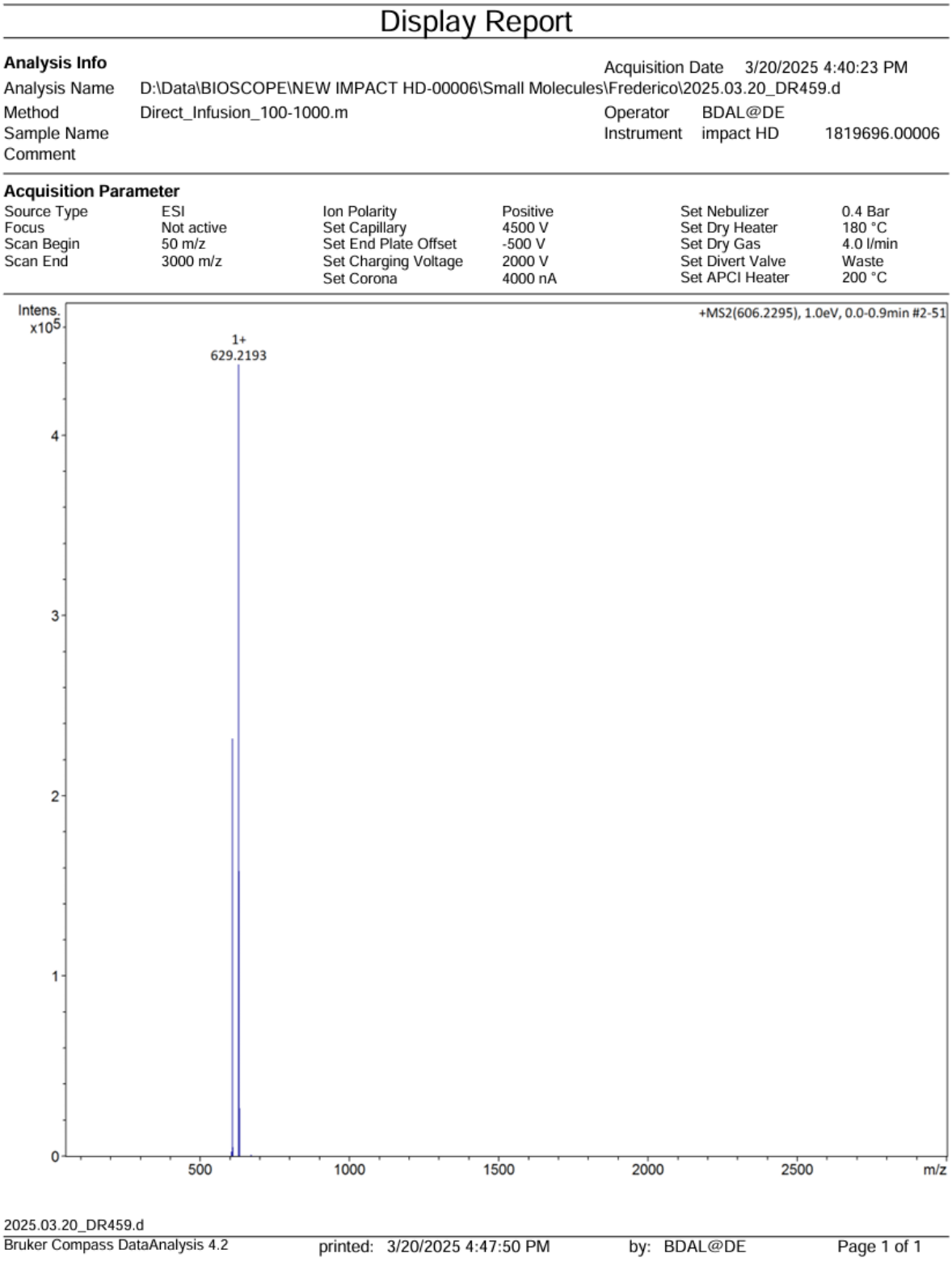


Figure 4–11. ESI-HRMS spectrum of compound **L3**.

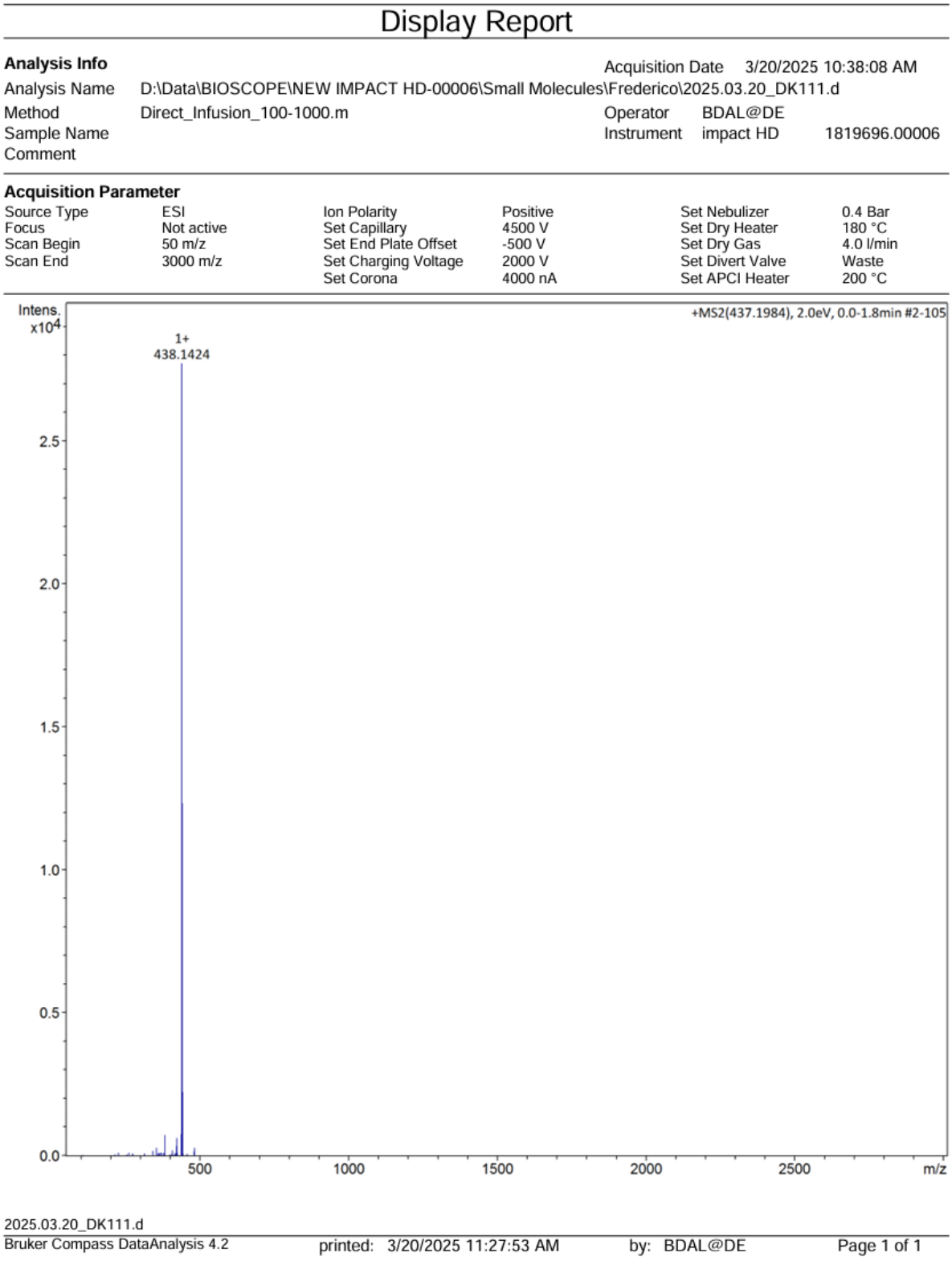


Figure 4–12. ESI-HRMS spectrum of compound **L4**.

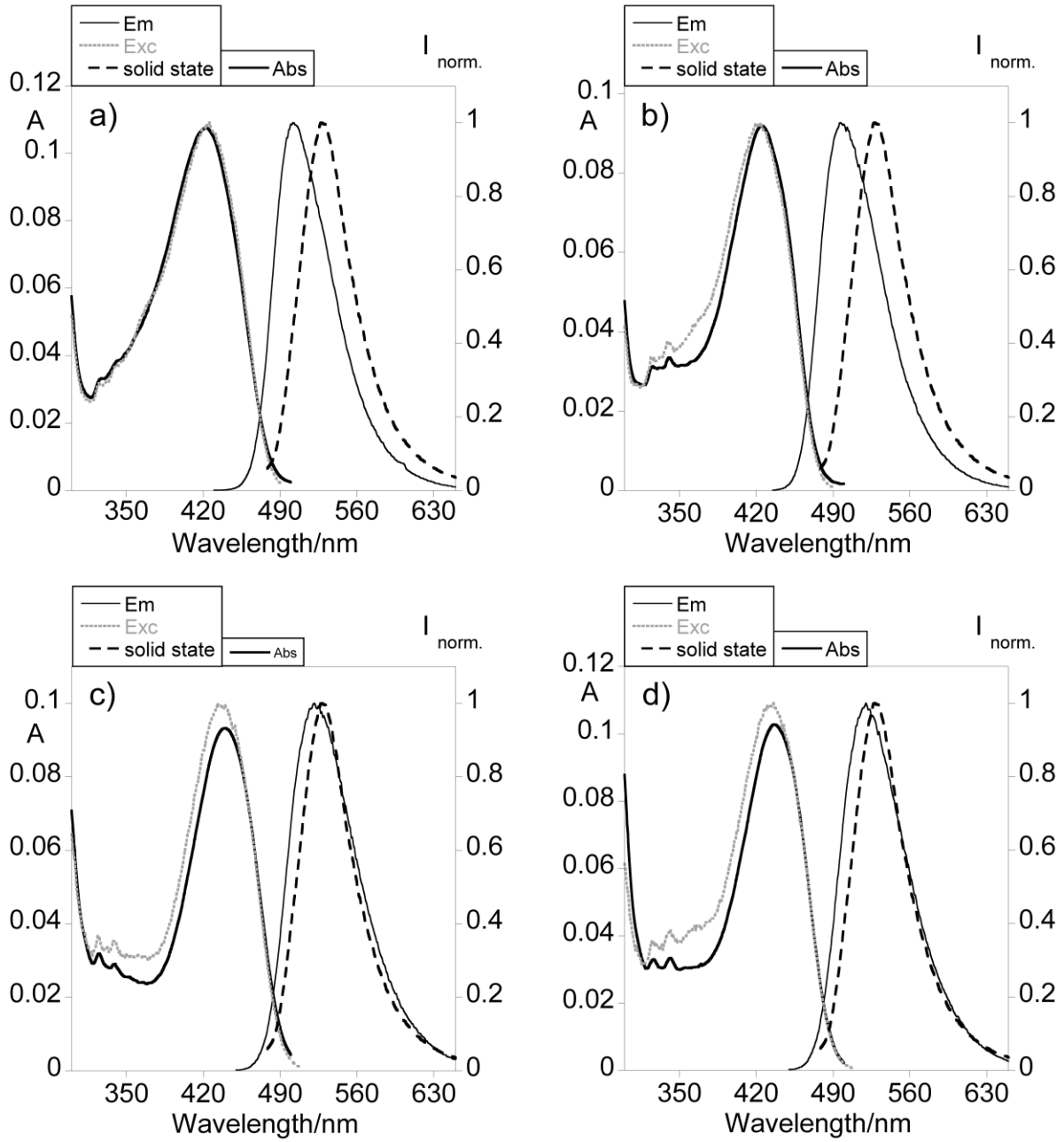


Figure 4–13. Photophysical characterization of **L1** in (a) chloroform, (b) THF, (c) ethanol and (d) DMSO.

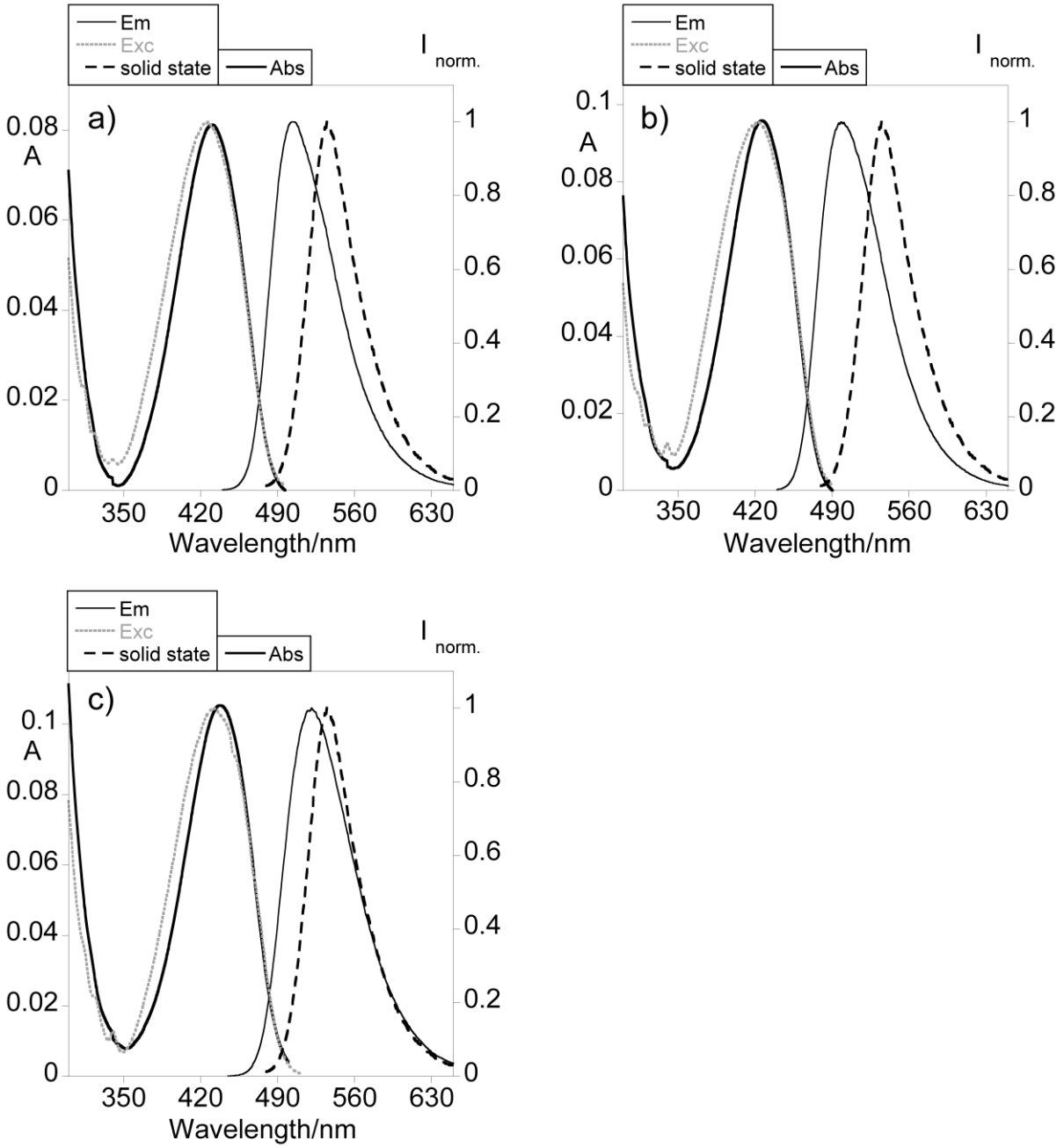


Figure 4–14. Photophysical characterization of **L2** in (a) chloroform, (b) THF and (c) DMSO.

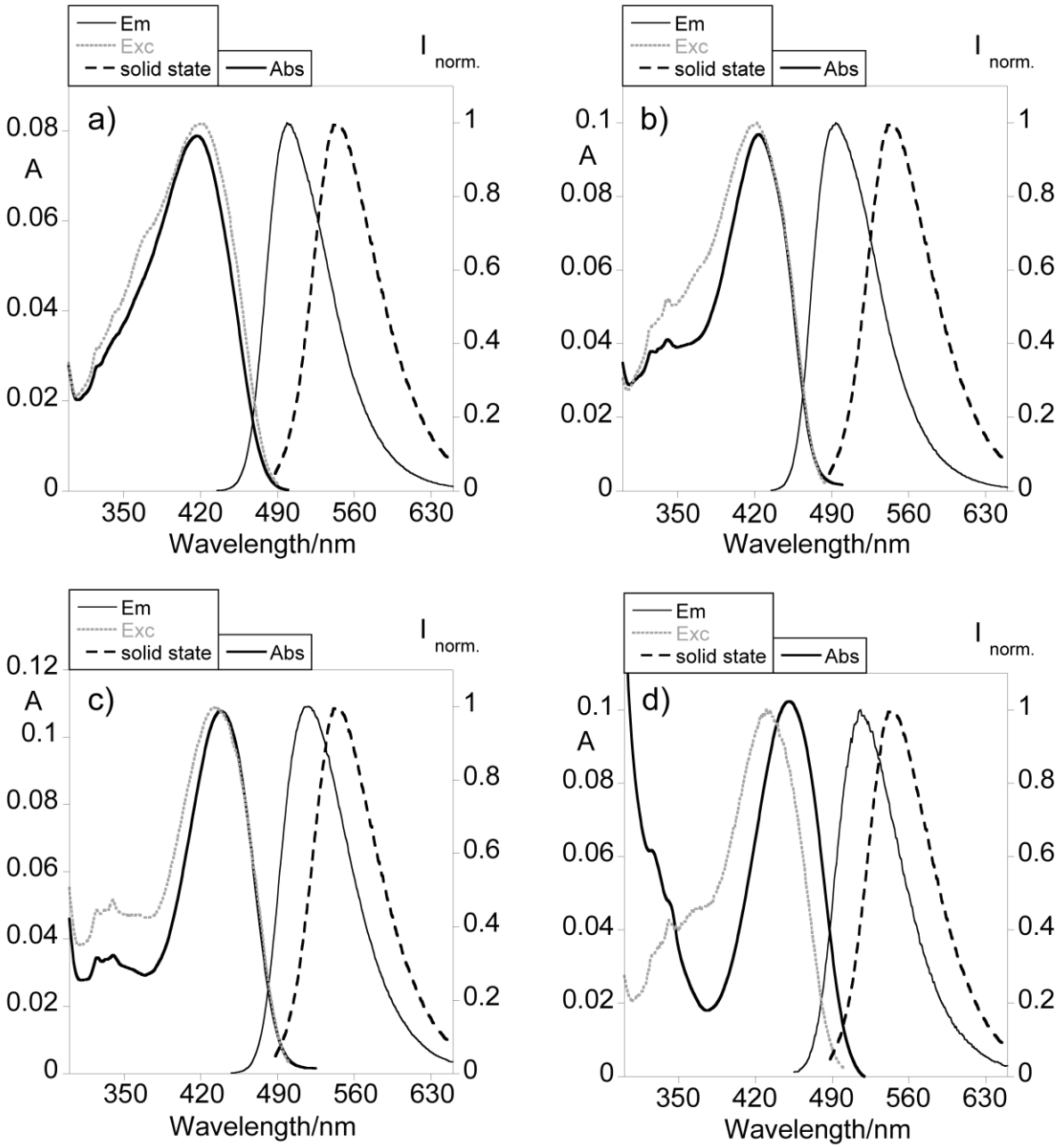


Figure 4–15. Photophysical characterization of **L3** in (a) chloroform, (b) THF, (c) ethanol and (d) DMSO.

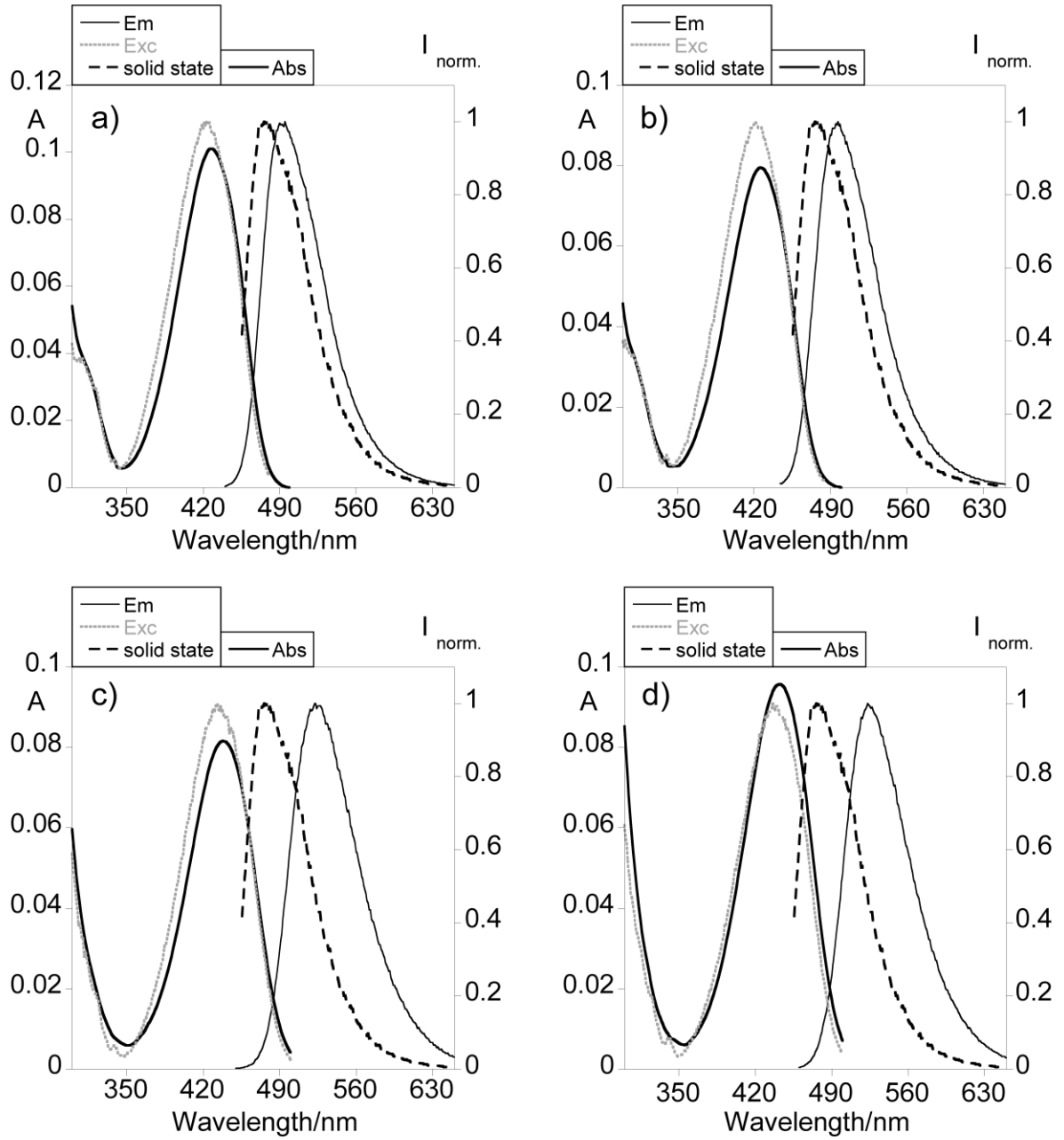


Figure 4–16. Photophysical characterization of **L4** in (a) chloroform, (b) THF, (c) ethanol and (d) DMSO.

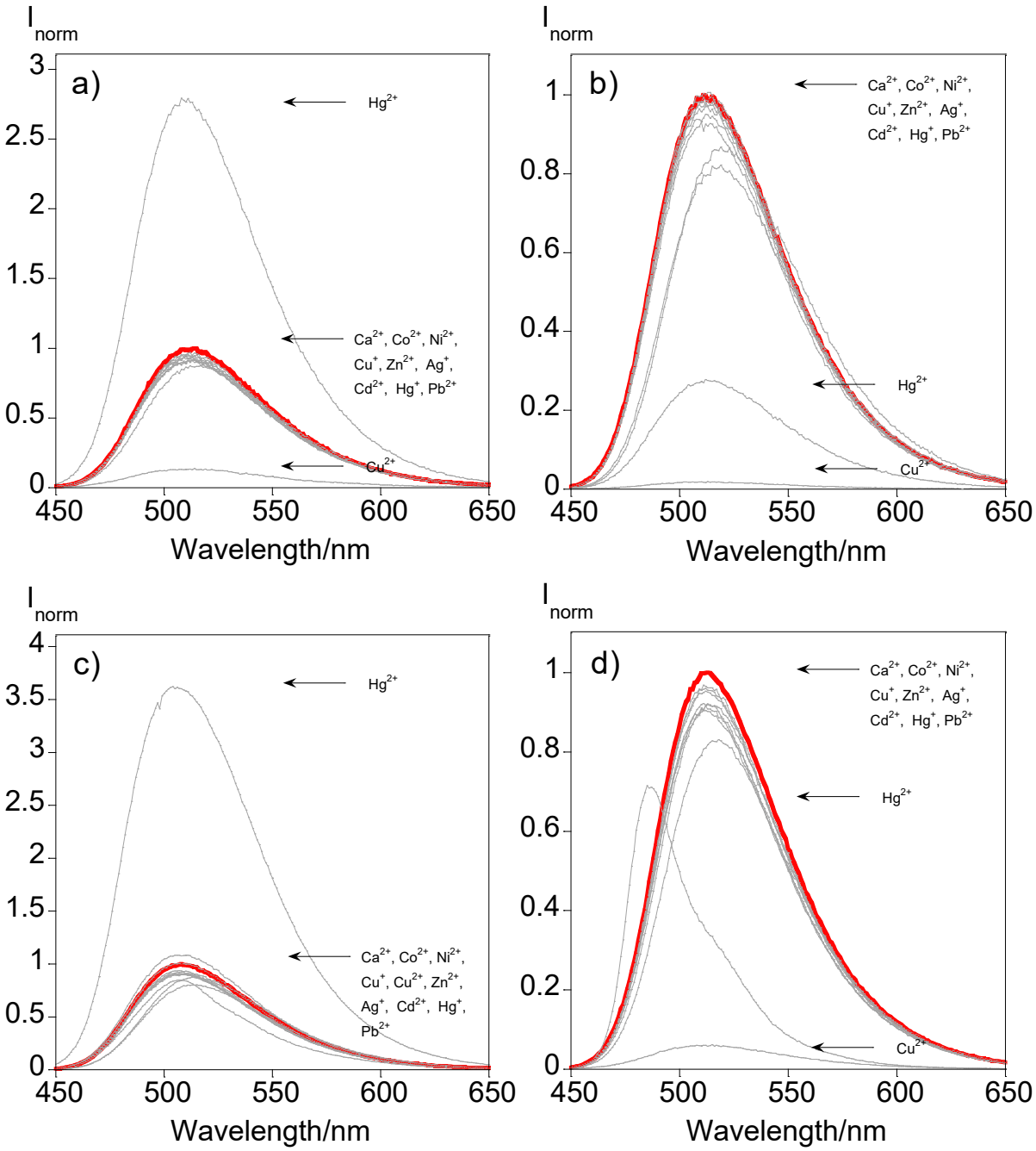


Figure 4–17. Emission spectra after the addition of 10 eq. of each metal for **L1** (a), **L2** (b), **L3** (c) and **L4** (d). For clarity of the reader the red spectrum corresponds to the initial fluorescence.

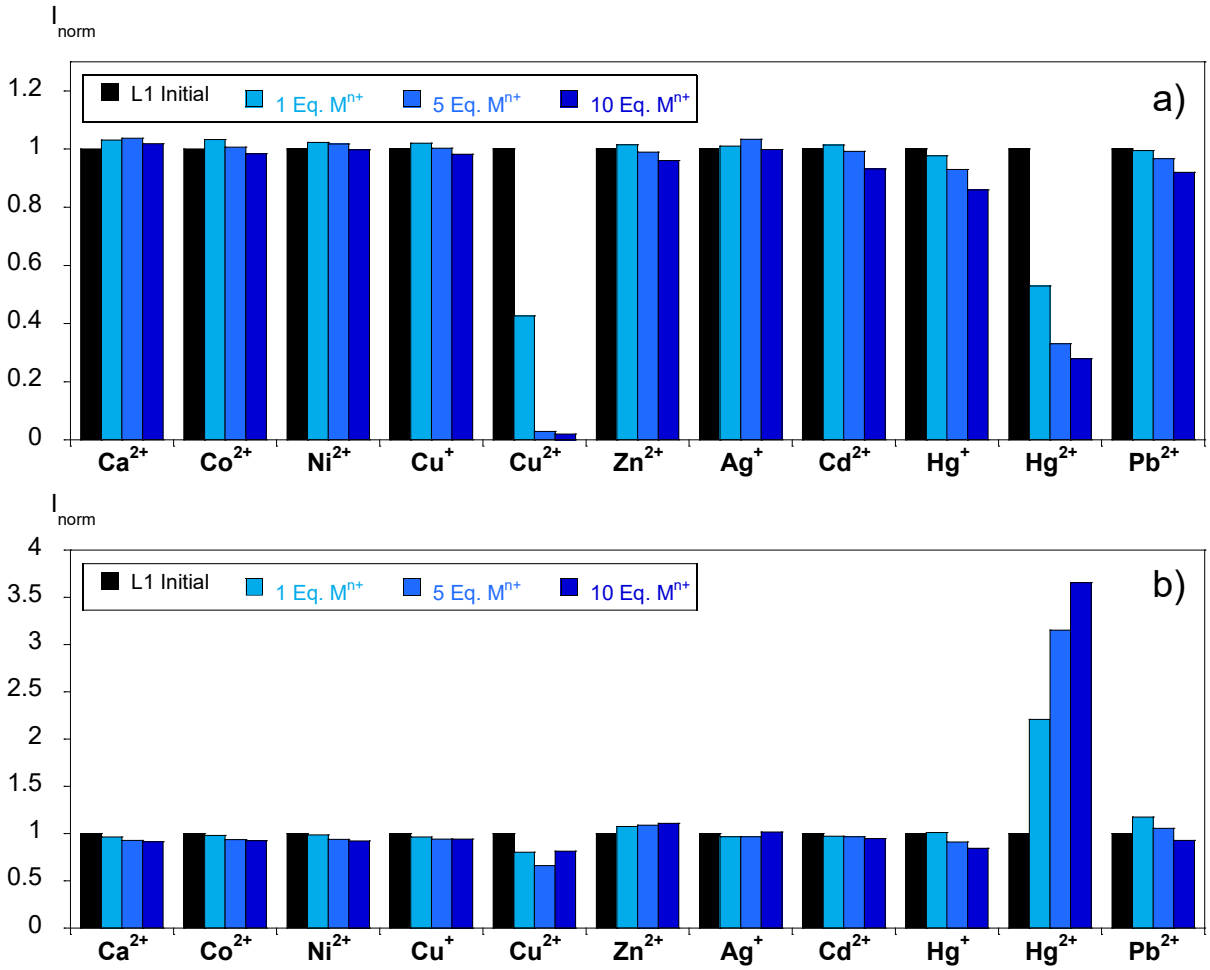


Figure 4–18. Normalized emission intensity of **L2** (a) and **L3** (b) upon addition of 1, 5, and 10 equivalents of Ca^{2+}, Co^{2+}, Ni^{2+}, Cu^{+}, Cu^{2+}, Zn^{2+}, Ag^{+}, Cd^{2+}, Hg^{+}, Hg^{2+} and Pb^{2+} metal ions. ([**L2**] = [**L3**] = 10μM). Emission spectra after the addition of 10 eq. of each metal for **L1** (c) and **L3** (d). For clarity of the reader the red spectrum corresponds to the initial fluorescence.

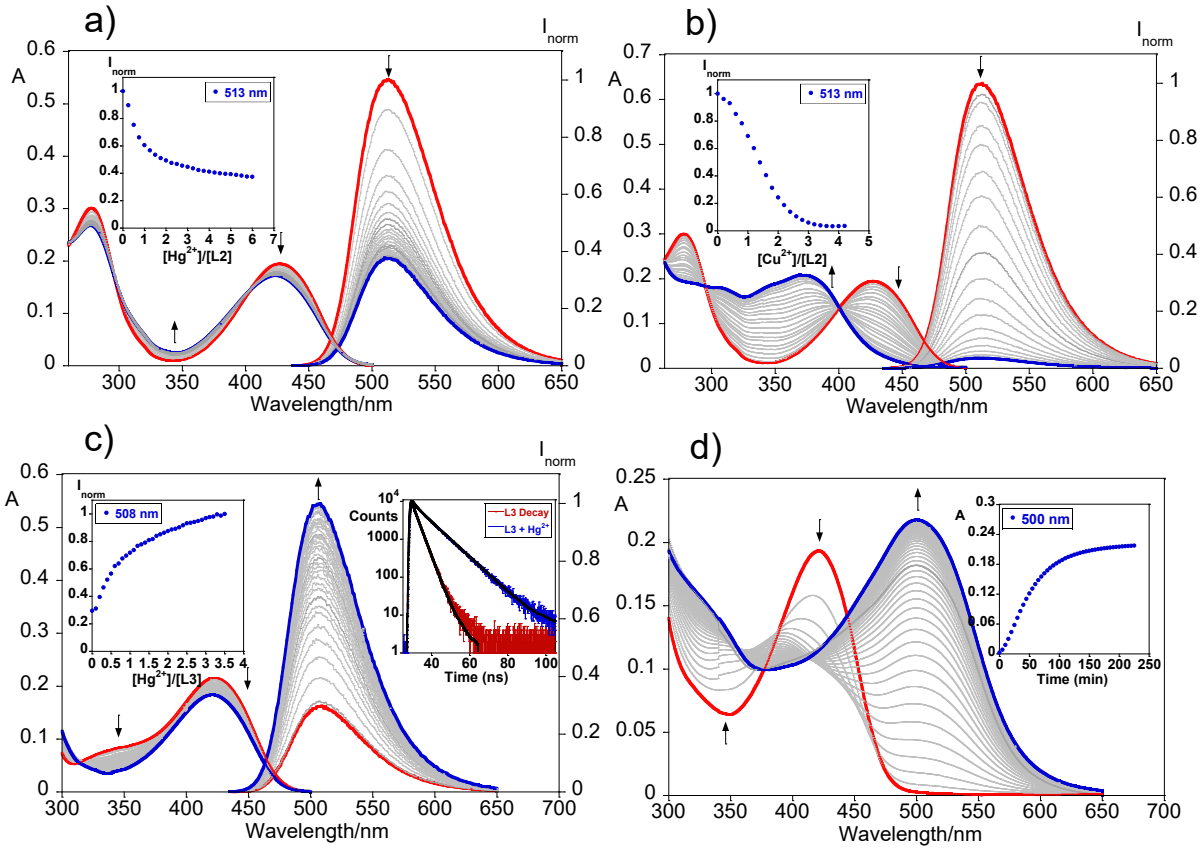


Figure 4–19. UV-Vis and luminescent titration of compound **L2** (a) upon continuous 4.8 μL additions of Hg^{2+} ([**L2**] = 10 μM; [Hg^{2+}] = 1.54 mM). The inset represents the emission of [Hg^{2+}]/[**L2**] at 513 nm. UV-Vis and luminescent titration of compound **L2** (b) upon continuous 20 μL additions of Cu^{2+} ions ([**L2**] = 10 μM; [Cu^{2+}] = 0.3 mM). The inset represents the emission of [Cu^{2+}]/[**L2**] at 513 nm. UV-Vis and luminescent titration of compound **L3** (c) upon continuous 10 μL additions of Hg^{2+} ([**L3**] = 10 μM; [Hg^{2+}] = 0.3 mM). The inset represents the emission of [Hg^{2+}]/[**L3**] at 508 nm (left) and the time-resolved fluorescence decay profile of **L3** before and after the titration with Hg^{2+} ions (right). UV-vis time continuous spectra of **L3** (d) after the addition of 8 eq. of Cu^{2+} ([**L3**] = 10 μM). The inset represents the time-dependent response of the absorbance at l = 500 nm (right). For clarity of the reader the red spectrum represents the initial spectrum and the blue at the end point of the titration while the black curves in the fluorescent decay profile represent the fitting obtained.

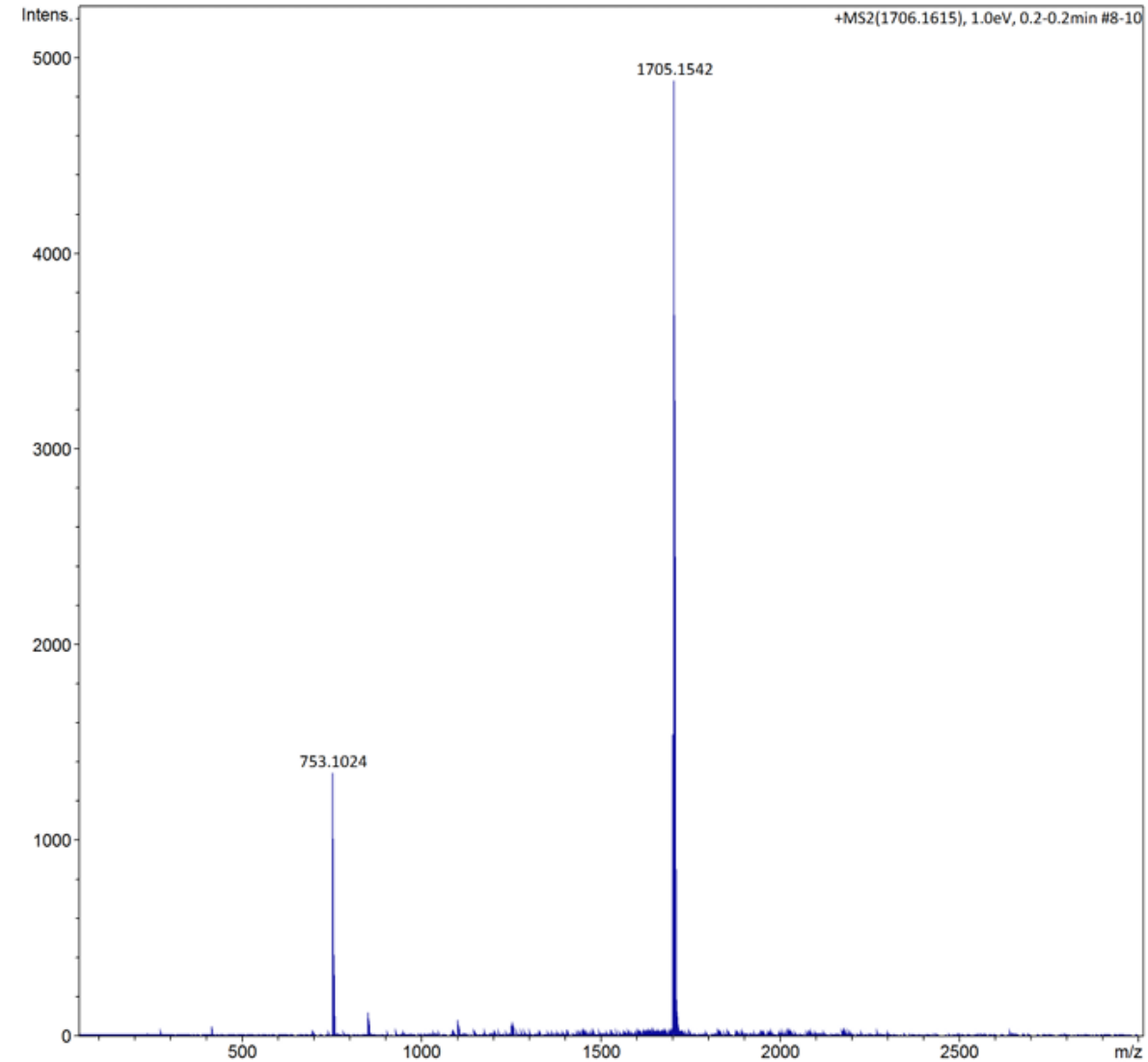
Display Report

Analysis Info

Analysis Name	D:\Data\BIOSCOPE\NEW IMPACT HD-00006\Small Molecules\Frederico\DR196Hg-1.d	Acquisition Date	3/24/2025 5:23:50 PM
Method	Small Molecules_Hg.m	Operator	BDAL@DE
Sample Name	DR196Hg	Instrument	impact HD 1819696.00006
Comment			

Acquisition Parameter

Source Type	ESI	Ion Polarity	Positive	Set Nebulizer	0.4 Bar
Focus	Not active	Set Capillary	4500 V	Set Dry Heater	180 °C
Scan Begin	50 m/z	Set End Plate Offset	-500 V	Set Dry Gas	4.0 l/min
Scan End	3000 m/z	Set Charging Voltage	2000 V	Set Divert Valve	Source
		Set Corona	0 nA	Set APCI Heater	0 °C



DR196Hg-1.d

Bruker Compass DataAnalysis 4.2 printed: 3/24/2025 3:40:26 PM by: BDAL@DE Page 1 of 1

Figure 4–20. ESI-HRMS spectrum of compound **L1** after the addition of Hg^{2+}.

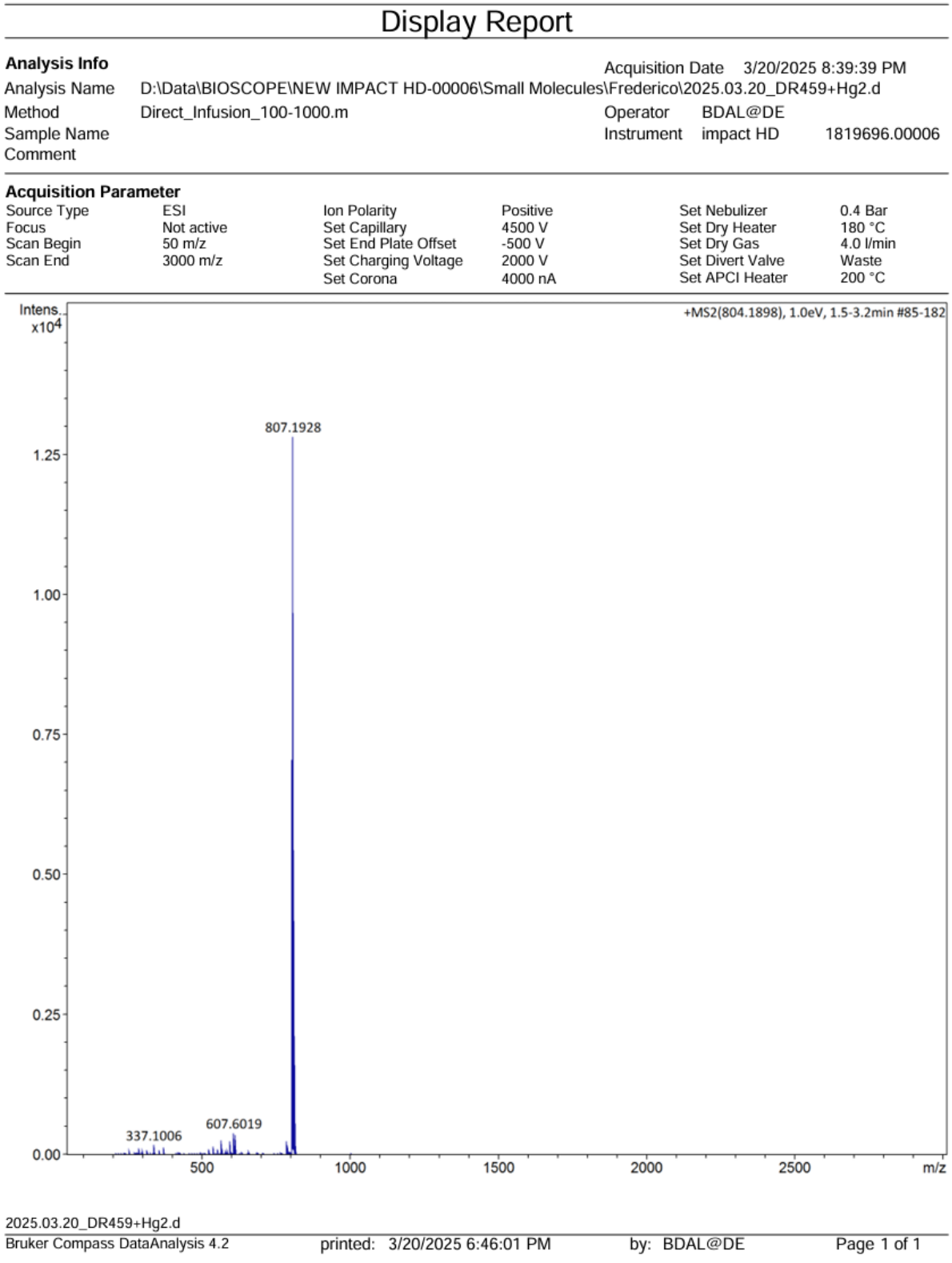


Figure 4–21. ESI-HRMS spectrum of compound **L3** after the addition of Hg^{2+}.

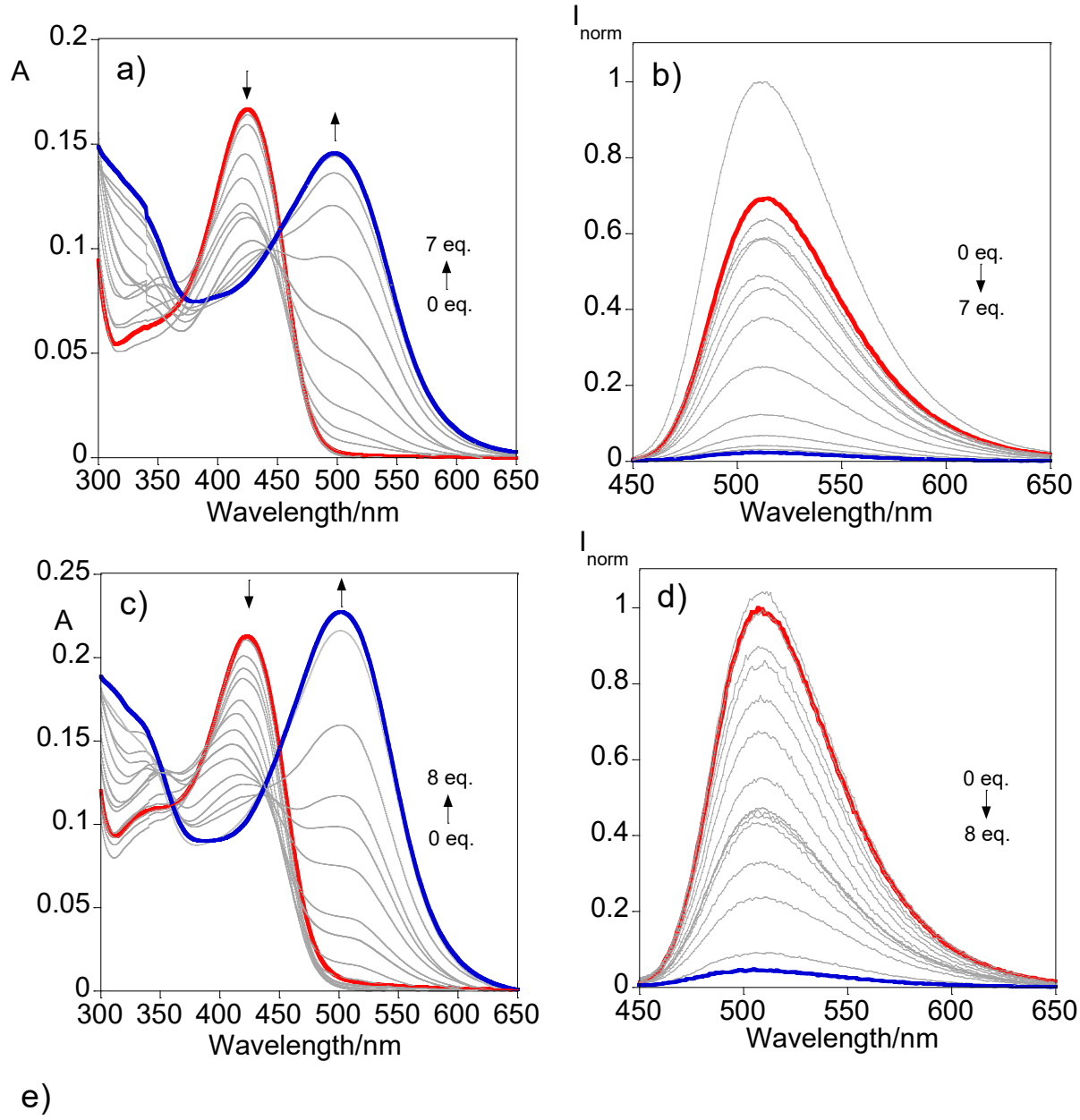


Figure 4–22. Absorption (a, c) and emission (b, d) spectra of the batch titrations recorded 24 hours after the incremental addition of 0.5 eq. of Cu^{2+} to a solution of (a, b) **L1** and (c, d) **L3** until it reached 7 and 8 eq., respectively ([**L1**] = [**L3**] = 10μM). Image of the batch titration of **L1**.

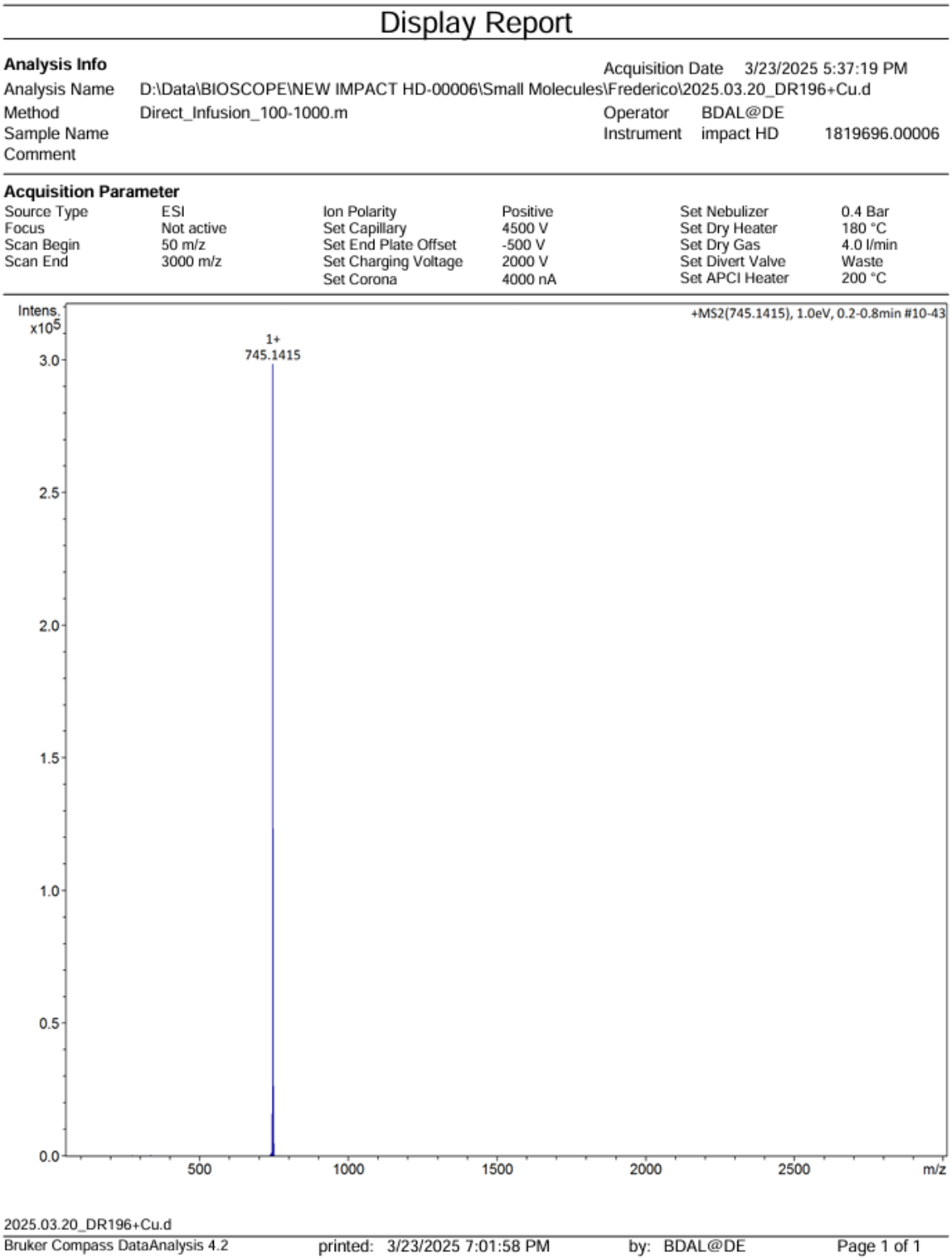


Figure 4–23. ESI-HRMS spectrum of compound **L1** after the addition of Cu^{2+}.

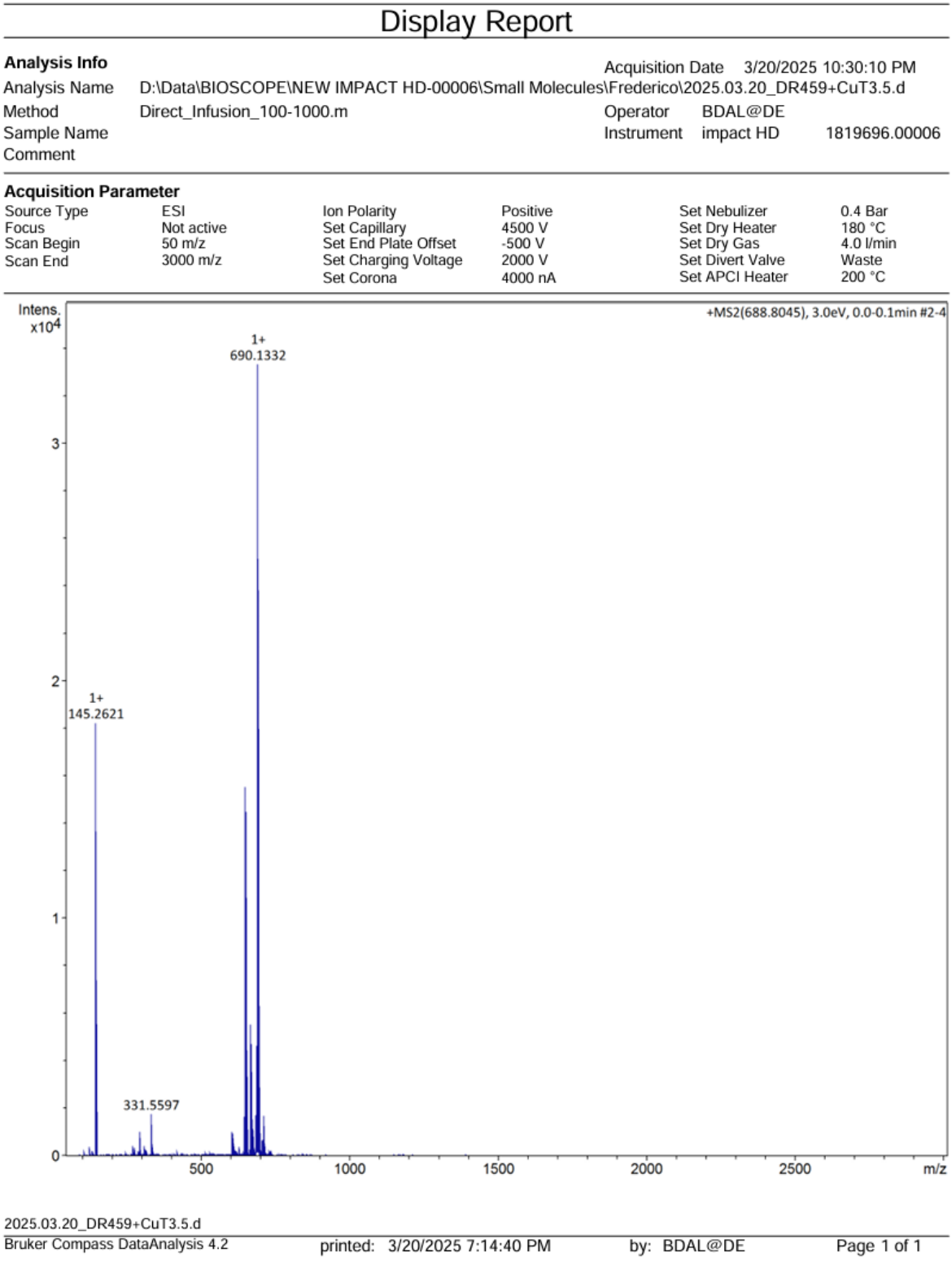


Figure 4–24. ESI-HRMS spectrum of compound **L3** after the addition of Cu^{2+}.

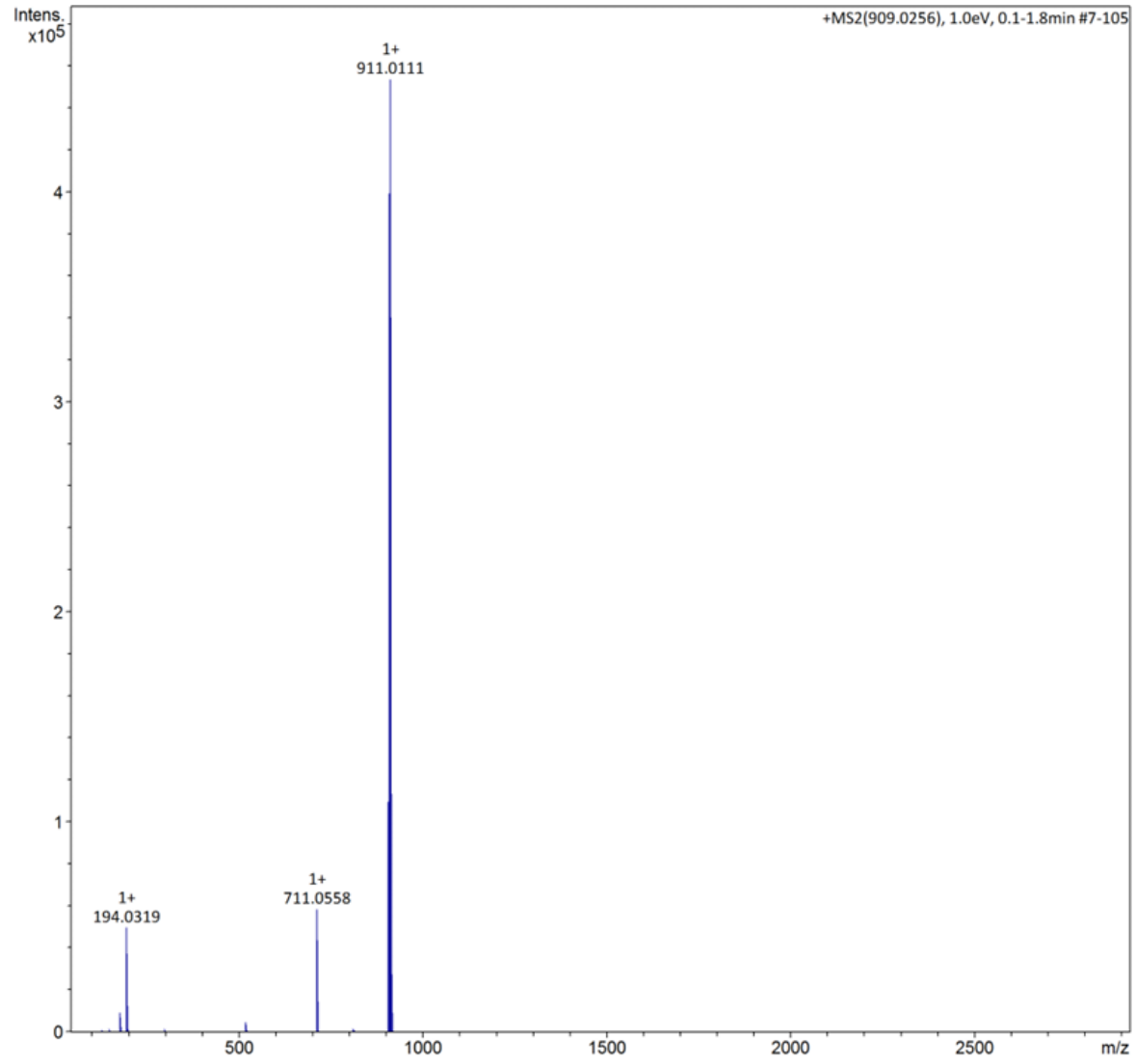
Display Report

Analysis Info

Analysis Name	D:\Data\BIOSCOPE\NEW IMPACT HD-00006\Small Molecules\Frederico\2025.03.20_DR375+Hg_T1.5min.d	Acquisition Date	3/27/2025 12:34:53 PM
Method	Direct_Infusion_100-1000.m	Operator	BDAL@DE
Sample Name		Instrument	impact HD 1819696.00006
Comment			

Acquisition Parameter

Source Type	ESI	Ion Polarity	Positive	Set Nebulizer	0.4 Bar
Focus	Not active	Set Capillary	4500 V	Set Dry Heater	180 °C
Scan Begin	50 m/z	Set End Plate Offset	-500 V	Set Dry Gas	4.0 l/min
Scan End	3000 m/z	Set Charging Voltage	2000 V	Set Divert Valve	Waste
		Set Corona	4000 nA	Set APCI Heater	200 °C



2025.03.20_DR375+Hg_T1.5min.d
Bruker Compass DataAnalysis 4.2 printed: 3/27/2025 12:44:13 PM by: BDAL@DE Page 1 of 1

Figure 4–25. ESI-HRMS spectrum of compound **L2** after the addition of Hg^{2+}.

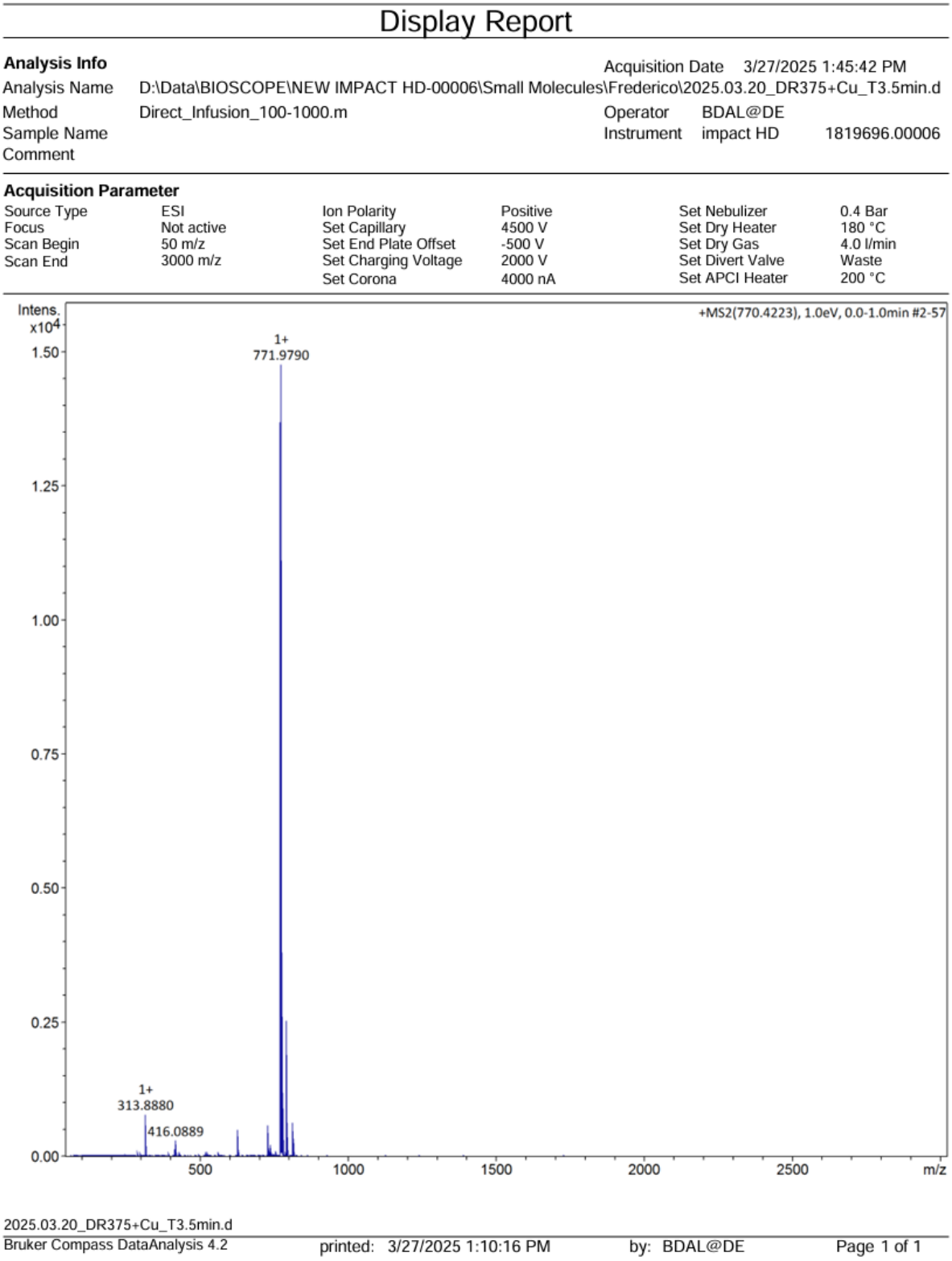


Figure 4–26. ESI-HRMS spectrum of compound **L2** after the addition of Cu^{2+}.

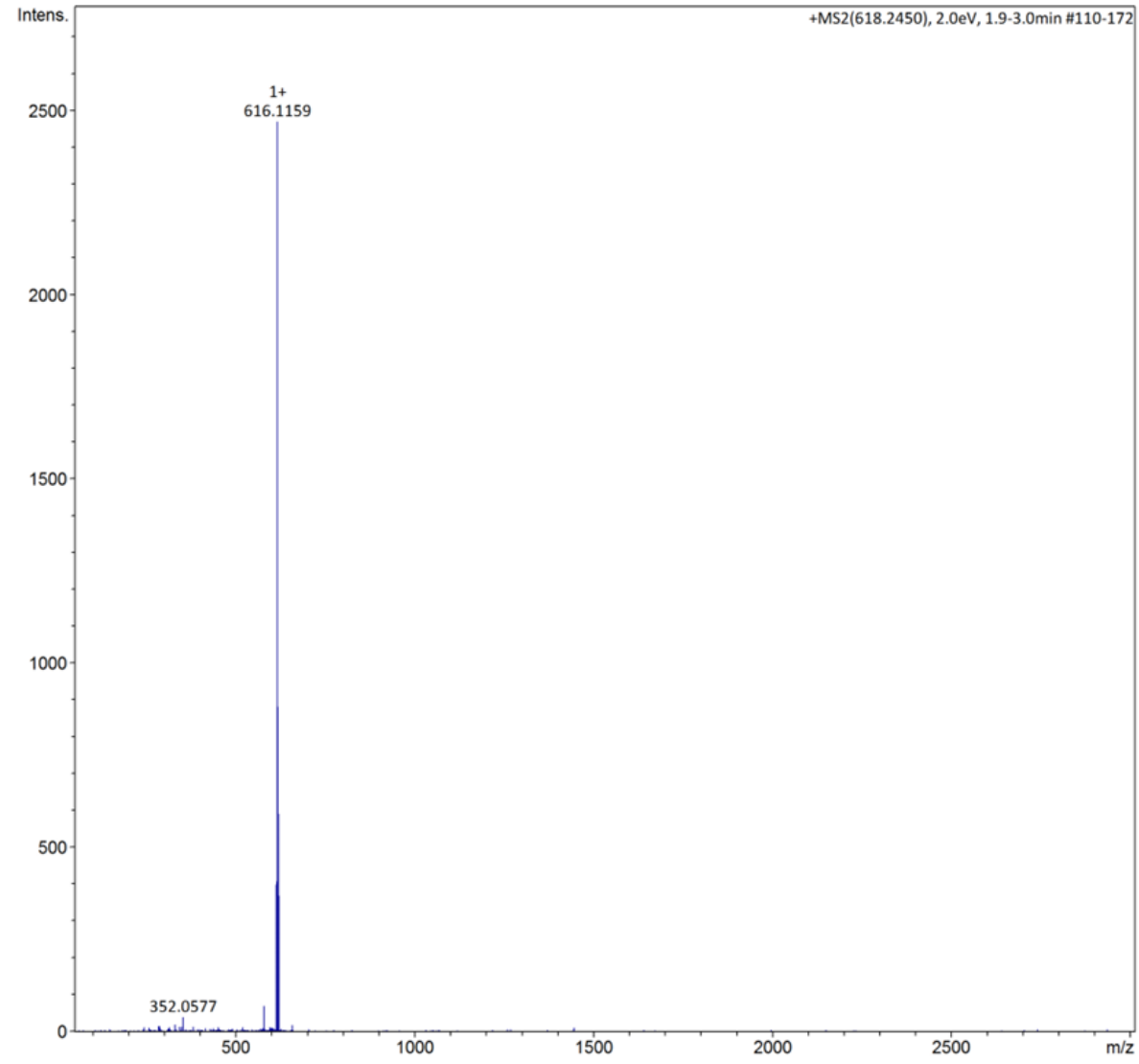
Display Report

Analysis Info

Analysis Name	D:\Data\BIOSCOPE\NEW IMPACT HD-00006\Small Molecules\Frederico\2025.03.20_DK111+Hg.d	Acquisition Date	3/20/2025 11:30:24 AM
Method	Direct_Infusion_100-1000.m	Operator	BDAL@DE
Sample Name		Instrument	impact HD 1819696.00006
Comment			

Acquisition Parameter

Source Type	ESI	Ion Polarity	Positive	Set Nebulizer	0.4 Bar
Focus	Not active	Set Capillary	4500 V	Set Dry Heater	180 °C
Scan Begin	50 m/z	Set End Plate Offset	-500 V	Set Dry Gas	4.0 l/min
Scan End	3000 m/z	Set Charging Voltage	2000 V	Set Divert Valve	Waste
		Set Corona	4000 nA	Set APCI Heater	200 °C



2025.03.20_DK111+Hg.d

Bruker Compass DataAnalysis 4.2 printed: 3/23/2025 3:22:03 PM by: BDAL@DE Page 1 of 1

Figure 4–27. ESI-HRMS spectrum of compound **L4** after the addition of Hg^{2+}.

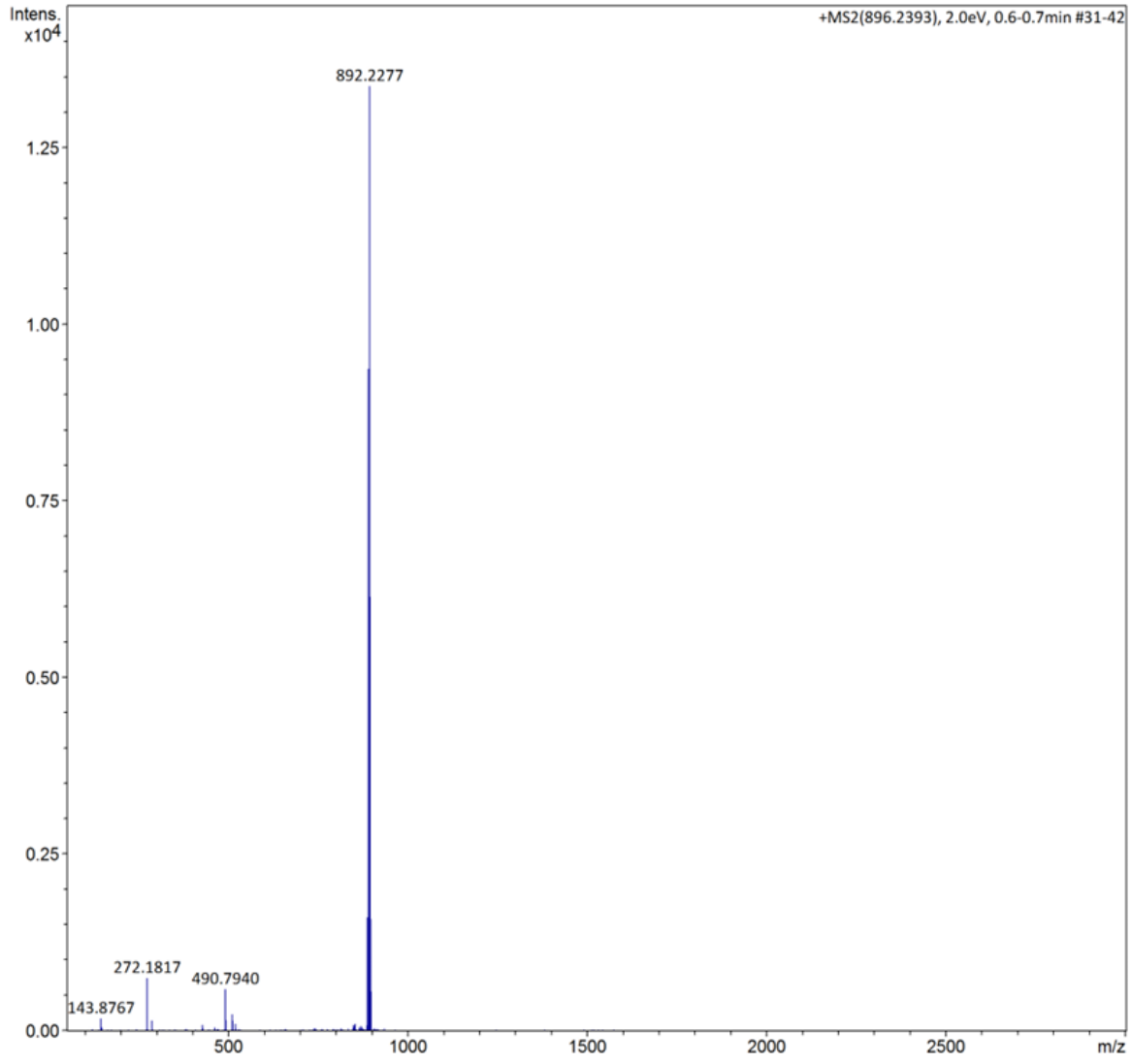
Display Report

Analysis Info

Analysis Name	D:\Data\BIOSCOPE\NEW IMPACT HD-00006\Small Molecules\Frederico\2025.03.20_DK111+Cu_T3.5.d	Acquisition Date	3/20/2025 3:15:52 PM
Method	Direct_Infusion_100-1000.m	Operator	BDAL@DE
Sample Name		Instrument	impact HD 1819696.00006
Comment			

Acquisition Parameter

Source Type	ESI	Ion Polarity	Positive	Set Nebulizer	0.4 Bar
Focus	Not active	Set Capillary	4500 V	Set Dry Heater	180 °C
Scan Begin	50 m/z	Set End Plate Offset	-500 V	Set Dry Gas	4.0 l/min
Scan End	3000 m/z	Set Charging Voltage	2000 V	Set Divert Valve	Waste
		Set Corona	4000 nA	Set APCI Heater	200 °C



2025.03.20_DK111+Cu_T3.5.d

Bruker Compass DataAnalysis 4.2 printed: 3/20/2025 2:38:33 PM by: BDAL@DE Page 1 of 1

Figure 4–28. ESI-HRMS spectrum of compound **L4** after the addition of Cu^{2+}.

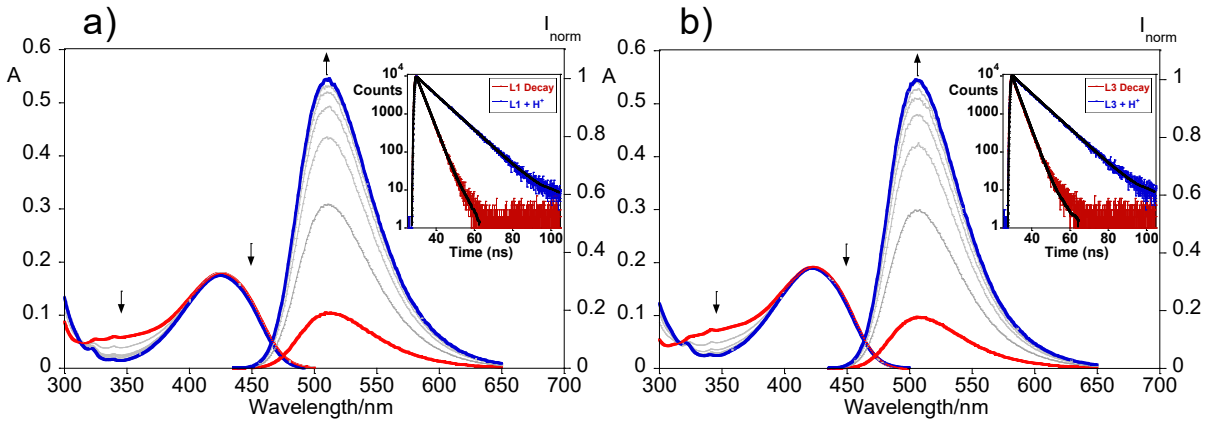


Figure 4–29. UV-Vis and luminescent titration of compound **L1** (a) and **L3** (b) upon continuous 10 μL additions of H^+ ([**L3**] = 10 μM; [H^+] = 0.3 mM). The inset represents the time-resolved fluorescence decay profile of **L1** and **L3** before and after the titration with H^+ ions.

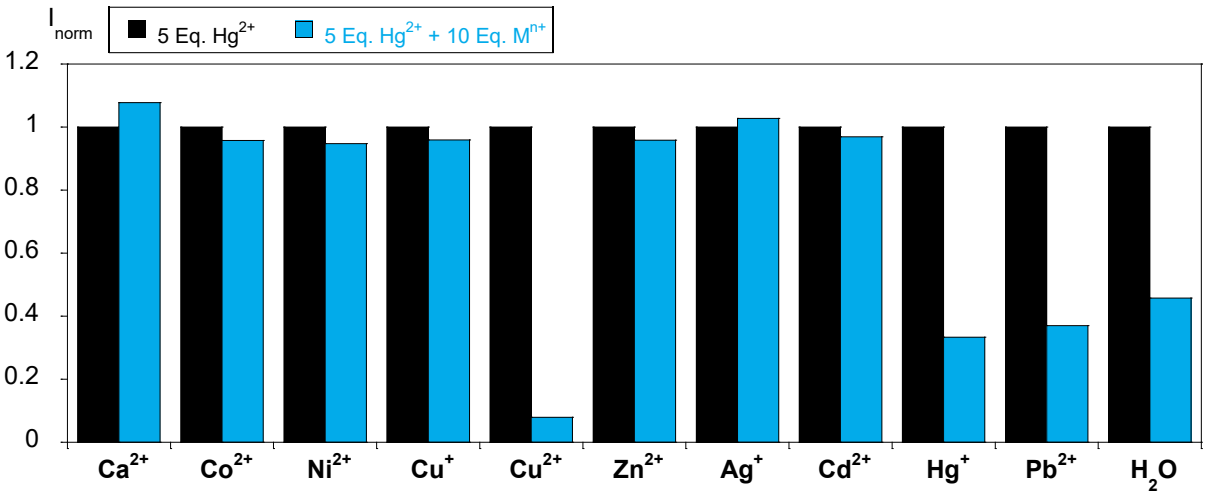


Figure 4–30. Normalized emission response of **L3** (a) in the presence of 5 equivalents Hg^{2+} and additional metal ions in acetonitrile. ([**L3**] = 10μM, T = 298K).

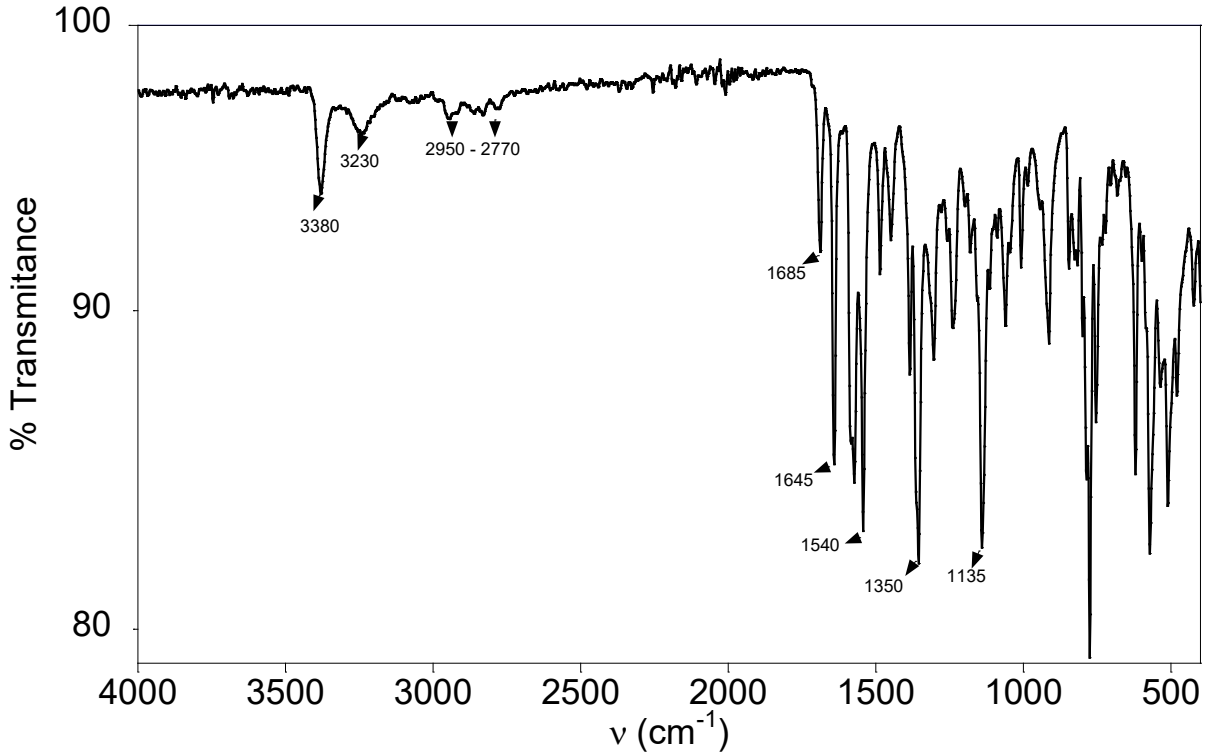


Figure 4–31. Infrared spectrum of compound **L1**.

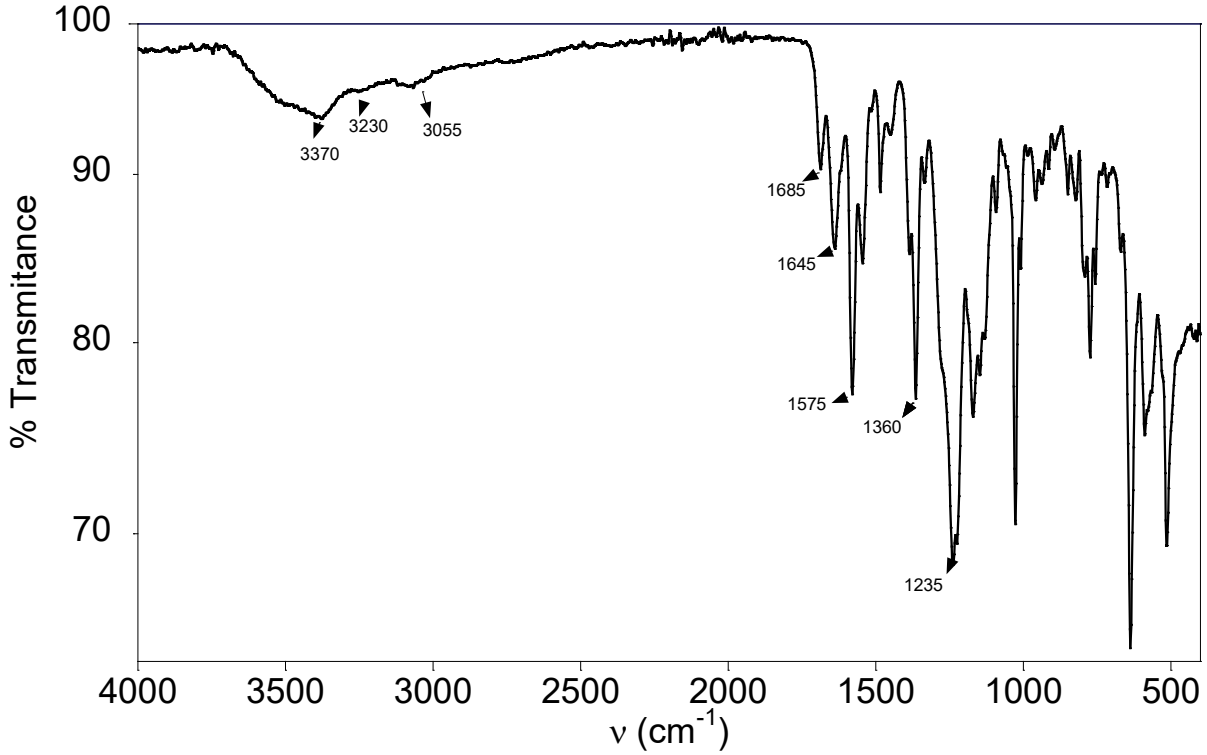


Figure 4–32. Infrared spectrum of $[Hg(II)\mathbf{L1}_2]^{2+}$.

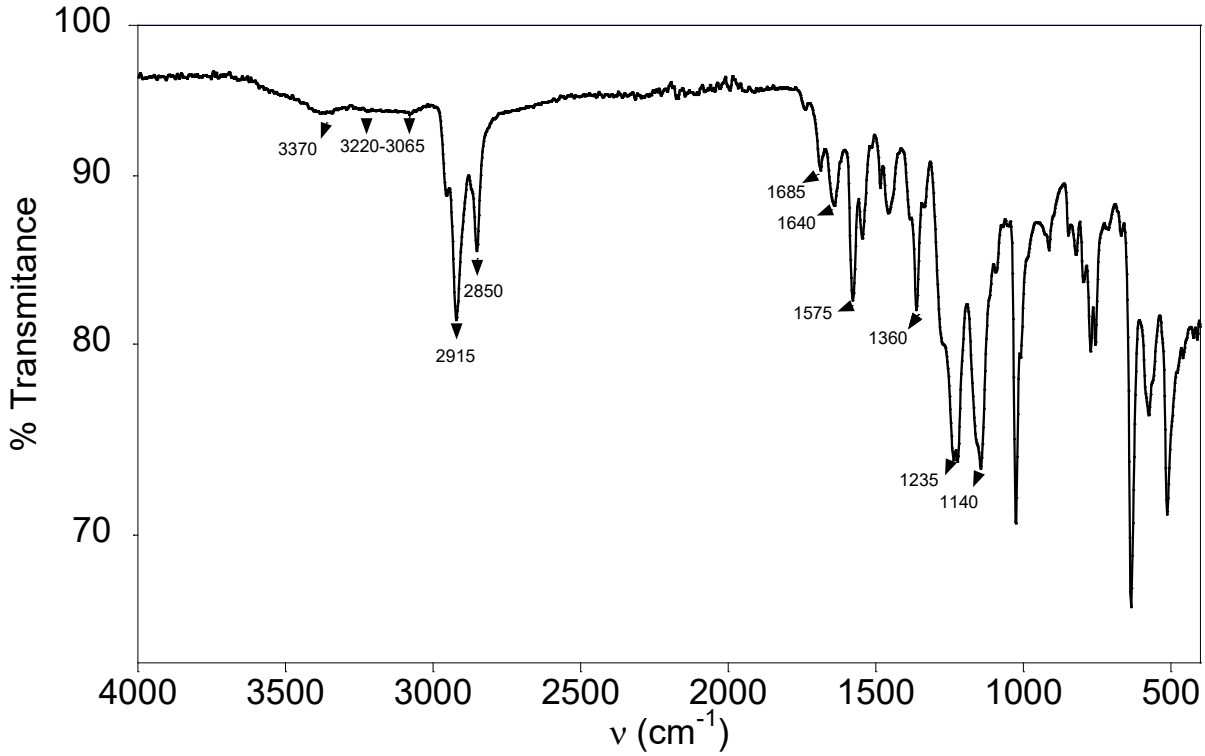


Figure 4–33. Infrared spectrum of $[Cu(II)\mathbf{L1}_2]^{2+}$.

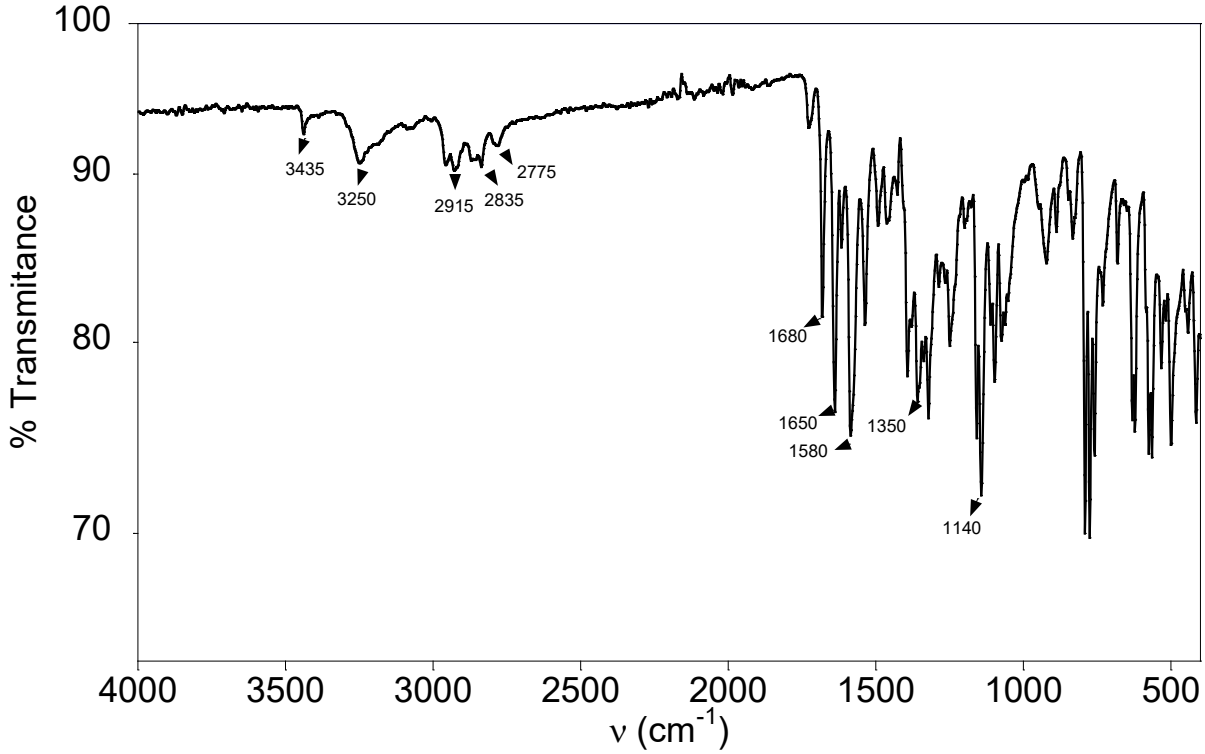


Figure 4–34. Infrared spectrum of compound **L3**.

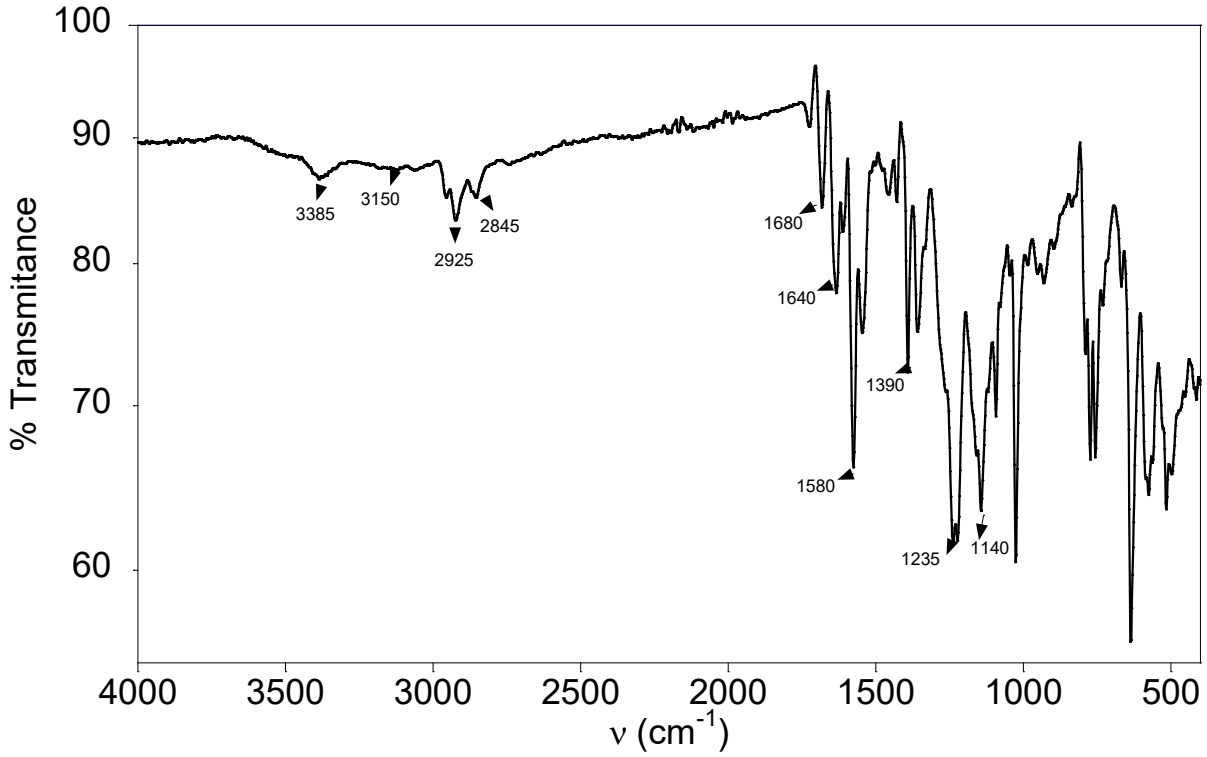


Figure 4–35. Infrared spectrum of $[Hg(II)\mathbf{L3}_2]^{2+}$.

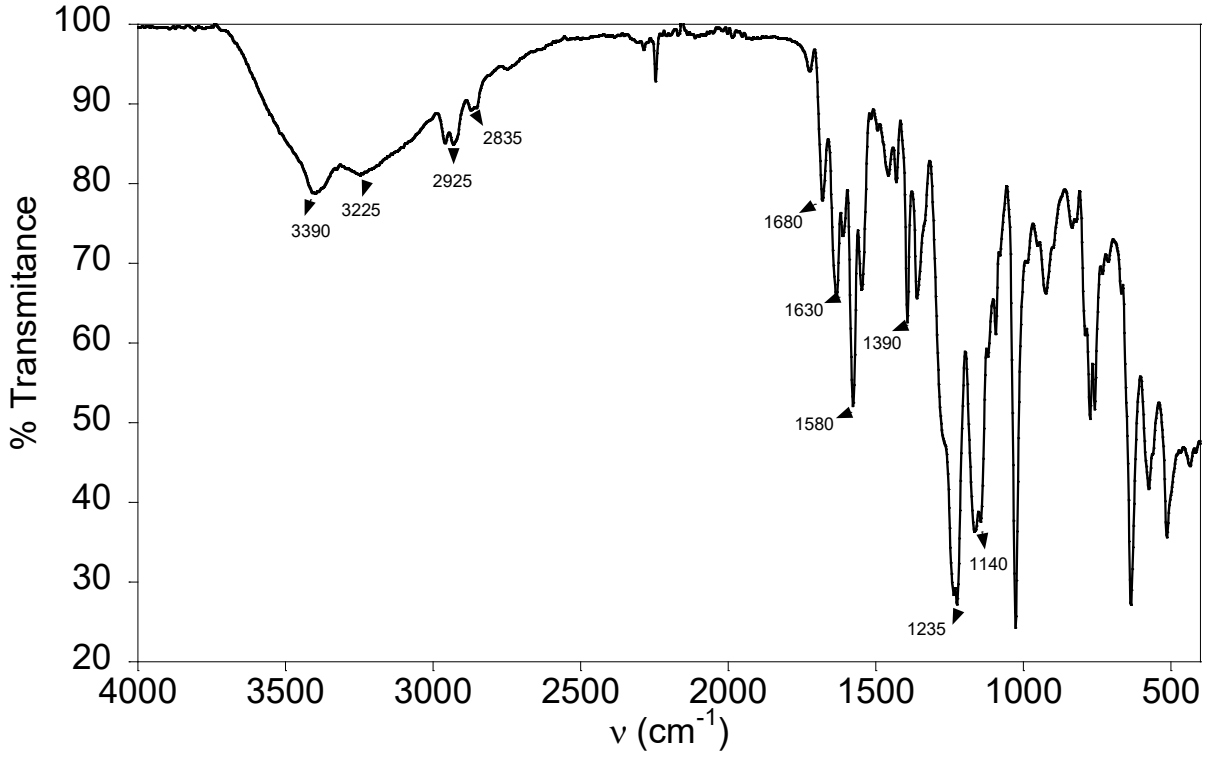


Figure 4–36. Infrared spectrum of $[Cu(II)\mathbf{L3}_2]^{2+}$.

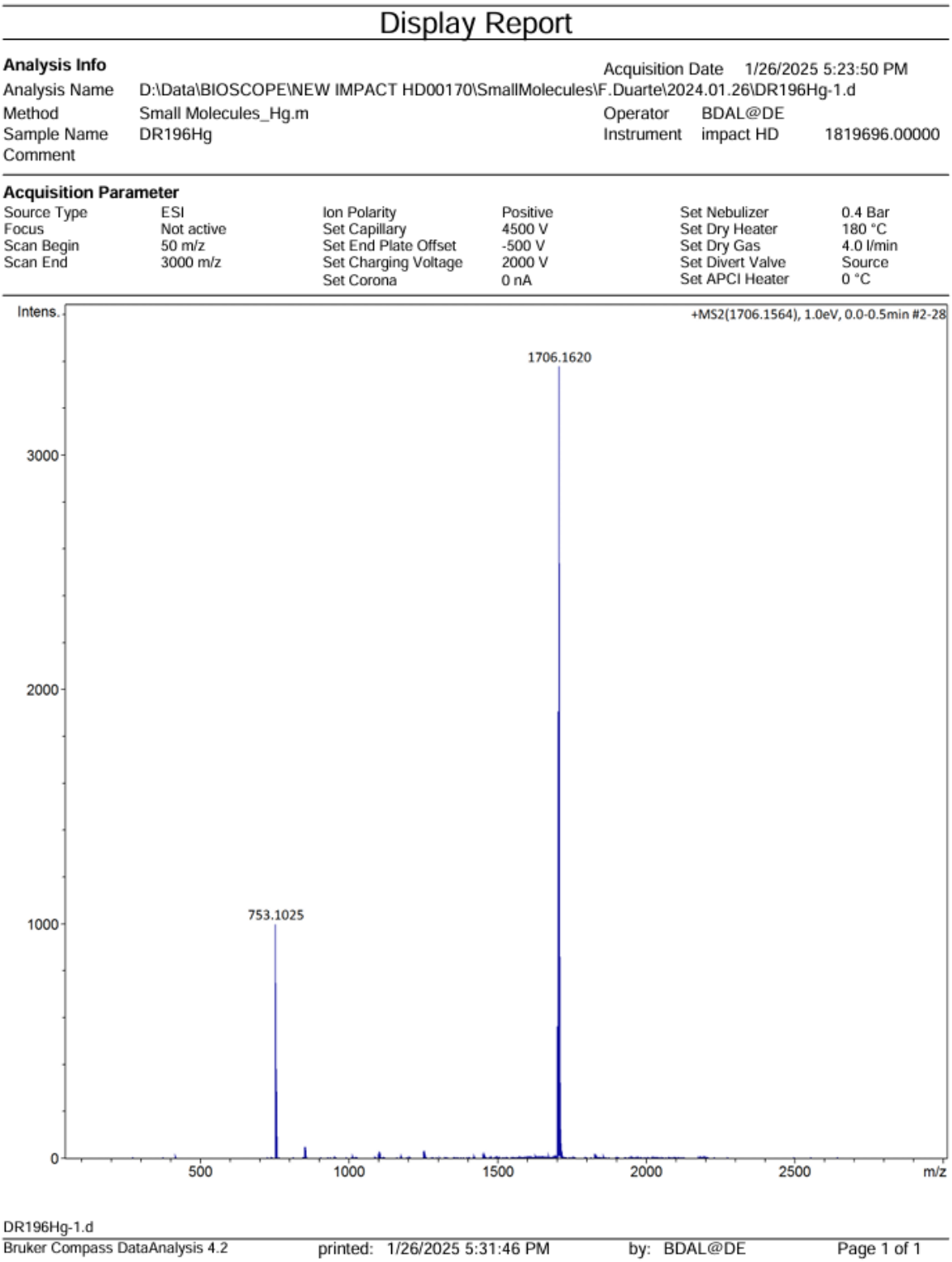


Figure 4–37. ESI-HRMS spectrum of $[Hg(II)\mathbf{L1}_2]^{2+}$.

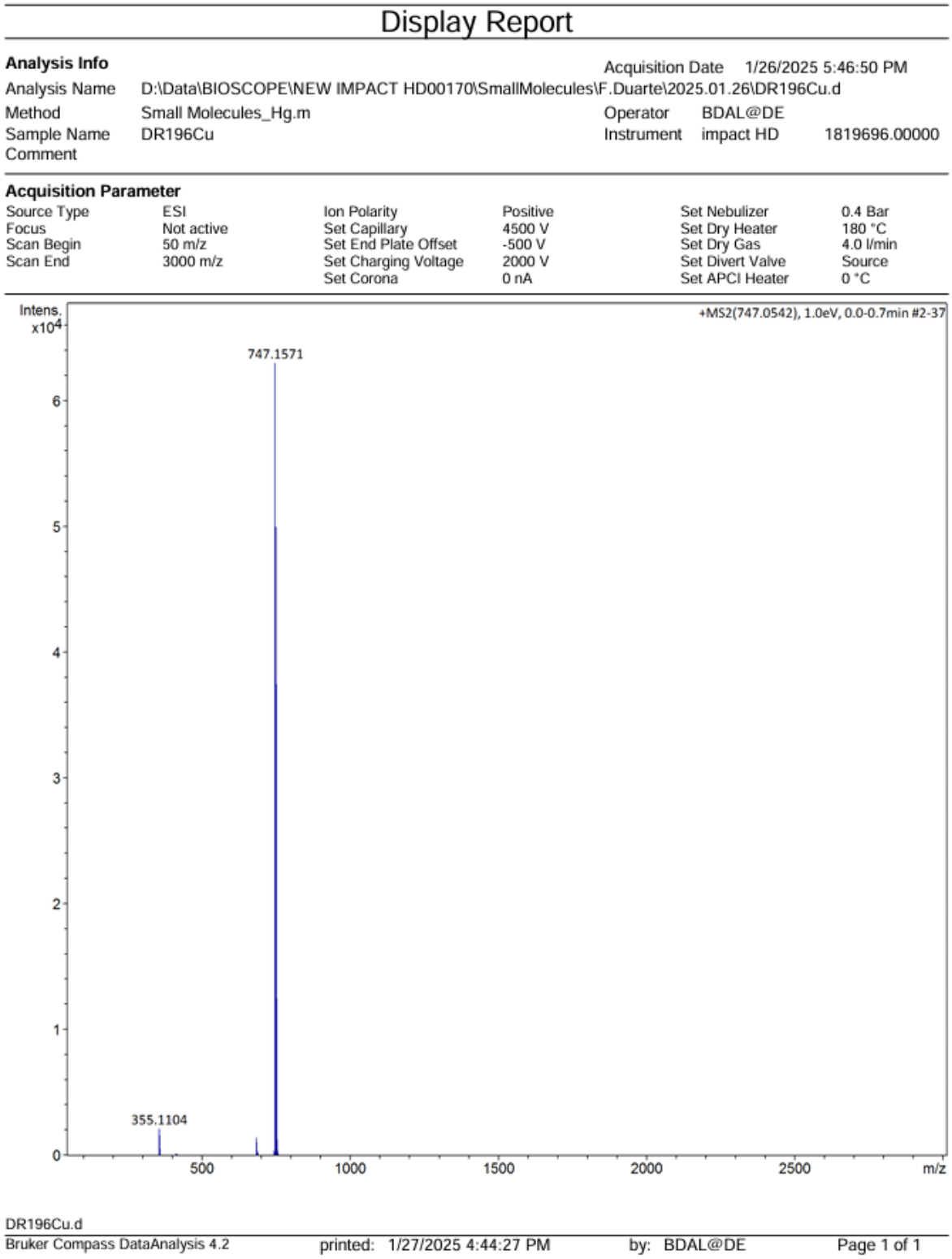


Figure 4–38. ESI-HRMS spectrum of $[Cu(II)\mathbf{L1}_2]^{2+}$.

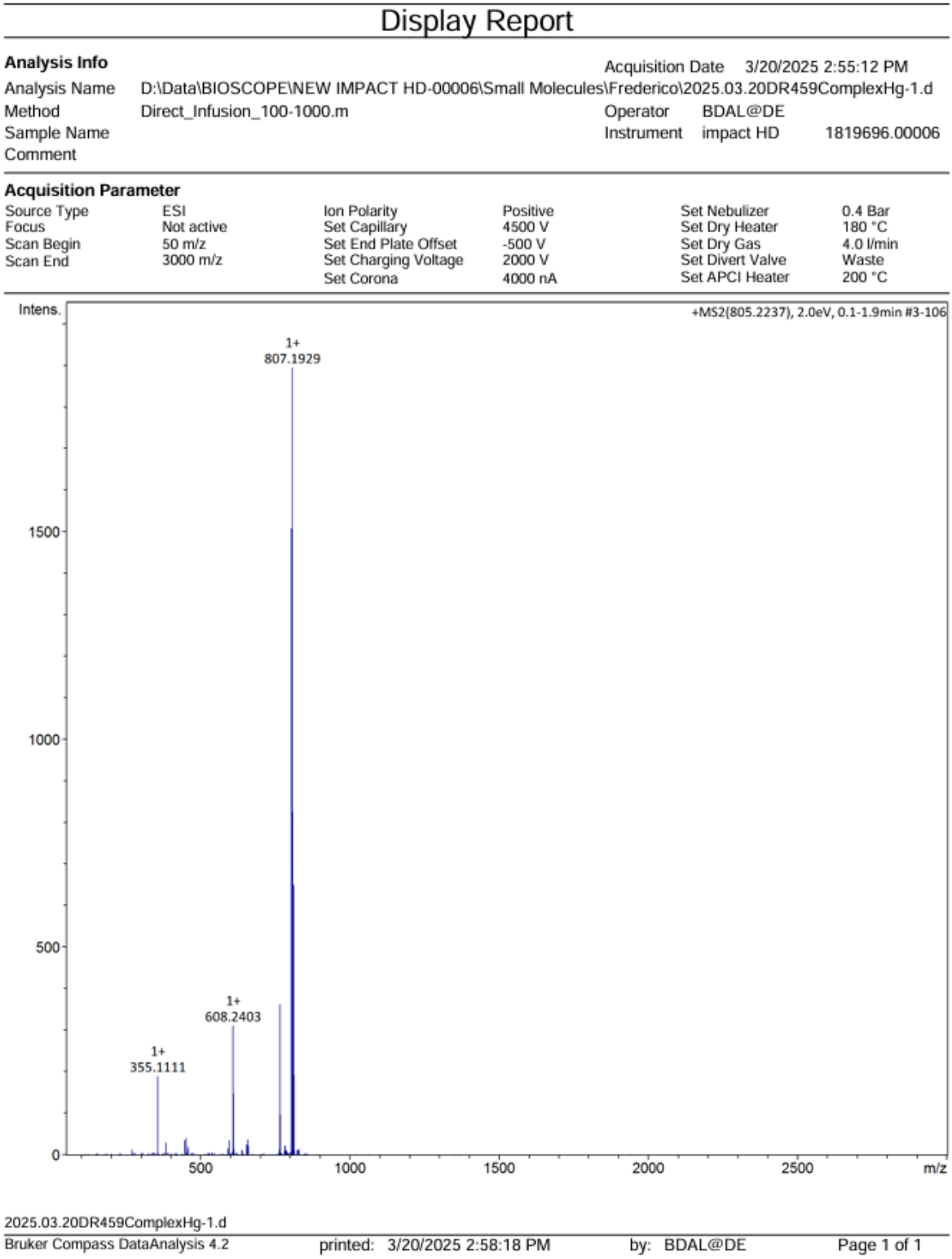


Figure 4–39. ESI-HRMS spectrum of $[Hg(II)\mathbf{L3}_2]^{2+}$.

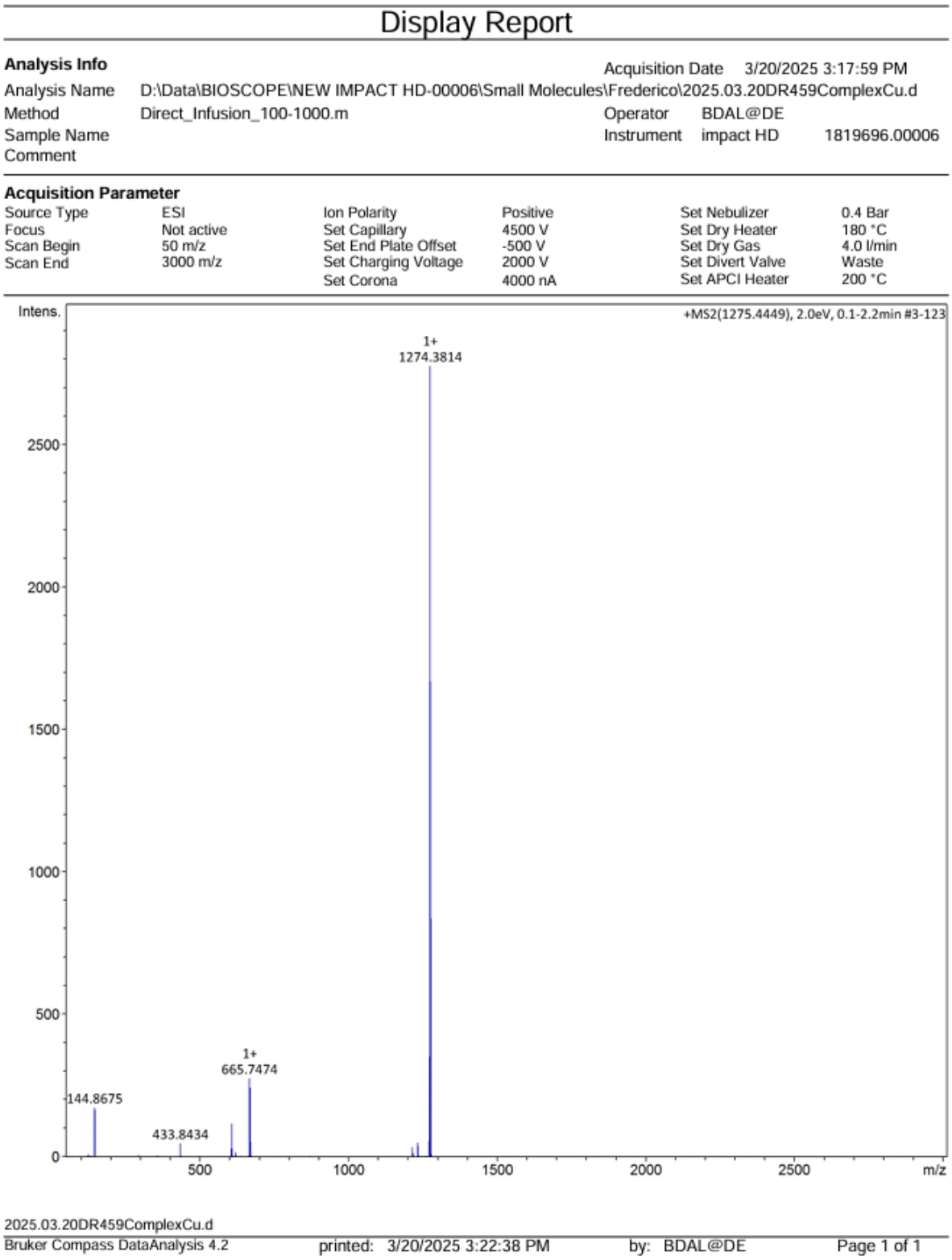


Figure 4–40. ESI-HRMS spectrum of $[Cu(II)\mathbf{L3}_2]^{2+}$.

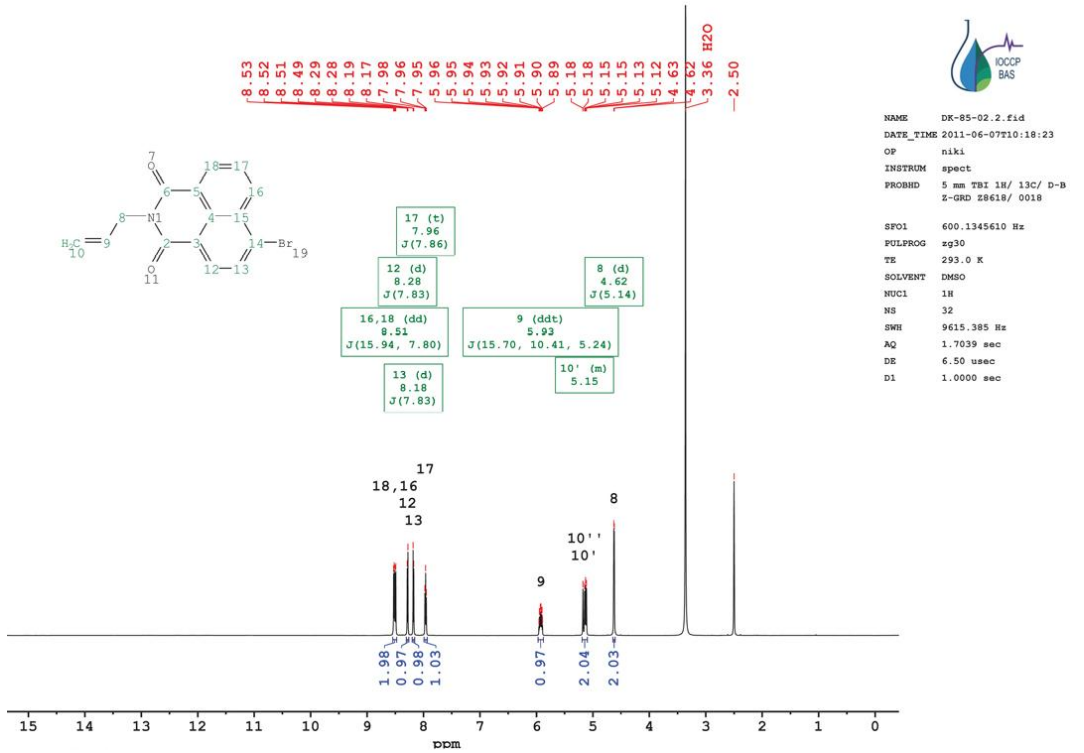


Figure 4–41. ^{1}H-NMR spectrum of compound **3** in DMSO.

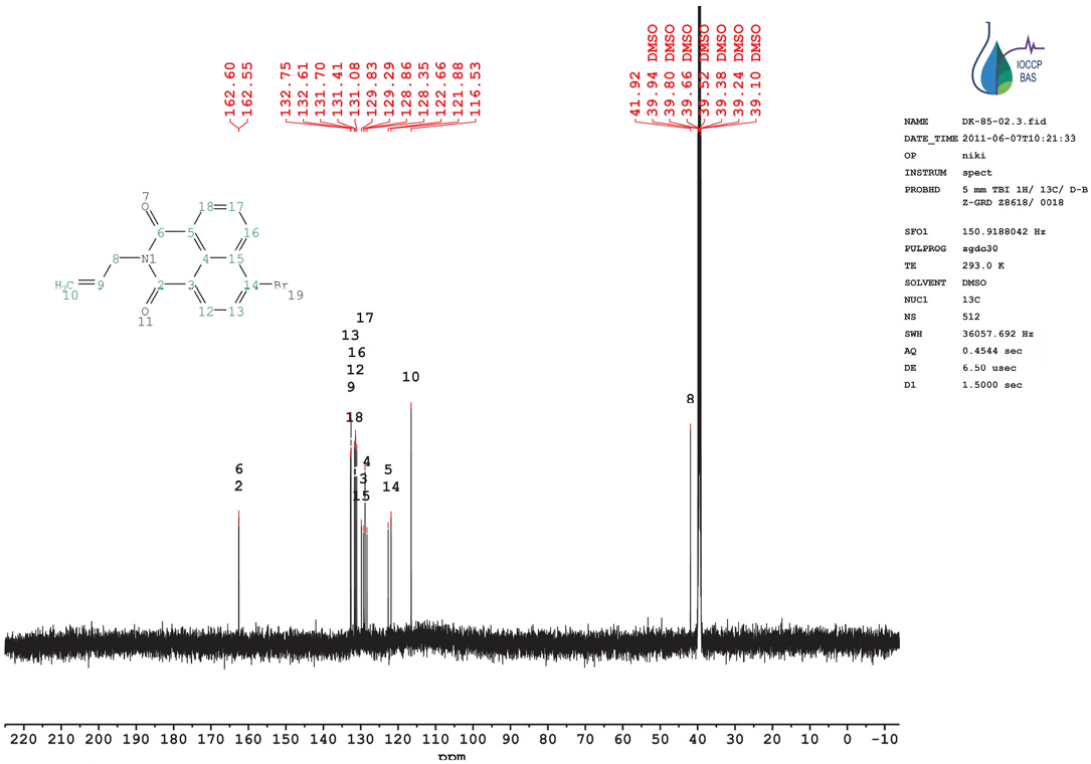


Figure 4–42. ^{13}C-NMR spectrum of compound **3** in DMSO.

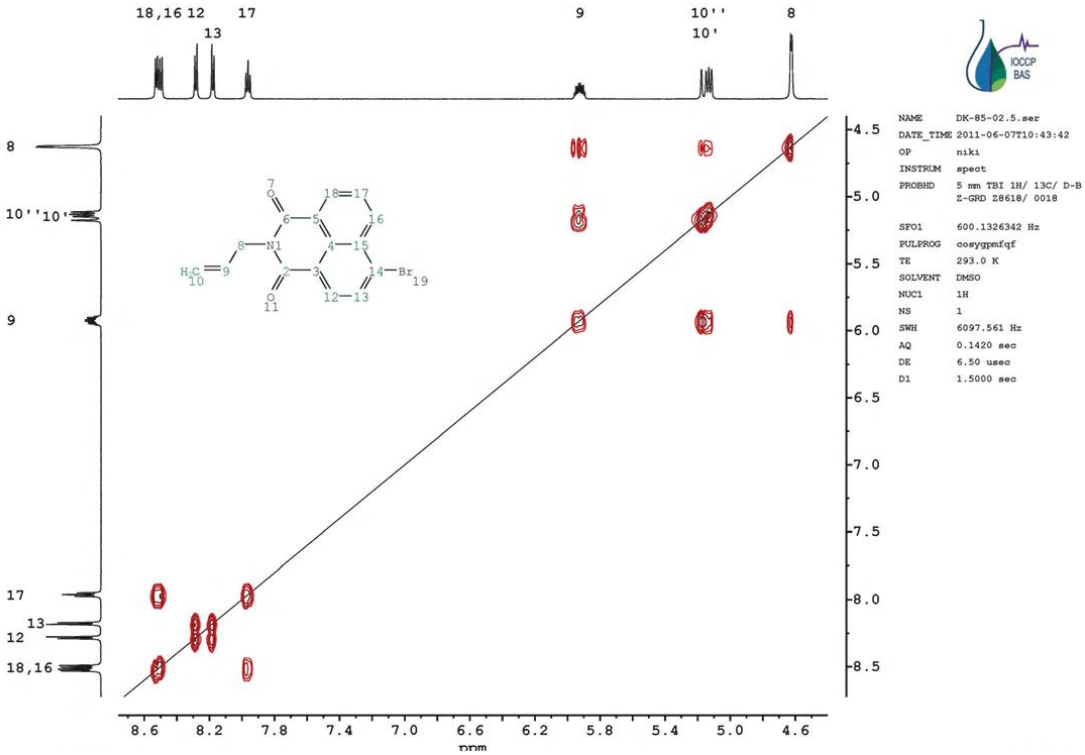


Figure 4–43. COSY-NMR spectrum of compound **3** in DMSO.

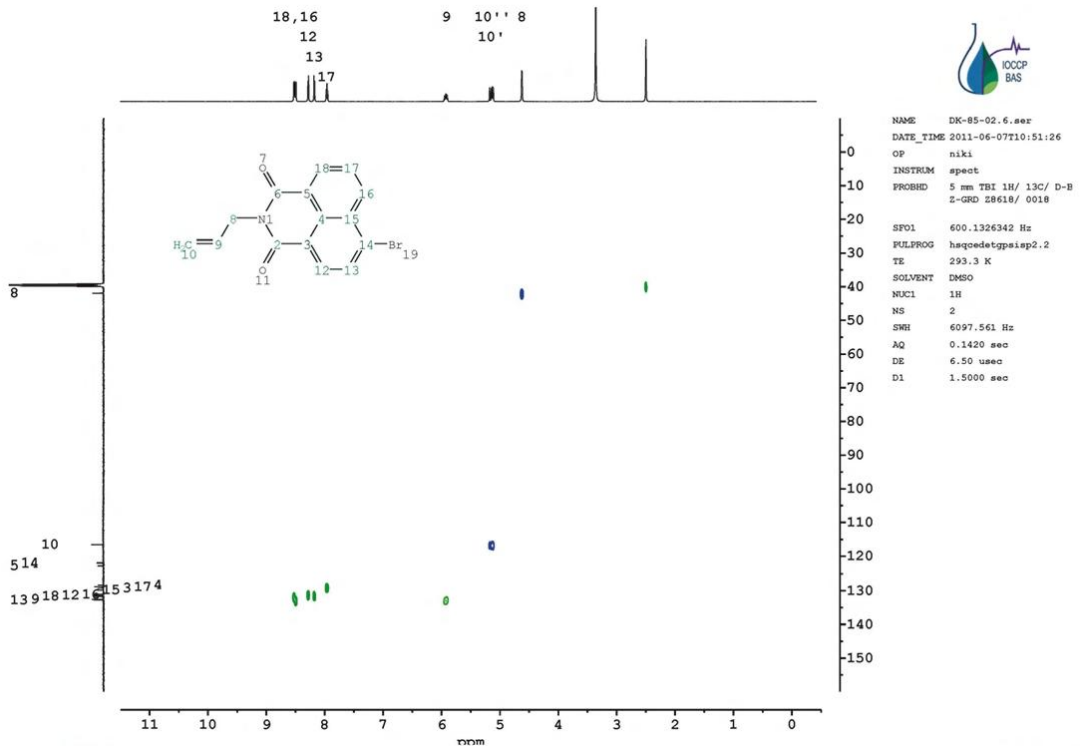


Figure 4–44. HSQC-NMR spectrum of compound **3** in DMSO.

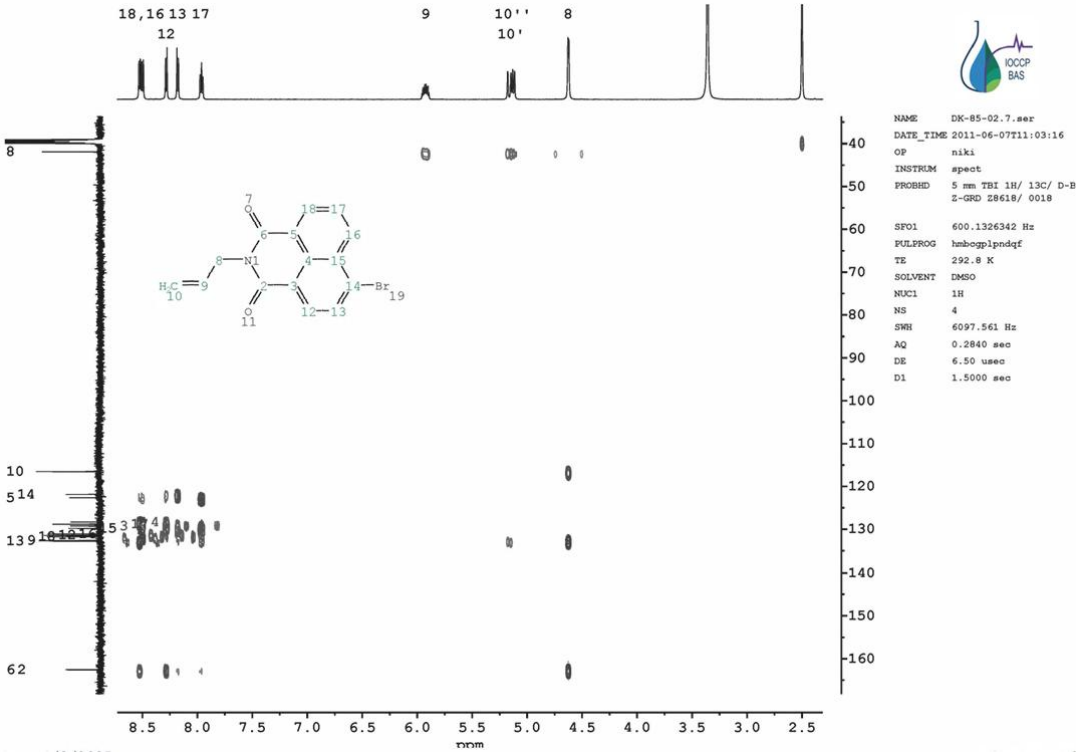


Figure 4–45. HMBC-NMR spectrum of compound **3** in DMSO.

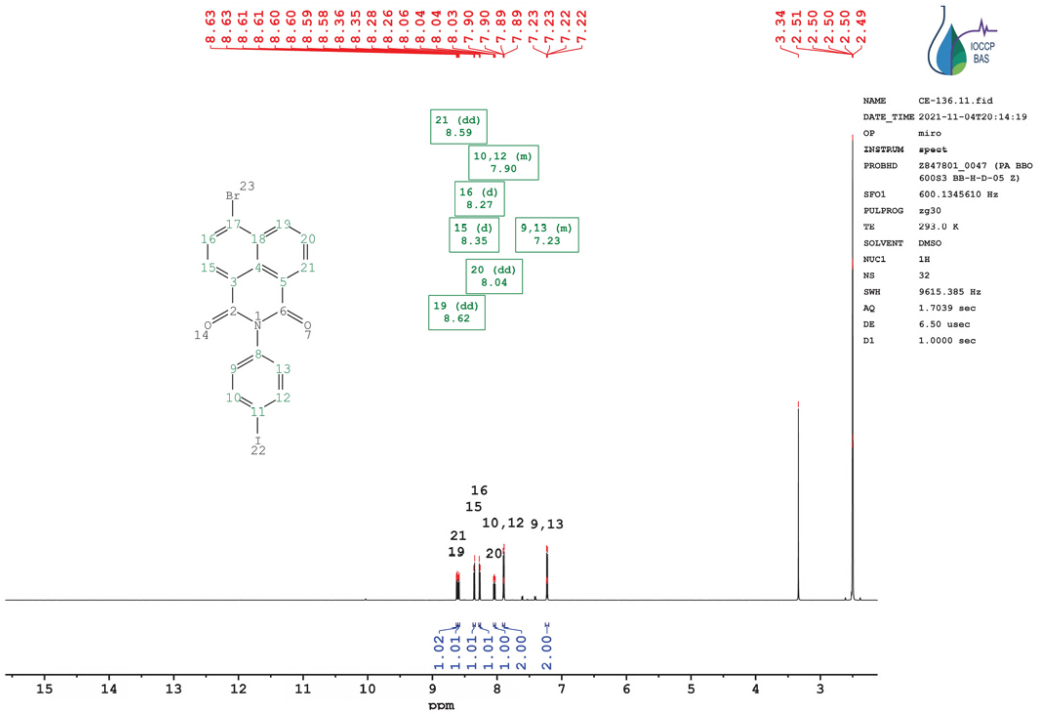


Figure 4–46. ^{1}H-NMR spectrum of compound **5** in DMSO.

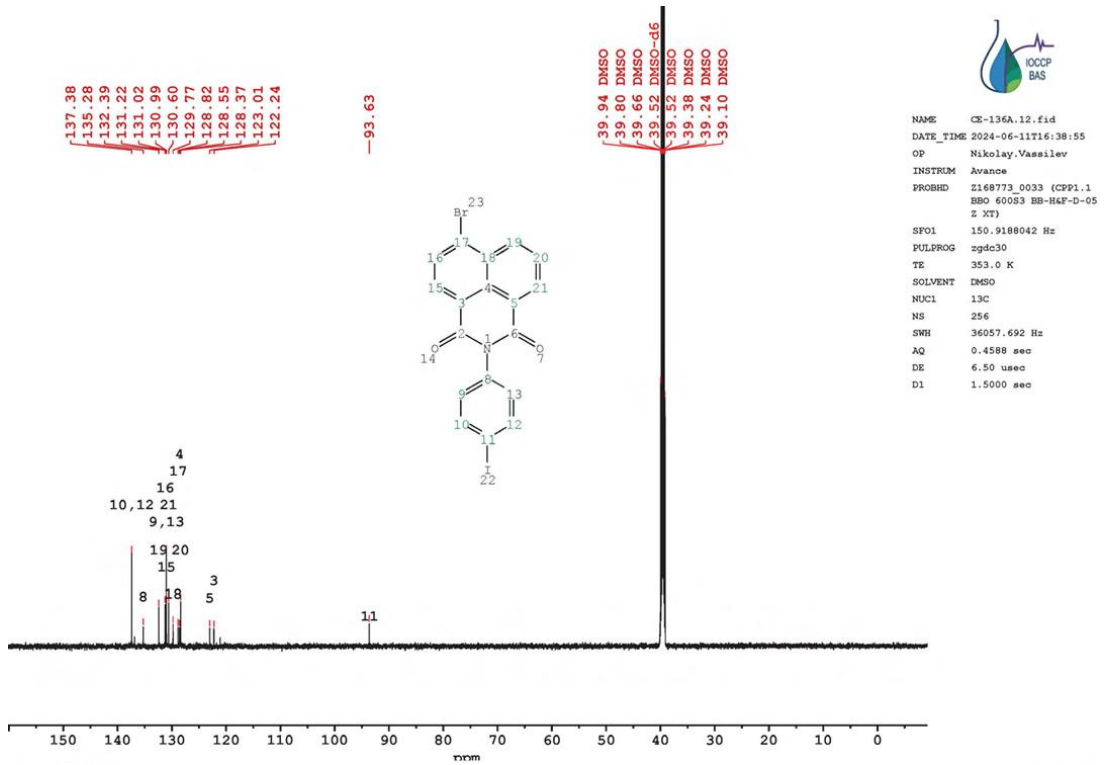


Figure 4–47. ^{13}C-NMR spectrum of compound **5** in DMSO.

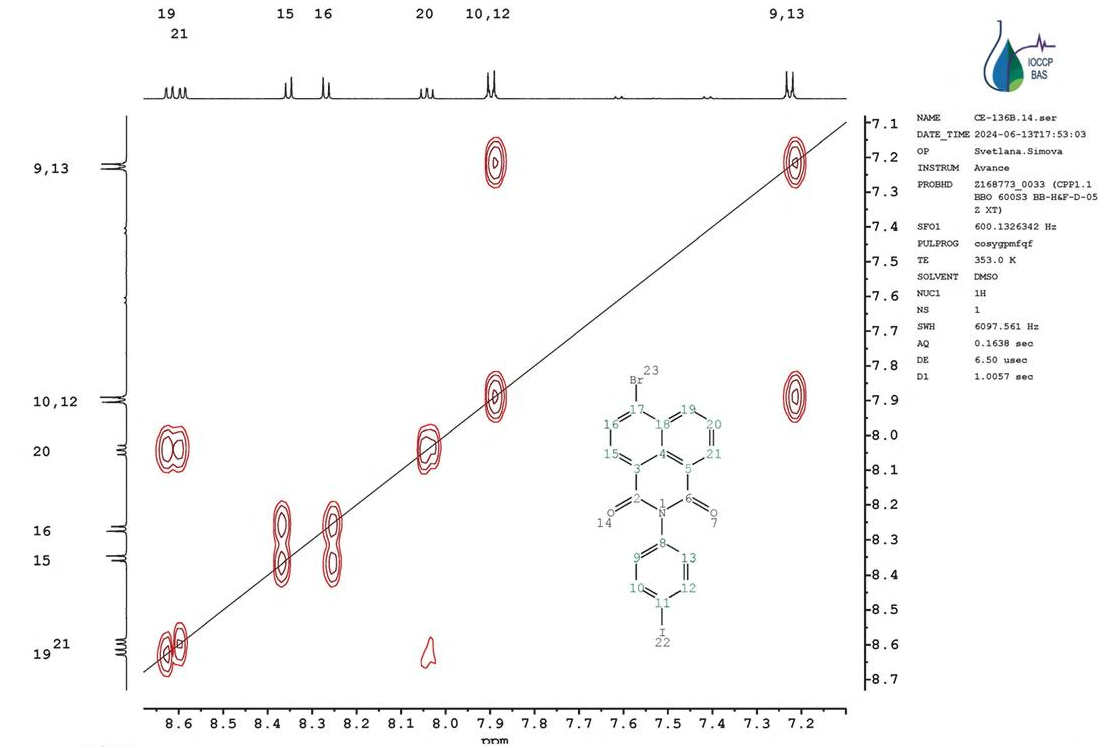


Figure 4–48. COSY-NMR spectrum of compound **5** in DMSO.

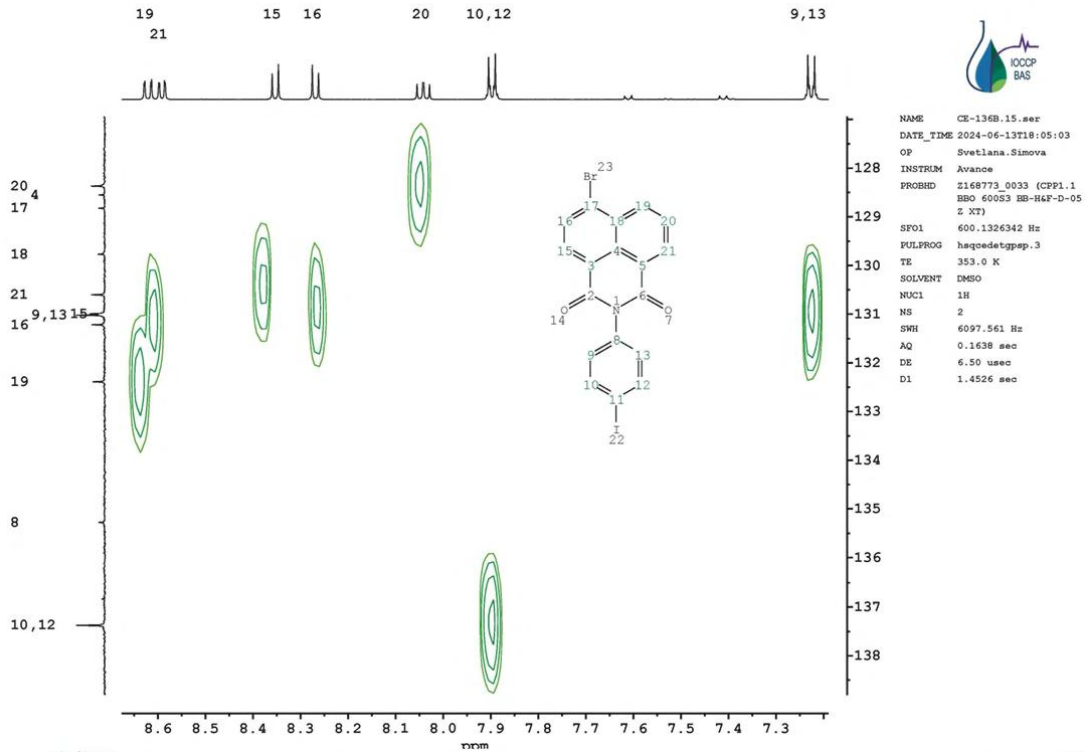


Figure 4–49. HSQC-NMR spectrum of compound **5** in DMSO.

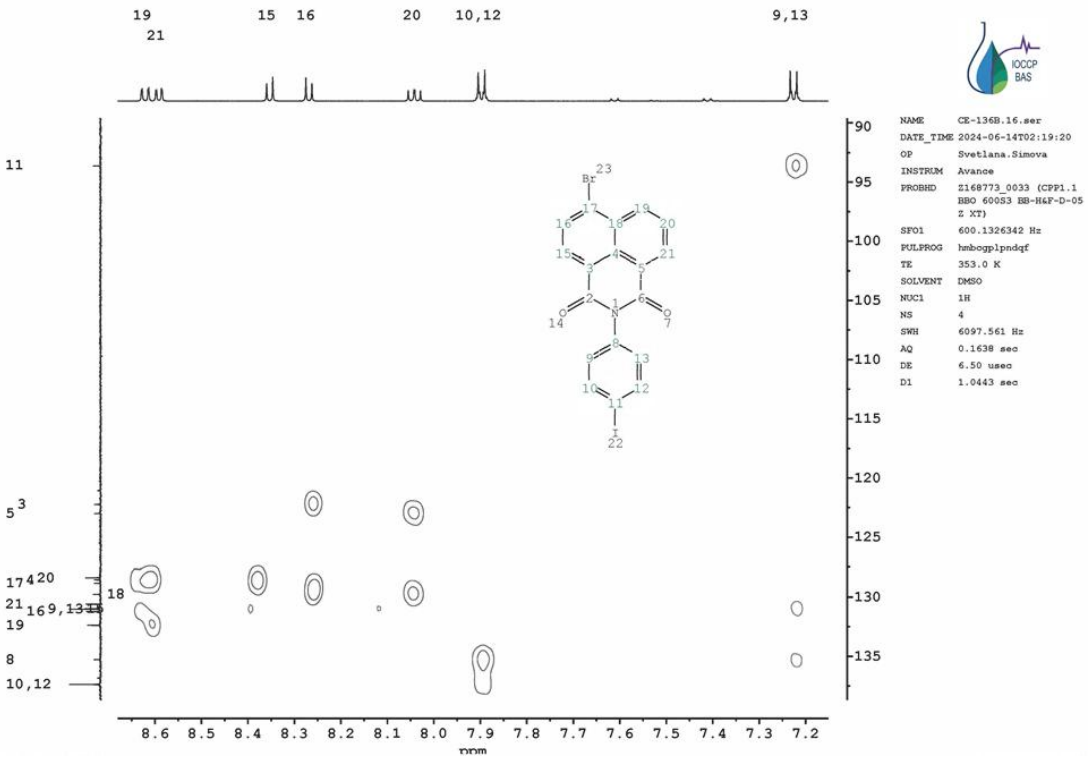


Figure 4–50. HMBC-NMR spectrum of compound **5** in DMSO.

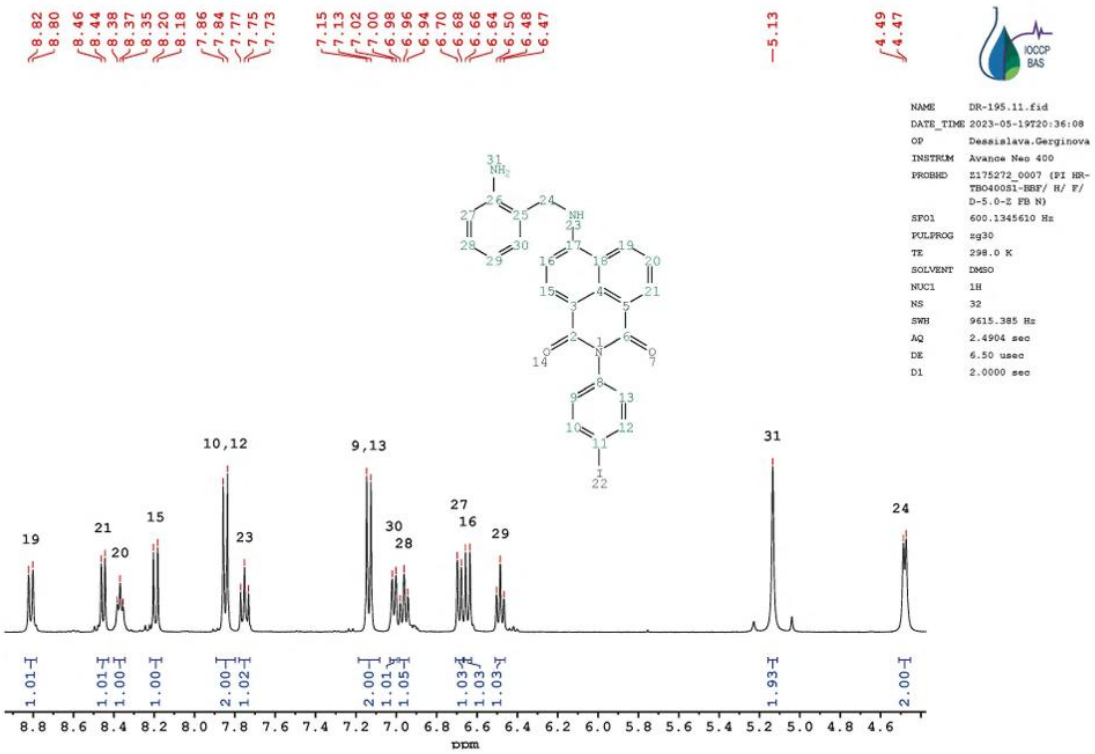


Figure 4–51. ^{1}H-NMR spectrum of compound **7** in DMSO.

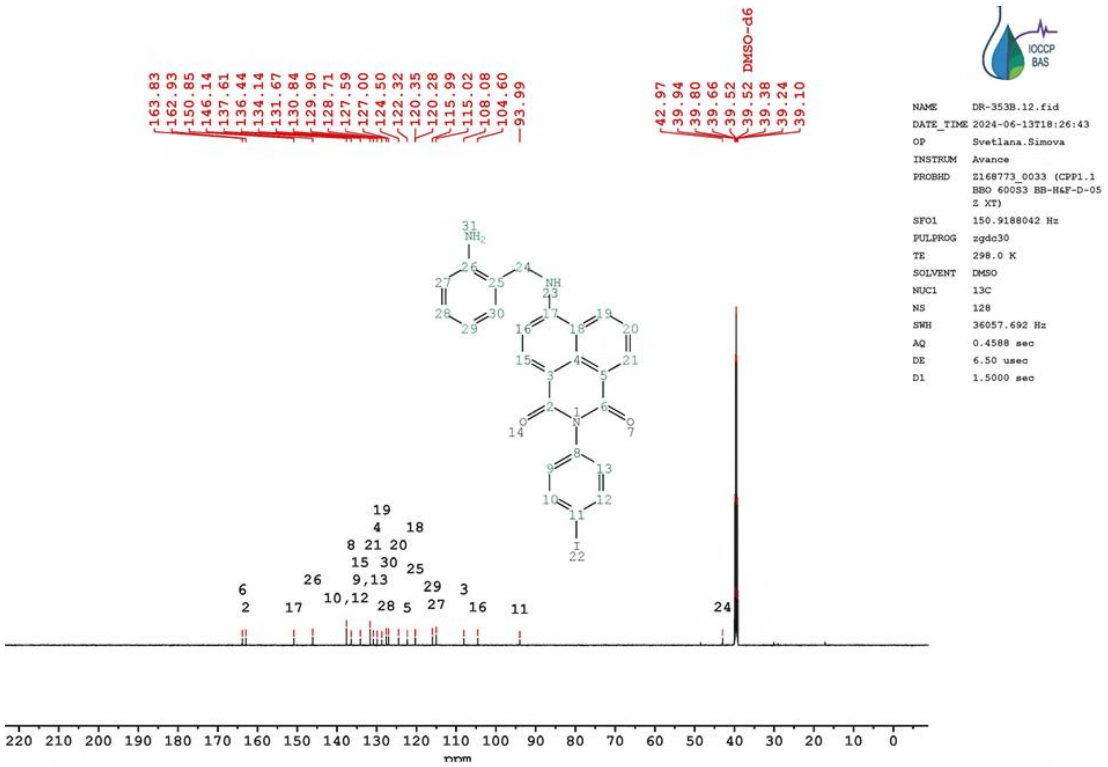


Figure 4–52. ^{13}C-NMR spectrum of compound **7** in DMSO.

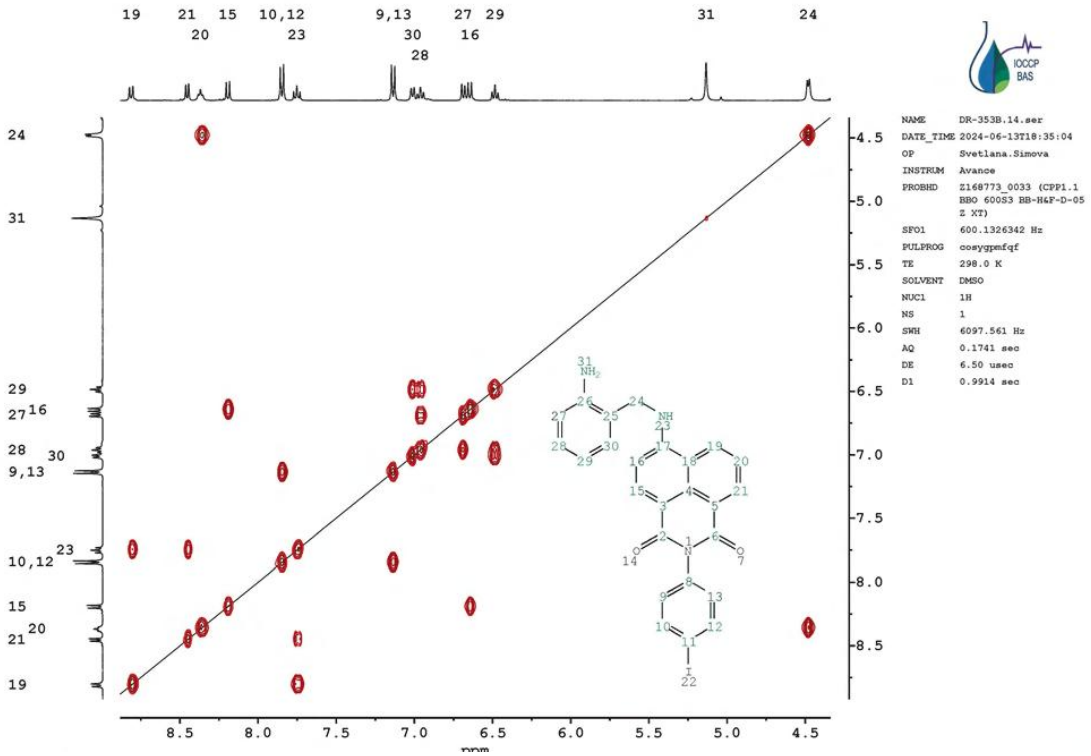


Figure 4–53. COSY-NMR spectrum of compound **7** in DMSO.

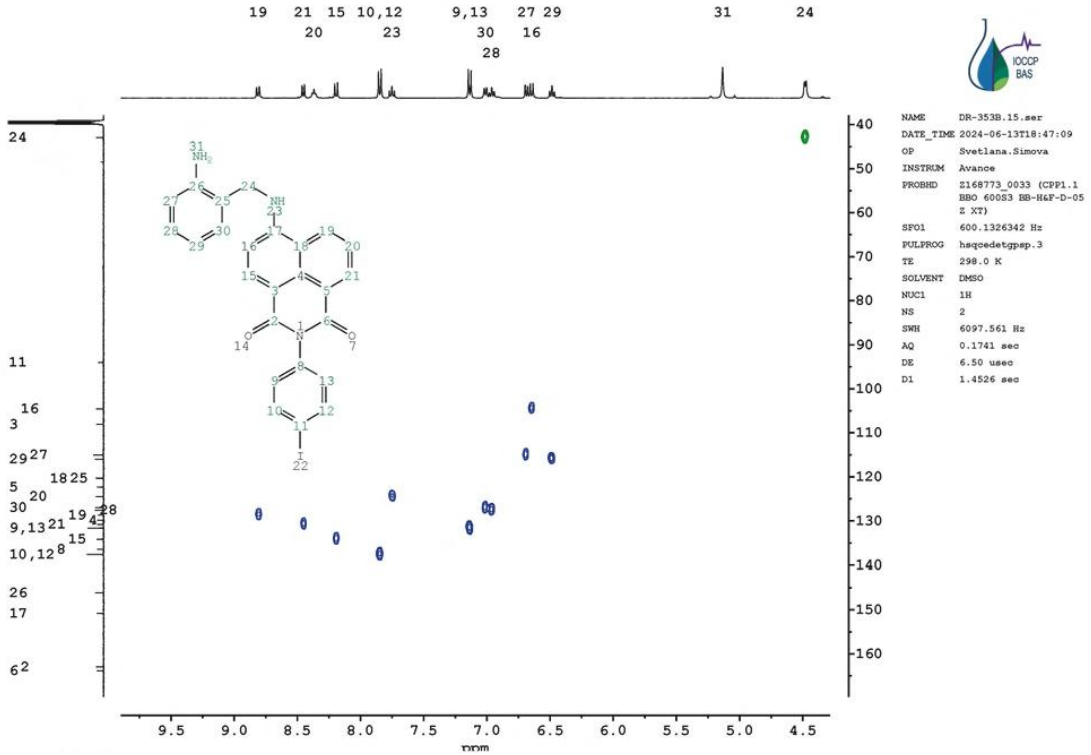


Figure 4–54. HSQC-NMR spectrum of compound **7** in DMSO.

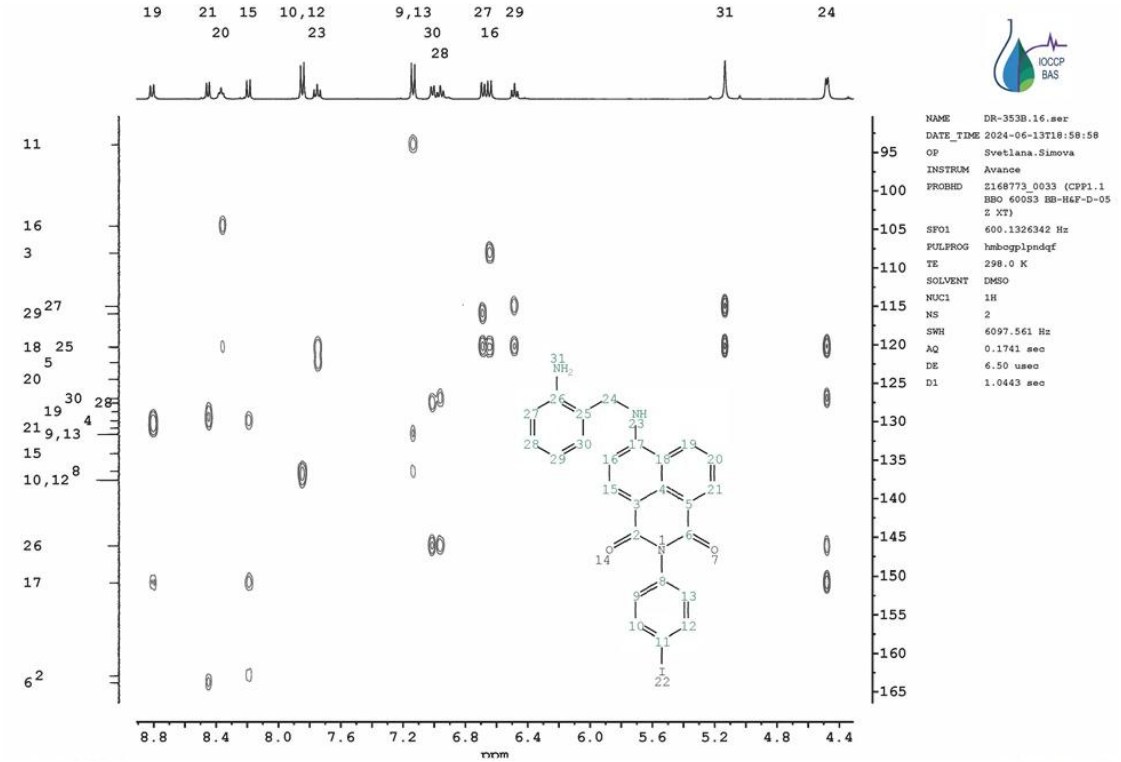


Figure 4–55. HMBC-NMR spectrum of compound **7** in DMSO.

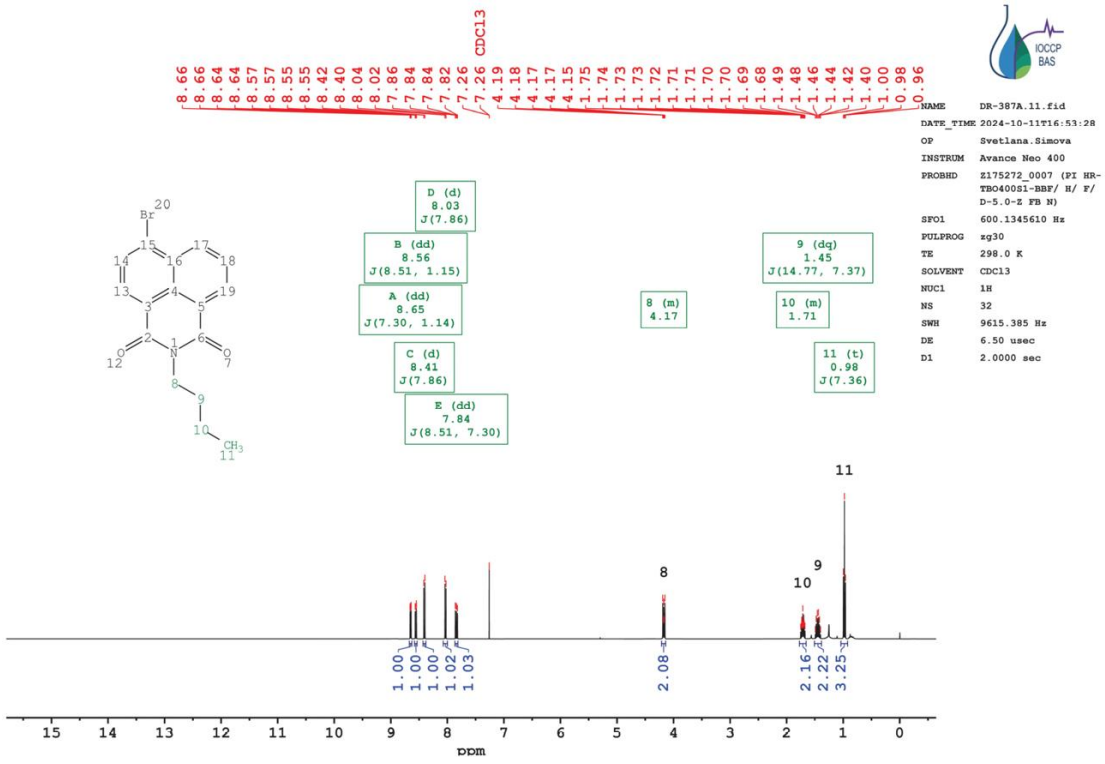


Figure 4–56. ^{1}H-NMR spectrum of compound **9** in chloroform.

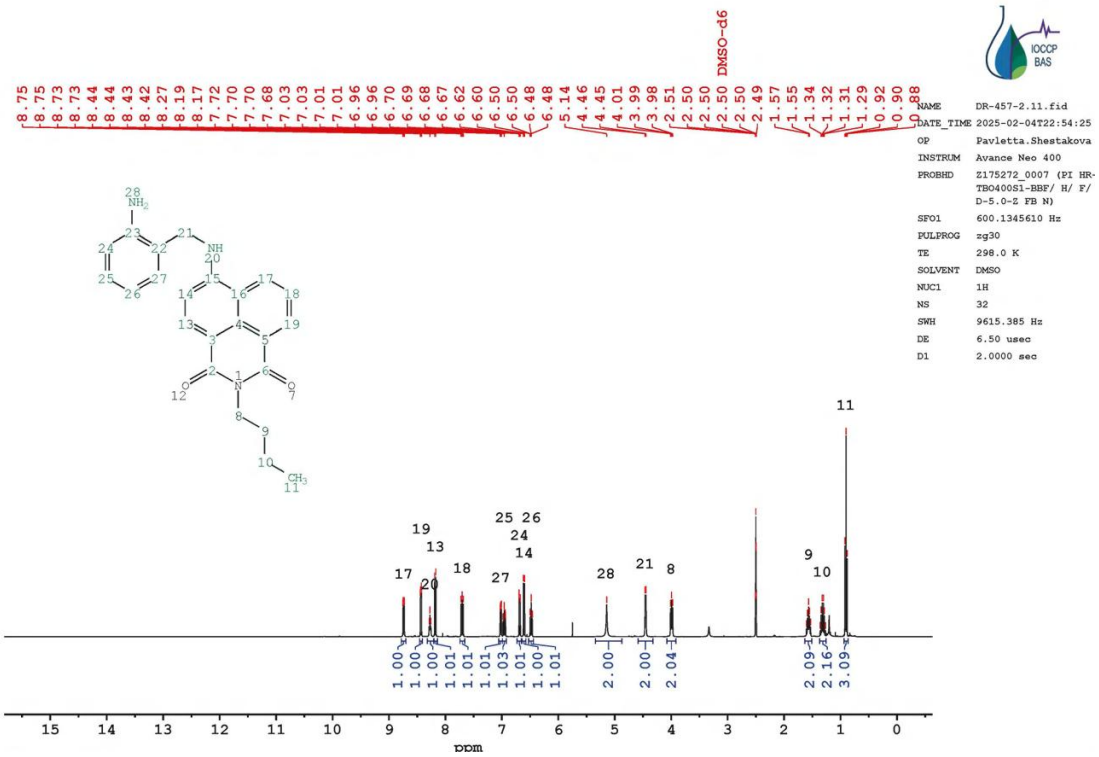


Figure 4–57. ^{1}H-NMR spectrum of compound **10** in DMSO.

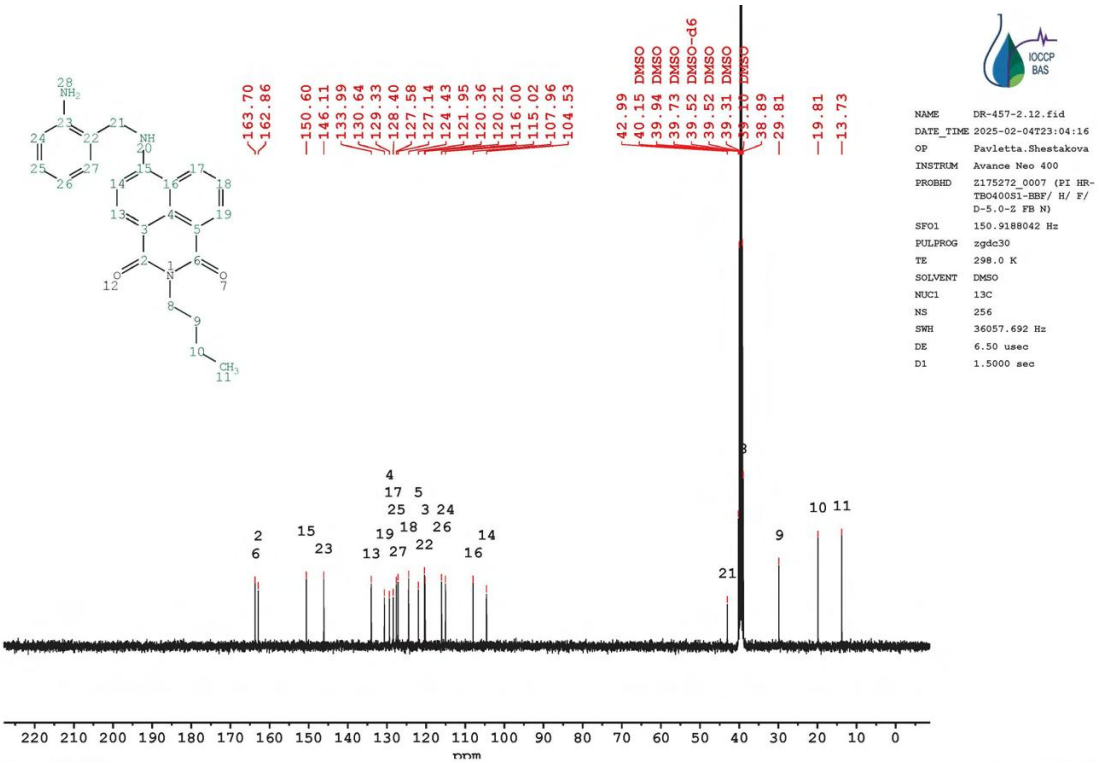


Figure 4–58. ^{13}C-NMR spectrum of compound **10** in DMSO.

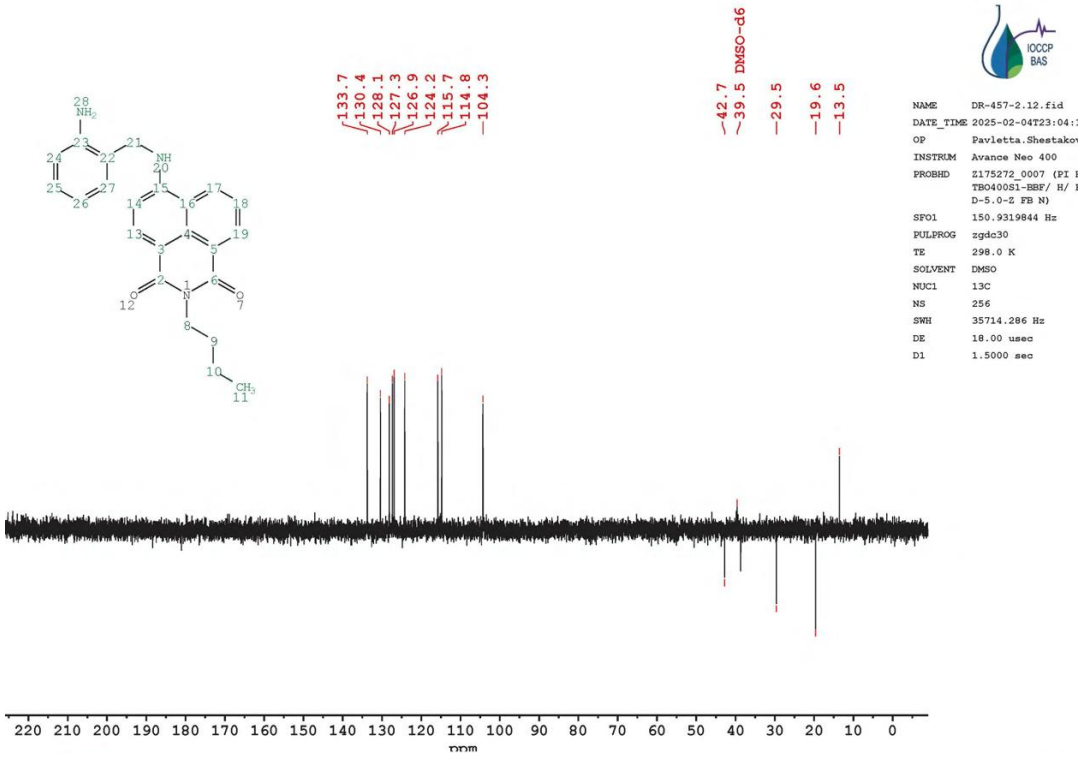


Figure 4–59. DEPT135-NMR spectrum of compound **10** in DMSO.

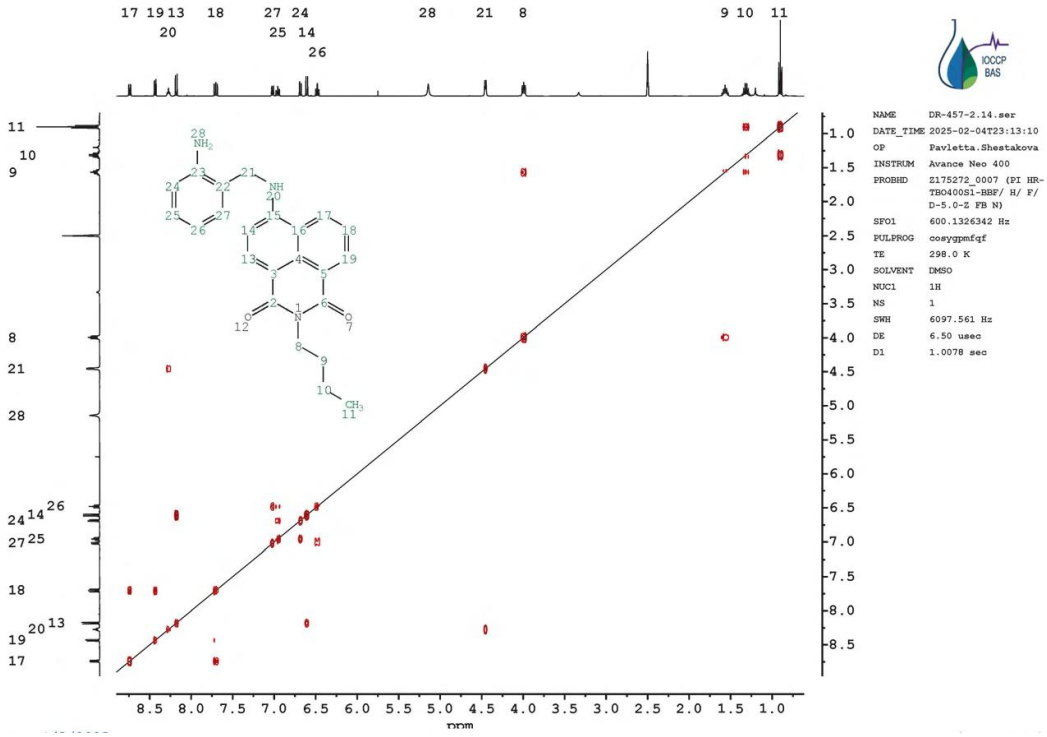


Figure 4–60. COSY-NMR spectrum of compound **10** in DMSO.

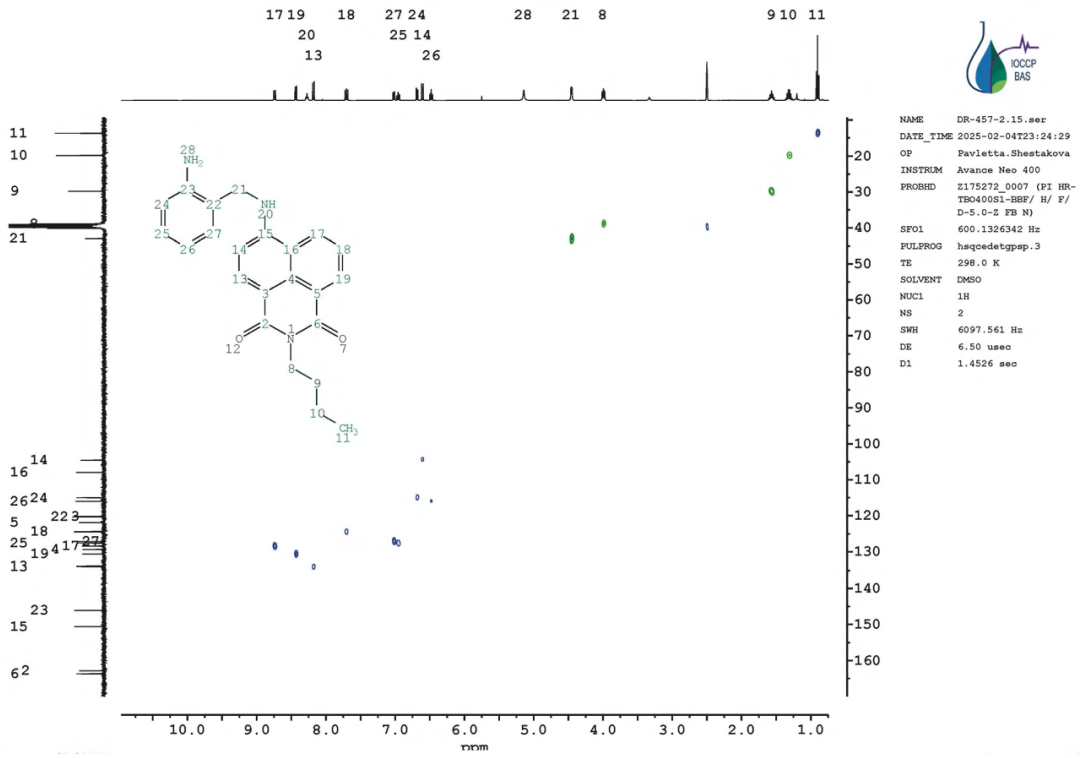


Figure 4–61. HSQC-NMR spectrum of compound **10** in DMSO.

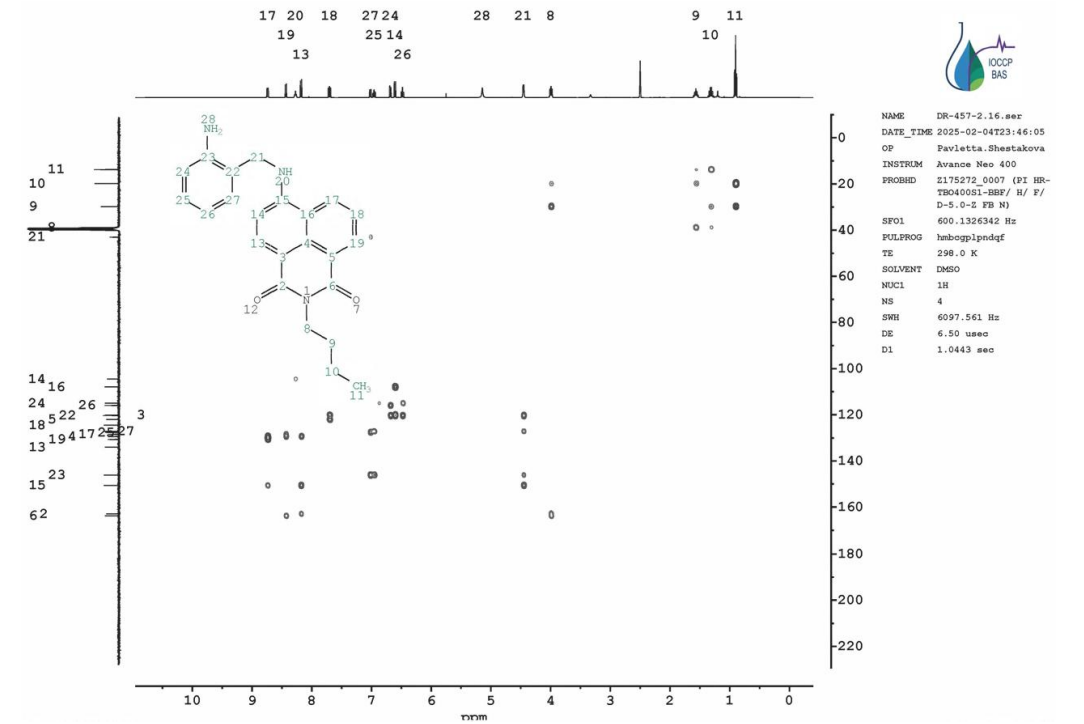


Figure 4–62. HMBC-NMR spectrum of compound **10** in DMSO.

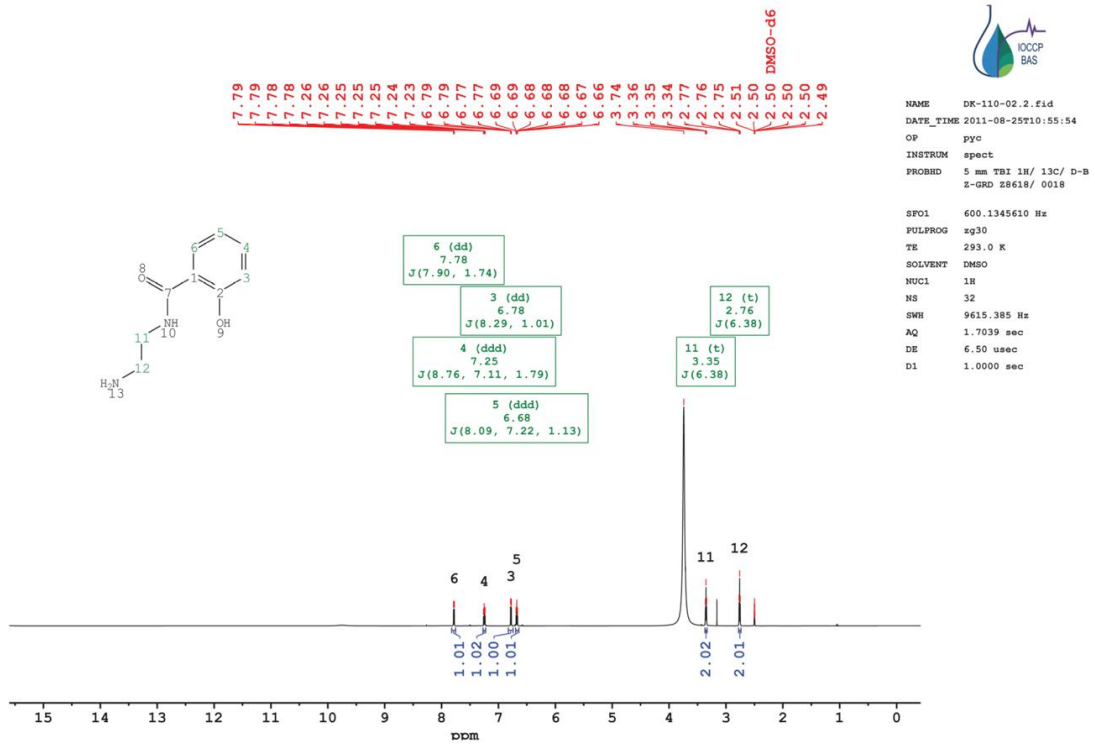


Figure 4–63. ^{1}H-NMR spectrum of compound **13** in DMSO.

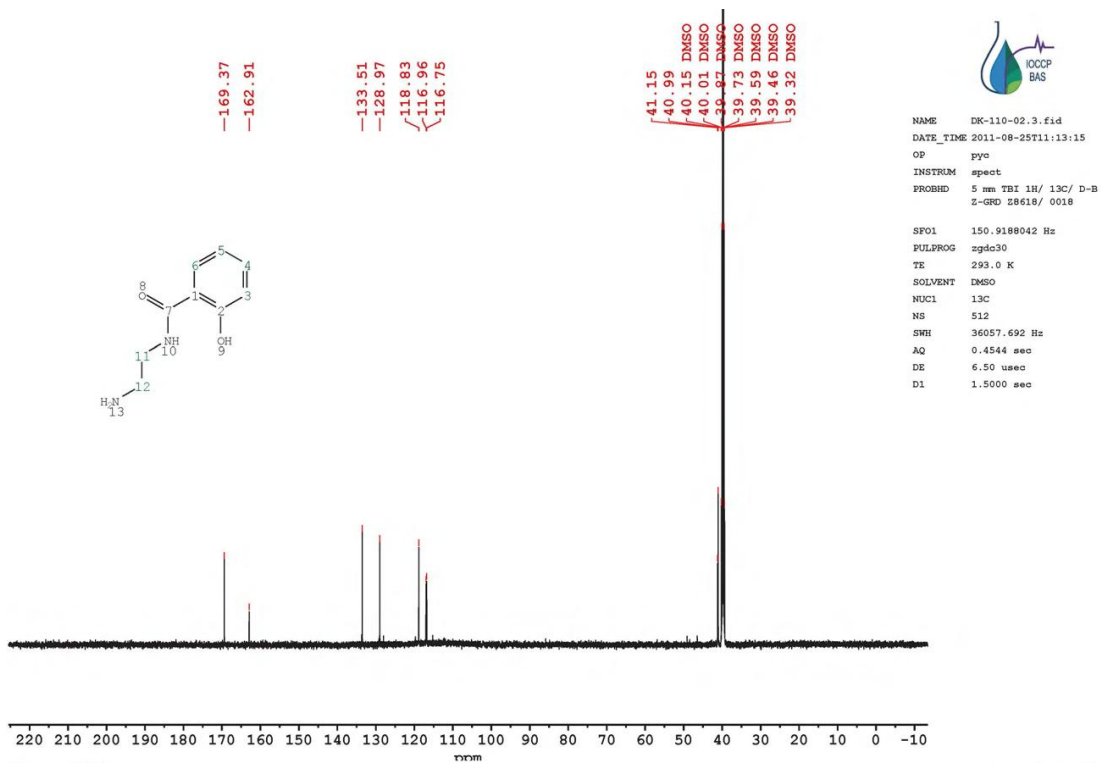


Figure 4–64. ^{13}C-NMR spectrum of compound **13** in DMSO.

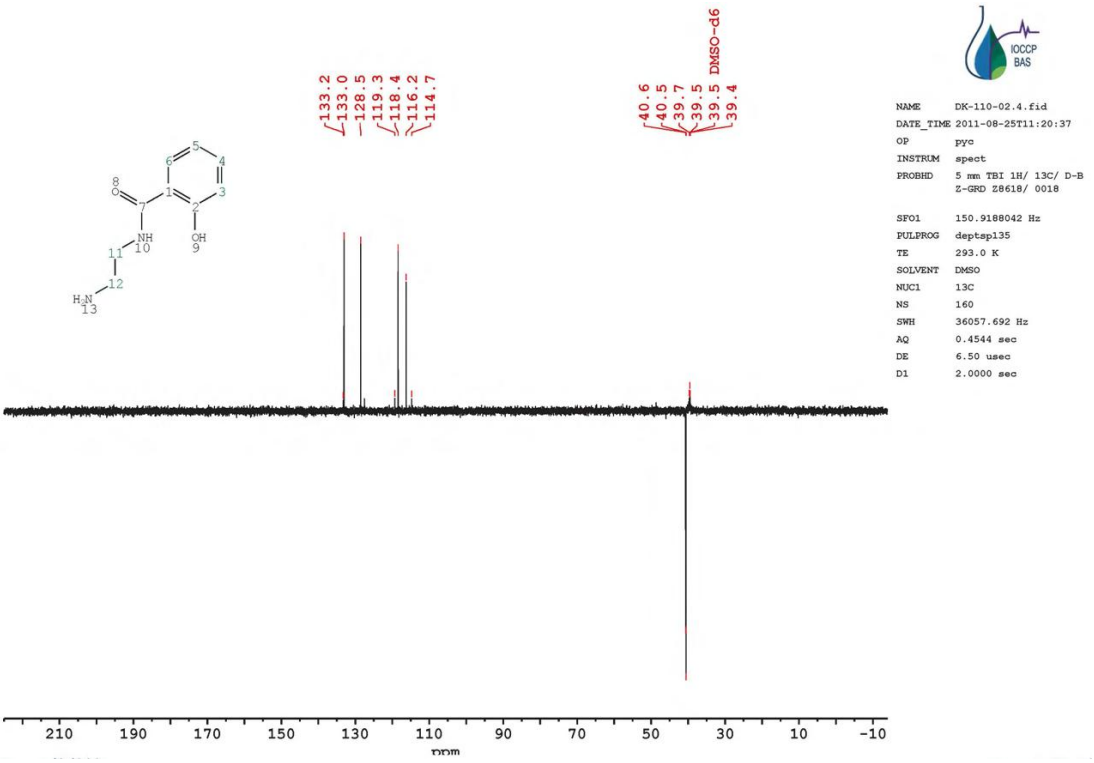


Figure 4–65. DEPT135-NMR spectrum of compound **13** in DMSO.

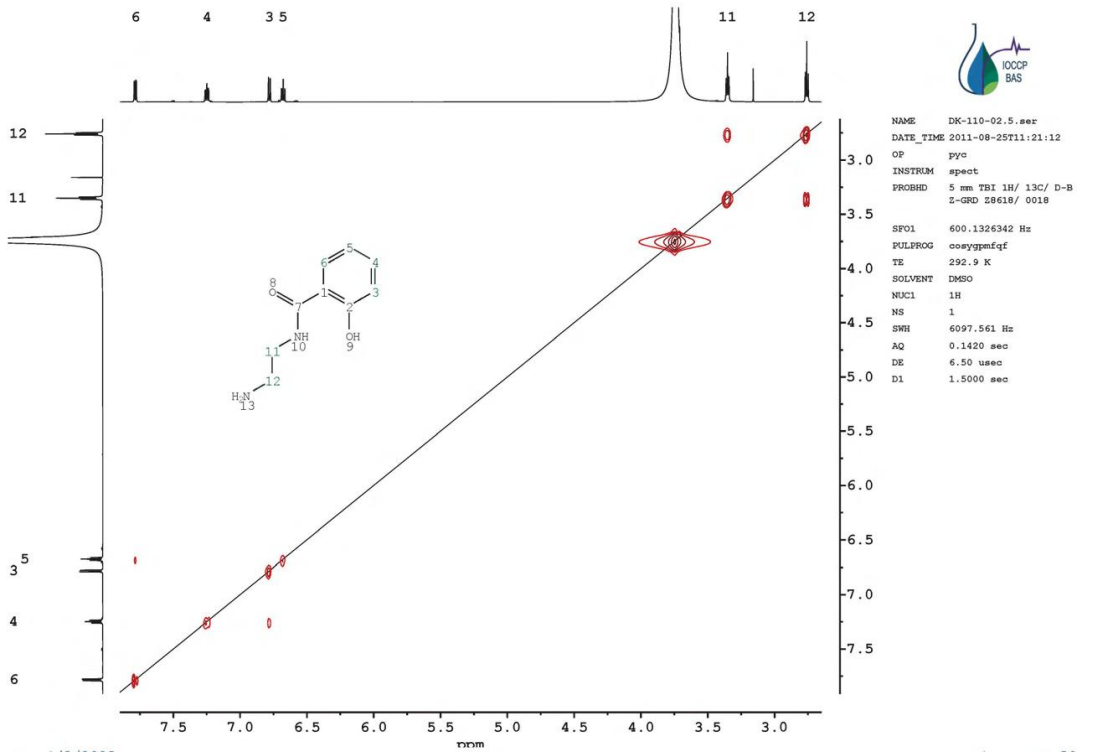


Figure 4–66. COSY-NMR spectrum of compound **13** in DMSO.

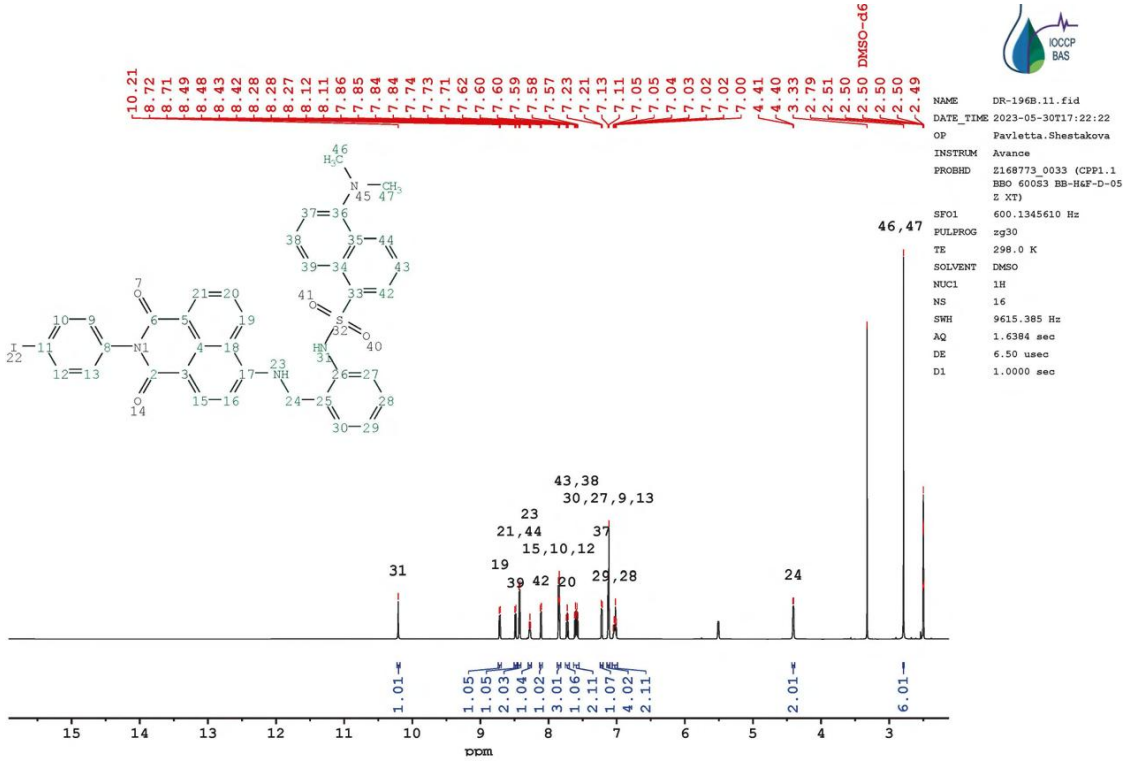


Figure 4–67. ^{1}H-NMR spectrum of compound **L1** in DMSO.

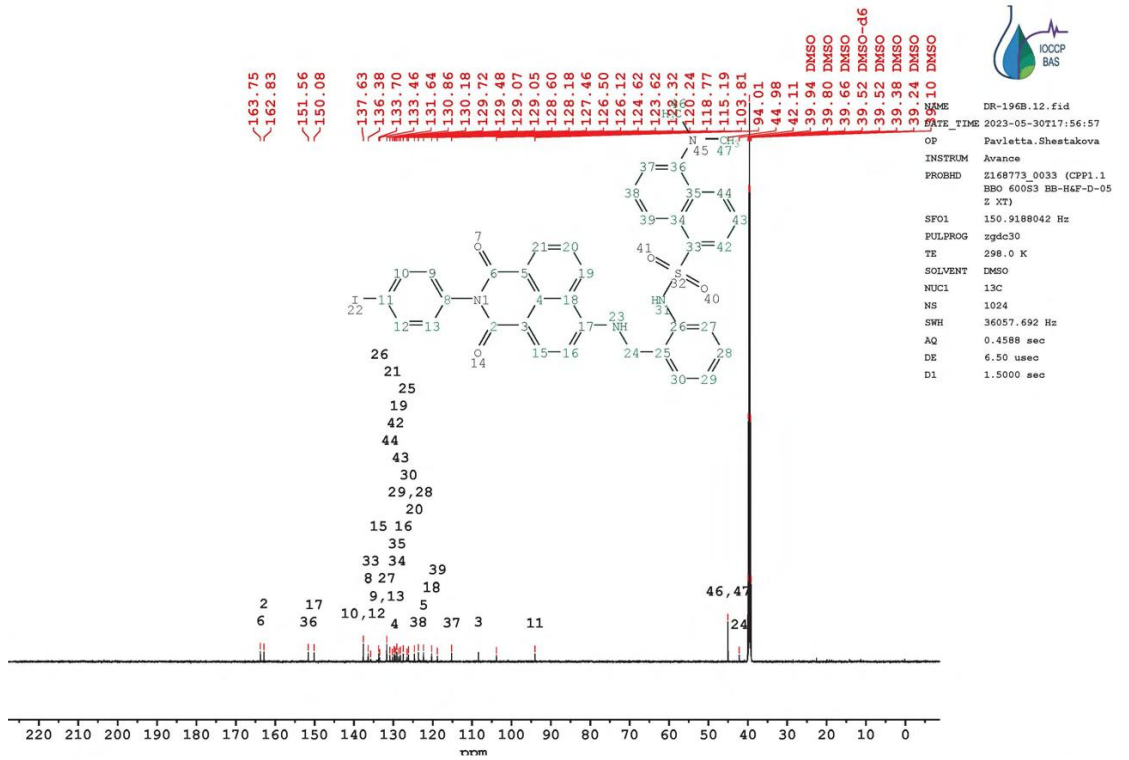


Figure 4–68. ^{13}C-NMR spectrum of compound **L1** in DMSO.

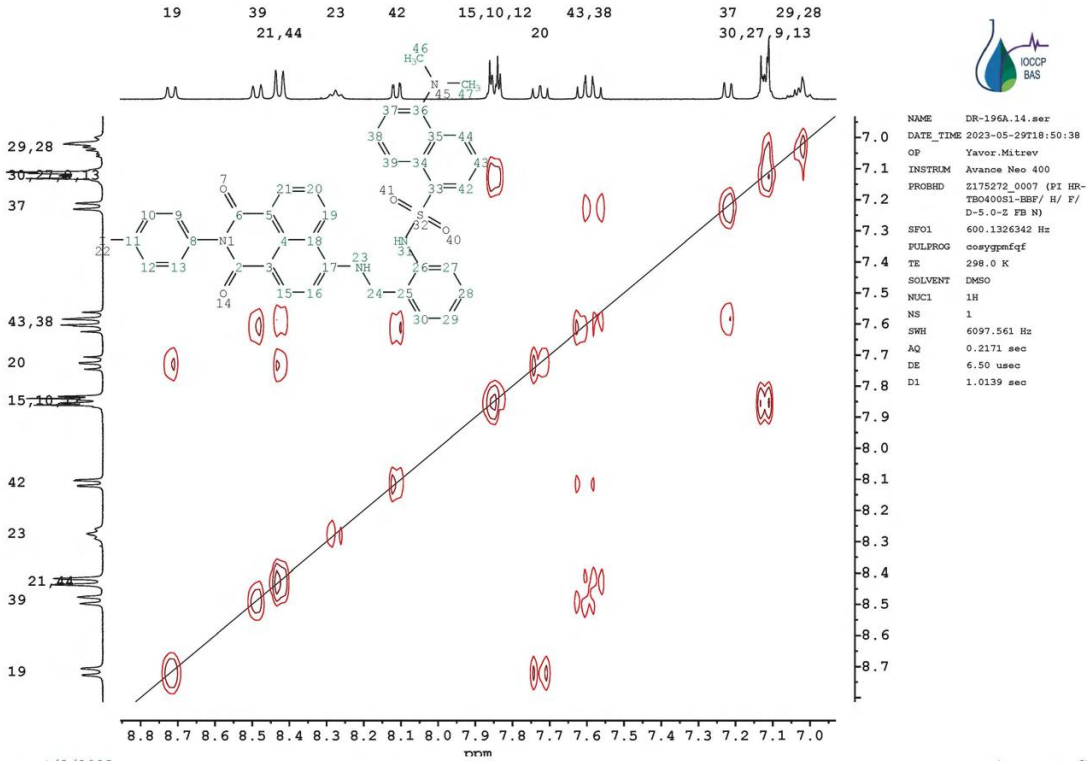


Figure 4–69. COSY-NMR spectrum of compound **L1** in DMSO.

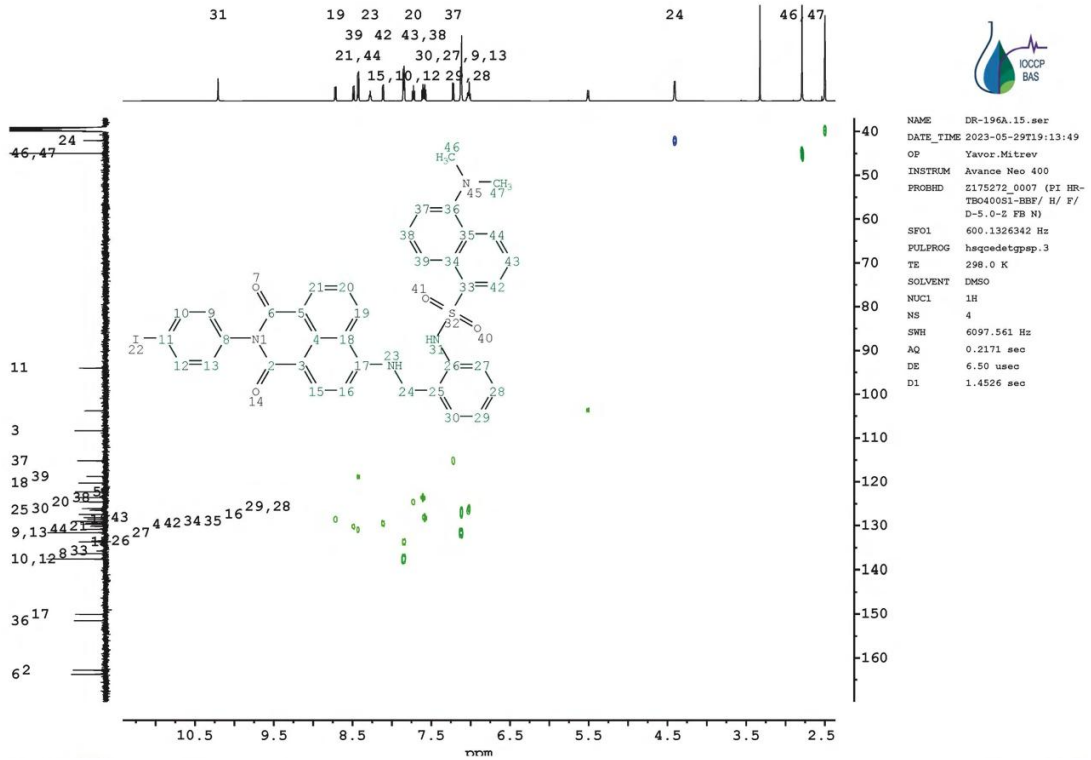


Figure 4–70. HSQC-NMR spectrum of compound **L1** in DMSO.

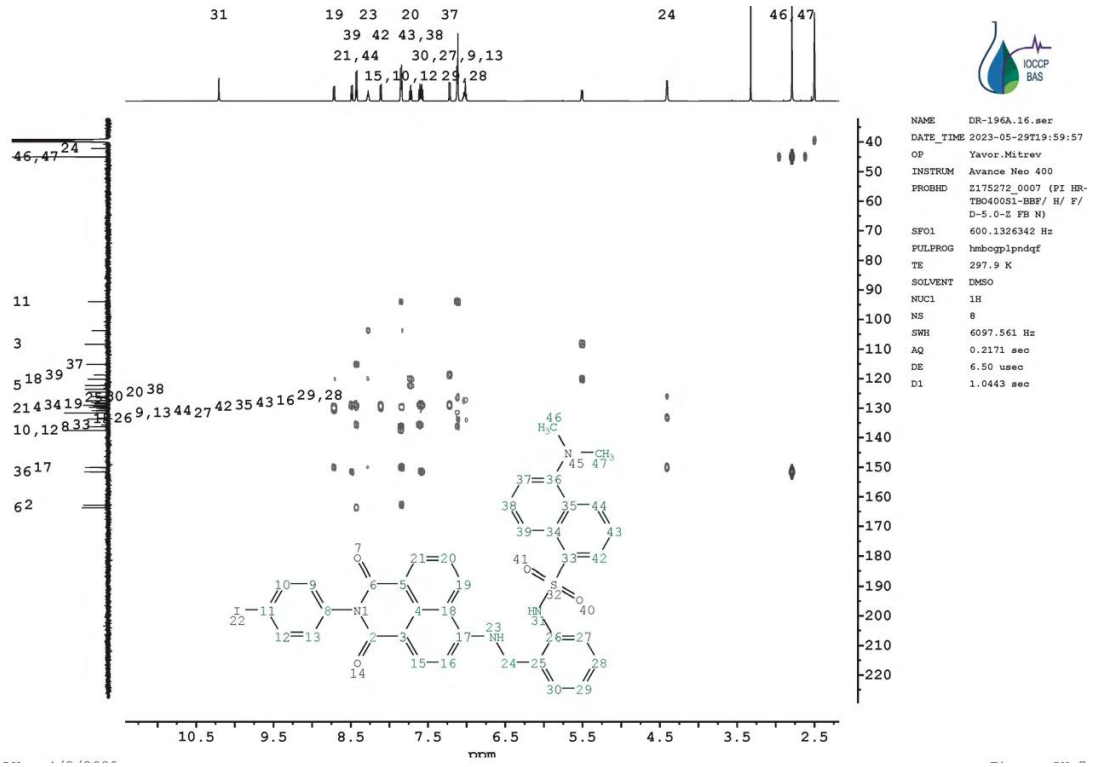


Figure 4–71. HMBC-NMR spectrum of compound **L1** in DMSO.

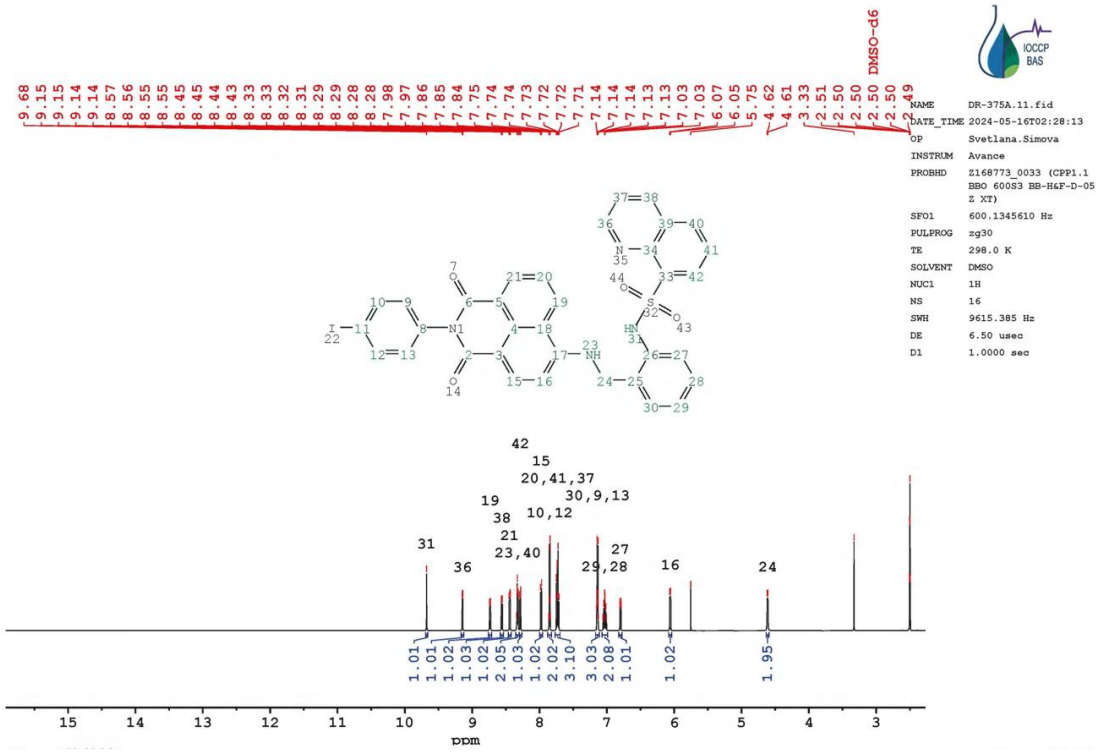


Figure 4–72. ^{1}H-NMR spectrum of compound **L2** in DMSO.

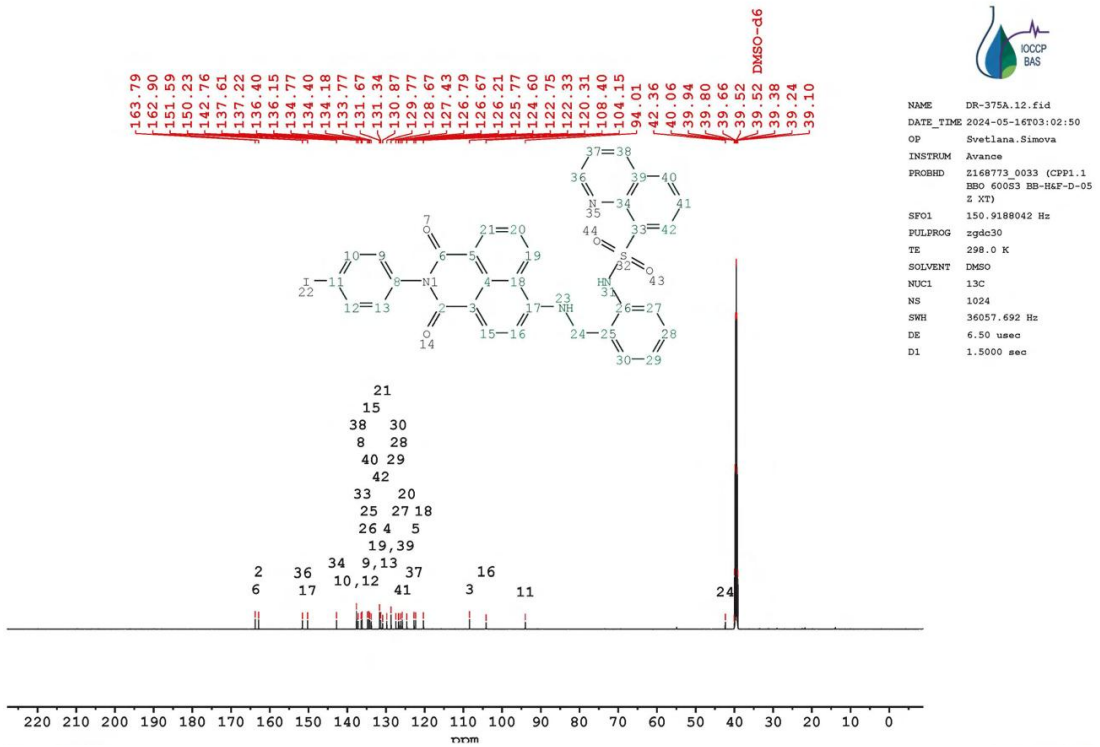


Figure 4–73. ^{13}C-NMR spectrum of compound **L2** in DMSO.

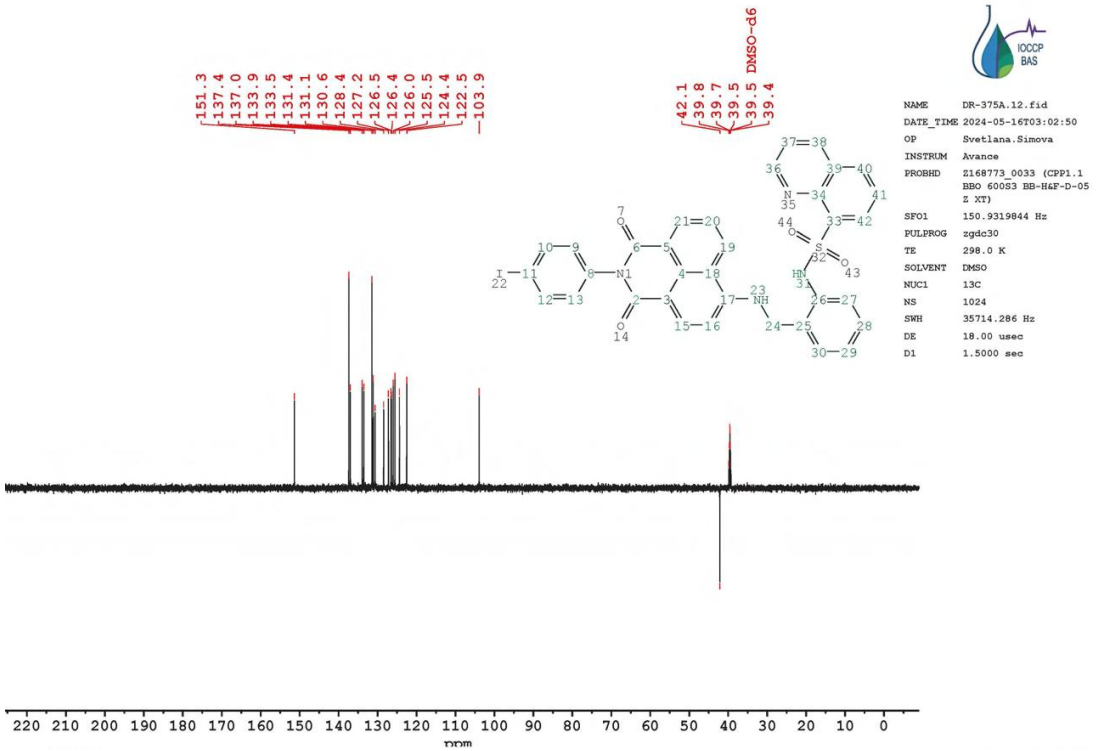


Figure 4–74. DEPT135-NMR spectrum of compound **L2** in DMSO.

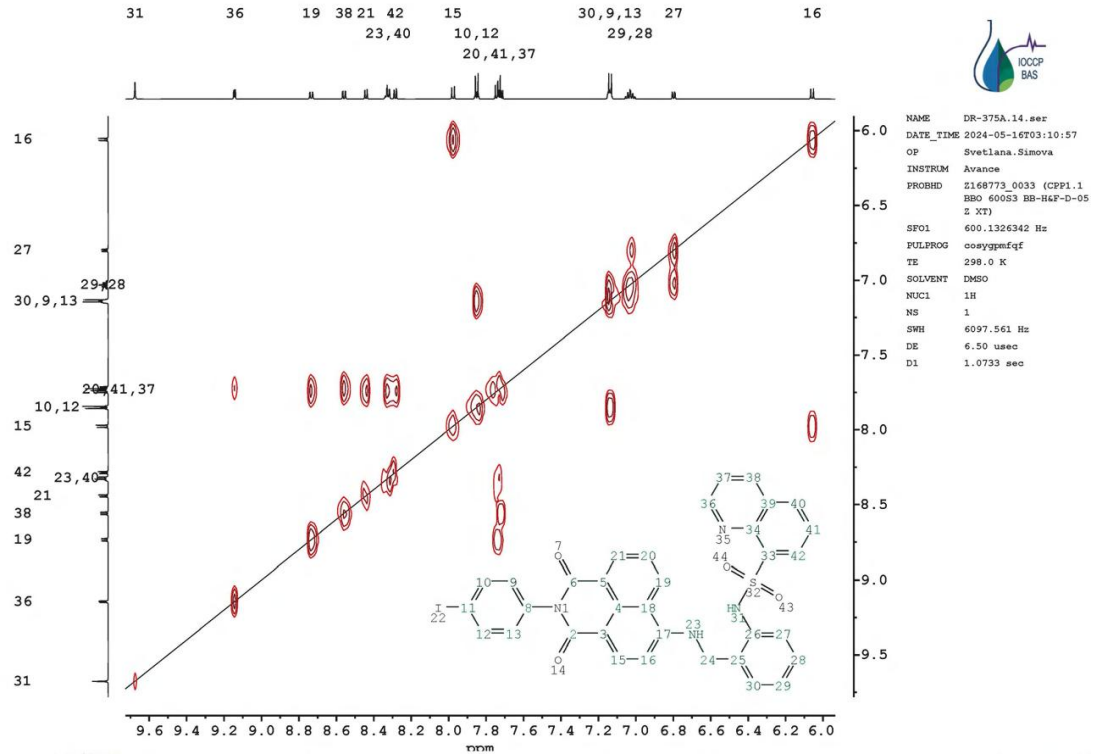


Figure 4–75. COSY-NMR spectrum of compound **L2** in DMSO.

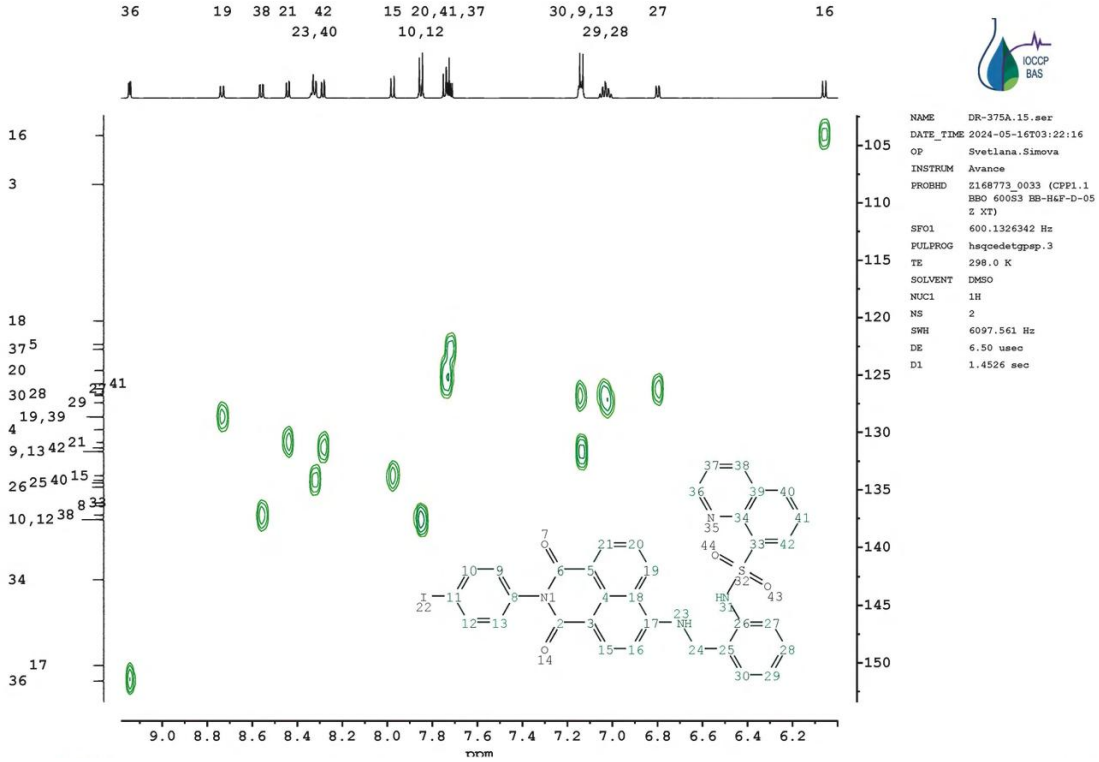


Figure 4–76. HSQC-NMR spectrum of compound **L2** in DMSO.

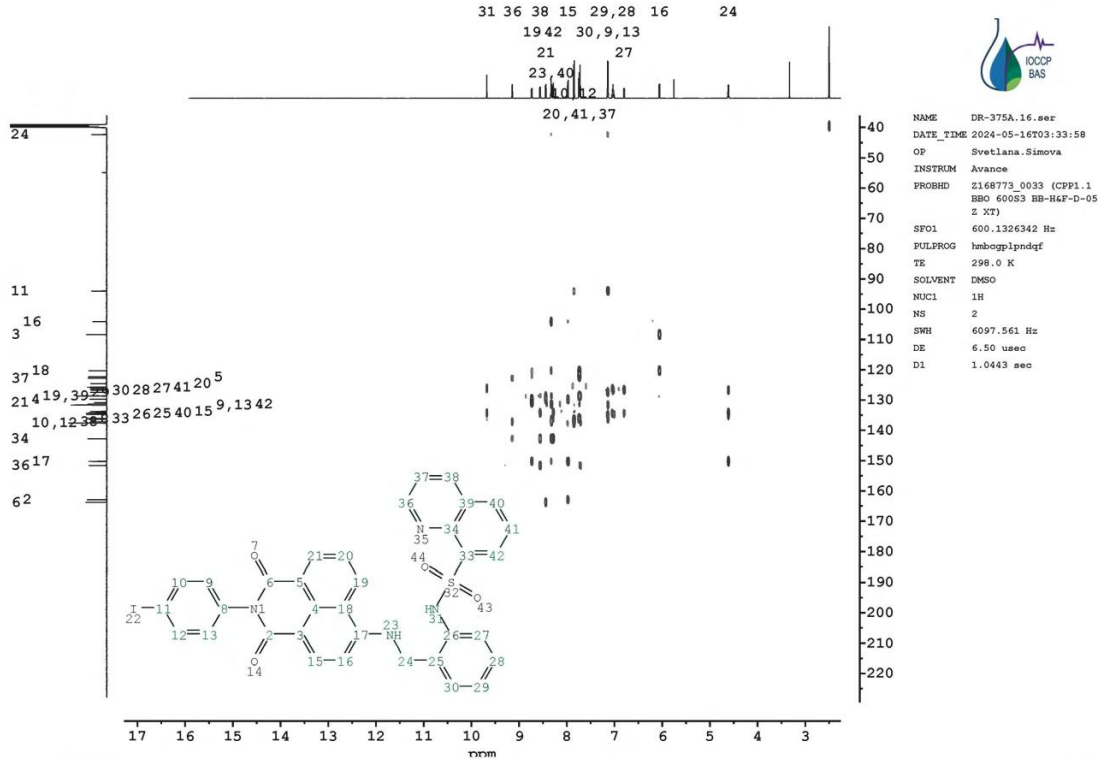


Figure 4–77. HMBC-NMR spectrum of compound **L2** in DMSO.

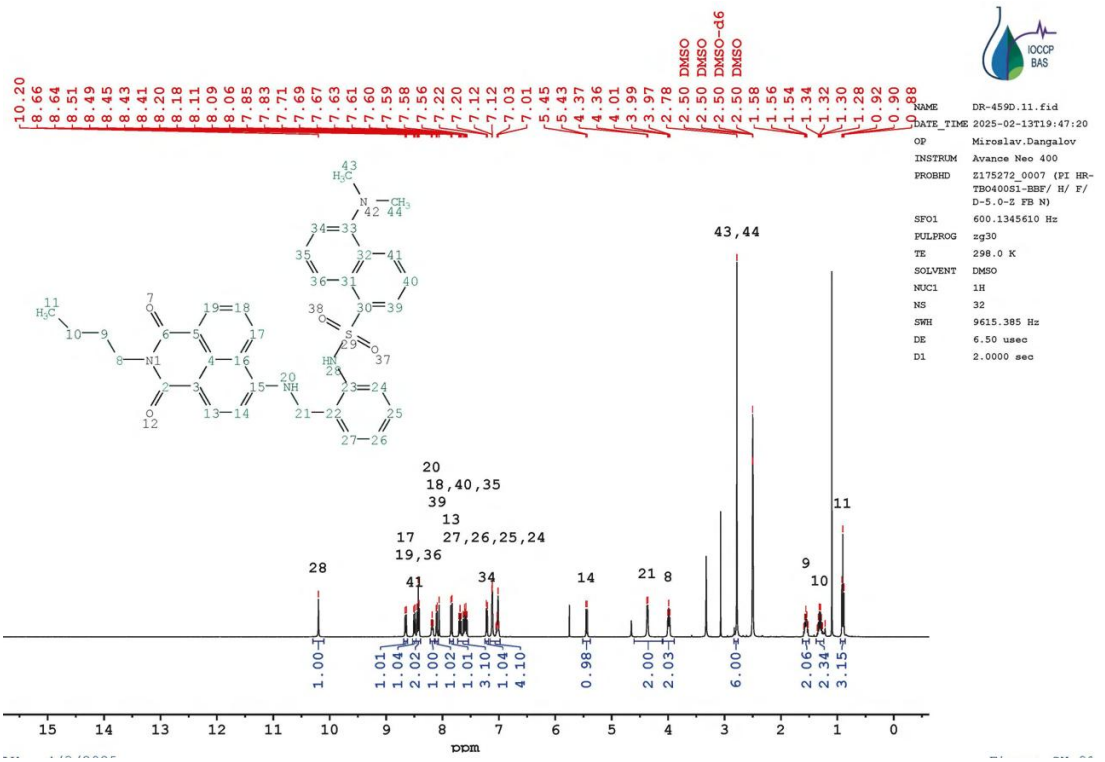


Figure 4–78. ^{1}H-NMR spectrum of compound **L3** in DMSO.

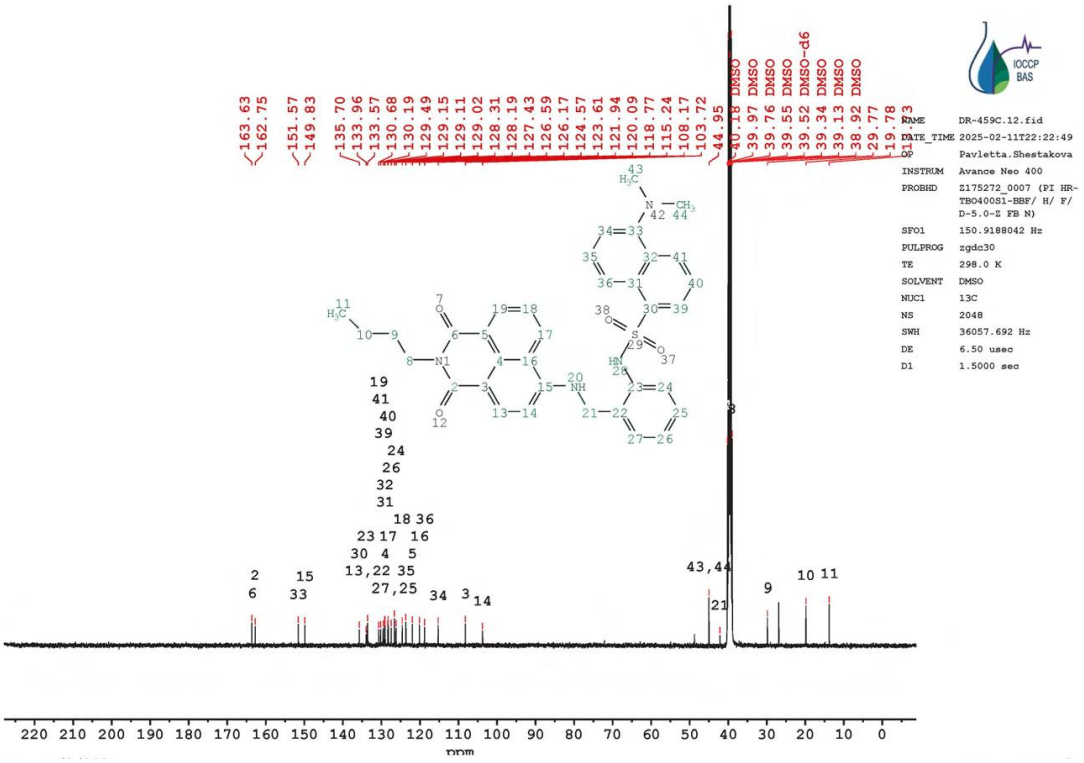


Figure 4–79. ^{13}C-NMR spectrum of compound **L3** in DMSO.

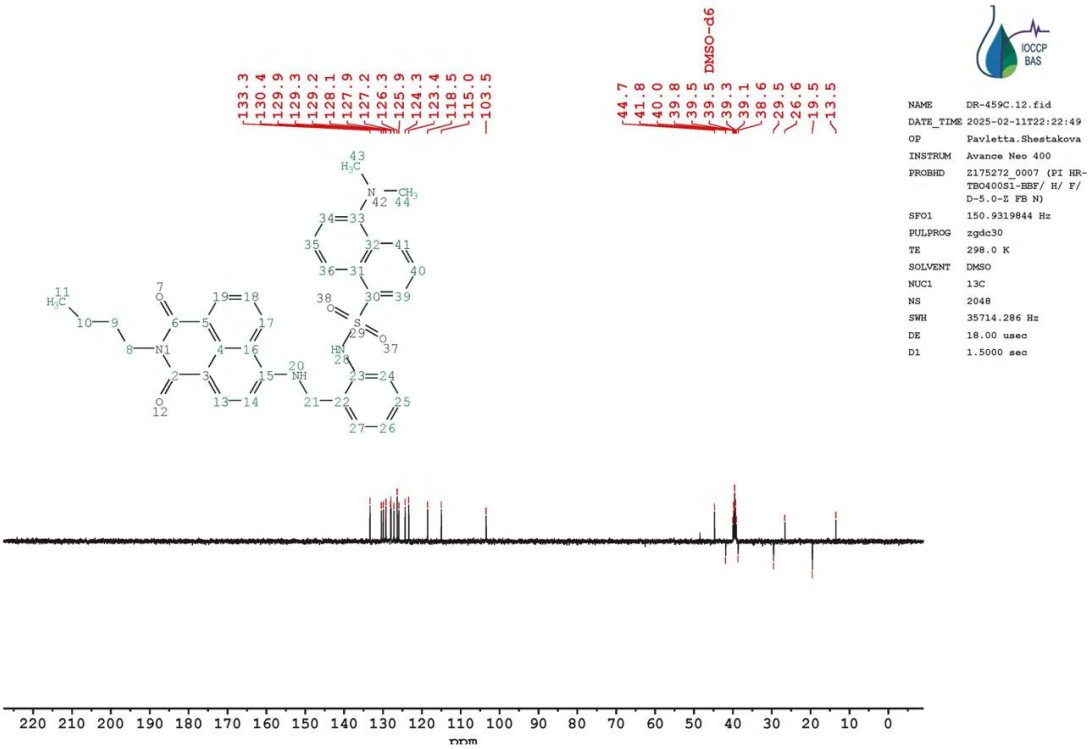


Figure 4–80. DEPT135-NMR spectrum of compound **L3** in DMSO.

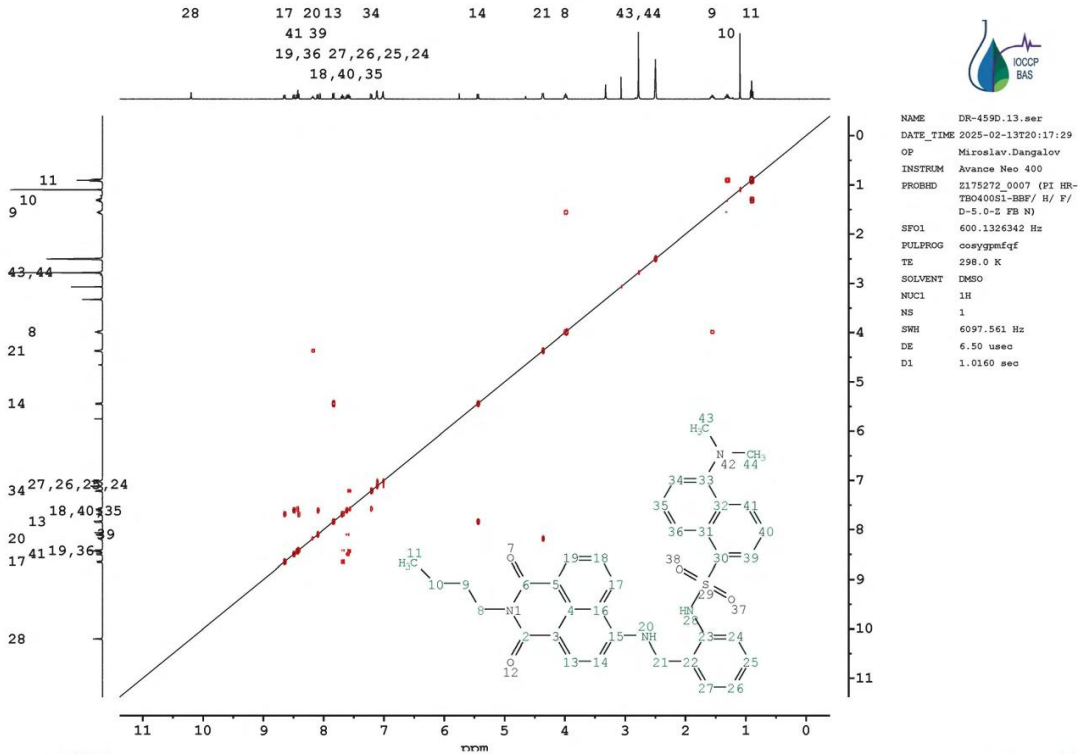


Figure 4–81. COSY-NMR spectrum of compound **L3** in DMSO.

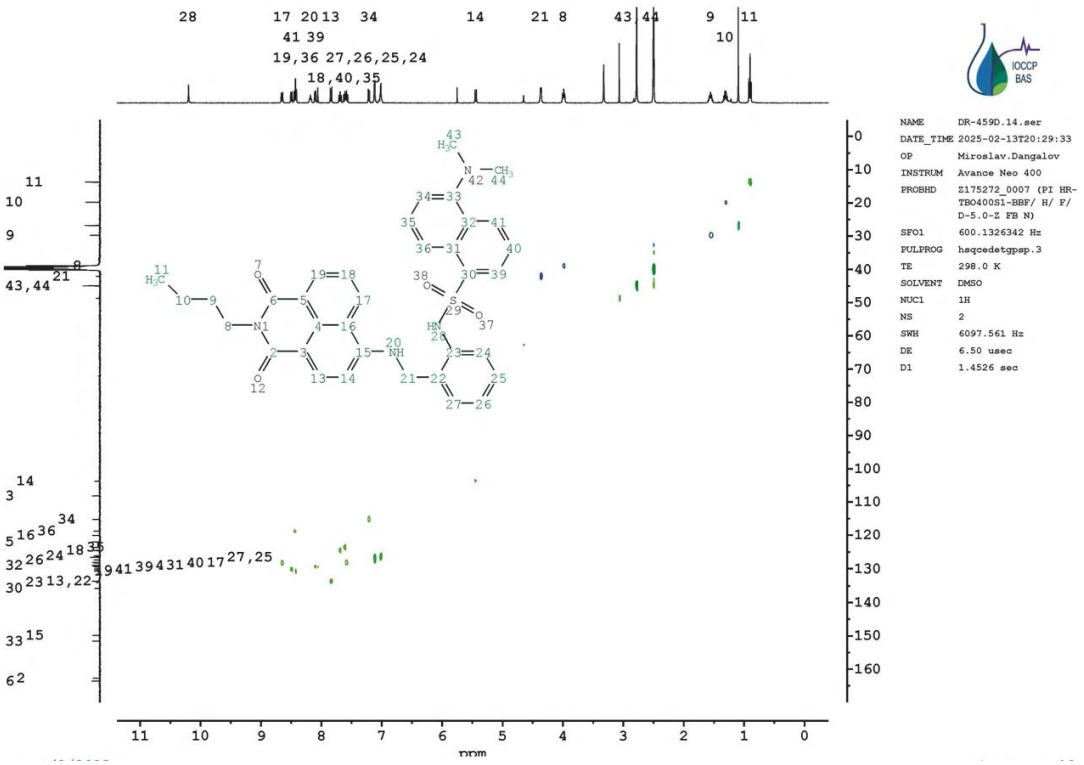


Figure 4–82. HSQC-NMR spectrum of compound **L3** in DMSO.

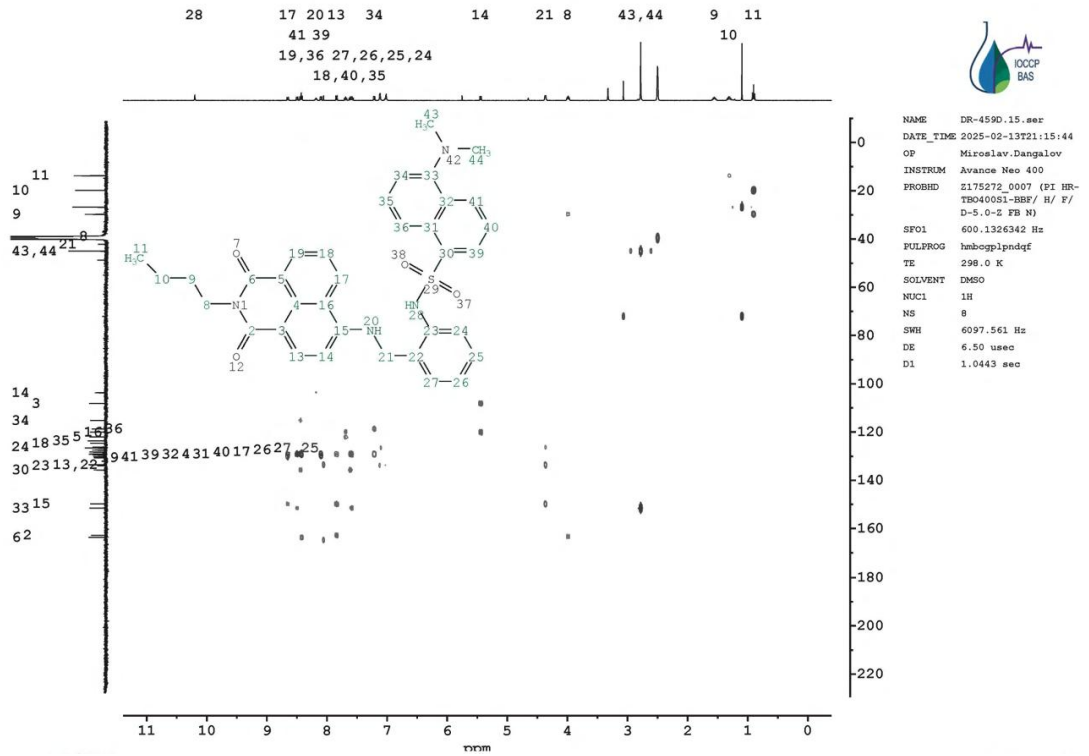


Figure 4–83. HMBC-NMR spectrum of compound **L3** in DMSO.

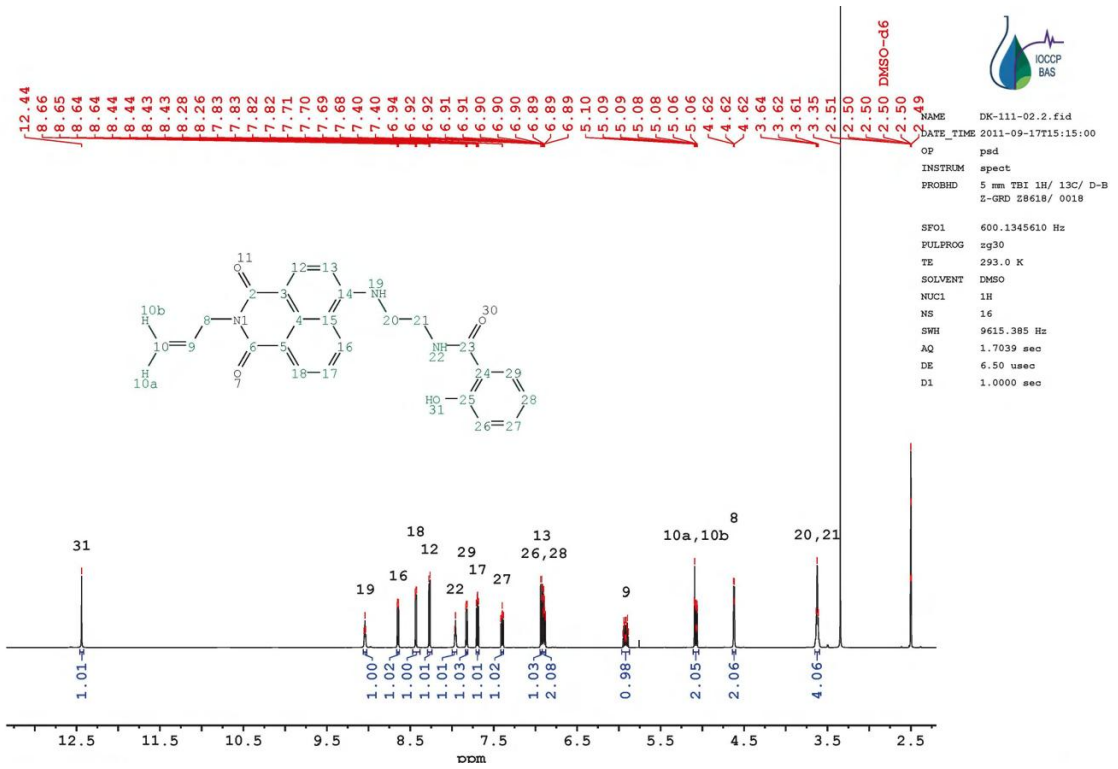


Figure 4–84. ^{1}H-NMR spectrum of compound **L4** in DMSO.

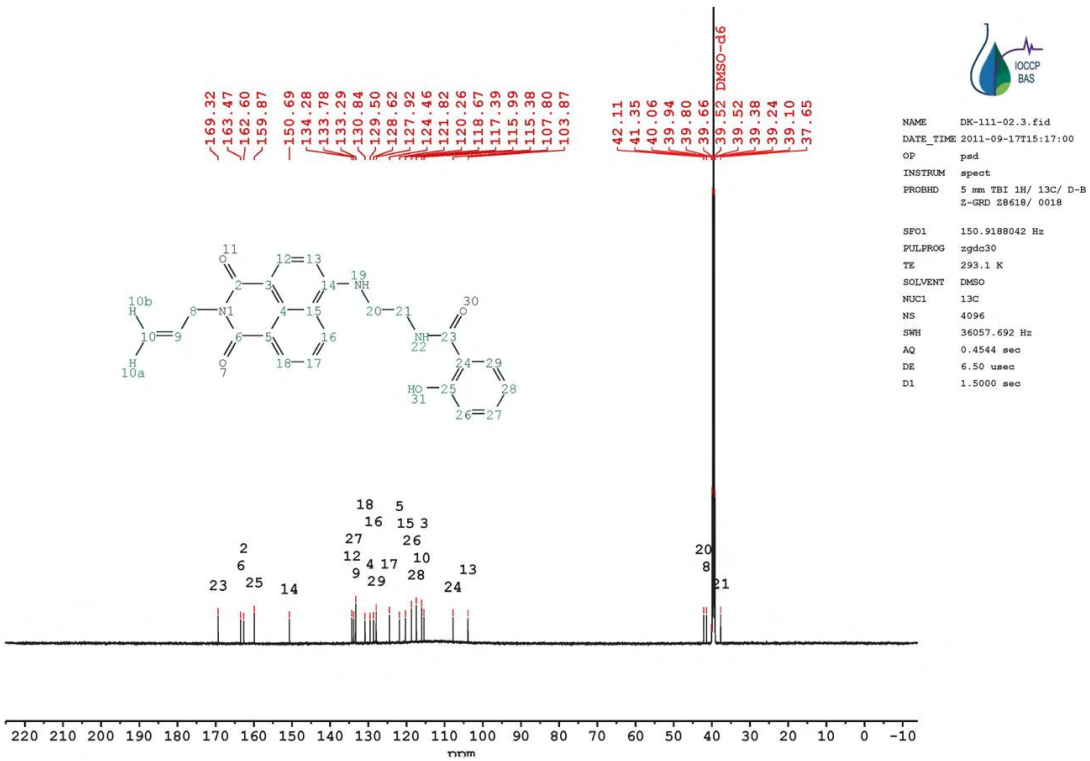


Figure 4–85. ^{13}C-NMR spectrum of compound **L4** in DMSO.

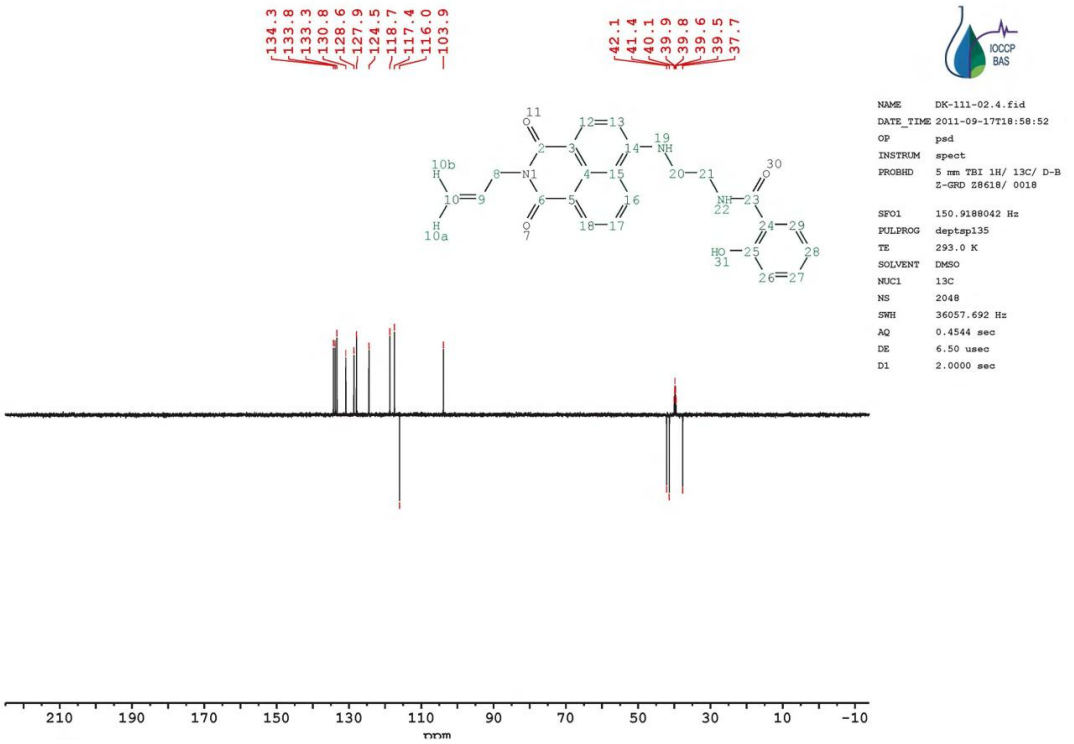


Figure 4–86. DEPT135-NMR spectrum of compound **L4** in DMSO.

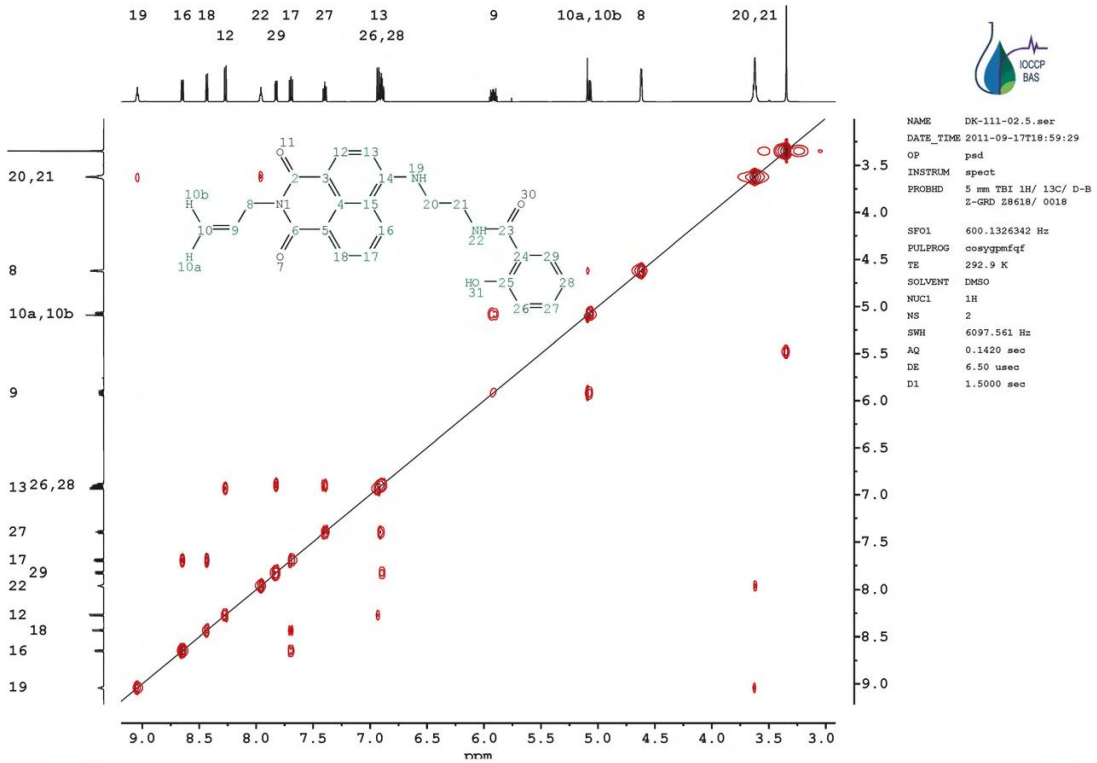


Figure 4–87. COSY-NMR spectrum of compound **L4** in DMSO.

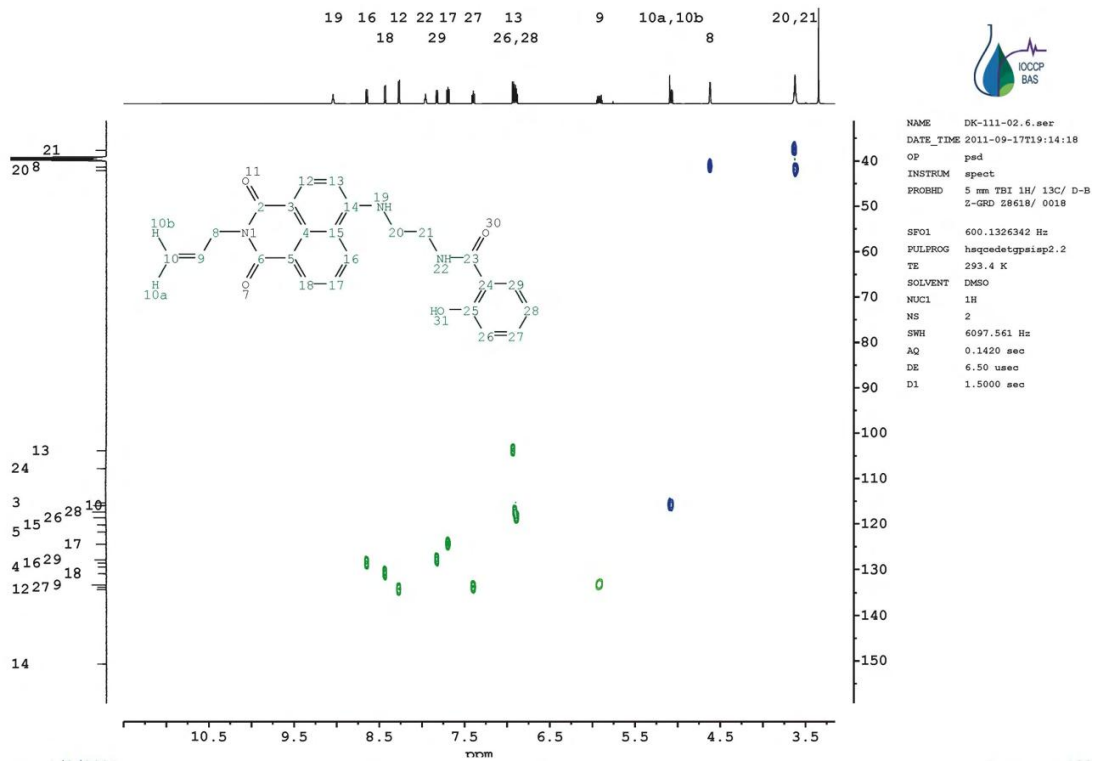


Figure 4–88. HSQC-NMR spectrum of compound **L4** in DMSO.

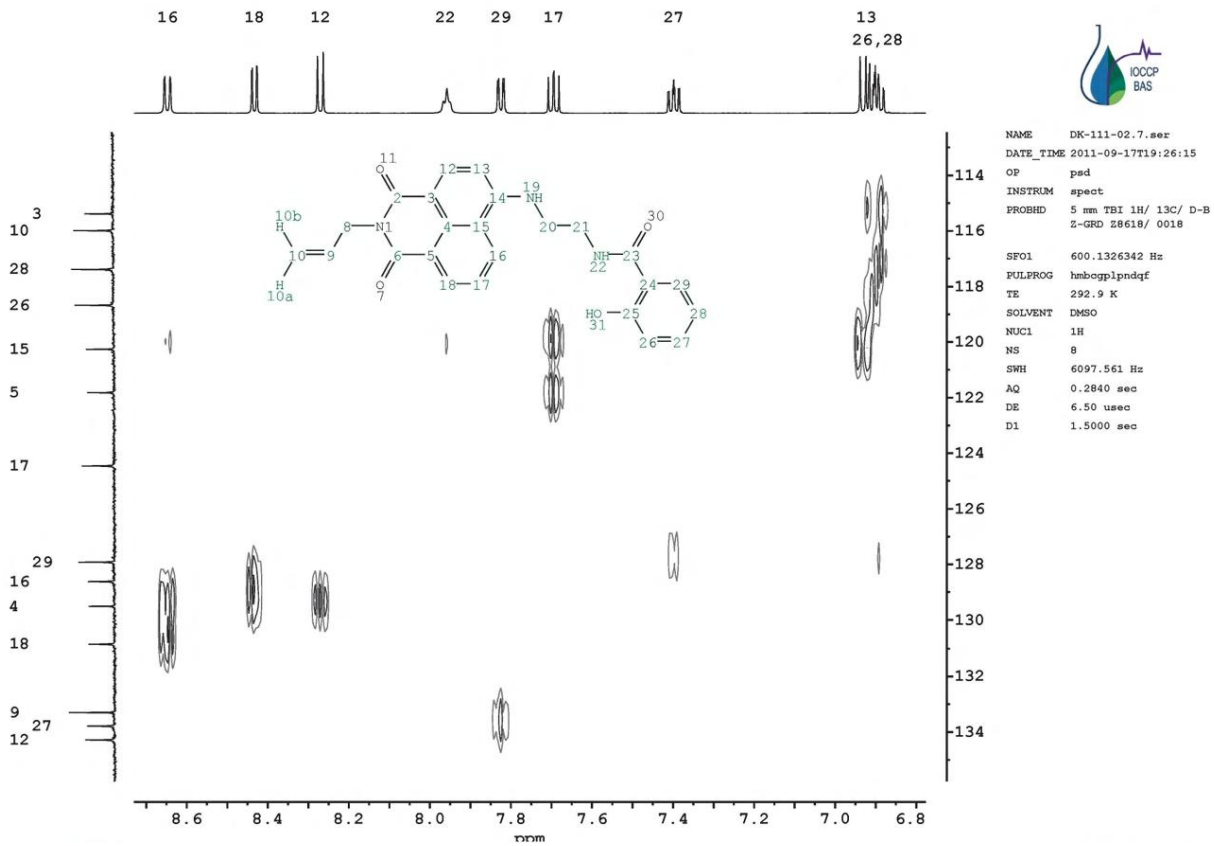


Figure 4–89. HMBC-NMR spectrum of compound **L4** in DMSO.

4.7 Contributions & Aknowledgements

4.7.1 Author Contributions

Frederico Duarte: Formal analysis, Investigation, Writing - Original Draft, Writing - Review & Editing, Visualization.

Diogo Torres: Formal analysis, Investigation, Writing - Original Draft, Writing - Review & Editing, Visualization.

Georgi Dobrikov: Methodology, Validation, Formal Analysis, Investigation, Writing - Original Draft, Writing - Review & Editing, Resources, Visualization.

Atanas Kurutos: Methodology, Validation, Formal Analysis, Investigation, Conceptualization Writing - Original Draft, Writing - Review & Editing, Resources, Visualization, Supervision, Funding acquisition.

Luisa B. Maia: Formal analysis, Investigation, Writing - Original Draft, Writing - Review & Editing, Visualization.

Ivaylo Slavchev Investigation & Review & Editing.

Jose Luis Capelo-Martinez: Resources, Writing - Review & Editing, Funding acquisition.

Hugo M. Santos: Investigation, Resources, Validation, Writing - Review & Editing, Funding acquisition

Carlos Lodeiro: Conceptualization, Methodology, Validation, Formal Analysis, Investigation, Resources, Writing - Review & Editing, Resources, Visualization, Supervision, Funding acquisition, Project administration

4.7.2 Acknowledgments

This work was supported by the Associate Laboratory for Green Chemistry LAQV which is financed by national funds from *Fundação para a Ciência e Tecnologia and Ministério da Ciência, Tecnologia e Ensino Superior* (FCT/MCTES) through the projects UIDB/50006/2020 and UIDP/50006/2020. PROTEOMASS Scientific Society (Portugal) is acknowledged by the funding provided through the General Funding Grant 2024-2025, and by the funding provided to the Laboratory for Biological Mass Spectrometry Isabel Moura (#PM001/2019 and #PM003/2016). F.D. thanks to FCT/MCTES (Portugal) for his doctoral grant 2021.05161.BD. H. M. S. acknowledges the Associate Laboratory for Green Chemistry LAQV (LA/P/0008/2020) funded by FCT/MCTES for his research contract. This work was supported by the Associate Laboratory for Green Chemistry - LAQV (UIDB/50006/2020 (DOI: 10.54499/UIDB/50006/2020) and

UIDP/50006/2020 (DOI: 10.54499/UIDP/50006/2020)), which are financed by national funds from Fundacão para a Ciência e a Tecnologia, MCTES (FCT/MCTES). LBM also thanks to FCT/MCTES, for the CEEC-Ind Program Contract. C.L. and H. M.S thanks the Royal Society of Chemistry for the Sustainable Laboratory Grants 2023 reference L23-8861107285.

The financial support by the Bulgarian National Science Fund (BNSF) under grant – "Novel styryl and polymethine fluorophores as potential theranostic agents "contract N◦ КП-06-М59/1 from 15.11.2021 is gratefully acknowledged by A.K. This work is also developed and acknowledged by A.K. as part of contract №: BG-RRP-2.004-0002-C01, Laboratory of Organic Functional Materials (Project BiOrgaMCT), Procedure BG-RRP-2.004 „Establishing of a network of research higher education institutions in Bulgaria", funded by BULGARIAN NATIONAL RECOVERY AND RESILIENCE PLAN".

G. D. thanks to the European Regional Development Fund within the Operational Programme Science and Education for Smart Growth 2014 - 2020 under the Project Center of Excellence: National center of mechatronics and clean technologies - BG05M2OP001-1.001-0008 for the financial support.

This work received support from PT national funds (FCT/MCTES, *Fundação para a Ciência e Tecnologia* and *Ministério da Ciência, Tecnologia e Ensino Superior)* through the projects UIDB/50006/2020 and UIDP/50006/2020. This work received support from PROTEOMASS Scientific Society through the General Funding Grant 2022-2023, and the projects #PM001/2019 and #PM003/2016. This work is also developed and acknowledged by A.K. as part of contract №: BG-RRP-2.004-0002-C01, Laboratory of Organic Functional Materials (Project BiOrgaMCT), Procedure BG-RRP-2.004 „Establishing of a network of research higher education institutions in Bulgaria", funded by BULGARIAN NATIONAL RECOVERY AND RESILIENCE PLAN".

4.8 References

[1] X. Yuan, T. H. Leng, Z. Q. Guo, C. Y. Wang, J. Z. Li, W. W. Yang and W. H. Zhu, A FRET-based dual-channel turn-on fluorescence probe for the detection of Hg^{2+} in living cells, *Dyes and Pigments* **161** (2019) 403–410. DOI: 10.1016/j.dyepig.2018.09.078.

[2] Y. Wang, J. Zhou, L. Zhao and B. Xu, A dual-responsive and highly sensitive fluorescent probe for Cu^{2+} and pH based on a dansyl derivative, *Dyes and Pigments* **180** (2020) 108513. DOI: 10.1016/j.dyepig.2020.108513.

[3] P. Wei, L. Xiao, Y. Gou, F. He, D. Zhou, Y. Liu, B. Xu, P. Wang and Y. Zhou, Fluorescent "on–off–on" probe based on copper peptide backbone for specific detection of Cu(II) and

hydrogen sulfide and its applications in cell imaging, real water samples and test strips, *Microchem. J.* **182** (2022) 107848. DOI: 10.1016/j.microc.2022.107848.

[4] R. Nagarajan, H. I. Ryoo, B. D. Vanjare, N. Gyu Choi and K. Hwan Lee, Novel phenylalanine derivative-based turn-off fluorescent chemosensor for selective Cu^{2+} detection in physiological pH, *J. Photochem. Photobiol. A Chem.* **418** (2021) 113435. DOI: 10.1016/j.jphotochem.2021.113435.

[5] L. He, Q. Li, Y. Zhang, K. Huang, B. Du and L. Liang, A naphthalimide functionalized fluoran with AIE effect for ratiometric sensing Hg^{2+} and cell imaging application *Spectrochim. Acta A Mol. Biomol. Spectrosc*. **296** (2023) 122672.

[6] L. Hu, K. Xie, A. Gao, Y. Hu and A. Hou, Synthesis of novel triazine-quinoline-appended naphthalimide sensors for Hg(II) recognition and their structure-activity relationship, *Dyes and Pigments* **199** (2022) 110048.

[7] Y. Li, Z. Ren, Y. Ge, C. Di, J. Zhou, J. Wu and L. Jia, A novel peptide fluorescent probe based on different fluorescence responses for detection of mercury species and hydrogen sulfide, *Microchem. J.* **184** (2023) 108160.

[8] F. Duarte, I. Pereira-Gomes, G. M. Dobrikov, J. Galhano, C. S. B. Gomes, A. Kurutos, H. M. Santos, E. Oliveira, M. Paula Duarte, J. Luis Capelo-Martinez and C. Lodeiro, Antimicrobial profile and Turn-On sensing of cyanide and water traces using a dual chromophoric Dansyl-Acridine conjugate as multifunctional system. *Microchem. J.* **205** (2024) 111237.

[9] H. Xu, Y. Xiao, Y. Liu and W. Sun, Research Progress on Naphthalimide Fluorescent Probes, *Adv. Sensor Res.* **3** (2024) 2300032.

[10] Y. G. Gao, K. Dang, W. J. Zhang, F. L. Liu, S. Patil, A. Qadir, A. X. Ding and A. R. Qian, A 1,8-naphthalimide-[12]aneN_3 derivative for efficient Cu^{2+} recognition, lysosome staining and siRNA delivery, *Colloids Surf. B Biointerfaces* **185** (2022) 110607.

[11] Z. Bao, C. Qin, J. jun Wang, J. Sun, L. Dai, G. Chen and F. Mei, A sensitive and selective probe for visual detection of Cu^{2+} based on 1,8-naphthalimidederivative, *Sens. Actuators B Chem.* **265** (2018) 234–241.

[12] H. Wang, J. Cui, X. Fang, W. Zhang, J. Wang, S. Chen and J. Qian, Fluorescent detection of copper ions with acylhydrazine-based probes: Effects of substitute and its position, *Dyes and Pigments* **197** (2022) 109954.

[13] F. C. Ho, Y. J. Huang, C. C. Weng, C. H. Wu, Y. K. Li, J. I. Wu and H. C. Lin, Efficien t FRET Approaches toward Copper(II) and Cyanide Detections via Host−Guest Interactions of Photo-Switchable [2]Pseudo-Rotaxane Polymers Containing Naphthalimide and Merocyanine Moieties, *ACS Appl. Mater. Interfaces* **12** (2020) 53257–53273.

[14] C. Liu, J. Xu, F. Yang, W. Zhou, Z. Li, L. Wei and M. Yu, Nanomolar $Cu^{2+}$and F^{-} naked-eye detection with a 1,8-naphthalimide-based colorimetric probe, *Sens. Actuators B Chem.* **212** (2015) 364–370.

[15] Z. Li, J. T. Hou, S. Wang, L. Zhu, X. He and J. Shen, Recent advances of luminescent sensors for iron and copper: Platforms, mechanisms, and bio-applications, *Coord. Chem. Rev.* **469** (2022) 214695.

[16] S. Ghosh, S. Ghosh, S. Ranjan Dhara, N. Baildya and K. Ghosh, Naphthalimide-based new architecture for fluorescence turn-on sensing of Cu^{2+} and colorimetric detection of F^{-}/CN^{-}, *Methods* **225** (2024) 13–19.

[17] H. Cai, Y. Liang, L. Huang and J. Wang, Relay detection of Cu^{2+} and bovine serum albumin by a dansyl derivative-based fluorescent probe, *Spectrochim. Acta A Mol. Biomol. Spectrosc.* **277** (2022) 121281.

[18] Z. Guo, Q. Wang, D. Zhou, Y. An, P. Wang and F. Liao, A novel peptide-based fluorescent probe with a large stokes shift for rapid and sequential detection of Cu^{2+} and CN^{-} in aqueous systems and live cells, *Spectrochim. Acta A Mol. Biomol. Spectrosc.* **264** (2022) 120257.

[19] Y. L. Liu, L. Yang, P. Li, S. J. Li, L. Li, X. X. Pang, F. Ye and Y. Fu, A novel colorimetric and "turn-off" fluorescent probe based on catalyzed hydrolysis reaction for detection of Cu^{2+} in real water and in living cells, *Spectrochim. Acta A Mol. Biomol. Spectrosc.* **227** (2020) 117540.

[20] Y. Fu, X. X. Pang, Z. Q. Wang, Q. Chai and F. Ye, A highly sensitive and selective fluorescent probe for determination of Cu(II) and application in live cell imaging, *Spectrochim. Acta A Mol. Biomol. Spectrosc.* **208** (2019) 198–205.

[21] B. Guo, X. Pan, Y. Liu, L. Nie, H. Zhao, Y. Liu, J. Jing and X. Zhang, A reversible water-soluble naphthalimide-based chemosensor for imaging of cellular copper(II) ion and cysteine, *Sens. Actuators B Chem.* **256** (2018) 632–638.

[22] Y. Liu, B. Jiang, L. Zhao, L. Zhao, Q. Wang, C. Wang and B. Xu, A dansyl-based fluorescent probe for sensing Cu^{2+} in aqueous solution, *Spectrochim. Acta A Mol. Biomol. Spectrosc.* **261** (2021) 120009.

[23] S. Liang, Q. Tong, X. Qin, X. Liao, Q. Li and G. Yan, A hydrophilic naphthalimide-based fluorescence chemosensor for Cu^{2+} ion: Sensing properties, cell imaging and molecular logic behavior, *Spectrochim. Acta A Mol. Biomol. Spectrosc.* **230** (2020) 118029.

[24] S. Y. Park, W. Kim, S. H. Park, J. Han, J. Lee, C. Kang and M. H. Lee, An endoplasmic reticulum-selective ratiometric fluorescent probe for imaging a copper pool, *Chem. Comm.* **53** (2017) 4457–4460.

[25] H. Jiang, Z. Li, Y. Kang, L. Ding, S. Qiao, S. Jia, W. Luo and W. Liu, A two-photon fluorescent probe for Cu^{2+}based on dansyl moiety and its application in bioimaging, *Sens. Actuators B Chem.* **242** (2017) 112–117.

[26] B. Uttam, S. Polepalli, S. Sinha, A. Majumder and C. P. Rao, Selective Sensing and Removal of Mercury Ions by Encapsulating Dansyl Appended Calix[4]Conjugate in a Zeolitic Imidazolate Framework as an Organic−Inorganic Hybrid Nanomaterial, *ACS. Nano Mater.* **5** (2022) 11371–11380.

[27] H. Cheng, F. Yi, J. Sun, A. Li, X. Zhang, D. Guan, Y. Qu and J. Cao, A naphthalimide-based fluorescent probe with a benzoylthiourea trigger for detection of Hg(II) in cosmetics, *Dyes and Pigments* **226** (2024) 112135.

[28] C. Yang, Y. Li, N. Wu, Y. Zhang, W. Feng, M. Yu and Z. Li, Ratiometric upconversion luminescence nanoprobes for quick sensing of Hg^{2+} and cells imaging, *Sens. Actuators B Chem.* **326** (2021) 128841.

[29] X. Pang, J. Dong, L. Gao, L. Wang, S. Yu, J. Kong and L. Li, Dansyl-peptide dual-functional fluorescent chemosensor for Hg^{2+} and biothiols, *Dyes and Pigments* **173** (2020) 107888.

[30] A. Aliberti, P. Vaiano, A. Caporale, M. Consales, M. Ruvo and A. Cusano, Fluorescent chemosensors for Hg^{2+} detection in aqueous environment, *Sens. Actuators B Chem.* **247** (2017) 727–735.

[31] Y. Shinohara, K. Tsukamoto and H. Maeda, A fluorescent turn-on probe for Hg^{2+} with a high contrast designed by manipulating functional groups tethered to naphthalimide, *J. Photochem. Photobiol. A Chem.* **371** (2019) 407–413.

[32] P. Wang, Y. An and J. Wu, Highly sensitive turn-on detection of mercury(II) in aqueous solutions and live cells with a chemosensor based on tyrosine, *Spectrochim. Acta A Mol. Biomol. Spectrosc.* **230** (2020) 118004.

[33] M. Graves, M. S. Elioff, E. S. Knorr, J. B. Griffith and J. Hu, A fluorescent turn-on sensor for mercury (II) ions in near neutral poly (metharylic acid) solution, *Spectrochim. Acta A Mol. Biomol. Spectrosc.* **282** (2022) 121702.

[34] P. Srivastava, M. Verma, S. Sivakumar and A. K. Patra, A smart FRET probe exhibiting a molecular keypad lock device based on rapid detection of nitric oxide mediated by Cu^{2+} ion, *Sens. Actuators B Chem.* **291** (2019) 478–484.

[35] T. Mishra, S. Guria, J. Sadhukhan, D. Das, M. K. Das, S. S. Adhikari, S. Maity and P. Maiti, A naphthalimide appended rhodamine based biocompatible fluorescent probe: Chemosensor for selective detection of Hg^{2+} ion, live cell imaging and DFT study, *J. Photochem. Photobiol. A Chem.* **446** (2024) 115168.

[36] J. Gao, Y. He, Y. Chen, D. Song, Y. Zhang, F. Qi, Z. Guo and W. He, Reversible FRET Fluorescent Probe for Ratiometric Tracking of Endogenous Fe^{3+} in Ferroptosis, *Inorg. Chem.* **59** (2020) 10920–10927.

[37] H. J. Lee, M. J. Cho and S. K. Chang, Ratiometric Signaling of Hypochlorite by the Oxidative Cleavage of Sulfonhydrazide-Based Rhodamine−Dansyl Dyad, *Inorg. Chem*. **54** (2015) 8644–8649.

[38] F. Martins, A. Granja, S. Reis, P. Gameiro, G. Barone, M. G. P. M. S. Neves and A. M. G. Silva, Synthesis, fluorescence and theoretical insights into a novel FRET-based dansyl-rhodamine sensor for the in vitro detection of toxic bioaccumulated Hg(II) ions, *Spectrochim. Acta A Mol. Biomol. Spectrosc.* **329** (2025) 125534.

[39] N. Li, W. Qin, Y. Chen, K. Liu, S. Wang and F. Kong, Construction of a robust polarity sensitive platform and its application for tracking of lipid droplets decrease under oxidative stress in live cells, *Sens. Actuators B Chem.* **346** (2021) 130491.

[40] D. Yang, X. T. Wu, X. J. Cao and B. X. Zhao, A reversible ratiometric fluorescence probe for fast detection of trace water in different organic solvents, *Dyes and Pigments* **170** (2019) 107558.

[41] C. Zheng, X. Zhang, A. Gao, M. Ju, A. Hou and K. Xie, Adjustable multimodality fluorescence emissions and photochromism of functional molecular device containing double chromophores with intramolecular FRET process, *Dyes and Pigments* **228** (2024) 112238.

[42] J. Zhao, J. Zhang, B. Hu, C. Gao, Z. Li, Z. Sun and J. You, *Spectrochim. Acta A Mol. Biomol. Spectrosc.* **286** (2023) 121965.

[43] H. Lee, H. S. Lee, J. H. Reibenspies and R. D. Hancock, Mechanism of "Turn-on" Fluorescent Sensors for Mercury(II) in Solution and Its Implications for Ligand Design, *Inorg. Chem.* **51** (2012) 10904–10915.

[44] W. Deng, S. Li, M. Zhou, M. Zheng, P. Wang and Y. An, Ratiometric peptide-based fluorescent probe with large Stokes shift for detection of Hg^{2+} and S^{2-} and its applications in cells imaging and smartphone-assisted recognition, *Spectrochim. Acta A Mol. Biomol. Spectrosc.* **315** (2024) 124306.

[45] L. Zhang, P. Zhao, S. Yu, J. Kong, L. Gao and L. Li, Dansyl-modified tryptophan fluorescence sensor for highly sensitive and selective detection of Hg^{2+} in aqueous solutions, *Microchem. J.* **200** (2024) 110520.

[46] R. Tamizhselvi, R. Bhaskar, M. Beena, A. Palaniappan, S. K. A. Kumar and A. A. Napoleon, A dual responsive bis-thiophene affixed thiosemicarbazide based chemosensor for

colorimetrically Hg^{2+} and fluorometrically Cu^{2+} ions and their applications in live cell imaging, *Spectrochim. Acta A Mol. Biomol. Spectrosc.* **322** (2024) 124766.

[47] W. J. Shi, C. F. Li, Y. Huang, H. ya Tan, Y. F. Wei, F. Liu, L. X. Feng, L. Zheng, G. S. Chen and J. wu Yan, A remarkable colorimetric probe for fluorescent ratiometric and ON-OFF discriminative detection of Hg^{2+} and Cu^{2+} by double-channel imaging in living cells, *Dyes and Pigments* **171** (2019) 107782.

[48] L. L. Chang, Q. Gao, S. Liu, C. C. Hu, W. J. Zhou and M. M. Zheng, Selective and differential detection of Hg^{2+} and Cu^{2+} with use of a single rhodamine hydrazone-type probe in the absence and presence of UV irradiation, *Dyes and Pigments* **153** (2018) 117–124.

[49] N. Kundu, M. Maity, P. B. Chatterjee, S. J. Teat, A. Endo and M. Chaudhury, Reporting a Unique Example of Electronic Bistability Observed in the Form of Valence Tautomerism with a Copper(II) Helicate of a Redox-Active Nitrogenous Heterocyclic Ligand. *J. Am. Chem. Soc.* **133** (2011) 20104–20107. O. Sato, J. Tao and Y. Z. Zhang, Control of Magnetic Properties through External Stimuli, *Angew. Chem. Int. Ed.* **46** (2007) 2152-2187.

[50] O. Sato, J. Tao and Y. Z. Zhang, Control of Magnetic Properties through External Stimuli, *Angew. Chem. Int. Ed.* **46** (2007) 2152-2187. DOI: 10.1002/anie.200602205.

[51] S. Wiesner, A. Wagner, E. Kaifer and H. J. Himmel, A Valence Tautomeric Dinuclear Copper Tetrakisguanidine Complex, *Chem. Eur. J.* **22** (2016) 10438–10445.

[52] T. Tezgerevska, K. G. Alley and C. Boskovic, Valence tautomerism in metal complexes: Stimulated and reversible intramolecular electron transfer between metal centers and organic ligands, *Coord. Chem. Rev.* **268** (2014) 23-40.

[53] G. K. Gransbury, B. N. Livesay, J. T. Janetzki, M. A. Hay, R. W. Gable, M. P. Shores, A. Starikova and C. Boskovic, Understanding the Origin of One-orTwo-Step Valence Tautomeric Transitions in Bis(dioxolene)-Bridged Dinuclear Cobalt Complexes, *J. Am. Chem. Soc.* **142** (2020) 10692–10704.

[54] K. M. Hess, I. F. Leach, L. Wijtenhorst, H. Lee and J. E. M. N. Klein, Valence Tautomerism Induced Proton Coupled Electron Transfer: X-H Bond Oxidation with a Dinuclear Au(II) Hydroxide Complex, *Angew. Chem. Int. Ed.* **63** (2024) e202318916.

[55] D. G. Lonnon, T. L. Sang and S. B. Colbran, Valence Tautomerism and Coordinative Lability in Copper(II)-Imidazolyl-Semiquinonate Anion Radical Models for the Cu_B Center in Cytochrome *c* Oxidases, *J. Am. Chem. Soc.* **129** (2007) 5800–5801.

[56] C. Sambiagio, S. P. Marsden, A. J. Blacker and P. C. McGowan, Copper catalysed Ullmann type chemistry: from mechanistic aspects to modern development, *Chem. Soc. Rev.* **43** (2014) 3525-3550.

[57] D. M. Andrada, S. M. Soria-Castro, D. A. Caminos, J. E. Argüello and A. B. Peñéñory, Understanding the Heteroatom Effect on the Ullmann Copper-Catalyzed Cross-Coupling of X-Arylation (*X* =NH, O, S) Mechanism, *Catalysts* **7** (2017) 388.

[58] S. Strekalova, A. Kononov, I. Rizvanov and Y. Budnikova, Acetonitrile and benzonitrile as versatile amino sources in copper-catalyzed mild electrochemical C–H amidation reactions. *RSC Adv.* **11** (2021) 37540–37543.

[59] Z. Xu, M. X. Zhang, G. Li, X. Chen, S. H. Liu, H. Chen and J. Yin, Naphthalimide-sulfonamide fused dansyl-sulfonamide fluorescent probe for tracking glutathione of lysosome with a dual-emission manner, *Dyes and Pigments* **171** (2019) 107685.

[60] S. Das and P. Sahoo, A colorimetric sensor for hydrogen sulfide: Detection from biogas and quantitative estimation in water, *Sens. Actuators B Chem.* **291** (2019) 287–292.

[61] K. Bin Li, D. Zhou, X. P. He and G. R. Chen, Ratiometric glyco-probe for transient determination of thiophenol in full aqueous solution and river water, *Dyes and Pigments* **116** (2015) 52–57.

[62] Y. Kong, X. Wan, Z. Liu, F. Chen, F. Wu, G. Qin, D. Cao and Y. Cui, A novel dansyl-naphthalimide fluorescent probe for visualizing nitroxyl (HNO) in biological systems, *Sens. Actuators B Chem.* **350** (2022) 130852.

[63] I. B. Berlman, Handbook of fluorescence spectra of aromatic molecules. New York, USA: academic Press; 1971.

[64] D. Macdougall and W. B. Crummett, Guidelines for data acquisition and data quality evaluation in environmental chemistry, Anal*. Chem.*, **52** (1980) 2242–2249.

[65] G. L. Long and J. D. Winefordner, Limit of Detection A Closer Look at the IUPAC Definition, Anal*. Chem.* **55** (1983) 713A-724A.

[66] N. Bagherzadeh and A. Reza Sardarian, Green approach to new library of 1,8-naphthalimide fluorophores employing C-C and C-N cross coupling reactions by novel, durable, and reusable magnetic nanocatalyst bearing nickel (0) complex of 1,10-phenanthroline, *J. Photochem. Photobio.l A Chem.* **449** (2024) 115345.

[67] G. Huang, C. Li, X. Han, S. O. Aderinto, K. Shen, S. Mao and H. Wu, Sensitive and selective detection of Cu(II) ion: A new effective 1,8-naphthalimide-based fluorescence 'turn off' sensor, *Luminescence* **33** (2018) 660–669.

[68] A. Schulz, J. Wotschadlo, T. Heinze and G. J. Mohr, Fluorescent nanoparticles for ratiometric pH-monitoring in the neutral range, *J. Mater. Chem.* **20** (2010) 1475–1482.

[69] T. L. Benanti, P. Saejueng and D. Venkataraman, Segregated assemblies in bridged electron-rich and electron-poor p-conjugated moieties, *Chem. Comm.* (2007) 692–694.

[70] P. Chinapang, V. Ruangpornvisuti, M. Sukwattanasinitt and P. Rashatasakhon, Ferrocenyl derivative of 1,8-naphthalimide as a new turn-on f luorescent sensor for Au(III) ion, *Dyes and Pigments* **112** (2015) 236–238.

[71] F. M. Pfeffer, M. Seter, N. Lewcenko and N. W. Barnett, Fluorescent anion sensors based on 4-amino-1,8-naphthalimide that employ the 4-amino N–H, *Tetrahedron Lett.* **47** (2006) 5241–5245.

[72] T. Lim, J. Y. Ryoo, M. Jang and M. S. Han, Ligand-free Suzuki–Miyaura cross-coupling with low Pd content: rapid development by a fluorescence-based high-throughput screening method, *Org. Biomol. Chem.* **19** (2021) 1009–1016.

[73] R. Ohtani, Y. Anegawa, H. Watanabe, Y. Tajima, M. Kinoshita, N. Matsumori, K. Kawano, S. Yanaka, K. Kato, M. Nakamura, M. Ohba and S. Hayami, Metal Complex Lipids for Fluid–Fluid Phase Separation in Coassembled Phospholipid Membranes, *Angew. Chem. Int. Ed.* **60** (2021) 13603–13608.

[74] K. Cheng, Q. Z. Zheng, Y. Qian, L. Shi, J. Zhao and H. L. Zhu, Synthesis, antibacterial activities and molecular docking studies of peptide and Schiff bases as targeted antibiotics, *Bioorg. Med. Chem.* **17** (2009) 7861–7871.

[75] S. C. Dash and A. C. Dash, Proximity effect on the general base catalysed hydrolysis of amide linkage: The role of cationic surfactant, CTABr, *J. Chem. Sci.* **123** (2011) 497-507.

[76] E. Oliveira, R. M. F. Baptista, S. P. G. Costa, M. M. M. Raposo and C. Lodeiro, Solvatochromic Effects of bis(indolyl)thienylaril derivatives as new Colored Materials, *Photochem. Photobiol. Sci.* **13** (2014) 492–498.

[77] S. Mocanu, G. Ionita and I. Matei, Solvatochromic characteristics of dansyl molecular probes bearing alkyl diamine chains, *Spectrochim. Acta - Part A Mol. Biomol. Spectrosc.* **237** (2020) 118413.

[78] E. M. Nolan and S. J. Lippard, Tools and Tactics for the Optical Detection of Mercuric Ion, *Chem. Rev.* **108** (2008) 3443-3480.

[79] P. Gans, A. Sabatini and A. Vacca, Investigation of equilibria in solution. Determination of equilibrium constants with the HYPERQUAD suite of programs, *Talanta,* **43** (1996) 1739–1753.

[80] J. Peisach and W. E. Blumberg, Structural Implications Derived from the Analysis of Electron Paramagnetic Resonance Spectra of Natural and Artificial Copper Proteins, *Arch. Biochem. Biophys.* **165** (1974) 691-708.

[81] M.C. Biesinger, Advanced analysis of copper X-ray photoelectron spectra, *Surf. Interface Anal.* **49** (2017) 1325–1334.

[82] D. Alders, F.C. Voogt, T. Hibma, G.A. Sawatzky, Nonlocal screening effects in 2 p x-ray photoemission spectroscopy of NiO (100), *Phys Rev B* **54** (1996) 7716–7719.

5

ENHANCING WATER SENSING VIA AGGREGATION-INDUCED EMISSION (AIE) AND SOLVATOFLUOROCHROMIC STUDIES USING TWO NEW DANSYL DERIVATIVES CONTAINING A DISULFIDE BOUND: POLLUTANT METAL IONS DETECTION AND PREPARATION OF WATER-SOLUBLE FLUORESCENT POLYMERIC PARTICLES

Frederico Duarte, Georgi Dobrikov, Atanas Kurutos, Hugo M. Santos, Javier Fernández-Lodeiro, Jose Luis Capelo-Martinez, Elisabete Oliveira, Carlos Lodeiro

Dyes and Pigments 218 (2023) 111428 Doi: 10.1016/j.dyepig.2023.111428

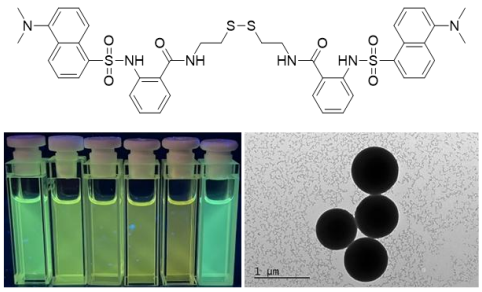
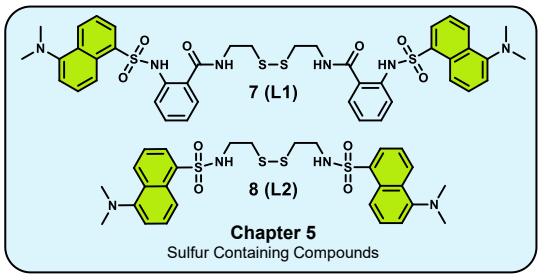


Figure 5–1. Graphical abstract.



Contribution to this work: Photophysical characterization; Preparation of polymeric doped microparticles; Sensing experiments of metal ions; Aggregation studies; Writing original draft.

5.1 Abstract

Polarity-sensitive dansyl derivatives **L1** and **L2** were synthesized and their ability to sense pollutant metal ions was investigated. All compounds were found to be highly sensitive towards Cu^{2+} and Hg^{2+} metal ions, while **L2** being able to detect and quantify Hg^{2+} concentrations as low as 2.5 μM. Both **L1** and **L2** exhibit positive solvatofluorochromic behaviour, modulated in the presence of water, which in turn results in fluorescence enhancement *via* aggregation-induced emission (AIE). Seeking stability and water solubility, luminescent **L1**-based polystyrene-block-polybutadiene-block-polystyrene (SBS) microparticles (size: 520 ± 76 nm) were successfully prepared while maintaining the fluorescence emission of fluorophore **L1** (ϕ = 22%). This work exemplifies the multiple properties of dansyl-derivatives and their promising applications in biomedicine and environmental fields.

5.2 Introduction

Over the past decades, the unique properties of dansyl derivatives have made them a useful tool for environmental science, analytical chemistry, biosensors and biological imaging. [1-9] The low intensity-excitation wavelengths of dansyl derivatives and high fluorescence quantum yield, provide strong conditions to be applied as biological probes and in the development of chemical sensors for the detection of heavy and transition metal ions. [10] The high sensitivity and selectivity of the dansyl moiety enhance the applicability for detecting these ions at low concentrations in the environment. The rather low detection limits reported of the dansyl derivatives for Cu^{2+}, ranging between 0.2 μM and 0.9 μM for Cu^{2+} and 140 nM for Hg^{2+}, respectively, turn it into a valuable vehicle for pollution control and environmental monitoring. [11-13] Additionally, their solvatochromic effect makes them suitable for imaging and environmental control, since changes in solvent polarity result in wavelength shifts in the absorption and emission bands. [1]

Numerous organic dyes express excellent fluorescent properties in solution, however, at higher concentrations or in the solid state, aggregation of these dyes results in a decrease in the intensity emission signal, due to non-radiative transitions. Since the first discovery in 2001 of fluorophores with aggregation-induced emission (AIE) reported by *Tang et. al.* [14], increasing popularity has been observed due to their high sensitivity, and selectivity. [15-18] In the AIE water-based mechanism, water modulates the aggregation state of the fluorophore,

resulting in fluorescence enhancement, providing a simple and direct way to monitor water content in complex environments, such as biological samples and industrial processes. [19-21]

Despite the plethora of available analytical methods for water detection, fluorescence-based techniques stand out to be the most rapid, sensitive and cost-effective approach. In fluorescent-based water sensors, as organic molecules, water can be detected by employing fluorescence "turn-off", "turn-on" or ratiometric methods. In the previous methods, photo-induced electron transfer (PET) and aggregation-induced emission (AIE) are some of the mechanisms discussed. [21] Among others, dansyl derivatives have been widely used as water sensors in organic solvents since they exhibit a strong fluorescence response to water content. [21] AIE platform has also been extensively used as a metal ion- responsive luminescent probe due to its sensitivity to the environment. [22,23]

However, the hydrophobicity of AIE-active organic compounds is still a challenging task when considering aqueous media applications. This challenge could be overcome by developing water soluble polymeric nanoparticles, opening new opportunities in biomedicine and environmental areas. [24,25] Fluorescent dye-doped polymer nanoparticles have shown great potential, providing significant improvements in sensitivity, stability, and enhanced fluorescence being many fold-brighter compared to traditional organic dyes. Dye-loaded polymer NPs allow high dye loading without aggregation-caused quenching (ACQ). Only recently were reported strategies to overcome ACQ in polymer nanoparticles, such as the design of organic compounds with the ability of AIE, resulting in increased fluorescence quantum yield and photostability. [2,26-29]

For more than twenty years the main focus of our research group has been devoted to sensing pollutant metal ions and anions using fluorescent polyamines [30-32], macrocycles, porphyrins or corroles [33,34], sulphur-containing sensors [35], and nanoparticles [36].

Based on our experience, in this work, two dansyl derivatives (L1 and L2) were synthesized and fully characterized. These two compounds contain two dansyl derivatives linked by a disulfide bridge (-S-S-). Studies in the literature reveal that compounds containing two chromophores linked by a bridge can increase sensitivity, specificity, stabilization, and lifetime [37,38]. Moreover, the presence of an S-S bridge has advantages for biological applications, such as detecting protein-protein interactions or conformational changes in a target protein. [39]

Aiming the creation of new breakthroughs in the state of the art, the multiple properties and advantages above-mentioned of dansyl derivatives were fully explored, such as (i) the solvatochromic effect, (ii) sensing ability towards pollutant metal ions, (iii) water detection in organic solvent *via* AIE, photostability, as well as (iv) the production of dansyl derivative (**L1**)

doped polystyrene-block-polybutadiene-block-polystyrene (SBS) microparticles (L1@SBS) [40], aiming higher fluorescence quantum yields *via* AIE in water.

5.3 Experimental Section

5.3.1 Materials

The metal salts: $Cu(OTf)_2$, $Cd(OTf)_2$, $Co(OTf)_2$, Ag(OTf), $Pb(OTf)_2$, $Zn(OTf)_2$, $Ni(OTf)_2$ and $Ca(OTf)_2$ were purchased from Solchemar, while $Hg(OTf)_2$, dansyl amide and all solvents were acquired from Sigma Aldrich without requiring additional steps of purification. Spectroscopy grade solvents were used for measuring the electronic and fluorescence spectra – acetonitrile (CH_3CN), chloroform ($CHCl_3$), toluene, ethanol (EtOH), dimethylsulfoxide (DMSO) and tetrahydrofuran (THF). Poly(styrene-butadiene-styrene) (SBS) was purchased from Sigma-Aldrich (St. Louis, MO, USA). Mili-Q ultrapure water was used in all experiments. The analytical grade reagents and solvents needed for the synthesis of the target dansyl derivatives were purchased from Alfa Aesar, Fluka, Fluorochem Ltd, Merck, TCI, and Sigma-Aldrich, and were utilized as received. TLC was used to monitor the reaction outcome (Merck silica gel 60 F254 precoated TLC plates - 0.2 mm thick). Purification of the crude products was achieved by column chromatography employing silica gel as a stationary phase. Details about the employed mobile phases are given in the corresponding synthetic protocols listed below.

5.3.2 Instrumentation

Dynamic light scattering (DLS) data has been obtained from a Malvern Zetasizer Nano series (Worcestershire, WR14 1XZ, UK) from PROTEOMASS Scientific Society-BIOSCOPE Facility Lab. Samples have been analyzed at a scattering angle of 90° and at a temperature of 25°C while supported in a glass cell. The z-potential measurement of microparticles was performed using a dip-cell.

High-Resolution Mass Spectrometry analyses were carried out in the Laboratory for Biological Mass Spectrometry–Isabel Moura (PROTEOMASS Scientific Society Facility), using UHR ESI-Qq-TOF IMPACT HD (Bruker-Daltonics, Bremen, Germany). Compounds were dissolved in 50% (v/v) Acetonitrile containing 0.1% (v/v) aqueous formic acid to obtain a working solution of 0.1 µg/mL. Mass spectrometry analysis was carried out by the direct infusion of the compound solutions into the ESI source. MS data were acquired in positive polarity over the mass

range of 80 – 1300 m/z. (Capillary voltage: 4500 V, End plate offset: -500 V, Charging voltage: 2000 V, Corona: 4000 nA, Nebulizer gas: 0.4 Bar, Dry Heater: 180°C, Dry gas: 4.0 L/min).

Transmission electron microscopy (TEM) images were obtained using a JOEL JEM 1010 transmission electron microscope from the CACTI, University of Vigo (Spain), operating at 100 kV. Samples were prepared by dropping 5 µL of the colloidal suspension on a copper grid coated with a continuous carbon film, and the solvent was allowed to evaporate. The size of particles and histograms were calculated from TEM images using the ImageJ software (Image 1.51h, Wayne Rasband, National Institutes of Health, Bethesda, MD, USA).

UV-Vis absorption spectra were recorded with a JASCO V-650 spectrophotometer, while fluorescence emission was on a HORIBA Scientific FLUOROMAX-4 spectrofluorimeter from PROTEOMASS Scientific Society Facility. All samples were carried out at 293 K with recourse to rectangular quartz cells of 10 mm in width. Visualization of the TLC was performed using a Vilber UV Lamp (BVL-6.LC dual wavelength 254 nm/365 nm, operational power of 2×6 Watts). Using a combination of ^{1}H-NMR, ^{13}C-NMR, 2-D COSY, HSQC, HMBC, and high-resolution mass spectrometry, all compounds' chemical identities were verified. Using 5 mm tubes on a Bruker Avance II+ 600 spectrometer, the ^{1}H-NMR and ^{13}C-NMR spectra were measured in $CDCl_3$ at 293 K at operating frequencies of 600.13 MHz and 150.92 MHz, respectively. ^{1}H and ^{13}C NMR spectra were calibrated to the signal of tetramethylsilane (TMS), δ=0.00. Chemical shifts are measured to an accuracy of 0.01 parts per million (ppm). The coupling constants (*J*) are shown with a precision of 0.1 and represented in Hz. The spin multiplicity in the 1H-NMR was denoted by the abbreviations *s* = singlet, *d* = doublet, *t* = triplet, *q* = quartet, *dd* = doublet of doublets, *dt* = doublet of triplets, *td* = triplet of doublets, and *m* = multiplet.

5.3.3 Synthetic procedures

5.3.3.1 Synthesis of L1

Synthesis of intermediate *N,N'*-(disulfanediylbis(ethane-2,1-diyl))bis(2-aminobenzamide) (**3**):

In a 100 ml flask charged with 50 mL dry dichloromethane (DCM) were added consequently anthranilic acid (**2**) (0.600 g, 4.38 mmol, 2.2 eq.), diamine **1** as di-HCl salt (0.450 g, 1.99 mmol, 1.0 eq.), diisopropylethylamine (DIPEA) (1.54 g, 1.97 mL, 11.93 mmol, 6.0 eq.) and TBTU (1.41 g, 4.38 mmol, 2.2 eq.). The formed clear solution was stirred at r.t. for 41 h. TLC of reaction mixture – DCM:methyl-*tert*-butyl ether (MTBE) = 5:1, x2. Workup: dilution with 30 mL DCM and washing with 1% aq. citric acid, sat. aq. $NaHCO_3$ and finally with water. The organic phase was

dried over anhydrous Na_2SO_4, filtered and evaporated to dryness. This crude product was purified by column chromatography: 75 g silica; phase 1 - DCM:MTBE=5:1 (to remove contaminations); phase 2 - DCM:MTBE=5:2 (for product). After solvent evaporation and drying *in vacuo*, product **3** was obtained as a white powder (0.760 g, 99%). m.p. 132-133°C. ^{1}H NMR (600 MHz, $CDCl_3$) δ 7.38 (*dd*, *J* = 7.9, 1.5 Hz, 2H, H-5), 7.20 (*m*, 2H, H-3), 6.78 (*s*, 2H, CO-N<u>H</u>), 6.72 – 6.57 (*m*, 4H, H-2 and H-4), 5.48 (*s*, 4H, N<u>H</u>$_2$), 3.76 (*q*, *J* = 6.3 Hz, 4H, H-7), 2.95 (*t*, *J* = 6.4 Hz, 4H, H-8). ^{13}C NMR (151 MHz, $CDCl_3$) δ 169.56 (2C, <u>C</u>=O), 148.74 (2C, C-1), 132.49 (2C, <u>C</u>H$_{arom.}$), 127.40 (2C, <u>C</u>H$_{arom.}$), 117.34 (2C, <u>C</u>H$_{arom.}$), 116.69 (2C, <u>C</u>H$_{arom.}$), 115.82 (2C, C-6), 38.61 (2C, C-7 or C-8), 38.04 (2C, C-7 or C-8).

Synthesis of *N,N'*-(disulfanediylbis(ethane-2,1-diyl))bis(2-((5-(dimethylamino)naphthalene)-1-sulfonamido)benzamide) (**L1**)

Compound **3** (0.300 g, 0.77 mmol, 1.0 eq.) was dissolved in 5 mL dry pyridine. Then dansyl chloride (0.456 g, 1.69 mmol, 2.2 eq.) was added and the formed clear solution was stirred at r.t. for 72 h. Workup: excess of conc. aq. citric acid was added and extracted with DCM. The organic phase was washed with water, dried over anhydrous Na_2SO_4, filtered and evaporated to dryness. This crude product was purified by column chromatography: 70 g silica, phase DCM:MTBE=20:1. After solvent evaporation and drying *in vacuo*, product **L1** was obtained as a yellow powder (0.510 g, 78%). m.p. 123-124°C. ^{1}H NMR (600 MHz, $CDCl_3$) δ 11.17 (*s*, 2H, SO_2-N<u>H</u>), 8.46 (*dt*, *J* = 8.6, 1.1 Hz, 2H, H-9), 8.32 (*d*, *J* = 8.6 Hz, 2H, H-4), 8.23 (*dd*, *J* = 7.3, 1.2 Hz, 2H, H-7), 7.55 – 7.47 (*m*, 4H, H-3 and H-15), 7.43 (*dd*, *J* = 8.5, 7.3 Hz, 2H, H-8), 7.30 (*dd*, *J* = 7.9, 1.5 Hz, 2H, H-12), 7.26 (*m*, 2H, H-13), 7.12 (*d*, *J* = 7.6 Hz, 2H, H-2), 6.88 (*td*, *J* = 7.5, 1.1 Hz, 2H, H-14), 6.62 (*t*, *J* = 5.9 Hz, 2H, CO-N<u>H</u>), 3.54 (*q*, *J* = 6.3 Hz, 4H, H-17), 2.82 (*s*, 12H, C<u>H</u>$_3$), 2.78 (*t*, *J* = 6.3 Hz, 4H, H-18). ^{13}C NMR (151 MHz, $CDCl_3$) δ 168.67 (2C, <u>C</u>O-NH), 151.77 (2C, C-1), 138.71 (2C, C-11), 134.63 (2C, C-6), 132.62 (2C, C-13), 130.77 (2C, C-9), 129.91 (2C, C-7), 129.79 (2C, C-5 or C-10), 129.46 (2C, C-5 or C-10), 128.39 (2C, C-15), 126.88 (2C, C-12), 123.01 (2C, C-8 or C-14), 122.99 (2C, C-8 or C-14), 120.53 (2C, C-16), 119.84 (2C, C-3), 118.96 (2C, C-4), 115.31 (2C, C-2), 45.39 (4C, <u>C</u>H$_3$), 38.83 (2C, C-17 or C-18), 37.41 (2C, C-17 or C-18). ESI-HRMS: $[M+H]^+$ for $C_{42}H_{44}N_6O_6S_4$ = 857.2270 (- 0.9 ppm), $[M+2H]^{2+}$ $C_{42}H_{44}N_6O_6S_4$ = 429.1175 (- 0.1 ppm). Calculated $[M+H]^+$ for $C_{42}H_{44}N_6O_6S_4$ = 857.227794, and $[M+2H]^{2+}$ $C_{42}H_{44}N_6O_6S_4$ = 429.117535.

5.3.3.2 Synthesis of L2

Synthesis of *N,N'*-(disulfanediylbis(ethane-2,1-diyl))bis(5-(dimethylamino)naphthalene-1-sulfonamide) (**L2**)

Diamine **1** as di-HCl salt (0.250 g, 1.11 mmol, 1.0 eq.) and Et_3N (0.560 g, 0.77 mL, 5.55 mmol, 5.0 eq.) were dissolved in 50 mL dry DCM and cooled to 5°C using an ice-water bath. Then dansyl chloride (0.659 g, 2.44 mmol, 2.2 eq.) was added in one portion and the formed clear mixture was stirred for 30 min at 5°C, followed by 20 h at r.t. TLC of reaction mixture – DCM:MTBE=5:1, x1. Workup: dilution with 30 mL DCM and washing with 1% aq. citric acid and water. The organic phase was dried over anhydr. Na_2SO_4, filtered, and evaporated to dryness. The crude product was purified by column chromatography: 70 g silica, phase DCM:MTBE=10:1. After evaporation of phase and drying *in vacuo*, product **L2** was obtained as a yellow powder (0.65 g, 95%). m.p. 74-75°C. ^{1}H NMR (600 MHz, $CDCl_3$) δ 8.54 (*dd*, *J* = 8.5, 1.1 Hz, 2H, H-9), 8.27 – 8.22 (*m*, 4H, H-4 and H-7), 7.55 (*dd*, *J* = 8.7, 7.5 Hz, 2H, H-3), 7.52 (*dd*, *J* = 8.5, 7.3 Hz, 2H, H-8), 7.18 (*d*, *J* = 7.6 Hz, 2H, H-2), 5.21 (*t*, *J* = 6.3 Hz, 2H, SO_2-N<u>H</u>), 3.10 (*q*, *J* = 6.3 Hz, 4H, H-11), 2.89 (*s*, 12H, C<u>H</u>$_3$), 2.49 (*t*, *J* = 6.3 Hz, 4H, H-12). ^{13}C NMR (151 MHz, $CDCl_3$) δ 152.05 (2C, C-1), 134.38 (2C, C-6), 130.69 (2C, C-9), 129.86 (2C, C-5 or C-10), 129.69 (2C, C-3), 129.47 (2C, C-5 or C-10), 128.60 (2C, C-7), 123.19 (2C, C-8), 118.55 (2C, C-4), 115.30 (2C, C-2), 45.42 (4C, <u>C</u>H$_3$), 41.56 (2C, C-11), 37.73 (2C, C-12). ESI-HRMS: $[M+H]^+$ for $C_{28}H_{34}N_4O_4S_4$ = 619.1543 (1.2 ppm), and $[M+2H]^{2+}$ for $C_{28}H_{34}N_4O_4S_4$ = 310.0811 (2.2 ppm). Calculated $[M+H]^+$ for $C_{28}H_{34}N_4O_4S_4$ = 619.153566 and $[M+2H]^{2+}$ for $C_{28}H_{34}N_4O_4S_4$ = 310.080421.

5.3.4 Spectrophotometric and spectroflurimetric measurements

5.3.4.1 Photophysical characterization and titrations

The spectroscopic characterizations and titrations were performed using stock solutions of compounds **L1** and **L2** (ca. 10^{-3} M) in various organic solvents (CH_3CN, EtOH, DMSO, $CHCl_3$, toluene and THF), prepared by dissolving the appropriate amount of the selected compound in a 10 mL volumetric flask. The studied solutions were prepared by appropriate dilution of the stock solutions to 10^{-5} – 10^{-6} M.

Titrations of **L1** and **L2** were carried out by the addition of microliter aliquots of standard solutions of Ca^{2+}, Co^{2+}, Ni^{2+}, Cu^{2+}, Zn^{2+}, Ag^+, Cd^{2+}, Hg^{2+}, Pb^{2+} ions in acetonitrile. A correction for the absorbed light was performed when necessary.

Spectra of solid samples were collected with a Horiba-Jobin-Yvon Fluoromax-4® spectrofluorometer using an optic fibre connected to the equipment, by exciting the solid compounds at appropriated λ (nm). All measurements were performed at 298 K.

Additionally, mixtures containing different water fractions (f_w), (f_w = 0%, 17%, 33%, 55%, 67% and 83%) with a final concentration of 10 mM were prepared and characterized by absorption and emission spectroscopy.

Table 5-1. Spectroscopic polarity parameters, physical properties of the different solvents. ε_r : relative permittivity; η: refractive index; α: the solvent's HBD acidity; β: the solvent´s HBA basicity; π^*: the solvent´s dipolarity/polarizability.

Solvent	ε_r	α	β	π^*	η
DMSO	47.24	0	0.76	1.00	1.47
CH_3CN	35.94	0.19	0.40	0.66	1.34
EtOH	24.30	0.86	0.75	0.54	1.36
THF	7.58	0	0.55	0.58	1.40
$CHCl_3$	4.89	0.20	0.10	0.69	1.44
Toluene	2.38	0	0.11	0.54	1.49

5.3.4.2 Fluorescence quantum yield and Lifetime

Relative photoluminescence quantum yield measurements were conducted using a solution of dansyl amide in acetonitrile as the reference standard. This approach was employed to quantify the relative quantum yields of both compounds when dissolved in acetonitrile (ϕ_F = 0.37), while the remaining ones were measured relative to the standard solution of dansyl amide in DMSO (ϕ_F = 0.61), as well as for both compounds in f_w = 83%. [41] The quantum yield for the polymeric particles of **L1** was obtained relative to the compound itself in chloroform. Tempro Fluorescence Lifetime System with a Nanoled pulsed diode controller from Horiba Jobin-Yvon (PROTEOMASS Scientific Society Facility) was used to perform lifetime measurements

5.3.5 Synthesis of polymeric microparticles

A solution of polymer matrix styrene-butadiene-styrene block copolymer (SBS) (50 mg) in 2 mL of tetrahydrofuran (THF) was prepared and heated at 70°C for 5 min aiming to allow solubilization. When the solution was cooled back to room temperature, an aliquot of 0.6 mL was quickly added to **L1** (0.5 mg) and transferred over 2.4 mL of deionized water, maintaining a magnetic stirring at 400 rpm for 5 min. The resulting mixture was stored at 20°C in the dark for 24 h for oil-in-water droplets stabilization. The final particles were obtained after evaporation of THF at room temperature for 24 h. Before use, a filtration step using glass membranes

with a pore size of 10–15 µm was performed to remove potential non-encapsulated **L1** and polymer precipitates.

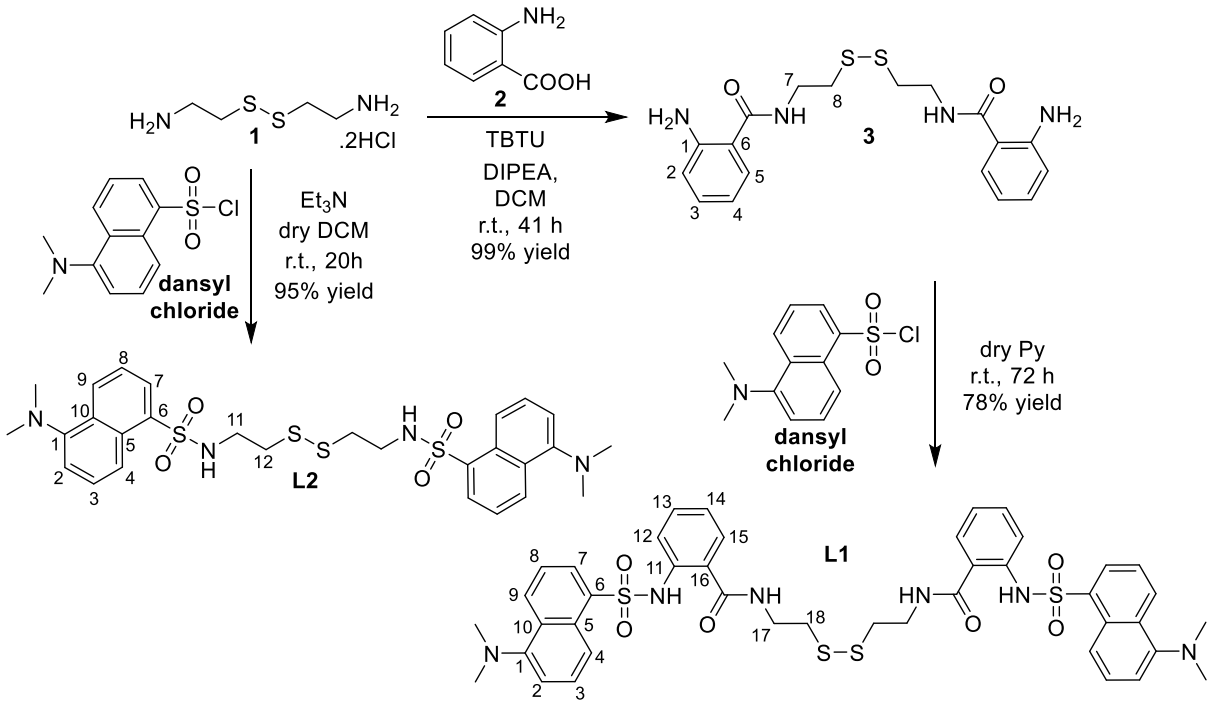
5.3.6 Determination of the detection and quantification limits (LOD and LOQ)

For the determination of the detection limit (LOD) and the quantification limit (LOQ), ten different measurements of a solution containing the selected probe were collected without the addition of any metal ion (y_{blank}). The LOD and LOQ were determined using the formulas:
LOD = y_{dl} = y_{blank} + 3std, where y_{dl} = signal detection limit and std = standard deviation.
LOQ = y_{dl} = y_{blank} + 10std, where y_{dl} = signal detection limit and std = standard deviation.
Additionally, small amounts of the metal ion were added to a solution containing **L1** and **L2**, to determine the minimal detectable and quantified concentration out of the LOD and LOQ values, respectively.

5.4 Results & Discussion

5.4.1 Synthesis

The synthesis of the target sulfonamides **L1** and **L2** was accomplished according to Scheme 5-1. Compound **L1** was synthesized in two steps. The first step includes the preparation of intermediate **3** quantitative starting from anthranilic acid (**2**) and **1** (both commercial products) proceeding at ambient temperature, by implementation of classical conditions of the peptide synthesis - presence of coupling reagent 2-(1*H*-benzotriazole-1-yl)-1,1,3,3-tetramethylaminium tetrafluoroborate (TBTU) under basic conditions (excess of DIPEA in dichloromethane). After isolation and purification, compound **3** was reacted with commercial dansyl chloride in dry pyridine (Py) at r.t. to furnish **L1** in 78% yield. Direct acylation of the diamine **1** with dansyl chloride (with excess of tryethylamine) in dry dichloromethane (DCM) affords the target product **L2** in 95% yield. The preparation of this compound was previously reported in the literature, concerning an investigation of fluorescent thiomaleimides. [42]



Scheme 5-1. Synthetic approach to the preparation of the target **L1** and **L2** fluorophores.

It is known from the literature, that dithio groups in ligands are able to form stable chelating complexes with transition and heavy metals [43-45], with or without S-S bond breaking. This is the main reason for introducing the dithio function in **L1** and **L2**. Moreover, dithio compounds have an advantage over their corresponding thiols because they are more stable and resistant to oxidation from air. This is important in order to obtain and store ligands in pure form, without the need of special conditions (i.e. inert atmosphere).

5.4.2 Photophysical characterization

Figure 5–2 shows the main photophysical characterization of **L1** and **L2** evaluated at 298 K in acetonitrile. Compounds **L1** and **L2** exhibit two main absorption bands at 332 nm and 340 nm, respectively, which is a hallmark of the π-π* transition of the dansyl chromophore, being colourless when observed by the unaided eye. Concerning the emission properties, fluorophore **L1** shows a maximum emission band located at 527 nm and **L2** at 518 nm, both of which emit an intense green colour under UV light. In the solid state, the emission of both compounds is characterized by a pronounced blue-shift of about 20 nm compared to the solution. Hence, 507 nm and 499 nm for **L1** and **L2**, respectively. The incorporation of a benzene ring as in the case of **L1** leads to a red-shift in the emission wavelength, as well as, in the solid state compared to **L2**, due to extending the conjugation, with the consequent decrease in fluorescence

quantum yield, rendering a compound less stable in the excited state, thus shortening its life-time (see Figure 5–2).

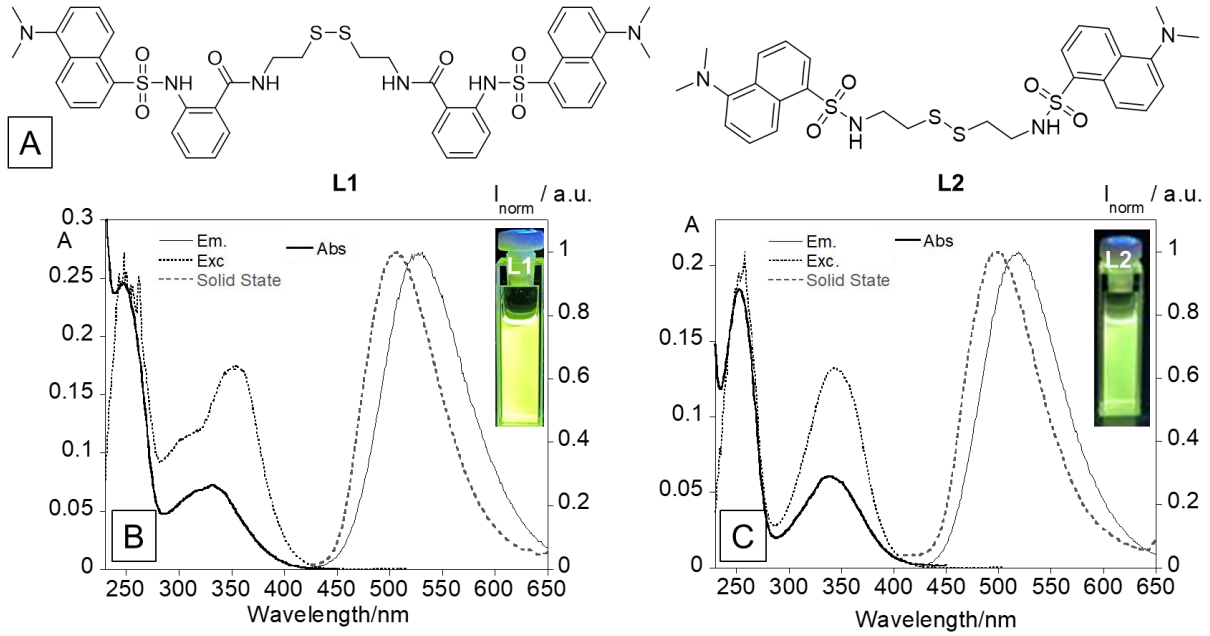


Figure 5–2. (A) Chemical structure of dansyl derivatives **L1** and **L2**. Absorption, excitation, emission and solid-state emission spectra for **L1** (B) and **L2** (C) in CH_3CN ([**L1**]=[**L2**]= 6 μM).

Table 5-2. Photophysical data of the dansyl derivatives **L1** and **L2** evaluated in organic solvents.

Cpd	Solv	λ_{abs} [nm]	λ_{em} [nm]	ε (10^4) [cm^{-1} M^{-1}]	Stokes shift [cm^{-1}]	ϕ(%)	λ_{em}^{Solid} [nm]	t[ns]
L1	DMSO	347	535	1.05	10127	30	507	14
	CH_3CN	332	527	0.94	11145	29		10
	EtOH	330	520	0.91	11072	24		13
	THF	336	507	1.11	10038	47		13
	$CHCl_3$	343	504	0.85	9313	52		14
	Toluene	341	498	1.03	9245	49		12
L2	DMSO	337	520	1.37	10443	59	499	17
	CH_3CN	340	518	0.99	10107	34		12
	EtOH	338	514	1.13	10131	33		13
	THF	336	497	1.20	9641	50		12
	$CHCl_3$	340	498	1.02	9331	56		15
	Toluene	338	488	0.83	9094	57		12

In order to evaluate the sensitivity of **L1** and **L2** to solvent polarity, both compounds were characterized and studied in six different solvents, including DMSO, CH_3CN, EtOH, THF, $CHCl_3$ and toluene (Figure 5–9 to Figure 5–12).

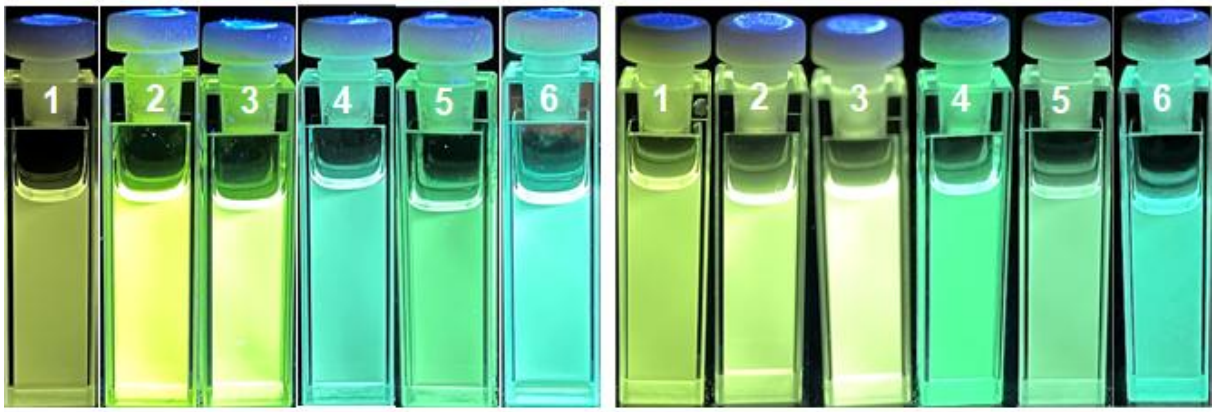
As can be seen in Table 5-2, in absorption despite their different maximum bands in all solvents, there is no correlation with the solvent polarity increase. However, in the emission, a red shift of the maximum bands is verified, from 498 nm to 535 nm in **L1** and from 488 nm to 520 nm in **L2**, as the polarity of the solvent increases.

Thus, polar solvents appear to have a significant impact on the stabilization of the compounds, where L1 and L2 exhibit greater stabilization of the excited state in these solvents. Based on the observed shifts in the emission spectra, **L1** and **L2** are denominated positive solvatofluorochromic. This phenomenon has important applications in imaging, biology and biomedicine to measure local polarity in biological structures. [46]

To shed more light on the **L1** and **L2** solvatofluorochromic behaviour, and to quantitatively characterize the solute-solvent interactions, the multiparametric fitting of the Kamlet-Taft equation (Equation 1) was performed allowing the determination of the three solute-dependent parameters (υ_0, a, b and p).

$$\upsilon = \upsilon_0 + a\alpha + b\beta + p\pi^* \qquad \text{(Equation 1)}$$

Where υ_0 is the value of emission in a reference solvent; parameters a, b and p are the responses of the solute property to the solvent property, α: the solvent's hydrogen bond donor (HBD) acidity; β: the solvent's hydrogen bond acceptor (HBA) basicity; π^*: the solvent's dipolarity /polarizability (Table 5-1). [47,48] Figure 5–3 shows the images of **L1** and **L2** under a UV light lamp and based on the fitting linear plots of $\upsilon_{exp.}$ versus $\upsilon_{calc.}$, the fitted parameters (υ0, a, b and p), the slope and correlation coefficients.



	L1				L2	
	υ_0	a	b	p	Slope	R^2
L1	21244	-388	-885	-1861	0.99	0.99
L2	21531	-707	-664	-1796	0.99	1

Figure 5–3. (Top) Images of **L1** and **L2** under a UV light lamp. Polarity decreases from 1 to 6 (1 – DMSO; 2 – CH_3CN; 3 – EtOH; 4 – THF; 5 – $CHCl_3$; 6 – toluene). (Down) υ_0, a, b and p-values, in cm^{-1}, slope and correlation coefficients obtained from Kamlet–Taft multiparametric fitting of the emission data.

According to the Kamlet-Taft parameters of each compound, **L2** is more polar than **L1**, which could be attributed to differences in their molecular structure. On the other hand, **L1** has the highest polarizability, having the ability to be distorted by an external electric field, which could also be related to its molecular size and shape.

5.4.3 Metal Ion sensing

The sensorial ability of dansyl derivatives **L1** and **L2** was studied towards metal ions, such as, Ca^{2+}, Co^{2+}, Ni^{2+}, Cu^{2+}, Zn^{2+}, Ag^{+}, Cd^{2+}, Hg^{2+} and Pb^{2+} in acetonitrile. Figure 5–4 shows the maximum emission at 527 nm and 518 nm of **L1** and **L2** upon the addition of 1, 5 and 10 equivalents of the above-mentioned metal ions, respectively. Both compounds exhibit unprecedented sensitivity to Cu^{2+} and Hg^{2+} metal ions (see Figure 5–4).

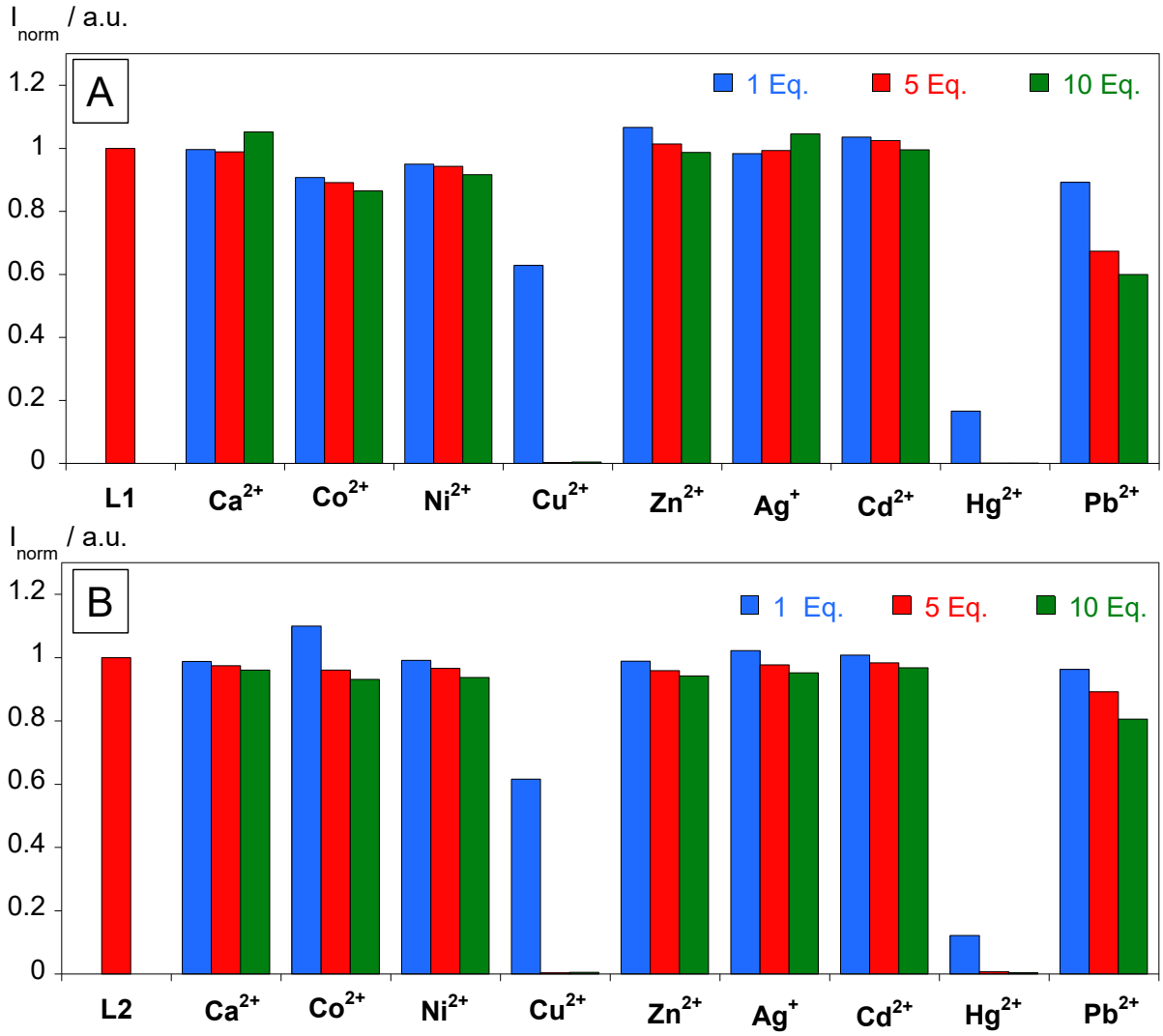


Figure 5–4. Maximum emission intensities of **L1** (A) and **L2** (B) upon the addition of 1, 5 and 10 equivalents of Ca^{2+}, Co^{2+}, Ni^{2+}, Cu^{2+}, Zn^{2+}, Ag^{+}, Cd^{2+}, Hg^{2+} and Pb^{2+} metal ions. ([**L1**] =[**L2**] = 20μM, λ_{emL1} = 527 nm, λ_{emL2} = 518 nm, T = 298K).

Figure 5–5 represents the absorption and emission spectra at increasing amounts of Cu^{2+} (A, C) and Hg^{2+} (B, D) for **L1** and **L2**, respectively. The addition of Cu^{2+} and Hg^{2+} promotes similar spectral behaviour in the absorption, where it is observed a decrease in the absorption at 332 nm, 340 nm and an increase in the absorbance at 290 nm and 255 nm for **L1** and **L2**, respectively. Regarding the emission spectra, in both cases, a quenching in the emission intensity at 527 nm (**L1**) and 518 nm (**L2**) is visualized. Paramagnetic transition metal ions, such as Cu^{2+} with unfilled d orbital shells, are commonly identified by the chelation enhancement of quenching (CHEQ effect), which occurs through either electron transfer or energy transfer mechanisms. However, Hg^{2+}, being a diamagnetic d10 metal, is an exception to this trend. In

the case of Hg^{2+}, quenching can also be attributed to spin-orbit coupling, which serves as the primary pathway for the nonradiative deactivation (K_{nr}) process. [49]

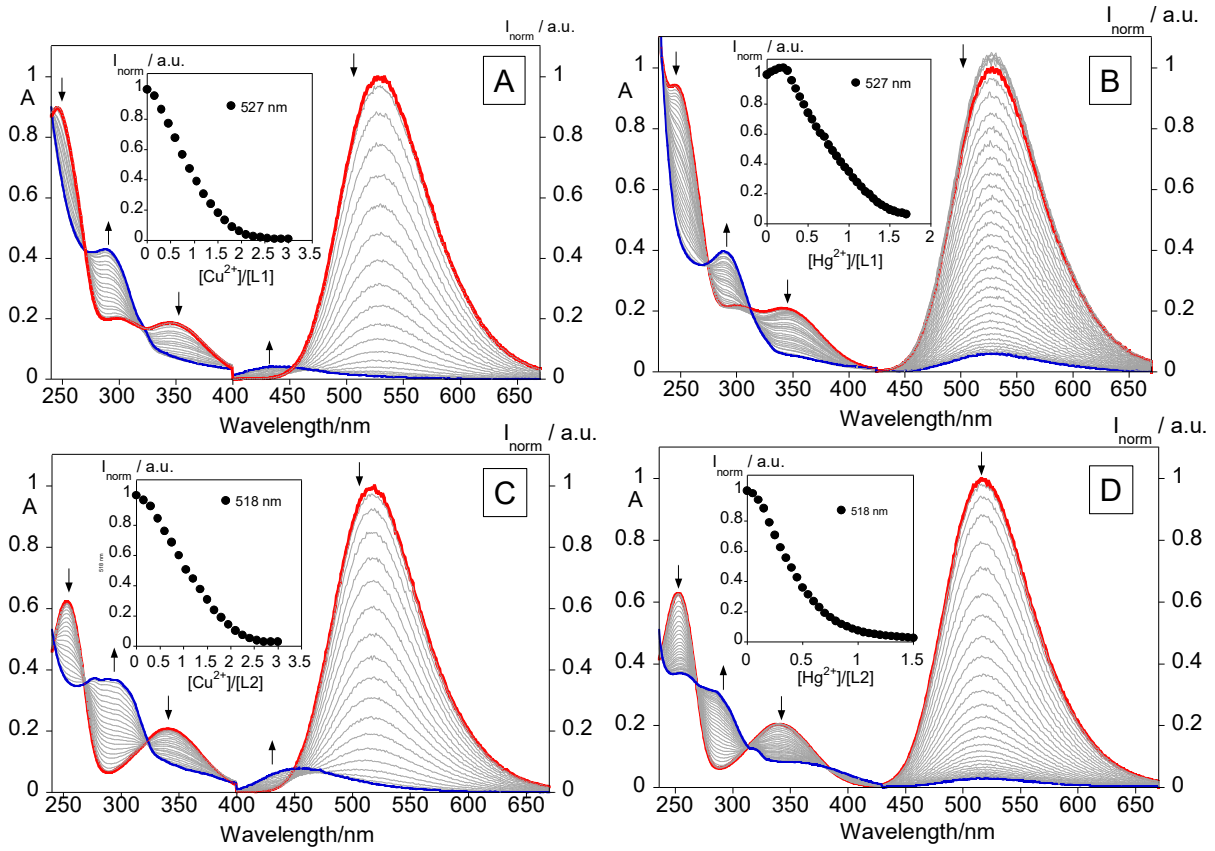


Figure 5–5. Spectrophotometric and spectrofluorimetric titrations of compounds **L1** (A, B) and **L2** (C, D) with increased additions of Cu^{2+} (A, C), and Hg^{2+} (B, D) in CH_3CN. The inset represents the emission (A-D) as a function of $[Cu^{2+}]/[\mathbf{L1}]$ at 527 nm (A), of $[Cu^{2+}]/[\mathbf{L2}]$ at 518 nm (C), of $[Hg^{2+}]/[\mathbf{L1}]$ at 527 nm (B) and of $[Hg^{2+}]/[\mathbf{L2}]$ at 518 nm (D). [**L1**] = [**L2**] = 20 μM, λ_{excL1}=332 nm, λ_{excL2}=340 nm,T = 298 K).

The stability constants were calculated through HypSpec program [50], as well as the minimal detectable and quantified amount of Cu^{2+} and Hg^{2+} in acetonitrile for both compounds and the data are summarized in Table 5-3.

Table 5-3. Stability association constants and stoichiometry for the complexes formed **L1** and **L2** with Cu^{2+} and Hg^{2+} ions, in CH_3CN. Minimal detectable (LOD) and quantified (LOQ) amounts (μM) of Cu^{2+} and Hg^{2+} metal ions (M) **L1** and **L2.** LOD and LOQ were measured by emission at 527 nm and 518 nm for **L1** and **L2**, respectively.

Compounds	Metal (M)	Association constants ($LogK_{ass.}$), L:M	LOD (μM)	LOQ (μM)
L1	Cu^{2+}	5.11 ± 0.06 (1:1)	7.5	15.0
	Hg^{2+}	5.00 ± 0.01 (1:1)	8.0	14.0
L2	Cu^{2+}	4.59 ± 0.01 (1:1)	6.0	13.5
	Hg^{2+}	6.38 ± 0.06 (1:1)	2.5	4.50

The stability constants reveal the formation of mononuclear species for Cu^{2+} and Hg^{2+} in both compounds. The highest constant was obtained for compound **L2** for Hg^{2+} with a value of $LogK_{ass.} = 6.38 \pm 0.06$.

The lowest detectable and quantifiable amounts were also determined for **L2** (2.5 μM and 4.5 μM), indicating that it has a high affinity for binding with Hg^{2+} ions, having the potential to be useful in applications such as environmental monitoring, where the presence of Hg^{2+} needs to be detected and quantified at low concentrations.

Regarding both structures and accordingly, with Pearson's Law, it can be predicted that the metal ion will coordinate with the S (bridge) and N donor atoms.

The structure of **L2** seems to play a significant role in the observed values. The absence of benzene moiety in the dansyl-derived fluorophore reduces the stereochemical hindrance, making it easier and more accessible for the metal ion to coordinate with the ligand.

5.4.4 Exploring dansyl derivatives behaviour in aqueous media

In order to understand the stability of the compounds in water, **L1** and **L2** were measured by absorption and emission in different mixtures, varying the ratio of acetonitrile to water. As can be seen in Figure 5–6 the increase of water led to a decrease in the emission intensity in both compounds up to 67% of water, after that value in 83% of water, an increase of the base-line was observed, which is indicative of the formation of aggregates. Moreover, an increase in the emission intensity and a blue shift are observed, surpassing in the case of **L1**, the emission intensity of the ligand in 100 % of acetonitrile.

Such behaviour was confirmed by the emission observed under the UV light lamp (see Figure 5–7), where the sample containing 83% of water appears to be the most emissive in both cases. The fluorescence quantum yield was determined, and a value of $\phi = 25\%$ and $\phi = 13\%$ were calculated for **L1** and **L2**, respectively. In the case of **L1** the fluorescence quantum yield was similar to the one observed in acetonitrile.

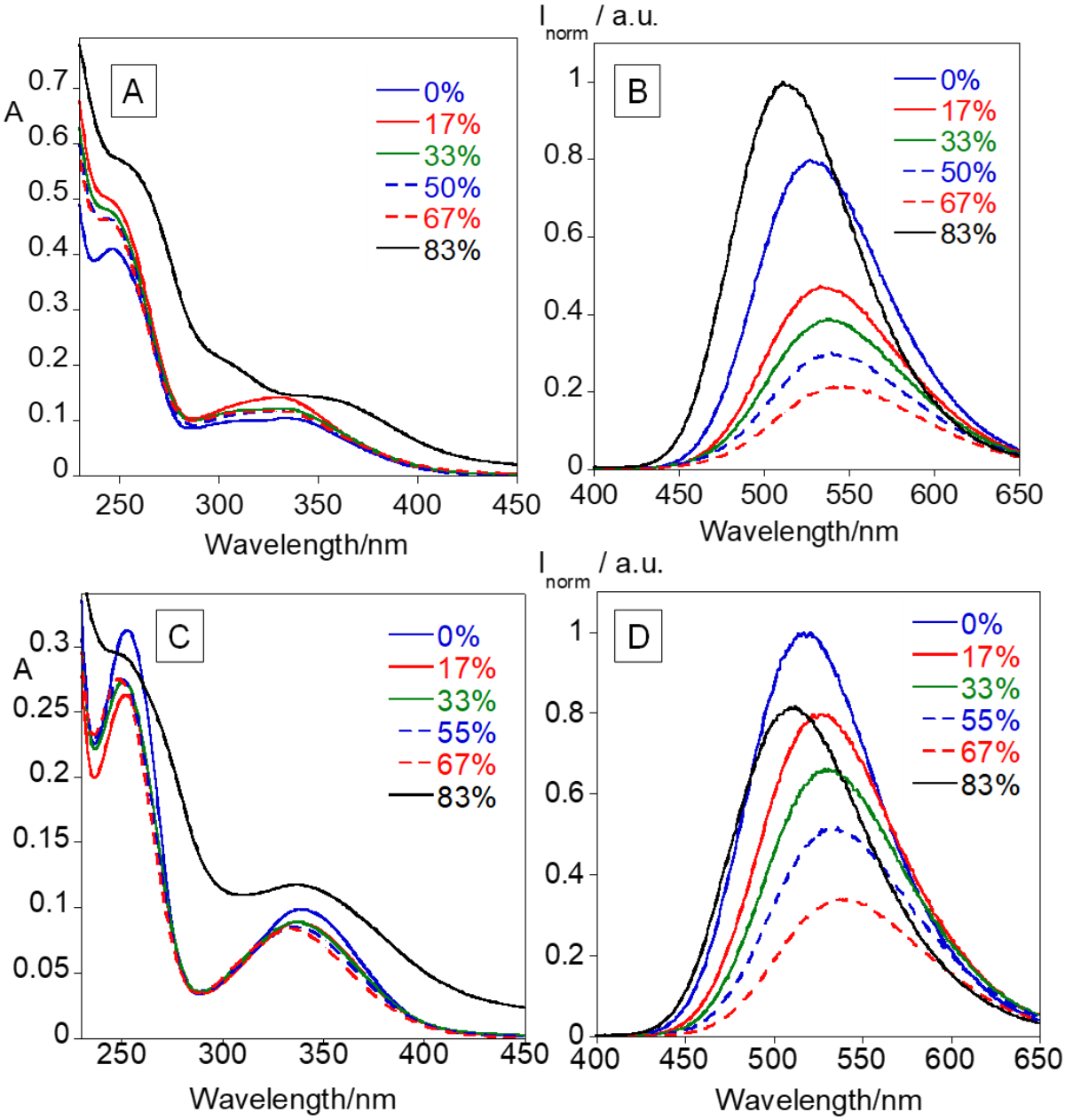


Figure 5–6. Absorption (A, C) and emission spectra (B, D) of **L1** (A,B) and **L2** (C,D) in CH_3CN with different water fraction f_w(0%, 17%, 33%, 55%, 67%, 83%). [**L1**]=[**L2**] = 10 μM, T = 298K.

In the presence of water (17 to 63%), molecules with active intramolecular rotation consume excited-state energy through non-radiative relaxation, leading to a decrease in the emission signal. However, when the concentration of these molecules reaches a certain threshold, in this case around 87%, the physical constraints imposed by aggregation can restrict their motion and prevent non-radiative relaxation. This can promote radiative decay, leading to a significant increase in the emission intensity. Thus, the aggregation-induced emission (AIE) effect arises from the restriction of motion due to physical constraints imposed by aggregation.

[51] These results are consistent with another experiment in which, while maintaining the same water percentage (87%), an increase in the concentration of ligand **L1** resulted in an enhanced aggregation-induced emission (AIE) effect. Consequently, there was an increase in the emission intensity (see Figure 5–13).

To explore deeply this observation, the solutions were measured by dynamic light scattering, resulting in monodispersed peaks (PDI_{L1} = 0.02; PDI_{L2} = 0.06) with hydrodynamic sizes of 124 ± 2 nm (**L1**) and 188 ±1.6 nm (**L2**).

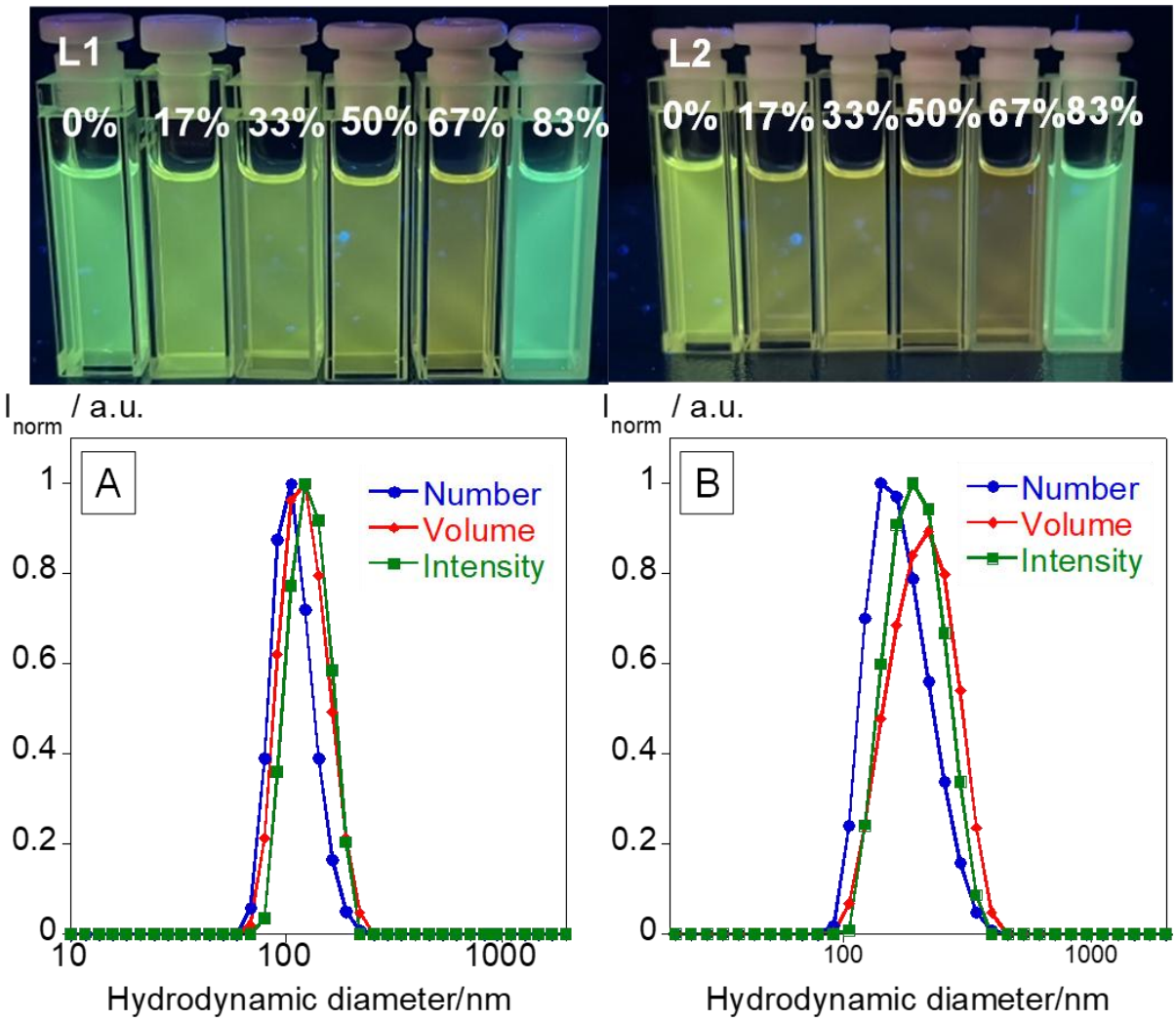


Figure 5–7. (Top) Images of **L1** and **L2** in CH_3CN with different water fraction f_w (0%, 17%, 33%, 55%, 67%, 83%). [**L1**]=[**L2**] = 10 μM, T = 298K. Size according to number, volume, and intensity distributions of a solution of CH_3CN/water solution of **L1** (A) and **L2** (B) with f_w = 83%.

These results confirmed the formation of aggregates in **L1** and **L2**. Based on other examples reported in the literature [18], herein the water modulates the aggregation state of the chromophore resulting in fluorescence enhancement *via* AIE mechanism, providing a wide

range of multiple applications in complex environments. However, these organic compounds could present some drawbacks, such as poor water solubility, leading to latter precipitation of the aggregates.

5.4.5 L1 doped SBS polymeric microparticles

Due to the observed AIE phenomenon of current compounds in aqueous media and our past works concerning the development of systems that would allow highly hydrophobic and water quenched sensors to maintain their properties in water, Poly(styrene-butadiene-styrene) SBS polymeric microparticles containing compound **L1** were synthesized using the precipitation method, a green method that minimizes waste generation [27,28]. SBS matrix was chosen due to its intrinsic chemical formula, the presence of benzene moieties would potentially improve the stability of these microparticles by staking interactions with the same moiety present in the ligand.

The use of polymeric particles was in this case applied as a measure to enhance the dispersion of the ligand in aqueous media, as well as for improving the AIE effect´s stability and bioavailability of the compound. The resulting SBS particles were characterized by fluorescence emission, dynamic light scattering (DLS) and transmission electron microscopy (TEM).

The dansyl-derivative **L1** is highly hydrophobic, but when incorporated into a polymeric matrix leads to stable and highly emissive microparticles dispersed in water, with a fluorescence quantum yield of 22%.

The results showed that the particles presented a spherical shape and that the ligand was successfully encapsulated within the polymeric matrix (see Figure 5–8 and Figure 5–14), resulting in high emissive microparticles, with green emission and a maximum emission band at 505 nm in water. Additionally, the microparticles present a size of 628 ± 22 nm (PDI: 0.07±0.04) by DLS, a zeta potential of -27 ± 0.7, and a size of 520 ± 76 nm measured by TEM.

In this work, the use of SBS particles as a carrier for dansyl derivative **L1** has the potential to improve its solubility, stability, and bioavailability, making it a promising approach for drug delivery and bioimaging.

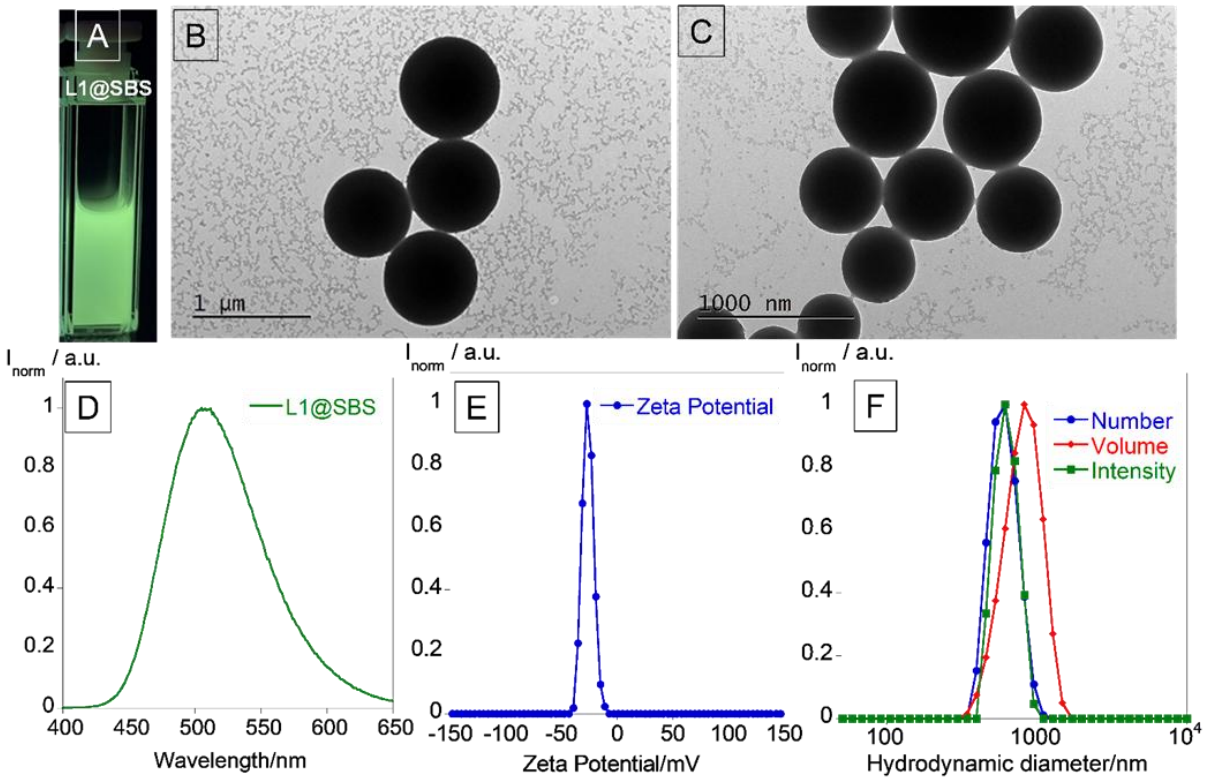


Figure 5–8. (A) Image of **L1**@SBS particles under UV-lamp; (B, C) TEM images of the **L1**@SBS particles, (D, E and F) Emission spectrum, zeta potential and hydrodynamic size of **L1**@SBS particles.

5.5 Conclusions

In current work, we present the synthesis of two fluorescent sensors abbreviated as **L1** and **L2**, bearing dual dansyl moieties linked together by a disulfide bridge. Implementation of the classical condition of peptide synthesis for compound **L1** was used for the introduction of the benzene moiety, in order to tune the photophysical characteristics of this fluorophore in relation to **L2**. Due to the common knowledge of the dansyl derivatives to manifest solvato-fluorochromism, extensive work has been carried out aiming to better understand the effect of different solvents on the emission properties. Positive solvatofluorochromism was observed for both **L1** and **L2** chromophores, and the Kamlet-Taft equation was applied to further understand the solute-solvent interactions. Alongside that, the presence of heteroatoms plays a crucial role in the sensing of metal ions, and so **L1** and **L2** were used as sensors to shed light on their potential for environmental remediation. Both compounds have been found to modulate their photophysical characteristics in the presence of Hg^{2+} and Cu^{2+} with quenching of the emission signal. Stability association constants and stoichiometry suggest mononuclear species for Cu^{2+} and Hg^{2+} in both compounds. Compound **L2** was found to exhibit the highest

constant towards Hg^{2+} with a value of $LogK_{ass.}$ = 6.38 with a LOD and LOQ of 2.5 μM and 4.5 μM. With the intention to further explore these compounds, their behavior in water was studied and found to manifest AIE enhancement at high fractions of water content with the formation of aggregates, as DLS suggests, with hydrodynamic sizes of 124 ± 2 nm (**L1**) and 188 ±1.6 nm (**L2**). Being in line with our previous efforts to characterize compounds once hydrophobic and unable to manifest emission properties due to water acting as a quencher, SBS polymeric doped microparticles were synthesized using an oil-in-water approach doped with **L1** to stabilize the AIE effect. TEM images suggest the formation of stable microparticles with a size of 520 ± 76 nm showing a green emission centered at 505 nm in water. Therefore, dansyl-derived compounds still provide value for their great photophysical characteristics, alongside their potential for bioimaging or drug delivery.

5.6 Supplementary material

5.6.1 Supplementary figures

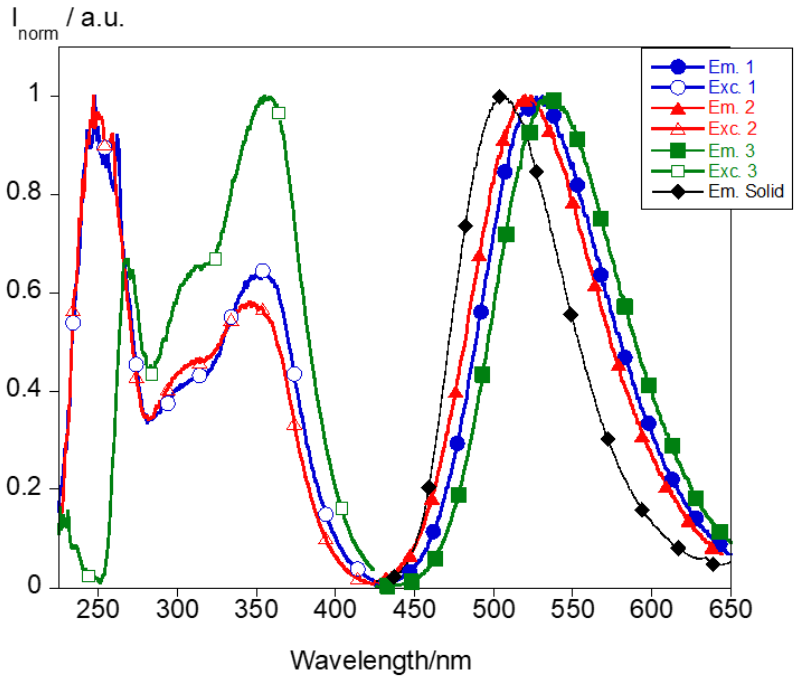


Figure 5–9. Emission, excitation and solid-state emission spectra of compound **L1** in 1) acetonitrile, 2) ethanol and 3) DMSO ([**L1**] = 6 μM).

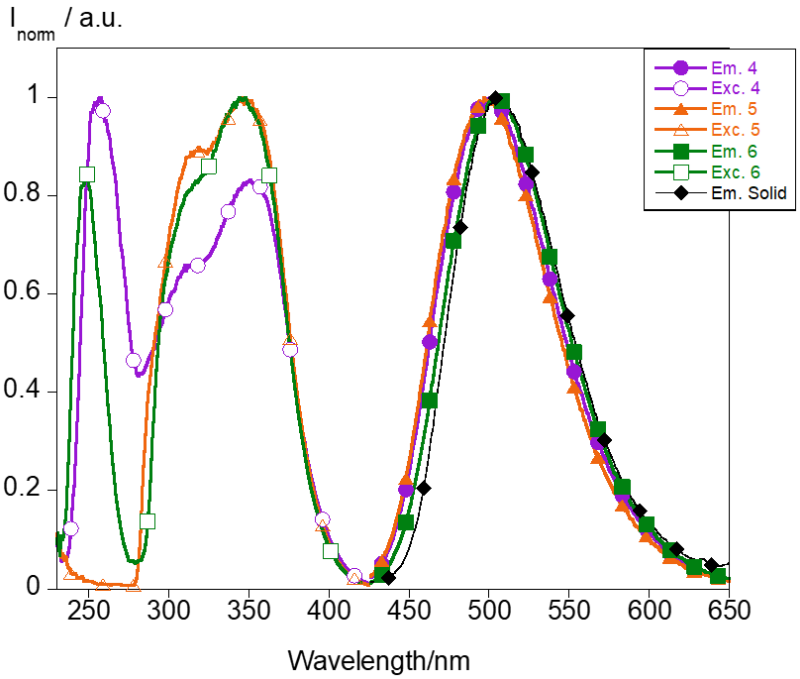


Figure 5–10. Emission, excitation, and solid-state emission spectra of compound **L1** in 4) chloroform, 5) toluene and 6) THF ([**L1**] = 6 μM).

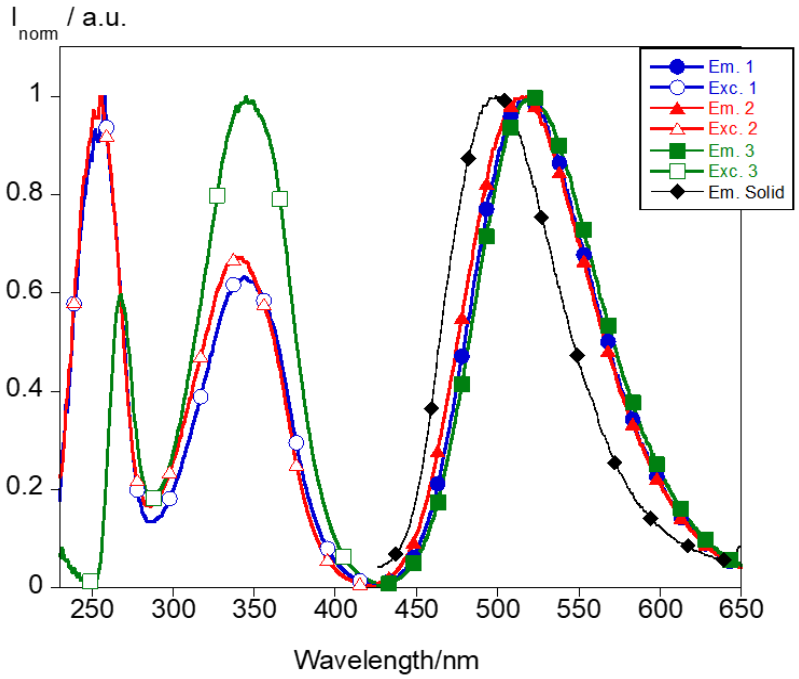


Figure 5–11. Emission, excitation and solid-state emission spectra of compound **L2** in1) acetonitrile, 2) ethanol and 3) DMSO ([**L2**] = 6 μM).

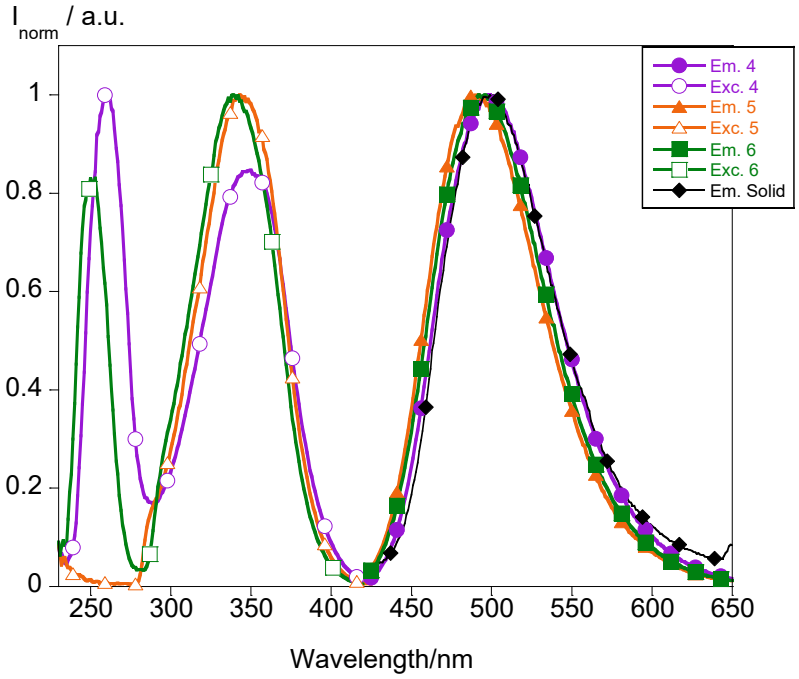


Figure 5–12. Emission, excitation, and solid-state emission spectra of compound **L2** in 4) chloroform, 5) toluene and 6) THF ([**L2**] = 6 μM).

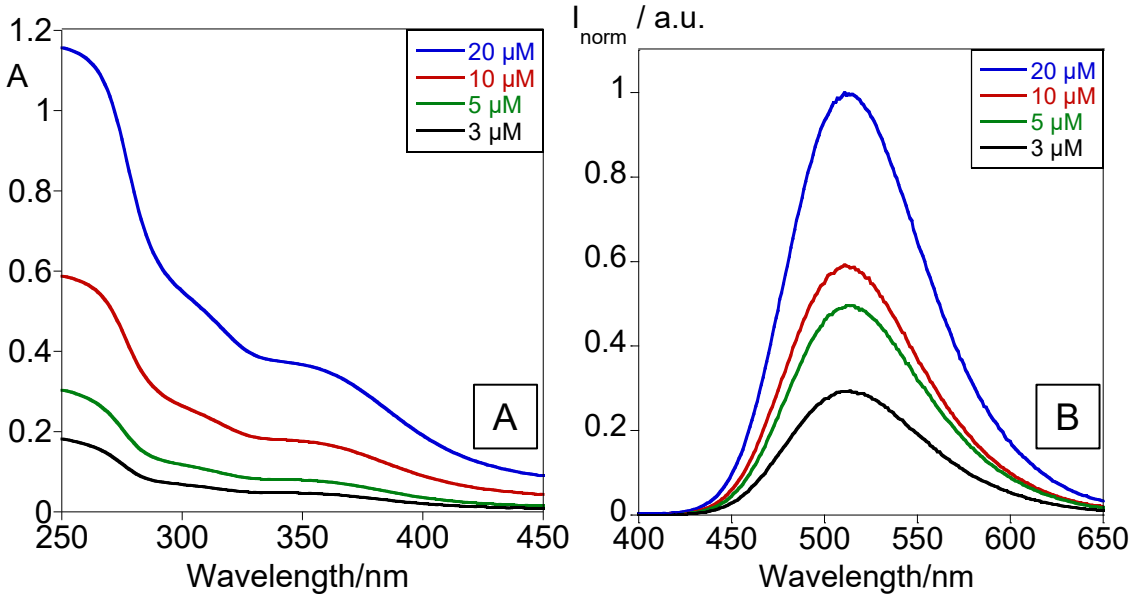


Figure 5–13. Absorption (A) and emission spectra (B) of **L1** in CH_3CN with water fraction f_w (83%) in different concentrations, T = 298K.

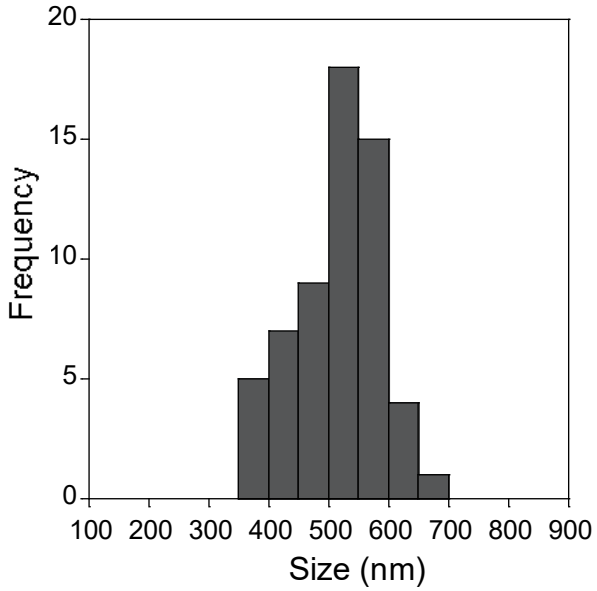


Figure 5–14. Size histogram of L1@SBS nanoparticles.

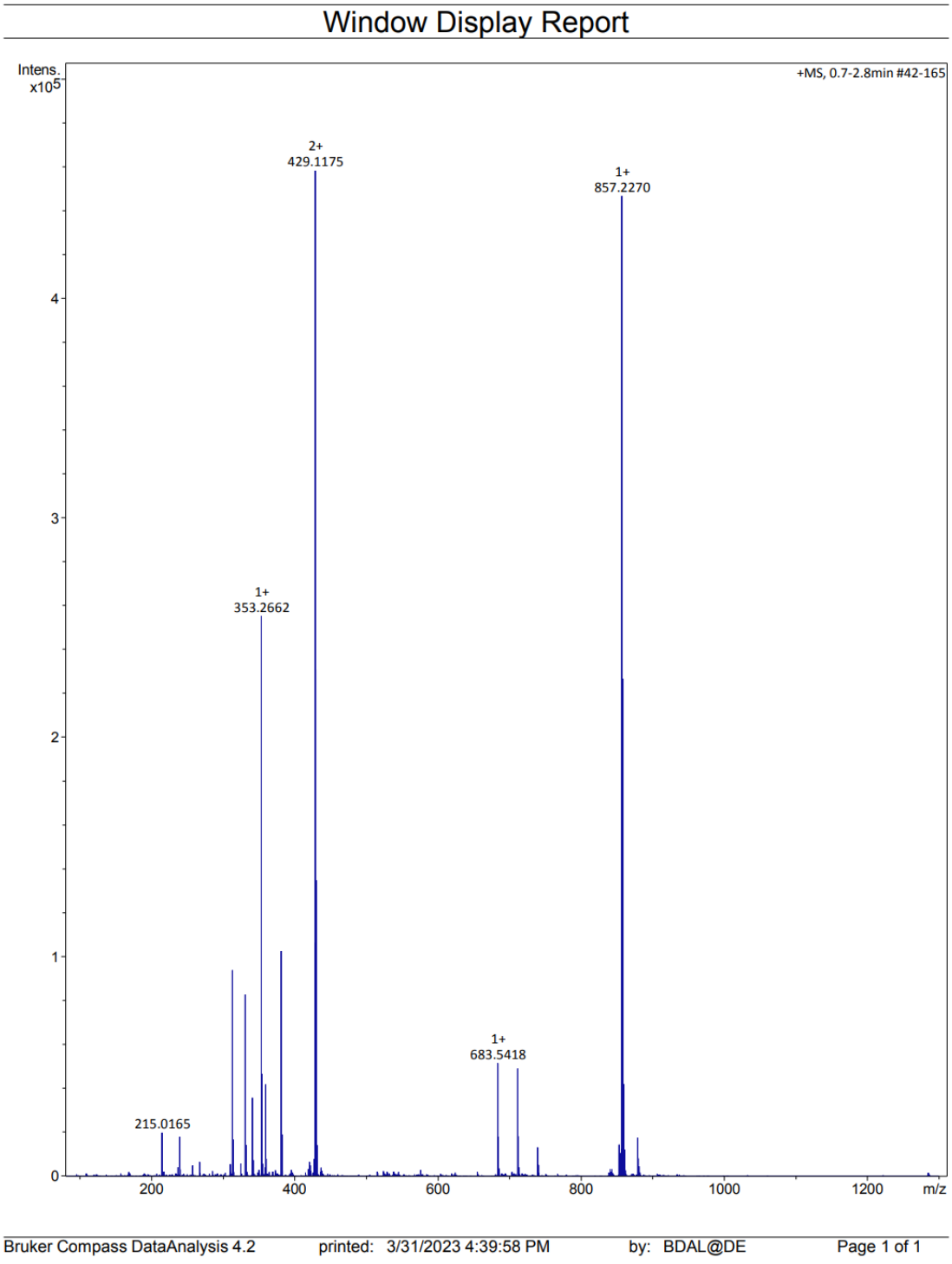


Figure 5–15. ESI-HRMS spectrum of compound **L1**.

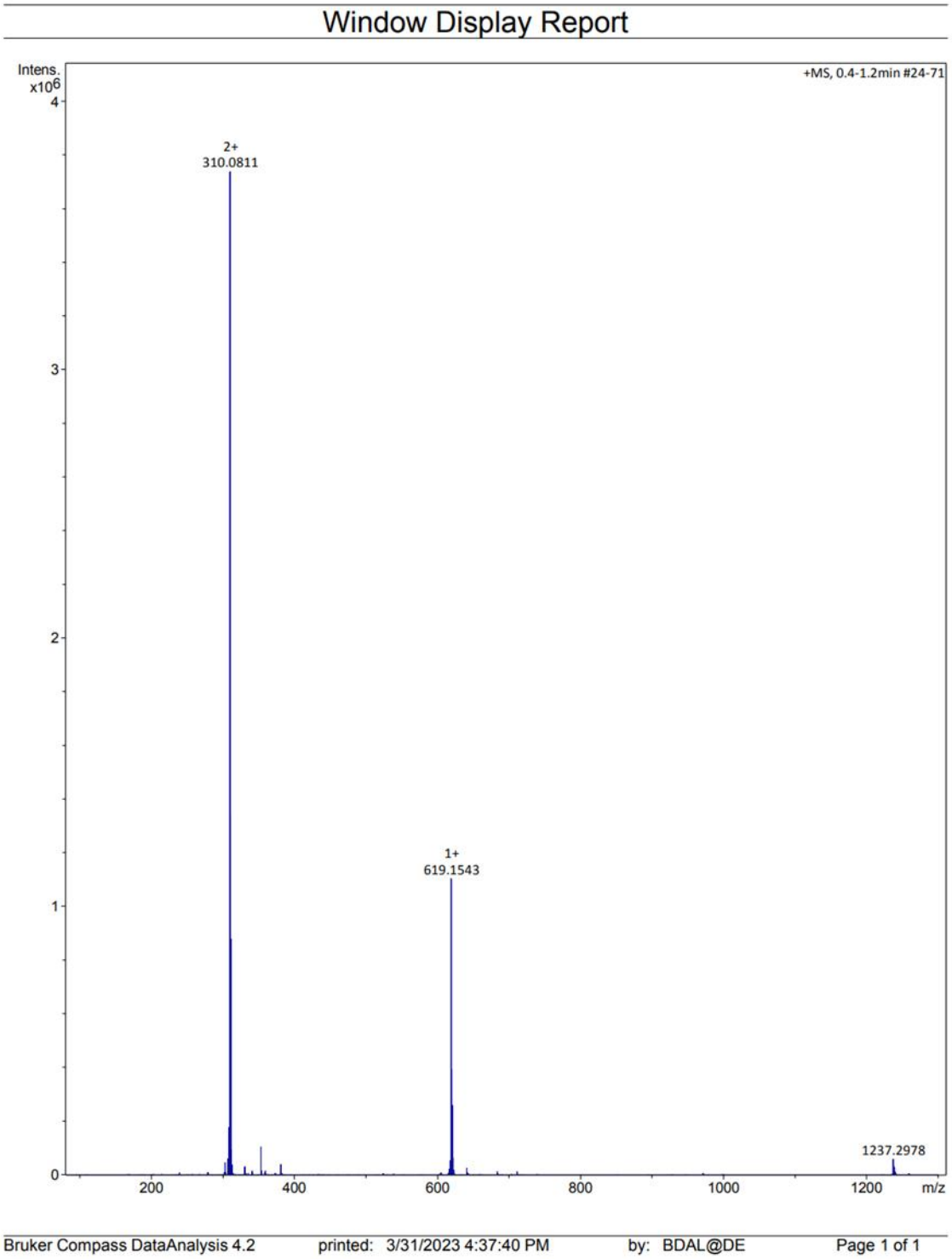


Figure 5–16. ESI-HRMS spectrum of compound **L2**.

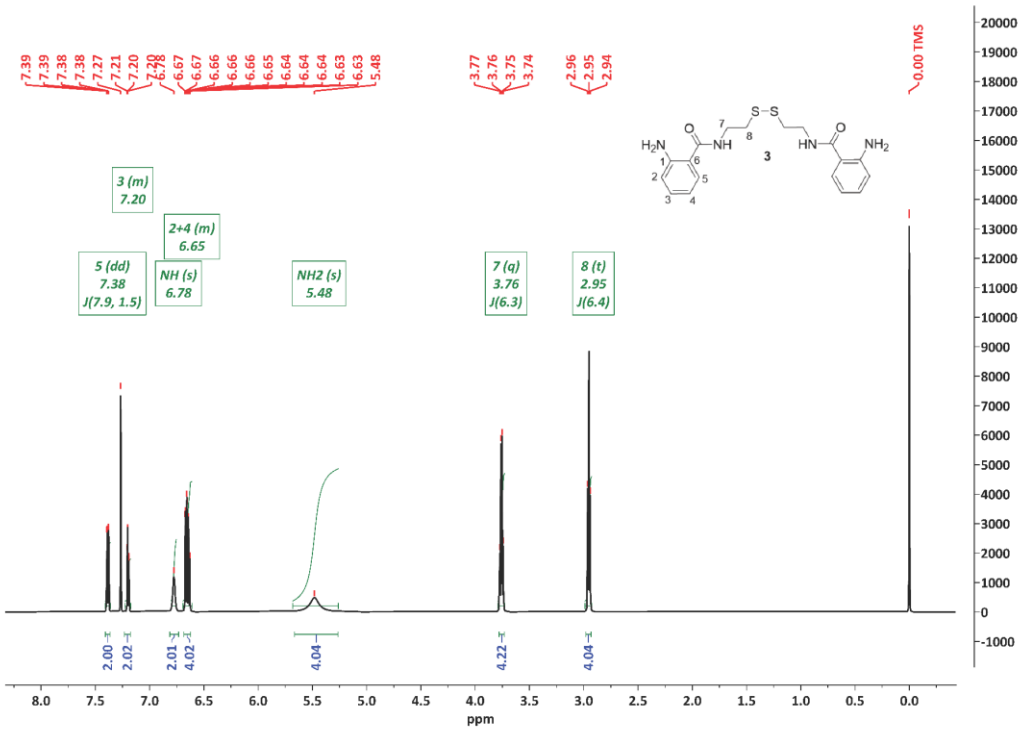


Figure 5–17. ^{1}H-NMR spectrum of compound **3**.

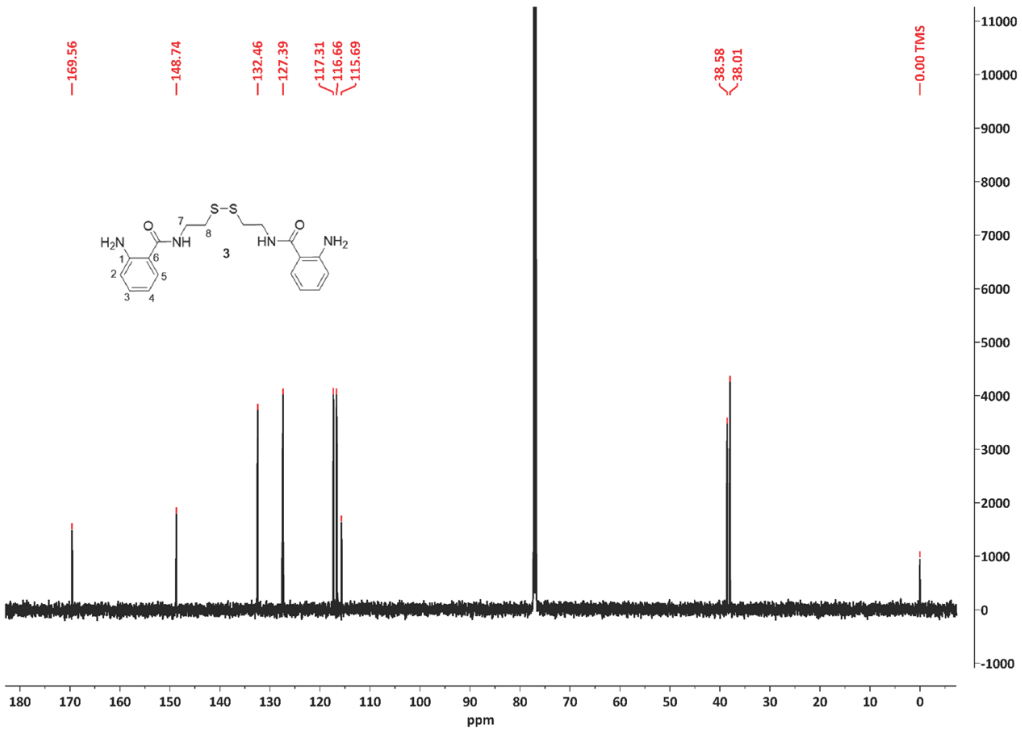


Figure 5–18. ^{13}C-NMR spectrum of compound **3**.

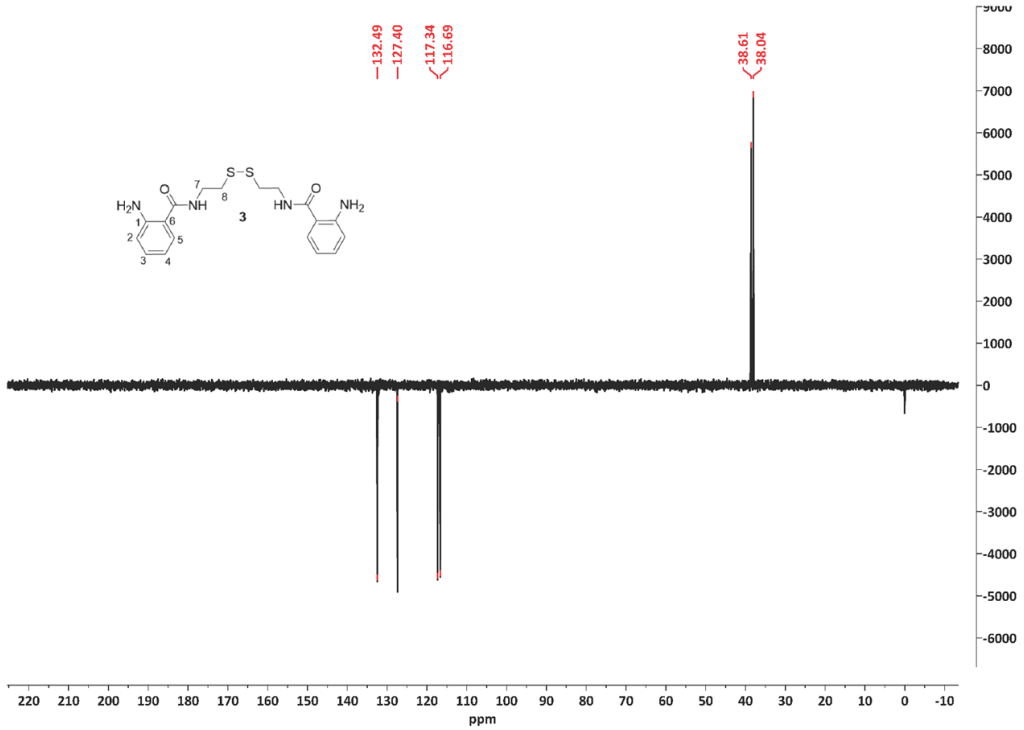


Figure 5–19. DEPT135-NMR spectrum of compound **3**.

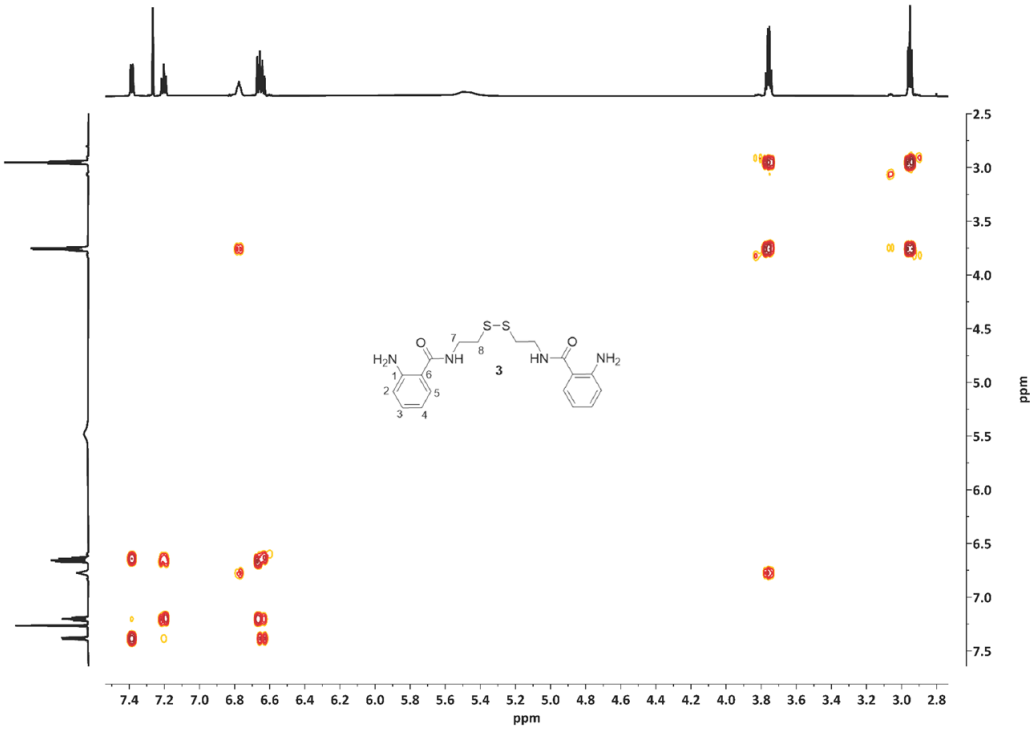


Figure 5–20. COSY-NMR spectrum of compound **3**.

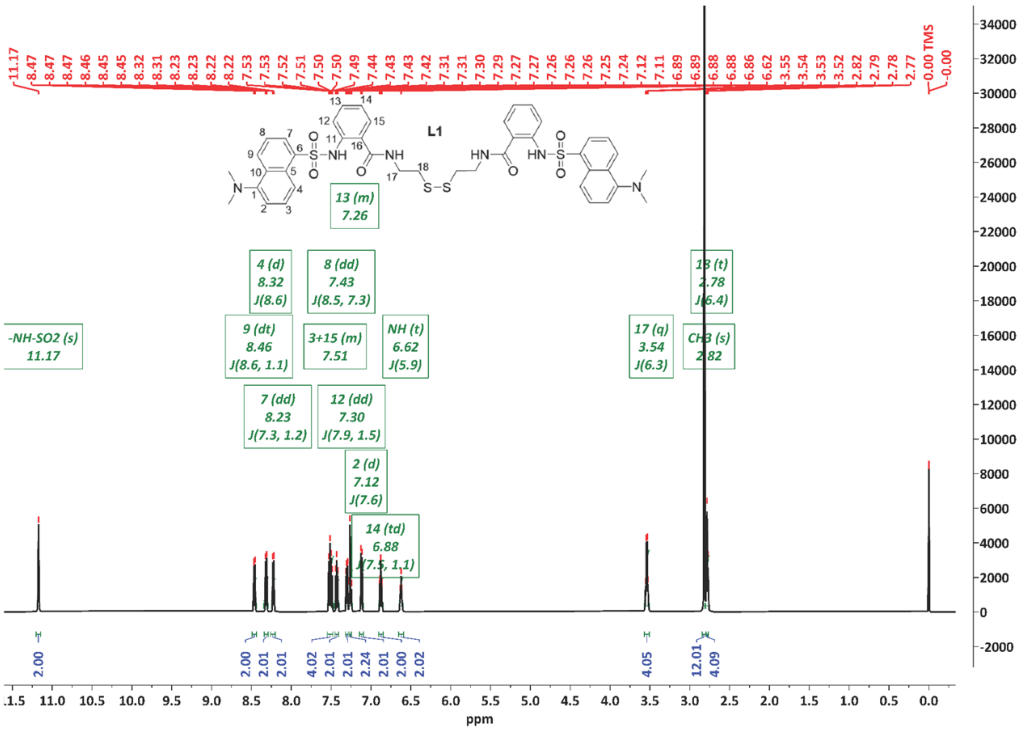


Figure 5–21. ^{1}H-NMR spectrum of compound **L1**.

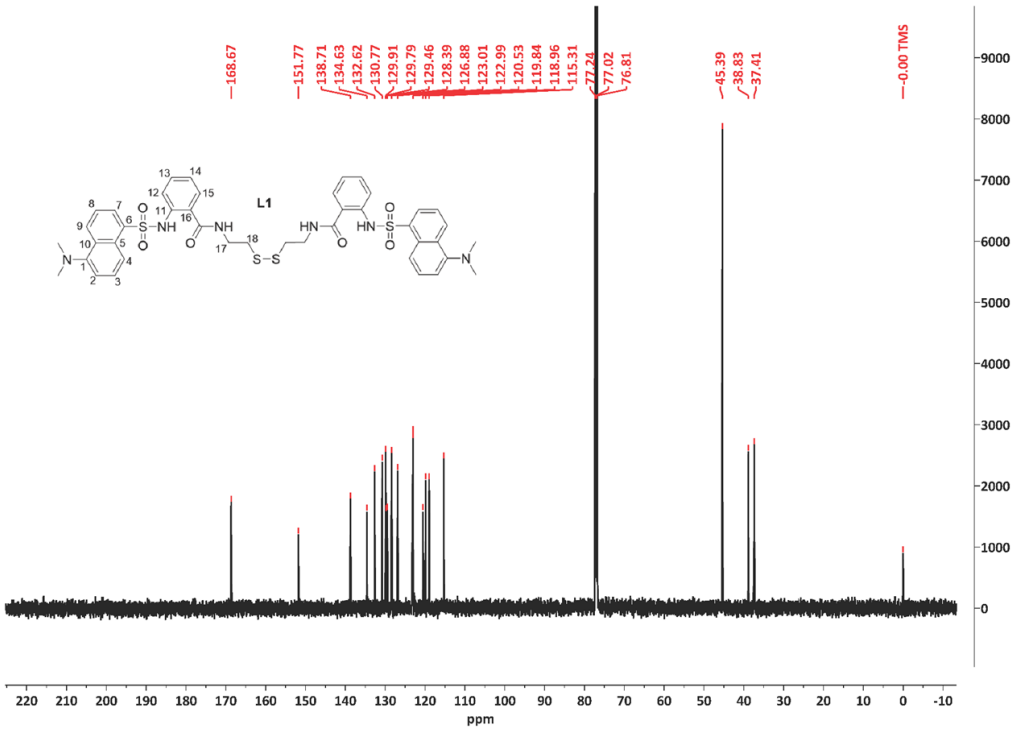


Figure 5–22. ^{13}C-NMR spectrum of compound **L1**.

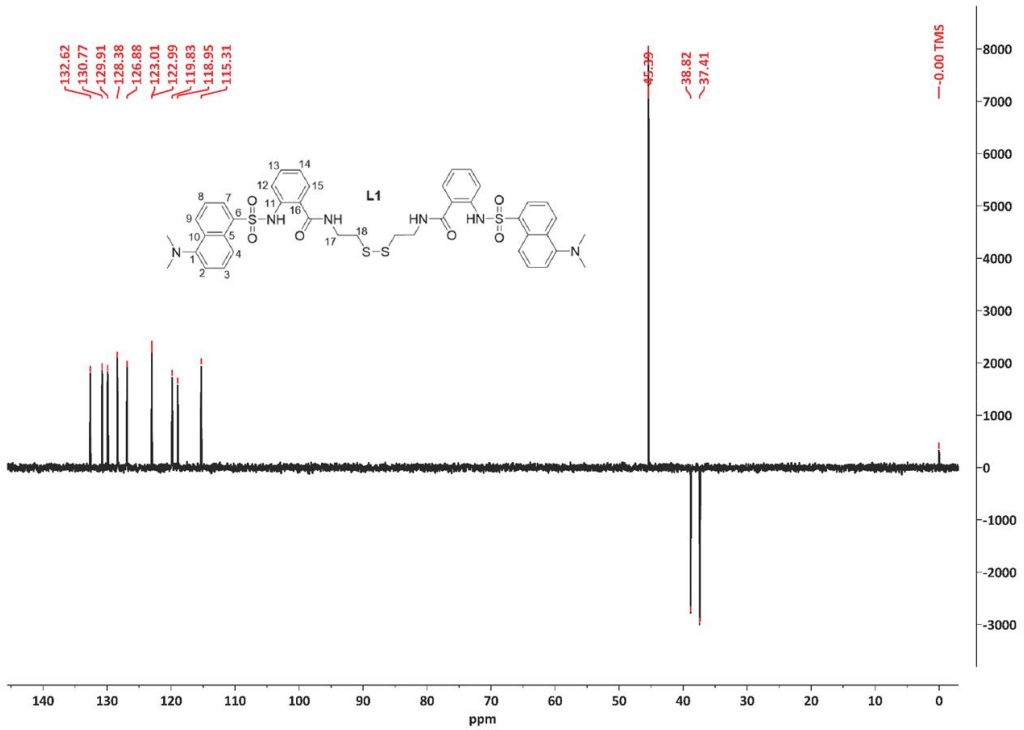


Figure 5–23. DEPT135-NMR spectrum of compound **L1**.

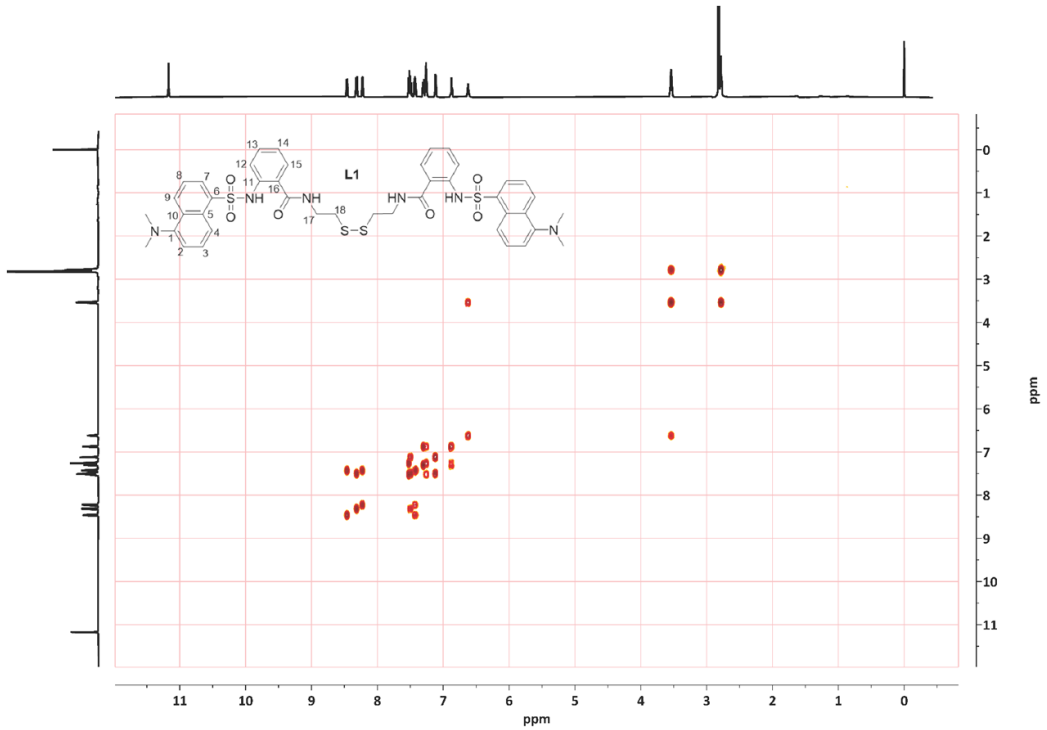


Figure 5–24. COSY-NMR spectrum of compound **L1**.

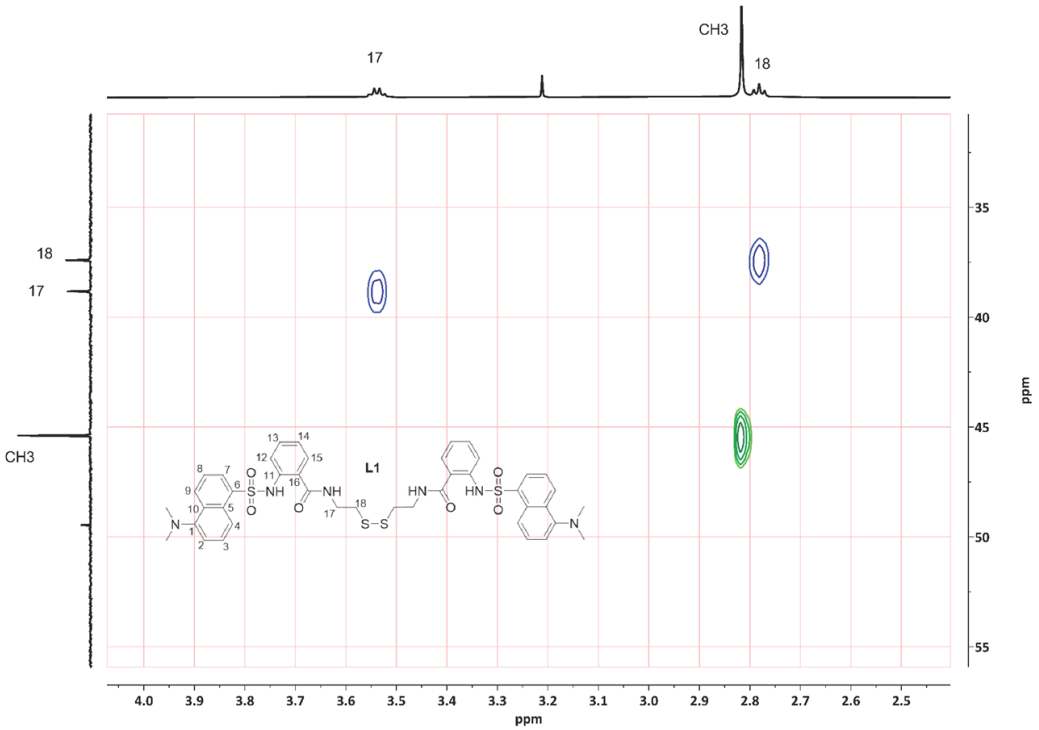


Figure 5–25. HSQC-NMR spectrum of compound **L1** (details).

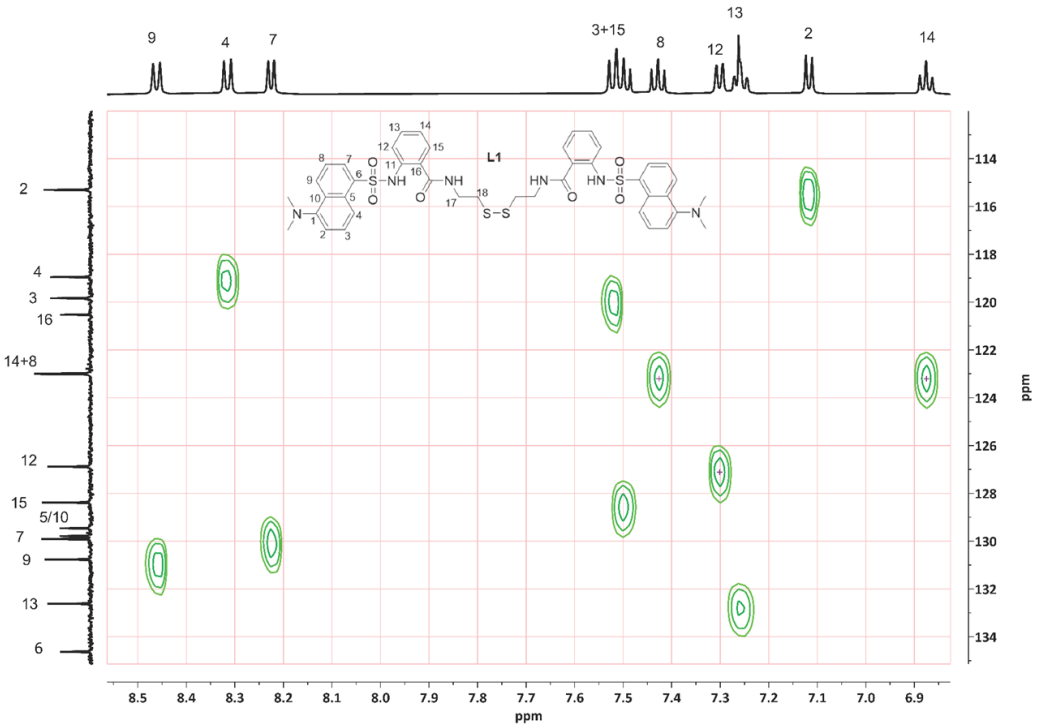


Figure 5–26. HSQC-NMR spectrum of compound **L1** (details).

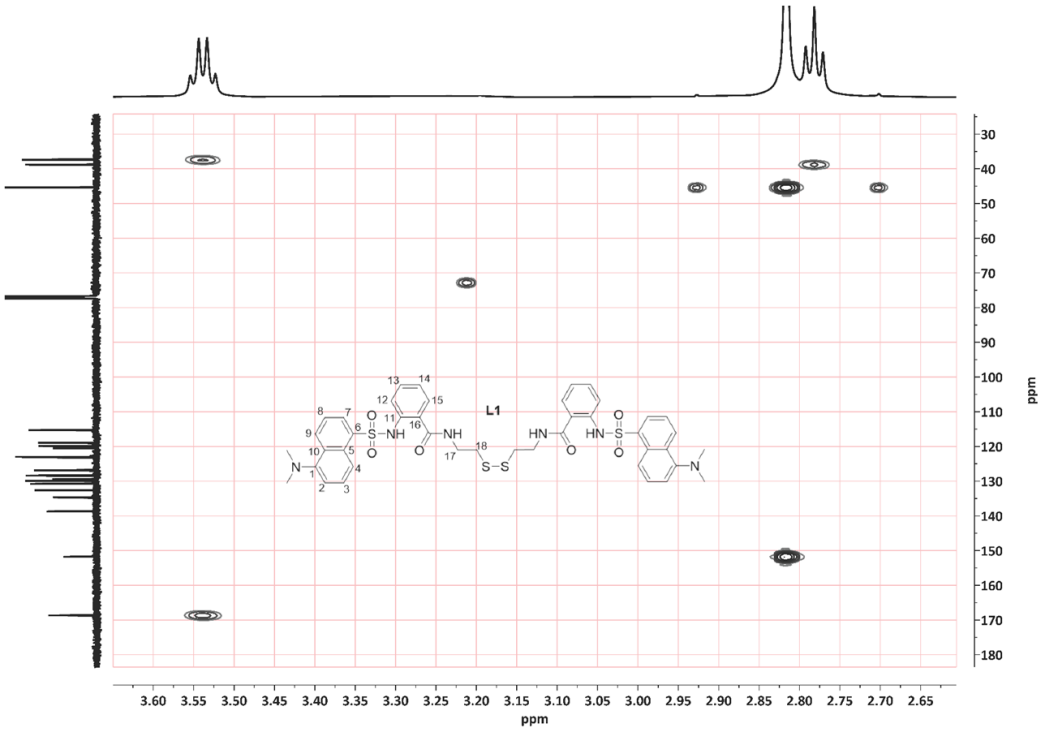


Figure 5–27. HSQC-NMR spectrum of compound **L1** (details).

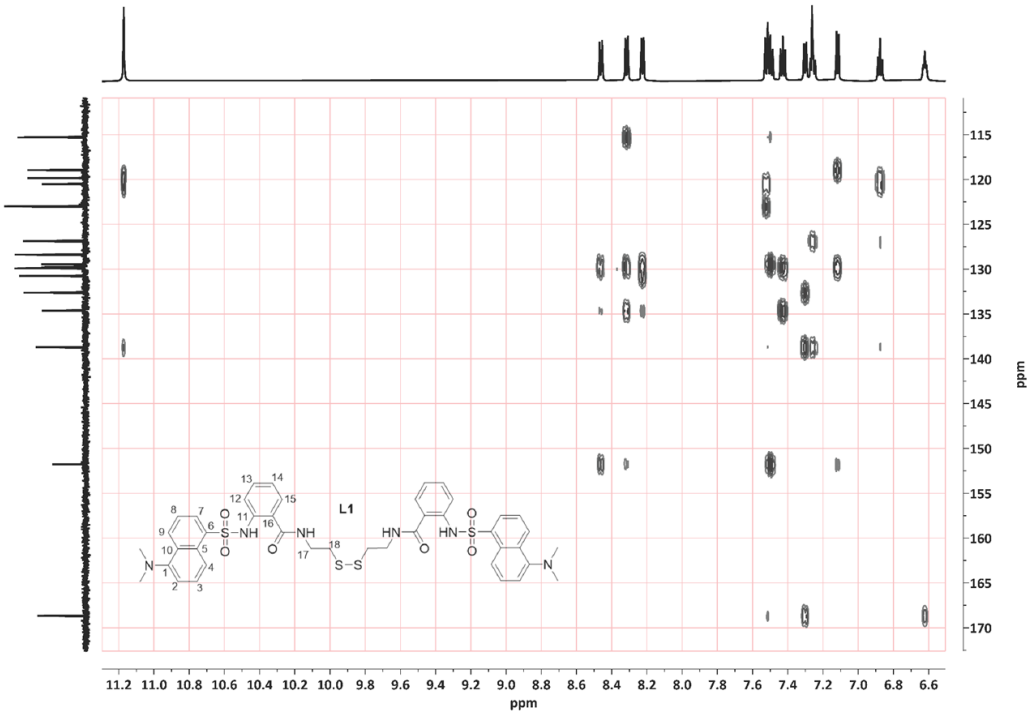


Figure 5–28. HMBC-NMR spectrum of compound **L1** (details).

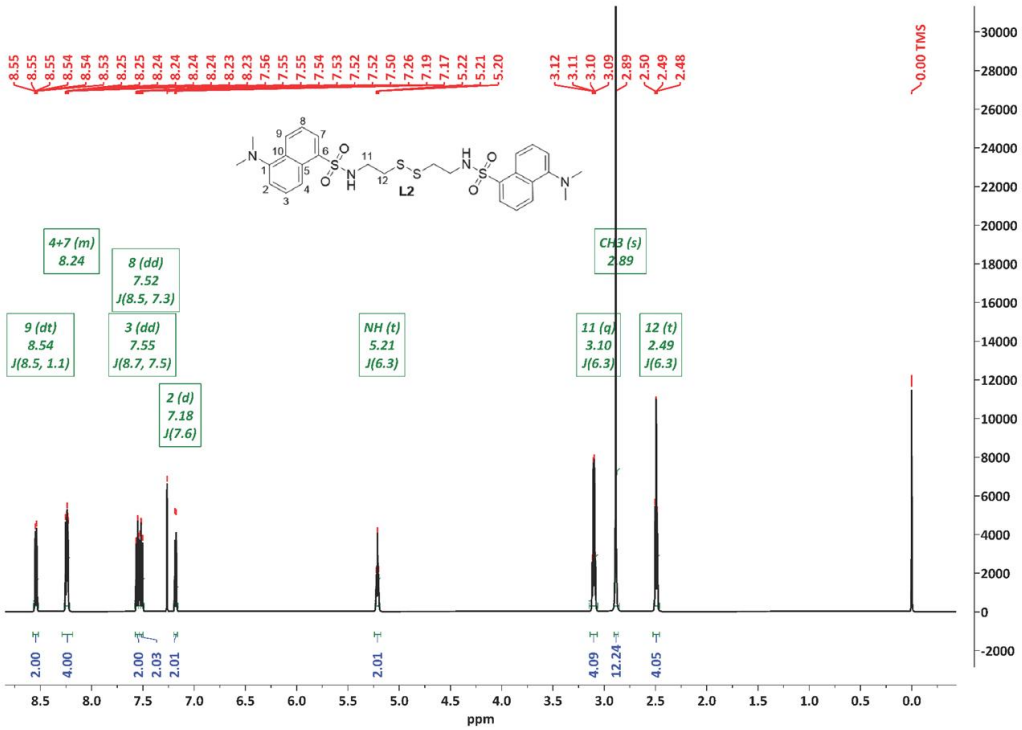


Figure 5–29. ^{1}H-NMR spectrum of compound **L2**.

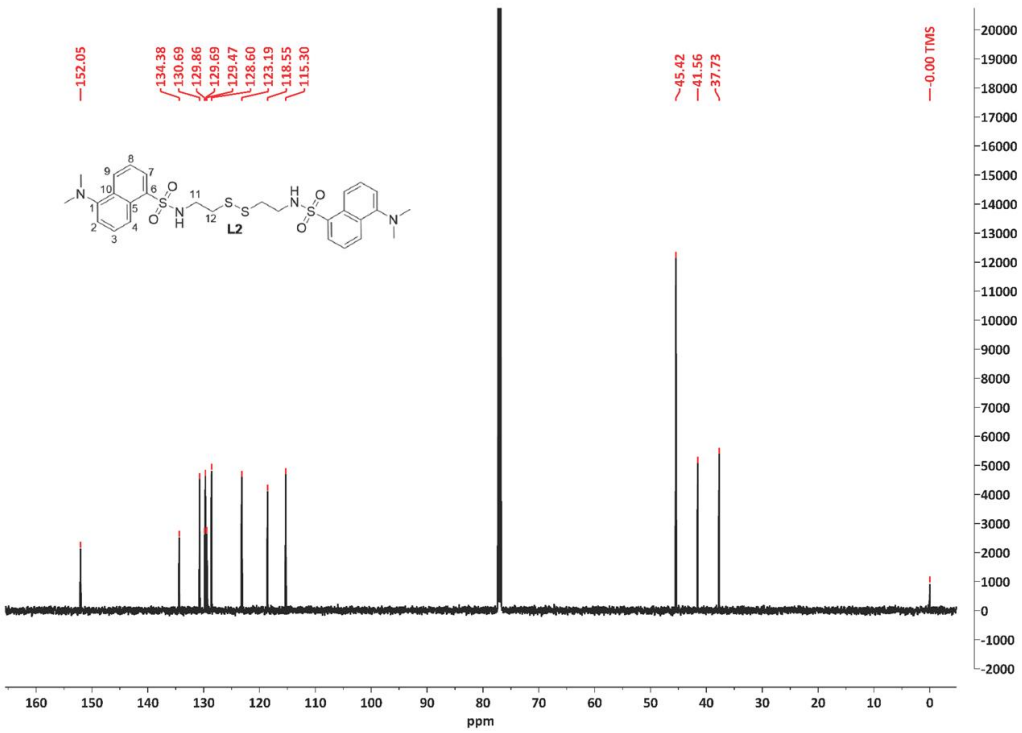


Figure 5–30. ^{13}C-NMR spectrum of compound **L2**.

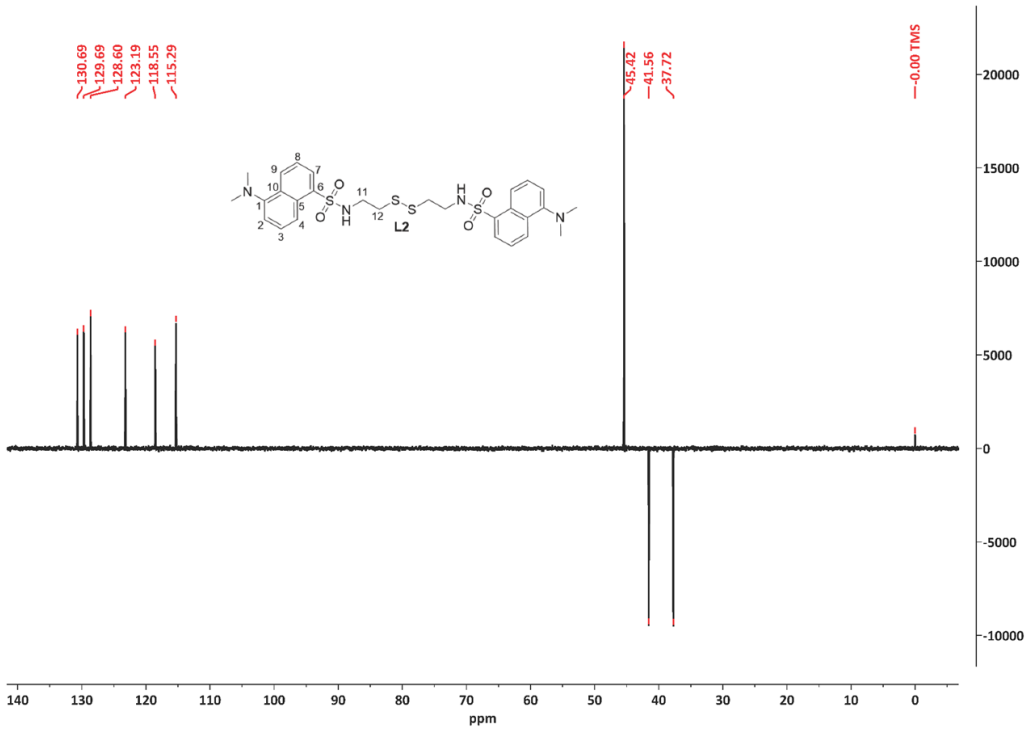


Figure 5–31. DEPT135-NMR spectrum of compound **L2**.

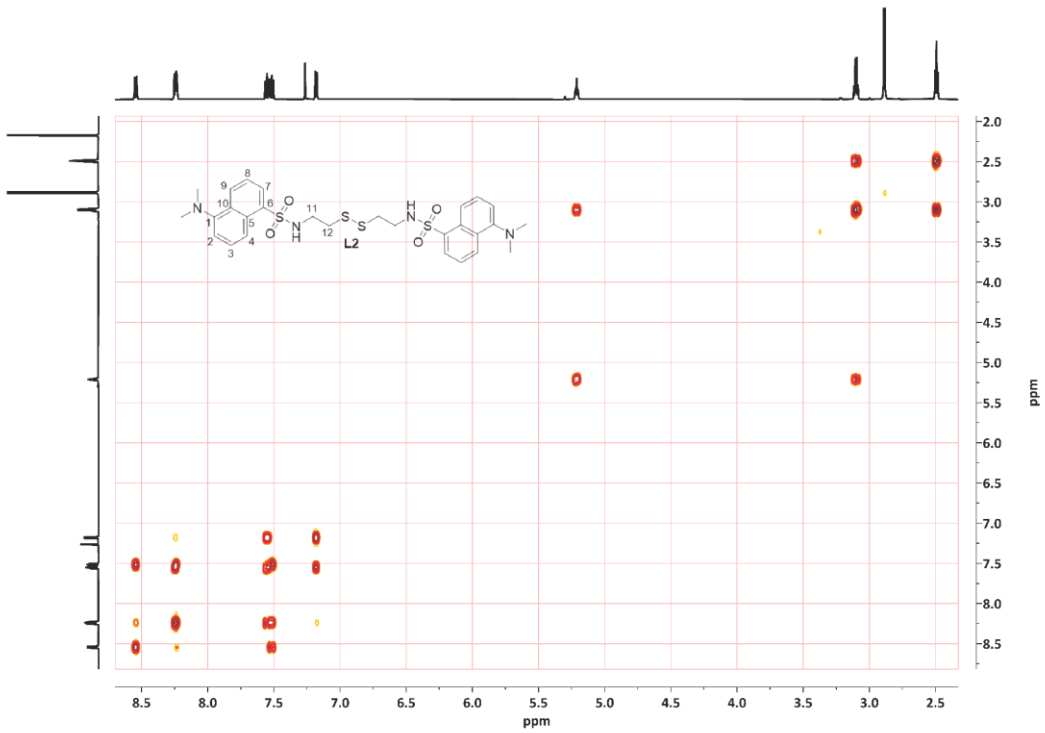


Figure 5–32. COSY-NMR spectrum of compound **L2**.

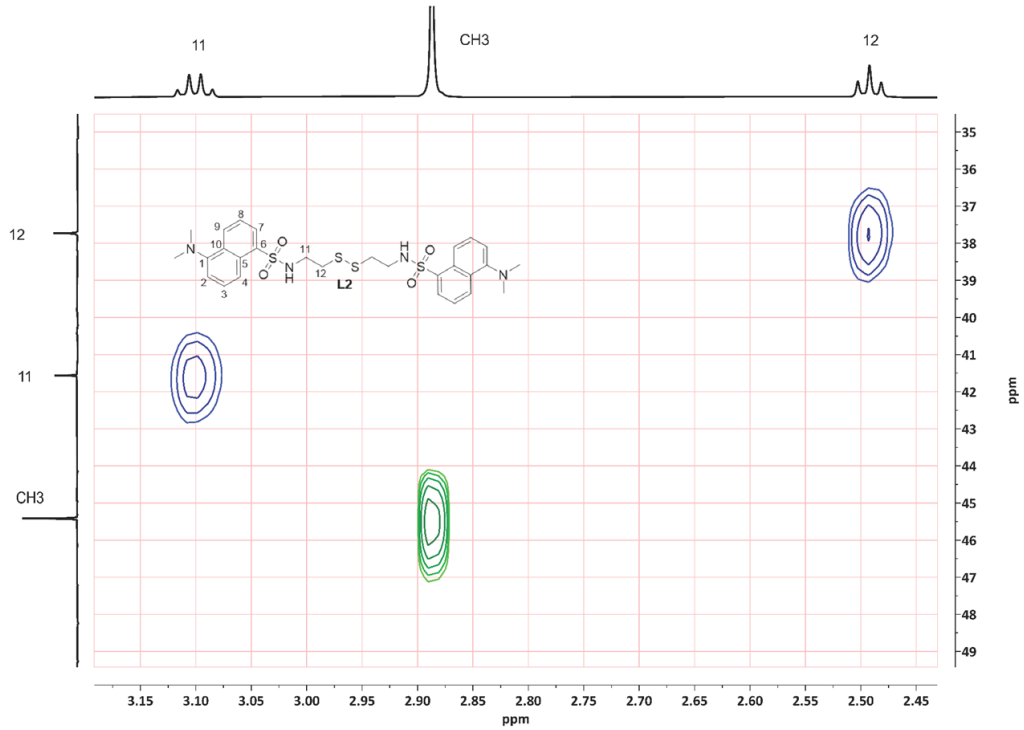


Figure 5–33. HSQC-NMR spectrum of compound **L2** (details).

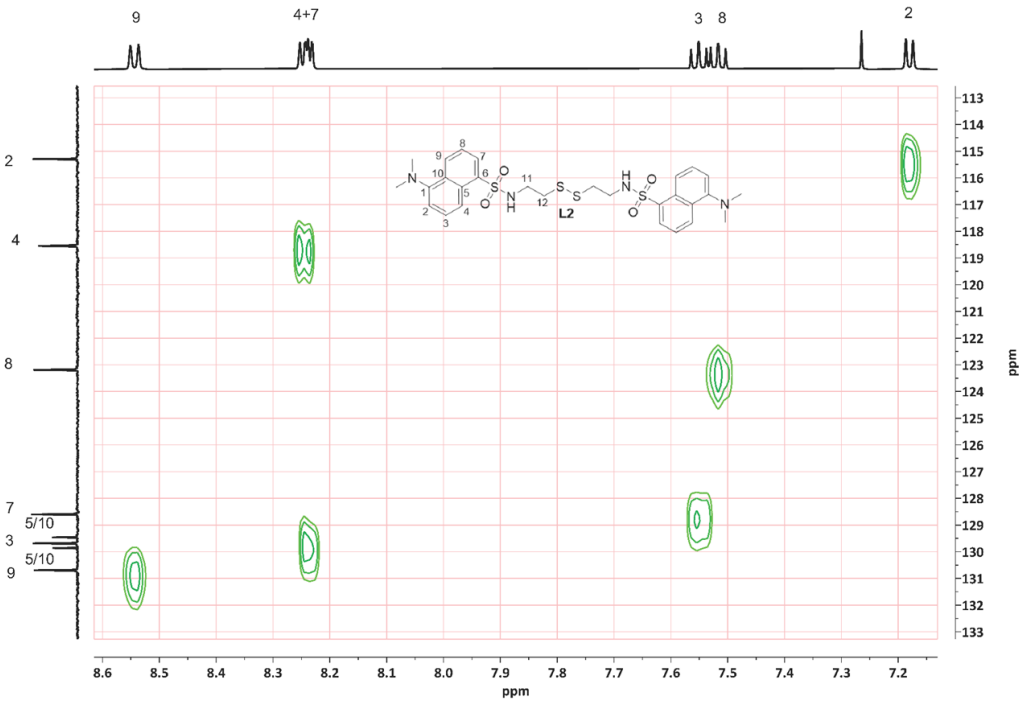


Figure 5–34. HSQC-NMR spectrum of compound **L2** (details).

5.7 Contributions & Aknowledgements

5.7.1 Author Contributions

Frederico Duarte: Formal analysis, Investigation, Writing - Original Draft, Writing - Review & Editing, Visualization.

Georgi Dobrikov: Methodology, Validation, Formal Analysis, Investigation, Writing - Original Draft, Writing - Review & Editing, Resources, Visualization.

Atanas Kurutos: Methodology, Validation, Formal Analysis, Investigation, Writing - Original Draft, Writing - Review & Editing, Resources, Visualization.

Javier Fernandez Lodeiro: Investigation, Resources, Validation, Writing - Review & Editing.

Jose Luis Capelo-Martinez: Resources, Writing - Review & Editing, Funding acquisition.

Hugo M. Santos: Investigation, Resources, Validation, Writing - Review & Editing.

Elisabete Oliveira: Conceptualization, Methodology, Validation, Formal Analysis, Investigation, Resources, Writing - Original Draft, Writing - Review & Editing, Resources, Visualization, supervision, Funding acquisition.

Carlos Lodeiro: Conceptualization, Methodology, Validation, Formal Analysis, Investigation, Resources, Writing - Review & Editing, Resources, Visualization, supervision, Funding acquisition, Project administration

5.7.2 Acknowledgments

This work was supported by the Associate Laboratory for Green Chemistry - LAQV which is financed by national funds from FCT/MCTES (UIDB/50006/2020 and UIDP/50006/2020) as well as the PROTEOMASS Scientific Society (Portugal) for funding support (General Funding Grant 2022-2023). F.D. thanks to FCT/MEC (Portugal) for his doctoral grant 2021.05161.BD. E.O thanks FCT/MEC (Portugal) for the individual contract, CEECIND/00648/2017. J.F-.L. thanks the FC/MEC (Portugal) for the individual research contract DL57. HMS acknowledges the Associate Laboratory for Green Chemistry-LAQV (LA/P/0008/2020) funded by FCT/MCTES for his research contract.

The financial support by the Bulgarian National Science Fund (BNSF) under grant – "Novel styryl and polymethine fluorophores as potential theranostic agents "contract N◦ КП-06-М59/1 from 15.11.2021 is gratefully acknowledged by A.K. This work is also developed and acknowledged by A.K. as part of contract №: BG-RRP-2.004-0002-C01, Laboratory of Organic Functional Materials (Project BiOrgaMCT), Procedure BG-RRP-2.004, Establishing of a network of

research higher education institutions in Bulgaria", funded by BULGARIAN NATIONAL RECOVERY AND RESILIENCE PLAN".

G.D. thanks to the European Regional Development Fund within the Operational Programme Science and Education for Smart Growth 2014 - 2020 under the Project Center of Exellence: National center of mechatronics and clean technologies - BG05M2OP001-1.001-0008 for the financial support.

5.8 References

[1] Y. Zhang, B. Lei, X. Zhang, Intramolecular energy transfer dyes as temperature- and polarity-sensitive fluorescence probes, *Dyes and Pigments* **205** (2022) 110492. DOI: 10.1016/j.dyepig.2022.110492.

[2] A. Reisch, A.S. Klymchenko, Fluorescent Polymer Nanoparticles Based on Dyes: Seeking Brighter Tools for Bioimaging, *Small* **12** (2016) 1968–1992. DOI: 10.1002/smll.201503396.

[3] R. Nishiyabu, Y. Sugino, Y. Kubo, White-light emitting boronate microparticles for potential use as reusable bright chemosensors in water, *Chem. Commun*. **49** (2013) 9869–9871. DOI: 10.1039/c3cc45739g.

[4] Y. Cui, F. Li, X. Zhang, Controlling fluorescence resonance energy transfer of donor-acceptor dyes by Diels-Alder dynamic covalent bonds, *Chem. Commun.* **57** (2021) 3275–3278. DOI: 10.1039/d1cc00165e.

[5] A.F. Sierra, D. Hernández-Alonso, M.A. Romero, J.A. González-Delgado, U. Pischel, P. Ballester, Optical Supramolecular Sensing of Creatinine, *J. Am. Chem. Soc.* **142** (2020) 4276–4284. DOI: 10.1021/jacs.9b12071.

[6] Y. Pan, C. Zhang, S.H. Liu, Y. Tan, J. Yin, Fluorescent switch based on dithienylethene with dansulfonamide in multimedium, *Dyes and Pigments* **181** (2020) 108546. DOI: 10.1016/j.dyepig.2020.108546.

[7] Y. Zhang, B. Lei, X. Zhang, Reversible, controllable white-light emission of dye systems by dynamic covalent furan moiety exchange, *Chem. Commun.* **58** (2022) 5261–5264. DOI: 10.1039/d2cc01309f.

[8] Z. Shi, J. Wu, Q. Song, R. Göstl, A. Herrmann, Toward Drug Release Using Polymer Mechanochemical Disulfide Scission, *J. Am. Chem. Soc.* **142** (2020) 14725–14732. DOI: 10.1021/jacs.0c07077.

[9] E.O. Dare, V. Vendrell-Criado, M.C. Jiménez, R. Pérez-Ruiz, D. Díaz Díaz, Highly efficient latent fingerprint detection by eight-dansyl-functionalized octasilsesquioxane nanohybrids, *Dyes and Pigments* **184** (2021) 108841. DOI: 10.1016/j.dyepig.2020.108841.

[10] W.M. Pazin, A.K.A. Almeida, V. Manzoni, J.M.M. Dias, A.C.F. De Abreu, M. Navarro, A.S. Ito, A.S. Ribeiro, I.N. De Oliveira, Thermal and solvatochromic effects on the emission properties of a thienyl-based dansyl derivative, *RSC. Adv.* **10** (2020) 28484–28491. DOI: 10.1039/d0ra05949h.

[11] H. Jiang, Z. Li, Y. Kang, L. Ding, S. Qiao, S. Jia, W. Luo, W. Liu, A two-photon fluorescent probe for Cu^{2+} based on dansyl moiety and its application in bioimaging, *Sens. Actuators B Chem.* **242** (2017) 112–117. DOI: 10.1016/j.snb.2016.11.033.

[12] A. Thangaraj, V. Bhardwaj, S.K. Sahoo, A multi-analyte selective dansyl derivative for the fluorescence detection of Cu(II) and cysteine, *Photochem. and Photobiol. Sci.* **18** (2019) 1533–1539. DOI: 10.1039/c9pp00080a.

[13] Y. Wang, J. Zhou, L. Zhao, B. Xu, A dual-responsive and highly sensitive fluorescent probe for Cu^{2+} and pH based on a dansyl derivative, *Dyes and Pigments* **180** (2020) 108513. DOI: 10.1016/j.dyepig.2020.108513.

[14] J. Luo, Z. Xie, Z. Xie, J.W.Y. Lam, L. Cheng, H. Chen, C. Qiu, H.S. Kwok, X. Zhan, Y. Liu, D. Zhu, B.Z. Tang, Aggregation-induced emission of 1-methyl-1,2,3,4,5-pentaphenylsilole, *Chem. Commun.* **18** (2001) 1740–1741. DOI: 10.1039/b105159h.

[15] J. Zhang, H. Shen, X. Liu, X. Yang, S.L. Broman, H. Wang, Q. Li, J.W.Y. Lam, H. Zhang, M. Cacciarini, M.B. Nielsen, B.Z. Tang, A Dihydroazulene-Based Photofluorochromic AIE System for Rewritable 4D Information Encryption, *Angew. Chem. Int. Ed.* **61** (2022) e202208460. DOI: 10.1002/anie.202208460.

[16] Y. Bin Ruan, A. Depauw, I. Leray, Aggregation-induced emission enhancement upon Al^{3+} complexation with a tetrasulfonated calix[4]bisazacrown fluorescent molecular sensor, *Org. Biomol. Chem.* **12** (2014) 4335–4341. DOI: 10.1039/c4ob00187g.

[17] M. Gao, B.Z. Tang, Fluorescent Sensors Based on Aggregation-Induced Emission: Recent Advances and Perspectives, *ACS Sens.* **2** (2017) 1382–1399. DOI: 10.1021/acssensors.7b00551.

[18] Z. Ruan, H. Zheng, C. Deng, X. Cheng, X. Ruan, S. Lv, Y. Chen, S. Liu, J. Lin, A simple AIE-active triphenylamine derivative for supersensitive detection of water in organic solvents with noticeable fluorescence color change, *Dyes and Pigments* **204** (2022) 110476. DOI: 10.1016/j.dyepig.2022.110476.

[19] H. Sun, X.X. Tang, B.X. Miao, Y. Yang, Z. Ni, A new AIE and TICT-active tetraphenylethene-based thiazole compound: Synthesis, structure, photophysical properties and application for water detection in organic solvents, *Sens. Actuators B Chem.* **267** (2018) 448–456. DOI: 10.1016/j.snb.2018.04.022.

[20] Z. Song, W. Zhang, M. Jiang, H.H.Y. Sung, R.T.K. Kwok, H. Nie, I.D. Williams, B. Liu, B.Z. Tang, Synthesis of Imidazole-Based AIEgens with Wide Color Tunability and Exploration of their Biological Applications, *Adv. Funct. Mater.* **26** (2016) 824–832. DOI: 10.1002/adfm.201503788.

[21] J. Wang, X. Zhang, H.B. Liu, Highly sensitive pyrene–dansyl conjugate-based fluorescent sensor for discriminative detection of water in organic solvents, *Dyes and Pigments* **182** (2020) 108685. DOI: 10.1016/j.dyepig.2020.108685.

[22] P. Alam, N.L.C. Leung, J. Zhang, R.T.K. Kwok, J.W.Y. Lam, B.Z. Tang, AIE-based luminescence probes for metal ion detection, *Coord. Chem. Rev.* **429** (2021) 213693. DOI: 10.1016/j.ccr.2020.213693.

[23] H. Wan, Q. Xu, P. Gu, H. Li, D. Chen, N. Li, J. He, J. Lu, AIE-based fluorescent sensors for low concentration toxic ion detection in water, *J. Hazard. Mater.* **403** (2021) 123656. DOI: 10.1016/j.jhazmat.2020.123656.

[24] Y. Jiang, J. McNeill, Light-harvesting and amplified energy transfer in conjugated polymer nanoparticles, *Chem. Rev.* **117** (2017) 838–859. DOI: 10.1021/acs.chemrev.6b00419.

[25] Q. Wan, Q. Huang, M. Liu, D. Xu, H. Huang, X. Zhang, Y. Wei, Aggregation-induced emission active luminescent polymeric nanoparticles: Non-covalent fabrication methodologies and biomedical applications, *Appl. Mater. Today.* **9** (2017) 145–160. DOI: 10.1016/j.apmt.2017.06.004.

[26] A. Suriya Prabha, R. Dorothy, S. Jancirani, S. Rajendran, G. Singh, S. Senthil Kumaran, Recent advances in the study of toxicity of polymer-based nanomaterials, in: *Nanotoxicity, Elsevier*, 2020: p. 143–165. DOI: 10.1016/B978-0-12-819943-5.00007-5.

[27] F. Duarte, C. Cuerva, C. Fernández-Lodeiro, J. Fernández-Lodeiro, R. Jiménez, M. Cano, C. Lodeiro, Polymer micro and nanoparticles containing B(III) compounds as emissive soft materials for cargo encapsulation and temperature-dependent applications, *Nanomaterials* **11** (2021) 3437. DOI: 10.3390/nano11123437.

[28] B. González-Tobío, F. Duarte, A. Arribas-Delgado, C. Fernández-Lodeiro, J. Fernández-Lodeiro, M. Cano, C. Lodeiro, C. Cuerva, Tuning and reviving the luminescence of a new class of pyridyl β-diketonate Eu(III) metallomesogens: From molecules to entrapment in polymer particles, *Dyes and Pigments* **204** (2022) 110440. DOI: 10.1016/j.dyepig.2022.110440.

[29] X. Zhang, K. Wang, M. Liu, X. Zhang, L. Tao, Y. Chen, Y. Wei, Polymeric AIE-based nano-probes for biomedical applications: Recent advances and perspectives, *Nanoscale* **7** (2015) 11486–11508. DOI: 10.1039/c5nr01444a.

[30] C. Lodeiro, J.L. Capelo, J.C. Mejuto, E. Oliveira, H.M. Santos, B. Pedras, C. Nuñez, Light and colour as analytical detection tools: A journey into the periodic table using polyamines to bio-inspired systems as chemosensors, *Chem. Soc. Rev.* **39** (2010) 2948–2976. DOI: 10.1039/b819787n.

[31] C. Lodeiro, J.C. Lima, A.J. Parola, J.S. Seixas de Melo, J.L. Capelo, B. Covelo, A. Tamayo, B. Pedras, Intramolecular excimer formation and sensing behavior of new fluorimetric probes and their interactions with metal cations and barbituric acids, *Sens. Actuators B Chem.* **115** (2006) 276–286. DOI: 10.1016/j.snb.2005.09.010.

[32] C. Lodeiro, F. Pina, Luminescent and chromogenic molecular probes based on polyamines and related compounds, *Coord. Chem. Rev.* **253** (2009) 1353–1383. DOI: 10.1016/j.ccr.2008.09.008.

[33] N.M.M. Moura, C. Núñez, S.M. Santos, M.A.F. Faustino, J.A.S. Cavaleiro, M.G.P.M.S. Neves, J.L. Capelo, C. Lodeiro, Synthesis, spectroscopy studies, and theoretical calculations of new fluorescent probes based on pyrazole containing porphyrins for Zn(II), Cd(II), and Hg(II) optical detection, *Inorg. Chem.* **53** (2014) 6149–6158. DOI: 10.1021/ic500634y.

[34] R. Lamelas, V. García, A. Liñares, R. Bastida, E. Labisbal, A. Fernández-Lodeiro, C. Lodeiro, C. Núñez, L. Valencia, Novel trans-disubstituted hexaaza-macrocyclic ligands containing pyridine head units: Synthesis, disubstitution and colorimetric properties, *Sens. Actuators B Chem.* **225** (2016) 481–491. DOI: 10.1016/j.snb.2015.11.090.

[35] A.C. Gonçalves, J.L. Capelo, C. Lodeiro, A.A.D. Santos, A seleno-pyrene selective probe for Hg^{2+} detection in either aqueous or aprotic systems, *Sens. Actuators B Chem.* **239** (2017) 311–318. DOI: 10.1016/j.snb.2016.08.014.

[36] E. Oliveira, C. Núñez, H.M. Santos, J. Fernández-Lodeiro, A. Fernández-Lodeiro, J.L. Capelo, C. Lodeiro, Revisiting the use of gold and silver functionalised nanoparticles as colorimetric and fluorometric chemosensors for metal ions, *Sens. Actuators B Chem.* **212** (2015) 297–328. https://doi.org/10.1016/j.snb.2015.02.026.

[37] L.J. Ma, J. Liu, L. Deng, M. Zhao, Z. Deng, X. Li, J. Tang, L. Yang, Selective and sensitive fluorescence-shift probes based on two dansyl groups for mercury(II) ion detection, *Photochem. and Photobiol. Sci.* **13** (2014) 1521–1528. DOI: 10.1039/c4pp00094c.

[38] N. Qureshi, S. Ehtisham-Ul-Haque, M. Abbas, M. Yameen, M. Farooq Azhar, G. Mahmoudi, A. Nazir, M. Iqbal, Synthesis of fluorescent di-dansyl substituted ethoxy compound:

A selective sensor for antimony and thallium metals detection, *Journal of Materials Research and Technology* **8** (2019) 1576–1580. DOI: 10.1016/j.jmrt.2017.12.007.

[39] A. Jose, M. Porel, Probing the interactions of dansyl appended sequence-defined oligomers with serum albumins: Effect of functionality, hydrophobicity, and architecture, J. Photochem. Photobiol. A Chem. **439** (2023) 114640. DOI: 10.1016/j.jphotochem.2023.114640.

[40] G. Pedro, F. Duarte, D.A. Cheptsov, N.Y. Volodin, I. V. Ivanov, H.M. Santos, J.L. Capelo-Martinez, C. Cuerva, E. Oliveira, V.F. Traven, C. Lodeiro, Exploring Coumarin-Based Boron Emissive Complexes as Temperature Thermometers in Polymer-Supported Materials, *Sensors* **23** (2023) 1689. DOI: 10.3390/s23031689.

[41] M. Montalti, A. Credi, L. Prodi MG, Montalti M, Credi A, Prodi L GM. Handbook of Photochemistry. 3rd ed. BOCA: Taylor & Francis, Boca Raton; 2006.

[42] J. Youziel, A.R. Akhbar, Q. Aziz, M.E.B. Smith, S. Caddick, A. Tinker, J.R. Baker, Bromo- and thiomaleimides as a new class of thiol-mediated fluorescence "turn-on" reagents, *Org. Biomol. Chem.* **12** (2014) 557–560. DOI: 10.1039/c3ob42141d.

[43] S.J.S. Flora, Structural, Chemical and Biological Aspects of Antioxidants for Strategies Against Metal and Metalloid Exposure. *Oxid. Med. Cell. Longev.* **2** (2009) 191–206. DOI: 10.4161/oxim.2.4.9112.

[44] M.T. Muhammad, M.N. Khan, Kinetics, mechanistic and synergistic studies of Alpha lipoic acid with hydrogen peroxide, *Journal of Saudi Chemical Society* **21** (2017) 123–131. DOI: 10.1016/j.jscs.2015.01.008.

[45] N. Mora-Diez, R. Monreal-Corona, J. Biddlecombe, A. Ippolito, Theoretical study of the iron complexes with lipoic and dihydrolipoic acids: Exploring secondary antioxidant activity, *Antioxidants* **9** (2020) 674. https://doi.org/10.3390/antiox9080674.

[46] L. Espinar-Barranco, P. Luque-Navarro, M.A. Strnad, P. Herrero-Foncubierta, L. Crovetto, D. Miguel, M.D. Giron, A. Orte, J.M. Cuerva, R. Salto, J.M. Alvarez-Pez, J.M. Paredes, A solvatofluorochromic silicon-substituted xanthene dye useful in bioimaging, *Dyes and Pigments* **168** (2019) 264–272. DOI: 10.1016/j.dyepig.2019.04.024.

[47] A. Ghanadzadeh Gilani, M. Moghadam, M.S. Zakerhamidi, Solvatochromism of Nile red in anisotropic media, *Dyes and Pigments* **92** (2012) 1052–1057. DOI: 10.1016/j.dyepig.2011.07.018.

[48] J. Nootem, C. Sattayanon, S. Namuangruk, P. Rashatasakhon, W. Wattanathana, G. Tumcharern, K. Chansaenpak, Solvatochromic triazaborolopyridinium probes toward ultra-sensitive trace water detection in organic solvents, *Dyes and Pigments* **181** (2020) 108554. https://doi.org/10.1016/j.dyepig.2020.108554.

[49] E. Oliveira, R.M.F. Baptista, S.P.G. Costa, M.M.M. Raposo, C. Lodeiro, Exploring the emissive properties of New Azacrown compounds bearing aryl, furyl, or thienyl moieties: A special case of chelation enhancement of fluorescence upon interaction with Ca^{2+}, Cu^{2+}, or Ni^{2+}, *Inorg. Chem.* **49** (2010) 10847–10857. DOI: 10.1021/ic101095y.

[50] P. Garw, A. Sabatinib, A. Vaccab, Investigation of equilibria in solution. Determination of equilibrium constants with the HYPERQUAD suite of programs, *Talanta* **43** (1996) 1739-1753. DOI: 10.1016/0039-9140(96)01958-3.

[51] H. Wang, E. Zhao, J.W.Y. Lam, B.Z. Tang, AIE luminogens: emission brightened by aggregation, *Materials Today* **18** (2015) 365–377.DOI: 10.1016/j.mattod.2015.03.004

6

DEVELOPMENT OF FLUOROCHROMIC POLYMER DOPED MATERIALS AS PLATFORMS FOR TEMPERATURE SENSING USING THREE DANSYL DERIVATIVES BEARING A SULFUR BRIDGE.

Frederico Duarte, Georgi Dobrikov, Atanas Kurutos, Jose Luis Capelo-Martinez, Hugo M. Santos, Elisabete Oliveira, Carlos Lodeiro

Journal of Photochemistry & Photobiology, A: Chemistry 445 (2023) 115033 Doi: 10.1016/j.jphotochem.2023.115033

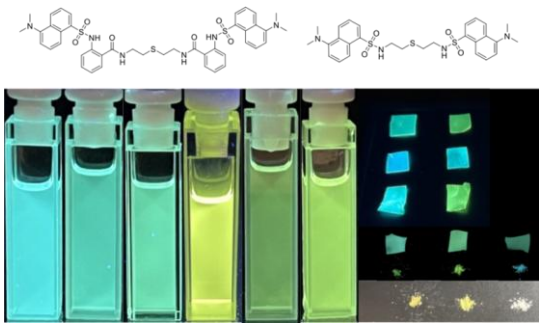
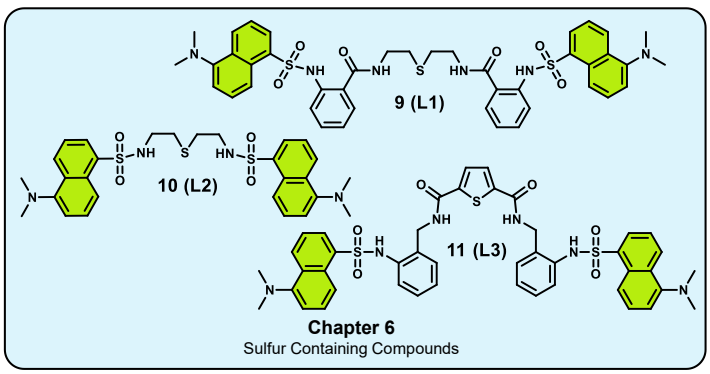


Figure 6–1. Graphical Abstract



Contribution to this work: Photophysical characterization; Preparation of polymeric doped thin films; Sensing experiments of metal ions; Temperature-dependent studies; Writing original draft.

6.1 Abstract

Three novel bis-dansyl derivatives bearing a sulfur bridge have been synthesized, fully characterized, and their photophysical characterization studied in solution, as well as, in the solid state. All compounds exhibit fluorescence emission with quantum yields up to 60%, which vary significantly depending on the solvent used, and the inherent molecular structure. Moreover, these compounds demonstrate positive solvatofluorochromic behaviour emitting from bluish-green to yellow. Kamlet-Taft studies were performed to better understand the solute-solvent interactions. Due to the intrinsic characteristics of the compounds, efforts were made to understand their potential usefulness for environmental remediation and thus metal ion sensing studies were investigated. Compounds **L1** and **L2** showed high sensitivity to Cu^{2+} and Hg^{2+} ions and were found to modulate their emission extensively, with **L2** capable of detecting and quantifying up to 4 μM of Hg^{2+}. Considering the solid-state emission of these compounds, the application towards temperature sensing was put forth. **L3** was found to quench its emission in a linear relation with temperature up to 170 ºC. Several doped polymer thin films were fabricated, which served as a platform to establish a linear relation with temperature beyond their melting point. Polymethylmetacrylate (PMMA) films emitted up to temperatures of 218 ºC, which could be fully restored at room temperature. These results suggest the potential application of these bis-chromophoric compounds as molecular thermometers.

6.2 Introduction

Probes and sensors conceptualized using fluorescent dyes offer inherent value due to their remarkable optical properties [1–3]. Among them, compounds based on 1-(dimethylamino)-naphthalene-5- sulfonyl or dansyl derivatives, have received consistent attention since they often exhibit broad emission spectra, high quantum yields and are robust enough under different external conditions [4–9]. This brought up to light a multitude of possible applications, ranging from biological targets such as the detection of oxygen reactive species [10], imaging [8,11–15], and monitoring of organ systems [6], to the detection of heavy and transition metal ions [12–20] and even water traces [4].

Our group has been working on metal ion detection for the last fifteen years [21–24]. Among them, the heavy and transition metal ions including Hg^{2+} and Cu^{2+} have gathered considerable attention. Hg^{2+} is a potential hazardous and toxic environmental pollutant that cause immunotoxic and neurotoxic effects in humans, leading to damage of the central nervous

system and organ failure. On the other hand, Cu^{2+} is abundant in the body and plays a crucial role in diverse biological processes and cellular functioning. Abnormal concentration of Cu^{2+} may lead to the disruption of metabolic processes and neurodegenerative diseases such as Alzheimer's and Wilson diseases [14,17,25]. The U.S. Environmental Protection Agency has set admissible levels of Hg^{2+} and Cu^{2+} in drinking water to be 10 nM and 20 mM, respectively. Therefore, the development of fluorescent sensors for the detection of these transition metals is of utmost importance [12,17].

Considering the constant search for improved sensors for metal ions, Anna Aliberti *et. al.* designed several dansyl-amino acids capable of detecting Hg^{2+}. Among them, N-dansylated methionine was the chemosensor that showed the best performance in terms of sensitivity, with a limit of detection (LOD) value of 140 nM. To improve the LOD of this chemosensor, a portable experimental set-up based on an optical fiber probe was developed, which was able to increase the LOD to 5 nM, meeting the requirements of the Environmental Protection Agency. However, application to water-based matrices was found to be unfruitful due to the coordinating ability of chloride anions towards Hg^{2+} [16]. Similarly, Bhawna Uttam *et. al.* developed a dansyl appended calix[4]arene on the lower rim, which selectively detected Hg^{2+} with a LOD value of 560 nM. MTT assay was performed using HeLa cells confirming its biocompatibility, and strong fluorescence was visualized by confocal microscopy. The removal of Hg^{2+} from water sources was also addressed by embedding the sensor on a zeolitic imidazolate framework with 5% encapsulation. ICP-MS studies suggested a 95% removal of Hg^{2+} from water using the hybrid metal-organic framework (MOF), displaying excellent selectivity even in the solid state [13].

On the other hand, the employment of dansyl derivatives towards sensing of Cu^{2+} ions have been put forward by Huie Jiang *et. al.* whom developed a novel fluorescent probe trough a nucleophilic substitution reaction between dansyl chloride and 2-(piperazin-1-yl)ethanol at room temperature. The compound was found to be selective and sensitive for Cu^{2+} ions, causing the red shift and quenching of the emission and presented a low detection limit of 0.18 mL. Furthermore, this compound was successfully applied for the monitorization of Cu^{2+} ions in living cells particularly A549 cells using two-photon confocal fluorescence imaging [12]. Additionally, Rajendran Nagarajan *et. al.* have synthesized an unnatural amino acid-based phenylalanine that has been linked to dansyl and benzoxazole moieties. Competitive studies with other metal ions showed a selective quenching towards Cu^{2+} ions within aqueous organic media with physiological pH with an LOD value of 3.0 mL. Further water analysis studies indicated

the usefulness of this compound being capable of recovering 99.92% of the Cu^{2+} ions in spiked tap and drinking water samples [25].

On the other hand, solvatochromism is another well-known and fairly common property among dansyl derivatives, as the dipole moment undergoes considerable changes as the solvent polarity increases, resulting in a significant Stokes shift [7,26–29]. However, further, research is needed to develop probes with high solvatochromism that do not succumb to aggregation-caused fluorescence quenching (ACQ) effects in hydrophilic and hydrophobic environments [8,30]. A more prevalent example of the contrast between these two types of environments is within cells, where different regions and organelles exhibit varying affinities for water. Na Li *et al.* have developed a robust polarity sensor to address this issue, which can track the decrease of lipid droplets when subjected to oxidative stress in live cells. The system involves the covalent bond between dansyl chloride and nile red derivative, capable of sensing polarity changes in both green and red detection channels. The fluorophore was found useful in both environments since the dansyl moiety was resistant to ACQ, while nile red changed the fluorescence in the red channel with high linearity of aqueous composition. This dual emission also provided the experimental results supporting the conclusion that oxidative stress leads to a sharp decrease in lipid droplets [8].

Fluorescent dye-doped solid support materials have generated great interest, as they have the potential to improve the intrinsic properties of the dye, such as stability against quenchers, sensitivity, fluorescence and prevention of aggregation-caused quenching (ACQ) [31,32]. These multifunctioning materials can be applied as sensors for pH [33,34], transition metals [17], temperature and smart materials [34–38] and even low-cost antibacterial polymers for biomedical and food packaging [39]. Given the diverse implementation of dansyl derivatives into multifunctional solid materials [31,40–42], and our recent knowledge on bis-dansyl derivatives bearing a disulfide bridge [43], the three dansyl derivatives **L1**, **L2** and **L3** bearing single sulfur bridges were synthesized and fully characterized. Above mentioned ligands were designed in order to demonstrate good complexation ability toward heavy metals. Presence of multiple amide bonds [44] as well as sulfur with aliphatic substituents in one molecule [45,46] ensure chelating effect of the ligands. Discovery of solvatochromic effect was accomplished alongside with their ability to sense pollutant metal ions, and incorporated into polymer thin films of polystyrene-block-polybutadiene-block-polystyrene (SBS), Poly(methylmethacrylate) (PMMA), Polyvinyl alcohol and poly(styrene-butadiene-styrene) co-polymer (PVA:PVP) and thermoplastic polyurethane (TPU) towards the development of temperature-smart materials.

6.3 Experimental Section

6.3.1 Materials

Spectroscopy grade solvents were used for photophysical experiments – ethanol (EtOH), toluene, tetrahydrofuran (THF), acetonitrile (CH_3CN), dimethylsulfoxyde (DMSO), dimethylformamide (DMF), chloroform ($CHCl_3$). Puriss. p.a. grade solvents were used after distillation for synthesis and purification of compounds – dichloromethane (DCM), petroleum ether (PE), methyl *tert*-butyl ether (MTBE), ethanol (EtOH).

Trifluoromethanesulfonate salts of Cu(II), Cd(II), Co(II), Ag(I), Pb(II), Zn(II), Ni(II) and Ca(II) have been obtained from Solchemar, while $Hg(OTf)_2$, dansylamide and all solvents were purchased from Sigma Aldrich without the necessity of performing additional steps of purification. Poly(methylmethacrylate), PMMA (MW ~ 350,000, Tg 105 °C) polyvinylpyrrolidone, PVP (MW ~40,000, Tg 170 °C), Polyvinyl alcohol (PVA, MW 27,000, Tg 85 °C) and poly(styrene-butadiene-styrene), SBS (Styrene 30 wt %, Tg 95 °C) were purchased from Sigma-Aldrich (St. Louis, MO, USA). The perfluoroalkoxy (PFA) supports for the fabrication of polymer films were purchased to Bohlender, Gmbh, Germany. Mili-Q ultrapure water was used in all experiments. The thermoplastic polyurethane TPU-A92 was offered by Huntsman (Germany)

6.3.2 Instrumentation

Visualization of the TLC was performed using a Vilber UV Lamp (BVL-6.LC dual wavelength 254 nm/365 nm, operational power of 2×6 Watts).

Using a combination of ^{1}H-NMR and ^{13}C-NMR all compounds' chemical identities were verified. Using 5 mm tubes on a Bruker Avance II+ 600 spectrometer, the ^{1}H-NMR and ^{13}C-NMR spectra were measured in $CDCl_3$ at 293 K at operating frequencies of 600.13 MHz and 150.92 MHz, respectively. ^{1}H and ^{13}C NMR spectra were calibrated to the signal of tetramethylsilane (TMS), δ=0.00. Chemical shifts are measured to an accuracy of 0.01 parts per million (ppm). The coupling constants (*J*) are shown with a precision of 0.1 and represented in Hz. The spin multiplicity in the 1H-NMR was denoted by the abbreviations s = singlet, d = doublet, t = triplet, q = quartet, dd = doublet of doublets, dt = doublet of triplets, td = triplet of doublets, and m = multiplet.

High-Resolution Mass Spectrometry analyses have been performed in the Laboratory for Biological Mass Spectrometry–Isabel Moura (PROTEOMASS Scientific Society Facility), using UHR ESI-Qq-TOF IMPACT HD (Bruker-Daltonics, Bremen, Germany). Samples of the

corresponding compounds were prepared by dissolution in 50% (v/v) Acetonitrile containing 0.1% (v/v) aqueous formic acid to obtain a working solution of 0.1 µg/mL. Mass spectrometry analysis was carried out by the direct infusion of the compound solutions into the ESI source. MS data were acquired in positive polarity over the mass range of 80 – 1300 m/z. (Capillary voltage: 4500 V, End plate offset: -500 V, Charging voltage: 2000 V, Corona: 4000 nA, Nebulizer gas: 0.4 Bar, Dry Heater: 180 °C, Dry gas: 4.0 L/min).

UV-Vis absorption spectra were recorded on a JASCO V-650 spectrophotometer and a fluorescence emission spectrum on a HORIBA Scientific FLUOROMAX-4 spectrofluorometer from BIOSCOPE-PROTEOMASS facilities.

6.3.3 Synthetic procedures

6.3.3.1 Synthesis of L1

N,N'-[thiobis(ethane-2,1-diyl)]bis(2-aminobenzamide) **(3)**:

In a 100 mL flask with 50 mL dry DCM were added consequently anthranilic acid (**2**) (2.51 g, 18.30 mmol, 2.2 eq.), diamine **1** (1.00 g, 0.95 mL, 8.32 mmol, 1.0 eq.), DIPEA (4.73 g, 6.05 mL, 36.60 mmol, 4.4 eq.) and TBTU (5.88 g, 18.30 mmol, 2.2 eq.). The formed clear solution was stirred at r.t. for 72 h. TLC of reaction mixture – DCM:MTBE=5:1, x1. Workup: dilution with 30 mL DCM and washing with distilled water, aq. K_2CO_3 and again with water. The organic phase was dried over anhydr. Na_2SO_4, filtered, and evaporated to dryness. This crude product was recrystallized from EtOH:H_2O=25:10 mL. The precipitate was filtered, washed with PE:MTBE=30:10 and dried *in vacuo* to give 2.22 g (74%) of pure **3** as white-off powder. M.p. 121-122°C. ^{1}H NMR (600 MHz, $CDCl_3$) δ 7.34 (*dd*, *J* = 7.9, 1.5 Hz, 2H), 7.20 (*ddd*, *J* = 8.4, 7.1, 1.5 Hz, 2H), 6.67 (*dd*, *J* = 8.2, 1.1 Hz, 2H), 6.65 – 6.60 (*m*, 4H), 5.48 (*s*, 4H), 3.62 (*q*, *J* = 6.2 Hz, 4H), 2.82 – 2.79 (*m*, 4H). ^{13}C NMR (151 MHz, $CDCl_3$) δ 169.61, 148.78, 132.53, 127.45, 117.44, 116.84, 116.01, 38.77, 31.83.

N,N'-[thiobis(ethane-2,1-diyl)]bis(2-[(5-(dimethylamino)naphthalene]-1-sulfonamido)benzamide) **(L1)**:

Compound **3** (0.250 g, 0.70 mmol, 1.0 eq.) was dissolved in 4 mL dry pyridine. Subsequently, dansyl chloride (0.452 g, 1.67 mmol, 2.4 eq.) was added and the formed clear solution was refluxed for 2 h. TLC of reaction mixture – DCM:MTBE=5:1, x1. Workup: after cooling an excess of conc. aq. citric acid was added and extracted with DCM. The organic phase was washed with water, dried over anhydr. Na_2SO_4, filtered, and evaporated to dryness. This crude

product was purified by column chromatography: 70 g silica, phase DCM:MTBE=20:1. After evaporation of phase and drying *in vacuo*, pure **L1** was obtained as bright yellow powder (0.31 g, 54%). M.p. 111-112°C. ^{1}H NMR (600 MHz, $CDCl_3$) δ 11.25 (*s*, 2H), 8.46 (*dt*, *J* = 8.6, 1.1 Hz, 2H), 8.33 (*dt*, *J* = 8.7, 0.9 Hz, 2H), 8.24 (*dd*, *J* = 7.3, 1.3 Hz, 2H), 7.55 – 7.47 (*m*, 4H), 7.43 (*dd*, *J* = 8.5, 7.3 Hz, 2H), 7.27 (*dd*, *J* = 7.9, 1.5 Hz, 2H), 7.28 – 7.21 (*m*, 2H), 7.11 (*dd*, *J* = 7.6, 0.9 Hz, 2H), 6.81 (*td*, *J* = 7.6, 1.2 Hz, 2H), 6.65 (*t*, *J* = 5.9 Hz, 2H), 3.44 (*q*, *J* = 6.4 Hz, 4H), 2.81 (*s*, 12H), 2.66 (*t*, *J* = 6.5 Hz, 4H). ^{13}C NMR (151 MHz, CDC l_3) δ 168.77, 151.91, 138.86, 134.80, 132.67, 130.91, 130.05, 129.93, 129.61, 128.51, 127.02, 123.13, 123.05, 120.62, 119.76, 119.12, 115.41, 45.51, 39.03, 31.50. ESI-MS: $[M+H]^+$ for $C_{42}H_{44}N_6O_6S_3$ = 825.2552 (-0.6 ppm), and $[M+2H]^{2+}$ for $C_{42}H_{44}N_6O_6S_3$ = 413.1307 (-1.9 ppm). Calculated $[M+H]^+$ for $C_{42}H_{44}N_6O_6S_3$ = 825.255723 and $[M+2H]^{2+}$ for $C_{42}H_{44}N_6O_6S_3$ = 413.131500.

6.3.3.2 Synthesis of L2

N,N'-(thiobis(ethane-2,1-diyl))bis(5-(dimethylamino)naphthalene-1-sulfonamide)**(L2)**:

Diamine **1** (0.089 g, 0.085 mL, 0.74 mmol, 1.0 eq.) and DIPEA (0.240 g, 0.32 mL, 1.85 mmol, 2.5 eq.) were dissolved in 50 mL dry DCM and cooled to 5°C (with ice-water). Then dansyl chloride (0.400 g, 1.48 mmol, 2.0 eq.) was added in one portion and the formed clear mixture was stirred for 30 min at 5°C, followed by 48 h at r.t. TLC of reaction mixture – DCM:MTBE=10:1, x1. Workup: dilution with 30 mL DCM and washing with 1% aq. citric acid and water. The organic phase was dried over anhydr. Na_2SO_4, filtered and evaporated to dryness. This crude product was purified by column chromatography: 70 g silica, phase DCM:MTBE=20:1. After evaporation of phase and drying *in vacuo*, pure **L2** was obtained as pale-yellow powder (0.20 g, 46%). M.p. 70-71°C. ^{1}H NMR (600 MHz, $CDCl_3$) δ 8.53 (*d*, *J* = 8.5 Hz, 2H), 8.24 (*d*, *J* = 8.6 Hz, 2H), 8.20 (*dd*, *J* = 7.3, 1.3 Hz, 2H), 7.54 (*dd*, *J* = 8.6, 7.5 Hz, 2H), 7.50 (*dd*, *J* = 8.5, 7.3 Hz, 2H), 7.17 (*d*, *J* = 7.5 Hz, 1H), 2.88 (*s*, 16H), 2.25 (*t*, *J* = 6.4 Hz, 4H). ^{13}C NMR (151 MHz, $CDCl_3$) δ 152.18, 134.53, 130.78, 129.96, 129.78, 129.59, 128.69, 123.32, 118.69, 115.41, 45.55, 42.00, 31.42. ESI-MS: $[M+H]^+$ for $C_{28}H_{34}N_4O_4S_3$ = 587.1811 (-0.7 ppm). Calculated $[M+H]^+$ for $C_{28}H_{34}N_4O_4S_3$ = 587.181495.

6.3.3.3 Synthesis of L3

N^{2},*N*^{5}-bis(2-aminobenzyl)thiophene-2,5-dicarboxamide **(6)**:

In a 100 mL flask with 50 ml dry DCM were added consequently diacid (**4**) (0.300 g, 1.74 mmol, 1.0 eq.), diamine **5** (0.45 g, 3.66 mmol, 2.1 eq.), DIPEA (1.24 g, 1.58 mL, 9.59 mmol, 5.5 eq.) and TBTU (1.23 g, 3.83 mmol, 2.2 eq.). The formed fine pale-yellow suspension was stirred

at r.t. for 20 h. Workup: the solvent was evaporated, and the formed solid product was dispersed in hot water and filtered. This crude product was crystalized from EtOH:H_2O = 40:5 mL, filtered and dried *in vacuo* to give 0.46 g (69%) of pure **6** as white powder. M.p. 214-215 °C (with decomp.). ^{1}H NMR (600 MHz, DMSO-d_6) δ 9.07 (t, *J* = 6.0 Hz, 1H), 7.75 (*s*, 1H), 7.02 (*dd*, *J* = 7.5, 1.6 Hz, 1H), 6.97 (*td*, *J* = 7.6, 1.6 Hz, 1H), 6.62 (*dd*, *J* = 7.9, 1.2 Hz, 1H), 6.51 (*td*, *J* = 7.4, 1.2 Hz, 1H), 5.12 (*s*, 2H), 4.29 (*d*, *J* = 6.1 Hz, 2H). ^{13}C NMR (151 MHz, DMSO-d_6) δ 160.97, 146.27, 143.05, 129.25, 128.50, 128.10, 121.62, 115.91, 114.78.

N^2,*N*^{5}-bis(2-((5-(dimethylamino)naphthalene)-1-sulfonamido)benzyl)thiophene-2,5-dicarboxamide **(L3)**:

Compound **6** (0.300 g, 0.79 mmol, 1.0 eq.) was dissolved in 5 mL dry pyridine. Then dansyl chloride (0.468 g, 1.73 mmol, 2.2 eq.) was added and the formed clear solution was stirred at r.t. for 72 h. TLC of reaction mixture – DCM:MTBE=5:1, x2. Workup: excess of conc. aq. citric acid was added and extracted with DCM. The organic phase was washed with water, dried over anhydr. Na_2SO_4, filtered, and evaporated to dryness. This crude product was purified by column chromatography: 70 g silica, phase 1 - DCM:MTBE=10:1 (for contaminations); phase 2 - DCM:MTBE=5:1 (for product). After evaporation of phase and drying *in vacuo*, pure **L3** was obtained as pale-yellow powder (0.51 g, 76%). M.p. 263-264°C. ^{1}H NMR (600 MHz, DMSO-d_6) δ 10.24 (s, 2H), 9.23 (t, *J* = 6.1 Hz, 2H), 8.47 (dt, *J* = 8.5, 1.1 Hz, 2H), 8.42 – 8.36 (m, 2H), 8.09 (dd, *J* = 7.3, 1.3 Hz, 2H), 7.76 (s, 2H), 7.57 (ddd, *J* = 11.9, 8.6, 7.4 Hz, 4H), 7.24 (dd, *J* = 7.7, 0.9 Hz, 2H), 7.20 – 7.15 (m, 2H), 7.12 – 7.05 (m, 4H), 6.90 – 6.85 (m, 2H), 4.32 (d, *J* = 6.1 Hz, 4H), 2.81 (s, 12H). ^{13}C NMR (151 MHz, DMSO-d_6) δ 161.39, 151.61, 142.64, 135.47, 134.49, 133.19, 130.31, 129.56, 129.07, 129.04, 128.27, 127.97, 125.91, 124.11, 123.69, 118.77, 115.35, 45.14. ESI-MS: $[M+H]^+$ for $C_{44}H_{42}N_6O_6S_3$ = 847.2389 (-1.3 ppm), and $[M+2H]^{2+}$ for $C_{42}H_{42}N_6O_6S_3$ = 424.1245 (1.9 ppm). Calculated $[M+H]^+$ for $C_{44}H_{42}N_6O_6S_3$ = 847.240073, and $[M+2H]^{2+}$ for $C_{42}H_{42}N_6O_6S_3$ = 424.123674.

6.3.4 Spectrophotometric and spectrofluorimetric measurements

6.3.4.1 Photophysical characterization and titrations

Photophysical characterizations and titrations were performed by preparation of stock solutions of compounds **L1**, **L2** and **L3** (ca. 10^{-3} M) in different solvents (CH_3CN, EtOH, DMSO, $CHCl_3$, Toluene, THF and DMF), by dissolution of an appropriate amount of the selected compound in a 10 mL volumetric flask. Further studies were carried out by appropriate dilution of

the stock solutions up to 10^{-5} – 10^{-6} M. Titrations of **L1** and **L2** were carried out by the addition of microliter aliquots of standard solutions of Ca^{2+}, Co^{2+}, Ni^{2+}, Cu^{2+}, Zn^{2+}, Ag^{+}, Cd^{2+}, Hg^{2+}, Pb^{2+} ions prepared in acetonitrile, while titrations of **L3** were carried out in DMSO. A correction for the absorbed light was performed when necessary. Luminescence spectra of the compounds in the solid state and of doped polymer thin films were recorded using of a fiber-optics device connected to the spectrofluorometer while exciting the samples at appropriated wavelength. The temperature dependent emission spectra were recorded by heating the samples over a hotplate with control over the temperature.

Table 6-1. Spectroscopic polarity parameters, physical properties of the different solvents. ε_r : relative permittivity; η: refractive index; α: the solvent's HBD acidity; β: the solvent´s HBA basicity; π^*: the solvent´s dipolarity/polarizability.

Solvent	ε_r	α	β	π^*	η
DMSO	47.24	0	0.76	1.00	1.47
DMF	38.4	0	0.69	0.88	1.43
CH_3CN	35.94	0.19	0.40	0.66	1.34
EtOH	24.30	0.86	0.75	0.54	1.36
THF	7.58	0	0.55	0.58	1.40
$CHCl_3$	4.89	0.20	0.10	0.69	1.44
Toluene	2.38	0	0.11	0.54	1.49

6.3.4.2 Fluorescence quantum yield and lifetime

Relative photoluminescence quantum yields were measured using dansyl amide in acetonitrile employed as a standard solution (ϕ_F = 0.37) for quantifying the relative QY of **L1** and **L2** dissolved in the same solvent and in DMSO for **L3**, while the remaining ones were measured relative to the standard solution of dansyl amide in DMSO (ϕ_F = 0.61) [47]. Tempro Fluorescence Lifetime System with a Nanoled pulsed diode controller from Horiba Jobin-Yvon (Proteomass Facilities) was used to perform lifetime measurements.

6.3.5 Determination of the detection and quantification limits (LOD and LOQ)

Determination of the detection limit (LOD) and quantification limit (LOQ) began by collecting ten independent measurements of a solution containing the selected probe and no

addition of any metal ion (y_{blank}). Final determination of the LOD and LOQ values followed the subsequent formulas [48,49]:

LOD = y_{dl} = y_{blank} + 3std, where y_{dl} = signal detection limit and std = standard deviation.

LOQ = y_{dl} = y_{blank} + 10std, where y_{dl} = signal detection limit and std = standard deviation.

The final step involved the determination of the minimal detectable and quantified concentration of metal ion by titration with the ligands.

6.3.6 Preparation of polymer Dye-Doped thin films

PMMA and SBS doped polymer thin films were obtained by slow evaporation of a 10 mL chloroform solution containing 100 mg of the corresponding polymer matrix and 0.5 mg of the selected compound.

PVA:PVP polymer films were prepared by dissolution of 200 mg of PVA and 50 mg of PVP in 1.5 mL miliQ water, while heating at 80 °C, with continuous stirring and 0.5 mg of the dansyl dyes were dissolved in 2 mL of EtOH and added to the hot mixture.

TPU doped polymer films were fabricated by dissolving 100 mg of the polymer matrix and 1 mg of the corresponding compounds in 10 mL of THF.

All mixtures were poured onto PFA supports with diameter of 5 cm to allow solvent evaporation at room temperature. All polymeric samples were prepared in triplicate.

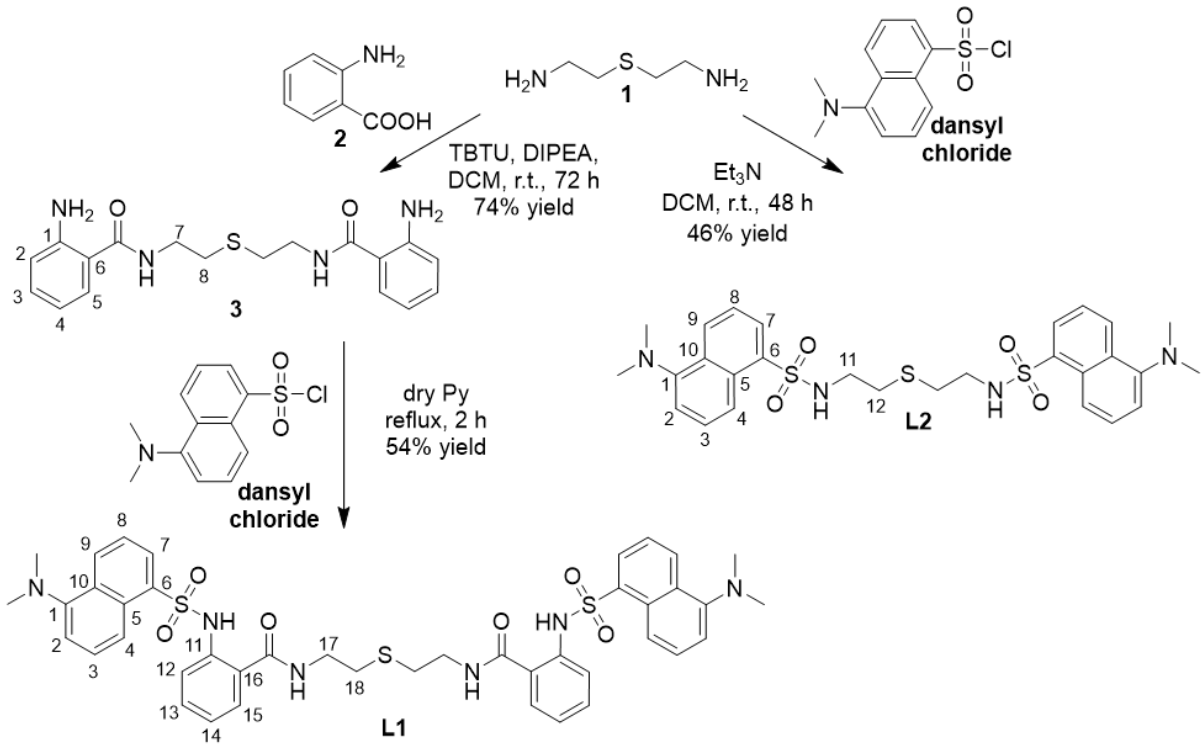
6.4 Results & Discussion

6.4.1 Synthesis

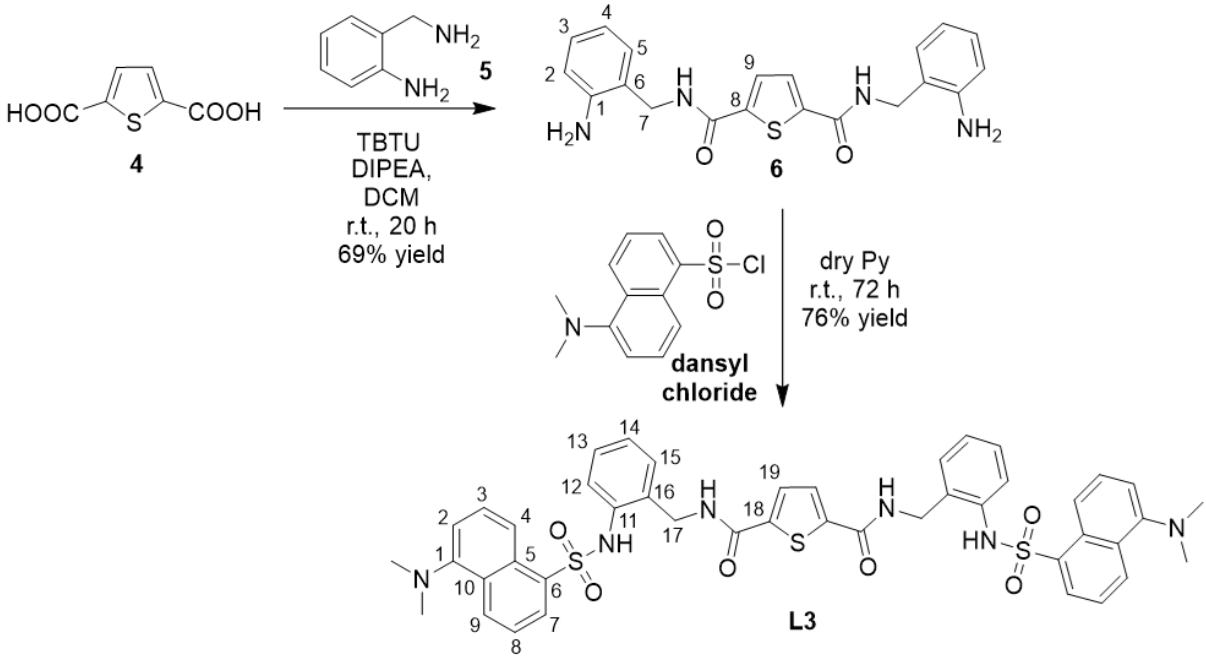
The synthesis of target compounds **L1** and **L2** was based on commercially available thiodiamine **1** (**Scheme 6-1**). Preparation of intermediate **3** was accomplished by direct coupling reaction of **1** with anthranilic acid (**2**). Due to better nucleophilicity of amino groups of **1**, preparation of **3** was performed in only one step and isolated with good yield without need of protection. Consequently, acylation of **3** with dansyl chloride in dry pyridine furnished the target product **L1** in good yield. The synthesis of compound **L2** was performed in one step starting from **1** and dansyl chloride, employing classical conditions (Et_3N in dry dichloromethane).

The preparation of ligand **L3** was conducted in two steps (Scheme 6-2). Intermediate **6** was prepared in one step from commercially available diacid **4** and diamine **5**, respectively. As in case of **3**, protection of **5** was not necessary. Acylation of **6** with excess of dansyl chloride in dry pyridine yields product **L3**. All intermediates and target compounds were obtained in good

yields and high purity after column chromatography. They were fully characterized by NMR, MS and melting point temperatures.



Scheme 6-1. Synthetic approach to the preparation of compounds **L1** and **L2.**



Scheme 6-2. Synthetic approach to the preparation of compound **L3.**

6.4.2 Photophysical characterization

The dansyl derived compounds exhibit luminescence properties both in solution and in the solid state. **Figure 6–2** displays the molecular structure alongside the photophysical data collected at 298 K for compound **L1** and **L2** in acetonitrile as well as in DMSO for **L3** as a representative example. The UV-Vis spectra show a band centered at 330, 340 and 350 nm; associated with the π-π^* transition of the dansyl chromophore, contributing to the visualization of colourless solutions in the naked eye. Upon excitation at the appropriate wavelength, the samples emit a greenish yellow light with a maxima at 524, 518 and 532 nm representative of a large stoke shift. On a relatable note, solid-state emission spectra show a wide band centered at 509, 499 and 469 nm, a considerable blue shift in relation to the emission in solution (Table 6-2).

Since dansyl derivatives are commonly associated with solvatochromism behavior, **L1**-**L3** were further studied for their photophysical properties in five different solvents to evaluate the sensitivity towards solvent polarity. Alongside in acetonitrile, **L1** and **L2** were further studied in DMSO, ethanol, THF, chloroform and toluene; Due to solubility restrictions **L3** was studied in THF and DMF (Figure 6–10 to Figure 6–14).

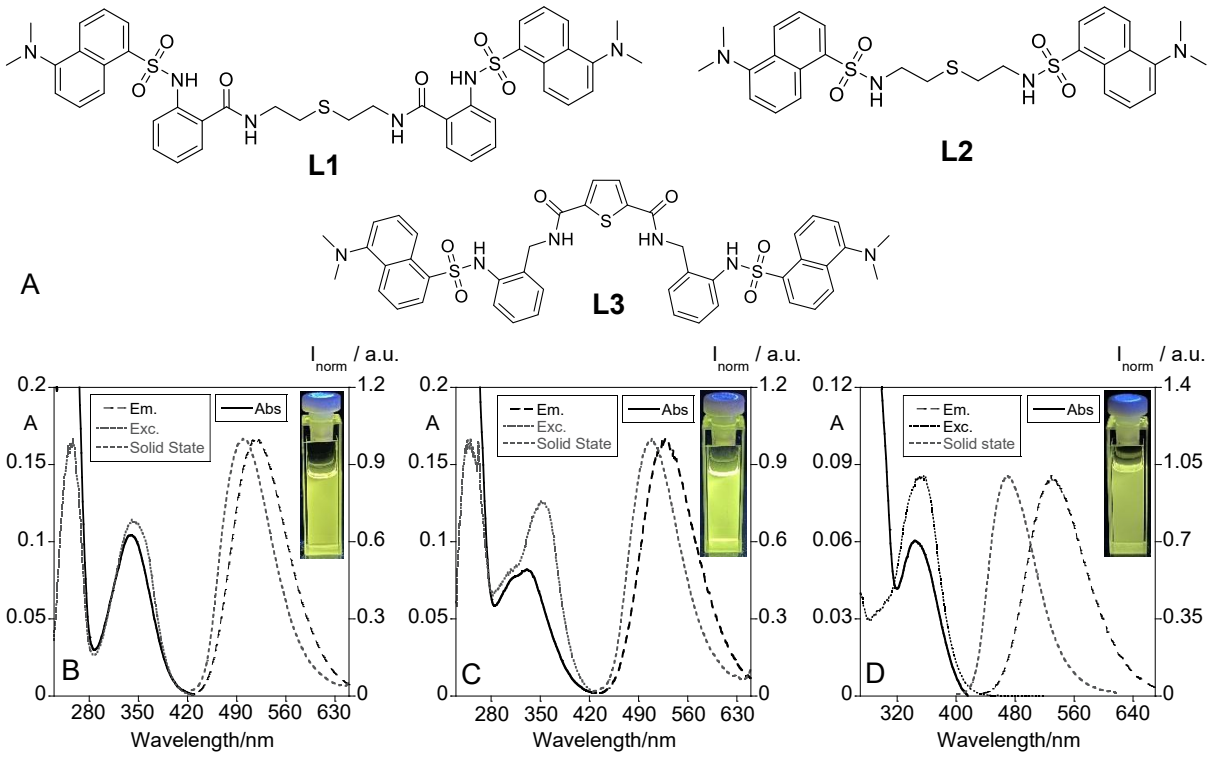


Figure 6–2. (A) Molecular structure of dansyl based compounds **L1**, **L2** and **L3**. Photophysical characterization of derivatives **L1** (B), **L2** (C) in acetonitrile and **L3** (D) in DMSO ([**L1**]=[**L2**]=[**L3**]= 6 μM).

Table 6-2. Absorption maximum wavelength in solution (λ_{abs}), emission maximum wavelength in solution (λ_{em}), molar absorption coefficients (ε), Stokes shift ($\Delta\lambda$), emission maximum in the solid state (λ_{em}^{Solid}), fluorescence quantum yields (ϕ), brightness ($\varepsilon x\phi$), fluorescence lifetimes (τ) for compounds **L1** to **L3** performed in different organic solvents.

Cpd	Solv	λ_{abs} [nm]	λ_{em} [nm]	ε (10^4) [cm^{-1} M^{-1}]	Stokes shift [cm^{-1}]	ϕ(%)	Brightness ($cm^{-1}.M^{-1}$)	λ_{em}^{Solid} [nm]	τ[ns]
L1	DMSO	350	534	0.999	9845	24	2359	509	14
	CH_3CN	330	524	0.99	11219	27	2714		11
	EtOH	334	520	0.804	10709	17	1367		13
	THF	336	507	1.19	10038	47	5556		14
	$CHCl_3$	345	506	1.07	9223	51	5405		15
	Toluene	343	500	0.816	9155	51	4187		13
L2	DMSO	340	520	0.956	10181	48	4588	499	12
	CH_3CN	340	518	1.06	10106	35	3689		12
	EtOH	335	515	0.964	10433	33	3180		15
	THF	336	492	1.21	9437	52	6290		13
	$CHCl_3$	343	500	0.802	9155	60	4812		13
	Toluene	341	489	0.899	8876	53	4767		16
L3	DMF	336	523	1.16	10641	4	430	469	7.7
	DMSO	350	532	1.03	9774	10	1051		5.6
	THF	339	501	1.34	9538	7	978		6.6

Taking into consideration the analysis of Table 6-2, no correlation can be perceived following the absorption as the solvent polarity increases despite the differences in maximum bands. On the contrary, the same cannot be said for the emission, where a clear red shift of the emission maximum bands is seen, a shift from 500 to 536 nm for **L1**, from 489 to 520 nm for **L2** and from 339 to 350 nm for **L3** with increasing solvent polarity. In line with these findings, a conclusion can be taken based on the shifts observed regarding the emission spectra, demonstrating that **L1**, **L2** and **L3** exhibit a positive solvatofluorochromism.

To fully characterize **L1** and **L2's** solvatofluorochromic behaviour, and to quantify the solute-solvent interactions, three solute-dependent parameters (υ_0, a, b and p) have been determined through the multiparametric fitting of the kamlet-Taft equation (Equation 1).

$$\upsilon = \upsilon_0 + a\alpha + b\beta + p\pi^* \quad \text{(Equation 1)}$$

Where υ_0 represents the wavenumber value without dependence of solvent effects; parameters a, b and p are obtained through multiple regression analysis that reflect the underlying sensitivity of the probes photophysical behaviour to solvent polarity; α: hydrogen bond donor acidity (HBD); β: hydrogen bond acceptor basicity (HBA); π^*: stabilization of a charge or dipole without a specific dielectric interaction (Table 6-1) [29,50].

Figure 6–3 gathers the images taken under UV light lamp of **L1** and **L2** under a UV light lamp while Table 6-3 presents the fitted parameters (υ0, a, b and p) driven from the multiple regression analysis while the slope and correlation were obtained from the linear fitting of the plot $\upsilon_{exp.}$ versus $\upsilon_{calc.}$

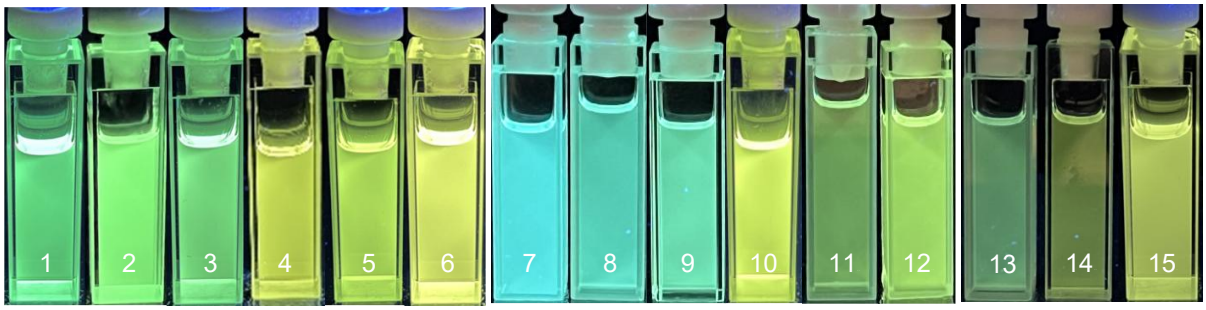


Figure 6–3. Images of **L1** (1-6), **L2** (7-12) and **L3** (13-15) in different organic solvents [Toluene (1,7); THF (2, 8, 13); Chloroform (3, 9); Acetonitrile (4, 10); Ethanol (5, 11); DMF (14); DMSO (6, 12, 15)] under a UV lamp.

Table 6-3. Independent fluorescence wavenumber (*υ*0), solvent polarity (*p*), HBD (*a*), HBA (*b*), slope and coefficient (R^2) of the linear fitting plot $\upsilon_{exp.}$ versus $\upsilon_{calc.}$

	υ0	a	b	p	Slope	R^2
L1	21144	-421	-721	-1848	0.99	0.99
L2	21790	-1032	-299	-2314	0.99	0.99
L3	21646	-1033	-301	-2626	0.99	0.99

From Table 6-3 it is perceived that **L3** has the highest polarizability making it more likely to be distorted by an external field.

6.4.3 Metal Ion sensing

Keeping in mind the potential value of these dansyl derivatives to be used towards the sensing of metal ions, additions of 1, 5 and 10 equivalents of Ca^{2+}, Co^{2+}, Ni^{2+}, Cu^{2+}, Zn^{2+}, Ag^{+}, Cd^{2+}, Hg^{2+} and Pb^{2+} in acetonitrile were performed. Figure 6–4 gathers the normalized emission

intensities at 524, 518 and 532 nm of compounds **L1**-**L3**, respectively, upon addition of the aforementioned metal ions. Compounds **L1** and **L2** showed sensitivity towards Cu^{2+} and Hg^{2+} metal ions while **L3** hasn't been found to have any meaningful variation on its emission after addition of 10 equivalents of each metal most likely due to the inherent rigidity of the system.

In face of the previous results, Figure 6–5 gathers the UV-Vis and luminescent titrations towards increasing amounts of Cu^{2+} (A, C) and Hg^{2+} (B, D) for **L1** and **L2**, respectively. Overall, the addition of both metal ions causes the continuous decrease of the absorbance maxima centered at 330 and 340 nm for **L1** and **L2**, respectively, while simultaneously a gradual formation of a band with a maximum around 300 nm is observed for both compounds, followed by the appearance of an additional band located around 370 nm in particular for **L2** when added Hg^{2+}. In terms of the emission spectra, a quenching on its intensity is observed in both cases at 524 (**L1**) and 518 nm (**L2**).

To fully characterize the sensing ability towards Cu^{2+} and Hg^{2+}, the stability constants were calculated with the aid of HypSpec software [51] alongside calculation of the detection and quantification limit parameters for both dansyl derivatives. The association constants, LOD and LOQ are included in Table 6-4.

Table 6-4 reveals that both probes assemble in mononuclear species with Cu^{2+} and Hg^{2+} with the highest constant belonging to **L2** towards Hg^{2+} with a stability constant value of $LogK_{ass.}$ = 6.38 ± 0.02. Ligand **L2** has also been found to exhibit the lowest LOD and LOQ values (4 μM and 7μM) being indicative of a higher affinity to bind with Hg^{2+} ions. These results highlight the potential usefulness of this probe in environmental remediation of Hg^{2+} ions where there is the need to monitor its presence in lower concentrations.

Regarding compound **L1**, the lower stability constants found for this compound may be due to the increased stereochemical hindrance promoted by the addition of the benzene moiety which in turn disables to some degree the accessibility for the coordination to occur.

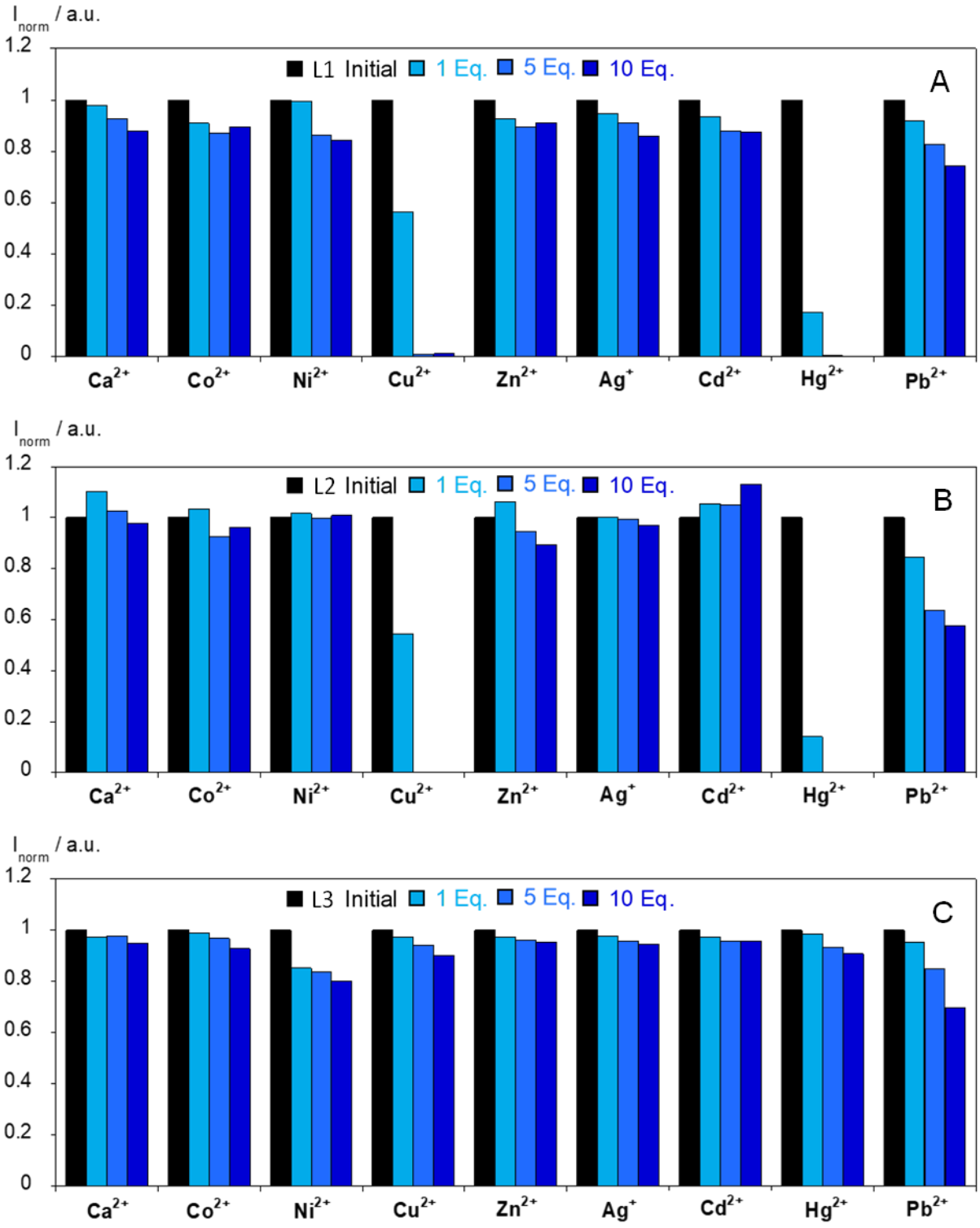


Figure 6–4. Normalized emission intensity of **L1** (A), **L2** (B) and **L3** (C) after addition of Ca^{2+}, Co^{2+}, Ni^{2+}, Cu^{2+}, Zn^{2+}, Ag^{+}, Cd^{2+}, Hg^{2+} and Pb^{2+} metal ions in successive proportions of 1, 5, and 10 equivalents in acetonitrile for **L1** and **L2** while in DMSO for **L3**. ([**L1**] = [**L2**] = [**L3**] = 20μM, $\lambda_{em\mathbf{L1}}$ = 524 nm, $\lambda_{em\mathbf{L2}}$ = 518 nm, $\lambda_{em\mathbf{L3}}$ = 532 nm, T = 298K).

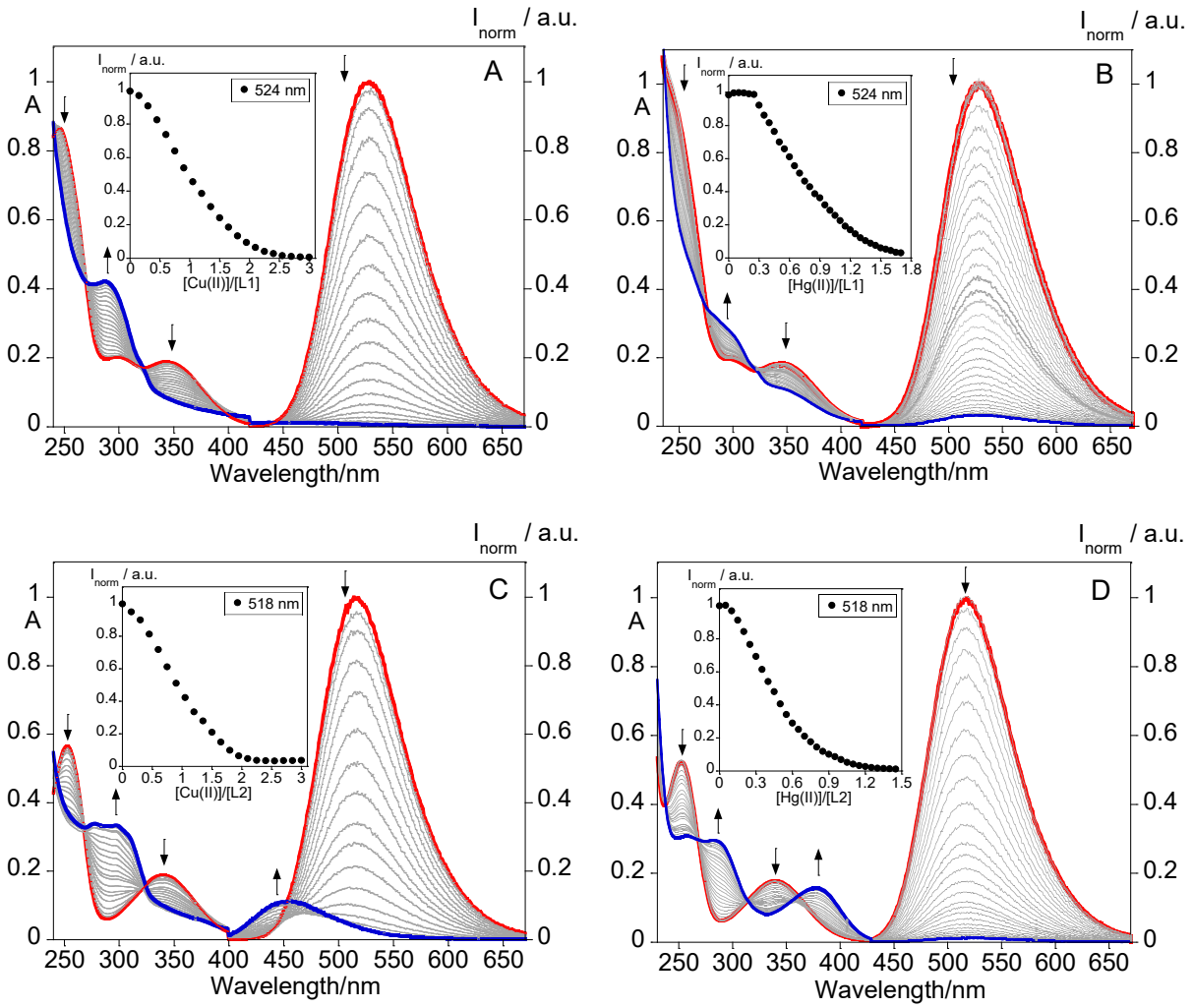


Figure 6–5. UV-Vis and luminescent titrations of compounds **L1** (A, B) and **L2** (C, D) upon continuous addition of 10 mL of Cu^{2+} (A, C; [Cu^{2+}] = 0.9 mM), and Hg^{2+} (B, D; [Hg^{2+}] = 0.3 mM) in acetonitrile. The inset represents the emission (A-D) as a function of [Cu^{2+}]/[**L1**] at 524 nm (A), of [Cu^{2+}]/[**L2**] at 518 nm (C), of [Hg^{2+}]/[**L1**] at 524 nm (B) and of [Hg^{2+}]/[**L2**] at 518 nm (D). [**L1**] = [**L2**] = 20 μM, $\lambda_{exc\mathbf{L1}}$=330 nm, $\lambda_{exc\mathbf{L2}}$=340 nm, T = 298 K).

Table 6-4. HypSpec's calculated association constants and stoichiometry for the probes **L1** and **L2** towards Cu^{2+} and Hg^{2+} ions, in CH_3CN alongside the respective values for the Minimal detectable (LOD) and quantified (LOQ) amounts (μM). LOD and LOQ were measured by the emission at 524 and 518 nm for **L1** and **L2**, respectively.

Compounds	Metal (M)	Association constants ($LogK_{ass.}$), L:M	LOD (μM)	LOQ (μM)
L1	Cu^{2+}	4.82 ± 0.03 (1:1)	6	15
	Hg^{2+}	5.29 ± 0.06 (1:1)	7	11
L2	Cu^{2+}	5.00 ± 0.04 (1:1)	6	15
	Hg^{2+}	6.38 ± 0.02 (1:1)	4	7

6.4.4 Studies using solid support compound L1

Surprisingly, the low solubility of compound **L1** in water offers an advantage when considering future practical applications. **L1** exhibits the lowest detection and quantification limit for Hg^{2+} metal ions in solution, making it suitable for supporting on low-cost, simple cellulose discs for the determination of Hg^{2+} in aqueous solutions.

Blank discs (*Liofilchem*) with a diameter of 6 mm were impregnated with a solution of **L1** ([**L1**] = 10 mM) in THF. After drying, the resulting white discs containing **L1** were briefly immersed for 5 s in water solutions with increasing concentrations of Hg^{2+} (0, 25, 50, 100, 200, 300, and 400 ppm). **Figure 6–6** illustrates the visual colour emission changes under a UV lamp. Notably, a visual detection of Hg^{2+} in water is possible from concentrations as low as 100 ppm. This method holds great potential for the development of portable and convenient in-the-field detection of Hg^{2+}.

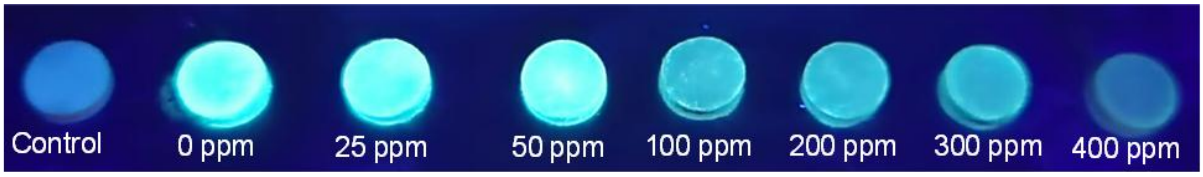


Figure 6–6. Visual changes in Blank Discs (*Liofilchem*) containing compound **L1** (10 mM) after immersion in water solutions containing increasing concentrations of Hg^{2+} metal ion (0-400 ppm).

6.4.5 Tuning the emission of dansyl derivatives towards temperature smart materials

Since **L1**-**L3** were found to exhibit emission in the solid state and manifest solvatofluorochromism due to the different properties of the solvents, the next intention is to modulate the emission of these ligands in solid supported materials to develop molecular thermometers through emission. In line with this premise, the compounds have been studied initially without the use of a solid supports. For this, emission of each probe has been recorded with the increase of temperature in the solid state. Figure 6–7 gathers the emission spectra and the plot of I_{nom} in relation to temperature for compound **L3**. The results suggest that **L3** manifests a linear relation of its emission and the increase of temperature between 30 and 129°C. The same behavior was also found during the cooling cycle. This compound was found to completely recover its emission by the end of the cooling cycle as it can be seen in Figure 6–7.

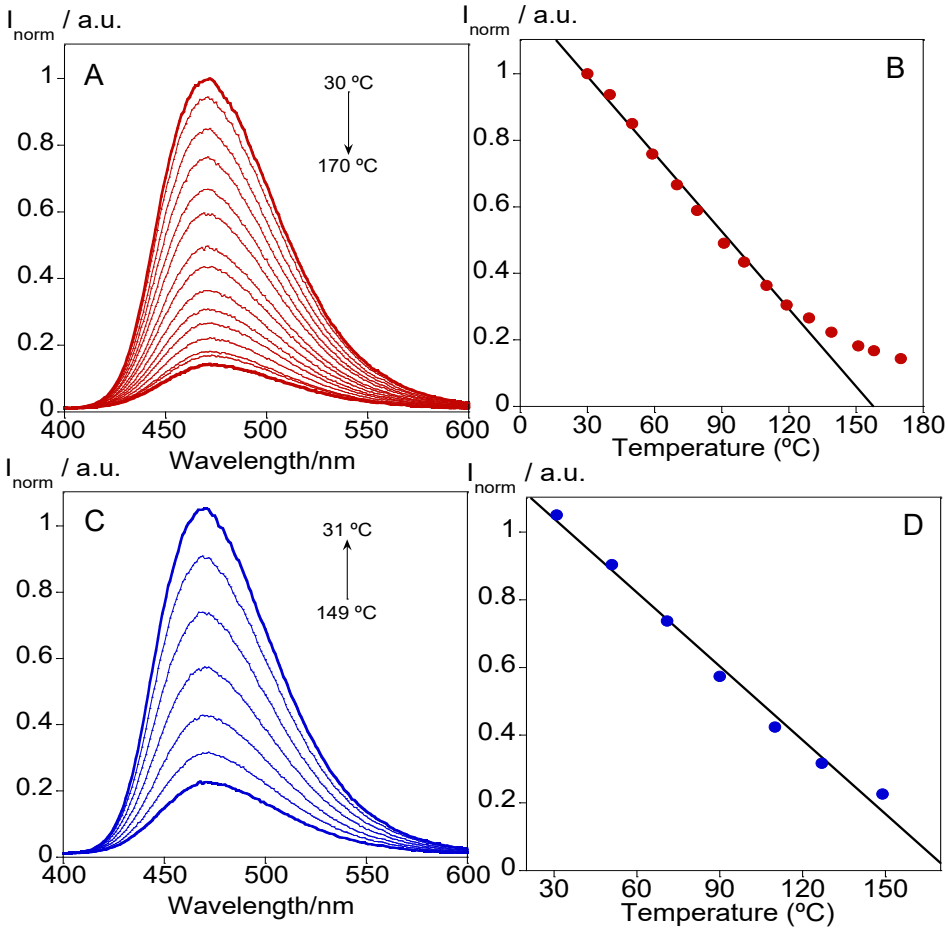


Figure 6–7. Temperature-dependent emission spectra of **L3** in the solid state (A) collected through a warming cycle between 30ºC to 170ºC. I_{norm}. vs. T plot recorded in the emission maximum at 472 nm upon heating (B) [30 to 129 ºC (Y= 1.2243 + 0.0077612x), yielding R=0.99663]. Temperature-dependent emission spectra of **L3** (C) collected through a cooling cycle between 31ºC to 149ºC. I_{norm}. vs. T plot recorded in the emission maximum at 472 nm upon cooling (D) [31 to 149 ºC (Y= 1.2571 + 0.0072628x), yielding R=0.99502].

Regarding compound **L1** and **L2**, a relation has been found between emission and temperature for **L1** between 30 and 70 ºC while no linearity was observed for **L2** as can be seen in Figure 6–15 and Figure 6–16. Also, after cooling the emission did not recover substantially, suggesting partial degradation of both compounds. This is most likely due to their low melting point around 112 and 70°C for compound **L1** and **L2**, respectively. The same was not found for compound **L3** since its melting point is 264°C. Thus, **L1** and **L3** have shown promising results allowing them to be used as temperature sensors, however applications may be hindered due to the lack of solid supports.

According with the previous findings, several polymers doped thin films have been developed as a next step to improve the sensing applications. Compound **L1** and **L2** were doped in PMMA, SBS, PVA:PVP and TPU while **L3**, due to solubility restrictions, has been doped only

in TPU. Figure 6–8 gathers the comparison between the emission spectra in the solid state and each emission of the different polymer thin films while Table 6-5 presents the corresponding emission maximum.

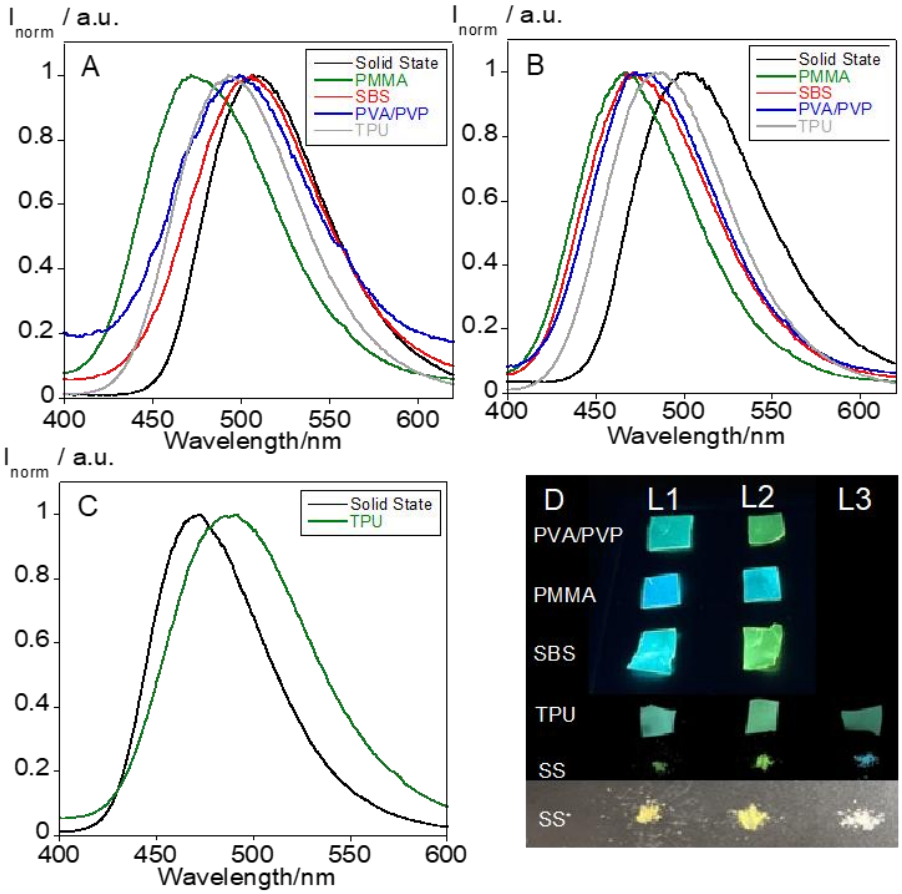


Figure 6–8. Comparison between the emission spectra of the different polymer thin films doped with (A) **L1**, (B) **L2** and (C) **L3** and the respective emission spectrum in the solid state. Images of the different polymer doped films and in the solid state under UV-light and under natural light (*) (D).

Table 6-5. Emission maximum in the solid state (λ_{em}^{Solid}), emission maximum of PMMA thin films (λ_{em}^{PMMA}), emission maximum of SBS thin films (λ_{em}^{SBS}), emission maximum of PVA/PVP thin films ($\lambda_{em}^{PVA/PVP}$), emission maximum of TPU thin films (λ_{em}^{TPU}).

Compounds	λ_{em}^{Solid} [nm]	λ_{em}^{PMMA} [nm]	λ_{em}^{SBS} [nm]	$\lambda_{em}^{PVA/PVP}$ [nm]	λ_{em}^{TPU} [nm]
L1	509	472	506	499	493
L2	499	467	471	472	487
L3	469	-	-	-	491

Overall, polymer thin films were successfully developed, and their emission properties were investigated. As it can be perceived by Figure 6–8, the molecular structure of the polymer

matrix is able to tune the final emission of the film by interacting with the probe. PMMA films display the largest blue-shift of 37 and 32 nm for **L1** and **L2**, respectively, without relevant input of the differences in molecular structure of both probes. However, for SBS and PVA/PVP more pronounced differences are observed due to the influence of the molecular structure. Compound **L1** tends to suffer less relevant blue-shifts on these polymer matrixes than **L2** most likely due to the increased compatibility that the benzene moieties provide while dispersed. Regarding TPU polymer thin films of **L1** and **L2**, blue shifts of 16 and 12 nm are observed. Nevertheless, the most interesting appears to be **L3** that when doped originates a red shift of 22 nm.

In face of the previous results, each polymer doped films were studied with variation in temperature aiming to better understand whether it is possible to humper the constrains that were found in the solid state for **L1** and **L2**. Figure 6–9 gathers the emission of the different polymer films doped with **L2**, as a representative example, alongside **L3** doped in TPU polymer film while polymer doped films of **L1** can be seen in Figure 6–17 to Figure 6–20.

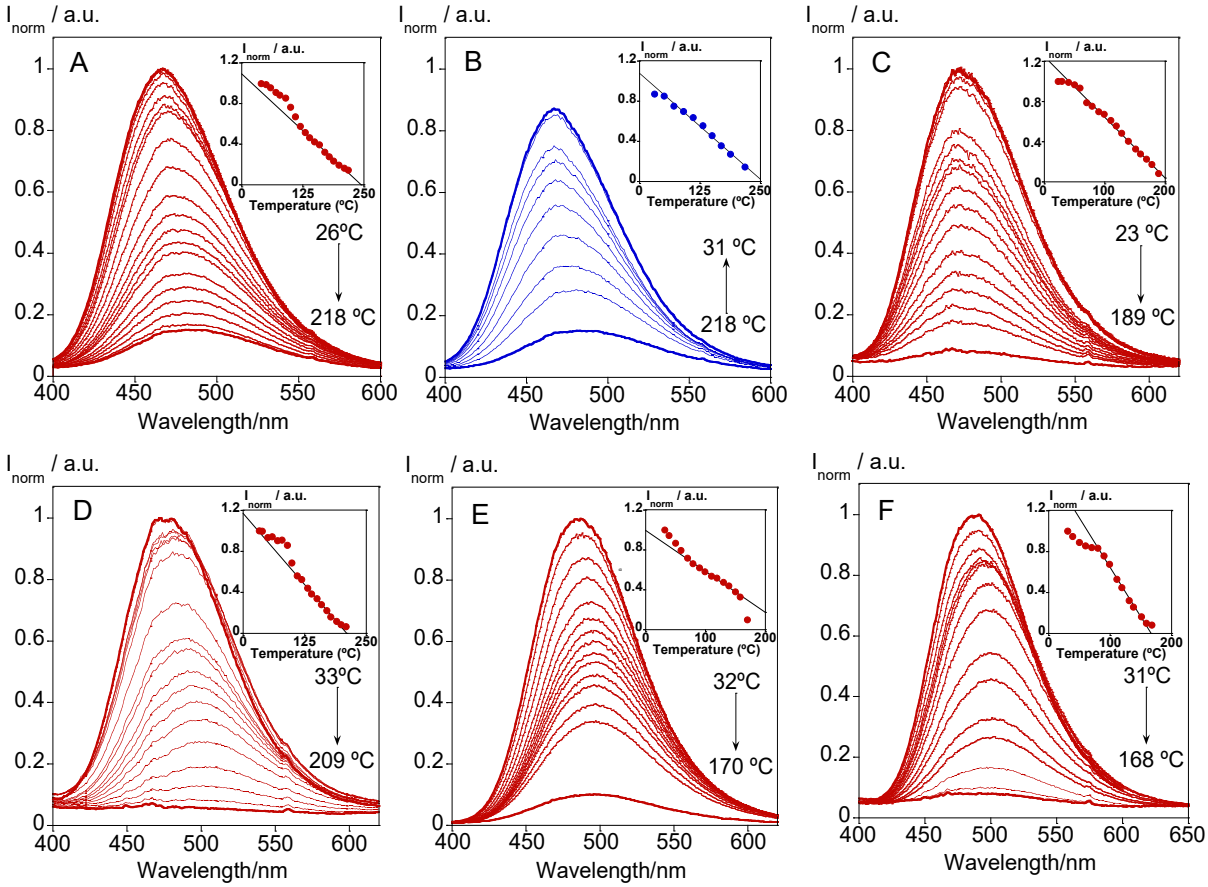


Figure 6–9. Temperature-dependent emission spectra of **L2** doped in (A) PMMA during heating cycle [Inset: I_{norm}. vs. T plot at 467 nm upon heating: 120 to 218 ºC (Y= 1.0919 - 0.004465x), yielding R=0.9948]; (B) PMMA during cooling cycle [Inset: I_{norm}. vs. T plot at 467 nm upon cooling: 51 to 218 ºC (Y= 1.0787 - 0.0042258x), yielding R=0.99644]; (C) SBS during heating cycle [Inset: I_{norm}. vs. T plot at 471 nm upon heating: 70 to 189 ºC (Y= 1.2484 -

0.0060553x), yielding R=0.99652]; (D) PVA/PVP during heating cycle [Inset: I_{norm}. vs. T plot at 472 nm upon heating: 110 to 199 ºC (Y= 1.1712 - 0.0055656x), yielding R=0.99736]; (E) TPU during heating cycle [Inset: I_{norm}. vs. T plot at 487 nm upon heating: 70 to 158 ºC (Y= 0.99593 - 0.00411x), yielding R=0.99574]. Temperature-dependent emission spectra of **L3** doped in (F) TPU during heating cycle [Inset: I_{norm}. vs. T plot at 491 nm upon heating: 80 to 159 ºC (Y= 1.611 - 0.0096602x), yielding R=0.99758].

Regarding the PMMA doped film, this material suffers its quenching with increments of temperature up to 218 ºC. Intriguingly, the behaviour observed for **L1** and **L2** in the solid state, due to their melting point, does not influence to the same extent the emission in the solid support. The polymer matrix serves as a media to maintain the emission at higher temperatures by providing sufficient conductivity which attenuates the thermal activated non-radiative processes that the compounds manifest. Likewise, as the cooling stage proceeds the emission gradually increases until it reaches room temperature and is capable of recovering 85% of the initial fluorescence. Additionally, linearity can be perceived from 120 to 218 ºC during heating and until 51ºC while cooling. It is also, interesting to note that the glass transition temperature of PMMA (T_g 105 ºC) do not seem to have any influence in the emission behaviour of the film. Remaining polymer supports were able to provide similar behaviour in relation to the emission properties with temperature. However, were not able to reach the same temperatures as PMMA and have been also found to not recover substantially their emission when cooled to room temperature (Figure 6–21) since they start to experience physical changes. On the other hand, linearity of the emission with temperature can still be perceived for SBS, PVA/PVP, and TPU between 70 to 189 ºC, 110 to 199 ºC and 70 and 158 ºC.

In the case of TPU doped with **L3**, the quenching of the emission is observed similarly as observed for the solid state, however linearity can only be seen between 80 to 159 ºC, while during cooling emission recovers 40% and shows linearity between 33 and 148 ºC (**Figure 6–22**). Nevertheless, in agreement with the other doped polymer materials studied, the incorporation of the probe onto a solid support provides the means to be applied as a molecular thermometer without restrictions imposed by their physical characteristic and, in this particular case, the polymer matrix can tune the emission wavelength to better suit the application.

6.5 Conclusions

In present work, three new bis-dansyl probes containing a sulfide bridge were synthesized and their photophysical properties were studied. Since dansyl compounds are known to exhibit solvatofluorochromism, photophysical studies were carried out in different solvents to fully evaluate the influence of each solvent's intrinsic characteristics on the probes' emission.

The equation of Kamlet-Taft was implemented to gain value insights into solute-solvent interactions, and positive solvatofluorochromism behaviour was observed for all compounds. The presence of heteroatoms also enables the study of how metal ions influence the probes' photophysical behaviour. From an environmental remediation perspective, **L1** and **L2** were found to quench their emission in the presence of Hg^{2+} and Cu^{2+} ions. Further calculations suggested that these compounds form mononuclear species with Cu^{2+} and Hg^{2+} and that **L2** has the highest association constant with Hg^{2+} ($LogK_{ass.}$ = 6.38) and an LOD and LOQ of 4 μM and 7μM, respectively. Finally, the probes were characterized in the solid state and doped in solid supports for the development of molecular thermometers PMMA, SBS, PVA/PVP, and TBU doped polymers were synthesized, and their luminescence was studied. The polymer matrix was found to modulate the emission maximum of all compounds and contribute to the emission at higher temperatures than those found in the solid state. Good linearity could also be observed at elevated temperatures, making these probes suitable candidates as temperature sensors in industrial applications.

6.6 Supplementary material

6.6.1 Supplementary figures & tables

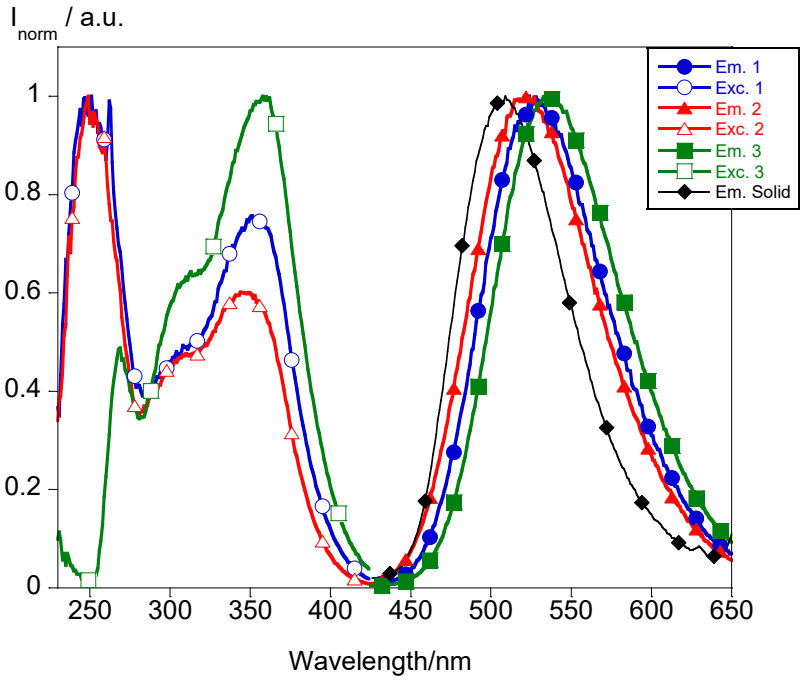


Figure 6–10. Emission, excitation and solid-state emission spectra of compound **L1** in: 1) acetonitrile, 2) ethanol and 3) DMSO ([**L**] = 6 μM).

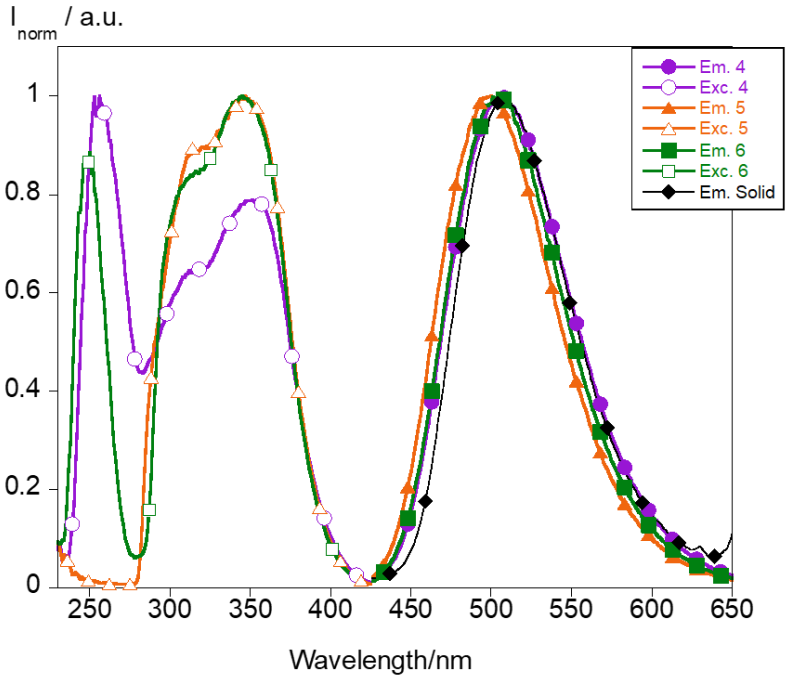


Figure 6–11. Emission, excitation, and solid-state emission spectra of compound **L1** in: 4) chloroform, 5) toluene and 6) THF ([**L**] = 6 μM).

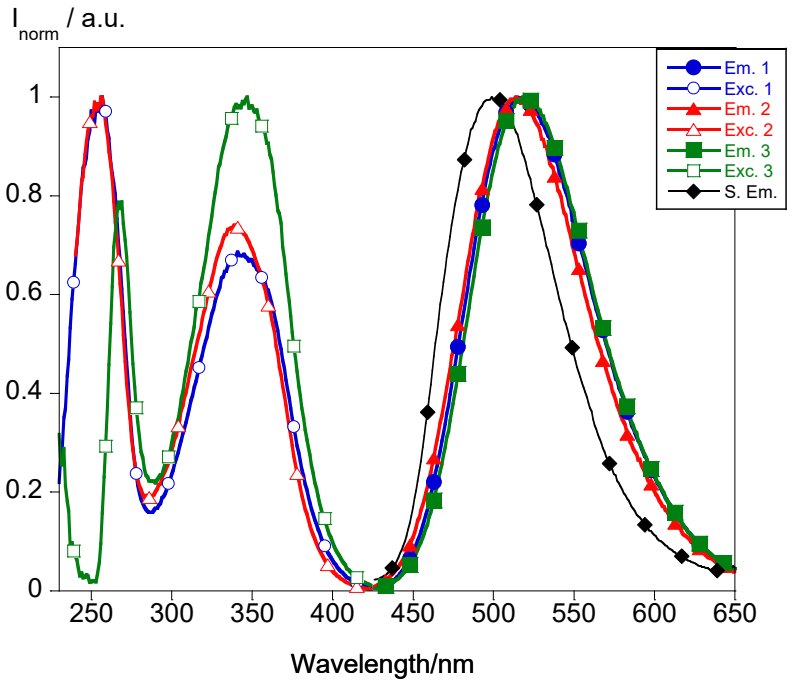


Figure 6–12. Emission, excitation and solid-state emission spectra of compound **L2** in: 1) acetonitrile, 2) ethanol and 3) DMSO ([**L**] = 10 μM).

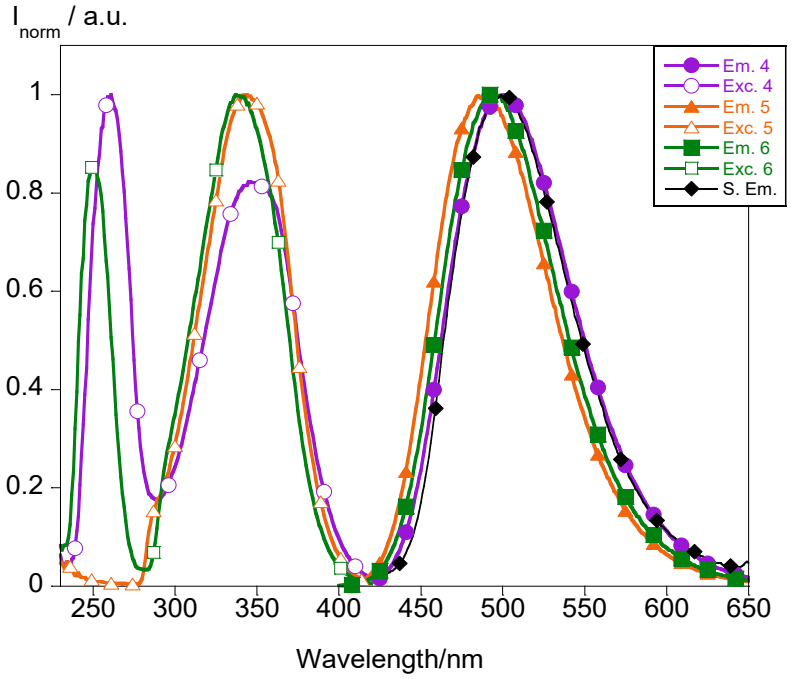


Figure 6–13. Emission, excitation, and solid-state emission of compound **L2** in: 4) chloroform, 5) toluene ([**L**] = 10 mM) and 6) THF ([**L**] = 6 mM)

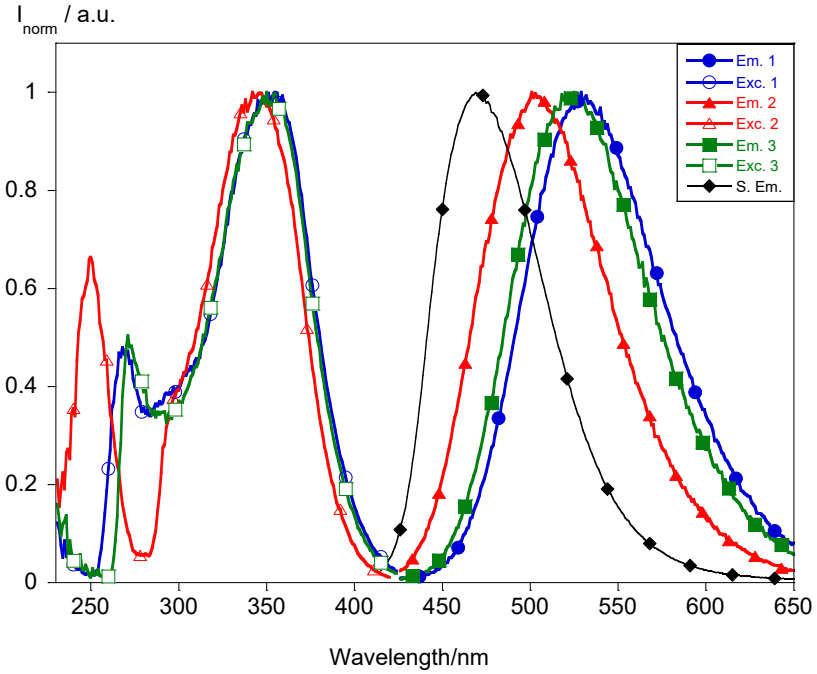


Figure 6–14. Emission, excitation, and solid-state emission of compound **L3** in: 1) DMSO, 2) THF and 3) DMF ([L] = 6 mM)

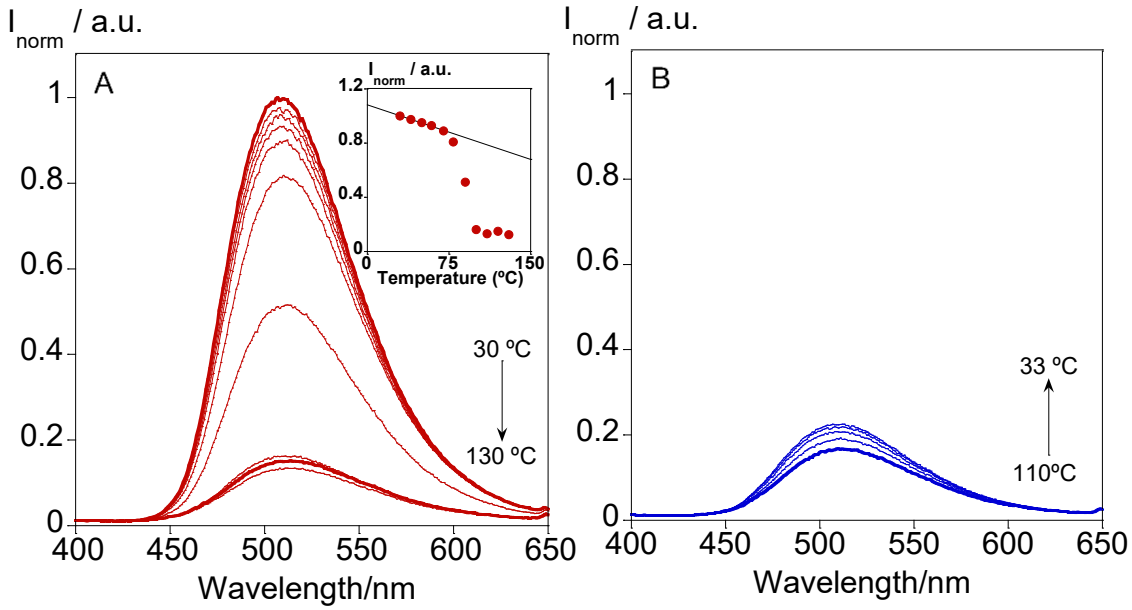


Figure 6–15. Temperature-dependent emission spectra of **L1** in the solid state (A) [Inset: I_{norm}. vs. T plot at 507 nm upon heating: 30 to 70ºC (Y=1.0825-0.0026806x), yielding R=0.9957]. Temperature-dependent emission spectra of **L1** (B) collected through a cooling cycle between 33ºC to 110ºC.

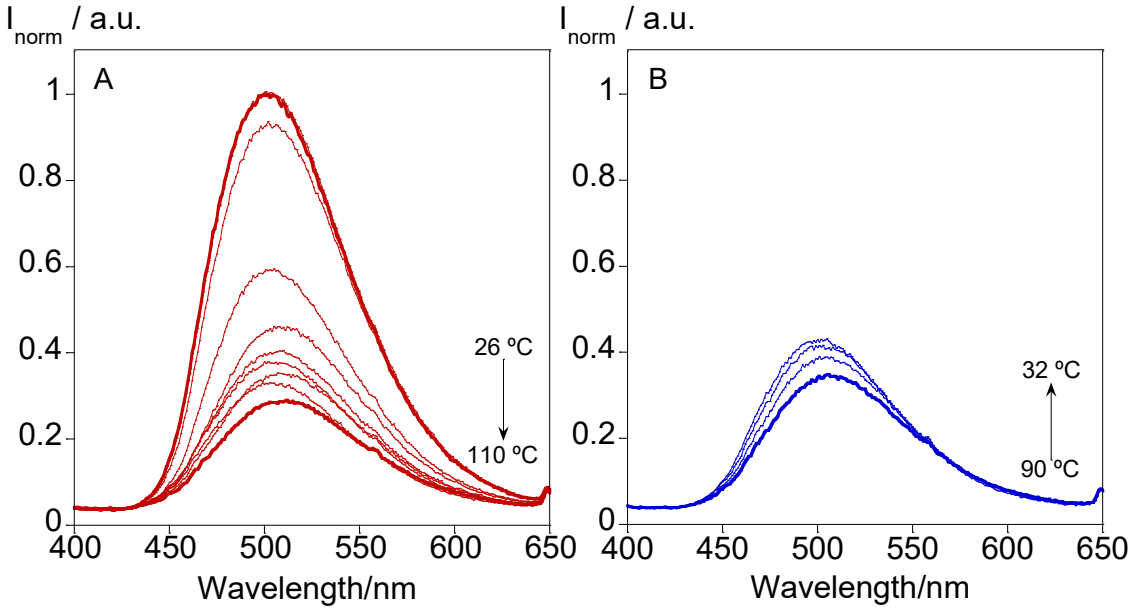


Figure 6–16. Temperature-dependent emission spectra of **L2** in the solid state (A) and (B) collected through a cooling cycle.

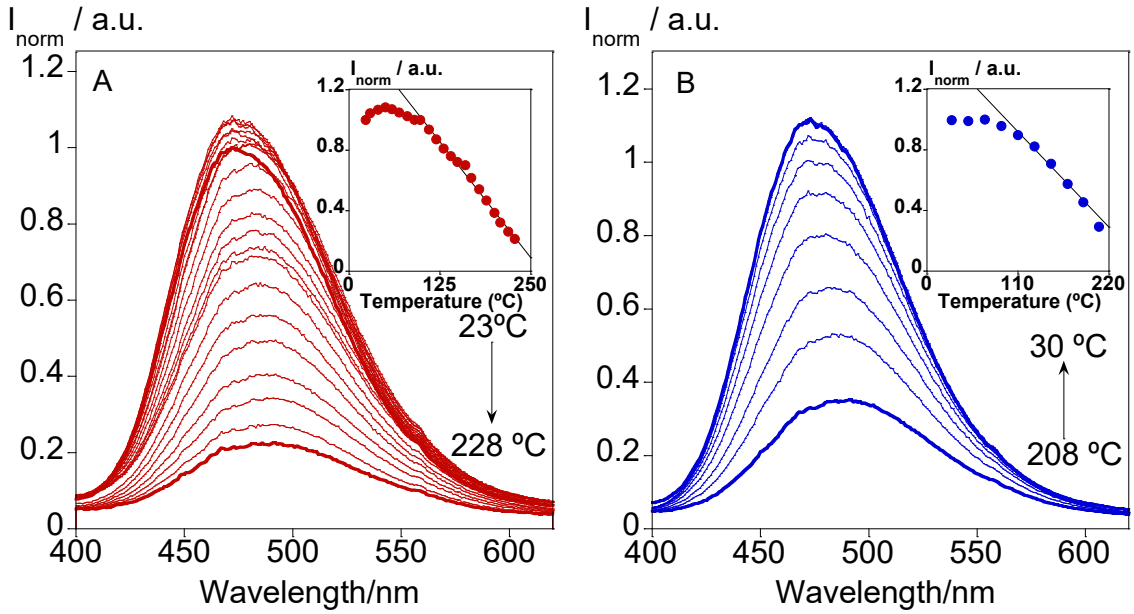


Figure 6–17. Temperature-dependent emission spectra of **L1** doped in (A) PMMA during heating cycle [Inset: I_{norm}. vs. T plot at 472 nm upon heating: 98 to 228ºC (Y=1.6211-0.0061283x), yielding R=0.9959]; (B) PMMA during cooling cycle [Inset: I_{norm}. vs. T plot at 472 nm upon cooling: 110 to 189ºC (Y= 1.5489 - 0.0057221x), yielding R=0.9949].

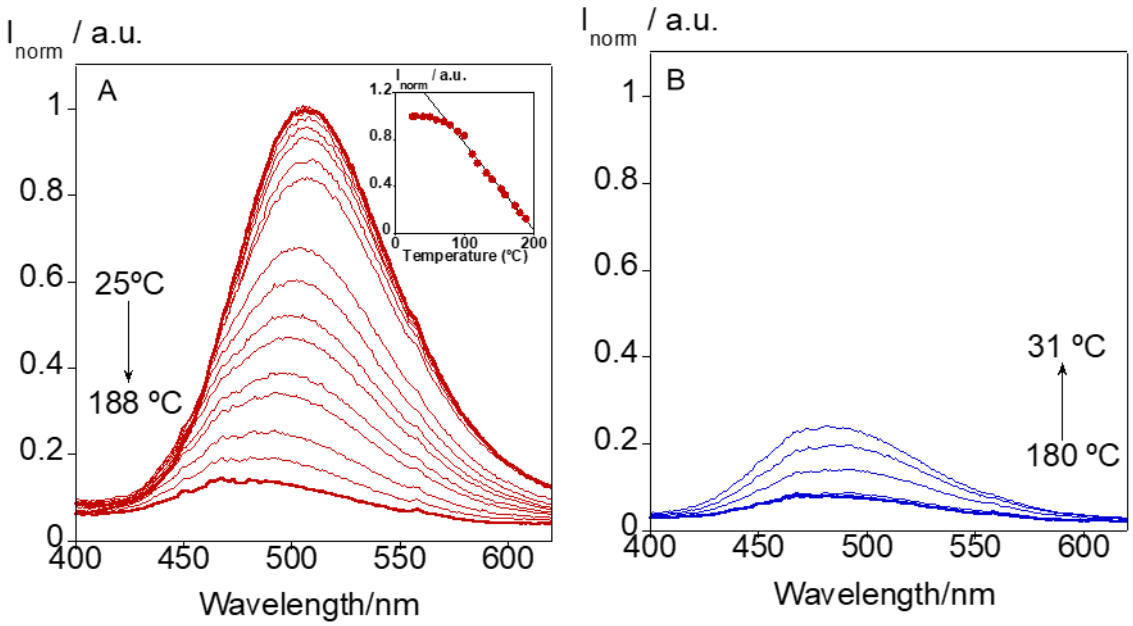


Figure 6–18. Temperature-dependent emission spectra of **L1** doped in (A) SBS during heating cycle [Inset: I_{norm}. vs. T plot at 506 nm upon heating: 70 to 188ºC (Y=1.5151-0.0074734x), yielding R=0.996]; (B) SBS during cooling cycle.

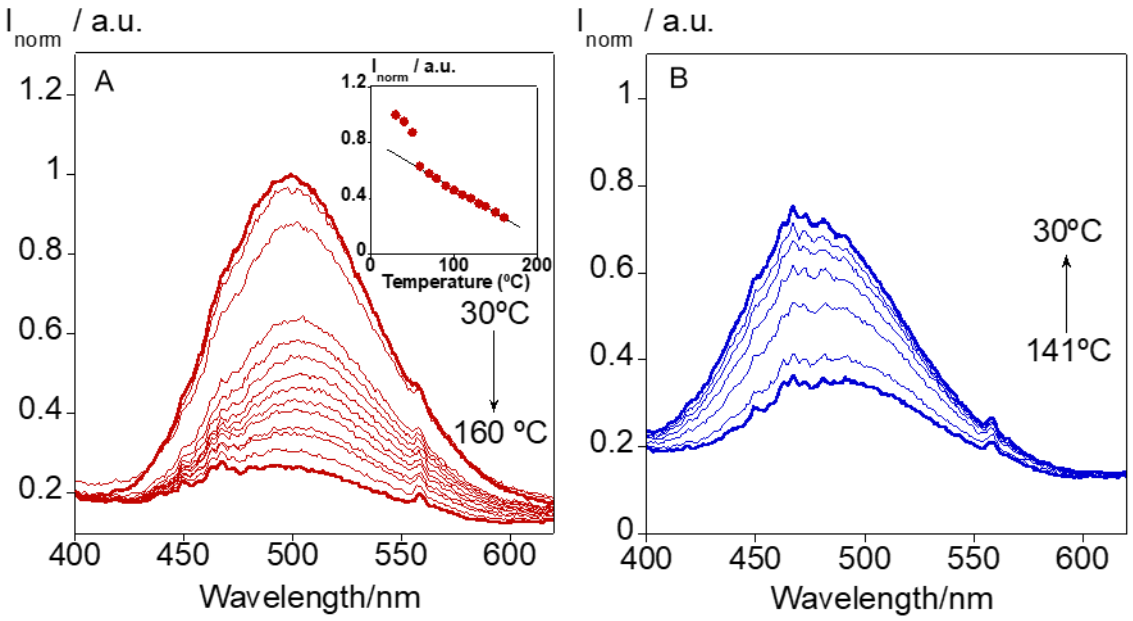


Figure 6–19. Temperature-dependent emission spectra of **L1** doped in (A) PVA/PVP during heating cycle [Inset: I_{norm}. vs. T plot at 499 nm upon heating: 70 to 160ºC (Y=0.82272-0.0035002x), yielding R=0.9971]; (B) PVA/PVP during cooling cycle.

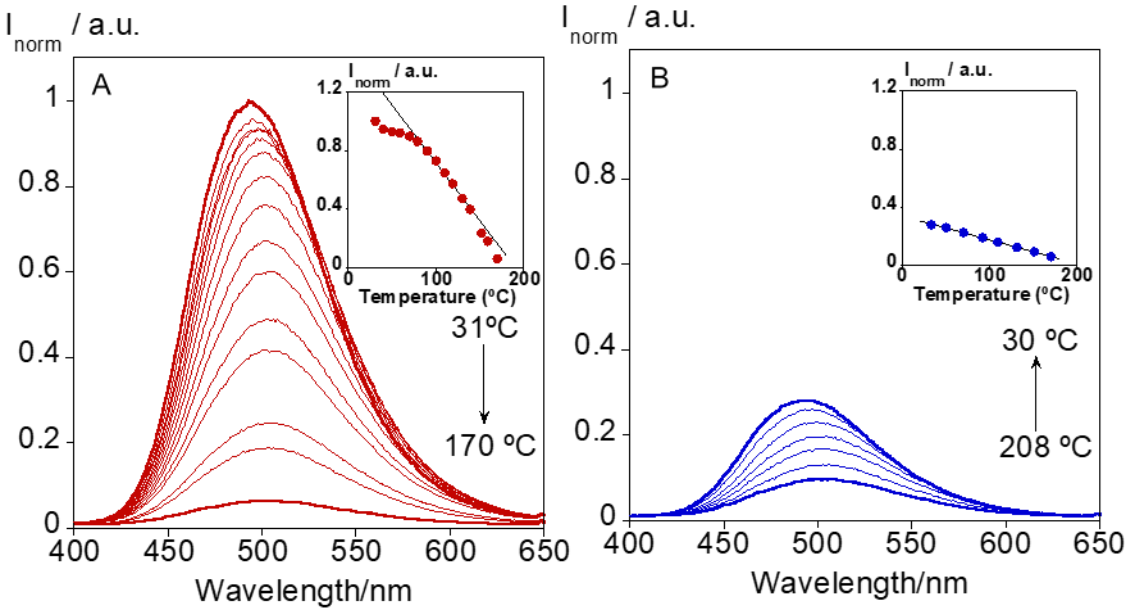


Figure 6–20. Temperature-dependent emission spectra of **L1** doped in (A) PVA/PVP during heating cycle [Inset: I_{norm}. vs. T plot at 493 nm upon heating: 79 to 139ºC (Y=1.5036-0.0078832x), yielding R=0.9972]; (B) PVA/PVP during cooling cycle [Inset: I_{norm}. vs. T plot at 493 nm upon heating: 33 to 170ºC (Y=0.33868-0.0016254x), yielding R=0.999]

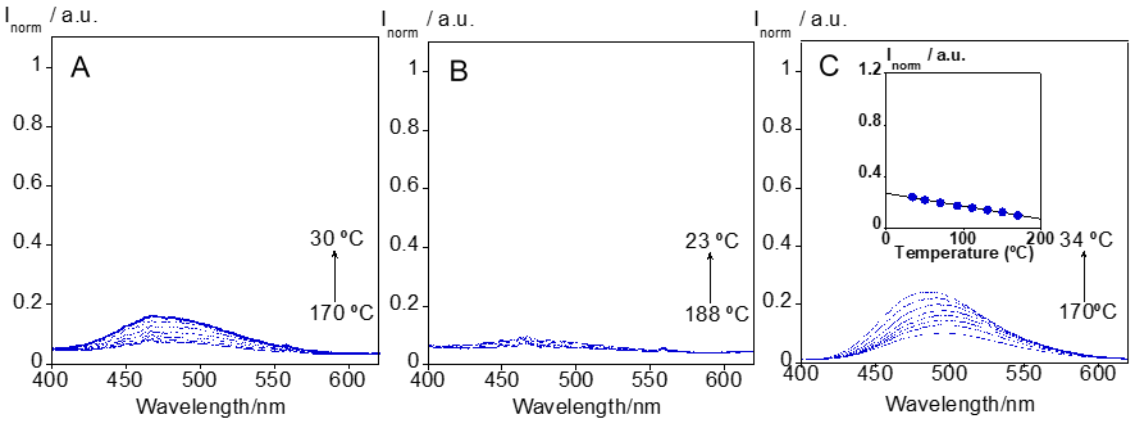


Figure 6–21. Temperature-dependent emission spectra of **L2** doped in (A) SBS (B) PVA/PVP and (C) TPU during cooling cycle [Inset: I_{norm}. vs. T plot at 487 nm upon cooling: 34 to 170ºC (Y=0.26991-0.0010004x), yielding R=0.9968].

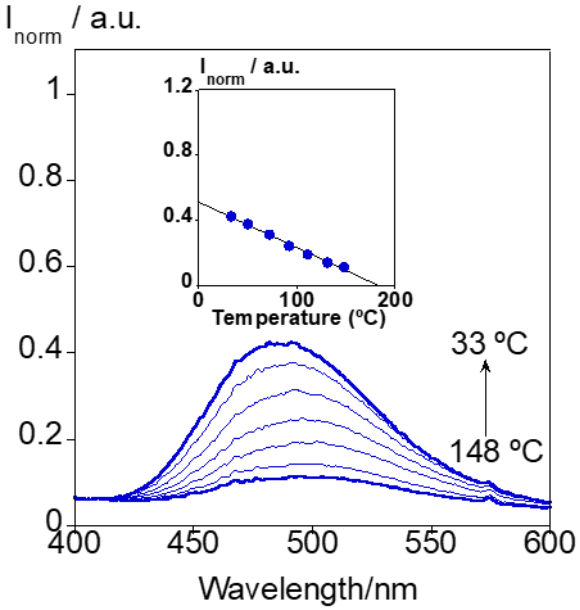


Figure 6–22. Temperature-dependent emission spectra of **L3** doped in TBU during heating cycle [Inset: I_{norm}. vs. T plot at 491 nm upon heating: 33 to 148ºC (Y=0.51427-0.0028025x), yielding R=0.9969].

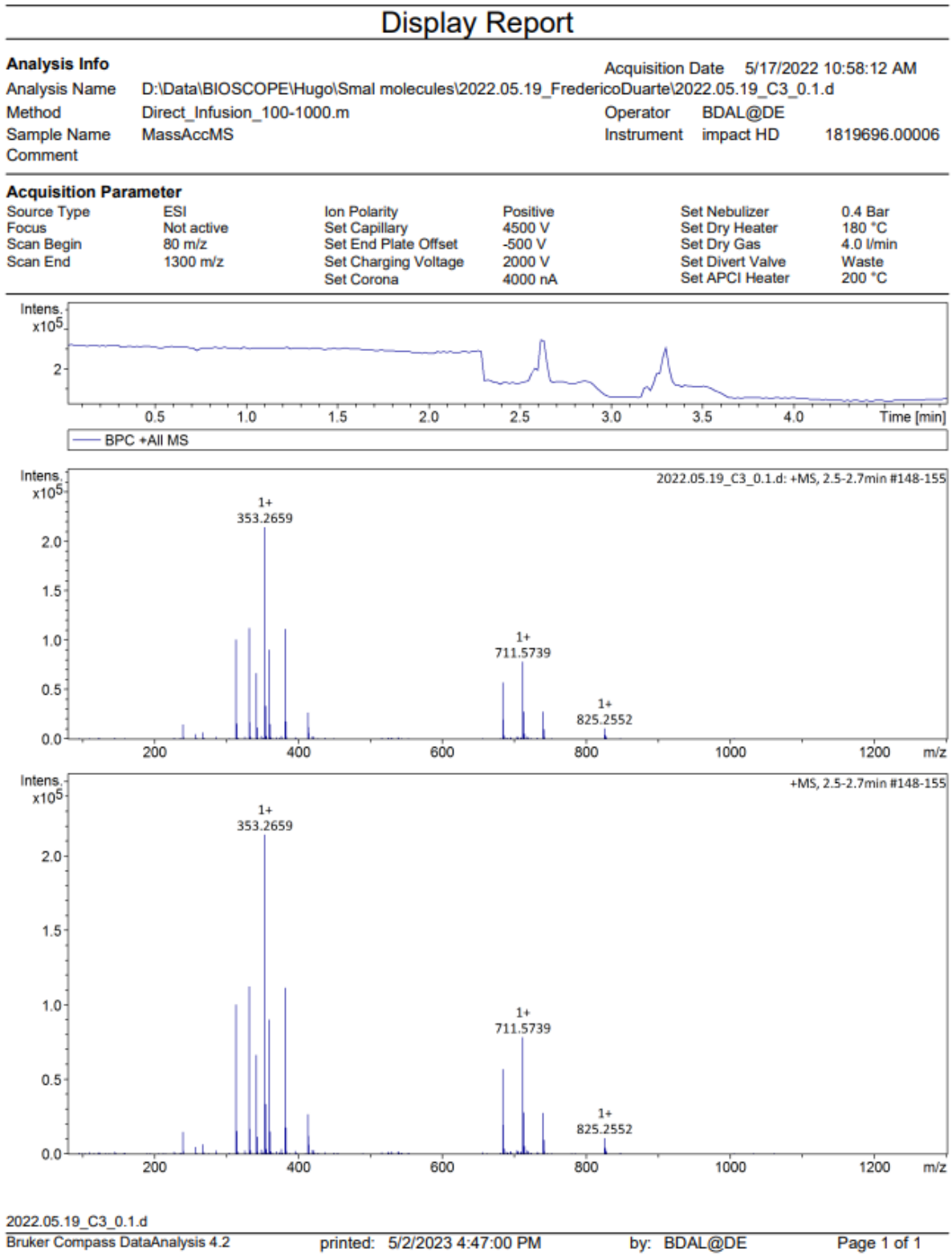


Figure 6–23. ESI-HRMS spectrum of compound **L1**.

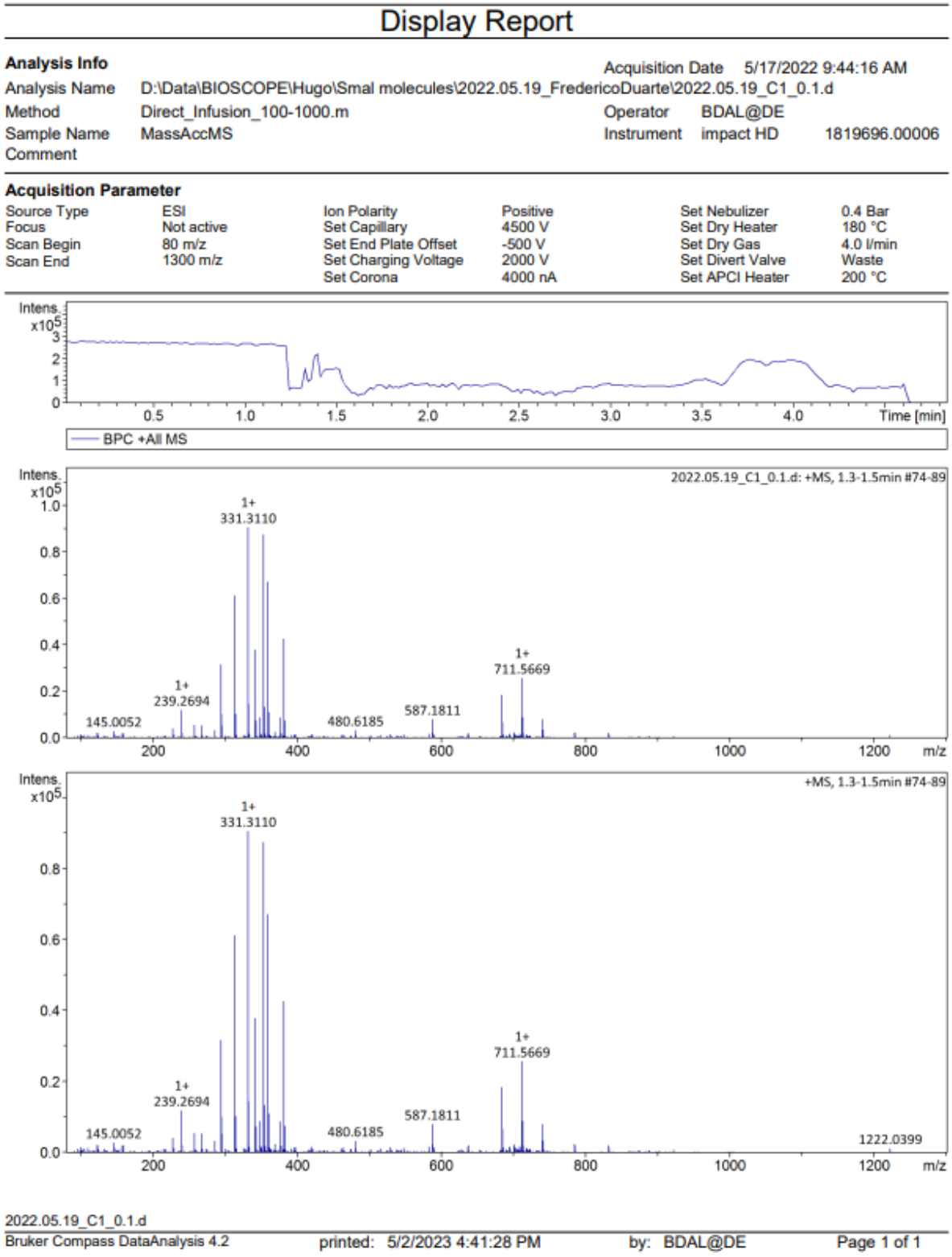


Figure 6–24. ESI-HRMS spectrum of compound **L2**.

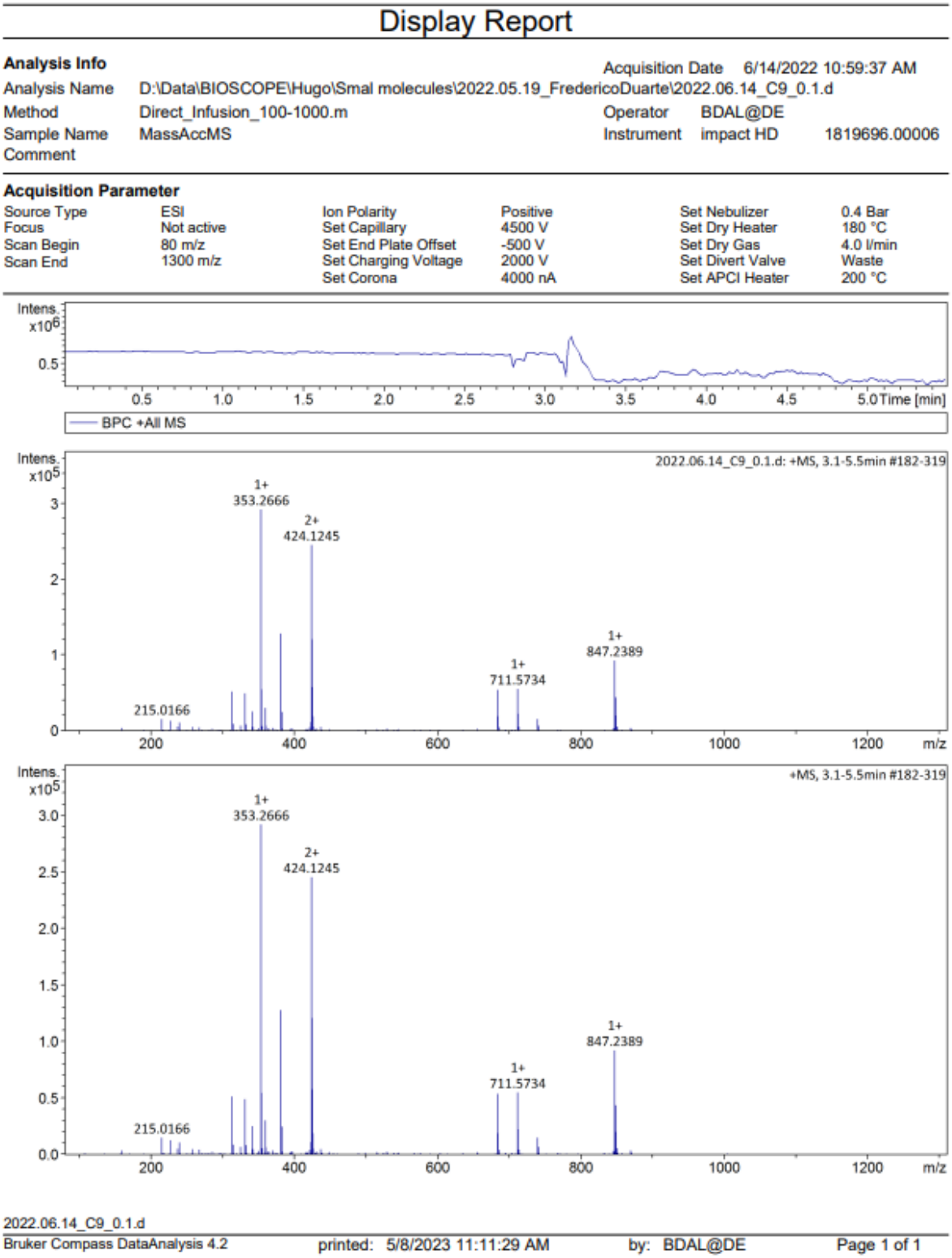


Figure 6–25. ESI-HRMS spectrum of compound **L3**.

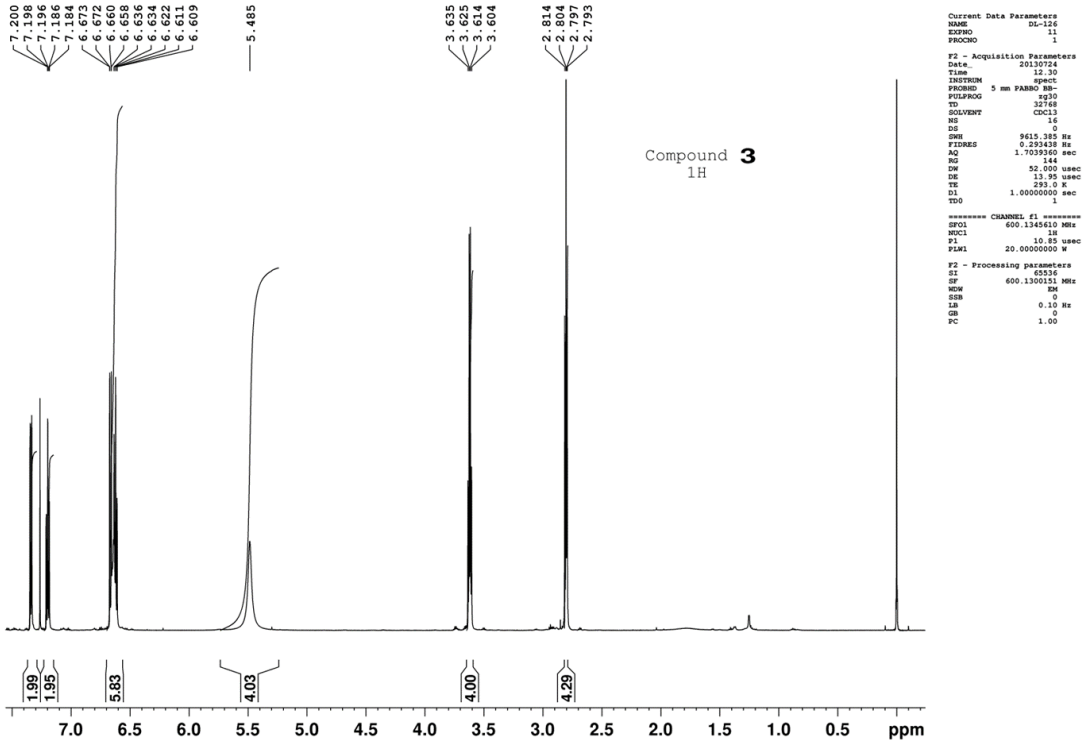


Figure 6–26. ^{1}H-NMR spectrum of compound **3**.

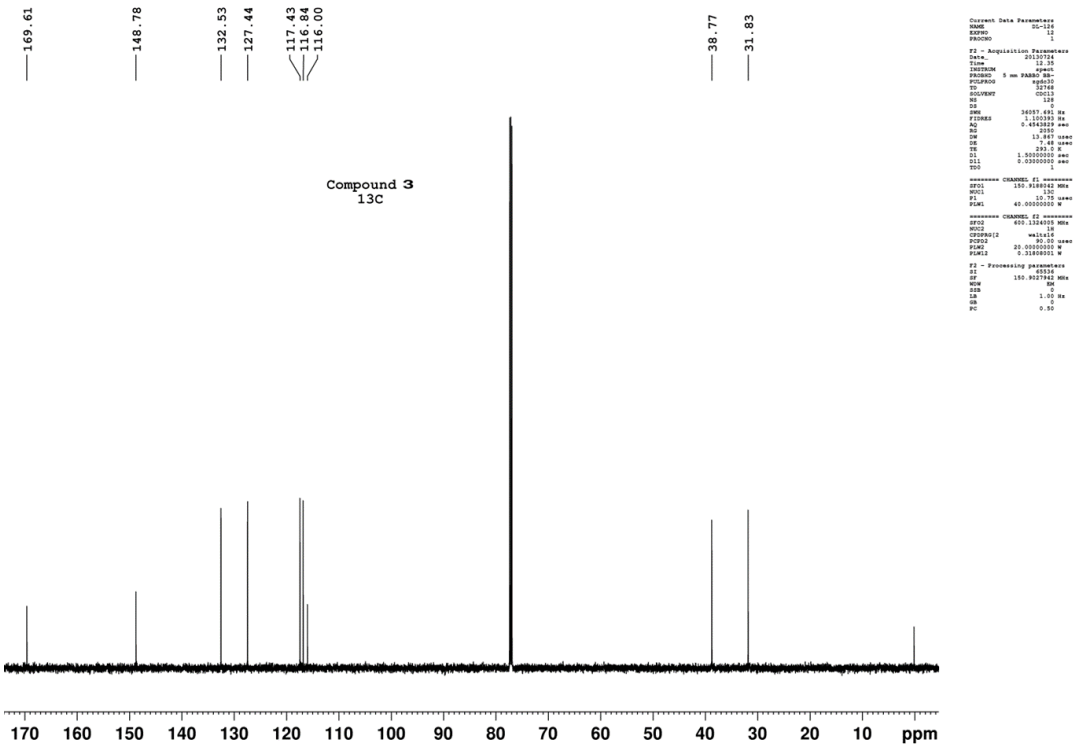


Figure 6–27. ^{13}C-NMR spectrum of compound **3**.

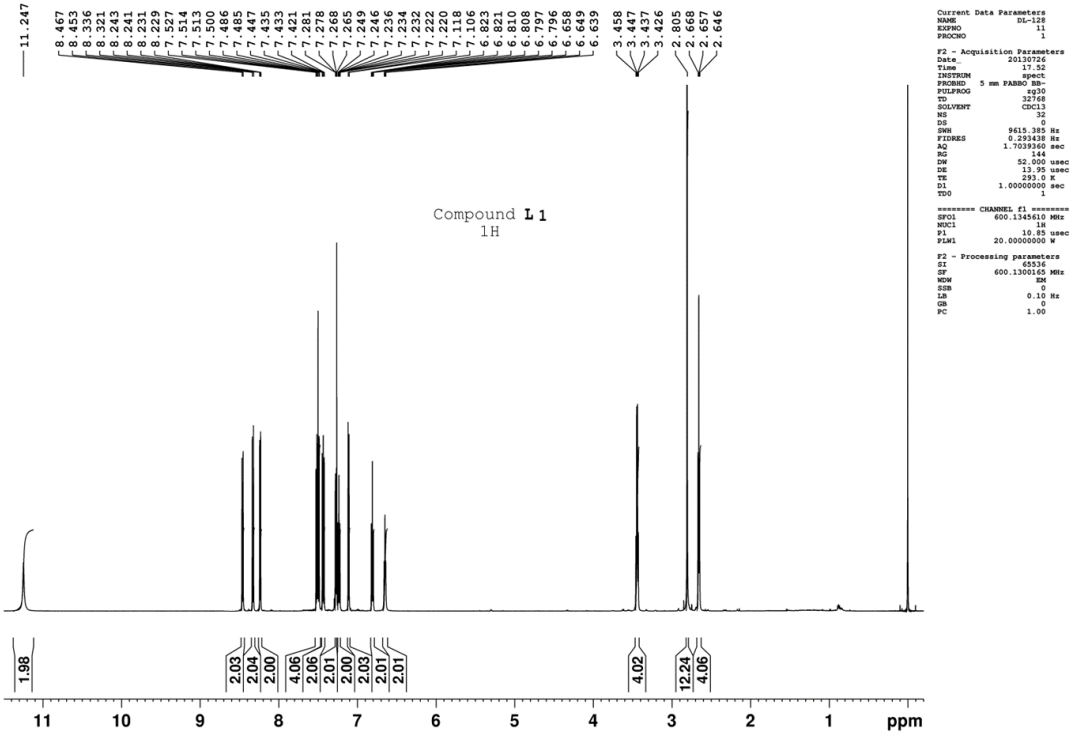


Figure 6–28. ^{1}H-NMR spectrum of compound **L1**.

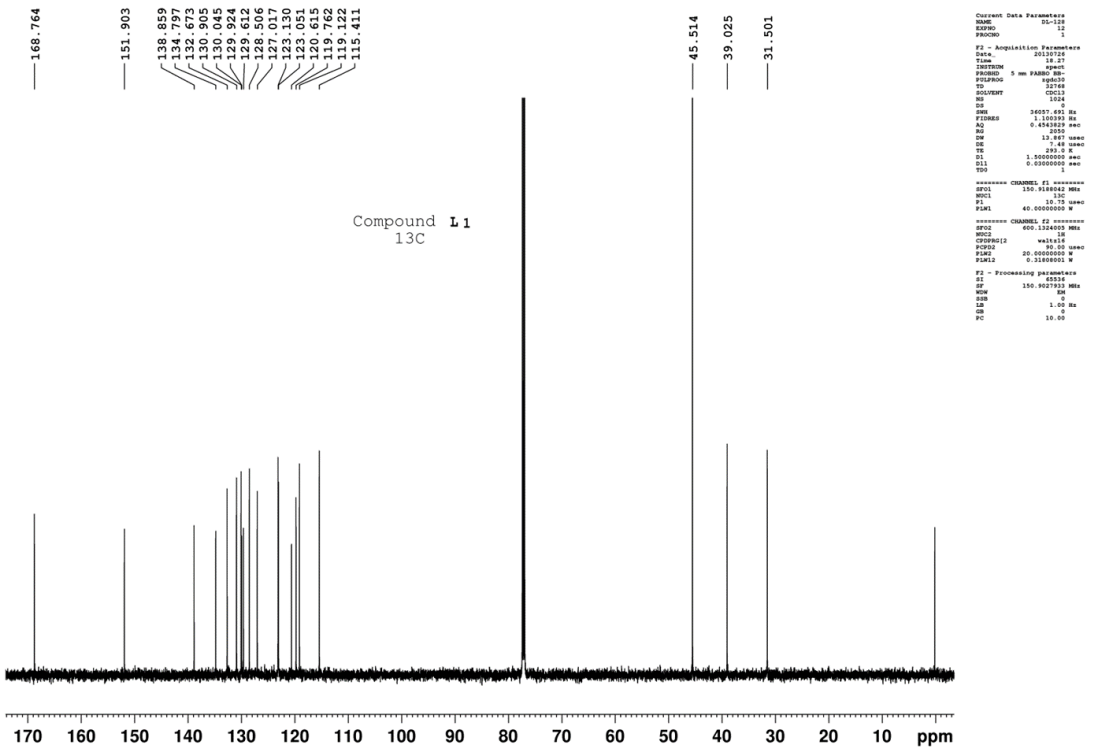


Figure 6–29. ^{13}C-NMR spectrum of compound **L1**.

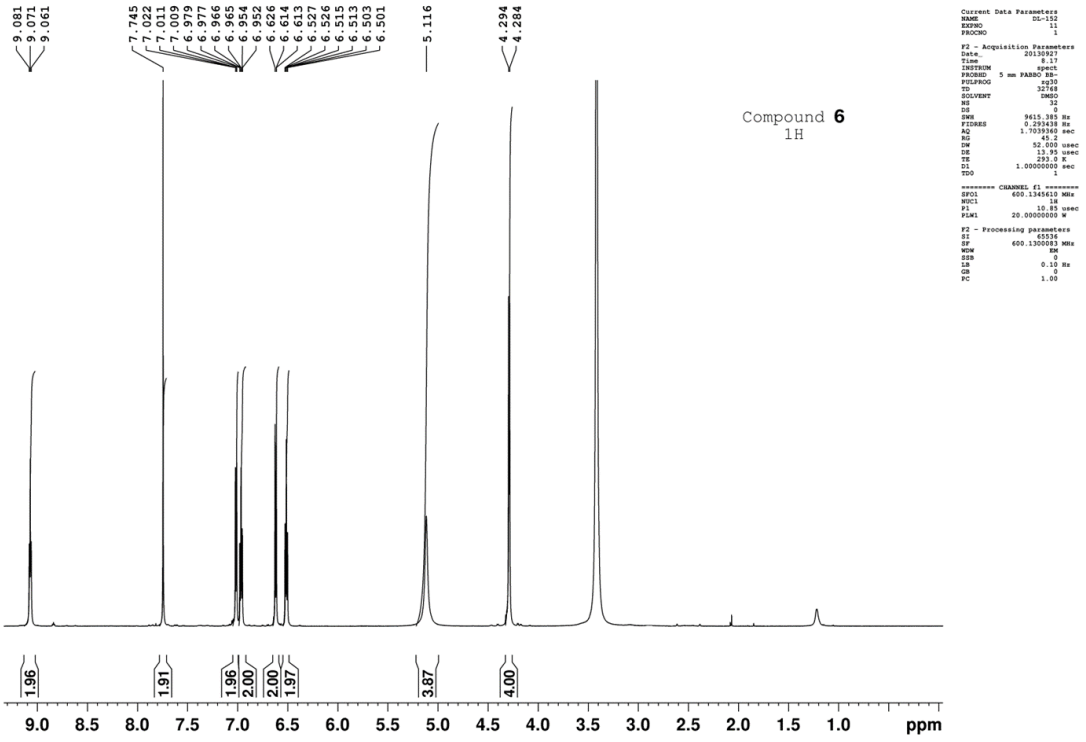


Figure 6–30. ^{1}H-NMR spectrum of compound **6**.

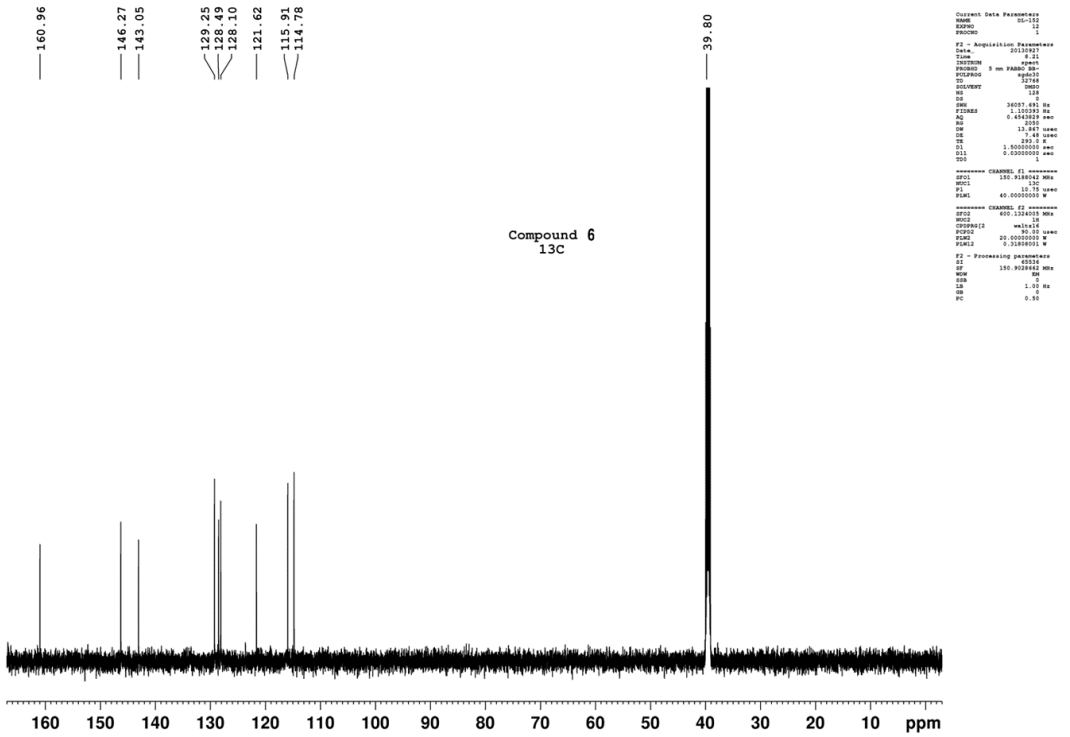


Figure 6–31. ^{13}C-NMR spectrum of compound **6**.

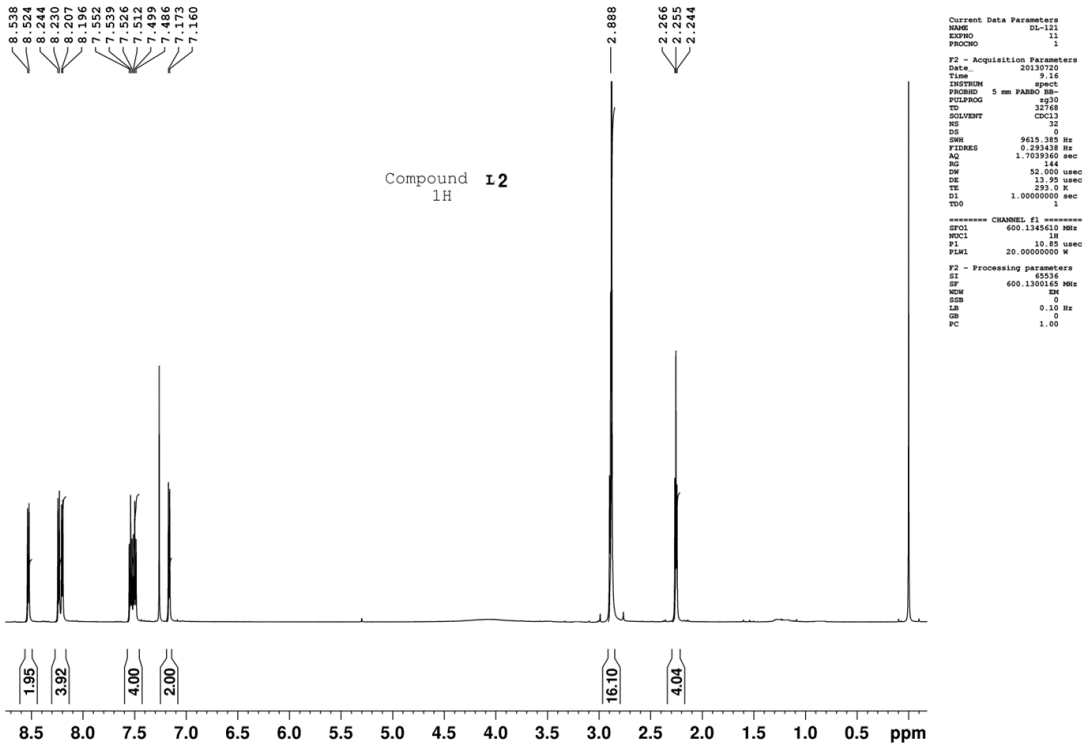


Figure 6–32. ^{1}H-NMR spectrum of compound **L2**.

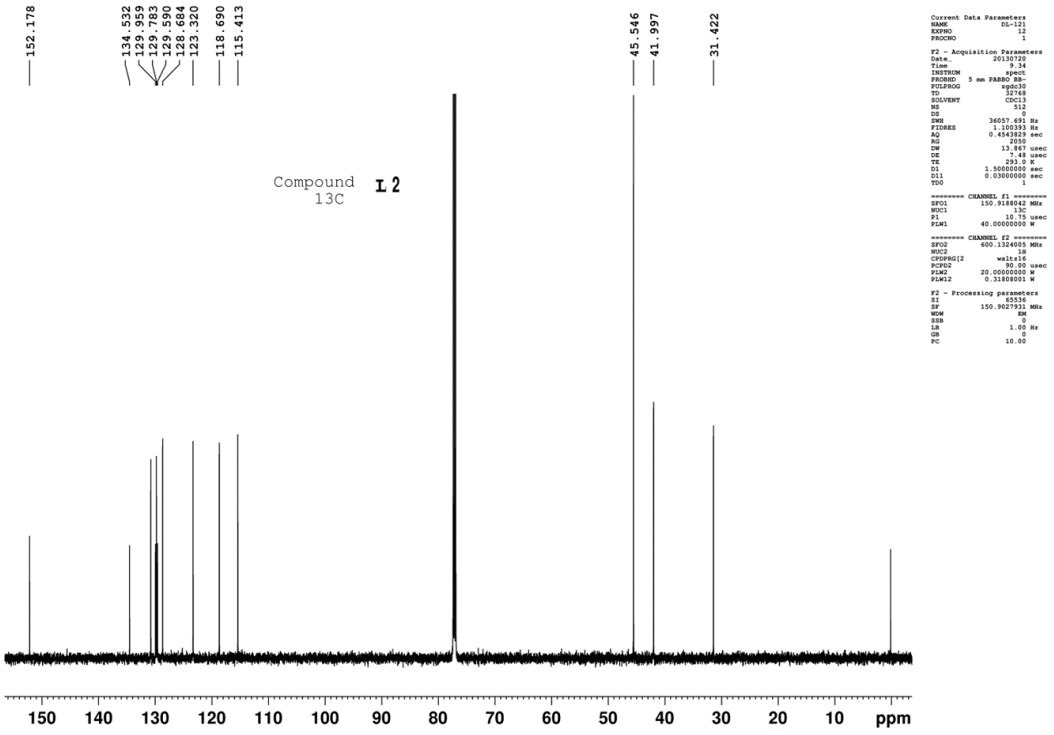


Figure 6–33. ^{13}C-NMR spectrum of compound **L2**.

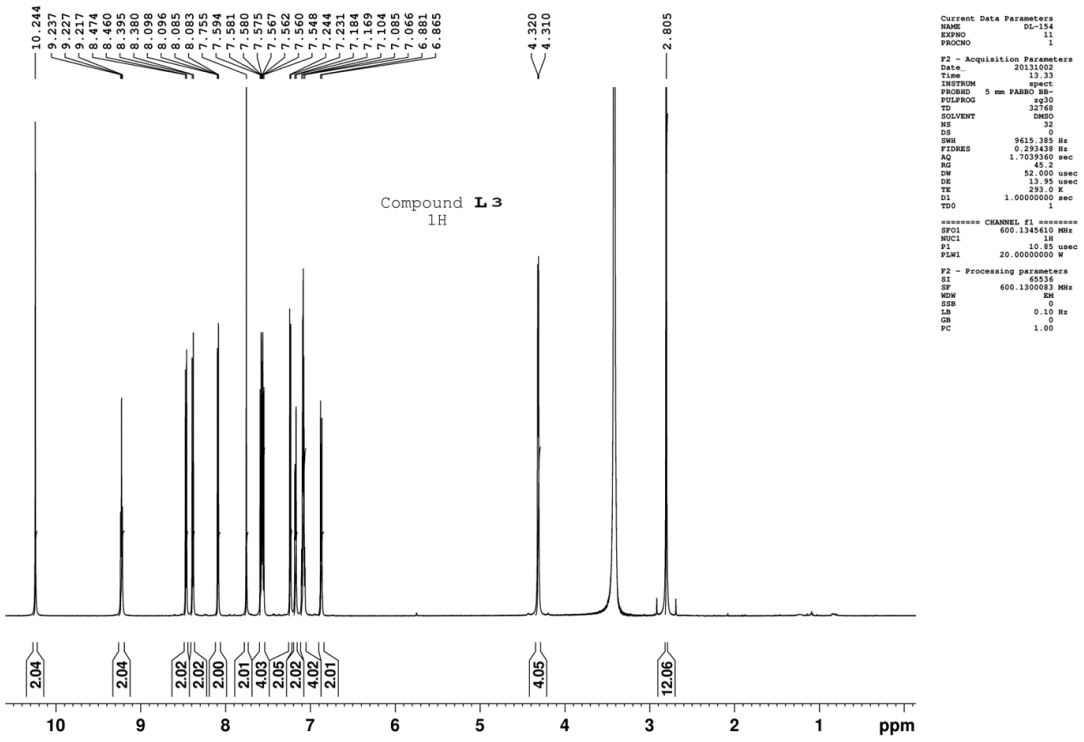


Figure 6–34. ^{1}H-NMR spectrum of compound **L3**.

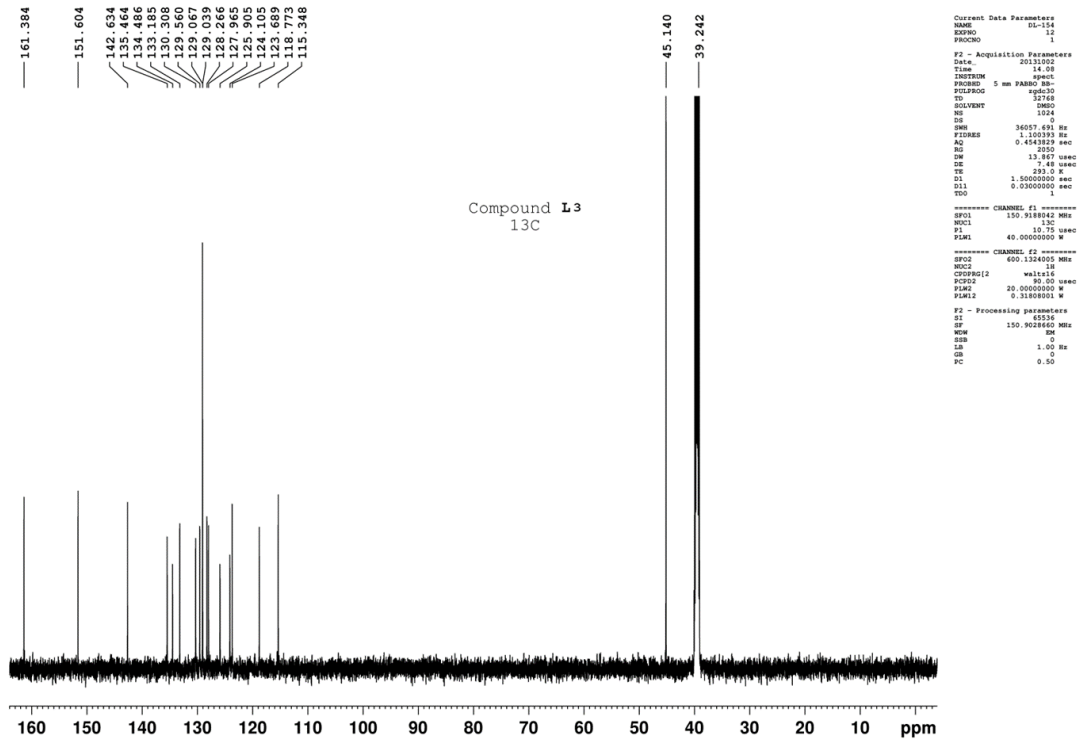


Figure 6–35. ^{13}C-NMR spectrum of compound **L3**.

6.7 Contributions & Aknowledgements

6.7.1 Author contributions

Frederico Duarte: Formal analysis, Investigation, Writing - Original Draft, Writing - Review & Editing, Visualization.

Georgi Dobrikov: Methodology, Validation, Formal Analysis, Investigation, Writing - Original Draft, Writing - Review & Editing, Resources, Visualization.

Atanas Kurutos: Methodology, Validation, Formal Analysis, Investigation, Writing - Original Draft, Writing - Review & Editing, Resources, Visualization.

Jose Luis Capelo-Martinez: Resources, Writing - Review & Editing, Funding acquisition.

Hugo M. Santos: Investigation, Resources, Validation, Writing - Review & Editing.

Elisabete Oliveira: Conceptualization, Methodology, Validation, Formal Analysis, Investigation, Resources, Writing - Original Draft, Writing - Review & Editing, Resources, Visualization, Supervision, Funding acquisition.

Carlos Lodeiro: Conceptualization, Methodology, Validation, Formal Analysis, Investigation, Resources, Writing - Review & Editing, Resources, Visualization, Supervision, Funding acquisition, Project administration

6.7.2 Acknowledgements

This work was supported by the Associate Laboratory for Green Chemistry LAQV which is financed by national funds from *Fundação para a Ciência e Tecnologia and Ministério da Ciência, Tecnologia e Ensino Superior* (FCT/MCTES) through the projects UIDB/50006/2020 and UIDP/50006/2020. PROTEOMASS Scientific Society (Portugal) is acknowledged by the funding provided through the General Funding Grant 2022-2023, and by the funding provided to the Laboratory for Biological Mass Spectrometry Isabel Moura (#PM001/2019 and #PM003/2016). F.D. thanks to FCT/MCTES (Portugal) for his doctoral grant 2021.05161.BD. E.O thanks FCT/MCTES (Portugal) for the individual contract, CEECIND/00648/2017. H. M. S. acknowledges the Associate Laboratory for Green Chemistry LAQV (LA/P/0008/2020) funded by FCT/MCTES for his research contract. The financial support by the Bulgarian National Science Fund (BNSF) under grant – "Novel styryl and polymethine fluorophores as potential theranostic agents "contract N◦ КП-06-М59/1 from 15.11.2021 is gratefully acknowledged by A.K. This work is also developed and acknowledged by A.K. as part of contract №: BG-RRP-2.004-0002-C01, Laboratory of Organic Functional Materials (Project BiOrgaMCT), Procedure BG-RRP-2.004

„Establishing of a network of research higher education institutions in Bulgaria", funded by BULGARIAN NATIONAL RECOVERY AND RESILIENCE PLAN".

G. D. thanks to the European Regional Development Fund within the Operational Programme Science and Education for Smart Growth 2014 - 2020 under the Project Center of Excellence: National center of mechatronics and clean technologies - BG05M2OP001-1.001-0008 for the financial support.

6.8 References

[1] E. O. Dare, V. Vendrell-Criado, M. C. Jiménez, R. Pérez-Ruiz and D. Díaz Díaz, Highly efficient latent fingerprint detection by eight-dansyl-functionalized octasilsesquioxane nanohybrids, *Dyes and Pigments* **184** (2021) 108841. DOI: 10.1016/j.dyepig.2020.108841.

[2] Y. Zhang, B. Lei and X. Zhang, Reversible, controllable white-light emission of dye systems by dynamic covalent furan moiety exchange, *Chem. Commun.* **58** (2022) 5261–5264. DOI: 10.1039/D2CC01309F.

[3] Y. Zhang, B. Lei and X. Zhang, Intramolecular energy transfer dyes as temperature- and polarity-sensitive fluorescence probes, *Dyes and Pigments* **205** (2022) 110492. DOI: 10.1016/j.dyepig.2022.110492.

[4] D. Yang, X. T. Wu, X. J. Cao and B. X. Zhao, A reversible ratiometric fluorescence probe for fast detection of trace water in different organic solvents, *Dyes and Pigments* **170** (2019) 107558. DOI: 10.1016/j.dyepig.2019.107558.

[5] Y. Cui, F. Li and X. Zhang, Controlling fluorescence resonance energy transfer of donor–acceptor dyes by Diels–Alder dynamic covalent bonds, *Chem. Commun.* **57** (2021) 3275–3278. DOI: 10.1039/D1CC00165E.

[6] A. F. Sierra, D. Hernández-Alonso, M. A. Romero, J. A. González-Delgado, U. Pischel and P. Ballester, Optical Supramolecular Sensing of Creatinine, *J. Am. Chem. Soc.* **142** (2020) 4276–4284. DOI: 10.1021/jacs.9b12071.

[7] W. M. Pazin, A. K. A. Almeida, V. Manzoni, J. M. M. Dias, A. C. F. De Abreu, M. Navarro, A. S. Ito, A. S. Ribeiro and I. N. De Oliveira, Thermal and solvatochromic effects on the emission properties of a thienyl-based dansyl derivative, *RSC Adv.* **10** (2020) 28484–28491. DOI: 10.1039/D0RA05949H.

[8] N. Li, W. Qin, Y. Chen, K. Liu, S. Wang and F. Kong, Construction of a robust polarity sensitive platform and its application for tracking of lipid droplets decrease under oxidative stress in live cells, *Sens. Actuators B Chem.* **346** (2021) 130491. DOI: 10.1016/j.snb.2021.130491.

[9] Y. Pan, C. Zhang, S. H. Liu, Y. Tan and J. Yin, Fluorescent switch based on dithienylethene with dansulfonamide in multimedium, *Dyes and Pigments* **181** (2020) 108546. DOI: 10.1016/j.dyepig.2020.108546.

[10] H. J. Lee, M. J. Cho and S. K. Chang, Ratiometric Signaling of Hypochlorite by the Oxidative Cleavage of Sulfonhydrazide-Based Rhodamine−Dansyl Dyad, *Inorg. Chem.* **54** (2015) 8644–8649. DOI: 10.1021/acs.inorgchem.5b01284.

[11] W. L. Wu, H. L. Ma, M. F. Huang, J. Y. Miao and B. X. Zhao, Mitochondria-targeted ratiometric fluorescent probe based on FRET for bisulfite, *Sens. Actuators B Chem.* **241** (2017) 239–244. DOI: 10.1016/j.snb.2016.10.028.

[12] H. Jiang, Z. Li, Y. Kang, L. Ding, S. Qiao, S. Jia, W. Luo and W. Liu, A two-photon fluorescent probe for Cu^{2+} based on dansyl moiety and its application in bioimaging, *Sens. Actuators B Chem.* **242** (2017) 112–117. DOI: 10.1016/j.snb.2016.11.033.

[13] B. Uttam, S. Polepalli, S. Sinha, A. Majumder and C. P. Rao, Selective Sensing and Removal of Mercury Ions by Encapsulating Dansyl Appended Calix[4]Conjugate in a Zeolitic Imidazolate Framework as an Organic−Inorganic Hybrid Nanomaterial, *ACS Appl. Nano Mater.* **5** (2022) 11371–11380. DOI: 10.1021/acsanm.2c02459.

[14] G. Donadio, R. Di Martino, R. Oliva, L. Petraccone, P. Del Vecchio, B. Di Luccia, E. Ricca, R. Isticato, A. Di Donato and E. Notomista, A new peptide-based fluorescent probe selective for zinc (II) and copper (II), *J. Mater. Chem. B* **4** (2016) 6979–6988. DOI: 10.1039/C6TB00671J.

[15] P. Wang, J. Wu, P. Su, C. Xu, Y. Ge, D. Liu, W. Liu and Y. Tang, Fluorescence "on-off-on" peptide-based chemosensor for selective detection of Cu^{2+} and S^{2-} and its application in living cells bioimaging, *Dalt. Trans.* **45** (2016) 16246–16254. DOI: 10.1039/C6DT03330J

[16] A. Aliberti, P. Vaiano, A. Caporale, M. Consales, M. Ruvo and A. Cusano, Fluorescent chemosensors for Hg^{2+} detection in aqueous environment, *Sens. Actuators B Chem.* **247** (2017) 727–735. DOI: 10.1016/j.snb.2017.03.026.

[17] X. Pang, J. Dong, L. Gao, L. Wang, S. Yu, J. Kong and L. Li, Dansyl-peptide dual-functional fluorescent chemosensor for Hg^{2+} and biothiols, *Dyes and Pigments* **173** (2020) 107888. DOI: 10.1016/j.dyepig.2019.107888.

[18] Y. Wang, J. Zhou, L. Zhao and B. Xu, A dual-responsive and highly sensitive fluorescent probe for Cu^{2+} and pH based on a dansyl derivative, *Dyes and Pigments* **180** (2020) 108513. DOI: 10.1016/j.dyepig.2020.108513.

[19] L. J. Ma, J. Liu, L. Deng, M. Zhao, Z. Deng, X. Li, J. Tang and L. Yang, Selective and sensitive fluorescence-shift probes based on two dansyl groups for mercury(II) ion detection *Photochem. Photobiol. Sci.* **13** (2014) 1521–1528. DOI: 10.1039/C4PP00094C.

[20] Y. B. Barot, V. Anand and R. Mishra, Di-Triphenylamine-based AIE active Schiff base for highly sensitive and selective fluorescence sensing of Cu^{2+} and Fe^{3+}, *J. Photochem. Photobiol. A Chem.* **426** (2022) 113785. DOI: 10.1016/j.jphotochem.2022.113785.

[21] J. Galhano, G. A. Marcelo, A. Kurutos, E. Bértolo, J. L. Capelo-Martinez, C. Lodeiro and E. Oliveira, Development of low-cost colourimetric and pH sensors based on PMMA@Cyanine polymers, *Dyes and Pigments* **200** (2022) 110154. DOI: 1016/j.dyepig.2022.110154.

[22] C. Lodeiro, J. L. Capelo, J. C. Mejuto, E. Oliveira, H. M. Santos, B. Pedras and C. Nuñez, Light and colour as analytical detection tools: A journey into the periodic table using polyamines to bio-inspired systems as chemosensors, *Chem. Soc. Rev.* **39** (2010) 2948–2976. DOI: 10.1039/B819787N.

[23] G. A. Marcelo, S. M. G. Pires, M. A. F. Faustino, M. M. Q. Simões, M. G. P. M. S. Neves, H. M. Santos, J. L. Capelo, J. P. Mota, C. Lodeiro and E. Oliveira, New dual colorimetric/fluorimetric probes for Hg^{2+} detection & extraction based on mesoporous SBA-16 nanoparticles containing porphyrin or rhodamine chromophores, *Dyes and Pigments* **161** (2019) 427–437 DOI: 10.1016/j.dyepig.2018.09.068.

[24] E. Oliveira, E. Bértolo, C. Núñez, V. Pilla, H. M. Santos, J. Fernández-Lodeiro, A. Fernández-Lodeiro, J. Djafari, J. L. Capelo and C. Lodeiro, Green and Red Fluorescent Dyes for Translational Applications in Imaging and Sensing Analytes: A Dual-Color Flag, *ChemistryOpen* **7** (2018) 9–52. DOI: 10.1002/open.201700135.

[25] R. Nagarajan, H. I. Ryoo, B. D. Vanjare, N. Gyu Choi and K. Hwan Lee, Novel phenylalanine derivative-based turn-off fluorescent chemosensor for selective Cu^{2+} detection in physiological pH, *J. Photochem. Photobiol. A Chem.* **418** (2021) 113435. DOI: 10.1016/j.jphotochem.2021.113435.

[26] T. N. Moshkina, E. V. Nosova, A. E. Kopotilova, M. I. Savchuk, I. L. Nikonov, D. S. Kopchuk, P. A. Slepukhin, G. A. Kim, G. N. Lipunova and V. N. Charushin, Synthesis and photophysical properties of pyridyl- and quinolinyl-substituted 4-(4-aminophenyl)quinazolines, *J. Photochem. Photobiol. A Chem.* **429** (2022) 113917. DOI: 10.1016/j.jphotochem.2022.113917.

[27] S. B. Yadav, S. Kothavale and N. Sekar, Triphenylamine and N-phenyl carbazole-based coumarin derivatives: Synthesis, solvatochromism, acidochromism, linear and nonlinear optical properties, *J. Photochem. Photobiol. A Chem.* **382** (2019) 111937. DOI: 10.1016/j.jphotochem.2019.111937.

[28] H. Sharma, R. Kakkar, S. Bishnoi and M. D. Milton, Synthesis of acceptor-donor-acceptor based phenothiazine-5-oxide aldehydes displaying large Stokes shift- "on-off-on"

acidofluorochromic switch and molecular logic gate operation, *J. Photochem. Photobiol. A Chem.* **430** (2022) 113944. DOI: 10.1016/j.jphotochem.2022.113944.

[29] S. Mocanu, G. Ionita and I. Matei, Solvatochromic characteristics of dansyl molecular probes bearing alkyl diamine chains, *Spectrochim. Acta - Part A Mol. Biomol. Spectrosc.* **237** (2020) 118413. DOI: 10.1016/j.saa.2020.118413.

[30] K. Li, J. Wang, Y. Li, Y. Si, J. He, X. Meng, H. Hou and B. Z. Tang, Combining two different strategies to overcome the aggregation caused quenching effect in the design of ratiometric fluorescence chemodosimeters for pH sensing, *Sens. Actuators B Chem.* **274** (2018) 654–661. DOI: 10.1016/j.snb.2018.07.109.

[31] S. Areti, S. Bandaru, D. S. Yarramala and C. P. Rao, Optimizing the Electron-Withdrawing Character on Benzenesulfonyl Moiety Attached to a Glyco-Conjugate to Impart Sensitive and Selective Sensing of Cyanide in HEPES Buffer and on Cellulose Paper and Silica Gel Strips, *Anal. Chem.* **87** (2015) 12396–12403. DOI: 10.1021/acs.analchem.5b04085.

[32] A. Pucci, Mechanochromic Fluorescent Polymers with Aggregation-Induced Emission Features, *Sensors* **19** (2019) 4969. DOI: 10.3390/s19224969.

[33] B. González-Tobío, F. Duarte, A. Arribas-Delgado, C. Fernández-Lodeiro, J. Fernández-Lodeiro, M. Cano, C. Lodeiro and C. Cuerva, Tuning and reviving the luminescence of a new class of pyridyl β-diketonate Eu(III) metallomesogens: From molecules to entrapment in polymer particles, *Dyes and Pigments* 204 (2022) 110440. DOI: 10.1016/j.dyepig.2022.110440.

[34] R. Jiménez, F. Duarte, S. Nuti, J. A. Campo, C. Lodeiro, M. Cano and C. Cuerva, Thermochromic and acidochromic properties of polymer films doped with pyridyl-β-diketonate boron(III) complexes, *Dyes and Pigments* **177** (2020) 108272. DOI: 10.1016/j.dyepig.2020.108272.

[35] S. Gupta and M. D. Milton, Novel Y-shaped AIEE-TICT active π-extended quinoxalines-based donor–acceptor molecules displaying acidofluorochromism and temperature dependent emission, *J. Photochem. Photobiol. A Chem.* **424** (2022) 113630. DOI: 10.1016/j.jphotochem.2021.113630.

[36] N. M. M. Moura, S. Valentini, V. Cheptene, A. Pucci, M. G. P. M. S. Neves, J. L. Capelo, C. Lodeiro and E. Oliveira, Multifunctional Porphyrin-based dyes for cations detection in solution and thermoresponsive low-cost materials, *Dyes and Pigments* **185** (2021) 108897. DOI: 10.1016/j.dyepig.2020.108897.

[37] C. Papucci, A. Dessì, C. Coppola, A. Sinicropi, G. Santi, M. Di Donato, M. Taddei, P. Foggi, L. Zani, G. Reginato, A. Pucci, M. Calamante and A. Mordini, Benzo[1,2-d:4,5-d′]bisthiazole fluorophores for luminescent solar concentrators: synthesis, optical properties and effect of the

polymer matrix on the device performances, *Dyes and Pigments* **188** (2021) 109207. DOI: 10.1016/j.dyepig.2021.109207.

[38] C. Micheletti, V. A. Dini, M. Carlotti, F. Fuso, D. Genovese, N. Zaccheroni, C. Gualandi and A. Pucci, Blending or Bonding? Mechanochromism of an Aggregachromic Mechanophore in a Thermoplastic Elastomer, *ACS Appl. Polym. Mater.* **5** (2023) 1545–1555. DOI: 10.1021/acsapm.2c02037.

[39] G. A. Marcelo, J. Galhano, M. P. Duarte, A. Kurutos, J. L. Capelo-Martínez, C. Lodeiro and E. Oliveira, Functional Cyanine-Based PVA:PVP Polymers as Antimicrobial Tools toward Food and Health-Care Bacterial Infections, *Macromol. Biosci.* **22** (2022) 1–12. DOI: 10.1002/mabi.202200244.

[40] L. M. Porosa, K. B. Mistry, A. Mocella, H. Deng, S. Hamzehi, A. Caschera, A. J. Lough, G. Wolfaardt and D. A. Foucher, Synthesis, structures and properties of self-assembling quaternary ammonium dansyl fluorescent tags for porous and non-porous surfaces, *J. Mater. Chem. B* **2** (2014) 1509–1520. DOI: 10.1039/C3TB21633K.

[41] Y. Y. Xiao, X. L. Gong, Y. Kang, Z. C. Jiang, S. Zhang and B. J. Li, Light-, pH- and thermal-responsive hydrogel with triple-shape memory effect, *Chem. Commun.* **52** (2016) 10609–10612. DOI: 10.1039/C6CC03587F.

[42] H. Yu, B. Zhao, J. Guo, K. Pan and J. Deng, Stimuli-responsive circularly polarized luminescent films with tunable emission, *J. Mater. Chem. C* **8** (2020) 1459–1465. DOI: 10.1039/C9TC06105C.

[43] F. Duarte, G. Dobrikov, A. Kurutos, H. M. Santos, J. Fernández-Lodeiro, J. L. Capelo-Martinez, E. Oliveira and C. Lodeiro, Enhancing water sensing via aggregation-induced emission (AIE) and solvatofluorochromic studies using two new dansyl derivatives containing a disulfide bound: Pollutant metal ions detection and preparation of water-soluble fluorescent polymeric particles, *Dyes and Pigments* **218** (2023) 111428. DOI: 10.1016/j.dyepig.2023.111428

[44] M. Carcelli, D. Rogolino, A. Bacchi, G. Rispoli, E. Fisicaro, C. Compari, M. Sechi, A. Stevaert and L. Naesens, Metal-Chelating 2-Hydroxyphenyl Amide Pharmacophore for Inhibition of Influenza Virus Endonuclease, *Mol. Pharm.* **11** (2014) 304–316. DOI: 10.1021/mp400482a.

[45] H. L. Yu, W. Y. Wang, B. Hong, Y. Zong, Y. L. Si and Z. Q. Hu, Variational first hyperpolarizabilities of 2,3-naphtho-15-crown-5 ether derivatives with cation-complexing: a potential and selective cation detector, *Phys. Chem. Chem. Phys.* **18** (2016) 26487–26494. DOI: 10.1039/C6CP04577D.

[46] A. Nion, P. Jiang, A. Popoff and D. Fichou, Rectangular Nanostructuring of Au(III) Surfaces by Self-Assembly of Size-Selected Thiacrown Ether Macrocycles, *J. Am. Chem. Soc.* **129** (2007) 2450–2451. DOI: 10.1021/ja068709e.

[47] M. Montalti, A. Credi, L. Prodi and M. T. Gandolfi, Handbook of Photochemistry, 3rd ed. BOCA: Taylor & Francis, Boca Raton; 2006.

[48] D. Macdougall and W. B. Crummett, Guidelines for data acquisition and data quality evaluation in environmental chemistry, Anal*. Chem.*, **52** (1980) 2242–2249. DOI: 10.1021/ac50064a004.

[49] G. L. Long and J. D. Winefordner, Limit of Detection A Closer Look at the IUPAC Definition, *Anal. Chem.* **55** (1983) 713A-724A. DOI: 10.1021/ac00258a724

[50] E. Oliveira, R. M. F. Baptista, S. P. G. Costa, M. M. M. Raposo and C. Lodeiro, Solvatochromic Effects of bis(indolyl)thienylaril derivatives as new Colored Materials, *Photochem. Photobiol. Sci.* **13** (2014) 492–498. DOI: 10.1039/C3PP50352F.

[51] P. Gans, A. Sabatini and A. Vacca, Investigation of equilibria in solution. Determination of equilibrium constants with the HYPERQUAD suite of programs, *Talanta* **43** (1996) 1739–1753. DOI: 10.1016/0039-9140(96)01958-3.

7

Design and Evaluation of Dansyl-Derived Chemosensors for Disulfide-Cleavage-Triggered Detection: Photophysical, Metal Sensing, and Thermometric Applications

Igor Lourenço, Frederico Duarte, Georgi M. Dobrikov, Atanas Kurutos, Ivaylo Slavchev, José Luis Capelo-Martínez, Hugo M. Santos, Carlos Lodeiro

Journal of Materials Chemistry C, 2025, 13, 6708 - 6719 Doi: 10.1039/d4tc04750h

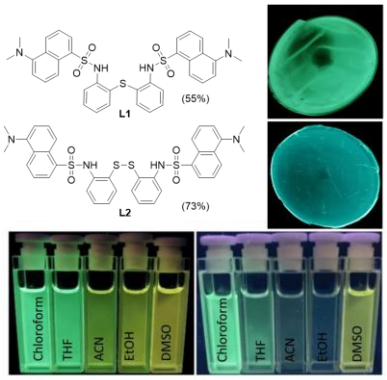
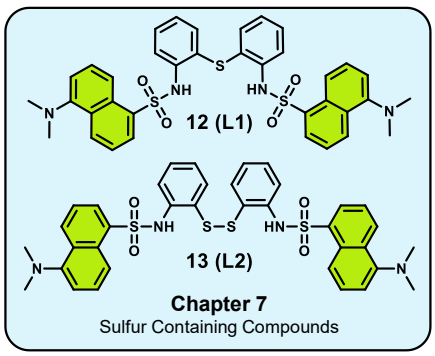


Figure 7–1. Graphical abstract.



Contribution to this work: Photophysical characterization; Preparation of polymeric doped thin films; Aggregation studies; Sensing experiments of metal ions and sodium dithionite; Temperature-dependent studies; Writing original draft.

7.1 Abstract

In this work, two new dansyl-derived chemosensors have been designed with the aim of developing a disulfide-cleavage-triggered probe. These stable new ligands, containing a thioether (L1) and a disulfide bridge (L2), have been synthesized and evaluated for their photophysical properties in both solution and solid state. Different fluorescence emission responses have been observed for both compounds due to the self-quenching nature of the disulfide bond compared to L1, with the latter reaching quantum yields close to 50%. Efforts to characterize solute-solvent interactions through Kamlet-Taft studies have revealed a positive solvatofluorochromic response for both compounds. Furthermore, the aggregation-induced emission phenomenon was demonstrated at increasing water fractions. The presence of free thiol groups enhances the complexation ability, making L1 particularly beneficial for sensing Cu^{2+} and Hg^{2+} ions, achieving detection limits as low as 2 μM in the case of mercury. Finally, incorporating L1 into polymer-doped films demonstrated promising results as molecular thermometers, while the response of L2 to sodium dithionite underscores its potential in disulfide-cleavage-triggered applications.

7.2 Introduction

The design of new sensors for metals and anions remains a topical area of chemistry in recent years. Contamination of water (including water in biological objects) with heavy metals is constantly growing, nonetheless, universally applicable and entirely effective sensors for their identification and elimination are not accessible. It is well known that most heavy metals (particularly Hg, Cu, Pb and Cd) possess high affinity to organic molecules containing sulfur, due to the formation of a strong donor-acceptor bond with this nonmetal element. Furthermore, the design of organosulfur fluorescent compounds may provide unique chemical properties that enable the interaction of particular substrates in biological systems. Some examples of biologically active substances include the aforementioned metal ions, reactive sulfur, oxygen and nitrogen species (RSS, ROS, RNS) and biomacromolecules [1]. Among the common classes of organosulfur compounds, thioether and disulfide bond containing probes may possess a complementary framework since efforts have been made to develop disulfide-cleavage-activated probes. This comes from the fact that disulfide bonds present strong reactivity or biological activity through reductive disulfide cleavage reaction producing two thiols, or the photocleavage reaction via a radical mechanism [2]. Several works have been published on the

basis of the presence of this bond for the sensing of biological relevant molecules and metal ions due to the often observed self-quenching effects through fluorescence resonance energy transfer or photoinduced electron transfer prior cleavage [3-9].

Over the last decades few studies offered sulfur containing ligands, possessing dansyl moiety as a source of fluorescence. Many of them were used for different applications – proteins labeling [10,11], immobilization onto polymers [12], enzyme detection [13], cell imaging [14] and metal ions detection [15,16]. In addition, the presence of sulfonamide functionality can significantly improve characteristics of such organic ligands [17] (especially their ability for complexation).

Our previous expertise in the synthesis of sulfur containing dansyl ligands for the detection of heavy metals, reveals that the incorporation of sulfur into aromatic rings leads to less efficient ligands. And vice versa – the best ligands contain sulfur, bound to aliphatic carbon chains [18,19]. Conversely, the existence of free thiol groups in the ligands provides optimal complexation capability; nevertheless, such compounds are often unstable and very susceptible to oxidation, even from atmospheric exposure.

In this work, we provide two novel stable ligands (Scheme 7-1, L1 and L2), including thio- and dithio- bridges connecting two identical dansyl-substituted aromatic groups. The chemical structures of these ligands were designed in order to ensure strong chelation of heavy metals by the introduction of sulfur atoms and sulfonamide functionalities. Furthermore, efforts have been made to highlight the photophysical contrast of both compounds towards the sensing of sodium dithionite or sodium hydrosulfite, $Na_2S_2O_4$, which is a strong reductant and broadly used in several industries as a bleaching agent, however classified as a highly toxic agent [20–25]. To the best of our knowledge, very few works have been published using dansyl moieties for the sensing of sodium dithionite with early reports from Nicholas Rattray et. al. where a sterically constrained bisdansyl chromophore would undergo fluorescent changes after reduction of the azo-bond locking group and the detection of azo-reductase expressing bacteria was also evaluated [26]. In contrast, Xingxing Cao et. al. where able to sense sodium dithionite by simultaneous immobilization in silicon nanowires a dansyl group and dabsyl group, the latter would act as quencher and recognizing group due the strong absorption at 470 nm overlapping with the dansyl group's emission. This system was found to exhibit high selectivity and good linearity between emission intensities and dithionite concentrations [27]. Finally, the aggregation induced emission (AIE) behaviour with increasing water fractions and the incorporation of L1 into polymeric thin films towards temperature dependent emission studies have been elucidated.

7.3 Experimental Section

7.3.1 Materials

Spectroscopy grade solvents, such as acetonitrile (CH_3CN), chloroform ($CHCl_3$), dimethylsulfoxide (DMSO), ethanol (EtOH), and tetrahydrofuran (THF), were used for the spectrophotometric and spectrofluorometric measurements. The starting fine chemicals (dansyl chloride (D0656 >98.0%(T)(HPLC)), 2,2'-thiodianiline (BD64353 98%) and 2,2'-disulfanediyldianiline (BD64662 98%)) used for the synthesis of the target fluorophores were purchased from TCI and BLD Pharm (China). Pyridine employed for the preparation of the target compounds was of analytical grade (p.a.) and dried over molecular sieve (3Å). Solvents for purification of compounds (petroleum ether (PE), dichloromethane (DCM) and methyl-*tert*-butyl ether (MTBE)) were of p.a. grade and were used without further purification. Silica gel (high-purity grade, pore size 60 Å, 230-400 mesh particle size, 40-63 µm particle size, for flash chromatography) employed for the column chromatography was purchased from Sigma Aldrich. Trifluoromethanesulfonate salts $Co(OTf)_2$, $Cu(OTf)_2$, $Zn(OTf)_2$, Ag(OTf), $Cd(OTf)_2$, were provided from Solchemar, while $Hg(OTf)_2$, $Pb(NO_3)_2$, CuBr and Hg_2Cl_2 were purchased from Sigma Aldrich. Poly(methyl methacrylate) (PMMA) (MW ≈ 350.000), IROGRAN® A 92 P 4637 (Polyether-based thermoplastic polyurethane (TPU)) was offered by Huntsman (Germany). The perfluoroalkoxy (PFA) supports for the fabrication of polymer films were purchased from Bohlender GmbH, Germany. Mili-Q ultrapure water was used in all experiments.

7.3.2 Instrumentation

The chemical identities of the compounds under investigation were confirmed through the utilization of various analytical techniques, including ^{1}H-NMR, ^{13}C-NMR, DEPT-135, 2-D COSY, 2D-HSQC, and 2-D HMBC NMR and 2-D NOESY spectroscopic techniques. The ^{1}H-NMR and ^{13}C-NMR spectra were acquired on a Bruker Avance II+600 spectrometer and Avance Neo 400 (Institute of Organic Chemistry with Centre of Phytochemistry - Bulgarian Academy of Sciences / NMR Centre) using 5 mm tubes. The measurements were performed in $CDCl_3$, CD_3CN, and DMSO-d_6 at 293K, with operating frequencies of 600.13 MHz / 400 MHz and 150.92 MHz / 100 MHz for the ^{1}H- and ^{13}C- nuclei, respectively. The ^{1}H- and ^{13}C- nuclear magnetic resonance (NMR) spectra were standardized using the reference signal of $CDCl_3$, CD_3CN, and DMSO-d_6 with a chemical shift value (δ) of 7.26 ppm / 1.94 ppm / 2.50 ppm for the ^{1}H-NMR and 77.16 ppm / 118.26 ppm, 39.52 ppm for the ^{13}C-NMR, respectively. The precision of

chemical changes is determined at a level of 0.01 ppm for the ^{1}H-NMR and 0.1 ppm for the ^{13}C-NMR. The coupling constants (*J*) are displayed with a precision of 0.1 and denoted in units of hertz (Hz). The spin multiplicity observed in the 1H- nuclear magnetic resonance (NMR) spectroscopy was represented using the following abbreviations: s for singlet, d for doublet, t for triplet, q for quartet, dd for doublet of doublets, dt for doublet of triplets, td for triplet of doublets, and m for multiplet. MestreNova v. 15.0 (Mestrelab Research S.L.) was used for processing the spectra.

High-Resolution Mass Spectrometry analyses have been performed in the Laboratory for Biological Mass Spectrometry–Isabel Moura (PROTEOMASS Scientific Society Facility), using UHR ESI-Qq-TOF IMPACT HD (Bruker-Daltonics, Bremen, Germany). Samples of the corresponding compounds were prepared by dissolution in 50% (v/v) Acetonitrile containing 0.1% (v/v) aqueous formic acid to obtain a working solution of 0.1 µg/mL. Mass spectrometry analysis was carried out by the direct infusion of the compound solutions into the ESI source. MS data were acquired in positive polarity over the mass range of 80 – 1300 m/z. (Capillary voltage: 4500 V, End plate offset: -500 V, Charging voltage: 2000 V, Corona: 4000 nA, Nebulizer gas: 0.4 Bar, Dry Heater: 180 °C, Dry gas: 4.0 L/min).

UV-Vis absorption spectra were recorded on a JASCO V-650 spectrophotometer. Otherwise stated, the fluorescence emission spectra were performed on a HORIBA Scientific FLUOROMAX-4 spectrofluorometer from BIOSCOPE-PROTEOMASS facilities. The second fluorometer equipment constitutes JASCO FP-8350. All photophysical experiments were carried out at 293 K using a quartz cell with 10 mm of optical path.

7.3.3 Synthetic procedures

7.3.3.1 Synthesis of L1

N,N'-(thiobis(2,1-phenylene))bis(5-(dimethylamino)naphthalene-1-sulfonamide) (**L1**):

Diamine **2** (1.0 equiv., 216 mg, 1.00 mmol) was dissolved in 3 mL dry pyridine in a 50 mL round bottom flask. Then an excess of dansyl chloride **1** (2.5 equiv., 674 mg, 2.50 mmol) was added as a solid and the formed mixture was stirred at 50°C for 18 h. The reaction outcome was monitored using TLC (mobile phase – DCM, developed 3 times). Workup: The reaction mixture was cooled down to room temperature, then excess of conc. aq. citric acid was added and extracted with DCM (2x40 mL). The organic phase was washed with water, dried over anhydr. Na_2SO_4 and evaporated to dryness. The crude product was purified by column chromatography: 65 g silica; DCM:MTBE=100:0.5 v/v. After the column chromatography, the product

was boiled with 4 mL PE, cooled down to r.t., decanted and dried *in vacuo* to furnish 375 mg (55%) of **L1** as a yellow powder. m.p. 113-114°C. ^{1}H-NMR (600.13 MHz, $CDCl_3$) δ 8.53 (*d*, *J* = 8.5 Hz, 1H), 8.26–8.20 (*m*, 2H), 7.47 (*dd*, *J* = 8.4, 7.5 Hz, 1H), 7.41 (*s*, 2H), 7.40–7.36 (*m*, 2H), 7.33 (*dd*, *J* = 8.2, 1.1 Hz, 1H), 7.11 (*d*, *J* = 7.5 Hz, 1H), 7.08–7.02 (*m*, 1H), 6.69 (*td*, *J* = 7.7, 1.2 Hz, 1H), 6.43 (*dd*, *J* = 7.9, 1.4 Hz, 1H), 2.86 (*s*, 12H). ^{13}C-NMR (150.92 MHz, $CDCl_3$) δ 152.1, 136.8, 134.2, 132.6, 131.3, 130.6, 130.0, 129.6, 129.2, 128.8, 125.7, 125.2, 123.1, 121.5, 118.7, 115.6, 45.6.

^{1}H NMR (400 MHz, CD_3CN) δ 8.52 (*dt*, *J* = 8.6, 1.0 Hz, 2H), 8.26 (*dt*, *J* = 8.7, 0.8 Hz, 2H), 8.20 (*dd*, *J* = 7.4, 1.3 Hz, 2H), 8.05 (*s*, 1H), 7.51 (*dd*, *J* = 8.5, 7.4 Hz, 2H), 7.44 (*dd*, *J* = 8.6, 7.6 Hz, 2H), 7.16 (*dd*, *J* = 7.6, 0.7 Hz, 2H), 7.12 (*dd*, *J* = 8.1, 1.4 Hz, 2H), 7.09 – 7.01 (*m*, 2H), 6.77 (*ddd*, *J* = 7.8, 7.3, 1.5 Hz, 2H), 6.45 (*dd*, *J* = 7.9, 1.4 Hz, 2H), 2.81 (*s*, 12H). ^{13}C NMR (101 MHz, CD_3CN) δ 152.95, 137.10, 135.35, 133.15, 131.96, 131.21, 130.58, 130.23, 129.84, 129.49, 128.32, 127.24, 124.12, 123.90, 119.51, 118.26, 116.41, 45.63.

^{1}H NMR (400 MHz, DMSO-d_6) δ 9.80 (*s*, 2H), 8.46 (*d*, *J* = 8.5 Hz, 2H), 8.31 (*d*, *J* = 8.7 Hz, 2H), 8.14 (*dd*, *J* = 7.4, 1.2 Hz, 2H), 7.57 (*dd*, *J* = 8.5, 7.4 Hz, 2H), 7.46 (*dd*, *J* = 8.6, 7.6 Hz, 2H), 7.19 (*d*, *J* = 7.1 Hz, 2H), 7.08 (*td*, *J* = 7.8, 1.5 Hz, 2H), 7.00 (*dd*, *J* = 8.1, 1.3 Hz, 2H), 6.86 (*td*, *J* = 7.6, 1.4 Hz, 2H), 6.53 (*dd*, *J* = 7.9, 1.4 Hz, 2H), 2.80 (*s*, 12H). ^{13}C NMR (101 MHz, DMSO-d_6) δ 151.27, 136.16, 135.28, 132.50, 130.26, 129.35, 129.27, 129.00, 128.95, 128.45, 128.09, 126.27, 123.85, 123.41, 118.86, 115.27, 45.04.

ESI-HRMS (**L1**): $[M+H]^+$ for $C_{36}H_{34}N_4O_4S_3$ = 683.1772 m/z (-6.3 ppm), $[M+2H]^{2+}$ $C_{36}H_{34}N_4O_4S_3$ = 342.0925 m/z (-5.5 ppm). Calculated $[M+H]^+$ for $C_{36}H_{34}N_4O_4S_3$ = 683.181495 m/z, and $[M+2H]^{2+}$ $C_{36}H_{34}N_4O_4S_3$ = 342.094386 m/z.

7.3.3.2 Synthesis of L2

Synthesis of *N,N'*-(disulfanediylbis(2,1-phenylene))bis(5-(dimethylamino)naphthalene-1-sulfonamide) (**L2**):

Diamine **3** (1.0 equiv., 248 mg, 1.00 mmol) was dissolved in 3 mL dry pyridine in a 50 ml round bottom flask. Then an excess of dansyl chloride **1** (2.5 equiv., 674 mg, 2.50 mmol) was added as a solid and the formed mixture was stirred at r.t. for 48 h. The reaction outcome was monitored using TLC (mobile phase – DCM, developed twice). Workup: excess of conc. aq. citric acid was added to the reaction mixture and extracted with DCM (2x40 mL). The organic phase was washed with water, dried over anhydr. Na_2SO_4 and evaporated to dryness. The crude product was purified by column chromatography: 65 g silica; DCM:MTBE=100:0.5 v/v. After the column chromatography, the product was boiled with 4 mL PE, cooled down to room temperature, decanted and dried *in vacuo* to yield 523 mg (73%) of **L2** as a yellow powder. m.p. 180-

181 °C. ^{1}H-NMR (600.13 MHz, $CDCl_3$) δ 8.48 (d, *J* = 8.5 Hz, 2H), 8.32 (d, *J* = 8.7 Hz, 2H), 8.25 (dd, *J* = 7.4, 1.3 Hz, 2H), 7.67 (s, 2H), 7.59 (dd, *J* = 8.6, 7.6 Hz, 2H), 7.53 (dd, *J* = 8.3, 1.2 Hz, 2H), 7.45 (dd, *J* = 8.5, 7.4 Hz, 2H), 7.22 (td, *J* = 8.0, 1.6 Hz, 2H), 7.16 (d, *J* = 7.3 Hz, 2H), 6.74 (td, *J* = 7.6, 1.3 Hz, 2H), 6.59 (dd, *J* = 7.7, 1.5 Hz, 2H), 2.80 (s, 12H). ^{13}C-NMR (150.92 MHz, $CDCl_3$) δ 152.1, 138.8, 136.5, 134.3, 132.0, 131.3, 130.4, 130.0, 129.7, 129.0, 124.2, 123.8, 123.1, 119.8, 118.9, 115.6, 45.5.

^{1}H NMR (400 MHz, CD_3CN) δ 8.50 (dt, *J* = 8.6, 1.1 Hz, 2H), 8.28 (d, *J* = 8.7 Hz, 2H), 8.11 (dd, *J* = 7.4, 1.3 Hz, 2H), 7.82 (s, 2H), 7.59 (dd, *J* = 8.7, 7.6 Hz, 2H), 7.49 (dd, *J* = 8.5, 7.4 Hz, 2H), 7.24 (dd, *J* = 7.6, 0.7 Hz, 2H), 7.22 – 7.14 (m, 4H), 6.92 (ddd, *J* = 7.9, 7.1, 1.7 Hz, 2H), 6.74 (dd, *J* = 7.9, 1.3 Hz, 2H), 2.78 (s, 12H). ^{13}C NMR (101 MHz, CD_3CN) δ 153.09, 137.23, 135.63, 133.18, 131.91, 131.01, 130.84, 130.64, 130.44, 130.13, 129.54, 127.21, 124.92, 124.16, 119.71, 118.26, 116.37, 45.59.

^{1}H NMR (400 MHz, DMSO-d_6) δ 10.23 (s, 2H), 8.47 (d, *J* = 8.5 Hz, 2H), 8.35 (d, *J* = 8.7 Hz, 2H), 7.97 (dd, *J* = 7.3, 1.2 Hz, 2H), 7.56 (ddd, *J* = 8.5, 7.5, 5.4 Hz, 4H), 7.25 (d, *J* = 7.0 Hz, 2H), 7.06 (m, 4H), 6.85 (dd, *J* = 7.8, 1.6 Hz, 2H), 6.75 (dd, J = 7.7, 1.5 Hz, 2H), 2.79 (s, 12H). ^{13}C NMR (101 MHz, DMSO-d_6) δ 151.34, 135.95, 134.71, 133.03, 130.10, 129.24, 129.06, 129.03, 128.53, 128.09, 127.93, 126.99, 125.49, 123.44, 119.20, 115.16, 45.03.

ESI-HRMS (**L2**): $[M+H]^+$ for $C_{36}H_{34}N_4O_4S_4$ = 715.1530 m/z (-0.8 ppm), $[M+2H]^{2+}$ $C_{36}H_{34}N_4O_4S_4$ = 358.0808 m/z (1.06 ppm). Calculated $[M+H]^+$ for $C_{36}H_{34}N_4O_4S_4$ = 715.153566 m/z, and $[M+2H]^{2+}$ $C_{36}H_{34}N_4O_4S_4$ = 358.080421 m/z.

7.3.4 Spectrophotometric and spectrofluorimetric measurements

7.3.4.1 Photophysical characterization and titrations

Stock solutions of each compound were prepared (*ca.* 10^{-3} M) in various solvents (CH_3CN, DMSO, EtOH, $CHCl_3$, and THF), by dissolving each ligand in a 10 mL volumetric flask and diluting with the corresponding solvent. The working solutions in the range of 10^{-5} – 10^{-6} M were subsequently prepared by diluting the stock solutions.

Titrations of **L1** were performed by successive additions of microliter aliquots of standard solutions of Cu^+, Cu^{2+}, Zn^{2+}, Ag^+, Cd^{2+}, Hg^+, Hg^{2+} ions prepared in acetonitrile. A correction for the absorbed light was performed when necessary. Temperature-dependent emission spectra were recorded by placing the material between quartz plates and using a temperature-controlled hotplate for variable temperature measurements. Additionally, mixtures with different water fractions (f_w = 0%, 17%, 33%, 55%, 67%, and 83%) were prepared at a final concentration

of 10 μM in THF and acetonitrile and characterized using absorption and emission spectroscopy. Luminescence spectra of the compounds in the solid state, as well as in doped polymer thin films, were obtained using a fiber-optic device connected to a spectrofluorometer, with samples excited at the appropriate wavelengths.

Table 7-1. Spectroscopic polarity parameters, physical properties of the different solvents. ε_r : relative permittivity; η: refractive index; α: the solvent's HBD acidity; β: the solvent´s HBA basicity; π^*: the solvent´s dipolarity/polarizability.

Solvent	ε_r	α	β	π^*	η
DMSO	47.24	0	0.76	1.00	1.47
CH_3CN	35.94	0.19	0.40	0.66	1.34
EtOH	24.30	0.86	0.75	0.54	1.36
THF	7.58	0	0.55	0.58	1.40
$CHCl_3$	4.89	0.20	0.10	0.69	1.44

7.3.4.2 Fluorescence quantum yield and lifetime

The relative photoluminescence quantum yields were evaluated using a solution of dansylamide in DMSO (ϕ_F = 0.61) as a reference standard to quantify the relative QY of **L1** and **L2** in all tested solvents [28]. Lifetime measurements were conducted using a Tempro Fluorescence Lifetime System equipped with a Horiba Jobin-Yvon NanoLed pulsed diode controller. All experiments were performed at 293 K.

7.3.5 Determination of the detection and quantification limits (LOD and LOQ)

The determination of the limit of detection (LOD) and limit of quantification (LOQ) started with the collection of ten independent measurements of a solution containing the chosen probe, devoid of any metal ion addition (y_{blank}). Final determination of the LOD and LOQ values followed the subsequent formulas: [29,30]

LOD = $y_{dl} = y_{blank} + 3std$, where y_{dl} = signal detection limit and std = standard deviation.

LOQ = $y_{dl} = y_{blank} + 10std$, where y_{dl} = signal detection limit and std = standard deviation.

The final step involved the determination of the minimal detectable and quantified concentration of metal ion by titration with the ligands.

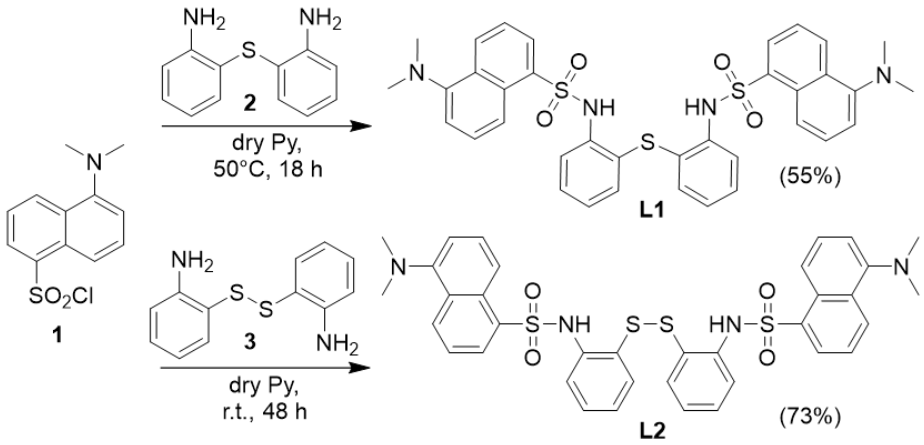
7.3.6 Procedure of polymeric thin films doped with L1

Doped polymer films were fabricated by measuring 100 mg of polymer into one vial and 0.5 mg of compound **L1** in another. To dissolve the polymers, 10 mL of solvent was added to the polymer vial (tetrahydrofuran for TPU and chloroform for PMMA), and 1 mL of solvent was added to the compound vial. For the polyether-based thermoplastic polyurethane (TPU), stirring was required for dissolution, while for the polymethyl methacrylate (PMMA), slight heating along with stirring was necessary. Once both solutions were fully dissolved, the compound solution was combined with the polymer solution and mixed. The resulting mixture was then poured into a perfluoroalkoxyalkane (PFA) mold with a 5 cm diameter and a 15 mL capacity, sourced from Bohlender, GmbH, Germany.

7.4 Results & Discussion

7.4.1 Synthesis

As in our recent study [18], the target compounds **L1** and **L2** were synthesised in dry pyridine via the reaction of dansyl chloride (**1**) with commercially available amines **2** and **3**, respectively (Scheme 7-1). Since **3** is presumably sensitive to oxidation, synthesis of **L2** was carried out at room temperature. Both **L1** and **L2** were isolated in pure form and good yields after column chromatography. They were unambiguously characterized by using different 1D and 2D NMR experimental techniques, melting point temperatures and HRMS.



Scheme 7-1. Synthetic approach to the preparation of dansyl derivatives **L1** and **L2**.

7.4.2 Photophysical characterization

The bisdansylated compounds **L1** and **L2** bearing single sulfur and disulfide bonds were studied according to their photophysical properties both in solution and in the solid state. Figure 7–2 displays the chemical structure alongside the photoluminescent data in acetonitrile with the remaining solvents gathered Figure 7–8 and Figure 7–9 while a summary of all the data is present in Table 7-2.

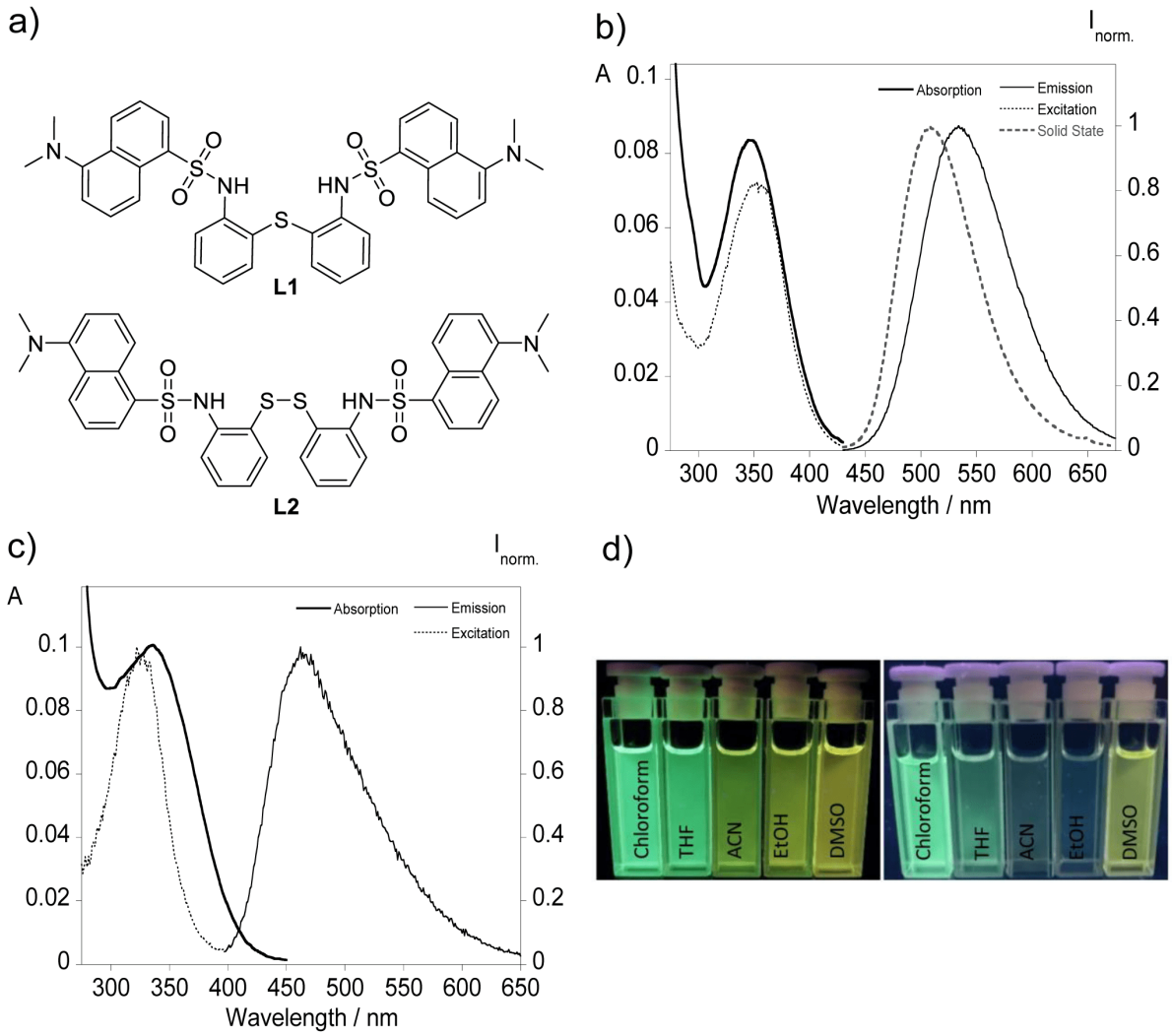


Figure 7–2. (a) Molecular structure of the dansyl derived compounds **L1** and **L2** bearing single sulfur and disulfide bridges. Photophysical characterization of derivatives **L1** (b) and **L2** (c) in acetonitrile ([**L1**] = [**L2**] = 10 μM). Images under UV light (365 nm) for (d) **L1** (left) and **L2** (right) in different solvents varying polarity.

UV-Vis spectral data of both compounds reveal a maximum centered at *ca.* 345 and 335 nm corresponding to the π-π* transition of dansyl chromophore supporting the observation of colorless solutions under the naked eye. Clear differences rise upon proper excitation of the samples with the visualization of a greenish light with emission maximum centered at 535 for **L1** and a faint bluish green emission characterized by a maximum around 464 nm is observed for **L2**. This behaviour is present across all solvents used and it can be visually identified in Figure 7–2d with the reason behind it being the presence of each type of sulfur bond that links both chromophores. Disulfide bonds when incorporated in fluorescent molecules are often associated with the quenching of the emission by promoting photoinduced electron transfer (PeT) or Föster resonance energy transfer (FRET) [3-9] This divergence observed between both ligands presents a key advantage that will be explored further ahead. On a similar subject, solid state emission is only present for **L1** with a maximum around 508 nm that is blue-shifted compared with in solution resembling the emission profile of chloroform and THF.

Table 7-2. Absorption maximum wavelength in solution (λ_{abs}), emission maximum wavelength in solution (λ_{em}), molar absorption coefficients (ε), Stokes shift (Δλ), fluorescence quantum yields (ϕ), emission maximum in the solid state (λ_{em}^{Solid}), fluorescence lifetimes (τ) for compounds **L1** and **L2** in various solvents.

Cpd	Solv	λ_{abs} [nm]	λ_{em} [nm]	ε (10^4) [cm^{-1} M^{-1}]	Stokes shift [cm^{-1}]	ϕ(%)	λ_{em}^{Solid} [nm]	τ[ns]
L1	DMSO	345	545	0.76	10637	17.7	508	12.6
	EtOH	340	525	0.81	10364	21.2		11.4
	CH_3CN	345	535	0.86	10294	18.8		11.7
	THF	343	511	0.88	9804	41.1		13.7
	$CHCl_3$	350	510	1.01	8964	48.3		15.5
L2	DMSO	340	529	0.91	10508	4.6	_	4.8
	EtOH	335	508	0.98	10166	2.9		7.3
	CH_3CN	340	464	0.98	8299	2.5		10.6
	THF	330	500	1.24	10303	3.5		12.5
	$CHCl_3$	333	487	1.21	9496	3.6		12.9

The fluorescence quantum yields of the two compounds were also evaluated, using dansylamide as a standard for compounds **L1** and **L2**, with compound **L1** reaching a quantum yield of 0.48 in chloroform and for compound **L2** expected lower values were obtained across all solvents with fluorescence efficiency was observed below 5%. Time-correlated single photon

counting suggests double digit nanosecond times among all solvents between 11.4 and 15.5 ns for **L1** while apolar solvents provide higher fluorescence lifetimes.

The presence of a solvent environment notably influences the stabilization of the ligand's excited state, primarily due to changes in the fluorophore's dipole moment. Considering the data gathered in Table 7-2, it is perceivable a correlation between the increase in solvent polarity and the energy gap, translating to greater Stokes shift, ultimately resulting in a bathochromic shift. This shift can be attributed to a positive solvatofluorochromic effect, where the environment-sensitive dansyl derivatives adjust their fluorescence maximum wavelength in response to solvent polarity, a behavior clearly illustrated in Figure 7–2.

In response to these results, significant efforts have been focused on thoroughly describing the interactions between the solvent and the molecule.
To this end, three solute-dependent parameters (υ0, a, b, and p) have been determined via multiparametric fitting using the Kamlet-Taft equation (Equation 1).

$$\upsilon = \upsilon_0 + a\alpha + b\beta + p\pi^* \qquad \text{(Equation 1)}$$

Where υ_0 denotes the wavenumber value in a reference solvent, the parameters a, b, and p are derived from multiple regression analysis and represent the sensitivity of the probe's photophysical behavior to solvent polarity. Specifically, α: indicates hydrogen bond donor acidity (HBD), β: represents hydrogen bond acceptor basicity (HBA), and π^*: reflects the stabilization of a charge or dipole in the absence of specific dielectric interactions (see Table 7-1) [31,32]. Table 7-3 summarizes the reference wavenumber value υ_0, the fitted parameters (a, b and p) with the slopes and correlation coefficients attained through the fitting of a linear plot of $\upsilon_{exp.}$ versus υ_{calc}, by applying the Kamler-Taft model excluding acetonitrile.

Table 7-3. Independent fluorescence wavenumber (*υ0*), solvent polarity (*p*), HBD (*a*), HBA (*b*), slope and coefficient (R^2) of the linear fitting plot $\upsilon_{exp.}$ versus $\upsilon_{calc.}$

	υ0	a	b	p	Slope	R^2
L1	21492	-509	-911	-2451	1.00	1
L2	21943	-65	-1652	-1784	1.00	1

Key distinctions can be elucidated regarding the predisposition of each compound towards the characteristics of different solvents. The fitted parameters reveal low hydrogen bond donor sensitivity with extended negative values for **L1**, while **L2** is more prone to stabilization

by solvents with higher hydrogen bond acceptor character due to the presence of an extra electronegative atom that forms a disulfide bridge. Additionally, highly polarizable solvents can stabilize the excited state of **L1** more effectively, as the more negative p value suggests higher polarizability, leading to stronger solvation effects.

7.4.3 Aggregation induced emission behaviour in water

The assessment of the photophysical properties of **L1** with different ratios of water in THF and acetonitrile mixtures have been followed by absorption and fluorescence spectroscopy.

Figure 7–3 illustrates that the augmentation of the water fraction results in a reduction in fluorescence in both solvents, accompanied by a little red shift in emission until reaching 67% water content. The absorption profile changes significantly in the mixture of 83% water content with the rise of the baseline indicating the presence of aggregates. This phenomenon translates into substantial changes in the emission profile by the sudden increase in fluorescence intensity followed by a hypsochromic shift suggesting an aggregation induced emission (AIE) effect. In the case of THF the emission intensity surpasses the initial one while in acetonitrile it is equalized with associated fluorescence quantum yields of 12% and 8% respectively. The heterogeneity observed in the absorbance measurements led us to further characterize the presence of aggregates through dynamic light scattering analysis. The results, gathered in Figure 7–3, suggest hydrodynamic sizes of 142.5 ± 7.9 nm (THF/Water) and 146.0 ± 2.5 nm (Acetonitrile/Water) with associated polydispersity index values of 0.037 ± 0.07 and 0.045 ± 0.01, respectively.

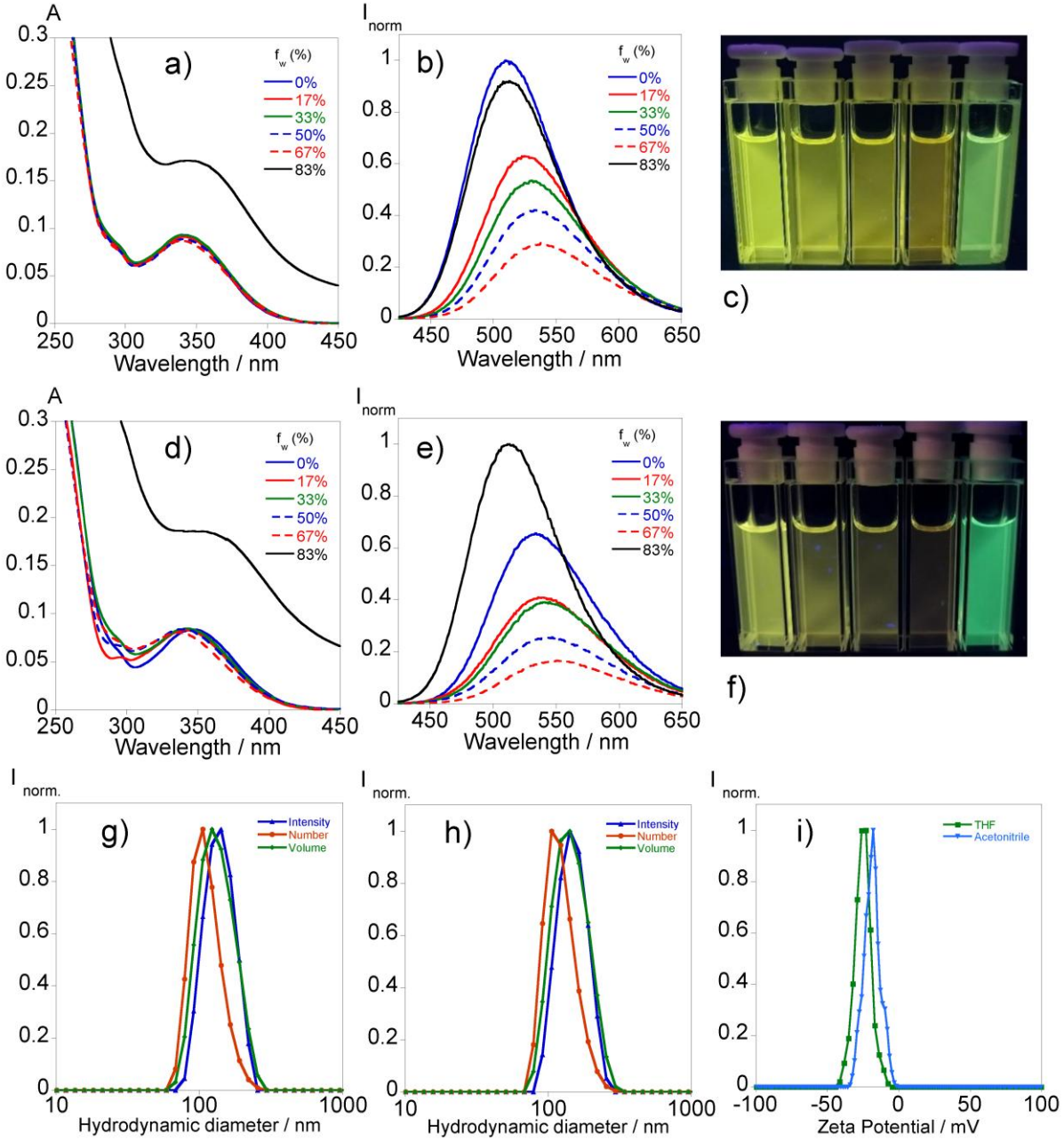


Figure 7–3. Absorption (a,d) and emission spectra (b,e) of **L1** in THF (a,b) and in acetonitrile (d,e) with different water fractions f_w (0%, 17%, 33%, 55%, 67%, 83%), [**L1**]= 10 μM. Images of **L1** in (c) THF and (f) acetonitrile with different water fractions under UV light (365 nm). Hydrodinamic diameter of **L1** aggregates in THF (g) and acetonitrile (h) according to number, volume, and intensity distributions and zeta potential (i) of the solutions of 83% water fractions.

7.4.4 Metal Ions Sensing

Dansyl derivatives have shown promise as efficient probes for the detection of metal ions, specifically evaluating the efficacy of compound **L1** was carried out, since **L2** showed negligible emission from the start. For this reason, several metal ions including Co^{2+}, Cu^{+}, Cu^{2+},

Zn^{2+}, Ag^{+}, Cd^{2+}, Hg^{+}, Hg^{2+} in acetonitrile and Pb^{2+} in water were tested. Figure 7–4 consolidates the response on the emission intensity with the addition of 0.5, 1, and 5 equivalents of the metal ions. Notably, the absorption and emission spectra showed significant variations exclusively in the presence of mercury(II) and copper(II) ions. The introduction of a single equivalent of each metal ion significantly diminished the emission signal. Furthermore, the fluorescence intensity was completely quenched upon the addition of 5 equivalents. This signifies that both compounds exhibit high selectivity for these particular metal ions.

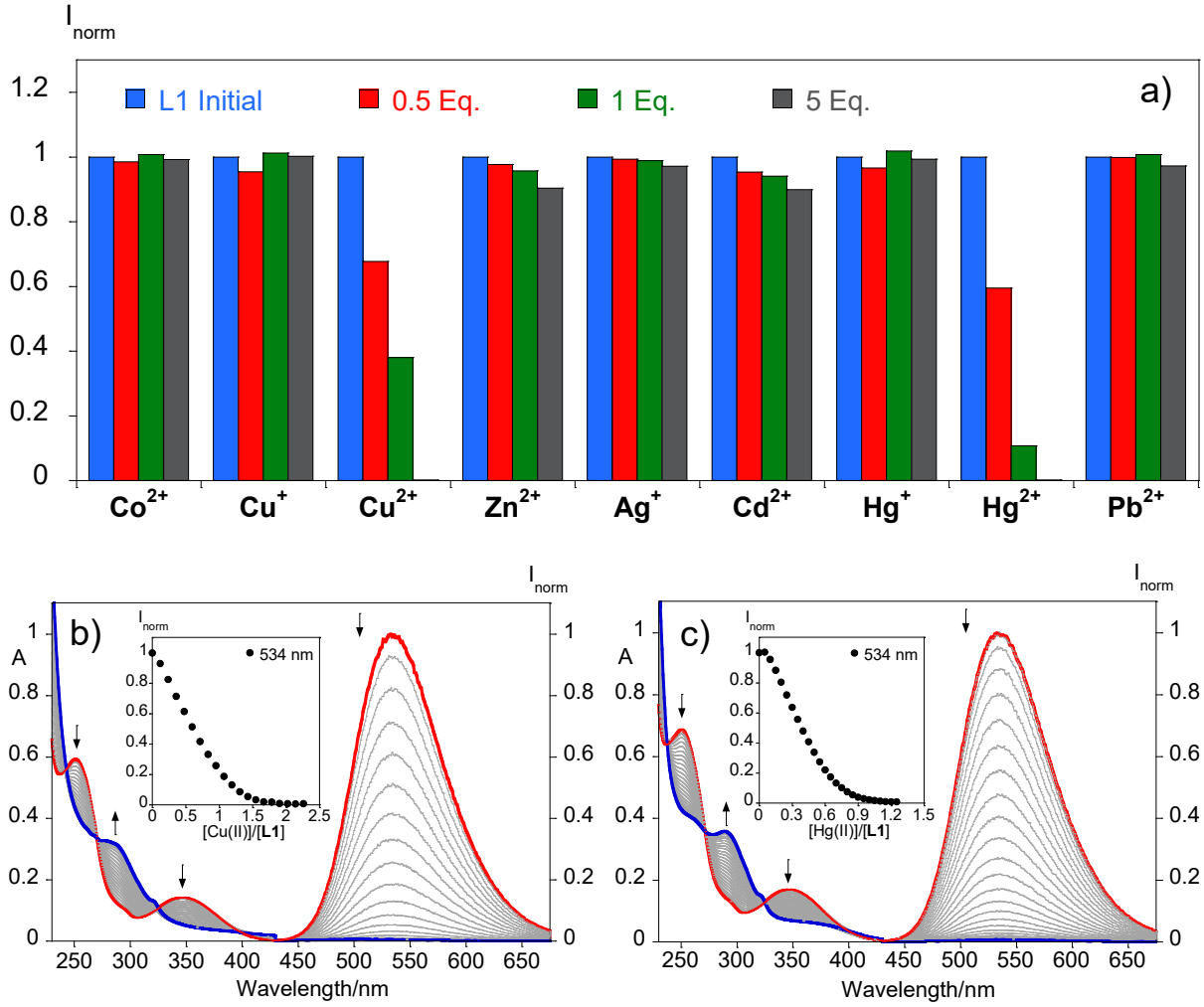


Figure 7–4. Maximum emission intensities of **L1** (a) after the addition of 0.5, 1, and 5 equivalents of Co^{2+}, Cu^{+}, Cu^{2+}, Zn^{2+}, Ag^{+}, Cd^{2+}, Hg^{+}, Hg^{2+} and Pb^{2+} metal ions in acetonitrile. Spectrophotometric and spectrofluorometric titrations of compound **L1** with increased additions of Cu^{2+} ([**L1**] = 16.8 μM) (b) and Hg^{2+} ([**L1**] = 20 μM) (c) in acetonitrile. The inset represents the emission as a function of [Cu^{2+}]/[**L1**] at 534 nm (b), of [Hg^{2+}]/[**L1**] at 534 nm (c).

The efficacy of compound L1 in detecting Cu^{2+} and Hg^{2+} metal ions was promising, prompting titrations with these metals in acetonitrile. Figure 7–4 shows the spectrophotometric and spectrofluorometric titrations towards both metals exhibiting similar absorption

spectral behaviour with a decrease in absorption at 250 nm and 347 nm and an increase in the absorbance at 289 nm. As for the emission spectra, a suppression of the emission intensity was observed at 534 nm. Figure 7–4 also shows the fluctuation of the emission intensity maxima of compound **L1** with the increasing of metal concentration in solution. The suppression of the emission caused by Hg^{2+} comes from the fact that, as a heavy atom, it has its photophysical properties such as spin-orbit coupling, making non-radiative pathways competing with fluorescence and therefore having a mechanism for quenching the emission after chelation (CHEQ). The Cu^{2+} ion is also commonly detected by CHEQ due to its paramagnetic nature by having unpaired electrons in the d-layer, which occurs through either electron transfer or energy transfer mechanisms. However, once filled Cu^{+} becomes a CHEF system, which is why Cu^{+} does not quench the emission intensity of compound **L1**. This system can recognize either Cu^{2+} from Cu^{+} and Hg^{2+} from Hg^{+} being a good example for metal speciation.

As a favorable characteristic of a molecular probe, the binding reversibility of **L1** with Hg^{2+} and Cu^{2+} was evaluated against a competitive ligand, i.e., Na_2EDTA. As shown in Figure 7–13, the addition of 2.2 equivalents of Cu^{2+} leads to fluorescence quenching of **L1** that showed no significant recovery of the emission intensity following the addition of equimolar Na_2EDTA, indicating that the complex formed is not reversible in the presence of this competitive ligand. In contract, the addition of 1.0 equivalents of Hg^{2+} also causes the fluorescence quenching, however, the emission intensity is recovered with equimolar Na_2EDTA in solution, suggesting the regeneration of free **L1**. These reversibility studies were performed 5 times (Figure 7–13) providing the results to support the capacity for **L1** to be a reversible fluorescent probe for the detection of Hg^{2+} but not for Cu^{2+}. Furthermore, the formation of the complexes have been followed by ESI-HRMS suggesting the stoichiometric proportion of 1:1 as it can be seen in Figure 7–14 and Figure 7–15. (**L1+Cu^{2+}**): $[M+H]^+$ for $C_{36}H_{34}CuN_4O_4S_3$ = 746.1111 m/z (-0.01 ppm). Calculated $[M+H]^+$ for $C_{36}H_{34}CuN_4O_4S_3$ = 746.111093 m/z. (**L1+Hg^{2+}**): $[M+H]^+$ for $C_{36}H_{34}HgN_4O_4S_3$ = 885.1519 m/z (-0.2 ppm). Calculated $[M+H]^+$ for $C_{36}H_{34}HgN_4O_4S_3$ = 885.152138 m/z.

To thoroughly evaluate the sensing capabilities for Hg^{2+} and Cu^{2+} ions, the interaction constants of all complexes were calculated using the HypSpec software [33]. Additionally, the detection and quantification limit parameters for both compounds in relation to Hg^{2+} and Cu^{2+} were determined. The association constants, along with the LOD (Limit of Detection) and LOQ (Limit of Quantification), are provided in Table 7-4.

Table 7-4. Association constants using HypSpec software for compounds **L1** towards Hg^{2+} and Cu^{2+} ions with included stoichiometry in acetonitrile. Respective values for the detection limit (LOD) and quantification limit (LOQ) amounts (μM) were measured following the emission at 534 nm.

Compounds	Metal (M)	Association constants ($LogK_{ass.}$), L:M	LOD (μM)	LOQ (μM)
L1	Cu^{2+}	5.73 ± 0.01 (1:1)	4	8
	Hg^{2+}	5.80 ± 0.02 (1:1)	2	4

The stability constants values for **L1** towards both metal ions evidence similar values in a stoichiometric proportion of 1:1 ligand to metal with a slightly higher value in the case of Hg^{2+} ($LogK_{ass.} = 5.80 \pm 0.02$).

The detection and quantification limits have also been determined reaching values as low as 2 and 4 μM for Hg^{2+}, respectively. These values indicate that **L1** could be highly useful in applications such as environmental monitoring, where it is crucial to detect and measure Hg^{2+} at low concentrations.

7.4.5 Sensing of sodium dithionite

The potential use of L2 in the induced turn-on sensing of sodium dithionite by disulfide bond cleavage has been evaluated in light of the duality observed in the photophysical profile of both compounds, which is a result of the self-quenching characteristic of disulfide systems.

Figure 7–5 gathers the UV-vis and the fluorescence response in acetonitrile upon consecutive additions of an aqueous solution of sodium dithionite up to 9 equivalents alongside the visual representation of the turn-on effect after addition of 5 equivalents, while the batch-based sensing can be seen in Figure 7–16.

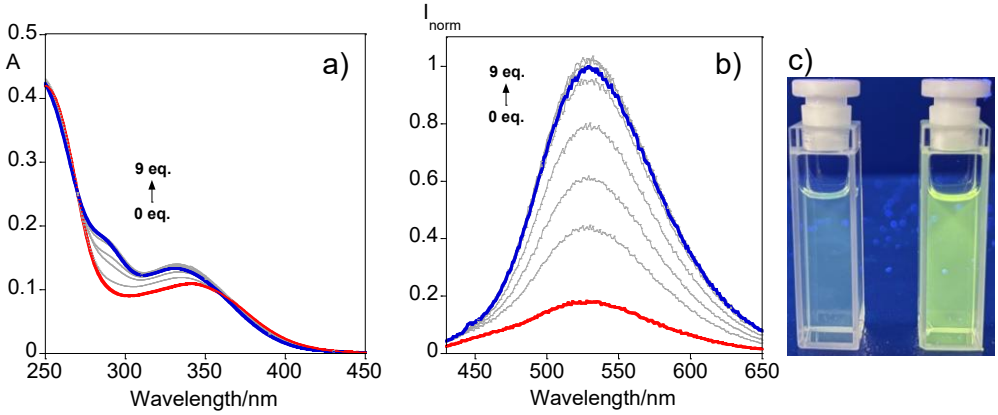


Figure 7–5. UV-vis (a) and emission (b) spectra response after the addition of up to 9 equivalents of sodium dithionite to **L2** solution in acetonitrile. Image under the UV-light (365 nm) (c) of the initial solution (left) and after addition of 5 equivalents (right).

Figure 7–5 reveals that as the concentration of dithionite increases, a progressive blue shift of the absorption profile is noticed with the emergence of a shoulder around 290 nm. Regarding the fluorescence response, results show that the emission band observed initially successively increases with the addition of dithionite indicating the cleavage of the disulfide bond. Also, ESI-HRMS adds support to this suggestion due to the formation of the monomer moiety depicted in Figure 7–17. ($[M+H]^+$ for $C_{18}H_{18}N_2O_2S_2$ = 359.0882 m/z (-0.1 ppm), calculated $[M+H]^+$ for $C_{18}H_{18}N_2O_2S_2$ = 359.088246 m/z) This behavior can be perceived through Figure 7–5c where a turn-on sensing mechanism is observed highlighting the usefulness of compound **L2** for disulfide-cleavage-activated applications.

Although a clear contribution of compound **L2** towards the development of new disulfide-based chemosensors has been established, some considerations might become useful for the improvement of future designs of these types of compounds. We propose that improving the selectivity of the sensor molecule must be considered since these compounds may interact with multiple analytes. Some examples include the soft character of sulfur atoms that can be easily combined with Hg^{2+} as an example of a soft metal according to Hard-Soft-Acid-Base theory or the implications of the reducing environment when applying for a specific reactive species in a biological system. This can be avoided through the design of a multiple lock design method to counteract false positives. Considerations about water solubility should be fulfilled alongside biocompatibility by implementing changes in their molecular structure. Finally, a switch-on or clear-cut ratiometric fluorescent mechanism may provide a comfortable level of certainty regarding the physical property changes in these systems [1,2].

7.4.6 NMR titrations of the free ligands

The full structural elucidation of the free ligands **L1** and **L2** was achieved with the help of 1D and 2D NMR experiments carried out in various solvents including $CDCl_3$ (Figure 7–18 to Figure 7–22 for **L1**, Figure 7–35 to Figure 7–39 for **L2**), CD_3CN (Figure 7–23 to Figure 7–28 for **L1**, Figure 7–40 to Figure 7–45 for **L2**), and DMSO-d_6 (Figure 7–29 to Figure 7–34 for **L1**, Figure 7–46 to Figure 7–51 for **L2**). Besides the acetonitrile-d_3, deuterated DMSO was also employed as an alternative bearing in mind the relatively poor solubility of the salts (mercury(II) acetate, copper(II) triflate, sodium dithionite) in CD_3CN. For all experiments we used 1 equiv. of each salt as the maximum amount in order to obtain clear NMR working solutions of suitable concentration.

The experiment of **L1** with mercury(II) acetate in acetonitrile-d_3 (Figure 7–54 and Figure 7–55) revealed almost no visible change with respect to the chemical shifts for the ^1H- and the

^{13}C-NMR spectra. The only notable difference involves broadening of the NH signal, which nevertheless retained the integral for a total of 2 protons. Changing the media to DMSO-d_6 the ^{1}H-NMR spectra of **L1** with Hg^{2+} resulted in rather noisy spectra (including broad baseline) with side bands around the main signals, the appearance of two new multiplets, namely a triplet a doublet of doublets (with a small $J_{H\text{-}H}$ coupling constant) at 6.30 ppm, along with a new doublet at about 8.69 ppm (Figure 7–58). The full identification of the mixture is hampered taking into consideration the broad signals and baseline, which remain broad and noisy even after 29 days. Despite the non-emissive nature of **L2** preventing the evaluation of the sensing abilities through fluorescent techniques, attempts to record spectra of **L2** in deuterated acetonitrile after the addition of 1 equiv. Hg^{2+} only showed once again very broad signals along the whole spectral range (Figure 7–61). The shape remained unaltered over several days. To shed more light, we attempted to perform the same measurement in DMSO-d_6. In the case of ligand **L2** changing the solvent revealed very pronounced spectral changes, pointing out to the spontaneous formation of a new product (Figure 7–64 and Figure 7–65). Intriguingly, the presence of mercury (II) acetate exhibits more pronounced spectral changes in DMSO-d_6 for both **L1** and **L2**. The addition of Hg^{2+} to **L2** resulted in the complete disappearance of the NH proton. The new spectra showed no sign of either an NH, or an SH proton signals. With respect to the ^{13}C-NMR spectra, the most pronounced changes were found for the 2 carbon atoms on the benzene ring, which are attached to the nitrogen and sulfur heteroatoms (Figure 7–65). We assume that the S-S bond is most likely cleaved while Hg is allocated between the two heteroatoms.

While keeping the DMSO-d_6 as the working media, the addition of 1 equiv. of copper(II) triflate to ligand **L2** (Figure 7–62 and Figure 7–63) showed no difference in comparison to the pure ligand as seen from the ^{1}H-NMR, where only minor shift of the majority of the signals is present in the carbon spectra. In the ^{13}C-NMR the triflate quartet with a $J_{C\text{-}F}$ coupling constant of around 320 Hz (123.87 ppm, 120.95 ppm, 117.75 ppm, 114.20 ppm) was also reported (**Figure 7–63**). The shape of the ^{1}H-NMR spectrum remained the same after 17 days. Therefore, we repeated the same experiment in acetonitrile-d_3 (Figure 7–60). Likewise to the data obtained in DMSO-d_6, the ^{13}C-NMR in acetonitrile- d_3 comprises the triflate quartet with a $J_{C\text{-}F}$ coupling constant of around 320 Hz (126.74 ppm, 123.55 ppm, 120.36 ppm, 117.19 ppm as). The addition of 1 equiv. copper(II) triflate to ligand **L1** (Figure 7–56) guides to only negligible changes (about 0.02-0.03 ppm towards the stronger field) as seen from the ^{1}H-NMR spectra in DMSO-d_6 (Figure 7–56). By analogy, the ^{13}C-NMR exhibits shift of around 0.6 ppm for all signals (Figure 7–57). Both spectra of the free ligand and after the addition of copper(II) triflate appear to be

highly similar accounting for the same number of protons and carbons in the chemical structure of the fluorophore. In turn, working with acetonitrile-d_3 for **L2** showed somehow more pronounced shifts for both the ^{1}H- and the ^{13}C-NMR spectra (Figure 7–59 and Figure 7–60). In particular, several shifts are observed for the whole dansyl moiety (including the dimethylamino group and the aromatic protons), whereas the *o*-substituted benzene ring remains unaltered. A shift of the signals was present for the $N(CH_3)_2$ - from 2.81 ppm to 3.04 ppm when copper(II) triflate is added (Figure 7–59). The ^{13}C- spectra also show distinctive changes, even to the carbon atom directly linked to the dimethylamino group, since approximately 5 ppm shift is evident (Figure 7–57). **L2** also exhibits the characteristic triflate quartet with a $J_{C\text{-}F}$ coupling constant of around 320 Hz (126.74 ppm, 123.56 ppm, 120.37 ppm, 117.19 ppm). Ligand **L2** exhibits very distinctive shifts in acetonitrile-d_3 - mainly relative to the dansyl moiety (up to 0.5 ppm). In particular, the singlet corresponding to the methyl protons of $N(CH_3)_2$ shift from 2.78 ppm to 3.41 ppm (Figure 7–59). Notable changes are also evident in the ^{13}C-NMR spectra, where the carbon attached to the dimethylamino shifts from 153.09 ppm to 139.51 ppm (Figure 7–60). Other dansyl carbon signals also move by about 4-5 ppm. On the other hand, only minor changes were visible for the benzene ring containing the two ortho S and N heteroatoms (Figure 7–60).

The addition of 1 equiv. sodium dithionite to **L2** in acetonitrile-d_3 (Figure 7–66 and Figure 7–68) furnished the appearance of new proton signals allocated at 9.82 (s), 8.20 (dd), 7.53 (m), 7.44 (dd), 7.38 (dd), 7.29 (m), 7.05 (td) and a negligible change of the NH shift from 7.82 (s) to 7.86 (s). The kinetics of this experiment are very slow, since even after 30 days we observe a mixture of the free ligand (about 57%) and an additional product (about 43%) - the ratio was determined based on integration of the ^{1}H-NMR. Due to the low concentration and the very poor solubility of sodium dithionite in acetonitrile, clear HMBC cross peaks of the XH signals were not observed. Despite the relatively low concentration, the NOESY experiment also did not yield any further information. This in turn hampered the full assignment of the newly developed product in deuterated acetonitrile. Next, we attempted to repeat the experiment in deuterated DMSO (Figure 7–67 and

Figure 7–69). Despite changing the media, the solubility of the dithionite salt was not notably enhanced. Adding 1 equiv. of sodium dithionite to ligand **L2** in DMSO-d_6 yielded broadening of the NH proton at 10.22 ppm (no disappearance - integral is maintained), while a new sharp signal was developed around 9.86 ppm (Figure 7–67). Several new signals were developed over time of which the more evident were found centered at 8.24 ppm (dt), 8.18 ppm (dd), 7.60 ppm (m), 7.42 ppm (dt), 7.40 ppm (t). In parallel, the intensity of several

multiplets was diminished, while others were enhanced accompanied by the appearance of overlapping multiplets. Accounting of the relatively clear region around the dimethylamino protons, we accounted for a mixture of at least two main components (ligand + newly formed product) in almost equal quantities (Figure 7–67). This slow transformation to about 50% of a new product takes more than 24 days under these experimental conditions. Bearing in mind the strong overlap of majority of the aromatic protons, full identification of the mixture by means of NMR is currently limited and beyond the scope of our current investigation.

7.4.7 Temperature dependent emission of polymer doped films

Since compound **L1** has manifested solvatochromism aligned with the fact that is the only compound exhibiting emission in the solid state, efforts have been put forth for the design of solid supports that would act as molecular thermometers. Bearing this in mind, doped polymer films have been produced following the procedure depicted in the experimental section using PMMA and TPU as polymer matrixes. Figure 7–6 gathers the emission spectra of **L1** in solid state and doped in the polymer materials together with the images under natural and UV light.

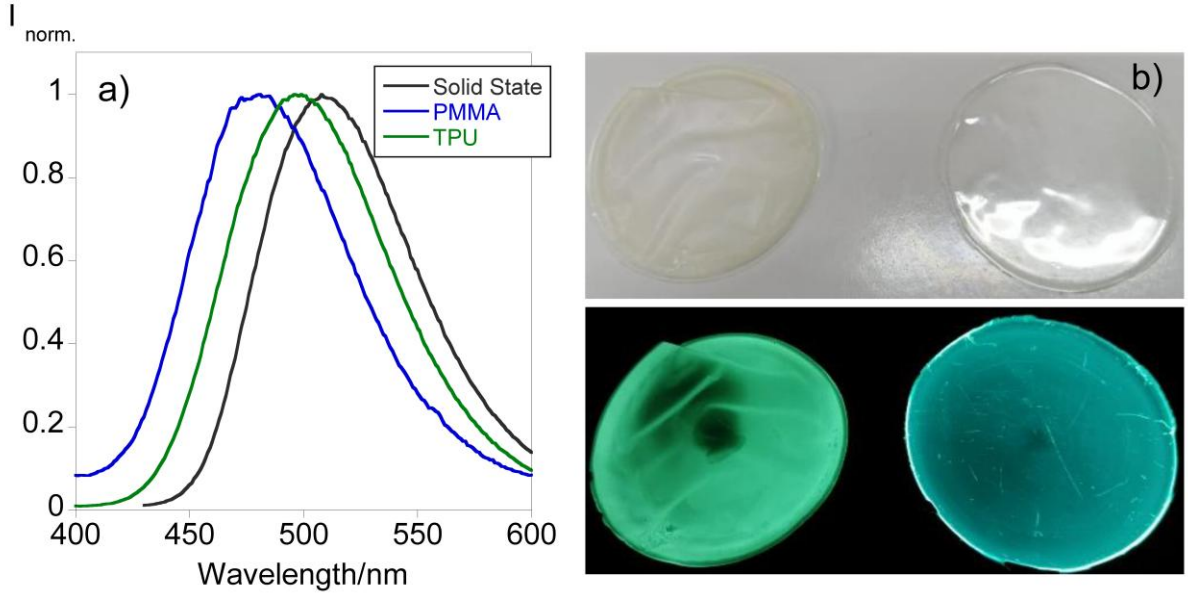


Figure 7–6. Comparison between the emission spectra of the different polymer thin films doped with (a) **L1** and (b) images under natural (up) and UV light (down) of TPU (left) and PMMA (right).

Attending Figure 7–6, it is perceivable that both polymer matrixes are able to shift the emission of the final material causing a blue shift from 508 in solid state to 496 and 481 nm in TPU and PMMA, respectively. This phenomenon is also tangible in the images of the polymers found in Figure 7–6 since TPU shows a greenish emission while PMMA's emission resembles

more bluish color. These observations have been described in previous works demonstrating the potential of the use of dansyl compounds towards the development of tunable solid materials for diverse applications [18]. Considering these findings, the fabricated polymer doped materials have been tested to be used as molecular thermometers by recording the emission at different temperatures. Figure 7–7 gathers the temperature dependent emission spectra of both doped materials.

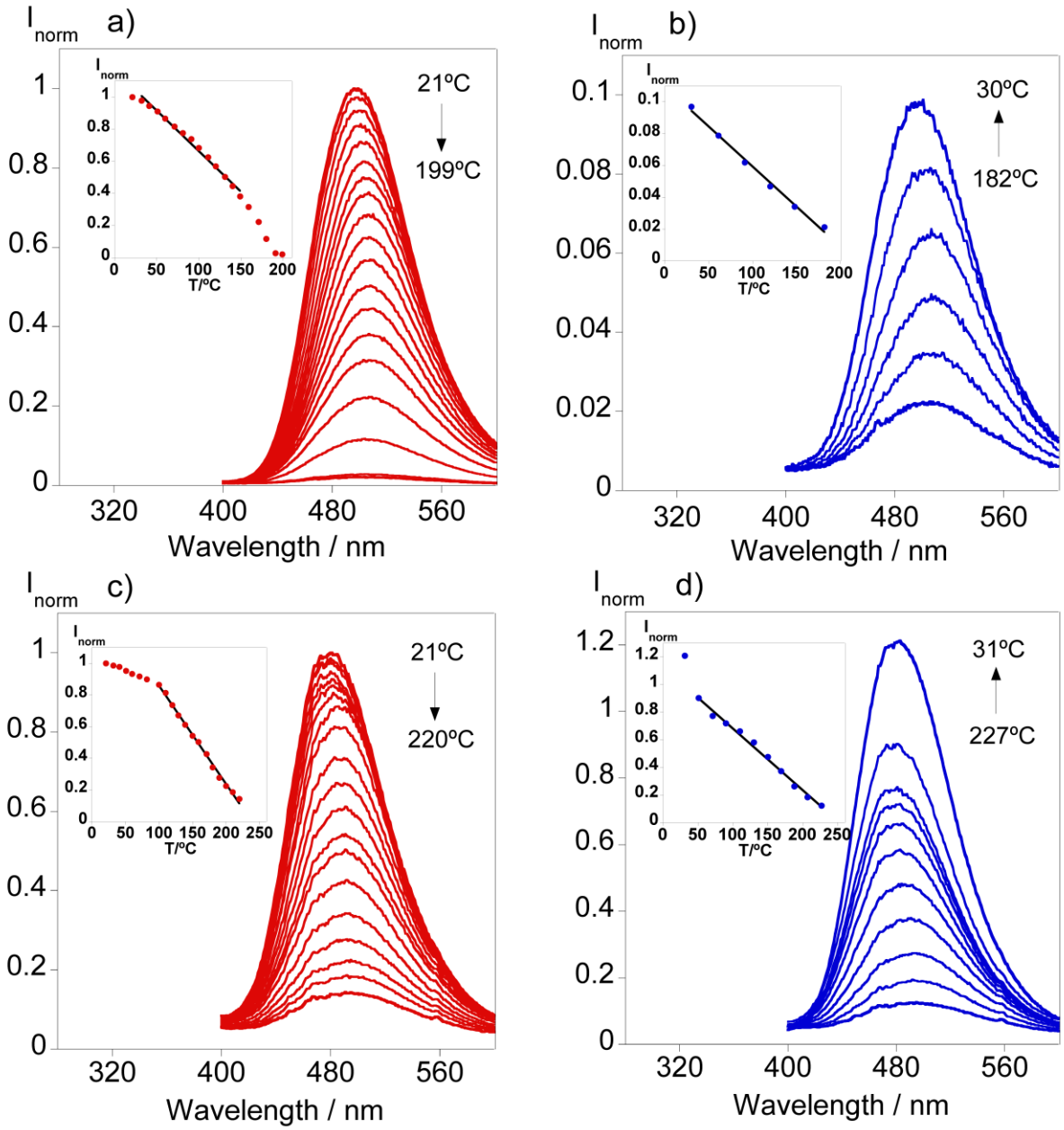


Figure 7–7. Temperature-dependent emission spectra of **L1** doped in (a) TPU during heating cycle [Inset: I_{norm}. vs. T plot at 496 nm upon heating: 32 to 149ºC (Y= 1.1685 - 0.0050481x), yielding R=0.9902]; (b) TPU during cooling cycle [Inset: I_{norm}. vs. T plot at 496 nm upon cooling: 30 to 182ºC (Y= 0.10949 - 0.0050184x), yielding R=0.9933]; (c) PMMA during heating cycle [Inset: I_{norm}. vs. T plot at 481 nm upon heating: 100 to 220ºC (Y= 1.481 - 0.0062098x),

yielding R=0.9963]; (d) PMMA during cooling cycle [Inset: $I_{norm.}$ vs. T plot at 481 nm upon cooling: 51 to 227ºC (Y= 1.1278 - 0.0044644x), yielding R=0.9925].

A reduction in the fluorescence signal is seen in both polymeric materials as the temperature increases, reaching values of up to 227ºC. Regarding the TPU doped material, a clear total quenching of the fluorescence signal was achieved at 200ºC. Throughout the increases in temperature over the course of the cycle, linearity has been found between 32 and 149ºC, however, only 10% of the initial emission is restored after cooling suggesting that further increases in temperature may cause physical damage to the polymer preventing reusability of the material.

In the case of PMMA doped with **L1**, higher temperatures could be achieved in this solid substrate alongside a linearity range at higher temperatures between 100 to 200ºC shifting its potential towards industrial applications. During the cooling cycle, linearity was maintained as the temperature decreased and in contrast with the TPU substrate, the physical changes enabled the recovery of the emission past the initial one due to the increased rigidity observed. Thus, these materials provide insights towards the design of solid materials that can be tuned on their emission depending on the polymer matrix used and the linearity of the fluorescence signal sustain the use of these doped polymers as thermometers.

7.5 Conclusions

Two new dansyl compounds bearing thio- and dithio- functionality were synthesized and their photophysical characteristics have been investigated. Using the Kamlet-Taft equation, the solute-solvent interactions were analyzed in detail, revealing a positive solvatofluorochromic behavior for both compounds. Additionally, the compounds showed enhanced emission in the presence of water, exhibiting aggregation-induced emission (AIE) at high water content. This AIE effect was further confirmed by dynamic light scattering experiments, which revealed hydrodynamic sizes of 142.5 ± 7.9 nm (THF/water) and 146.0 ± 2.5 nm (acetonitrile/water) for **L1**. Taking an environmental remediation standpoint, **L1** was found sensitive to Hg^{2+} and Cu^{2+} ions by modulating their emission profile with the highest association constant towards Hg^{2+} (Log $K_{ass.}$= 5.80) in tandem with the lowest LOD and LOQ values of 2 and 4 μM, respectively. Given that the key photophysical differences were attributed to the presence of disulfide bridge in **L2** promoting self-quenching behavior, a proof of concept for sodium dithionite sensing was put forth to highlight the potential use of this compound towards disulfide-cleavage-triggered sensing. Finally, the PMMA and TPU polymer doped films were fabricated

in order to demonstrate the possibility to modulate the emission maximum wavelength in the solid state and the use of these materials as molecular thermometers have been elucidated.

7.6 Supplementary material

7.6.1 Determination of the limit of detection and quantification (LOD and LOQ)

The determination of the Limit of Detection (LOD) and Limit of Quantification (LOQ) began by recording several emission intensities for L1 at the working concentration without the addition of any metal at 534 nm. The measured intensities were as follows: 3325880; 3210490; 3263120; 3208930; 3347470; 3296160; 3326780; 3251750; 3230730. The average emission intensity and its standard deviation were calculated to be 3273478 ± 49572. Using the equations provided in Section 1.5 of the experimental section, the LOD and LOQ were determined to be 3124760 and 2777751, respectively.

To express the LOD and LOQ in terms of concentration, extrapolation was performed by comparing these values with the intensities obtained after each addition of metal.

7.6.2 Supplementary figures & tables

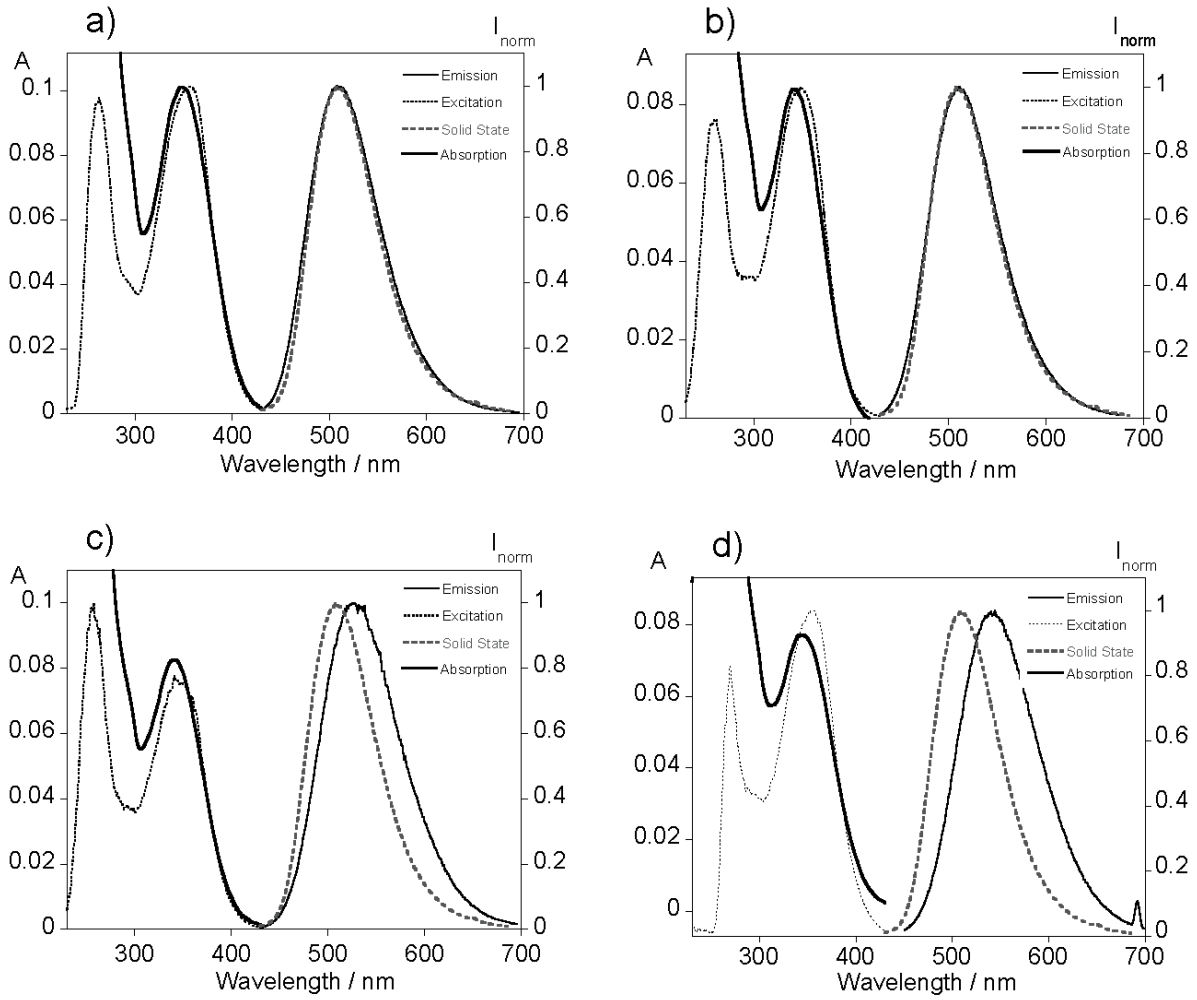


Figure 7–8. Ptophysical characterization of L1 in a) chloroform, b) THF, c) ethanol and d) DMSO.

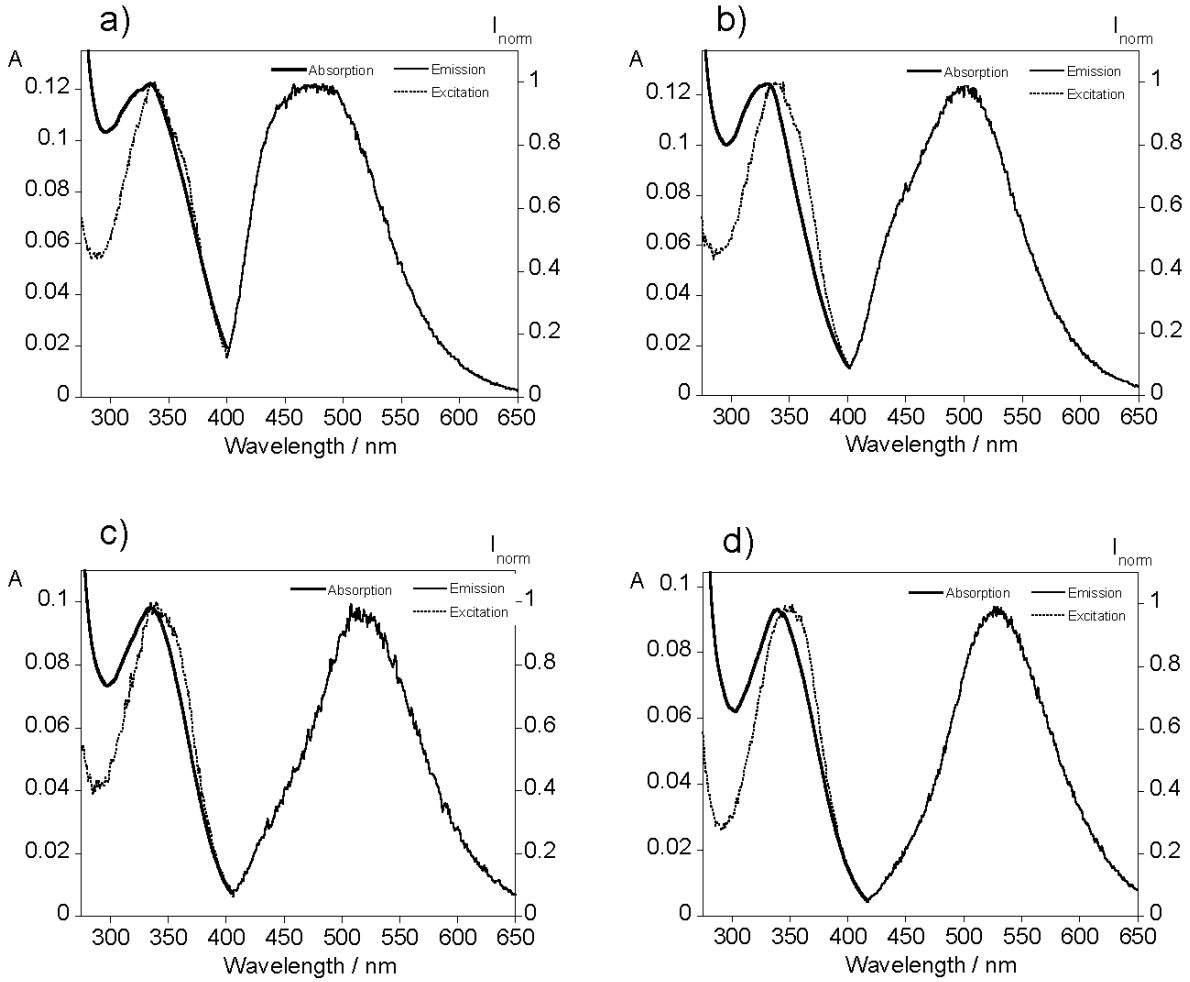


Figure 7–9. Photophysical characterization of L2 in a) chloroform, b) THF, c) ethanol and d) DMSO.

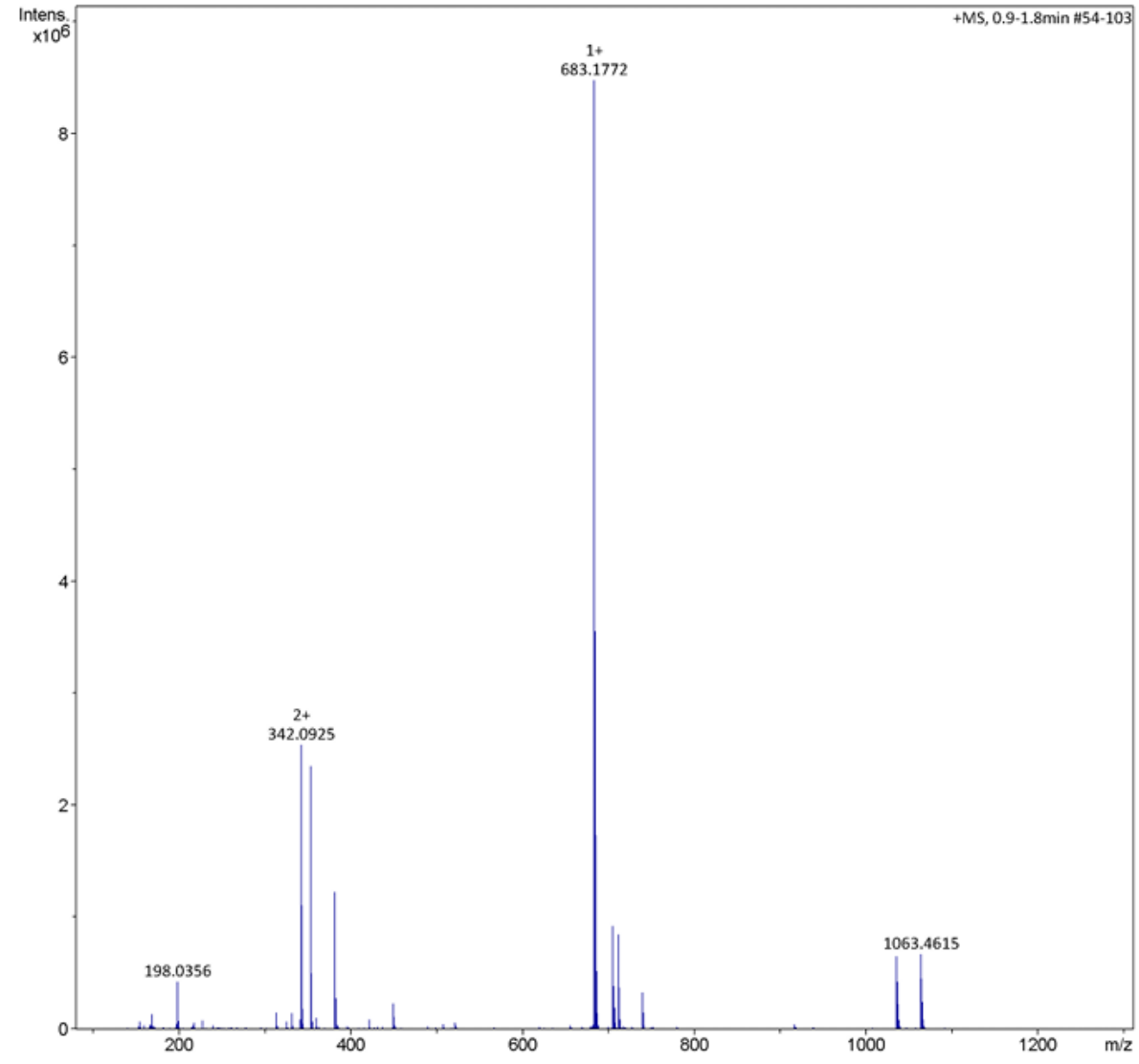
Display Report

Analysis Info

Analysis Name	D:\Data\BIOSCOPE\Hugo\Smal molecules\2024.01.10-Frederico\DR-P165.d	Acquisition Date	11-Jan-24 10:18:20 AM
Method	Direct_Infusion_100-1000.m	Operator	BDAL@DE
Sample Name	MassAccMS	Instrument	impact HD 1819696.00006
Comment			

Acquisition Parameter

Source Type	ESI	Ion Polarity	Positive	Set Nebulizer	0.4 Bar
Focus	Not active	Set Capillary	4500 V	Set Dry Heater	180 °C
Scan Begin	80 m/z	Set End Plate Offset	-500 V	Set Dry Gas	4.0 l/min
Scan End	1300 m/z	Set Charging Voltage	2000 V	Set Divert Valve	Waste
		Set Corona	4000 nA	Set APCI Heater	200 °C



DR-P165.d

Bruker Compass DataAnalysis 4.2 printed: 02-Feb-24 1:41:43 PM by: BDAL@DE Page 1 of 1

Figure 7–10. ESI-HRMS spectrum of compound L1.

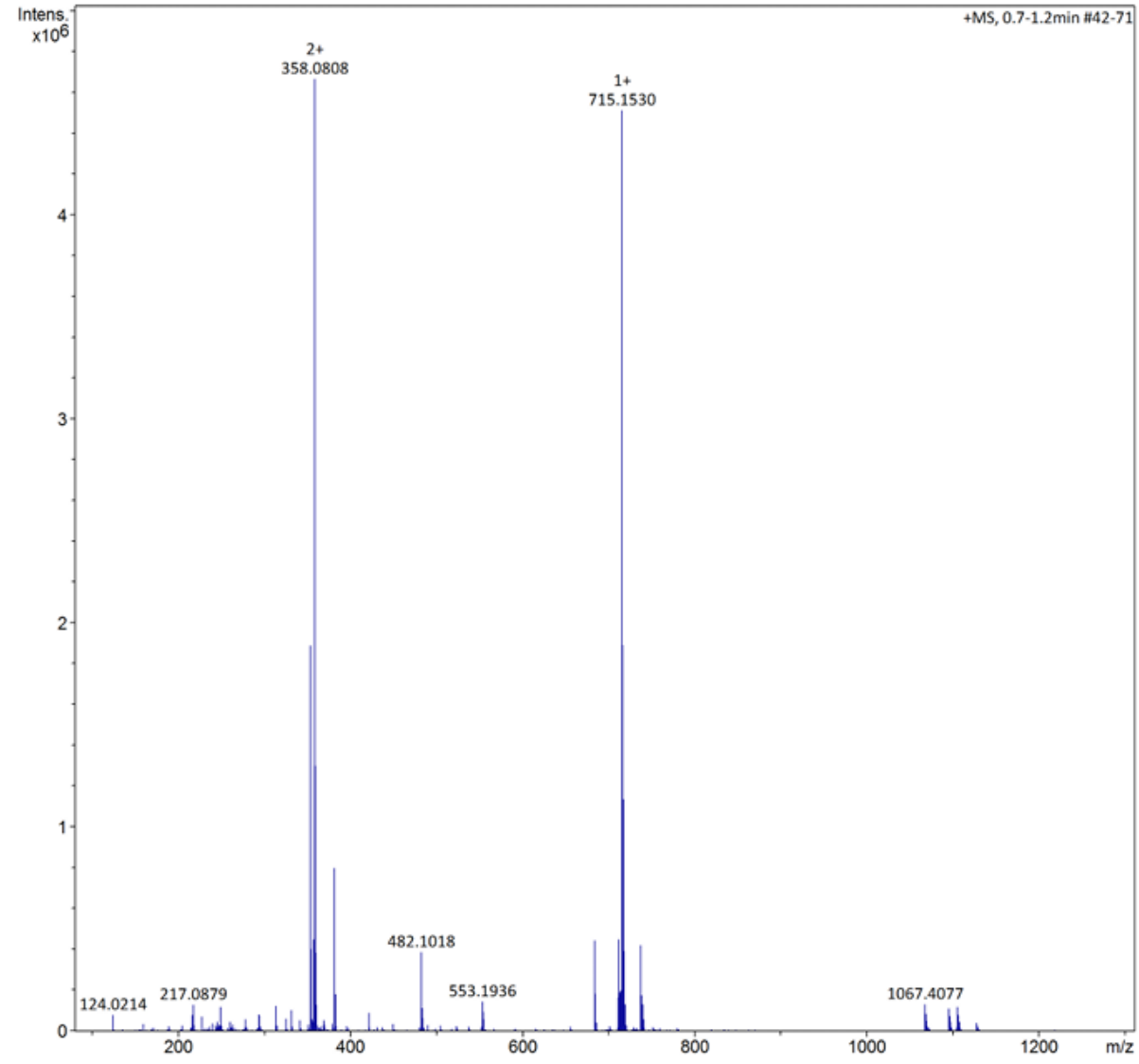
Display Report

Analysis Info

Analysis Name	D:\Data\BIOSCOPE\Hugo\Smal molecules\2024.04.17-Frederico\DR292.1.d	Acquisition Date	17-Apr-24 4:11:45 PM
Method	Direct_Infusion_100-1000.m	Operator	BDAL@DE
Sample Name	ACN	Instrument	impact HD 1819696.00006
Comment			

Acquisition Parameter

Source Type	ESI	Ion Polarity	Positive	Set Nebulizer	0.4 Bar
Focus	Not active	Set Capillary	4500 V	Set Dry Heater	180 °C
Scan Begin	80 m/z	Set End Plate Offset	-500 V	Set Dry Gas	4.0 l/min
Scan End	1300 m/z	Set Charging Voltage	2000 V	Set Divert Valve	Waste
		Set Corona	4000 nA	Set APCI Heater	200 °C



DR292.1.d

Bruker Compass DataAnalysis 4.2 printed: 05-Jun-24 11:25:29 AM by: BDAL@DE Page 1 of 1

Figure 7–11. ESI-HRMS spectrum of compound L2.

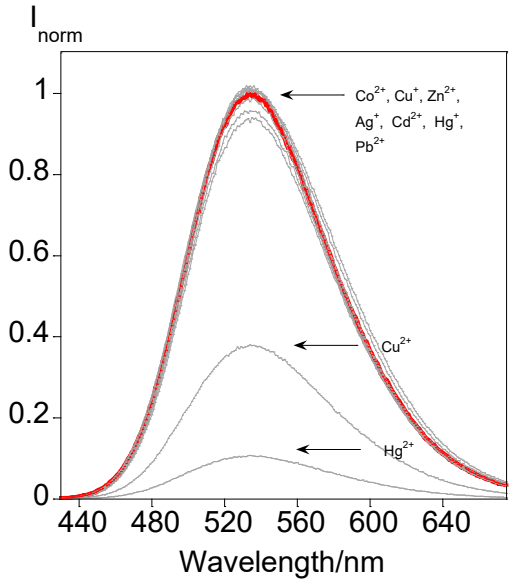


Figure 7–12. Emission spectra after the addition of 1 eq. of each metal. For clarity of the reader the red spectrum corresponds L1.

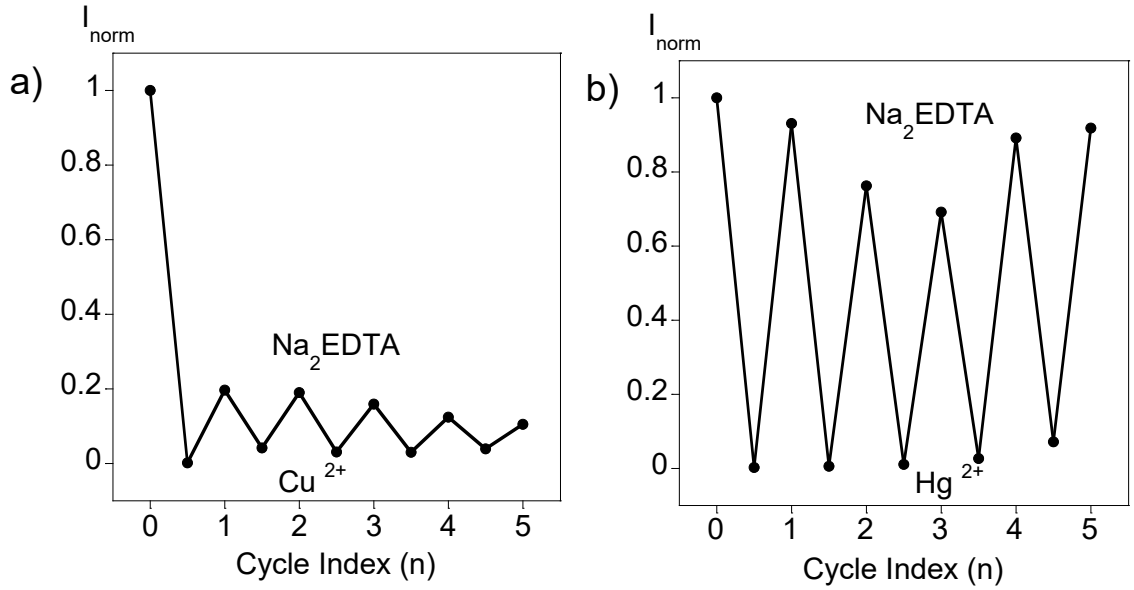


Figure 7–13. Reversible changes of fluorescence intensity at 533 nm of L1 upon addition of a) Cu_{2+} and b) Hg_{2+} with Na_2EDTA alternately.

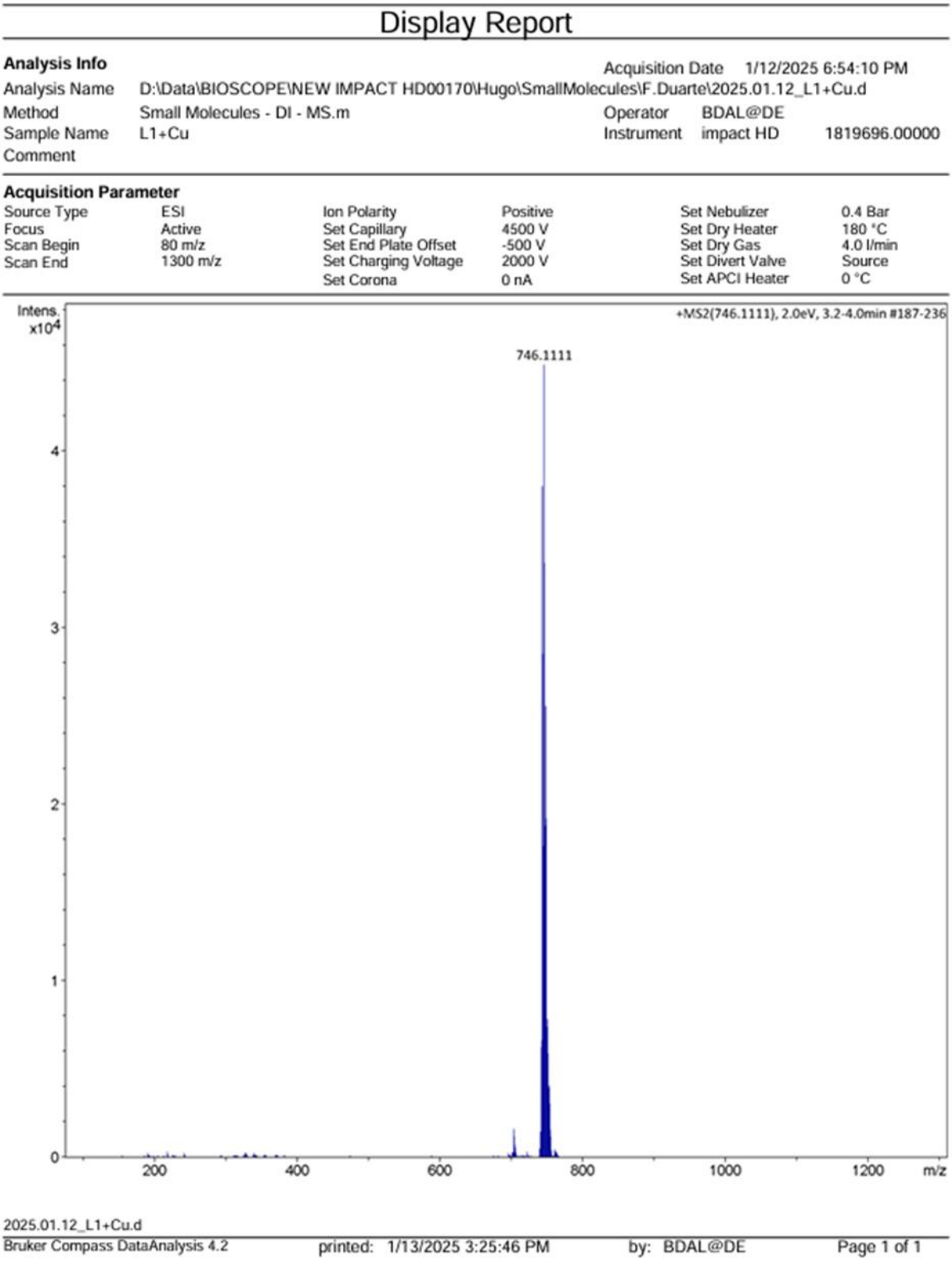


Figure 7–14. ESI-HRMS spectrum of compound L1+Cu^{2+} complex.

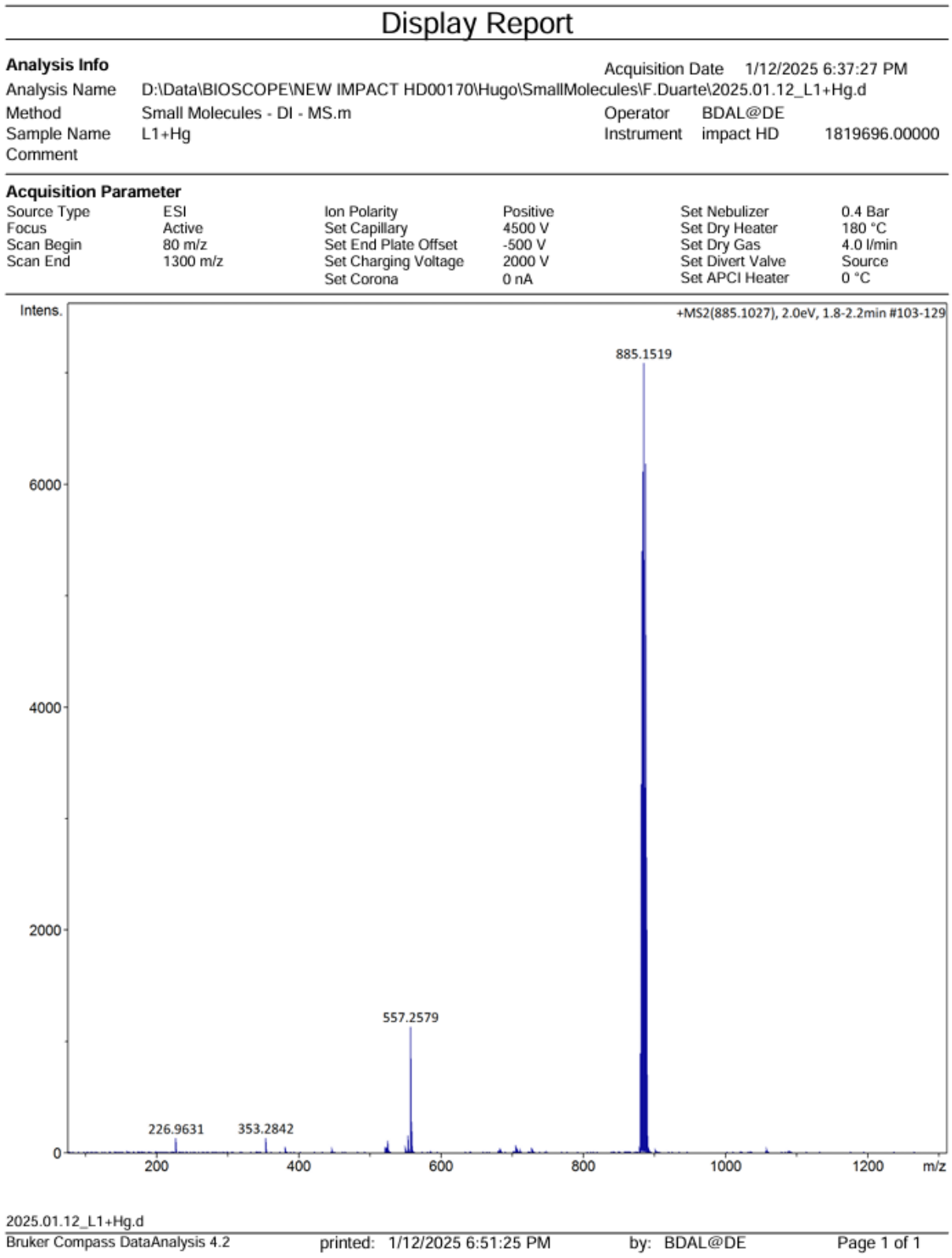


Figure 7–15. ESI-HRMS spectrum of compound L1+Hg^{2+} complex.

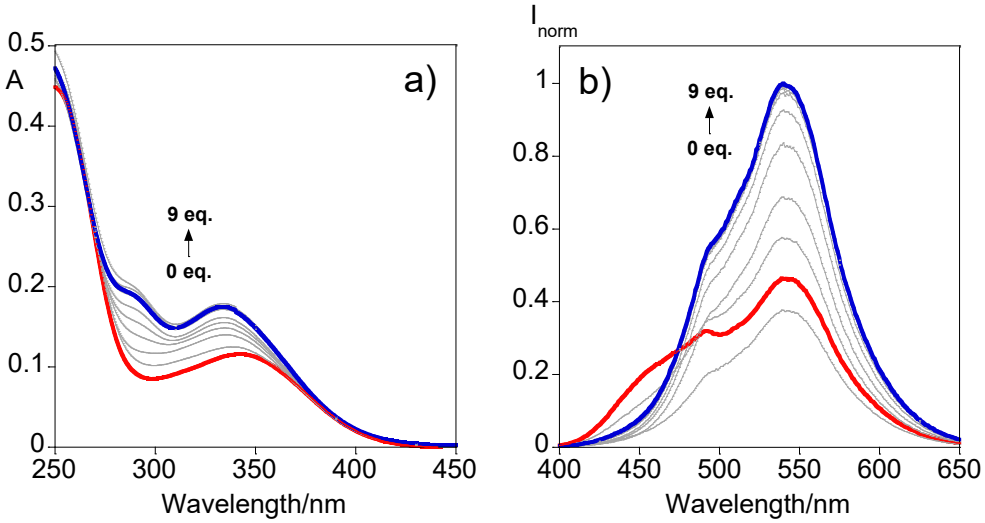


Figure 7–16. UV-vis (a) and emission (performed in JASCO FP-8350) (b) spectra response after the addition of up to 9 equivalents of sodium dithionite.

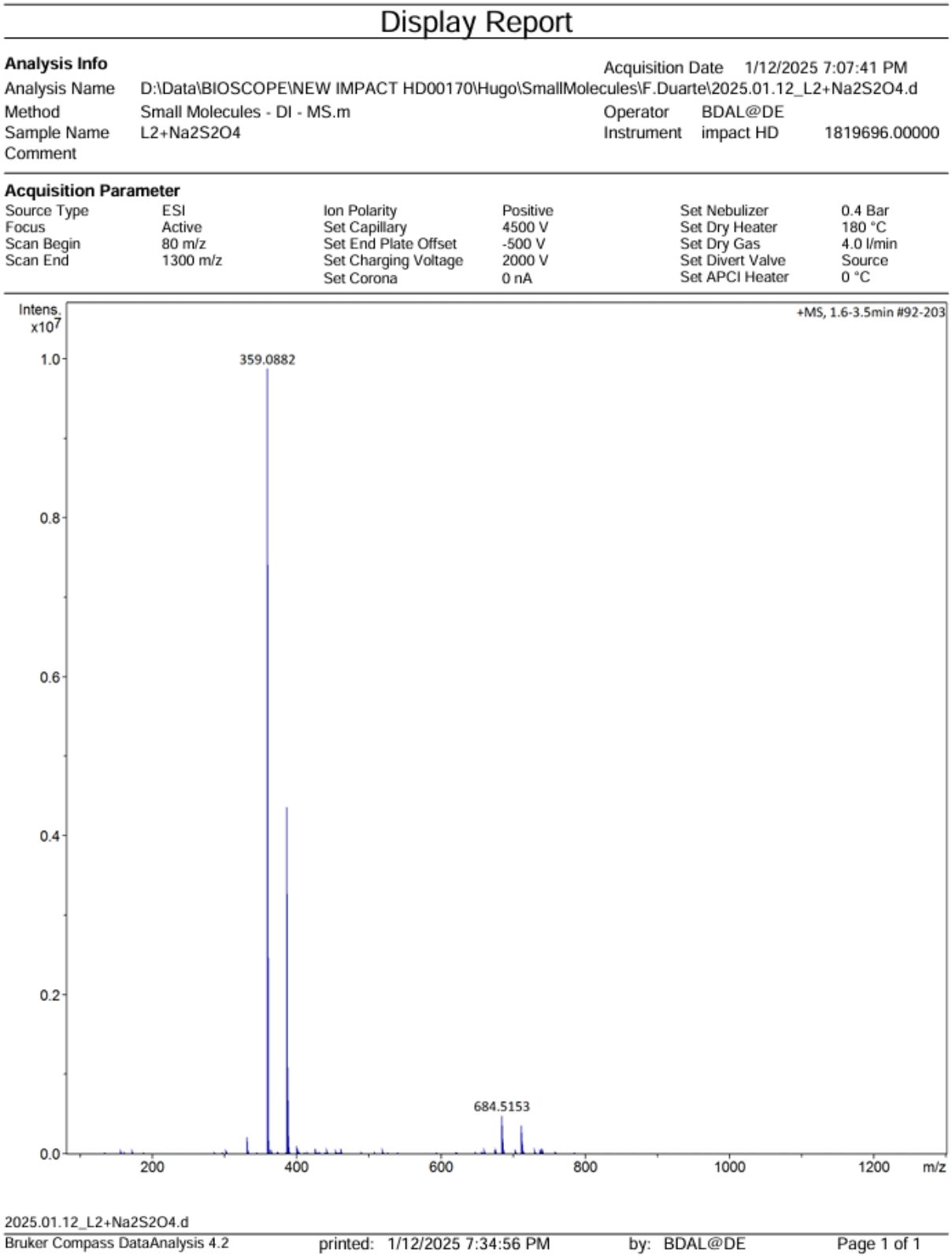


Figure 7–17. ESI-HRMS spectrum of compound L2 after the addition of $Na_2S_2O_4$.

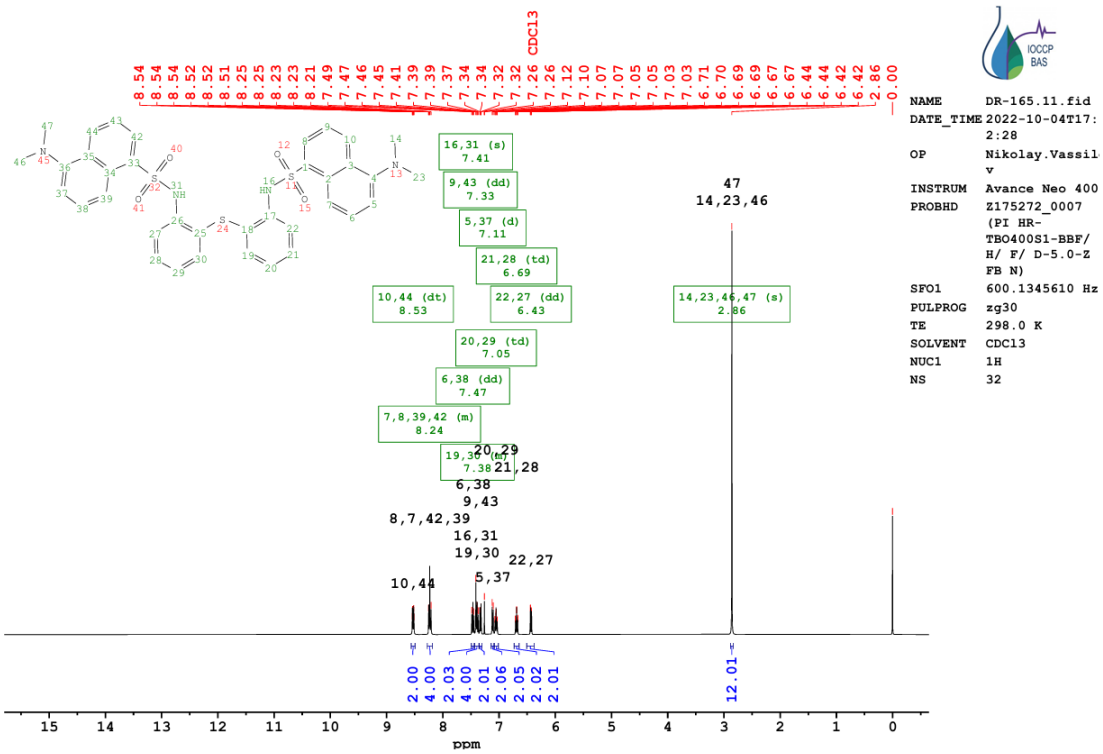


Figure 7–18. ^{1}H-NMR spectrum of compound **L1** in chloroform.

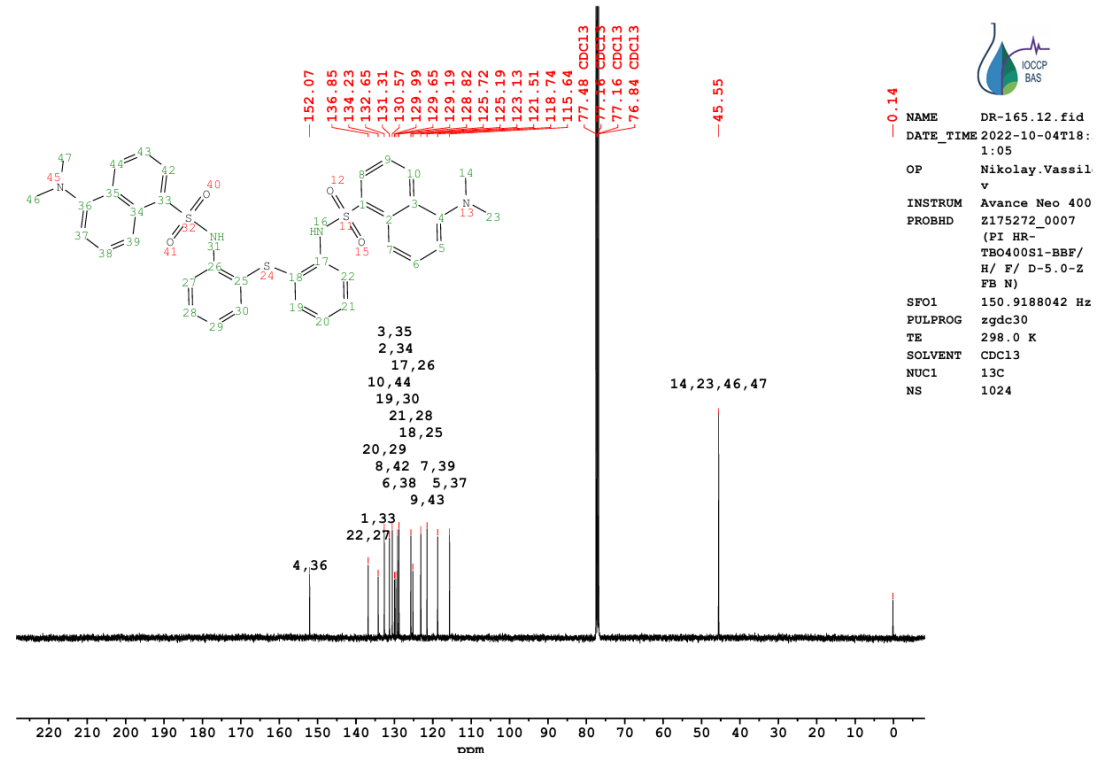


Figure 7–19. ^{13}C-NMR spectrum of compound **L1** in chloroform.

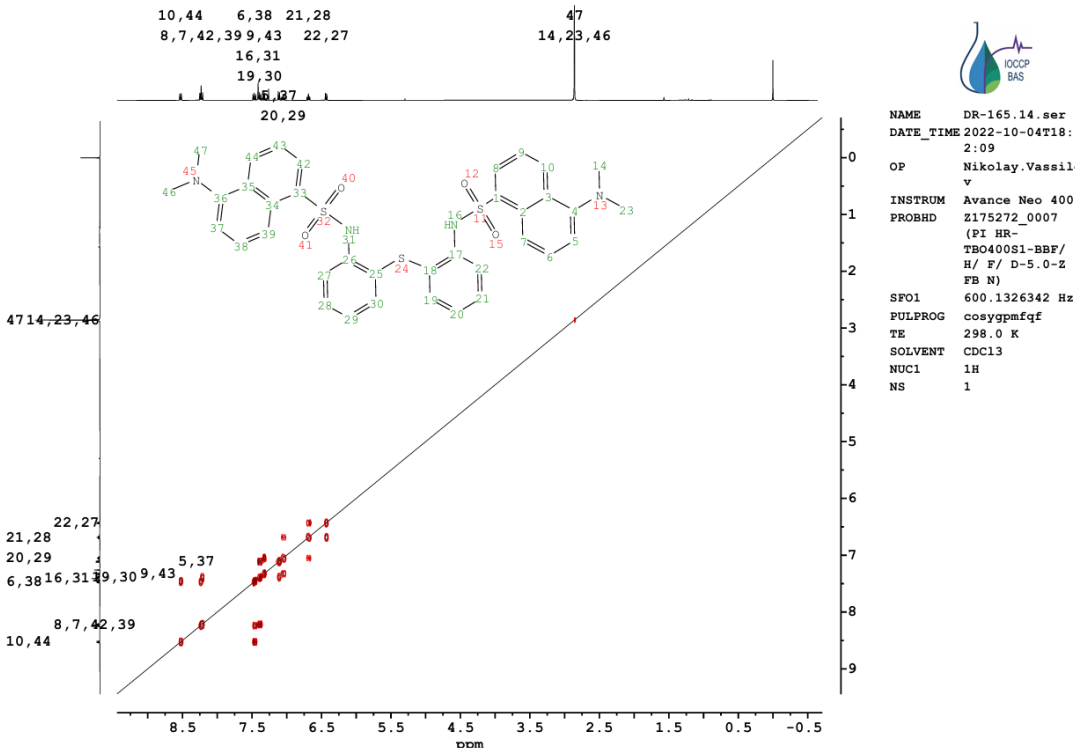


Figure 7–20. COSY-NMR spectrum of compound **L1** in chloroform.

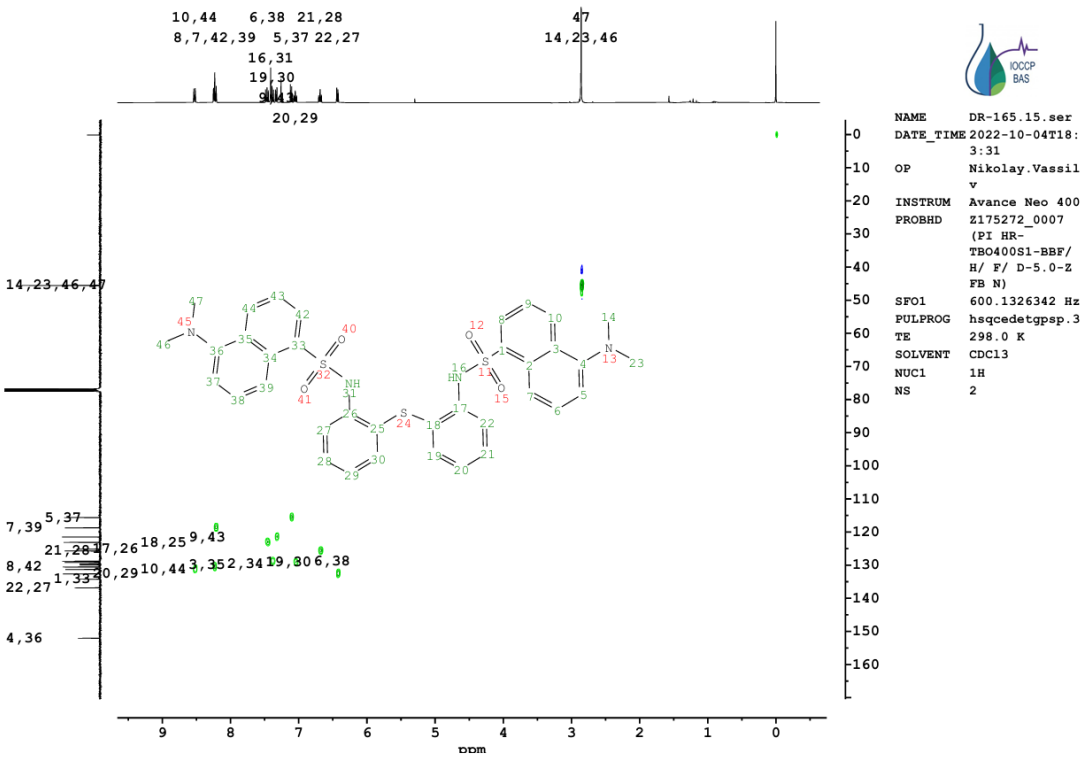


Figure 7–21. HSQC-NMR spectrum of compound **L1** in chloroform.

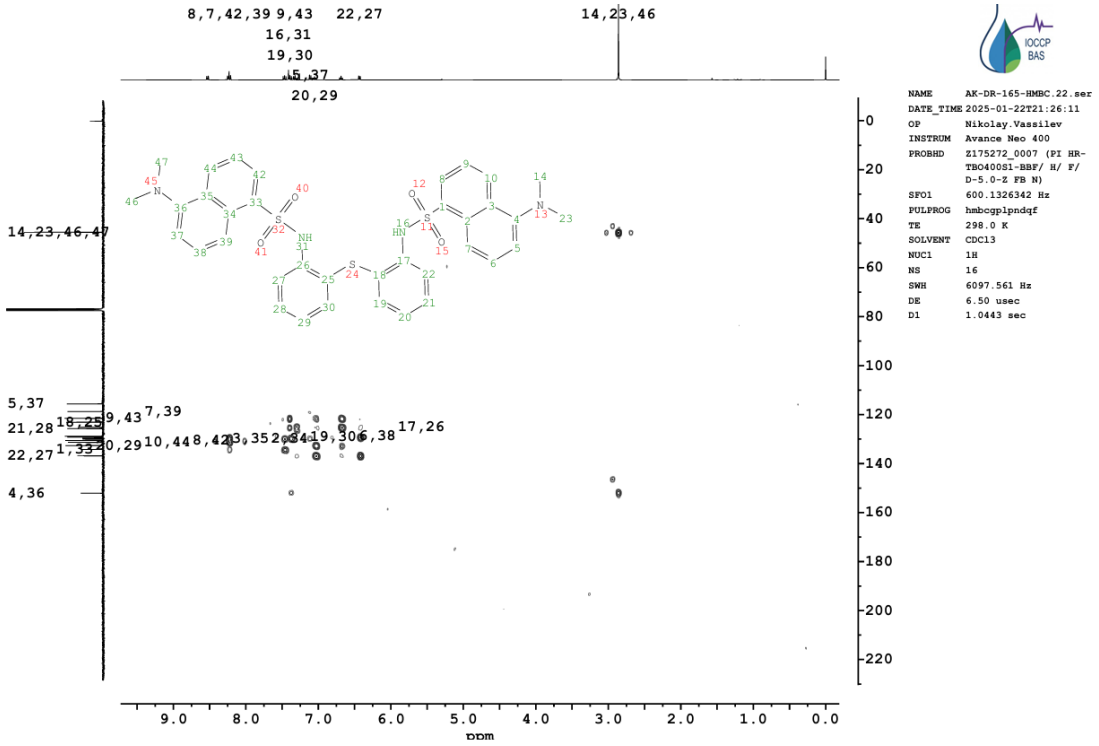


Figure 7–22. HMBC-NMR spectrum of compound **L1** in chloroform.

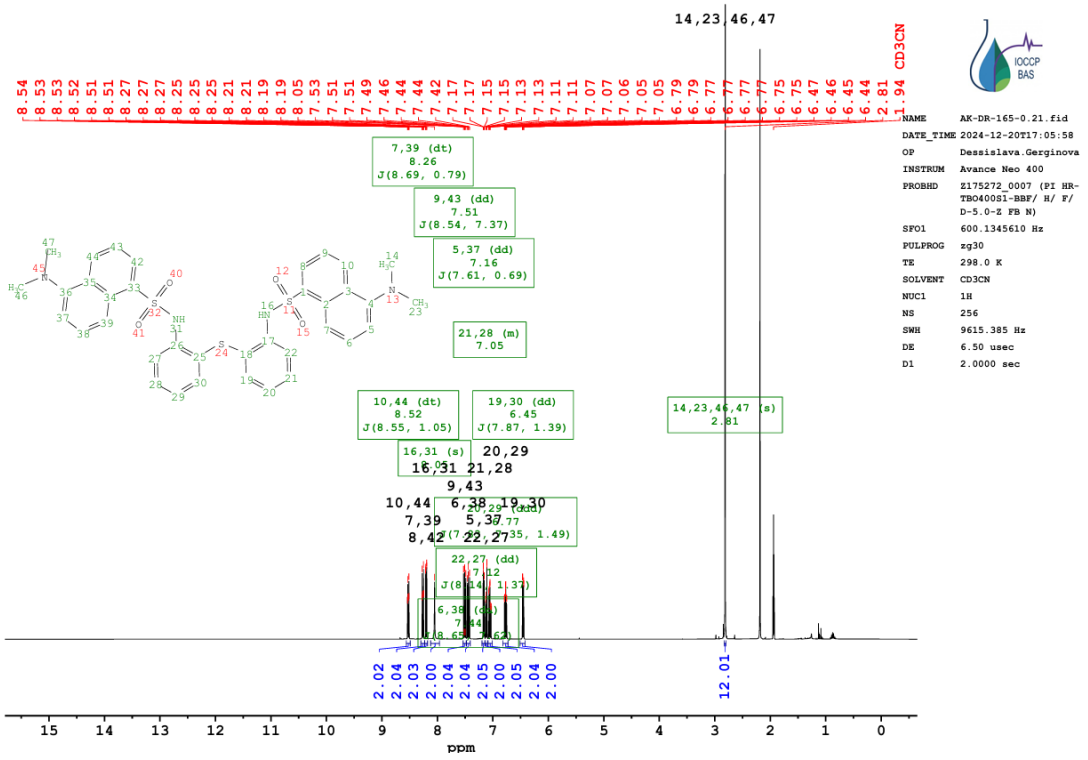


Figure 7–23. ^{1}H-NMR spectrum of compound **L1** in acetonitrile.

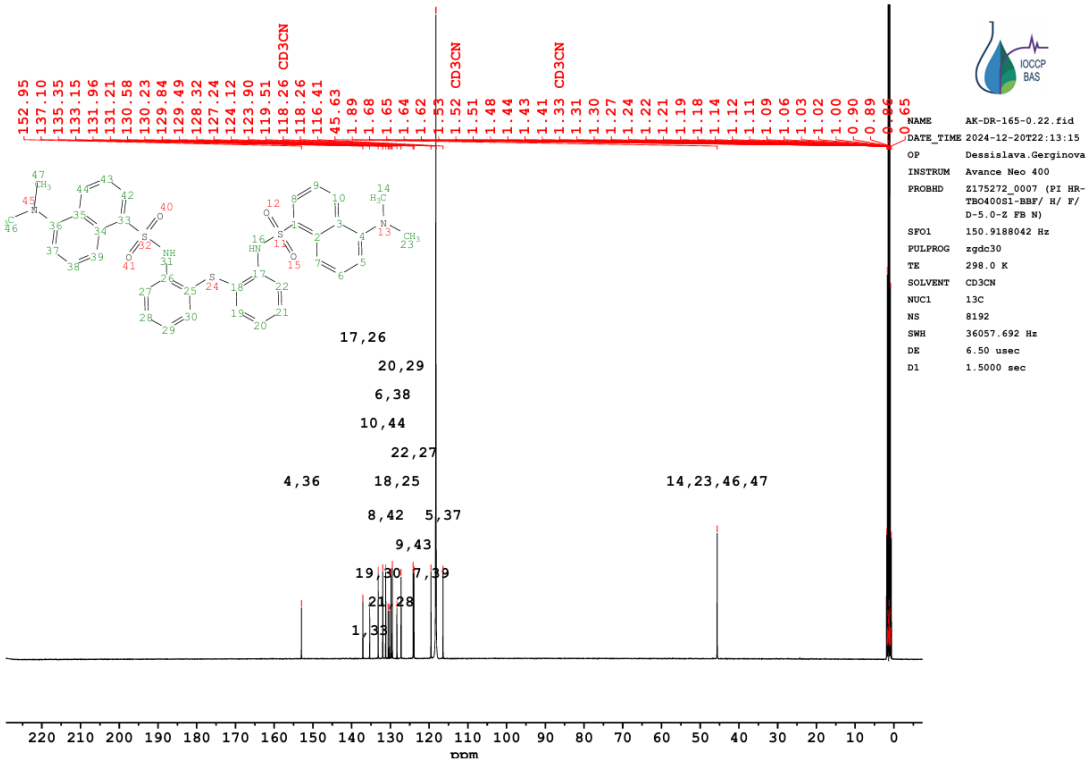


Figure 7–24. ^{13}C-NMR spectrum of compound **L1** in acetonitrile.

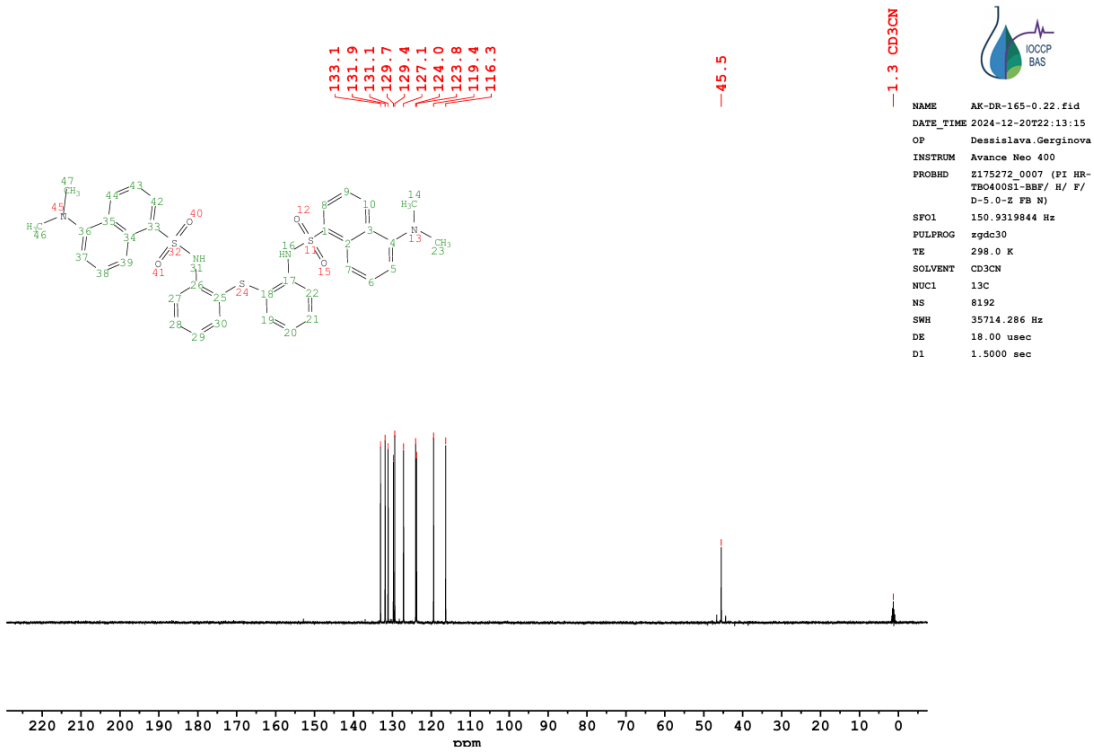


Figure 7–25. DEPT135-NMR spectrum of compound L1 in acetonitrile.

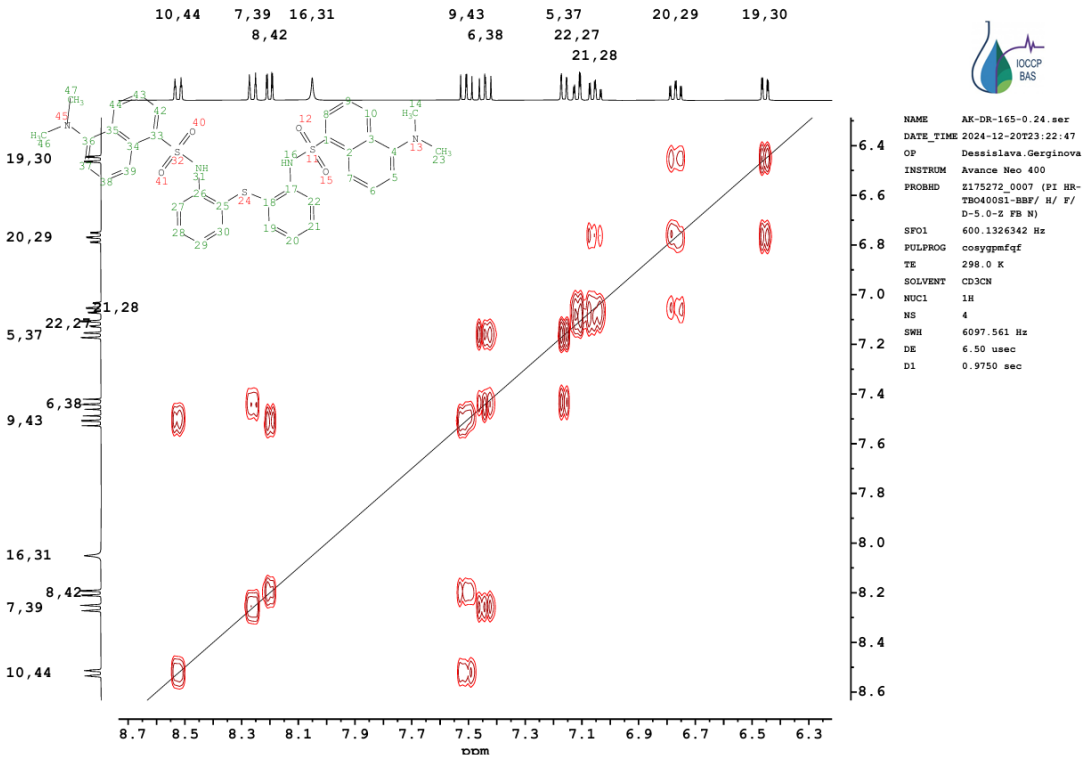


Figure 7–26. COSY-NMR spectrum of compound **L1** in acetonitrile.

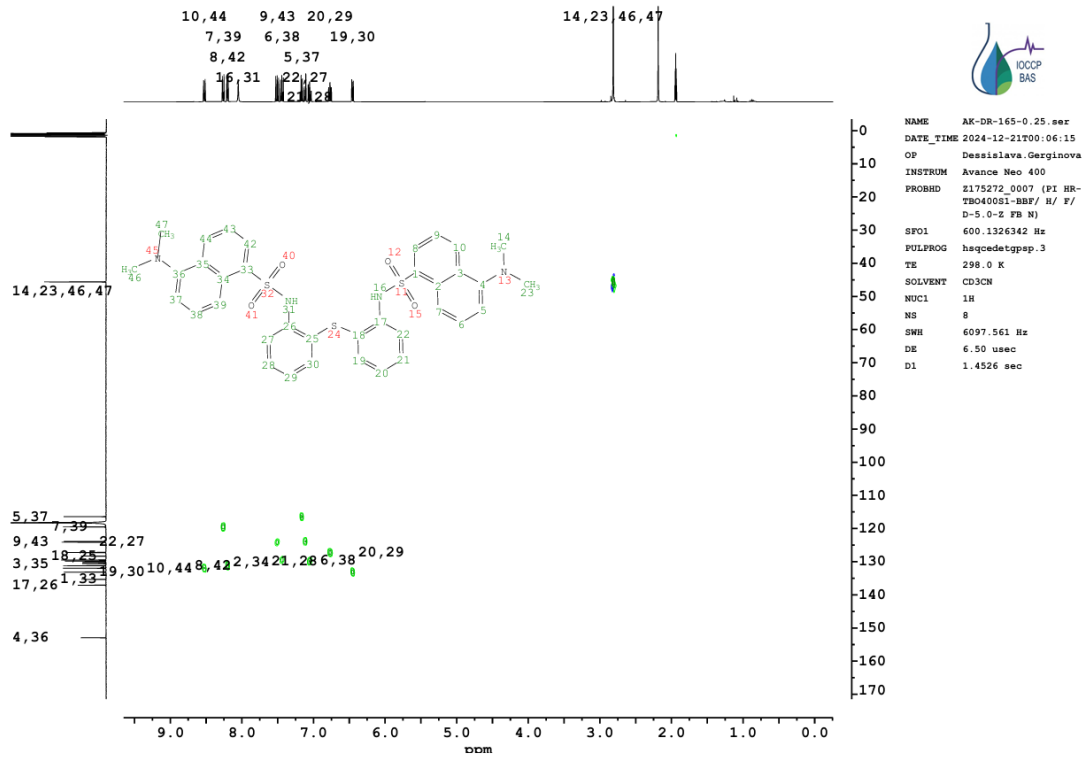


Figure 7–27. HSQC-NMR spectrum of compound **L1** in acetonitrile.

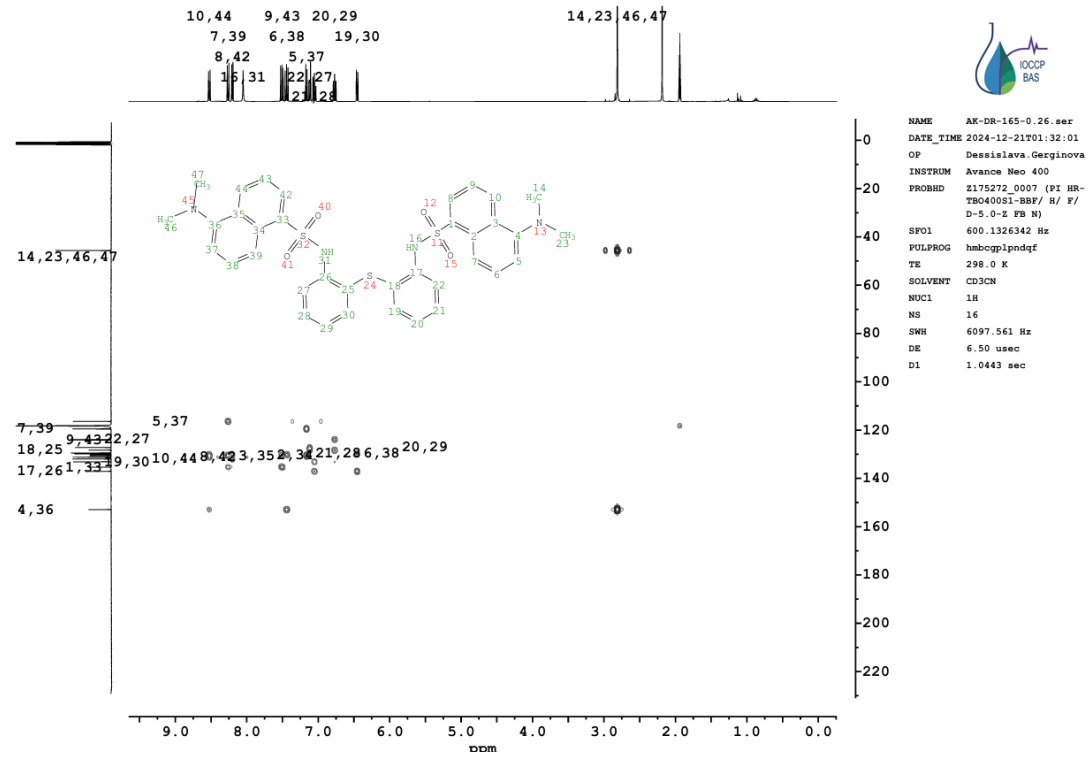


Figure 7–28. HMBC-NMR spectrum of compound **L1** in acetonitrile.

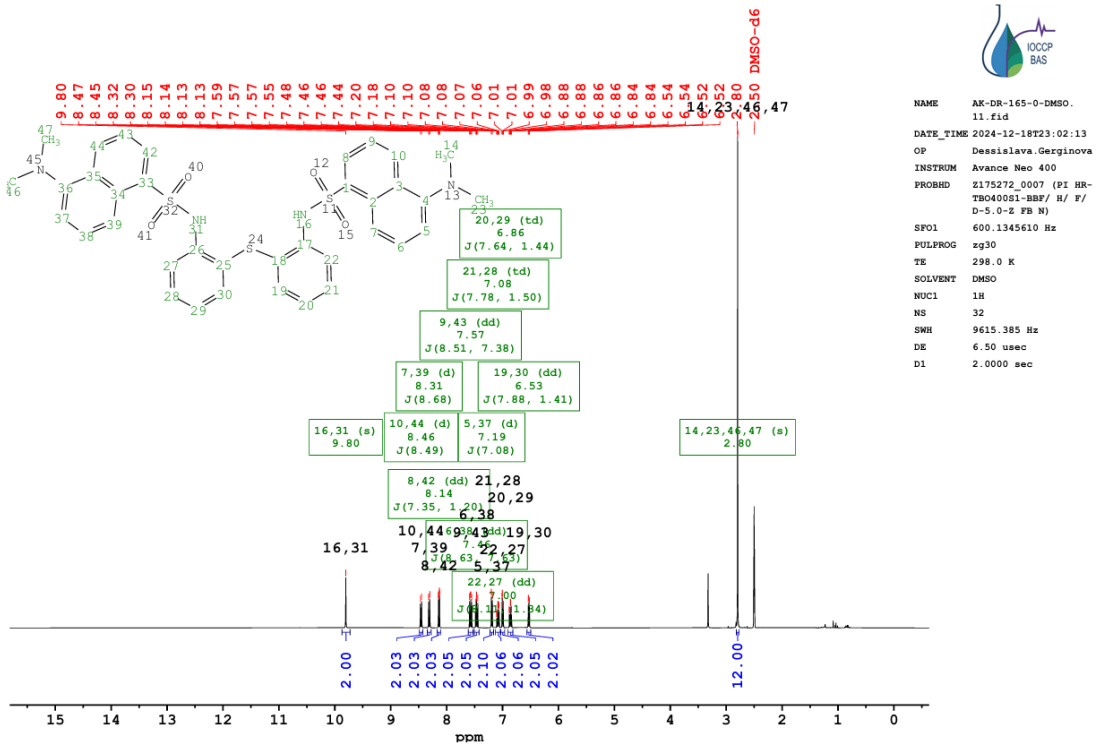


Figure 7–29. ^{1}H-NMR spectrum of compound **L1** in DMSO.

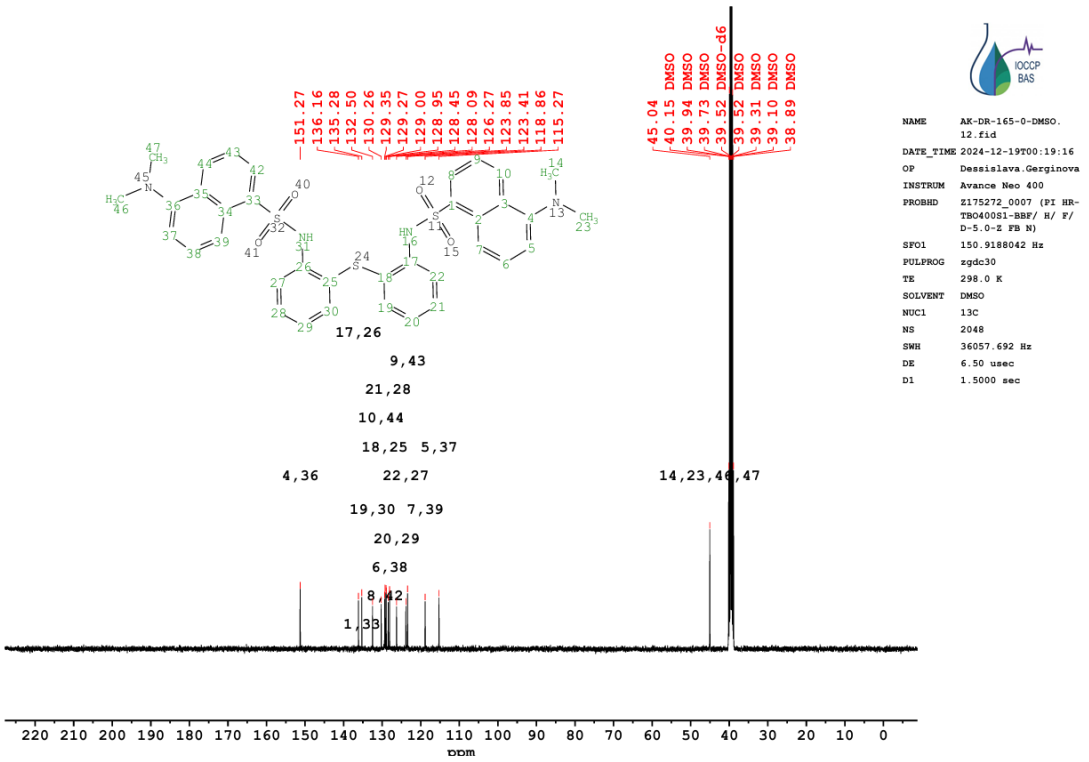


Figure 7–30. ^{13}C-NMR spectrum of compound **L1** in DMSO.

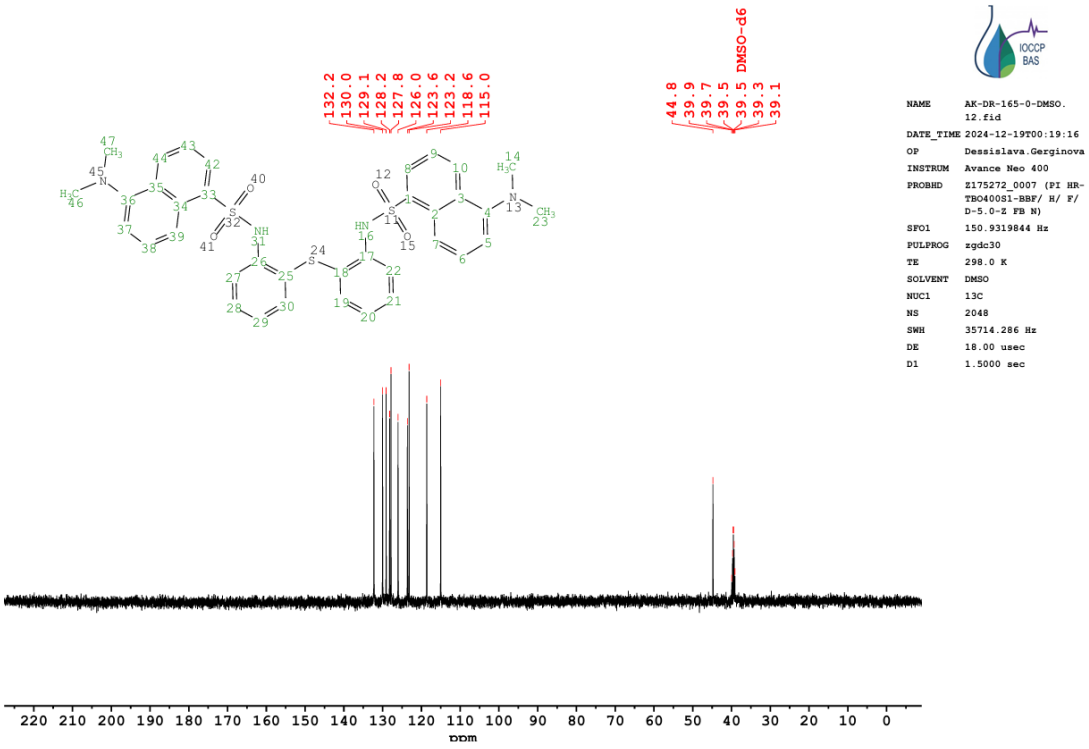


Figure 7–31. DEPT135-NMR spectrum of compound L1 in DMSO.

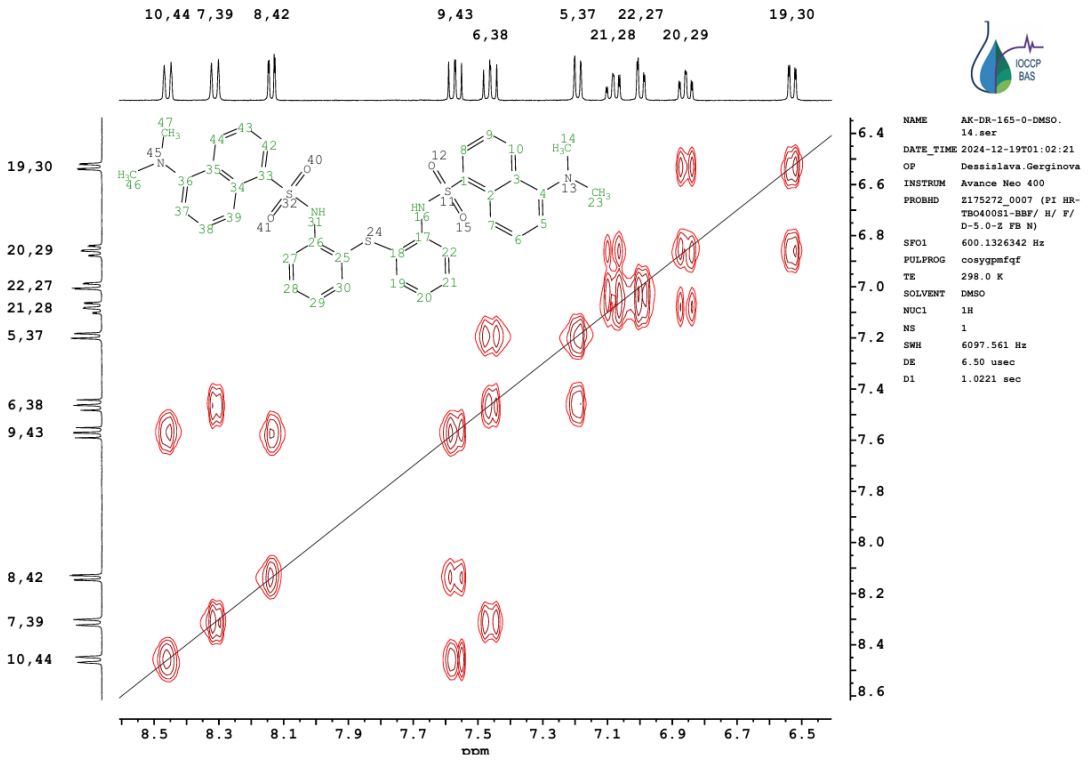


Figure 7–32. COSY-NMR spectrum of compound L1 in DMSO.

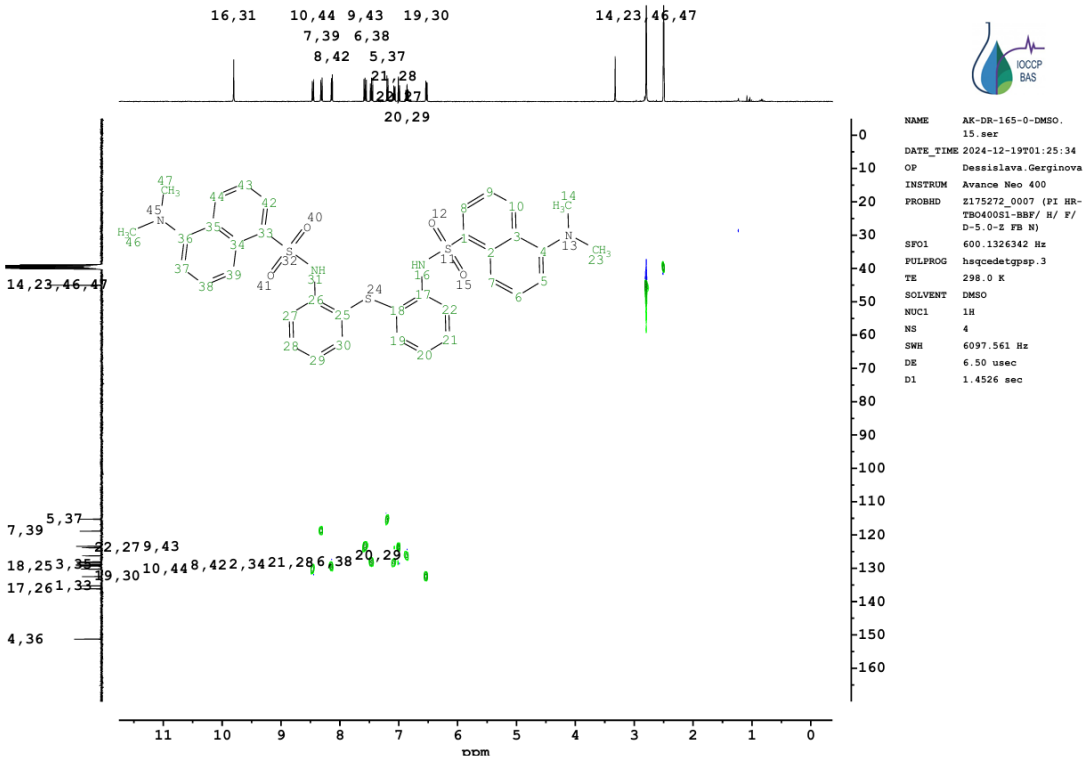


Figure 7–33. HSQC-NMR spectrum of compound **L1** in DMSO.

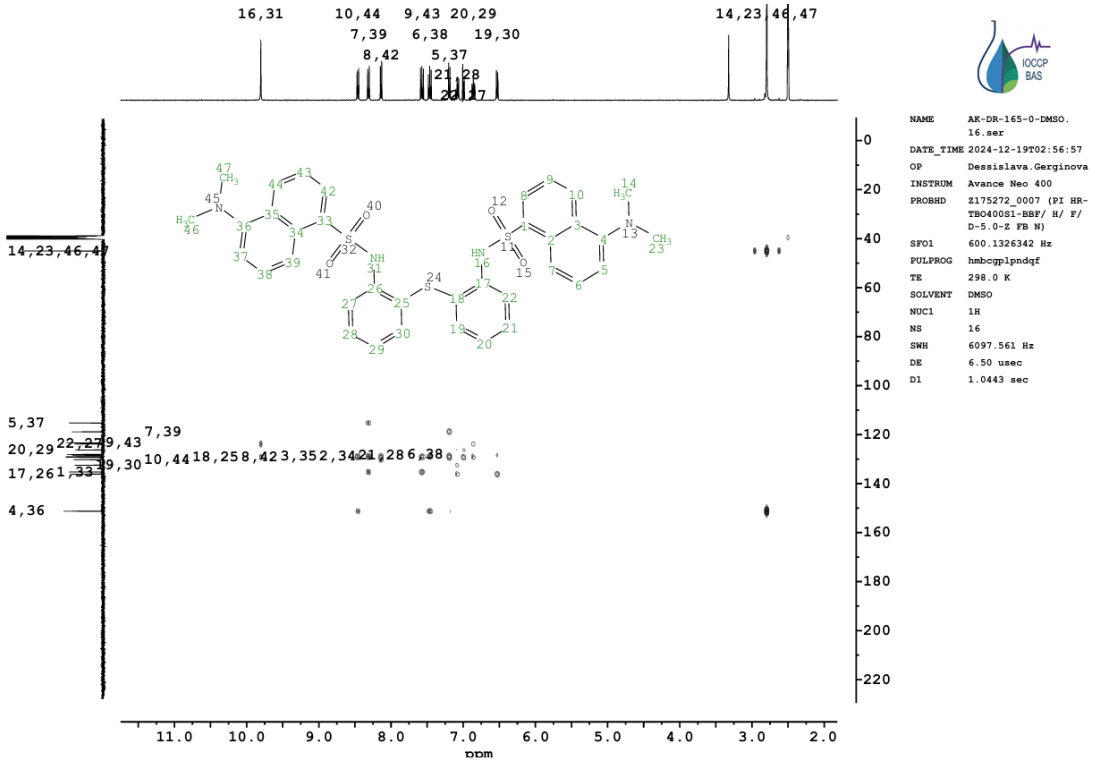


Figure 7–34. HMBC-NMR spectrum of compound L1 in DMSO.

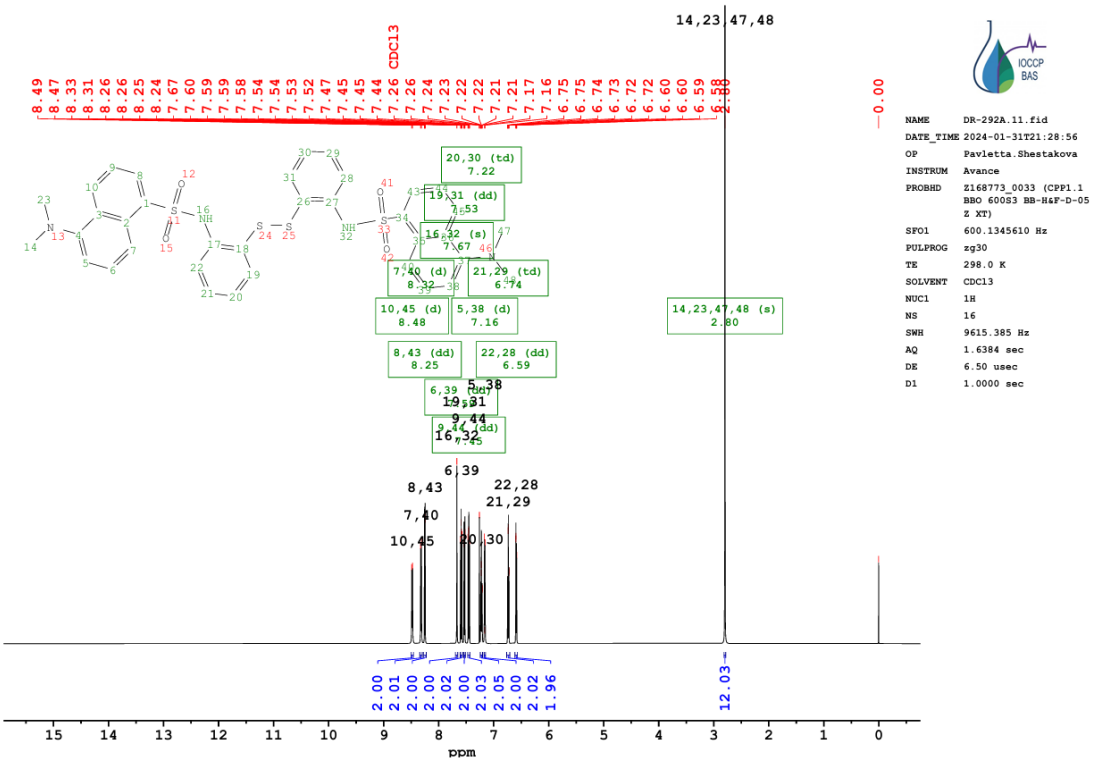


Figure 7–35. ^{1}H-NMR spectrum of compound **L2** in chloroform.

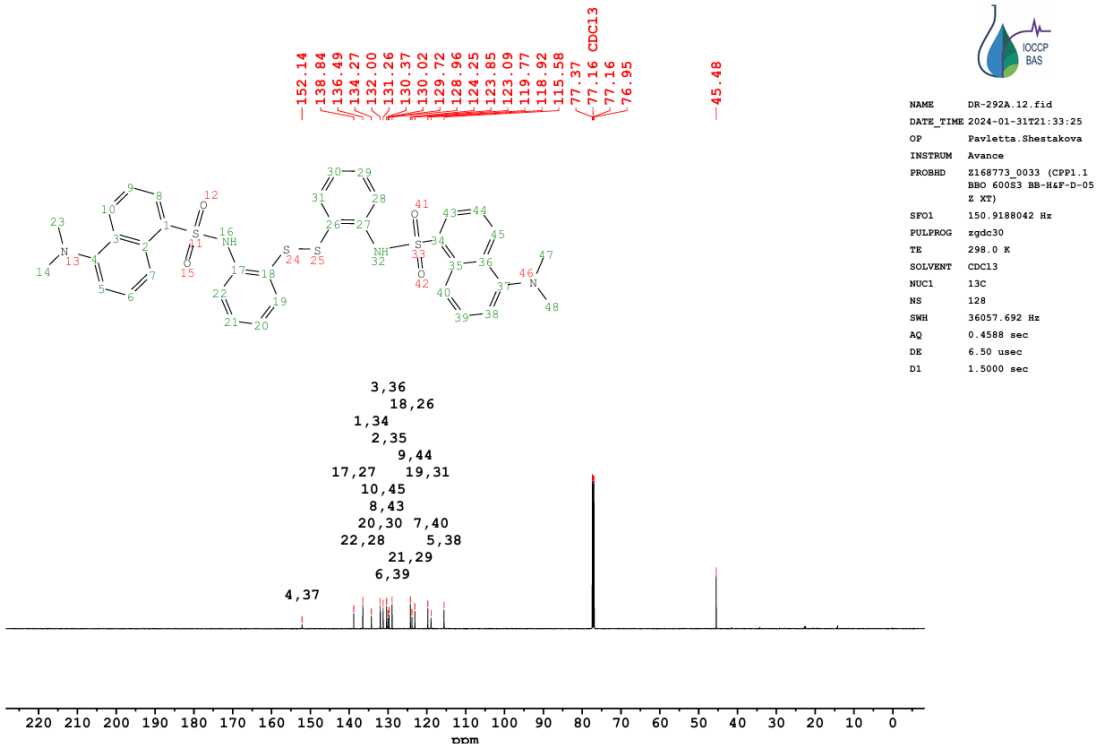


Figure 7–36. ^{13}C-NMR spectrum of compound **L2** in chloroform.

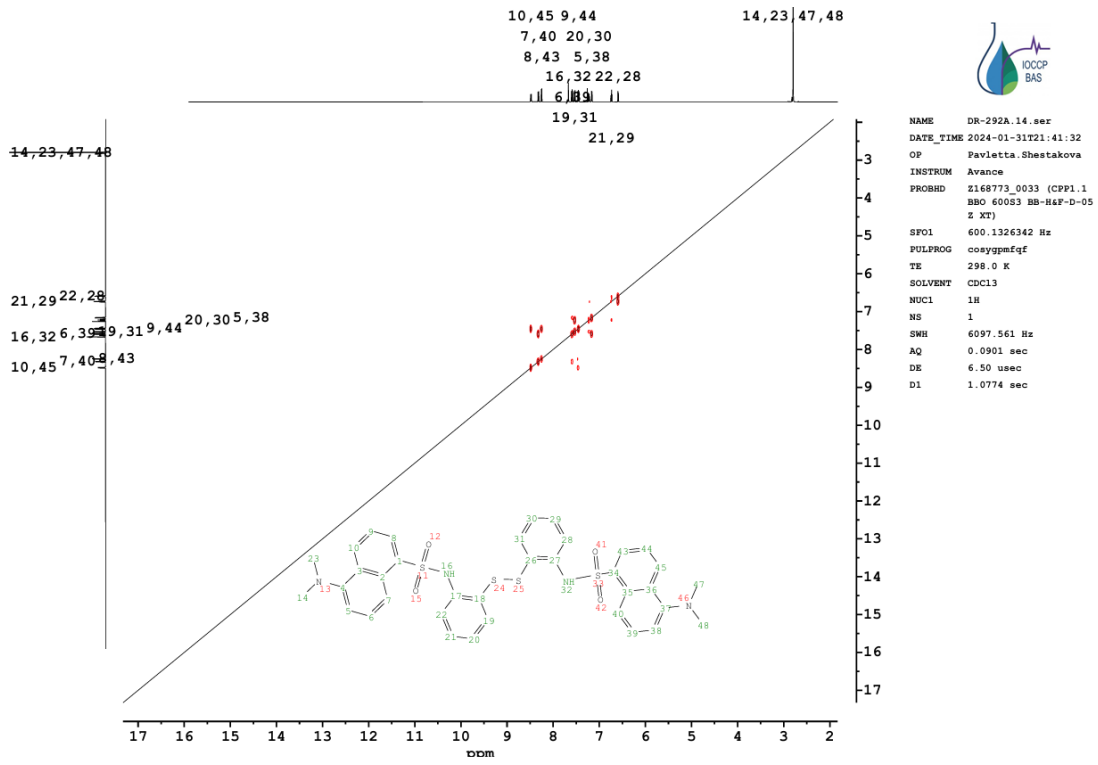


Figure 7–37. COSY-NMR spectrum of compound **L2** in chloroform.

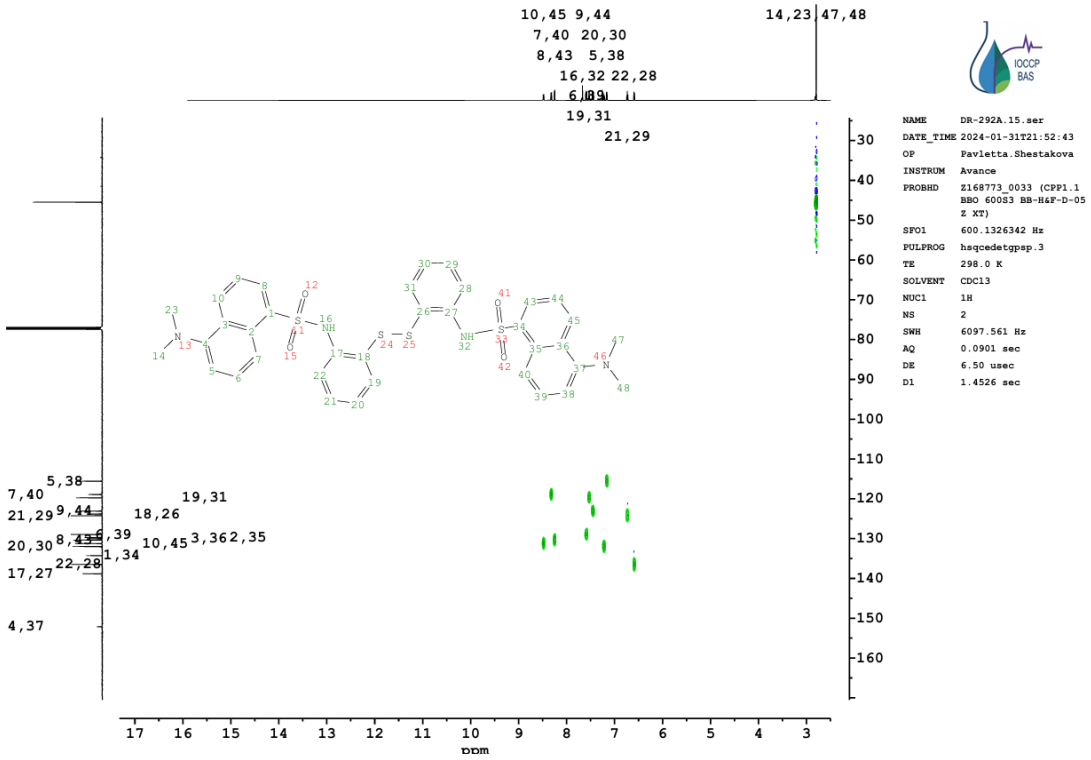


Figure 7–38. HSQC-NMR spectrum of compound **L2** in chloroform.

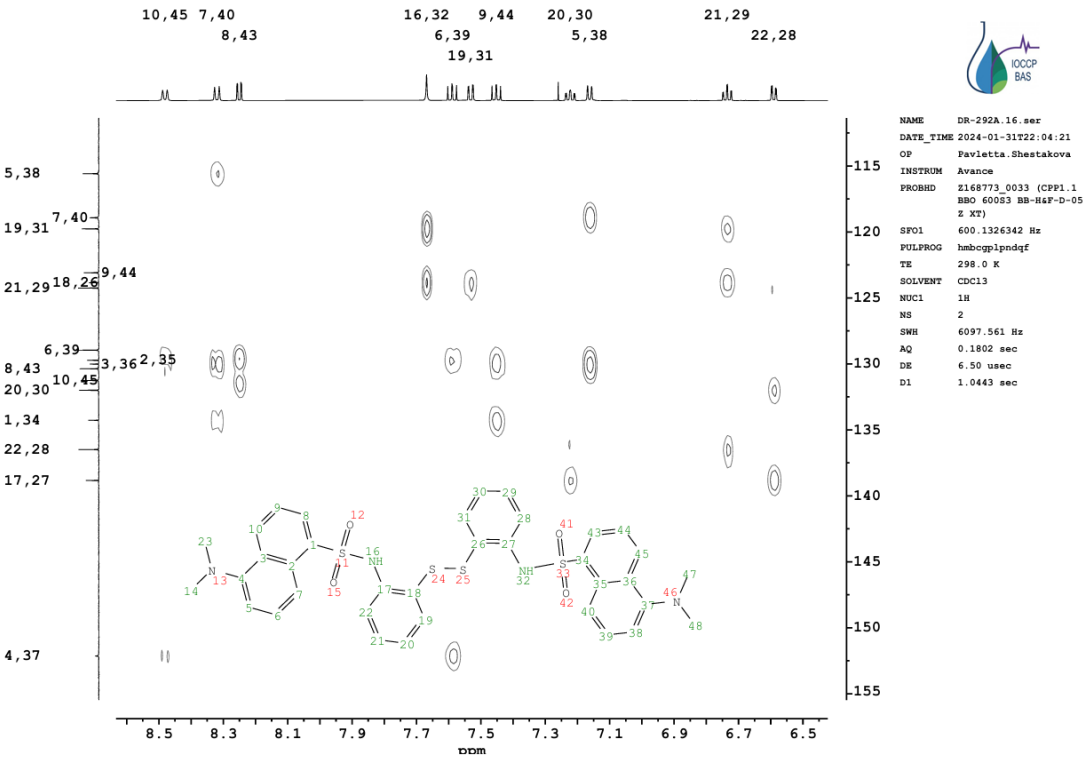


Figure 7–39. HMBC-NMR spectrum of compound **L2** in chloroform.

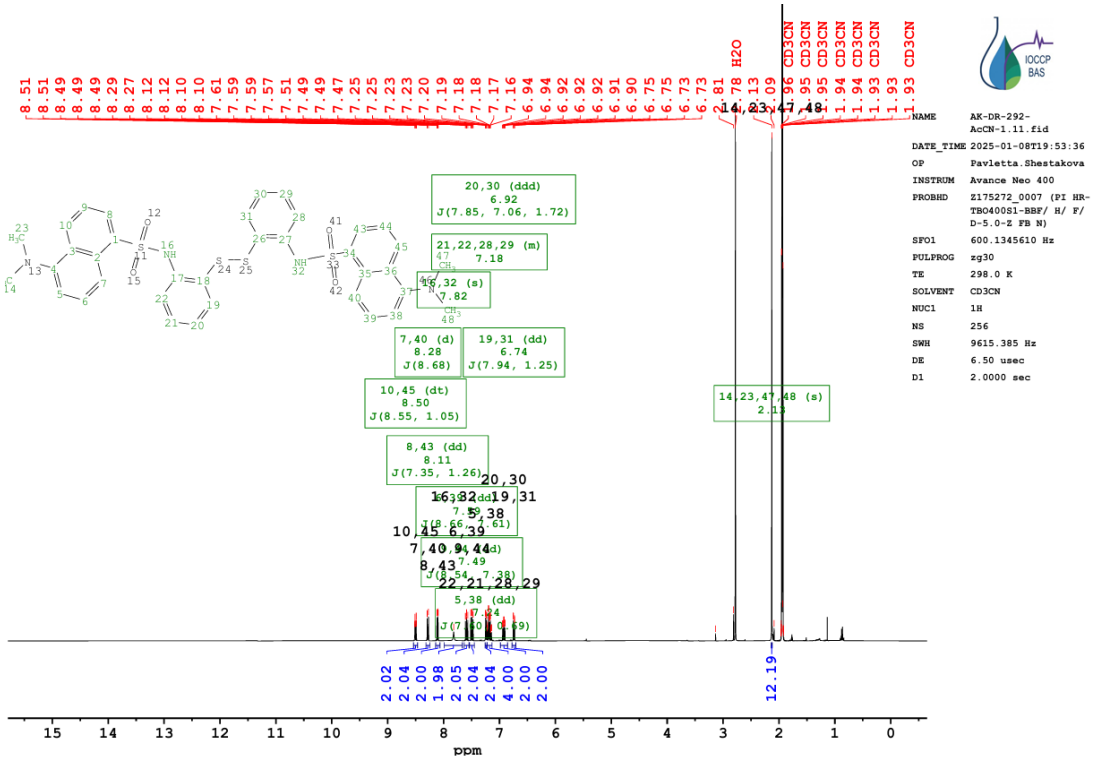


Figure 7–40. ^{1}H-NMR spectrum of compound **L2** in acetonitrile.

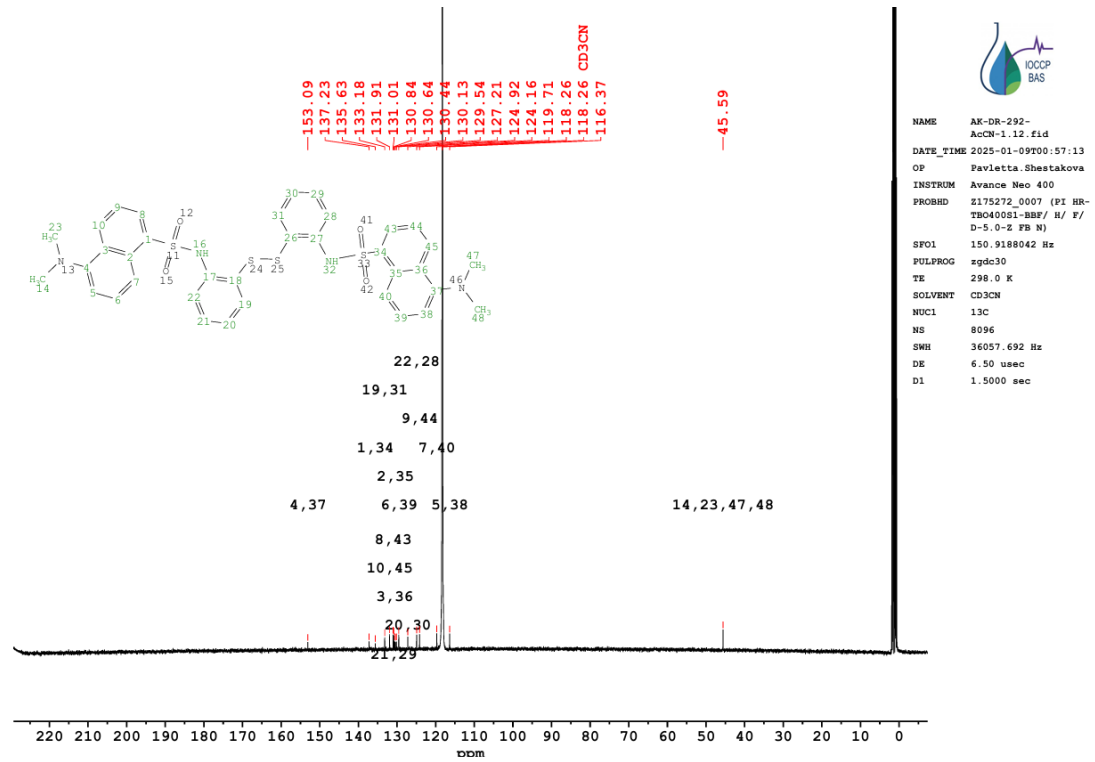


Figure 7–41. ^{13}C-NMR spectrum of compound **L2** in acetonitrile.

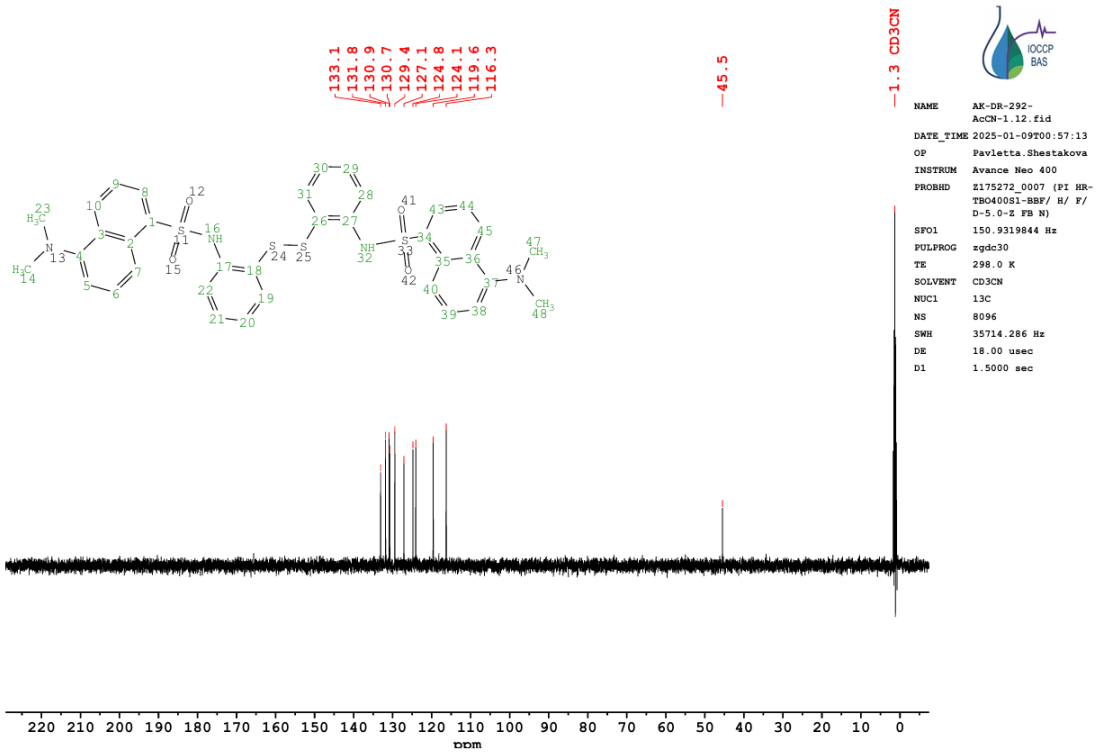


Figure 7–42. DEPT135-NMR spectrum of compound L1 in acetonitrile.

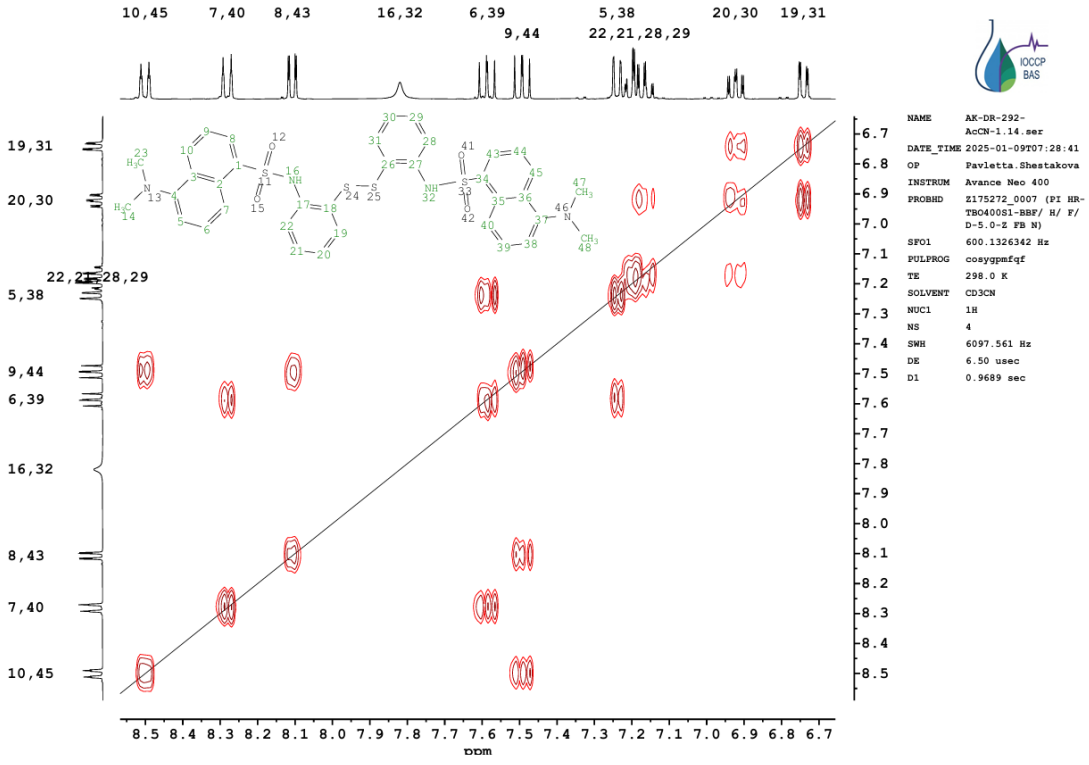


Figure 7–43. COSY-NMR spectrum of compound **L2** in acetonitrile.

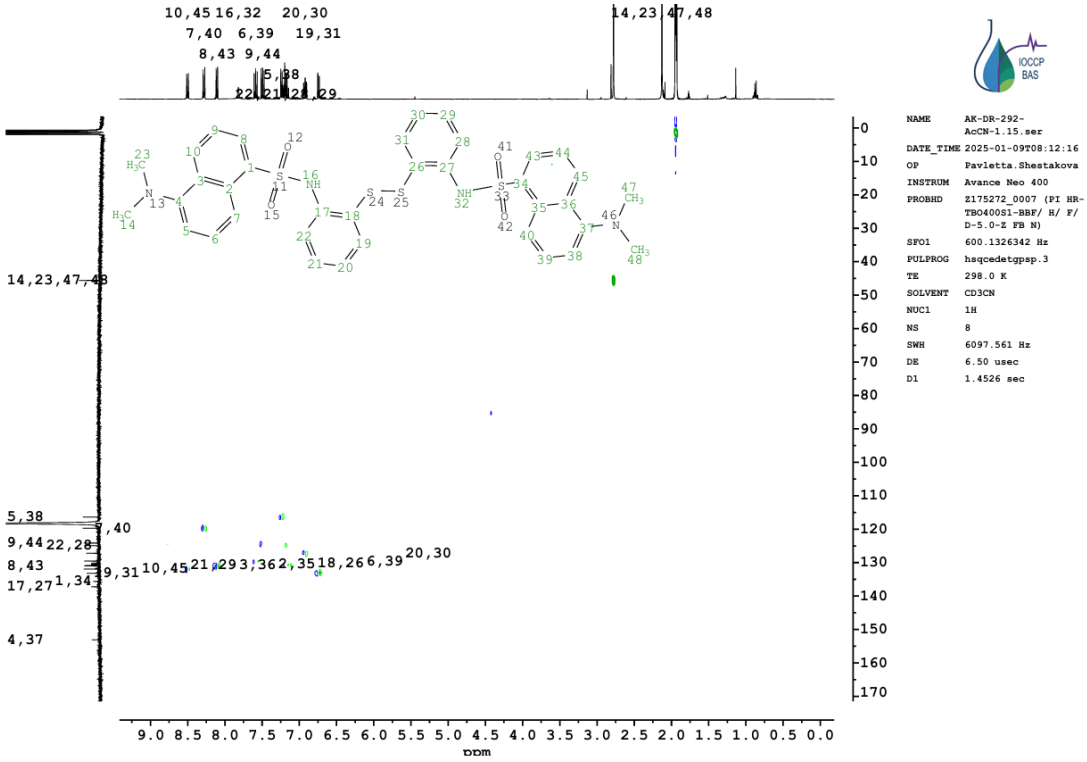


Figure 7–44. HSQC-NMR spectrum of compound **L2** in acetonitrile.

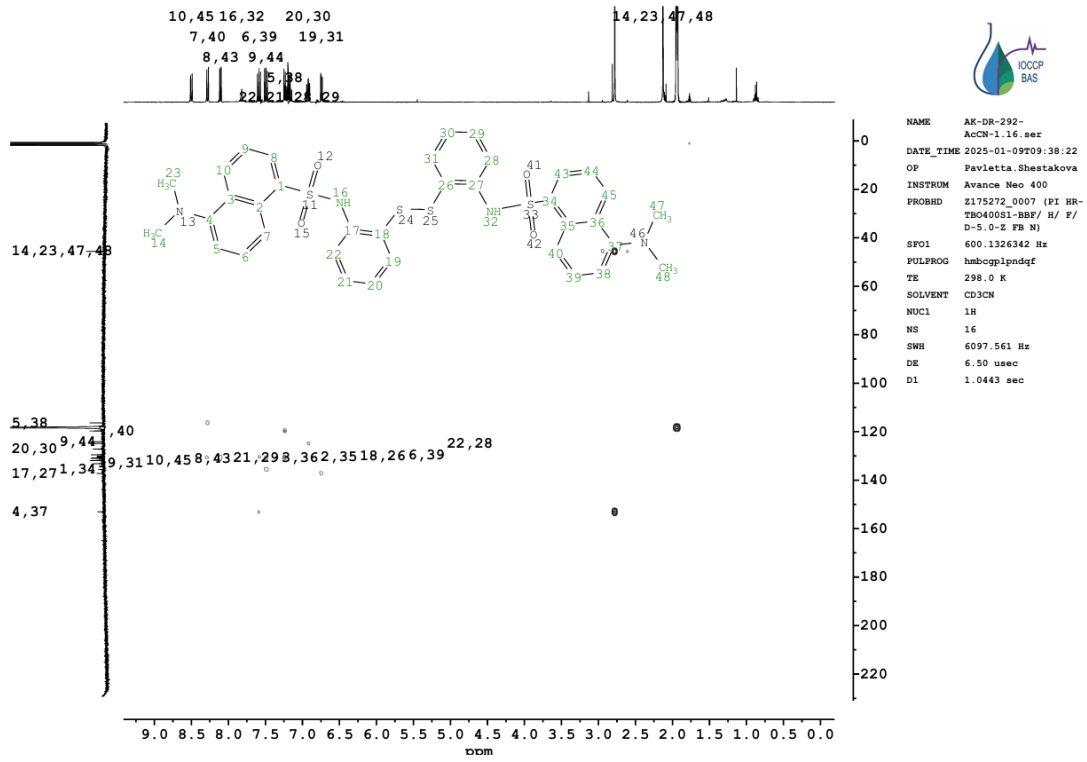


Figure 7–45. HMBC-NMR spectrum of compound **L2** in acetonitrile.

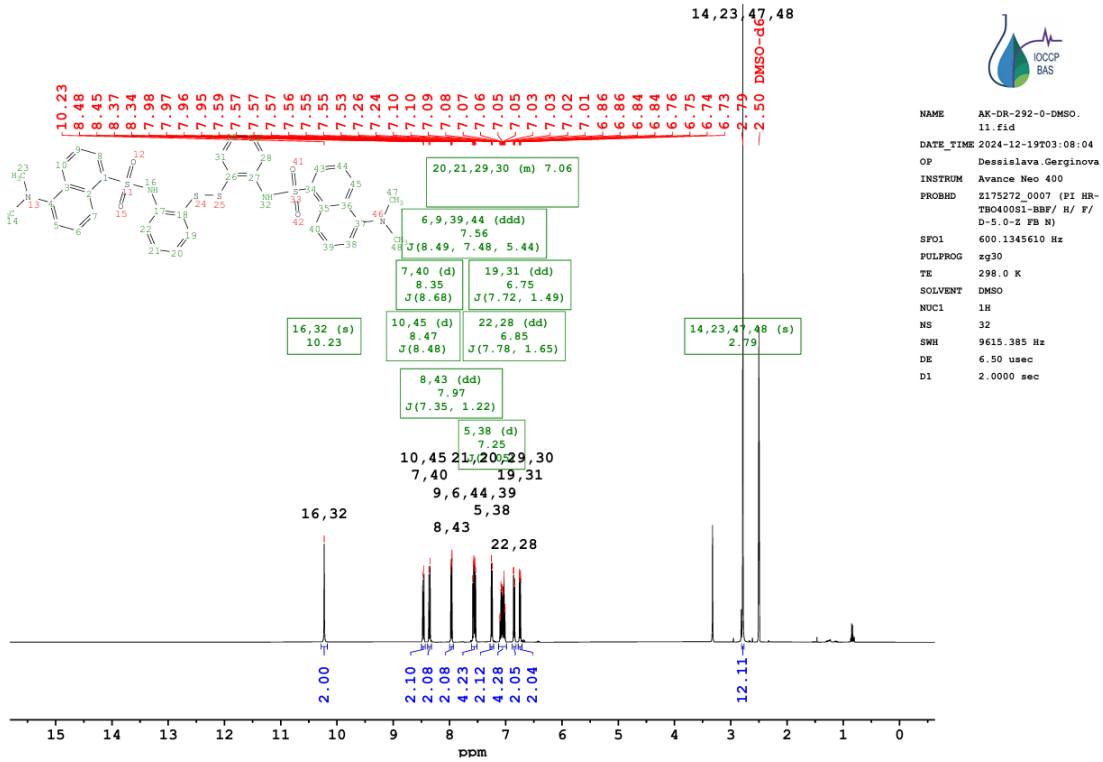


Figure 7–46. ^{1}H-NMR spectrum of compound **L2** in DMSO.

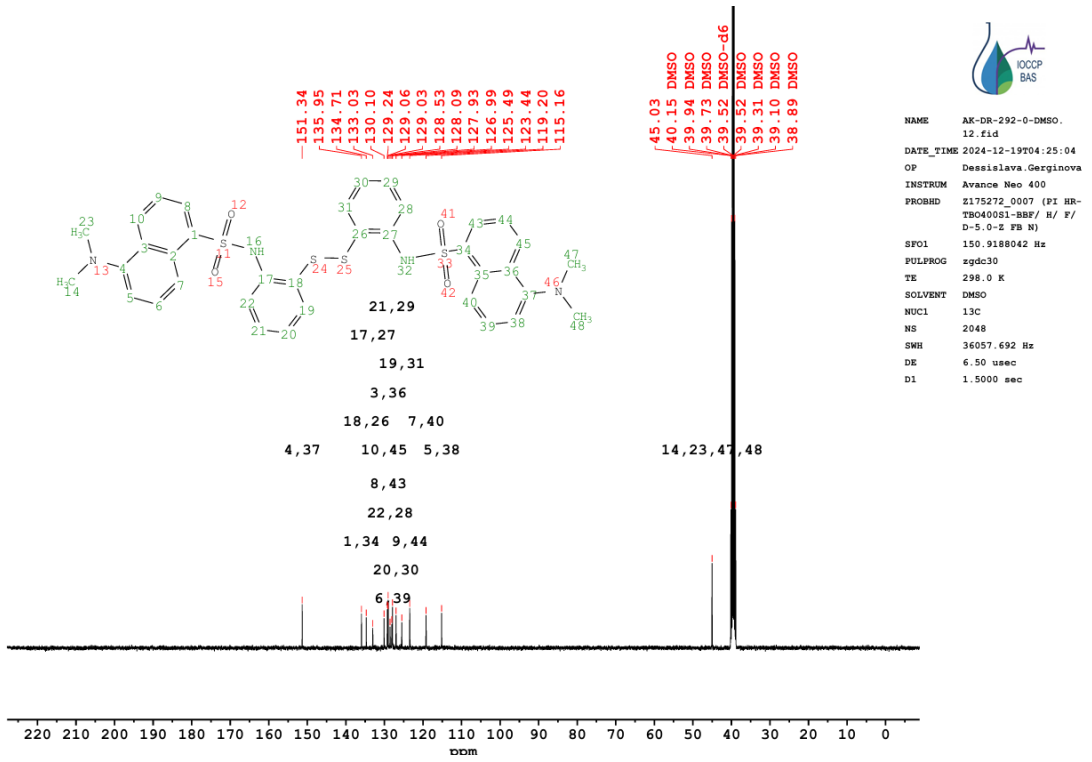


Figure 7–47. ^{13}C-NMR spectrum of compound **L2** in DMSO.

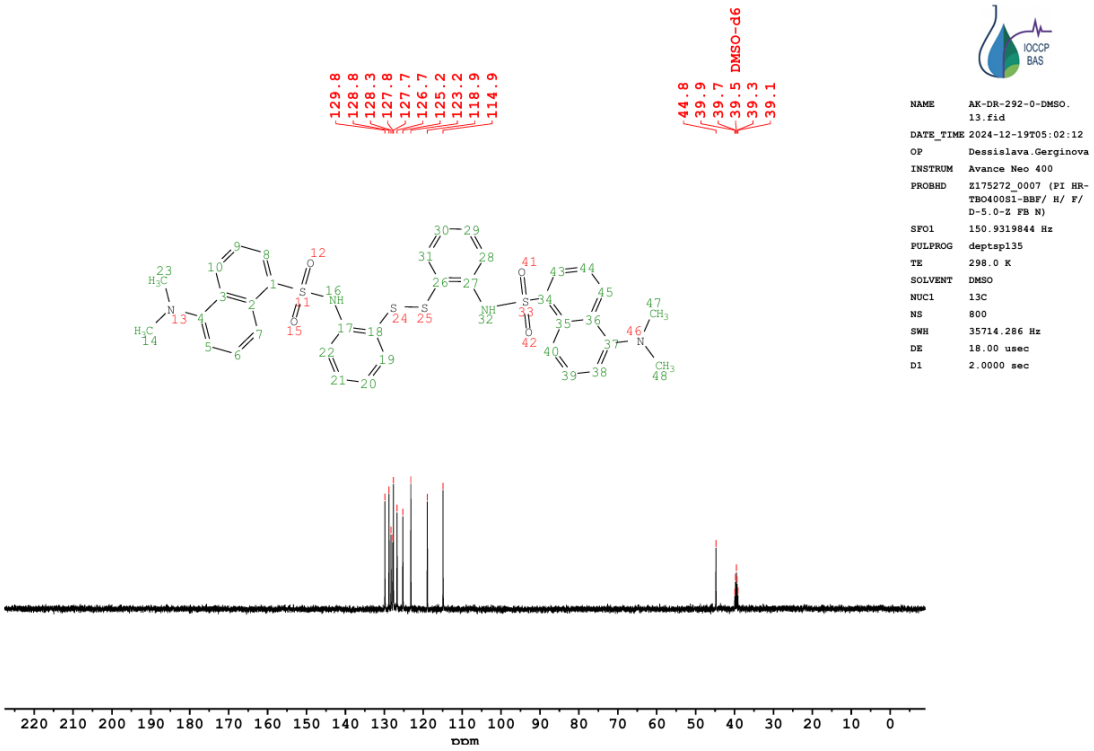


Figure 7–48. DEPT135-NMR spectrum of compound L2 in DMSO.

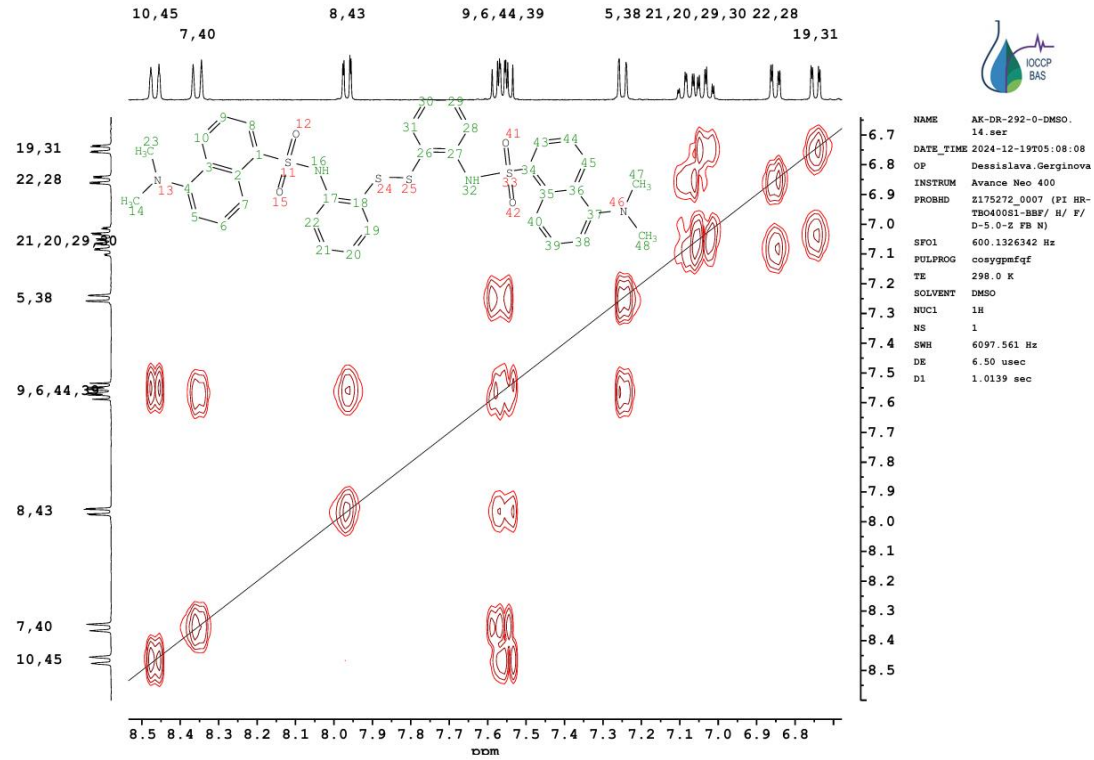


Figure 7–49. COSY-NMR spectrum of compound L2 in DMSO.

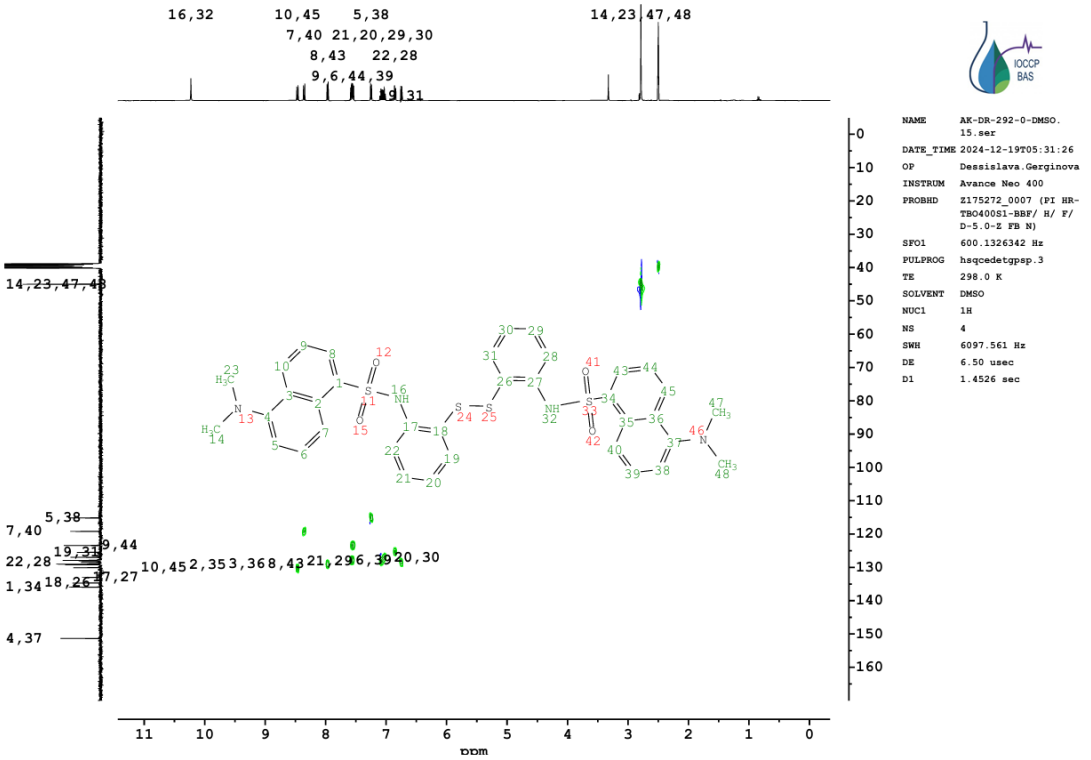


Figure 7–50. HSQC-NMR spectrum of compound **L2** in DMSO.

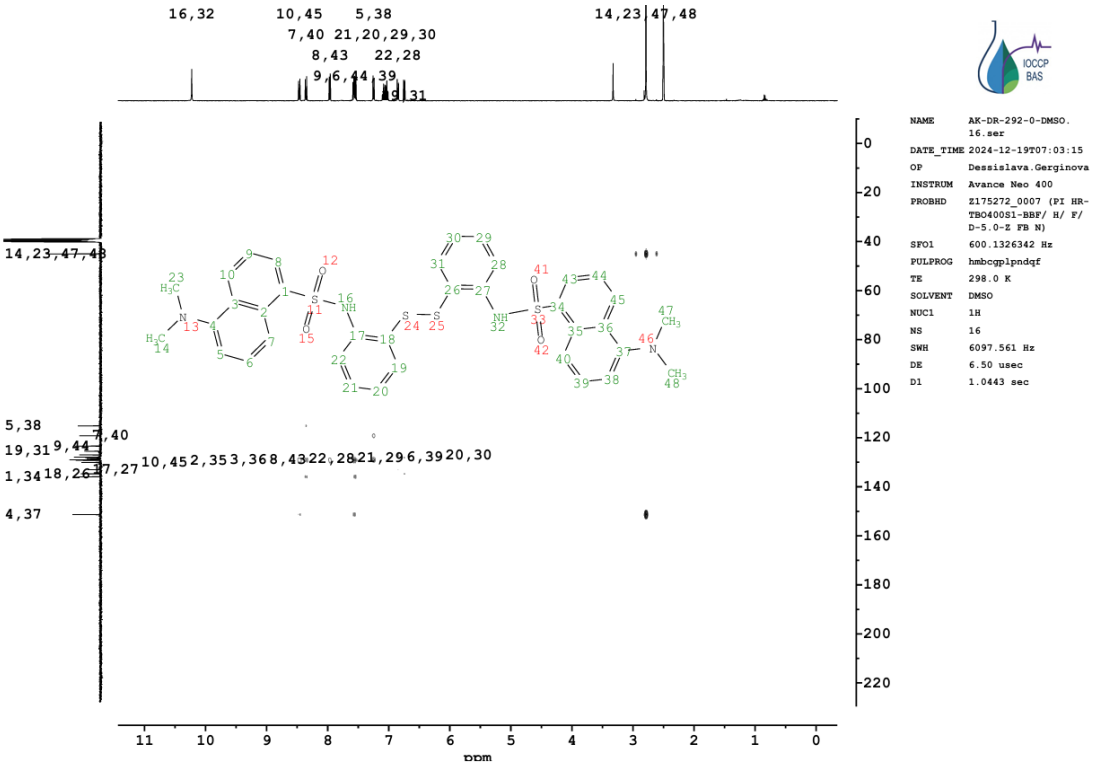


Figure 7–51. HMBC-NMR spectrum of compound L1 in DMSO.

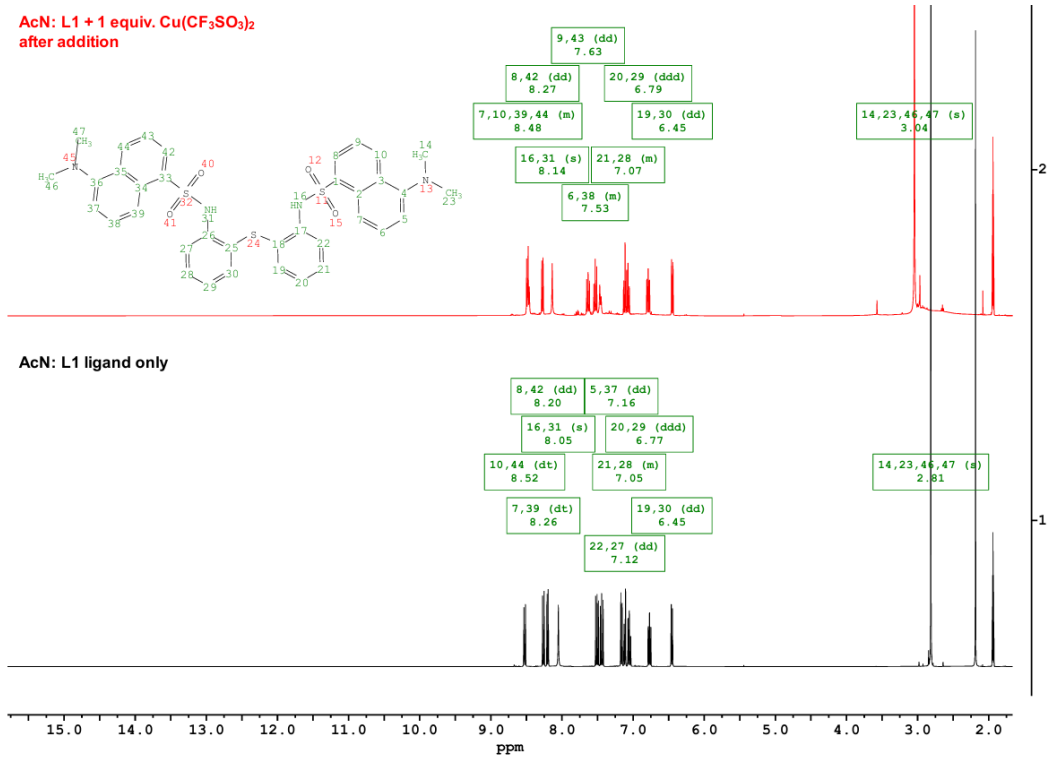


Figure 7–52. Comparison between ^{1}H-NMR spectra of compound L1 in acetonitrile before and after the addition of 1 eq. of Cu^{2+}.

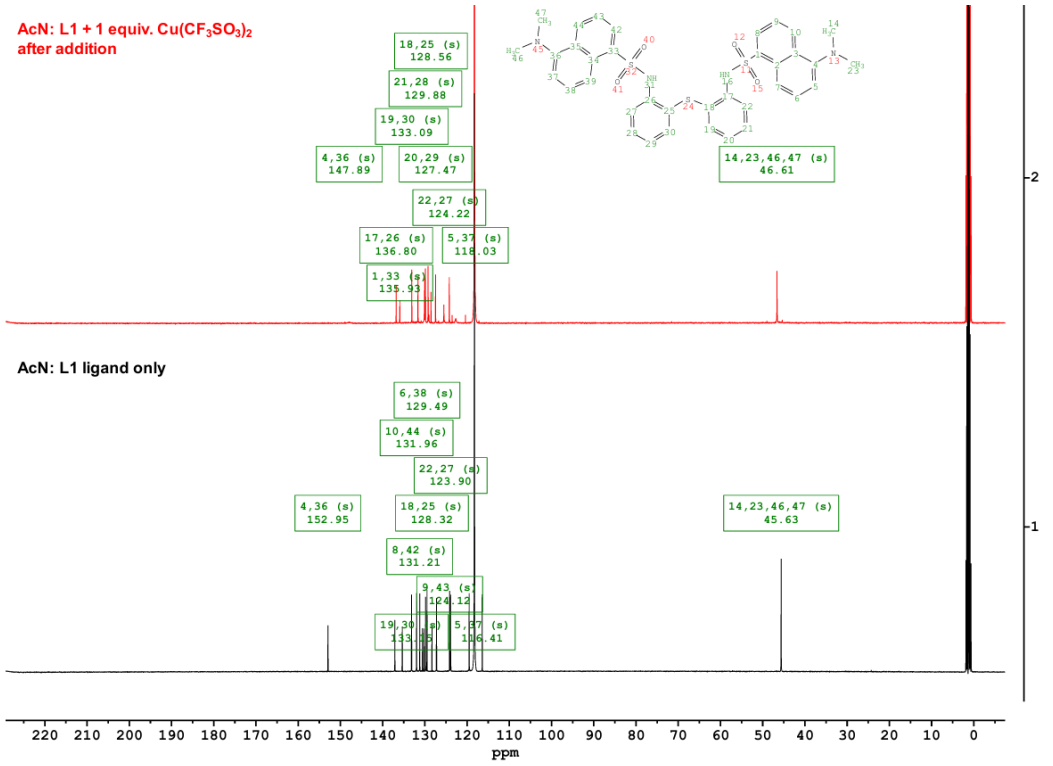


Figure 7–53. Comparison between ^{13}C-NMR spectra of compound **L1** in acetonitrile before and after the addition of 1 eq. of Cu^{2+}.

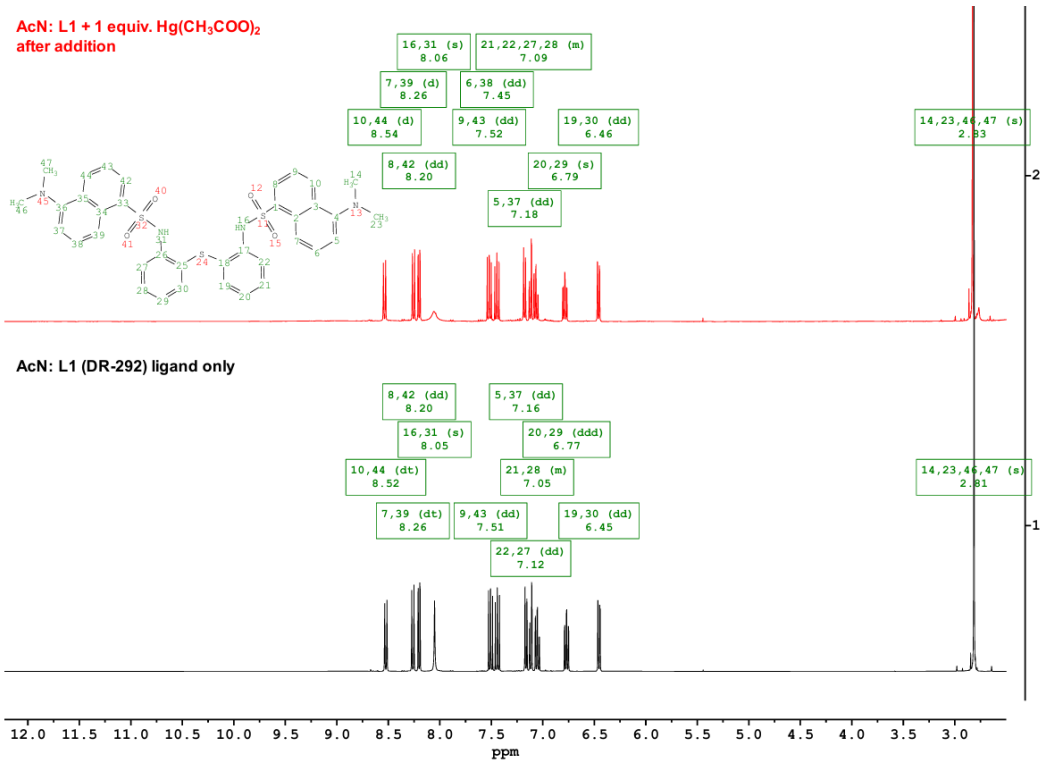


Figure 7–54. Comparison between ^{1}H-NMR spectra of compound **L1** in acetonitrile before and after the addition of 1 eq. of Hg^{2+}.

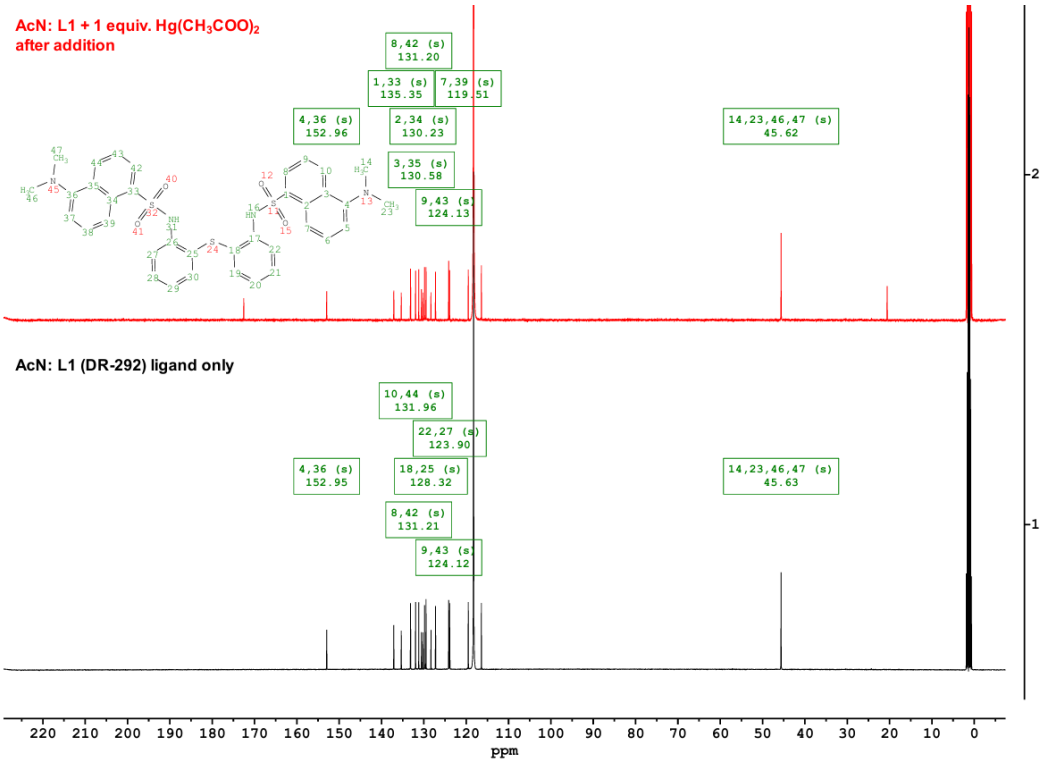


Figure 7–55. Comparison between ^{13}C-NMR spectra of compound **L1** in acetonitrile before and after the addition of 1 eq. of Hg^{2+}.

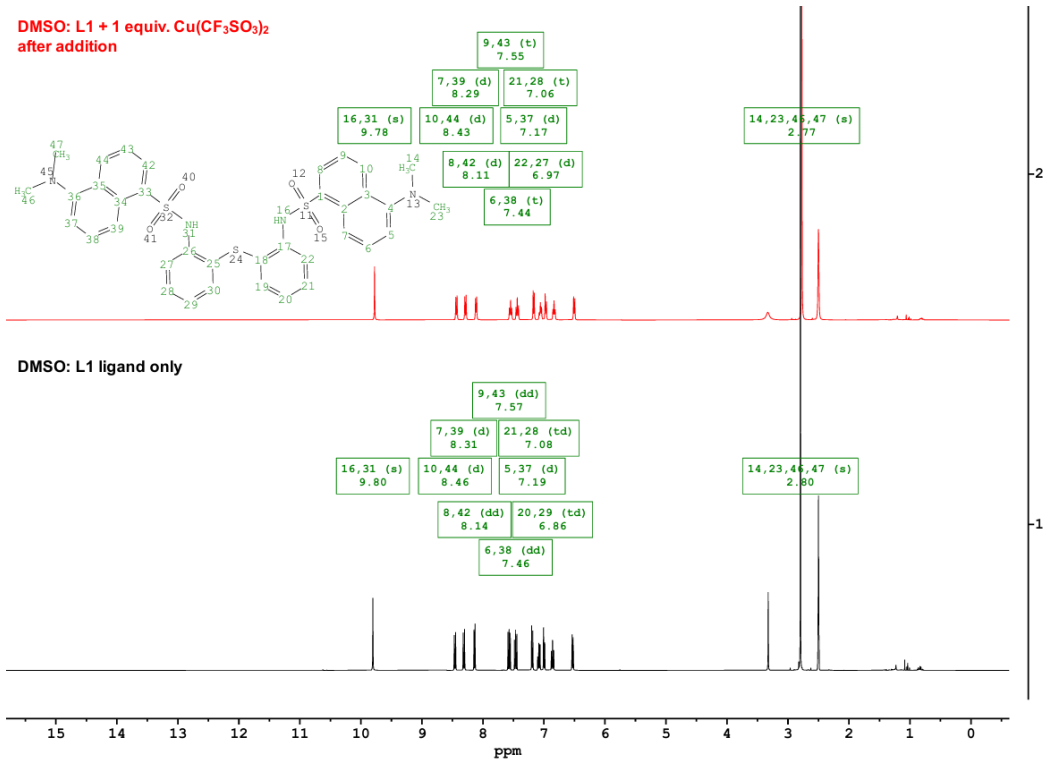


Figure 7–56. Comparison between ^{1}H-NMR spectra of compound **L1** in DMSO before and after the addition of 1 eq. of Cu^{2+}.

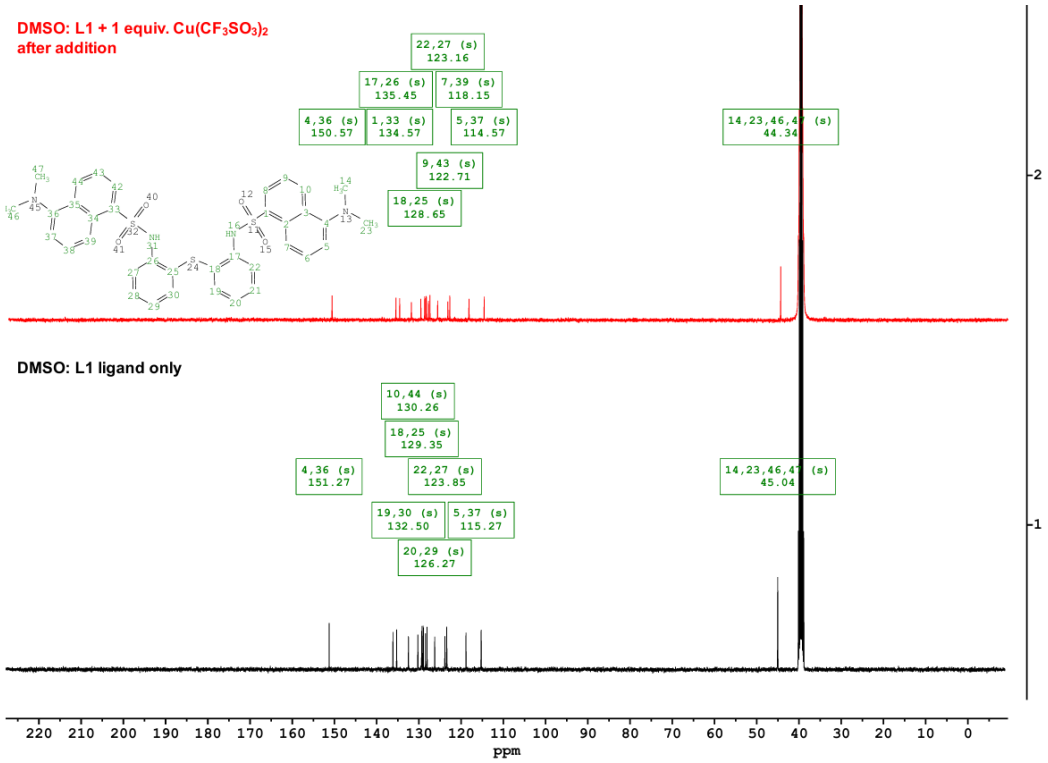


Figure 7–57. Comparison between ^{13}C-NMR spectra of compound **L1** in DMSO before and after the addition of 1 eq. of Cu^{2+}.

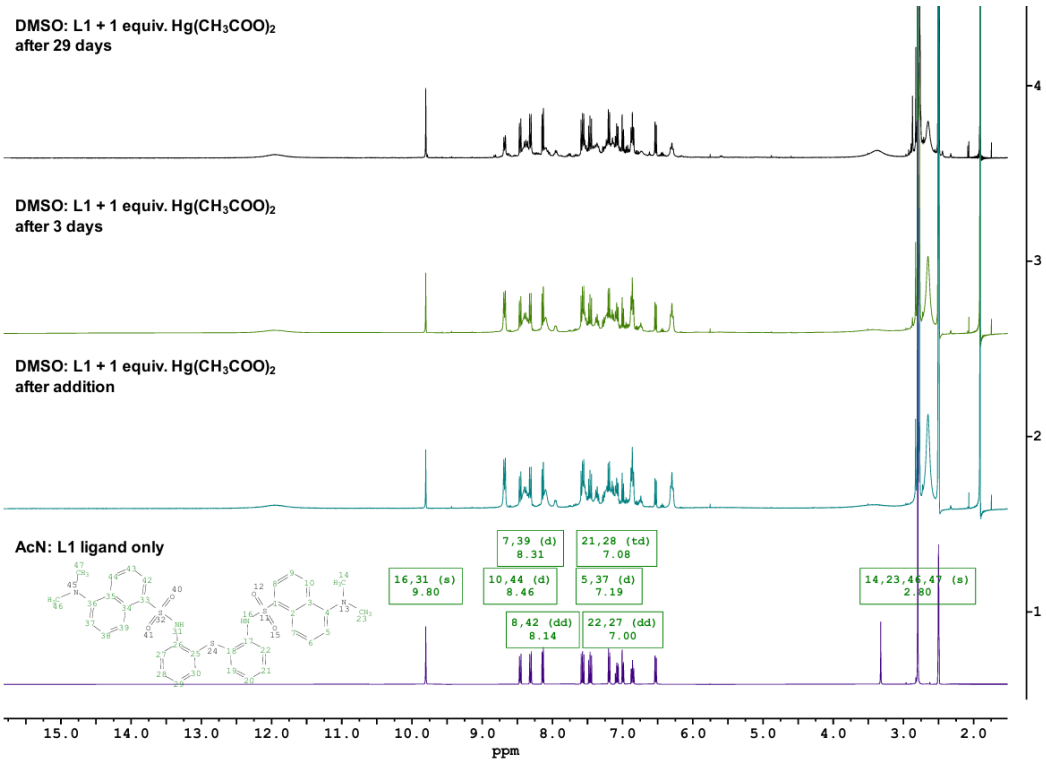


Figure 7–58. Comparison between ^{1}H-NMR spectra of compound **L1** in DMSO before and after the addition of 1 eq. of Hg^{2+} at different timepoints.

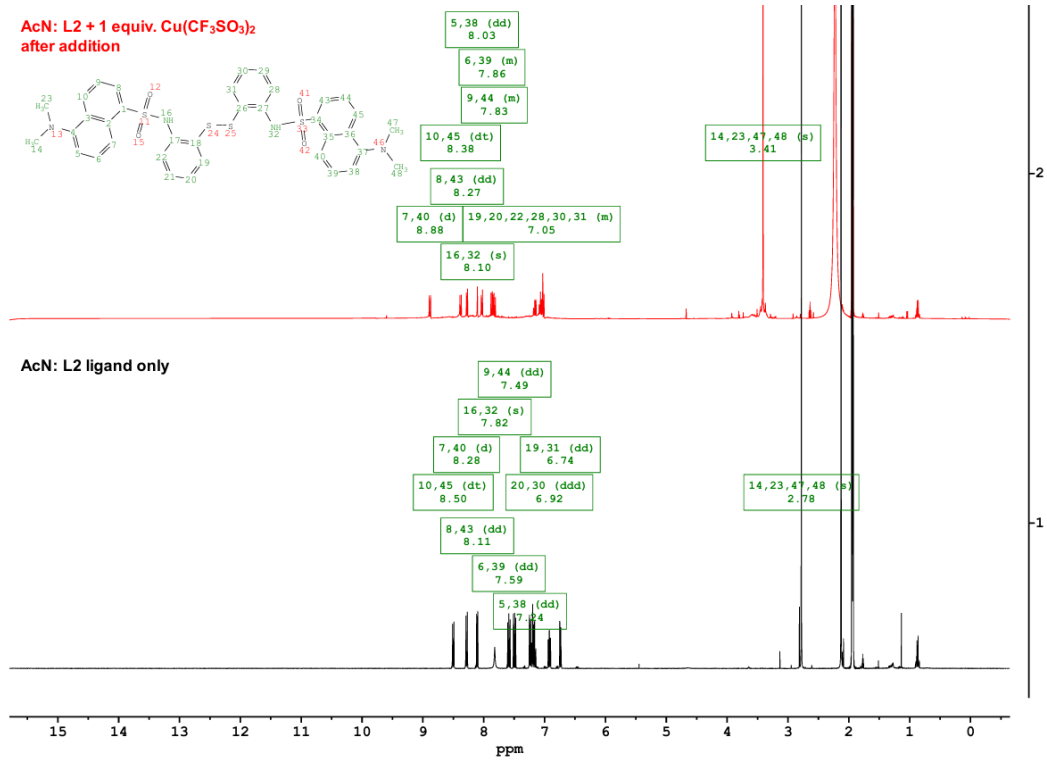


Figure 7–59. Comparison between ^{1}H-NMR spectra of compound **L2** in acetonitrile before and after the addition of 1 eq. of Cu^{2+}.

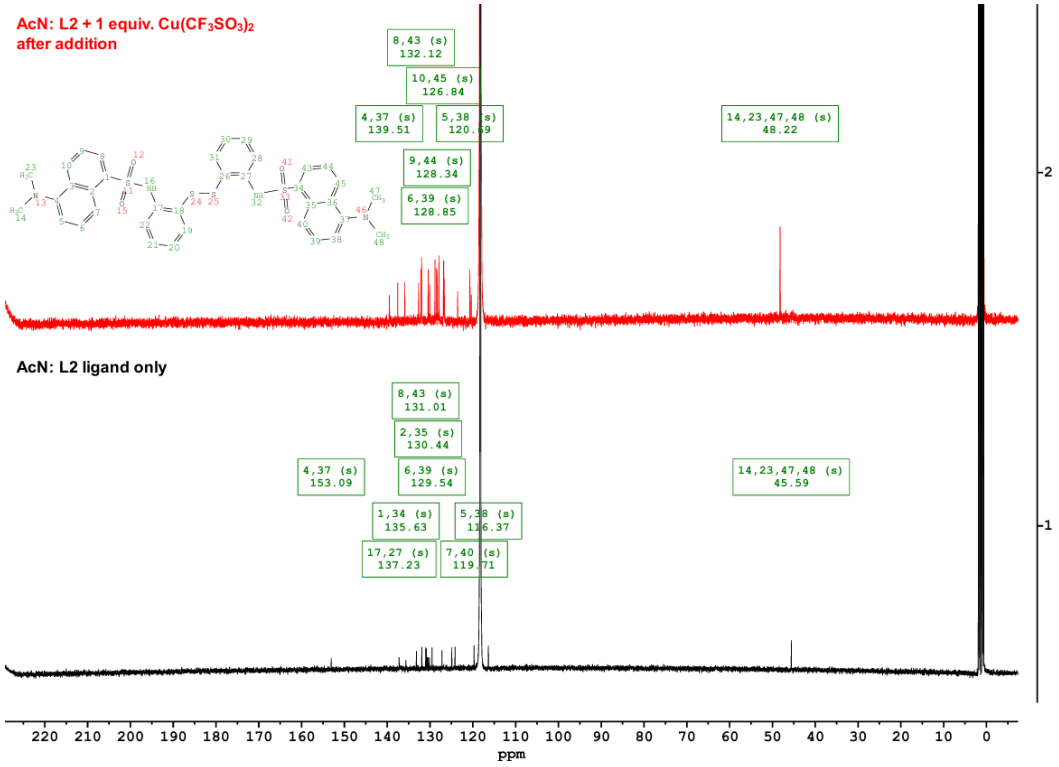


Figure 7–60. Comparison between ^{13}C-NMR spectra of compound **L2** in acetonitrile before and after the addition of 1 eq. of Cu^{2+}.

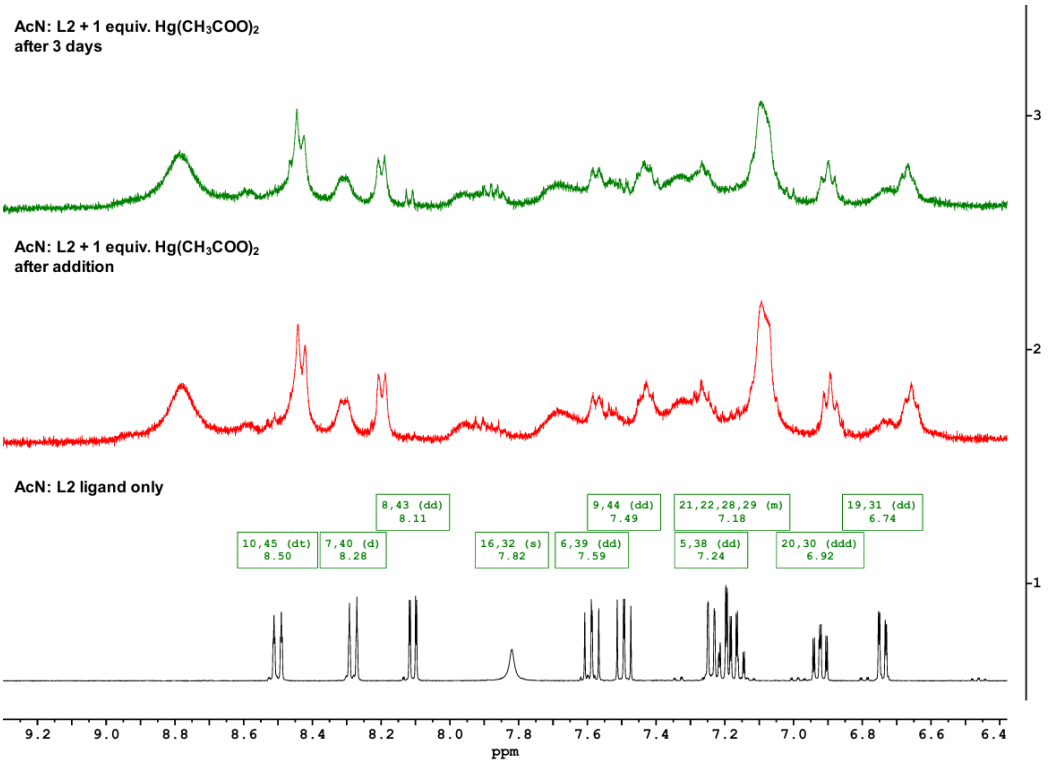


Figure 7–61. Comparison between ^{1}H-NMR spectra of compound **L2** in acetonitrile before and after the addition of 1 eq. of Hg^{2+} at different timepoints.

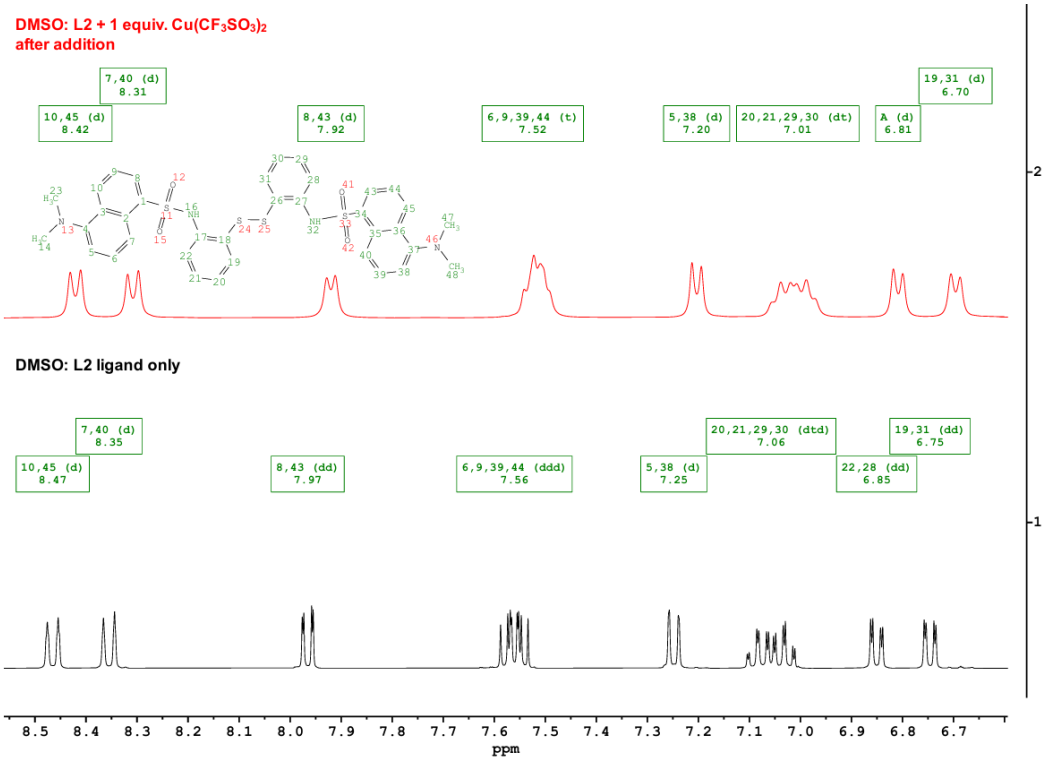


Figure 7–62. Comparison between ^{1}H-NMR spectra of compound **L2** in DMSO before and after the addition of 1 eq. of Cu^{2+}.

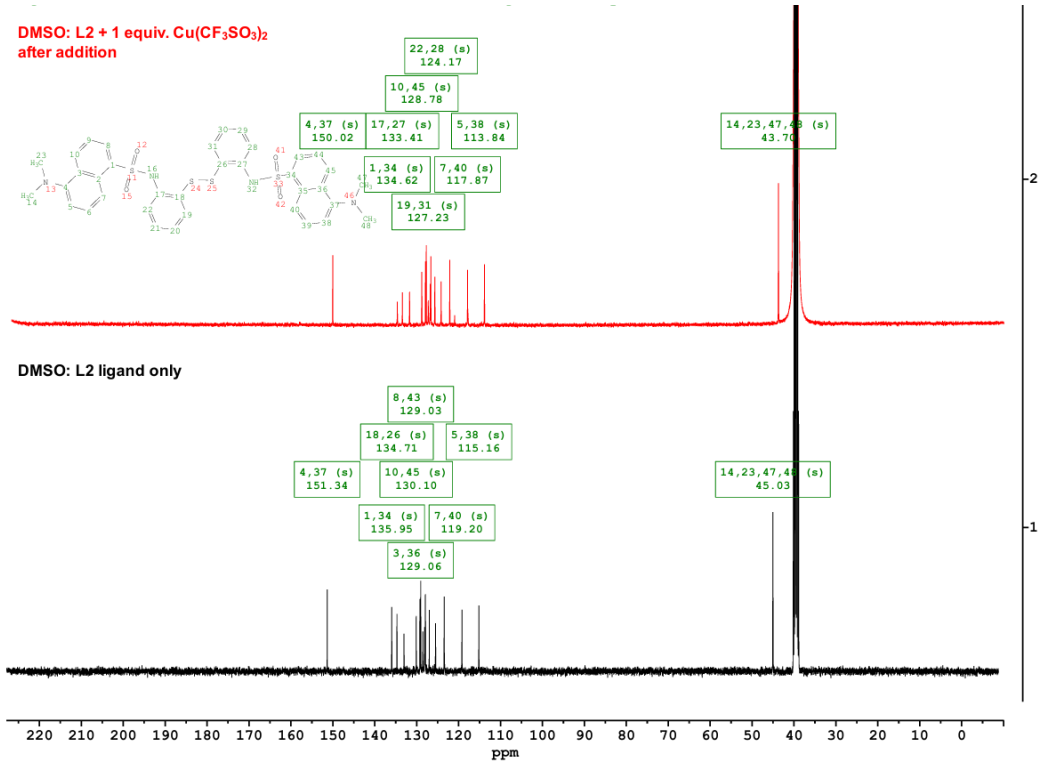


Figure 7–63. Comparison between ^{13}C-NMR spectra of compound **L2** in DMSO before and after the addition of 1 eq. of Cu^{2+}.

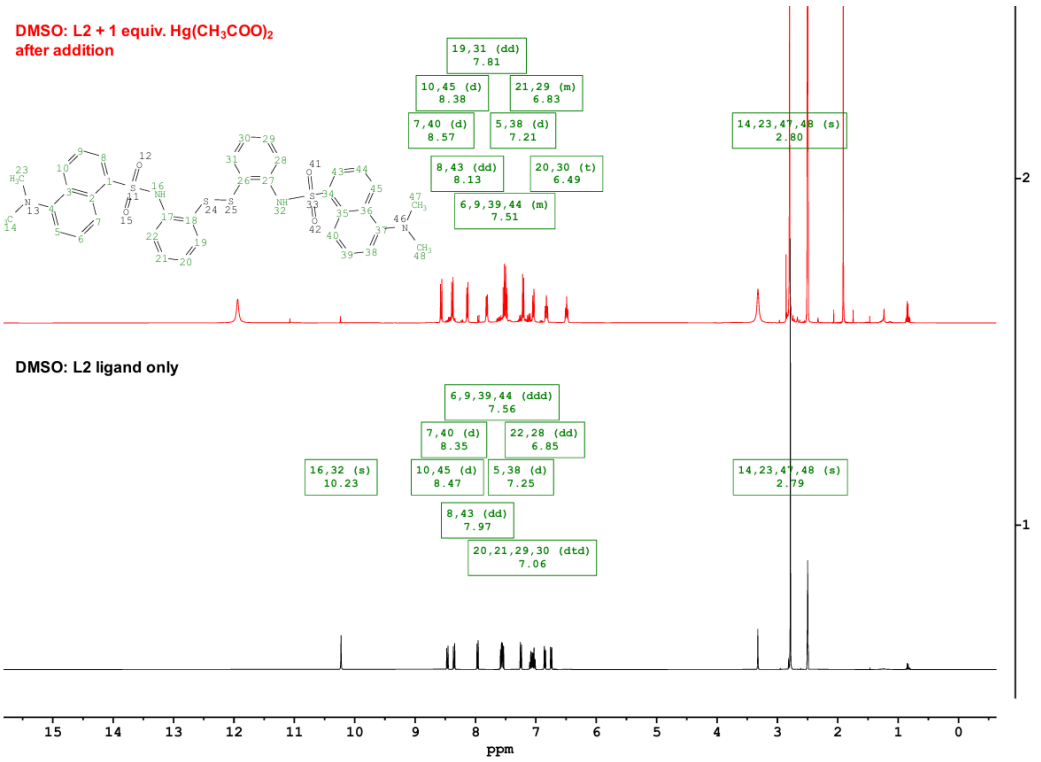


Figure 7–64. Comparison between ^{1}H-NMR spectra of compound **L2** in DMSO before and after the addition of 1 eq. of Hg^{2+}.

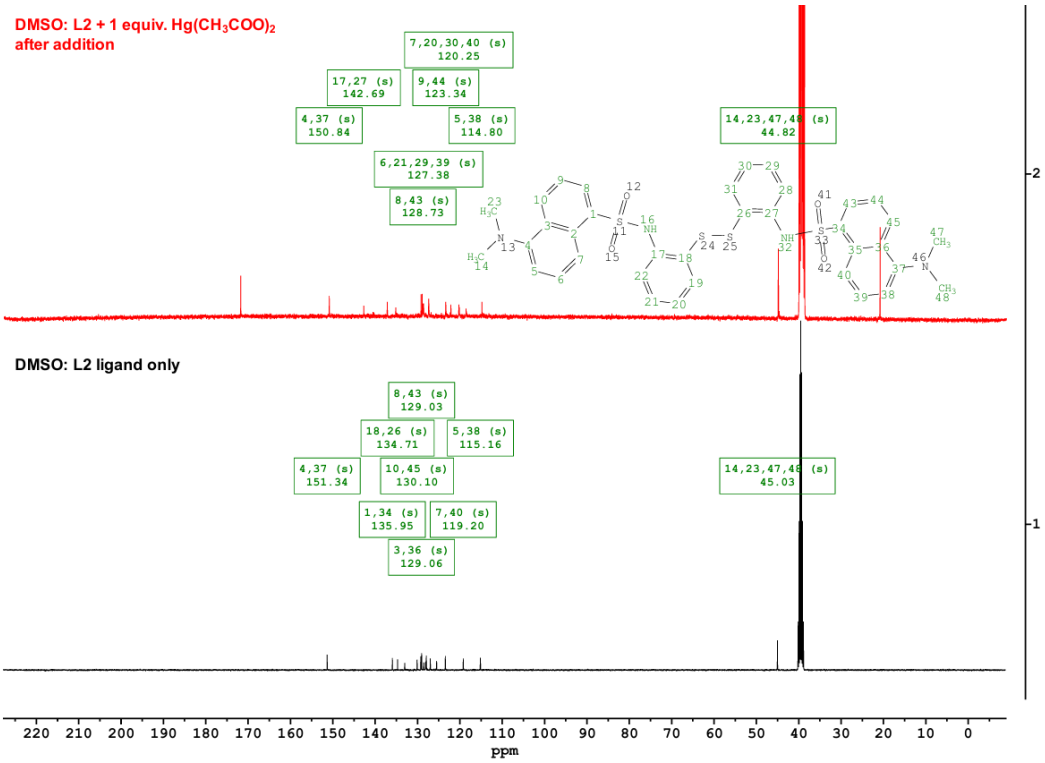


Figure 7–65. Comparison between ^{13}C-NMR spectra of compound **L2** in DMSO before and after the addition of 1 eq. of Hg^{2+}.

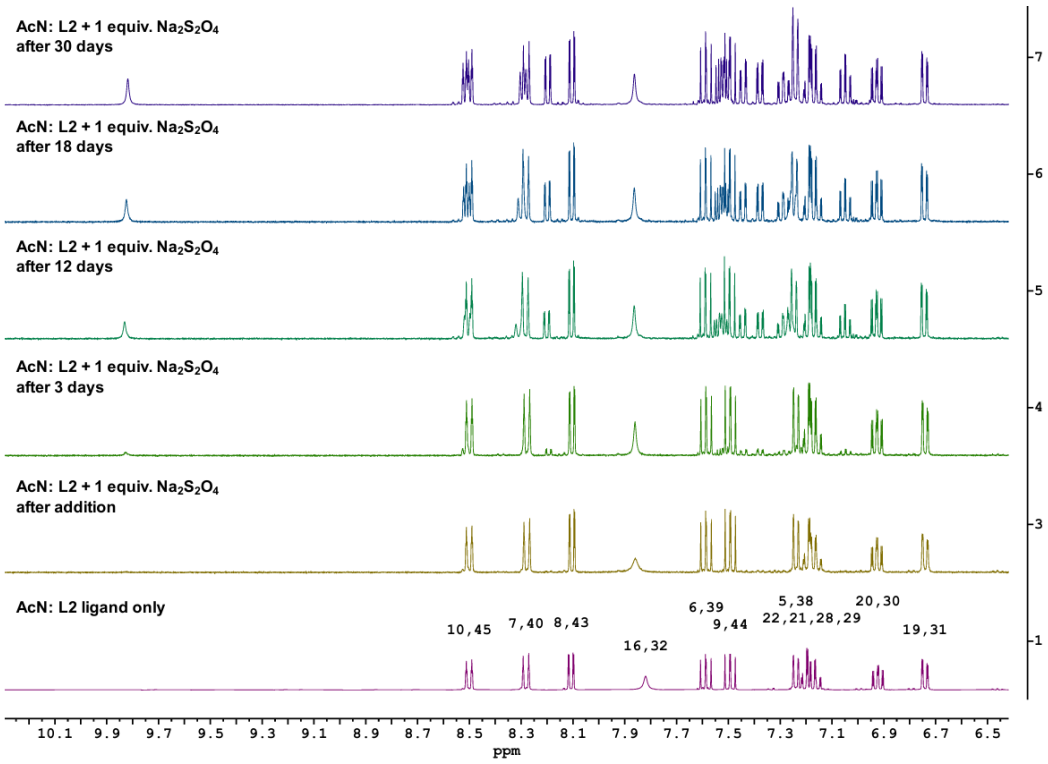


Figure 7–66. Comparison between ^{1}H-NMR spectra of compound **L2** in acetonitrile before and after the addition of 1 eq. of $Na_2S_2O_4$ at different timepoints.

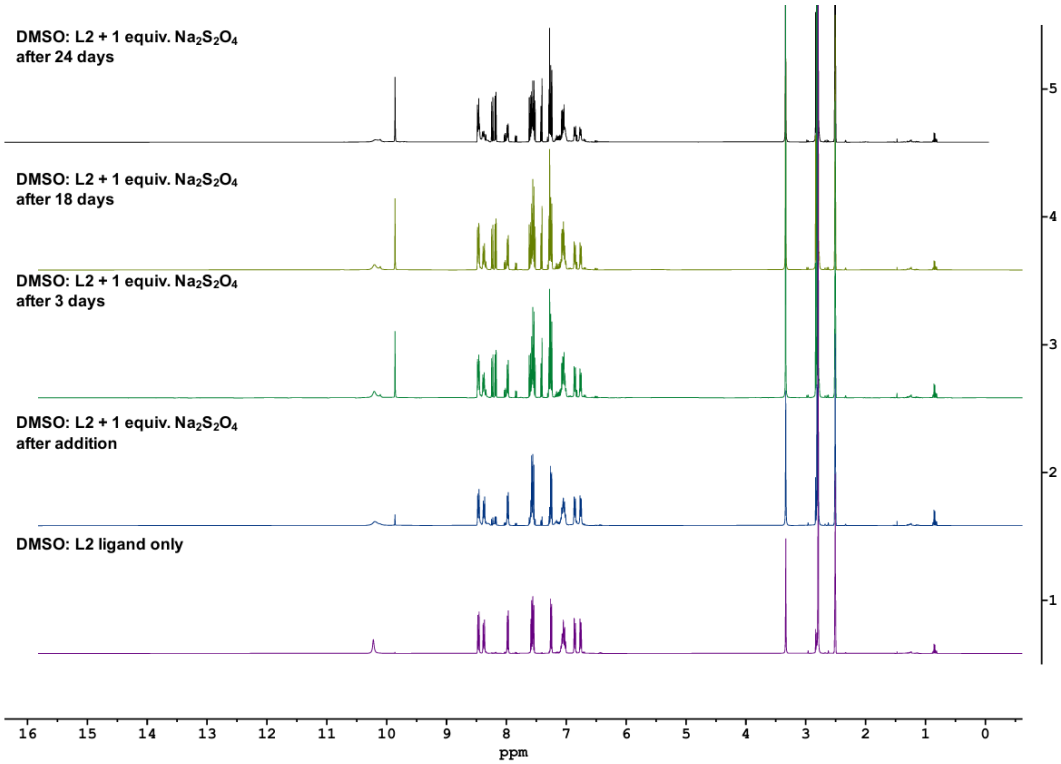


Figure 7–67. Comparison between ^{1}H-NMR spectra of compound **L2** in DMSO before and after the addition of 1 eq. of $Na_2S_2O_4$ at different timepoints.

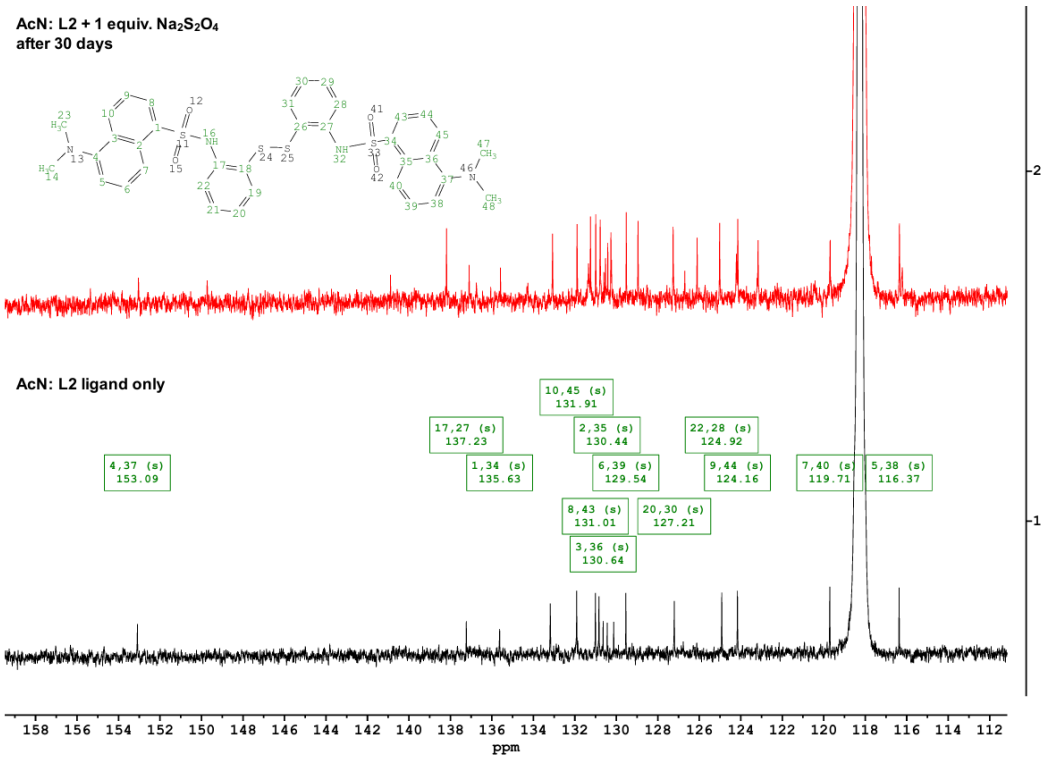


Figure 7–68. Comparison between ^{13}C-NMR spectra of compound **L2** in acetonitrile before and after the addition of 1 eq. of $Na_2S_2O_4$.

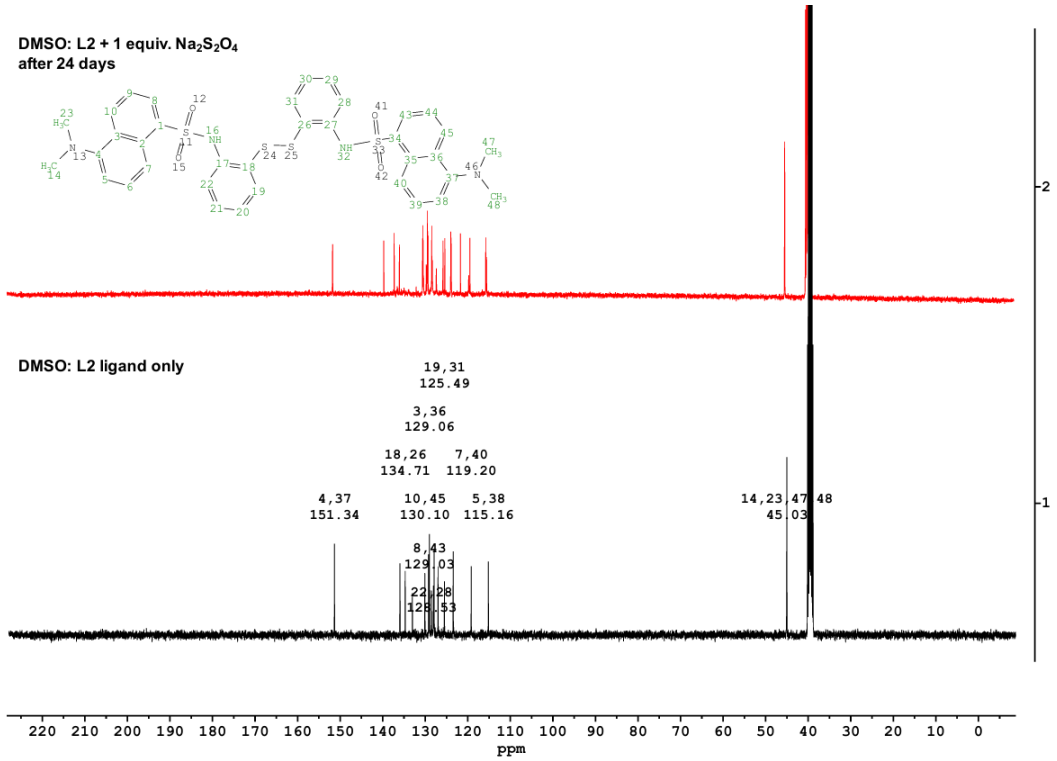


Figure 7–69. Comparison between ^{13}C-NMR spectra of compound **L2** in DMSO before and after the addition of 1 eq. of $Na_2S_2O_4$.

7.7 Contributions & Aknowledgements

7.7.1 Author Contributions

Igor Lourenço: Formal analysis, Investigation, Writing - Original Draft, Writing - Review & Editing, Visualization.

Frederico Duarte: Formal analysis, Investigation, Writing - Original Draft, Writing - Review & Editing, Visualization.

Georgi Dobrikov: Methodology, Validation, Formal Analysis, Investigation, Writing - Original Draft, Writing - Review & Editing, Resources, Visualization.

Atanas Kurutos: Conceptualization, Methodology, Validation, Formal Analysis, Investigation, Writing - Original Draft, Writing - Review & Editing, Resources, Visualization. Supervision, Funding acquisition.

Ivaylo Slavchev: Investigation

Jose Luis Capelo-Martinez: Resources, Writing - Review & Editing, Funding acquisition.

Hugo M. Santos: Investigation, Resources, Validation, Writing - Review & Editing.

Carlos Lodeiro: Conceptualization, Methodology, Validation, Formal Analysis, Investigation, Resources, Writing - Review & Editing, Resources, Visualization, Supervision, Funding acquisition, Project administration

7.7.2 Acknowledgments

This work was supported by the Associate Laboratory for Green Chemistry LAQV which is financed by national funds from *Fundação para a Ciência e Tecnologia and Ministério da Ciência, Tecnologia e Ensino Superior* (FCT/MCTES) through the projects UIDB/50006/2020 and UIDP/50006/2020. PROTEOMASS Scientific Society (Portugal) is acknowledged by the funding provided through the General Funding Grant 2023-2024, and by the funding provided to the Laboratory for Biological Mass Spectrometry Isabel Moura (#PM001/2019 and #PM003/2016). F.D. thanks to FCT/MCTES (Portugal) for his doctoral grant 2021.05161.BD. H. M. S. acknowledges the Associate Laboratory for Green Chemistry LAQV (LA/P/0008/2020) funded by FCT/MCTES for his research contract. The financial support by the Bulgarian National Science Fund (BNSF) under grant – "Novel styryl and polymethine fluorophores as potential theranostic

agents "contract N◦ КП-06-М59/1 from 15.11.2021 is gratefully acknowledged by A.K. This work is also developed and acknowledged by A.K. as part of contract №: BG-RRP-2.004-0002-C01, Laboratory of Organic Functional Materials (Project BiOrgaMCT), Procedure BG-RRP-2.004 „Establishing of a network of research higher education institutions in Bulgaria", funded by BULGARIAN NATIONAL RECOVERY AND RESILIENCE PLAN".

G. D. acknowledges that this work was supported by European Regional Development Fund under "Research Innovation and Digitization for Smart Transformation" program 2021-2027 under the Project BG16RFPR002-1.014-0006 "National Centre of Excellence Mechatronics and Clean Technologies". Research equipment of this project was used for experimental work.

7.8 References

[1] G. Hu, H. dong Xu and J. Fang, Sulfur-based fluorescent probes for biological analysis: A review, *Talanta* **279** (2024) 126515. DOI: 10.1016/j.talanta.2024.126515

[2] M. H. Lee, Z. Yang, C. W. Lim, Y. H. Lee, S. Dongbang, C. Kang and J. S. Kim, Disulfide-Cleavage-Triggered Chemosensors and Their Biological Applications, *Chem. Rev.* **113** (2013) 5071–5109. DOI: 10.1021/cr300358b

[3] Y. Zhang, S. Xia, S. Wan, T. E. Steenwinkel, T. Vohs, R. L. Luck, T. Werner and H. Liu, Ratiometric Detection of Glutathione Based on Disulfide Linkage Rupture between a FRET Coumarin Donor and a Rhodamine Acceptor, *ChemBioChem* **22** (2021) 2282–2291. DOI: 10.1002/cbic.202100108

[4] Z. Zheng, Y. Huyan, H. Li, S. Sun and Y. Xu, A lysosome-targetable near infrared fluorescent probe for glutathione sensing and live-cell imaging, *Sens. Actuators B Chem.* **309** (2019) 127065. DOI: 10.1016/j.snb.2019.127065.

[5] Z. Wang, R. Jing, Y. Li, D. Song, Y. Wan, N. Fukui, H. Shinokubo, Z. Kuang and A. Xia, Intrinsic Photostability in Dithiolonaphthalimide Achieved by Disulfide Bond-Induced Excited-State Quenching, *J. of Phys. Chem. Lett.* **14** (2023) 8485–8492. DOI: 10.1021/acs.jpclett.3c02260

[6] G. J. S. Cheng, J. M. Qin, X. Li and Q. Y. Cao, A naphthalimide-based fluorescent probe with mitochondria targeting for GSH sensing and cancer cell recognition, *Dyes and Pigments* **211** (2023) 111089. DOI: 10.1016/j.dyepig.2023.111089

[7] J. Mishra, R. Kaur, A. K. Ganguli and N. Kaur, Urea/thiourea based dipodal nanoreceptors: Aqueous medium fluorescent chemosensor for Zn(II) and Hg(II) ions by photoinduced electron transfer, *Microchemical Journal* **206** (2024) 111501. DOI: 10.1016/j.microc.2024.111501.

[8] J. Qiang, Y. Wang, Y. Li, Z. Guo, L. Jiang, F. Wang, S. Lu and X. Chen, A dual-locked near-infrared fluorescent probe based on ESIPT and FRET for improved discrimination between normal and cancer cells, *Sens. Actuators B Chem.* **405** (2024) 135344. DOI: 10.1016/j.snb.2024.135344.

[9] A. K. Ghosh, A. H. Khan and P. K. Das, Naphthalimide-Based AIEgens for Sensing Protein Disulfide Isomerase through Thiol−Disulfide Redox Exchange, *Anal. Chem.* **95** (2023) 13638–13648. DOI: 10.1021/acs.analchem.3c02442

[10] J. Torres-Kolbus, C. Chou, J. Liu and A. Deiters, Synthesis of Non-linear Protein Dimers through a Genetically Encoded Thiol-ene Reaction, *PLoS One* **9(9)** (2014) e105467. DOI: 10.1371/journal.pone.0105467.

[11] Y. Li, M. Yang, Y. Huang, X. Song, L. Liu and P. R. Chen, Genetically encoded alkenyl–pyrrolysine analogues for thiol–ene reaction mediated site-specific protein labeling, *Chem. Sci.* **3** (2012) 2766–2770. DOI: 10.1039/C2SC20433A.

[12] J. Sánchez-Bodón, M. Diaz-Galbarriatu, L. Pérez-Álvarez, J. L. Vilas-Vilela and I. Moreno-Benítez, Expanding (Bio)Conjugation Strategies: Metal-Free Thiol-Yne Photo-Click Reaction for Immobilization onto PLLA Surfaces, *Coatings* **14** (2024) 839. DOI: 10.3390/coatings14070839.

[13] H. Kurosaki, H. Yasuzawa, Y. Yamaguchi, W. Jin, Y. Arakawa and M. Goto, Detection of a metallo--lactamase (IMP-1) by fluorescent probes having dansyl and thiol groups, *Org. Biomol. Chem.* **1** (2003) 17–20. DOI: 10.1039/ b209086d.

[14] J. Youziel, A. R. Akhbar, Q. Aziz, M. E. B. Smith, S. Caddick, A. Tinker and J. R. Baker, Bromo- and thiomaleimides as a new class of thiol-mediated fluorescence 'turn-on' reagents, *Org. Biomol. Chem.* **12** (2014) 557–560. DOI: 10.1039/c3ob42141d

[15] V. Tharmaraj and K. Pitchumani, A highly selective ratiometric fluorescent chemosensor for Cu(II) based on dansyl-functionalized thiol stabilized silver nanoparticles, *J. Mater. Chem. B* **1** (2013) 1962–1967. DOI: 10.1039/c3tb00534h

[16] A. Jose, R. Sahadevan, M. Vijay, S. Sadhukhan and M. Porel, Dansyl-appended sequence-defined oligomers for selective ultrasensitive detection of Hg^{2+} in water, paper strips, living cells and its efficient removal, *Sens. Actuators B Chem.* **380** (2023) 133335. DOI: 10.1016/j.snb.2023.133335.

[17] M. Batool, Z. Afzal, H. M. Junaid, A. R. Solangi and A. Hassan, Sulfonamides as Optical Chemosensors, *Crit. Rev. Anal. Chem.* **54:5** (2024) 954–981. DOI: 10.1080/10408347.2022.2105135

[18] F. Duarte, G. Dobrikov, A. Kurutos, J. L. Capelo-Martinez, H. M. Santos, E. Oliveira and C. Lodeiro, Development of fluorochromic polymer doped materials as platforms for temperature

sensing using three dansyl derivatives bearing a sulfur bridge, *J. Photochem. Photobiol. A Chem.* **445** (2023) 115033. DOI: 10.1016/j.jphotochem.2023.115033

[19] G. Pedro, F. Duarte, G. M. Dobrikov, A. Kurutos, H. M. Santos, J. L. Capelo-Martínez, E. Oliveira and C. Lodeiro, Optical evaluation of dansyl derivatives and their implementation in low-cost and flexible dye-doped PMMA platforms for efficient detection of hazardous chemical vapours, *Dyes and Pigments* **224** (2024) 112042. DOI: 10.1016/j.dyepig.2024.112042

[20] Y. Zha, R. Xin, M. Zhang, X. Cui and N. Li, Stimuli-responsive azobenzene-quantum dots for multi-sensing of dithionite, hypochlorite, and azoreductase, *Microchimica Acta* **187** (2020) 481. DOI: 10.1007/s00604-020-04455-9

[21] J. Li, X. Yu, D. Shu, H. Liu, M. Gu, K. Zhang, G. Mao, S. Yang and R. Yang, Accelerated Activity-Based Sensing by Fluorogenic Reporter Engineering Enables to Rapidly Determine Unstable Analyte, *Anal. Chem.* **96** (2024) 7723–7729. DOI: 10.1021/acs.analchem.4c00945

[22] B. Dong, W. Song, X. Kong, N. Zhang and W. Lin, Visualizing cellular sodium hydrosulfite (Na2S2O4) using azo-based fluorescent probes with a high signal-to-noise ratio, *J. Mater. Chem. B* **7** (2019) 730–733. DOI: 10.1039/c8tb02487a

[23] A. Chevalier, C. Mercier, L. Saurel, S. Orenga, P. Y. Renard and A. Romieu, The first latent green fluorophores for the detection of azoreductase activity in bacterial cultures, *Chem. Commun.* **49** (2013) 8815–8817. DOI: 10.1039/c3cc44798g

[24] X. Yu, L. Xiang, S. Yang, S. Qu, X. Zeng, Y. Zhou and R. Yang, A near-infrared fluorogenic probe with fast response for detecting sodium dithionite in living cells, *Spectrochim. Acta A Mol. Biomol. Spectrosc.* **245** (2021) 118887. DOI: 10.1016/j.saa.2020.118887

[25] S. Wang, W. Wu, J. Lv, Q. Qi and W. Huang, Fast detection of sodium dithionite in sugar using a xanthylium-based f luorescent probe, *Food Chem.* **452** (2024) 139547. DOI:10.1016/j.foodchem.2024.139547

[26] N. J. W. Rattray, W. A. Zalloum, D. Mansell, J. Latimer, M. Jaffar, E. V. Bichenkova and S. Freeman, Chemical and bacterial reduction of azo-probes: monitoring a conformational change using fluorescence spectroscopy, *Tetrahedron* **69** (2013) 2758–2766. DOI: 10.1016/j.tet.2013.01.086

[27] X. Cao, L. Mu, M. Chen and G. She, A facile fluorescent sensor based on silicon nanowires for dithionite, *Appl. Surf. Sci.* **441** 2018 388–393. DOI: 10.1016/j.apsusc.2018.01.313

[28] M. Montalti, A. Credi, L. Prodi MG, Montalti M, Credi A, Prodi L GM. Handbook of Photochemistry. 3rd ed. BOCA: Taylor & Francis, Boca Raton; 2006.

[29] D. Macdougall and W. B. Crummett, Guidelines for data acquisition and data quality evaluation in environmental chemistry, *Anal. Chem.* **52** (1980) 2242–2249, DOI. 10.1021/ac50064a004

[30] G. L. Long and J. D. Winefordner, Limit of Detection A Closer Look at the IUPAC Definition, *Anal. Chem.* **55** (1983) 713A-724A, 10.1021/ac00258a724.

[31] S. Mocanu, G. Ionita and I. Matei, Solvatochromic characteristics of dansyl molecular probes bearing alkyl diamine chains, *Spectrochim. Acta - Part A Mol. Biomol. Spectrosc.* **237** (2020) 118413, DOI: 10.1016/j.saa.2020.118413

[32] E. Oliveira, R. M. F. Baptista, S. P. G. Costa, M. M. M. Raposo and C. Lodeiro, Solvatochromic Effects of bis(indolyl)thienylaril derivatives as new Colored Materials, *Photochem. Photobiol. Sci.* **13** (2014) 492–498, DOI: 10.1039/C3PP50352F

[32] P. Gans, A. Sabatini and A. Vacca, Investigation of equilibria in solution. Determination of equilibrium constants with the HYPERQUAD suite of programs, *Talanta*, **43** (1996) 1739–1753, DOI: 10.1016/0039-9140(96)01958-3.

8

TETRA DANSYLAMIDES SUBSTITUTED CYCLEN AND CYCLAM MACROCYCLES AS FLUORESCENT SENSING PROBES FOR METAL IONS AND TEMPERATURE-RESPONSIVE MATERIALS IN DOPPED POLYMERS

Inês Pereira-Gomes, Frederico Duarte, Georgi M. Dobrikov, Ivaylo Slavchev, Atanas Kurutos, Jose Luis Capelo-Martinez, Hugo M. Santos, Carlos Lodeiro

Dyes and Pigments 232 (2025) 112461 Doi: 10.1016/j.dyepig.2024.112461

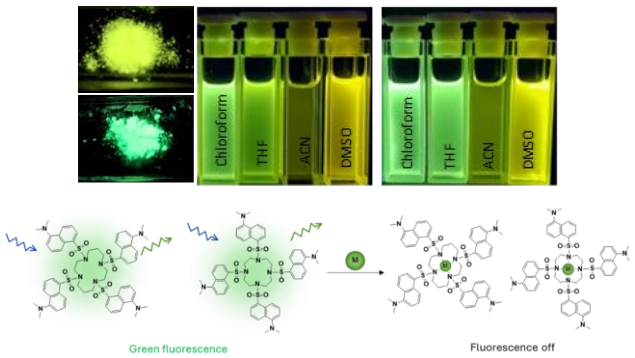
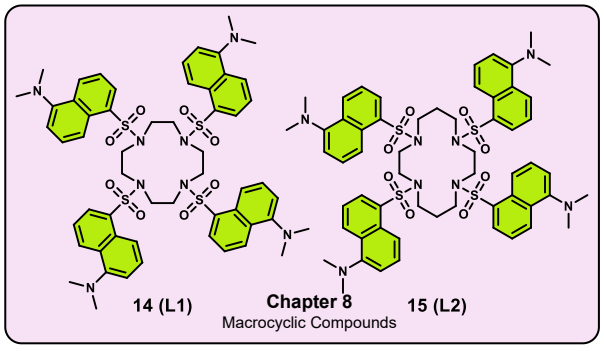


Figure 8–1. Graphical abstract.



Contribution to this work: Photophysical characterization; Preparation of polymeric doped thin films; Aggregation studies; Sensing experiments of metal ions; Temperature-dependent studies; Writing original draft.

8.1 Abstract

Two novel tetra-dansyl derivatives incorporating cyclen (1,4,7,10-tetraazacyclododecane) and cyclam (1,4,8,11-tetraazacyclotetradecane) macrocycles have been synthesized, thoroughly characterized, and their photophysical properties examined, both in solution and in the solid state. These compounds exhibit fluorescence emission with quantum yields up to 40%, varying significantly with different solvents. They also display positive solvatofluorochromic behavior, with emissions ranging from green to yellow colours. Kamlet-Taft studies were conducted to better understand solute-solvent interactions. Furthermore, aggregation-induced emission was observed in solutions with high water content, confirmed via dynamic light scattering. Given the intrinsic properties of these compounds, their potential for environmental remediation was explored through metal ion sensing studies. Compounds **L1** and **L2** demonstrated high sensitivity to Cu^{2+} and Hg^{2+} ions, significantly modulating their emission, with **L2** capable of detecting and quantifying Hg^{2+} concentrations as low as 2-3 μM. Additionally, the solid-state emission of these compounds encouraged an investigation into their potential as temperature sensors. Several doped polymer thin films were fabricated, establishing a linear relationship with temperature beyond their melting point. These findings suggest that these tetra-chromophoric compounds hold promise as molecular thermometers.

8.2 Introduction

Probes and sensors employing fluorescent dyes are highly beneficial due to their exceptional optical features. Among this extensive group, dansyl derivatives have consistently been used throughout the decades amidst their consistent photophysical properties, namely large Stokes shift, high fluorescence quantum yields and the well-known strong dependence of the emission properties on the surrounding environment. [1-5] The detection of heavy metals and transition metal ions is extensively documented in the literature, given the wide range of applications to which dansyl derivatives have been put to use, especially for Cu^{2+} [1,2,4,6-10], Zn^{2+} [11,12], Ag^{2+} [13], Cd^{2+} [14], Hg^{2+} [1,4,15-18] and Pb^{2+}[19].

Given the current efforts to develop new dyes, aza-crown compounds, namely cyclen (1,4,7,10-Tetraazacyclododecane) and cyclam (1,4,8,11-Tetraazacyclotetradecane) were employed as good candidates to their versatility and wide range of applications including in the fields of medicine [20,21], magnetic resonance imaging [22-24], catalysis [25-27] and pollutant degradation [28]. Within this context, azamacrocyclic tetramines can readily be functionalized

and demonstrate robust binding to a diverse array of cations. [29] An example of this was demonstrated by Hava Ozay *et al.* where p(2-hydroxyethyl methacrylate-co-tetraacrylic cyclen) (p(HEMA-co-TACYC)) hydrogels were synthesized with the intention to transfer the copper ion binding ability of cyclen into the hydrogel structure. The designed hydrogels showed selective colorimetric sensor behaviour towards Cu^{2+} in all aqueous media and when submitted to metal ion mixtures. [30]

Functionalization of these macrocycles with fluorophores is supported by the literature, namely with anthracene, naphthalimide, rhodamine and BODIPY. [29,31,32] Xiao Fang *et al.* have synthesized a BODIPY-based fluorescent probe with a cyclen moiety that improved water solubility, followed by Cu^{2+} binding. The selective turn-on fluorescent behaviour for H_2S was elucidated with a LOD of 1.1 nM. Additionally, the complex was effectively utilized for imaging exogenous H_2S generated from Na_2S and GYY4137 in H9c2 and U87 cells. [31]

Based on an extensive literature search, the dansylation of aza-crown compounds is in its early stages with very early reports focused on mono dansylated cyclen. [33,34] More recently, this compound was used for the formation of metal complexes in various matrices. [35-38] The presence of metal ions binding to the basic nitrogen atoms of this derivative is crucial for the creation of a stable complex. Rivas *et al.* demonstrated that coordination of metal ions with other heteroatoms outside the aza-crown ring is also feasible. [39] Due to the negligible cytotoxicity, good penetration and photostability, Yang *et al.* have been successful in using this compound for specific lysosome labeling in various cell lines. [40] To the best of our knowledge, only a few mentions of dansyl derivatives of cyclam are reported in the art. [41-45] In this study, we successfully synthesized symmetric tetra dansyl derived compounds of cyclam and cyclen for the first time. These newly developed fluorophores were then fully characterized according to their photophysical properties. The Kamlet-Taft equation was used to explain the solvatochromism behaviour of functionalizing the aza-crown with four dansyl units. The tuning of the emission using water as co-solvent led to an aggregation induced emission in high water fraction and was confirmed by dynamic light scattering. The above-mentioned ligands were designed in order to demonstrate good complexation ability toward heavy metals and so efforts to elucidate their ability to sense pollutant metal ions was put forth. Finally, incorporation into polymer thin films KURARITY (L44285) and IROGRAN (A 92 P 4637) towards the development of temperature-smart materials was carried out.

8.3 Experimental Section

8.3.1 Materials

Spectroscopy grade solvents, such as acetonitrile (CH_3CN), chloroform ($CHCl_3$), dimethylsulfoxide (DMSO), ethanol (EtOH), and tetrahydrofuran (THF), were used for spectrophotometric and spectrofluorimetric measurements. All solvents used for the synthesis and purification of the target compounds (dichloromethane (DCM) and methyl-tert-butyl ether (MTBE)) were of analytical grade (p.a.) and dried over molecular sieve (3Å). The starting fine chemicals (cyclam (1,4,8,11-Tetraazacyclotetradecane), cyclen (1,4,7,10-Tetraazacyclododecane), diisopropylethylamine (DIPEA) and dansyl chloride) used for the synthesis of the target fluorophores were purchased from Sigma Aldrich, Tokyo Chemical Industry Co. Ltd., and BLDPharm. Silica gel (high-purity grade, pore size 60 Å, 230-400 mesh particle size, 40-63 µm particle size, for flash chromatography) employed for the column chromatography was purchased from Sigma Aldrich. Trifluoromethanesulfonate salts of $Co(OTf)_2$, $Ni(OTf)_2$, $Cu(OTf)_2$, $Zn(OTf)_2$, Ag(OTf), $Cd(OTf)_2$, were provided from Solchemar, while $Hg(OTf)_2$ and $Ca(BF_4)_2H_2O$ were purchased from Sigma Aldrich. KURARITY^{TM} LA4285 Kurashiki, Okayama, Japan; the thermoplastic polyurethane TPU-A92 was offered by Huntsman (Germany). The perfluoroalkoxy (PFA) supports for the fabrication of polymer films were purchased to Bohlender, Gmbh, Germany. Mili-Q ultrapure water was used in all experiments.

8.3.2 Instrumentation

The chemical identities of the compounds under investigation were confirmed through the utilization of various analytical techniques, including ^{1}H-NMR, ^{13}C-NMR, DEPT-135, 2-D COSY, 2D-HSQC, and 2-D HMBC NMR spectroscopic techniques. The ^{1}H-NMR and ^{13}C-NMR spectra were acquired on a Bruker Avance II+600 spectrometer (Institute of Organic Chemistry with Centre of Phytochemistry - Bulgarian Academy of Sciences / NMR Centre) using 5 mm tubes. The measurements were performed in $CDCl_3$ at 293K, with operating frequencies of 600.13 MHz and 150.92 MHz for the ^{1}H- and ^{13}C- nuclei, respectively. The ^{1}H- and ^{13}C- nuclear magnetic resonance (NMR) spectra were standardized using the reference signal of $CDCl_3$ with a chemical shift value (δ) of 7.26 ppm for the ^{1}H-NMR and 77.16 ppm for the ^{13}C-NMR, respectively. The precision of chemical changes is determined at a level of 0.01 ppm. The coupling constants (*J*) are displayed with a precision of 0.1 and denoted in units of hertz (Hz). The spin multiplicity observed in the 1H- nuclear magnetic resonance (NMR) spectroscopy was

represented using the following abbreviations: s for singlet, d for doublet, t for triplet, q for quartet, dd for doublet of doublets, dt for doublet of triplets, td for triplet of doublets, and m for multiplet. MestreNova v. 14.1.1 (Mestrelab Research S.L.) was used for processing the spectra. High-Resolution Mass Spectrometry analyses have been performed in the Laboratory for Biological Mass Spectrometry–Isabel Moura (PROTEOMASS Scientific Society Facility), using UHR ESI-Qq-TOF IMPACT HD (Bruker-Daltonics, Bremen, Germany). Samples of the corresponding compounds were prepared by dissolution in 50% (v/v) Acetonitrile containing 0.1% (v/v) aqueous formic acid to obtain a working solution of 0.1 µg/mL. Mass spectrometry analysis was carried out by the direct infusion of the compound solutions into the ESI source. MS data were acquired in positive polarity over the mass range of 80 – 1300 m/z. (Capillary voltage: 4500 V, End plate offset: -500 V, Charging voltage: 2000 V, Corona: 4000 nA, Nebulizer gas: 0.4 Bar, Dry Heater: 180 °C, Dry gas: 4.0 L/min).

UV-Vis absorption spectra were recorded on a JASCO V-650 spectrophotometer and the fluorescence emission spectrum on a HORIBA Scientific FLUOROMAX-4 spectrofluorometer from BIOSCOPE-PROTEOMASS facilities. Otherwise stated, all photophysical experiments were carried out at 293 K using a quartz cell with 10 mm of optical path.

8.3.3 Synthetic procedures

8.3.3.1 General procedure for the synthesis of L1 and L2

Cyclic tetraamine (1.0 eq. of **2** or **3**) and dry DIPEA (8.0 eq.) were dissolved in 50 mL dry DCM, and the formed clear solution was cooled down to 5°C with ice-water. Dansyl chloride (4.5 eq.) was added in one portion and stirring was maintained for 30 min at this temperature. Subsequently, the reaction mixture was stirred for 4 days at r.t. The reaction outcome was monitored by TLC (mobile phase - DCM:MTBE=100:1 v/v). Workup: the reaction mixture was diluted with DCM and washed consequently with aq. citric acid (x1), aq. K_2CO_3 (x1) and distilled water (x1). The organic phase was dried over anhydr. Na_2SO_4 and the solvent was evaporated to dryness. The crude product was purified by silica gel column chromatography affording compounds **L1** or **L2**, respectively.

8.3.3.2 Data for 5,5',5'',5'''-(1,4,7,10-tetraazacyclododecane-1,4,7,10-tetrasulfonyl)tetrakis(*N,N*-dimethylnaphthalen-1-amine) (L1)

This compound was prepared according to the general synthetic procedure described above using cyclen (**2**) (1.00 mmol, 0.172 g, 1 eq.), DIPEA (8.00 mmol, 1.39 mL, 1.39 mL) and

dansyl chloride (4.50 mmol, 1.214 g, 4.5 eq.) (**1**). Column chromatography: stationary phase - 75 g silica gel; Mobile phase - DCM:MTBE=75:1v/v. The target product **L1** was obtained in 0.984 g (89%) as a light-yellow powder. m.p. 178-179°C. ^{1}H NMR (600 MHz, $CDCl_3$) δ 8.57 (*d*, *J* = 8.5 Hz, 4H), 8.49 (*d*, *J* = 8.7 Hz, 4H), 8.01 (*dd*, *J* = 7.4, 1.2 Hz, 4H), 7.53 (*td*, *J* = 9.0, 7.5 Hz, 8H), 7.18 (*d*, *J* = 7.1 Hz, 1H), 3.67 (*s*, 16H), 2.89 (*s*, 24H). ^{13}C NMR (151 MHz, $CDCl_3$) δ 151.83, 133.19, 130.79, 130.74, 130.44, 129.63, 128.57, 123.35, 119.82, 115.50, 51.34, 45.56, 0.14. ESI-MS: $[M+H]^+$ for $C_{56}H_{64}N_8O_8S_4$= 1105.3758 m/z (-4 ppm), calculated $[M+H]^+$ for $C_{56}H_{64}N_8O_8S_4$= 1105.3803 m/z; $[M+2H]^{2+}$ for $C_{56}H_{64}N_8O_8S_4$= 533.1937 m/z (-0.1 ppm), calculated $[M+2H]^{2+}$ for $C_{56}H_{64}N_8O_8S_4$= 533.1938 m/z. EA Found C: 60,21; H: 5.95; N: 9.22 and S: 10.95%. $C_{56}H_{64}N_8O_8S_4$ requires C: 60.85; H: 5.84; N: 10.14 and S: 11.60%.

8.3.3.3 Data for 5,5',5'',5'''-(1,4,8,11-tetraazacyclotetradecane-1,4,8,11-tetrasulfonyl)tetrakis(*N*,*N*-dimethylnaphthalen-1-amine) (L2)

L2 compound was prepared according to the general synthetic procedure described above, employing cyclam (1.00 mmol, 0.200 g, 1 eq.) (**3**), DIPEA (8.00 mmol, 1.39 mL, 1.39 ml) and dansyl chloride (4.50 mmol, 1.214 g, 4.5 eq.) (**1**). Column chromatography: stationary phase - 75 g silica gel; Mobile phase - DCM:MTBE=25:1 v/v. The target product **L2** was obtained in 1.025 g (90%) as a light-yellow powder. m.p. 227-228°C. ^{1}H NMR (600 MHz, $CDCl_3$) δ 8.55 (*d*, *J* = 8.5 Hz, 4H), 8.33 (*d*, *J* = 8.7 Hz, 4H), 8.04 (*dd*, *J* = 7.3, 1.2 Hz, 4H), 7.52 (*ddd*, *J* = 8.5, 7.5, 1.2 Hz, 8H), 7.17 (*d*, *J* = 7.3 Hz, 4H), 3.37 (*s*, 8H), 3.31 (*t*, *J* = 7.0 Hz, 8H), 2.88 (*s*, 24H), 1.95 (*p*, *J* = 7.1 Hz, 4H). ^{13}C NMR (151 MHz, $CDCl_3$) δ 151.89, 133.62, 130.75, 130.33, 130.28, 129.91, 128.50, 123.35, 119.55, 115.48, 48.14, 47.21, 45.55, 27.65, 0.13. ESI-MS: $[M+H]^+$ for $C_{58}H_{68}N_8O_8S_4$= 1133.4077 m/z (-3.4 ppm), calculated $[M+H]^+$ for $C_{58}H_{68}N_8O_8S_4$= 1133.4116 m/z; $[M+2H]^{2+}$ for $C_{58}H_{68}N_8O_8S_4$= 567.2103 m/z (1.6 ppm), calculated $[M+2H]^{2+}$ for $C_{58}H_{68}N_8O_8S_4$= 567.2094 m/z. EA Found C: 61,13; H: 6.24; N: 9.67 and S: 11.30. $C_{58}H_{68}N_8O_8S_4$ requires C: 61.46; H: 6.05; N: 9.89 and S: 11.32%.

8.3.4 Spectrophotometric and spectroflurimetric measurements

8.3.4.1 Photophysical characterizatio and titrations

Photophysical measurements began with the preparation of stock solutions of compounds **L1** and **L2** (*ca.* 10^{-3} M) in various solvents (CH_3CN, DMSO, $CHCl_3$, and THF), by dissolving each ligand in a 10 mL volumetric flask and diluting with the corresponding solvent. The working solutions in the range of 10^{-5} – 10^{-6} M were then prepared by dilution of the stock solutions.

Titrations of **L1** and **L2** were performed by successive additions of microliter aliquots of standard solutions of Ca^{2+}, Co^{2+}, Ni^{2+}, Cu^{2+}, Zn^{2+}, Ag^{+}, Cd^{2+}, Hg^{2+} ions prepared in acetonitrile. A correction for the absorbed light was performed when necessary. The temperature dependent emission spectra were recorded by encapsulating the material between quartz plates, and over a hotplate with temperature control for measurements at variable temperature. Additionally, mixtures containing different water fractions (f_w), (f_w = 0%, 17%, 33%, 55%, 67% and 83%) with a final concentration of 10 mM were prepared and characterized by absorption and emission spectroscopy. Luminescence spectra of the compounds in the solid state and of doped polymer thin films were recorded using a fiber-optics device connected to the spectrofluorometer while exciting the samples at appropriated wavelength.

Table 8-1. Spectroscopic polarity parameters, physical properties of the different solvents. ε_r: relative permittivity; η: refractive index; α: the solvent's HBD acidity; β: the solvent´s HBA basicity; π^*: the solvent´s dipolarity/polarizability.

Solvent	ε_r	α	β	π^*	η
DMSO	47.24	0	0.76	1.00	1.47
CH_3CN	35.94	0.19	0.40	0.66	1.34
THF	7.58	0	0.55	0.58	1.40
$CHCl_3$	4.89	0.20	0.10	0.69	1.44

8.3.4.2 Fluorescence quantum yield and lifetime

The evaluation of the relative photoluminescence quantum yields was performed by preparing a solution of dansylamide in DMSO (ϕ_F = 0.61) as reference standard for quantifying the relative QY of **L1** and **L2** in all studied solvents. [46] Lifetime measurements were recorded on a Tempro Fluorescence Lifetime System with a Horiba Jobin-Yvon NanoLed pulsed diode controller. All measurements were carried out at 293 K.

8.3.5 Determination of the detection and quantification limits (LOD and LOQ)

Determination of the detection limit (LOD) and quantification limit (LOQ) began by collecting ten independent measurements of a solution containing the selected probe and no addition of any metal ion (y_{blank}). Final determination of the LOD and LOQ values followed the subsequent formulas [47,48]

LOD = y_{dl} = y_{blank} + 3std, where y_{dl} = signal detection limit and std = standard deviation.

LOQ = y_{dl} = y_{blank} + 10std, where y_{dl} = signal detection limit and std = standard deviation.

The final step involved the determination of the minimal detectable and quantified concentration of metal ion by titration with the ligands.

8.3.6 Preparation of the polymer dye-doped thin films

8.3.6.1 KURARITY L44285 film

Production began by weighting 100 mg of polymer in a vial and was dissolved in 5 mL of chloroform whereas 1 mg of the compound (**L1** or **L2**) was weighted in a separate vial and dissolved in 1 mL of chloroform. Then, the polymer solution was stirred aided by heating at 70 ºC and when the polymer was completely dissolved, the compound solution was added, and they were mixed.

8.3.6.2 IROGRAN A 92 P 4637

TPU's solution was prepared by weighting 100 mg of this polymeric material in a vial and in another vial was weighed 1 mg of the compound. The amount of TPU weighted was dissolved in 10 mL of THF over stirring at room temperature until it was totally dissolved. The dye solution was prepared in THF for **L1-2** and then added to the polymer solution.

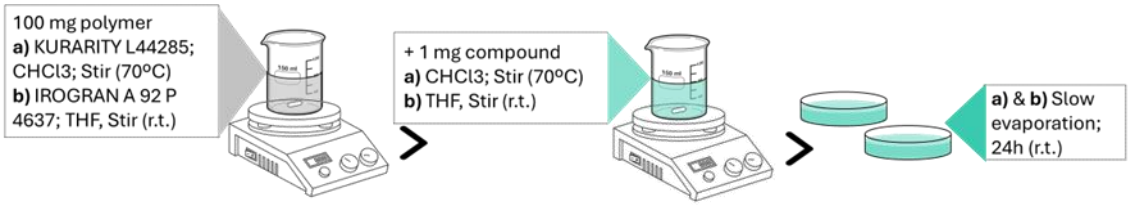


Figure 8–2. The method of synthesis of a) KURARITY L44285 and b) IROGRAN 4 92 P 4637 films.

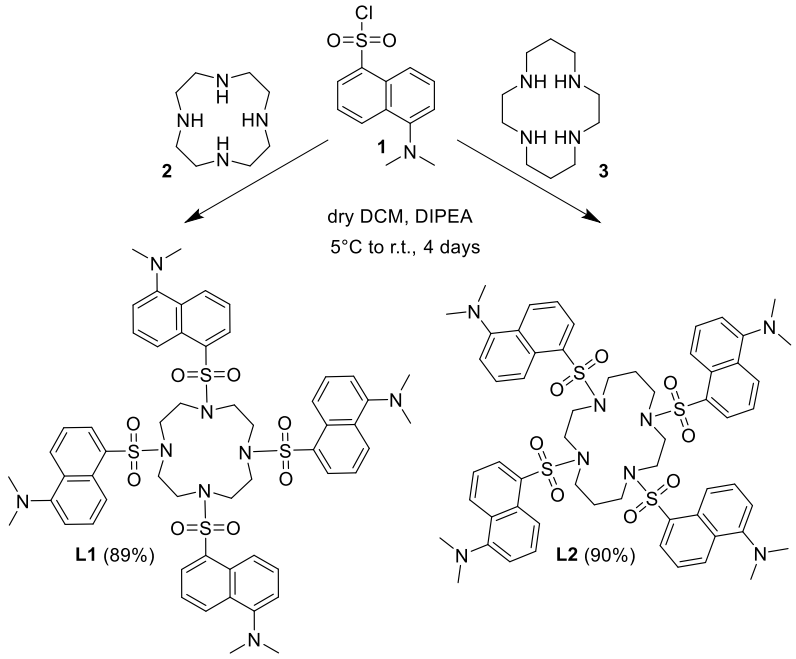
The resulting solution from the mixture of the compound solution and the polymer solution was poured into a perfluoro alkoxy alkane, PFA, support with 5 cm of diameter and left it to slow evaporation at room temperature during *ca.* 24h.

8.4 Results & Discussion

8.4.1 Synthesis

The synthesis of both compounds **L1** and **L2** was accomplished under classical conditions for the preparation of sulfonamides from amines and sulphochlorides (**Scheme 8-1**). Both cyclen (**2**) and cyclam (**3**) were dissolved in dry DCM and reacted with an excess of dansyl chloride

(**1**) in the presence of dry DIPEA. Analytical samples of **L1** and **L2** were obtained after column chromatography on silica gel and were fully characterized by 1D- and 2D-NMR spectroscopic techniques, HRMS and melting point temperatures.



Scheme 8-1. Synthetic approach to the preparation of the target compounds **L1** and **L2**.

8.4.2 Photophysical characterization

The tetradansylated derived compounds of cyclen and cyclam exhibit photoluminescent properties both in solution and in the solid state. Figure 8–3 shows the molecular representation side by side with photophysical data of compound **L1** and **L2** in chloroform recorded at 298K as a representative example (Figure 8–11 and Figure 8–12) while the data in all solvents are summarized in Table 8-2.

Considering the UV-Vis spectra, **L1** and **L2**, show a maximum at *ca.* 344 nm which is assigned to the π - π* transition of dansyl chromophore contributing to the absence of any colour visible to the naked eye. Upon excitation at the appropriate wavelength, the samples emit a greenish light with a maximum centered around 502nm and 499 nm, characteristic for the dansyl moiety due to the intramolecular charge-transfer (ICT) band between the *N,N*-dimethylamine (donor) and the sulfonamide (acceptor) functions, resulting in a Stokes shift of 9149 and 9029 cm^{-1}. On a relatable note, significant disparities can be noted regarding the solid-state emission spectra on both compounds where a wide band centered at 508 nm is recorded for **L1** much similar to the one in chloroform solution, while for **L2**, a clear, blue-shifted emission is evident accompanied by an emission maximum at 487 nm.

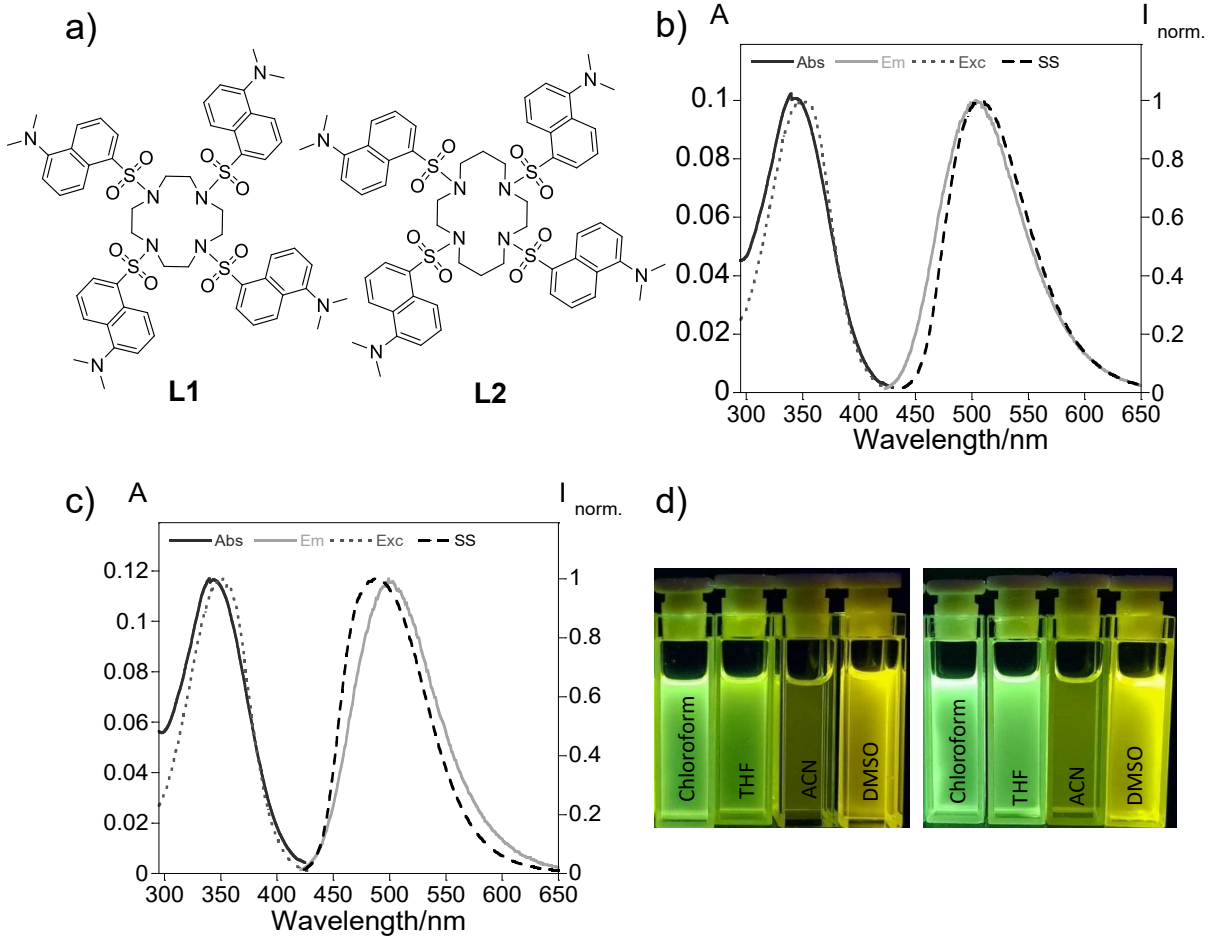


Figure 8–3. (a) Molecular structure of tetradansylated cyclen and cyclam derived compounds **L1** and **L2**. Photophysical characterization of derivatives **L1** (b) and **L2** (c) in chloroform ([**L1**] = [**L2**] = 5 μM). Images under UV light for (d) **L1** (left) and **L2** (right) in different solvents.

The fluorescence quantum yield has been determined using dansyl amide as a standard for both dansyl derivatives. Significantly higher values of 35% and 41% have been attained for **L1** and **L2** in chloroform, while for the remaining solvents, values were in the range of 24 to 34 %. Double digit nanosecond times were observed from time-resolved fluorescence decay curves for all solvents sitting in the range of 12. 4 to 15.2 ns, however, no relevant association can be determined between the characteristics of the solvent and compounds studied.

Table 8-2. Absorption maximum wavelength in solution (λ_{abs}), emission maximum wavelength in solution (λ_{em}), molar absorption coefficients (ε), Stokes shift (Δλ), fluorescence quantum yields (ϕ), emission maximum in the solid state (λ_{em}^{Solid}), brightness (ε x ϕ), fluorescence lifetimes (τ) for compounds **L1** and **L2** in various solvents.

Cpd	Solv	λ_{abs} [nm]	λ_{em} [nm]	ε (10^4) [cm^{-1} M^{-1}]	Stoke shift [cm^{-1}]	ϕ (%)	Brightness (10^3) ε χ ϕ ($cm^{-1}.M^{-1}$)	λ_{em}^{Solid} [nm]	t[ns]
L1	DMSO	347	532	2.23	10021	28	6.24	508	13.6
	CH_3CN	344	527	2.38	10094	24	5.71		12.4
	THF	340	508	2.25	9726	30	6.75		15.1
	$CHCl_3$	344	502	2.01	9149	35	7.04		14.8
L2	DMSO	345	529	1.95	10081	34	6.63	487	15.2
	CH_3CN	342	523	2.26	10119	28	6.33		13.4
	THF	340	502	2.09	9491	27	5.64		13.9
	$CHCl_3$	344	499	2.33	9029	41	7.04		15.2

However, the presence of a solvent environment significantly affects the stabilization of the ligand's excited state due to the alteration of the fluorophore's dipole moment. Based on the information presented in Table 8-1, the increase in solvent polarity is accompanied by an increase of the energy gap and, consequently, an increase in Stoke's shift, which translate into a bathochromic shift. The shift presented can be related to a positive solvatofluorochromic effect due to the capacity of the environment-sensitive dyes to change their fluorescence maximum wavelength aligned with the solvent polarity, behaviour well noticed in **Figure 8–3**.

Aligned with these observations, efforts have been made to thoroughly characterize the interactions between the solvent and the compound. To achieve this, three solute-dependent parameters (υ_0, a, b and p) have been determined through the multiparametric fitting of the Kamlet-Taft equation (Equation 1).

$$\upsilon = \upsilon_0 + a\alpha + b\beta + p\pi^* \qquad \text{(Equation 1)}$$

Where υ_0 represents the wavenumber value in a reference solvent; parameters a, b and p are obtained through multiple regression analysis that reflect the underlying sensitivity of the probes photophysical behaviour to solvent polarity; α: hydrogen bond donor acidity (HBD); β: hydrogen bond acceptor basicity (HBA); π^*: stabilization of a charge or dipole without a specific dielectric interaction (Table 8-1). [49,50]

Table 8-3. Independent fluorescence wavenumber ($\upsilon 0$), solvent polarity (*p*), HBD (*a*), HBA (*b*), slope and coefficient (R^2) of the linear fitting plot $\upsilon_{exp.}$ versus $\upsilon_{calc.}$

	υ0	a	b	p	Slope	R^2
L1	21795	-6245	-3399	-415	1.00	1
L2	22197	-6548	-3357	-741	1.00	1

Table 8-3 presents the reference wavenumber value υ_0, the fitted parameters (a, b and p) alongside the slopes and correlation coefficients obtained through the fitting of a linear plot of $\upsilon_{exp.}$ versus υ_{calc}, by applying the Kamler-Taft model. It is perceptible for both compounds extended negative values of a and b parameters, where some relevant differences are present in the predisposition towards hydrogen bond donor sensitivity being **L2** more slightly prone to be influenced by protic solvents. Finally, large negative p value observed for **L2** indicates a more instability towards highly polarizable solvents presumably due to the increase in size with less rigidity due to the introduction of two carbons in the macrocycle.

8.4.3 Exploring the behavior in aqueous media

Solutions with different ratios of water in THF were prepared and measured by absorption and fluorescence emission spectroscopy in order to evaluate the optical properties of the ligands when exposed to water. Figure 8–4 shows that the increase of water content is responsible for a decrease in the emission intensity to 67% following a bathochromic shift, while at 83% of water content, an increase on luminescence intensity (ca. 40%) is evident without a shift when comparing to the initial solution. This increase of emission intensity with water fraction of 83% translates on a fluorescence quantum yield values increase (ϕL1=49,7%; ϕL2=50,4%) than in the absence of water (ϕL1=30%; ϕL2=27%), which suggest an aggregation induced emission (AIE) effect, i.e., when in the vast majority of water medium, the ligand molecules tend to aggregate and restrict the intramolecular rotation blocking the non-radiative relaxation. [51,52] While in the presence of 67% of water, both ligands reveal some solubility issues as shown in Figure 8–4, where some precipitate is observed which contributes also to the decrease of the emission signal and clarifies the decrease in the absorption profile.

Initially, when the water content is increased, there is a notable rise in the baseline as seen in the absorption spectra of the solution containing 83% water. The observed rise in the absorbance measurement can be attributed to a light scattering artifact caused by the presence of aggregates, which adds to the inherent heterogeneity. Through dynamic light

scattering, the solutions were measured resulting on different polydispersity index, PDI_{L1}=0,127; PDI_{L2}=0.049 with hydrodynamic sizes of 134±3 nm (**L1**) and 98±1 nm (**L2**), and zeta potential of -18±1 mV (**L1**) and -22±2 mV (**L2**). The PDI obtained reflects the presence of monodisperse aggregates for the two compounds, with slightly differences on the size and zeta potential due to the molecular organization in aggregates.

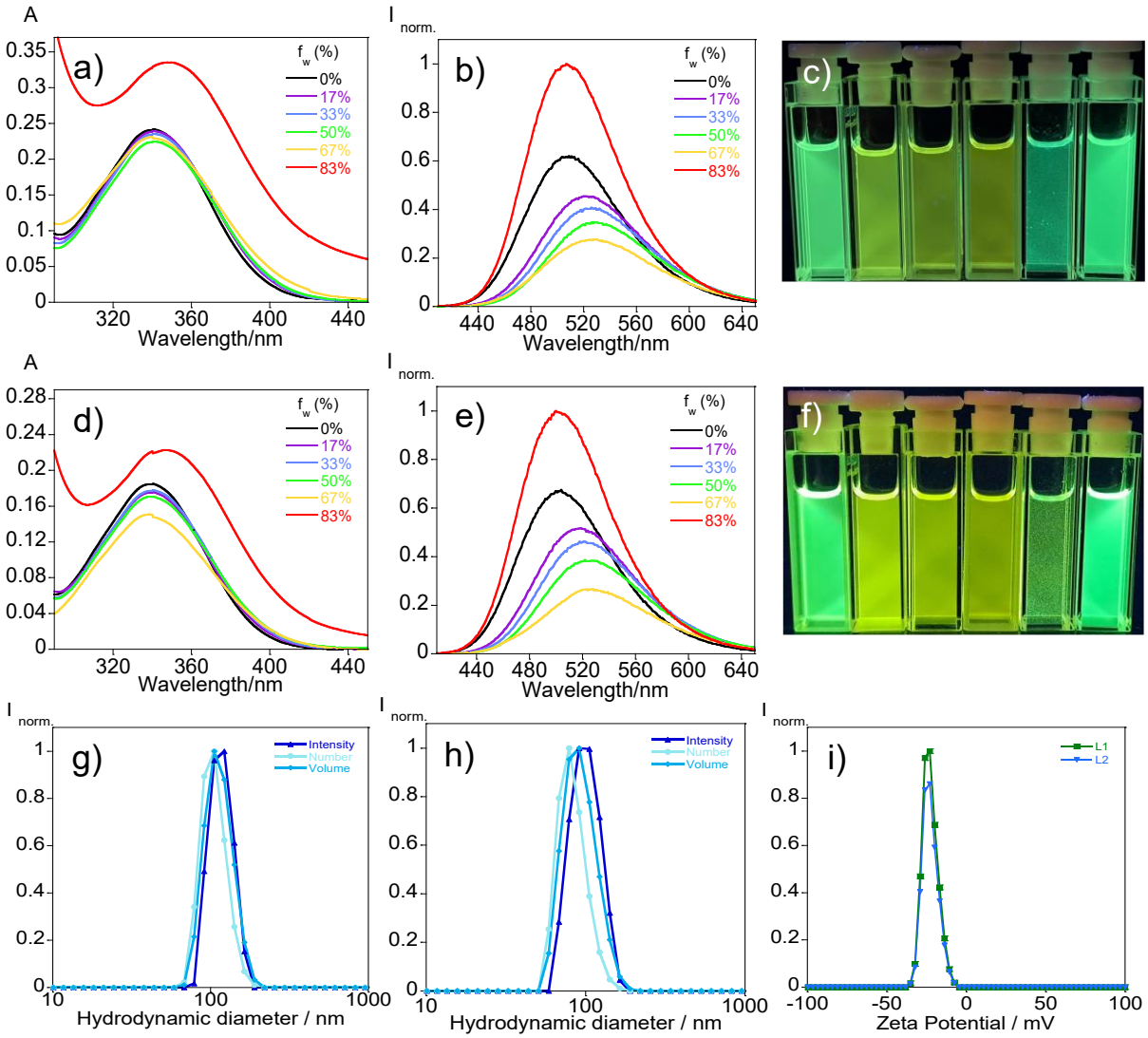


Figure 8–4. Absorption (a,d) and emission spectra (b,e) of **L1** (a,b) and **L2** (d,e) in THF with different water fractions f_w (0%, 17%, 33%, 55%, 67%, 83%), [**L1**]=[**L2**]= 10 μM. Images of **L1** (c) and **L2** (f) in THF with different water fractions. Hydrodynamic diameter of **L1** (g) and **L2** (h) aggregates according to number, volume, and intensity distributions and zeta potential (i) of a solution of THF/water with f_w = 83%.

8.4.4 Metal ion sensing

Considering the possible use of dansyl derivatives for detecting metal ions, we evaluated the capacity of **L1** and **L2** to sense metal ions, including, Ca^{2+}, Co^{2+}, Ni^{2+}, Cu^{2+}, Zn^{2+}, Ag^{+}, Cd^{2+},

Hg^{2+}, which were evaluated in acetonitrile. Figure 8–5 illustrates the impact on the emission intensity when 1, 5, and 10 equivalents of the aforementioned metal ions are added. It is evident that the absorption and emission spectra only exhibited significant spectrum alterations in the presence of mercury(II) and copper(II) ions. By adding only 1 equivalent of both metal ions, the emission signal is significantly reduced. Subsequently, adding 5 equivalents completely suppresses the fluorescence intensity. Thus, both compounds exhibit strong selectivity for the specified metal ions.

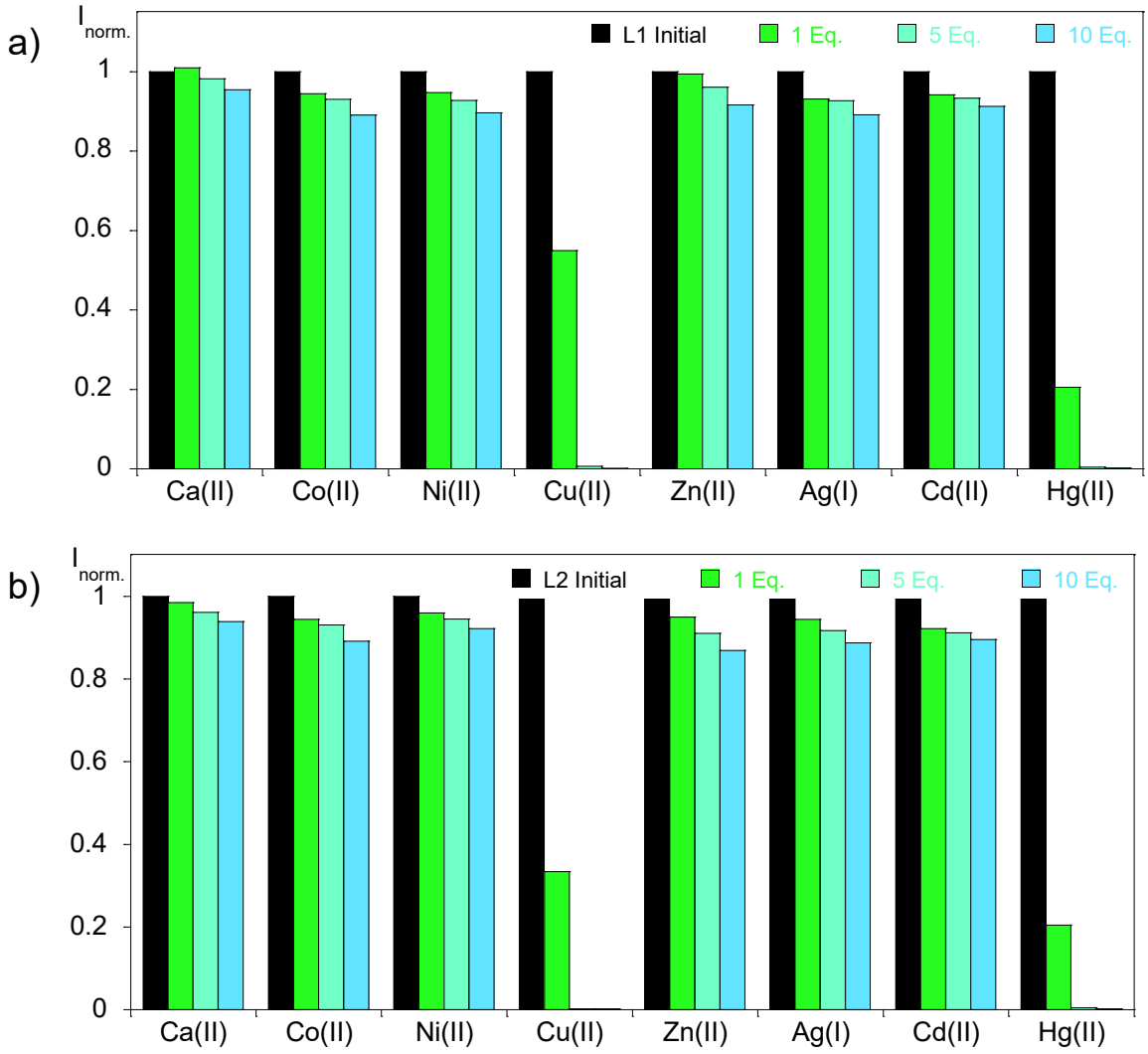


Figure 8–5. Normalized emission intensity of **L1** (a) and **L2** (b) upon addition of 1, 5, and 10 equivalents of Ca^{2+}, Co^{2+}, Ni^{2+}, Cu^{2+}, Zn^{2+}, Ag^{+}, Cd^{2+}, and Hg^{2+} metal ions in acetonitrile. ([**L1**] = [**L2**] = 5 μM, T = 298K).

Thereby, Figure 8–6 displays the titrations of **L1** and **L2**, in acetonitrile, upon successive addition of Cu^{2+} (a, c) and Hg^{2+} (b, d) microliter aliquots, respectively, conducted through spectrophoto- and spectrofluorimetric devices.

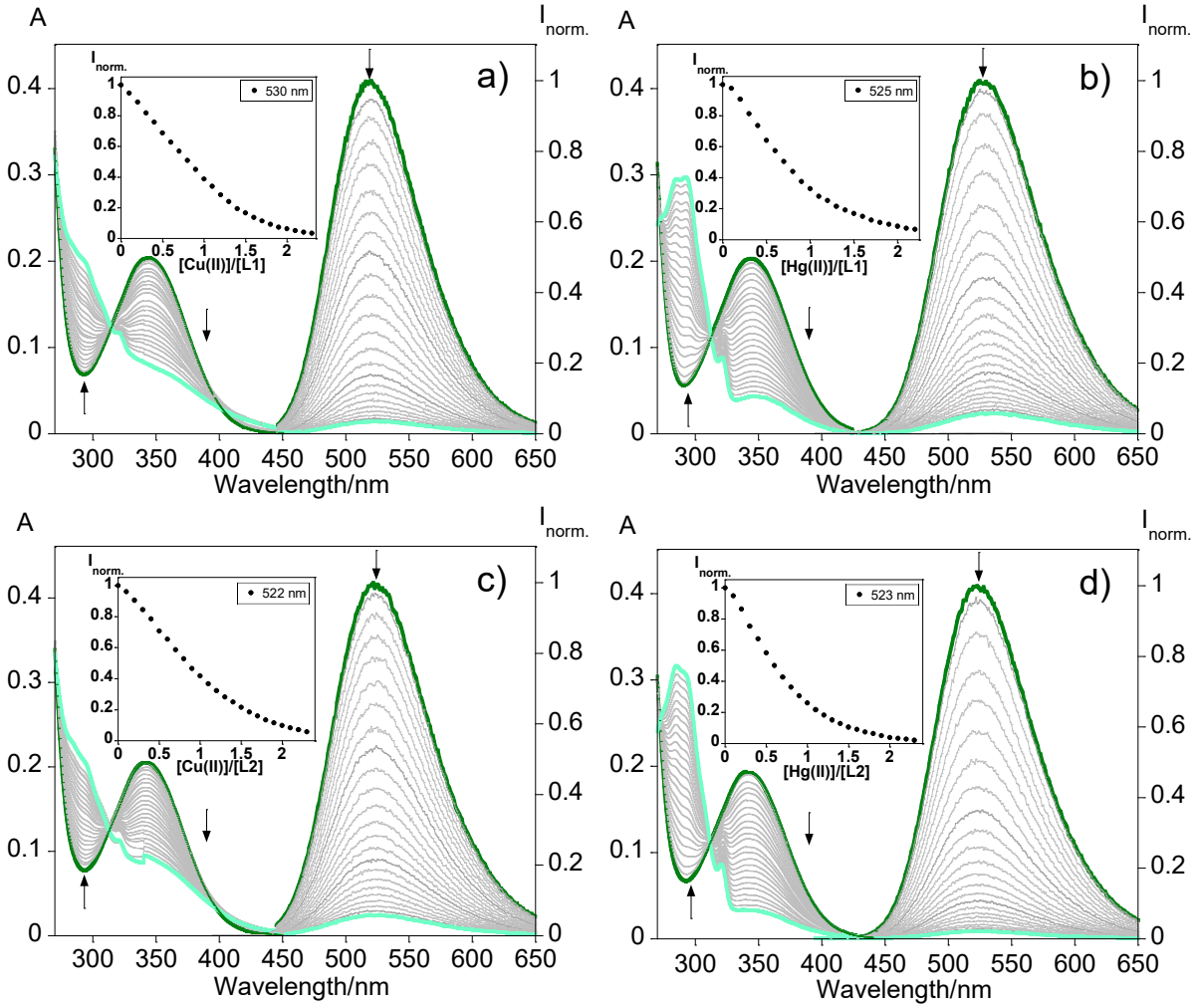


Figure 8–6. Spectrophotometric and spectrofluorimetric titrations of compounds **L1** (a, b) and **L2** (c, d) with increased additions of Cu^{2+} (a, c), and Hg^{2+} (b, d) in CH_3CN. The inset represents the emission (a-d) as a function of $[Cu^{2+}]/[\mathbf{L1}]$ at 530 nm (a), of $[Cu^{2+}]/[\mathbf{L2}]$ at 525 nm (c), of $[Hg^{2+}]/[\mathbf{L1}]$ at 525 nm (b) and of $[Hg^{2+}]/[\mathbf{L2}]$ at 523 nm (d). [**L1**] = [**L2**] = 5 μM, T = 298 K).

The progressive addition of Cu^{2+} ions results, generally, in a decrease on both the absorption and the emission spectra. The absorption spectra display a decrease of the main band centred at 345 nm and 342 nm for **L1** and **L2**, respectively. A remarkable decrease in luminescence intensity is also observed without noticing any particular shift of the maxima (530 nm and 522 nm for **L1** and **L2**, respectively). Copper ion is a paramagnetic transition metal with an unfilled d orbital that can induce mechanisms like electron transfer or energy transfer caused quenching, consequently, the quenching in luminescence is observed.

Similarly, as Hg^{2+} solution is gradually added, a decrease is noted on the main absorption band at 344 nm without any shift. Looking to the spectrofluorimetric data, at 525 nm for **L1**, a quenching of the emission's intensity occurs, causing an almost complete suppression upon added 2 equivalents of the metal ion and, consequently, the formation of a plateau. Attending

to Figure 8–6 (c and d), an analogous behaviour is verified for **L2**. Hg^{2+} ions exhibit diamagnetic properties with a d10 configuration and large atomic number, in that case, the formation of heavy atom complexes can lead to non-radiative deactivation explaining the observations.

Therefore, considering that in the presence of Cu^{2+} and Hg^{2+}, both ligands show an absorption and a fluorescence decay, while a chelation enhanced quenching effect (CHEQ) phenomenon is suggested, where **L1** and **L2** coordinate to the metal ion resulting in the corresponding complexes evidenced by Figure 8–7. [53-61]

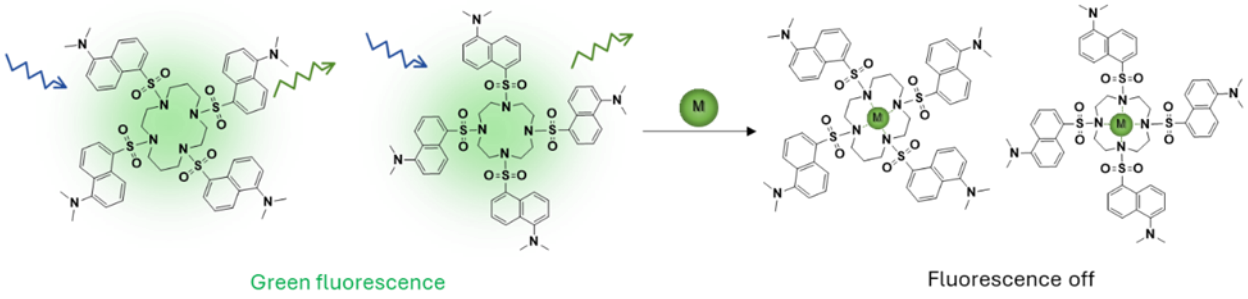


Figure 8–7. General representation of the chelation enhanced quenching effect after complexation with Cu^{2+} and Hg^{2+} metal ions.

In order to completely assess the sensing ability towards Hg^{2+} and Cu^{2+}, the HypSpec software [62] was used for the calculation of the interaction constants of all complexes. Furthermore, the determination of the detection and quantification limit parameters of both compounds towards both has been fulfilled. The association constants, LOD and LOQ are included in Table 8-4.

Table 8-4. Association constants using HypSpec software for compounds **L1** and **L2** towards Hg^{2+} and Cu^{2+} ions with included stoichiometry in acetonitrile. Respective values for the detection limit (LOD) and quantification limit (LOQ) amounts (μM) were measured following the emission maximum wavelength.

Compounds	Metal (M)	Association constants ($LogK_{ass.}$), L:M	LOD (μM)	LOQ (μM)
L1	Cu^{2+}	5.613 ± 0.002 (1:1)	2.9	3.4
	Hg^{2+}	5.104 ± 0.002 (1:1)	3.5	3.8
L2	Cu^{2+}	5.870 ± 0.003 (1:1)	2.8	4.4
	Hg^{2+}	5.047 ± 0.002 (1:1)	2.0	3.0

The stability constants were evaluated based on the stoichiometry 1:1 (L:M) by keeping in mind the complex centers evidenced by the ligand structures. The stability constants values for **L1** and **L2** towards both metal ions clarify the high affinity between both species being the

highest constant found for **L2** towards Cu^{2+} with a value of $LogK_{ass.}$ = 5.870 ± 0.003. Thus, detectable differences rise while considering the two macrocycles specially for Cu^{2+} sensing in the observed values since the presence of two more carbons provide the flexibility to better accommodate the metal ion.

The lowest detectable and quantifiable amounts were determined for **L2** (2.0 μM and 3.0 μM), having the potential to be useful in applications such as environmental monitoring, where the presence of Hg^{2+} needs to be detected and quantified at low concentrations.

8.4.5 Designing temperature-responsive materials using dansyl derivative emission

Since **L1** and **L2** have shown solid-state emission and exhibit solvatofluorochromism due to the varying properties of different solvents, the next step is to modulate the emission of these ligands in solid-supported materials to develop molecular thermometers based on their emission properties. Initially, these compounds have been studied without the use of solid supports. To this end, the emission of each probe was recorded as the temperature increased in the solid state. Figure 8–8 presents the emission spectra and the plot of I_{norm} versus temperature for compound both compounds. While heating, both compounds display a quenching in the fluorescence emission, linear at certain ranges, in the case of **L1**, with no visible shift with respect to the maxima band. Between ca. 40°C to 110°C a linear behaviour is evident, therefore, within this range, this ligand can function as a probe in optical sensing due to its photochemical stability. However, around 120°C, a sudden decrease in intensity was observed compromising the recovery of luminescence (only *ca.* 20%, Figure 8–13). The decrease in the fluorescence intensity with increasing temperature is caused by the loss of intermolecular interactions that leads to the melting point observed at 178º C in the case of **L1**.

In another way, **L2** can maintain a steady emission and there is no observation of a sharp quenching on the fluorescence intensity until 200ºC due to the higher melting point observed for this compound at 227º C, characteristic that provides the recovery of *ca.* 90% of the emission (Figure 8–13).

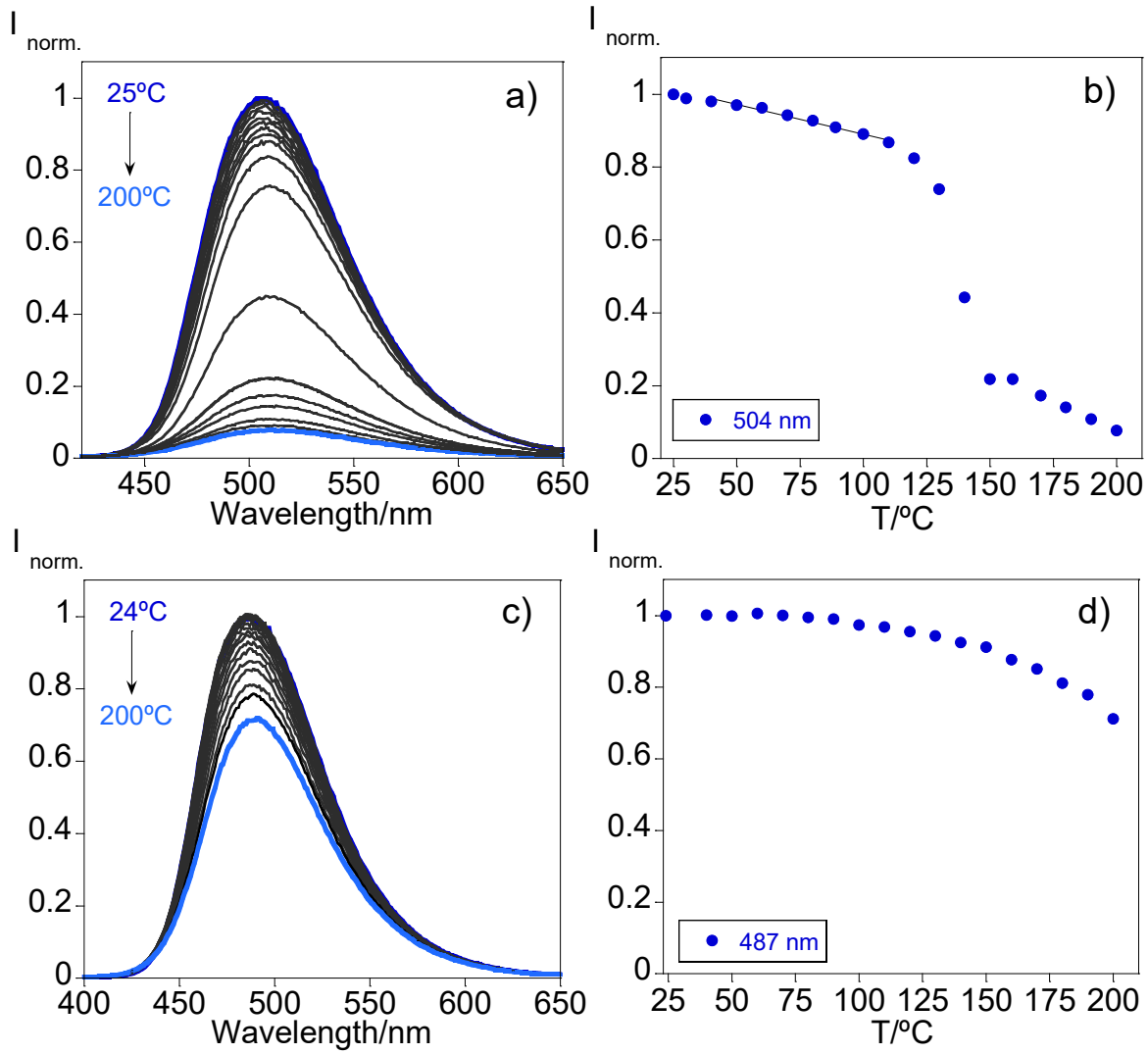


Figure 8–8. Temperature-dependent emission spectra of **L1** in the solid state (a) collected through a warming cycle between 25ºC to 200ºC. $I_{norm.}$ vs. T plot recorded in the emission maximum at 504 nm upon heating (b) [40 to 110 ºC (Y= 1.0529 - 0.0016231x), yielding R=0.99139]. Temperature-dependent emission spectra of **L2** (d) collected through a warming cycle between 24ºC to 200ºC. $I_{norm.}$ vs. T plot recorded in the emission maximum at 487 nm upon heating (d).

Building on previous findings, several doped polymer thin films have been developed to enhance sensing applications. Following the synthesis procedure of Figure 8–2, compounds L1 and L2 were doped into Kurarity and TPU. Figure 8–9 compares the emission spectra of these compounds in their solid state with their emission in the various polymer thin films.

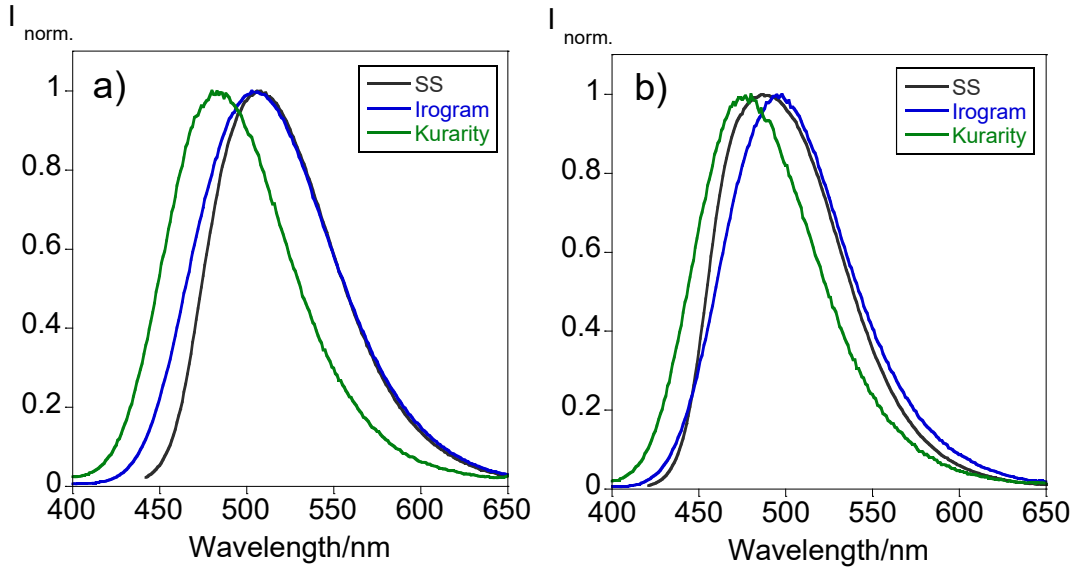


Figure 8–9. Comparison between the emission spectra of the different polymer thin films doped with (a) L1 and (b) L2 and the respective emission spectrum in the solid state.

In summary, polymer thin films were effectively created, and their emission characteristics were examined. Figure 8–9 clearly shows that the Kurarity of the polymer matrix can adjust the final emission of the film by interacting with the probe, causing a blue shift in the emission to 480 nm for both compounds. On another hand, the Irogran films maintain the emission maximum wavelength observed in the solid state. Similar behaviours have been observed in a previous work demonstrating the modulation of the emission using polymer matrix of dansyl derivatives. [1]

Considering the previous results, the polymer-doped films were studied under varying temperatures to determine if the constraints found in the solid state for **L1** and **L2** could be mitigated. Figure 8–10 presents the temperature dependent emission spectra of **L1** doped in both Kurarity and Irogran polymer matrixes as a representative example. The emission spectra for polymer-doped films of **L2** can be found in Figure 8–15.

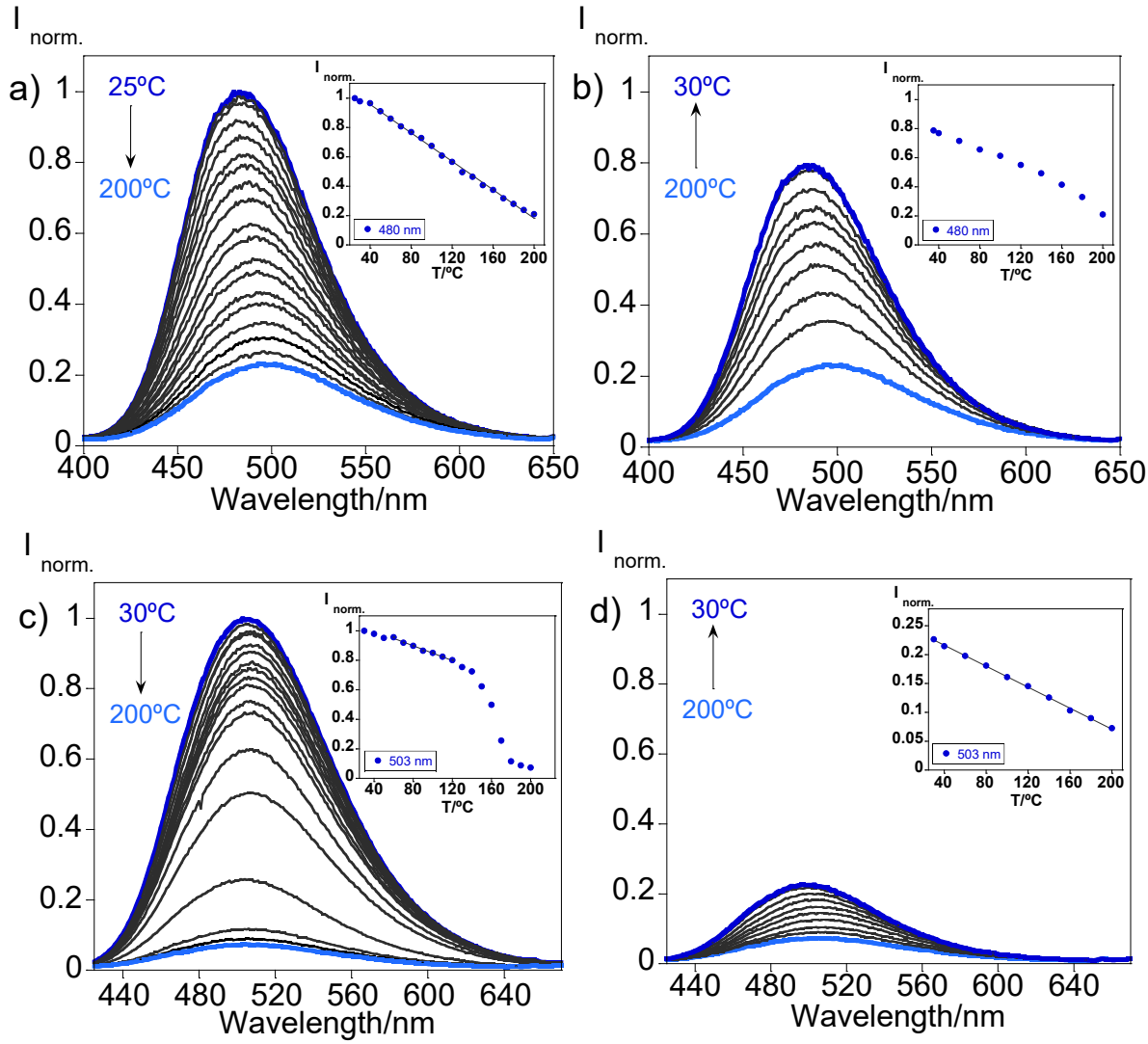


Figure 8–10. Temperature-dependent emission spectra of **L1** doped in (a) Kurarity during heating cycle [Inset: $I_{norm.}$ vs. T plot at 480 nm upon heating: 40 to 200 ºC (Y= 1.151 - 0.004844x), yielding R=0.9975]; (b) Kurarity during cooling cycle [Inset: $I_{norm.}$ vs. T plot at 480 nm upon cooling]; (c) Irogran during heating cycle [Inset: $I_{norm.}$ vs. T plot at 503 nm upon heating: 60 to 120 ºC (Y= 1.099 - 0.00251x), yielding R=0.9916]; (d) Irogran during cooling cycle [Inset: $I_{norm.}$ vs. T plot at 503 nm upon cooling: 30 to 200 ºC (Y= 0.2527 - 0.0009083x), yielding R=0.9989];

An attenuation of the emission is observed in both polymer-doped films as the temperature increases, up to a maximum of 200°C. Intriguingly, the behavior of **L1** in its solid state, as influenced by its melting point, does not have an impact on the emission profile in Kurarity. In this case, the polymer matrix functions as a medium to maintain emission at higher temperatures by offering adequate conductivity, thereby reducing the thermally activated non-radiative processes displayed by the compounds and prevent the melting. During the temperature variation cycle, it is possible to perceive linearity from 40°C to 200°C and a recovering to 80% of the initial fluorescence is observed after cooling. Regarding the Irogran doped material, it

exhibited the same behavior as in its solid state, which hindered the restoration of the emission at the end of the cycle.

In the case of **L2** doped materials (Figure 8–15) similar ranges of linearity have been found when doped in Kurarity with also almost complete recovery of the emission while for Irogran the fast quenching at 150°C hampered the emission rise at 25°C to reach past 25%. These data show that by attaching the probe to a solid substrate, it can be used as a molecular thermometer without being limited by its physical properties.

8.5 Conclusions

Two fluorophores, based on tetradansylated cyclen and cyclam, were synthesized and their photoluminescent characteristics were investigated. Efforts were undertaken to study the photophysical features of dansyl compounds in various solvents to fully understand the impact of each solvent's intrinsic properties on the emission of the probes, considering that dansyl compounds commonly display solvatofluorochromism. Implementation of the Kamlet-Taft equation expressed in detail the solute-solvent interactions with a positive solvatofluorochromism behaviour is present for both compounds. Furthermore, the compounds were found to modulate their emission in the presence of water expressing aggregation induced emission at high water content that was confirmed by dynamic light scattering experiments with hydrodynamic sizes of 134±3 nm (**L1**) and 98±1 nm (**L2**). From an environmental remediation perspective, **L1** and **L2** were found to quench their emission in the presence of Hg^{2+} and Cu^{2+} ions. Mononuclear species were proposed with Cu^{2+} and Hg^{2+} and that **L2** has the highest association constant with Cu^{2+} (Log $K_{ass.}$=5.87) while the lowest LOD and LOQ was found for Hg^{2+} of 2 μM and 3 μM, respectively. Finally, the probes were characterized in the solid state and incorporated into solid supports to develop molecular thermometers. Polymers such as Kurarity and TPU were doped with the compounds, and their luminescence properties were studied. The polymer matrix Kurarity was discovered to regulate the emission maxima for both compounds. The probes demonstrated excellent linearity throughout the heating cycle, rendering them highly appropriate for utilization as temperature sensors in industrial applications.

8.6 Supplementary material

8.6.1 Supplementary figures & tables

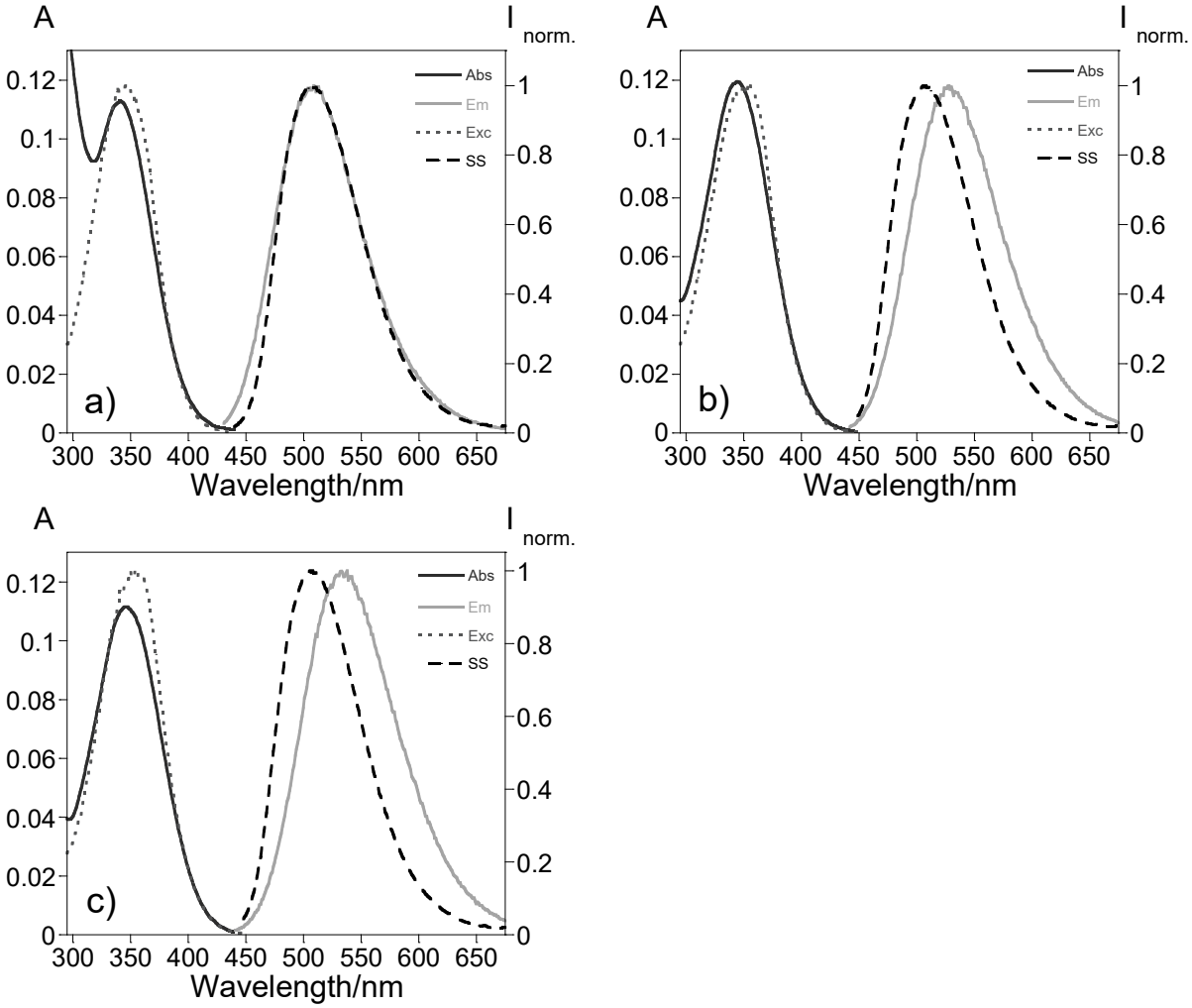


Figure 8–11. Photophysical characterization of L1 in (a) THF, (b) Acetonitrile and (c) DMSO.

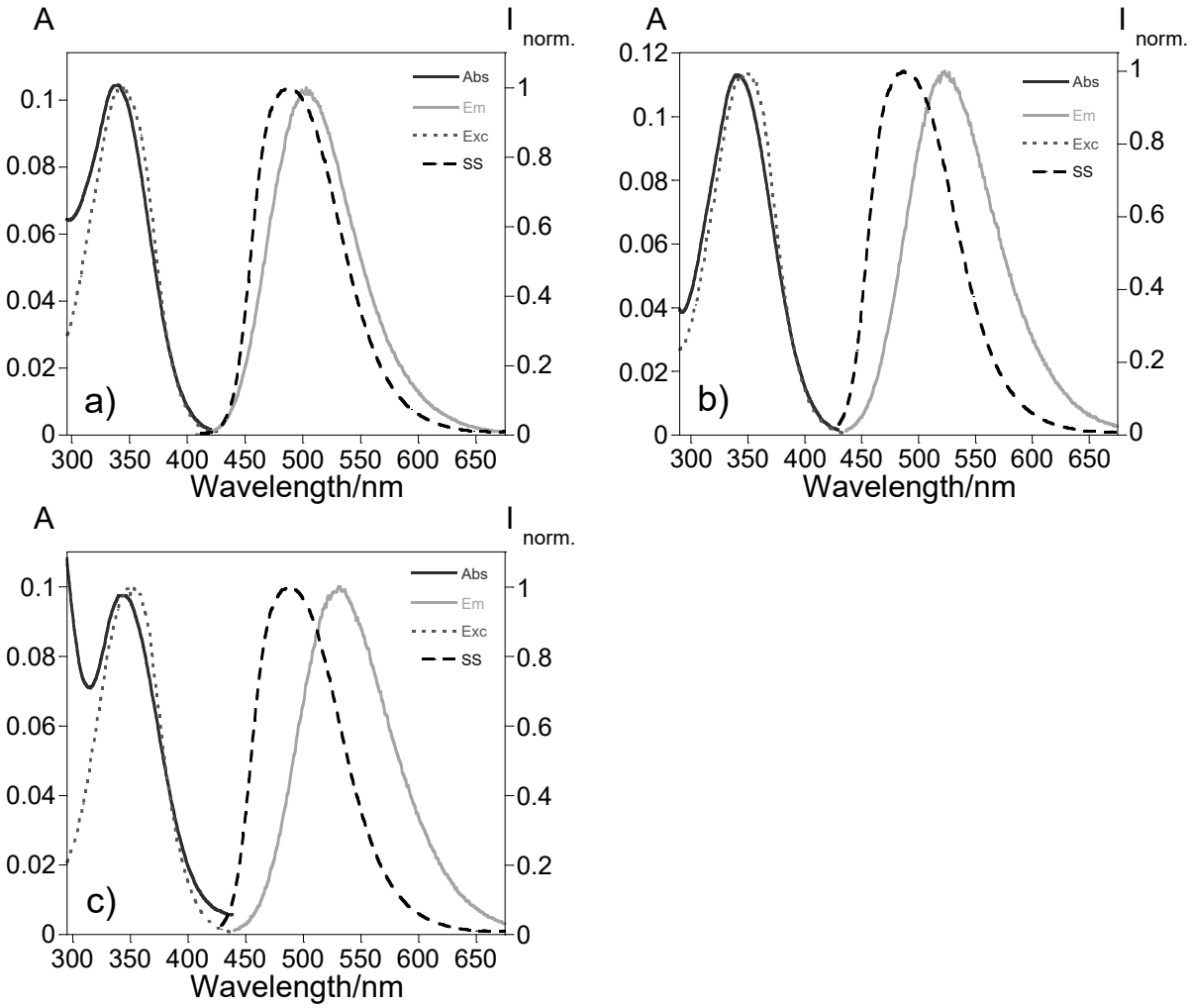


Figure 8–12. Photophysical characterization of L2 in (a) THF, (b) Acetonitrile and (c) DMSO.

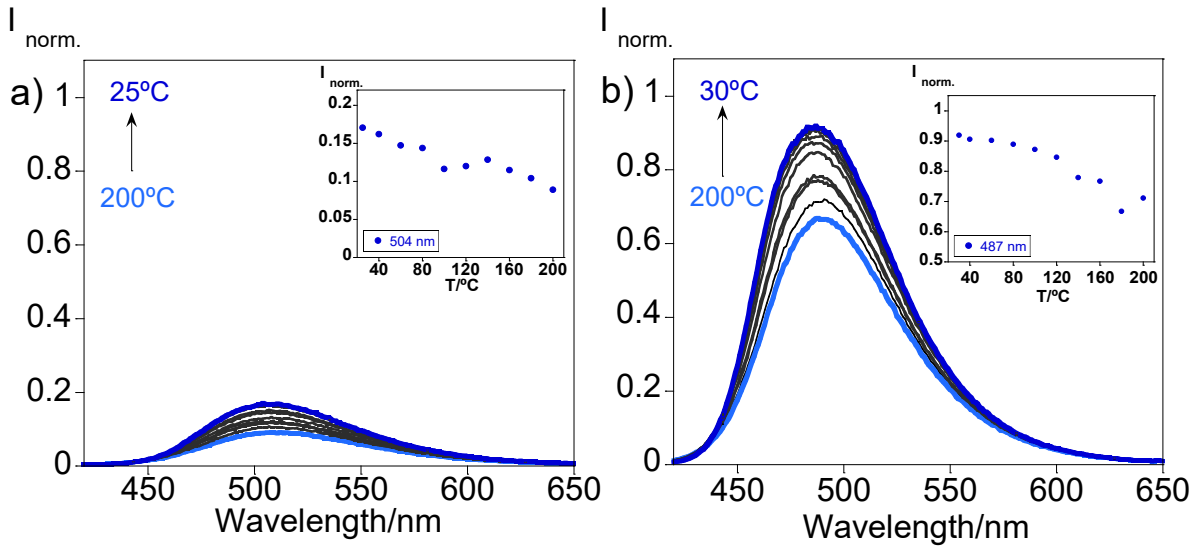


Figure 8–13. Temperature-dependent emission spectra of (a) L1 and (b) L2 in the solid state collected through a cooling cycle between 25ºC to 200ºC. $I_{norm.}$ vs. T plot recorded in the emission maximum at 504 nm and 487 nm upon cooling for L1 and L2, respectively.

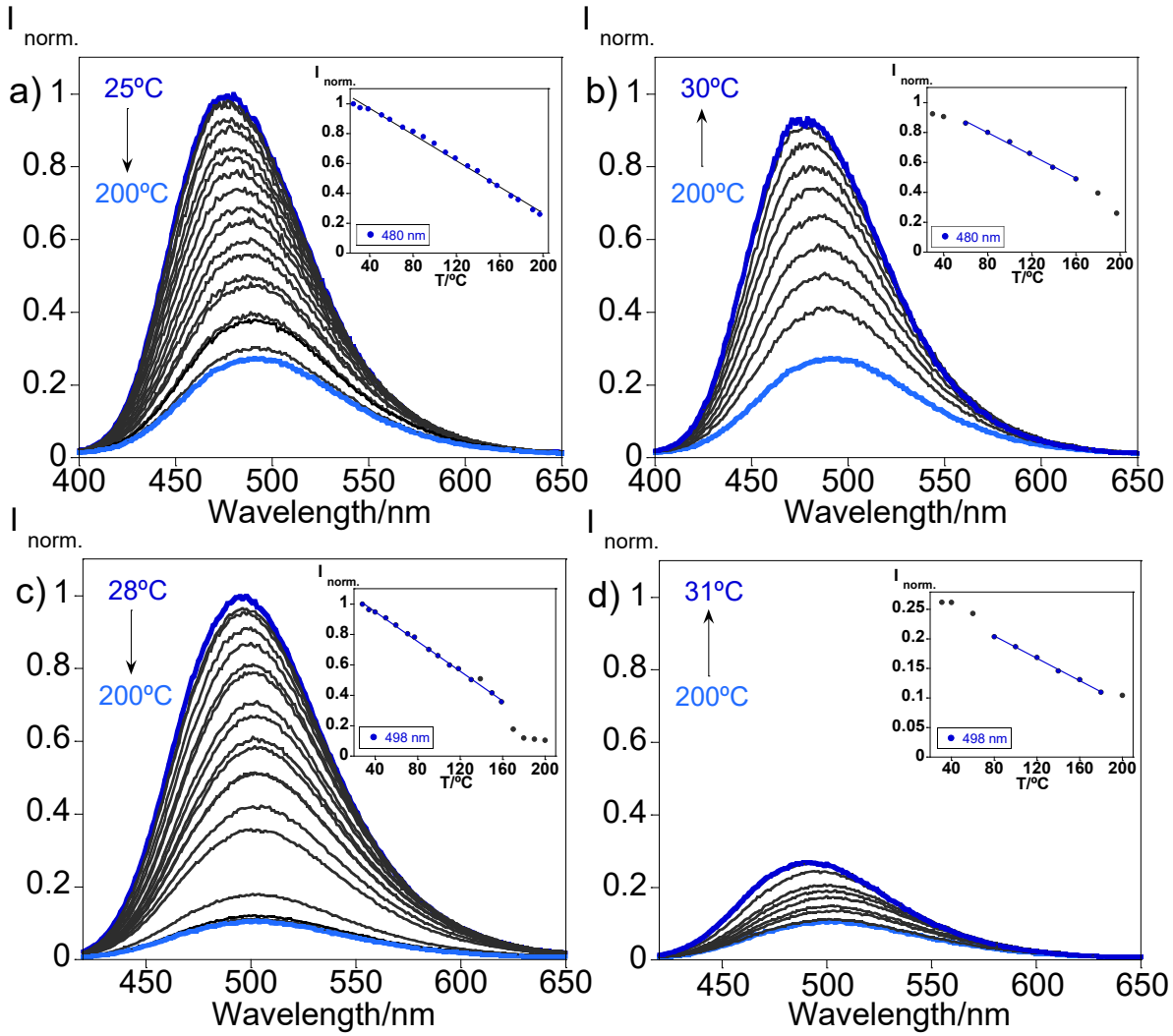


Figure 8–14. Temperature-dependent emission spectra of L2 doped in (a) Kurarity during heating cycle [Inset: Inorm. vs. T plot at 480 nm upon heating: 25 to 200 ºC (Y= 1.1452 - 0.0044x), yielding R=0.9938]; (b) Kurarity during cooling cycle [Inset: Inorm. vs. T plot at 480 nm upon cooling 60 to 160 ºC (Y= 1.1035 - 0.0038x), yielding R=0.9948]; (c) Irogram during heating cycle [Inset: Inorm. vs. T plot at 498 nm upon heating: 28 to 159 ºC (Y= 1.1402 - 0.0048x), yielding R=0.9959]; (d) Irogram during cooling cycle [Inset: Inorm. vs. T plot at 498 nm upon cooling: 80 to 180 ºC (Y= 0.28 - 0.0009x), yielding R=0.9979].

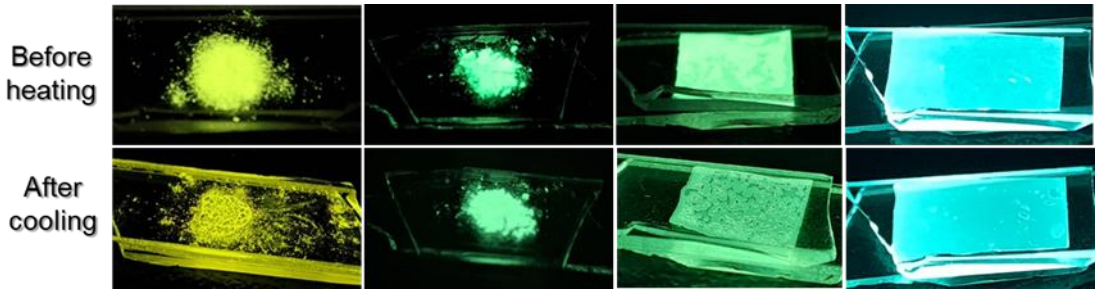


Figure 8–15. L1 and L2 in solid-state (left and right, respectively) and at polymer films, L1 in IROGRAN and L2 in KURARITY (left and right, respectively) under an UV light before heating and after cooling.

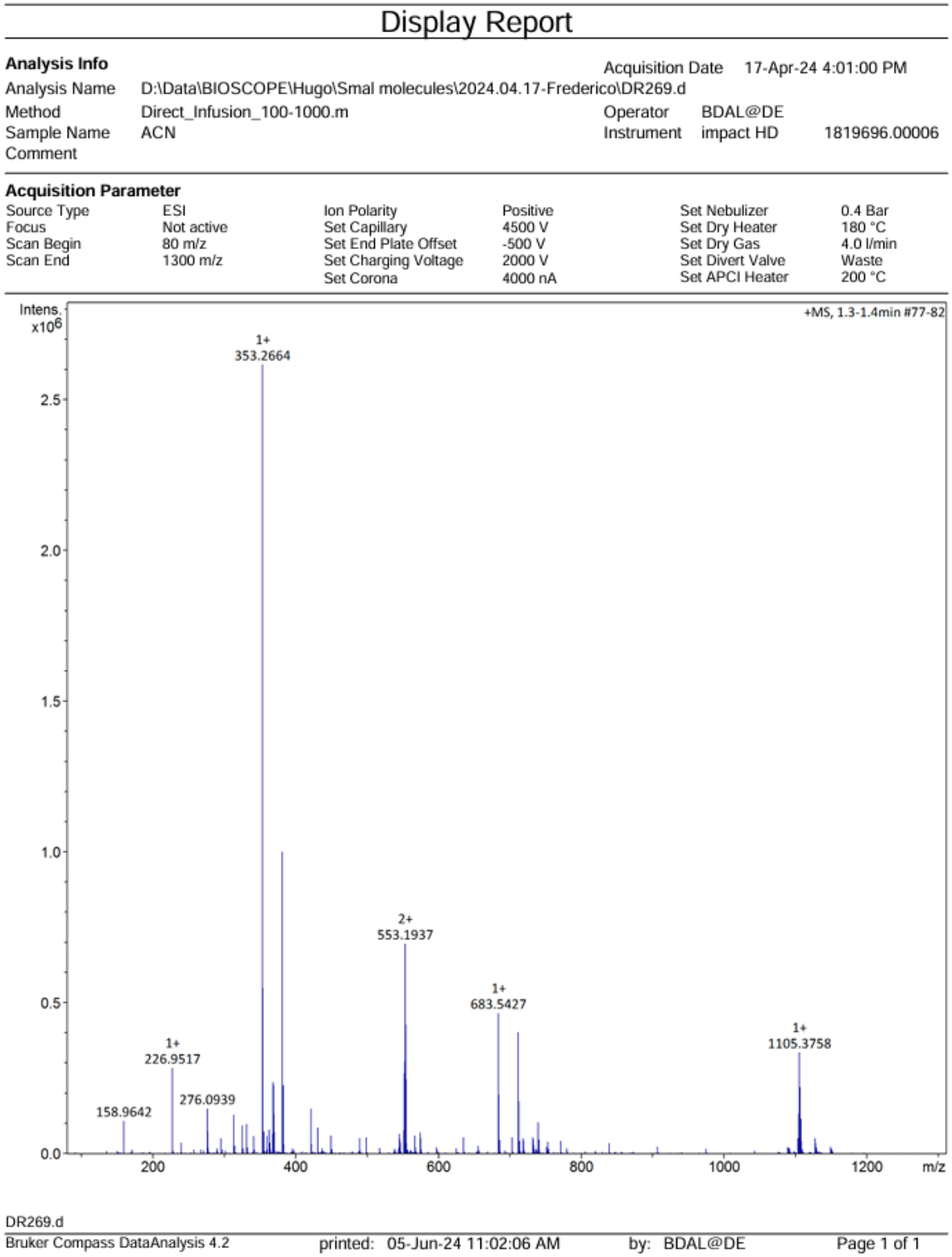


Figure 8–16. ESI-HRMS spectrum of compound L1.

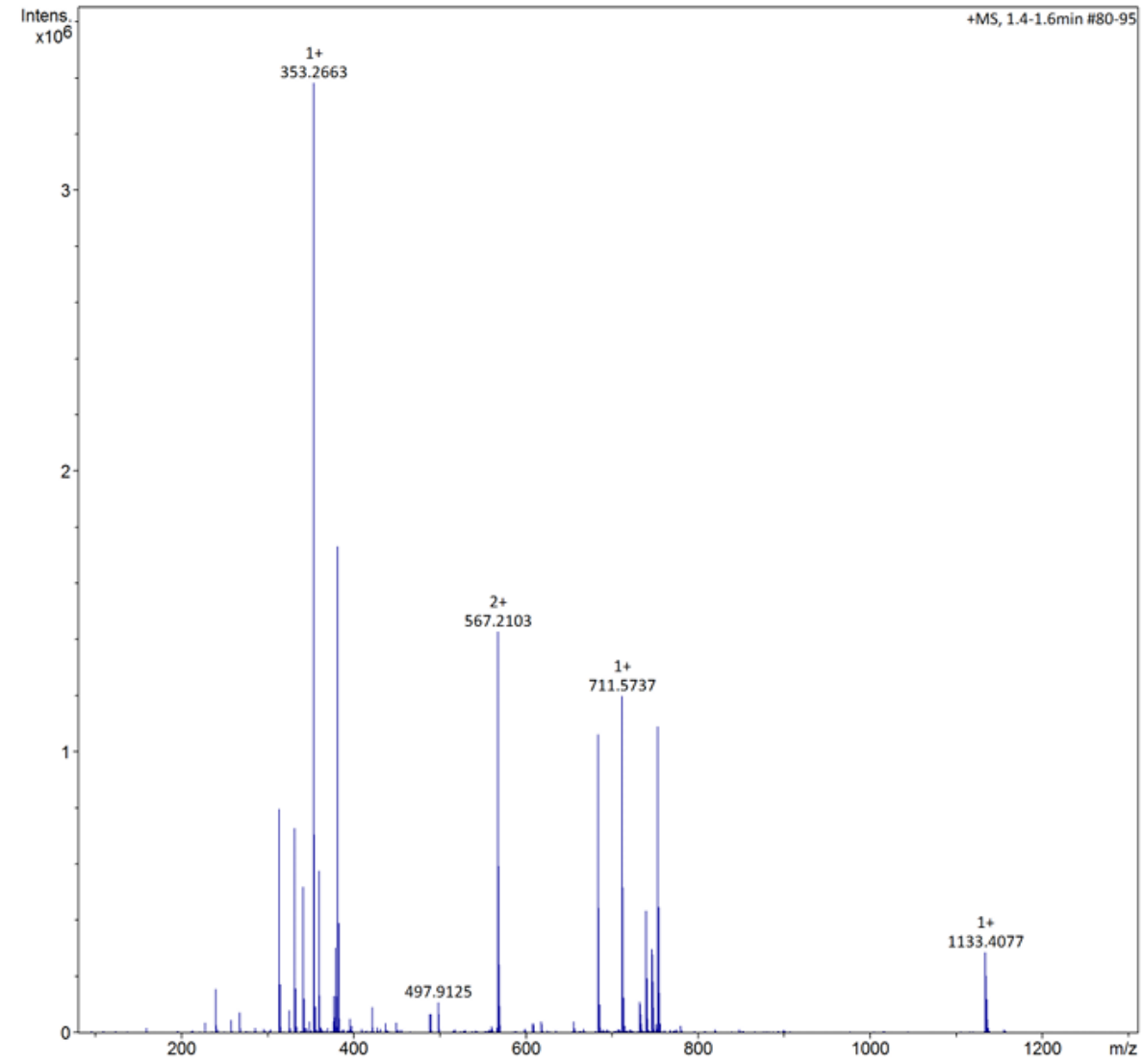
Display Report

Analysis Info

Analysis Name	D:\Data\BIOSCOPE\Hugo\Smal molecules\2024.04.17-Frederico\DR274.d	Acquisition Date	17-Apr-24 3:51:27 PM
Method	Direct_Infusion_100-1000.m	Operator	BDAL@DE
Sample Name	ACN	Instrument	impact HD 1819696.00006
Comment			

Acquisition Parameter

Source Type	ESI	Ion Polarity	Positive	Set Nebulizer	0.4 Bar
Focus	Not active	Set Capillary	4500 V	Set Dry Heater	180 °C
Scan Begin	80 m/z	Set End Plate Offset	-500 V	Set Dry Gas	4.0 l/min
Scan End	1300 m/z	Set Charging Voltage	2000 V	Set Divert Valve	Waste
		Set Corona	4000 nA	Set APCI Heater	200 °C



DR274.d

Bruker Compass DataAnalysis 4.2 printed: 05-Jun-24 11:24:15 AM by: BDAL@DE Page 1 of 1

Figure 8–17. ESI-HRMS spectrum of compound L1.

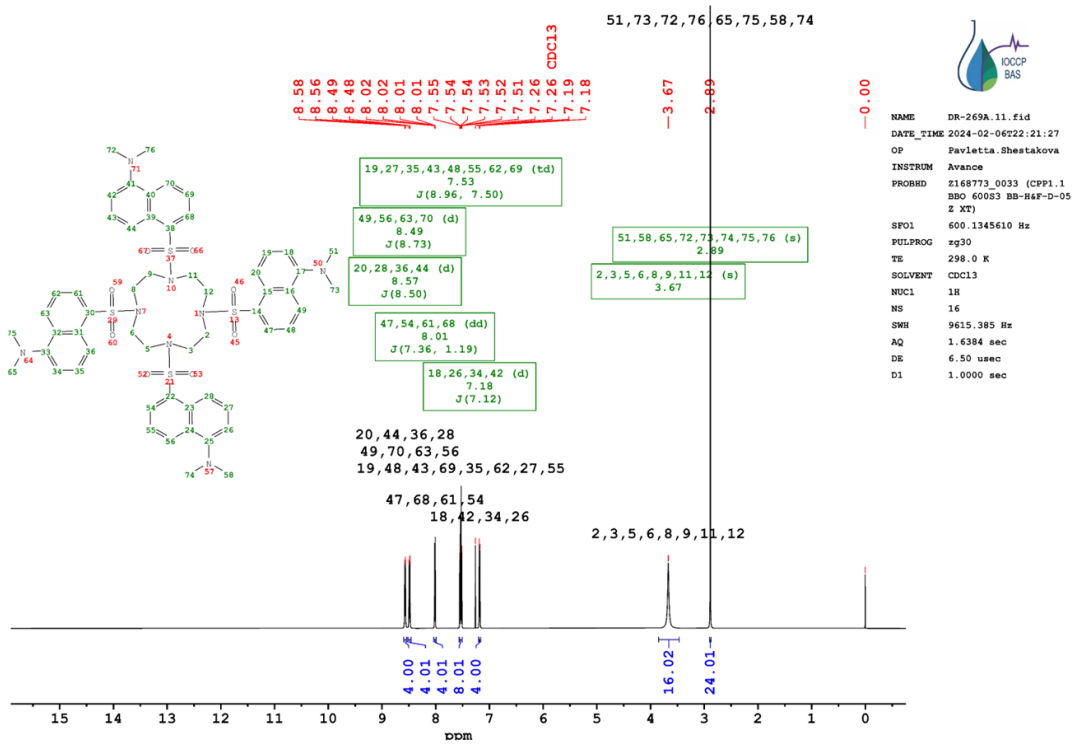


Figure 8–18. ^{1}H-NMR spectrum of compound **L1**.

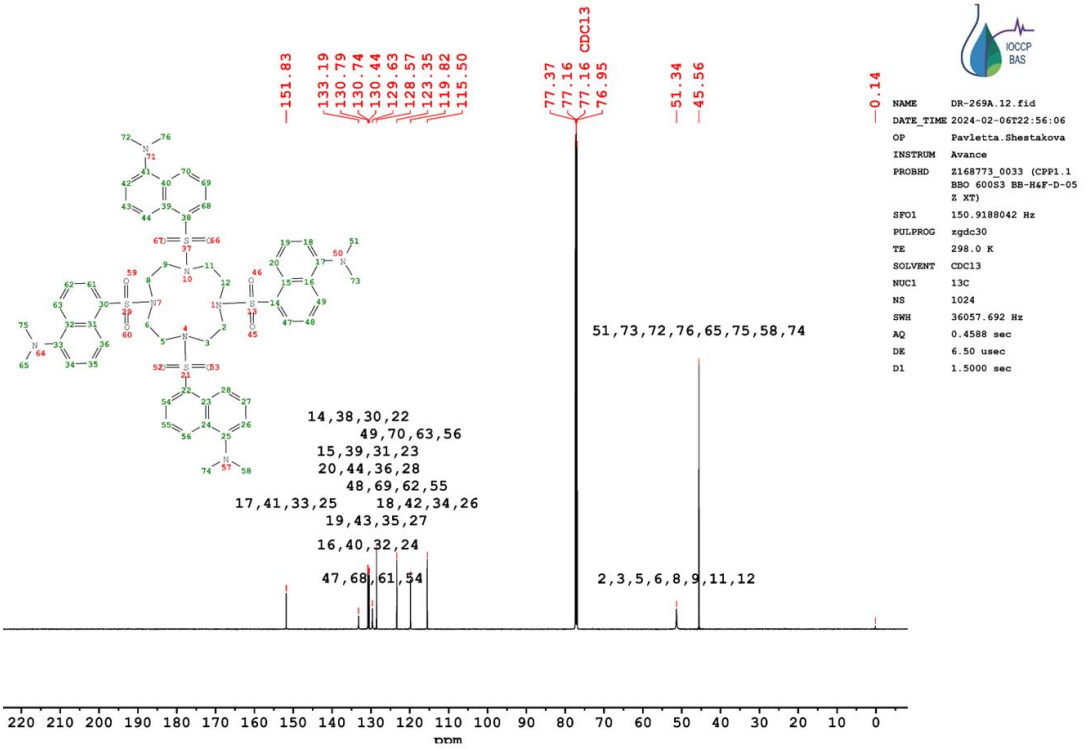


Figure 8–19. ^{13}C-NMR spectrum of compound **L1**.

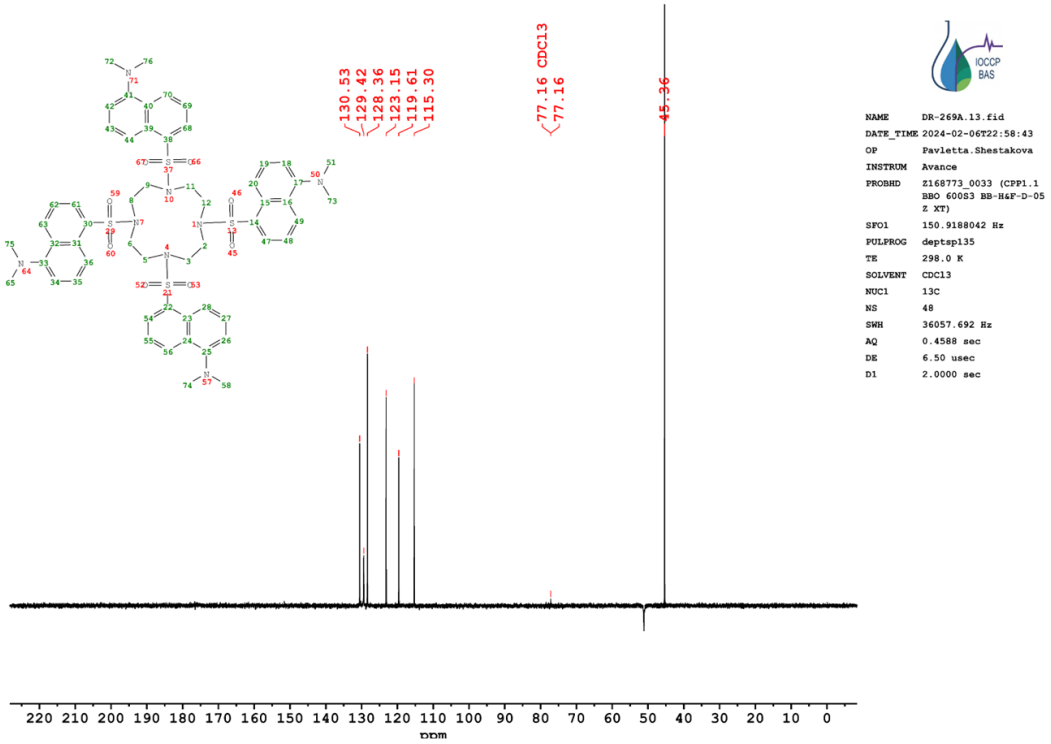


Figure 8–20. DEPT135-NMR spectrum of compound **L1**

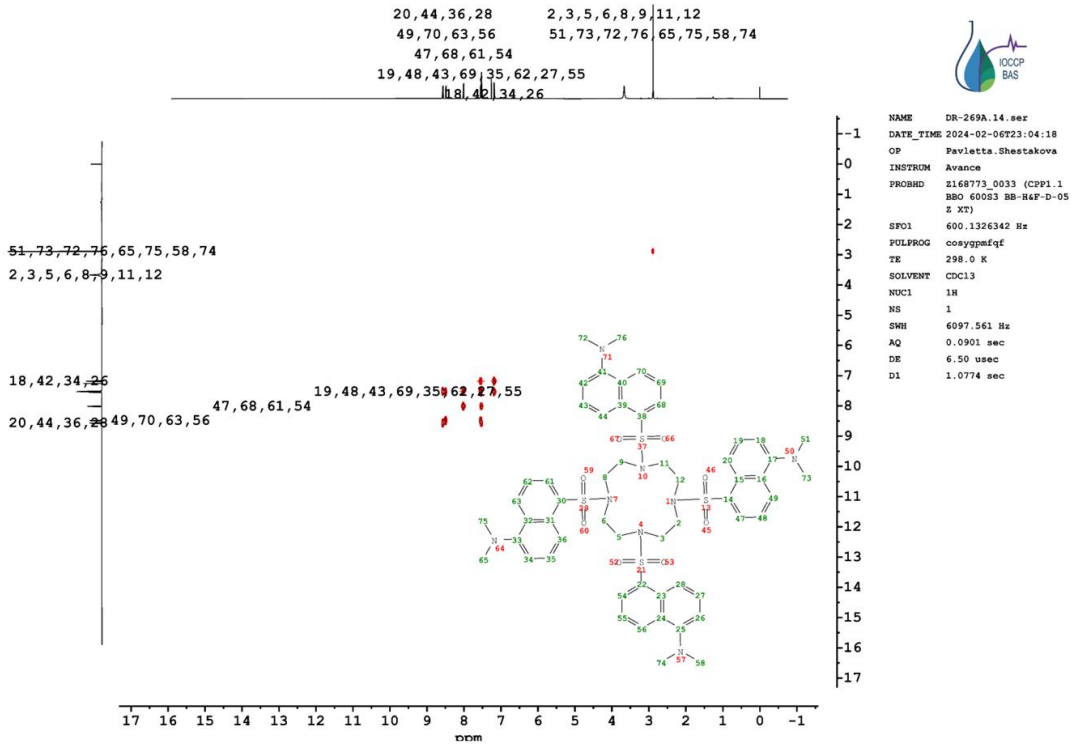


Figure 8–21. COSY-NMR spectrum of compound **L1**.

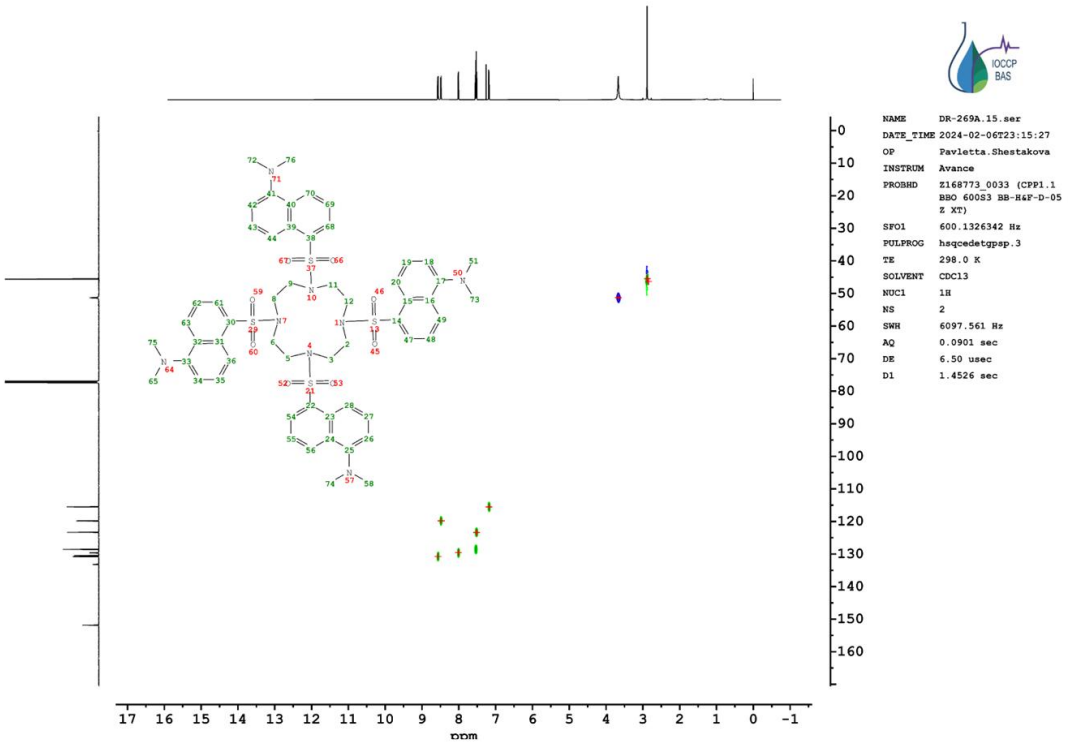


Figure 8–22. HSQC-NMR spectrum of compound **L1**

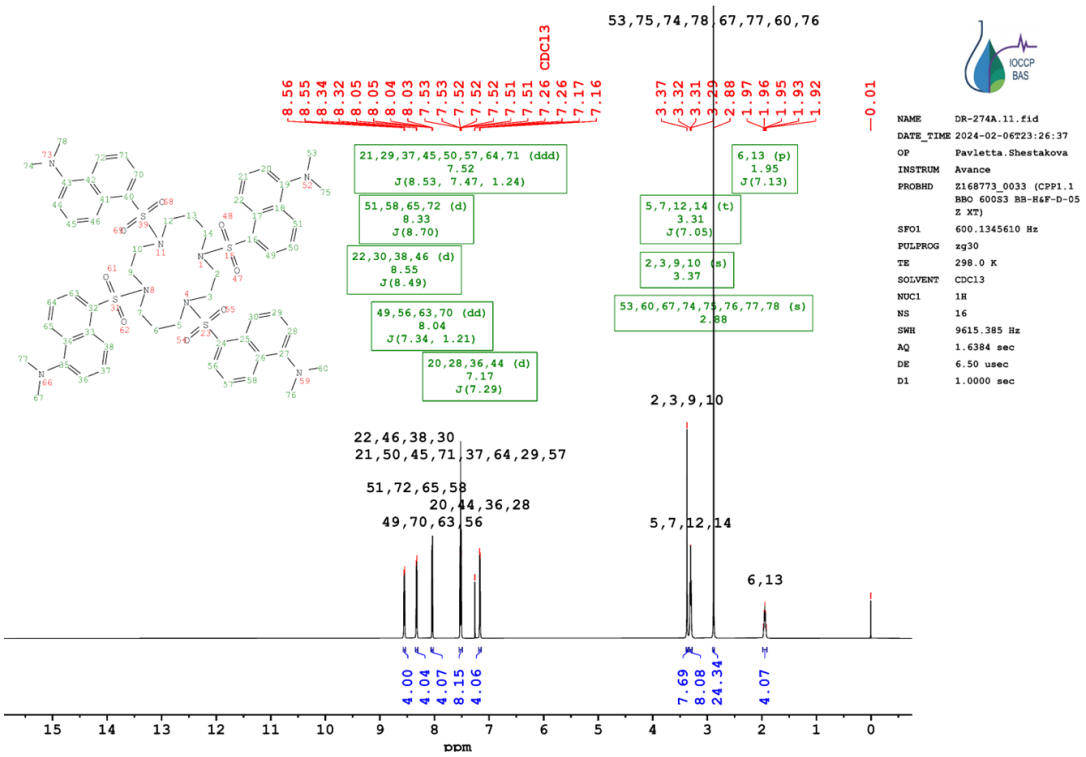


Figure 8–23. ^{1}H-NMR spectrum of compound **L1**.

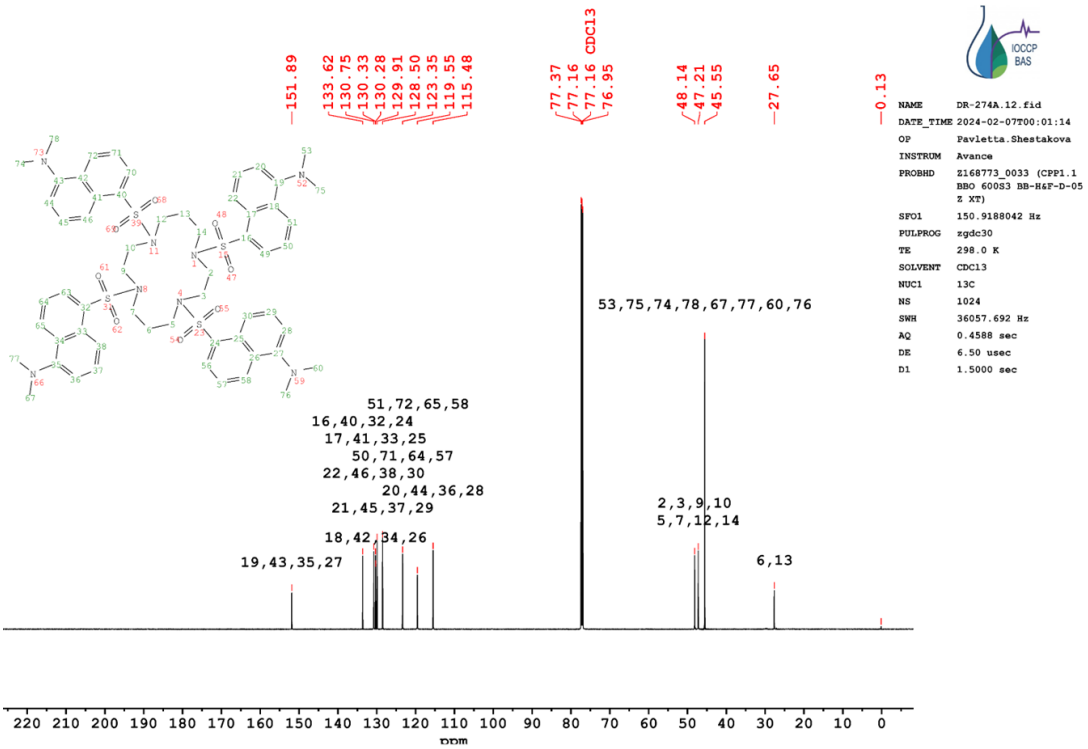


Figure 8–24. ^{13}C-NMR spectrum of compound **L2**.

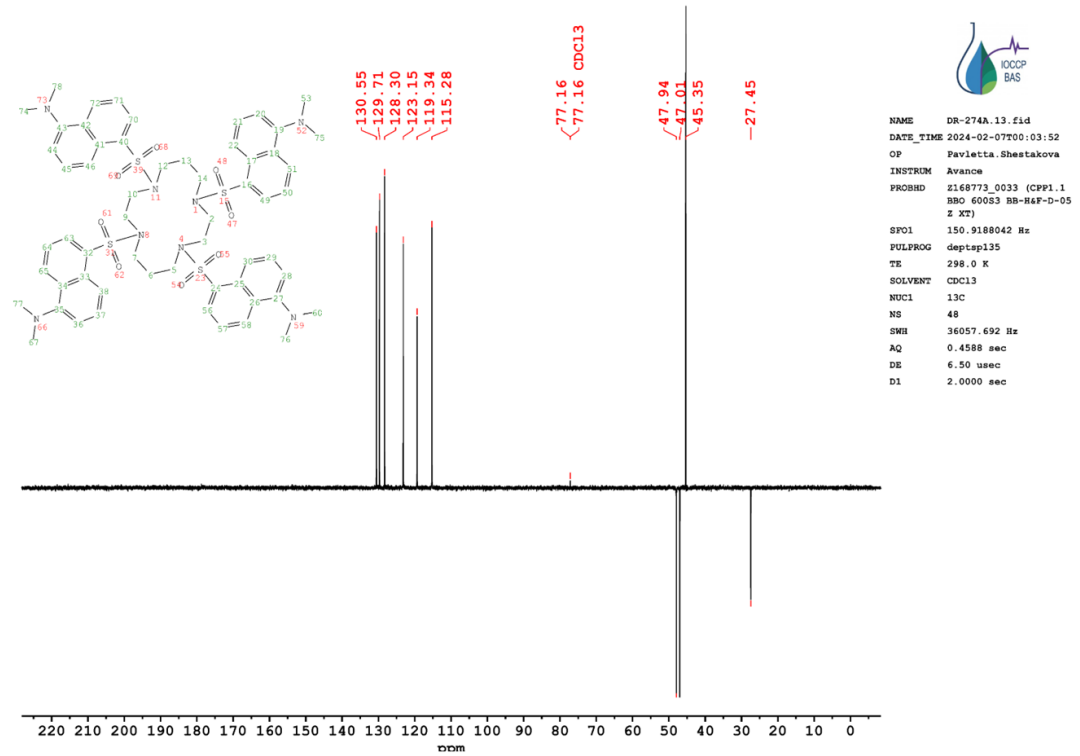


Figure 8–25. DEPT135-NMR spectrum of compound **L2**.

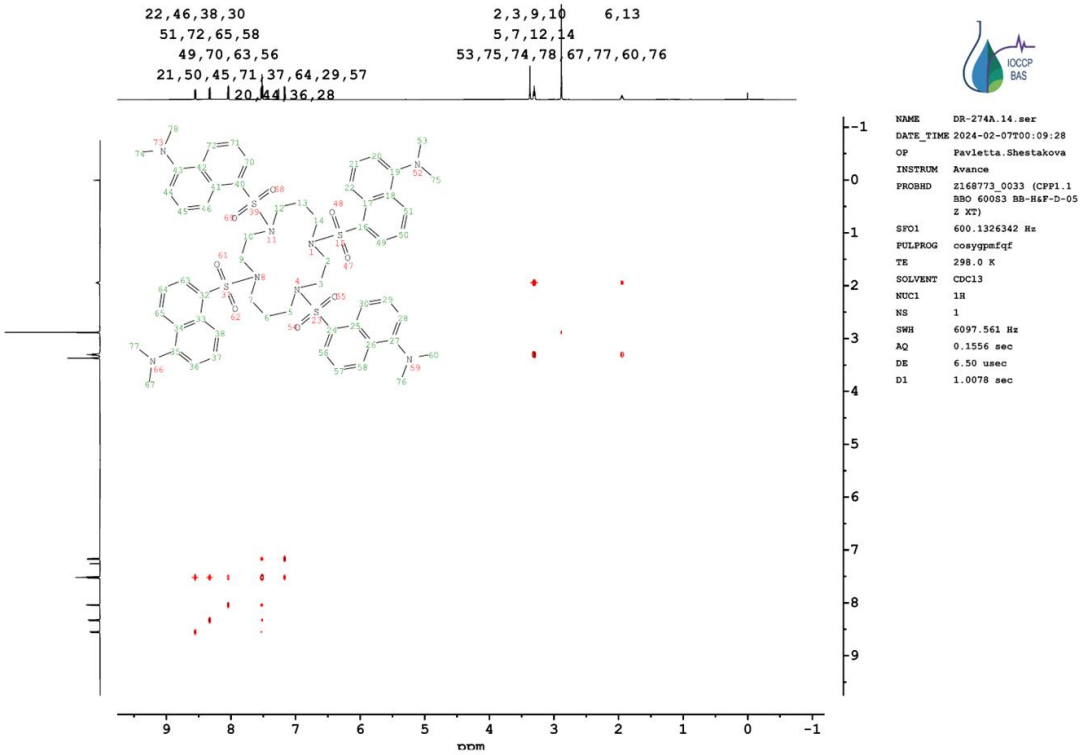


Figure 8–26. COSY-NMR spectrum of compound **L2**.

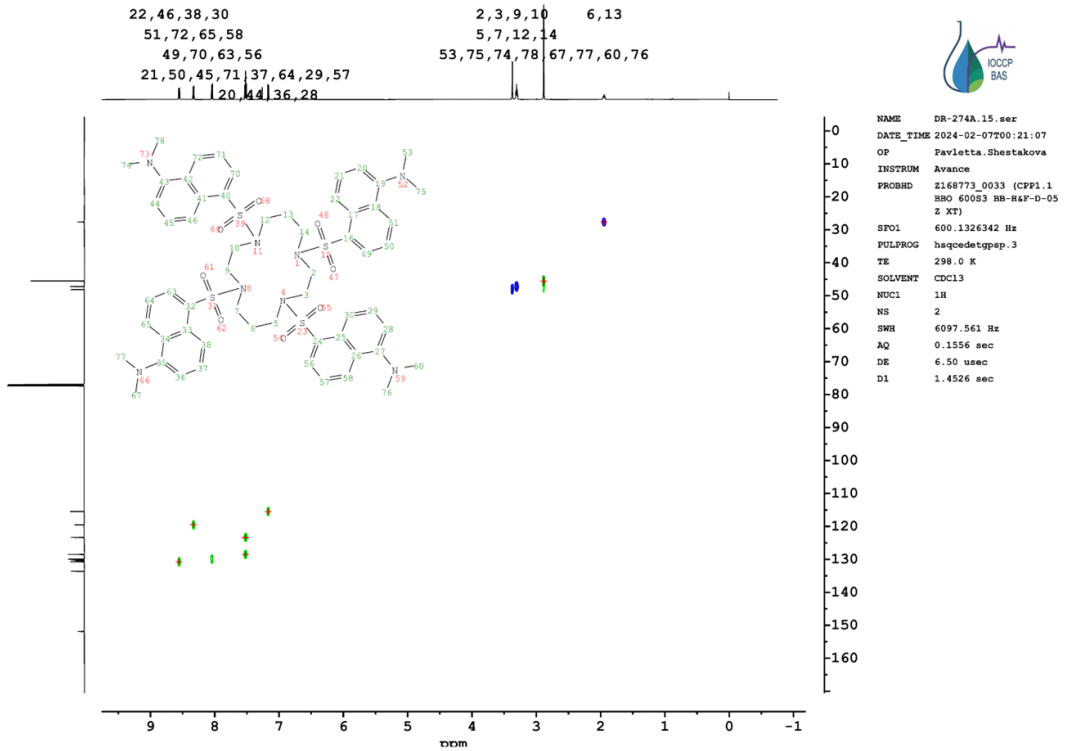


Figure 8–27. HSQC-NMR spectrum of compound **L2**.

8.7 Contributions & Aknowledgements

8.7.1 Author Contributions

Inês Pereira-Gomes: Formal analysis, Investigation, Writing - Original Draft, Writing - Review & Editing, Visualization.

Frederico Duarte: Formal analysis, Investigation, Writing - Original Draft, Writing - Review & Editing, Visualization.

Georgi Dobrikov: Methodology, Validation, Formal Analysis, Investigation, Writing - Original Draft, Writing - Review & Editing, Resources, Visualization.

Ivaylo Slavchev: Investigation.

Atanas Kurutos: Methodology, Validation, Formal Analysis, Investigation, Conceptualization, Writing - Original Draft, Writing - Review & Editing, Resources, Visualization. Supervision, Funding acquisition.

Jose Luis Capelo-Martinez: Resources, Writing - Review & Editing, Funding acquisition.

Hugo M. Santos: Investigation, Resources, Validation, Writing - Review & Editing.

Carlos Lodeiro: Conceptualization, Methodology, Validation, Formal Analysis, Investigation, Resources, Writing - Review & Editing, Resources, Visualization, Supervision, Funding acquisition, Project administration

8.7.2 Acknowledgments

This work was supported by the Associate Laboratory for Green Chemistry LAQV which is financed by national funds from *Fundação para a Ciência e Tecnologia and Ministério da Ciência, Tecnologia e Ensino Superior* (FCT/MCTES) through the projects UIDB/50006/2020 and UIDP/50006/2020. PROTEOMASS Scientific Society (Portugal) is acknowledged by the funding provided through the General Funding Grant 2022-2023, and by the funding provided to the Laboratory for Biological Mass Spectrometry Isabel Moura (#PM001/2019 and #PM003/2016). F.D. thanks to FCT/MCTES (Portugal) for his doctoral grant 2021.05161.BD. H. M. S. acknowledges the Associate Laboratory for Green Chemistry LAQV (LA/P/0008/2020) funded by FCT/MCTES for his research contract. The financial support by the Bulgarian National Science Fund (BNSF) under grant – "Novel styryl and polymethine fluorophores as potential theranostic agents "contract N◦ КП-06-М59/1 from 15.11.2021 is gratefully acknowledged by A.K. This work is also developed and acknowledged by A.K. as part of contract №: BG-RRP-2.004-0002-C01, Laboratory of Organic Functional Materials (Project BiOrgaMCT), Procedure BG-RRP-2.004

„Establishing of a network of research higher education institutions in Bulgaria", funded by BULGARIAN NATIONAL RECOVERY AND RESILIENCE PLAN".

G. D. thanks to the European Regional Development Fund within the Operational Programme Science and Education for Smart Growth 2014 - 2020 under the Project Center of Excellence: National center of mechatronics and clean technologies - BG05M2OP001-1.001-0008 for the financial support.

8.8 References

[1] F. Duarte, G. Dobrikov, A. Kurutos, J. L. Capelo-Martinez, H. M. Santos, E. Oliveira and C. Lodeiro, Development of fluorochromic polymer doped materials as platforms for temperature sensing using three dansyl derivatives bearing a sulfur bridge, *J. Photochem. Photobiol. A Chem.* **445** (2023) 115033. DOI: 10.1016/j.jphotochem.2023.115033.

[2] H. Jiang, Z. Li, Y. Kang, L. Ding, S. Qiao, S. Jia, W. Luo and W. Liu, A two-photon fluorescent probe for Cu^{2+} based on dansyl moiety and its application in bioimaging, *Sens. Actuators B Chem.* **242** (2017) 112–117. DOI: http://dx.doi.org/10.1016/j.snb.2016.11.033

[3] I. Pisagatti, D. Crisafulli, A. Pappalardo, G. Trusso Sfrazzetto, A. Notti, F. Nastasi, M. F. Parisi, N. Micali, G. Gattuso and V. Villari, Photoinduced electron transfer in host-guest interactions of a viologen derivative with a didansyl-pillar[5]arene, *Mater. Today Chem.* **24** (2022) 100841. DOI: 10.1016/j.mtchem.2022.100841.

[4] F. Duarte, G. Dobrikov, A. Kurutos, H. M. Santos, J. Fernández-Lodeiro, J. L. Capelo-Martinez, E. Oliveira and C. Lodeiro, Enhancing water sensing via aggregation-induced emission (AIE) and solvatofluorochromic studies using two new dansyl derivatives containing a disulfide bound: Pollutant metal ions detection and preparation of water-soluble fluorescent polymeric particles, *Dyes and Pigments* **218** (2023) 111428. DOI: 10.1016/j.dyepig.2023.111428

[5] A. Aliberti, P. Vaiano, A. Caporale, M. Consales, M. Ruvo and A. Cusano, Fluorescent chemosensors for Hg^{2+} detection in aqueous environment, *Sens. Actuators B Chem.* **247** (2017) 727–735. DOI: 10.1016/j.snb.2017.03.026.

[6] P. Wei, L. Xiao, Y. Gou, F. He, D. Zhou, Y. Liu, B. Xu, P. Wang and Y. Zhou, Fluorescent "on–off–on" probe based on copper peptide backbone for specific detection of Cu(II) and hydrogen sulfide and its applications in cell imaging, real water samples and test strips, *Microchemical Journal* **182** (2022) 107848. DOI: 10.1016/j.microc.2022.107848

[7] P. Srivastava, M. Verma, S. Sivakumar and A. K. Patra, A smart FRET probe exhibiting a molecular keypad lock device based on rapid detection of nitric oxide mediated by Cu^{2+} ion, *Sens. Actuators B Chem.* **291** (2019) 478–484. DOI: 10.1016/j.snb.2019.04.093

[8] H. Cai, Y. Liang, L. Huang and J. Wang, Relay detection of Cu^{2+} and bovine serum albumin by a dansyl derivative-based fluorescent probe, *Spectrochim. Acta A Mol. Biomol. Spectrosc.* **277** (2022) 121281. DOI: 10.1016/j.saa.2022.121281

[9] Y. Wang, J. Zhou, L. Zhao and B. Xu, A dual-responsive and highly sensitive fluorescent probe for Cu^{2+} and pH based on a dansyl derivative, *Dyes and Pigments* **180** (2020) 108513. DOI: 10.1016/j.dyepig.2020.108513.

[10] Y. Liu, B. Jiang, L. Zhao, L. Zhao, Q. Wang, C. Wang and B. Xu, A dansyl-based fluorescent probe for sensing Cu^{2+} in aqueous solution, *Spectrochim. Acta A Mol. Biomol. Spectrosc.* **261** (2021) 120009. DOI: 10.1016/j.saa.2021.120009.

[11] P. Wang, D. Zhou and B. Chen, High selective and sensitive detection of Zn(II) using tetrapeptide-based dansyl fluorescent chemosensor and its application in cell imaging, *Spectrochim. Acta A Mol. Biomol. Spectrosc.* **204** (2018) 735–742. DOI: 10.1016/j.saa.2018.07.001

[12] P. Wang and J. Wu, Highly selective and sensitive detection of Zn(II) and Cu(II) ions using a novel peptide fluorescent probe by two different mechanisms and its application in live cell imaging, *Spectrochim. Acta A Mol. Biomol. Spectrosc.* **208** (2019) 140–149. DOI: 10.1016/j.saa.2018.09.054

[13] P. Su, Z. Zhu, J. Wang, B. Cheng, W. Wu, K. Iqbal and Y. Tang, A biomolecule-based fluorescence chemosensor for sequential detection of Ag^{+} and H_2S in 100% aqueous solution and living cells, *Sens. Actuators B Chem.* **273** (2018) 93–100. DOI: 10.1016/j.snb.2018.06.037

[14] P. Wang, D. Zhou and B. Chen, A fluorescent dansyl-based peptide probe for highly selective and sensitive detect Cd^{2+} ions and its application in living cell imaging, *Spectrochim. Acta A Mol. Biomol. Spectrosc.* **207** (2019) 276–283. DOI: 10.1016/j.saa.2018.09.029

[15] L S. Yu, L. Gao, R. Li, C. Fu, W. Meng, L. Wang and L. Li, Ultrasensitive mercury ion and biothiol detection based on Dansyl-His-Pro-Gly-Asp-NH_2 fluorescent sensor, *Spectrochim. Acta A Mol. Biomol. Spectrosc.* **250** (2021) 119246. DOI: 10.1016/j.saa.2020.119246.

[16] Y. Li, Z. Ren, Y. Ge, C. Di, J. Zhou, J. Wu and L. Jia, A novel peptide fluorescent probe based on different fluorescence responses for detection of mercury species and hydrogen sulfide, *Microchemical Journal* **184** (2023) 108160. DOI: 10.1016/j.microc.2022.108160.

[17] X. Pang, J. Dong, L. Gao, L. Wang, S. Yu, J. Kong and L. Li, Dansyl-peptide dual-functional fluorescent chemosensor for Hg^{2+} and biothiols, *Dyes and Pigments* **173** (2020) 107888. DOI: 10.1016/j.dyepig.2019.107888.

[18] P. Wang, Y. An and J. Wu, Highly sensitive turn-on detection of mercury(II) in aqueous solutions and live cells with a chemosensor based on tyrosine, *Spectrochim. Acta A Mol. Biomol. Spectrosc*. **230** (2020) 118004. DOI: 10.1016/j.saa.2019.118004.

[19] C. L. Li, P. hsuan Lu, S. Y. Lin and A. T. Wu, A turn-on dansyl-based fluorescent chemosensor for the recognition of Pb^{2+}, *J. Photochem. Photobiol. A Chem*. **385** (2019) 112088. DOI: 10.1016/j.jphotochem.2019.112088.

[20] M. Tosato, M. Asti, M. Dalla Tiezza, L. Orian, D. Häussinger, R. Vogel, U. Köster, M. Jensen, A. Andrighetto, P. Pastore and V. Di Marco, Highly Stable Silver(I) Complexes with Cyclen-Based Ligands Bearing Sulfide Arms: A Step Toward Silver-111 Labeled Radiopharmaceuticals, *Inorg. Chem*. **59** (2020) 10907–10919. DOI: 10.1021/acs.inorgchem.0c01405.

[21] Z. F. Wang, X. F. Zhou, Q. C. Wei, Q. P. Qin, J. X. Li, M. X. Tan and S. H. Zhang, Novel bifluorescent Zn(II)–cryptolepine–cyclen complexes trigger apoptosis induced by nuclear and mitochondrial DNA damage in cisplatin-resistant lung tumor cells, *Eur. J. Med. Chem*. **238** (2022) 114418. DOI: 10.1016/j.ejmech.2022.114418.

[22] J. Blahut, K. Bernášek, A. Gálisová, V. Herynek, I. Císařová, J. Kotek, J. Lang, S. Matějková and P. Hermann, Paramagnetic ^{19}F Relaxation Enhancement in Nickel(II) Complexes of N-Trifluoroethyl Cyclam Derivatives and Cell Labeling for ^{19}F MRI, *Inorg. Chem*. **56** (2017) 13337–13348. DOI: 10.1021/acs.inorgchem.7b02119

[23] T. L. Cheung, L. K. B. Tam, W. S. Tam, L. Zhang, H. Y. Kai, W. Thor, Y. Wu, P. L. Lam, Y. H. Yeung, C. Xie, H. F. Chau, W. S. Lo, T. Zhang and K. L. Wong, Facile Peptide Macrocyclization and Multifunctionalization via Cyclen Installation, *Small Methods* 2024 2400006. DOI: 10.1002/smtd.202400006.

[24] E. M. Surender, S. Comby, S. Martyn, B. Cavanagh, T. C. Lee, D. F. Brougham and T. Gunnlaugsson, Cyclen lanthanide-based micellar structures for application as luminescent [Eu(III)] and magnetic [Gd(III)] resonance imaging (MRI) contrast agents, *Chem. Commun.* **52** (2016) 10858–10861. DOI: 10.1039/C6CC03092K.

[25] M. Naher, C. Su, J. R. Harmer, C. M. Williams and P. V. Bernhardt, Macrocyclic Copper(II) Complexes as Catalysts for Electrochemically Mediated Atom TransfeR, *Inorg. Chem*. **63** (2024) 6453–6464. DOI: 10.1021/acs.inorgchem.4c00311

[26] A. Annunziata, R. Esposito, G. Gatto, M. E. Cucciolito, A. Tuzi, A. Macchioni and F. Ruffo, Iron(III) Complexes with Cross-Bridged Cyclams: Synthesis and Use in Alcohol and Water Oxidation Catalysis, *Eur. J. Inorg. Chem*. **2018** (2018) 3304–3311. DOI: 10.1002/ejic.201800451

[27] C. Ollier, A. Méndez-Ardoy, F. Ortega-Caballero, J. L. Jiménez-Blanco, N. Le Bris and R. Tripier, Extending the Scope of the *C*-Functionalization of Cyclam via Copper(I)-Catalyzed

Alkyne–Azide Cycloaddition to Bifunctional Chelators of Interest, *J. Org. Chem.* **89** (2024) 5988–5999. DOI: 10.1021/acs.joc.3c02854.

[28] Y. Yu, P. Tan, X. Huang, J. Tao, Y. Liu, R. J. Zeng, M. Chen and S. Zhou, Homogeneous activation of peroxymonosulfate using a low-dosage cross bridged cyclam manganese(II) complex for organic pollutant degradation via a nonradical pathway, *J. Hazard Mater*. **394** (2020) 122560. DOI: 10.1016/j.jhazmat.2020.122560.

[29] J. K. H. Wong, M. H. Todd and P. J. Rutledge, Recent Advances in Macrocyclic Fluorescent Probes for Ion Sensing, *Molecules* **22** (2017) 200. DOI: 10.3390/molecules22020200.

[30] S H. Ozay, Z. Gungor, B. Yilmaz, P. Ilgin and O. Ozay, Dual use of colorimetric sensor and selective copper removal from aqueous media with novel p(HEMA-co-TACYC) hydrogels: Cyclen derivative as both monomer and crosslinker, *J. Hazard Mater*. **389** (2020) 121848. DOI: 10.1016/j.jhazmat.2019.121848.

[31] X. Fang, S. Wang, Q. Wang, J. Gong, L. Li, H. Lu, P. Xue, Z. Ren and X. Wang, A highly selective and sensitive fluorescence probe based on BODIPY-cyclen for hydrogen sulfide detection in living cells and serum, *Talanta* **268** (2024) 125339. DOI: 10.1016/j.talanta.2023.125339.

[32] M. D. Tomczyk, K. Matczak, M. Skonieczna, P. Chulkin, M. Denel-Bobrowska, D. Różycka, S. Rykowski, A. B. Olejniczak and K. Walczak, Synthesis and in vitro cytotoxic activity of dye-linker-macrocycle conjugates with variable linker length and components, *Bioorg. Chem*. **140** (2023) 106782. DOI: 10.1016/j.bioorg.2023.106782.

[33] S. Aoki, H. Kawatani, T. Goto, E. Kimura and M. Shiro, A Double-Functionalized Cyclen with Carbamoyl and Dansyl Groups (Cyclen = 1,4,7,10-Tetraazacyclododecane): A Selective Fluorescent Probe for Y^{3+} and La^{3+}, *J. Am. Chem. Soc*. **123** (2001) 1123–1132. DOI: 10.1021/ja0033786

[34] M. P. Lowe and D. Parker, pH Switched sensitisation of europium(III) by a dansyl group, Inorganica Chim. Acta **317** (2001) 163-173. DOI: 10.1016/S0020-1693(01)00346-2

[35] K. E. Siters, M. A. Fountain and J. R. Morrow, Selective Binding of Zn^{2+} Complexes to Human Telomeric G-Quadruplex DNA, *Inorg. Chem*. **53** (2014) 11540–11551. DOI: 10.1021/ic501484p

[36] I. M. A. Del Mundo, K. E. Siters, M. A. Fountain and J. R. Morrow, Structural Basis for Bifunctional Zinc(II) Macrocyclic Complex Recognition of Thymine Bulges in DNA, *Inorg. Chem*. **51** (2012) 5444–5457. DOI: 10.1021/ic3004245

[37] J. Y. Kim, S. Sarkar, K. N. Bobba, P. T. Huynh, A. Bhise and J. Yoo, Development of dansyl based copper(ii) complex to detect hydrogen sulfide in hypoxia, *Org. Biomol. Chem.* **17** (2019) 7088–7094. DOI: 10.1039/C9OB00948E

[38] L. L. O'neil and O. Wiest, A Selective, Noncovalent Assay for Base Flipping in DNA, *J. Am. Chem. Soc.* **127** (2005) 16800–16801. DOI: 10.1021/ja056274+.

[39] C. Rivas, G. J. Stasiuk, M. Sae-Heng and N. J. Long, Towards understanding the design of dual-modal MR/fluorescent probes to sense zinc ions, *Dalton. Trans.* **44** (2015) 4976–4985. DOI: 10.1039/C4DT02981J.

[40] L. Yang, J. Zhao, J. Wang, G. Han, B. Liu, W. Zhang, Y. Fu, M. Y. Han, Z. Wang and Z. Zhang, An azacyclo-localizing fluorescent probe for the specific labeling of lysosome and autolysosome, *Talanta* **216** (2020) 120941. DOI: 10.1016/j.talanta.2020.120941.

[41] G. Xue, J. S. Bradshaw, H. Song, R. T. Bronson, P. B. Savage, K. E. Krakowiak, R. M. Izatt, L. Prodi, M. Montalti and N. Zaccheroni, A convenient synthesis and preliminary photophysical study of novel fluoroionophores: macrocyclic polyamines containing two dansylamidoethyl side arms, *Tetrahedron* **57** (2001) 87–91. DOI: 10.1016/S0040-4020(00)00999-6.

[42] L. Fabbrizzi, F. Foti, M. Licchelli, P. M. Maccarini, D. Sacchi and M. Zema, Light-Emitting Molecular Machines: pH-Induced Intramolecular Motions in a Fluorescent Nickel(II) Scorpionate Complex, *Chemistry - A European Journal* **8** (2002) 4965–4972. DOI: 10.1002/1521-3765(20021104)8:21<4965::AID-CHEM4965>3.0.CO;2-X.

[43] G. Bergamini, A. Sottilotta, M. Maestri, P. Ceroni and F. Vögtle, Cyclam-Cored Dendrimers Appended with Four Dendrons of Two Different Types: Intradendrimer Energy Transfer, *Chem. Asian J.* **5** (2010) 1884–1895. DOI: 10.1002/asia.201000170.

[44] Z. S. Pillai, P. Ceroni, M. Kubeil, J. M. Heldt, H. Stephan and G. Bergamini, Dendrimers as Nd^{3+} ligands: Effect of Generation on the Efficiency of the Sensitized Lanthanide Emission, *Chem. Asian J.* **8** (2013) 771–777. DOI: 10.1002/asia.201201065.

[45] B. Branchi, P. Ceroni, G. Bergamini, V. Balzani, M. Maestri, J. Van Heyst, S. K. Lee, F. Luppertz and F. Vögtle, A Cyclam Core Dendrimer Containing Dansyl and Oligoethylene Glycol Chains in the Branches: Protonation and Metal Coordination, *Chemistry - A European Journal* **12** (2016) 8926–8934. DOI: 10.1002/chem.200601129.

[46] M. Montalti, A. Credi, L. Prodi MG, Montalti M, Credi A, Prodi L GM. Handbook of Photochemistry. 3rd ed. BOCA: Taylor & Francis, Boca Raton; 2006.

[47] D. Macdougall and W. B. Crummett, Guidelines for data acquisition and data quality evaluation in environmental chemistry, *Anal. Chem.* **52** (1980) 2242–2249. DOI. 10.1021/ac50064a004.

[48] G. L. Long and J. D. Winefordner, Limit of Detection A Closer Look at the IUPAC Definition, *Anal. Chem.* **55** (1983) 713A-724A. https://doi.org/10.1021/ac00258a724.

[49] S. Mocanu, G. Ionita and I. Matei, Solvatochromic characteristics of dansyl molecular probes bearing alkyl diamine chains, *Spectrochim. Acta - Part A Mol. Biomol. Spectrosc.* **237** (2020) 118413. DOI: 10.1016/j.saa.2020.118413.

[50] E. Oliveira, R. M. F. Baptista, S. P. G. Costa, M. M. M. Raposo and C. Lodeiro, Solvatochromic Effects of bis(indolyl)thienylaril derivatives as new Colored Materials, *Photochem. Photobiol. Sci.* **13** (2014) 492–498. DOI: 10.1039/C3PP50352F.

[51] P. Alam, N. L. C. Leung, J. Zhang, R. T. K. Kwok, J. W. Y. Lam and B. Z. Tang, AIE-based luminescence probes for metal ion detection, *Coord. Chem. Rev.* **429** (2021) 213693. DOI: 10.1016/j.ccr.2020.213693.

[52] H. Wang, E. Zhao, J. W. Y. Lam and B. Z. Tang, AIE luminogens: emission brightened by aggregation, *Materials Today* **18** (2015) 365–377. DOI: 10.1016/j.mattod.2015.03.004.

[53] F. Koucký, J. Kotek, I. Císařová, J. Havlíčková, V. Kubíček and P. Hermann, Transition metal complexes of cyclam with two 2,2,2-trifluoroethylphosphinate pendant arms as probes for ^{19}F magnetic resonance imaging, *Dalton. Trans.* **52** (2023) 12208–12223. DOI: https://doi.org/10.1039/D3DT01420G.

[54] M. M. Le Roy, S. Héry, N. Saffon-Merceron, C. Platas-Iglesias, T. Troadec and R. Tripier, A Phosphine Oxide-Functionalized Cyclam as a Specific, Copper(II) Chelator *Inorg. Chem.* **62** (2023) 8112–8122. DOI: 10.1021/acs.inorgchem.3c00329.

[55] M. Naher, C. Su, J. R. Harmer, C. M. Williams and P. V. Bernhardt, Macrocyclic Copper(II) Complexes as Catalysts for Electrochemically Mediated Atom Transfer, *Inorg. Chem.* **63** (2024) 6453–6464. DOI: 10.1021/acs.inorgchem.4c00311.

[56] X. Li, L. Pan, F. Yang and L. Yang, Blue Carbon Dot-Based Portable Smartphone Platform for Visualization of Copper(II), *ACS Appl. Nano Mater.* **5** (2022) 9252–9259. DOI: 10.1021/acsanm.2c01595.

[57] E. Lelong, J. M. Suh, G. Kim, D. Esteban-Gómez, M. Cordier, M. H. Lim, R. Delgado, G. Royal, C. Platas-Iglesias, H. Bernard and R. Tripier, *Inorg. Chem.* **60** (2021) 10857–10872. DOI: 10.1021/acs.inorgchem.1c01572.

[58] A. M. Brown, J. L. Butman, R. Lengacher, N. P. Vargo, K. E. Martin, A. Koller, D. Śmiłowicz, E. Boros and J. R. Robinson, *N,N*-Alkylation Clarifies the Role of *N*- and *O*-Protonated Intermediates in Cyclen-Based ^{64}Cu Radiopharmaceuticals, *Inorg. Chem.* **62** (2023) 1362–1376. DOI: 10.1021/acs.inorgchem.2c02907.

[59] S. Almada, L. B. Maia, J. C. Waerenborgh, B. J. C. Vieira, N. P. Mira, E. R. Silva, F. Cerqueira, E. Pinto and L. G. Alves, Cyclam-based iron(III) and copper(II) complexes: synthesis, characterization and application as antifungal agents, *New J. of Chem.* **46** (2022) 16764–16770. DOI: 10.1039/D2NJ03161B.

[60] H. Zhang, J. Song, S. Wang, Q. Song, H. Guo and Z. Li, Recent progress in macrocyclic chemosensors for lead, cadmium and mercury heavy metal ions, *Dyes and Pigments* **216** (2023) 111380. DOI: 10.1016/j.dyepig.2023.111380.

[61] M. Tosato, P. Randhawa, M. Asti, L. B. S. Hemmingsen, C. A. O'Shea, P. Thaveenrasingam, S. P. A. Sauer, S. Chen, C. Graiff, I. Menegazzo, M. Baron, V. Radchenko, C. F. Ramogida and V. Di Marco, Capturing Mercury-197m/g for Auger Electron Therapy and Cancer Theranostic with Sulfur-Containing Cyclen-Based Macrocycles, *Inorg. Chem.* **63** (2024) 14241-14255. DOI: 10.1021/acs.inorgchem.4c02418

[62] P. Gans, A. Sabatini and A. Vacca, Investigation of equilibria in solution. Determination of equilibrium constants with the HYPERQUAD suite of programs, *Talanta* **43** (1996) 1739–1753. DOI: 10.1016/0039-9140(96)01958-3.

9

Engineering Multifunctional Cyclen Fluorophores: Bridging Metal Ion Detection, Self-Assembly and Nanocolloid Applications

Frederico Duarte, Cristián Cuerva, Georgi M. Dobrikov, Atanas Kurutos, Nikolay G. Vassilev, Javier Fernández-Lodeiro, José Luis Capelo-Martinez, Hugo M. Santos, Carlos Lodeiro

Spectrochimica Acta Part A: Molecular and Biomolecular Spectroscopy 349 (2026) 127285
Doi: doi.org/10.1016/j.saa.2025.127285

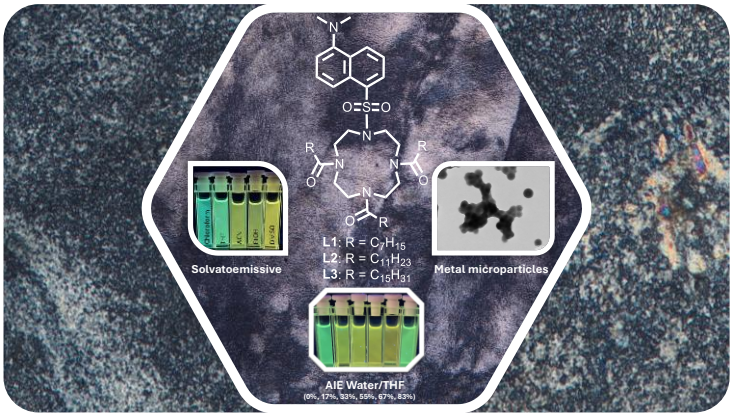
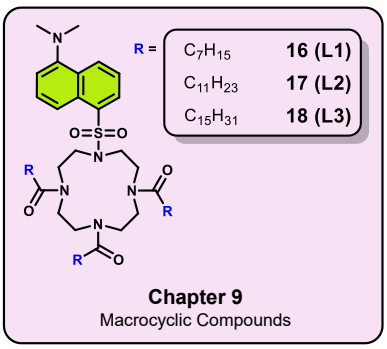


Figure 9–1. Graphical abstract.



Contribution to this work: Photophysical characterization; Synthesis of platinum nanoparticles; Polarized optical microscopy observations; Differential scanning calorimetry experiments; Aggregation studies; Sensing experiments of metal ions; Temperature-dependent studies; Writing original draft.

9.1 Abstract

We report the design, synthesis, and comprehensive characterization of three novel monodansylated cyclen derivatives (**L1**–**L3**), each bearing alkyl side chains of varying lengths (n = 8, 12, 16), developed as multifunctional fluorophores. Polarized optical microscopy (POM) and differential scanning calorimetry (DSC) were employed to evaluate mesomorphism, a property often associated with extended alkyl chains. These compounds exhibited pronounced solvatochromic behavior and high fluorescence quantum yields, reaching up to 55% in chloroform. The influence of solvent polarity on their photophysical properties was quantitatively analyzed using the Kamlet–Taft equation. Self-assembly behavior in THF–water mixtures revealed aggregation-induced emission (AIE), with emission profiles varying according to alkyl chain length, as confirmed by dynamic light scattering (DLS) and fluorescence lifetime measurements. Selective detection of Cu^{2+} and Hg^{2+} ions by **L1** was demonstrated through significant fluorescence quenching, with detection limits of 2 μM and 40 μM, respectively. Additionally, **L3** functioned effectively as a stabilizing agent in the colloidal synthesis of platinum nanoparticles, resulting in spherical nanostructures with low polydispersity, as confirmed by transmission electron microscopy (TEM) and DLS. These results highlight the versatile utility of alkylated dansyl–cyclen hybrids as fluorescent probes with self-assembly properties useful as nanomaterial stabilizers for advanced functional applications.

9.2 Introduction

The advancement of environmental monitoring, imaging, and medical diagnostics has been significantly influenced by the development of fluorescent probes and sensors. Dansyl (5-dimethylaminonaphthalene-1-sulfonyl) derivatives have endured as a fundamental class of fluorophores over time as a result of their well-established photophysical properties, which are present in the extensive collection of fluorescent dyes. These include large Stokes shifts, high fluorescence quantum yields, and a strong modulation of emission characteristics on the surrounding microenvironment. [1,2] However, modern design of dansyl-derived fluorophores have shifted away from traditional single-function probes to advanced multiresponsive compounds towards pH, polarity, metal ions, with special focus towards the sensing of Hg(II) and Cu(II), and materials science. [3-12]

In recent studies, several fluorophores have been functionalized with azamacrocycle groups to enhance their applications. [13,14] Dansyl-based azamacrocyclic compounds are no

exception, with various examples being reported in the literature that combine the advantages of the dansyl fluorophore and azamacrocyclic scaffolds improving selectivity, sensitivity and biological compatibility. [1,15-18]

Our previous studies on tetra-dansylated cyclen and cyclam derivatives have demonstrated pronounced emission modulation in response to solvent polarity reaching fluorescence quantum yields up to 41% in chloroform. Dependence of the emission in the presence of higher fractions of water content in tetrahydrofuran (THF), demonstrated aggregation-induced emission (AIE) accompanied with the rise of the quantum yield. The formation of nanoaggregates was followed by dynamic light scattering (DLS) analysis, which achieved an average size of 134±3 nm for the dansyl bearing a cyclen moiety. The application of these compounds towards metal ion remediation demonstrated the quenching of emission and the formation of mononuclear species with Hg^{2+} and Cu^{2+} reaching a limit of detection and quantification up to 2 mM and 3 mM, respectively. [1]

Modification of the cyclen core with flexible alkyl side chains has recently emerged as an effective strategy to enhance its amphiphilic character. [19,20] The hydrophobic nature of the alkyl substituents not only improves solubility in nonpolar media but also promotes anisotropic molecular alignment. Liquid crystals (LCs) represent an intermediate state of matter that combines the fluidity of liquids with the structural order of crystalline solids, which is possible given their anisotropic molecular nature. [21] In turn, fluorescent liquid crystals (FLCs), a subclass of LCs, have attained increasing attention since they provide new platforms for the development of advanced materials in various research fields. [22-27] These structural adaptations open new opportunities for designing cyclen-based LC materials with tunable self-assembly behavior, metal coordination, and supramolecular material applications.

Since their anisotropic and self-organizing nature, liquid crystals can intersect with nanoparticle synthesis serving as a stabilizing agent or template media, functioning similarly to surfactants in respect to guiding growth, controlling morphology and preventing aggregation. In particular, colloidal syntheses of platinum nanoparticles have gained wide adoption owing to their relative simplicity, controllable reaction parameters, and strong potential for scalable production which may benefit from such templating approaches. [28]

Thus, we report the synthesis and characterization of three monodansylated cyclen compounds (**L1**-**L3**), each bearing a set of alkyl side chains of varying lengths on the remaining nitrogen atoms. The primary distinction being the length of these side chains. Polarized optical microscopy (POM) and differential scanning calorimetry (DSC) were employed to evaluate potential mesomorphic behaviour. Additionally, their photophysical properties were investigated,

and solvent–solute interactions were analyzed using the Kamlet–Taft equation. The effect of alkyl chain length on AIE behavior was examined in THF–water mixtures and monitored via DLS. Given the cyclen core's well-known ability to coordinate metal ions, the compounds were also evaluated for their potential in metal remediation. Finally, colloidal platinum nanoparticles were synthesized through an accessible route in which the cyclen compounds acted as stabilizing agents.

9.3 Experimental Section

9.3.1 Materials

All solvents used for the synthesis and purification including dichloromethane (DCM) and methyl-tert-butyl ether (MTBE) were of analytical grade (p.a.) and dried over molecular sieve (3 Å). The starting fine chemicals - cyclen (1,4,7,10-Tetraazacyclododecane), *N,N*-diisopropylethylamine (DIPEA), dansyl chloride, Octanoyl chloride, Dodecanoyl chloride, and Hexadecanoyl chloride used for the synthesis of the target fluorophores were purchased from Sigma Aldrich, Tokyo Chemical Industry Co. Ltd., and BLDPharm and utilized as received. Silica gel (high-purity grade, pore size 60 Å, 230–400 mesh particle size, 40–63 μm particle size, for flash chromatography) employed for the column chromatography was purchased from Sigma Aldrich.

Spectroscopy grade solvents, such as acetonitrile (CH_3CN), chloroform ($CHCl_3$), dimethyl sulfoxide (DMSO), ethanol (EtOH), and tetrahydrofuran (THF), were used for spectrophotometric and spectrofluorimetric measurements. Trifluoromethanesulfonate salts $Ca(OTf)_2$, $Co(OTf)_2$, $Ni(OTf)_2$, $Cu(OTf)_2$, $Zn(OTf)_2$, Ag(OTf) and $Cd(OTf)_2$, were provided from Solchemar, while $Cu(NCCH_3)_4(OTf)$, $Hg(OTf)_2$, $HgCl_2$ and $Pb(ClO_4)\cdot 3H_2O$ were purchased from Sigma Aldrich.

9.3.2 Instrumentation

The chemical identities of all compounds were confirmed by a combination of ^{1}H-NMR, ^{13}C-NMR, 2D-COSY, 2D-HSQC, and 2D-HMBC spectroscopic techniques. Utilizing 5 mm tubes on a Bruker Avance II+ 600 spectrometer (Institute of Organic Chemistry with Centre of Phytochemistry-Bulgarian Academy of Sciences / NMR Centre), the ^{1}H-NMR and ^{13}C-NMR spectra were acquired in Trichloroethylene-d_1 (TCE), with spectrometer operating frequencies of 600.13 MHz and 150.92 MHz, respectively. The ^{1}H-NMR and 13C-NMR spectra were standardized to the tetramethylsilane (TMS) signal at δ = 0.00 ppm. Chemical changes were quantified with a

precision of 0.01 parts per million (ppm). The coupling constants (*J*) were given with an accuracy of 0.1 Hz. The spin multiplicity in the ^{1}H-NMR is represented by the following abbreviations: s = singlet, d = doublet, t = triplet, q = quartet, dd = doublet of doublets, dt = doublet of triplets, td = triplet of doublets, and m = multiplet.

^{1}H spectra (0.05 M in 0.6 ml TCE) were recorded on a Bruker Avance Neo instrument (5 mm BBO CryoProbe Prodigy) at 600.18 MHz in steps of 10 K in the interval between 243 K and 393 K. The sample temperature was controlled by the temperature control system (BSVT) and BCU-II cooling unit. ^{1}H NMR spectra were acquired using a spectral width of 10 kHz, an acquisition time of 1.7 s and 32 scans, zerofilled to 64k datapoints (0.15 Hz per point) and processed without apodization.

High-Resolution Mass Spectrometry analyses have been performed in the Laboratory for Biological Mass Spectrometry–Isabel Moura (PROTEOMASS Scientific Society Facility), using UHR ESI-Qq-TOF IMPACT HD (Bruker-Daltonics, Bremen, Germany). Samples of the corresponding compounds were prepared by dissolution in 50% (v/v) Acetonitrile containing 0.1% (v/v) aqueous formic acid to obtain a working solution of 0.1 µg/mL. Mass spectrometry analysis was carried out by the direct infusion of the compound solutions into the ESI source. MS data were acquired in positive polarity over the mass range of 80 – 1300 m/z. (Capillary voltage: 4500 V, End plate offset: -500 V, Charging voltage: 2000 V, Corona: 4000 nA, Nebulizer gas: 0.4 Bar, Dry Heater: 180°C, Dry gas: 4.0 L/min).

Polarized optical microscopy (POM) observations were carried out by using an Olympus BX50 microscope equipped with a Linkam THMS 600 heating stage. The transition temperatures and their associated enthalpy data were determined with a PerkinElmer Pyris 1 differential scanning calorimeter. Samples were hermetically sealed in aluminum pans and measurements were carried out with heating and cooling rates of 10 K min^{-1}.

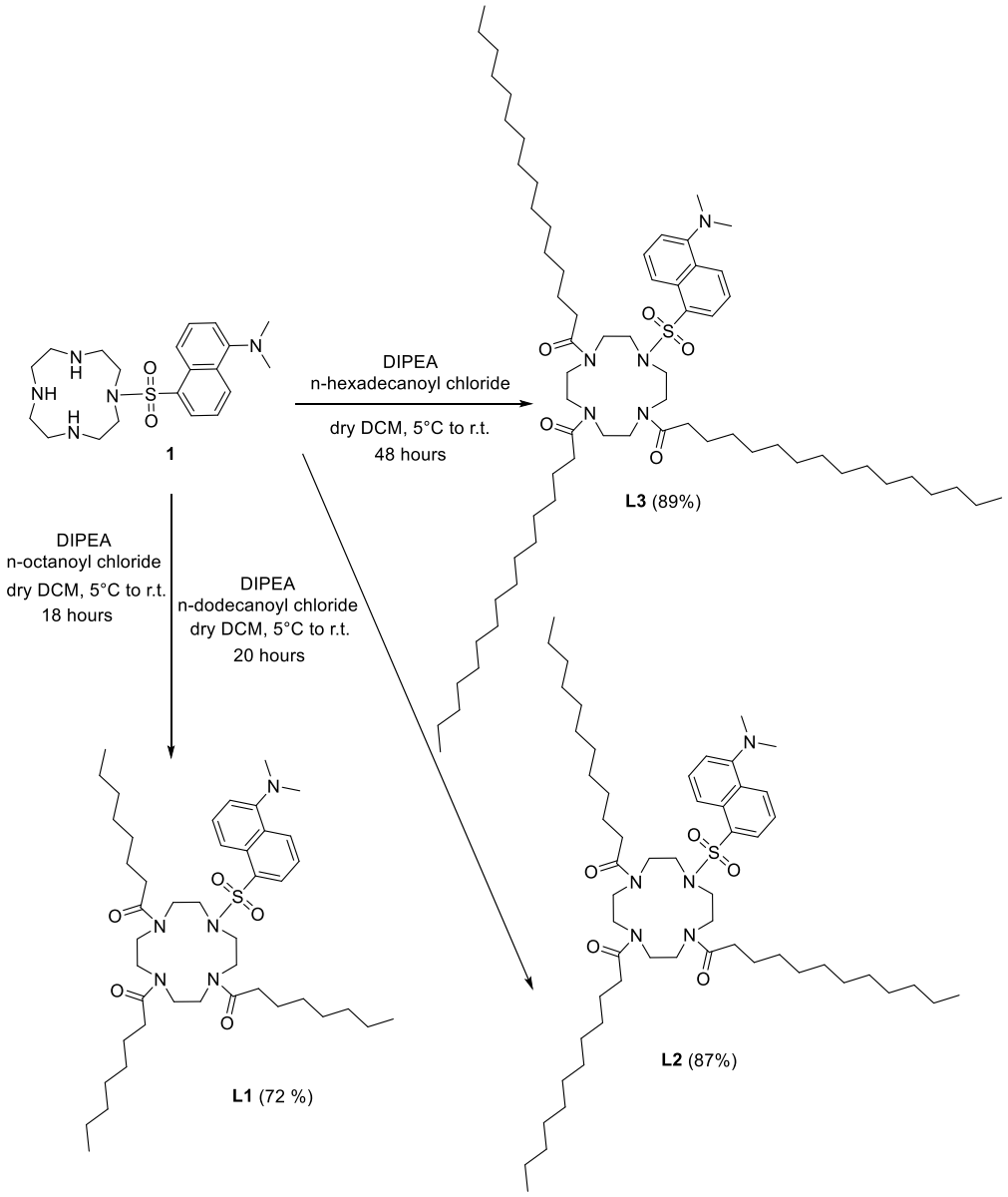
The UV-Vis absorption spectra were recorded using a JASCO V-650 spectrophotometer, while the fluorescence emission spectra were measured with a HORIBA Scientific FLUOROMAX-4 spectrofluorometer. Otherwise stated, all photophysical experiments were performed at 293 K using quartz cells with 10 mm optical path. Spectra of solid samples were collected using an optic fiber coupled to the spectrofluorometer by exciting the solid compounds at the appropriated wavelength. Fluorescence lifetime measurements were performed on TemPro, Deltahub Nanoled of Horiba Jobin-Yvon, using a 390 nm Nanoled. All instrumentation was provided by PROTEOMASS-BIOSCOPE facility.

Transmission electron microscopy (TEM) images were obtained using a JOEL JEM 1400 transmission electron microscope from the i3S, University of Porto (Portugal), operating at 80

kV. Samples were prepared by dropping 5 µL of the colloidal suspension on a copper grid coated with a continuous carbon film, and the solvent was allowed to evaporate.

Dynamic light scattering (DLS) data wasen obtained on a Malvern Zetasizer Nano series (Worcestershire, WR14 1XZ, UK) from PROTEOMASS Scientific Society-BIOSCOPE Facility Lab. The samples were analyzed at a scattering angle of 90º and at a temperature of 25 ºC and 20 ºC for water and ethanol, respectively, while supported in a glass cell. The z-potential measurement of microparticles was performed using a dip-cell.

9.3.3 Synthetic procedures



Scheme 9-1. Synthetic approach to the preparation of L1-L3.

9.3.3.1 Synthesis of L1

Synthesis of 1,1',1''-(10-(5-(dimethylamino)naphthalen-1-ylsulfonyl)-1,4,7,10-tetraaza-cyclododecane-1,4,7-triyl)trioctan-1-one

Ds-cyclen **1** (0.36 mmol, 144 mg, 1 equiv.) and DIPEA (3.55 mmol, 0.62 mL, 10 equiv.) were dissolved in 25 mL of dry DCM resulting in the formation of a clear yellow solution, which was cooled down to 5°C. n-Octanoyl chloride (2.13 mmol, 0.36 mL, 6 equiv.) was added dropwise at this temperature and the mixture was stirred for 30 min (**Scheme 9-1**). The colour changed to red, but the solution remains clear. Stirring was maintained for 18 h at r.t. The reaction mixture was worked up with DCM and consequently washed with conc. aq. citric acid, brine, aq. $NaHCO_3$ and water. The organic phase was dried over anhydr. Na_2SO_4 and the flask content was evaporated to dryness. The target product was subjected to purification by column chromatography on a silica gel employing DCM:MTBE=10:1 v/v as a mobile phase to furnish 0.200 g (72%) of a thick yellow oil. ^{1}H NMR (TCE, 600 MHz, 393K) δ = 0.91 (*t*, *J*=7.0 Hz, 6H, H-8''), 0.91 (*t*, *J*=7.0 Hz, 3H, H-8''), 1.30-1.37 (*m*, 24H, H-4' to H-7' and H-4'' to H-7''), 1.64-1.67 (*m*, 6H, H-3' and H-3''), 2.27 (*t*, *J*=7.3 Hz, 4H, H-2''), 2.32 (*t*, *J*=7.4 Hz, 2H, H-2'), 2.91 (*s*, 6H, NCH_3), 3.31 (*bs*, 4H, H-9 and H-11), 3.56 (*bs*, 4H, H-2 and H-6), 3.62 (*bs*, 4H, H-8 and H-12), 3.79 (*bs*, 4H, H-3 and H-5), 7.22 (*d*, *J*=7.6 Hz, 1H, H-6'''), 7.55 (*t*, *J*=7.5 Hz, 1H, H-3), 7.56 (*t*, *J*=7.2 Hz, 1H, H-7'''), 8.07 (*d*, *J*=7.2 Hz, 1H, H-2'''), 8.53 (*d*, *J*=8.6 Hz, 1H, H-8'''), 8.63 (*d*, *J*=8.3 Hz, 1H, H-4''').

^{13}C NMR (TCE, 150 MHz, 393K) δ = 14.19 (C-8' and C-8''), 22.85 (C-7' and C-7''), 25.69 (C-3''), 25.81 (C-3'), 29.36 and 29.40 and 29.82 and 29.89 and 29.97 (C-4' to C5' and C-4'' to C5''), 32.03 (C-6' and C-6''), 33.67 (C-2'), 34.08 (C-2''), 45.69 (NCH_3), 49.51 (C-3 and C-5), 49.87 (C-8 and C-12), 50.26 (C-2 and C-6), 51.78 (C-9 and C-11), 116.18 (C-6), 119.92 (C-8), 123.43 (C-3), 128.85 (C-7'''), 130.77 (C-2'''), 131.02 (C-8a'''), 131.59 (C-4'''), 131.65 (C-4a'''), 132.68 (C-1'''), 152.48 (C-5'''), 174.35 (C-1'), 174.99 (C-1'').

9.3.3.2 Synthesis of L2

Synthesis of 1,1',1''-{10-[5-(dimethylamino)naphthalene-1-sulfonyl]-1,4,7,10-tetraazacyclododecane-1,4,7-triyl}tri(dodecan-1-one)

Ds-cyclen 1 (0.50 mmol, 201 mg, 1 equiv.) and DIPEA (4.96 mmol, 0.86 mL, 10 equiv.) were dissolved in 25 mL dry DCM resulting in the formation of a clear yellow solution, which was cooled down to 5 °C. n-Dodecanoyl chloride (2.48 mmol, 0.58 mL, 5 equiv.) was added dropwise at this temperature and the mixture was stirred for 30 min (Scheme 9-1). The colour changed to orange-red, but the solution remains clear. Stirring was maintained for 20 h at r.t. The reaction mixture was worked up with DCM and washed consequently with conc. aq. citric

acid, brine, aq. $NaHCO_3$ and water. The organic phase was dried over anhydr. Na_2SO_4 and the flask content was evaporated to dryness. The target product was subjected to purification by column chromatography on a silica gel employing DCM:MTBE=10:1 v/v as a mobile phase to furnish 0.411 g (87%) of a thick yellow oil. ^{1}H NMR (TCE, 600 MHz, 393K) δ = 0.90 (*t*, *J*=7.0 Hz, 6H, H-12''), 0.91 (*t*, *J*=7.0 Hz, 3H, H-12'), 1.28-1.38 (*m*, 48H, H-4' to H-11' and H-4'' to H-11''), 1.62-1.68 (*m*, 6H, H-3' and H-3''), 2.28 (*t*, *J*=7.4 Hz, 4H, H-2''), 2.32 (*t*, *J*=7.4 Hz, 2H, H-2'), 2.91 (*s*, 6H, NCH_3), 3.32 (*t*, *J*=4.6 Hz, 4H, H-9 and H-11), 3.57 (*t*, *J*=6.0 Hz, 4H, H-2 and H-6), 3.62 (*t*, *J*=4.8 Hz, 4H, H-8 and H-12), 3.79 (*t*, *J*=5.9 Hz, 4H, H-3 and H-5), 7.21 (*d*, *J*=7.1 Hz, 1H, H-6'''), 7.54 (*t*, *J*=8.7 Hz, 1H, H-3'''), 7.55 (*t*, *J*=8.8 Hz, 1H, H-7'''), 8.07 (*dd*, *J*=1.2, 7.4 Hz, 1H, H-2'''), 8.52 (*d*, *J*=8.7 Hz, 1H, H-8'''), 8.62 (*d*, *J*=8.5 Hz, 1H, H-4''').

^{13}C NMR (TCE, 150 MHz, 393K) δ = 14.19 (C-12' and C-12''), 22.88 (C-11' and C-11''), 25.70 (C-3''), 25.82 (C-3'), 29.56 and 29.77 and 29.81 and 29.84 and 29.88 and 29.91 and 29.93 and 29.95 (C-4' to C9' and C-4'' to C9''), 32.20 (C-10' and C-10''), 33.68 (C-2'), 34.08 (C-2''), 45.64 (NCH_3), 49.49 (C-3 and C-5), 49.85 (C-8 and C-12), 50.23 (C-2 and C-6), 51.77 (C-9 and C-11), 116.14 (C-6'''), 119.81 (C-8'''), 123.35 (C-3'''), 128.85 (C-7'''), 130.73 (C-2'''), 131.10 (C-8a'''), 131.59 (C-4'''), 131.65 (C-4a'''), 132.74 (C-1'''), 152.67 (C-5'''), 174.33 (C1'), 174.97 (C-1'').

9.3.3.3 Synthesis of L3

Synthesis of 1,1',1''-{10-[5-(dimethylamino)naphthalene-1-sulfonyl]-1,4,7,10-tetraazacyclododecane-1,4,7-triyl}tri(hexadecan-1-one)

Ds-cyclen **1** (0.41 mmol, 168 mg, 1 equiv.) and DIPEA (4.14 mmol, 0.72 mL, 10 equiv.) were dissolved in 50 mL of dry DCM resulting in the formation of a clear yellow solution, which was cooled down to 5 °C. n-Hexadecanoyl chloride (2.07 mmol, 0.57 mL, 5 equiv.) was added dropwise at this temperature and the mixture was stirred for 30 min (**Scheme 9-1**). The colour changed to orange-red, but the solution remains clear. Stirring was maintained for 48 h at r.t. The reaction mixture was worked up by stirring with 1% aq. NaOH for 2 hours, followed by extraction with DCM (2 x 50 mL). The combined organic phase was consequently washed with conc. aq. citric acid, brine, aq. $NaHCO_3$ and water. The organic phase was dried over anhydr. Na_2SO_4 and the flask content was evaporated to dryness. The target product was subjected to purification by column chromatography on a silica gel employing DCM:MTBE=20:1 v/v as a mobile phase to furnish 1.421 g (89%) of a yellow solid. ^{1}H NMR (TCE, 600 MHz, 393K) δ = 0.90 (*t*, *J*=7.0 Hz, 6H, H-16''), 0.91 (*t*, *J*=6.7 Hz, 3H, H-16'), 1.30-1.39 (*m*, 66H, H-4' to H-15' and H-4'' to H-15''), 1.63-1.67 (*m*, 6H, H-3' and H-3''), 2.28 (*t*, *J*=7.4 Hz, 4H, H-2''), 2.32 (*t*, *J*=7.3 Hz, 2H, H-2'), 2.91 (*s*, 6H, NCH_3), 3.32 (*t*, *J*=4.2 Hz, 4H, H-9 and H-11), 3.57 (*t*, *J*=5.9 Hz, 4H, H-2 and H-

6), 3.62 (*t*, *J*=4.6 Hz, 4H, H-8 and H-12), 3.79 (*t*, *J*=5.8 Hz, 4H, H-3 and H-5), 7.21 (*d*, *J*=7.5 Hz, 1H, H-6‴), 7.54 (*t*, *J*=8.7 Hz, 1H, H-3‴), 7.55 (*t*, *J*=8.6 Hz, 1H, H-7‴), 8.07 (*d*, *J*=7.3 Hz, 1H, H-2‴), 8.52 (*d*, *J*=8.7 Hz, 1H, H-8‴), 8.62 (*d*, *J*=8.5 Hz, 1H, H-4‴).

^{13}C NMR (TCE, 150 MHz, 393K) δ = 14.19 (C-16′ and C-16″), 22.89 (C-15′ and C-15″), 25.71 (C-3″), 25.83 (C-3′), 29.58 and 29.79 and 29.83 and 29.86 and 29.90 and 29.93 and 29.96 and 29.98 (C-4′ to C13′ and C-4″ to C13″), 32.21 (C-14′ and C-14″), 33.68 (C-2′), 34.09 (C-2″), 45.65 (NCH_3), 49.49 (C-3 and C-5), 49.86 (C-8 and C-12), 50.23 (C-2 and C-6), 51.73 (C-9 and C-11), 116.14 (C-6‴), 119.83 (C-8‴), 123.36 (C-3‴), 128.85 (C-7‴), 130.74 (C-2‴), 131.09 (C-8a‴), 131.59 (C-4‴), 131.65 (C-4a‴), 132.75 (C-1‴), 152.66 (C-5‴), 174.32 (C-1′), 175.01 (C-1″).

9.3.4 Spectrophotometric and spectrofluorimetric measurements

9.3.4.1 Photophysical characterization and titrations

Stock solutions of each compound (approximately 1 mM) were prepared in various solvents (CH_3CN, DMSO, EtOH, $CHCl_3$, and THF), by dissolving the respective ligand in a 10 mL volumetric flask and diluting with the chosen solvent. Working solutions, ranging from 10 μM to 1 μM, were obtained by further dilution of the stock solutions.

Titration experiments with ligand L1 were conducted through the stepwise addition of microliter aliquots of standard metal ion solutions (Ca^{2+}, Co^{2+}, Ni^{2+}, Cu^{+}, Cu^{2+}, Zn^{2+}, Ag^{+}, Cd^{2+}, and Hg^{2+}) in acetonitrile. For Hg^{+} and Pb^{2+}, aqueous solutions were used. Absorbance corrections were applied where necessary.

To study the aggregation effects, mixtures with varying water fractions (f_w = 0%, 17%, 33%, 55%, 67% and 83%) were prepared in THF at a final concentration of 10 μM and characterized using absorption and emission spectroscopy.

Table 9-1. Spectroscopic polarity parameters, physical properties of the different solvents. ε_r: relative permitivity; η: refractive index; α: the solvent's HBD acidity; β: the solvent´s HBA basicity; π*: the solvent´s dipolarity/polarizability.

Solvent	ε_r	α	β	π*	η
DMSO	47.24	0	0.76	1.00	1.47
CH_3CN	35.94	0.19	0.40	0.66	1.34
EtOH	24.30	0.86	0.75	0.54	1.36
THF	7.58	0	0.55	0.58	1.40
$CHCl_3$	4.89	0.20	0.10	0.69	1.44

9.3.4.2 Fluorescence quantum yield and lifetime

The relative photoluminescence quantum yields were evaluated using dansylamide dissolved in DMSO (ϕ_F = 0.61) as a reference standard for quantifying the QY of each compound across all tested solvents. [29] Fluorescence lifetime measurements were conducted using a Tempro Fluorescence Lifetime System equipped with a Horiba Jobin-Yvon NanoLed pulsed diode controller. All experiments were performed at 293 K.

9.3.5 Determination of the detection and quantification limits (LOD and LOQ)

The determination of the detection limit (LOD) and quantification limit (LOQ) began with ten independent measurements of a solution containing the selected probe, without the addition of any metal ions (y_{blank}). The LOD and LOQ were then calculated using the following equations. LOD = y_{dl} = y_{blank} + 3std and LOQ = y_{dl} = y_{blank} + 10std, where y_{dl} = signal detection limit and std = standard deviation.

Finally, titrations with the ligands were carried out to determine the lowest concentrations of metal ions that could be reliably detected and quantified. [30,31]

9.3.6 DFT calculations

All calculations were performed by means of quantum chemical calculations at the density functional theory (DFT) level using Gaussian16 program package. [32] The geometries of all compounds have been fully optimized and the corresponding transition states were localized using B3LYP [33] functional with 6-31+G(d,p) basis set. [34] The nature of all critical points was confirmed by means of the vibrational analysis. The ΔH, ΔS and ΔG values were calculated at T = 298.15 K at the same level of theory including zero-point energy and vibrational, rotational and translational thermal energy corrections.

9.3.7 Colloidal synthesis of platinum nanoparticles

Synthesis of platinum nanoparticles began with the preparation of an aqueous solution of K_2PtCl_4 with a concentration of 2.72 mM. Compound **L3** was used as a stabilizing agent in different ratios of metal:**L3** (1:1, 1:2, 1:5, 1:7.5, 1:10). In a round-bottom flask, 10 mL of ethanol was added to the weighted compound **L3** (0.29 mM, 0.53 mM, 1.36 mM, 2.05 mM, 2.66 mM) and heated to 87ºC to allow solubilization. Then, 1 mL of the platinum solution was added, and

the solution was allowed to run for ten minutes. The resulting solutions were centrifuged three times for thirty minutes at 6000 rpm in ethanol.

9.4 Results & Discussion

9.4.1 Conformational Analysis and Molecular Geometry

The NMR spectra of the obtained and purified compounds display signals indicating a mixture of conformers, with their exchange occurring slowly on the NMR time scale. Variable temperature ^{1}H NMR spectra of compounds **L1**-**L3** were measured in TCE in order to reach slow and fast exchange limits. As the temperature decreases, the separation of signals of rotamers increases. However, at 243K (Figure 9–12, Figure 9–18, Figure 9–24), the signals were still broad and we were not able to reach slow exchange regime. With increasing the temperatures to 393K (Figure 9–12, Figure 9–18, Figure 9–24) the fast exchange regime was reached and we were able to measure ^{1}H, ^{13}C, 2D COSY, 2D HSQC and 2D HMBC NMR spectra allowing full structure elucidation of the new compounds.

To investigate the exchange behavior of the new compounds in solution, we performed DFT calculations on a model compound in which all long alkane chains were replaced with methyl. There are four possible conformations of the cyclen ring [35] depending on the *R* or *S* configurations of the chiral nitrogen atoms. In our case, the substitution of the amine protons with rather bulky substituents reduces the possible conformations to one with alternating up and down substituents. Reaction coordinate type calculations using variation of the dihedral angles around the S-N and S-C bonds estimate a barrier in the range 5-8 kcal/mol. However, reaction coordinate type calculations using variation of the dihedral angles of the three amide bonds estimate rotation barriers in the range 15-18 kcal/mol, revealing that these restricted rotations are responsible for the dynamic behavior of the NMR spectra of the **L1**-**L3** compound. Eight conformers with *syn* and *anti* conformations around the three amide bonds are possible (Figure 9–2). The B3LYP/6-31+G(d,p) calculated thermodynamic parameters of all eight GS stereoisomers at 298 K are presented in Table 9-2. The most preferable conformer is GS5 (*syn, syn, syn*). The exchange between the ground state structures GS1 (*syn, anti, anti*) and GS2 (*syn, anti, syn*) of the model compound together with the two transition states TS12 and TS21 are illustrated in Scheme 9-2. Further optimizations of transition state (TS) structures during the rotation around amide bonds allow localization of all TS geometries and estimation of rotational barriers (Table 9-10).

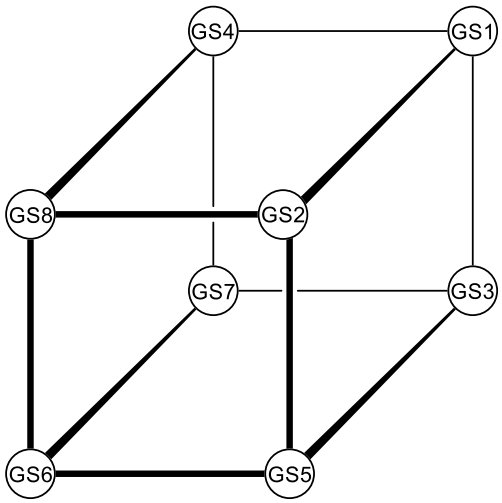
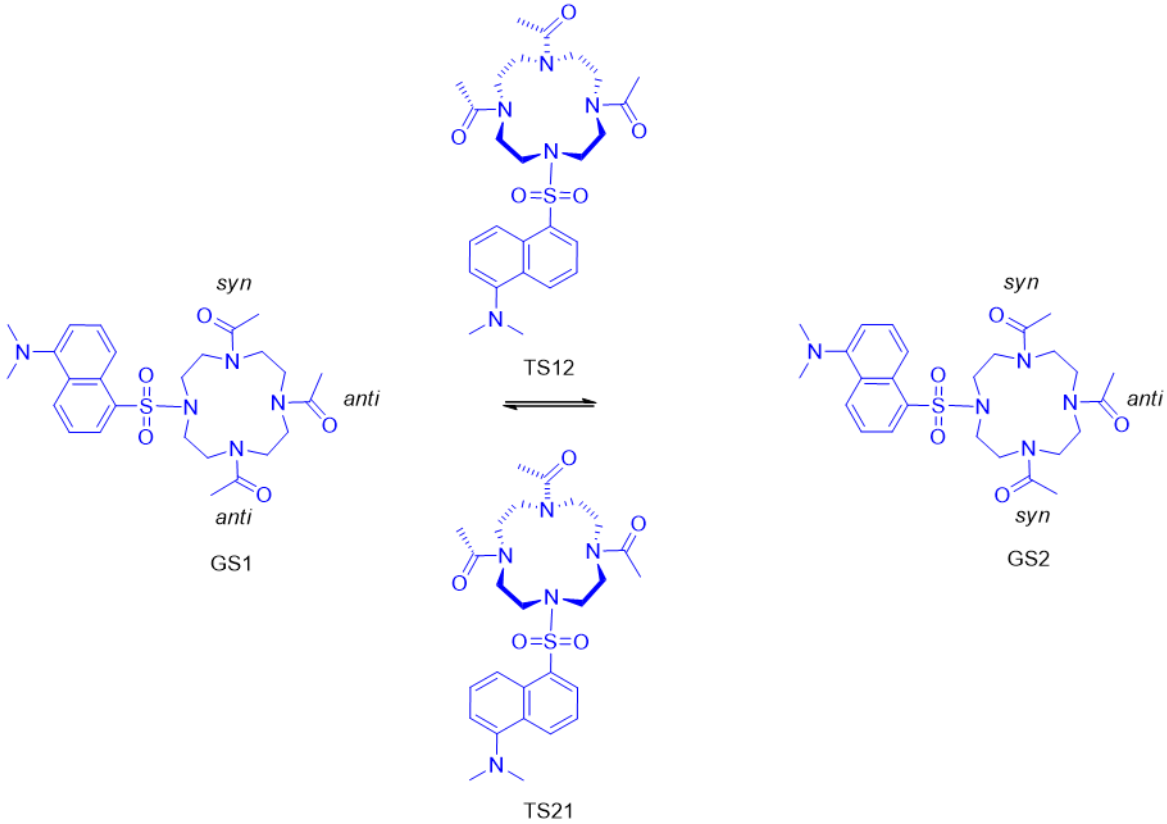


Figure 9–2. Cube vertices representing the eight conformations of model compound and the edges mapping out the exchange pathways. The nomenclature of all conformations is presented in Table 9-2.



Scheme 9-2. Exchange between GS1 (*syn, anti, anti*) and GS2 (*syn, anti, anti*) ground state structures of the model compound. The two transition states TS12 and TS21 are also presented.

Table 9-2. B3LYP/6-31+G(d,p) calculated thermodynamic parameters for stereoisomers at 298 K.

Stereoisomer	Nomenclature	ΔH≠ (kcal/mol)	ΔS≠ (e.u.)	ΔG≠ (kcal/mol)	Populations (%)
GS1	syn,anti,anti	0	0	0	0.002
GS2	syn,anti,syn	-3.05	7.89	-5.41	22.1
GS3	syn,syn,anti	-4.34	2.76	-5.16	14.5
GS4	anti,anti,anti	-2.97	5.97	-4.74	7.2
GS5	syn,syn,syn	-3.32	7.62	-5.59	30.2
GS6	anti,syn,syn	-2.25	8.34	-4.73	7.1
GS7	anti,syn,anti	-3.21	6.92	-5.23	17.6
GS8	anti,anti,syn	-1.33	8.03	-3.72	1.3

9.4.2 Mesomorphic behavior

Polarized light optical microscopy (POM) and differential scanning calorimetry (DSC) studies were conducted to determine if the new compounds bearing terminal alkyl chains exhibit mesomorphism. The optical observations under polarized light show that compounds **L2** and **L3** form a fluidic and birefringent liquid-crystalline mesophase just before melting into the isotropic liquid, as demonstrated in Figure 9–3. In accordance with the POM studies, the corresponding DSC thermograms displayed a unique and broad endothermic peak that involves both the solid-mesophase and the mesophase-isotrope phase transitions. The onset temperatures and the enthalpy values are gathered in Table 9-3. Note that no exothermic peaks appear in the thermograms upon cooling. In fact, the formation of the mesophase from the isotrope was not observed by POM at the expected temperature, neither the solidification process. This feature can only be understood if a hysteresis phenomenon [36] occurs during the heating and cooling cycles. To verify this behavior, samples were allowed to cool slowly, and solidification was finally observed after several hours at r.t.

Regarding the mesophase nature, it could be possible that the mesophases are columnar, based on the disc-like shape of these molecules (see Scheme 9-1). Regrettably, the narrow temperature range of just some degrees in which the mesophases are stable prevented analyzing their supramolecular organization by powder X-ray diffraction experiments, and the texture of the mesophases observed under polarized light did not allow their identification either.

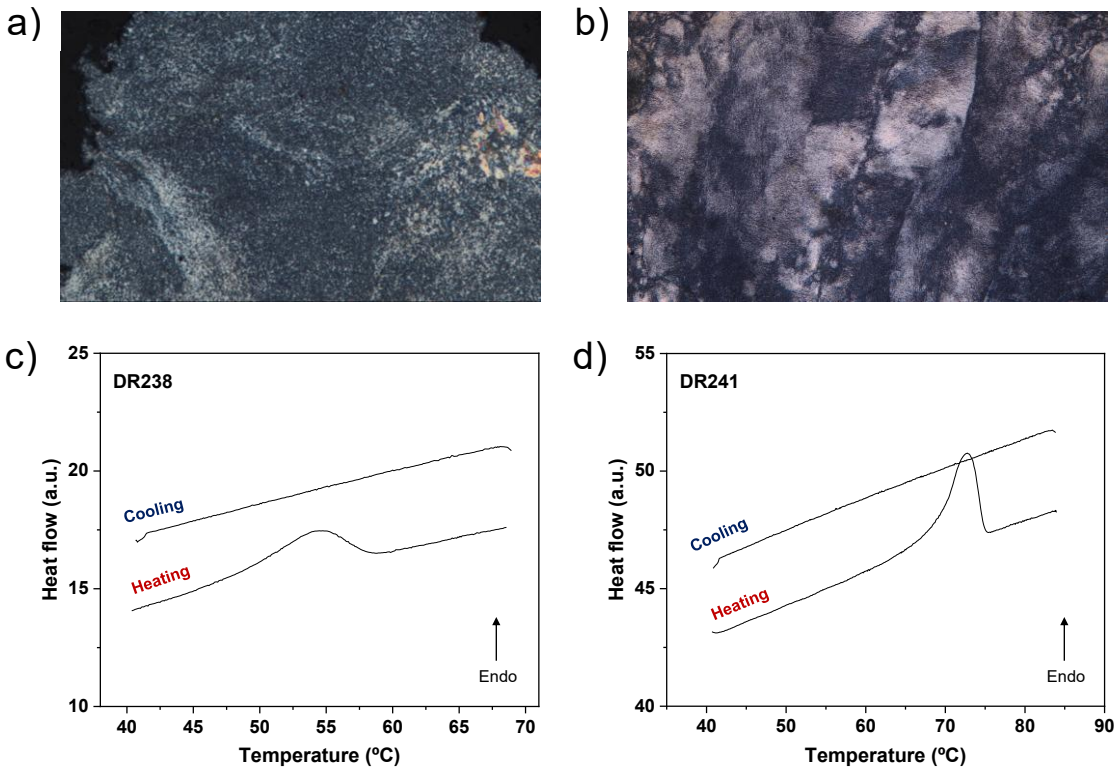


Figure 9–3. (a,b) Textures of the mesophases observed by POM for (a) **L2** and (b) **L3**, at 43 and 68 ºC, respectively, in the first heating cycle. (c,d) DSC thermograms registered in the first heating and cooling cycles.

Table 9-3. Phase behavior of **L2** and **L3** established by DSC.

Compound	Transition[a]	Onset temperature[b] (ºC)	ΔH ($kJmol^{-1}$)
L2	Cr → M → I	47	47.8
L3	Cr → M → I	68	80.3

[a] Cr = solid, M = mesophase, I = isotrope. [b] Onset temperature determined by DSC.

9.4.3 Photophysical characterization

The monodansylated cyclen compounds bearing different alkyl side chains exhibit photophysical properties both in solution as well as in the solid state. The complete photophysical data are provided in Figure 9–4, as well as Table 9-4 and in Figure 9–28 to Figure 9–30 of the supporting information. Special focus has been given to the investigation of **L1** in various solvents given the constraints associated with the increment in length of the alkyl side chains in terms of solubility for **L2** and **L3**.

Providing a closer look at the UV-Vis spectra, all compounds display a broad absorption band with a maximum centered between 341 and 350 nm depending on the employed solven, associated with the π - π* transition of dansyl chromophore promoting the absence of any colour in the visible region. As we consider each solvent used, the excitation of the solutions at the appropriate wavelength for **L1** results in a shift of the emission from 504 to 537 nm enabling the display of solvatochromism that it will be further explored and can be confirmed by Figure 9–4c. Although no confirmation of solvatochromism is possible for **L2** and **L3**, due to solubility limitations, no evidence has been found in chloroform or THF that could suggest any influence of the length of the alkyl side chains onto the photophysical properties given the similarities observed. Furthermore, large Stokes shifts, commonly found for dansyl derivatives, were observed ranging from 8730 to 10113 cm^{-1}. On a relatable note, solid-state emission spectra were recorded for all compounds exhibiting an emission maximum between 486 and 498 nm that is blue-shifted in comparison to all the spectra recorded in solution.

Finally, elucidation in terms of fluorescence quantum yield efficiency and characterization of fluorescence lifetime decay were investigated and are summarized in Table 9-4. Once again, the solvent used was found to influence the quantum yield efficiency with lower values for more polar solvents starting from 26% in ethanol and reaching a maximum of up to 55% in chloroform as **L1** is considered. In turn, the time-resolved fluorescence decay curves give us insights into the double-digit nanosecond times sitting in the range of 12 to 14.98 ns with no relevant association between this parameter and the solvent used.

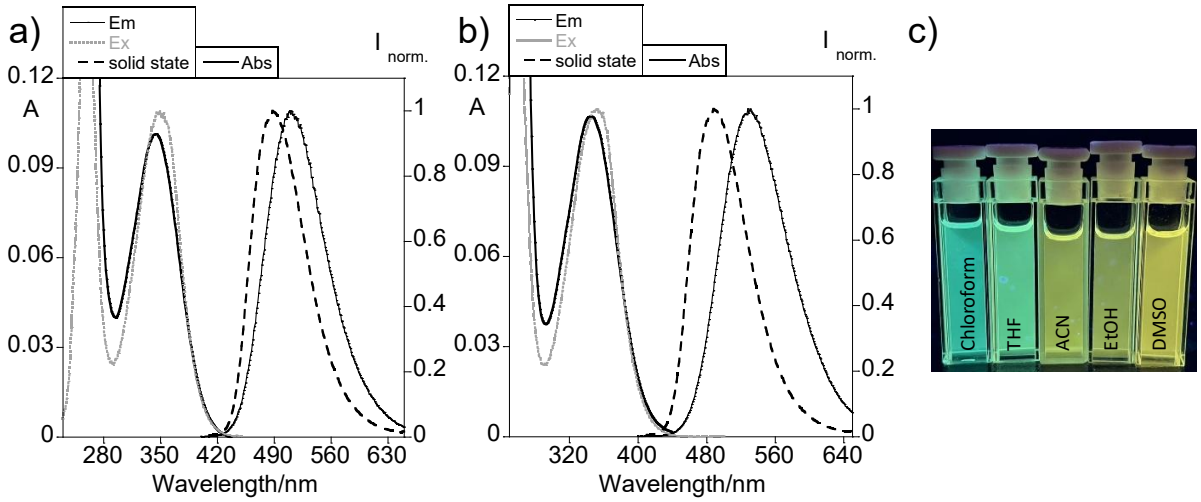


Figure 9–4. Photoluminescent characterization of compound **L1** in THF (a) and acetonitrile (b). Image (c) under UV light (365 nm) of **L1** dissolved in various solvents.

Table 9-4. Absorption maximum wavelength in solution (λ_{abs}), emission maximum wavelength in solution (λ_{em}), molar absorption coefficients (ε), Stokes shift ($\Delta\lambda$), emission maximum in the solid state (λ_{em}^{Solid}), fluorescence quantum yields (ϕ), fluorescence lifetimes (τ) for compounds **L1** to **L3** in different solvents.

Cpd	Solv	λ_{abs} [nm]	λ_{em} [nm]	ε (10^4) [cm^{-1} M^{-1}]	Stokes shift [cm^{-1}]	ϕ(%)	λ_{em}^{Solid} [nm]	τ[ns]
L1	DMSO	348	537	0.466	10113	32	486	14.29
	EtOH	345	526	0.534	9974	26		12.04
	CH_3CN	345	531	0.557	10153	40		12.56
	THF	341	508	0.497	9640	42		13.30
	$CHCl_3$	350	504	0.500	8730	55		14.98
L2	THF	340	509	0.494	9765	43	488	13.36
	$CHCl_3$	350	503	0.460	8691	57		14.98
L3	THF	341	508	0.507	9640	44	498	13.48
	$CHCl_3$	350	502	0.524	8651	54		15.03

As mentioned before, efforts were placed to investigate the solvatochromic behavior of these dansyl derivatives given the visual detection of a color change under UV radiation from bluish green to yellow. This transition with the increase in solvent polarity relates to positive solvatochromism and has been characterized by their solvent-compound interactions through the multiparametric fitting of the Kamlet-Taft equation (Equation 1).

$$\upsilon = \upsilon_0 + a\alpha + b\beta + p\pi^* \quad \text{(Equation 1)}$$

Where υ_0 represents the wavenumber value in a reference solvent; the solute dependent parameters a, b and p are obtained through multiple regression analysis that elucidate the susceptibility for the probes' photophysical behavior to be influenced by solvent polarity; α: hydrogen bond donor acidity (HBD); β: hydrogen bond acceptor basicity (HBA); π^*: stabilization of a charge or dipole without a specific dielectric interaction (Table 9-1). [37,38]

Table 9-5. Independent fluorescence wavenumber ($\upsilon 0$), solvent polarity (p), HBD (a), HBA (b), slope and coefficient (R^2) of the linear fitting plot $\upsilon_{exp.}$ versus $\upsilon_{calc.}$

	υ0	a	b	p	Slope	R^2
L1	21440	-618	-1105	-1978	1.00	1.00

Table 9-5 gathers the reference wavenumber value υ_0, the fitted parameters (a, b and p) along with the slopes and correlation coefficients obtained through the fitting of a linear plot of $\upsilon_{exp.}$ versus υ_{calc}, by applying the Kamler-Taft model excluding acetonitrile.

The Kamlet-Taft analysis of the solvatochromic behavior reveals that the observed positive solvatochromism for **L1** is primarily driven by solvent polarity effects. The observed negative coefficients suggest that any increase of the solvent parameters leads to a bathochromic shift in the emission spectrum in accordance with what is observed experimentally. Among these values, the largest is associated with p parameter suggesting that dipolarity and polarizability of the solvent have the strongest influence on the spectral shifts. In turn, hydrogen bond basicity also plays a comparatively smaller role, while hydrogen bond acidity employs the least effect.

9.4.4 Modulation of aggregation induced emission in water.

The assessment of the formation of aggregates, according to the implementation of different alkyl side chains in the compounds under investigation, was accomplished with different ratios of water in THF, and were followed by photophysical and dynamic light scattering techniques. Figure 9–5 illustrates the absorption and the emission profile at increasing water fraction (f_w) whereas Table 9-6 summarizes the DLS data alongside the quantum yield and lifetime measurements of the high f_w samples of all compounds. As far as the emission and the absorption profiles are concerned, key changes can be perceived with increasing alkyl side chains. Figure 9–5a-c demonstrate that the absorption profile suffers changes with the slight increase of the baseline at f_w = 83% for all compounds and a larger increase at 67% for the latter two compounds, without variation of the absorption maximum wavelength. These increases serve as evidence for the formation of aggregates at high water content ratios. DLS data help consolidate these findings with the identification of aggregates with an average size between 66.8 and 106.8 nm considering the f_w = 83%. Interestingly, larger aggregates were identified for the mixtures of f_w = 67% but only for compounds **L2** and **L3** with an average size of 322.1 and 298.5 nm, respectively, suggesting that the formation of these aggregates can only be stabilized by the implementation of larger alkyl side chains.

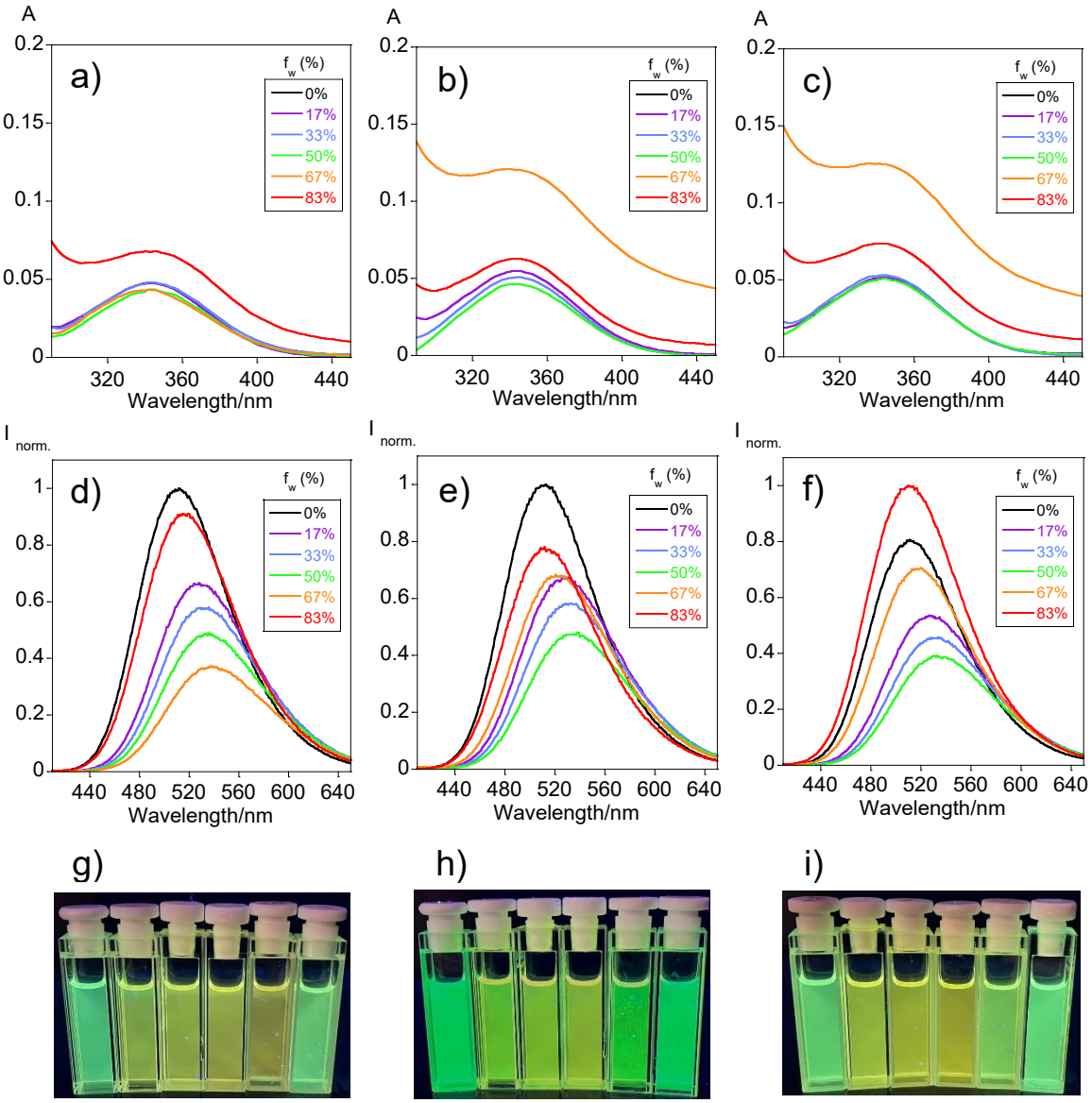


Figure 9–5. Absorption (a-c) and emission (d-e) spectra of **L1** (a,d), **L2** (b,e) and **L3** (c,f) in different mixtures THF and water fractions f_w (0%, 17%, 33%, 55%, 67%, 83%). Images of **L1** (g), **L2** (h) and **L3** (i) with different water fractions under UV light (365 nm). The images are displayed in increasing water fraction order.

The photoluminescent profile of these mixtures is characterized by a continuous quenching of the emission as the water content increases in tandem with a bathochromic shift of the fluorescence emission maximum, that can be visualized in Figure 9–5d-f in combination with the images under UV light (Figure 9–5g-i). Deviations from this are observed with the increase of the emission close to the original one for **L1** at f_w = 83%. A similar behaviour is addressed for **L2** with an additional regain of emission for f_w = 67% whereas for **L3** the emission at f_w = 83% was recorded past the original one. The aggregation induced emission was then characterized for its quantum yield, suggesting values from 16% to 40% and the identification of two fluorescence lifetimes for each mixture indicates the presence of different relaxation pathways.

Being the contribution of T_1 lower than T_2 while the latter resembles in great length the ones found for the other solvents used.

Table 9-6. Dynamic light scattering data, quantum yield and lifetime measurements of each compound in different mixtures of THF and water.

f_w(%)	Z-Average (nm)	PDI	ζ-Potential (mV)	ϕ(%)	τ[ns]
L1 (83%)	98.6 ± 4.2	0.19 ± 0.13	-24.6 ± 1.1	26	T_1 = 1.4; T_2 = 16.0
L2 (67%)	322.1 ± 5.2	0.09 ± 0.03	-17.5 ± 0.4	16	T_1 = 4.5; T_2 = 14.0
L2 (83%)	66.8 ± 0.5	0.16 ± 0.02	-18.7 ± 0.4	28	T_1 = 4.8; T_2 = 17.1
L3 (67%)	298.5 ± 4.1	0.05 ± 0.01	-8.4 ± 0.9	20	T_1 = 3.5; T_2 = 15.3
L3 (83%)	132.7 ± 0.7	0.06 ± 0.01	-25.1 ± 1.3	40	T_1 = 8.4; T_2 = 18.1

9.4.5 Metal ion detection

Given the established usefulness of dansyl derivatives for metal ion detection, **L1** has been evaluated for this application. Hence, acetonitrile solutions of several metal ions; namely Ca^{2+}, Co^{2+}, Ni^{2+}, Cu^{+}, Cu^{2+}, Zn^{2+}, Ag^{+}, Cd^{2+}, and Hg^{2+} were used, while Hg^{+} and Pb^{2+} were prepared in aqueous solution. These metal ions have been added to **L1** in proportions of 1, 5, and 10 equivalents, and their corresponding emission intensities are shown in Figure 9–6. Clear modulation of the emission intensity was found in the presence of copper(II) ions due to the extensive quenching of the emission with only 1 equivalent followed by the total absence of emission in the case of 5 equivalents. It is also noteworthy to mention the much less pronounced effect of mercury(II) on the quenching of **L1**.

Despite the visible difference in magnitude, titrations of compound **L1** with Cu^{2+} and Hg^{2+} metal ions were carried out in acetonitrile. The absorption and luminescent behaviour were recorded and are gathered in Figure 9–6. The spectrophotometric and spectrofluorimetric titrations yielded results that were consistent for both metals.

For both cases the absorption spectral behaviour is characterized by a decrease of the absorption band centered at 345 nm and an opposite move for the band found at 290 nm, additionally for Hg^{2+}, a substantial decrease at 250 nm was observed. Furthermore, both titrations evolve with the presence of one and two isosbestic points for Cu^{2+} and Hg^{2+}, respectively, assuring a complexation interaction among these species. Regarding the fluorescence emission spectra, a suppression was followed at 530 nm, showing this fluctuation of the emission intensity maxima of **L1** in both insets of Figure 9–6b and Figure 9–6c. The emission quenching

observed with Hg^{2+} is presumably due to its nature as a heavy atom, which enhances spin-orbit coupling and facilitates non-radiative decay pathways that compete with fluorescence. As a result, chelation with Hg^{2+} leads to chelation-enhanced quenching (CHEQ). Likewise, Cu^{2+} is often detected via CHEQ, owing to its paramagnetic nature arising from unpaired electrons in its d-orbitals. This quenching occurs through various mechanisms such as either electron transfer or energy transfer. In contrast, the closed-shell configuration of Cu^{+} makes it incapable of quenching fluorescence. Thus, this system can effectively distinguish between Cu^{2+} and Cu^{+}, as well as Hg^{2+} and Hg^{+}, serving as a useful tool for metal ion speciation.

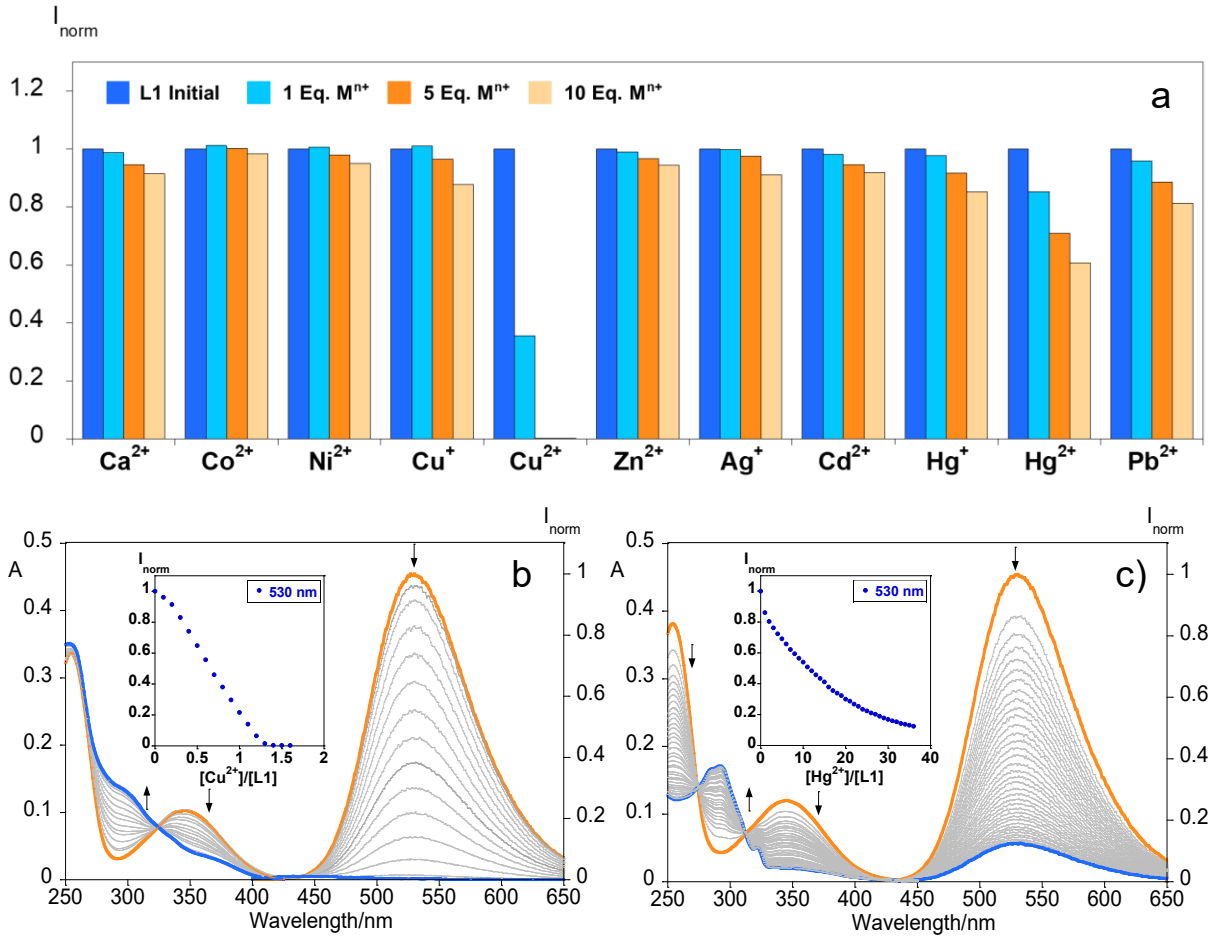


Figure 9–6. Maximum emission intensities of **L1** in acetonitrile (a) after the addition of 1, 5, and 10 equivalents of Ca^{2+}, Co^{2+}, Ni^{2+}, Cu^{+}, Cu^{2+}, Zn^{2+}, Ag^{+}, Cd^{2+} and Hg^{2+} in acetonitrile while Hg^{+} and Pb^{2+} metal ions were in aqueous solution. Spectrophotometric and spectrofluorometric titrations of compound **L1** with increased additions of Cu^{2+} (b) and Hg^{2+} (c) in acetonitrile. The inset represents the emission as a function of $[Cu^{2+}]/[\mathbf{L1}]$ at 530 nm (b), of $[Hg^{2+}]/[\mathbf{L1}]$ at 530 nm (c).

The complete assessment of the sensing profile for Cu^{2+} and Hg^{2+} was accomplished with the use of the HypSpec software[191] to determine the interaction constants. Additionally,

limits of detection (LOD) and quantification (LOQ) were evaluated. Table 9-7 presents the association constants along with the corresponding LOD and LOQ values.

Table 9-7. Association constants and stoichiometry for compound **L1** in the sensing of Hg^{2+} and Cu^{2+} ions in acetonitrile, determined using HypSpec software. Detection limit (LOD) and quantification limit (LOQ) values (in μM) were calculated based on emission intensity at 530 nm.

Compounds	Metal (M)	Association constants ($LogK_{ass.}$), L:M	LOD (μM)	LOQ (μM)
L1	Cu^{2+}	4.73 ± 0.01 (1:1)	2	6
	Hg^{2+}	3.10 ± 0.01 (1:1)	40	60

The proposed interaction constants have in consideration the stoichiometric ratio of 1:1 (L:M) provided the well-defined cyclen core as the coordination site. Naturally, the highest association constant was found for Cu^{2+} with a value of $Log K_{ass.}$ = 4.73 ± 0.01. This large gap in the interaction constants between **L1** and both metal ions may be assigned to the imposed rigidity of the tertiary amides which hinder the most favorable conformation of the core. This effect allied with the larger size of the Hg^{2+} ion, translates to a more challenging sensing of this metal. In our previous work, where the tetra dansylation of cyclen core was accomplished, these hindrances were not evident, which inturn promoted a slightly higher constant in the case of Cu^{2+} that were in par with Hg^{2+}. [1] Furthermore, the lowest detectable amounts corresponded to Cu^{2+} (2 μM and 6 μM) indicating its potential suitability for applications such as environmental monitoring, where detecting and quantifying low levels of Cu^{2+} is essential.

9.4.6 Colloidal synthesis of platinum nanoparticles

Considering the capacity of these compounds to self-assemble in solution, together with the mesomorphic properties conferred by the alkyl chains in the cyclen core, we redirected our focus to investigate these compounds in the colloidal production of platinum particles. Given the simplicity and vast literature surrounding the methodologies for the synthesis of these nanomaterials, our approach employs ethanol as a reducing agent and **L3** was used in order to explore it as stabilizing. [28] As expressed in the experimental section, several syntheses were accomplished by varying the ratio of the compound's concentration while maintaining the platinum salt's concentration constant. All the resulting colloidal solutions were followed by DLS while, from the selected Pt@1:5 AND Pt@1:10, TEM images were obtained. Overall, this synthesis method allows the intended formation of platinum particles, with **L3** acting as an effective stabilizing agent. Due to their non-plasmonic nature, no characteristic absorption

bands have been found (Figure 9–31). However, DLS data presented in Table 9-8 reveal variations in the average particle size, depending on the L3 ratio used, ranging from 157.5±1.0 to 229.7±11.5 nm. The associated polydispersity index (PDI) values indicate a low degree of polydispersity across all samples. Complementary transmission electron microscopy (TEM) images (Figure 9–32 and Figure 9–33) further support the formation of spherical particles. These images reveal a clear contrast between the dense metal core and the surrounding **L3** layer, which serves to inhibit coalescence. These results open for consideration the use of new synthesizable molecules as stabilizing agents and as a method of functionalization broadening the range of applications.

Table 9-8. Dynamic light scattering data for the obtained particles.

Particles	Z-Average (nm)	PDI
Pt@1:1	194.1 ± 3.2	0.23 ± 0.01
Pt@1:2	157.5 ± 1.0	0.17 ± 0.02
Pt@1:5	187.0 ± 0.9	0.20 ± 0.03
Pt@1:7.5	229.7 ± 11.5	0.30 ± 0.05
Pt@1:10	225.4 ± 4.9	0.23 ± 0.01

9.5 Conclusions

In this study, three novel monodansylated cyclen derivatives (**L1**–**L3**), functionalized with alkyl chains of varying lengths, were successfully synthesized and characterized. POM experiments showed that **L2** and **L3** exhibit a fluidic and birefringent liquid-crystalline mesophase immediately before transitioning into the isotropic liquid. Meanwhile, thermograms revealed a distinct and broad endothermic peak corresponding to both the solid-to-mesophase and mesophase-to-isotropic phase transitions.

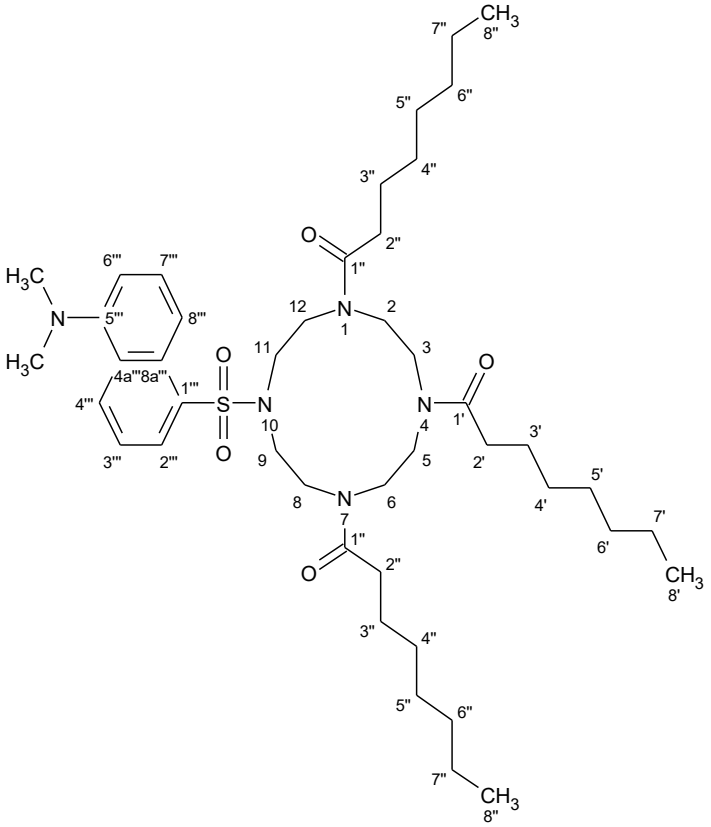
Photophysical studies were carried out in several solvents, revealing a positive solvatofluorochromism behavior, which was quantitatively analyzed using the Kamlet–Taft equation, providing relevant information regarding solute–solvent interactions. Different mixtures of aqueous environments promoted tunable photophysical properties through AIE, which was found to be dependent on the length of the alkyl chains. DLS provided the means to determine the size of the formed aggregates, which were also monitored by fluorescence decay lifetime measurements.

As a reference example, **L1** was used to establish the interaction potential toward metal ions, demonstrating efficient fluorescence quenching in the presence of Cu^{2+} and Hg^{2+} ions, reaching a detection limit of 2 μM for the former metal ion, with an association constant of log K_{ass} = 4.73. Notably, the system was able to differentiate between Cu^{+}/Cu^{2+} and Hg^{+}/Hg^{2+}, offering added analytical value.

Given its embedded multifunctional design, **L3** served as an effective stabilizing agent in the colloidal synthesis of platinum nanoparticles. TEM images revealed spherical-shaped particles, while DLS data showed that the hydrodynamic diameters were centered between 157.5 ± 1.0 and 229.7 ± 11.5 nm, depending on the salt-to-ligand ratio used. This result illustrates the versatility of these macrocyclic fluorophores, not only as responsive sensors but also as functional components in nanomaterial synthesis.

9.6 Supplementary material

9.6.1 Supplementary figures & tables



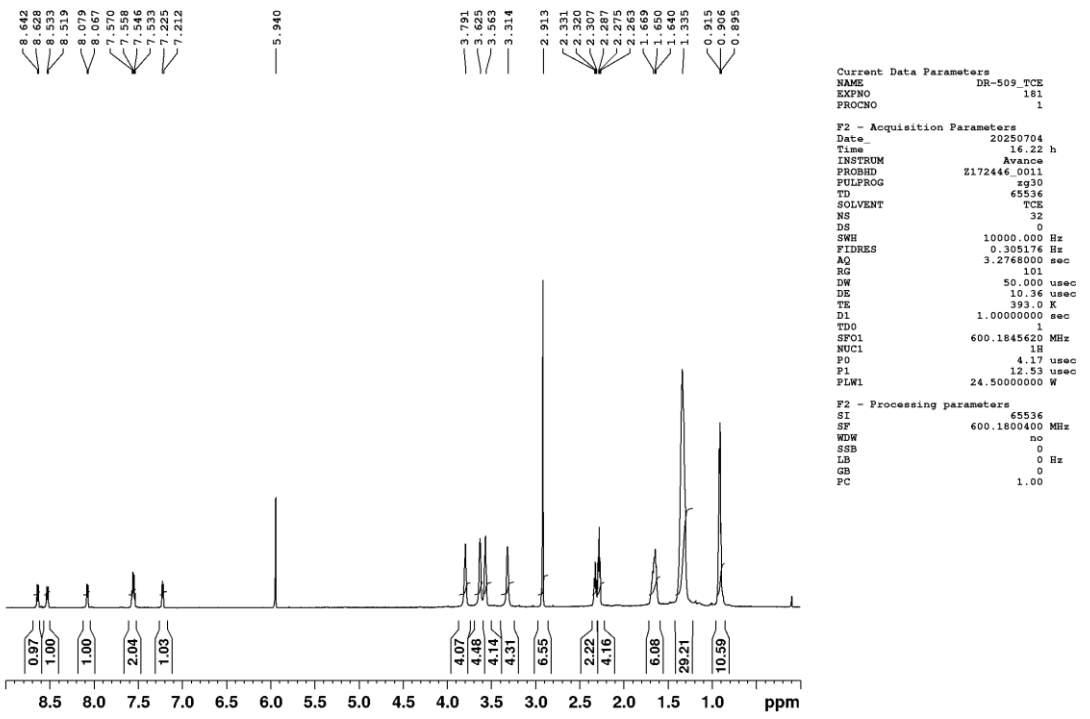


Figure 9–7. ^{1}H NMR spectrum of compound **L1** in TCE-d_2 at 393 K.

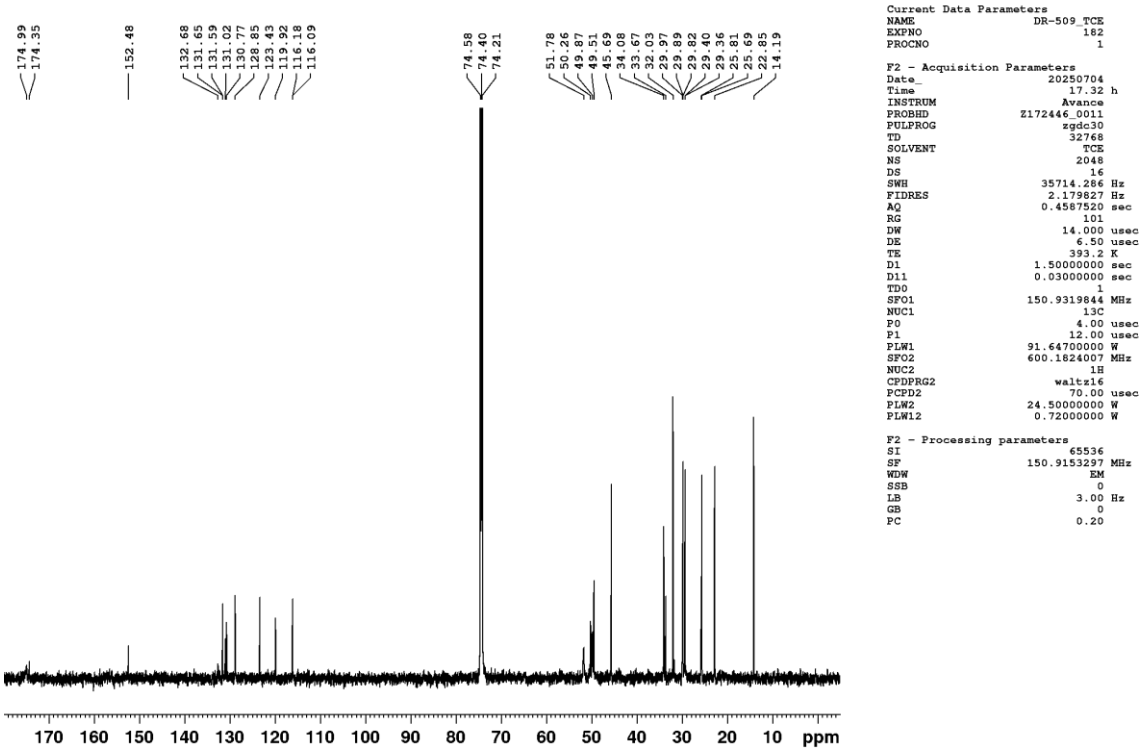


Figure 9–8. ^{13}C NMR spectrum of compound **L1** in TCE-d_2 at 393 K.

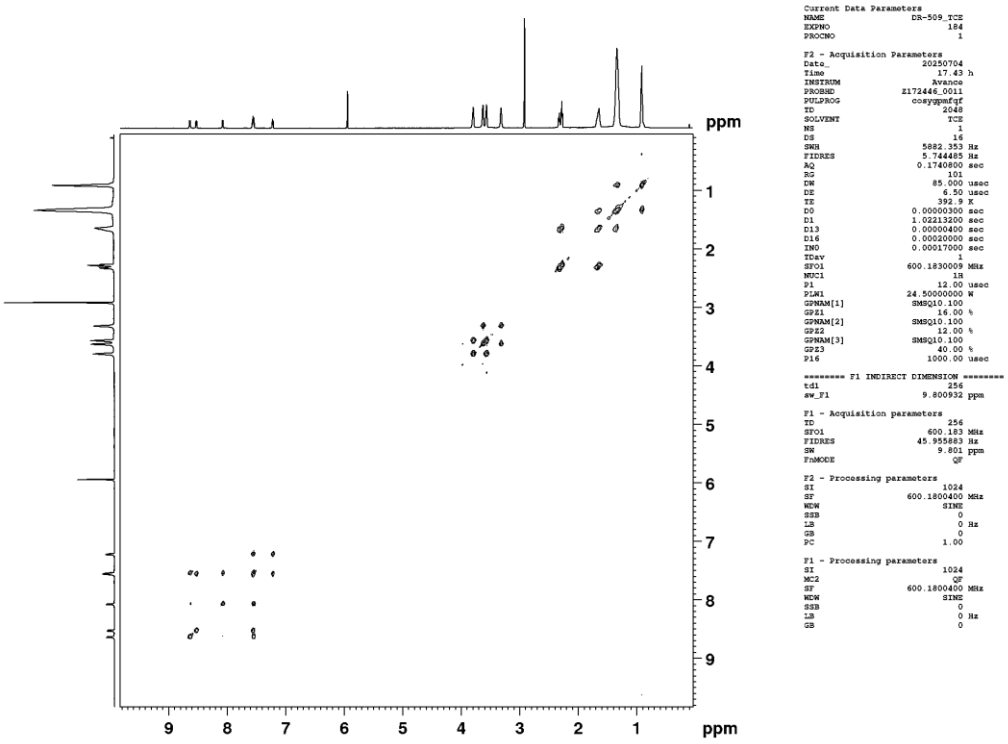


Figure 9–9. COSY NMR spectrum of compound **L1** in TCE-d_2 at 393 K.

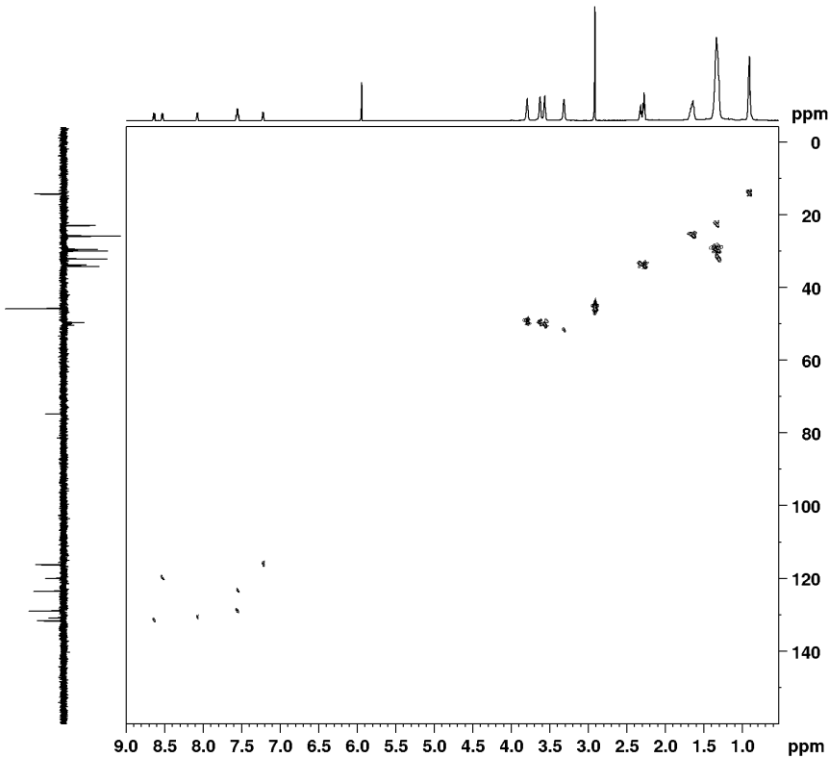


Figure 9–10. HSQC NMR spectrum of compound **L1** in TCE-d_2 at 393 K.

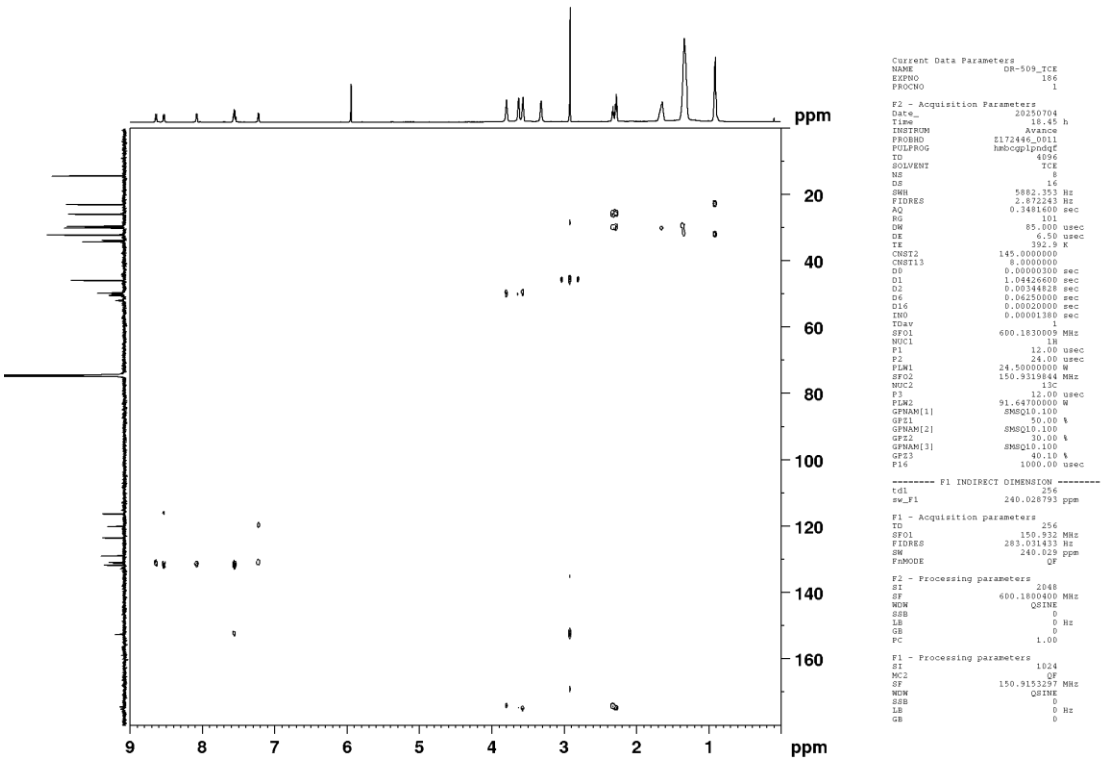


Figure 9–11. HMBC NMR spectrum of compound **L1** in TCE-d_2 at 393 K.

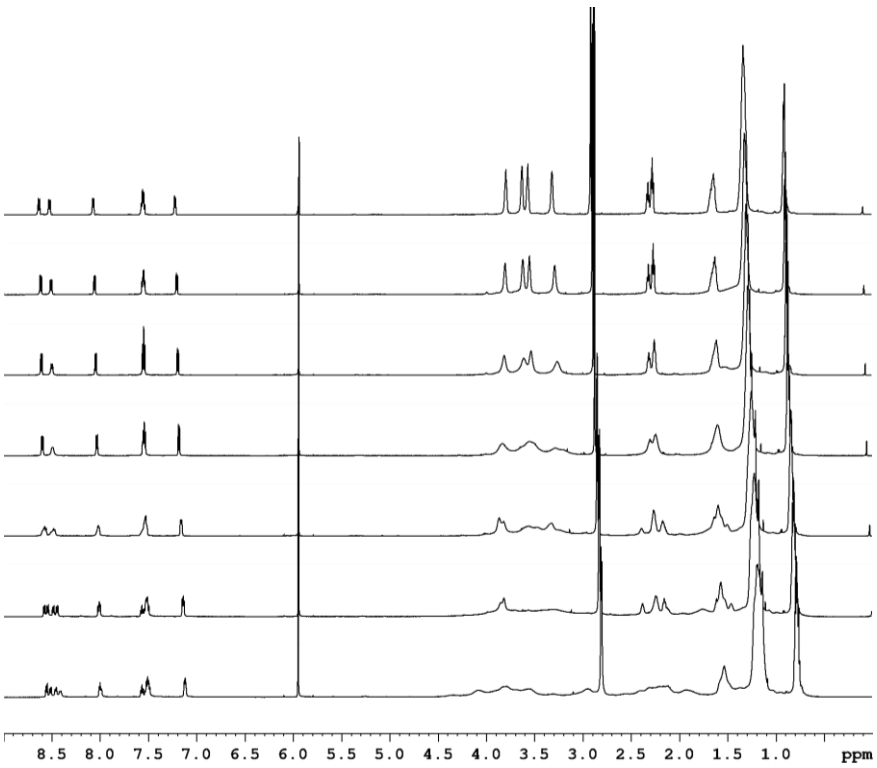


Figure 9–12. Stack plot of ^{1}H NMR spectra of compound **L1** in TCE-d_2 at 243, 273, 298, 333, 353, 373 and 393 K.

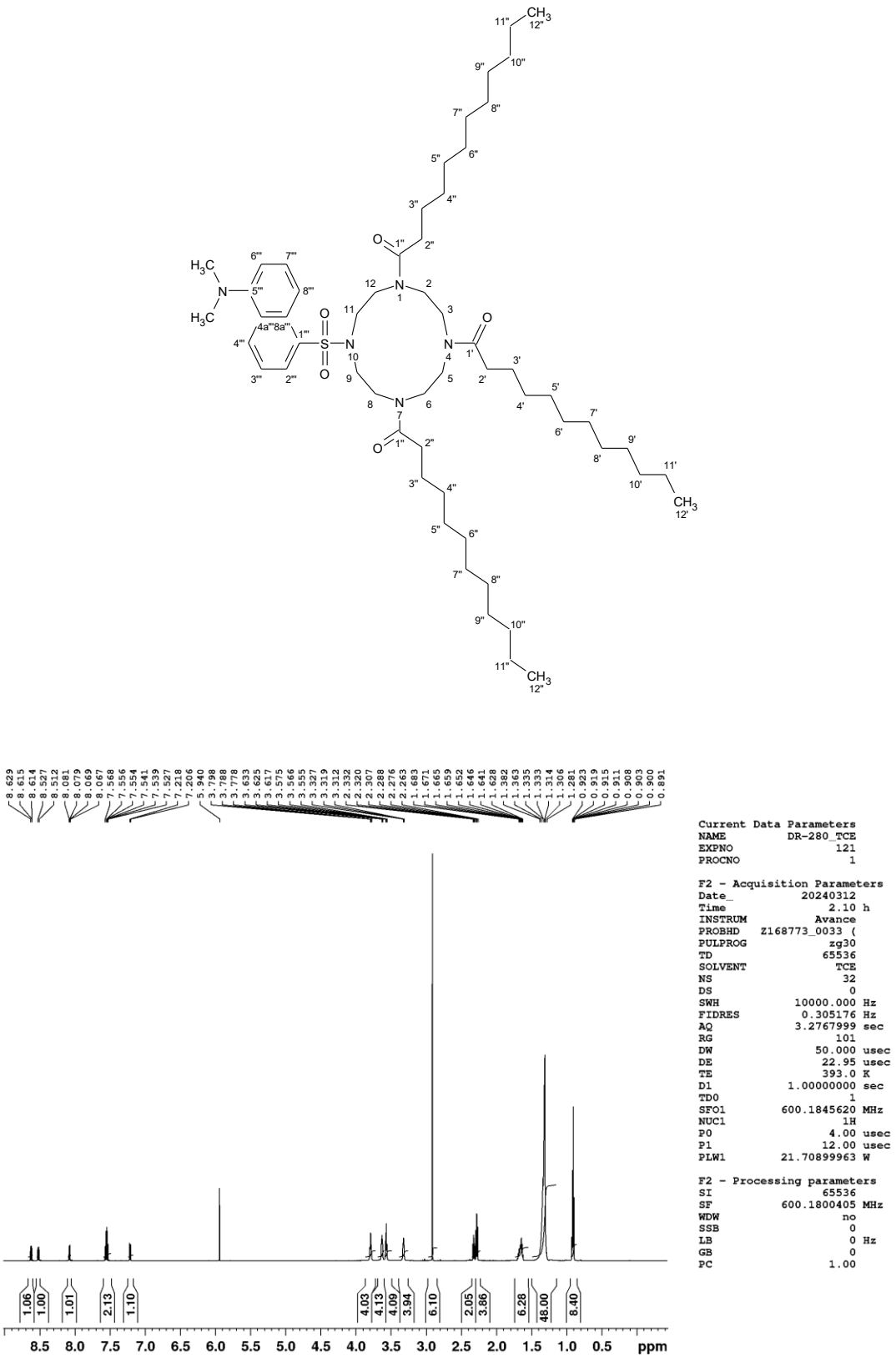


Figure 9–13. ^{1}H NMR spectrum of compound **L2** in TCE-d_2 at 393 K.

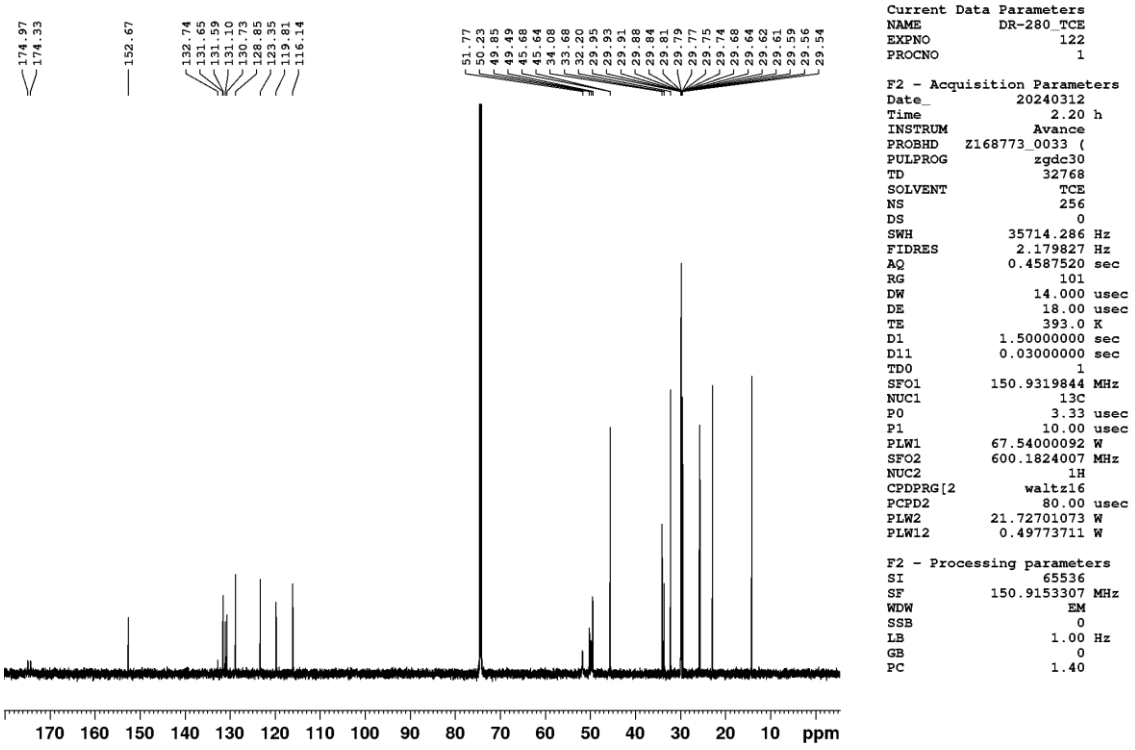


Figure 9–14. ^{13}C NMR spectrum of compound **L2** in TCE-d_2 at 393 K.

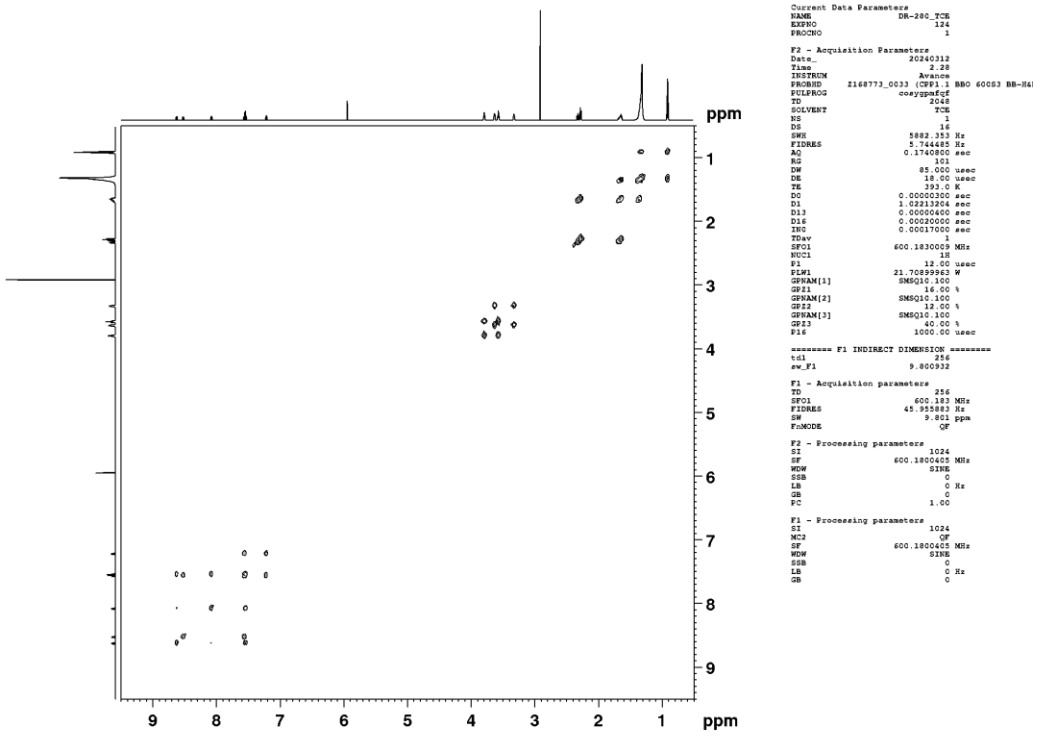


Figure 9–15. 2D COSY NMR spectrum of compound **L2** in TCE-d_2 at 393 K.

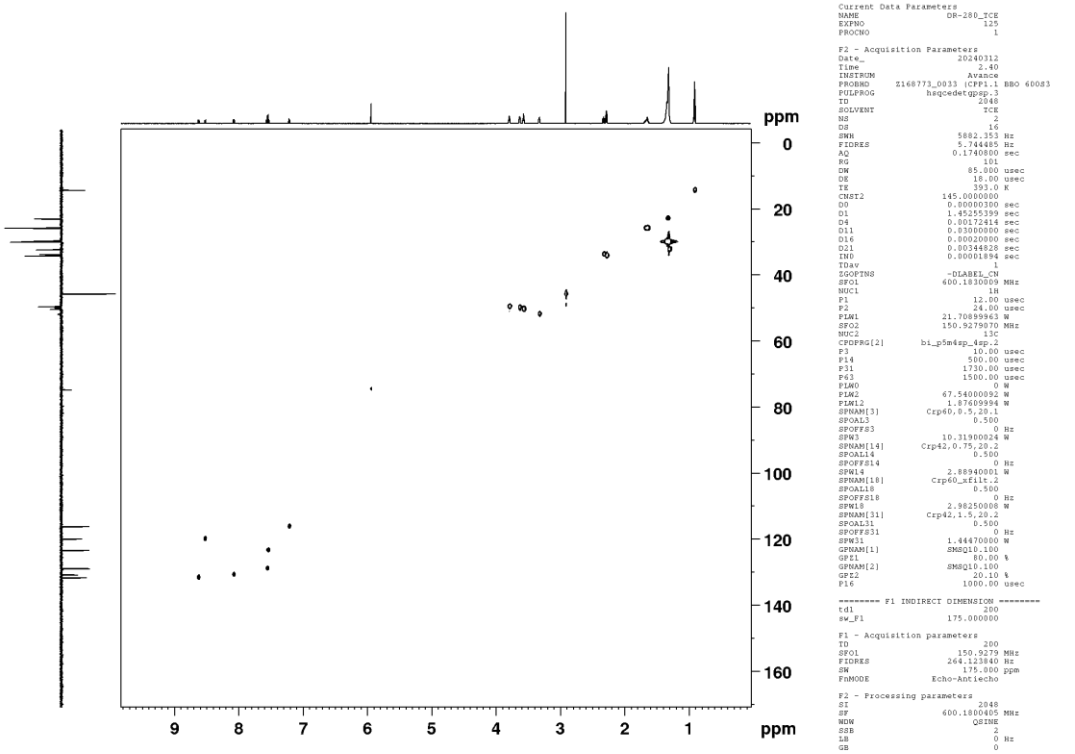


Figure 9–16. 2D HSQC NMR spectrum of compound **L2** in TCE-d_2 at 393 K.

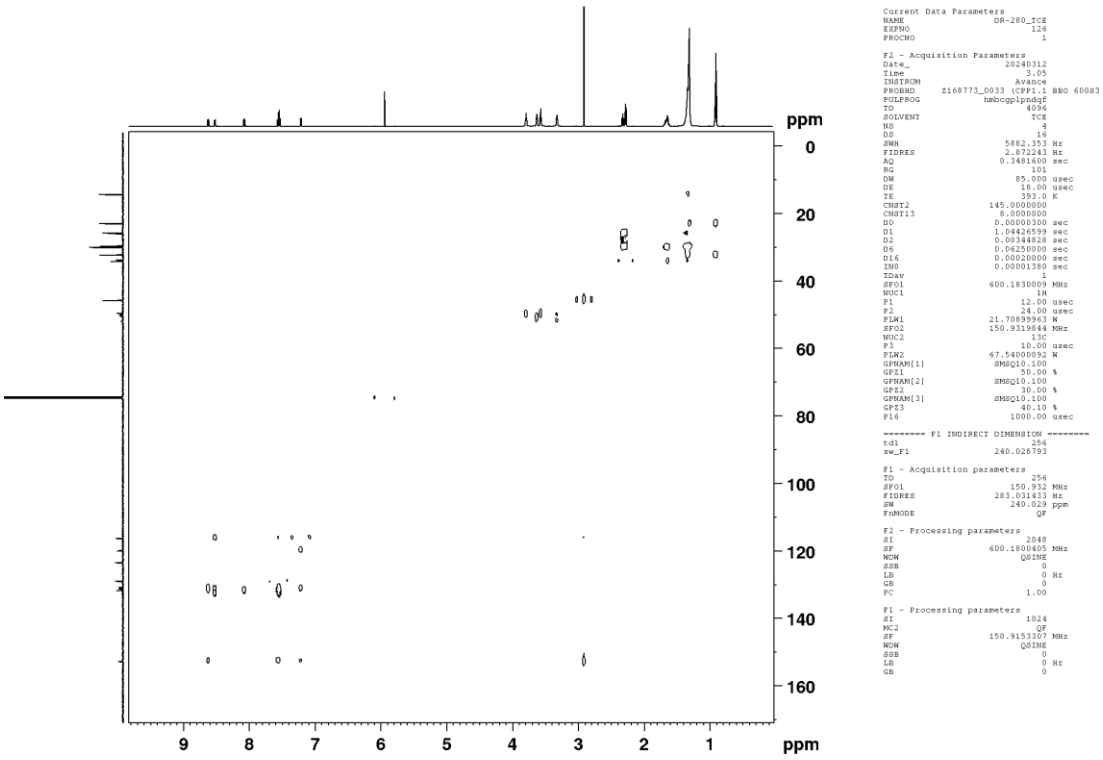


Figure 9–17. 2D HMBC NMR spectrum of compound **L2** in TCE-d_2 at 393 K.

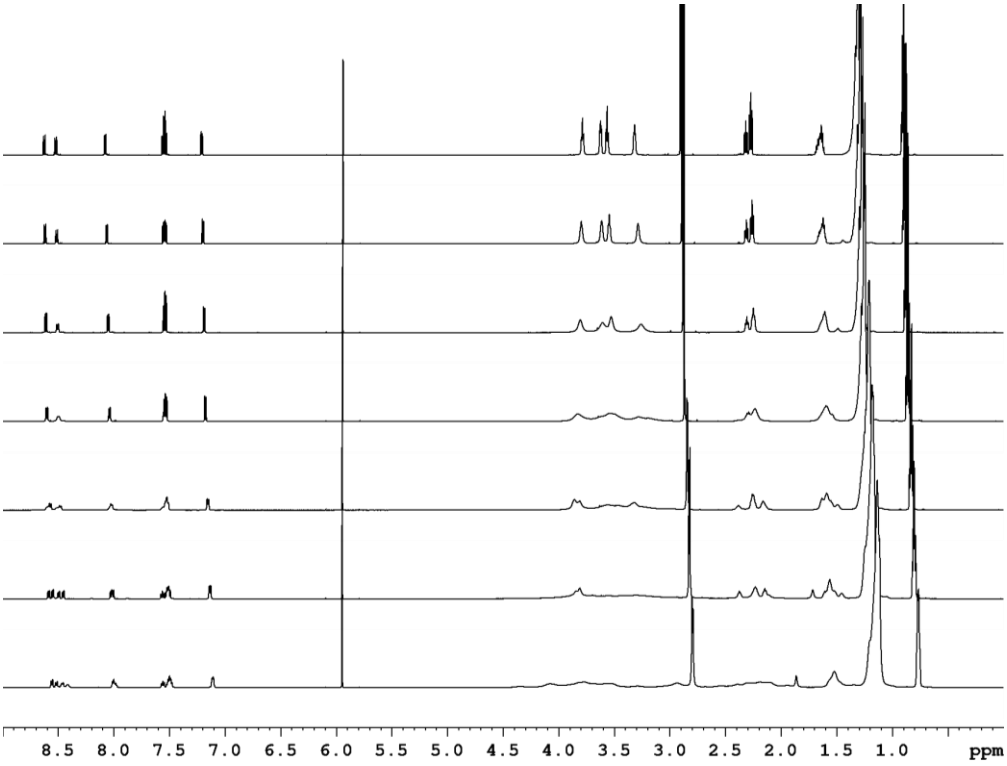
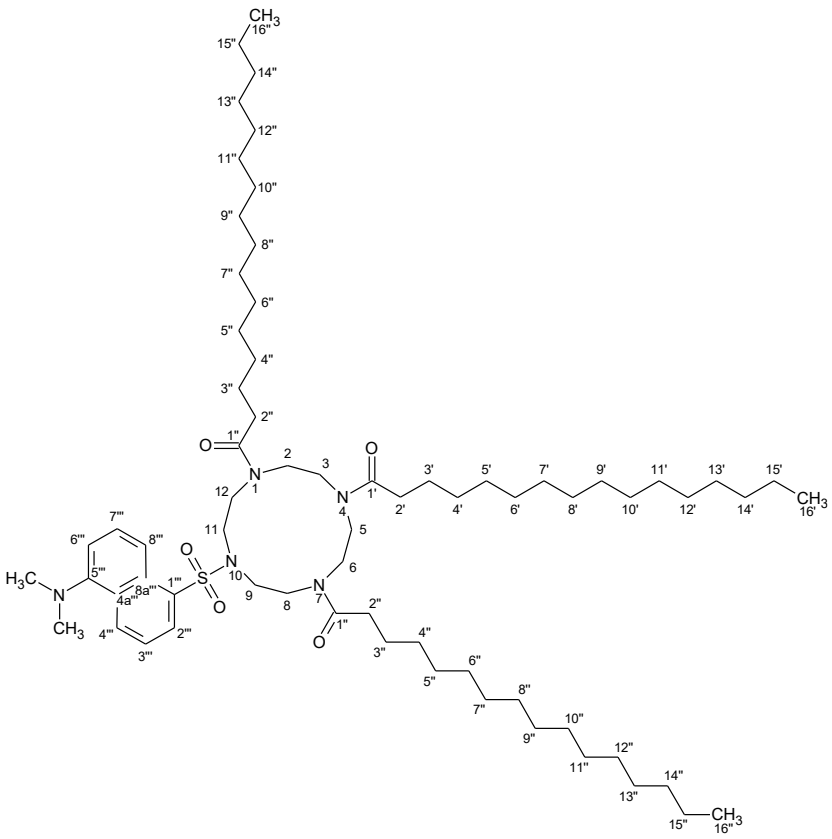
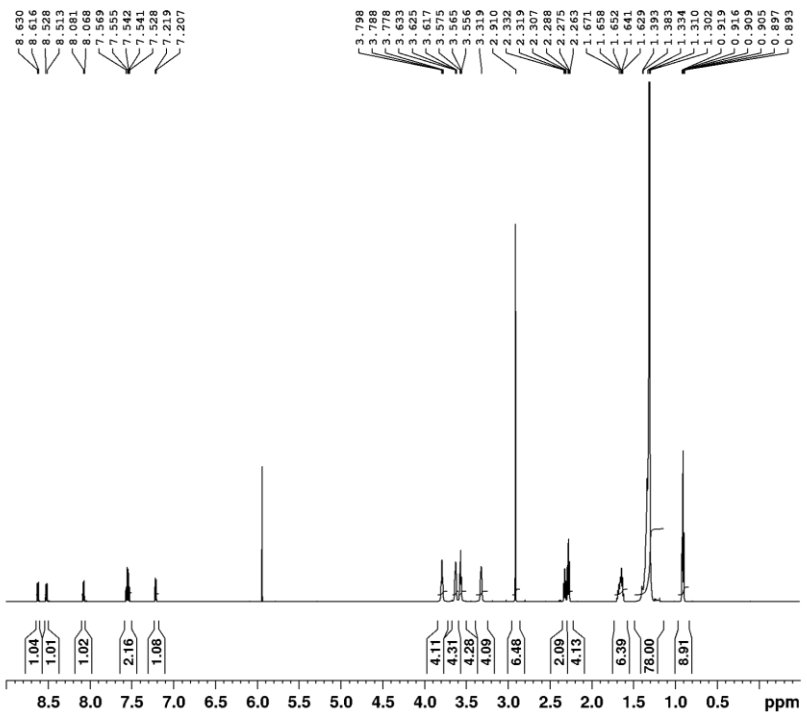


Figure 9–18. Stack plot of ^{1}H NMR spectra of compound **L2** in TCE-d_2 at 243, 273, 298, 333, 353, 373 and 393 K.



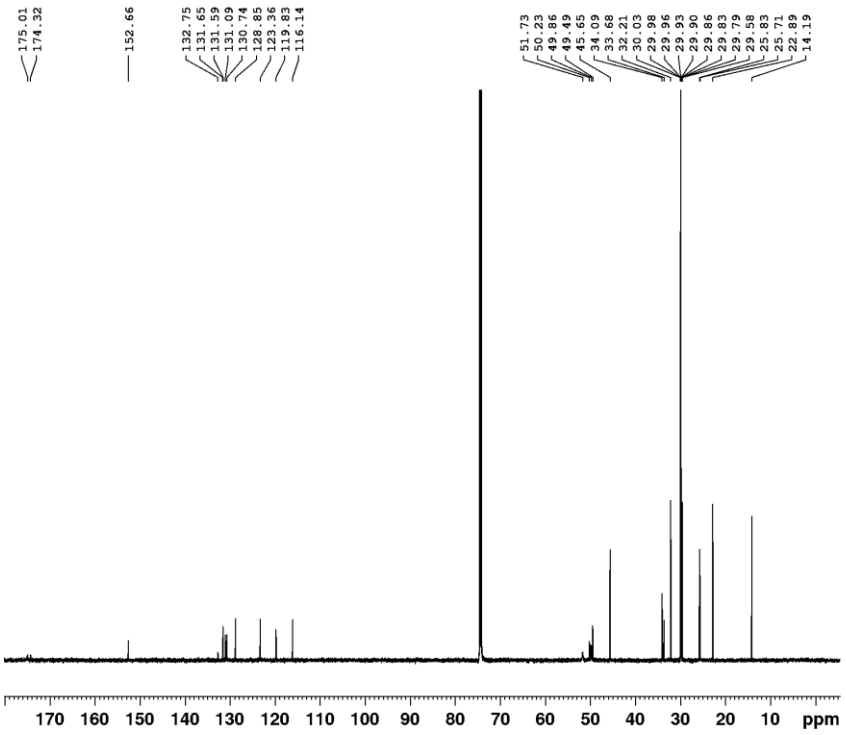



```
Current Data Parameters
NAME          DR-263_TCE
EXPNO                 91
PROCNO                 1

F2 - Acquisition Parameters
Date_           20240313
Time              15.38 h
INSTRUM           Avance
PROBHD   Z168773_0033 (
PULPROG             zg30
TD                 65536
SOLVENT              TCE
NS                    32
DS                     0
SWH           10000.000 Hz
FIDRES         0.305176 Hz
AQ             3.2767999 sec
RG                   101
DW              50.000 usec
DE              22.95 usec
TE                393.0 K
D1            1.00000000 sec
TD0                    1
SFO1         600.1845620 MHz
NUC1                  1H
P0                 4.00 usec
P1                12.00 usec
PLW1         21.70899963 W

F2 - Processing parameters
SI                 65536
SF           600.1800405 MHz
WDW                   no
SSB                    0
LB                     0 Hz
GB                     0
PC                  1.00
```

Figure 9–19. ^{1}H NMR spectrum of compound **L3** in TCE-d_2 at 393 K.




```
Current Data Parameters
NAME          DR-263_TCE
EXPNO                 92
PROCNO                 1

F2 - Acquisition Parameters
Date_           20240313
Time              16.18 h
INSTRUM           Avance
PROBHD   Z168773_0033 (
PULPROG           zgdc30
TD                 32768
SOLVENT              TCE
NS                  1024
DS                     0
SWH           35714.286 Hz
FIDRES         2.179827 Hz
AQ             0.4587520 sec
RG                   101
DW              14.000 usec
DE              18.00 usec
TE                393.0 K
D1            1.50000000 sec
D11           0.03000000 sec
TD0                    1
SFO1         150.9319844 MHz
NUC1                 13C
P0                 3.33 usec
P1                10.00 usec
PLW1         67.54000092 W
SFO2         600.1824007 MHz
NUC2                  1H
CPDPRG[2         waltz16
PCPD2             80.00 usec
PLW2         21.72701073 W
PLW12         0.49773711 W

F2 - Processing parameters
SI                 65536
SF           150.9153302 MHz
WDW                   EM
SSB                    0
LB                  1.00 Hz
GB                     0
PC                  1.40
```

Figure 9–20. ^{13}C NMR spectrum of compound **L3** in TCE-d_2 at 393 K.

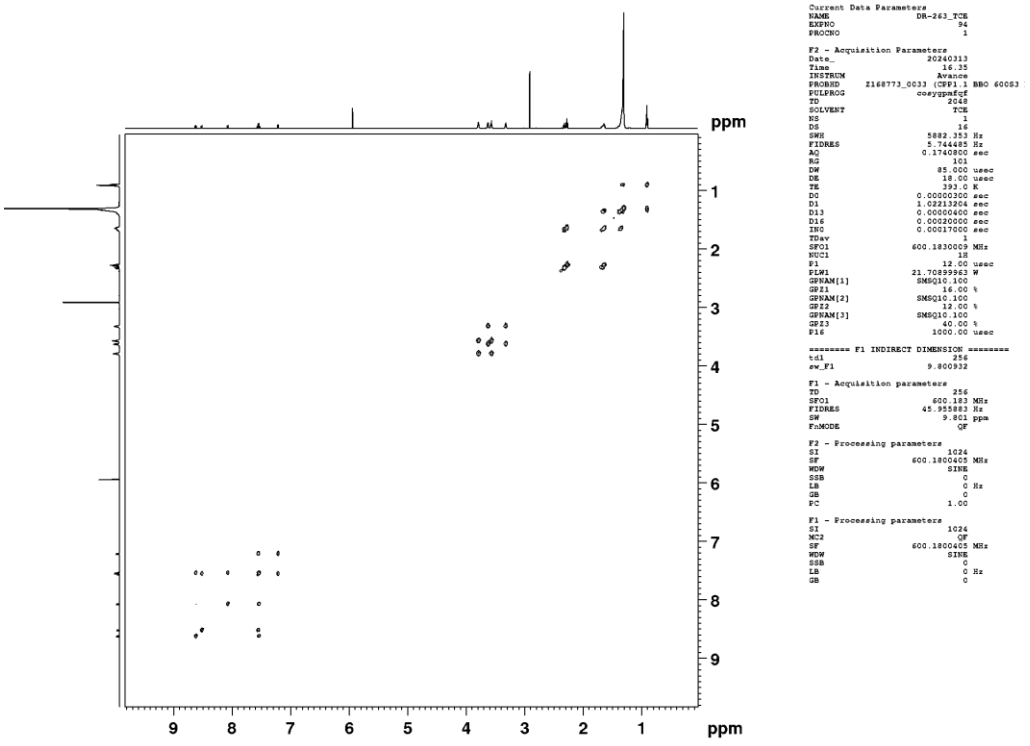


Figure 9–21. COSY NMR spectrum of compound **L3** in TCE-d_2 at 393 K.

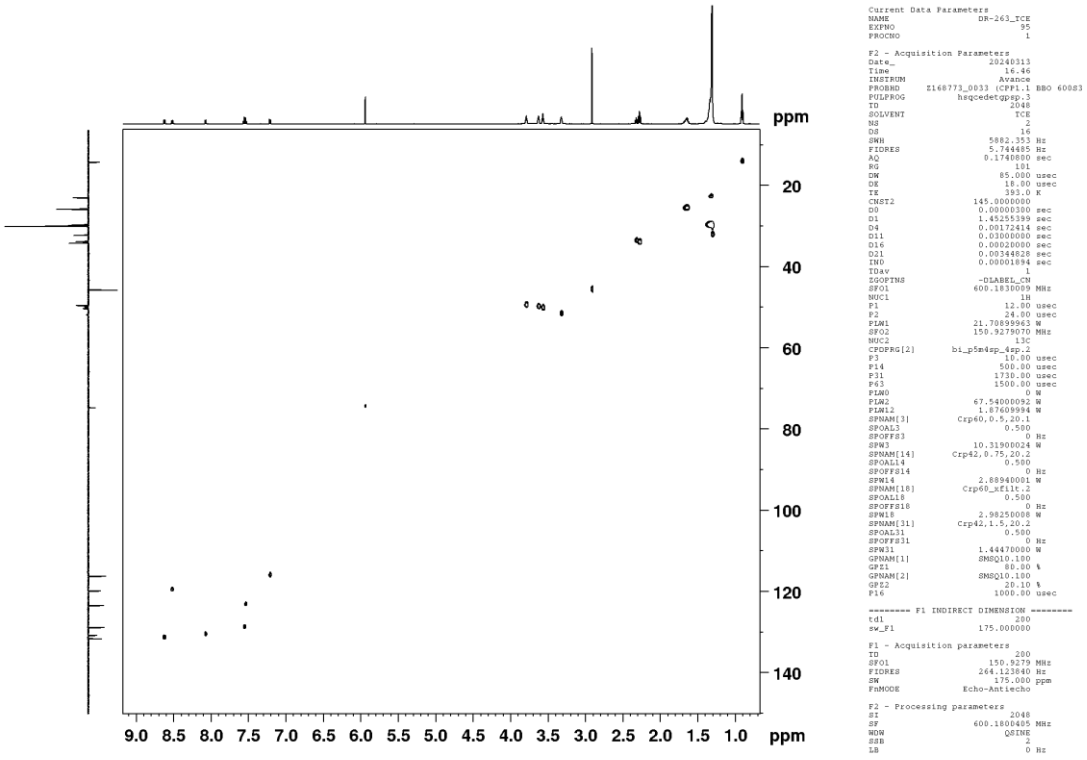


Figure 9–22. HSQC NMR spectrum of compound **L3** in TCE-d_2 at 393 K.

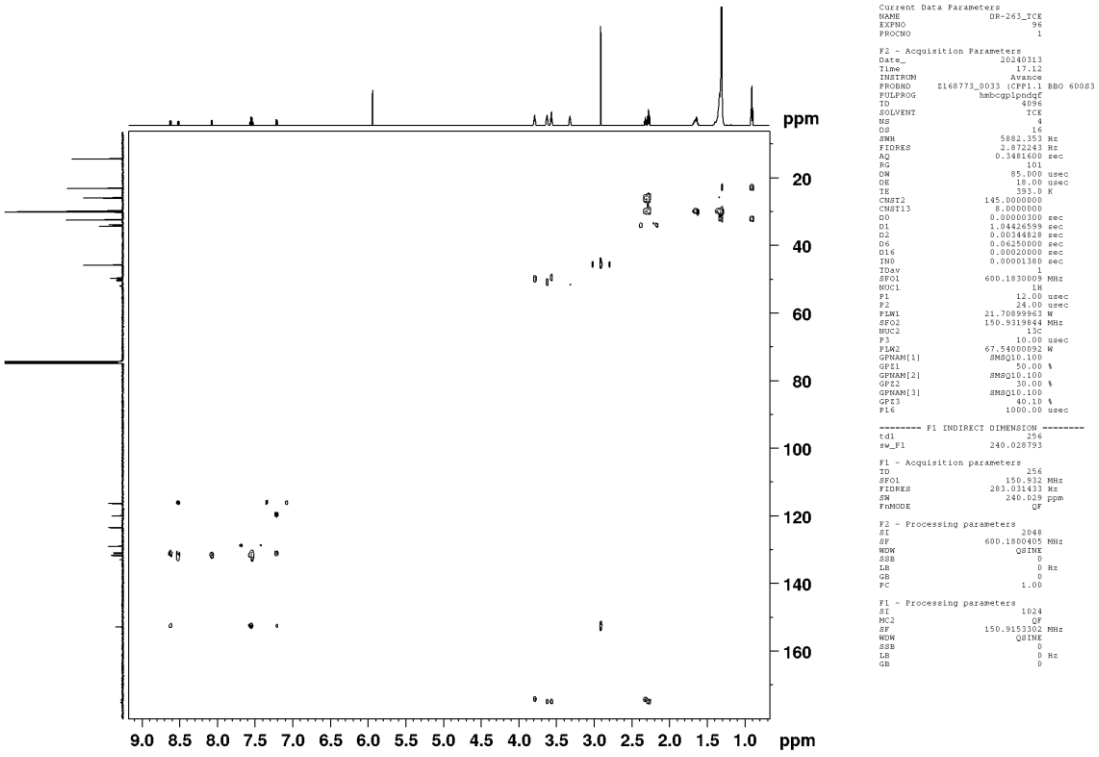


Figure 9–23. HMBC NMR spectrum of compound **L3** in TCE-d_2 at 393 K.

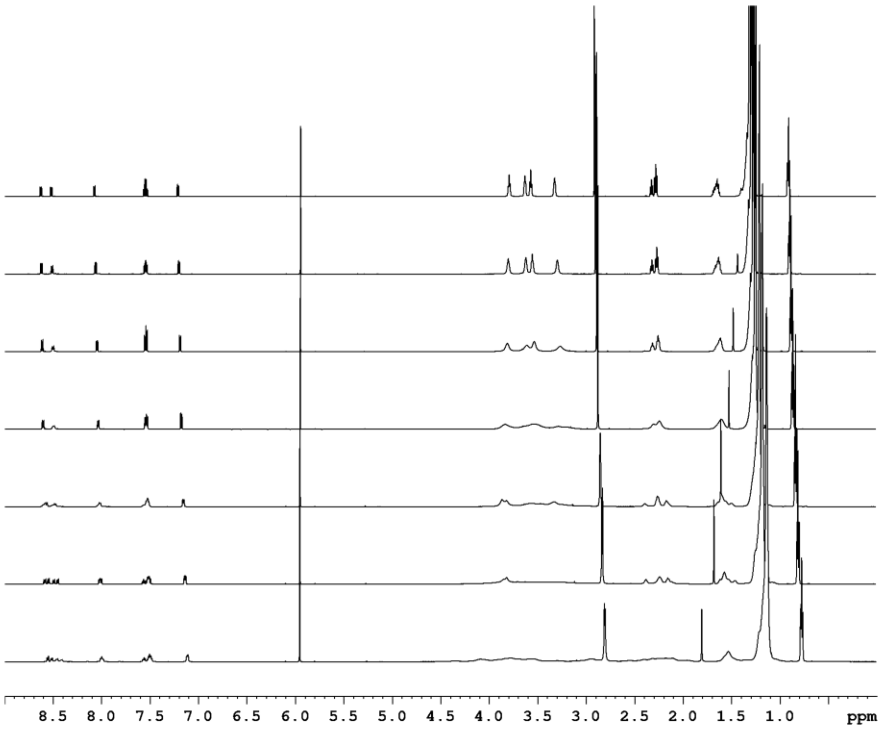


Figure 9–24. Stack plot of ^{1}H NMR spectra of compound **L3** in TCE-d_2 at 243, 273, 298, 333, 353, 373 and 393 K.

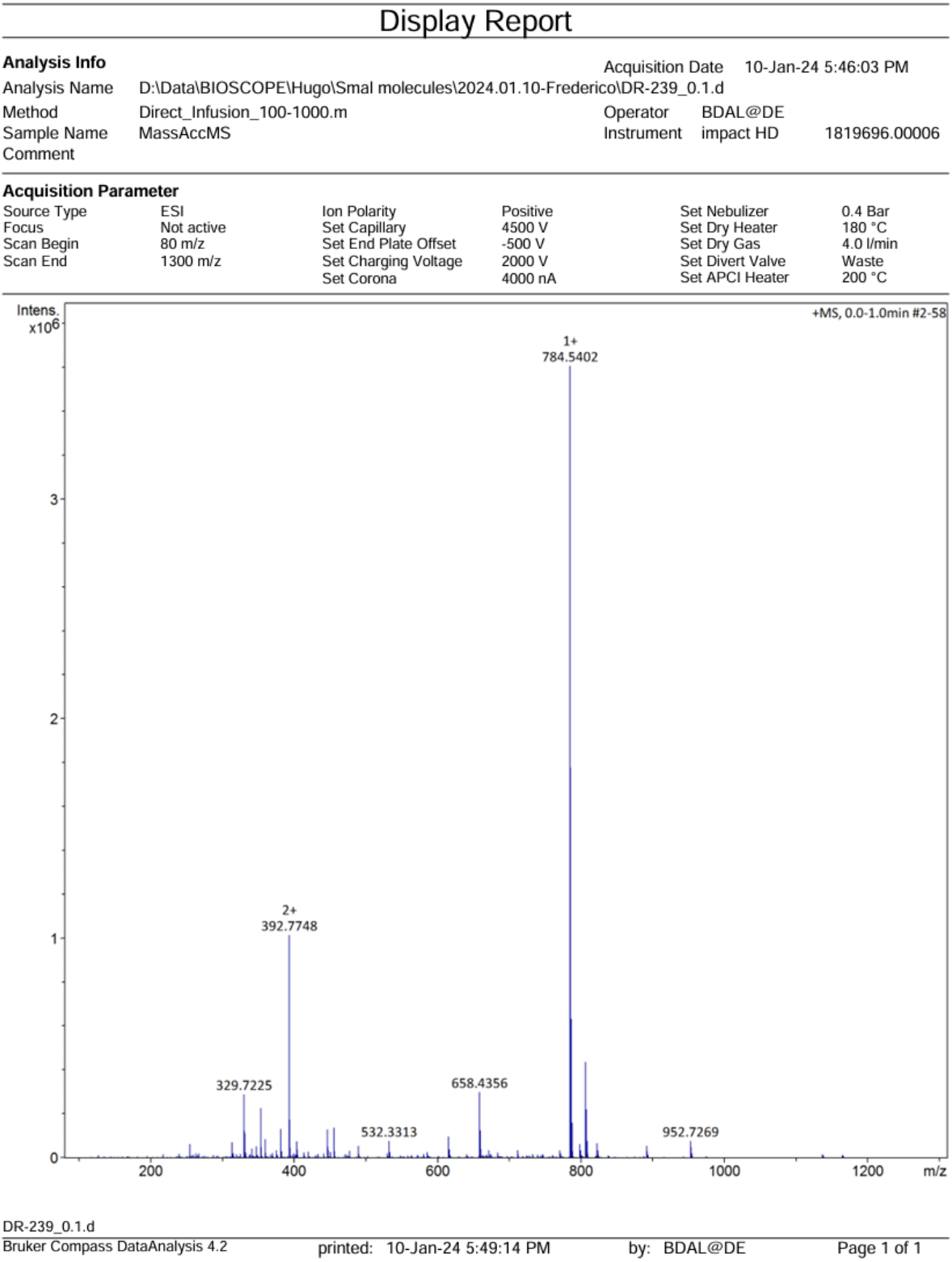


Figure 9–25. ESI-HRMS spectrum of compound **L1**.

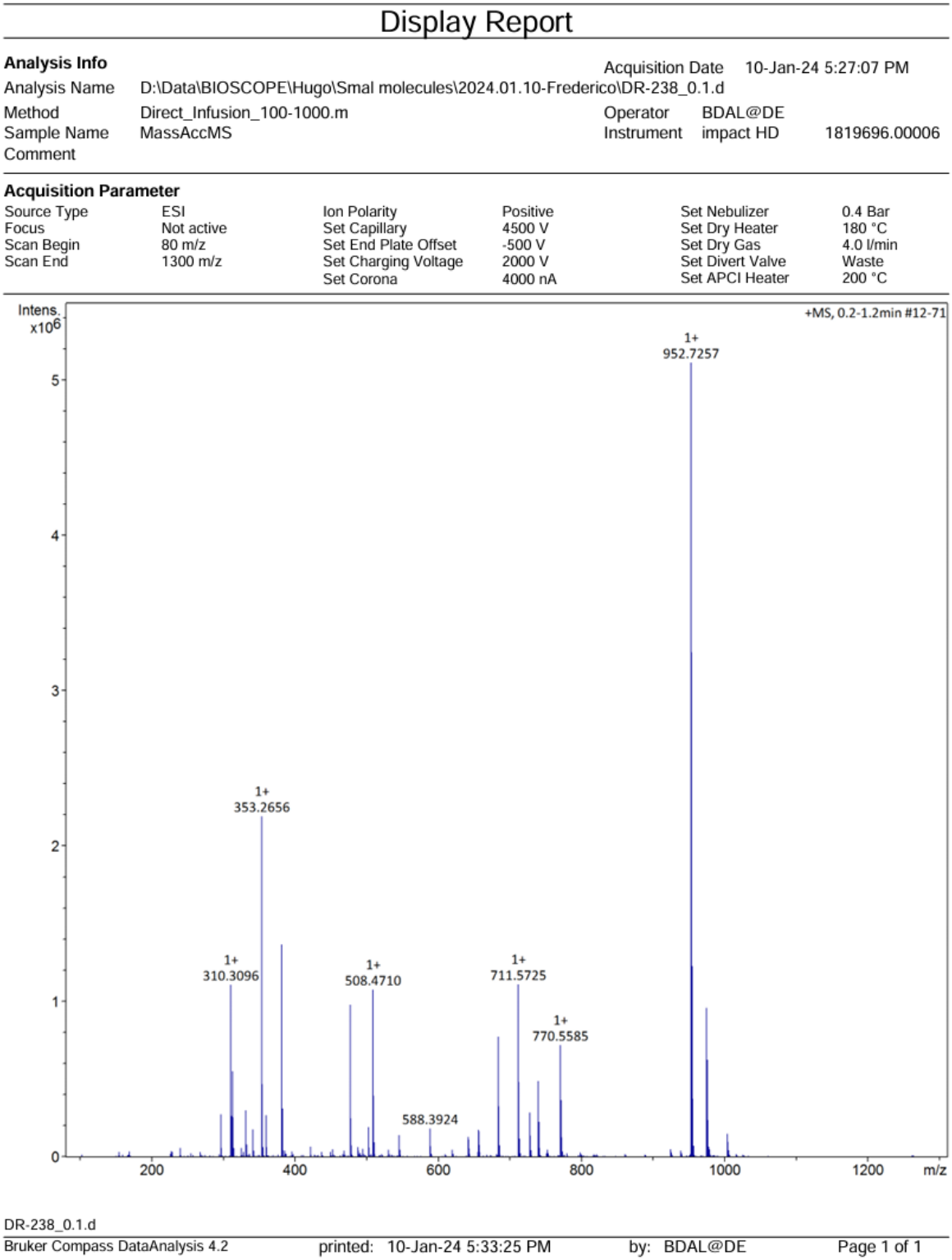


Figure 9–26. ESI-HRMS spectrum of compound **L2**.

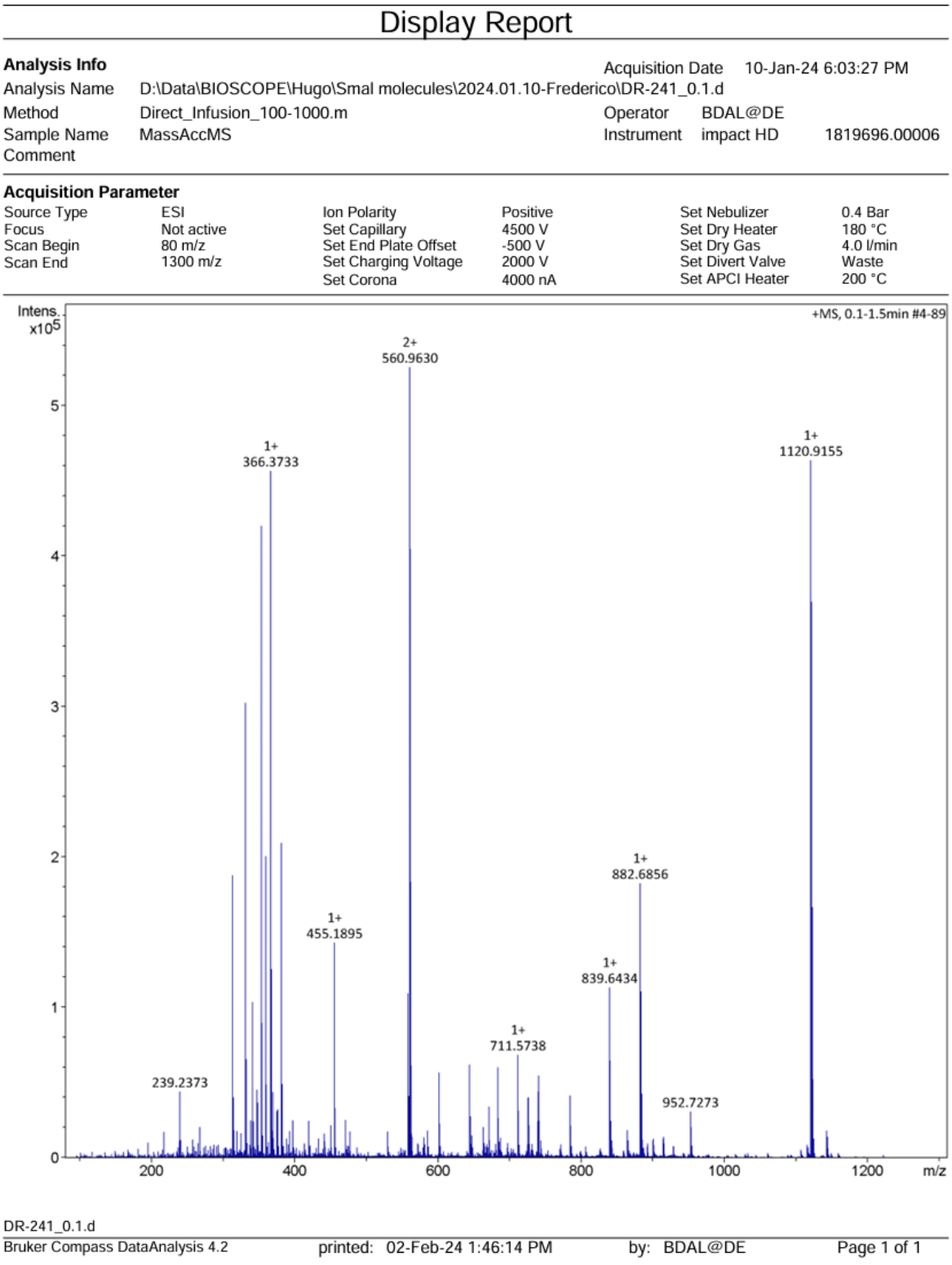


Figure 9–27. ESI-HRMS spectrum of compound **L3**.

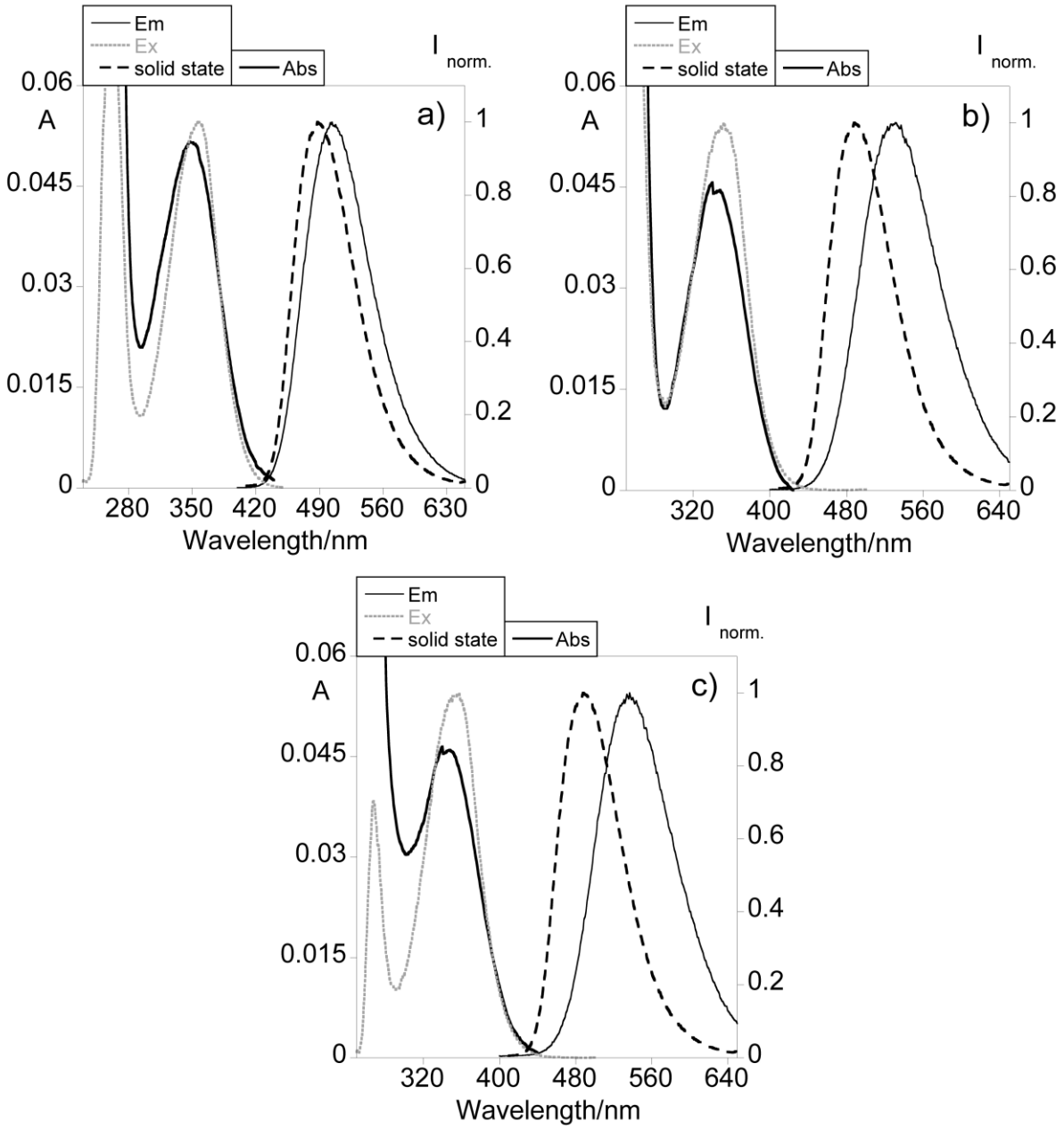


Figure 9–28. Photophysical characterization of **L1** in a) chloroform, b) ethanol and d) DMSO.

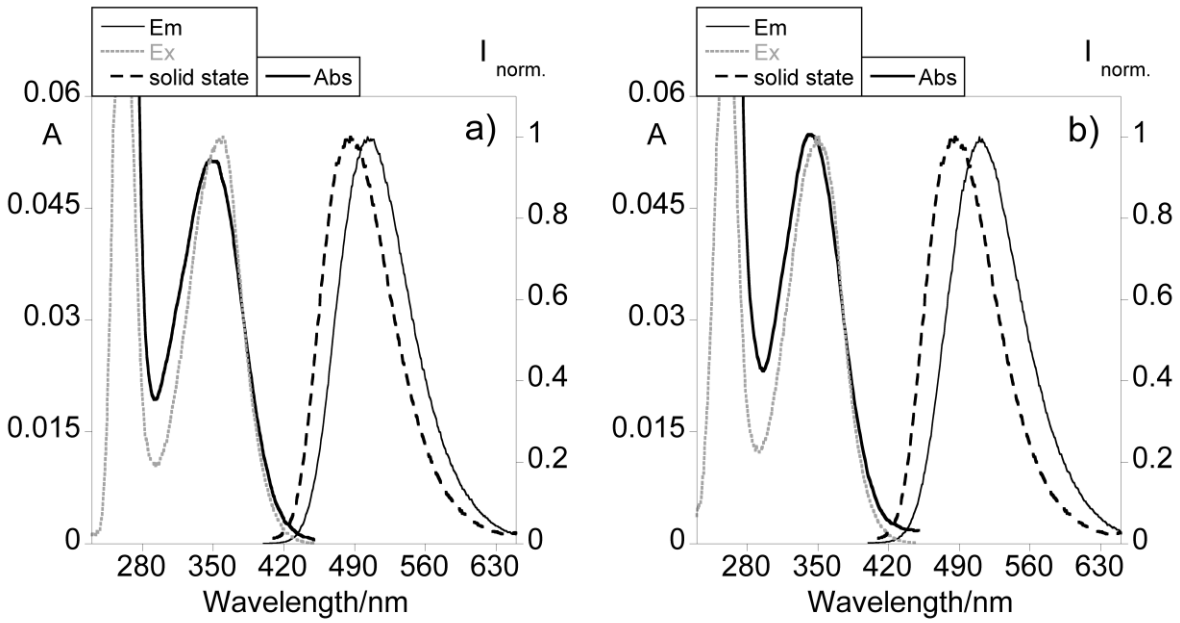


Figure 9–29. Photophysical characterization of **L2** in a) chloroform and b) THF.

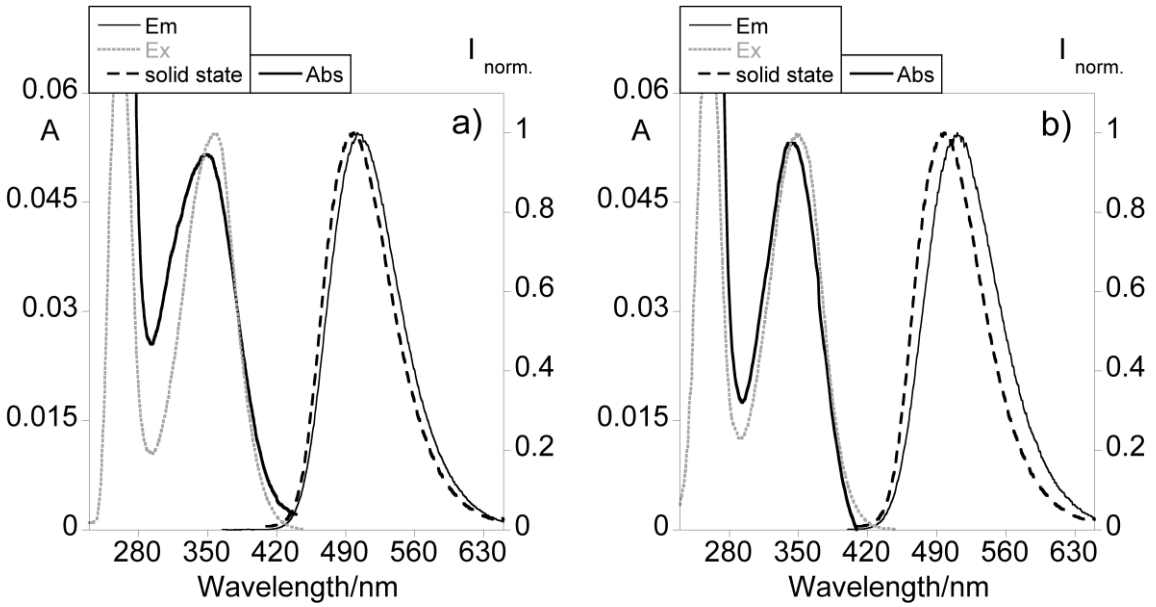


Figure 9–30. Photophysical characterization of **L3** in a) chloroform and b) THF.

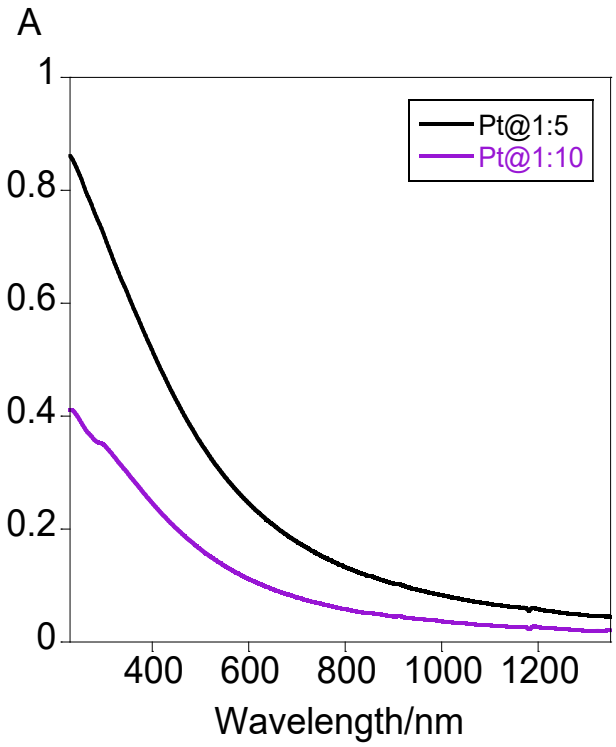


Figure 9–31. UV-vis spectra of Pt@1:5 and Pt@1:10.

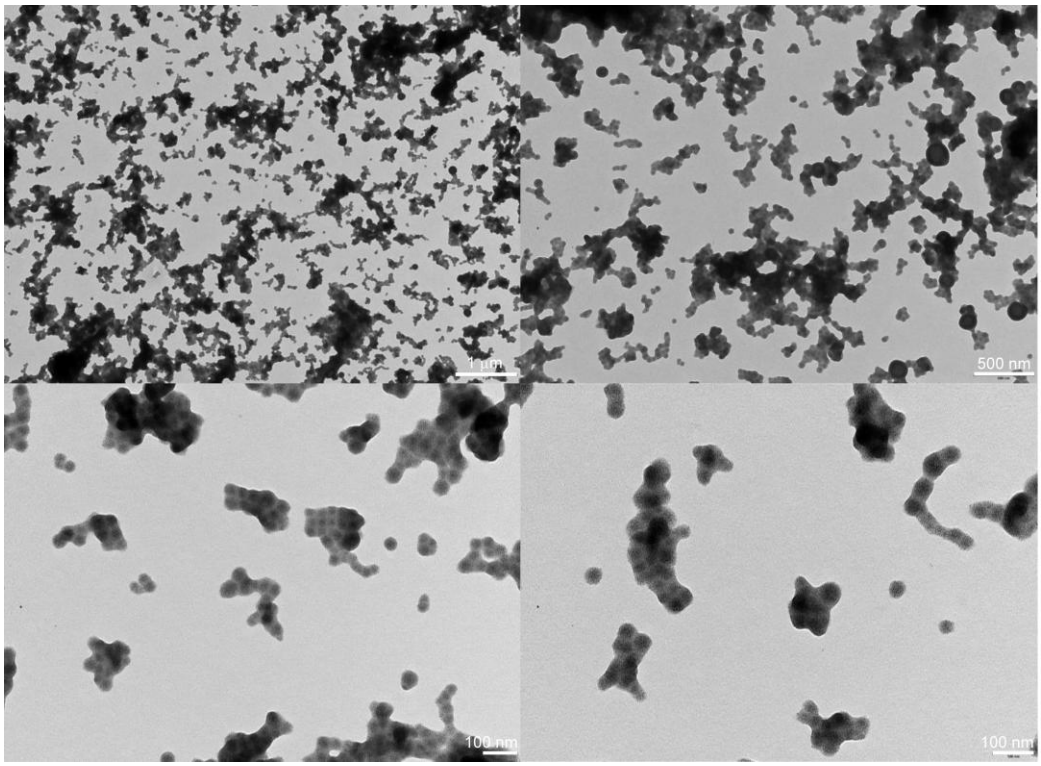


Figure 9–32. Transmission electron microscopy (TEM) images of Pt@1:5.

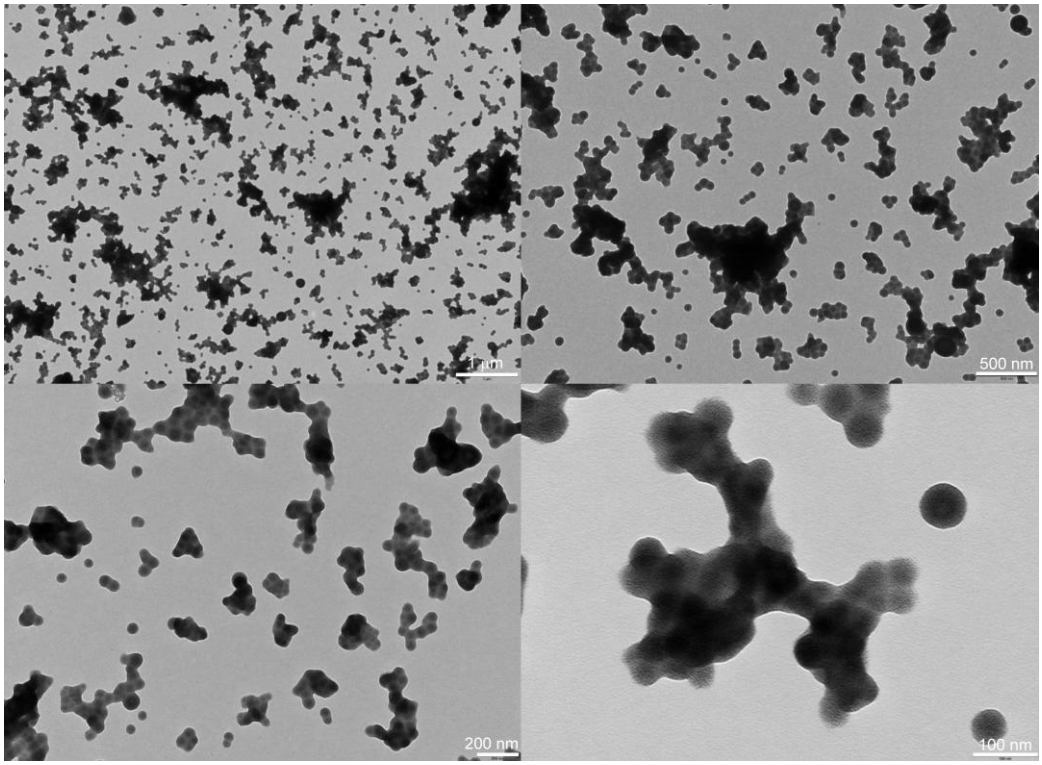
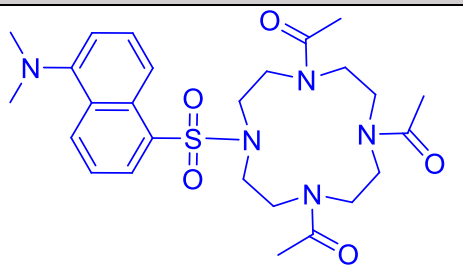
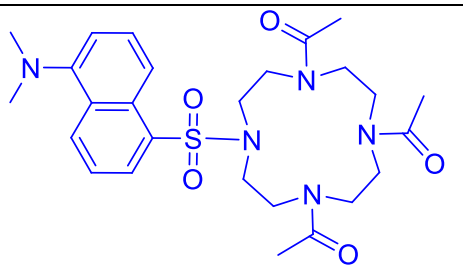
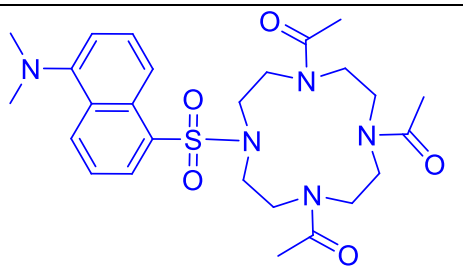
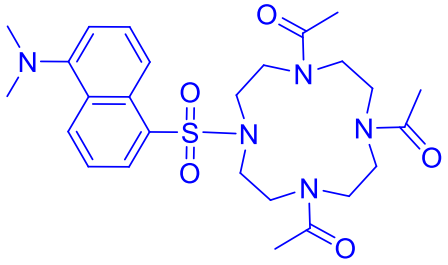
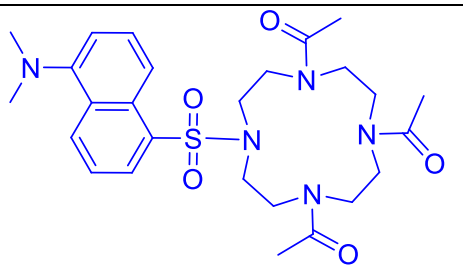
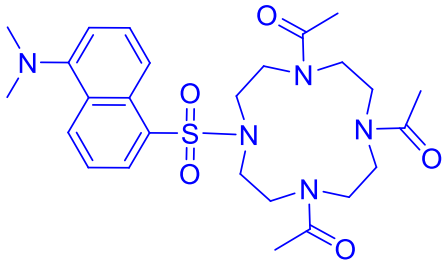
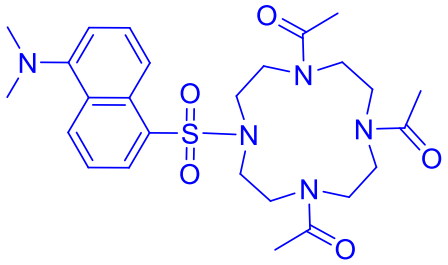
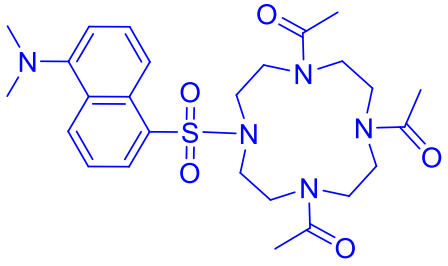


Figure 9–33. Transmission electron microscopy (TEM) images of Pt@1:10.

Table 9-9. DFT calculated ground state (GS) conformations of model compound

Stereoisomer	Nomenclature	Formulae
GS1	*syn,anti,anti*	
GS2	*syn,anti,syn*	

GS3	*syn,syn,anti*	
GS4	*anti,anti,anti*	
GS5	*syn,syn,syn*	
GS6	*anti,syn,syn*	
GS7	*anti,syn,anti*	
GS8	*anti,anti,syn*	

Cartesian coordinates of the SMD(DMF)//B3LYP/6-31+G(d,p) optimized GS geometries:

GS1

C	5.62311000	-0.56053600	-0.19043600
C	5.32773900	-1.91012900	-0.26938600
C	4.03038400	-2.38088000	0.02756200
C	3.02106900	-1.52287900	0.40056600
C	3.25035800	-0.11771800	0.44391600
C	4.56950000	0.37185500	0.12708100
C	2.25389800	0.86288100	0.78125700
C	2.55065000	2.21426400	0.81267700
C	3.83400500	2.67265600	0.45163100
C	4.81259100	1.77004200	0.10193600
S	0.51315700	0.47218200	1.15671600
O	0.42536500	-0.87212800	1.74116400
O	-0.01443700	1.62398800	1.89763600
N	6.92842600	-0.04818900	-0.43258700
C	7.77980000	-0.83358400	-1.31957900
C	7.65523300	0.36983100	0.77394100
N	-0.35334000	0.42949200	-0.31270700
C	-0.06367200	-0.72009400	-1.21238400
C	-0.65328400	-2.07875300	-0.81439600
N	-2.11589300	-2.22856700	-0.95558300
C	-2.83932700	-2.80158300	0.19593600
C	-4.14269200	-2.12598800	0.66097400
N	-4.02564800	-0.78098900	1.22512800
C	-4.29121700	0.33201500	0.28639700
C	-3.50256500	1.61906600	0.59755000
N	-2.90299600	2.24323700	-0.60300700
C	-1.52181900	2.71171300	-0.48906600
C	-0.45518000	1.73759700	-1.01356200
C	-3.75211200	2.64867800	-1.60055600
C	-4.21931000	-0.54307000	2.56877900
C	-2.56818800	-2.34317200	-2.25521200
C	-4.02866700	-1.69780900	3.54357300
C	-3.17625700	3.41792300	-2.78316600
C	-4.00092300	-2.77441600	-2.51943700
O	-4.95873400	2.39685000	-1.55199100
O	-4.51743700	0.57658000	2.98220900
O	-1.82328100	-2.08576600	-3.20438900
H	6.10230300	-2.62499800	-0.52333500
H	3.83678200	-3.44923800	-0.00666200
H	2.05797600	-1.91486400	0.69161900
H	1.78911700	2.91831200	1.12607600
H	4.03800500	3.73879800	0.44197100
H	5.78940900	2.11487100	-0.21616800

H	8.64080800	-0.22203700	-1.60735300
H	7.22944000	-1.10068100	-2.22494700
H	8.16833300	-1.75752600	-0.85529100
H	8.02576800	-0.49635400	1.34917000
H	8.51346400	0.98580600	0.48576000
H	7.01082800	0.95923300	1.42766300
H	1.01864900	-0.85593800	-1.34374200
H	-0.46409100	-0.46000800	-2.19026900
H	-0.16740800	-2.81112200	-1.47185300
H	-0.39163000	-2.30969700	0.21475900
H	-3.07467800	-3.85909800	0.00112000
H	-2.14445200	-2.78447200	1.03673500
H	-4.87439600	-2.08772900	-0.15050200
H	-4.57136300	-2.79777600	1.40928500
H	-5.36406600	0.54719800	0.26072500
H	-3.99792000	-0.02332500	-0.70123700
H	-4.15494200	2.34134000	1.09406900
H	-2.68208300	1.38954300	1.27423600
H	-1.39904200	3.63981500	-1.05460000
H	-1.32409600	2.95105400	0.55639500
H	-0.68826700	1.49831100	-2.05304300
H	0.51409600	2.25869300	-1.02436800
H	-3.19973500	-2.35864700	3.27631200
H	-4.94304300	-2.29919800	3.61324600
H	-3.83877400	-1.26215200	4.52486500
H	-2.25384200	2.98075400	-3.17633400
H	-2.96635000	4.45730600	-2.50420800
H	-3.93358200	3.42178500	-3.56716800
H	-4.34274300	-3.58298000	-1.86787300
H	-4.04959300	-3.10169300	-3.55827900
H	-4.68377700	-1.92674100	-2.39953600

GS2

C	-5.48811600	0.61080400	-1.10212500
C	-5.12642300	1.94647600	-1.06808700
C	-4.00956500	2.37154200	-0.31604100
C	-3.24895500	1.48019900	0.40626900
C	-3.54063700	0.08748200	0.36224900
C	-4.66671500	-0.35700900	-0.41942500
C	-2.77609300	-0.92405900	1.03774500
C	-3.10169700	-2.26395900	0.94806200
C	-4.18149300	-2.67970800	0.14053400
C	-4.93469200	-1.74715300	-0.53556600
S	-1.27320900	-0.56354400	1.99052300
O	-1.40649600	0.72877500	2.67364500

O	-0.96716500	-1.78435400	2.74861800
N	-6.63549800	0.14656100	-1.80703500
C	-7.06994000	0.95260200	-2.94186900
C	-7.76915200	-0.22454200	-0.95034600
N	-0.03123000	-0.38437900	0.87562100
C	0.43397000	0.94458200	0.46378000
C	1.55572200	1.49754700	1.37392300
N	2.37167800	2.55886100	0.75575800
C	3.80671200	2.33958600	0.55670100
C	4.23553400	1.92349700	-0.88674300
N	4.75786600	0.56121700	-1.01316200
C	3.78394200	-0.54023500	-1.01809700
C	4.00329400	-1.58371300	0.10012600
N	2.90032200	-2.53817300	0.19206600
C	1.74293500	-2.20377900	1.03009900
C	0.53293500	-1.59509500	0.26334600
C	2.86305100	-3.73457200	-0.49200100
C	6.04136200	0.25988200	-1.41538400
C	1.76834800	3.78140700	0.55655400
C	7.07026500	1.37789800	-1.49168400
C	4.10239000	-4.16101700	-1.26261400
C	2.61934700	4.92759300	0.02776300
O	1.85987000	-4.44798900	-0.45193200
O	6.35133700	-0.89791700	-1.69840300
O	0.57480800	3.94534700	0.80458600
H	-5.72228000	2.68693400	-1.59009500
H	-3.76749500	3.42970000	-0.27823100
H	-2.44888500	1.84363500	1.03503500
H	-2.51511700	-2.99134100	1.49659900
H	-4.39933800	-3.73886500	0.04519600
H	-5.73809700	-2.06164200	-1.19140500
H	-7.79239600	0.37274300	-3.52530400
H	-6.21616100	1.18433500	-3.58335900
H	-7.56066200	1.89882100	-2.65072200
H	-8.28622500	0.66363200	-0.54675200
H	-8.48947900	-0.80835400	-1.53322400
H	-7.43291400	-0.83171300	-0.10876000
H	-0.39013900	1.65498900	0.45727100
H	0.78917100	0.85908000	-0.56969300
H	1.09368300	1.87880800	2.28947000
H	2.23498300	0.68997500	1.64903600
H	4.34456800	3.24875100	0.83726200
H	4.13312300	1.56752000	1.25798700
H	3.37076900	2.03323700	-1.55322100
H	4.99615800	2.61481900	-1.24813700

H	3.81848200	-1.04811200	-1.98864900
H	2.79485400	-0.09389100	-0.91094200
H	4.94273200	-2.10402600	-0.08049300
H	4.09797400	-1.07497000	1.06586700
H	1.42001600	-3.11217000	1.54030700
H	2.07705000	-1.49866400	1.79340500
H	0.83044600	-1.33642300	-0.75789200
H	-0.24959700	-2.35045000	0.16717300
H	7.08931700	1.99908300	-0.59109700
H	6.88281000	2.03051600	-2.35193300
H	8.04509400	0.90892800	-1.62424100
H	3.83896200	-5.04621200	-1.84115300
H	4.91204500	-4.42204300	-0.57134500
H	4.48483400	-3.38689500	-1.93345900
H	3.32517600	5.27641800	0.79063200
H	1.94490600	5.74737200	-0.21843800
H	3.19421700	4.65616800	-0.86293000

GS3

C	5.69486000	0.14562800	0.72712700
C	5.37117700	0.74180800	1.93311700
C	4.07562200	1.25588300	2.15637700
C	3.09457400	1.18085900	1.19391700
C	3.35203900	0.52588500	-0.04483200
C	4.67005400	-0.01305100	-0.27528600
C	2.38750300	0.35782700	-1.09879000
C	2.71346300	-0.27527600	-2.28600400
C	3.99338700	-0.83678300	-2.46742400
C	4.94064000	-0.72085300	-1.47533700
S	0.64933200	0.88562600	-0.99261000
O	0.51731200	1.99904000	-0.04520000
O	0.17912500	1.03809900	-2.37763100
N	7.00123300	-0.34046300	0.44046200
C	7.80701500	-0.74961100	1.58601800
C	7.77556400	0.49671100	-0.48596800
N	-0.25419900	-0.39264300	-0.33869900
C	-0.05135100	-0.65565300	1.10916500
C	-1.04332300	0.03376800	2.05904200
N	-2.44116700	-0.44152000	2.05424300
C	-3.51638500	0.57121000	2.16801700
C	-4.49806200	0.67397600	0.97845900
N	-4.10920200	1.62196500	-0.06861400
C	-3.15308200	1.17523400	-1.08376300
C	-3.64622400	0.00739000	-1.97886900
N	-2.97299700	-1.28202000	-1.73762900

C	-1.60716300	-1.42924300	-2.25467000
C	-0.47914100	-1.56445300	-1.21370900
C	-3.69995000	-2.31714500	-1.19950500
C	-4.52189700	2.92698400	0.07699200
C	-2.66270100	-1.75129400	2.41944700
C	-4.15574800	3.93550200	-1.00409800
C	-3.05309000	-3.68754400	-1.07145300
C	-4.08871300	-2.20840000	2.67747000
O	-4.85596800	-2.15452400	-0.79383700
O	-5.18387300	3.28270500	1.05562600
O	-1.72525100	-2.55101400	2.53367900
H	6.12323100	0.85483600	2.70585300
H	3.86078600	1.75281700	3.09809800
H	2.13374000	1.64463500	1.36329700
H	1.97870500	-0.32856100	-3.08029400
H	4.21970700	-1.36699900	-3.38719800
H	5.91362200	-1.18432200	-1.58831100
H	8.66954200	-1.31581000	1.22053000
H	7.22141500	-1.39922400	2.24095600
H	8.19280400	0.09797000	2.17998600
H	8.14669100	1.41372400	0.00366800
H	8.63647200	-0.07055000	-0.85485800
H	7.16513400	0.79284200	-1.34025500
H	0.94744400	-0.33173900	1.41682100
H	-0.09247300	-1.73084900	1.26752000
H	-0.62940900	-0.09932900	3.06946600
H	-1.05538200	1.10140500	1.83809700
H	-4.09852900	0.37015600	3.07264600
H	-3.04559600	1.54383700	2.32332800
H	-4.65336800	-0.30253000	0.51695800
H	-5.45638900	1.01915100	1.36978300
H	-2.22753400	0.86893500	-0.59318300
H	-2.90036400	2.02454300	-1.71447300
H	-4.71577600	-0.15305500	-1.84344500
H	-3.47517200	0.26778700	-3.02952700
H	-1.54476500	-2.31095700	-2.90460700
H	-1.40062700	-0.56265700	-2.88135000
H	-0.69151500	-2.40007000	-0.54616900
H	0.43798900	-1.83058000	-1.75952200
H	-4.69334200	4.85569500	-0.77578700
H	-4.43397500	3.59704300	-2.00714000
H	-3.08144500	4.14980600	-1.00509500
H	-2.53169800	-3.76061300	-0.11025800
H	-2.34497800	-3.93164500	-1.86621800
H	-3.85848800	-4.42302900	-1.06761100

H	-4.53665700	-1.67188000	3.52086800
H	-4.04715000	-3.26971400	2.92197600
H	-4.73282800	-2.06894200	1.80511000

GS4

C	5.76059400	0.40003900	0.20137600
C	5.52887600	1.75524800	0.35976000
C	4.27362800	2.31286900	0.03428000
C	3.24085100	1.53632300	-0.44036600
C	3.40020900	0.12604400	-0.56284200
C	4.67792200	-0.45212800	-0.22530000
C	2.37444400	-0.77845200	-1.00903900
C	2.60841100	-2.13739500	-1.13080700
C	3.85168500	-2.68423200	-0.75297500
C	4.85291800	-1.85920900	-0.29284600
S	0.66632600	-0.27939200	-1.38367100
O	0.62846800	1.12301700	-1.80491000
O	0.10401700	-1.33148400	-2.23900600
N	7.02669100	-0.19471900	0.46117600
C	7.87482900	0.48432300	1.43524500
C	7.78652900	-0.56595700	-0.74093100
N	-0.23014000	-0.36074300	0.07280000
C	0.09469800	0.66852400	1.08533400
C	-1.15285100	1.31126600	1.72118100
N	-1.86029600	2.25074500	0.85717900
C	-2.79297700	1.69034700	-0.12589500
C	-4.25938500	1.67490600	0.36672000
N	-5.02115000	0.55938600	-0.18927300
C	-4.86676500	-0.75701500	0.44735000
C	-3.96444200	-1.75038500	-0.33083200
N	-2.92261000	-2.39986100	0.50186000
C	-1.57117100	-2.55937100	-0.05400400
C	-0.45852900	-1.72075500	0.62060600
C	-3.38317400	-3.21370500	1.51440300
C	-5.84513700	0.64265200	-1.28494100
C	-1.74769700	3.61856200	0.93217200
C	-6.07325700	2.00992000	-1.91229700
C	-2.38306800	-4.07990500	2.26944600
C	-0.75149500	4.21016600	1.92035200
O	-4.57871300	-3.25237800	1.80398900
O	-6.39309700	-0.36460400	-1.73778800
O	-2.43801800	4.34972700	0.22163800
H	6.32563400	2.41020700	0.69392000
H	4.13534600	3.38670600	0.12298800
H	2.31804900	1.99951700	-0.75817600

H	1.82893100	-2.77771100	-1.52624500
H	4.00612000	-3.75679100	-0.81666600
H	5.79647100	-2.27464400	0.04091900
H	8.69154900	-0.18867700	1.71456000
H	7.29841400	0.71725400	2.33386500
H	8.32768500	1.41632500	1.05299100
H	8.22469300	0.31743700	-1.23654600
H	8.59934600	-1.24419700	-0.46136200
H	7.14459300	-1.07428400	-1.46164500
H	0.67404300	1.45816900	0.60890700
H	0.71847200	0.22912900	1.87816800
H	-1.85622000	0.53100000	2.03774800
H	-0.83406200	1.82370800	2.63130100
H	-2.70868900	2.26492600	-1.05057500
H	-2.46135100	0.67545600	-0.33525400
H	-4.27156000	1.58042800	1.45927900
H	-4.74144700	2.62317600	0.13068700
H	-5.85498200	-1.19773600	0.57612500
H	-4.44869700	-0.58791100	1.44158400
H	-4.59226600	-2.52116500	-0.78866300
H	-3.44916800	-1.22299800	-1.13414600
H	-1.27237500	-3.60998200	0.01661900
H	-1.60172400	-2.32434600	-1.11656400
H	-0.71318100	-1.58083700	1.67387200
H	0.47995600	-2.29436000	0.60259500
H	-5.13794500	2.50010200	-2.19960400
H	-6.60192900	2.67923200	-1.22454100
H	-6.68691000	1.86227900	-2.80073400
H	-1.45034600	-3.56639300	2.51732100
H	-2.12868300	-4.96764300	1.67796600
H	-2.86755100	-4.41191400	3.18779200
H	-0.69628700	5.28025100	1.72144600
H	0.24852500	3.77532300	1.82595800
H	-1.08627100	4.06728500	2.95436900

GS5

C	-5.44923500	0.55002600	-1.23621900
C	-5.09121600	1.85573300	-1.52608400
C	-3.97036600	2.45076100	-0.90664000
C	-3.20549200	1.76100300	0.00645300
C	-3.49772900	0.40100900	0.30392400
C	-4.62023200	-0.22357800	-0.34629200
C	-2.72610200	-0.41291100	1.19972000
C	-3.02615700	-1.74253700	1.41990400
C	-4.10096900	-2.34764100	0.73391400

C	-4.87134800	-1.60555100	-0.13221200
S	-1.26091000	0.20975700	2.06661300
O	-1.48869600	1.58045000	2.54141900
O	-0.86831600	-0.84264500	3.01586600
N	-6.59697200	-0.07238600	-1.80349600
C	-7.04856600	0.44573100	-3.08949600
C	-7.72069800	-0.24766200	-0.87411600
N	-0.06508600	0.31531700	0.88897800
C	0.54068400	1.60810100	0.54546300
C	1.77647300	2.01375600	1.40330100
N	2.94667400	2.45691900	0.63592800
C	4.01011900	1.49636200	0.34879800
C	3.75518300	0.70870000	-0.95618000
N	4.68012000	-0.41338600	-1.17210400
C	4.10925200	-1.75796100	-1.27431300
C	3.73517100	-2.43022300	0.08547200
N	2.30411800	-2.62955300	0.32466800
C	1.55808900	-1.61709500	1.09431500
C	0.42941300	-0.92832100	0.29055200
C	1.64984400	-3.80632700	0.03295800
C	5.97586900	-0.09492000	-1.51673200
C	2.95817300	3.76433400	0.19632900
C	6.95614300	-1.22061800	-1.81059400
C	2.42326600	-4.90710900	-0.67966100
C	4.21436400	4.28163900	-0.48661200
O	0.46937200	-3.96601500	0.34108600
O	6.33469700	1.08164100	-1.57771900
O	1.98594900	4.49654700	0.38194200
H	-5.69152200	2.44831300	-2.20732000
H	-3.73087800	3.48641000	-1.13024200
H	-2.39902500	2.26290500	0.52099300
H	-2.41802800	-2.31879200	2.10690500
H	-4.29843800	-3.40475700	0.88067000
H	-5.67208600	-2.07421200	-0.69242900
H	-7.77039400	-0.25872500	-3.51519000
H	-6.20262800	0.52892200	-3.77622500
H	-7.54576300	1.42996200	-3.01981100
H	-8.24704100	0.70400800	-0.68378000
H	-8.43653500	-0.95916600	-1.29925400
H	-7.37184200	-0.63848500	0.08258500
H	-0.21525000	2.38636900	0.63565600
H	0.82081000	1.55867800	-0.51217000
H	1.48745300	2.82762100	2.07074000
H	2.08568300	1.17031500	2.02369200
H	4.97075000	2.00407200	0.27297700

H	4.08097800	0.80117600	1.19248500
H	2.74614400	0.29609700	-0.94277900
H	3.82313200	1.39831300	-1.80485200
H	4.82176100	-2.39126000	-1.80246000
H	3.20997300	-1.71205800	-1.90060600
H	4.23846500	-3.39709000	0.15204900
H	4.13772800	-1.82326500	0.90144400
H	1.11682000	-2.08057000	1.98033100
H	2.28159800	-0.87399600	1.42981800
H	0.77652000	-0.68415600	-0.72018700
H	-0.39465000	-1.63516400	0.17289600
H	6.73746300	-1.69496400	-2.77406400
H	6.95219700	-1.99788100	-1.04039800
H	7.94958700	-0.77588500	-1.86563100
H	1.70237500	-5.66570600	-0.98375500
H	3.15278800	-5.37345700	-0.00729900
H	2.96036900	-4.54748700	-1.56271500
H	5.03352400	4.37163000	0.23617300
H	3.98716700	5.27191100	-0.88083200
H	4.56572600	3.63784600	-1.29749200

GS6

C	-5.48050100	0.26106500	-1.33155400
C	-4.98778600	1.33112500	-2.05974400
C	-3.77810000	1.95962400	-1.69121800
C	-3.05485700	1.53858200	-0.59846000
C	-3.48824400	0.41289700	0.15453200
C	-4.70330000	-0.25422600	-0.23179800
C	-2.77252900	-0.13102200	1.27224700
C	-3.20803000	-1.25570300	1.94397100
C	-4.37515200	-1.92397100	1.51682300
C	-5.09671600	-1.43672900	0.45028700
S	-1.22701100	0.59079300	1.87151500
O	-1.33023900	2.05750600	1.93068100
O	-0.85125600	-0.16318400	3.07758400
N	-6.71564200	-0.37097800	-1.64189800
C	-7.16921800	-0.27108000	-3.02440600
C	-7.80655400	-0.08778700	-0.69951200
N	-0.11607600	0.27586600	0.65054000
C	0.73125300	1.36679600	0.14838500
C	1.72096000	2.00678500	1.16305900
N	2.94457500	2.50531300	0.53378900
C	4.05569100	1.56416600	0.33269700
C	4.25017400	1.09086400	-1.13223600
N	4.72319500	-0.29724300	-1.25118400

C	3.72388500	-1.36467000	-1.17961600
C	3.66821700	-2.14945400	0.16571900
N	2.32186200	-2.59824100	0.52112900
C	1.44540100	-1.65303500	1.23064000
C	0.26285600	-1.11733200	0.38092200
C	1.83209900	-3.86445000	0.30023700
C	6.05679000	-0.51763900	-1.53942600
C	3.15422600	3.81829300	0.17161700
C	6.49105500	-1.94963000	-1.82361700
C	2.74636200	-4.89275300	-0.34885800
C	2.05748000	4.83067100	0.46497000
O	0.68293000	-4.15675800	0.63203400
O	6.86805700	0.40277400	-1.58207000
O	4.20899900	4.15948200	-0.36202300
H	-5.54702600	1.72172000	-2.90237100
H	-3.43369300	2.81574900	-2.26443600
H	-2.16962800	2.07921300	-0.29567600
H	-2.63553800	-1.62703600	2.78582100
H	-4.68455300	-2.83321700	2.02219900
H	-5.96987300	-1.96927200	0.09173200
H	-7.98507300	-0.98494600	-3.17564900
H	-6.35428100	-0.53105100	-3.70433600
H	-7.54930300	0.73079100	-3.29310500
H	-8.21963900	0.92543600	-0.84528800
H	-8.61251400	-0.81406800	-0.84776400
H	-7.45660500	-0.16536200	0.33056300
H	0.09997200	2.15205900	-0.27783700
H	1.29406700	0.93389900	-0.68154600
H	1.21707400	2.81195600	1.69612000
H	1.99997700	1.26984200	1.92181100
H	4.98038700	2.03658900	0.67419000
H	3.86143900	0.70452100	0.97727000
H	3.30082800	1.16994800	-1.67316900
H	4.97446100	1.73596000	-1.62703100
H	3.86075400	-2.06866500	-2.00739400
H	2.75006400	-0.89858200	-1.34081100
H	4.33662300	-3.01071300	0.13112500
H	4.03973000	-1.50678800	0.96939000
H	1.05310700	-2.13511800	2.12907700
H	2.07125300	-0.82058900	1.55106800
H	0.51367200	-1.17864000	-0.68399600
H	-0.60883400	-1.75803400	0.52381800
H	5.99376200	-2.34989000	-2.71432700
H	6.28050500	-2.62424600	-0.98838600
H	7.56621300	-1.93418700	-1.99931600

H	2.14705800	-5.78018700	-0.55084200
H	3.56659500	-5.17074100	0.32264500
H	3.18373600	-4.53606000	-1.28649900
H	1.08239700	4.52568400	0.07371100
H	2.35157600	5.77197500	0.00124000
H	1.94735600	4.98947000	1.54348800

GS7

C	-5.37460300	0.30175900	-1.38111500
C	-4.80660200	1.37709700	-2.04393300
C	-3.58670900	1.93500700	-1.60323300
C	-2.92440900	1.43465700	-0.50514800
C	-3.43270200	0.29705000	0.17926000
C	-4.66294300	-0.29441900	-0.27751400
C	-2.78111300	-0.32848400	1.29348200
C	-3.29791800	-1.45403800	1.90477000
C	-4.48147100	-2.04439900	1.41292200
C	-5.13771500	-1.48160900	0.34092800
S	-1.21952500	0.28711800	1.97371600
O	-1.26973000	1.74831500	2.12665800
O	-0.91112100	-0.56701700	3.13123000
N	-6.62372000	-0.25873800	-1.76205300
C	-7.01911900	-0.08232600	-3.15535000
C	-7.73673300	0.03772800	-0.84921500
N	-0.07323400	-0.00127100	0.78050200
C	0.75702800	1.09889700	0.26974900
C	1.79007600	1.67949800	1.26798000
N	2.77742900	2.54364100	0.62179600
C	4.05732600	1.96209500	0.19224800
C	4.07168900	1.36893400	-1.24922600
N	4.61476500	0.00919600	-1.36215800
C	3.70267800	-1.12763900	-1.24334100
C	3.55632400	-1.63521100	0.21073500
N	2.44960900	-2.57940300	0.41102800
C	1.29613200	-2.14513400	1.20377900
C	0.19459800	-1.38953700	0.39456400
C	2.63177300	-3.86224900	-0.05315600
C	5.97162200	-0.12484100	-1.58494700
C	2.58842500	3.89975400	0.43252700
C	6.51931000	-1.52056600	-1.84195600
C	1.53449300	-4.88679600	0.19137700
C	1.34950600	4.54130600	1.04050500
O	3.66387100	-4.17250200	-0.65053900
O	6.70954900	0.85900000	-1.60519400
O	3.41303800	4.57712200	-0.17800300

H	-5.31502500	1.82779300	-2.88864300
H	-3.18515400	2.80015700	-2.12300100
H	-2.03206700	1.92508300	-0.14421100
H	-2.77742800	-1.88214200	2.75350200
H	-4.85836300	-2.95148800	1.87480000
H	-6.02273000	-1.95452400	-0.06850200
H	-7.85871900	-0.75203200	-3.36613000
H	-6.19087400	-0.35093300	-3.81548800
H	-7.34474000	0.94549800	-3.39465600
H	-8.09793900	1.07361900	-0.96920700
H	-8.56782900	-0.64423900	-1.05656900
H	-7.43094000	-0.09550900	0.18919600
H	0.11812200	1.91093100	-0.08827000
H	1.27124600	0.69659100	-0.60494600
H	1.25785500	2.22447900	2.04877300
H	2.32362600	0.86493000	1.76550800
H	4.80747300	2.75022100	0.25675200
H	4.32899400	1.18455900	0.91171300
H	3.05542400	1.35569900	-1.65318700
H	4.67423500	2.01444500	-1.88903300
H	4.03757200	-1.95390700	-1.87041200
H	2.72458200	-0.81722800	-1.62630200
H	4.49113300	-2.11777200	0.51270200
H	3.38709100	-0.79258900	0.88044900
H	0.85369400	-3.01634900	1.68689800
H	1.64788100	-1.50139400	2.01415300
H	0.46378100	-1.38758700	-0.66676000
H	-0.74827900	-1.94007500	0.46629400
H	6.19662500	-1.88256700	-2.82509100
H	6.20041500	-2.25934600	-1.10205500
H	7.60671800	-1.44895700	-1.83802000
H	1.79362200	-5.78127000	-0.37464500
H	0.54861300	-4.53340300	-0.12599900
H	1.47156900	-5.15242800	1.25270500
H	0.42082500	4.01321900	0.81011800
H	1.29044600	5.56024100	0.65862800
H	1.43850100	4.58186800	2.13231100

GS8

C	5.74789400	0.36932100	0.19801500
C	5.51900800	1.73335400	0.24381600
C	4.26915200	2.26603000	-0.13920500
C	3.23873800	1.45652600	-0.56099000
C	3.39492300	0.04048600	-0.56806700
C	4.66710600	-0.51177200	-0.17081800

C	2.37169200	-0.89519600	-0.95201100
C	2.60331000	-2.26009500	-0.96189000
C	3.84033600	-2.77749500	-0.52696400
C	4.83864800	-1.91995800	-0.12309100
S	0.67104200	-0.42463200	-1.39164400
O	0.64041100	0.94646400	-1.90318100
O	0.12501500	-1.53012500	-2.18935800
N	7.00908200	-0.20595100	0.51926700
C	7.84795900	0.54705700	1.44595900
C	7.78151900	-0.67218100	-0.64101600
N	-0.25570700	-0.41077700	0.05296700
C	0.10494400	0.65381200	1.01902200
C	-1.11608600	1.38872300	1.60735200
N	-1.71091700	2.38988800	0.72949100
C	-2.70415400	1.92595200	-0.24758600
C	-4.13159300	1.86268000	0.35151200
N	-4.94055300	0.74752600	-0.14990400
C	-4.72873900	-0.56793500	0.46129400
C	-3.82704400	-1.52571800	-0.36156400
N	-2.96522500	-2.39388500	0.46654300
C	-1.58510500	-2.61903500	0.01519100
C	-0.50514100	-1.73432800	0.67761300
C	-3.60095600	-3.25581800	1.33215500
C	-5.95340200	1.01529200	-1.04827500
C	-1.43896200	3.73831400	0.80646300
C	-6.86868400	-0.13565400	-1.44319900
C	-2.75661700	-4.23311500	2.13853000
C	-0.39386200	4.20376700	1.81436900
O	-4.82511000	-3.23491700	1.46485100
O	-6.12833600	2.14155000	-1.50992300
O	-2.01940400	4.55153900	0.09115200
H	6.31413500	2.41128900	0.53302500
H	4.13305200	3.34374900	-0.13861400
H	2.32077700	1.89575600	-0.92394300
H	1.82779100	-2.92863200	-1.31628600
H	3.99282300	-3.85197600	-0.50327700
H	5.77751900	-2.30893200	0.25312700
H	8.65921600	-0.10321900	1.78801600
H	7.26172800	0.85256900	2.31601100
H	8.30821400	1.44438900	0.99574600
H	8.22677900	0.16862200	-1.20026000
H	8.58991300	-1.32690700	-0.29939400
H	7.14658400	-1.23550400	-1.32622800
H	0.72899600	1.39062100	0.51554100
H	0.69903200	0.22196100	1.83814500

H	-1.88995300	0.66207400	1.88371400
H	-0.79922200	1.86297600	2.53886200
H	-2.68440300	2.60377100	-1.10107000
H	-2.38232300	0.94350300	-0.59004800
H	-4.06033200	1.75924700	1.44181100
H	-4.66383100	2.78824300	0.13279300
H	-5.68215700	-1.05210300	0.66559700
H	-4.25851500	-0.40145300	1.43493900
H	-4.44903000	-2.15514200	-1.01049300
H	-3.16646800	-0.94073500	-1.00053000
H	-1.31647800	-3.65855700	0.21402300
H	-1.54331900	-2.49507800	-1.06694400
H	-0.80909000	-1.53093700	1.70800200
H	0.43411700	-2.30493900	0.73721200
H	-7.48523800	-0.45609000	-0.59581100
H	-6.31955400	-1.01039700	-1.80245200
H	-7.52296100	0.22635800	-2.23584400
H	-1.83022800	-3.79548200	2.52109800
H	-2.49287900	-5.10644100	1.53045800
H	-3.36734800	-4.57626500	2.97387200
H	-0.20404100	5.25827500	1.61525500
H	0.54746200	3.64986400	1.74186800
H	-0.76411200	4.10785200	2.84182100

Table 9-10. B3LYP/6-31+G(d,p) calculated activation parameters for the exchange processes of the studied model compound.

Barrier	$\Delta H^{\neq}$(298 K)	$\Delta S^{\neq}$(298 K)	$\Delta G^{\neq}$(298 K)	$\Delta G^{\neq}$(298 K)^{eff}
TS12—GS1	20.0	0.0	20.0	
TS21—GS1	13.5	0.7	13.3	13.3
TS12—GS2	23.1	−7.9	25.4	
TS21—GS2	16.6	−7.2	18.7	18.7
TS13—GS1	13.0	−1.8	13.6	13.6
TS31—GS1	16.3	−2.9	17.2	
TS13—GS3	17.4	−4.6	18.7	18.7
TS31—GS3	20.6	−5.7	22.3	
TS14—GS1	19.5	−0.2	19.5	
TS41—GS1	14.8	1.9	14.3	14.3
TS14—GS4	22.4	−6.2	24.3	
TS41—GS4	17.8	−4.1	19.0	19.0

TS25—GS2	14.9	-9.2	17.6	
TS52—GS2	13.2	-10.1	16.2	16.2
TS25—GS5	15.2	-9.0	17.8	
TS52—GS5	13.5	-9.8	16.4	16.3
TS28—GS2	23.0	-5.6	24.7	
TS82—GS2	16.5	-5.9	18.3	18.3
TS28—GS8	21.3	-5.7	23.0	
TS82—GS8	14.8	-6.0	16.6	16.6
TS35—GS3	16.6	-1.1	16.9	
TS53—GS3	25.3	-5.4	26.9	16.9
TS35—GS5	15.6	-5.9	17.3	
TS53—GS5	24.3	-10.2	27.4	17.3
TS37—GS3	23.6	-2.6	24.3	
TS73—GS3	13.2	-0.7	13.4	13.4
TS37—GS7	22.4	-6.8	24.5	
TS73—GS7	12.0	-4.8	13.5	13.5
TS47—GS4	18.9	-5.3	20.5	
TS74—GS4	18.3	-6.1	20.1	19.9
TS47—GS7	19.2	-6.2	21.0	
TS74—GS7	18.5	-7.0	20.6	20.4
TS48—GS4	16.6	0.8	16.3	
TS84—GS4	16.5	-5.5	18.1	16.3
TS48—GS8	14.9	-1.2	15.3	
TS84—GS8	14.8	-7.6	17.1	15.3
TS56—GS5	15.2	-9.0	17.8	
TS65—GC5	13.5	-9.8	16.4	16.3
TS56—GS6	14.1	-9.7	17.0	
TS65—GS6	12.4	-10.5	15.5	15.5
TS67—GS6	15.9	-1.5	16.3	
TS76—GC6	15.7	-7.9	18.1	16.3
TS67—GS7	16.8	-0.1	16.9	
TS76—GS7	16.7	-6.5	18.6	16.8
TS68—GS6	18.2	-7.7	20.5	
TS86—GC6	17.6	-8.5	20.1	19.9
TS68—GS8	20.8	-7.4	19.5	

TS86—GS8	16.7	-8.2	19.1	18.8

9.7 Contributions & Aknowledgements

9.7.1 Author Contributions

Frederico Duarte: Formal analysis, Investigation, Writing - Original Draft, Writing - Review & Editing, Visualization.

Cristián Cuerva: Methodology, Validation, Formal Analysis, Investigation, Writing - Review & Editing, Resources, Visualization, Supervision, Funding acquisition

Georgi Dobrikov: Methodology, Validation, Formal Analysis, Investigation, Writing - Original Draft, Writing - Review & Editing, Resources, Visualization.

Atanas Kurutos: Methodology, Validation, Formal Analysis, Investigation, Conceptualization Writing - Original Draft, Writing - Review & Editing, Resources, Visualization, Supervision, Funding acquisition.

Nikolay G. Vassilev: Investigation, Visualization, Writing - Original Draft.

Jose Luis Capelo-Martinez: Resources, Writing - Review & Editing, Funding acquisition.

Hugo M. Santos: Investigation, Resources, Validation, Writing - Review & Editing.

Carlos Lodeiro: Conceptualization, Methodology, Validation, Formal Analysis, Investigation, Resources, Writing - Review & Editing, Visualization, Supervision, Funding acquisition, Project administration.

9.7.2 Acknowledgments

This work was supported by the Associate Laboratory for Green Chemistry LAQV which is financed by national funds from *Fundação para a Ciência e Tecnologia and Ministério da Ciência, Tecnologia e Ensino Superior* (FCT/MCTES) through the projects UIDB/50006/2020 and UIDP/50006/2020. PROTEOMASS Scientific Society (Portugal) is acknowledged by the funding provided through the General Funding Grant 2024-2025, and by the funding provided to the Laboratory for Biological Mass Spectrometry Isabel Moura (#PM001/2019 and #PM003/2016). F.D. thanks to FCT/MCTES (Portugal) for his doctoral grant 2021.05161.BD. H. M. S.

acknowledges the Associate Laboratory for Green Chemistry LAQV (LA/P/0008/2020) funded by FCT/MCTES for his research contract. This work was supported by the Associate Laboratory for Green Chemistry - LAQV (UIDB/50006/2020 (DOI: 10.54499/UIDB/50006/2020) and UIDP/50006/2020 (DOI: 10.54499/UIDP/50006/2020)), which are financed by national funds from Fundacão para a Ciência e a Tecnologia, MCTES (FCT/MCTES). C.L. and H. M.S thanks the Royal Society of Chemistry for the Sustainable Laboratory Grants 2023 reference L23-8861107285.

The financial support by the Bulgarian National Science Fund (BNSF) under grant – "Novel styryl and polymethine fluorophores as potential theranostic agents "contract N◦ КП-06-М59/1 from 15.11.2021 is gratefully acknowledged by A.K. This work is also developed and acknowledged by A.K. as part of contract №: BG-RRP-2.004-0002-C01, Laboratory of Organic Functional Materials (Project BiOrgaMCT), Procedure BG-RRP-2.004 „Establishing of a network of research higher education institutions in Bulgaria", funded by BULGARIAN NATIONAL RECOVERY AND RESILIENCE PLAN".

G. D. thanks to the European Regional Development Fund within the Operational Programme Science and Education for Smart Growth 2014 - 2020 under the Project Center of Excellence: National center of mechatronics and clean technologies - BG05M2OP001-1.001-0008 for the financial support. Research equipment of Distributed Research Infrastructure INFRAMAT, part of the Bulgarian National Roadmap for Research Infrastructures, supported by the Bulgarian Ministry of Education and Science, was used in this investigation and acknowledged by N.G.V.

This work received support from PT national funds (FCT/MCTES, *Fundação para a Ciência e Tecnologia* and *Ministério da Ciência, Tecnologia e Ensino Superior)* through the projects UIDB/50006/2020 and UIDP/50006/2020. This work received support from PROTEOMASS Scientific Society through the General Funding Grant 2022-2023, and the projects #PM001/2019 and #PM003/2016. This work is also developed and acknowledged by A.K. as part of contract №: BG-RRP-2.004-0002-C01, Laboratory of Organic Functional Materials (Project BiOrgaMCT), Procedure BG-RRP-2.004 „Establishing of a network of research higher education institutions in Bulgaria", funded by BULGARIAN NATIONAL RECOVERY AND RESILIENCE PLAN". Research equipment of Distributed Research Infrastructure INFRAMAT, part of the Bulgarian National Roadmap for Research Infrastructures, supported by the Bulgarian Ministry of Education and Science, was used in this investigation and acknowledged by N.G.V.

9.8 References

[1] I. Pereira-Gomes, F. Duarte, G. M. Dobrikov, I. Slavchev, A. Kurutos, J. L. Capelo-Martinez, H. M. Santos and C. Lodeiro, Tetra dansylamides substituted cyclen and cyclam macrocycles as fluorescent sensing probes for metal ions and temperature-responsive materials in dopped polymers, *Dyes and Pigments* **232** (2025) 112461, DOI:10.1016/j.dyepig.2024.112461.

[2] Y. Wang, J. Zhou, L. Zhao and B. Xu, A dual-responsive and highly sensitive fluorescent probe for Cu^{2+} and pH based on a dansyl derivative, *Dyes and Pigments* **180** (2020) 108513. DOI: 10.1016/j.dyepig.2020.108513.

[3] W. Deng, S. Li, M. Zhou, M. Zheng, P. Wang and Y. An, Ratiometric peptide-based fluorescent probe with large Stokes shift for detection of Hg^{2+} and S^{2-} and its applications in cells imaging and smartphone-assisted recognition, *Spectrochim. Acta A Mol. Biomol. Spectrosc.* **315** (2024) 124306. DOI:10.1016/j.saa.2024.124306.

[4] L. Zhang, P. Zhao, S. Yu, J. Kong, L. Gao and L. Li, Dansyl-modified tryptophan fluorescence sensor for highly sensitive and selective detection of Hg^{2+} in aqueous solutions, *Microchem. J.* **200** (2024) 110520. DOI:10.1016/j.microc.2024.110520.

[5] B. Uttam, S. Polepalli, S. Sinha, A. Majumder and C. P. Rao, Selective Sensing and Removal of Mercury Ions by Encapsulating Dansyl Appended Calix[4]Conjugate in a Zeolitic Imidazolate Framework as an Organic−Inorganic Hybrid Nanomaterial, *ACS Appl. Nano Mater.* **5** (2022) 11371–11380. DOI:10.1021/acsanm.2c02459.

[6] A. Aliberti, P. Vaiano, A. Caporale, M. Consales, M. Ruvo and A. Cusano, Fluorescent chemosensors for Hg^{2+} detection in aqueous environment, *Sens. Actuators B Chem.* **247** (2017) 727–735. DOI:10.1016/j.snb.2017.03.026.

[7] P. Wang, Y. An and J. Wu, Highly sensitive turn-on detection of mercury(II) in aqueous solutions and live cells with a chemosensor based on tyrosine, *Spectrochim. Acta A Mol. Biomol. Spectrosc.* **230** (2020) 118004. DOI:10.1016/j.saa.2019.118004.

[8] J. Y. Kim, S. Sarkar, K. N. Bobba, P. T. Huynh, A. Bhise and J. Yoo, Development of dansyl based copper(ii) complex to detect hydrogen sulfide in hypoxia, *Org. Biomol. Chem.*, **17** (2019) 7088–7094. DOI: https://doi.org/10.1039/C9OB00948E.

[9] R. Nagarajan, H. I. Ryoo, B. D. Vanjare, N. Gyu Choi and K. Hwan Lee, Novel phenylalanine derivative-based turn-off fluorescent chemosensor for selective Cu^{2+} detection in physiological pH, *J. Photochem. Photobiol. A Chem.* **418** (2021) 113435. DOI:10.1016/j.jphotochem.2021.113435.

[10] H. Jiang, Z. Li, Y. Kang, L. Ding, S. Qiao, S. Jia, W. Luo and W. Liu, A two-photon fluorescent probe for Cu^{2+} based on dansyl moiety and its application in bioimaging, *Sens. Actuators B Chem.* **242** (2017) 242 112–117. DOI:10.1016/j.snb.2016.11.033.

[11] Y. Liu, B. Jiang, L. Zhao, L. Zhao, Q. Wang, C. Wang and B. Xu, A dansyl-based fluorescent probe for sensing Cu^{2+} in aqueous solution, *Spectrochim. Acta A Mol. Biomol. Spectrosc.* **261** (2021) 120009. DOI:10.1016/j.saa.2021.120009.

[12] G. Pedro, F. Duarte, G. M. Dobrikov, A. Kurutos, H. M. Santos, J. L. Capelo-Martínez, E. Oliveira and C. Lodeiro, Optical evaluation of dansyl derivatives and their implementation in low-cost and flexible dye-doped PMMA platforms for efficient detection of hazardous chemical vapours, *Dyes and Pigments* **224** (2024) 112042. DOI:10.1016/j.dyepig.2024.112042.

[13] X. Fang, S. Wang, Q. Wang, J. Gong, L. Li, H. Lu, P. Xue, Z. Ren and X. Wang, A highly selective and sensitive fluorescence probe based on BODIPY-cyclen for hydrogen sulfide detection in living cells and serum, *Talanta* **268** (2024) 125339. DOI:10.1016/j.talanta.2023.125339.

[14] M. D. Tomczyk, K. Matczak, M. Skonieczna, P. Chulkin, M. Denel-Bobrowska, D. Różycka, S. Rykowski, A. B. Olejniczak and K. Walczak, Synthesis and in vitro cytotoxic activity of dye-linker-macrocycle conjugates with variable linker length and components, *Bioorg. Chem.* **140** (2023) 106782, DOI:10.1016/j.bioorg.2023.106782.

[15] K. E. Siters, M. A. Fountain and J. R. Morrow, Selective Binding of Zn^{2+} Complexes to Human Telomeric G-Quadruplex DNA, *Inorg. Chem.* **53** (2014) 11540–11551. DOI: 10.1021/ic501484p.

[16] C. Rivas, G. J. Stasiuk, M. Sae-Heng and N. J. Long, Towards understanding the design of dual-modal MR/fluorescent probes to sense zinc ions, *Dalton Transactions*, **44** (2015) 4976–4985. DOI: 10.1039/C4DT02981J.

[17] L. Yang, J. Zhao, J. Wang, G. Han, B. Liu, W. Zhang, Y. Fu, M. Y. Han, Z. Wang and Z. Zhang, An azacyclo-localizing fluorescent probe for the specific labeling of lysosome and autolysosome, *Talanta*, **216** (2020) 120941. DOI:10.1016/j.talanta.2020.120941.

[18] D. Paderni, D. Lopez, A. Ciavarella, M. Montanari, G. Panza, M. Voccia, M. Formica, B. Canonico, E. Macedi, S. Papa and V. Fusi, A new macrocyclic dansyl-cyclen fluorescent probe for the identification of mildly acidic intracellular compartments, *Inorg. Chim. Acta* **581** (2025) 122620. DOI:10.1016/j.ica.2025.122620.

[19] M. Tosato, M. Asti, M. Dalla Tiezza, L. Orian, D. Häussinger, R. Vogel, U. Köster, M. Jensen, A. Andrighetto, P. Pastore and V. Di Marco, Highly Stable Silver(I) Complexes with Cyclen-Based Ligands Bearing Sulfide Arms: A Step Toward Silver-111 Labeled Radiopharmaceuticals, *Inorg. Chem.* **59** (2020) 10907–10919. DOI:10.1021/acs.inorgchem.0c01405.

[20] E. M. Surender, S. Comby, S. Martyn, B. Cavanagh, T. C. Lee, D. F. Brougham and T. Gunnlaugsson, Cyclen lanthanide-based micellar structures for application as luminescent [Eu(III)] and magnetic [Gd(III)] resonance imaging (MRI) contrast agents, *Chem. Commun.* **52** (2016) 10858–10861. DOI:10.1039/C6CC03092K.

[21] S. Rani, S. Prasad Gupta, M. Gupta and S. Kumar Pal, Color-tunable photoluminescent discotic liquid crystal based on perylene – Pentaalkynylbenzene triad, *J. Mol. Liq.* **385** (2023) 122202. DOI:10.1016/j.molliq.2023.122202.

[22] N. Wang, W. Bi, Y. Liu, S. Xu, K. Wang and S. Cao, Recent progress of fluorescent liquid crystals, *J. Mol. Liq.* **432** (2025) 127741. DOI: 10.1016/j.molliq.2025.127741.

[23] Q. Q. Xiong, J. Y. Wu, H. S. Zhang, J. F. Gao, S. Y. Ma and X. Z. He, Liquid crystal polymers with dual properties of fluorescence and selective reflection-design, synthesis and characterization, *Liq. Cryst.* **51** (2024) 696–710. DOI:10.1080/02678292.2024.2321453.

[24] Y. Li, Y. Shen, K. Liu, Y. Quan and Y. Cheng, Tunable AI-CPL behavior by regulation of microstructure of AIE-active Isomers through chiral emissive liquid crystals, *Dyes and Pigments* **186** (2021) 109001. DOI: 10.1016/j.dyepig.2020.109001.

[25] F. Duarte, K. Morice, T. Ghanem, D. Puchán Sánchez, P. Blanchard, C. S. B. Gomes, S. Herrero, C. Cabanetos, C. Cuerva, J. Luis Capelo-Martinez and C. Lodeiro, Harnessing liquid crystal attributes of near-unit photoluminescent benzothioxanthene photosensitizers: Photophysical profiling in solution, solid state, and polymer matrix embedding, *J. Mol. Liq.* **409** (2024) 125424. DOI:10.1016/j.molliq.2024.125424.

[26] A. Kumar and G. Singh, Recent advances and future perspectives of photoluminescent liquid crystals and their nanocomposites for emissive displays and other tunable photonic devices, *J. Mol. Liq.* **386** (2023) 122607. DOI: 10.1016/j.molliq.2023.122607.

[27] Y. Li, K. Yao, Y. Chen, Y. Quan and Y. Cheng, Full-Color and White Circularly Polarized Luminescence Promoted by Liquid Crystal Self-Assembly Containing Chiral Naphthalimide Dyes, *Adv. Optical Mater.* **9** (2021) 2100961 DOI:10.1002/adom.202100961.

[28] J. Quinson and K. M. Ø. Jensen, From platinum atoms in molecules to colloidal nanoparticles: A review on reduction, nucleation and growth mechanisms, *Adv. Colloid Interface Sci.* **286** (2020) 102300. DOI: 10.1016/j.cis.2020.102300.

[29] M. Montalti, A. Credi, L. Prodi MG, Montalti M, Credi A, Prodi L GM. Handbook of Photochemistry. 3rd ed. BOCA: Taylor & Francis, Boca Raton; 2006.

[30] D. Macdougall and W. B. Crummett, Guidelines for data acquisition and data quality evaluation in environmental chemistry, *Anal. Chem.* **52** (1980) 2242–2249. DOI:10.1021/ac50064a004.

[31] G. L. Long and J. D. Winefordner, Limit of Detection A Closer Look at the IUPAC Definition, *Anal. Chem.* **55** (1983) 713A-724A. DOI:10.1021/ac00258a724.

[32] Gaussian 16, Revision C.01, M. J. Frisch, G. W. Trucks, H. B. Schlegel, G. E. Scuseria, M. A. Robb, J. R. Cheeseman, G. Scalmani, V. Barone, G. A. Petersson, H. Nakatsuji, X. Li, M. Caricato, A. V. Marenich, J. Bloino, B. G. Janesko, R. Gomperts, B. Mennucci, H. P. Hratchian, J. V. Ortiz, A. F. Izmaylov, J. L. Sonnenberg, D. Williams-Young, F. Ding, F. Lipparini, F. Egidi, J. Goings, B. Peng, A. Petrone, T. Henderson, D. Ranasinghe, V. G. Zakrzewski, J. Gao, N. Rega, G. Zheng, W. Liang, M. Hada, M. Ehara, K. Toyota, R. Fukuda, J. Hasegawa, M. Ishida, T. Nakajima, Y. Honda, O. Kitao, H. Nakai, T. Vreven, K. Throssell, J. A. Montgomery, Jr., J. E. Peralta, F. Ogliaro, M. J. Bearpark, J. J. Heyd, E. N. Brothers, K. N. Kudin, V. N. Staroverov, T. A. Keith, R. Kobayashi, J. Normand, K. Raghavachari, A. P. Rendell, J. C. Burant, S. S. Iyengar, J. Tomasi, M. Cossi, J. M. Millam, M. Klene, C. Adamo, R. Cammi, J. W. Ochterski, R. L. Martin, K. Morokuma, O. Farkas, J. B. Foresman, and D. J. Fox, Gaussian, Inc., Wallingford CT, 2016.

[33] A. D. Becke, Density-functional thermochemistry. III. The role of exact exchange, *J. Chem. Phys.* **58 (**1993) 5648–5652. DOI:10.1063/1.464913.

[34] P. C. Hariharan and J. A. Pople, The Influence of Polarization Functions on Molecular Orbital Hydrogenation Energies, *Theoret. Chim. Acta (Berl.)* **28** (1993) 213-222. DOI:10.1007/BF00533485.

[35] M. Meyer, V. Dahaoui-Gindrey, C. Lecomte and R. Guilard, Conformations and coordination schemes of carboxylate and carbamoyl derivatives of the tetraazamacrocycles cyclen and cyclam, and the relation to their protonation states, *Coord. Chem. Rev.* **178**-**180** (1998) 1313-1405. DOI:10.1016/S0010-8545(98)00169-6.

[36] D. Lu, X. Xu, X. Zhang, W. Xie and Y. Gao, Study on Influencing Factors of Phase Transition Hysteresis in the Phase Change Energy Storage, *Materials* **15** (2022) 2775. DOI:10.3390/ma15082775

[37] S. Mocanu, G. Ionita and I. Matei, Solvatochromic characteristics of dansyl molecular probes bearing alkyl diamine chains, *Spectrochim. Acta A Mol. Biomol. Spectrosc.* **237** (2020) 118413. DOI:10.1016/j.saa.2020.118413.

[38] E. Oliveira, R. M. F. Baptista, S. P. G. Costa, M. M. M. Raposo and C. Lodeiro, Solvatochromic Effects of bis(indolyl)thienylaril derivatives as new Colored Materials, *Photochem. Photobiol. Sci.* **13** (2014) 492–498. DOI:10.1039/C3PP50352F.

[39] P. Gans, A. Sabatini and A. Vacca, Investigation of equilibria in solution. Determination of equilibrium constants with the HYPERQUAD suite of programs, *Talanta,* **43** (1996) 1739–1753. DOI:10.1016/0039-9140(96)01958-3.

10

General Conclusions

The present works show a diverse collection of studies that jointly advance the field of fluorescent molecular probes, functional materials, and their applications in sensing, environmental remediation, and biomedical technologies. Through the design, synthesis, and photophysical characterization of eighteen related dansyl-based fluorophores, this research offers innovative contributions addressing current challenges in chemical sensing, material engineering, and multifunctional analytical platforms.

By pursuing the various objectives explored throughout these studies, several significant advancements were achieved, contributing to both fundamental photophysical understanding and practical technological development:

i. Development of tailored fluorophores with tunable emission was achieved through structural variations such as introducing heteroatoms, disulfide bridges, macrocyclic cores, or dyad architectures. These modifications enabled systematic control over solvatochromism, intramolecular charge transfer, AIE behavior, and acid/base responsiveness. The findings provide valuable insight into excited-state processes and expand the chemical space of functional fluorophores.

ii. Metal-ion sensing capabilities were strongly demonstrated, particularly for environmentally and biologically relevant species such as Hg^{2+}, Cu^{2+}, and CN^{-}. Through multiple studies, the compounds showed selective turn-on or quenching responses, high association constants, and low LOD/LOQ values, highlighting their analytical potential. Mechanistic investigations including PET modulation and dyad redox interplay further reinforce their suitability for targeted detection strategies.

iii. Aggregation-induced emission and water-dependent emission modulation were widely observed and exploited. Through careful solvent screening, Kamlet–Taft multiparametric analyses, and DLS characterization, the studies clarified how

hydrophobicity, solvent polarity, and molecular architecture rule aggregation and emission enhancement. Such insights not only strengthen the understanding of AIE mechanisms but also support the development of aqueous-stable imaging and sensing systems.

iv. Integration of fluorophores into polymer matrices such as PMMA, PVA/PVP, SBS, Irogran®-TPU and Kurarity proved essential to extend their applicability. Polymer-doped films and microparticles enabled enhanced stability, modulation of emission maxima, thermal linearity, and suitability for real-world application. These hybrid materials demonstrated utility as molecular thermometers, acid sensors, and fluorescent carriers, underscoring the versatility of polymer-fluorophore composites.

v. Biological relevance and antimicrobial potential were demonstrated through incorporation of selected fluorophores into polymeric materials and microparticles for bio-applications. The observed antimicrobial activity, particularly against clinically relevant strains, illustrates a promising avenue for the development of functional coatings and biomedical materials.

vi. Lastly, nanomaterial stabilization and functionalization were accomplished using particularly versatile fluorophores, enabling the controlled synthesis of metal nanoparticles with defined morphologies and aggregate sizes. This dual sensing-stabilizing ability highlights the broader utility of these compounds in nanotechnology and catalysis.

This doctoral work significantly advances the understanding of how molecular design governs photophysical behavior, how these properties can be tailored for precise sensing functions, and how polymer incorporation or nano structuring can translate molecular phenomena into practical tools. Beyond contributing new compounds and analytical methods, this research opens new perspectives for multifunctional materials with environmental, industrial, and biomedical relevance.

11

FUTURE PERSPECTIVES

Building on the substantial advances achieved throughout this work, multiple routes emerge for future exploration to further expand the impact of fluorescent molecular probes, functional polymers, and photophysical methodologies across sensing, environmental, and biomedical applications. These directions aim to transform the current scientific findings into more versatile technological solutions.

i. Broadening sensing applications across diverse analytes. Future work could extend the sensitivity and selectivity of the synthesized fluorophores toward a wider range of environmentally and biologically relevant species, such as reactive oxygen/nitrogen species or emerging pollutants. Structural modifications guided by computational design may further enhance turn-on responses, AIE behavior, or redox-mediated sensing, enabling the development of next-generation analytical probes.

ii. Advancing polymer–fluorophore hybrid materials. Building on the promising results obtained with PMMA, TPU, SBS, and other matrices, future efforts could focus on designing smart polymer platforms with programmable mechanical, chemical, and thermal responses. These may include self-healing polymers, biodegradable supports, or flexible films for wearable sensing devices. Such systems could help translate molecular sensing mechanisms into deployable real-world technologies.

iii. Development of micro- and nanoscale carriers for biomedical use. The successful fabrication of fluorescent microparticles opens the path toward expanding into nanoscale architectures suitable for drug delivery, bioimaging, and antimicrobial therapies. Functionalization with targeting agents, responsive release systems, or dual-mode imaging capabilities may allow precise clinical applications, especially in infection detection, cellular tracking, or localized therapeutic delivery.

iv. Integration of computational modeling and machine learning. Emerging AI-driven methods can be applied to predict photophysical behavior, optimize structural modifications, and automate spectral data analysis. Machine-learning models could accelerate the identification of structure-property relationships, improving the rational design of new fluorophores and enabling real-time analysis of sensing signals in complex environments.

v. Exploration of catalytic and redox-active functionalities. The observation of ligand-mediated copper reduction highlights the potential of certain compounds as active components in catalytic systems. Future work may focus on designing dyad or macrocyclic architectures tailored for photocatalysis, environmental remediation, or metal-mediated organic transformations, linking photophysical properties with catalytic performance.

vi. Translation to industrial and environmental monitoring platforms. Given the robustness of the polymer-doped thermal sensors and the high selectivity of metal-ion probes, future development could involve integrating these materials into commercial devices such as temperature-responsive indicators, on-site pollutant monitors, or optical sensor arrays. Collaborations with industry may accelerate the deployment of these materials in manufacturing, environmental surveillance, and quality-control settings.

vii. Establishing multidisciplinary research networks. To fully realize the translational potential of these findings, expanding collaborations between chemists, materials scientists, environmental engineers, and biomedical researchers will be essential. International partnerships and shared research infrastructures can facilitate the scaling of sensing materials, clinical validation of bioimaging probes, and exploration of new polymer–fluorophore technologies.

By pursuing these future directions with some already underway, the research can continue to advance the fields of photophysics, sensing science, and functional materials. These efforts will help pave the way for innovative analytical platforms, multifunctional hybrid systems, and new strategies for environmental and biomedical applications, marking a promising trajectory toward more effective technological solutions.

A

Published Paper in Microchemical Journal - Corresponding to Chapter 3

Microchemical Journal 205 (2024) 111237

Contents lists available at ScienceDirect

Microchemical Journal

journal homepage: www.elsevier.com/locate/microc

Antimicrobial profile and Turn-On sensing of cyanide and water traces using a dual chromophoric Dansyl-Acridine conjugate as multifunctional system

Frederico Duarte [a,1], Inês Pereira-Gomes [a,2], Georgi M. Dobrikov [b,3], Joana Galhano [a,4], Clara S.B. Gomes [c,5], Atanas Kurutos [b,d,6,*], Hugo M. Santos [a,e,7], Elisabete Oliveira [a,e,8,*], Maria Paula Duarte [f,9], José Luis Capelo-Martinez [a,e,10], Carlos Lodeiro [a,e,*]

[a] BIOSCOPE Research Group, LAQV-REQUIMTE, Chemistry Department, NOVA School of Science and Technology, FCT NOVA, Universidade NOVA de Lisboa, 2829-516 Caparica, Portugal
[b] Institute of Organic Chemistry with Centre of Phytochemistry, Bulgarian Academy of Sciences, Acad. G. Bonchev str., bl. 9, 1113 Sofia, Bulgaria
[c] LAQV-REQUIMTE, Department of Chemistry, NOVA School of Science and Technology, NOVA FCT, NOVA University of Lisbon, 2829-516 Caparica, Portugal
[d] University of Chemical Technology and Metallurgy, 8 St. Kliment Ohridski blvd, 1756 Sofia, Bulgaria
[e] PROTEOMASS Scientific Society, 2825-466 Costa de Caparica, Portugal
[f] MEtRICs, Chemistry Department, NOVA School of Science and Technology, FCT NOVA, Universidade NOVA de Lisboa, 2829-516 Caparica, Portugal

ARTICLE INFO

Keywords:
Multifunctional materials
Water trace
Acidochromism
Cyanide sensing
Polymer particles
Antimicrobial activity

ABSTRACT

9-aminocridine derivatives bearing a dimethylmethanimidamide, **L1**, and the dyad conjugate dansyl-acridine, **L2**, were synthesized and their ability to be used as multifunctional materials using different polymer matrixes was investigated. **L1** was found to modulate its emission in the presence of traces of water with a turn-on effect and to this end was used for the detection of water traces in organic solvents with a LOD and LOQ of 0.0028 and 0.0121 (V%) in acetonitrile, respectively. Due to the observed acidochromism for this compound and the different behaviour in acetonitrile and chloroform due to different stabilization of the excited state a turn-off and turn-on effect was observed for respective solvents. PMMA polymer doped films aided on the elucidation for this compound to be used as a sensor of strong acids. Furthermore, compound **L2** was found fruitful for the detection of cyanide through an acid base anion sensing. Incorporation of these compounds in PVA:PVP polymer films and Irogran® microparticles were carried out to assess their antimicrobial profile.

1. Introduction

Fluorescent chemosensors have exhibited extraordinary optical qualities in various applications during the past decades due to their exceptional sensitivity, quickness, and non-invasive nature. As an example, the 1-(dimethylamino)-naphthalene-5-sulfonyl or dansyl derivatives which often present high fluorescence quantum yields, a significant Stokes Shift and the solvatochromism behaviour that provide

* Corresponding authors.
E-mail addresses: akouroutos@gmail.com (A. Kurutos), ej.oliveira@fct.unl.pt (E. Oliveira), cle@fct.unl.pt (C. Lodeiro).
[1] Frederico Duarte: 0000-0001-5274-7139
[2] Inês Pereira-Gomes: 0009-0001-6086-8499.
[3] Georgi M. Dobrikov: 0000-0003-0437-2162.
[4] Joana Galhano: 0000-0002-7149-1682.
[5] Clara S.B. Gomes: 0000-0003-3672-0045.
[6] Atanas Kurutos: 0000-0002-6847-198X.
[7] Hugo M. Santos: 0000-0002-6032-8679.
[8] Elisabete Oliveira: 0000-0002-8339-4820.
[9] Maria Paula Duarte: 0000-0002-8699-0070
[10] José Luis Capelo-Martinez: 0000-0001-6276-8507.

https://doi.org/10.1016/j.microc.2024.111237
Received 6 July 2024; Received in revised form 15 July 2024; Accepted 17 July 2024
Available online 18 July 2024
0026-265X/© 2024 The Author(s). Published by Elsevier B.V. This is an open access article under the CC BY-NC-ND license (http://creativecommons.org/licenses/by-nc-nd/4.0/).

the robustness necessary to be useful for the development of biosensors and biological imaging [1–4].

One potential downside of these systems is that the fluorescence changes often occur in either a single emission or ratiometric response. Recently, several successful examples based on dual fluorescence probes bearing a dansyl unit have been reported, which amplify the manners of fluorescence signals, improve the signal-to-noise ratio, and provide a wider region of emission [5]. Dithienylethene and diarylethene photoswitches [6,7], carbazole and triphenylamine-based energy donors [8], pyrene [9,10], naphthalimide [5,11], and rhodamine [12–14] are only a few examples.

In line with the premise of designing more versatile multifunctional dual fluorescent molecules, acridine and its derivatives become good candidates due to their sensing purposes. In the field of fluorescence sensors, different photophysical events might arise from a variety of chemical processes involving water such as hydrolysis, protonation and deprotonation reactions and molecular aggregation [15]. It is also noteworthy to highlight the relevance of monitoring water as an analyte in several applications such as chemical production, petroleum-based fuel and food processing [10,12,16–18].

Therefore, acridine derivatives become relevant since in aqueous solution they can adopt two prototropic forms (pKa ~5.3), namely the neutral and protonated forms. Each form has a characteristic fluorescence spectrum allowing acridine derivatives to be used as pH sensitive probes [19,20].

In the realm of material science, there's a pressing demand for molecular sensors capable of detecting acidic species. Polymer materials emerge as ideal candidates that enable the detection of the targeted process, ensure the device's stability, and are cost-effective, and adaptable for production. With this in mind, Sandra Medel *et al.* have synthesized a hyperbranched polyeteramide functionalized with six acridine groups as a fluorescent acid sensor in solution as well as in solid polymer films exhibiting an increase in the fluorescence emission [21]. Due to the known contribution of acridine derivatives towards anticancer and antibacterial development fields [22–26], the authors have tested the synthesized polymer film against five bacteria (Gram-positive and Gram-negative) as well as two yeasts, exhibiting high antimicrobial activity [21].

In this work, two compounds (**L1** and **L2**) based on the dyad dansyl-acridine have been synthesized with the intention to be used as multifunctional materials. Compound **L1** was found to be synthesized only in the presence of a sulfonyl chloride group while **L2** constitutes both chromophores. Their photophysical and sensorial recognition properties were investigated. The sensing of water traces as well as the acidochromism effect of **L1** was investigated in solution and polymer thin films of polymethylmethacrylate (PMMA). The turn-on effect of **L2** towards cyanide was demonstrated and the mechanism of interaction elucidated. The antimicrobial activity of both compounds was investigated in solution as well as in doped polymer films of polyvinyl alcohol and polyvinylpyrrolidone co-polymer (PVA:PVP) and the thermoplastic polyurethane TPU-A92 (Irogran®). Polymer doped particles of the latter polymer were also synthesized and characterized as proof of concept for antimicrobial purposes.

2. Experimental section

2.1. Materials

All reagents and solvents employed for the synthesis and purification of the target compounds were purchased with purity > 98 % from Fluorochem Ltd (United Kingdom), Sigma-Aldrich (St Louis, Missouri, United States) or Tokyo Chemical Industry Co., Ltd (TCI). Photophysical experiments were carried out using spectroscopy grade solvents: ethanol (EtOH), acetonitrile (CH_3CN), chloroform ($CHCl_3$).

The synthesis and purification steps were accomplished using puriss p.a. grade solvents: dichloromethane (DCM), dimethylformamide (DMF), petroleum ether (PE), methanol (MeOH), methyl *tert*-butyl ether (MTBE).

Poly(methylmethacrylate), PMMA (MW~350,000, T_g 105 °C), polyvinylpyrrolidone, PVP (MW~40,000, T_g 170 °C), Polyvinyl alcohol (PVA, MW 27,000, T_g 85 °C) were purchased from Sigma-Aldrich (St. Louis, MO, USA) and the thermoplastic polyurethane TPU-A92 (Irogran®) was offered by Huntsman (Germany).

The perfluoroalkoxy (PFA) supports for the fabrication of polymer films were purchased to Bohlender, Gmbh, Germany. Mili-Q ultrapure water was used in all experiments.

2.2. Instrumentation

The chemical identities of the compounds under investigation were confirmed through the utilization of various analytical techniques, including ^{1}H NMR, ^{13}C NMR, DEPT-135, 2-D COSY, 2D-HSQC, and 2-D HMBC techniques. The ^{1}H NMR and ^{13}C NMR spectra were acquired on a Bruker Avance II+600 spectrometer and Bruker Avance Neo 400 (Institute of Organic Chemistry with Centre of Phytochemistry – Bulgarian Academy of Sciences / NMR Centre) using 5 mm tubes. The measurements were performed in $CDCl_3$ and DMSO-d6 at 293 K, with operating frequencies of 600.13 MHz / 400.13 MHz and 150.92 MHz / 100.62 MHz for the 1H and 13C nuclei, respectively. The ^{1}H- and ^{13}C-nuclear magnetic resonance (NMR) spectra were standardized using the reference signal of tetramethylsilane (TMS) with a chemical shift value (δ) of 0.00. The precision of chemical changes is determined at a level of 0.01 ppm. The coupling constants (J) are displayed with a precision of 0.1 and denoted in units of hertz (Hz). The spin multiplicity observed in the ^{1}H nuclear magnetic resonance (NMR) spectroscopy was represented using the following abbreviations: s for singlet, d for doublet, t for triplet, q for quartet, dd for doublet of doublets, dt for doublet of triplets, td for triplet of doublets, and m for multiplet. MestreNova v. 14.1.1 (Mestrelab Research S.L.) was used for processing the spectra. High-Resolution Mass Spectrometry analyses have been performed in the Laboratory for Biological Mass Spectrometry–Isabel Moura (PROTEOMASS Scientific Society Facility), using UHR ESI-Qq-TOF IMPACT HD (Bruker-Daltonics, Bremen, Germany). Samples of the corresponding compounds were prepared by dissolution in 50 % (v/v) Acetonitrile containing 0.1 % (v/v) aqueous formic acid to obtain a working solution of 0.1 μg/mL. Mass spectrometry analysis was carried out by the direct infusion of the compound solutions into the ESI source. MS data were acquired in positive polarity over the mass range of 80 – 1300 *m/z*. (Capillary voltage: 4500 V, End plate offset: −500 V, Charging voltage: 2000 V, Corona: 4000nA, Nebulizer gas: 0.4 Bar, Dry Heater: 180 °C, Dry gas: 4.0 L/min).

Photophysical studies were performed at 293 K using a JASCO V-650 spectrophotometer to obtain the UV–Vis absorption spectra and a HORIBA Scientific FLUOROMAX-4 spectrofluorometer for recording fluorescence spectra. Both instruments were from BIOSCOPE-PROTEOMASS facilities. Quartz cells with 10 mm optical path were used.

Crystals of compounds **L1HCl** and **L1HOTf** suitable for single-crystal X-ray analysis were selected, covered with Fomblin (polyfluoro ether oil) and mounted on a nylon loop. The data was collected at 110(2) K on a Bruker D8 Venture diffractometer equipped with a Photon II detector and an Oxford Cryostems Cooler, using graphite monochromated Mo-Kα radiation (λ = 0.71073 Å). The data was processed using the APEX4 suite software package, which includes integration and scaling (SAINT), absorption corrections (SADABS [27]) and space group determination (XPREP). Structure solution and refinement were done using direct methods with the programs SHELXT 2018/2 and SHELXL-2019/2 [28,29] inbuilt in APEX and WinGX-Version 2021.3 [30] software packages. All non-hydrogen atoms were refined anisotropically and, except for the N–H atom, all hydrogen atoms were inserted in idealized positions and allowed to refine riding on the parent carbon atom with C–H distances of 0.98 Å, 1.00 Å and 0.95 Å for methyl, methine and

aromatic H atoms, respectively. The molecular diagrams were drawn with Mercury [31]. Crystal and structure refinement data are given in Table S1. The data was deposited in the CCDC under deposit numbers 2,346,365 for **L1HC** and 2,346,366 for **L1HOTf**.

2.3. Synthetic procedures

2.3.1. Synthesis of L1

N'-(9-Acridinyl)-N,N-dimethylformamidine:

9-aminoacridine (300 mg, 1.54 mmol, 1.0 eq.) and K_2CO_3 (426 mg, 3.08 mmol, 2.0 eq.) were added consequently into a 50 mL flask containing 25 mL dimethylformamide and the resulting solution was stirred at room temperature for 10 min and then tosyl chloride (587 mg, 3.07 mmol, 2.0 eq.) was added. The formed heterogenous solution was further stirred at 70 °C for 3 h. TLC of reaction mixture – mobile phase DCM:MeOH=10:1 (v/v). Workup: the solution was left to cool down to room temperature and filtrated to remove the K_2CO_3, and the resulting clear solution was diluted with 120 mL of distilled water and decantated with 30 mL of $CHCl_3$ three times. The organic phase was concentrated *in vacuo* and diluted with 120 mL of water repeating the previous operation twice to remove the DMF. The concentrated mixture was then passed through a column using silica gel (70–230 mesh) as stationary phase and a mixture of DCM:MeOH=10:1 (v/v) as the eluent to give 95 mg (24 %) of compound **L1** as an orange powder. M.p. 141–142 °C. ^{1}H NMR (400 MHz, $CDCl_3$) δ 8.15 (d, J=9.74 Hz, 4H), 7.71 (ddd, J=8.43, 6.55, 1.31 Hz, 2H), 7.57 (s, 1H), 7.39 (m, 2H), 3.29 (s, 3H), 3.14 (s, 3H). ^{13}C NMR (101 MHz, $CDCl_3$) δ 156.46, 154.15, 149.25, 130.24, 128.75, 124.83, 123.77, 120.36, 40.34, 34.62. ESI-MS: $[M+H]^+$ without formic acid for $C_{16}H_{15}N_3$ = 250.1342 (−0.1 ppm) and $[M+H]^+$ with formic acid for $C_{16}H_{15}N_3$ = 250.1346 (−0.3 ppm).

2.3.2. Synthesis of L2

N-(acridin-9-yl)-5-(dimethylamino)naphthalene-1-sulfonamide.

Aminoacridine-base (327 mg, 1.68 mmol, 1.0 eq.) was suspended in 4 mL dry NMP (*N*-methylpyrrolidone), and NaH (65 mg, 1.68 mmol, 1.0 eq. – 65 % dispersed in mineral oil) was added. The mixture was stirred at room temperature for 15 min, until the formation of a brown solution. Then DsCl (dansyl chloride) (545 mg, 2.02 mmol, 1.2 eq.) was added and the resulting mixture was further stirred at room temperature for 72 h. Subsequently, 35 mL of distilled water was added, and the formed gray precipitate was filtered, washed with distilled water and PE (petroleum ether), then dried. The obtained gray powder was suspended in DCM and filtered through a silica gel pad (mobile phase DCM: MTBE=4:1 v/v). After evaporation under reduced pressure the product was recrystallized from 12 mL of 96 % EtOH. The formed precipitate was decanted and further boiled with 5 mL of MTBE (methyl *tert*-butyl ether). After cooling down to room temperature, it was decanted and dried in *vacuo* to furnish 153 mg (21 %) of yellow powder. M.p. 266 °C. ^{1}H NMR (400 MHz, DMSO) δ 12.92 (s, 1H), 8.63 (dd, J=8.6, 1.0 Hz, 2H), 8.45 (d, J=8.5 Hz, 1H), 8.34 (d, J=8.7 Hz, 1H), 8.27 (dd, J=7.3, 1.1 Hz, 1H), 7.84 (ddd, J=8.3, 6.9, 1.3 Hz, 2H), 7.72 (d, J=8.0 Hz, 2H), 7.64 (dd, J=8.5, 7.3 Hz, 1H), 7.46 (dd, J=8.6, 7.6 Hz, 1H), 7.31 (ddd, J=8.3, 6.9, 1.1 Hz, 2H), 7.22 (d, J=7.1 Hz, 1H), 2.86 (s, 6H).^{13}C NMR (101 MHz, DMSO) δ 159.38, 151.12, 140.67, 140.00, 134.33, 129.25, 129.15, 128.53, 128.47, 127.13, 125.37, 123.55, 122.25, 120.23, 118.22, 117.75, 114.81, 45.11, 40.15, 39.94, 39.73, 39.52, 39.31, 39.10, 38.89. ESI-MS: $[M+H]^+$ for $C_{25}H_{21}N_3O_2S$=428.1421 (−1.4 ppm), calculated $[M+H]^+$ for $C_{25}H_{21}N_3O_2S$=428.1427 *m/z*.

2.4. Spectrophotometric and spectrofluorimetric measurements

2.4.1. Photophysical characterization and titrations

Spectroscopic studies were carried out in various organic solvents (EtOH, CH_3CN, THF, $CHCl_3$) by preparing a stock solution (ca. 10^{-3} M) through dissolution of an appropriate amount of the corresponding compound in a 10 mL volumetric flask. The photophysical analysis were performed by preparation of diluted working solutions with concentration ranging from 10^{-5} to 10^{-6} M.

Solid state and doped polymer thin films' emission spectra were obtained using a fiber-optics device connected to the spectrofluorometer by excitation of the samples choosing an appropriate wavelength.

2.4.2. Fluorescence quantum yield and lifetime

Relative photoluminescence quantum yields were evaluated using 9-aminoacridine in absolute ethanol as a standard solution (ϕ_F=0.99) and the relative QY formula was applied taking into consideration each spectra's area [32]. Lifetime measurements were performed on a Tempro Fluorescence Lifetime System equipped with a pulsed diode Nanoled controller from Horiba Jobin-Yvon from the BIOSCOPE-PROTEOMASS facilities.

2.5. Determination of the detection and quantification limits (LOD and LOQ)

Determination of the detection limit (LOD) and quantification limit (LOQ) began by collecting ten independent measurements of a solution containing the selected probe and no addition of any analyte (yblank). Final determination of the LOD and LOQ values followed the subsequent formulas [33,34]:

LOD=$y_{dl} = y_{blank} + 3std$, where y_{dl} = signal detection limit and std = standard deviation.

LOQ=$y_{dl} = y_{blank} + 10std$, where y_{dl} = signal detection limit and std = standard deviation. The final step involved the determination of the minimal detectable and quantified concentration of analyte by titration with the ligands.

2.6. Preparation of polymer Dye-Doped thin films

PMMA doped thin films were prepared by weighting 100 mg of the polymer matrix and allowed to dissolve in $CHCl_3$ at a temperature of 50 °C. After cooling down to room temperature, 0.5 mg of **L1** were added to the solution.

The synthesis of PVA:PVP polymers commenced by utilizing a solution comprising 0.5 mg of **L1** and **L2** was prepared in 3 mL of ethanol. Another solution containing 200 mg of PVA and 50 mg of PVP was prepared in 2 mL of milliQ water and 3 mL of ethanol. This mixture was stirred and heated over a hotplate at ca. 60 °C until PVA and PVP were completely dissolved. The dye solution was then added to the polymer solution, and the mixture was kept on stirring and further placed under ultrasound.

TPU's solution was prepared by weighting 100 mg of this polymeric material and 0.5 mg of the compound in separate vials. The amount of TPU weighted was dissolved in 10 mL of THF over stirring at room temperature until it was totally dissolved. The dye solution was prepared in 1.5 mL of ethanol. This solution was after added to the Irogran® solution and sonicated on ultrasound.

All solutions were poured onto perfluoroalkoxy (PFA) supports of 5 cm diameter favouring solvent evaporation at room temperature over 24 h.

2.7. Synthesis of polymeric microparticles

A solution of polymer matrix thermoplastic polyurethane TPU-A92 (100 mg) in 10 mL of tetrahydrofuran (THF) was prepared and allowed to stir until complete solubilization was achieved. An aliquot of 0.6 mL of this solution was quickly added to **L1** and **L2** (0.5 mg) and transferred over 2.4 mL of deionized water, maintaining a magnetic stirring at 400 rpm for 5 min. For non-doped Irogran® particles the 0.6

mL aliquot was added directly to the 2.4 mL of deionized water. The resulting mixtures were stored at 20 °C in the dark for 24 h for oil-in-water droplets stabilization. The final particles were obtained after evaporation of THF at room temperature for 24 h. Before use, a filtration step using glass membranes with a pore size of 10–15 μm was performed to remove potential non-encapsulated **L1**, **L2** and polymer precipitates.

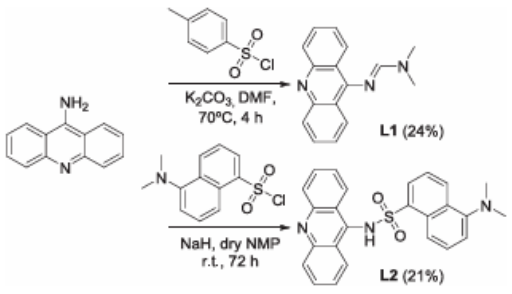
2.8. Antimicrobial assays

Four bacterial strains were chosen due to their relevance in antibiotic resistance in industrial and environmental fields: *Escherichia coli* (ATCC® 8739™), *Staphylococcus aureus* (ATCC® 6538™), *Enterococcus faecalis* (ATCC® 29212™) and *Salmonella enterica* subsp. *enterica* serovar *Choleraesuis* (ATCC® 10708™).

Bacterial stocks were maintained in appropriate broth containing 15 % v/v glycerol at −70 °C. After thawing, the stocks were inoculated onto TSA plates and incubated for 24 h at 35 ± 2 °C. Bacterial suspensions with a density equivalent to 0.5 on the McFarland scale (determined using a DEN-1B McFarland Densitometer, Grant-bio) were prepared in a saline medium (0.85 % m/v), resulting in a bacterial concentration of approximately 1.5×10^8 Colony Forming Units (CFU)/mL. The first stock solution was used for solid polymeric evaluation assays on an agar plate, while 1:10 dilutions of bacterial stocks were used for liquid assays.

Samples **L1**, **L2** and control 9-aminoacridine (**CAA**) were dissolved in DMSO to obtain a stock concentration of 1 mg/mL. Irogran® polymeric nanoparticles doped with **L1** were used as synthetized, with a concentration of **L1** inside the nanoparticles of 0.14 mg/mL. A 2-fold dilution series was prepared in 96-well plates using Mueller-Hinton broth (MHB), ranging from a maximum concentration of 100 μg/mL to a minimum concentration of 0.20 μg/mL for compounds and from 14 to 0.03 μg/mL for polymeric nanoparticles. Each well was then inoculated with the bacterial stocks to achieve a bacterial concentration of approximately 10^6 CFU/mL for all tested bacterial strains. The plates were then incubated 24 h at 35 ± 2 °C. The following day, the plates were collected, and the minimum inhibitory concentration (MIC) was accessed by optical density quantification at 600 nm in a CLARIOStar Spectrophotometer (BMG Labtech) at the PROTEOMASS Scientific Society Facility.

To evaluate the antimicrobial effect of the prepared doped polymers (**L1**@PVA:PVP, **L2**@PVA:PVP, **L1**@Irogran®, **L2**@Irogran®), 1 x 1 cm pieces of each were placed into a Mueller-Hintor Agar (MHA) plates, which were previously inoculated with each bacterial strain. The plates were incubated at 35 ± 2 °C for 24 h. Control films (9-aminoacridine (**CAA**)-doped and non-doped PVA:PVP and Irogran®) were also evaluated. Bacterial growth was visually evaluated in MHA plates and inhibition zones were measured in squared centimeters (cm^2). Asepsis conditions were achieved in a VBH Laminar Flow Hood (Steril). All incubations were performed in a Mermmet Incubator B10 (Vikat Ekinox).



Scheme 1. Synthetic approach to the preparation of the acridine derivatives under investigation.

3. Results and discussion

3.1. Synthesis

The synthesis of the target compound **L1** was achieved by utilizing the primary amine present in the commercially available 9-aminoacridine **1** (Scheme 1). The preparation of **L1** was accomplished by formation of an imine bond between **1** and dimethylformamide molecules also serving as the reaction media. It is noteworthy that this compound is only able to be formed in the presence of a sulfonyl group, in this case, tosyl chloride was used, instead of dansyl chloride for being an inexpensive reagent, also in the presence of potassium carbonate. No evidence was found for the formation of **L1** in the absence of tosyl chloride. This was favored due to the amine group's decreased reactivity as part of the aromatic system, as well as the delocalization of the nitrogen's lone pair of electrons within the ring. We suggest that the mechanism might involve the bond between the oxygen atom and the sulfur atom of the tosyl group aided by the nitrogen of the dimethyl group allowing the nitrogen of **1** to perform a nucleophilic attack to the aldehyde's carbon. The target compound was obtained in good yield after purification by column chromatography. NMR, MS, and melting point temperatures have been applied for the characterization of the compound. There is no indication that the imine bond decomposes in the presence of acidic or aqueous solutions, which will be examined subsequently. Acylation of 9-aminoacridine is a rather complicated procedure, due to tautomerism of this compound and, respectively weak nucleophilicity of the amino group. There are only few such examples of acyl-aminoacridines that can be found in the literature [35]. The synthesis of the target compound **L2** was performed with preliminary activation of the free 9-aminoacridine base by using a strong base (NaH in dry *N*-methylpyrrolidone), followed by the addition of dansyl chloride. The yield of the target compound **L2** after purification is 21 %.

Compound **L1** crystallized as pale-yellow crystals in the triclinic system, *P*-1 space group, in the form of acridinium cations with either chloride (**L1HCl**) or triflate (**L1HOTf**) as counterions. Their molecular structure is depicted in Figure S6, and selected bond lengths and angles are presented in Table S2.

L1HCl and **L1HOTf** have very similar crystal structures, with planar acridinium backbones, due to the aromatic nature of the fragment (Table S2) and an imine moiety, formed from the reaction of 9-aminoacridine with dimethylformamide. Both compounds have an *E* configuration and bond distances and angles within the reported values for similar compounds. [36] The main difference between these two derivatives, apart from the counterion, is the dihedral angle between the acridinium moiety and the imine fragment. In the case of **L1HCl**, this dihedral angle is slightly more pronounced with a value of 51.06(13) ° compared to 44.05(11) ° for **L1HOTf**. The supramolecular arrangement in these derivatives is generated from the formation of classical (N–H…O) and non-classical (C–H…O) hydrogen bonds, halogen (Cl…Cl, C–H…Cl, N–H…Cl and C–H…F) and π…π interactions (Figure S7).

3.2. Photophysical characterization

The 9-aminoacridine derived compounds exhibit luminescent properties both in solution and in the solid state. Both compounds have been synthesized with the intention of serving as multifunctional compounds and will be investigated in accordance with this principle. Figure S8 presents the chemical structures alongside the photophysical data performed at 293 K for compounds **L1** in acetonitrile and **L2** in chloroform as a representative example while Table 1 gathers all the photophysical data of the studied compounds.

The UV–Vis spectra exhibit notable disparities between the two compounds. In the case of **L1**, a band with a peak centered at 393 nm and a slight secondary peak allocated at 450 nm are detected, contributing to a faint pale green color visible to the human eye. Consequently, two sharp maximums centered around 415 and 440 nm in conjunction with a

broader shoulder at 400 nm constitute the absorption fingerprint of **L2.**

Upon excitation at the appropriate wavelength, a blue-greenish light with a maximum at 486 nm can be observed for **L1** in all solvents. In turn, compound **L2** has not been found to be emissive in solution and will be discussed further ahead. Regarding the solid-state emission, a red-shifted band from the one in solution is present with an emission maximum at 520 nm for **L1**, as well as an emission band centered at 587 nm for **L2** (Table 1). Concerning the fluorescence quantum yield, for **L1** a dependence according to the solvent is noticeable being in ethanol where the fluorescence quantum yield is higher of around 29 %. Lifetime measurements, by instance, present single digit nanosecond times for **L1** that vary significantly with the solvent.

3.3. Sensing of water molecules

Due to **L1**'s rather low solubility in water, various combinations were prepared using different water fractions in acetonitrile. The final concentration of **L1** was kept constant throughout. Fig. 1 displays the absorption and emission spectra of these mixtures where an interesting increase in the emission is perceived between 0 % and 17 % water fraction with minimal spectral variation regarding the one in pure acetonitrile. A yellow-greenish color begins to appear at the naked eye as the water content rises, and the absorption profile begins to develop, reaching a maximum at 430 nm with shoulders at 405 and 450 nm. When the water content is increased above 17 %, the emission of the various solutions declines until 83 % of the initial intensity is reached. When comparing the combination in pure acetonitrile, it was discovered that the fluorescence quantum yield for the most emissive mixture increased from 12 % to 20 %. This initial behaviour should be attributed to the different solvation sphere of **L1** possibly enabling hydrogen bridged between water molecules and the nitrogen of the aromatic ring.

Keeping in mind these results, efforts were made to establish if **L1** would be suited for water detection in organic solvents. For this purpose, subsequent additions of small aliquots of water have been added to a solution of **L1** in dried acetonitrile in order to determine a relation between the increase of the emission and the water content.

This experiment was performed through setting up a batch composed of several 3 mL solutions of **L1** and increasing total volumes in sums of 20 μL was added to each solution. As previously hypothesized, small quantities of water content can indeed increase the emission of **L1**. Fig. 1a gathers the spectra in acetonitrile where an increase in the emission up to 60 % in noticeable when added a total of 200 μL of water. The possibility for this system to be used as a sensor of water molecules in organic solvents is now supported by Fig. 1b where two different linear regressions can be established, the first from its initial emission up to 100 μL of water added, and the second until 200 μL. To fully characterize the usefulness of **L1** towards water tracing, calculation of the detection and quantification limit parameters were found to be 0.0028 and 0.0121 (V%), respectively.

3.4. Acidochromic behaviour

In line with the hypothesis that the nitrogen of the aromatic ring is capable of conducting hydrogen bonds with water molecules, we were interested in determining if **L1** would manifest acidochromism in solution and in solid supported thin films. For this, consecutive titrations of HCl and NaOH were performed to establish if also this behaviour would be reversible. Fig. 2a gathers the absorption and emission spectra corresponding to each last addition of HCl and NaOH and the initial spectra are provided for better clarity while Fig. 2b displays the emission of **L1** in relation to each addition in an equivalent manner. The complete titrations can be seen in Figure S10. The obtained results show that **L1** exhibits acidochromic behaviour in solution with the quenching of the emission as the concentration of HCl increases accompanied by a change in the absorption profile similarly seen previously. With the addition of NaOH the absorption returns to the initial maximum at 393 nm and the emission is recovered suggesting that the imine bond is intact. The increase of the emission past the initial one could be attributed to the increasing deprotonation of **L1** alongside the increasing formation of hydrogen bonds with water molecules.

In order to gain a deeper understanding of this acidochromic behavior, other investigations have been conducted, including a titration with trifluoroacetic acid in chloroform. As can be seen in Fig. 2c, the absorption profile is similar to the titration in acetonitrile with the progressive increase of a redshifted band. However, in this case only the 430 nm maximum is well established. In a surprisingly manner, the emission in chloroform changes completely by increasing its emission with increments of the acid equivalents in contrast with what was observed in acetonitrile. Fig. 2d offers a better understanding of this increase alongside the images under UV light. We suggest that the chloroform molecules stabilize differently the excited state of **L1** enabling the excited state proton transfer phenomenon, since the excitation spectra shown in Figure S9 is much similar to the absorption spectrum at the endpoint of the titration with TFA [37].

Since **L1** was able to manifest acidochromism in solution, the next step was to apply this behavior for the sensing of acidic solutions and environments. For this reason, PMMA polymer thin films were produced due to our previous experience with this polymer matrix.[38] For this purpose, an aqueous solution of HCl (12 M) was prepared and the polymer film doped with **L1** was submerged for 10 min. The prototype maintained its physical integrity and we observed a color change from light green to yellow (Fig. 2g). The emission of the film recorded before and after the treatment can be seen in Fig. 2e where the polymer maintains its emission maximum around 485 nm, however, after treatment the emission is substantially quenched. In order to check if the polymer had any degree of reusability, the previously treated polymer thin film was submerged in an aqueous solution of NH_3, and in fact the emission is restored practically to the initial one (Fig. 2e). To better assess the applicability of this material in the field of luminescent sensors, several cycles were performed, and as can be seen in Fig. 2f, the quenching of the emission in contact with an acidic media and its recovery in direct contact with ammonia are maintained for at least five cycles. Further experiments were performed by introducing the doped material in HCl solutions at varying concentrations from 6 – 10 M, however the 10-minute mark for these solutions is not able to significantly alter the emission profile of the film (Figure S11). Studies performed by exposing this material to atmospheres of these gases also demonstrated difficulties to fully protonate and reverse the acidochromic behaviour to its initial emission (Figure S12).

Table 1
Absorption maximum wavelength in solution (λ_{abs}), emission maximum wavelength in solution (λ_{em}), molar absorption coefficients (ε), Stokes shift ($\Delta\lambda$), emission maximum in the solid state (λ_{em}^{Solid}), fluorescence quantum yields (ϕ), fluorescence lifetimes (τ) for compound L1 and L2 in different solvents.

Cpd		λ_{abs} [nm]	λ_{em} [nm]	ε [10^4 cm^{-1} M^{-1}]	Stokes shift [cm^{-1}]	ϕ (%)	τ [ns]	λ_{em}^{Solid} [nm]
	EtOH	393	486	1.01	4869	29	2.8	
L1	CH_3CN	393	486	0.84		12	7.4	520
	$CHCl_3$	393	486	1.35		17	9.2	
L2	$CHCl_3$	439	–	2.79	–	–	–	587
	THF	439	–	2.84	–	–	–	

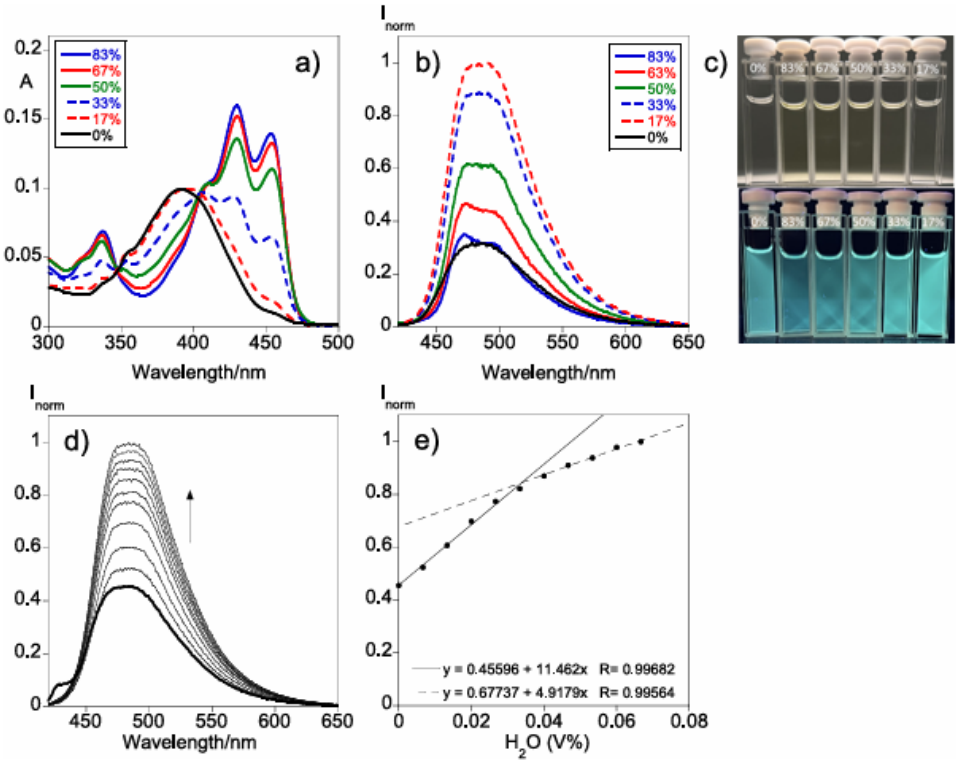


Fig. 1. (a) Absorption, (b) emission spectra and (c) images of **L1** in acetonitrile with different water fractions (f_w = 0 %, 17 %, 33 %, 55 %, 67 %, 83 %) at natural light (up) and under UV light (down, 365 nm). (d) Emission spectra (λ_{excL1} = 395 nm) and (e) plot of the normalized emission intensities at 490 nm of **L1** in acetonitrile with increasing amounts of water aliquots (0 %-0.067 %, v/v) with the corresponding linear regressions. [L] = 10 μM, T=293 K.

3.5. Acid-base anion sensing

Taking into consideration that **L2** does not exhibit emission in solution, our first approach was to access if the compound was synthesized in the protonated form. Accompanied with several other examples in the literature of dansyl probes [39–43], **L2** was used towards the sensing of anions and additions of 1, 5 and 10 equivalents of CN^-, F^-, Br^-, Cl^- in chloroform were performed. Fig. 3a assembles the normalized emission intensities at 476 nm, upon the addition of the aforementioned anions. Surprisingly, **L2** showed sensitivity towards CN^- and F^- ions evidenced by a turn-on effect of the emission. Due to the more basic character of the cyanide anion, the turn-on effect was accomplished before 5 equivalents while F^- ions were not able to reach the same intensities even at 10 equivalents.

In line with the previous results, Fig. 3b gathers the UV–Vis and luminescent titrations towards increasing amounts of CN^- for **L2** in chloroform. Overall, the addition of the anion causes the continuous decrease of the absorbance maxima centered at 418 and 440 nm. In terms of the emission spectra, an enhancement of its intensity is observed with well-defined maxima at 476 nm and 505 nm with a shoulder at 546 nm. Similar behaviour was observed in THF (Figure S13). This progression with consequent additions of cyanide resembles the same behaviour of **L1** observed in acetonitrile when added OH^- ions with the loss of the characteristic absorption band and the increase in emission (Figure S14). In addition, the re-establish of the characteristic dansyl absorption band becomes evident at the endpoint of the titration.

To fully characterize the luminescence of the resultant species and the sensing ability towards CN^- the quantum yield alongside the lifetime measurement were obtained and the stability constants were calculated with the aid of HypSpec software [44]. Table 2 reveals that **L2** has the largest constant in the presence of CN^- ions in chloroform with a constant value of $LogK_{ass.}$ = 4.23. Ligand **L2** was also found to exhibit a higher quantum yield of 29 % in chloroform. Regarding lifetime measurements, a biexponential decay fitting was used for both solutions providing two distinct lifetimes due to the equilibrium of two species. Lifetime $\mathbf{T_1}$ was found to contribute in one third and in half for chloroform and THF, respectively, with a value of 1.1 and 1.2 ns. By contrast, $\mathbf{T_2}$ was the predominant lifetime of 3.9 and 2.7 ns as chloroform and THF are considered.

3.6. Polymeric particles

Considering our efforts on the development of systems that allow highly hydrophobic, and water quenched sensors to maintain their properties in water [4,45], Irogran® polymeric microparticles doped with **L1** were synthesized using the precipitation method as well as undoped particles. These polymeric particles were used in this case as an additional carrier for the assessment of the antimicrobial effect for both **L1** as a proof of concept due to poor encapsulation of **L2** into the

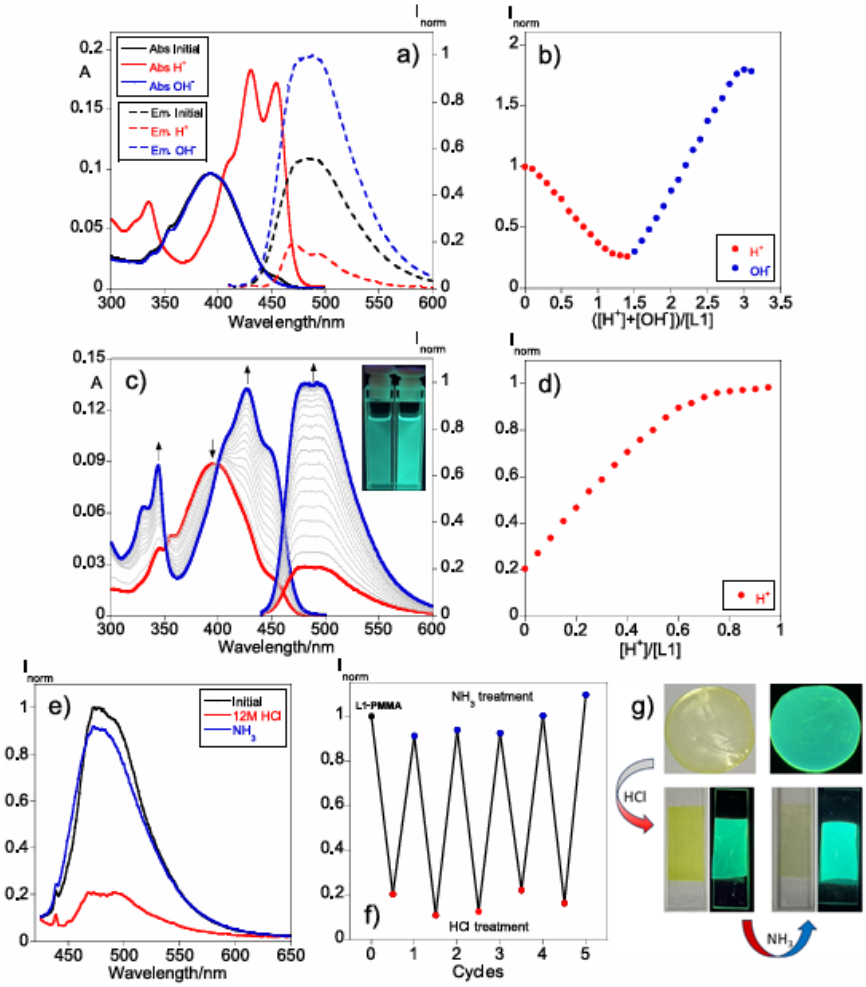


Fig. 2. (a) Absorption and emission spectra of **L1** in acetonitrile after the addition of 1.4 eq. of H^+ followed by 1.6 eq. of OH^- ($[H^+] = [OH^-] = 0.6$ mM) and (b) the emission as a function of ($[H^+] + [OH^-]$/[**L1**]) at 487 nm. (c) Spectrophotometric and spectrofluorimetric titrations of compounds **L1** with increased additions of 10 μL of trifluoroacetic acid ([TFA] = 0.15 mM, ($\lambda_{exc L1}$ = 400 nm)) in chloroform and (d) the emission as a function of [H^+]/[**L1**] at 487 nm. Inset images of the solution of **L1** in chloroform prior (left) and after (right) the titration under UV light (365 nm). Acidochromic behaviour of **L1-PMMA**. (e) Normalised emission spectra recorded after treatment with HCl solution (12 M) followed by immersion in a NH_3 solution (25 % in water), (f) normalized emission intensity maximum at 474 nm after successive cycles of HCl/NH_3 treatments by immersion in the corresponding aqueous solutions. (g) Images of the reversible acidochromic behaviour of **L1-PMMA** taken with the naked eye (left) and under UV light (right).

particles. The resulting Irogran® particles were characterized by dynamic light scattering (DLS) and transmission electron microscopy (TEM). The results showed that the particles present a spherical shape (Figure S15), while DLS data is included in Table 3.

Overall, DLS data suggest a smaller average size for the undoped Irogran® particles that increase considering the size of the compound introduced. Polydispersity index values suggest a mono distribution of size range and the zeta potential shows a negative surface charge indicative of good stability.

3.7. Antimicrobial assays

The antibacterial activity of acridine derivatives **L1** and **L2** against Gram-negative (*E. coli*, *S. enterica*) and Gram-positive (*S. aureus*, *E. faecalis*) bacteria was evaluated by broth microdilution assays. The bacterial strains were incubated for 24 h with a gradient concentration of each derivative from 100 to 0.20 μg/mL (see Fig. 4).

Fig. 4 summarizes the results obtained for the acridine derivatives **L1** and **L2**, as well as the control sample 9-aminoacridine (CAA). In general, the control CAA demonstrated antibacterial activity against all tested strains, with MIC_{50} values of 3.13 μg/mL for *E. coli*, 25 μg/mL for

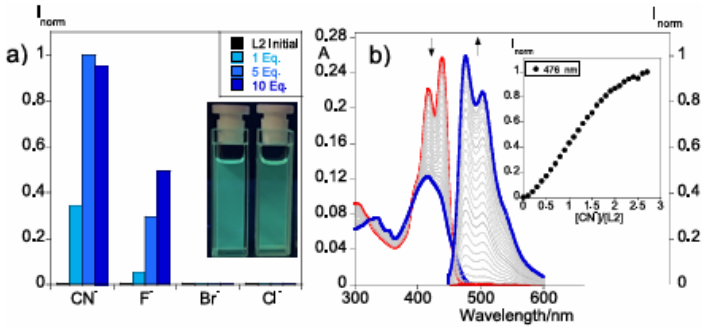


Fig. 3. (a) Normalized emission intensity of **L2** after addition of CN^-, F^-, Br^-, Cl^- in successive proportions of 1, 5, and 10 equivalents in chloroform and inset image under UV light after the addition of 10 eq. of CN^- ions in a solution of chloroform (left) and THF (right) of **L2** ([**L2**] = 10 μM, λ_{emL2} = 476 nm, T=298 K). (b) UV–Vis and luminescent titrations of compounds **L2** upon continuous addition of 10 μL of CN^- ([CN^-] = 0.3 mM; [**L2**] = 10 μM, (λ_{excL1} = 439 nm)), in chloroform. Inset: Emission as a function of [CN^-]/[**L2**] at 476 nm. For clarity of the reader the red spectra correspond to the initial spectrum and the blue to the endpoint of the titration. (For interpretation of the references to color in this figure legend, the reader is referred to the web version of this article.)

Table 2
HypSpec's calculated association constants for the probe **L2** towards CN^- ions, fluorescence quantum yields (ϕ), and fluorescence lifetimes (τ) for compound **L2** after addition of CN^- ions in different solvents.

Cpd		Association constants ($LogK_{ass.}$)	ϕ (%)	τ[ns]
L2	$CHCl_3$	4.23 ± 0.0018	29	T_1 = 1.2; T_2 = 3.9
	THF	3.62 ± 0.0015	16	T_1 = 1.1; T_2 = 2.7

Table 3
Dynamic light scattering data for the obtained particles.

Particles	Z-Average (nm)	PDI	ζ-Potential (mV)
@Nano	181 ± 4	0.17 ± 0.01	−39.6 ± 0.7
L1@Nano	189 ± 5	0.20 ± 0.01	−39.9 ± 1.1

S. aureus and *E. faecalis*, and 12.5 μg/mL for *S. enterica*, indicating greater efficacy against Gram-negative bacteria. Compound **L1** exhibited MIC_{50} values of 12.5 μg/mL for *E. coli*,100 μg/mL for *S. aureus* and *S. enterica*, and 25 μg/mL for *E. faecalis*. On the other hand, **L2** showed an MIC_{50} value of 100 μg/mL for all tested strains.

The MIC_{50} values observed for the control compound CAA align with previously reported data in the literature, where 9-aminoacridine is known for its broad-spectrum antibacterial activity, particularly against Gram-negative bacteria. Typical MIC values for 9-aminoacridine compound are 8–32 μg/mL for *E. coli*, 32 μg/mL for *S. aureus* and 64 μg/mL for *E. faecalis* [46].

For compound **L1**, the MIC_{50} values indicate more significant antibacterial activity than **L2**, particularly against *E. coli* and *E. faecalis*. Although the antibacterial activity is lower compared to CAA, these compounds may have several advantages, such as reduced toxicity, increased selectivity, versatility, and improved environmental impact. As acridine derivatives are known for their cytotoxicity, modifications in the chemical structure can lead to reduced toxicity, making them safer for environmental and industrial uses.

To explore the versatility of **L1** and **L2**, they were integrated into polymer materials, such as PVA:PVP, and Irogran®, aiming to produce antibacterial coatings and films for diverse industrial applications. For these assays, the polymers were placed in contact with inoculated MHA plates and incubated for 24 h to ensure bacterial growth. Non-doped polymers were used as controls. Additionally, based on the results obtained, Irogran® polymeric nanoparticles doped with **L1** were also synthesized, and their antibacterial activity was evaluated through a broth microdilution assay.

Fig. 5 summarizes the results achieved for these assays. Firstly, no significant antibacterial activity was detected for the control non-doped PVA:PVP polymers, demonstrating once again their biocompatible profile [47]. A similar profile was obtained for PVA:PVP@**L2** polymers, with no inhibitory behavior observed for any bacterial strains tested.

Conversely, for PVA:PVP@**L1**, no bacterial growth was observed at the agar-polymer interface for *E. coli*, *S. aureus*, and *E. faecalis*, with a slight color diffusion in the latter two, demonstrating some antibacterial properties.

Irogran® polymers exhibit intrinsic antibacterial properties, presenting no bacterial growth under the polymers in *E. faecalis* and *S. enterica*, as also previously reported in the literature. [48] The same behavior was verified for Irogran®@**L2** in *E. coli*, *E. faecalis* and *S. enterica* and for Irogran®@**L1** in all bacterial strains, with a halo formation of 9 cm^2 in *E. faecalis*, consistent with the release of some compound to the medium and their subsequent diffusion throughout. This increased inhibition zone observed with Irogran®@**L1** in *E. faecalis* suggests that combining Irogran® with **L1** may create a synergistic effect, enhancing the antibacterial efficacy.

Considering these results, Irogran® polymeric microparticles were thus synthesized with compound **L1** and tested against the same bacterial strains with undoped Irogran® microparticles, within a lower concentration range from 0.03 to 14 μg/mL. Surprisingly, the Irogran® microparticles doped with **L1** (**L1**@Nano) exhibit unprecedented selectivity, achieving an MIC_{50} value of 14 μg/mL for *E. faecalis*. This value is 2-fold lower than the obtained MIC_{50} of free **L1** in solution, indicating enhanced efficacy in the microparticle formulation and further validating the occurrence of possible synergistic mechanisms between the two.

4. Conclusions

In this work, two 9-aminoacridine based fluorophores were synthesized with the intention to explore their photophysical properties using different polymer matrixes as multifunctional materials. **L1** was found to modulate its emission in the presence of trace amounts of water, exhibiting a turn-on effect. This property was utilized for detecting water traces in organic solvents, achieving a limit of detection (LOD) of 0.0028 V% and a limit of quantification (LOQ) of 0.0121 V% in acetonitrile. Additionally, **L1** displayed acidochromism and showed different behaviors in acetonitrile and chloroform due to the varying stabilization of the excited state, resulting in turn-off and turn-on effects in these

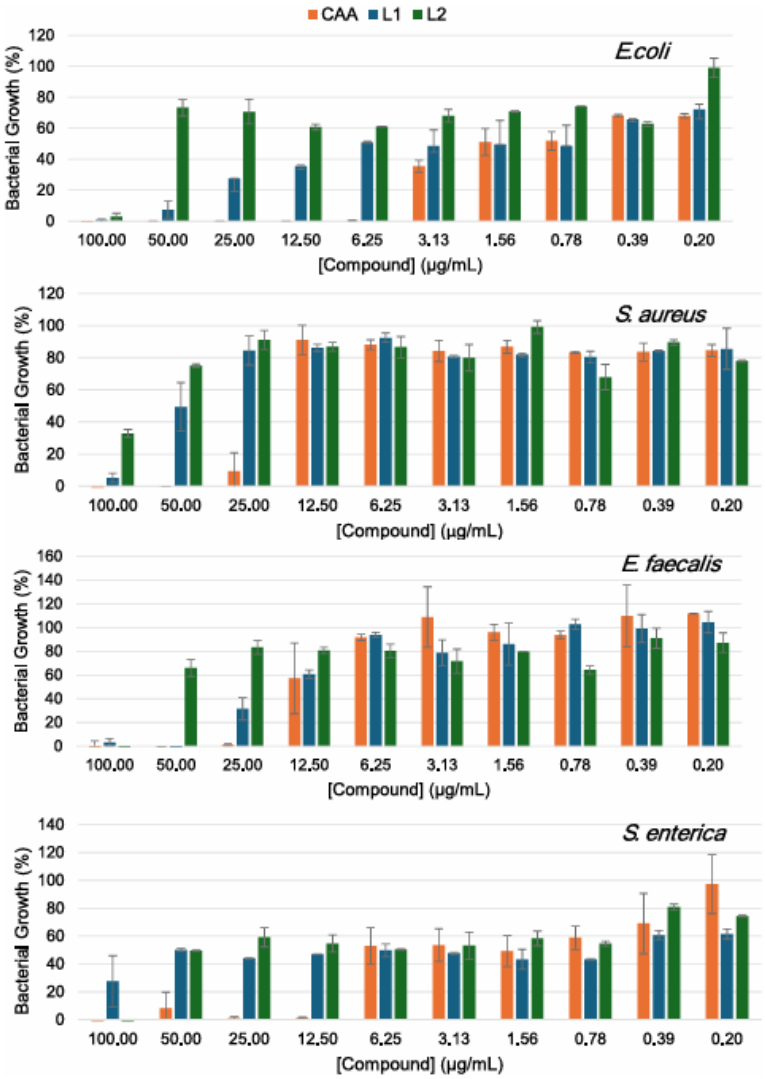


Fig. 4. Bacterial growth profile against Gram-negative and Gram-positive bacteria of compounds **L1**, **L2** and **CAA** (9-aminoacridine:control).

respective solvents. PMMA polymer doped films were useful in the demonstration for this compound to be used as a sensor for strong acids, and the reusability of this material has been elucidated through various cycles. Due to the photophysical similarities of the synthesized **L2** and the protonated **L1**, a proposed acid-base anion sensing was carried out for cyanide. This led to a turn-on effect on the emission and a full characterization of the emission was performed resulting in an increment of the quantum yield to 29 % and an association constant of $LogK_{ass.} = 4.23$ in chloroform. Finally, the antibacterial profile of the newly synthesized compounds was performed through broth microdilution assay and integrated into polymer materials, such as PVA:PVP, and Irogran®, aiming to produce antibacterial coatings and films for diverse industrial applications. As a proof of concept, undoped and doped with **L1** Irogran® microparticles were synthesized using an oil-in-water method as an additional carrier for the assessment of the antimicrobial effect, achieving an MIC_{50} value of 14 µg/mL for *E. faecalis*.

Funding

This work received support from PT national funds (FCT/MCTES, *Fundação para a Ciência e Tecnologia* and *Ministério da Ciência, Tecnologia e Ensino Superior)* through the projects UIDB/50006/2020 and UIDP/50006/2020. This work received support from PROTEOMASS Scientific Society through the General Funding Grant 2022–2023, and the projects

a)

	PVA:PVP	PVA:PVP@L1	PVA:PVP@L2	PVA:PVP@CAA	Irogran	Irogran@L1	Irogran@L2	Irogran@CAA
E. coli	Growth	No growth No halo	Growth	No growth Halo: 3.7 cm²	Growth	No growth No halo	No growth No halo	No growth Halo: 2.9 cm²
S. aureus	Growth	No growth No halo*	Growth	No growth Halo: 2.2 cm²	Growth	No growth No halo*	Growth	No growth Halo: 2.4 cm²
E. faecalis	Growth	No growth No halo*	ND	No growth Halo: 2.4 cm²	No growth No halo	No growth* Halo: 9.0 cm²	No growth No halo	No growth Halo: 1.5 cm²
S. enterica	Growth	Growth	Growth	No growth Halo: 3.3 cm²	No growth No halo	No growth No halo*	No growth No halo	No growth Halo: 3.4 cm²

b)

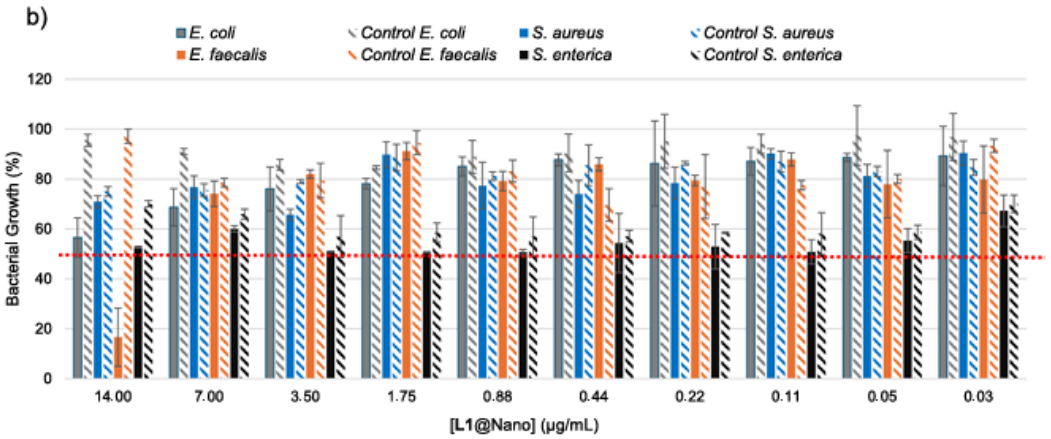


Fig. 5. (**a**) Results of antibacterial assays of PVA:PVP and Irogran® polymers (*color diffusion to the media), and (**b**) Bacterial growth profile against Gram-negative and Gram-positive bacteria of free and **L1** doped Irogran® nanoparticles.

#PM001/2019 and #PM003/2016. This work is also developed and acknowledged by A.K. as part of contract BG-RRP-2.004–0002-C01, Laboratory of Organic Functional Materials (Project BiOrgaMCT), Procedure BG-RRP-2.004, Establishing of a network of research higher education institutions in Bulgaria", funded by BULGARIAN NATIONAL RECOVERY AND RESILIENCE PLAN".

CRediT authorship contribution statement

Frederico Duarte: Writing – review & editing, Writing – original draft, Visualization, Validation, Software, Methodology, Investigation, Formal analysis, Data curation. **Inês Pereira-Gomes:** Writing – review & editing, Validation, Software, Investigation, Formal analysis. **Georgi M. Dobrikov:** Writing – review & editing, Software, Methodology, Investigation, Funding acquisition, Conceptualization. **Joana Galhano:** Writing – review & editing, Software, Investigation, Formal analysis, Data curation. **Clara S.B. Gomes:** Writing – review & editing, Investigation, Formal analysis, Data curation, Writing – original draft. **Atanas Kurutos:** Writing – review & editing, Writing – original draft, Visualization, Software, Resources, Investigation, Funding acquisition, Formal analysis, Data curation, Conceptualization. **Hugo M. Santos:** Writing – review & editing, Writing – original draft, Visualization, Resources, Investigation, Funding acquisition, Formal analysis, Data curation. **Elisabete Oliveira:** Writing – review & editing, Visualization, Software, Methodology, Investigation, Formal analysis, Data curation, Writing – original draft, Resources, Funding acquisition, Supervision. **Maria Paula Duarte:** Writing – review & editing, Validation, Software, Investigation, Funding acquisition, Data curation. **José Luis Capelo-Martinez:** Writing – review & editing, Visualization, Validation, Resources, Funding acquisition. **Carlos Lodeiro:** Writing – review & editing, Writing – original draft, Validation, Supervision, Resources, Project administration, Funding acquisition, Formal analysis, Conceptualization.

Declaration of competing interest

The authors declare the following financial interests/personal relationships which may be considered as potential competing interests: Carlos Lodeiro reports financial support was provided by Proteomass Scientific Society. Jose Luis Capelo-Martinez reports financial support was provided by Proteomass Scientific Society. If there are other authors, they declare that they have no known competing financial interests or personal relationships that could have appeared to influence the work reported in this paper.

Data availability

Data will be made available on request.

Acknowledgements

This work was supported by the Associate Laboratory for Green Chemistry LAQV which is financed by national funds from *Fundação para a Ciência e Tecnologia and* Ministério da Ciência, Tecnologia e

Ensino Superior (FCT/MCTES) through the projects UIDB/50006/2020 (https://doi.org/10.54499/UIDB/50006/2020) and UIDP/50006/2020 (https://doi.org/10.54499/UIDP/50006/2020). PROTEOMASS Scientific Society (Portugal) is acknowledged by the funding provided through the General Funding Grants 2022-2023, and by the funding provided to the Laboratory for Biological Mass Spectrometry Isabel Moura (#PM001/2019 and #PM003/2016). F.D. and J.G. thank FCT/MCTES (Portugal) for their doctoral grants 2021.05161.BD. and 2022.09495.BD., respectively. EO thanks FCT/MEC (Portugal) for the individual contract, CEECIND/05280/2022. H. M. S. and C. S. B. G. acknowledges the Associate Laboratory for Green Chemistry LAQV (LA/P/0008/2020 – https://doi.org/10.54499/LA/P/0008/2020) funded by FCT/MCTES for his research contract. This work is also developed and acknowledged by A.K. as part of contract BG-RRP-2.004-0002-C01, Laboratory of Organic Functional Materials (Project BiOrgaMCT), Procedure BG-RRP-2.004, Establishing of a network of research higher education institutions in Bulgaria", funded by BULGARIAN NATIONAL RECOVERY AND RESILIENCE PLAN". G. D. thanks to the European Regional Development Fund (Bulgaria) within the Operational Programme Science and Education for Smart Growth 2014 - 2020 under the Project Center of Excellence: National center of mechatronics and clean technologies - BG05M2OP001-1.001-0008 for the financial support. C. S. B. Gomes acknowledges the XTAL – Macromolecular Crystallography group (UCIBIO and i4HB) for granting access to the X-ray diffractometer. X-Ray infrastructure financed by FCT-MCTES through project RECI/BBBBEP/0124/2012.

Appendix A. Supplementary data

Supplementary data to this article can be found online at https://doi.org/10.1016/j.microc.2024.111237.

References

[1] I. Pisagatti, D. Crisafulli, A. Pappalardo, G. Trusso Sfrazzetto, A. Notti, F. Nastasi, M. F. Parisi, N. Micali, G. Gattuso and V. Villari, Photoinduced electron transfer in host-guest interactions of a viologen derivative with a didansyl-pillar[5]arene, *Mater. Today Chem.*, **24** (2022) 1000841, 10.1016/j.mtchem.2022.100841.

[2] E. O. Dare, V. Vendrell-Criado, M. C. Jiménez, R. Pérez-Ruiz and D. Díaz Díaz, Highly efficient latent fingerprint detection by eight-dansyl-functionalized octasilsesquioxane nanohybrids, *Dyes Pigm.*, **184** (2021) 108841, 10.1016/j.dyepig.2020.108841.

[3] F. Duarte, G. Dobrikov, A. Kurutos, J.L. Capelo-Martinez, H.M. Santos, E. Oliveira, C. Lodeiro, Development of fluorochromic polymer doped materials as platforms for temperature sensing using three dansyl derivatives bearing a sulfur bridge, J. Photochem. Photobiol. A Chem. 445 (2023) 115033, https://doi.org/10.1016/j.jphotochem.2023.115033.

[4] F. Duarte, G. Dobrikov, A. Kurutos, H.M. Santos, J. Fernández-Lodeiro, J.L. Capelo-Martinez, E. Oliveira, C. Lodeiro, Enhancing water sensing via aggregation-induced emission (AIE) and solvatofluorochromic studies using two new dansyl derivatives containing a disulfide bound: Pollutant metal ions detection and preparation of water-soluble fluorescent polymeric particles, Dyes Pigm. 218 (2023) 111428, https://doi.org/10.1016/j.dyepig.2023.111428.

[5] Z. Xu, M.X. Zhang, G. Li, X. Chen, S.H. Liu, H. Chen, J. Yin, Naphthalimide-sulfonamide fused dansyl-sulfonamide fluorescent probe for tracking glutathione of lysosome with a dual-emission manner, Dyes Pigm. 171 (2019) 107685, https://doi.org/10.1016/j.dyepig.2019.107685.

[6] H. Cheng, P. Ma, Y. Wang, G. Hu, S. Fang, Y. Fang, Y. Lin, Photoswitchable and Water-Soluble Fluorescent Nano-Aggregates Based on a Diarylethene-Dansyl Dyad and Liposome, Chem. Asian J. 12 (2017) 248–253, https://doi.org/10.1002/asia.201601501.

[7] Y. Pan, C. Zhang, S.H. Liu, Y. Tan, J. Yin, Fluorescent switch based on dithienylethene with dansulfonamide in multimedium, Dyes Pigm. 181 (2020) 108546, https://doi.org/10.1016/j.dyepig.2020.108546.

[8] Y. Cui, F. Li, X. Zhang, Controlling fluorescence resonance energy transfer of donor–acceptor dyes by Diels-Alder dynamic covalent bonds, Chem. Commun. 57 (2021) 3275–3278, https://doi.org/10.1039/d1cc00165e.

[9] Y. Zhang, B. Lei, X. Zhang, Reversible, controllable white-light emission of dye systems by dynamic covalent furan moiety exchange, Chem. Commun. 58 (2022) 5261–5264, https://doi.org/10.1039/d2cc01309f.

[10] J. Wang, X. Zhang, H.B. Liu, Highly sensitive pyrene–dansyl conjugate-based fluorescent sensor for discriminative detection of water in organic solvents, Dyes Pigm. 182 (2020) 108685, https://doi.org/10.1016/j.dyepig.2020.108685.

[11] S. Das, P. Sahoo, A colorimetric sensor for hydrogen sulfide: Detection from biogas and quantitative estimation in water, Sens Actuators B Chem 291 (2019) 287–292, https://doi.org/10.1016/j.snb.2019.04.089.

[12] D. Yang, X.T. Wu, X.J. Cao, B.X. Zhao, A reversible ratiometric fluorescence probe for fast detection of trace water in different organic solvents, Dyes Pigm. 170 (2019) 107558, https://doi.org/10.1016/j.dyepig.2019.107558.

[13] P. Srivastava, M. Verma, S. Sivakumar, A.K. Patra, A smart FRET probe exhibiting a molecular keypad lock device based on rapid detection of nitric oxide mediated by Cu2+ ion, Sens Actuators B Chem 291 (2019) 478–484, https://doi.org/10.1016/j.snb.2019.04.093.

[14] J. Gao, Y. He, Y. Chen, D. Song, Y. Zhang, F. Qi, Z. Guo, W. He, Reversible FRET Fluorescent Probe for Ratiometric Tracking of Endogenous Fe3+ in Ferroptosis, Inorg. Chem. 59 (2020) 10920–10927, https://doi.org/10.1021/acs.inorgchem.0c01412.

[15] P.P. Dash, A.K. Ghosh, P. Mohanty, R. Behura, S. Behera, B.R. Jali, S.K. Sahoo, Advances on fluorescence chemosensors for selective detection of water, Talanta 275 (2024) 126089, https://doi.org/10.1016/j.talanta.2024.126089.

[16] H. Sun, X.X. Tang, B.X. Miao, Y. Yang, Z. Ni, A new AIE and TICT-active tetraphenylethene-based thiazole compound: Synthesis, structure, photophysical properties and application for water detection in organic solvents, Sens Actuators B Chem 267 (2018) 448–456, https://doi.org/10.1016/j.snb.2018.04.022.

[17] H. Sun, X.X. Tang, R. Zhang, W.H. Sun, B.X. Miao, Y. Zhao, Z.H. Ni, Tetraphenylethene-substituted benzothiadiazoles: AIE and TICT properties, tunable intramolecular conjugation and application in detecting trace water in organic solvents, Dyes Pigm. 174 (2020) 108051, https://doi.org/10.1016/j.dyepig.2019.108051.

[18] L. Cai, X. Sun, W. He, R. Hu, B. Liu, J. Shen, A solvatochromic AIE tetrahydro[5]helicene derivative as fluorescent probes for water in organic solvents and highly sensitive sensors for glyceryl monostearate, Talanta 206 (2020) 120214, https://doi.org/10.1016/j.talanta.2019.120214.

[19] T. Yin, S. Zhang, M. Li, C. Redshaw, X.L. Ni, Macrocycle encapsulation triggered supramolecular pKa shift: A fluorescence indicator for detecting octreotide in aqueous solution, Sens Actuators B Chem 281 (2019) 568–573, https://doi.org/10.1016/j.snb.2018.10.136.

[20] H. Zhou, Y. Zhao, X. Chen, S. Zhang, Ultrafast spectroscopic studies of the pH responsive 9-acridinecarboxylic acid as a ratiometric and fluorescence lifetime pH indicator, Microchem J. 176 (2022) 107240, https://doi.org/10.1016/j.microc.2022.107240.

[21] S. Medel, E. Martínez-Campos, D. Acitores, E. Vassileva-Tonkova, I. Grabchev, P. Bosch, Synthesis and spectroscopic properties of a new fluorescent acridine hyperbranched polymer: Applications to acid sensing and as antimicrobial agent, Eur. Polym. J. 102 (2018) 19–29, https://doi.org/10.1016/j.eurpolymj.2018.03.008.

[22] J. Franco Pinto, A. Fillion, P. Duchambon, S. Bombard, A. Granzhan, Acridine–O^6-benzylguanine hybrids: Synthesis, DNA binding, MGMT inhibition and antiproliferative activity, Eur. J. Med. Chem. 227 (2022) 113909, https://doi.org/10.1016/j.ejmech.2021.113909.

[23] M. Vilková, M. Hudáčová, N. Palušeková, R. Jendželovský, M. Almáši, T. Béres, P. Fedoročko, M. Kožurková, Acridine Based N-Acylhydrazone Derivatives as Potential Anticancer Agents: Synthesis Characterization and ctDNA/HSA Spectroscopic Binding Properties, *Molecules* 27 (2022) 2883, https://doi.org/10.3390/molecules27092883.

[24] S. Zhang, H. Wu, C.S. Day, U. Bierbach, Platinum-Acridine Agents with High Activity in Cancers Expressing the Solute Carrier MATE1 (SLC47A1), ACS Med. Chem. Lett. 14 (2023) 1122–1128, https://doi.org/10.1021/acsmedchemlett.3c00266.

[25] E. Abdelaziz, N.M. El-Deeb, M.F. Zayed, A.M. Hasanein, I.E.T. El Sayed, E. I. Elmongy, E.A. Kamoun, Synthesis and *in*-vitro anti-proliferative with antimicrobial activity of new coumarin containing heterocycles hybrids, Sci Rep 13 (2023) 22791, https://doi.org/10.1038/s41598-023-50170-9.

[26] O. Sharhan, T. Heidelberg, N.M. Hashim, W.M. Al-Madhagi, H.M. Ali, Benzimidazolium-acridine-based silver N-heterocyclic carbene complexes as potential anti-bacterial and anti-cancer drug, Inorganica Chim. Acta 504 (2020) 119462, https://doi.org/10.1016/j.ica.2020.119462.

[27] L. Krause, R. Herbst-Irmer, G.M. Sheldrick, D. Stalke, Comparison of silver and molybdenum microfocus X-ray sources for single-crystal structure determination, J Appl Crystallogr 48 (2015) 3–10, https://doi.org/10.1107/S1600576714022985.

[28] G.M. Sheldrick, Crystal structure refinement with SHELXL, Acta Crystallogr C Struct Chem 71 (2015) 3–8, https://doi.org/10.1107/S2053229614024218.

[29] C.B. Hübschle, G.M. Sheldrick, B. Dittrich, ShelXle: a Qt graphical user interface for SHELXL, J Appl Crystallogr 44 (2011) 1281–1284, https://doi.org/10.1107/S0021889811043202.

[30] L. J. Farrugia, WinGX and ORTEP for Windows: an update, J Appl Crystallogr 45 (2012) 849–854. DOI:10.1107/S0021889812029111.

[31] C.F. MacRae, I. Sovago, S.J. Cottrell, P.T.A. Galek, P. McCabe, E. Pidcock, M. Platings, G.P. Shields, J.S. Stevens, M. Towler, P.A. Wood, Mercury 4.0: from visualization to analysis, design and prediction, J Appl Crystallogr 53 (2020) 226–235, https://doi.org/10.1107/S1600576719014092.

[32] S.J. Strickler, R.A. Berg, Relationship between Absorption Intensity and Fluorescence Lifetime of Molecules, J Chem Phys 37 (1962) 814–822, https://doi.org/10.1063/1.1733166.

[33] D. Macdougall, W.B. Crummett, Guidelines for data acquisition and data quality evaluation in environmental chemistry, Anal. Chem. 52 (1980) 2242–2249, https://doi.org/10.1021/ac50064a004.

[34] G.L. Long, J.D. Winefordner, Limit of Detection A Closer Look at the IUPAC Definition, Anal. Chem. 55 (1983) 713A–A724, https://doi.org/10.1021/ac00258a724.

[35] A.A. Taherpour, D. Kvaskoff, P.V. Bernhardt, C. Wentrup, 9-Azidoacridine and 9-acridinylnitrene, J Phys Org Chem 23 (2010) 382–389, https://doi.org/10.1002/poc.1657.
[36] C.R. Groom, I.J. Bruno, M.P. Lightfoot, S.C. Ward, The Cambridge Structural Database, Acta Crystallogr B Struct Sci Cryst Eng Mater 72 (2016) 171–179, https://doi.org/10.1107/S2052520616003954.
[37] P. Zhou, K. Han, Unraveling the Detailed Mechanism of Excited-State Proton Transfer, Acc. Chem. Res. 51 (2018) 1681–1690, https://doi.org/10.1021/acs.accounts.8b00172.
[38] G. Pedro, F. Duarte, G.M. Dobrikov, A. Kurutos, H.M. Santos, J.L. Capelo-Martínez, E. Oliveira, C. Lodeiro, Optical evaluation of dansyl derivatives and their implementation in low-cost and flexible dye-doped PMMA platforms for efficient detection of hazardous chemical vapours, Dyes Pigm. 224 (2024) 112042, https://doi.org/10.1016/j.dyepig.2024.112042.
[39] E. Jeong, S. Yoon, H.S. Lee, A. Kumar, P.S. Chae, TURN-ON fluorescence detection of cyanide using an ensemble system consisting of a dansyl-based cationic probe and dicyanovinyl derivative, Dyes Pigm. 162 (2019) 348–357, https://doi.org/10.1016/j.dyepig.2018.10.033.
[40] F. Hu, M. Cao, J. Huang, Z. Chen, D. Wu, Z. Xu, S.H. Liu, J. Yin, Sulfonamide and urea-based anions chemosensors, Dyes Pigm. 119 (2015) 108–115, https://doi.org/10.1016/j.dyepig.2015.03.036.
[41] S. Areti, S. Bandaru, D.S. Yarramala, C.P. Rao, Optimizing the Electron-Withdrawing Character on Benzenesulfonyl Moiety Attached to a Glyco-Conjugate to Impart Sensitive and Selective Sensing of Cyanide in HEPES Buffer and on Cellulose Paper and Silica Gel Strips, Ana.l Chem. 87 (2015) 12396–12403, https://doi.org/10.1021/acs.analchem.5b04085.
[42] L.L. Xi, X.F. Guo, C.L. Wang, W.L. Wu, M.F. Huang, J.Y. Miao, B.X. Zhao, A near-infrared ratiometric fluorescent probe for rapid and selective detection of hypochlorous acid in aqueous solution and living cells, Sens Actuators B Chem 255 (2018) 666–671, https://doi.org/10.1016/j.snb.2017.08.073.
[43] Z. Guo, Q. Wang, D. Zhou, Y. An, P. Wang, F. Liao, A novel peptide-based fluorescent probe with a large stokes shift for rapid and sequential detection of Cu^{2+} and CN^{-} in aqueous systems and live cells, Spectrochim Acta A Mol Biomol Spectrosc 264 (2022) 120257, https://doi.org/10.1016/j.saa.2021.120257.
[44] P. Gans, A. Sabatini and A. Vacca, Investigation of equilibria in solution. Determination of equilibrium constants with the HYPERQUAD suite of programs, *Talanta*, **43** (1996) 1739–1753. 10.1016/0039-9140(96)01958-3.
[45] B. González-Tobío, F. Duarte, A. Arribas-Delgado, C. Fernández-Lodeiro, J. Fernández-Lodeiro, M. Cano, C. Lodeiro, C. Cuerva, Tuning and reviving the luminescence of a new class of pyridyl β-diketonate Eu(III) metallomesogens: From molecules to entrapment in polymer particles, Dyes Pigm. 204 (2022) 110440, https://doi.org/10.1016/j.dyepig.2022.110440.
[46] P. She, Y. Li, Z. Li, S. Liu, Y. Yang, L. Li, L. Zhou and Y. Wu, Repurposing 9-Aminoacridine as an Adjuvant Enhances the Antimicrobial Effects of Rifampin against Multidrug-Resistant Klebsiella pneumoniae, *Microbiol. Spectr.*, 11:e04474-22, 10.1128/spectrum.04474-22.
[47] G.A. Marcelo, J. Galhano, M.P. Duarte, A. Kurutos, J.L. Capelo-Martínez, C. Lodeiro, E. Oliveira, Functional Cyanine-Based PVA:PVP Polymers as Antimicrobial Tools toward Food and Health-Care Bacterial Infections, Macromol. Biosci. 22 (2022) 2200244, https://doi.org/10.1002/mabi.202200244.
[48] S. Nuti, A. Fernández-Lodeiro, J. Galhano, E. Oliveira, M.P. Duarte, J.L. Capelo-Martínez, C. Lodeiro, J. Fernández-Lodeiro, Tailoring Mesoporous Silica-Coated Silver Nanoparticles and Polyurethane-Doped Films for Enhanced Antimicrobial Applications, Nanomaterials 14 (2024) 462, https://doi.org/10.3390/nano14050462.

.

B

Published Paper in Dyes and Pigments - Corresponding to Chapter 4

Dyes and Pigments 243 (2025) 113088

Contents lists available at ScienceDirect

Dyes and Pigments

journal homepage: www.elsevier.com/locate/dyepig

A dual-responsive Dansyl–Naphthalimide system for Hg(II) CHEF detection and ligand-mediated Cu(II) reduction with catalytic relevance

Frederico Duarte [a], Diogo Torres [a], Georgi M. Dobrikov [b,c,*], Atanas Kurutos [b,d,**], Luisa B. Maia [e], Oleksandr Bondarchuk [f], Ivaylo Slavchev [b], Jose Luis Capelo-Martínez [a,g], Hugo M. Santos [a,g], Carlos Lodeiro [a,g,***]

[a] BIOSCOPE Research Group, LAQV-REQUIMTE, Chemistry Department, NOVA School of Science and Technology, FCT NOVA, Universidade NOVA de Lisboa, 2829-516, Caparica, Portugal
[b] Institute of Organic Chemistry with Centre of Phytochemistry, Bulgarian Academy of Sciences, Acad. G. Bonchev Str., Bl. 9, 1113, Sofia, Bulgaria
[c] National Centre of Excellence Mechatronics and Clean Technologies, Sofia, Bulgaria
[d] University of Chemical Technology and Metallurgy, 8 St. Kliment Ohridski Blvd, 1756, Sofia, Bulgaria
[e] LAQV-REQUIMTE, Chemistry Department, NOVA School of Science and Technology, FCT NOVA, Universidade NOVA de Lisboa, 2829-516, Caparica, Portugal
[f] International Iberian Nanotechnology Laboratory - INL, Avenida Mestre José Veiga S/n, 4715-330, Braga, Portugal
[g] PROTEOMASS Scientific Society, 2825-466, Caparica, Portugal

ARTICLE INFO

Keywords:
Dansyl
Naphtilimide
Copper(II)
Mercury(II)
Sensing
Ligand-mediated reduction

ABSTRACT

We report a compelling structure–property relationship in a series of four naphthalimide-derived ligands, engineered for the selective and differential detection of Hg(II) and Cu(II) ions. By integrating a dansyl moiety, we induce intramolecular electron transfer that gives rise to two non-redox-innocent dyad systems. Notably, the detection of Hg(II) operates through a rare chelation-enhanced fluorescence (CHEF) mechanism, an unusual pathway considering the heavy atom effect typically associated with mercury. In contrast, the Cu(II) dyads reveal striking reduction of Cu(II) to Cu(I) in solution, driven by ligand-to-metal electron transfer, as conclusively demonstrated via EPR and XPS analysis. Furthermore, introducing a catalytic substrate probe highlights that this redox transformation is the bottleneck in catalytic efficiency. These findings provide deep mechanistic insights and position these ligands as versatile platforms for dual-mode ion sensing and redox-responsive catalysis.

1. Introduction

The design of luminescent probes for heavy and transition metal ions detection have gathered substantial attention due to their impact in environmental and biological assays [1]. Among these metal ions, divalent copper is known for being the third most abundant metal ion in the human body which are crucial in a wide range of biological processes and is linked to neurodegenerative illnesses [2–4]. In turn, high toxicity is the main reason why there is a constant demand for the monitorization of mercury in the environment in order to remediate the potential threat to public health [1,5–7].

In light of the considerable progresses over the decades, dansyl and naphthalimide derivatives have been consistent fluorophores exhibiting strong biocompatibility and reliable photophysical properties. High fluorescence quantum yields, large Stokes shift and solvatochromic behavior are common characteristics related to dansyl derivatives while the tunable emission profiles of naphthalimide dyes by simple modification of the core offer the novelty and versatility as sensors towards heavy and transition metal ions [1,8,9]. Notably, the use of these dyes towards Cu(II) [10–25] and Hg(II) [6,7,26–33] are well entrenched in the literature. However, the main strategies employed for these systems often rely only on fluorescence changes in single-emission windows that

* Corresponding author. Institute of Organic Chemistry with Centre of Phytochemistry, Bulgarian Academy of Sciences, Acad. G. Bonchev Str., Bl. 9, 1113 Sofia, Bulgaria
** Corresponding author. Institute of Organic Chemistry with Centre of Phytochemistry, Bulgarian Academy of Sciences, Acad. G. Bonchev Str., Bl. 9, 1113 Sofia, Bulgaria
*** Corresponding author. BIOSCOPE Research Group, LAQV-REQUIMTE, Chemistry Department, NOVA School of Science and Technology, FCT NOVA, Universidade NOVA de Lisboa, 2829-516 Caparica, Portugal.
E-mail addresses: Georgi.Dobrikov@orgchm.bas.bg (G.M. Dobrikov), atanas.kurutos@orgchm.bas.org (A. Kurutos), cle@fct.unl.pt (C. Lodeiro).

https://doi.org/10.1016/j.dyepig.2025.113088
Received 21 June 2025; Received in revised form 30 July 2025; Accepted 30 July 2025
Available online 5 August 2025
0143-7208/© 2025 The Authors. Published by Elsevier Ltd. This is an open access article under the CC BY-NC-ND license (http://creativecommons.org/licenses/by-nc-nd/4.0/).

may be hindered by environmental effects. Consequently, an increase in demand for the design of more efficient sensors that provide signal fidelity, dual-channel or ratiometric approaches have become more frequent to provide high signal-to-noise ratio and mitigate environmental interference [1,8]. Dual fluorescence probes emerge as optimal choices providing a broader window of emission with enhanced fluorescence signal modalities. Some examples explore the utility of both dansyl and naphthalimide fluorophores as excited dye donors towards Föster resonance energy transfer (FRET) systems for metal ion sensing in conjunction with rhodamines [1,5,34–38] as well as other dyes across diverse applications [8,39–42].

When considering the most desirable fluorescent sensor for metal ions, one may consider those that display chelation-enhanced fluorescence (CHEF) the best suited. However, the large spin-orbit coupling constant of Hg(II) and the paramagnetic nature of Cu(II) causes the majority of sensors towards these metals to be "turn-off" in nature [43]. Some of the aforementioned dyad systems avoid these hindrances due to the initial presence of a photoinduced electron-transfer (PeT) effect [1,5,35] that prevents an excited electron to relax radiatively to ground state since an electron from a lone pair that is higher in energy drops to the SOMO-H of the fluorophore. The coordination of the metal ion can stabilize the donor orbital lowering its energy below from the ground state restoring fluorescence with a few examples of this behavior applied in dansyl systems for the detection of Hg(II) [43–45]. Furthermore, strategic multiple-ion-responsive sensors with built-in selective and differential detection are of upmost importance with several examples reported in the literature towards Cu(II) and Hg(II) [46–48].

Among the transition-metal compounds, in some cases, it is possible to observe reversible intramolecular electron-transfer between the metal and the ligand provided that the two electronic states are close-lying, energetically speaking. Valence tautomerism or redox isomerism rises from this notion when one or more non-redox-innocent ligand coordinates with a redox-active metal center and are capable of reversibly shift the electronic charge distribution [49,50]. However, electron delocalization must be avoided so that the two valence tautomers can be differentiated. Such processes of charge-distribution expand the scope and applicability since these systems are provided with unique physical properties and are found in nature in enzymatic processes [51]. The most known valence tautomeric systems are found for cobalt using dioxolane ligands accompanied with fewer examples of other metal complexes such as manganese, nickel, iron, ruthenium and others [50,52–54]. Copper can also form valence tautomerism since electronic and structural changes between Cu(I) and Cu(II) can create a barrier in energy sufficient enough to prevent charge delocalization so that they can be distinguishable. However, examples that fall outside of dioxolane and related structures are considered as rather rare [49,51,55]. Furthermore, copper shows some advantages over other metals in terms of catalysis since it is more cost-effective and has garnered industrial interest. For this reason, copper-catalyzed cross coupling Ullmann type reactions have become a very useful process to build several types of bonds while ancillary chelating ligands have brought reliability and mildness to these systems [56–58].

In this work, four new naphthalimide derived compounds (Scheme 2, **L1** to **L4**), from which two are dansyl-substituted dyad systems were successfully synthesized. Exploration of the interaction between dansyl and naphthalimide in dyad systems, to the best of our knowledge, is not well explored with only a handful works reported [59–62]. Bearing this in mind, efforts have been put forth to establish a structure/photophysical properties relation by intentional modification of the naphthalimide core and the presence or absence of the dansyl moiety. The complete characterization of the photophysical properties in a diverse array of solvents provided the foundation for the use of the Kamlet-Taft equation to assess the solvatochromism behavior of these systems. Due to the existence of well-defined coordination sites, these fluorophores have been tested for differential detection of metal ions owing to the occurrence of energy transfer processes in dual fluorescence probes. The determination of association constants and sensing limit parameters along with metal ion selectivity experiments were implemented. ESI-HRMS was employed to follow the complex formation in solution and to compare with the synthesized isolated complexes. Moreover, electron paramagnetic resonance spectroscopy (EPR) and X-ray Photoelectron Spectroscopy (XPS) were deemed beneficial for the elucidation of the ligand-mediated chemical reduction between the dyad systems and Cu^{2+} ions. Finally, the integration of iodophenyl moiety was found fruitful to establish the usefulness of these dyad compounds as ancillary chelating ligands for copper-catalyzed reactions.

2. Results and discussion

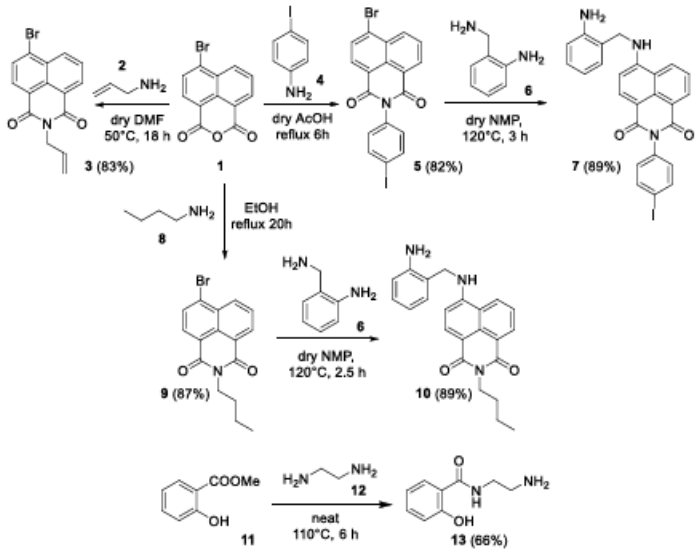
2.1. Synthesis

For the preparation of the target compounds (**L1**-**L4**), intermediates **3**, **5**, **7**, **9**, **10** and **13** were synthesized as shown in Scheme 1. Compound of **3** (83 %) was synthesized starting from **1** and **2** in dry DMF according to a protocol reported in the literature [63–65]. The synthesis of compound **5** was described by Benati et al. [66] and Chinapang et al. [67], however our attempt furnished **5** in increased yield (82 % after crystallization). Naphthalimide **7** (89 % after crystallization) is a new compound, though an analogue is described elsewhere [68]. Synthesis of bromide **9** from **1** and amine **8** was described in multiple studies, nevertheless we followed the procedure of Lim et al. [69] as the most suitable for our investigation (almost quantitative yield of **9**). Since **9** is well characterized, we performed only ^{1}H NMR spectra to confirm its chemical structure. Like compound **7**, intermediate **10** (89 % after column chromatography) was prepared from **9** and the diamine **6** in dry *N*-methylpyrrolidone. As a new compound, it was fully characterized by various 1D and 2D NMR techniques (Figures SX 1-129, Supplementary Material), melting point temperatures, and mass spectra. Although existing literature synthetic procedures report low yielded [70–72], amine **13** was readily prepared by heating of methyl salicylate (**11**) with ethylenediamine (**12**) under solvent free conditions. Compound **13** was purified by column chromatography and isolated in good yield (66 %).

The target compounds **L1** and **L2** were prepared by heating the intermediate **7** in dry pyridine with sulfonyl chlorides **14** and **15**, respectively (Scheme 2). **L1** (54 %) and **L2** (77 %) were isolated after silica gel column chromatography. Ligand **L3** was prepared from **10** and dansyl chloride (**14**) by using the same procedure, as in case of **L1** and **L2**. However, the yield of compound **L3** (23 %) was significantly decreased, due to the need of implementation of triple column chromatography. The synthetic approach to the preparation of **L4** (14 %) involves the use of intermediates **3** and **13**. The reaction was performed in dry 2-methoxyethanol at 110 °C (Scheme 2). The target compounds **L1**-**L4** as well as all new intermediate products were fully characterized by 1D and 2D NMR spectroscopic techniques (Figs. S1–129, Supplementary Material), HRMS and melting point temperatures.

2.2. Photophysical characterization

The conjugated dansyl-naphthalimide and single naphthalimide derived compounds manifest luminescent properties both in solution and in the solid state. Fig. 1 compiles the molecular structure accompanied by the photoluminescent data of all compounds in acetonitrile recorded at 298 K as a representative example (Figure S5-S8) while Table 1 exhibits all the photophysical data of the compounds under investigation. The UV–Vis spectra in acetonitrile shows an absorption band maximum centered at 425 and 429 nm, contributing to the display of yellow solutions to the naked eye. Upon excitation at the appropriate wavelength, the samples emit a greenish yellow light with a maximum allocated around 515 nm resulting in a Stokes shift between 4150 and 3854 cm^{-1}. On a relatable note, significant disparities can be noted regarding the solid-state emission spectra since compounds **L1** to **L3**



Scheme 1. Synthesis of intermediates **3**, **5**, **7**, **9**, **10** and **13**.

progressively display a red-shifted wide band centered at 528, 535 and 546 nm as in solution is concerned, while the opposite is found for **L4**, a clear, blue-shifted emission is observed with an emission maximum of 476 nm.

Overall, from a quantum yield perspective, higher values were obtained in the case of **L2** and **L4**, reaching values up to 69 % in THF, while for **L1** and **L3** the presence of the dansyl unit translates a lower general trend of values, being the fluorescent mechanism most efficient in chloroform. Single digit nanosecond times were obtained from lifetime measurements for the majority of solvents being **L1** and **L3** the ones that present more variability as each solvent is considered while more prevalent values were found for **L2** and **L4**.

Considering the well-documented solvatochromic behavior of dansyl and naphthalimide derivatives and given the visually detected solvent dependent color change under UV lamp (Fig. 1f and g), compounds **L1** to **L4** manifest positive solvatochromism due to the change in color from green to yellow with increasing solvent polarity. In line with these observations, efforts have been made to fully characterize the occurring solvent-compound interactions, and for this, three solute-dependent parameters (υ_0, a, b and p) have been determined through the multiparametric fitting of the Kamlet-Taft equation (Equation (1)).

$$\upsilon = \upsilon_0 + a\alpha + b\beta + p\pi^* \quad \text{(Equation 1)}$$

Where υ_0 represents the wavenumber value in a reference solvent; parameters a, b and p are obtained through multiple regression analysis that reflect the underlying sensitivity of the probes photophysical behavior to solvent polarity; α: hydrogen bond donor acidity (HBD); β: hydrogen bond acceptor basicity (HBA); π^*: stabilization of a charge or dipole without a specific dielectric interaction (Table S1) [73,74].

Table 2 summarizes the reference wavenumber value υ_0, the fitted parameters (a, b and p) alongside the slopes and correlation coefficients obtained through the fitting of a linear plot of $\upsilon_{exp.}$ versus υ_{calc}, by applying the Kamler-Taft model excluding acetonitrile.

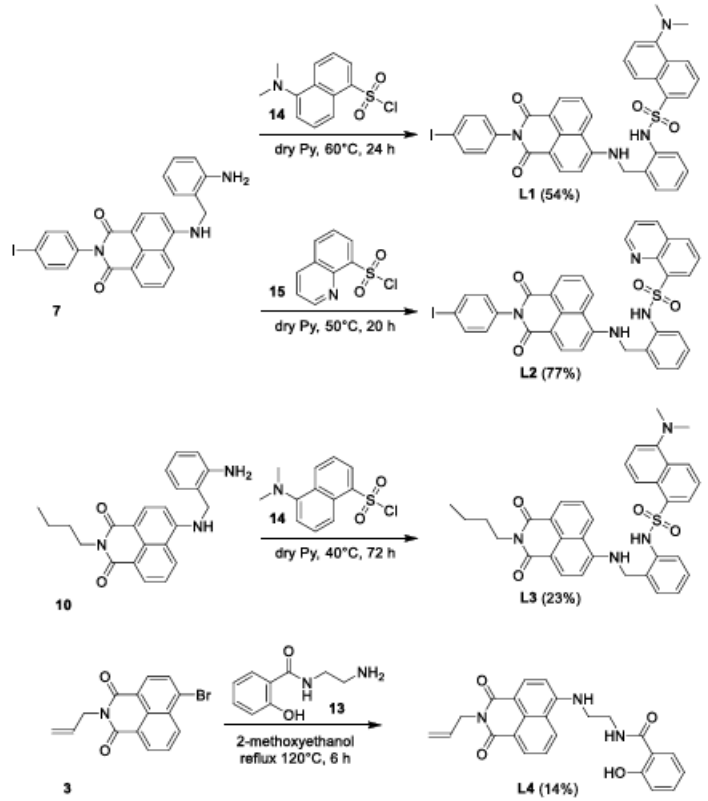
Interestingly, all compounds present negative values of both a and b parameters, however, key inferences can be considered by comparing the dual and single chromophoric compounds. While the hydrogen bond donor sensitivity is roughly the same for **L1**, **L3** and **L4**, compound **L2** is 2-fold more susceptible to being influenced by protic solvents due to the quinoline group. Differences also rise in terms of sensitivity towards hydrogen bond acceptor interactions. Compound **L1** and **L3** are two-fold and three-fold less prone to be afflicted by the basic character of the solvent in regard to **L2** and **L3**, respectively. Finally, large negative p values indicate that the excited state of all compounds can be stabilized to the same degree by highly polarizable solvents.

2.3. Metal ions sensing

Given the extensive literature on the application of dansyl and naphthalimide derivatives towards the sensing of metal ions and presence of well-defined coordination sites of the compounds in investigation, additions in acetonitrile of 1, 5 and 10 equivalents Ca^{2+}, Co^{2+}, Ni^{2+}, Cu^{+}, Cu^{2+}, Zn^{2+}, Ag^{+}, Cd^{2+}, Hg^{+}, Hg^{2+} and Pb^{2+} were performed. Fig. 2 contains the normalized intensities at 515 and 513 nm of compounds **L1** and **L4** upon addition of each metal ion while **L2** and **L3** can be seen in .Figure S10

All compounds show sensitivity towards Cu^{2+} and Hg^{2+} metal ions, however, it is noteworthy to highlight a chelation enhancement of fluorescence of **L1** and **L3** towards Hg^{2+} while the exact opposite was found in the case of compound **L2** and **L4**. It is noteworthy to highlight a shift of the emission band of **L4** to 493 nm towards the sensing of Hg^{2+} that can be seen in Figure S9 and will be discussed further ahead. In terms of Cu^{2+} a general quenching of the emission was observed across all compounds.

In line with the previous results, Fig. 3 exhibits the spectrophoto- and spectrofluorimetric titrations in response to increasing concentrations of Hg^{2+} and Cu^{2+} for **L1** and **L4**, and Figure S11 for **L2** and **L3**. Overall, consecutive additions of Hg^{2+} ions cause a relative no change of the absorbance maxima centered at 425 nm for **L1** while simultaneously a gradual increase of the emission intensity is observed maintaining its maximum at around 515 nm. This change is associated with an increase in the quantum yield from 7.5 % to 24.6 % and a fluorescence decay of 9.36 ns representing an almost 2-fold increase (Fig. 3a). A similar behavior was observed for **L3** with an increase in the quantum yield to



Scheme 2. Synthetic approach to the preparation of the target compounds **L1**-**L4**.

31.5 % with the same 2-fold increase in fluorescence decay to 9.31 ns (Figure S11). ESI-HRMS elucidates the formation of 2:1 (L:M) complex for **L1** (Figure S12; $[M+H]^+$ for $C_{74}H_{56}HgI_2N_8O_8S_2$ = 1705.1542 *m/z* (0.002 ppm). Calculated $[M+H]^+$ for $C_{74}H_{56}HgI_2N_8O_8S_2$ = 1705.154197 *m/z*) while a 1:1 complex has been detected for **L3** (Figure S13; $[M+H]^+$ for $C_{35}H_{32}HgN_4O_4S$ = 807.1928 *m/z* (0.05 ppm). Calculated $[M+H]^+$ for $C_{35}H_{32}HgN_4O_4S$ = 807.192756 *m/z*)

The absorption response of **L1** and **L3** during the batch titration recorded 24 h after the addition increments of 0.5 eq. of Cu^{2+} until 7 eq. and 8 eq., respectively, showed the continuous decrease of the 425 nm band leading to the emergence of a band centered at 500 nm while a quenching of the emission was observed (Figure S14). When viewed by the unaided eye a progressive transition from yellow to pink solution was evident. To better characterize this behavior the progression of the absorption profile through time was recorded and is expressed in Fig. 3b and Figure S11 for **L1** and **L3**, respectively. The results suggest the same general trend observed for the batch titration with a bathochromic shift of the absorption profile, which stabilizes around 220 min past the addition. Taking into consideration the time lapse, the formation of a complex with an inferior molecular weight than the original ligand has been found for **L1** (Figure S15; ESI-HRMS $[M+H]^+$ for $C_{39}H_{31}CuN_5O_5S$ = 745.1415 *m/z* (0.05 ppm). Calculated $[M+H]^+$ for $C_{39}H_{31}CuN_5O_5S$ = 745.141464 *m/z*) whereas for **L3**, the complex found shows no signs of ligand's cleavage at the same timepoint (Figure S16; ESI-HRMS $[M+Na]^+$ for $C_{35}H_{32}CuN_4O_4S$ = 690.1332 *m/z* (−0.07 ppm). Calculated $[M+Na]^+$ for $C_{35}H_{32}CuN_4O_4S$ = 690.133245 *m/z*) Although a better understanding of this phenomenon will be discussed and supported further ahead, early indications suggest that the iodophenyl moiety suffers changes in result of the complexation with Cu^{2+}. However, this has not demonstrated to be the limiting factor on the colorimetric response since in the absence of the iodophenyl moiety, **L3** showed the same behavior.

The introduction of the quinoline moiety in place of the dansyl unit in compound **L2** gives a stark contrast in the sensing mechanism of the aforementioned metal ions (Figure S11). In the case of Hg^{2+}, a generic quenching of the emission is observed with very few changes to the absorption profile. For Cu^{2+} an attenuation of the 427 nm absorption band and the formation of a band at around 370 nm in parallel with the quenching of the emission is observed. In this case, no changes in the resulting transparent solution of **L2** were detected in the upcoming hours after the experiment took place, highlighting the necessity for the presence of the dansyl moiety in both the turn-on effect and the colorimetric response. Complexation in 1:1 ratio has been found towards Hg^{2+} (Figure S17; ESI-HRMS $[M+H]^+$ for $C_{34}H_{21}HgIN_4O_4S$ = 911.0111 *m/z* (−0.03 ppm). Calculated $[M+H]^+$ $C_{34}H_{21}HgIN_4O_4S$ = 911.011127 *m/z*) and Cu^{2+} (Figure S18; ESI-HRMS $[M+H]^+$ for $C_{34}H_{21}CuIN_4O_4S$ = 771.9690 *m/z* (−0.9 ppm). Calculated $[M+H]^+$ $C_{34}H_{21}CuIN_4O_4S$ = 771.969698 *m/z*). Some attention should be given to the fact that, in contrast to the case of **L1**, the iodophenyl moiety of **L2** maintained its integrity demonstrating a close association between the distinct

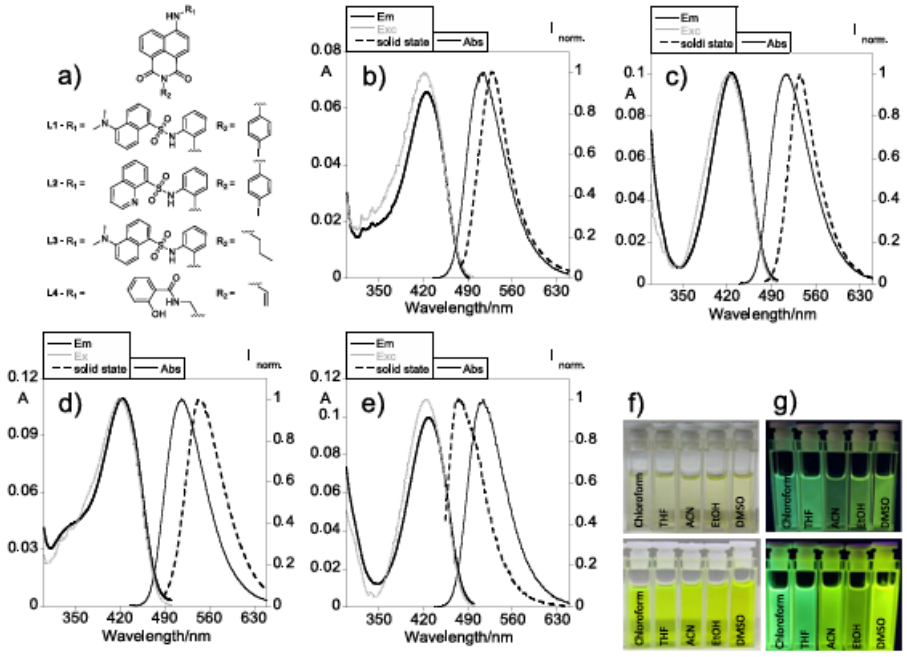


Fig. 1. (A) Molecular structure of dual dansyl-naphthalimide and naphthalimide derived compounds **L1** to **L4**. Photophysical characterization of compounds **L1** to **L4** ((b) to (e)) in acetonitrile ([**L1**] to [**L4**] = 5 μM). Images under natural light (left) and irradiated under UV light (right) for (f) **L1** and (g) **L4** in different solvents, as representative example.

Table 1
Absorption maximum wavelength in solution (λ_{abs}), emission maximum wavelength in solution (λ_{em}), molar absorption coefficients (ε), Stokes shift ($\Delta\lambda$), fluorescence quantum yields (ϕ), emission maximum in the solid state (λ_{em}^{Solid}), fluorescence lifetimes (τ) for compounds **L1** to **L4** in various solvents.

Cpd.	Solv.	λ_{abs} [nm]	λ_{em} [nm]	ε (10^4) [cm^{-1} M^{-1}]	Stokes shift [cm^{-1}]	ϕ (%)	λ_{em}^{Solid} [nm]	τ[ns]
L1	DMSO	437	520	2.18	3652	15	528	5.9
	EtOH	439	521	1.99	3585	18		6.7
	CH_3CN	425	515	2.15	4111	7.5		3.3
	THF	425	497	1.70	3408	24		5.3
	$CHCl_3$	422	502	2.04	3776	33		7.1
L2	DMSO	438	521	2.09	3637	46	535	8.5
	CH_3CN	427	513	1.92	3926	35		7.5
	THF	427	498	1.74	3338	39		6.7
	$CHCl_3$	430	505	1.61	3453	53		8.0
L3	DMSO	448	516	2.17	2942	4.3		5.9
	EtOH	438	518	2.23	3526	20		7.1
	CH_3CN	425	516	2.16	4150	8.4	546	3.2
	THF	424	494	1.90	3342	26		5.6
	$CHCl_3$	418	499	1.51	3883	32		7.3
L4	DMSO	442	524	1.84	3540	43	476	10.3
	EtOH	438	523	1.61	3710	37		9.2
	CH_3CN	429	514	1.85	3854	44		10.4
	THF	426	497	1.81	3353	69		9.3
	$CHCl_3$	427	494	1.98	3176	42		9.1

properties of **L1** and Cu^{2+} ions.

Furthermore, the sensing abilities of compound **L4** towards Hg^{2+} ions are characterized by the progressive formation of a red-shifted band with a maximum centered at 465 nm accompanied by a shoulder at 445 nm. With respect to the emission spectra, a progressive quenching on its intensity is observed with the emergence of an emission maximum at 493 and a shoulder at 518 nm. Fluorescence decay curves set the initial emission with a lifetime of 10.4 ns that after addition of Hg^{2+} ions decreases to a lifetime value of 5.1 ns. The formation of a 1:1 complex towards Hg^{2+} has been detected using **L4** (Figure S19; ESI-HRMS $[M+H]^+$ for $C_{24}H_{19}HgN_3O_4$ = 616.1159 *m/z* (0.02 ppm). Calculated $[M+H]^+$ for $C_{24}H_{19}HgN_3O_4$ = 616.115890 *m/z*) The sensing capabilities of **L4** towards Cu^{2+} focus on the suppression of the absorption band and the rise of a new band centered at 350 nm while a continuous quenching

Table 2
Independent fluorescence wavenumber ($\upsilon 0$), solvent polarity (p), HBD (a), HBA (b), slope and coefficient (R^2) of the linear fitting plot $\upsilon_{exp.}$ versus $\upsilon_{calc.}$

	υ_0	a	b	p	Slope	R [2]
L1	21474	−1053	−481	−1878	1.00	1.00
L2	21500	−2134	−753	−1733	1.00	1.00
L3	21556	−1066	−468	−1821	1.00	1.00
L4	21855	−979	−1167	−1884	1.00	1.00

of the emission is observed until the addition of 10 eq. of the metal ion. For this case, ESI-HRMS suggests a 2:1 complex (Figure S20; ESI-HRMS $[M+H]^+$ for $C_{48}H_{40}CuN_6O_8$ = 892.2277 m/z (0.07 ppm). Calculated $[M+H]^+$ for $C_{48}H_{40}CuN_6O_8$ = 892.227636 m/z).

Given the results observed for the dyad systems **L1** and **L3**, we propose that these compounds manifest a photoinduced electron transfer in solution, the coordinating Hg^{2+} metal ion subsequently stabilizes the donor orbital lowering its energy further below from the ground state preventing PeT and restoring fluorescence. Hyunjung Lee et al. [43] highlighted this reasoning in modulating the fluorescence properties of Hg^{2+} complexes with also several examples reported in the literature of the turn-on sensing of Hg^{2+} [75]. In accordance with these observations and keeping in mind that PeT behavior can also be mitigated by protonation, several eq. additions of H^+ were performed for **L1** and **L3** demonstrating the same increase in fluorescence (Figure S21). Lifetime measurements help consolidate these findings with very similar increases of the decay's curves to 9.34 and 9.47 ns for **L1** and **L3**, respectively, a phenomenon much comparable as observed towards Hg^{2+} ions.

These factors facilitate the comprehension of the highly coveted potential to detect both Hg^{2+} and Cu^{2+} in the same system without falling in the predicament of the "turn-off" behavior due to the large spin-orbit coupling constant of Hg^{2+} and the paramagnetic nature of Cu^{2+}. The incorporation of the dansyl unit enables dual-function sensing: a "turn-on" fluorescence response for Hg^{2+} detection and a distinct colorimetric response for Cu^{2+} with the overall detection mechanisms depicted in Fig. 4. The colorimetric detection of Cu^{2+} will be discussed in more detail further ahead.

2.4. Anti-interference performance in Hg^{2+} detection

The interference effect that metal ions might promote on the turn-on detection ability of **L1** and **L3** for Hg^{2+} has been investigated by the addition of 10 eq. of each metal to a solution of each compound already containing 5 eq. of Hg^{2+}. As shown in Fig. 5 and Figure S22, the Hg^{2+} dependent fluorescence emission was not significantly altered by the presence of Ca^{2+} and the transition metal ions Co^{2+}, Ni^{2+}, Cu^{+}, Zn^{2+}, Ag^{+}, Cd^{2+}, Hg^{+}, and Pb^{2+} except for Cu^{2+} that causes a decrease in the enhanced fluorescent response towards Hg^{2+}. This behavior could be attributed to the paramagnetic nature of Cu^{2+} that may interact to different sites in the molecule or accept electrons from fluorophore's excited state. Furthermore, compound **L3** was found susceptible to water molecules in which Hg^{+} and Pb^{2+} were dissolved, exhibiting interference on the interpretation of these metal ions.

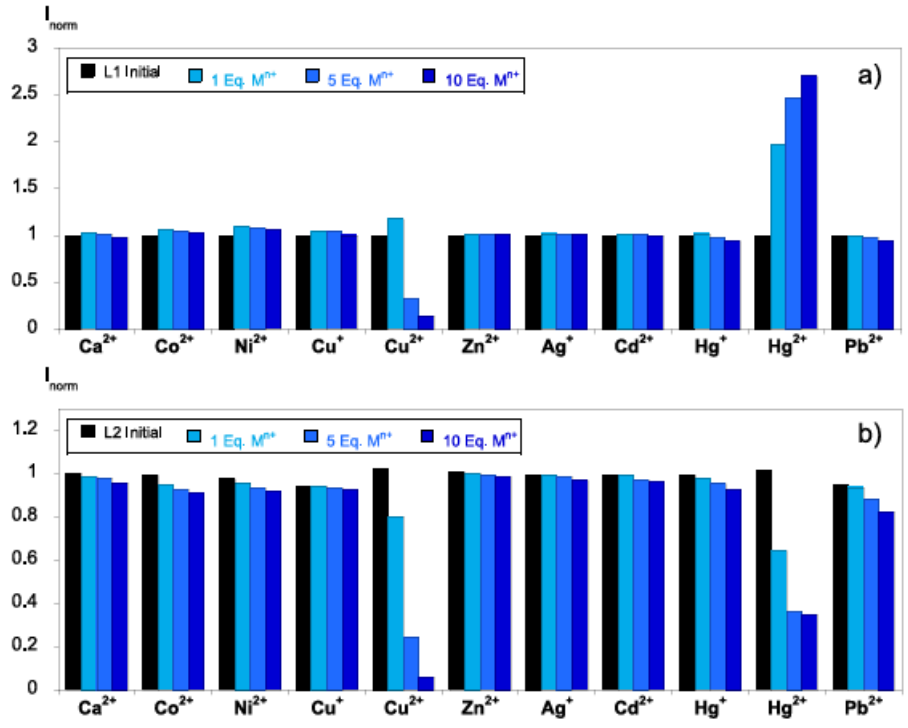


Fig. 2. Normalized emission intensity of **L1** (a) and **L4** (b) upon addition of 1, 5, and 10 equivalents of Ca^{2+}, Co^{2+}, Ni^{2+}, Cu^{+}, Cu^{2+}, Zn^{2+}, Ag^{+}, Cd^{2+}, Hg^{+}, Hg^{2+} and Pb^{2+} metal ions. ([**L1**] = [**L4**] = 10 μM, λ_{emL1} = 515 nm, λ_{emL4} = 513 nm, T = 298 K).

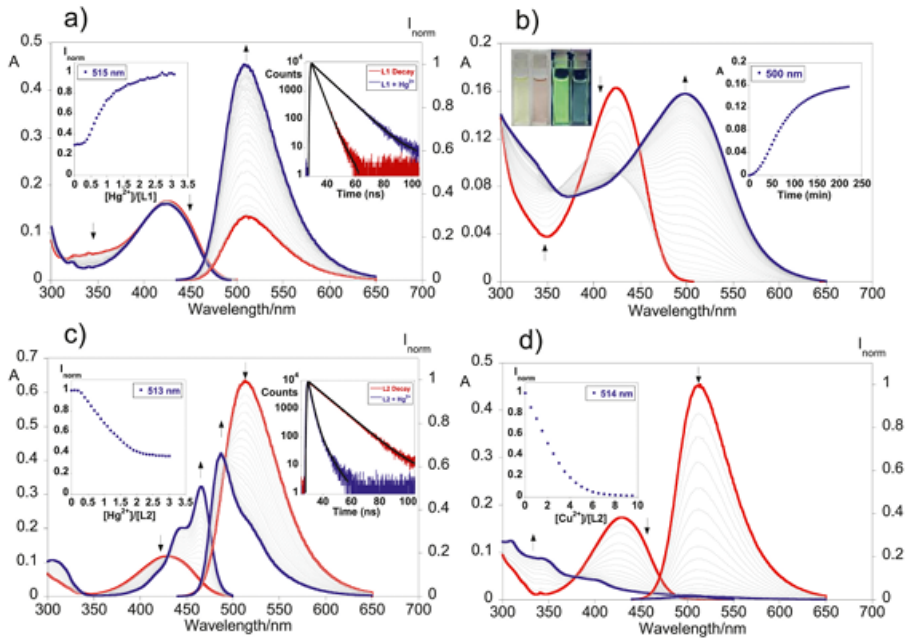


Fig. 3. UV–Vis and luminescent titration of compound **L1** (a) upon continuous 10 μL additions of Hg^{2+} ([**L1**] = 10 μM; [Hg^{2+}] = 0.225 mM). The inset represents the emission of [Hg^{2+}]/[**L1**] at 515 nm (left) and the time-resolved fluorescence decay profile of **L1** before and after the titration with Hg^{2+} ions (right). UV–vis time continuous spectra of **L1** (b) after the addition of 7 eq. of Cu^{2+} ([**L1**] = 10 μM). The inlet represents the images under natural light and UV light (left) and the time-dependent response of the absorbance at λ = 500 nm (right). UV–Vis and luminescent titration of compound **L4** (c) upon continuous 10 μL additions of Hg^{2+} ([**L4**] = 5 μM; [Hg^{2+}] 0.15 mM). The inlet represents the emission of [Hg^{2+}]/[**L4**] at 513 nm (left) and the time-resolved fluorescence decay profile of **L4** before and after the titration with Hg^{2+} ions (right). UV–Vis and luminescent titration of compound **L4** (d) upon continuous 10 μL additions of Cu^{2+} ions ([**L4**] = 10 μM; [Cu^{2+}] = 1.5 mM). The inlet represents the emission of [Cu^{2+}]/[**L4**] at 514 nm. For clarity of the reader the red spectrum represents the initial spectrum and the blue at the end point of the titration while the black curves in the fluorescent decay profile represent the fitting obtained. (For interpretation of the references to color in this figure legend, the reader is referred to the Web version of this article.)

2.5. Determination of association constants and sensing limit parameters

In order to completely assess the sensing ability of all compounds towards Hg^{2+} and Cu^{2+}, the HypSpec software [76] was used for the evaluation of the stability constants. Also, the determination of the detection and the quantification limit parameters towards both metal ions has been fulfilled. The association constants, LOD and LOQ are summarized in Table 3.

Table 3 reveals the association constants considering the stoichiometry 2:1 and 1:1 (L:M) for Hg^{2+} and Cu^{2+} in accordance with the data obtained from mass spectrometry for complex formation is concerned. The constants that relate to the stoichiometry of 2:1 were found to be very similar using **L1** and **L4** for Hg^{2+} and Cu^{2+}, respectively. Among the remaining systems, stoichiometry 1:1 was prevalent, attributing to **L2** the highest association constant towards Hg^{2+} with an association constant of 5.54 ± 0.03. In terms of LOD and LOQ, values were found to range between 1 to 8 and 2–12 μM, respectively, attributing the lowest values for the sensing of Hg^{2+} using **L3**.

2.6. Characterization of L1 and L3 complexes with Hg^{2+} and Cu^{2+}

Given the extensive studies in solution that provided the complete framework for the differentiation towards the sensing of Hg^{2+} and Cu^{2+} using **L1** and **L3**, our interest shifted in the direction of obtaining the complexes in solid form. All complexes were successfully synthesized, and a complete description of the procedures can be found in the experimental section.

The structural characterization of the complexes was achieved by FTIR and the proposed formulations were also confirmed by HRMS. The solid-state FTIR spectra of **L1** and **L3** provided the expected bands for the dansyl and naphthalimide moieties (Figures S22-S27). Complexes of **L1** showed the broadening of the 3500 to 3000 cm^{-1} regions especially the band dedicated to the ν(*N*–H) with the unchanged profile of the dicarboximide group, between 1680 and 1575 cm^{-1}, suggesting the well stablished coordination site of the secondary amines spacer. Furthermore, the dedicated region for the ν(S=O) + ν(C–N) bands, between 1350 and 1130 cm^{-1}, showed an increase in strength due to the presence of the triflate counterion, consolidating this finding. Concerning the Cu^{2+} complex, the increase of the bands at 2915 and 2850 cm^{-1} suggests a change in the molecular structure. The ESI-HRMS spectrum suggests the formation of a 2:1 (L:M) Hg^{2+} complex with a *m/z* of 1706.1620 (Figure S29) in accordance with the findings in solution. In turn, a smaller ion than the ligand with a *m/z* of 747.1571 (Figure S30) was found for the Cu^{2+} complex similarly detected in solution, as mentioned previously which help illustrate the emergence of the band typically associated with aliphatic C–H stretches found in the FTIR spectrum. Thus, this demonstrates that iodine is no longer present in the molecular structure and will be discussed further ahead.

The complexation of Hg^{2+} and Cu^{2+} with compound **L3** shares the same changes in comparison to **L1**, broadening of the 3500 to 3000 cm^{-1}

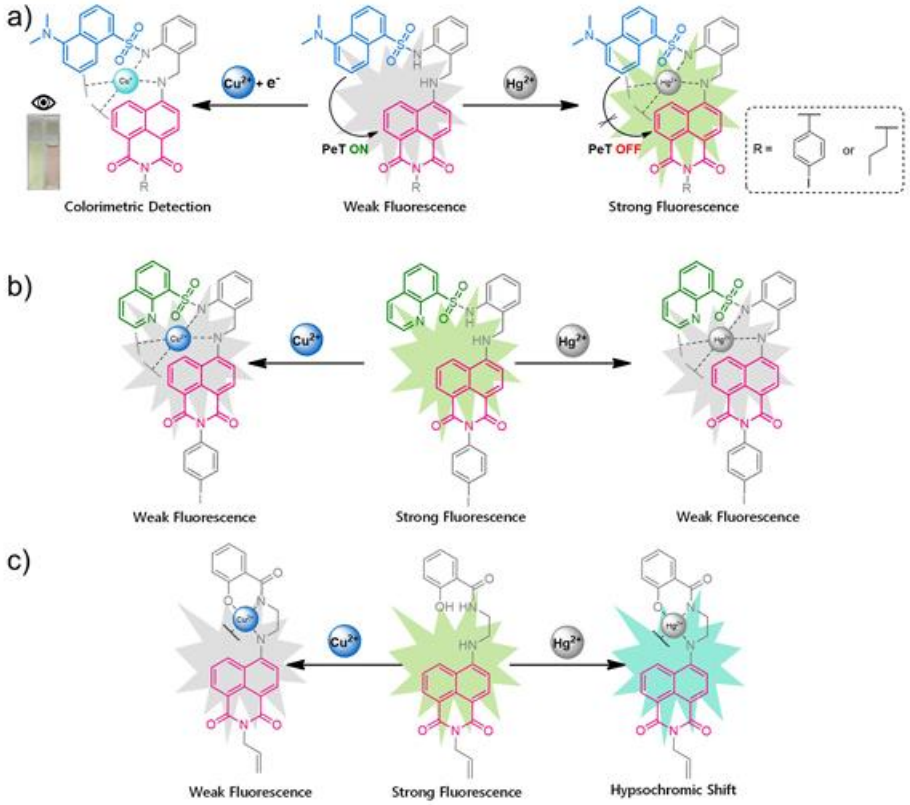


Fig. 4. Proposed mechanism after complexation with Cu^{2+} and Hg^{2+} metal ions for (a) **L1** and **L3**, (b) **L2** and (c) **L4**.

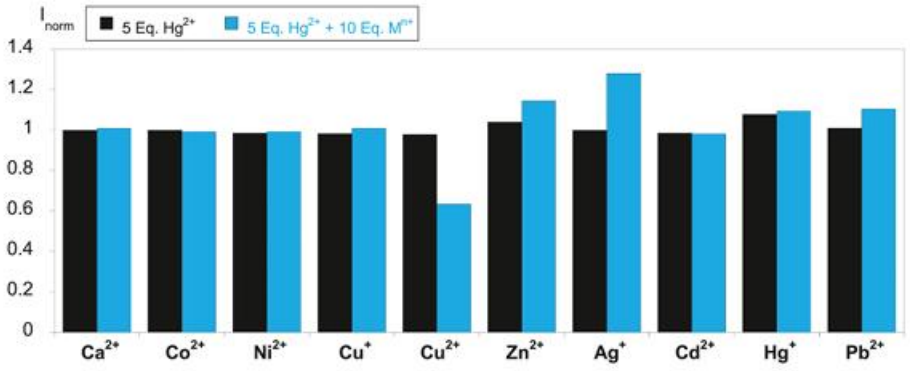


Fig. 5. Normalized emission response of **L1** in the presence of 5 equivalents Hg^{2+} and upon the addition of metal ions in acetonitrile. ([**L1**] = 10 μM, λ_{emL1} = 515 nm, T = 298 K).

region while keeping the dicarboximide profile and the increase of the ν(S=O) + ν(C–N) bands suggesting the presence of triflate counterion. Both complexes were followed by ESI-HRMS giving insight of the formation of a 1:1 Hg^{2+} complex with an *m/z* of 807.1929 (Figure S31) as it was found in solution, whereas the Cu^{2+} complex would preferably adopt a 2:1 stoichiometry in the solid state with an *m/z* of 1274.3814

Table 3
Association constants evaluated employing HypSpec software for compounds **L1** to **L4** towards Hg^{2+} and Cu^{2+} ions with included stoichiometry in acetonitrile. Respective values for the detection limit (LOD) and quantification limit (LOQ) amounts (μM).

Compounds	Metal (M)	Association constants ($LogK_{ass}$), L:M	LOD (μM)	LOQ (μM)
L1	Hg^{2+}	9.39 ± 0.01 (2:1)	5.1	7.3
L2	Cu^{2+}	4.83 ± 0.03 (1:1)	8	12
	Hg^{2+}	5.54 ± 0.03 (1:1)	2.5	5
L3	Hg^{2+}	5.07 ± 0.04 (1:1)	1	2
L4	Cu^{2+}	9.37 ± 0.05 (2:1)	5	9.9
	Hg^{2+}	4.73 ± 0.04 (1:1)	3.9	7.1

(Figure S32).

2.7. Interaction mechanism study of L1 with Cu^{2+}

To shed more light on the phenomenon underlying the **L1** and **L3** photophysical characteristics upon the introduction of Cu^{2+}, the time evolution of the **L1**:Cu^{2+} complex was studied by means of EPR and X-ray photoelectron spectroscopy.

At 1:4, the EPR of L1:Cu^{2+} displays a broad axial spectrum, characteristic of Cu^{2+} (Fig. 6a, brown line), with $g// > g_{\perp} > 2$, where only two of the expected copper four $g//$ lines are visible. No super-hyperfine interactions were identified. Noteworthy, L1:Cu^{2+} displays the same key spectral features as Cu^{2+} (in acetonitrile solution, without L1; Fig. 6a, green line), indicating that only copper not coordinated to L1 is being observed in the EPR spectrum of L1:Cu^{2+}. The spectrum likely arises from heterogeneous copper species coordinated by four oxygen atoms, as suggested by the $g// \approx 2.414$ and $A// \approx 138 \times 10^{-4} cm^{-1}$ values [77].

The L1:Cu^{2+} 1:4 spectrum intensity decreases with time (Fig. 6b, light blue line), clearly showing that Cu^{2+} is being reduced to the EPR silent Cu^{+}, and, after 75 min (Fig. 6a, light orange line), almost all copper (2.0 mM) was reduced. For L1:Cu^{2+} 1:7 and 1:10, similar spectra were obtained and their intensity also decreased with time (Fig. 6b, blue and dark blue lines, respectively). These results clearly demonstrate that L1 reduces copper. Moreover, because no spectral evidence of a L1:Cu^{2+} complex was observed, these results suggest that copper is reduced upon coordination/reaction with L1 (reduction would take place within 30–60s, the minimum time required to mix L1 and copper and freeze the solution, under our experimental conditions).

To be able to reduce copper, L1 needs to be oxidized by one electron, giving rise to an initial (transient) cation radical species, $L1^{\bullet+}$. The observation of such radical is dependent on its lifetime and, if the species is present in a low accumulated concentration, its EPR signal can be greatly obscured by the broad copper signal. In this context, the small feature at $g \approx 2.004$ observed in the 45 s spectra of **L1**:Cu^{2+} 1:4 (Fig. 6a, brown line) can be taken as an evidence of a radical formation in very low amounts; for longer times, no such feature can be identified. Alternatively, **L1** can be oxidized by two electrons to yield 2 Cu^{+}. After the initial (1 or 2-electron) oxidation, each **L1** molecule ought to undergo additional oxidation events, involving a total of four electrons, to account for the complete copper reduction observed in **L1**:Cu^{2+} 1:4 after 75 min (Fig. 6a, light orange line, and Fig. 6b, light blue line). Noteworthy, when an excess of copper is used (**L1**:Cu^{2+} 1:7 and 1:10), the amount of Cu^{2+} reduced is approximately the same. For a **L1**:Cu^{2+} 1:4 (0.5:2.0 mM) ratio, (almost) no copper remains in the Cu^{2+} state; for 1:7 (0.5:3.5 mM) and 1:10 (0.5:5.0 mM) ratios, approximately 1.5 (3.5–2.0) and 3 (5.0–2.0) equivalents remain in the Cu^{2+} state, respectively (Fig. 6b). These results give further support to the suggestion that **L1** is able to promote a global 4-electron redox process with copper.

X-ray photoelectron spectroscopy was deployed to further gain insight into the oxidation states of Cu in the compounds under study after various treatments. Fig. 7a presents Cu2p spectra for the **L1**:Cu^{2+} compound with a concentration ratio of 1:4 as prepared (black curve) and after 4 h in a vacuum (red curve). Fig. 7b presents Cu2p spectra for the **L1**:Cu^{2+} compound with a concentration ratio of 1:1 as prepared (green curve) and for the $[Cu(II)\mathbf{L1}]^{2+}$ complex. All the Cu2p spectra have a complex multipeak structure, which includes doublets due to spin-orbit splitting (Cu2p3/2 and Cu2p1/2 peaks) and satellites in the binding energy range of ~938–948 eV. The complex structure of the

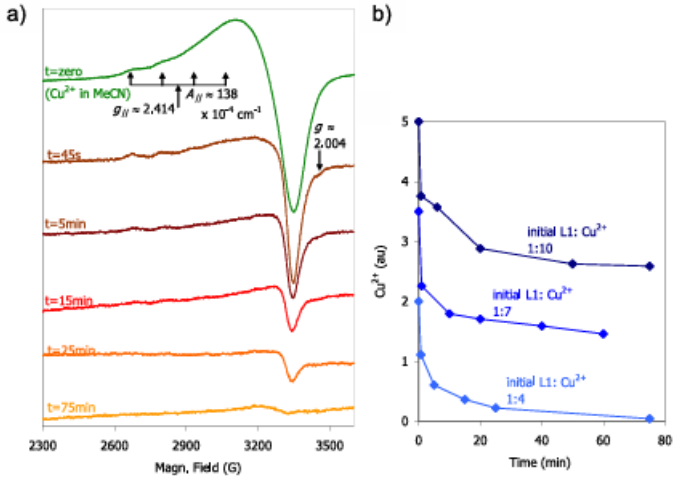


Fig. 6. (A) EPR spectra at 77 K of L1:Cu^{2+} 1:4 (0.5 mM:2.0 mM) in MeCN, at time zero (green line) and after 45s (brown), 5 min (dark red), 15 min (red), 25 min (orange) and 75 min (light orange). (b) Cu^{2+} reduction as a function of time, upon mixing L1 and Cu^{2+} at 1:4 (0.5:2.0 mM; light blue line), 1:7 (0.5:3.5 mM; blue) and 1:10 (0.5:5.0 mM; dark blue) ratios. Cu^{2+} concentration values (in arbitrary units, au) were determined from the respective EPR spectra intensity (double spectrum integration). (For interpretation of the references to color in this figure legend, the reader is referred to the Web version of this article.)

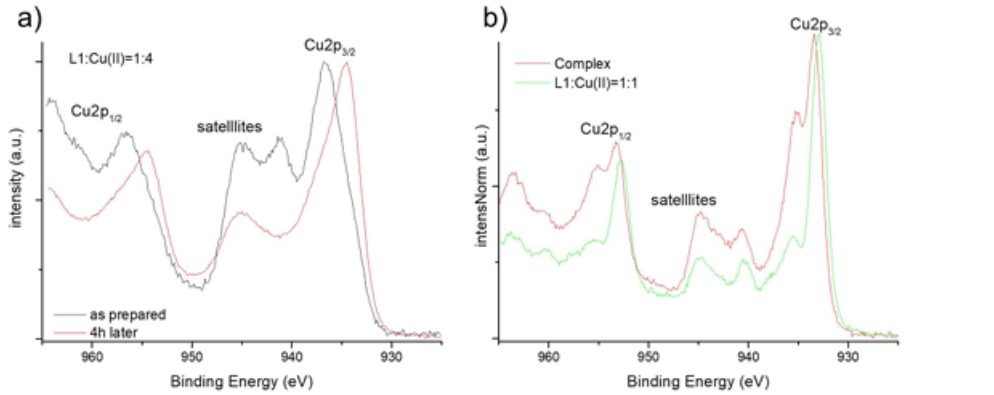


Fig. 7. Cu2p XPS spectra (a) after the addition of **L1** and Cu^{2+} in proportion 1:4 as prepared and 4 h later while (b) exhibits the spectra of the $[Cu(II)\mathbf{L1}]^{2+}$ complex and in proportion 1:1 (L:M).

Cu2p XPS spectra indicates a mixture of copper oxidation states. Strong satellites in the Cu2p spectra are an indication of the Cu^{2+} oxidation state [78].

The Cu2p3/2 peaks in the spectra of the **L1**:Cu^{2+} = 1:4 compound (Fig. 7a) as prepared and after 4 h, show a wide, asymmetric shape with peak positions shifted to 933–935 eV. In the case of the **L1**:Cu^{2+} = 1:1 and $[Cu(II)\mathbf{L1}]^{2+}$, the Cu2p3/2 peaks split into two components with maximum positions at ~933 and ~935 eV. Given the position of the main peak at ~933 eV and the presence of satellites, one can tentatively conclude that the **L1**:Cu^{2+} = 1:1 and $[Cu(II)\mathbf{L1}]^{2+}$ compounds contain a mixture of Cu^{1+} and Cu^{2+} species. An interesting observation is the splitting of the main Cu2p3/2 peak with an additional maximum at ~935 eV. The trivial explanation for this peak would be to assign it to an oxidation state higher than 2+. However, this peak splitting appears similar to that observed in the Ni2p spectra of NiO and is often mistakenly assigned to Ni^{3+}. It has been shown that the 2p peak splitting can be explained by the nonlocal screening of the core hole created during ionization of the 2p level by electrons donated by nearest and non-nearest ligands, while maintaining the 2+ oxidation state of Ni ions [79].

It is noteworthy to analyze the relative intensity of the satellite peaks with respect to the intensity of the main Cu2p3/2 peaks. Fig. 7a, shows that the relative intensity of the satellites substantially decreased after 4 h. In the case of the **L1**:Cu^{2+} = 1:1 compound, the relative satellite intensities are smaller than those in the **L1**:Cu^{2+} = 1:4 compound. The decrease in satellites can indicate the reduction of Cu^{2+} species by mixing with the **L1** substance. After 4 h, Cu^{2+} species are still present in the **L1**:Cu^{2+} = 1:4 compound as well as in the **L1**:Cu^{2+} = 1:1 compound, as evidenced by the Cu2p XPS spectra. This could also be due to surface oxidation of the studied materials, which is detectable by the surface-sensitive XPS technique (information depth up to ~10 nm).

Provided the evidence that showed the copper reduction using **L1** and **L3** from EPR and XPS experiments and bearing in mind the PeT process that could be mitigated and applied for the sensing of Hg^{2+}, we propose that both compounds perform a ligand-mediated chemical reduction of Cu^{2+} to Cu^{+}. The presence of an intramolecular electron-transfer process leads to a shift of the electronic charge distribution and the identification of the Cu^{+} state, that can also be colorimetrically identified with a change in the absorption profile from yellow to pink. Given the absence of any indication of reversibility or equilibrium between Cu^{2+} and Cu^{+} states provided by EPR data, these systems cannot achieve valence tautomerism. Furthermore, the introduction of iodophenyl serves as a catalysis substrate probe, in which only **L1** was able to catalyze the cleavage of the carbon-iodine bond from within itself. This is mediated by the formation of the Cu^{+} complex evidenced by the formation of a complex with lower molecular weight. The reduction of copper was found the limiting factor since compound **L2**, that does not manifest intramolecular electron-transfer, would not catalyze the carbon-halogen bond given that does not reduce the copper ion. Thus, we propose that **L1** self-catalyzed an amidation of benzene through an Ullman-type reaction using acetonitrile as amino source demonstrating in this way the usefulness of these dyad systems for catalysis [56–58].

3. Conclusions

In summary, we report the synthesis and characterization of four new naphthalimide derived ligands for the differential detection of Hg (II) and Cu(II) ions. Photophysical characterization in various solvents prompted us to characterize the solvent-compound interactions through the multiparametric fitting of the Kamlet-Taft equation and underlying solvatochromism. An understanding of the photophysical properties in dyad systems has been accomplished by comparison between the introduction of a quinoline or dansyl moiety to the naphthalimide core. Intramolecular electron transfer was possible in two compounds by introduction of a dansyl moiety constituting in two non-redox-innocent dyad systems. Application of these compounds to the sensing of metal ions, particularly of Hg(II) and Cu(II) ions, proved to be effective in avoiding the well-known suppression that these ions cause to fluorescent systems. A clear turn-on or CHEF effect of the emission was detected while sensing Hg(II) ions since it lowers the energy of the lone pair further from the ground state that would cause the initial quenching. A differential detection of Cu(II) ions was achieved by a colorimetric response accompanied by the intramolecular electron transfer. In this case, the two electronic states of the non-redox-innocent ligand and the redox-active metal center are close enough to observe ligand-mediated chemical reduction of Cu^{2+}. Application of EPR and XPS provided the evidences to establish a reduction of the copper(II) center to copper(I) promoted by the underlying close connection between the dansyl and naphthalimide units of the dyad. Finally, the resulting copper complexes were found the only suited compounds to be tested in the future for their catalysis properties since the cleavage of the carbon-halogen bond implemented as a probe was only mediated by prior reduction to copper (I).

CRediT authorship contribution statement

Frederico Duarte: Writing – review & editing, Writing – original draft, Validation, Software, Methodology, Investigation, Formal analysis, Data curation. **Diogo Torres:** Writing – original draft, Visualization, Methodology, Investigation. **Georgi M. Dobrikov:** Writing – review & editing, Writing – original draft, Validation, Resources, Investigation, Funding acquisition, Formal analysis, Conceptualization. **Atanas Kurutos:** Writing – review & editing, Writing – original draft, Visualization, Supervision, Resources, Methodology, Investigation, Funding acquisition, Formal analysis, Conceptualization. **Luisa B. Maia:** Writing – review & editing, Writing – original draft, Resources, Investigation, Formal analysis. **Oleksandr Bondarchuk:** Writing – original draft, Resources, Methodology, Investigation, Formal analysis. **Ivaylo Slavchev:** Writing – original draft, Methodology, Investigation. **Jose Luis Capelo-Martínez:** Writing – review & editing, Writing – original draft, Validation, Resources, Methodology, Funding acquisition, Formal analysis, Data curation. **Hugo M. Santos:** Writing – review & editing, Writing – original draft, Visualization, Validation, Resources, Investigation, Funding acquisition, Formal analysis, Data curation. **Carlos Lodeiro:** Writing – review & editing, Writing – original draft, Visualization, Validation, Supervision, Software, Resources, Project administration, Methodology, Investigation, Funding acquisition, Formal analysis, Data curation, Conceptualization.

Declaration of competing interest

The authors declare that they have no known competing financial interests or personal relationships that could have appeared to influence the work reported in this paper.

Funding

This work received support from PT national funds (FCT/MCTES, *Fundação para a Ciência e Tecnologia* and *Ministério da Ciência, Tecnologia e Ensino Superior)* through the projects UIDB/50006/2020 and UIDP/50006/2020. This work received support from PROTEOMASS Scientific Society through the General Funding Grant 2024–2025, and the projects #PM001/2019 and #PM003/2016. This work is also developed and acknowledged by A.K. as part of contract №: BG-RRP-2.004-0002-C01, Laboratory of Organic Functional Materials (Project BiOrgaMCT), Procedure BG-RRP-2.004 „Establishing of a network of research higher education institutions in Bulgaria", funded by BULGARIAN NATIONAL RECOVERY AND RESILIENCE PLAN".

Declaration of competing interest

The authors declare the following financial interests/personal relationships which may be considered as potential competing interests: Given his role as Executive Editor, Professor Carlos Lodeiro Y Espiño had no involvement in the peer review of this article and had no access to information regarding its peer review. Full responsibility for the editorial process for this article was delegated to another journal editor.

Acknowledgements

This work was financed by national funds from FCT - Fundação para a Ciência e a Tecnologia, I.P., under the scope of the project UID/50006/2023 of the Associate Laboratory for Green Chemistry - LAQV REQUIMTE. PROTEOMASS Scientific Society (Portugal) is acknowledged by the funding provided through the General Funding Grant 2024–2025, and by the funding provided to the Laboratory for Biological Mass Spectrometry Isabel Moura (#PM001/2019 and #PM003/2016). F.D. thanks to FCT/MCTES (Portugal) for his doctoral grant 2021.05161. BD. H. M. S. acknowledges the Associate Laboratory for Green Chemistry LAQV (LA/P/0008/2020) funded by FCT/MCTES for his research contract. This work was supported by the Associate Laboratory for Green Chemistry - LAQV (UIDB/50006/2020 (DOI: 10.54499/UIDB/50006/2020) and UIDP/50006/2020 (DOI: 10.54499/UIDP/50006/2020)), which are financed by national funds from Fundacão para a Ciência e a Tecnologia, MCTES (FCT/MCTES). LBM also thanks to FCT/MCTES, for the CEEC-Ind Program Contract. C.L. and H. M.S thanks the Royal Society of Chemistry for the Sustainable Laboratory Grants 2023 reference L23-8861107285.

The financial support by the Bulgarian National Science Fund (BNSF) under grant – "Novel styryl and polymethine fluorophores as potential theranostic agents "contract № КП-06-М59/1 from November 15, 2021 is gratefully acknowledged by A.K. This work is also developed and acknowledged by A.K. as part of contract №: BG-RRP-2.004-0002-C01, Laboratory of Organic Functional Materials (Project BiOrgaMCT), Procedure BG-RRP-2.004 „Establishing of a network of research higher education institutions in Bulgaria", funded by BULGARIAN NATIONAL RECOVERY AND RESILIENCE PLAN".

G. D. thanks to the European Regional Development Fund within the Operational Programme Science and Education for Smart Growth 2014–2020 under the Project Center of Excellence: National center of mechatronics and clean technologies - BG05M2OP001-1.001-0008 for the financial support.

Appendix A. Supplementary data

Supplementary data to this article can be found online at https://doi.org/10.1016/j.dyepig.2025.113088.

Data availability

Data will be made available on request.

References

[1] Yuan X, Leng TH, Guo ZQ, Wang CY, Li JZ, Yang WW, Zhu WH. A FRET-Based dual-channel turn-on fluorescence probe for the detection of Hg^{2+} in living cells. Dyes Pigments 2019;161:403–10. https://doi.org/10.1016/j.dyepig.2018.09.078.

[2] Wang Y, Zhou J, Zhao L, Xu B. A dual-responsive and highly sensitive fluorescent probe for Cu^{2+} and pH based on a dansyl derivative. Dyes Pigments 2020;180:108513. https://doi.org/10.1016/j.dyepig.2020.108513.

[3] Wei P, Xiao L, Gou Y, He F, Zhou D, Liu Y, Xu B, Wang P, Zhou Y. Fluorescent "on–off–on" probe based on copper peptide backbone for specific detection of Cu (II) and hydrogen sulfide and its applications in cell imaging, real water samples and test strips. Microchem J 2022;182:107848. https://doi.org/10.1016/j.microc.2022.107848.

[4] Nagarajan R, Ryoo HI, Vanjare BD, Gyu Choi N, Hwan Lee K. Novel phenylalanine derivative-based turn-off fluorescent chemosensor for selective Cu^{2+} detection in physiological pH. J Photochem Photobiol Chem 2021;418:113435. https://doi.org/10.1016/j.jphotochem.2021.113435.

[5] He L, Li Q, Zhang Y, Huang K, Du B, Liang L. A naphthalimide functionalized fluoran with AIE effect for ratiometric sensing Hg^{2+} and cell imaging application. Spectrochim Acta Mol Biomol Spectrosc 2023;296:122672.

[6] Hu L, Xie K, Gao A, Hu Y, Hou A. Synthesis of novel triazine-quinoline-appended naphthalimide sensors for Hg(II) recognition and their structure-activity relationship. Dyes Pigments 2022;199:110048.

[7] Li Y, Ren Z, Ge Y, Di C, Zhou J, Wu J, Jia L. A novel peptide fluorescent probe based on different fluorescence responses for detection of Mercury species and hydrogen sulfide. Microchem J 2023;184:108160.

[8] Duarte F, Pereira-Gomes I, Dobrikov GM, Galhano J, Gomes CSB, Kurutos A, Santos HM, Oliveira E, Paula Duarte M, Luis Capelo-Martinez J, Lodeiro C. Antimicrobial profile and Turn-On sensing of cyanide and water traces using a dual chromophoric dansyl-acridine conjugate as multifunctional system. Microchem J 2024;205:111237.

[9] Xu H, Xiao Y, Liu Y, Sun W. Research progress on naphthalimide fluorescent probes. Adv Sensor Res 2024;3:2300032.

[10] Gao YG, Dang K, Zhang WJ, Liu FL, Patil S, Qadir A, Ding AX, Qian AR, A 1,8-naphthalimide-[12]. $aneN_5$ derivative for efficient Cu^{2+} recognition, lysosome staining and siRNA delivery. Colloids Surf B Biointerfaces 2022;185:110607.

[11] Bao Z, Qin C, jun Wang J, Sun J, Dai L, Chen G, Mei F. A sensitive and selective probe for visual detection of Cu^{2+} based on 1,8-naphthalimidederivative. Sens Actuators B Chem 2018;265:234–41.

[12] Wang H, Cui J, Fang X, Zhang W, Wang J, Chen S, Qian J. Fluorescent detection of copper ions with acylhydrazine-based probes: effects of substitute and its position. Dyes Pigments 2022;197:109954.

[13] Ho FC, Huang YJ, Weng CC, Wu CH, Li YK, Wu JI, Lin HC. Efficien t FRET approaches toward Copper(II) and cyanide detections via host–guest interactions

of photo-switchable [2]Pseudo-Rotaxane polymers containing naphthalimide and merocyanine moieties. ACS Appl Mater Interfaces 2020;12:53257–73.
[14] Liu C, Xu J, Yang F, Zhou W, Li Z, Wei L, Yu M. Nanomolar $Cu^{2+}$and F^- naked-eye detection with a 1,8-naphthalimide-based colorimetric probe. Sens Actuators B Chem 2015;212:364–70.
[15] Li Z, Hou JT, Wang S, Zhu L, He X, Shen J. Recent advances of luminescent sensors for iron and copper: platforms, mechanisms, and bio-applications. Coord Chem Rev 2022;469:214695.
[16] Ghosh S, Ghosh S, Ranjan Dhara S, Baildya N, Ghosh K. Naphthalimide-based new architecture for fluorescence turn-on sensing of Cu^{2+} and colorimetric detection of F^-/CN^-. Methods 2024;225:13–9.
[17] Cai H, Liang Y, Huang L, Wang J. Relay detection of Cu^{2+} and bovine serum albumin by a dansyl derivative-based fluorescent probe. Spectrochim Acta Mol Biomol Spectrosc 2022;277:121281.
[18] Guo Z, Wang Q, Zhou D, An Y, Wang P, Liao F. A novel peptide-based fluorescent probe with a large stokes shift for rapid and sequential detection of Cu^{2+} and CN^- in aqueous systems and live cells. Spectrochim Acta Mol Biomol Spectrosc 2022;264:120257.
[19] Liu YL, Yang L, Li P, Li SJ, Li L, Pang XX, Ye F, Fu Y. A novel colorimetric and "turn-off" fluorescent probe based on catalyzed hydrolysis reaction for detection of Cu^{2+} in real water and in living cells. Spectrochim Acta Mol Biomol Spectrosc 2020;227:117540.
[20] Fu Y, Pang XX, Wang ZQ, Chai Q, Ye F. A highly sensitive and selective fluorescent probe for determination of Cu(II) and application in live cell imaging. Spectrochim Acta Mol Biomol Spectrosc 2019;208:198–205.
[21] Guo B, Pan X, Liu Y, Nie L, Zhao H, Liu Y, Jing J, Zhang X. A reversible water-soluble naphthalimide-based chemosensor for imaging of cellular copper(II) ion and cysteine. Sens Actuators B Chem 2018;256:632–8.
[22] Liu Y, Jiang B, Zhao L, Zhao L, Wang Q, Wang C, Xu B. A dansyl-based fluorescent probe for sensing Cu^{2+} in aqueous solution. Spectrochim Acta Mol Biomol Spectrosc 2021;261:120009.
[23] Liang S, Tong Q, Qin X, Liao X, Li Q, Yan G. A hydrophilic naphthalimide-based fluorescence chemosensor for Cu^{2+} ion: sensing properties, cell imaging and molecular logic behavior. Spectrochim Acta Mol Biomol Spectrosc 2020;230:118029.
[24] Park SY, Kim W, Park SH, Han J, Lee J, Kang C, Lee MH. An endoplasmic reticulum-selective ratiometric fluorescent probe for imaging a copper pool. Chem Comm 2017;53:4457–60.
[25] Jiang H, Li Z, Kang Y, Ding L, Qiao S, Jia S, Luo W, Liu W. A two-photon fluorescent probe for Cu^{2+}based on dansyl moiety and its application in bioimaging. Sens Actuators B Chem 2017;242:112–7.
[26] Uttam B, Polepalli S, Sinha S, Majumder A, Rao CP. Selective sensing and removal of mercury ions by encapsulating dansyl appended Calix[4]Conjugate in a zeolitic imidazolate framework as an organic–inorganic hybrid nanomaterial. ACS Nano Mater 2022;5:11371–80.
[27] Cheng H, Yi F, Sun J, Li A, Zhang X, Guan D, Qu Y, Cao J. A naphthalimide-based fluorescent probe with a benzoylthiourea trigger for detection of Hg(II) in cosmetics. Dyes Pigments 2024;226:112135.
[28] Yang C, Li Y, Wu N, Zhang Y, Feng W, Yu M, Li Z. Ratiometric upconversion luminescence nanoprobes for quick sensing of Hg^{2+} and cells imaging. Sens Actuators B Chem 2021;326:128841.
[29] Pang X, Dong J, Gao L, Wang L, Yu S, Kong J, Li L. Dansyl-peptide dual-functional fluorescent chemosensor for Hg^{2+} and biothiols. Dyes Pigments 2020;173:107888.
[30] Aliberti A, Vaiano P, Caporale A, Consales M, Ruvo M, Cusano A. Fluorescent chemosensors for Hg^{2+} detection in aqueous environment. Sens Actuators B Chem 2017;247:727–35.
[31] Shinohara Y, Tsukamoto K, Maeda H. A fluorescent turn-on probe for Hg^{2+} with a high contrast designed by manipulating functional groups tethered to naphthalimide. J Photochem Photobiol Chem 2019;371:407–13.
[32] Wang P, An Y, Wu J. Highly sensitive turn-on detection of mercury(II) in aqueous solutions and live cells with a chemosensor based on tyrosine. Spectrochim Acta Mol Biomol Spectrosc 2020;230:118004.
[33] Graves M, Elioff MS, Knorr ES, Griffith JB, Hu J. A fluorescent turn-on sensor for Mercury (II) ions in near neutral poly (metharylic acid) solution. Spectrochim Acta Mol Biomol Spectrosc 2022;282:121702.
[34] Srivastava P, Verma M, Sivakumar S, Patra AK. A smart FRET probe exhibiting a molecular keypad lock device based on rapid detection of nitric oxide mediated by Cu^{2+} ion. Sens Actuators B Chem 2019;291:478–84.
[35] Mishra T, Guria S, Sadhukhan J, Das D, Das MK, Adhikari SS, Maity S, Maiti P. A naphthalimide appended rhodamine based biocompatible fluorescent probe: chemosensor for selective detection of Hg^{2+} ion, live cell imaging and DFT study. J Photochem Photobiol Chem 2024;446:115168.
[36] Gao J, He Y, Chen Y, Song D, Zhang Y, Qi F, Guo Z, He W. Reversible FRET fluorescent probe for ratiometric tracking of endogenous Fe^{3+} in ferroptosis. Inorg Chem 2020;59:10920–7.
[37] Lee HJ, Cho MJ, Chang SK. Ratiometric signaling of hypochlorite by the oxidative cleavage of Sulfonhydrazide-Based rhodamine–dansyl dyad. Inorg Chem 2015;54:8644–9.
[38] Martins F, Granja A, Reis S, Gameiro P, Barone G, Neves MGPMS, Silva AMG. Synthesis, fluorescence and theoretical insights into a novel FRET-Based dansyl-rhodamine sensor for the in vitro detection of toxic bioaccumulated Hg(II) ions. Spectrochim Acta Mol Biomol Spectrosc 2025;329:125534.
[39] Li N, Qin W, Chen Y, Liu K, Wang S, Kong F. Construction of a robust polarity sensitive platform and its application for tracking of lipid droplets decrease under oxidative stress in live cells. Sens Actuators B Chem 2021;346:130491.
[40] Yang D, Wu XT, Cao XJ, Zhao BX. A reversible ratiometric fluorescence probe for fast detection of trace water in different organic solvents. Dyes Pigments 2019;170:107558.
[41] Zheng C, Zhang X, Gao A, Ju M, Hou A, Xie K. Adjustable multimodality fluorescence emissions and photochromism of functional molecular device containing double chromophores with intramolecular FRET process. Dyes Pigments 2024;228:112238.
[42] Zhao J, Zhang J, Hu B, Gao C, Li Z, Sun Z, You J. Spectrochim Acta Mol Biomol Spectrosc 2023;286:121965.
[43] Lee H, Lee HS, Reibenspies JH, Hancock RD. Mechanism of "Turn-on" fluorescent sensors for Mercury(II) in solution and its implications for ligand design. Inorg Chem 2012;51:10904–15.
[44] Deng W, Li S, Zhou M, Zheng M, Wang P, An Y. Ratiometric peptide-based fluorescent probe with large stokes shift for detection of Hg^{2+} and S^{2-} and its applications in cells imaging and smartphone-assisted recognition. Spectrochim Acta Mol Biomol Spectrosc 2024;315:124306.
[45] Zhang L, Zhao P, Yu S, Kong J, Gao L, Li L. Dansyl-modified tryptophan fluorescence sensor for highly sensitive and selective detection of Hg^{2+} in aqueous solutions. Microchem J 2024;200:110520.
[46] Tamizhselvi R, Bhaskar R, Beena M, Palaniappan A, Kumar SKA, Napoleon AA. A dual responsive bis-thiophene affixed thiosemicarbazide based chemosensor for colorimetrically Hg^{2+} and fluorometrically Cu^{2+} ions and their applications in live cell imaging. Spectrochim Acta Mol Biomol Spectrosc 2024;322:124766.
[47] Shi WJ, Li CF, Huang Y, ya Tan H, Wei YF, Liu F, Feng LX, Zheng L, Chen GS, wu Yan J. A remarkable colorimetric probe for fluorescent ratiometric and ON-OFF discriminative detection of Hg^{2+} and Cu^{2+} by double-channel imaging in living cells. Dyes Pigments 2019;171:107782.
[48] Chang LL, Gao Q, Liu S, Hu CC, Zhou WJ, Zheng MM. Selective and differential detection of Hg^{2+} and Cu^{2+} with use of a single rhodamine hydrazone-type probe in the absence and presence of UV irradiation. Dyes Pigments 2018;153:117–24.
[49] [a] Kundu N, Maity M, Chatterjee PB, Teat SJ, Endo A, Chaudhury M. Reporting a Unique Example of Electronic Bistability Observed in the Form of Valence Tautomerism with a Copper(II) Helicate of a Redox-Active Nitrogenous Heterocyclic Ligand. J Am Chem Soc 2011;133:20104–7.[b] Sato O, Tao J, Zhang YZ. Control of Magnetic Properties through External Stimuli. Angew Chem Int Ed 2007;46:2152–87.
[50] Sato O, Tao J, Zhang YZ. Control of magnetic properties through external stimuli. Angew Chem Int Ed 2007;46:2152–87. https://doi.org/10.1002/anie.200602205.
[51] Wiesner S, Wagner A, Kaifer E, Himmel HJ. A valence tautomeric dinuclear copper tetrakisguanidine complex. Chem Eur J 2016;22:10438–45.
[52] Tezgerevska T, Alley KG, Boskovic C. Valence tautomerism in metal complexes: stimulated and reversible intramolecular electron transfer between metal centers and organic ligands. Coord Chem Rev 2014;268:23–40.
[53] Gransbury GK, Livesay BN, Janetzki JT, Hay MA, Gable RW, Shores MP, Starikova A, Boskovic C. Understanding the origin of one-ortwo-step valence tautomeric transitions in bis(dioxolene)-bridged dinuclear cobalt complexes. J Am Chem Soc 2020;142:10692–704.
[54] Hess KM, Leach IF, Wijtenhorst L, Lee H, Klein JEMN. Valence tautomerism induced proton coupled electron transfer: X-H bond oxidation with a dinuclear Au (II) hydroxide complex. Angew Chem Int Ed 2024;63:e202318916.
[55] Lennon DG, Sang TL, Colbran SB. Valence tautomerism and coordinative lability in Copper(II)-Imidazolyl-Semiquinonate anion radical models for the Cu_B center in cytochrome *c* oxidases. J Am Chem Soc 2007;129:5800–1.
[56] Sambiagio C, Marsden SP, Blacker AJ, McGowan PC. Copper catalysed ullmann type chemistry: from mechanistic aspects to modern development. Chem Soc Rev 2014;43:3525–50.
[57] Andrada DM, Soria-Castro SM, Caminos DA, Argüello JE, Peñéñory AB. Understanding the heteroatom effect on the ullmann copper-catalyzed cross-coupling of X-Arylation (*X* =NH, O, S) mechanism. Catalysts 2017;7:388.
[58] Strekalova S, Kononov A, Rizvanov I, Budnikova Y. Acetonitrile and benzonitrile as versatile amino sources in copper-catalyzed mild electrochemical C–H amidation reactions. RSC Adv 2021;11:37540–3.
[59] Xu Z, Zhang MX, Li G, Chen X, Liu SH, Chen H, Yin J. Naphthalimide-sulfonamide fused dansyl-sulfonamide fluorescent probe for tracking glutathione of lysosome with a dual-emission manner. Dyes Pigments 2019;171:107685.
[60] Das S, Sahoo P. A colorimetric sensor for hydrogen sulfide: detection from biogas and quantitative estimation in water. Sens Actuators B Chem 2019;291:287–92.
[61] Bin Li K, Zhou D, He XP, Chen GR. Ratiometric glyco-probe for transient determination of thiophenol in full aqueous solution and river water. Dyes Pigments 2015;116:52–7.
[62] Kong Y, Wan X, Liu Z, Chen F, Wu F, Qin G, Cao D, Cui Y. A novel dansyl-naphthalimide fluorescent probe for visualizing nitroxyl (HNO) in biological systems. Sens Actuators B Chem 2022;350:130852.
[63] Bagherzadeh N, Reza Sardarian A. Green approach to new library of 1,8-naphthalimide fluorophores employing C-C and C-N cross coupling reactions by novel, durable, and reusable magnetic nanocatalyst bearing nickel (0) complex of 1,10-phenanthroline. J Photochem Photobiol Chem 2024;449:115345.
[64] Huang G, Li C, Han X, Aderinto SO, Shen K, Mao S, Wu H. Sensitive and selective detection of Cu(II) ion: a new effective 1,8-naphthalimide-based fluorescence 'turn off' sensor. Luminescence 2018;33:660–9.
[65] Schulz A, Wotschadlo J, Heinze T, Mohr GJ. Fluorescent nanoparticles for ratiometric pH-monitoring in the neutral range. J Mater Chem 2010;20:1475–82.
[66] Benanti TL, Saejueng P, Venkataraman D. Segregated assemblies in bridged electron-rich and electron-poor p-conjugated moieties. Chem Comm 2007:692–4.

[67] Chinapang P, Ruangpornvisuti V, Sukwattanasinitt M, Rashatasakhon P. Ferrocenyl derivative of 1,8-naphthalimide as a new turn-on f luorescent sensor for Au(III) ion. Dyes Pigments 2015;112:236–8.
[68] Pfeffer FM, Seter M, Lewcenko N, Barnett NW. Fluorescent anion sensors based on 4-amino-1,8-naphthalimide that employ the 4-amino N–H. Tetrahedron Lett 2006; 47:5241–5.
[69] Lim T, Ryoo JY, Jang M, Han MS. Ligand-free suzuki–miyaura cross-coupling with low Pd content: rapid development by a fluorescence-based high-throughput screening method. Org Biomol Chem 2021;19:1009–16.
[70] Ohtani R, Anegawa Y, Watanabe H, Tajima Y, Kinoshita M, Matsumori N, Kawano K, Yanaka S, Kato K, Nakamura M, Ohba M, Hayami S. Metal complex lipids for fluid–fluid phase separation in coassembled phospholipid membranes. Angew Chem Int Ed 2021;60:13603–8.
[71] Cheng K, Zheng QZ, Qian Y, Shi L, Zhao J, Zhu HL. Synthesis, antibacterial activities and molecular docking studies of peptide and schiff bases as targeted antibiotics. Bioorg Med Chem 2009;17:7861–71.
[72] Dash SC, Dash AC. Proximity effect on the general base catalysed hydrolysis of amide linkage: the role of cationic surfactant, CTABr. J Chem Sci 2011;123: 497–507.
[73] Oliveira E, Baptista RMF, Costa SPG, Raposo MMM, Lodeiro C. Solvatochromic effects of bis(indolyl)thienylaril derivatives as new colored materials. Photochem Photobiol Sci 2014;13:492–8.
[74] Mocanu S, Ionita G, Matei I. Solvatochromic characteristics of dansyl molecular probes bearing alkyl diamine chains. Spectrochim Acta Part A Mol Biomol Spectrosc 2020;237:118413.
[75] Nolan EM, Lippard SJ. Tools and tactics for the optical detection of mercuric ion. Chem Rev 2008;108:3443–80.
[76] Gans P, Sabatini A, Vacca A. Investigation of equilibria in solution. Determination of equilibrium constants with the HYPERQUAD suite of programs. Talanta 1996; 43:1739–53.
[77] Peisach J, Blumberg WE. Structural implications derived from the analysis of electron paramagnetic resonance spectra of natural and artificial copper proteins. Arch Biochem Biophys 1974;165:691–708.
[78] Biesinger MC. Advanced analysis of copper X-ray photoelectron spectra. Surf Interface Anal 2017;49:1325–34.
[79] Alders D, Voogt FC, Hibma T, Sawatzky GA. Nonlocal screening effects in 2 p x-ray photoemission spectroscopy of NiO (100). Phys Rev B 1996;54:7716–9.

.

C

Published Paper in Dyes and Pigments - Corresponding to Chapter 5

Dyes and Pigments 218 (2023) 111428

Contents lists available at ScienceDirect

Dyes and Pigments

journal homepage: www.elsevier.com/locate/dyepig

Enhancing water sensing via aggregation-induced emission (AIE) and solvatofluorochromic studies using two new dansyl derivatives containing a disulfide bound: Pollutant metal ions detection and preparation of water-soluble fluorescent polymeric particles

Frederico Duarte [a], Georgi Dobrikov [b,***], Atanas Kurutos [b,c], Hugo M. Santos [a,d], Javier Fernández-Lodeiro [a,d], Jose Luis Capelo-Martinez [a,d], Elisabete Oliveira [a,d,**], Carlos Lodeiro [a,d,*]

[a] BIOSCOPE Research Group, LAQV-REQUIMTE, Chemistry Department, NOVA School of Science and Technology, FCT NOVA, Universidade NOVA de Lisboa, 2829-516, Caparica, Portugal
[b] Institute of Organic Chemistry with Centre of Phytochemistry, Bulgarian Academy of Sciences, Acad. G. Bonchev str., bl. 9, 1113, Sofia, Bulgaria
[c] University of Chemical Technology and Metallurgy, 8 St. Kliment Ohridski blvd, 1756, Sofia, Bulgaria
[d] PROTEOMASS Scientific Society, Rua dos Inventores, Madam Parque, Caparica Campus, 2829-516, Caparica, Portugal

ARTICLE INFO

Keywords:
Polystyrene-block-polybutadiene-block-polystyrene (SBS) microparticles
Dansyl derivatives
Metal ions
AIE effect
Solvatochromism

ABSTRACT

Polarity-sensitive dansyl derivatives **L1** and **L2** were synthesized and their ability to sense pollutant metal ions was investigated. All compounds were found to be highly sensitive towards Cu^{2+} and Hg^{2+} metal ions, while **L2** being able to detect and quantify Hg^{2+} concentrations as low as 2.5 μM. Both **L1** and **L2** exhibit positive solvatofluorochromic behaviour, modulated in the presence of water, which in turn results in fluorescence enhancement *via* aggregation-induced emission (AIE). Seeking stability and water solubility, luminescent **L1**-based polystyrene-block-polybutadiene-block-polystyrene (SBS) microparticles (size: 520 ± 76 nm) were successfully prepared while maintaining the fluorescence emission of fluorophore **L1** (φ = 22%). This work exemplifies the multiple properties of dansyl-derivatives and their promising applications in biomedicine and environmental fields.

1. Introduction

Over the past decades, the unique properties of dansyl derivatives have made them a useful tool for environmental science, analytical chemistry, biosensors and biological imaging [1–9]. The low intensity-excitation wavelengths of dansyl derivatives and high fluorescence quantum yield, provide strong conditions to be applied as biological probes and in the development of chemical sensors for the detection of heavy and transition metal ions [10]. The high sensitivity and selectivity of the dansyl moiety enhance the applicability for detecting these ions at low concentrations in the environment. The rather low detection limits reported of the dansyl derivatives for Cu^{2+}, ranging between 0.2 μM and 0.9 μM for Cu^{2+} and 140 nM for Hg^{2+}, respectively, turn it into a valuable vehicle for pollution control and environmental monitoring [11–13]. Additionally, their solvatochromic effect makes them suitable for imaging and environmental control, since changes in solvent polarity result in wavelength shifts in the absorption and emission bands [1].

Numerous organic dyes express excellent fluorescent properties in solution, however, at higher concentrations or in the solid state, aggregation of these dyes results in a decrease in the intensity emission signal, due to non-radiative transitions. Since the first discovery in 2001 of fluorophores with aggregation-induced emission (AIE) reported by *Tang* et al. [14], increasing popularity has been observed due to their high sensitivity, and selectivity [15–18]. In the AIE water-based mechanism, water modulates the aggregation state of the fluorophore,

* Corresponding author. PROTEOMASS Scientific Society, Rua dos Inventores, Madam Parque, Caparica Campus, 2829-516, Caparica, Portugal.
** Corresponding author. PROTEOMASS Scientific Society, Rua dos Inventores, Madam Parque, Caparica Campus, 2829-516, Caparica, Portugal.
*** Corresponding author.
E-mail addresses: Georgi.Dobrikov@orgchm.bas.bg (G. Dobrikov), ej.oliveira@fct.unl.pt (E. Oliveira), cle@fct.unl.pt (C. Lodeiro).

https://doi.org/10.1016/j.dyepig.2023.111428
Received 14 April 2023; Received in revised form 21 May 2023; Accepted 22 May 2023
Available online 5 June 2023
0143-7208/© 2023 The Authors. Published by Elsevier Ltd. This is an open access article under the CC BY-NC-ND license (http://creativecommons.org/licenses/by-nc-nd/4.0/).

resulting in fluorescence enhancement, providing a simple and direct way to monitor water content in complex environments, such as biological samples and industrial processes [19–21].

Despite the plethora of available analytical methods for water detection, fluorescence-based techniques stand out to be the most rapid, sensitive and cost-effective approach. In fluorescent-based water sensors, as organic molecules, water can be detected by employing fluorescence "turn-off", "turn-on" or ratiometric methods. In the previous methods, photo-induced electron transfer (PET) and aggregation-induced emission (AIE) are some of the mechanisms discussed [21]. Among others, dansyl derivatives have been widely used as water sensors in organic solvents since they exhibit a strong fluorescence response to water content [21]. AIE platform has also been extensively used as a metal ion-responsive luminescent probe due to its sensitivity to the environment [22,23].

However, the hydrophobicity of AIE-active organic compounds is still a challenging task when considering aqueous media applications. This challenge could be overcome by developing water soluble polymeric nanoparticles, opening new opportunities in biomedicine and environmental areas [24,25]. Fluorescent dye-doped polymer nanoparticles have shown great potential, providing significant improvements in sensitivity, stability, and enhanced fluorescence being many fold-brighter compared to traditional organic dyes. Dye-loaded polymer NPs allow high dye loading without aggregation-caused quenching (ACQ). Only recently were reported strategies to overcome ACQ in polymer nanoparticles, such as the design of organic compounds with the ability of AIE, resulting in increased fluorescence quantum yield and photostability [2,26–29].

For more than twenty years the main focus of our research group has been devoted to sensing pollutant metal ions and anions using fluorescent polyamines [30–32], macrocycles, porphyrins or corroles [33,34], sulphur-containing sensors [35], and nanoparticles [36].

Based on our experience, in this work, two dansyl derivatives (L1 and L2) were synthesized and fully characterized. These two compounds contain two dansyl derivatives linked by a disulfide bridge (-S-S-). Studies in the literature reveal that compounds containing two chromophores linked by a bridge can increase sensitivity, specificity, stabilization, and lifetime [37,38]. Moreover, the presence of an S–S bridge has advantages for biological applications, such as detecting protein-protein interactions or conformational changes in a target protein [39].

Aiming the creation of new breakthroughs in the state of the art, the multiple properties and advantages above-mentioned of dansyl derivatives were fully explored, such as (i) the solvatochromic effect, (ii) sensing ability towards pollutant metal ions, (iii) water detection in organic solvent *via* AIE, photostability, as well as (iv) the production of dansyl derivative (L1) doped polystyrene-block-polybutadiene-block-polystyrene (SBS) microparticles (L1@SBS) [40], aiming higher fluorescence quantum yields *via* AIE in water.

2. Experimental section

2.1. Materials

The metal salts: $Cu(OTf)_2$, $Cd(OTf)_2$, $Co(OTf)_2$, $Ag(OTf)$, $Pb(OTf)_2$, $Zn(OTf)_2$, $Ni(OTf)_2$ and $Ca(OTf)_2$ were purchased from Solchemar, while $Hg(OTf)_2$, dansyl amide and all solvents were acquired from Sigma Aldrich without requiring additional steps of purification. Spectroscopy grade solvents were used for measuring the electronic and fluorescence spectra – acetonitrile (CH_3CN), chloroform ($CHCl_3$), toluene, ethanol (EtOH), dimethylsulfoxide (DMSO) and tetrahydrofuran (THF). Poly (styrene-butadiene-styrene) (SBS) was purchased from Sigma-Aldrich (St. Louis, MO, USA). Mili-Q ultrapure water was used in all experiments. The analytical grade reagents and solvents needed for the synthesis of the target dansyl derivatives were purchased from Alfa Aesar, Fluka, Fluorochem Ltd, Merck, TCI, and Sigma-Aldrich, and were utilized as received. TLC was used to monitor the reaction outcome (Merck silica gel 60 F254 precoated TLC plates - 0.2 mm thick). Purification of the crude products was achieved by column chromatography employing silica gel as a stationary phase. Details about the employed mobile phases are given in the corresponding synthetic protocols listed below.

2.2. Instrumentation

Dynamic light scattering (DLS) data has been obtained from a Malvern Zetasizer Nano series (Worcestershire, WR14 1XZ, UK) from PROTEOMASS Scientific Society-BIOSCOPE Facility Lab. Samples have been analyzed at a scattering angle of 90° and at a temperature of 25 °C while supported in a glass cell. The z-potential measurement of microparticles was performed using a dip-cell.

High-Resolution Mass Spectrometry analyses were carried out in the Laboratory for Biological Mass Spectrometry–Isabel Moura (PROTEOMASS Scientific Society Facility), using UHR ESI-Qq-TOF IMPACT HD (Bruker-Daltonics, Bremen, Germany). Compounds were dissolved in 50% (v/v) Acetonitrile containing 0.1% (v/v) aqueous formic acid to obtain a working solution of 0.1 μg/mL. Mass spectrometry analysis was carried out by the direct infusion of the compound solutions into the ESI source. MS data were acquired in positive polarity over the mass range of 80–1300 *m/z*. (Capillary voltage: 4500 V, End plate offset: −500 V, Charging voltage: 2000 V, Corona: 4000 nA, Nebulizer gas: 0.4 Bar, Dry Heater: 180 °C, Dry gas: 4.0 L/min).

Transmission electron microscopy (TEM) images were obtained using a JOEL JEM 1010 transmission electron microscope from the CACTI, University of Vigo (Spain), operating at 100 kV. Samples were prepared by dropping 5 μL of the colloidal suspension on a copper grid coated with a continuous carbon film, and the solvent was allowed to evaporate. The size of particles and histograms were calculated from TEM images using the ImageJ software (Image 1.51 h, Wayne Rasband, National Institutes of Health, Bethesda, MD, USA).

UV–Vis absorption spectra were recorded with a JASCO V-650 spectrophotometer, while fluorescence emission was on a HORIBA Scientific FLUOROMAX-4 spectrofluorimeter from PROTEOMASS Scientific Society Facility. All samples were carried out at 293 K with recourse to rectangular quartz cells of 10 mm in width. Visualization of the TLC was performed using a Vilber UV Lamp (BVL-6.LC dual wavelength 254 nm/365 nm, operational power of 2 × 6 Watts). Using a combination of ^{1}H NMR, ^{13}C NMR, 2-D COSY, HSQC, HMBC, and high-resolution mass spectrometry, all compounds' chemical identities were verified. Using 5 mm tubes on a Bruker Avance II+ 600 spectrometer, the ^{1}H NMR and ^{13}C NMR spectra were measured in $CDCl_3$ at 293 K at operating frequencies of 600.13 MHz and 150.92 MHz, respectively. ^{1}H and ^{13}C NMR spectra were calibrated to the signal of tetramethylsilane (TMS), δ = 0.00. Chemical shifts are measured to an accuracy of 0.01 parts per million (ppm). The coupling constants (*J*) are shown with a precision of 0.1 and represented in Hz. The spin multiplicity in the 1H NMR was denoted by the abbreviations s = singlet, d = doublet, t = triplet, q = quartet, dd = doublet of doublets, dt = doublet of triplets, td = triplet of doublets, and m = multiplet.

2.3. Synthetic procedures

2.3.1. Synthesis of *L1* and *L2*

2.3.1.1. Synthesis of intermediate N,N'-(disulfanediylbis(ethane-2,1-diyl)) bis(2-aminobenzamide) (3). In a 100 ml flask charged with 50 mL dry dichloromethane (DCM) were added consequently anthranilic acid (**2**) (0.600 g, 4.38 mmol, 2.2 eq.), diamine **1** as di-HCl salt (0.450 g, 1.99 mmol, 1.0 eq.), diisopropylethylamine (DIPEA) (1.54 g, 1.97 mL, 11.93 mmol, 6.0 eq.) and TBTU (1.41 g, 4.38 mmol, 2.2 eq.). The formed clear solution was stirred at r.t. for 41 h. TLC of reaction mixture – DCM:

methyl-*tert*-butyl ether (MTBE) = 5:1, x2. Workup: dilution with 30 mL DCM and washing with 1% aq. citric acid, sat. aq. $NaHCO_3$ and finally with water. The organic phase was dried over anhydrous Na_2SO_4, filtered and evaporated to dryness. This crude product was purified by column chromatography: 75 g silica; phase 1 - DCM:MTBE = 5:1 (to remove contaminations); phase 2 - DCM:MTBE = 5:2 (for product). After solvent evaporation and drying *in vacuo*, product **3** was obtained as a white powder (0.760 g, 99%). m.p. 132–133 °C. ^{1}H NMR (600 MHz, $CDCl_3$) δ 7.38 (dd, *J* = 7.9, 1.5 Hz, 2H, H-5), 7.20 (m, 2H, H-3), 6.78 (s, 2H, CO–N<u>H</u>), 6.72–6.57 (m, 4H, H-2 and H-4), 5.48 (s, 4H, N<u>H</u>$_2$), 3.76 (q, *J* = 6.3 Hz, 4H, H-7), 2.95 (t, *J* = 6.4 Hz, 4H, H-8). ^{13}C NMR (151 MHz, $CDCl_3$) δ 169.56 (2C, <u>C</u>=O), 148.74 (2C, C-1), 132.49 (2C, <u>C</u>H$_{arom.}$), 127.40 (2C, <u>C</u>H$_{arom.}$), 117.34 (2C, <u>C</u>H$_{arom.}$), 116.69 (2C, <u>C</u>H$_{arom.}$), 115.82 (2C, C-6), 38.61 (2C, C-7 or C-8), 38.04 (2C, C-7 or C-8) (Figure S1).

*2.3.1.2. Synthesis of N,N′-(disulfanediylbis(ethane-2,1-diyl))bis(2-((5-(dimethylamino)naphthalene)-1-sulfonamido)benzamide) (**L1**).* Compound **3** (0.300 g, 0.77 mmol, 1.0 eq.) was dissolved in 5 mL dry pyridine. Then dansyl chloride (0.456 g, 1.69 mmol, 2.2 eq.) was added and the formed clear solution was stirred at r.t. for 72 h. Workup: excess of conc. aq. citric acid was added and extracted with DCM. The organic phase was washed with water, dried over anhydrous Na_2SO_4, filtered and evaporated to dryness. This crude product was purified by column chromatography: 70 g silica, phase DCM:MTBE = 20:1. After solvent evaporation and drying *in vacuo*, product **L1** was obtained as a yellow powder (0.510 g, 78%). m.p. 123–124 °C. ^{1}H NMR (600 MHz, $CDCl_3$) δ 11.17 (s, 2H, SO_2–N<u>H</u>), 8.46 (dt, *J* = 8.6, 1.1 Hz, 2H, H-9), 8.32 (d, *J* = 8.6 Hz, 2H, H-4), 8.23 (dd, *J* = 7.3, 1.2 Hz, 2H, H-7), 7.55–7.47 (m, 4H, H-3 and H-15), 7.43 (dd, *J* = 8.5, 7.3 Hz, 2H, H-8), 7.30 (dd, *J* = 7.9, 1.5 Hz, 2H, H-12), 7.26 (m, 2H, H-13), 7.12 (d, *J* = 7.6 Hz, 2H, H-2), 6.88 (td, *J* = 7.5, 1.1 Hz, 2H, H-14), 6.62 (t, *J* = 5.9 Hz, 2H, CO–N<u>H</u>), 3.54 (q, *J* = 6.3 Hz, 4H, H-17), 2.82 (s, 12H, C<u>H</u>$_3$), 2.78 (t, *J* = 6.3 Hz, 4H, H-18). ^{13}C NMR (151 MHz, $CDCl_3$) δ 168.67 (2C, <u>C</u>O–NH), 151.77 (2C, C-1), 138.71 (2C, C-11), 134.63 (2C, C-6), 132.62 (2C, C-13), 130.77 (2C, C-9), 129.91 (2C, C-7), 129.79 (2C, C-5 or C-10), 129.46 (2C, C-5 or C-10), 128.39 (2C, C-15), 126.88 (2C, C-12), 123.01 (2C, C-8 or C-14), 122.99 (2C, C-8 or C-14), 120.53 (2C, C-16), 119.84 (2C, C-3), 118.96 (2C, C-4), 115.31 (2C, C-2), 45.39 (4C, <u>C</u>H$_3$), 38.83 (2C, C-17 or C-18), 37.41 (2C, C-17 or C-18). ESI-HRMS: $[M+H]^+$ for $C_{42}H_{44}N_6O_6S_4$ = 857.2270 (- 0.9 ppm), $[M+2H]^{2+}$ $C_{42}H_{44}N_6O_6S_4$ = 429.1175 (- 0.1 ppm). Calculated $[M+H]^+$ for $C_{42}H_{44}N_6O_6S_4$ = 857.227794, and $[M+2H]^{2+}$ $C_{42}H_{44}N_6O_6S_4$ = 429.117535 (Figures S2, S4).

*2.3.1.3. Synthesis of N,N′-(disulfanediylbis(ethane-2,1-diyl))bis(5-(dimethylamino)naphthalene-1-sulfonamide) (**L2**).* Diamine **1** as di-HCl salt (0.250 g, 1.11 mmol, 1.0 eq.) and Et_3N (0.560 g, 0.77 mL, 5.55 mmol, 5.0 eq.) were dissolved in 50 mL dry DCM and cooled to 5 °C using an ice-water bath. Then dansyl chloride (0.659 g, 2.44 mmol, 2.2 eq.) was added in one portion and the formed clear mixture was stirred for 30 min at 5 °C, followed by 20 h at r.t. TLC of reaction mixture – DCM: MTBE = 5:1, x1. Workup: dilution with 30 mL DCM and washing with 1% aq. citric acid and water. The organic phase was dried over anhydr. Na_2SO_4, filtered, and evaporated to dryness. The crude product was purified by column chromatography: 70 g silica, phase DCM:MTBE = 10:1. After evaporation of phase and drying *in vacuo*, product **L2** was obtained as a yellow powder (0.65 g, 95%). m.p. 74–75 °C. ^{1}H NMR (600 MHz, $CDCl_3$) δ 8.54 (dd, *J* = 8.5, 1.1 Hz, 2H, H-9), 8.27–8.22 (m, 4H, H-4 and H-7), 7.55 (dd, *J* = 8.7, 7.5 Hz, 2H, H-3), 7.52 (dd, *J* = 8.5, 7.3 Hz, 2H, H-8), 7.18 (d, *J* = 7.6 Hz, 2H, H-2), 5.21 (t, *J* = 6.3 Hz, 2H, SO_2–N<u>H</u>), 3.10 (q, *J* = 6.3 Hz, 4H, H-11), 2.89 (s, 12H, C<u>H</u>$_3$), 2.49 (t, *J* = 6.3 Hz, 4H, H-12). ^{13}C NMR (151 MHz, $CDCl_3$) δ 152.05 (2C, C-1), 134.38 (2C, C-6), 130.69 (2C, C-9), 129.86 (2C, C-5 or C-10), 129.69 (2C, C-3), 129.47 (2C, C-5 or C-10), 128.60 (2C, C-7), 123.19 (2C, C-8), 118.55 (2C, C-4), 115.30 (2C, C-2), 45.42 (4C, <u>C</u>H$_3$), 41.56 (2C, C-11), 37.73 (2C, C-12). ESI-HRMS: $[M+H]^+$ for $C_{28}H_{34}N_4O_4S_4$ = 619.1543 (1.2 ppm), and $[M+2H]^{2+}$ for $C_{28}H_{34}N_4O_4S_4$ = 310.0811 (2.2 ppm). Calculated $[M+H]^+$ for $C_{28}H_{34}N_4O_4S_4$ = 619.153566 and $[M+2H]^{2+}$ for $C_{28}H_{34}N_4O_4S_4$ = 310.080421 (Figures S3, S5).

2.4. Spectrophotometric and spectrofluorimetric measurements

2.4.1. Photophysical characterization and titrations

The spectroscopic characterizations and titrations were performed using stock solutions of compounds **L1** and **L2** (ca. 10^{-3} M) in various organic solvents (CH_3CN, EtOH, DMSO, $CHCl_3$, toluene and THF), prepared by dissolving the appropriate amount of the selected compound in a 10 mL volumetric flask. The studied solutions were prepared by appropriate dilution of the stock solutions to 10^{-5} – 10^{-6} M.

Titrations of **L1** and **L2** were carried out by the addition of microliter aliquots of standard solutions of Ca^{2+}, Co^{2+}, Ni^{2+}, Cu^{2+}, Zn^{2+}, Ag^+, Cd^{2+}, Hg^{2+}, Pb^{2+} ions in acetonitrile. A correction for the absorbed light was performed when necessary.

Spectra of solid samples were collected with a Horiba-Jobin-Yvon Fluoromax-4® spectrofluorometer using an optic fibre connected to the equipment, by exciting the solid compounds at appropriated λ (nm). All measurements were performed at 298 K.

Additionally, mixtures containing different water fractions (f_w), (f_w = 0%, 17%, 33%, 55%, 67% and 83%) with a final concentration of 10 mM were prepared and characterized by absorption and emission spectroscopy.

2.4.2. Fluorescence quantum yield and lifetime

Relative photoluminescence quantum yield measurements were conducted using a solution of dansyl amide in acetonitrile as the reference standard. This approach was employed to quantify the relative quantum yields of both compounds when dissolved in the same solvent (φ_F = 0.37), while the remaining ones were measured relative to the standard solution of dansyl amide in DMSO (φ_F = 0.61), as well as for both compounds in f_w = 83% [41]. The quantum yield for the polymeric particles of **L1** was obtained relative to the compound itself in chloroform. Tempro Fluorescence Lifetime System with a Nanoled pulsed diode controller from Horiba Jobin-Yvon (PROTEOMASS Scientific Society Facility) was used to perform lifetime measurements.

2.5. Synthesis of L1 polymeric microparticles

A solution of polymer matrix styrene-butadiene-styrene block copolymer (SBS) (50 mg) in 2 mL of tetrahydrofuran (THF) was prepared and heated at 70 °C for 5 min aiming to allow solubilization. When the solution was cooled back to room temperature, an aliquot of 0.6 mL was quickly added to **L1** (0.5 mg) and transferred over 2.4 mL of deionized water, maintaining a magnetic stirring at 400 rpm for 5 min. The resulting mixture was stored at 20 °C in the dark for 24 h for oil-in-water droplets stabilization. The final particles were obtained after evaporation of THF at room temperature for 24 h. Before use, a filtration step using glass membranes with a pore size of 10–15 μm was performed to remove potential non-encapsulated **L1** and polymer precipitates.

2.6. Determination of the detection and quantification limits (LOD and LOQ)

For the determination of the detection limit (LOD) and the quantification limit (LOQ), ten different measurements of a solution containing the selected probe were collected without the addition of any metal ion (y_{blank}). The LOD and LOQ were determined using the formulas:

LOD = $y_{dl} = y_{blank} + 3std$, where y_{dl} = signal detection limit and std = standard deviation.

LOQ = $y_{dl} = y_{blank} + 10std$, where y_{dl} = signal detection limit and std = standard deviation.

Additionally, small amounts of the metal ion were added to a solution containing **L1** and **L2**, to determine the minimal detectable and quantified concentration out of the LOD and LOQ values, respectively.

3. Results and discussion

3.1. Synthesis

The synthesis of the target sulfonamides **L1** and **L2** was accomplished according to Scheme 1. Compound **L1** was synthesized in two steps. The first step includes the preparation of intermediate **3** quantitative starting from anthranilic acid (**2**) and **1** (both commercial products) proceeding at ambient temperature, by implementation of classical conditions of the peptide synthesis - presence of coupling reagent 2-(1*H*-benzotriazole-1-yl)-1,1,3,3-tetramethylaminium tetrafluoroborate (TBTU) under basic conditions (excess of DIPEA in dichloromethane). After isolation and purification, compound **3** was reacted with commercial dansyl chloride in dry pyridine (Py) at r.t. to furnish **L1** in 78% yield. Direct acylation of the diamine **1** with dansyl chloride (with excess of tryethylamine) in dry dichloromethane (DCM) affords the target product **L2** in 95% yield. The preparation of this compound was previously reported in the literature, concerning an investigation of fluorescent thiomaleimides [42].

It is known from the literature, that dithio groups in ligands are able to form stable chelating complexes with transition and heavy metals [43–45], with or without S–S bond breaking. This is the main reason for introducing the dithio function in L1 and L2. Moreover, dithio compounds have an advantage over their corresponding thiols because they are more stable and resistant to oxidation from air. This is important in order to obtain and store ligands in pure form, without the need of special conditions (i.e. inert atmosphere).

3.2. Photophysical characterization

Fig. 1 shows the main photophysical characterization of **L1** and **L2** evaluated at 298 K in acetonitrile. Compounds **L1** and **L2** exhibit two main absorption bands at 332 nm and 340 nm, respectively, which is a hallmark of the π-π* transition of the dansyl chromophore, being colourless when observed by the unaided eye. Concerning the emission properties, fluorophore **L1** shows a maximum emission band located at 527 nm and **L2** at 518 nm, both of which emit an intense green colour under UV light. In the solid state, the emission of both compounds is characterized by a pronounced blue-shift of about 20 nm compared to the solution. Hence, 507 nm and 499 nm for **L1** and **L2**, respectively. The incorporation of a benzene ring as in the case of **L1** leads to a red-shift in the emission wavelength, as well as, in the solid state compared to **L2**, due to extending the conjugation, with the consequent decrease in fluorescence quantum yield and brightness, rendering a compound less stable in the excited state, thus shortening its lifetime (see Fig. 1D).

In order to evaluate the sensitivity of **L1** and **L2** to solvent polarity, both compounds were characterized and studied in six different solvents, including DMSO, CH_3CN, EtOH, THF, $CHCl_3$ and toluene (Figures S6-S9).

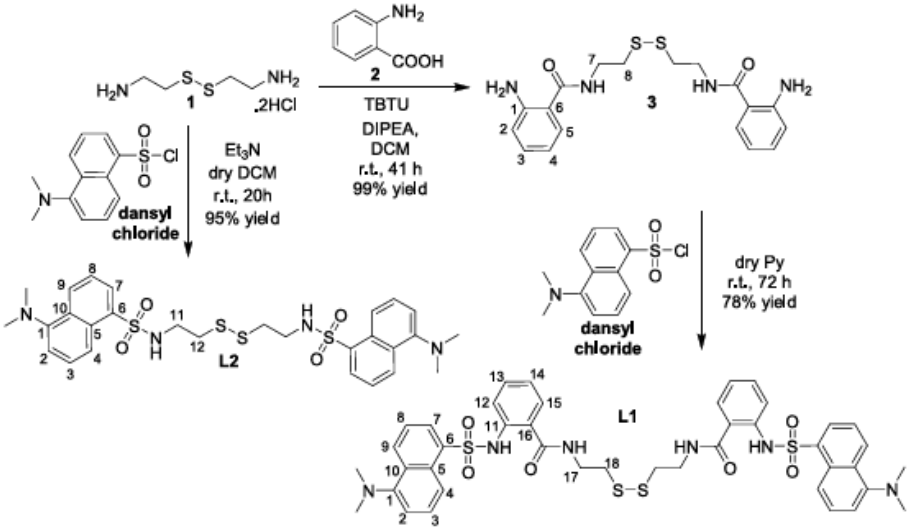
As can be seen in Table 2, in absorption despite their different maximum bands in all solvents, there is no correlation with the solvent polarity increase. However, in the emission, a red shift of the maximum bands is verified, from 498 nm to 535 nm in **L1** and from 488 nm to 520 nm in **L2**, as the polarity of the solvent increase.

Thus, in the excited state polar solvents appear to have a significant impact on the stabilization of the compounds, where **L1** and **L2** appear to be more stable in the excited state than in the ground state. Based on the observed shifts in the emission spectra, **L1** and **L2** are denominated positive solvatofluorochromic. This phenomenon has important applications in imaging, biology and biomedicine to measure local polarity in biological structures [46].

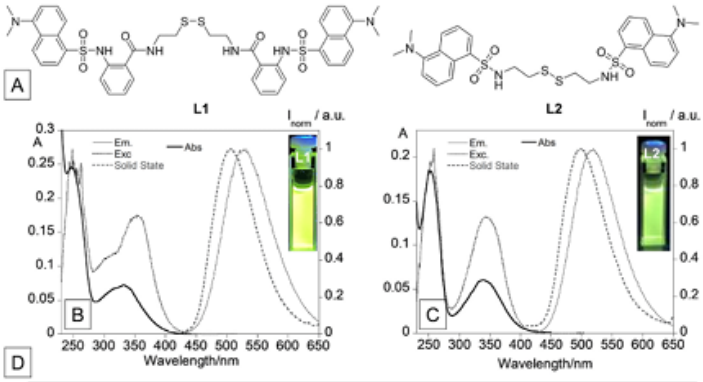
To shed more light on the **L1** and **L2** solvatofluorochromic behaviour, and to quantitatively characterize the solute-solvent interactions, the multiparametric fitting of the Kamlet-Taft equation (Equation (1)) was performed allowing the determination of the three solute-dependent parameters (υ_0, a, b and p).

$$\upsilon = \upsilon_0 + a\alpha + b\beta + p\pi^* \quad \text{(Equation 1)}$$

where υ_0 is the value of emission in a reference solvent; parameters a, b and p are the responses of the solute property to the solvent property, α: the solvent's hydrogen bond donor (HBD) acidity; β: the solvent's hydrogen bond acceptor (HBA) basicity; π*: the solvent's dipolarity/



Scheme 1. Synthetic approach to the preparation of the target **L1** and **L2** fluorophores.



Compound	λ_{abs} (nm)	λ_{em} (nm)	ε ($cm^{-1}.M^{-1}$)	Stokes shift (cm^{-1})	$\lambda_{em\ solid}$ (nm)	ϕ (%)	Brightness ε χ ϕ ($cm^{-1}.M^{-1}$)	τ (ns)
L1	332	527	9357	51282	507	29	2741	10
L2	340	518	9904	56179	499	34	3416	12

Fig. 1. (A) Chemical structure of dansyl derivatives **L1** and **L2**. Absorption, excitation, emission and solid-state emission spectra for **L1** (B) and **L2** (C) in CH_3CN ([**L1**] = [**L2**] = 6 μM). (D) Main photophysical data of compounds **L1** and **L2**.

Table 1
Spectroscopic polarity parameters, physical properties of the different solvents. ε_r: relative permittivity; η: refractive index; α: the solvent's HBD acidity; β: the solvent's HBA basicity; π*: the solvent's dipolarity/polarizability.

Solvent	ε_r	α	β	π*	η
DMSO	47.24	0	0.76	1.00	1.47
CH_3CN	35.94	0.19	0.40	0.66	1.34
EtOH	24.30	0.86	0.75	0.54	1.36
THF	7.58	0	0.55	0.58	1.40
$CHCl_3$	4.89	0.20	0.10	0.69	1.44
Toluene	2.38	0	0.11	0.54	1.49

polarizability (Table 1) [47,48].

Fig. 2 shows the images of **L1** and **L2** under a UV light lamp and based on the fitting linear plots of $\upsilon_{exp.}$ versus $\upsilon_{calc.}$, the fitted parameters (υ0, a, b and p), the slope and correlation coefficients.

According to the Kamlet-Taft parameters of each compound, **L2** is more polar than **L1**, which could be attributed to differences in their molecular structure. On the other hand, **L1** has the highest polarizability, having the ability to be distorted by an external electric field, which could also be related to its molecular size and shape.

3.3. Metal ions sensing

The sensorial ability of dansyl derivatives **L1** and **L2** was studied towards metal ions, such as, Ca^{2+}, Co^{2+}, Ni^{2+}, Cu^{2+}, Zn^{2+}, Ag^{+}, Cd^{2+}, Hg^{2+} and Pb^{2+} in acetonitrile. Fig. 3 shows the maximum emission at 527 nm and 518 nm of **L1** and **L2** upon the addition of 1, 5 and 10 equivalents of the above-mentioned metal ions, respectively. Both compounds exhibit unprecedented sensitivity to Cu^{2+} and Hg^{2+} metal ions (see Fig. 3).

Fig. 4 represents the absorption and emission spectra at increasing amounts of Cu^{2+} (A, C) and Hg^{2+} (B, D) for **L1** and **L2**, respectively. The addition of Cu^{2+} and Hg^{2+} promotes similar spectral behaviour in the absorption, where it is observed a decrease in the absorption at 332 nm, 340 nm and an increase in the absorbance at 290 nm and 255 nm for **L1** and **L2**, respectively. Regarding the emission spectra, in both cases, a quenching in the emission intensity at 527 nm (**L1**) and 518 nm (**L2**) is visualized. Paramagnetic transition metal ions, such as Cu^{2+} with unfilled d orbital shells, are commonly identified by the chelation enhancement of quenching (CHEQ effect), which occurs through either electron transfer or energy transfer mechanisms. However, Hg^{2+}, being a diamagnetic d10 metal, is an exception to this trend. In the case of Hg^{2+}, quenching can also be attributed to spin-orbit coupling, which serves as the primary pathway for the nonradiative deactivation (K_{nr}) process [49].

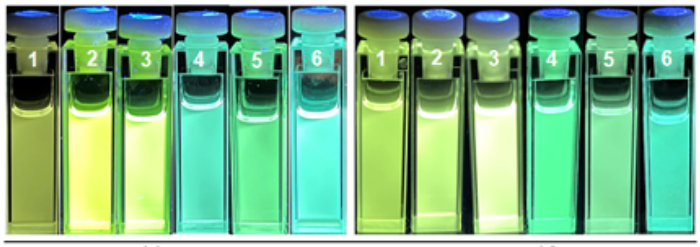
The stability constants were calculated through HypSpec program [50], as well as the minimal detectable and quantified amount of Cu^{2+} and Hg^{2+} in acetonitrile for both compounds and the data are summarized in Table 3.

The stability constants reveal the formation of mononuclear species for Cu^{2+} and Hg^{2+} in both compounds. The highest constant was obtained for compound **L2** for Hg^{2+} with a value of $LogK_{ass.} = 6.38 \pm 0.06$.

The lowest detectable and quantifiable amounts were also determined for **L2** (2.5 μM and 4.5 μM), indicating that it has a high affinity for binding with Hg^{2+} ions, having the potential to be useful in

Table 2
Photophysical data of the dansyl derivatives **L1** and **L2** evaluated in organic solvents.

Solvent	λ (nm)				ε (10^4 cm^{-1} M^{-1})		Stokes shift (cm^{-1})		φ (%)		τ (ns)	
	L1 (Abs.)	L1 (Em.)	L2 (Abs.)	L2 (Em.)	L1	L2	L1	L2	L1	L2	L1	L2
DMSO	347	535	337	520	1.0506	1.3706	53191	54644	30	59	14	17
CH_3CN	332	527	340	518	0.9357	0.9904	51282	56179	29	34	10	12
EtOH	330	520	338	514	0.9058	1.1285	52631	56818	24	33	13	13
THF	336	507	336	497	1.1135	1.2022	58479	64102	47	50	13	12
$CHCl_3$	343	504	340	498	0.8526	1.0200	62111	62500	52	56	14	15
Toluene	341	498	338	488	1.0325	0.8259	63694	66666	49	57	12	12



	L1			L2		
	υ_0	a	b	p	Slope	R^2
L1	21244	-388	-885	-1861	0.99	0.99
L2	21531	-707	-664	-1796	0.99	1

Fig. 2. (Top) Images of **L1** and **L2** under a UV light lamp. Polarity decrease from 1 to 6 (1 – DMSO; 2 – CH_3CN; 3 – EtOH; 4 – THF; 5 – $CHCl_3$; 6 – toluene). (Down) υ_0, a, b and p-values, in cm^{-1}, slope and correlation coefficients obtained from Kamlet–Taft multiparametric fitting of the emission data.

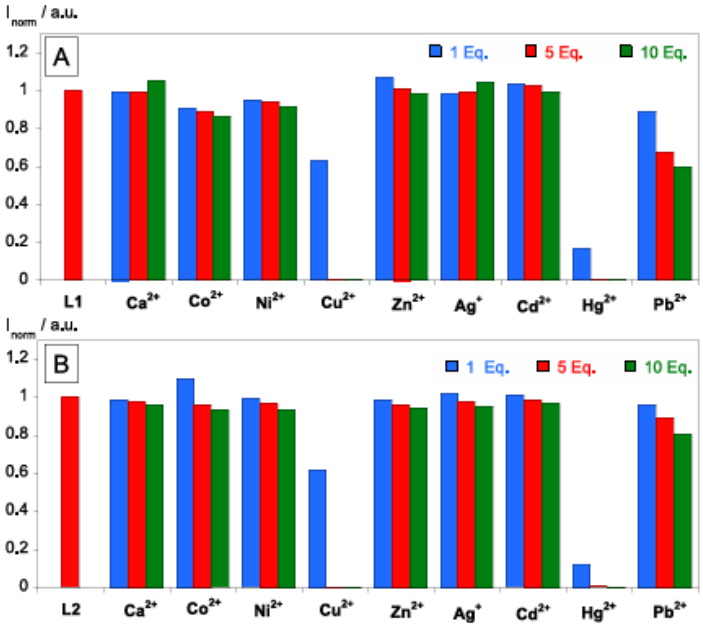


Fig. 3. Maximum emission intensities of **L1** (A) and **L2** (B) upon the addition of 1, 5 and 10 equivalents of Ca^{2+}, Co^{2+}, Ni^{2+}, Cu^{2+}, Zn^{2+}, Ag^{+}, Cd^{2+}, Hg^{2+} and Pb^{2+} metal ions. ([**L1**] = [**L2**] = 20 μM, $\lambda_{em,L1}$ = 527 nm, $\lambda_{em,L2}$ = 518 nm, T = 298 K).

applications such as environmental monitoring, where the presence of Hg^{2+} needs to be detected and quantified at low concentrations.

Regarding both structures and accordingly, with Pearson's Law, it can be predicted that the metal ion will coordinate with the S (bridge) and N donor atoms.

The structure of **L2** seems to play a significant role in the observed values. The absence of benzene moiety in the dansyl-derived fluorophore reduces the stereochemical hindrance, making it easier and more accessible for the metal ion to coordinate with the ligand.

3.4. Exploring dansyl derivatives behaviour in aqueous media

In order to understand the stability of the compounds in water, **L1** and **L2** were measured by absorption and emission in different mixtures, varying the ratio of acetonitrile to water. As can be seen in Fig. 5 the increase of water led to a decrease in the emission intensity in both compounds up to 67% of water, after that value in 83% of water, an increase of the baseline was observed, which is indicative of the formation of aggregates. Moreover, an increase in the emission intensity and a blue shift are observed, surpassing in the case of **L1**, the emission intensity of the ligand in 100% of acetonitrile.

Such behaviour was confirmed by the emission observed under the

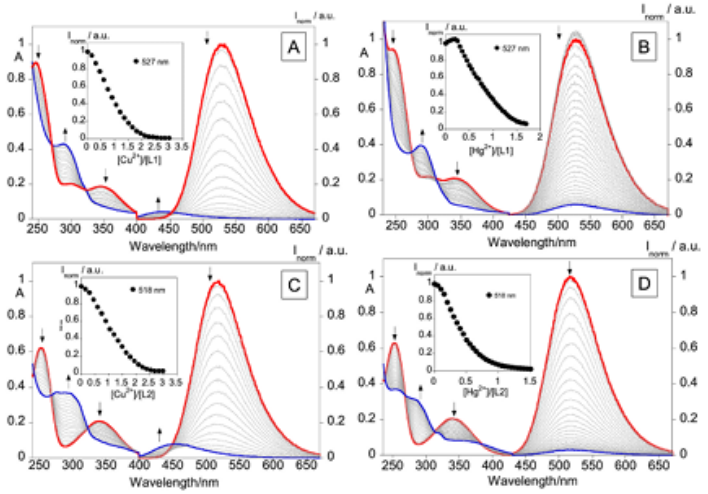


Fig. 4. Spectrophotometric and spectrofluorimetric titrations of compounds **L1** (A, B) and **L2** (C, D) with increased additions of Cu^{2+} (A, C), and Hg^{2+} (B, D) in CH_3CN. The inset represents the emission (A–D) as a function of $[Cu^{2+}]/[\mathbf{L1}]$ at 527 nm (A), of $[Cu^{2+}]/[\mathbf{L2}]$ at 518 nm (C), of $[Hg^{2+}]/[\mathbf{L1}]$ at 527 nm (B) and of $[Hg^{2+}]/[\mathbf{L2}]$ at 518 nm (D). $[\mathbf{L1}] = [\mathbf{L2}] = 20$ μM, $\lambda_{exc,L1} = 332$ nm, $\lambda_{exc,L2} = 340$ nm,T = 298 K).

Table 3
Stability association constants and stoichiometry for the complexes formed **L1** and **L2** with Cu^{2+} and Hg^{2+} ions, in CH_3CN. Minimal detectable (LOD) and quantified (LOQ) amounts (μM) of Cu^{2+} and Hg^{2+} metal ions (M) **L1** and **L2**. LOD and LOQ were measured by emission at 527 nm and 518 nm for **L1** and **L2**, respectively.

Compounds	Metal (M)	Association constants ($LogK_{ass.}$), L:M	LOD (μM)	LOQ (μM)
L1	Cu^{2+}	5.11 ± 0.06 (1:1)	7.5	15.0
	Hg^{2+}	5.00 ± 0.01 (1:1)	8.0	14.0
L2	Cu^{2+}	4.59 ± 0.01 (1:1)	6.0	13.5
	Hg^{2+}	6.38 ± 0.06 (1:1)	2.5	4.50

UV light lamp (see Fig. 6), where the sample containing 83% of water appears to be the most emissive in both cases. The fluorescence quantum yield was determined, and a value of φ = 25% and φ = 13% were calculated for **L1** and **L2**, respectively. In the case of **L1** the fluorescence quantum yield was similar to the one observed in acetonitrile.

In the presence of water (17–63%), molecules with active intramolecular rotation consume excited-state energy through non-radiative relaxation, leading to a decrease in the emission signal. However, when the concentration of these molecules reaches a certain threshold, in this case around 87%, the physical constraints imposed by aggregation can restrict their motion and prevent non-radiative relaxation. This can promote radiative decay, leading to a significant increase in the emission intensity. Thus, the aggregation-induced emission (AIE) effect arises from the restriction of motion due to physical constraints imposed by aggregation [51]. These results are consistent with another experiment in which, while maintaining the same water percentage (87%), an increase in the concentration of ligand **L1** resulted in an enhanced aggregation-induced emission (AIE) effect. Consequently, there was an increase in the emission intensity (see Figure S10).

To explore deeply this observation, the solutions were measured by dynamic light scattering, resulting in monodispersed peaks (PDI_{L1} = 0.02; PDI_{L2} = 0.06) with hydrodynamic sizes of 124 ± 2 nm (**L1**) and 188 ± 1.6 nm (**L2**).

These results confirmed the formation of aggregates in L1 and L2. Based on other examples reported in the literature [18], herein the water modulates the aggregation state of the chromophore resulting in fluorescence enhancement *via* AIE mechanism, providing a wide range of multiple applications in complex environments. However, these organic compounds could present some drawbacks, such as poor water solubility, leading to latter precipitation of the aggregates.

3.5. L1 doped SBS polymeric microparticles

Due to the observed AIE phenomenon of current compounds in aqueous media and our past works concerning the development of systems that would allow highly hydrophobic and water quenched sensors to maintain their properties in water, Poly(styrene-butadiene-styrene) SBS polymeric microparticles containing compound L1 were synthesized using the precipitation method, a green method that minimizes waste generation [27,28]. SBS matrix was chosen due to its intrinsic chemical formula, the presence of benzene moieties would potentially improve the stability of these microparticles by staking interactions with the same moiety present in the ligand.

The use of polymeric particles was in this case applied as a measure to enhance the dispersion of the ligand in aqueous media, as well as for improving the AIE effect's stability and bioavailability of the compound. The resulting SBS particles were characterized by fluorescence emission, dynamic light scattering (DLS) and transmission electron microscopy (TEM).

The dansyl-derivative L1 is highly hydrophobic, but when incorporated into a polymeric matrix leads to stable and highly emissive microparticles dispersed in water, with a fluorescence quantum yield of 22%.

The results showed that the particles presented a spherical shape and that the ligand was successfully encapsulated within the polymeric matrix (see Fig. 7 and S11), resulting in high emissive microparticles, with green emission and a maximum emission band at 505 nm in water. Additionally, the microparticles present a size of 628 ± 22 nm (PDI: 0.07 ± 0.04) by DLS, a zeta potential of −27 ± 0.7, and a size of 520 ± 76 nm measured by TEM.

In this work, the use of SBS particles as a carrier for dansyl derivative **L1** has the potential to improve its solubility, stability, and

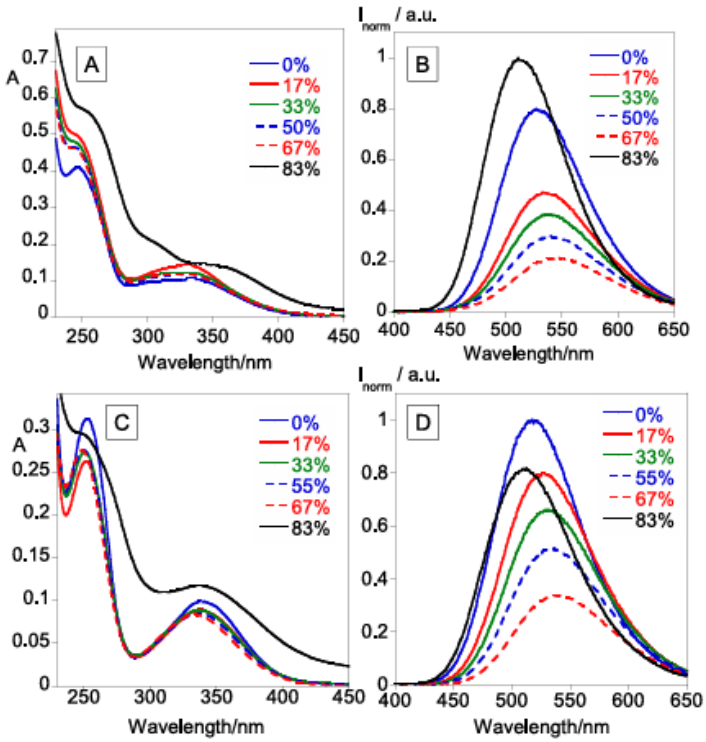


Fig. 5. Absorption (A, C) and emission spectra (B, D) of **L1** (A,B) and **L2** (C,D) in CH_3CN with different water fraction f_w (0%, 17%, 33%, 55%, 67%, 83%). [**L1**] = [**L2**] = 10 μM, T = 298 K.

bioavailability, making it a promising approach for drug delivery and bioimaging.

4. Conclusions

In current work, we present the synthesis of two fluorescent sensors abbreviated as L1 and L2, bearing dual dansyl moieties linked together by a disulfide bridge. Implementation of the classical condition of peptide synthesis for compound L1 was used for the introduction of the benzene moiety, in order to tune the photophysical characteristics of this fluorophore in relation to L2. Due to the common knowledge of the dansyl derivatives to manifest solvatofluorochromism, extensive work has been carried out aiming to better understand the effect of different solvents on the emission properties. Positive solvatofluorochromism was observed for both L1 and L2 chromophores, and the Kamlet-Taft equation was applied to further understand the solute-solvent interactions. Alongside that, the presence of heteroatoms plays a crucial role in the sensing of metal ions, and so L1 and L2 were used as sensors to shed light on their potential for environmental remediation. Both compounds have been found to modulate their photophysical characteristics in the presence of Hg^{2+} and Cu^{2+} with quenching of the emission signal. Stability association constants and stoichiometry suggest mononuclear species for Cu^{2+} and Hg^{2+} in both compounds. Compound L2 was found to exhibit the highest constant towards Hg^{2+} with a value of $LogK_{ass}$ = 6.38 with a LOD and LOQ of 2.5 μM and 4.5 μM. With the intention to further explore these compounds, their behaviour in water was studied and found to manifest AIE enhancement at high fractions of water content with the formation of aggregates, as DLS suggests, with hydrodynamic sizes of 124 ± 2 nm (L1) and 188 ± 1.6 nm (L2). Being in line with our previous efforts to characterize compounds once hydrophobic and unable to manifest emission properties due to water acting as a quencher, SBS polymeric doped microparticles were synthesized using an oil-in-water approach doped with L1 to stabilize the AIE effect. TEM images suggest the formation of stable microparticles with a size of 520 ± 76 nm showing a green emission centred at 505 nm in water. Therefore, dansyl-derived compounds still provide value for their great photophysical characteristics, alongside their potential for bioimaging or drug delivery.

CRediT authorship contribution statement

Frederico Duarte: Formal analysis, Investigation, Writing - Original Draft, Writing - Review & Editing, Visualization. Georgi Dobrikov: Methodology, Validation, Formal Analysis, Investigation, Writing - Original Draft, Writing - Review & Editing, Resources, Visualization. Atanas Kurutos: Methodology, Validation, Formal Analysis, Investigation, Writing - Original Draft, Writing - Review & Editing, Resources, Visualization. Javier Fernandez Lodeiro: Investigation, Resources, Validation, Writing - Review & Editing. Jose Luis Capelo-Martinez: Resources, Writing - Review & Editing, Funding acquisition. Hugo M. Santos: Investigation, Resources, Validation, Writing - Review & Editing. Elisabete Oliveira: Conceptualization, Methodology, Validation, Formal Analysis, Investigation, Resources, Writing - Original Draft, Writing - Review & Editing, Resources, Visualization, supervision,

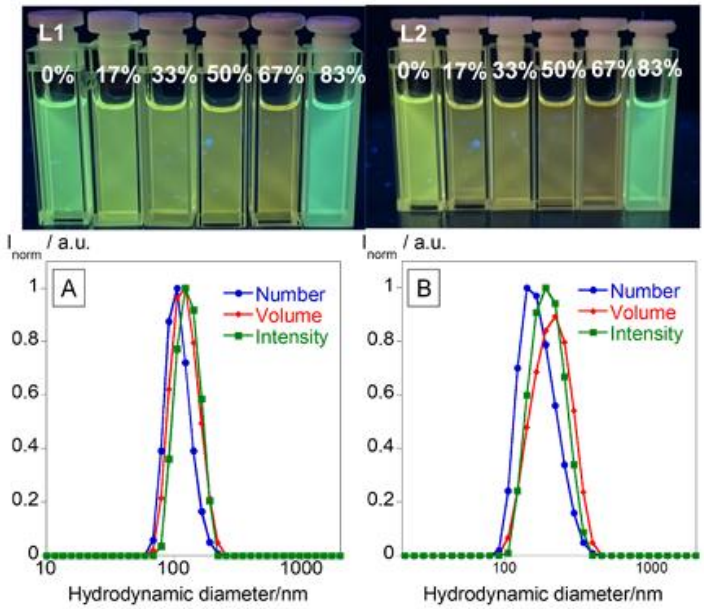


Fig. 6. (Top) Images of **L1** and **L2** in CH_3CN with different water fraction f_w (0%, 17%, 33%, 55%, 67%, 83%). [**L1**] = [**L2**] = 10 μM, T = 298 K. Size according to number, volume, and intensity distributions of a solution of CH_3CN/water solution of **L1** (A) and **L2** (B) with f_w = 83%.

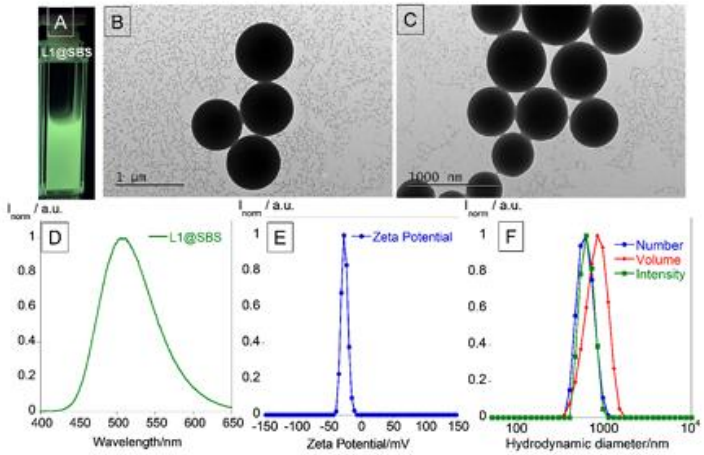


Fig. 7. (A) Image of **L1**@SBS particles under UV-lamp; (B, C) TEM images of the **L1**@SBS particles, (D, E and F) Emission spectrum, zeta potential and hydrodynamic size of **L1**@SBS particles.

Funding acquisition. Carlos Lodeiro: Conceptualization, Methodology, Validation, Formal Analysis, Investigation, Resources, Writing - Review & Editing, Resources, Visualization, supervision, Funding acquisition, Project administration.

Declaration of competing interest

The authors declare that they have no known competing financial interests or personal relationships that could have appeared to influence the work reported in this paper.

Data availability

Data will be made available on request.

Acknowledgements

This work was supported by the Associate Laboratory for Green Chemistry - LAQV which is financed by national funds from FCT/MCTES (UIDB/50006/2020 and UIDP/50006/2020) as well as the PROTEOMASS Scientific Society (Portugal) for funding support (General Funding Grant 2022–2023). F.D. thanks to FCT/MEC (Portugal) for his doctoral grant 2021.05161.BD. E.O thanks FCT/MEC (Portugal) for the individual contract, CEECIND/00648/2017. J.F-.L. thanks the FCT/MEC (Portugal) for the individual research contract DL57. HMS acknowledges the Associate Laboratory for Green Chemistry-LAQV (LA/P/0008/2020) funded by FCT/MCTES for his research contract.

The financial support by the Bulgarian National Science Fund (BNSF) under grant – "Novel styryl and polymethine fluorophores as potential theranostic agents "contract № КП-06-М59/1 from 15.11.2021 is gratefully acknowledged by A.K. This work is also developed and acknowledged by A.K. as part of contract №: BG-RRP-2.004-0002-C01, Laboratory of Organic Functional Materials (Project BiOrgaMCT), Procedure BG-RRP-2.004, Establishing of a network of research higher education institutions in Bulgaria", funded by BULGARIAN NATIONAL RECOVERY AND RESILIENCE PLAN".

G.D. thanks to the European Regional Development Fund within the Operational Programme Science and Education for Smart Growth 2014–2020 under the Project Center of Exellence: National center of mechatronics and clean technologies - BG05M2OP001-1.001-0008 for the financial support.

Appendix A. Supplementary data

Supplementary data to this article can be found online at https://doi.org/10.1016/j.dyepig.2023.111428.

References

[1] Zhang Y, Lei B, Zhang X. Intramolecular energy transfer dyes as temperature- and polarity-sensitive fluorescence probes. Dyes Pigments 2022;205:110492. https://doi.org/10.1016/j.dyepig.2022.110492.

[2] Reisch A, Klymchenko AS. Fluorescent polymer nanoparticles based on dyes: seeking brighter tools for bioimaging. Small 2016;12:1968–92. https://doi.org/10.1002/smll.201503396.

[3] Nishiyabu R, Sugino Y, Kubo Y. White-light emitting boronate microparticles for potential use as reusable bright chemosensors in water. Chem Commun 2013;49:9869. https://doi.org/10.1039/c3cc45739g.

[4] Cui Y, Li F, Zhang X. Controlling fluorescence resonance energy transfer of donor–acceptor dyes by Diels–Alder dynamic covalent bonds. Chem Commun 2021;57:3275–8. https://doi.org/10.1039/D1CC00165E.

[5] Sierra AF, Hernández-Alonso D, Romero MA, González-Delgado JA, Pischel U, Ballester P. Optical supramolecular sensing of creatinine. J Am Chem Soc 2020;142:4276–84. https://doi.org/10.1021/jacs.9b12071.

[6] Pan Y, Zhang C, Liu SH, Tan Y, Yin J. Fluorescent switch based on dithienylethene with dansulfonamide in multimedium. Dyes Pigments 2020;181:108546. https://doi.org/10.1016/j.dyepig.2020.108546.

[7] Zhang Y, Lei B, Zhang X. Reversible, controllable white-light emission of dye systems by dynamic covalent furan moiety exchange. Chem Commun 2022;58:5261–4. https://doi.org/10.1039/D2CC01309F.

[8] Shi Z, Wu J, Song Q, Gostl R, Herrmann A. Toward drug release using polymer mechanochemical disulfide scission. J Am Chem Soc 2020;142:14725–32. https://doi.org/10.1021/jacs.0c07077.

[9] Dare EO, Vendrell-Criado V, Jiménez MC, Pérez-Ruiz R, Díaz Díaz D. Highly efficient latent fingerprint detection by eight-dansyl-functionalized octasilsesquioxane nanohybrids. Dyes Pigments 2021;184:108841. https://doi.org/10.1016/j.dyepig.2020.108841.

[10] Pazin WM, Almeida AKA, Manzoni V, Dias JMM, de Abreu ACF, Navarro M, et al. Thermal and solvatochromic effects on the emission properties of a thienyl-based dansyl derivative. RSC Adv 2020;10:28484–91. https://doi.org/10.1039/D0RA05949H.

[11] Jiang H, Li Z, Kang Y, Ding L, Qiao S, Jia S, et al. A two-photon fluorescent probe for Cu2+ based on dansyl moiety and its application in bioimaging. Sensor Actuator B Chem 2017;242:112–7. https://doi.org/10.1016/j.snb.2016.11.033.

[12] Thangaraj A, Bhardwaj V, Sahoo SK. A multi-analyte selective dansyl derivative for the fluorescence detection of Cu(ii) and cysteine. Photochem Photobiol Sci 2019;18:1533–9. https://doi.org/10.1039/c9pp00080a.

[13] Wang Y, Zhou J, Zhao L, Xu B. A dual-responsive and highly sensitive fluorescent probe for Cu2+ and pH based on a dansyl derivative. Dyes Pigments 2020;180:108513. https://doi.org/10.1016/j.dyepig.2020.108513.

[14] Luo J, Xie Z, Lam JWY, Cheng L, Tang BZ, Chen H, et al. Aggregation-induced emission of 1-methyl-1,2,3,4,5-pentaphenylsilole. Chem Commun 2001:1740. https://doi.org/10.1039/b105159h. –1.

[15] Zhang J, Shen H, Liu X, Yang X, Broman SL, Wang H, et al. A dihydroazulene-based photofluorochromic AIE system for rewritable 4D information encryption. Angew Chem Int Ed 2022;61. https://doi.org/10.1002/anie.202208460.

[16] Ruan Y-B, Depauw A, Leray I. Aggregation-induced emission enhancement upon Al $^{3+}$ complexation with a tetrasulfonated calix[4]bisazacrown fluorescent molecular sensor. Org Biomol Chem 2014;12:4335–41. https://doi.org/10.1039/C4OB00187G.

[17] Gao M, Tang BZ. Fluorescent sensors based on aggregation-induced emission: recent advances and perspectives. ACS Sens 2017;2:1382–99. https://doi.org/10.1021/acssensors.7b00551.

[18] Ruan Z, Zheng H, Deng C, Cheng X, Ruan X, Lv S, et al. A simple AIE-active triphenylamine derivative for supersensitive detection of water in organic solvents with noticeable fluorescence color change. Dyes Pigments 2022;204:110476. https://doi.org/10.1016/j.dyepig.2022.110476.

[19] Sun H, Tang X-X, Miao B-X, Yang Y, Ni Z. A new AIE and TICT-active tetraphenylethene-based thiazole compound: synthesis, structure, photophysical properties and application for water detection in organic solvents. Sensor Actuator B Chem 2018;267:448–56. https://doi.org/10.1016/j.snb.2018.04.022.

[20] Song Z, Zhang W, Jiang M, Sung HHY, Kwok RTK, Nie H, et al. Synthesis of imidazole-based AIEgens with wide color tunability and exploration of their biological applications. Adv Funct Mater 2016;26:824–32. https://doi.org/10.1002/adfm.201503788.

[21] Wang J, Zhang X, Liu H-B. Highly sensitive pyrene–dansyl conjugate-based fluorescent sensor for discriminative detection of water in organic solvents. Dyes Pigments 2020;182:108685. https://doi.org/10.1016/j.dyepig.2020.108685.

[22] Alam P, Leung NLC, Zhang J, Kwok RTK, Lam JWY, Tang BZ. AIE-based luminescence probes for metal ion detection. Coord Chem Rev 2021;429:213693. https://doi.org/10.1016/j.ccr.2020.213693.

[23] Wan H, Xu Q, Gu P, Li H, Chen D, Li N, et al. AIE-based fluorescent sensors for low concentration toxic ion detection in water. J Hazard Mater 2021;403:123656. https://doi.org/10.1016/j.jhazmat.2020.123656.

[24] Jiang Y, McNeill J. Light-harvesting and amplified energy transfer in conjugated polymer nanoparticles. Chem Rev 2017;117:838–59. https://doi.org/10.1021/acs.chemrev.6b00419.

[25] Wan Q, Huang Q, Liu M, Xu D, Huang H, Zhang X, et al. Aggregation-induced emission active luminescent polymeric nanoparticles: non-covalent fabrication methodologies and biomedical applications. Appl Mater Today 2017;9:145–60. https://doi.org/10.1016/j.apmt.2017.06.004.

[26] Suriya Prabha A, Dorothy R, Jancirani S, Rajendran S, Singh G, Senthil Kumaran S. Recent advances in the study of toxicity of polymer-based nanomaterials. Nanotoxicity, Elsevier; 2020. p. 143–65. https://doi.org/10.1016/B978-0-12-819943-5.00007-5.

[27] Duarte F, Cuerva C, Fernández-Lodeiro C, Fernández-Lodeiro J, Jiménez R, Cano M, et al. Polymer micro and nanoparticles containing B(III) compounds as emissive soft materials for cargo encapsulation and temperature-dependent applications. Nanomaterials 2021;11:3437. https://doi.org/10.3390/nano11123437.

[28] González-Tobío B, Duarte F, Arribas-Delgado A, Fernández-Lodeiro C, Fernández-Lodeiro J, Cano M, et al. Tuning and reviving the luminescence of a new class of pyridyl β-diketonate Eu(III) metallomesogens: from molecules to entrapment in polymer particles. Dyes Pigments 2022;204:110440. https://doi.org/10.1016/j.dyepig.2022.110440.

[29] Zhang X, Wang K, Liu M, Zhang X, Tao L, Chen Y, et al. Polymeric AIE-based nanoprobes for biomedical applications: recent advances and perspectives. Nanoscale 2015;7:11486–508. https://doi.org/10.1039/C5NR01444A.

[30] Lodeiro C, Capelo JL, Mejuto JC, Oliveira E, Santos HM, Pedras B, et al. Light and colour as analytical detection tools: a journey into the periodic table using polyamines to bio-inspired systems as chemosensors. Chem Soc Rev 2010;39:2948. https://doi.org/10.1039/b819787n.

[31] Lodeiro C, Lima JC, Parola AJ, Seixas de Melo JS, Capelo JL, Covelo B, et al. Intramolecular excimer formation and sensing behavior of new fluorimetric probes and their interactions with metal cations and barbituric acids. Sensor Actuator B Chem 2006;115:276–86. https://doi.org/10.1016/j.snb.2005.09.010.

[32] Lodeiro C, Pina F. Luminescent and chromogenic molecular probes based on polyamines and related compounds. Coord Chem Rev 2009;253:1353–83. https://doi.org/10.1016/j.ccr.2008.09.008.

[33] Moura NMM, Núñez C, Santos SM, Faustino MAF, Cavaleiro JAS, Neves MGPMS, et al. Synthesis, spectroscopy studies, and theoretical calculations of new fluorescent probes based on pyrazole containing porphyrins for Zn(II), Cd(II), and Hg(II) optical detection. Inorg Chem 2014;53:6149–58. https://doi.org/10.1021/ic500634y.

[34] Lamelas R, García V, Linares A, Bastida R, Labisbal E, Fernández-Lodeiro A, et al. Novel trans-disubstituted hexaaza-macrocyclic ligands containing pyridine head units: synthesis, disubstitution and colorimetric properties. Sensor Actuator B Chem 2016;225:481–91. https://doi.org/10.1016/j.snb.2015.11.090.

[35] Gonc AC, Luis J, Lodeiro C, Dos AA. Sensors and Actuators B : chemical A seleno-pyrene selective probe for Hg 2 + detection in either aqueous or aprotic systems, vol. 239; 2017. p. 311–8. https://doi.org/10.1016/j.snb.2016.08.014.

[36] Oliveira E, Núñez C, Santos HM, Fernández-Lodeiro J, Fernández-Lodeiro A, Capelo JL, et al. Revisiting the use of gold and silver functionalised nanoparticles as colorimetric and fluorometric chemosensors for metal ions. Sensor Actuator B Chem 2015;212:297–328. https://doi.org/10.1016/j.snb.2015.02.026.

[37] Ma L-J, Liu J, Deng L, Zhao M, Deng Z, Li X, et al. Selective and sensitive fluorescence-shift probes based on two dansyl groups for mercury(ii) ion detection. Photochem Photobiol Sci 2014;13:1521–8. https://doi.org/10.1039/c4pp00094c.
[38] Qureshi N, Ehtisham-ul-Haque S, Abbas M, Yameen M, Farooq Azhar M, Mahmoudi G, et al. Synthesis of fluorescent di-dansyl substituted ethoxy compound: a selective sensor for antimony and thallium metals detection. J Mater Res Technol 2019;8:1576–80. https://doi.org/10.1016/j.jmrt.2017.12.007.
[39] Jose A, Porel M. Probing the interactions of dansyl appended sequence-defined oligomers with serum albumins: effect of functionality, hydrophobicity, and architecture. J Photochem Photobiol Chem 2023;439:114640. https://doi.org/10.1016/j.jphotochem.2023.114640.
[40] Pedro G, Duarte F, Cheptsov DA, Nyu Volodin, Ivanov IV, Santos HM, et al. Exploring coumarin-based boron emissive complexes as temperature thermometers in polymer-supported materials. Sensors 2023;23:1689. https://doi.org/10.3390/s23031689.
[41] Montalti M, Credi A, Prodi L, Mg, Montalti M, Credi A, Prodi LGM. Handbook of photochemistry. third ed. BOCA: Taylor & Francis, Boca Raton; 2006.
[42] Youziel J, Akhbar AR, Aziz Q, Smith MEB, Caddick S, Tinker A, et al. Bromo- and thiomaleimides as a new class of thiol-mediated fluorescence 'turn-on' reagents. Org Biomol Chem 2014;12:557–60. https://doi.org/10.1039/C3OB42141D.
[43] Flora SJS. Structural, chemical and biological aspects of antioxidants for strategies against metal and metalloid exposure. Oxid Med Cell Longev 2009;2:191–206. https://doi.org/10.4161/oxim.2.4.9112.
[44] Muhammad MT, Khan MN. Kinetics, mechanistic and synergistic studies of Alpha lipoic acid with hydrogen peroxide. J Saudi Chem Soc 2017;21:123–31. https://doi.org/10.1016/j.jscs.2015.01.008.
[45] Monreal-Corona R, Biddlecombe J, Ippolito A, Mora-Diez N. Theoretical study of the iron complexes with lipoic and dihydrolipoic acids: exploring secondary antioxidant activity. Antioxidants 2020;9:674. https://doi.org/10.3390/antiox9080674.
[46] Espinar-Barranco L, Luque-Navarro P, Strnad MA, Herrero-Foncubierta P, Crovetto L, Miguel D, et al. A solvatofluorochromic silicon-substituted xanthene dye useful in bioimaging. Dyes Pigments 2019;168:264–72. https://doi.org/10.1016/j.dyepig.2019.04.024.
[47] Ghanadzadeh Gilani A, Moghadam M, Zakerhamidi MS. Solvatochromism of Nile red in anisotropic media. Dyes Pigments 2012;92:1052–7. https://doi.org/10.1016/j.dyepig.2011.07.018.
[48] Nootem J, Sattayanon C, Namuangruk S, Rashatasakhon P, Wattanathana W, Tumcharern G, et al. Solvatochromic triazaborolopyridinium probes toward ultra-sensitive trace water detection in organic solvents. Dyes Pigments 2020;181:108554. https://doi.org/10.1016/j.dyepig.2020.108554.
[49] Oliveira E, Baptista RMF, Costa SPG, Raposo MMM, Lodeiro C. Exploring the emissive properties of new azacrown compounds bearing aryl, furyl, or thienyl moieties: a special case of chelation enhancement of fluorescence upon interaction with Ca^{2+}, Cu^{2+}, or Ni^{2+}. Inorg Chem 2010;49:10847–57. https://doi.org/10.1021/ic101095y.
[50] Gans P, Sabatini A, Vacca A. Investigation of equilibria in solution. Determination of equilibrium constants with the HYPERQUAD suite of programs. Talanta 1996;43:1739–53. https://doi.org/10.1016/0039-9140(96)01958-3.
[51] Wang H, Zhao E, Lam JWY, Tang BZ. AIE luminogens: emission brightened by aggregation. Mater Today 2015;18:365–77. https://doi.org/10.1016/j.mattod.2015.03.004.

.

D

Published Paper in Journal of Photochemistry & Photobiology, A: Chemistry - Corresponding to Chapter 6

Journal of Photochemistry & Photobiology, A: Chemistry 445 (2023) 115033

Contents lists available at ScienceDirect

Journal of Photochemistry & Photobiology, A: Chemistry

journal homepage: www.elsevier.com/locate/jphotochem

Development of fluorochromic polymer doped materials as platforms for temperature sensing using three dansyl derivatives bearing a sulfur bridge

Frederico Duarte [a], Georgi Dobrikov [b,*], Atanas Kurutos [b,c], Jose Luis Capelo-Martinez [a,d], Hugo M. Santos [a,d], Elisabete Oliveira [a,d,*], Carlos Lodeiro [a,d,*]

[a] BIOSCOPE Research Group, LAQV-REQUIMTE, Chemistry Department, NOVA School of Science and Technology, FCT NOVA, Universidade NOVA de Lisboa, 2829-516 Caparica, Portugal
[b] Institute of Organic Chemistry with Centre of Phytochemistry, Bulgarian Academy of Sciences, Acad. G. Bonchev str., bl. 9, 1113 Sofia, Bulgaria
[c] University of Chemical Technology and Metallurgy, 8 St. Kliment Ohridski blvd, 1756 Sofia, Bulgaria
[d] PROTEOMASS Scientific Society, Departmental Building, BIOSCOPE Group laboratories, Ground Floor, FCT-NOVA Caparica Campus, 2829-516 Caparica, Portugal

ARTICLE INFO

Keywords:
Polymers
Dansyl derivatives
Metal ions
Sensors
Solvatochromism
Temperature

ABSTRACT

Three novel bis-dansyl derivatives bearing a sulfur bridge have been synthesized, fully characterized, and their photophysical characterization studied in solution, as well as, in the solid state. All compounds exhibit fluorescence emission with quantum yields up to 60%, which vary significantly depending on the solvent used, and the inherent molecular structure. Moreover, these compounds demonstrate positive solvatofluorochromic behaviour emitting from bluish-green to yellow. Kamlet-Taft studies were performed to better understand the solute–solvent interactions. Due to the intrinsic characteristics of the compounds, efforts were made to understand their potential usefulness for environmental remediation and thus metal ion sensing studies were investigated. Compounds **L1** and **L2** showed high sensitivity to Cu^{2+} and Hg^{2+} ions and were found to modulate their emission extensively, with **L2** capable of detecting and quantifying up to 4 μM of Hg^{2+}. Considering the solid-state emission of these compounds, the application towards temperature sensing was put forth. **L3** was found to quench its emission in a linear relation with temperature up to 170 °C. Several doped polymer thin films were fabricated, which served as a platform to establish a linear relation with temperature beyond their melting point. Polymethylmetacrylate (PMMA) films emitted up to temperatures of 218 °C, which could be fully restored at room temperature. These results suggest the potential application of these bis-chromophoric compounds as molecular thermometers.

1. Introduction

Probes and sensors conceptualized using fluorescent dyes offer inherent value due to their remarkable optical properties [1–3]. Among them, compounds based on 1-(dimethylamino)-naphthalene-5- sulfonyl or dansyl derivatives, have received consistent attention since they often exhibit broad emission spectra, high quantum yields and are robust enough under different external conditions [4–9]. This brought up to light a multitude of possible applications, ranging from biological targets such as the detection of oxygen reactive species [10], imaging [8,11–15], and monitoring of organ systems [6], to the detection of heavy and transition metal ions [12–20] and even water traces [4].

Our group has been working on metal ion detection for the last fifteen years [21–24]. Among them, the heavy and transition metal ions including Hg^{2+} and Cu^{2+} have gathered considerable attention. Hg^{2+} is a potential hazardous and toxic environmental pollutant that cause immunotoxic and neurotoxic effects in humans, leading to damage of the central nervous system and organ failure. On the other hand, Cu^{2+} is abundant in the body and plays a crucial role in diverse biological processes and cellular functioning. Abnormal concentration of Cu^{2+} may lead to the disruption of metabolic processes and neurodegenerative diseases such as Alzheimer's and Wilson diseases [14,17,25]. The U.S. Environmental Protection Agency has set admissible levels of Hg^{2+} and Cu^{2+} in drinking water to be 10 nM and 20 μM, respectively. Therefore, the development of fluorescent sensors for the detection of these transition metals is of utmost importance [12,17].

* Corresponding authors at: BIOSCOPE Research Group, LAQV-REQUIMTE, Chemistry Department, NOVA School of Science and Technology, FCT NOVA, Universidade NOVA de Lisboa, 2829-516 Caparica, Portugal.
E-mail addresses: Georgi.Dobrikov@orgchm.bas.bg (G. Dobrikov), ej.oliveira@fct.unl.pt (E. Oliveira), cle@fct.unl.pt (C. Lodeiro).

https://doi.org/10.1016/j.jphotochem.2023.115033
Received 23 May 2023; Received in revised form 20 July 2023; Accepted 22 July 2023
Available online 25 July 2023
1010-6030/© 2023 The Author(s). Published by Elsevier B.V. This is an open access article under the CC BY-NC-ND license (http://creativecommons.org/licenses/by-nc-nd/4.0/).

Considering the constant search for improved sensors for metal ions, Anna Aliberti *et. al.* designed several dansyl-amino acids capable of detecting Hg^{2+}. Among them, N-dansylated methionine was the chemosensor that showed the best performance in terms of sensitivity, with a limit of detection (LOD) value of 140 nM. To improve the LOD of this chemosensor, a portable experimental set-up based on an optical fiber probe was developed, which was able to increase the LOD to 5 nM, meeting the requirements of the Environmental Protection Agency. However, application to water-based matrices was found to be unfruitful due to the coordinating ability of chloride anions towards Hg^{2+} [16]. Similarly, Bhawna Uttam *et. al.* developed a dansyl appended calix[4] arene on the lower rim, which selectively detected Hg^{2+} with a LOD value of 560 nM. MTT assay was performed using HeLa cells confirming its biocompatibility, and strong fluorescence was visualized by confocal microscopy. The removal of Hg^{2+} from water sources was also addressed by embedding the sensor on a zeolitic imidazolate framework with 5% encapsulation. ICP-MS studies suggested a 95% removal of Hg^{2+} from water using the hybrid metal–organic framework (MOF), displaying excellent selectivity even in the solid state [13].

On the other hand, the employment of dansyl derivatives towards sensing of Cu^{2+} ions have been put forward by Huie Jiang *et. al.* whom developed a novel fluorescent probe through a nucleophilic substitution reaction between dansyl chloride and 2-(piperazin-1-yl)ethanol at room temperature. The compound was found to be selective and sensitive for Cu^{2+} ions, causing the red shift and quenching of the emission and presented a low detection limit of 0.18 μM. Furthermore, this compound was successfully applied for the monitorization of Cu^{2+} ions in living cells particularly A549 cells using two-photon confocal fluorescence imaging [12]. Additionally, Rajendran Nagarajan *et. al.* have synthesized an unnatural amino acid-based phenylalanine that has been linked to dansyl and benzoxazole moieties. Competitive studies with other metal ions showed a selective quenching towards Cu^{2+} ions within aqueous organic media with physiological pH with a LOD value of 3.0 μM. Further water analysis studies indicated the usefulness of this compound being capable of recovering 99.92% of the Cu^{2+} ions in spiked tap and drinking water samples [25].

On the other hand, solvatochromism is another well-known and fairly common property among dansyl derivatives, as the dipole moment undergoes considerable changes as the solvent polarity increases, resulting in a significant Stokes shift [7,26–29]. However, further, research is needed to develop probes with high solvatochromism that do not succumb to aggregation-caused fluorescence quenching (ACQ) effects in hydrophilic and hydrophobic environments [8,30]. A more prevalent example of the contrast between these two types of environments is within cells, where different regions and organelles exhibit varying affinities for water. Na Li *et al.* have developed a robust polarity sensor to address this issue, which can track the decrease of lipid droplets when subjected to oxidative stress in live cells. The system involves the covalent bond between dansyl chloride and nile red derivative, capable of sensing polarity changes in both green and red detection channels. The fluorophore was found useful in both environments since the dansyl moiety was resistant to ACQ, while nile red changed the fluorescence in the red channel with high linearity of aqueous composition. This dual emission also provided the experimental results supporting the conclusion that oxidative stress leads to a sharp decrease in lipid droplets [8].

Fluorescent dye-doped solid support materials have generated great interest, as they have the potential to improve the intrinsic properties of the dye, such as stability against quenchers, sensitivity, fluorescence and prevention of aggregation-caused quenching (ACQ) [31,32]. These multifunctioning materials can be applied as sensors for pH [33,34], transition metals [17], temperature and smart materials [34–38] and even low-cost antibacterial polymers for biomedical and food packaging [39]. Given the diverse implementation of dansyl derivatives into multifunctional solid materials [31,40–42], and our recent knowledge on bis-dansyl derivatives bearing a disulfide bridge [43], the three dansyl derivatives **L1**, **L2** and **L3** bearing single sulfur bridges were synthesized and fully characterized. Above mentioned ligands were designed in order to demonstrate good complexation ability toward heavy metals. Presence of multiple amide bonds [44] as well as sulfur with aliphatic substituents in one molecule [45,46] ensure chelating effect of the ligands. Discovery of solvatochromic effect was accomplished alongside with their ability to sense pollutant metal ions, and incorporated into polymer thin films of polystyrene-block-polybutadiene-block-polystyrene (SBS), Poly(methylmethacrylate) (PMMA), Polyvinyl alcohol and poly(styrene–butadiene–styrene) copolymer (PVA:PVP) and thermoplastic polyurethane (TPU) towards the development of temperature-smart materials.

2. Experimental section

2.1. Materials

Spectroscopy grade solvents were used for photophysical experiments – ethanol (EtOH), toluene, tetrahydrofuran (THF), acetonitrile (CH_3CN), dimethylsulfoxyde (DMSO), dimethylformamide (DMF), chloroform ($CHCl_3$). Puriss. p.a. grade solvents were used after distillation for synthesis and purification of compounds – dichloromethane (DCM), petroleum ether (PE), methyl *tert*-butyl ether (MTBE), ethanol (EtOH).

Trifluoromethanesulfonate salts of Cu(II), Cd(II), Co(II), Ag(I), Pb (II), Zn(II), Ni(II) and Ca(II) have been obtained from Solchemar, while $Hg(OTf)_2$, dansyl amide and all solvents were purchased from Sigma Aldrich without the necessity of performing additional steps of purification. Poly(methylmethacrylate), PMMA (MW ~ 350,000, Tg 105 °C) polyvinylpyrrolidone, PVP (MW ~ 40,000, Tg 170 °C), Polyvinyl alcohol (PVA, MW 27,000, Tg 85 °C) and poly(styrene–butadiene–styrene), SBS (Styrene 30 wt%, Tg 95 °C) were purchased from Sigma-Aldrich (St. Louis, MO, USA). The perfluoroalkoxy (PFA) supports for the fabrication of polymer films were purchased to Bohlender, Gmbh, Germany. Mili-Q ultrapure water was used in all experiments. The thermoplastic polyurethane TPU-A92 was offered by Huntsman (Germany).

2.2. Instrumentation

Visualization of the TLC was performed using a Vilber UV Lamp (BVL-6.LC dual wavelength 254 nm/365 nm, operational power of 2 × 6 Watts).

Using a combination of ^{1}H NMR and ^{13}C NMR all compounds' chemical identities were verified. Using 5 mm tubes on a Bruker Avance II + 600 spectrometer, the ^{1}H NMR and ^{13}C NMR spectra were measured in $CDCl_3$ at 293 K at operating frequencies of 600.13 MHz and 150.92 MHz, respectively. ^{1}H and ^{13}C NMR spectra were calibrated to the signal of tetramethylsilane (TMS), $\delta = 0.00$. Chemical shifts are measured to an accuracy of 0.01 parts per million (ppm). The coupling constants (J) are shown with a precision of 0.1 and represented in Hz. The spin multiplicity in the 1H NMR was denoted by the abbreviations s = singlet, d = doublet, t = triplet, q = quartet, dd = doublet of doublets, dt = doublet of triplets, td = triplet of doublets, and m = multiplet.

High-Resolution Mass Spectrometry analyses have been performed in the Laboratory for Biological Mass Spectrometry–Isabel Moura (PROTEOMASS Scientific Society Facility), using UHR ESI-Qq-TOF IMPACT HD (Bruker-Daltonics, Bremen, Germany). Samples of the corresponding compounds were prepared by dissolution in 50% (v/v) Acetonitrile containing 0.1% (v/v) aqueous formic acid to obtain a working solution of 0.1 μg/mL. Mass spectrometry analysis was carried out by the direct infusion of the compound solutions into the ESI source. MS data were acquired in positive polarity over the mass range of 80–1300 m/z. (Capillary voltage: 4500 V, End plate offset: −500 V, Charging voltage: 2000 V, Corona: 4000 nA, Nebulizer gas: 0.4 Bar, Dry Heater: 180 °C, Dry gas: 4.0 L/min).

UV–Vis absorption spectra were recorded on a JASCO V-650 spectrophotometer and a fluorescence emission spectrum on a HORIBA Scientific FLUOROMAX-4 spectrofluorometer from BIOSCOPE-PROTEOMASS facilities.

2.3. Synthetic procedures

2.3.1. Synthesis of intermediates *3* and *6*

N,N'-(thiobis(ethane-2,1-diyl))bis(2-aminobenzamide) **(3)**:

In a 100 mL flask with 50 mL dry DCM were added consequently anthranilic acid (**2**) (2.51 g, 18.30 mmol, 2.2 eq.), diamine **1** (1.00 g, 0.95 mL, 8.32 mmol, 1.0 eq.), DIPEA (4.73 g, 6.05 mL, 36.60 mmol, 4.4 eq.) and TBTU (5.88 g, 18.30 mmol, 2.2 eq.). The formed clear solution was stirred at r.t. for 72 h. TLC of reaction mixture – DCM:MTBE = 5:1, x1. Workup: dilution with 30 mL DCM and washing with distilled water, aq. K_2CO_3 and again with water. The organic phase was dried over anhydr. Na_2SO_4, filtered, and evaporated to dryness. This crude product was recrystallized from EtOH:H_2O = 25:10 mL. The precipitate was filtered, washed with PE:MTBE = 30:10 and dried *in vacuo* to give 2.22 g (74%) of pure **3** as white-off powder. M.p. 121–122 °C. ^{1}H NMR (600 MHz, $CDCl_3$) δ 7.34 (dd, J = 7.9, 1.5 Hz, 2H), 7.20 (ddd, J = 8.4, 7.1, 1.5 Hz, 2H), 6.67 (dd, J = 8.2, 1.1 Hz, 2H), 6.65 – 6.60 (m, 4H), 5.48 (s, 4H), 3.62 (q, J = 6.2 Hz, 4H), 2.82 – 2.79 (m, 4H). ^{13}C NMR (151 MHz, $CDCl_3$) δ 169.61, 148.78, 132.53, 127.45, 117.44, 116.84, 116.01, 38.77, 31.83.

N^2,N^5-bis(2-aminobenzyl)thiophene-2,5-dicarboxamide **(6)**:

In a 100 mL flask with 50 mL dry DCM were added consequently diacid (**4**) (0.300 g, 1.74 mmol, 1.0 eq.), diamine **5** (0.45 g, 3.66 mmol, 2.1 eq.), DIPEA (1.24 g, 1.58 mL, 9.59 mmol, 5.5 eq.) and TBTU (1.23 g, 3.83 mmol, 2.2 eq.). The formed fine pale-yellow suspension was stirred at r.t. for 20 h. Workup: the solvent was evaporated, and the formed solid product was dispersed in hot water and filtered. This crude product was crystalized from EtOH:H_2O = 40:5 mL, filtered and dried *in vacuo* to give 0.46 g (69%) of pure **6** as white powder. M.p. 214–215 °C (with decomp.). ^{1}H NMR (600 MHz, DMSO-d_6) δ 9.07 (t, J = 6.0 Hz, 1H), 7.75 (s, 1H), 7.02 (dd, J = 7.5, 1.6 Hz, 1H), 6.97 (td, J = 7.6, 1.6 Hz, 1H), 6.62 (dd, J = 7.9, 1.2 Hz, 1H), 6.51 (td, J = 7.4, 1.2 Hz, 1H), 5.12 (s, 2H), 4.29 (d, J = 6.1 Hz, 2H). ^{13}C NMR (151 MHz, DMSO-d_6) δ 160.97, 146.27, 143.05, 129.25, 128.50, 128.10, 121.62, 115.91, 114.78.

2.3.2. Synthesis of *L1*, *L2* and *L3*

N,N'-(thiobis(ethane-2,1-diyl))bis(2-((5-(dimethylamino)naphthalene)-1-sulfonamido)benzamide) **(L1)**:

Compound **3** (0.250 g, 0.70 mmol, 1.0 eq.) was dissolved in 4 mL dry pyridine. Subsequently, dansyl chloride (0.452 g, 1.67 mmol, 2.4 eq.) was added and the formed clear solution was refluxed for 2 h. TLC of reaction mixture – DCM:MTBE = 5:1, x1. Workup: after cooling an excess of conc. aq. citric acid was added and extracted with DCM. The organic phase was washed with water, dried over anhydr. Na_2SO_4, filtered, and evaporated to dryness. This crude product was purified by column chromatography: 70 g silica, phase DCM:MTBE = 20:1. After evaporation of phase and drying *in vacuo*, pure **L1** was obtained as bright yellow powder (0.31 g, 54%). M.p. 111–112 °C. ^{1}H NMR (600 MHz, CDC**L3**) δ 11.25 (s, 2H), 8.46 (dt, J = 8.6, 1.1 Hz, 2H), 8.33 (dt, J = 8.7, 0.9 Hz, 2H), 8.24 (dd, J = 7.3, 1.3 Hz, 2H), 7.55 – 7.47 (m, 4H), 7.43 (dd, J = 8.5, 7.3 Hz, 2H), 7.27 (dd, J = 7.9, 1.5 Hz, 2H), 7.28 – 7.21 (m, 2H), 7.11 (dd, J = 7.6, 0.9 Hz, 2H), 6.81 (td, J = 7.6, 1.2 Hz, 2H), 6.65 (t, J = 5.9 Hz, 2H), 3.44 (q, J = 6.4 Hz, 4H), 2.81 (s, 12H), 2.66 (t, J = 6.5 Hz, 4H). ^{13}C NMR (151 MHz, CDC l_3) δ 168.77, 151.91, 138.86, 134.80, 132.67, 130.91, 130.05, 129.93, 129.61, 128.51, 127.02, 123.13, 123.05, 120.62, 119.76, 119.12, 115.41, 45.51, 39.03, 31.50. ESI-MS: $[M + H]^+$ for $C_{42}H_{44}N_6O_6S_3$ = 825.2552 (-0.6 ppm), and $[M + 2H]^{2+}$ for $C_{42}H_{44}N_6O_6S_3$ = 413.1307 (-1.9 ppm). Calculated $[M + H]^+$ for $C_{42}H_{44}N_6O_6S_3$ = 825.255723 and $[M + 2H]^{2+}$ for $C_{42}H_{44}N_6O_6S_3$ = 413.131500.

N,N'-(thiobis(ethane-2,1-diyl))bis(5-(dimethylamino)naphthalene-1-sulfonamide) **(L2)**:

Diamine **1** (0.089 g, 0.085 mL, 0.74 mmol, 1.0 eq.) and DIPEA (0.240 g, 0.32 mL, 1.85 mmol, 2.5 eq.) were dissolved in 50 mL dry DCM and cooled to 5 °C (with ice-water). Then dansyl chloride (0.400 g, 1.48 mmol, 2.0 eq.) was added in one portion and the formed clear mixture was stirred for 30 min at 5 °C, followed by 48 h at r.t. TLC of reaction mixture – DCM:MTBE = 10:1, x1. Workup: dilution with 30 mL DCM and washing with 1% aq. citric acid and water. The organic phase was dried over anhydr. Na_2SO_4, filtered and evaporated to dryness. This crude product was purified by column chromatography: 70 g silica, phase DCM:MTBE = 20:1. After evaporation of phase and drying *in vacuo*, pure **L2** was obtained as pale-yellow powder (0.20 g, 46%). M.p. 70–71 °C. ^{1}H NMR (600 MHz, CDC**L3**) δ 8.53 (d, J = 8.5 Hz, 2H), 8.24 (d, J = 8.6 Hz, 2H), 8.20 (dd, J = 7.3, 1.3 Hz, 2H), 7.54 (dd, J = 8.6, 7.5 Hz, 2H), 7.50 (dd, J = 8.5, 7.3 Hz, 2H), 7.17 (d, J = 7.5 Hz, 1H), 2.88 (s, 16H), 2.25 (t, J = 6.4 Hz, 4H). ^{13}C NMR (151 MHz, $CDCl_3$) δ 152.18, 134.53, 130.78, 129.96, 129.78, 129.59, 128.69, 123.32, 118.69, 115.41, 45.55, 42.00, 31.42. ESI-MS: $[M + H]^+$ for $C_{28}H_{34}N_4O_4S_3$ = 587.1811 (-0.7 ppm). Calculated $[M + H]^+$ for $C_{28}H_{34}N_4O_4S_3$ = 587.181495.

N^2,N^5-bis(2-((5-(dimethylamino)naphthalene)-1-sulfonamido) benzyl)thiophene-2,5-dicarboxamide **(L3)**:

Compound **6** (0.300 g, 0.79 mmol, 1.0 eq.) was dissolved in 5 mL dry pyridine. Then dansyl chloride (0.468 g, 1.73 mmol, 2.2 eq.) was added and the formed clear solution was stirred at r.t. for 72 h. TLC of reaction mixture – DCM:MTBE = 5:1, x2. Workup: excess of conc. aq. citric acid was added and extracted with DCM. The organic phase was washed with water, dried over anhydr. Na_2SO_4, filtered, and evaporated to dryness. This crude product was purified by column chromatography: 70 g silica, phase 1 - DCM:MTBE = 10:1 (for contaminations); phase 2 - DCM:MTBE = 5:1 (for product). After evaporation of phase and drying *in vacuo*, pure **L3** was obtained as pale-yellow powder (0.51 g, 76%). M.p. 263–264 °C. ^{1}H NMR (600 MHz, DMSO-d_6) δ 10.24 (s, 2H), 9.23 (t, J = 6.1 Hz, 2H), 8.47 (dt, J = 8.5, 1.1 Hz, 2H), 8.42 – 8.36 (m, 2H), 8.09 (dd, J = 7.3, 1.3 Hz, 2H), 7.76 (s, 2H), 7.57 (ddd, J = 11.9, 8.6, 7.4 Hz, 4H), 7.24 (dd, J = 7.7, 0.9 Hz, 2H), 7.20 – 7.15 (m, 2H), 7.12 – 7.05 (m, 4H), 6.90 – 6.85 (m, 2H), 4.32 (d, J = 6.1 Hz, 4H), 2.81 (s, 12H). ^{13}C NMR (151 MHz, DMSO-d_6) δ 161.39, 151.61, 142.64, 135.47, 134.49, 133.19, 130.31, 129.56, 129.07, 129.04, 128.27, 127.97, 125.91, 124.11, 123.69, 118.77, 115.35, 45.14. ESI-MS: $[M + H]^+$ for $C_{44}H_{42}N_6O_6S_3$ = 847.2389 (-1.3 ppm), and $[M + 2H]^{2+}$ for $C_{42}H_{42}N_6O_6S_3$ = 424.1245 (1.9 ppm). Calculated $[M + H]^+$ for $C_{44}H_{42}N_6O_6S_3$ = 847.240073, and $[M + 2H]^{2+}$ for $C_{42}H_{42}N_6O_6S_3$ = 424.123674.

2.4. Spectrophotometric and spectrofluorimetric measurements

2.4.1. Photophysical characterization and titrations

Photophysical characterizations and titrations were performed by preparation of stock solutions of compounds **L1**, **L2** and **L3** (ca. 10^{-3} M) in different solvents (CH_3CN, EtOH, DMSO, $CHCl_3$, Toluene, THF and DMF), by dissolution of an appropriate amount of the selected compound in a 10 mL volumetric flask. Further studies were carried out by appropriate dilution of the stock solutions up to 10^{-5} – 10^{-6} M.

Titrations of **L1** and **L2** were carried out by the addition of microliter aliquots of standard solutions of Ca^{2+}, Co^{2+}, Ni^{2+}, Cu^{2+}, Zn^{2+}, Ag^+, Cd^{2+}, Hg^{2+}, Pb^{2+} ions prepared in acetonitrile, while titrations of **L3** were carried out in DMSO. A correction for the absorbed light was performed when necessary. Luminescence spectra of the compounds in the solid state and of doped polymer thin films were recorded using of a fiber-optics device connected to the spectrofluorometer while exciting the samples at appropriated wavelength. The temperature dependent emission spectra were recorded by heating the samples over a hotplate with control over the temperature.

2.4.2. Fluorescence quantum yield and lifetime

Relative photoluminescence quantum yields were measured using

dansyl amide in acetonitrile employed as a standard solution ($\phi_F = 0.37$) for quantifying the relative QY of **L1** and **L2** dissolved in the same solvent and in DMSO for **L3**, while the remaining ones were measured relative to the standard solution of dansyl amide in DMSO ($\phi_F = 0.61$) [47]. Tempro Fluorescence Lifetime System with a Nanoled pulsed diode controller from Horiba Jobin-Yvon (Proteomass Facilities) was used to perform lifetime measurements.

2.5. Determination of the detection and quantification limits (LOD and LOQ)

Determination of the detection limit (LOD) and quantification limit (LOQ) began by collecting ten independent measurements of a solution containing the selected probe and no addition of any metal ion (y_{blank}). Final determination of the LOD and LOQ values followed the subsequent formulas [48,49]:

$LOD = y_{dl} = y_{blank} + 3std$, where y_{dl} = signal detection limit and std = standard deviation.

$LOQ = y_{dl} = y_{blank} + 10std$, where y_{dl} = signal detection limit and std = standard deviation.

The final step involved the determination of the minimal detectable and quantified concentration of metal ion by titration with the ligands.

2.6. Preparation of polymer Dye-Doped thin films

PMMA and SBS doped polymer thin films were obtained by slow evaporation of a 10 mL chloroform solution containing 100 mg of the corresponding polymer matrix and 0.5 mg of the selected compound.

PVA:PVP polymer films were prepared by dissolution of 200 mg of PVA and 50 mg of PVP in 1.5 mL miliQ water, while heating at 80 °C, with continuous stirring and 0.5 mg of the dansyl dyes were dissolved in 2 mL of EtOH and added to the hot mixture.

TPU doped polymer films were fabricated by dissolving 100 mg of the polymer matrix and 1 mg of the corresponding compounds in 10 mL of THF.

All mixtures were poured onto PFA supports with diameter of 5 cm to allow solvent evaporation at room temperature. All polymeric samples were prepared in triplicate.

3. Results and discussion

3.1. Synthesis

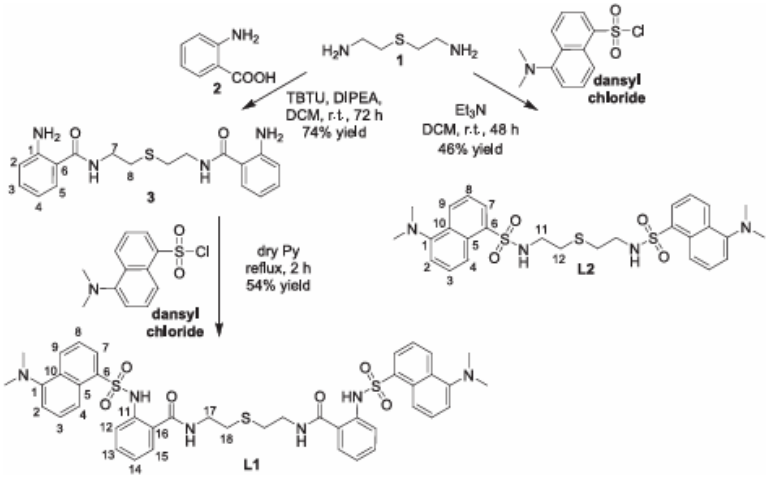
The synthesis of target compounds **L1** and **L2** was based on commercially available thio-diamine **1** (Scheme 1). Preparation of intermediate **3** was accomplished by direct coupling reaction of **1** with anthranilic acid (**2**). Due to better nucleophilicity of amino groups of **1**, preparation of **3** was performed in only one step and isolated with good yield without need of protection. Consequently, acylation of **3** with dansyl chloride in dry pyridine furnished the target product **L1** in good yield. The synthesis of compound **L2** was performed in one step starting from **1** and dansyl chloride, employing classical conditions (Et_3N in dry dichloromethane).

The preparation of ligand **L3** was conducted in two steps (Scheme 2). Intermediate **6** was prepared in one step from commercially available diacid **4** and diamine **5**, respectively. As in case of **3**, protection of **5** was not necessary. Acylation of **6** with excess of dansyl chloride in dry pyridine yields product **L3**. All intermediates and target compounds were obtained in good yields and high purity after column chromatography. They were fully characterized by NMR, MS and melting point temperatures.

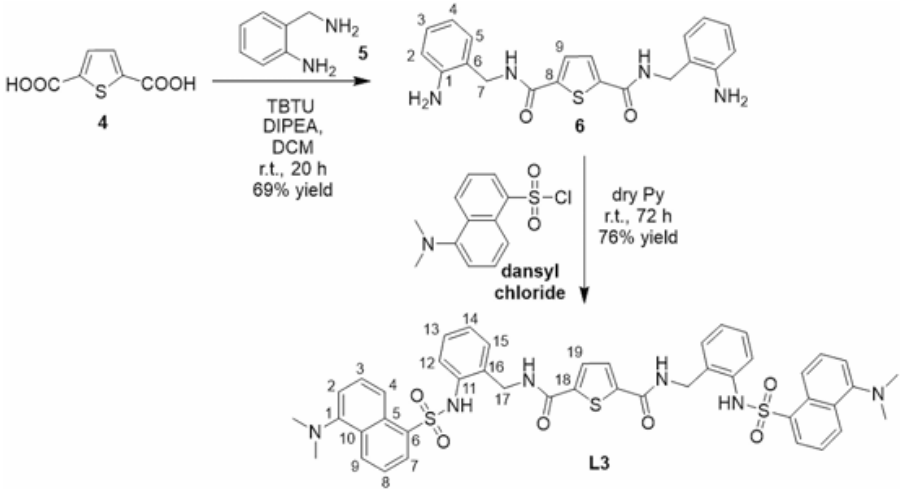
3.2. Photophysical characterization

The dansyl derived compounds exhibit luminescence properties both in solution and in the solid state. Fig. 1 displays the molecular structure alongside the photophysical data collected at 298 K for compound **L1** and **L2** in acetonitrile as well as in DMSO for **L3** as a representative example. The UV–Vis spectra show a band centered at 330, 340 and 350 nm; associated with the π-π* transition of the dansyl chromophore, contributing to the visualization of colourless solutions in the naked eye. Upon excitation at the appropriate wavelength, the samples emit a greenish yellow light with a maxima at 524, 518 and 532 nm representative of a large stoke shift. On a relatable note, solid-state emission spectra show a wide band centered at 509, 499 and 469 nm, a considerable blue shift in relation to the emission in solution (Table 2).

Since dansyl derivatives are commonly associated with solvatochromism behavior, **L1**-**L3** were further studied for their photophysical properties in five different solvents to evaluate the sensitivity towards solvent polarity. Alongside in acetonitrile, **L1** and **L2** were



Scheme 1. Synthetic approach to the preparation of compounds **L1** and **L2**.



Scheme 2. Synthetic approach to the preparation of compound **L3**.

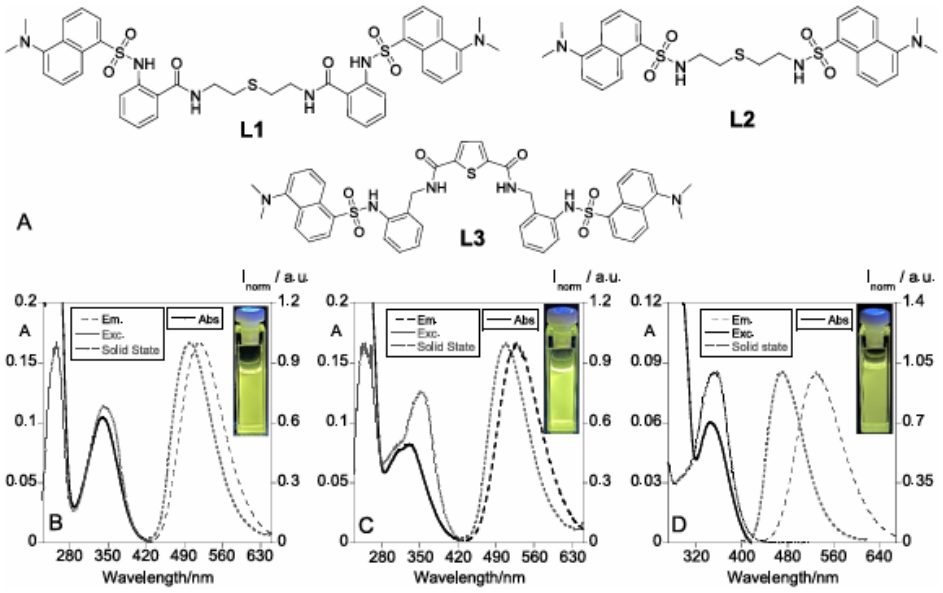


Fig. 1. (A) Molecular structure of dansyl based compounds **L1**, **L2** and **L3**. Photophysical characterization of derivatives **L1** (B), **L2** (C) in acetonitrile and **L3** (D) in DMSO ([**L1**] = [**L2**] = [**L3**] = 6 μM).

further studied in DMSO, ethanol, THF, chloroform and toluene; Due to solubility restrictions **L3** was studied in THF and DMF (Figs. S14–S18).

Taking into consideration the analysis of Table 3, no correlation can be perceived following the absorption as the solvent polarity increases despite the differences in maximum bands. On the contrary, the same cannot be said for the emission, where a clear red shift of the emission maximum bands is seen, a shift from 500 to 536 nm for **L1**, from 489 to 520 nm for **L2** and from 339 to 350 nm for **L3** with increasing solvent polarity. In line with these findings, a conclusion can be taken based on the shifts observed regarding the emission spectra, demonstrating that **L1**, **L2** and **L3** exhibit a positive solvatofluorochromism.

To fully characterize **L1** and **L2**'s solvatofluorochromic behaviour, and to quantify the solute–solvent interactions, three solute-dependent parameters (υ_0, a, b and p) have been determined through the multi-parametric fitting of the kamlet-Taft equation (Equation (1)).

Table 1
Spectroscopic polarity parameters, physical properties of the different solvents. ε_r: relative permittivity; η: refractive index; α: the solvent's HBD acidity; β: the solvents HBA basicity; π*: the solvent's dipolarity/polarizability.

Solvent	ε_r	α	β	π*	η
DMSO	47.24	0	0.76	1	1.47
DMF	38.4	0	0.69	0.88	1.43
CH_3CN	35.94	0.19	0.40	0.66	1.34
Ethanol	24.30	0.86	0.75	0.54	1.36
THF	7.58	0	0.55	0.58	1.40
$CHCl_3$	4.89	0.20	0.10	0.69	1.44
Toluene	2.38	0	0.11	0.54	1.49

$$\upsilon = \upsilon_0 + a\alpha + b\beta + p\pi^* \quad (1)$$

Where υ_0 represents the wavenumber value without dependence of solvent effects; parameters a, b and p are obtained through multiple regression analysis that reflect the underlying sensitivity of the probes photophysical behaviour to solvent polarity; α: hydrogen bond donor acidity (HBD); β: hydrogen bond acceptor basicity (HBA); π*: stabilization of a charge or dipole without a specific dielectric interaction (Table 1) [29,50].

Fig. 2 gathers the images taken under UV light lamp of **L1** and **L2** under a UV light lamp while Table 4 presents the fitted parameters (υ0, a, b and p) driven from the multiple regression analysis while the slope and correlation were obtained from the linear fitting of the plot $\upsilon_{exp.}$ versus $\upsilon_{calc.}$

From Table 4 it is perceived that **L3** has the highest polarizability making it more likely to be distorted by an external field.

3.3. Metal ions sensing

Keeping in mind the potential value of these dansyl derivatives to be used towards the sensing of metal ions, additions of 1, 5 and 10 equivalents of Ca^{2+}, Co^{2+}, Ni^{2+}, Cu^{2+}, Zn^{2+}, Ag^{+}, Cd^{2+}, Hg^{2+} and Pb^{2+} in acetonitrile were performed. Fig. 3 gathers the normalized emission intensities at 524, 518 and 532 nm of compounds **L1**-**L3**, respectively, upon addition of the aforementioned metal ions. Compounds **L1** and **L2** showed sensitivity towards Cu^{2+} and Hg^{2+} metal ions while **L3** hasn't been found to have any meaningful variation on its emission after addition of 10 equivalents of each metal most likely due to the inherent rigidity of the system.

In face of the previous results, Fig. 4 gathers the UV–Vis and luminescent titrations towards increasing amounts of Cu^{2+} (A, C) and Hg^{2+} (B, D) for **L1** and **L2**, respectively. Overall, the addition of both metal ions causes the continuous decrease of the absorbance maxima centered

Table 4
Independent fluorescence wavenumber (υ0), solvent polarity (*p*), HBD (*a*), HBA (*b*), slope and coefficient (R^2) of the linear fitting plot $\upsilon_{exp.}$ versus $\upsilon_{calc.}$

	υ_0	a	b	p	Slope	R^2
L1	21,144	−421	−721	−1848	0.99	0.99
L2	21,790	−1032	−299	−2314	0.99	0.99
L3	21,646	−1033	−301	−2626	0.99	0.99

Table 2
Absorption maximum wavelength in solution (λ_{abs}), emission maximum wavelength in solution (λ_{em}), molar absorption coefficients (ε), Stokes shift (Δλ), emission maximum in the solid state (λ_{em}^{Solid}), fluorescence quantum yields (ϕ), brightness (εxϕ), fluorescence lifetimes (τ) for compounds **L1** and **L2** in acetonitrile and **L3** in DMSO.

Cp.	λ_{abs} [nm]	λ_{em} [nm]	ε [10^4 cm^{-1} M^{-1}]	Stokes shift [10^4 cm^{-1}]	λ_{em}^{Solid} [nm]	ϕ (%)	Brightness (ε X ϕ) [10^3 cm^{-1} M^{-1}]	τ [ns]
L1	330	524	0.991	5.15	509	27	2.68	11
L2	340	518	1.06	5.62	499	35	3.71	12
L3	350	532	1.03	5.49	469	10	1.03	5.9

Table 3
Photophysical characterization of probes **L1** and **L2** performed in different organic solvents.

Cpd.	Solv.	λ_{abs} [nm]	λ_{em} [nm]	ε [10^4 cm^{-1} M^{-1}]	Stokes shift [10^4 cm^{-1}]	ϕ (%)	Brightness (ε X ϕ) [10^3 cm^{-1} M^{-1}]	τ [ns]
L1	DMSO	350	534	0.999	5.43	24	2.40	14
	EtOH	334	520	0.804	5.38	17	1.37	13
	THF	336	507	1.19	5.85	47	5.59	14
	$CHCl_3$	345	506	1.07	6.21	51	5.36	15
	Toluene	343	500	0.816	6.37	51	4.16	13
L2	DMSO	340	520	0.956	5.56	48	4.59	12
	EtOH	335	515	0.964	5.56	33	3.18	15
	THF	336	492	1.21	6.41	52	6.29	13
	$CHCl_3$	343	500	0.802	6.37	60	4.81	13
	Toluene	341	489	0.899	6.76	53	4.77	16
L3	DMF	336	523	1.16	5.35	3.6	0.428	7.7
	THF	339	501	1.34	6.17	7.3	0.978	6.6

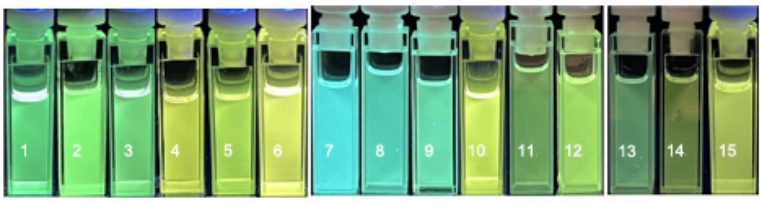


Fig. 2. Images of **L1** (1–6), **L2** (7–12) and **L3** (13–15) in different organic solvents [Toluene (1,7); THF (2, 8, 13); Chloroform (3, 9); Acetonitrile (4, 10); Ethanol (5, 11); DMF (14); DMSO (6, 12, 15)] under a UV lamp.

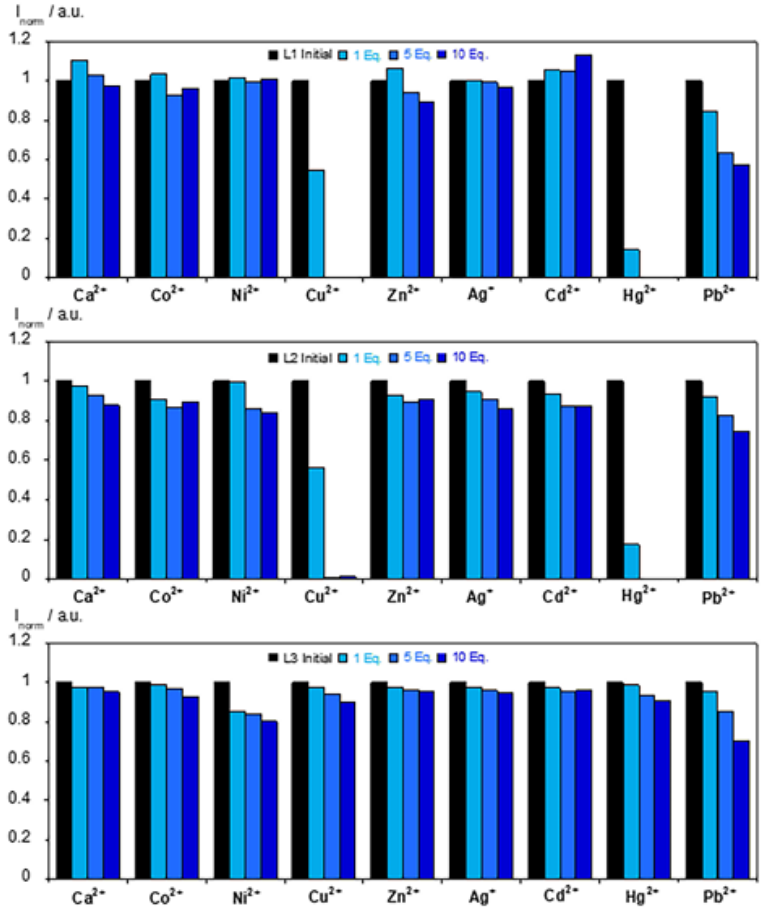


Fig. 3. Normalized emission intensity of **L1** (A), **L2** (B) and **L3** (C) after addition of Ca^{2+}, Co^{2+}, Ni^{2+}, Cu^{2+}, Zn^{2+}, Ag^{+}, Cd^{2+}, Hg^{2+} and Pb^{2+} metal ions in successive proportions of 1, 5, and 10 equivalents in acetonitrile for **L1** and **L2** while in DMSO for **L3**. ([**L1**] = [**L2**] = [**L3**] = 20 μM, λ_{emL1} = 524 nm, λ_{emL2} = 518 nm, λ_{emL3} = 532 nm, T = 298 K).

at 330 and 340 nm for **L1** and **L2**, respectively, while simultaneously a gradual formation of a band with a maximum around 300 nm is observed for both compounds, followed by the appearance of an additional band located around 370 nm in particular for **L2** when added Hg^{2+}. In terms of the emission spectra, a quenching on its intensity is observed in both cases at 524 (**L1**) and 518 nm (**L2**).

To fully characterize the sensing ability towards Cu^{2+} and Hg^{2+}, the stability constants were calculated with the aid of HypSpec software [51] alongside calculation of the detection and quantification limit parameters for both dansyl derivatives. The association constants, LOD and LOQ are included in Table 5.

Table 5 reveals that both probes assemble in mononuclear species with Cu^{2+} and Hg^{2+} with the highest constant belonging to **L2** towards Hg^{2+} with a stability constant value of $LogK_{ass.} = 6.38 \pm 0.02$. Ligand **L2** has also been found to exhibit the lowest LOD and LOQ values (4 μM and 7 μM) being indicative of a higher affinity to bind with Hg^{2+} ions. These results highlight the potential usefulness of this probe in environmental remediation of Hg^{2+} ions where there is the need to monitor its presence in lower concentrations.

Regarding compound **L1**, the lower stability constants found for this compound may be due to the increased stereochemical hindrance promoted by the addition of the benzene moiety which in turn disables to some degree the accessibility for the coordination to occur.

3.4. Studies using solid support compound L1

L1 in water offers an advantage when considering future practical applications. **L1** exhibits the lowest detection and quantification limit for Hg^{2+} metal ions in solution, making it suitable for supporting on low-cost, simple cellulose discs for the determination of Hg^{2+} in aqueous solutions.

Blank discs (*Liofilchem*) with a diameter of 6 mm were impregnated with a solution of **L1** ([**L1**] = 10 μM) in THF. After drying, the resulting white discs containing **L1** were briefly immersed for 5 s in water solutions with increasing concentrations of Hg^{2+} (0, 25, 50, 100, 200, 300, and 400 ppm). Fig. 5 illustrates the visual colour emission changes under

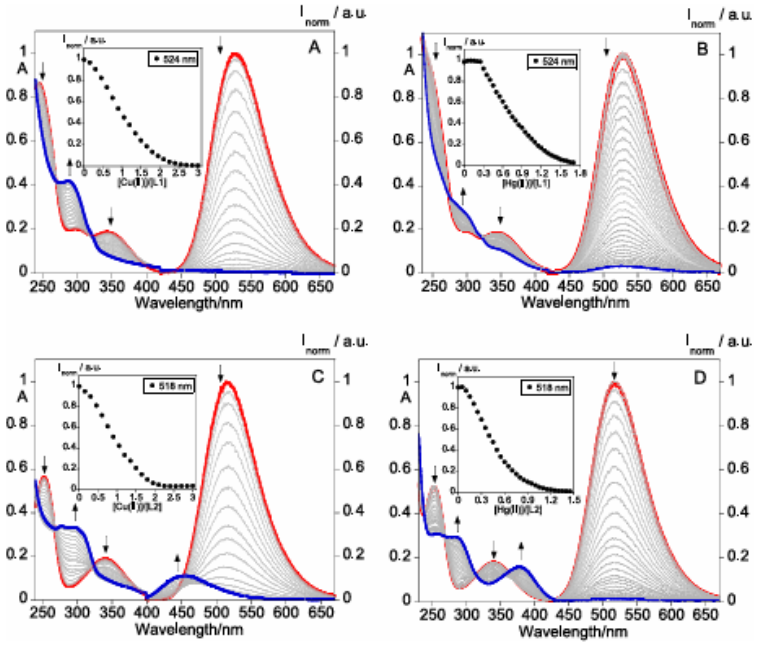


Fig. 4. UV–Vis and luminescent titrations of compounds **L1** (A, B) and **L2** (C, D) upon continuous addition of 10 μL of Cu^{2+} (A, C; $[Cu^{2+}] = 0.9$ mM), and Hg^{2+} (B, D; $[Hg^{2+}] = 0.3$ mM) in acetonitrile. The inset represents the emission (A-D) as a function of $[Cu^{2+}]/[\mathbf{L1}]$ at 524 nm (A), of $[Cu^{2+}]/[\mathbf{L2}]$ at 518 nm (C), of $[Hg^{2+}]/[\mathbf{L1}]$ at 524 nm (B) and of $[Hg^{2+}]/[\mathbf{L2}]$ at 518 nm (D). $[\mathbf{L1}] = [\mathbf{L2}] = 20$ μM, $\lambda_{exc,L1} = 330$ nm, $\lambda_{exc,L2} = 340$ nm, T = 298 K).

Table 5
HypSpec's calculated association constants and stoichiometry for the probes **L1** and **L2** towards Cu^{2+} and Hg^{2+} ions, in CH_3CN alongside the respective values for the Minimal detectable (LOD) and quantified (LOQ) amounts (μM). LOD and LOQ were measured by the emission at 524 and 518 nm for **L1** and **L2**, respectively.

Compounds	Metal (M)	Association constants ($LogK_{ass}$), L:M	LOD (μM)	LOQ (μM)
L1	Cu^{2+}	4.82 ± 0.03 (1:1)	6	15
	Hg^{2+}	5.29 ± 0.06 (1:1)	7	11
L2	Cu^{2+}	5.00 ± 0.04 (1:1)	6	15
	Hg^{2+}	6.38 ± 0.02 (1:1)	4	7

a UV lamp. Notably, a visual detection of Hg^{2+} in water is possible from concentrations as low as 100 ppm. This method holds great potential for the development of portable and convenient in-the-field detection of Hg^{2+}.

3.5. *Tuning the emission of dansyl derivatives towards temperature smart materials*

Since **L1**-**L3** were found to exhibit emission in the solid state and manifest solvatofluorochromism due to the different properties of the solvents, the next intention is to modulate the emission of these ligands in solid supported materials to develop molecular thermometers through emission. In line with this premise, the compounds have been studied initially without the use of a solid supports. For this, emission of each probe has been recorded with the increase of temperature in the solid state. Fig. 6 gathers the emission spectra and the plot of I_{nom} in relation to temperature for compound **L3**. The results suggest that **L3** manifests a linear relation of its emission and the increase of temperature between 30 and 129 °C. The same behavior was also found during the cooling cycle. This compound was found to completely recover its emission by the end of the cooling cycle as it can be seen in Fig. 6.

Regarding compound **L1** and **L2**, a relation has been found between emission and temperature for **L1** between 30 and 70 °C while no linearity was observed for **L2** as can be seen in Figs. S19 and S20. Also, after cooling the emission did not recover substantially suggesting partial degradation of both compounds. This is most likely due to their low melting point around 112 and 70 °C for compound **L1** and **L2**, respectively. The same was not found for compound **L3** since its melting point is 264 °C. Thus, **L1** and **L3** have shown promising results allowing them to be used as temperature sensors, however applications may be hindered due to the lack of solid supports.

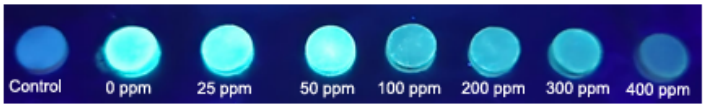


Fig. 5. Visual changes in Blank Discs (*Liofilchem*) containing compound **L1** (10 μM) after immersion in water solutions containing increasing concentrations of Hg^{2+} metal ion (0–400 ppm). [25 ppm = 50 μM; 50 ppm = 100 μM; 100 ppm = 200 μM; 200 ppm = 401 μM; 300 ppm = 602 μM; 400 ppm = 802 μM].

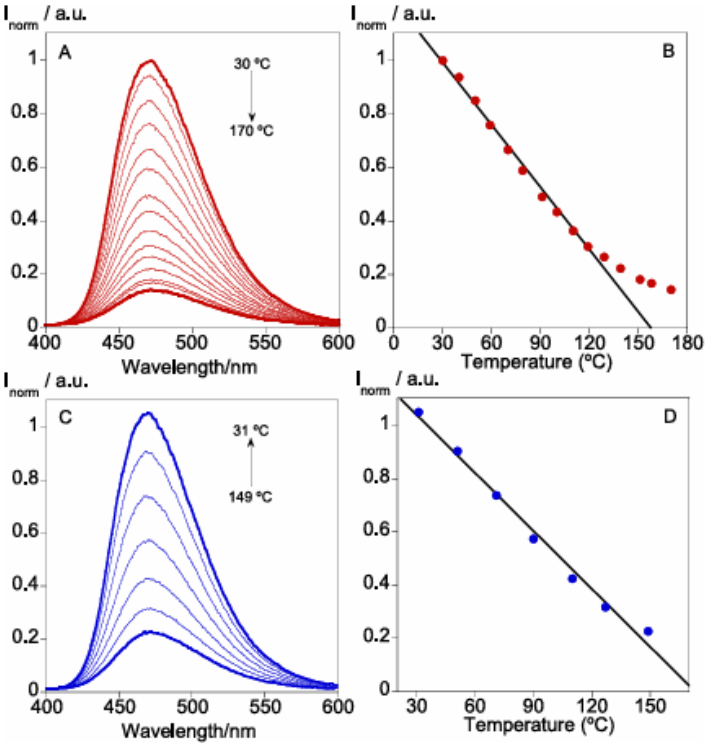


Fig. 6. Temperature-dependent emission spectra of **L3** in the solid state (A) collected through a warming cycle between 30 °C and 170 °C. $I_{norm.}$ vs. T plot recorded in the emission maximum at 472 nm upon heating (B) [30 to 129 °C (Y = 1.2243 + 0.0077612x), yielding R = 0.99663]. Temperature-dependent emission spectra of **L3** (C) collected through a cooling cycle between 31 °C and 149 °C. $I_{norm.}$ vs. T plot recorded in the emission maximum at 472 nm upon cooling (D) [31 to 149 °C (Y = 1.2571 + 0.0072628x), yielding R = 0.99502].

According with the previous findings, several polymers doped thin films have been developed as a next step to improve the sensing applications. Compound **L1** and **L2** were doped in PMMA, SBS, PVA:PVP and TPU while **L3**, due to solubility restrictions, has been doped only in TPU. Fig. 7 gathers the comparison between the emission spectra in the solid state and each emission of the different polymer thin films while Table 6 presents the corresponding emission maximum.

Overall, polymer thin films were successfully developed, and their emission properties were investigated. As it can be perceived by Fig. 7, the molecular structure of the polymer matrix is able to tune the final emission of the film by interacting with the probe. PMMA films display the largest blue-shift of 37 and 32 nm for **L1** and **L2**, respectively, without relevant input of the differences in molecular structure of both probes. However, for SBS and PVA/PVP more pronounced differences are observed due to the influence of the molecular structure. Compound **L1** tends to suffer less relevant blue-shifts on these polymer matrixes than **L2** most likely due to the increased compatibility that the benzene moieties provide while dispersed. Regarding TPU polymer thin films of **L1** and **L2**, blue shifts of 16 and 12 nm are observed. Nevertheless, the most interesting appears to be **L3** that when doped originates a red shift of 22 nm.

In face of the previous results, each polymer doped films were studied with variation in temperature aiming to better understand whether it is possible to humper the constrains that were found in the solid state for **L1** and **L2**. Fig. 8 gathers the emission of the different polymer films doped with **L2**, as a representative example, alongside **L3** doped in TPU polymer film while polymer doped films of **L1** can be seen in Figs. S21–S24.

Regarding the PMMA doped film, this material suffers its quenching with increments of temperature up to 218 °C. Intriguingly, the behaviour observed for **L1** and **L2** in the solid state, due to their melting point, does not influence to the same extent the emission in the solid support. The polymer matrix serves as a media to maintain the emission at higher temperatures by providing sufficient conductivity which attenuates the thermal activated non-radiative processes that the compounds manifest. Likewise, as the cooling stage proceeds the emission gradually increases until it reaches room temperature and is capable of recovering 85% of the initial fluorescence. Additionally, linearity can be perceived from 120 to 218 °C during heating and until 51 °C while cooling. It is also, interesting to note that the glass transition temperature of PMMA (T_g 105 °C) do not seem to have any influence in the emission behaviour of the film.

Remaining polymer supports were able to provide similar behaviour in relation to the emission properties with temperature. However, were not able to reach the same temperatures as PMMA and have been also found to not recover substantially their emission when cooled to room temperature (Fig. S25) since they start to experience physical changes. On the other hand, linearity of the emission with temperature can still be perceived for SBS, PVA/PVP, and TPU between 70 to 189 °C, 110 to 199 °C and 70 and 158 °C.

In the case of TPU doped with **L3**, the quenching of the emission is observed similarly as observed for the solid state, however linearity can only be seen between 80 and 159 °C, while during cooling emission recovers 40% and shows linearity between 33 and 148 °C (Fig. S26). Nevertheless, in agreement with the other doped polymer materials studied, the incorporation of the probe onto a solid support provides the means to be applied as a molecular thermometer without restrictions imposed by their physical characteristic and, in this particular case, the

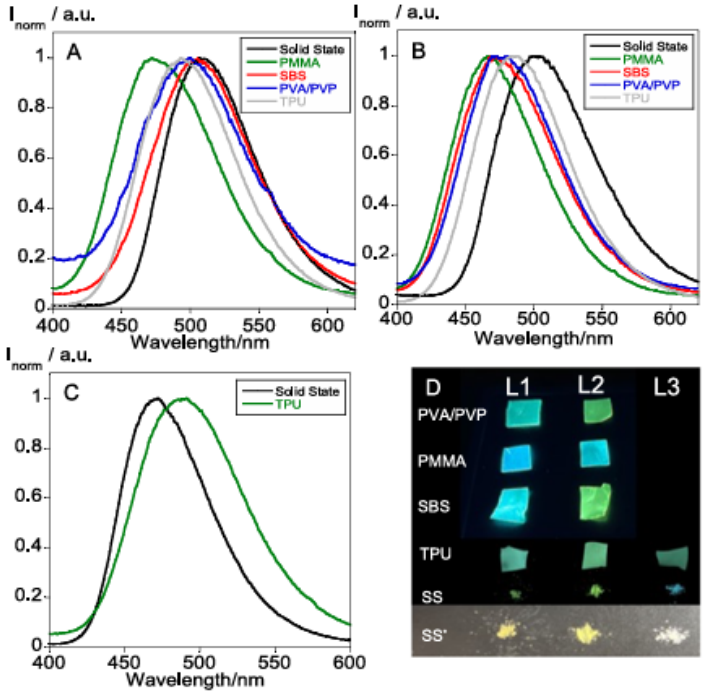


Fig. 7. Comparison between the emission spectra of the different polymer thin films doped with (A) L1, (B) L2 and (C) L3 and the respective emission spectrum in the solid state. Images of the different polymer doped films and in the solid state under UV-light and under natural light (*) (D).

Table 6
Emission maximum in the solid state (λ_{em}^{Solid}), emission maximum of PMMA thin films (λ_{em}^{PMMA}), emission maximum of SBS thin films (λ_{em}^{SBS}), emission maximum of PVA/PVP thin films ($\lambda_{em}^{PVA/PVP}$), emission maximum of TPU thin films (λ_{em}^{TPU}).

Compounds	λ_{em}^{Solid} [nm]	λ_{em}^{PMMA} [nm]	λ_{em}^{SBS} [nm]	$\lambda_{em}^{PVA/PVP}$ [nm]	λ_{em}^{TPU} [nm]
L1	509	472	506	499	493
L2	499	467	471	472	487
L3	469	–	–	–	491

polymer matrix can tune the emission wavelength to better suit the application.

4. Conclusions

In present work, three new bis-dansyl probes containing a sulfide bridge were synthesized and their photophysical properties were studied. Since dansyl compounds are known to exhibit solvatofluorochromism, photophysical studies were carried out in different solvents to fully evaluate the influence of each solvent's intrinsic characteristics on the probes' emission. The equation of Kamlet-Taft was implemented to gain value insights into solute–solvent interactions, and positive solvatofluorochromism behaviour was observed for all compounds. The presence of heteroatoms also enables the study of how metal ions influence the probes' photophysical behaviour. From an environmental remediation perspective, **L1** and **L2** were found to quench their emission in the presence of Hg^{2+} and Cu^{2+} ions. Further calculations suggested that these compounds form mononuclear species with Cu^{2+} and Hg^{2+} and that **L2** has the highest association constant with Hg^{2+} ($LogK_{ass.} = 6.38$) and an LOD and LOQ of 4 μM and 7 μM, respectively. Finally, the probes were characterized in the solid state and doped in solid supports for the development of molecular thermometers PMMA, SBS, PVA/PVP, and TBU doped polymers were synthesized, and their luminescence was studied. The polymer matrix was found to modulate the emission maximum of all compounds and contribute to the emission at higher temperatures than those found in the solid state. Good linearity could also be observed at elevated temperatures, making these probes suitable candidates as temperature sensors in industrial applications.

CRediT authorship contribution statement

Frederico Duarte: Conceptualization, Data curation, Writing – original draft, Writing – review & editing, Visualization, Investigation, Validation, Formal analysis, Methodology. **Georgi Dobrikov:** Conceptualization, Funding acquisition, Data curation, Writing – original draft, Writing – review & editing, Resources. **Atanas Kurutos:** Conceptualization, Funding acquisition, Data curation, Writing – original draft, Writing – review & editing, Resources. **Jose LuisCapelo-Martinez:** Funding acquisition, Writing – original draft, Writing – review & editing, Resources. **Elisabete Oliveira:** Conceptualization, Data curation, Writing – original draft, Writing – review & editing. **Carlos Lodeiro:** Conceptualization, Funding acquisition, Data curation, Writing – original draft, Writing – review & editing, Supervision, Resources.

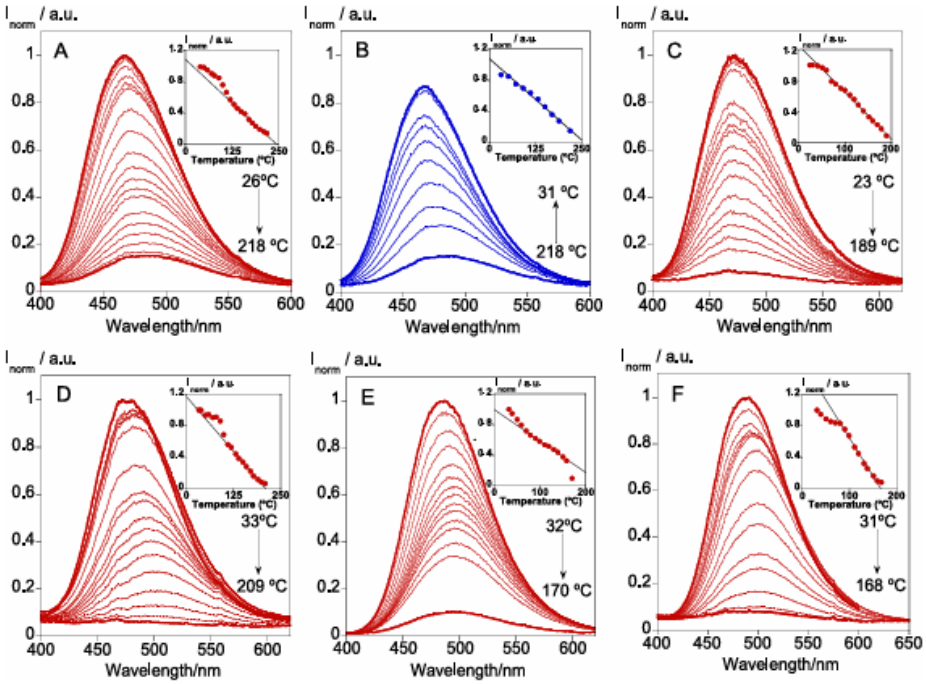


Fig. 8. Temperature-dependent emission spectra of **L2** doped in (A) PMMA during heating cycle [Inset: $I_{norm.}$ vs. T plot at 467 nm upon heating: 120 to 218 °C (Y = 1.0919–0.004465x), yielding R = 0.9948]; (B) PMMA during cooling cycle [Inset: $I_{norm.}$ vs. T plot at 467 nm upon cooling: 51 to 218 °C (Y = 1.0787–0.0042258x), yielding R = 0.99644]; (C) SBS during heating cycle [Inset: $I_{norm.}$ vs. T plot at 471 nm upon heating: 70 to 189 °C (Y = 1.2484–0.0060553x), yielding R = 0.99652]; (D) PVA/PVP during heating cycle [Inset: $I_{norm.}$ vs. T plot at 472 nm upon heating: 110 to 199 °C (Y = 1.1712–0.0055656x), yielding R = 0.99736]; (E) TPU during heating cycle [Inset: $I_{norm.}$ vs. T plot at 487 nm upon heating: 70 to 158 °C (Y = 0.99593–0.00411x), yielding R = 0.99574]. Temperature-dependent emission spectra of **L3** doped in (F) TPU during heating cycle [Inset: $I_{norm.}$ vs. T plot at 491 nm upon heating: 80 to 159 °C (Y = 1.611–0.0096602x), yielding R = 0.99758].

Declaration of Competing Interest

The authors declare that they have no known competing financial interests or personal relationships that could have appeared to influence the work reported in this paper.

Data availability

Data will be made available on request.

Acknowledgements

This work was supported by the Associate Laboratory for Green Chemistry LAQV which is financed by national funds from *Fundação para a Ciência e Tecnologia and Ministério da Ciência, Tecnologia e Ensino Superior* (FCT/MCTES) through the projects UIDB/50006/2020 and UIDP/50006/2020. PROTEOMASS Scientific Society (Portugal) is acknowledged by the funding provided through the General Funding Grant 2022-2023, and by the funding provided to the Laboratory for Biological Mass Spectrometry Isabel Moura (#PM001/2019 and #PM003/2016). F.D. thanks to FCT/MCTES (Portugal) for his doctoral grant 2021.05161.BD. E.O thanks FCT/MCTES (Portugal) for the individual contract, CEECIND/00648/2017. H. M. S. acknowledges the Associate Laboratory for Green Chemistry LAQV (LA/P/0008/2020) funded by FCT/MCTES for his research contract. The financial support by the Bulgarian National Science Fund (BNSF) under grant – "Novel styryl and polymethine fluorophores as potential theranostic agents" contract № KП-06-M59/1 from 15.11.2021 is gratefully acknowledged by A.K. This work is also developed and acknowledged by A.K. as part of contract №: BG-RRP-2.004-0002-C01, Laboratory of Organic Functional Materials (Project BiOrgaMCT), Procedure BG-RRP-2.004 „Establishing of a network of research higher education institutions in Bulgaria", funded by BULGARIAN NATIONAL RECOVERY AND RESILIENCE PLAN".

G. D. thanks to the European Regional Development Fund within the Operational Programme Science and Education for Smart Growth 2014 - 2020 under the Project Center of Excellence: National center of mechatronics and clean technologies - BG05M2OP001-1.001-0008 for the financial support.

Funding

This work received support from PT national funds (FCT/MCTES, *Fundação para a Ciência e Tecnologia* and *Ministério da Ciência, Tecnologia e Ensino Superior*) through the projects UIDB/50006/2020 and UIDP/50006/2020. This work received support from PROTEOMASS Scientific Society through the General Funding Grant 2022-2023, and the projects #PM001/2019 and #PM003/2016.

Appendix A. Supplementary data

Supplementary data to this article can be found online at https://doi.

org/10.1016/j.jphotochem.2023.115033.

References

[1] E.O. Dare, V. Vendrell-Criado, M.C. Jiménez, R. Pérez-Ruiz, D. Díaz Díaz, Highly efficient latent fingerprint detection by eight-dansyl-functionalized octasilsesquioxane nanohybrids, Dyes Pigm. 184 (2021) 108841.

[2] Y. Zhang, B. Lei, X. Zhang, Reversible, controllable white-light emission of dye systems by dynamic covalent furan moiety exchange, Chem. Commun. 58 (2022) 5261–5264, https://doi.org/10.1039/D2CC01309F.

[3] Y. Zhang, B. Lei, X. Zhang, Intramolecular energy transfer dyes as temperature- and polarity-sensitive fluorescence probes, Dye. Pigment. 205 (2022), 110492, https://doi.org/10.1016/j.dyepig.2022.110492.

[4] D. Yang, X.T. Wu, X.J. Cao, B.X. Zhao, A reversible ratiometric fluorescence probe for fast detection of trace water in different organic solvents, Dye. Pigment. 170 (2019), 107558, https://doi.org/10.1016/j.dyepig.2019.107558.

[5] Y. Cui, F. Li, X. Zhang, Controlling fluorescence resonance energy transfer of donor–acceptor dyes by Diels-Alder dynamic covalent bonds, Chem. Commun. 57 (2021) 3275–3278, https://doi.org/10.1039/D1CC00165E.

[6] A.F. Sierra, D. Hernández-Alonso, M.A. Romero, J.A. González-Delgado, U. Pischel, P. Ballester, Optical supramolecular sensing of creatinine, J. Am. Chem. Soc. 142 (2020) 4276–4284, https://doi.org/10.1021/jacs.9b12071.

[7] W.M. Pazin, A.K.A. Almeida, V. Manzoni, J.M.M. Dias, A.C.F. De Abreu, M. Navarro, A.S. Ito, A.S. Ribeiro, I.N. De Oliveira, Thermal and solvatochromic effects on the emission properties of a thienyl-based dansyl derivative, RSC Adv. 10 (2020) 28484–28491, https://doi.org/10.1039/D0RA05949H.

[8] N. Li, W. Qin, Y. Chen, K. Liu, S. Wang, F. Kong, Construction of a robust polarity sensitive platform and its application for tracking of lipid droplets decrease under oxidative stress in live cells, Sensors Actuators B Chem. 346 (2021), 130491, https://doi.org/10.1016/j.snb.2021.130491.

[9] Y. Pan, C. Zhang, S.H. Liu, Y. Tan, J. Yin, Fluorescent switch based on dithienylethene with dansulfonamide in multimedium, Dye. Pigment. 181 (2020), 108546, https://doi.org/10.1016/j.dyepig.2020.108546.

[10] H.J. Lee, M.J. Cho, S.K. Chang, Ratiometric signaling of hypochlorite by the oxidative cleavage of sulfonhydrazide-based rhodamine–Dansyl Dyad, Inorg. Chem. 54 (2015) 8644–8649, https://doi.org/10.1021/acs.inorgchem.5b01284.

[11] W.L. Wu, H.L. Ma, M.F. Huang, J.Y. Miao, B.X. Zhao, Mitochondria-targeted ratiometric fluorescent probe based on FRET for bisulfite, Sensors Actuators, B Chem. 241 (2017) 239–244, https://doi.org/10.1016/j.snb.2016.10.028.

[12] H. Jiang, Z. Li, Y. Kang, L. Ding, S. Qiao, S. Jia, W. Luo, W. Liu, A two-photon fluorescent probe for Cu2+ based on dansyl moiety and its application in bioimaging, Sensors Actuators, B Chem. 242 (2017) 112–117, https://doi.org/10.1016/j.snb.2016.11.033.

[13] B. Uttam, S. Polepalli, S. Sinha, A. Majumder, C.P. Rao, Selective sensing and removal of mercury ions by encapsulating dansyl appended calix[4]conjugate in a zeolitic imidazolate framework as an organic–inorganic hybrid nanomaterial, ACS Appl. Nano Mater. 5 (2022) 11371–11380, https://doi.org/10.1021/acsanm.2c02459.

[14] G. Donadio, R. Di Martino, R. Oliva, L. Petraccone, P. Del Vecchio, B. Di Luccia, E. Ricca, R. Isticato, A. Di Donato, E. Notomista, A new peptide-based fluorescent probe selective for zinc (II) and copper (II), J. Mater. Chem. B 4 (2016) 6979–6988, https://doi.org/10.1039/C6TB00671J.

[15] P. Wang, J. Wu, P. Su, C. Xu, Y. Ge, D. Liu, W. Liu, Y. Tang, Fluorescence "on-off-on" peptide-based chemosensor for selective detection of Cu2+ and S2- and its application in living cells bioimaging, Dalt. Trans. 45 (2016) 16246–16254, https://doi.org/10.1039/C6DT03330J.

[16] A. Aliberti, P. Vaiano, A. Caporale, M. Consales, M. Ruvo, A. Cusano, Fluorescent chemosensors for Hg2+ detection in aqueous environment, Sensors Actuators, B Chem. 247 (2017) 727–735, https://doi.org/10.1016/j.snb.2017.03.026.

[17] X. Pang, J. Dong, L. Gao, L. Wang, S. Yu, J. Kong, L. Li, Dansyl-peptide dual-functional fluorescent chemosensor for Hg2+ and biothiols, Dye. Pigment. 173 (2020), 107888, https://doi.org/10.1016/j.dyepig.2019.107888.

[18] Y. Wang, J. Zhou, L. Zhao, B. Xu, A dual-responsive and highly sensitive fluorescent probe for Cu^{2+} and pH based on a dansyl derivative, Dye. Pigment. 180 (2020), 108513, https://doi.org/10.1016/j.dyepig.2020.108513.

[19] L.J. Ma, J. Liu, L. Deng, M. Zhao, Z. Deng, X. Li, J. Tang, L. Yang, Selective and sensitive fluorescence-shift probes based on two dansyl groups for mercury(II) ion detection *Photochem*, Photobiol. Sci. 13 (2014) 1521–1528, https://doi.org/10.1039/C4PP00094C.

[20] Y.B. Barot, V. Anand, R. Mishra, Di-Triphenylamine-based AIE active Schiff base for highly sensitive and selective fluorescence sensing of Cu^{2+} and Fe^{3+}, J. Photochem. Photobiol. A Chem. 426 (2022), 113785 https://doi.org/10.1016/j.jphotochem.2022.113785.

[21] J. Galhano, G.A. Marcelo, A. Kurutos, E. Bértolo, J.L. Capelo-Martinez, C. Lodeiro, E. Oliveira, Development of low-cost colourimetric and pH sensors based on PMMA@Cyanine polymers, Dye. Pigment. 200 (2022), 110154, https://doi.org/10.1016/j.dyepig.2022.110154.

[22] C. Lodeiro, J.L. Capelo, J.C. Mejuto, E. Oliveira, H.M. Santos, B. Pedras, C. Nuñez, Light and colour as analytical detection tools: A journey into the periodic table using polyamines to bio-inspired systems as chemosensors, Chem. Soc. Rev. 39 (39) (2010) 2948–2976, https://doi.org/10.1039/B819787N.

[23] G.A. Marcelo, S.M.G. Pires, M.A.F. Faustino, M.M.Q. Simões, M.G.P.M.S. Neves, H. M. Santos, J.L. Capelo, J.P. Mota, C. Lodeiro, E. Oliveira, New dual colorimetric/fluorimetric probes for Hg2+ detection & extraction based on mesoporous SBA-16 nanoparticles containing porphyrin or rhodamine chromophores, Dye. Pigment. 161 (2019) 427–437, https://doi.org/10.1016/j.dyepig.2018.09.068.

[24] E. Oliveira, E. Bértolo, C. Núñez, V. Pilla, H.M. Santos, J. Fernández-Lodeiro, A. Fernández-Lodeiro, J. Djafari, J.L. Capelo, C. Lodeiro, Green and red fluorescent dyes for translational applications in imaging and sensing analytes: a dual-color flag, ChemistryOpen 7 (2018) 9–52, https://doi.org/10.1002/open.201700135.

[25] R. Nagarajan, H.-I. Ryoo, B.D. Vanjare, N. Gyu Choi, K.i. Hwan Lee, Novel phenylalanine derivative-based turn-off fluorescent chemosensor for selective Cu2 + detection in physiological pH, J. Photochem. Photobiol. A Chem. 418 (2021) 113435.

[26] T.N. Moshkina, E.V. Nosova, A.E. Kopotilova, M.I. Savchuk, I.L. Nikonov, D. S. Kopchuk, P.A. Slepukhin, G.A. Kim, G.N. Lipunova, V.N. Charushin, Synthesis and photophysical properties of pyridyl- and quinolinyl-substituted 4-(4-aminophenyl)quinazolines, J. Photochem. Photobiol. A Chem. 429 (2022), 113917, https://doi.org/10.1016/j.jphotochem.2022.113917.

[27] S.B. Yadav, S. Kothavale, N. Sekar, Triphenylamine and N-phenyl carbazole-based coumarin derivatives: Synthesis, solvatochromism, acidochromism, linear and nonlinear optical properties, J. Photochem. Photobiol. A Chem. 382 (2019), 111937, https://doi.org/10.1016/j.jphotochem.2019.111937.

[28] H. Sharma, R. Kakkar, S. Bishnoi, M.D. Milton, Synthesis of acceptor-donor-acceptor based phenothiazine-5-oxide aldehydes displaying large Stokes shift- "on-off-on" acidofluorochromic switch and molecular logic gate operation, J. Photochem. Photobiol. A Chem. 430 (2022), 113944, https://doi.org/10.1016/j.jphotochem.2022.113944.

[29] S. Mocanu, G. Ionita, I. Matei, Solvatochromic characteristics of dansyl molecular probes bearing alkyl diamine chains, Spectrochim. Acta A Mol. Biomol. Spectrosc. 237 (2020) 118413.

[30] K. Li, J. Wang, Y. Li, Y. Si, J. He, X. Meng, H. Hou, B.Z. Tang, Combining two different strategies to overcome the aggregation caused quenching effect in the design of ratiometric fluorescence chemodosimeters for pH sensing, Sensors Actuators, B Chem. 274 (2018) 654–661, https://doi.org/10.1016/j.snb.2018.07.109.

[31] S. Areti, S. Bandaru, D.S. Yarramala, C.P. Rao, Optimizing the electron-withdrawing character on benzenesulfonyl moiety attached to a glyco-conjugate to impart sensitive and selective sensing of cyanide in HEPES buffer and on cellulose paper and silica gel strips, Anal. Chem. 87 (2015) 12396–12403, https://doi.org/10.1021/acs.analchem.5b04085.

[32] A. Pucci, Mechanochromic fluorescent polymers with aggregation-induced emission features, Sensors 19 (2019) 4969, https://doi.org/10.3390/s19224969.

[33] B. González-Tobío, F. Duarte, A. Arribas-Delgado, C. Fernández-Lodeiro, J. Fernández-Lodeiro, M. Cano, C. Lodeiro, C. Cuerva, Tuning and reviving the luminescence of a new class of pyridyl β-diketonate Eu(III) metallomesogens: From molecules to entrapment in polymer particles, Dye. Pigment. 204 (2022), 110440, https://doi.org/10.1016/j.dyepig.2022.110440.

[34] R. Jiménez, F. Duarte, S. Nuti, J.A. Campo, C. Lodeiro, M. Cano, C. Cuerva, Thermochromic and acidochromic properties of polymer films doped with pyridyl-β-diketonate boron(III) complexes, Dye. Pigment. 177 (2020), 108272, https://doi.org/10.1016/j.dyepig.2020.108272.

[35] S. Gupta, M.D. Milton, Novel Y-shaped AIEE-TICT active π-extended quinoxalines-based donor–acceptor molecules displaying acidofluorochromism and temperature dependent emission, J. Photochem. Photobiol. A Chem. 424 (2022), 113630, https://doi.org/10.1016/j.jphotochem.2021.113630.

[36] N.M.M. Moura, S. Valentini, V. Cheptene, A. Pucci, M.G.P.M.S. Neves, J.L. Capelo, C. Lodeiro, E. Oliveira, Multifunctional Porphyrin-based dyes for cations detection in solution and thermoresponsive low-cost materials, Dye. Pigment. 185 (2021), 108897, https://doi.org/10.1016/j.dyepig.2020.108897.

[37] C. Papucci, A. Dessì, C. Coppola, A. Sinicropi, G. Santi, M. Di Donato, M. Taddei, P. Foggi, L. Zani, G. Reginato, A. Pucci, M. Calamante, A. Mordini, Benzo[1,2-d: 4,5-d']bisthiazole fluorophores for luminescent solar concentrators: synthesis, optical properties and effect of the polymer matrix on the device performances, Dye. Pigment. 188 (2021), 109207, https://doi.org/10.1016/j.dyepig.2021.109207.

[38] C. Micheletti, V.A. Dini, M. Carlotti, F. Fuso, D. Genovese, N. Zaccheroni, C. Gualandi, A. Pucci, Blending or Bonding? Mechanochromism of an Aggregachromic Mechanophore in a Thermoplastic Elastomer, ACS Appl. Polym. Mater. 5 (2023) 1545–1555, https://doi.org/10.1021/acsapm.2c02037.

[39] G.A. Marcelo, J. Galhano, M.P. Duarte, A. Kurutos, J.L. Capelo-Martínez, C. Lodeiro, E. Oliveira, Functional cyanine-based PVA:PVP polymers as antimicrobial tools toward food and health-care bacterial infections, Macromol. Biosci. 22 (2022) 1–12, https://doi.org/10.1002/mabi.202200244.

[40] L.M. Porosa, K.B. Mistry, A. Mocella, H. Deng, S. Hamzehi, A. Caschera, A.J. Lough, G. Wolfaardt, D.A. Foucher, Synthesis, structures and properties of self-assembling quaternary ammonium dansyl fluorescent tags for porous and non-porous surfaces, J. Mater. Chem. B 2 (2014) 1509–1520, https://doi.org/10.1039/C3TB21633K.

[41] Y.Y. Xiao, X.L. Gong, Y. Kang, Z.C. Jiang, S. Zhang, B.J. Li, Light-, pH- and thermal-responsive hydrogel with triple-shape memory effect, Chem. Commun. 52 (2016) 10609–10612, https://doi.org/10.1039/C6CC03587F.

[42] H. Yu, B. Zhao, J. Guo, K. Pan, J. Deng, Stimuli-responsive circularly polarized luminescent films with tunable emission, J. Mater. Chem. C 8 (2020) 1459–1465, https://doi.org/10.1039/C9TC06105C.

[43] F. Duarte, G. Dobrikov, A. Kurutos, H.M. Santos, J. Fernández-Lodeiro, J.L. Capelo-Martinez, E. Oliveira, C. Lodeiro, Enhancing water sensing via aggregation-induced emission (AIE) and solvatofluorochromic studies using two new dansyl derivatives containing a disulfide bound: Pollutant metal ions detection and preparation of water-soluble fluorescent polymeric particles, Dye. Pigment. 218 (2023), 111428, https://doi.org/10.1016/j.dyepig.2023.111428.

[44] M. Carcelli, D. Rogolino, A. Bacchi, G. Rispoli, E. Fisicaro, C. Compari, M. Sechi, A. Stevaert, L. Naesens, Metal-chelating 2-hydroxyphenyl amide pharmacophore for inhibition of influenza virus endonuclease, Mol. Pharm. 11 (2014) 304–316, https://doi.org/10.1021/mp400482a.
[45] H.L. Yu, W.Y. Wang, B. Hong, Y. Zong, Y.L. Si, Z.Q. Hu, Variational first hyperpolarizabilities of 2,3-naphtho-15-crown-5 ether derivatives with cation-complexing: a potential and selective cation detector, Phys. Chem. Chem. Phys. 18 (2016) 26487–26494, https://doi.org/10.1039/C6CP04577D.
[46] A. Nion, P. Jiang, A. Popoff, D. Fichou, Rectangular nanostructuring of Au(III) surfaces by self-assembly of size-selected thiacrown ether macrocycles, J. Am. Chem. Soc. 129 (2007) 2450–2451, https://doi.org/10.1021/ja068709e.
[47] M. Montalti, A. Credi, L. Prodi, M.T. Gandolfi, Handbook of Photochemistry, 3rd ed., Taylor & Francis, Boca Raton, BOCA, 2006.
[48] D. MacDougall, W.B. Crummett, et al., Guidelines for data acquisition and data quality evaluation in environmental chemistry, Anal. Chem. 52 (14) (1980) 2242–2249.
[49] G.L. Long, J.D. Winefordner, Limit of detection A closer look at the IUPAC definition, Anal. Chem. 55 (1983) 713A–A724, https://doi.org/10.1021/ac00258a724.
[50] E. Oliveira, R.M.F. Baptista, S.P.G. Costa, M.M.M. Raposo, C. Lodeiro, Solvatochromic effects of bis(indolyl)thienylaril derivatives as new colored materials, Photochem. Photobiol. Sci. 13 (2014) 492–498, https://doi.org/10.1039/C3PP50352F.
[51] P. Gans, A. Sabatini, A. Vacca, Investigation of equilibria in solution. Determination of equilibrium constants with the HYPERQUAD suite of programs, *Talanta* 43 (1996) 1739–1753, https://doi.org/10.1016/0039-9140(96)01958-3.

.

E

Published Paper in Journal of Materials Chemistry C - Corresponding to Chapter 7

Journal of Materials Chemistry C

ROYAL SOCIETY OF CHEMISTRY

PAPER



Cite this: J. Mater. Chem. C, 2025, 13, 6708

Design and evaluation of dansyl-derived chemosensors for disulfide-cleavage-triggered detection: photophysical, metal sensing, and thermometric applications†

Igor Lourenço,‡[a] Frederico Duarte,‡[a] Georgi M. Dobrikov,[bc] Atanas Kurutos,*[bd] Ivaylo Slavchev,[b] José Luis Capelo-Martínez,[ae] Hugo M. Santos[ae] and Carlos Lodeiro *[ae]

Received 8th November 2024, Accepted 5th February 2025

DOI: 10.1039/d4tc04750h

rsc.li/materials-c

In this work, two new dansyl-derived chemosensors have been designed with the aim of developing a disulfide-cleavage-triggered probe. These stable new ligands, containing a thioether (**L1**) and a disulfide bridge (**L2**), have been synthesized and evaluated for their photophysical properties in both solution and the solid state. Different fluorescence emission responses have been observed for both compounds due to the self-quenching nature of the disulfide bond in L2 compared to **L1**, with the latter reaching quantum yields close to 50%. Efforts to characterize solute–solvent interactions through Kamlet–Taft studies have revealed a positive solvatofluorochromic response for both compounds. Furthermore, the aggregation-induced emission phenomenon was demonstrated at increasing water fractions. The presence of free thiol groups enhances the complexation ability, making **L1** particularly beneficial for sensing Cu^{2+} and Hg^{2+} ions, achieving detection limits as low as 2 μM in the case of mercury. Finally, incorporating **L1** into polymer-doped films demonstrated promising results as molecular thermometers, while the response of **L2** to sodium dithionite underscores its potential for disulfide-cleavage-triggered applications.

1. Introduction

The design of new sensors for metals and anions has been a topical area of chemistry in recent years. Contamination of water (including water in biological objects) with heavy metals is continuously increasing. Nonetheless, universally applicable and entirely effective sensors for their detection and removal are not available. It is well known that most heavy metals (particularly Hg, Cu, Pb and Cd) possess high affinity to organic molecules containing sulfur, due to the formation of a strong donor–acceptor bond with this nonmetal element. Furthermore, the design of organosulfur fluorescent compounds may provide unique chemical properties that enable the interaction of particular substrates in biological systems. Some examples of biologically active substances include the aforementioned metal ions, reactive sulfur, oxygen and nitrogen species (RSS, ROS, and RNS) and biomacromolecules.[1] Among the common classes of organosulfur compounds, thioether and disulfide bond-containing probes may possess a complementary framework since efforts have been made to develop disulfide-cleavage-activated probes. This comes from the fact that disulfide bonds present strong reactivity or biological activity through the reductive disulfide cleavage reaction producing two thiols, or the photocleavage reaction *via* a radical mechanism.[2] Several studies have been published on the basis of the presence of this bond for the sensing of biologically relevant molecules and metal ions due to the often observed self-quenching effects through fluorescence resonance energy transfer or photoinduced electron transfer prior cleavage.[3–9]

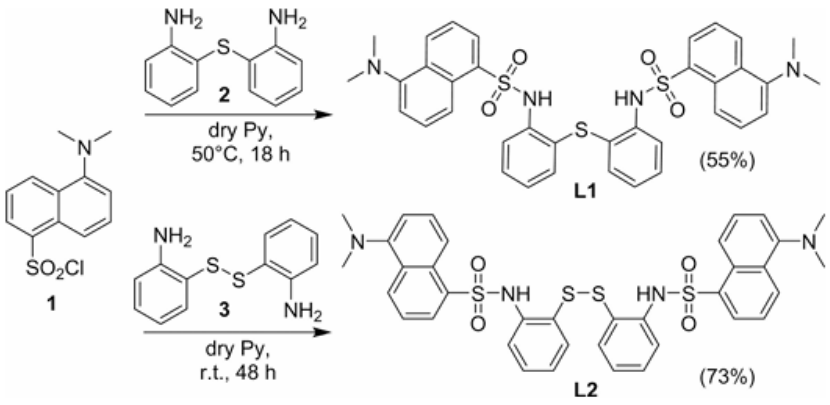
Over the last few decades, few studies have explored sulfur containing ligands, possessing a dansyl moiety as a source of fluorescence. Many of them were used for different applications such as protein labeling,[10,11] immobilization onto polymers,[12] enzyme detection,[13] cell imaging[14] and metal ion detection.[15,16] In addition, the presence of a sulfonamide functionality can

[a] BIOSCOPE Research Group, LAQV-REQUIMTE, Chemistry Department, NOVA School of Science and Technology, FCT NOVA, Universidade NOVA de Lisboa, 2829-516 Caparica, Portugal. E-mail: cle@fct.unl.pt
[b] Institute of Organic Chemistry with Centre of Phytochemistry, Bulgarian Academy of Sciences, Acad. G. Bonchev str., bl. 9, 1113 Sofia, Bulgaria. E-mail: Atanas.Kurutos@orgchm.bas.bg
[c] National Centre of Excellence Mechatronics and Clean Technologies, Sofia, Bulgaria
[d] University of Chemical Technology and Metallurgy, 8 St. Kliment Ohridski blvd, 1756 Sofia, Bulgaria
[e] PROTEOMASS Scientific Society, 2825-466 Costa de Caparica, Portugal

† Electronic supplementary information (ESI) available. See DOI: https://doi.org/10.1039/d4tc04750h

‡ These authors contributed equally to this work.

This journal is © The Royal Society of Chemistry 2025



Scheme 1 Synthetic approach to the preparation of dansyl derivatives **L1** and **L2**.

significantly improve the characteristics of such organic ligands[17] (especially their ability for complexation).

Our previous expertise in the synthesis of sulfur containing dansyl ligands for the detection of heavy metals reveals that the incorporation of sulfur into aromatic rings leads to less efficient ligands, whereas the best ligands contain sulfur, bound to aliphatic carbon chains.[18,19] Conversely, the existence of free thiol groups in the ligands provides optimal complexation capability; nevertheless, such compounds are often unstable and very susceptible to oxidation, even from atmospheric exposure.

In this work, we provide two novel stable ligands (Scheme 1, **L1** and **L2**), including thio- and dithio- bridges connecting two identical dansyl-substituted aromatic groups. The chemical structures of these ligands were designed in order to ensure strong chelation of heavy metals by the introduction of sulfur atoms and sulfonamide functionalities. Furthermore, efforts have been made to highlight the photophysical contrast of both compounds towards the sensing of sodium dithionite or sodium hydrosulfite, $Na_2S_2O_4$, which is a strong reductant and broadly used in several industries as a bleaching agent, however classified as a highly toxic agent.[20–25] To the best of our knowledge, very few studies have been published using dansyl moieties for the sensing of sodium dithionite with early reports from Nicholas Rattray *et al.* where a sterically constrained bisdansyl chromophore would undergo fluorescence changes after reduction of the azo-bond locking group, and the detection of azo-reductase expressing bacteria was also evaluated.[26] In contrast, Xingxing Cao *et al.* were able to sense sodium dithionite by simultaneous immobilization in silicon nanowires of a dansyl group and dabsyl group, the latter would act as a quencher and recognizing group due the strong absorption at 470 nm overlapping with the dansyl group's emission. This system was found to exhibit high selectivity and good linearity between emission intensities and dithionite concentrations.[27]

Finally, the aggregation-induced emission (AIE) behaviour with increasing water fractions and the incorporation of **L1** into polymeric thin films towards temperature-dependent emission studies have been elucidated.

2. Results and discussion

2.1. Synthesis

As in our recent study,[18] the target compounds **L1** and **L2** were synthesised in dry pyridine *via* the reaction of dansyl chloride (**1**) with commercially available amines **2** and **3**, respectively (Scheme 1). Since **3** is presumably sensitive to oxidation, synthesis of **L2** was carried out at room temperature. Both **L1** and **L2** were obtained in pure form and good yields after column chromatography. They were unambiguously characterized by using different 1D and 2D NMR experimental techniques, melting point temperatures and HRMS.

2.2. Photophysical characterization

The bisdansylated compounds **L1** and **L2** bearing single sulfur and disulfide bonds were studied according to their photophysical properties both in solution and in the solid state. Fig. 1 displays the chemical structure with the photoluminescence data in acetonitrile with the remaining solvents shown in Fig. S3 and S4 (ESI†) while a summary of all the data is present in Table 1.

The UV-vis spectral data of both compounds reveal maxima centered at *ca.* 345 and 335 nm corresponding to the π–π* transitions of the dansyl chromophore supporting the observation of colorless solutions with the naked eye. Clear differences rise upon proper excitation of the samples with the visualization of a greenish light with the emission maximum centered at 535 for **L1** and a faint bluish green emission characterized by a maximum around 464 nm observed for **L2**. This behaviour is present across all solvents used, and it can be visually identified in Fig. 1d with the reason behind it being the presence of each type of sulfur bond that links both chromophores. Disulfide bonds when incorporated in fluorescent molecules are often associated with the quenching of the emission by promoting

This journal is © The Royal Society of Chemistry 2025

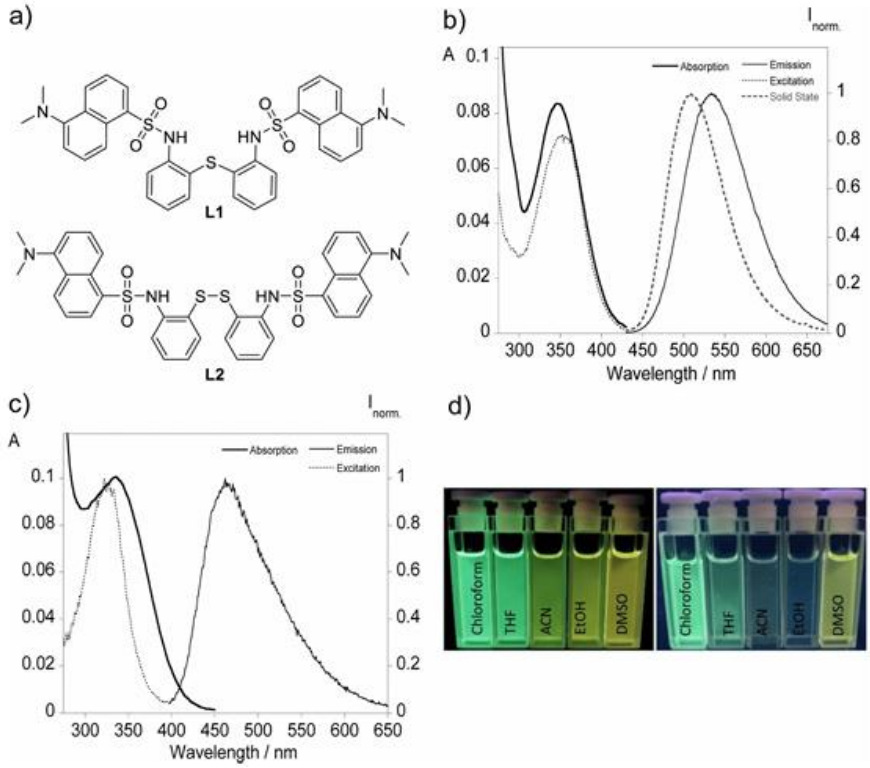


Fig. 1 (a) Molecular structure of the dansyl derived compounds **L1** and **L2** bearing single sulfur and disulfide bridges. Photophysical characterization of derivatives **L1** (b) and **L2** (c) in acetonitrile ([**L1**] = [**L2**] = 10 μM). Images under UV light (365 nm) of (d) **L1** (left) and **L2** (right) in different solvents with varying polarity.

photoinduced electron transfer (PeT) or Förster resonance energy transfer (FRET).[3–9] This divergence observed between both ligands presents a key advantage that will be explored further ahead. On a similar subject, solid state emission is only present for **L1** with a maximum around 508 nm that is blue-shifted compared with in solution resembling the emission profile of chloroform and THF.

The fluorescence quantum yields of the two compounds were also evaluated, using dansylamide as a standard for compounds **L1** and **L2**, with compound **L1** reaching a quantum yield of 0.48 in chloroform, and for compound **L2** the expected lower values were obtained across all solvents with fluorescence efficiency observed below 5%. Time-correlated single photon counting suggests double digit nanosecond times among all solvents between 11.4 and 15.5 ns for **L1** while apolar solvents provide higher fluorescence lifetimes.

The presence of a solvent environment notably influences the stabilization of the ligand's excited state, primarily due to changes in the fluorophore's dipole moment. Considering the data gathered in Table 1, a correlation between the increase in solvent polarity and the energy gap, translating to a greater Stokes shift, ultimately resulting in a bathochromic shift can be inferred. This shift can be attributed to a positive solvatofluorochromic effect,

Table 1 Absorption maximum wavelength in solution (λ_{abs}), emission maximum wavelength in solution (λ_{em}), molar absorption coefficients (ε), Stokes shift ($\Delta\lambda$), fluorescence quantum yields (ϕ), emission maximum in the solid state (λ_{em}^{Solid}), brightness ($\varepsilon \times \phi$), and fluorescence lifetimes (τ) of compounds **L1** and **L2** in various solvents

Cpd.	Solv.	λ_{abs} [nm]	λ_{em} [nm]	ε (10^4) [cm^{-1} M^{-1}]	Stokes shift [cm^{-1}]	Φ (%)	λ_{em}^{Solid} [nm]	τ [ns]
L1	DMSO	345	545	0.76	10 637	17.7	508	12.6
	EtOH	340	525	0.81	10 364	21.2		11.4
	CH_3CN	345	535	0.86	10 294	18.8		11.7
	THF	343	511	0.88	9804	41.1		13.7
	$CHCl_3$	350	510	1.01	8964	48.3		15.5
L2	DMSO	340	529	0.91	10 508	4.6	—	4.8
	EtOH	335	508	0.98	10 166	2.9		7.3
	CH_3CN	340	464	0.98	8299	2.5		10.6
	THF	330	500	1.24	10 303	3.5		12.5
	$CHCl_3$	333	487	1.21	9496	3.6		12.9

This journal is © The Royal Society of Chemistry 2025

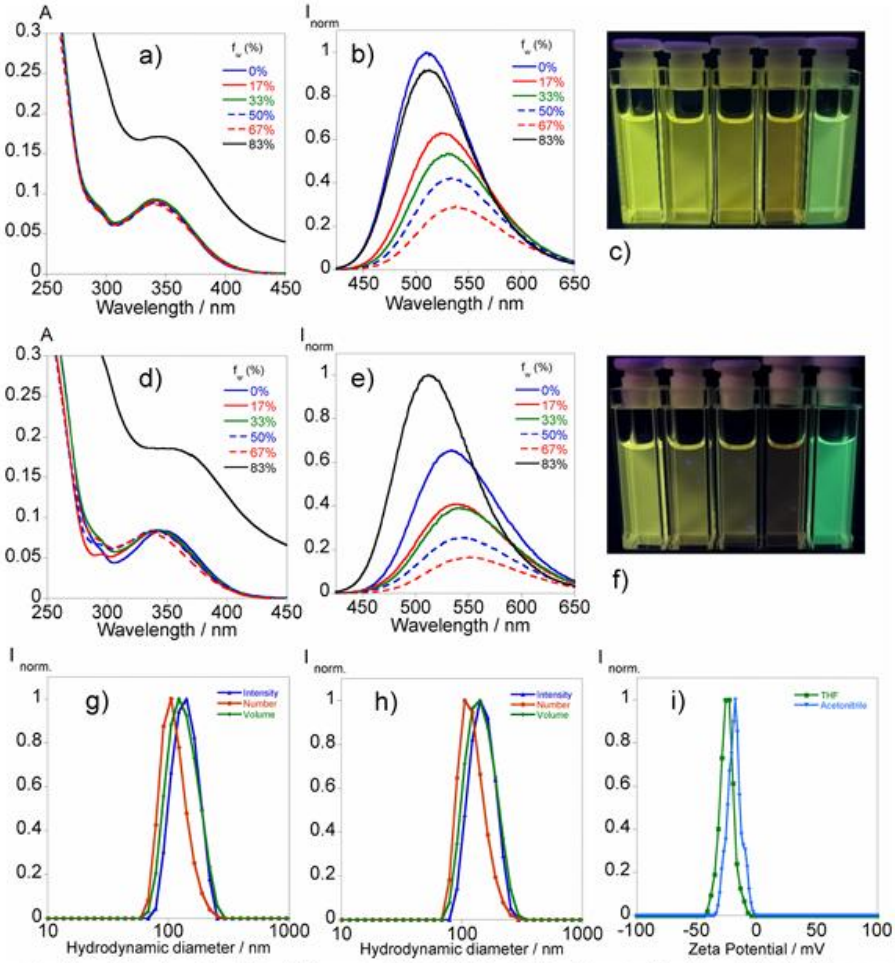


Fig. 2 Absorption ((a) and (d)) and emission ((b) and (e)) spectra of **L1** in THF ((a) and (b)) and in acetonitrile ((d) and (e)) with different water fractions f_w (0%, 17%, 33%, 55%, 67%, and 83%). [**L1**]= 10 μM. Images of **L1** in (c) THF and (f) acetonitrile with different water fractions under UV light (365 nm). The hydrodynamic diameter of **L1** aggregates in THF (g) and acetonitrile (h) according to the number, volume, and intensity distributions and zeta potential (i) of the solutions of 83% water fractions.

where the environment-sensitive dansyl derivatives adjust their fluorescence maximum wavelengths in response to solvent polarity, a behavior clearly illustrated in Fig. 2.

In response to these results, significant efforts have been focused on thoroughly describing the interactions between the solvent and the molecules.

To this end, three solute-dependent parameters (υ_0, a, b, and p) have been determined *via* multiparametric fitting using the Kamlet–Taft equation (eqn (1)).

$$\upsilon = \upsilon_0 + a\alpha + b\beta + p\pi^* \quad (1)$$

where υ_0 denotes the wavenumber value in a reference solvent and the parameters a, b, and p are derived from multiple regression analysis and represent the sensitivity of the probe's photophysical behavior to solvent polarity. Specifically, α indicates the hydrogen bond donor acidity (HBD), β represents the hydrogen bond acceptor basicity (HBA), and π^* reflects the stabilization of a charge or dipole in the absence of specific dielectric interactions (see Table S1, ESI†).[28,29]

Table 2 summarizes the reference wavenumber value υ_0, the fitted parameters (a, b and p) with the slopes and correlation coefficients attained through the fitting of a linear plot of

This journal is © The Royal Society of Chemistry 2025

Table 2 Independent fluorescence wavenumber (υ_0), solvent polarity (p), HBD (a), HBA (b), and slopes and coefficients (R^2) of the linear fitting plot $\upsilon_{exp.}$ *versus* υ_{calc}

	υ_0	a	b	p	Slope	R^2
L1	21 492	−509	−911	−2451	1.00	1
L2	21 943	−65	−1652	−1784	1.00	1

$\upsilon_{exp.}$ *versus* υ_{calc}, by applying the Kamler–Taft model excluding acetonitrile.

Key distinctions can be elucidated regarding the predisposition of each compound towards the characteristics of different solvents. The fitted parameters reveal low hydrogen bond donor sensitivity with extended negative values for **L1**, while **L2** is more prone to stabilization by solvents with more hydrogen bond acceptor character due to the presence of an extra electronegative atom that forms a disulfide bridge. Additionally, highly polarizable solvents can stabilize the excited state of **L1** more effectively, as the more negative p value suggests higher polarizability, leading to stronger solvation effects.

2.3. Aggregation-induced emission behaviour in water

The assessment of the photophysical properties of **L1** with different ratios of water in THF and acetonitrile mixtures has been conducted *via* absorption and fluorescence spectroscopy.

Fig. 2 illustrates that the augmentation of the water fraction results in a reduction in fluorescence in both solvents, accompanied by a little red shift in emission until reaching a 67% water content.

The absorption profile changes significantly in the mixture of 83% water content with the rise of the baseline indicating the presence of aggregates. This phenomenon translates into substantial changes in the emission profile by the sudden increase in the fluorescence intensity followed by a hypsochromic shift suggesting an aggregation-induced emission (AIE) effect. In the case of THF, the emission intensity surpasses the initial one while in acetonitrile it is equalized with the associated fluorescence quantum yields of 12% and 8%, respectively. The heterogeneity observed in the absorbance measurements led us to further characterize the presence of aggregates through dynamic light scattering analysis. The results,

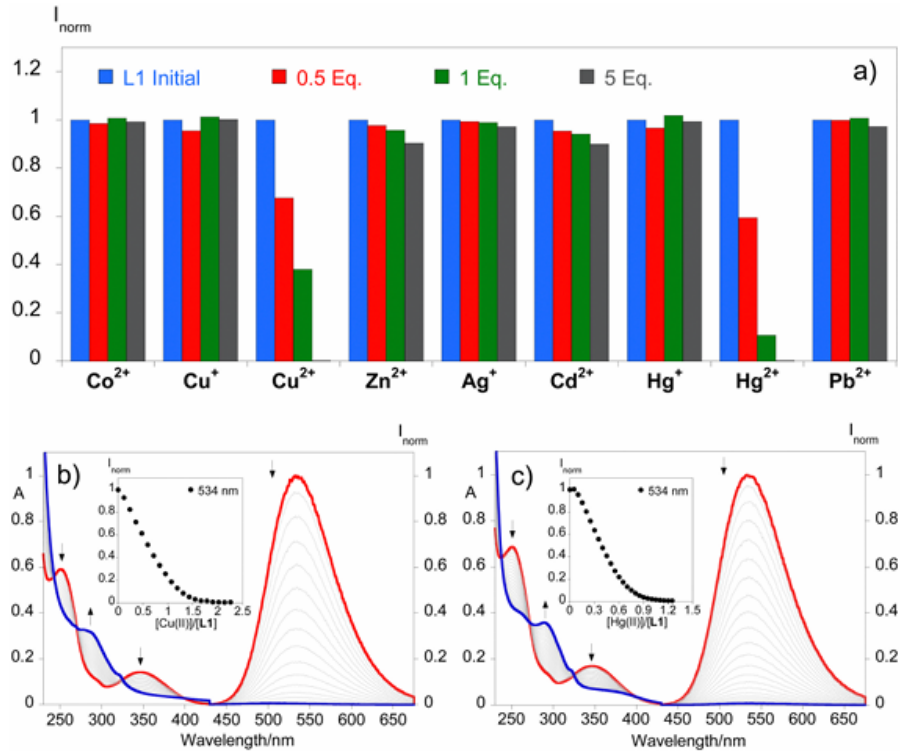


Fig. 3 Maximum emission intensities of **L1** (a) after the addition of 0.5, 1, and 5 equivalents of Co^{2+}, Cu^{+}, Cu^{2+}, Zn^{2+}, Ag^{+}, Cd^{2+}, Hg^{+}, Hg^{2+} and Pb^{2+} metal ions in acetonitrile. Spectrophotometric and spectrofluorometric titrations of compound **L1** with increased additions of Cu^{2+} ([**L1**] = 16.8 μM) (b) and Hg^{2+} ([**L1**] = 20 μM) (c) in acetonitrile. The insets present the emission as a function of $[Cu^{2+}]/[L1]$ at 534 nm (b) and $[Hg^{2+}]/[L1]$ at 534 nm (c).

 This journal is © The Royal Society of Chemistry 2025

presented in Fig. 2, suggest hydrodynamic sizes of 142.5 ± 7.9 nm (THF/water) and 146.0 ± 2.5 nm (acetonitrile/water) with associated polydispersity index values of 0.037 ± 0.07 and 0.045 ± 0.01, respectively.

2.4. Metal ion sensing

Dansyl derivatives have shown promise as efficient probes for the detection of metal ions, specifically evaluating the efficacy of compound **L1** was carried out, since **L2** showed negligible emission from the start. For this reason, several metal ions including Co^{2+}, Cu^{+}, Cu^{2+}, Zn^{2+}, Ag^{+}, Cd^{2+}, Hg^{+}, and Hg^{2+} in acetonitrile and Pb^{2+} in water were tested. Fig. 3 shows a consolidation of the changes in the emission intensity with the addition of 0.5, 1, and 5 equivalents of the metal ions. Notably, the absorption and emission spectra showed significant variations exclusively in the presence of mercury(II) and copper(II) ions. The introduction of a single equivalent of each metal ion significantly diminished the emission signal. Furthermore, the fluorescence intensity was completely quenched upon the addition of 5 equivalents.

This signifies that both compounds exhibit high selectivity for these particular metal ions.

The efficacy of compound **L1** in detecting Cu^{2+} and Hg^{2+} metal ions was promising, prompting titrations with these metals in acetonitrile. Fig. 3 shows the spectrophotometric and spectrofluorometric titrations towards both metals exhibiting similar absorption spectral behaviour with a decrease in absorption at 250 nm and 347 nm and an increase in the absorbance at 289 nm. As for the emission spectra, a suppression of the emission intensity was observed at 534 nm. Fig. 3 also shows the fluctuation of the emission intensity maxima of compound **L1** with the increase of the metal concentration in solution. The suppression of the emission caused by Hg^{2+} comes from the fact that, as a heavy atom, it has photophysical properties such as spin–orbit coupling, making non-radiative pathways compete with fluorescence and therefore having a mechanism for quenching the emission after chelation (CHEQ). The Cu^{2+} ion is also commonly detected by CHEQ due to its paramagnetic nature by having unpaired electrons in the d-layer, which occurs through either electron transfer or energy transfer mechanisms. However, once filled Cu^{+} becomes a CHEF system, which is why Cu^{+} does not quench the emission intensity of compound **L1**. This system can recognize either Cu^{2+} from Cu^{+} or Hg^{2+} from Hg^{+}, being a good example for metal speciation.

As a favorable characteristic of a molecular probe, the binding reversibility of **L1** with Hg^{2+} and Cu^{2+} was evaluated against a competitive ligand, *i.e.*, Na_2EDTA. As shown in Fig. S8 (ESI†), the addition of 2.2 equivalents of Cu^{2+} leads to fluorescence quenching of **L1** that showed no significant recovery of the emission intensity following the addition of equimolar Na_2EDTA, indicating that the complex formed is not reversible in the presence of this competitive ligand. In contrast, the addition of 1.0 equivalents of Hg^{2+} also causes fluorescence quenching; however, the emission intensity is recovered with equimolar Na_2EDTA in solution, suggesting the regeneration of free **L1**. These reversibility studies were performed 5 times (Fig. S6, ESI†), providing the results to support the capacity for **L1** to be a reversible fluorescent probe for the detection of Hg^{2+} but not for Cu^{2+}. Furthermore, the formation of the complexes has been followed by ESI-HRMS suggesting the stoichiometric proportion of 1 : 1 as it can be seen in Fig. S7 and S8 (ESI†). (**L1** + Cu^{2+}): $[M + H]^+$ for $C_{36}H_{34}CuN_4O_4S_3$ = 746.1111 *m*/*z* (−0.01 ppm). Calculated $[M + H]^+$ for $C_{36}H_{34}CuN_4O_4S_3$ = 746.111093 *m*/*z*. (**L1** + Hg^{2+}): $[M + H]^+$ for $C_{36}H_{34}HgN_4O_4S_3$ = 885.1519 *m*/*z* (−0.2 ppm). Calculated $[M + H]^+$ for $C_{36}H_{34}HgN_4O_4S_3$ = 885.152138 *m*/*z*.

Table 3 Association constants using HypSpec software for compounds **L1** and **L2** towards Hg^{2+} and Cu^{2+} ions with included stoichiometry in acetonitrile. The respective values for the detection limit (LOD) and quantification limit (LOQ) amounts (μM) were measured by the emission at 509 and 513 nm for **L1** and **L2**, respectively

Compounds	Metal (M)	Association constants ($\log K_{ass}$), L : M	LOD (μM)	LOQ (μM)
L1	Cu^{2+}	5.73 ± 0.01	4	8
	Hg^{2+}	5.80 ± 0.02	2	4

To thoroughly evaluate the sensing capabilities for Hg^{2+} and Cu^{2+} ions, the interaction constants of all complexes were calculated using HypSpec software.[30] Additionally, the detection and quantification limit parameters for both compounds in relation to Hg^{2+} and Cu^{2+} were determined. The association constants, along with the LOD (limit of detection) and LOQ (limit of quantification), are provided in Table 3.

The stability constant values for **L1** towards both metal ions evidence similar values in a stoichiometric proportion of 1 : 1 ligand to metal with a slightly higher value in the case of Hg^{2+} ($\log K_{ass.}$ = 5.80 ± 0.02).

The detection and quantification limits have also been determined, reaching values as low as 2 and 4 μM for Hg^{2+}, respectively. These values indicate that **L1** could be highly useful in applications such as environmental monitoring, where it is crucial to detect and measure Hg^{2+} at low concentrations.

2.5. Sensing of sodium dithionite

The potential use of **L2** in the induced turn-on sensing of sodium dithionite by disulfide bond cleavage has been evaluated in light of the duality observed in the photophysical profile of both compounds, which is a result of the self-quenching characteristic of disulfide systems. Fig. 4 shows the UV-vis and the fluorescence response in acetonitrile upon consecutive additions of an aqueous solution of sodium dithionite up to 9 equivalents alongside the visual representation of the turn-on effect after the addition of 5 equivalents, while the batch-based sensing can be seen in Fig. S9 (ESI†).

Fig. 4 reveals that as the concentration of dithionite increases, a progressive blue shift of the absorption profile is noticed with the emergence of a shoulder around 290 nm. Regarding the fluorescence response, the results show that the emission band observed initially successively increases with the addition of dithionite indicating the cleavage of the disulfide

This journal is © The Royal Society of Chemistry 2025

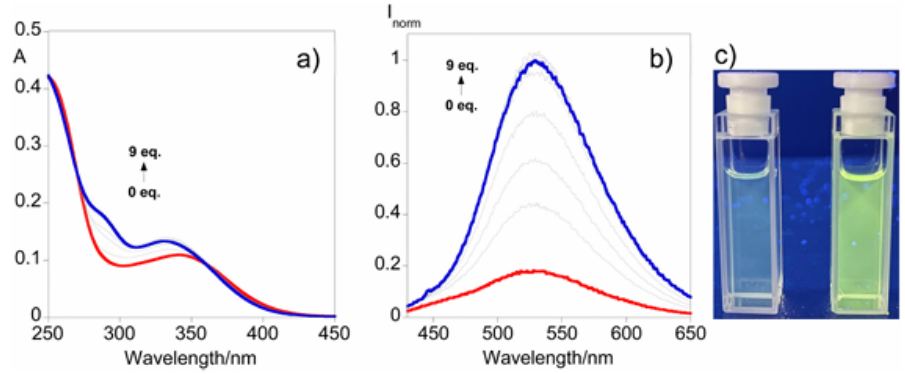


Fig. 4 UV-vis (a) and emission (b) spectral responses after the addition of up to 9 equivalents of sodium dithionite to **L2** solution in acetonitrile. The image under UV-light (365 nm) (c) of the initial solution (left) and after the addition of 5 equivalents (right).

bond. Also, ESI-HRMS adds support to this suggestion due to the formation of the monomer moiety depicted in Fig. S10 (ESI†). ([M + H]$^+$ for $C_{18}H_{18}N_2O_2S_2$ = 359.0882 *m/z* (−0.1 ppm) and calculated [M + H]$^+$ for $C_{18}H_{18}N_2O_2S_2$ = 359.088246 *m/z*.) This behavior can be perceived through Fig. 4c where a turn-on sensing mechanism is observed highlighting the usefulness of compound **L2** for disulfide-cleavage-activated applications.

Although a clear contribution of compound **L2** towards the development of new disulfide-based chemosensors has been established, some considerations might become useful for the improvement of the future design of these types of compounds. We propose that improving the selectivity of the sensor molecule must be considered since these compounds may interact with multiple analytes. Some examples include the soft character of sulfur atoms that can be easily combined with Hg^{2+} as an example of a soft metal according to the hard–soft–acid–base theory or the implications of the reducing environment when applying for a specific reactive species in a biological system. This can be avoided through the design of a multiple lock design method to counteract false positives. Considerations about water solubility should be fulfilled alongside biocompatibility by implementing changes in their molecular structure. Finally, a switch-on or clear-cut ratiometric fluorescence mechanism may provide a comfortable level of certainty regarding the physical property changes in these systems.[1,2]

2.6. NMR titrations of the free ligands

The full structural elucidation of the free ligands **L1** and **L2** was achieved with the help of 1D and 2D NMR experiments carried out in various solvents including $CDCl_3$ (Fig. SX1–SX20 for **L1** and Fig. SX59–SX82 for **L2**, ESI†), CD_3CN (Fig. SX21–SX40 for **L1** and Fig. SX83–SX98 for **L2**, ESI†), and DMSO-d_6 (Fig. SX41–SX58 for **L1** and Fig. SX99–SX115 for **L2**, ESI†). In addition to acetonitrile-d_3, deuterated DMSO was also employed as an alternative bearing in mind the relatively poor solubility of the salts (mercury(II) acetate, copper(II) triflate, and sodium dithionite) in CD_3CN. For all experiments we used 1 equiv. of each salt as the maximum amount in order to obtain clear NMR working solutions of suitable concentration.

The experiment of **L1** with mercury(II) acetate in acetonitrile-d_3 (Fig. SX145–SX171, ESI†) revealed almost no visible change with respect to the chemical shifts in the ^{1}H- and the ^{13}C-NMR spectra. The only notable difference involves broadening of the NH signal (Fig. SX164 and SX165, ESI†), which nevertheless retained the integral for a total of 2 protons. Changing the media to DMSO-d_6, the ^{1}H-NMR spectra of **L1** with Hg^{2+} resulted in rather noisy spectra (including a broad baseline) with side bands around the main signals, the appearance of two new multiplets, namely a triplet a doublet of doublets (with a small J_{H-H} coupling constant) at 6.30 ppm, along with a new doublet at about 8.69 ppm (Fig. SX192 and SX193, ESI†). The full identification of the mixture is hampered taking into consideration the broad signals and baseline, which remain broad and noisy even after 29 days. Despite the non-emissive nature of **L2** preventing the evaluation of the sensing capabilities through fluorescence techniques, attempts to record spectra of **L2** in deuterated acetonitrile after the addition of 1 equiv. of Hg^{2+} only showed very broad signals along the whole spectral range once again (Fig. SX200, ESI†). The shape remained unaltered over several days. To shed more light, we attempted to perform the same measurement in DMSO-d_6. In the case of ligand **L2**, changing the solvent revealed very pronounced spectral changes, pointing out to the spontaneous formation of a new product (Fig. SX225–SX246, ESI†). Intriguingly, the presence of mercury(II) acetate exhibits more pronounced spectral changes in DMSO-d_6 for both **L1** and **L2**. The addition of Hg^{2+} to **L2** resulted in the complete disappearance of the NH proton. The new spectra showed no sign of either an NH, or an SH proton signal. With respect to the ^{13}C-NMR spectra, the most pronounced changes were found for the 2 carbon atoms on the benzene ring, which are attached to the nitrogen and sulfur heteroatoms (Fig. SX245, ESI†). We assume that the S–S bond is most likely cleaved while Hg is allocated between the two heteroatoms.

 This journal is © The Royal Society of Chemistry 2025

While keeping DMSO-d_6 as the working media, the addition of 1 equiv. of copper(II) triflate to ligand **L2** (Fig. SX205–SX224, ESI†) showed no difference in comparison to the pure ligand as seen from the ^{1}H-NMR spectra, where only a minor shift of the majority of the signals is present in the carbon spectra. In the ^{13}C-NMR spectra, the triflate quartet with a J_{C-F} coupling constant of around 320 Hz (123.87 ppm, 120.95 ppm, 117.75 ppm, and 114.20 ppm) was also reported (Fig. SX209, ESI†). The shape of the ^{1}H-NMR spectrum remained the same after 17 days. Therefore, we repeated the same experiment in acetonitrile-d_3 (Fig. SX194–SX199, ESI†). Likewise to the data obtained in DMSO-d_6, the ^{13}C-NMR in acetonitrile-d_3 comprises the triflate quartet with a J_{C-F} coupling constant of around 320 Hz (126.74 ppm, 123.55 ppm, 120.36 ppm, and 117.19 ppm as). The addition of 1 equiv. of copper(II) triflate to ligand **L1** (Fig. SX188–SX191, ESI†) leads to only negligible changes (of about 0.02–0.03 ppm towards a stronger field) as seen from the ^{1}H-NMR spectra in DMSO-d_6 (Fig. SX188 and 189, ESI†). By analogy, the ^{13}C-NMR exhibits a shift of around 0.6 ppm for all signals (Fig. SX190 and 191, ESI†). Both spectra of the free ligand and after the addition of copper(II) triflate appear to be highly similar accounting for the same number of protons and carbons in the chemical structure of the fluorophore. In turn, working with acetonitrile-d_3 for **L2** showed somehow more pronounced shifts for both the ^{1}H- and the ^{13}C-NMR spectra (Fig. SX194–SX199, ESI†). In particular several shifts are observed for the whole dansyl moiety (including the dimethylamino group and the aromatic protons), whereas the *o*-substituted benzene ring remains unaltered. A shift of the signals was present for the $N(CH_3)_2$ - from 2.81 ppm to 3.04 ppm when copper(II) triflate is added (Fig. SX194, ESI†). The ^{13}C-spectra also show distinctive changes, even to the carbon atom directly linked to the dimethylamino group, since an approximately 5 ppm shift is evident (Fig. SX190, ESI†). **L2** also exhibits the characteristic triflate quartet with a J_{C-F} coupling constant of around 320 Hz (126.74 ppm, 123.56 ppm, 120.37 ppm, and 117.19 ppm). Ligand **L2** exhibits very distinctive shifts in acetonitrile-d_3 – mainly relative to the dansyl moiety (up to 0.5 ppm). In particular, the singlet corresponding to the methyl protons of $N(CH_3)_2$ shifts from 2.78 ppm to 3.41 ppm (Fig. SX194, ESI†). Notable changes are also evident in the ^{13}C-NMR spectra, where the carbon attached to the dimethylamino shifts from 153.09 ppm to 139.51 ppm (Fig. SX197, ESI†). Other dansyl carbon signals also move by about 4–5 ppm. On the other hand, only minor changes were visible for the benzene ring containing the two *ortho* S and N heteroatoms (Fig. SX198, ESI†).

The addition of 1 equiv. of sodium dithionite to **L2** in acetonitrile-d_3 (Fig. SX201–SX204, ESI†) furnished the appearance of new proton signals allocated at 9.82 (s), 8.20 (dd), 7.53 (m), 7.44 (dd), 7.38 (dd), 7.29 (m), and 7.05 (td) and a negligible change of the NH shift from 7.82 (s) to 7.86 (s). The kinetics of this experiment are very slow, since even after 30 days we observe a mixture of the free ligand (about 57%) and an additional product (about 43%) – the ratio was determined based on the integration of the ^{1}H-NMR. Due to the low concentration and the very poor solubility of sodium dithionite in acetonitrile, clear HMBC cross peaks of the XH signals were not observed. Despite the relatively low concentration, the NOESY experiment also did not yield any further information. This in turn hampered the full assignment of the newly developed product in deuterated acetonitrile. Next, we attempted to repeat the experiment in deuterated DMSO (Fig. SX247–SX254, ESI†). Despite changing the media, the solubility of the dithionite salt was not notably enhanced. Adding 1 equiv. of sodium dithionite to ligand **L2** in DMSO-d_6 yielded the broadening of the NH proton at 10.22 ppm (no disappearance – integral is retained), while a new sharp signal was developed around 9.86 ppm (Fig. SX248–SX250, ESI†). Several new signals were

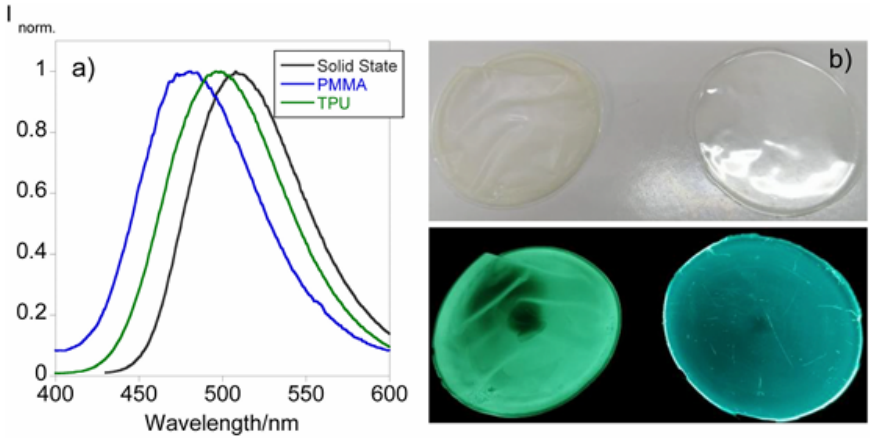


Fig. 5 Comparison between the emission spectra of the different polymer thin films doped with (a) **L1** and the (b) images under natural (up) and UV light (down) of TPU (left) and PMMA (right).

This journal is © The Royal Society of Chemistry 2025

developed over time of which the more evident were found centered at 8.24 ppm (dt), 8.18 ppm (dd), 7.60 ppm (m), 7.42 ppm (dt), and 7.40 ppm (t). In parallel, the intensity of several multiplets was diminished, while others were enhanced accompanied by the appearance of overlapping multiplets. Accounting for the relatively clear region around the dimethylamino protons, we accounted for a mixture of at least two main components (ligand + newly formed product) in almost equal quantities (Fig. SX250, ESI†). This slow transformation to about 50% of a new product takes more than 24 days under these experimental conditions. Bearing in mind the strong overlap of the majority of the aromatic protons, full identification of the mixture by means of NMR is currently limited and beyond the scope of our current investigation.

2.7. Temperature-dependent emission of polymer doped films

Since compound **L1** has manifested solvatochromism aligned with the fact that it is the only compound exhibiting emission in the solid state, efforts have been put forth for the design of solid supports that would act as molecular thermometers. Bearing this in mind, doped polymer films have been produced following the procedure depicted in the experimental section using PMMA and TPU as polymer matrixes. Fig. 5 shows the

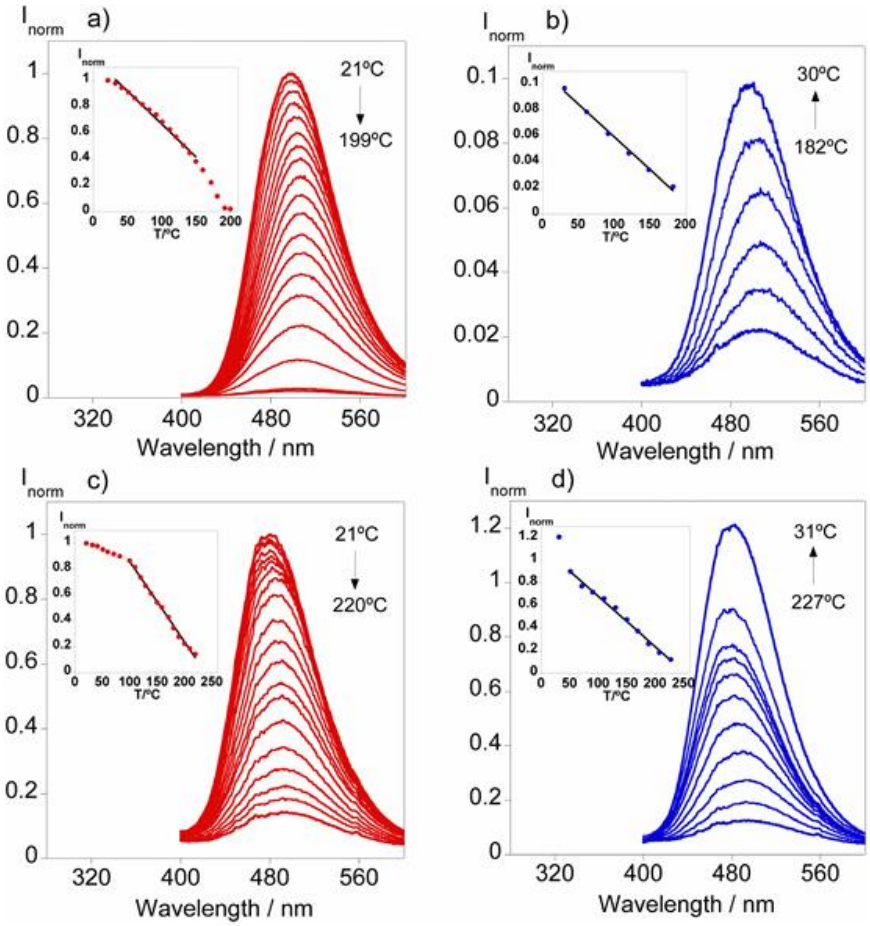


Fig. 6 Temperature-dependent emission spectra of **L1** doped in (a) TPU during the heating cycle [inset: I_{norm} vs. T plot at 496 nm upon heating: 32 to 149 °C (Y = 1.1685 − 0.0050481x), yielding R = 0.9902]; (b) TPU during the cooling cycle [inset: I_{norm} vs. T plot at 496 nm upon cooling: 30 to 182 °C (Y = 0.10949 − 0.0050184x), yielding R = 0.9933]; (c) PMMA during the heating cycle [inset: I_{norm} vs. T plot at 481 nm upon heating: 100 to 220 °C (Y = 1.481 − 0.0062098x), yielding R = 0.9963]; (d) PMMA during the cooling cycle [inset: I_{norm} vs. T plot at 481 nm upon cooling: 51 to 227 °C (Y = 1.1278 − 0.0044644x), yielding R = 0.9925].

 This journal is © The Royal Society of Chemistry 2025

emission spectra of **L1** in the solid state and doped in the polymer materials together with the images under natural and UV light.

From Fig. 5, it can be inferred that both polymer matrixes are able to shift the emission of the final material causing a blue shift from 508 in the solid state to 496 and 481 nm in TPU and PMMA, respectively. This phenomenon is also tangible in the images of the polymers found in Fig. 5 since TPU shows a greenish emission while PMMA's emission resembles a more bluish color. These observations have been described in previous studies demonstrating the potential of the use of dansyl compounds towards the development of tunable solid materials for diverse applications.[18] Considering these findings, the fabricated polymer doped materials have been tested to be used as molecular thermometers by recording the emission at different temperatures. Fig. 6 presents the temperature-dependent emission spectra of both doped materials.

A reduction in the fluorescence signal is seen in both polymeric materials as the temperature increases, reaching values of up to 227 °C. Regarding the TPU-doped material, a clear total quenching of the fluorescence signal was achieved at 200 °C. Throughout the increases in temperature over the course of the cycle, linearity has been found between 32 and 149 °C; however, only 10% of the initial emission is restored after cooling suggesting that further increases in temperature may cause physical damage to the polymer preventing reusability of the material.

In the case of PMMA doped with **L1**, higher temperatures could be achieved in this solid substrate along with a linearity range at higher temperatures between 100 and 200 °C shifting its potential towards industrial applications. During the cooling cycle, linearity was retained as the temperature decreased and in contrast with the TPU substrate, the physical changes enabled the recovery of the emission past the initial one due to the increased rigidity observed.

Thus, these materials provide insights into the design of solid materials that can be tuned in terms of their emission depending on the polymer matrix used, and the linearity of the fluorescence signal sustains the use of these doped polymers as thermometers.

3. Conclusions

Two new dansyl compounds bearing thio- and dithio- functionalities were synthesized and their photophysical characteristics were investigated. Using the Kamlet–Taft equation, the solute–solvent interactions were analyzed in detail, revealing a positive solvatofluorochromic behavior for both compounds. Additionally, the compounds showed enhanced emission in the presence of water, exhibiting aggregation-induced emission (AIE) at a high water content. This AIE effect was further confirmed by dynamic light scattering experiments, which revealed hydrodynamic sizes of 142.5 ± 7.9 nm (THF/water) and 146.0 ± 2.5 nm (acetonitrile/water) for **L1**. Taking an environmental remediation standpoint, **L1** was found sensitive to Hg^{2+} and Cu^{2+} ions by modulating their emission profile with the highest association constant towards Hg^{2+} ($\log K_{ass.} = 5.80$) in tandem with the lowest LOD and LOQ values of 2 and 4 μM, respectively. Given that the key photophysical differences were attributed to the presence of disulfide bridges in **L2** promoting self-quenching behavior, a proof of concept for sodium dithionite sensing was put forth to highlight the potential use of this compound towards disulfide-cleavage-triggered sensing. Finally, the PMMA and TPU polymer-doped films were fabricated in order to demonstrate the possibility of modulating the emission maximum wavelength in the solid state, and the use of these materials as molecular thermometers has been elucidated.

Author contributions

Igor Lourenço: formal analysis, investigation, writing – original draft, review & editing, and visualization. Frederico Duarte: formal analysis, investigation, writing – original draft, review & editing, and visualization. Georgi Dobrikov: methodology, validation, formal analysis, investigation, writing – original draft, review & editing, resources, and visualization. Atanas Kurutos: conceptualization, methodology, validation, formal analysis, investigation, writing – original draft, review & editing, resources, visualization, supervision, and funding acquisition. Ivaylo Slavchev: investigation. Jose Luis Capelo-Martinez: resources, writing – review & editing, and funding acquisition. Hugo M. Santos: investigation, resources, validation, and writing – review & editing. Carlos Lodeiro: conceptualization, methodology, validation, formal analysis, investigation, resources, writing – review & editing, visualization, supervision, funding acquisition, and project administration.

Data availability

Data will be made available on request.

Conflicts of interest

The authors declare that they have no known competing financial interests or personal relationships that could have appeared to influence the work reported in this paper.

Acknowledgements

This work received support from PT national funds (FCT/MCTES, *Fundação para a Ciência e Tecnologia* and *Ministério da Ciência, Tecnologia e Ensino Superior)* through the projects UIDB/50006/2020 and UIDP/50006/2020. This work received support from the PROTEOMASS Scientific Society through the General Funding Grant 2022-2023, and the projects #PM001/2019 and #PM003/2016. The financial support from the Bulgarian National Science Fund (BNSF) under grant – ''Novel styryl and polymethine fluorophores as potential theranostic agents'' contract No KP-06-M59/1 from 15.11.2021 is gratefully acknowledged by A. K. This work is also developed and acknowledged

This journal is © The Royal Society of Chemistry 2025

by A. K. as part of contract No: BG-RRP-2.004-0002-C01, Laboratory of Organic Functional Materials (Project BiOrgaMCT), Procedure BG-RRP-2.004 "Establishing of a network of research higher education institutions in Bulgaria", funded by the BULGARIAN NATIONAL RECOVERY AND RESILIENCE PLAN. This work was supported by the Associate Laboratory for Green Chemistry LAQV that is financed by the national funds from *Fundação para a Ciência e Tecnologia and Ministério da Ciência, Tecnologia e Ensino Superior* (FCT/MCTES) through the projects UIDB/50006/2020 and UIDP/50006/2020. The PROTEOMASS Scientific Society (Portugal) is acknowledged for the funding provided through the General Funding Grant 2023-2024 and for the funding provided to the Laboratory for Biological Mass Spectrometry Isabel Moura (#PM001/2019 and #PM003/2016). F. D. thanks the FCT/MCTES (Portugal) for his doctoral grant 2021.05161.BD. H. M. S. acknowledges the Associate Laboratory for Green Chemistry LAQV (LA/P/0008/2020) funded by the FCT/MCTES for his research contract. The financial support by the Bulgarian National Science Fund (BNSF) under grant – "Novel styryl and polymethine fluorophores as potential theranostic agents" contract No КП-06-М59/1 from 15.11.2021 is gratefully acknowledged by A. K. This work is also developed and acknowledged by A. K. as part of contract No: BG-RRP-2.004-0002-C01, Laboratory of Organic Functional Materials (Project BiOrgaMCT), Procedure BG-RRP-2.004 "Establishing of a network of research higher education institutions in Bulgaria", funded by the BULGARIAN NATIONAL RECOVERY AND RESILIENCE PLAN. G. D. acknowledges that this work was supported by the European Regional Development Fund under the "Research Innovation and Digitization for Smart Transformation" program 2021-2027 under the Project BG16RFPR002-1.014-0006 "National Centre of Excellence Mechatronics and Clean Technologies". Research equipment of this project was used for experimental work.

References

1 G. Hu, H. Dong Xu and J. Fang, Sulfur-based fluorescent probes for biological analysis: A review, *Talanta*, 2024, **279**, 126515, DOI: **10.1016/j.talanta.2024.126515**.

2 M. H. Lee, Z. Yang, C. W. Lim, Y. H. Lee, S. Dongbang, C. Kang and J. S. Kim, Disulfide-Cleavage-Triggered Chemosensors and Their Biological Applications, *Chem. Rev.*, 2013, **113**, 5071–5109, DOI: **10.1021/cr300358b**.

3 Y. Zhang, S. Xia, S. Wan, T. E. Steenwinkel, T. Vohs, R. L. Luck, T. Werner and H. Liu, Ratiometric Detection of Glutathione Based on Disulfide Linkage Rupture between a FRET Coumarin Donor and a Rhodamine Acceptor, *ChemBioChem*, 2021, **22**, 2282–2291, DOI: **10.1002/cbic.202100108**.

4 Z. Zheng, Y. Huyan, H. Li, S. Sun and Y. Xu, A lysosome-targetable near infrared fluorescent probe for glutathione sensing and live-cell imaging, *Sens. Actuators, B*, 2019, **309**, 127065, DOI: **10.1016/j.snb.2019.127065**.

5 Z. Wang, R. Jing, Y. Li, D. Song, Y. Wan, N. Fukui, H. Shinokubo, Z. Kuang and A. Xia, Intrinsic Photostability in Dithiolonaphthalimide Achieved by Disulfide Bond-Induced Excited-State Quenching, *J. Phys. Chem. Lett.*, 2023, **14**, 8485–8492, DOI: **10.1021/acs.jpclett.3c02260**.

6 G. J. S. Cheng, J. M. Qin, X. Li and Q. Y. Cao, A naphthalimide-based fluorescent probe with mitochondria targeting for GSH sensing and cancer cell recognition, *Dyes Pigm.*, 2023, **211**, 111089, DOI: **10.1016/j.dyepig.2023.111089**.

7 J. Mishra, R. Kaur, A. K. Ganguli and N. Kaur, Urea/thiourea based dipodal nanoreceptors: Aqueous medium fluorescent chemosensor for Zn(II) and Hg(II) ions by photoinduced electron transfer, *Microchem. J.*, 2024, **206**, 111501, DOI: **10.1016/j.microc.2024.111501**.

8 J. Qiang, Y. Wang, Y. Li, Z. Guo, L. Jiang, F. Wang, S. Lu and X. Chen, A dual-locked near-infrared fluorescent probe based on ESIPT and FRET for improved discrimination between normal and cancer cells, *Sens. Actuators, B*, 2024, **405**, 135344, DOI: **10.1016/j.snb.2024.135344**.

9 A. K. Ghosh, A. H. Khan and P. K. Das, Naphthalimide-Based AIEgens for Sensing Protein Disulfide Isomerase through Thiol–Disulfide Redox Exchange, *Anal. Chem.*, 2023, **95**, 13638–13648, DOI: **10.1021/acs.analchem.3c02442**.

10 J. Torres-Kolbus, C. Chou, J. Liu and A. Deiters, Synthesis of Non-linear Protein Dimers through a Genetically Encoded Thiol-ene Reaction, *PLoS One*, 2014, **9**(9), e105467, DOI: **10.1371/journal.pone.0105467**.

11 Y. Li, M. Yang, Y. Huang, X. Song, L. Liu and P. R. Chen, Genetically encoded alkenyl–pyrrolysine analogues for thiol–ene reaction mediated site-specific protein labeling, *Chem. Sci.*, 2012, **3**, 2766–2770, DOI: **10.1039/C2SC20433A**.

12 J. Sánchez-Bodón, M. Diaz-Galbarriatu, L. Pérez-Álvarez, J. L. Vilas-Vilela and I. Moreno-Benítez, Expanding (Bio)-Conjugation Strategies: Metal-Free Thiol-Yne Photo-Click Reaction for Immobilization onto PLLA Surfaces, *Coatings*, 2024, **14**, 839, DOI: **10.3390/coatings14070839**.

13 H. Kurosaki, H. Yasuzawa, Y. Yamaguchi, W. Jin, Y. Arakawa and M. Goto, Detection of a metallo-lactamase (IMP-1) by fluorescent probes having dansyl and thiol groups, *Org. Biomol. Chem.*, 2003, **1**, 17–20, DOI: **10.1039/b209086d**.

14 J. Youziel, A. R. Akhbar, Q. Aziz, M. E. B. Smith, S. Caddick, A. Tinker and J. R. Baker, Bromo- and thiomaleimides as a new class of thiol-mediated fluorescence 'turn-on' reagents, *Org. Biomol. Chem.*, 2014, **12**, 557–560, DOI: **10.1039/c3ob42141d**.

15 V. Tharmaraj and K. Pitchumani, A highly selective ratiometric fluorescent chemosensor for Cu(II) based on dansyl-functionalized thiol stabilized silver nanoparticles, *J. Mater. Chem. B*, 2013, **1**, 1962–1967, DOI: **10.1039/c3tb00534h**.

16 A. Jose, R. Sahadevan, M. Vijay, S. Sadhukhan and M. Porel, Dansyl-appended sequence-defined oligomers for selective ultrasensitive detection of Hg^{2+} in water, paper strips, living cells and its efficient removal, *Sens. Actuators, B*, 2023, **380**, 133335, DOI: **10.1016/j.snb.2023.133335**.

 This journal is © The Royal Society of Chemistry 2025

17 M. Batool, Z. Afzal, H. M. Junaid, A. R. Solangi and A. Hassan, Sulfonamides as Optical Chemosensors, *Crit. Rev. Anal. Chem.*, 2024, **54**(5), 954–981, DOI: 10.1080/10408347.2022.2105135.

18 F. Duarte, G. Dobrikov, A. Kurutos, J. L. Capelo-Martinez, H. M. Santos, E. Oliveira and C. Lodeiro, Development of fluorochromic polymer doped materials as platforms for temperature sensing using three dansyl derivatives bearing a sulfur bridge, *J. Photochem. Photobiol., A*, 2023, **445**, 115033, DOI: 10.1016/j.jphotochem.2023.115033.

19 G. Pedro, F. Duarte, G. M. Dobrikov, A. Kurutos, H. M. Santos, J. L. Capelo-Martínez, E. Oliveira and C. Lodeiro, Optical evaluation of dansyl derivatives and their implementation in low-cost and flexible dye-doped PMMA platforms for efficient detection of hazardous chemical vapours, *Dyes Pigm.*, 2024, **224**, 112042, DOI: 10.1016/j.dyepig.2024.112042.

20 Y. Zha, R. Xin, M. Zhang, X. Cui and N. Li, Stimuli-responsive azobenzene-quantum dots for multi-sensing of dithionite, hypochlorite, and azoreductase, *Microchim. Acta*, 2020, **187**, 481, DOI: 10.1007/s00604-020-04455-9.

21 J. Li, X. Yu, D. Shu, H. Liu, M. Gu, K. Zhang, G. Mao, S. Yang and R. Yang, Accelerated Activity-Based Sensing by Fluorogenic Reporter Engineering Enables to Rapidly Determine Unstable Analyte, *Anal. Chem.*, 2024, **96**, 7723–7729, DOI: 10.1021/acs.analchem.4c00945.

22 B. Dong, W. Song, X. Kong, N. Zhang and W. Lin, Visualizing cellular sodium hydrosulfite (Na2S2O4) using azo-based fluorescent probes with a high signal-to-noise ratio, *J. Mater. Chem. B*, 2019, **7**, 730–733, DOI: 10.1039/c8tb02487a.

23 A. Chevalier, C. Mercier, L. Saurel, S. Orenga, P. Y. Renard and A. Romieu, The first latent green fluorophores for the detection of azoreductase activity in bacterial cultures, *Chem. Commun.*, 2013, **49**, 8815–8817, DOI: 10.1039/c3cc44798g.

24 X. Yu, L. Xiang, S. Yang, S. Qu, X. Zeng, Y. Zhou and R. Yang, A near-infrared fluorogenic probe with fast response for detecting sodium dithionite in living cells, *Spectrochim. Acta, Part A*, 2021, **245**, 118887, DOI: 10.1016/j.saa.2020.118887.

25 S. Wang, W. Wu, J. Lv, Q. Qi and W. Huang, Fast detection of sodium dithionite in sugar using a xanthylium-based f luorescent probe, *Food Chem.*, 2024, **452**, 139547, DOI: 10.1016/j.foodchem.2024.139547.

26 N. J. W. Rattray, W. A. Zalloum, D. Mansell, J. Latimer, M. Jaffar, E. V. Bichenkova and S. Freeman, Chemical and bacterial reduction of azo-probes: monitoring a conformational change using fluorescence spectroscopy, *Tetrahedron*, 2013, **69**, 2758–2766, DOI: 10.1016/j.tet.2013.01.086.

27 X. Cao, L. Mu, M. Chen and G. She, A facile fluorescent sensor based on silicon nanowires for dithionite, *Appl. Surf. Sci.*, 2018, **441**, 388–393, DOI: 10.1016/j.apsusc.2018.01.313.

28 S. Mocanu, G. Ionita and I. Matei, Solvatochromic characteristics of dansyl molecular probes bearing alkyl diamine chains, *Spectrochim. Acta, Part A*, 2020, **237**, 118413, DOI: 10.1016/j.saa.2020.118413.

29 E. Oliveira, R. M. F. Baptista, S. P. G. Costa, M. M. M. Raposo and C. Lodeiro, Solvatochromic Effects of bis(indolyl)thienylaril derivatives as new Colored Materials, *Photochem. Photobiol. Sci.*, 2014, **13**, 492–498, DOI: 10.1039/C3PP50352F.

30 P. Gans, A. Sabatini and A. Vacca, Investigation of equilibria in solution. Determination of equilibrium constants with the HYPERQUAD suite of programs, *Talanta*, 1996, **43**, 1739–1753, DOI: 10.1016/0039-9140(96)01958-3.

This journal is © The Royal Society of Chemistry 2025

.

.

F

Published Paper in Dyes and Pigments- Corresponding to Chapter to Chapter 8

Dyes and Pigments 232 (2025) 112461

Contents lists available at ScienceDirect

Dyes and Pigments

journal homepage: www.elsevier.com/locate/dyepig

Tetra dansylamides substituted cyclen and cyclam macrocycles as fluorescent sensing probes for metal ions and temperature-responsive materials in dopped polymers

Inês Pereira-Gomes [a,1], Frederico Duarte [a,1], Georgi M. Dobrikov [b,**], Ivaylo Slavchev [b], Atanas Kurutos [b,c], Jose Luis Capelo-Martinez [a,d], Hugo M. Santos [a,d], Carlos Lodeiro [a,d,*]

[a] BIOSCOPE Research Group, LAQV-REQUIMTE, Chemistry Department, NOVA School of Science and Technology, FCT NOVA, Universidade NOVA de Lisboa, 2829-516, Caparica, Portugal
[b] Institute of Organic Chemistry with Centre of Phytochemistry, Bulgarian Academy of Sciences, Acad. G. Bonchev str., bl. 9, 1113, Sofia, Bulgaria
[c] University of Chemical Technology and Metallurgy, 8 St. Kliment Ohridski blvd, 1756, Sofia, Bulgaria
[d] PROTEOMASS Scientific Society, 2825-466, Costa de Caparica, Portugal

ARTICLE INFO

Keywords:
Polymers
Dansyl derivatives
Metal ions
Sensors
Solvatochromism
Temperature

ABSTRACT

Two novel tetra-dansyl derivatives incorporating cyclen (1,4,7,10-tetraazacyclododecane) and cyclam (1,4,8,11-tetraazacyclotetradecane) macrocycles have been synthesized, thoroughly characterized, and their photophysical properties examined, both in solution and in the solid state. These compounds exhibit fluorescence emission with quantum yields up to 40 %, varying significantly with different solvents. They also display positive solvato-fluorochromic behavior, with emissions ranging from green to yellow colours. Kamlet-Taft studies were conducted to better understand solute-solvent interactions. Furthermore, aggregation-induced emission was observed in solutions with high water content, confirmed via dynamic light scattering. Given the intrinsic properties of these compounds, their potential for environmental remediation was explored through metal ion sensing studies. Compounds **L1** and **L2** demonstrated high sensitivity to Cu^{2+} and Hg^{2+} ions, significantly modulating their emission, with **L2** capable of detecting and quantifying Hg^{2+} concentrations as low as 2–3 μM. Additionally, the solid-state emission of these compounds encouraged an investigation into their potential as temperature sensors. Several doped polymer thin films were fabricated, establishing a linear relationship with temperature beyond their melting point. These findings suggest that these tetra-chromophoric compounds hold promise as molecular thermometers.

1. Introduction

Probes and sensors employing fluorescent dyes are highly beneficial due to their exceptional optical features. Among this extensive group, dansyl derivatives have consistently been used throughout the decades amidst their consistent photophysical properties, namely large Stokes shift, high fluorescence quantum yields and the well-known strong dependence of the emission properties on the surrounding environment [1–5]. The detection of heavy metals and transition metal ions is extensively documented in the literature, given the wide range of applications to which dansyl derivatives have been put to use, especially for Cu^{2+} [1,2,4,6–10], Zn^{2+} [11,12], Ag^{2+} [13], Cd^{2+} [14], Hg^{2+} [1,4,15–18] and Pb^{2+} [19].

Given the current efforts to develop new dyes, aza-crown compounds, namely cyclen (1,4,7,10-Tetraazacyclododecane) and cyclam (1,4,8,11-Tetraazacyclotetradecane) were employed as good candidates to their versatility and wide range of applications including in the fields of medicine [20,21], magnetic resonance imaging [22–24], catalysis [25–27] and pollutant degradation [28]. Within this context, azamacrocyclic tetramines can readily be functionalized and demonstrate robust binding to a diverse array of cations [29]. An example of this was demonstrated by Hava Ozay et al. where p(2-hydroxyethyl

* Corresponding author. BIOSCOPE Research Group, LAQV-REQUIMTE, Chemistry Department, NOVA School of Science and Technology, FCT NOVA, Universidade NOVA de Lisboa, 2829-516, Caparica, Portugal.
** Corresponding author.
E-mail addresses: Georgi.Dobrikov@orgchm.bas.bg (G.M. Dobrikov), cle@fct.unl.pt (C. Lodeiro).
[1] These authors have contributed equally to the work.

https://doi.org/10.1016/j.dyepig.2024.112461
Received 25 July 2024; Received in revised form 11 September 2024; Accepted 13 September 2024
Available online 16 September 2024
0143-7208/© 2024 The Authors. Published by Elsevier Ltd. This is an open access article under the CC BY-NC-ND license (http://creativecommons.org/licenses/by-nc-nd/4.0/).

methacrylate-co-tetraacrylic cyclen) (p(HEMA-co-TACYC)) hydrogels were synthesized with the intention to transfer the copper ion binding ability of cyclen into the hydrogel structure. The designed hydrogels showed selective colorimetric sensor behaviour towards Cu^{2+} in all aqueous media and when submitted to metal ion mixtures [30].

Functionalization of these macrocycles with fluorophores is supported by the literature, namely with anthracene, naphthalimide, rhodamine and BODIPY [29,31,32]. Xiao Fang et al. have synthesized a BODIPY-based fluorescent probe with a cyclen moiety that improved water solubility, followed by Cu^{2+} binding. The selective turn-on fluorescent behaviour for H_2S was elucidated with a LOD of 1.1 nM. Additionally, the complex was effectively utilized for imaging exogenous H_2S generated from Na_2S and GYY4137 in H9c2 and U87 cells [31].

Based on an extensive literature search, the dansylation of aza-crown compounds is in its early stages with very early reports focused on mono dansylated cyclen [33,34]. More recently, this compound was used for the formation of metal complexes in various matrices [35–38]. The presence of metal ions binding to the basic nitrogen atoms of this derivative is crucial for the creation of a stable complex. Rivas et al. demonstrated that coordination of metal ions with other heteroatoms outside the aza-crown ring is also feasible [39]. Due to the negligible cytotoxicity, good penetration and photostability, Yang et al. have been successful in using this compound for specific lysosome labeling in various cell lines [40]. To the best of our knowledge, only a few mentions of dansyl derivatives of cyclam are reported in the art [41–45]. In this study, we successfully synthesized symmetric tetra dansyl derived compounds of cyclam and cyclen for the first time. These newly developed fluorophores were then fully characterized according to their photophysical properties. The Kamlet-Taft equation was used to explain the solvatochromism behaviour of functionalizing the aza-crown with four dansyl units. The tuning of the emission using water as co-solvent led to an aggregation induced emission in high water fraction and was confirmed by dynamic light scattering. The above-mentioned ligands were designed in order to demonstrate good complexation ability toward heavy metals and so efforts to elucidate their ability to sense pollutant metal ions was put forth. Finally, incorporation into polymer thin films KURARITY (L44285) and IROGRAN (A 92 P 4637) towards the development of temperature-smart materials was carried out.

2. Experimental section

2.1. Materials

Spectroscopy grade solvents, such as acetonitrile (CH_3CN), chloroform ($CHCl_3$), dimethylsulfoxide (DMSO), ethanol (EtOH), and tetrahydrofuran (THF), were used for spectrophotometric and spectrofluorimetric measurements. All solvents used for the synthesis and purification of the target compounds (dichloromethane (DCM) and methyl-*tert*-butyl ether (MTBE)) were of analytical grade (p.a.) and dried over molecular sieve (3 Å). The starting fine chemicals (cyclam (1,4,8,11-Tetraazacyclotetradecane), cyclen (1,4,7,10-Tetraazacyclododecane), diisopropylethylamine (DIPEA) and dansyl chloride) used for the synthesis of the target fluorophores were purchased from Sigma Aldrich, Tokyo Chemical Industry Co. Ltd., and BLDPharm. Silica gel (high-purity grade, pore size 60 Å, 230–400 mesh particle size, 40–63 μm particle size, for flash chromatography) employed for the column chromatography was purchased from Sigma Aldrich. Trifluoromethanesulfonate salts of $Co(OTf)_2$, $Ni(OTf)_2$, $Cu(OTf)_2$, $Zn(OTf)_2$, $Ag(OTf)$, $Cd(OTf)_2$, were provided from Solchemar, while $Hg(OTf)_2$ and $Ca(BF_4)_2H_2O$ were purchased from Sigma Aldrich. KURARITY™ LA4285 Kurashiki, Okayama, Japan; the thermoplastic polyurethane TPU-A92 was offered by Huntsman (Germany). The perfluoroalkoxy (PFA) supports for the fabrication of polymer films were purchased to Bohlender, Gmbh, Germany. Mili-Q ultrapure water was used in all experiments.

2.2. Instrumentation

The chemical identities of the compounds under investigation were confirmed through the utilization of various analytical techniques, including ^{1}H NMR, ^{13}C NMR, DEPT-135, 2-D COSY, 2D-HSQC, and 2-D HMBC NMR spectroscopic techniques. The ^{1}H NMR and ^{13}C NMR spectra were acquired on a Bruker Avance II+600 spectrometer (Institute of Organic Chemistry with Centre of Phytochemistry - Bulgarian Academy of Sciences/NMR Centre) using 5 mm tubes. The measurements were performed in $CDCl_3$ at 293K, with operating frequencies of 600.13 MHz and 150.92 MHz for the ^{1}H- and ^{13}C- nuclei, respectively. The ^{1}H- and ^{13}C- nuclear magnetic resonance (NMR) spectra were standardized using the reference signal of $CDCl_3$ with a chemical shift value (δ) of 7.26 ppm for the ^{1}H NMR and 77.16 ppm for the ^{13}C NMR, respectively. The precision of chemical changes is determined at a level of 0.01 ppm. The coupling constants (*J*) are displayed with a precision of 0.1 and denoted in units of hertz (Hz). The spin multiplicity observed in the 1H- nuclear magnetic resonance (NMR) spectroscopy was represented using the following abbreviations: s for singlet, d for doublet, t for triplet, q for quartet, dd for doublet of doublets, dt for doublet of triplets, td for triplet of doublets, and m for multiplet. MestreNova v. 14.1.1 (Mestrelab Research S.L.) was used for processing the spectra. High-Resolution Mass Spectrometry analyses have been performed in the Laboratory for Biological Mass Spectrometry–Isabel Moura (PROTEOMASS Scientific Society Facility), using UHR ESI-Qq-TOF IMPACT HD (Bruker-Daltonics, Bremen, Germany). Samples of the corresponding compounds were prepared by dissolution in 50 % (v/v) Acetonitrile containing 0.1 % (v/v) aqueous formic acid to obtain a working solution of 0.1 μg/mL. Mass spectrometry analysis was carried out by the direct infusion of the compound solutions into the ESI source. MS data were acquired in positive polarity over the mass range of 80–1300 m/z. (Capillary voltage: 4500 V, End plate offset: −500 V, Charging voltage: 2000 V, Corona: 4000 nA, Nebulizer gas: 0.4 Bar, Dry Heater: 180 °C, Dry gas: 4.0 L/min).

UV–Vis absorption spectra were recorded on a JASCO V-650 spectrophotometer and the fluorescence emission spectrum on a HORIBA Scientific FLUOROMAX-4 spectrofluorometer from BIOSCOPE-PROTEOMASS facilities. Otherwise stated, all photophysical experiments were carried out at 293 K using a quartz cell with 10 mm of optical path.

2.3. Synthetic procedures

2.3.1. General procedure (GP) for the synthesis of L1 and L2

Cyclic tetramine (1.0 eq. of **2** or **3**) and dry DIPEA (8.0 eq.) were dissolved in 50 mL dry DCM, and the formed clear solution was cooled down to 5 °C with ice-water. Dansyl chloride (4.5 eq.) was added in one portion and stirring was maintained for 30 min at this temperature. Subsequently, the reaction mixture was stirred for 4 days at r.t. The reaction outcome was monitored by TLC (mobile phase - DCM:MTBE = 100:1 v/v). Workup: the reaction mixture was diluted with DCM and washed consequently with aq. citric acid (x1), aq. K_2CO_3 (x1) and distilled water (x1). The organic phase was dried over anhydr. Na_2SO_4 and the solvent was evaporated to dryness. The crude product was purified by silica gel column chromatography affording compounds **L1** or **L2**, respectively.

2.3.2. Data for 5,5′,5″,5‴-(1,4,7,10-tetraazacyclododecane-1,4,7,10-tetrasulfonyl)tetrakis(N,N-dimethylnaphthalen-1-amine) (L1)

This compound was prepared according to the general synthetic procedure described above using cyclen (**2**) (1.00 mmol, 0.172 g, 1 eq.), DIPEA (8.00 mmol, 1.39 mL, 1.39 mL) and dansyl chloride (4.50 mmol, 1.214 g, 4.5 eq.) (**1**). Column chromatography: stationary phase - 75 g silica gel; Mobile phase - DCM:MTBE = 75:1v/v. The target product **L1** was obtained in 0.984 g (89 %) as a light-yellow powder. m.p. 178–179 °C. ^{1}H NMR (600 MHz, $CDCl_3$) δ 8.57 (d, *J* = 8.5 Hz, 4H), 8.49

(d, J = 8.7 Hz, 4H), 8.01 (dd, J = 7.4, 1.2 Hz, 4H), 7.53 (td, J = 9.0, 7.5 Hz, 8H), 7.18 (d, J = 7.1 Hz, 1H), 3.67 (s, 16H), 2.89 (s, 24H). ^{13}C NMR (151 MHz, $CDCl_3$) δ 151.83, 133.19, 130.79, 130.74, 130.44, 129.63, 128.57, 123.35, 119.82, 115.50, 51.34, 45.56, 0.14. ESI-MS: $[M+H]^+$ for $C_{56}H_{64}N_8O_8S_4$ = 1105.3758 m/z (−4 ppm), calculated $[M+H]^+$ for $C_{56}H_{64}N_8O_8S_4$ = 1105.3803 m/z; $[M+2H]^+$ for $C_{56}H_{64}N_8O_8S_4$ = 533.1937 m/z (−0.1 ppm), calculated $[M+2H]^+$ for $C_{56}H_{64}N_8O_8S_4$ = 533.1938 m/z. EA Found C: 60,21; H: 5.95; N: 9.22 and S: 10.95 %. $C_{56}H_{64}N_8O_8S_4$ requires C: 60.85; H: 5.84; N: 10.14 and S: 11.60 %.

2.3.3. Data for 5,5′,5″,5‴-(1,4,8,11-tetraazacyclotetradecane-1,4,8,11-tetrasulfonyl)tetrakis(N,N-dimethylnaphthalen-1-amine) (L2)

L2 compound was prepared according to the general synthetic procedure described above, employing cyclam (1.00 mmol, 0.200 g, 1 eq.) (**3**), DIPEA (8.00 mmol, 1.39 mL, 1.39 ml) and dansyl chloride (4.50 mmol, 1.214 g, 4.5 eq.) (**1**). Column chromatography: stationary phase - 75 g silica gel; Mobile phase - DCM:MTBE = 25:1 v/v. The target product **L2** was obtained in 1.025 g (90 %) as a light-yellow powder. m.p. 227–228 °C. ^{1}H NMR (600 MHz, $CDCl_3$) δ 8.55 (d, J = 8.5 Hz, 4H), 8.33 (d, J = 8.7 Hz, 4H), 8.04 (dd, J = 7.3, 1.2 Hz, 4H), 7.52 (ddd, J = 8.5, 7.5, 1.2 Hz, 8H), 7.17 (d, J = 7.3 Hz, 4H), 3.37 (s, 8H), 3.31 (t, J = 7.0 Hz, 8H), 2.88 (s, 24H), 1.95 (p, J = 7.1 Hz, 4H). ^{13}C NMR (151 MHz, $CDCl_3$) δ 151.89, 133.62, 130.75, 130.33, 130.28, 129.91, 128.50, 123.35, 119.55, 115.48, 48.14, 47.21, 45.55, 27.65, 0.13. ESI-MS: $[M+H]^+$ for $C_{58}H_{68}N_8O_8S_4$ = 1133.4077 m/z (−3.4 ppm), calculated $[M+H]^+$ for $C_{58}H_{68}N_8O_8S_4$ = 1133.4116 m/z; $[M+2H]^+$ for $C_{58}H_{68}N_8O_8S_4$ = 567.2103 m/z (1.6 ppm), calculated $[M+2H]^+$ for $C_{58}H_{68}N_8O_8S_4$ = 567.2094 m/z. EA Found C: 61,13; H: 6.24; N: 9.67 and S: 11.30. $C_{58}H_{68}N_8O_8S_4$ requires C: 61.46; H: 6.05; N: 9.89 and S: 11.32 %.

2.4. Spectrophotometric and spectrofluorimetric measurements

2.4.1. Photophysical characterization and titrations

Photophysical measurements began with the preparation of stock solutions of compounds **L1** and **L2** (*ca.* 10^{-3} M) in various solvents (CH_3CN, DMSO, $CHCl_3$, and THF), by dissolving each ligand in a 10 mL volumetric flask and diluting with the corresponding solvent. The working solutions in the range of $10^{-5} - 10^{-6}$ M were then prepared by dilution of the stock solutions.

Titrations of **L1** and **L2** were performed by successive additions of microliter aliquots of standard solutions of Ca^{2+}, Co^{2+}, Ni^{2+}, Cu^{2+}, Zn^{2+}, Ag^{+}, Cd^{2+}, Hg^{2+} ions prepared in acetonitrile. A correction for the absorbed light was performed when necessary. The temperature dependent emission spectra were recorded by encapsulating the material between quartz plates, and over a hotplate with temperature control for measurements at variable temperature. Additionally, mixtures containing different water fractions (f_w), (f_w = 0 %, 17 %, 33 %, 55 %, 67 % and 83 %) with a final concentration of 10 μM were prepared and characterized by absorption and emission spectroscopy. Luminescence spectra of the compounds in the solid state and of doped polymer thin films were recorded using a fiber-optics device connected to the spectrofluorometer while exciting the samples at appropriated wavelength.

2.4.2. Fluorescence quantum yield and lifetime

The evaluation of the relative photoluminescence quantum yields was performed by preparing a solution of dansylamide in DMSO (ϕ_F = 0.47) as reference standard for quantifying the relative QY of **L1** and **L2** in all studied solvents [46]. Lifetime measurements were recorded on a Tempro Fluorescence Lifetime System with a Horiba Jobin-Yvon NanoLed pulsed diode controller. All measurements were carried out at 293 K.

2.5. Determination of the detection and quantification limits (LOD and LOQ)

Determination of the detection limit (LOD) and quantification limit (LOQ) began by collecting ten independent measurements of a solution containing the selected probe and no addition of any metal ion (y_{blank}). Final determination of the LOD and LOQ values followed the subsequent formulas [47,48].

LOD = $y_{dl} = y_{blank} + 3std$, where y_{dl} = signal detection limit and std = standard deviation.

LOQ = $y_{dl} = y_{blank} + 10std$, where y_{dl} = signal detection limit and std = standard deviation.

The final step involved the determination of the minimal detectable and quantified concentration of metal ion by titration with the ligands.

2.6. Preparation of polymer dye-doped thin films

- **KURARITY** L44285 **film**

Production began by weighting 100 mg of polymer in a vial and was dissolved in 5 mL of chloroform whereas 1 mg of the compound (**L1** or **L2**) was weighted in a separate vial and dissolved in 1 mL of chloroform. Then, the polymer solution was stirred aided by heating at 70 °C and when the polymer was completely dissolved, the compound solution was added, and they were mixed.

- **IROGRAN A 92 P 4637**

TPU's solution was prepared by weighting 100 mg of this polymeric material in a vial and in another vial was weighed 1 mg of the compound. The amount of TPU weighted was dissolved in 10 mL of THF over stirring at room temperature until it was totally dissolved. The dye solution was prepared in THF for **L1**-2 and then added to the polymer solution.

The resulting solution from the mixture of the compound solution and the polymer solution was poured into a perfluoro alkoxy alkane, PFA, support with 5 cm of diameter and left it to slow evaporation at room temperature during *ca.* 24h.

3. Results and discussion

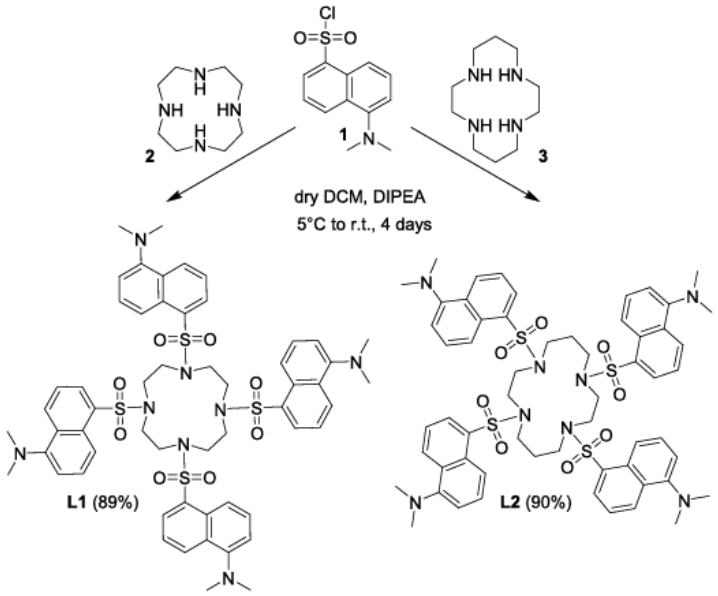
3.1. Synthesis

The synthesis of both compounds **L1** and **L2** was accomplished under classical conditions for the preparation of sulfonamides from amines and sulphochlorides (Scheme 1). Both cyclen (**2**) and cyclam (**3**) were dissolved in dry DCM and reacted with an excess of dansyl chloride (**1**) in the presence of dry DIPEA. Analytical samples of **L1** and **L2** were obtained after column chromatography on silica gel and were fully characterized by 1D and 2D-NMR spectroscopic techniques, HRMS and melting point temperatures.

3.2. Photophysical characterization

The tetradansylated derived compounds of cyclen and cyclam exhibit photoluminescent properties both in solution and in the solid state. Fig. 2 shows the molecular representation side by side with photophysical data of compound **L1** and **L2** in chloroform recorded at 293 K as a representative example (Figs. S5–S6) while the data in all solvents are summarized in Table 2.

Considering the UV–Vis spectra, **L1** and **L2**, show a maximum at *ca.* 344 nm which is assigned to the π - π* transition of dansyl chromophore contributing to the absence of any colour visible to the naked eye. Upon excitation at the appropriate wavelength, the samples emit a greenish light with a maximum centered around 502 nm and 499 nm, characteristic for the dansyl moiety due to the intramolecular charge-transfer



Scheme 1. Synthetic approach to the preparation of the target compounds **L1** and **L2**.

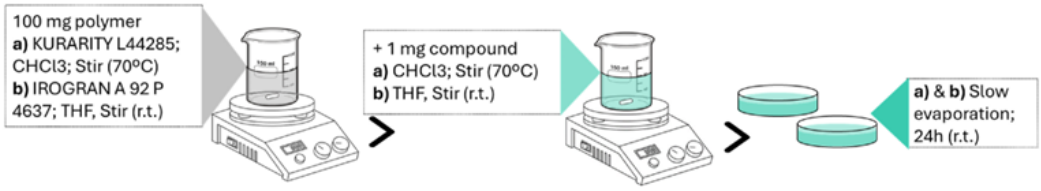


Fig. 1. The method of synthesis of a) KURARITY L44285 and b) IROGRAN 4 92 P 4637 films.

(ICT) band between the N,N′-dimethylamine (donor) and the sulfonamide (acceptor) functions, resulting in a Stokes shift of 9149 and 9029 cm^{-1}. On a relatable note, significant disparities can be noted regarding the solid-state emission spectra on both compounds where a wide band centered at 508 nm is recorded for **L1** much similar to the one in chloroform solution, while for **L2**, a clear, blue-shifted emission is evident accompanied by an emission maximum at 487 nm.

The fluorescence quantum yield has been determined using dansyl amide as a standard for both dansyl derivatives. Significantly higher values of 35 % and 41 % have been attained for **L1** and **L2** in chloroform, while for the remaining solvents, values were in the range of 24–34 %. Double digit nanosecond times were observed from time-resolved fluorescence decay curves for all solvents sitting in the range of 12.4–15.2 ns, however, no relevant association can be determined between the characteristics of the solvent and compounds studied.

However, the presence of a solvent environment significantly affects the stabilization of the ligand's excited state due to the alteration of the fluorophore's dipole moment. Based on the information presented in Table 1, the increase in solvent polarity is accompanied by an increase of the energy gap and, consequently, an increase in Stoke's shift, which translate into a bathochromic shift. The shift presented can be related to a positive solvatofluorochromic effect due to the capacity of the environment-sensitive dyes to change their fluorescence maximum wavelength aligned with the solvent polarity, behaviour well noticed in Fig. 2.

Aligned with these observations, efforts have been made to thoroughly characterize the interactions between the solvent and the compound. To achieve this, three solute-dependent parameters (υ_0, a, b and p) have been determined through the multiparametric fitting of the Kamlet-Taft equation (Equation (1)).

$$\upsilon = \upsilon_0 + a\alpha + b\beta + p\pi^* \quad \text{(Equation 1)}$$

Where υ_0 represents the wavenumber value in a reference solvent; parameters a, b and p are obtained through multiple regression analysis that reflect the underlying sensitivity of the probes photophysical behaviour to solvent polarity; α: hydrogen bond donor acidity (HBD); β: hydrogen bond acceptor basicity (HBA); π*: stabilization of a charge or dipole without a specific dielectric interaction (Table 1) [49,50].

Table 3 presents the reference wavenumber value υ_0, the fitted parameters (a, b and p) alongside the slopes and correlation coefficients obtained through the fitting of a linear plot of $\upsilon_{exp.}$ versus υ_{calc}, by applying the Kamler-Taft model. It is perceptible for both compounds extended negative values of a and b parameters, where some relevant differences are present in the predisposition towards hydrogen bond donor sensitivity being **L2** more slightly prone to be influenced by protic

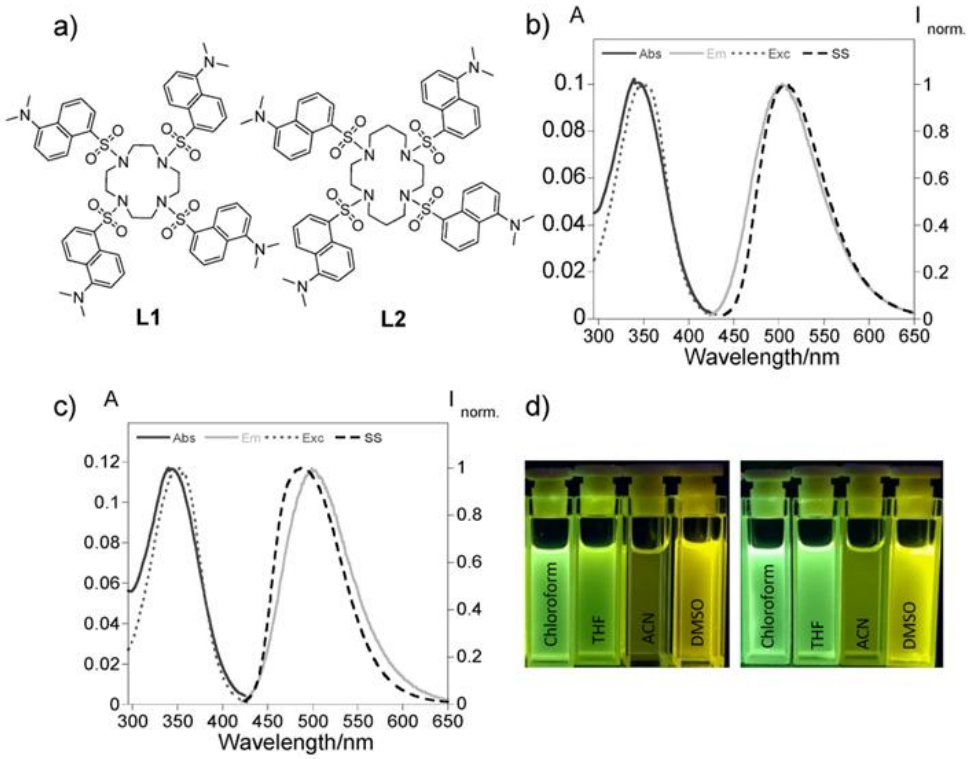


Fig. 2. (a) Molecular structure of tetradansylated cyclen and cyclam derived compounds **L1** and **L2**. Photophysical characterization of derivatives **L1** (b) and **L2** (c) in chloroform ([**L1**] = [**L2**] = 5 μM). Images under UV light for (d) **L1** (left) and **L2** (right) in different solvents.

Table 1
Spectroscopic polarity parameters, physical properties of the different solvents. ε_r: relative permittivity; η: refractive index; α: the solvent's HBD acidity; β: the solvent's HBA basicity; π*: the solvent's dipolarity/polarizability.

Solvent	ε_r	α	β	π*	η
DMSO	47.24	0	0.76	1.00	1.47
ACN	35.94	0.19	0.40	0.66	1.34
THF	7.58	0	0.55	0.58	1.40
$CHCl_3$	4.89	0.20	0.10	0.69	1.44

solvents. Finally, large negative p value observed for **L2** indicate a more instability towards highly polarizable solvents presumably due to the increase in size with less rigidity due to the introduction of two carbons in the macrocycle.

3.3. Exploring the behavior in aqueous media

Solutions with different ratios of water in THF were prepared and measured by absorption and fluorescence emission spectroscopy in

Table 3
Independent fluorescence wavenumber ($\upsilon 0$), solvent polarity (p), HBD (a), HBA (b), slope and coefficient (R^2) of the linear fitting plot $\upsilon_{exp.}$ versus $\upsilon_{calc.}$

	υ_0	a	b	p	Slope	R^2
L1	21795	−6245	−3399	−415	1.00	1
L2	22197	−6548	−3357	−741	1.00	1

Table 2
Absorption maximum wavelength in solution (λ_{abs}), emission maximum wavelength in solution (λ_{em}), molar absorption coefficients (ε), Stokes shift ($\Delta\lambda$), fluorescence quantum yields (ϕ), emission maximum in the solid state (λ_{em}^{Solid}), brightness (ε x ϕ), fluorescence lifetimes (τ) for compounds **L1** and **L2** in various solvents.

Cpd.	Solv.	λ_{abs} [nm]	λ_{em} [nm]	ε (10^4) [cm^{-1} M^{-1}]	Stokes shift [cm^{-1}]	ϕ (%)	λ_{em}^{Solid} [nm]	(ε x ϕ) (10^3) [cm^{-1} M^{-1}]	τ[ns]
L1	DMSO	347	532	2.23	10021	28	508	6.24	13.6
	CH_3CN	344	527	2.38	10094	24		5.71	12.4
	THF	340	508	2.25	9726	30		6.75	15.1
	$CHCl_3$	344	502	2.01	9149	35		7.04	14.8
L2	DMSO	345	529	1.95	10081	34	487	6.63	15.2
	CH_3CN	342	523	2.26	10119	28		6.33	13.4
	THF	340	502	2.09	9491	27		5.64	13.9
	$CHCl_3$	344	499	2.33	9029	41		7.04	15.2

order to evaluate the optical properties of the ligands when exposed to water. Fig. 3 shows that the increase of water content is responsible for a decrease in the emission intensity to 67 % following a bathochromic shift, while at 83 % of water content, an increase on luminescence intensity (ca. 40 %) is evident without a shift when comparing to the initial solution. This increase of emission intensity with water fraction of 83 % translates on a fluorescence quantum yield values increase (φL1 = 49,7 %; φL2 = 50,4 %) than in the absence of water (φL1 = 30 %; φL2 = 27 %), which suggest an aggregation induced emission (AIE) effect, i.e., when in the vast majority of water medium, the ligand molecules tend to aggregate and restrict the intramolecular rotation blocking the non-radiative relaxation [51,52]. While in the presence of 67 % of water, both ligands reveal some solubility issues as shown in Fig. 3, where some precipitate is observed which contributes also to the decrease of the emission signal and clarifies the decrease in the absorption profile.

Initially, when the water content is increased, there is a notable rise in the baseline as seen in the absorption spectra of the solution containing 83 % water. The observed rise in the absorbance measurement can be attributed to a light scattering artifact caused by the presence of aggregates, which adds to the inherent heterogeneity. Through dynamic light scattering, the solutions were measured resulting on different polydispersity index, PDI_{L1} = 0,127; PDI_{L2} = 0.049 with hydrodynamic sizes of 134 ± 3 nm (**L1**) and 98 ± 1 nm (**L2**), and zeta potential of −18 ± 1 mV (**L1**) and −22 ± 2 mV (**L2**). The PDI obtained reflect the presence of monodisperse aggregates for the two compounds, with slightly differences on the size and zeta potential due to the molecular organization in aggregates.

3.4. Metal ions sensing

Considering the possible use of dansyl derivatives for detecting metal ions, we evaluated the capacity of **L1** and **L2** to sense metal ions, including, Ca^{2+}, Co^{2+}, Ni^{2+}, Cu^{2+}, Zn^{2+}, Ag^{+}, Cd^{2+}, Hg^{2+}, which were evaluated in acetonitrile. Fig. 4 illustrates the impact on the emission

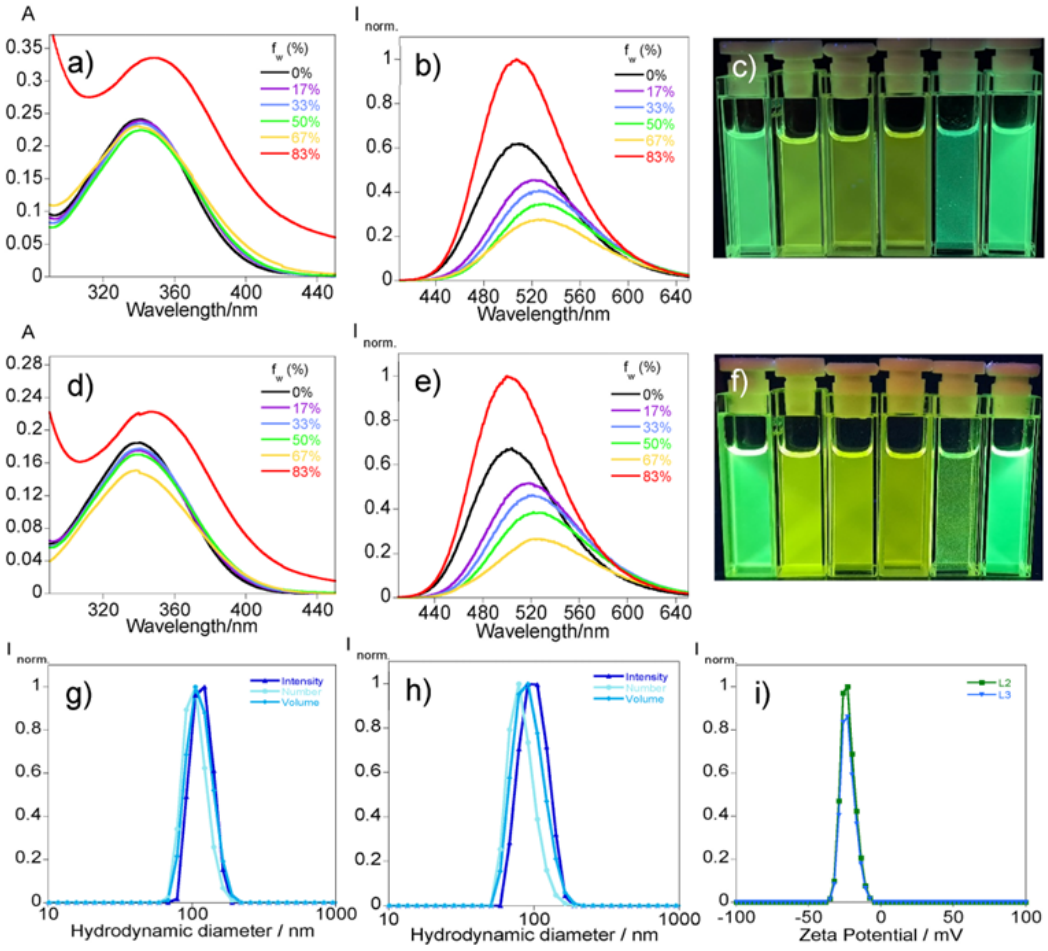


Fig. 3. Absorption (a,d) and emission spectra (b,e) of **L1** (a,b) and **L2** (d,e) in THF with different water fractions f_w (0 %, 17 %, 33 %, 55 %, 67 %, 83 %), [**L1**] = [**L2**] = 10 μM. Images of **L1** (c) and **L2** (f) in THF with different water fractions. Hydrodynamic diameter of **L1** (g) and **L2** (h) aggregates according to number, volume, and intensity distributions and zeta potential (i) of a solution of THF/water with f_w = 83 %.

intensity when 1, 5, and 10 equivalents of the aforementioned metal ions are added. It is evident that the absorption and emission spectra only exhibited significant spectrum alterations in the presence of mercury(II) and copper(II) ions. By adding only 1 equivalent of both metal ions, the emission signal is significantly reduced. Subsequently, adding 5 equivalents completely suppresses the fluorescence intensity. Thus, both compounds exhibit strong selectivity for the specified metal ions.

Thereby, Fig. 5 displays the titrations of **L1** and **L2**, in acetonitrile, upon successive addition of Cu^{2+} (a, c) and Hg^{2+} (b, d) microliter aliquots, respectively, conducted through spectrophoto- and spectrofluorimetric devices.

The progressive addition of Cu^{2+} ions results, generally, in a decrease on both the absorption and the emission spectra. The absorption spectra display a decrease of the main band centered at 345 nm and 342 nm for **L1** and **L2**, respectively. A remarkable decrease in luminescence intensity is also observed without noticing any particular shift of the maxima (530 nm and 522 nm for **L1** and **L2**, respectively). Copper ion is a paramagnetic transition metal with an unfilled d orbital that can induce mechanisms like electron transfer or energy transfer caused quenching, consequently, the quenching in luminescence is observed.

Similarly, as Hg^{2+} solution is gradually added, a decrease is noted on the main absorption band at 344 nm without any shift. Looking to the spectrofluorimetric data, at 525 nm for **L1**, a quenching of the emission's intensity occurs, causing an almost complete suppression upon added 2 equivalents of the metal ion and, consequently, the formation of a plateau. Attending to Fig. 5 (c and d), an analogous behaviour is verified for **L2**. Hg^{2+} ions exhibit diamagnetic properties with a d^{10} configuration and large atomic number, in that case, the formation of heavy atom complexes can lead to non-radiative deactivation explaining the observations.

Therefore, considering that in the presence of Cu^{2+} and Hg^{2+}, both ligands show an absorption and a fluorescence decay, while a chelation enhanced quenching effect (CHEQ) phenomenon is suggested, where **L1** and **L2** coordinate to the metal ion resulting in the corresponding complexes evidenced by Fig. 6 [53–61].

In order to completely assess the sensing ability towards Hg^{2+} and Cu^{2+}, the HypSpec software [62] was used for the calculation of the interaction constants of all complexes. Furthermore, the determination of the detection and quantification limit parameters of both compounds towards both has been fulfilled. The association constants, LOD and LOQ are included in Table 4.

The stability constants were evaluated based on the stoichiometry 1:1 (L:M) by keeping in mind the complex centers evidenced by the ligand structures. The stability constants values for **L1** and **L2** towards both metal ions clarify the high affinity between both species being the highest constant found for **L2** towards Cu^{2+} with a value of $LogK_{ass.} = 5.870 \pm 0.003$. Thus, detectable differences rise while considering the two macrocycles specially for Cu^{2+} sensing in the observed values since the presence of two more carbons provide the flexibility to better accommodate the metal ion.

The lowest detectable and quantifiable amounts were determined for **L2** (2.0 μM and 3.0 μM), having the potential to be useful in applications such as environmental monitoring, where the presence of Hg^{2+} needs to be detected and quantified at low concentrations.

3.5. Designing Temperature-Responsive materials using dansyl derivative emission

Since **L1** and **L2** have shown solid-state emission and exhibit solvatofluorochromism due to the varying properties of different solvents,

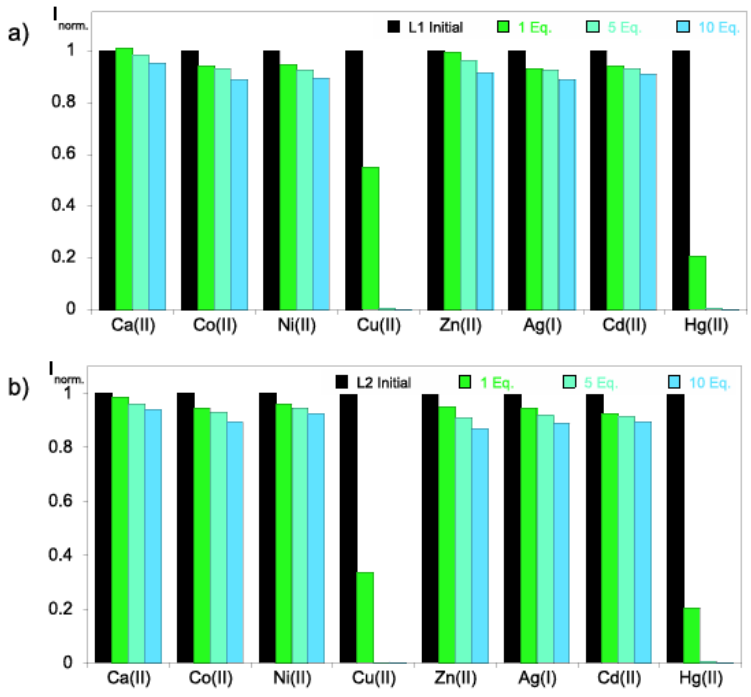


Fig. 4. Normalized emission intensity of **L1** (a) and **L2** (b) upon addition of 1, 5, and 10 equivalents of Ca^{2+}, Co^{2+}, Ni^{2+}, Cu^{2+}, Zn^{2+}, Ag^{+}, Cd^{2+}, and Hg^{2+} metal ions in acetonitrile. ([**L1**] = [**L2**] = 5 μM, T = 298K).

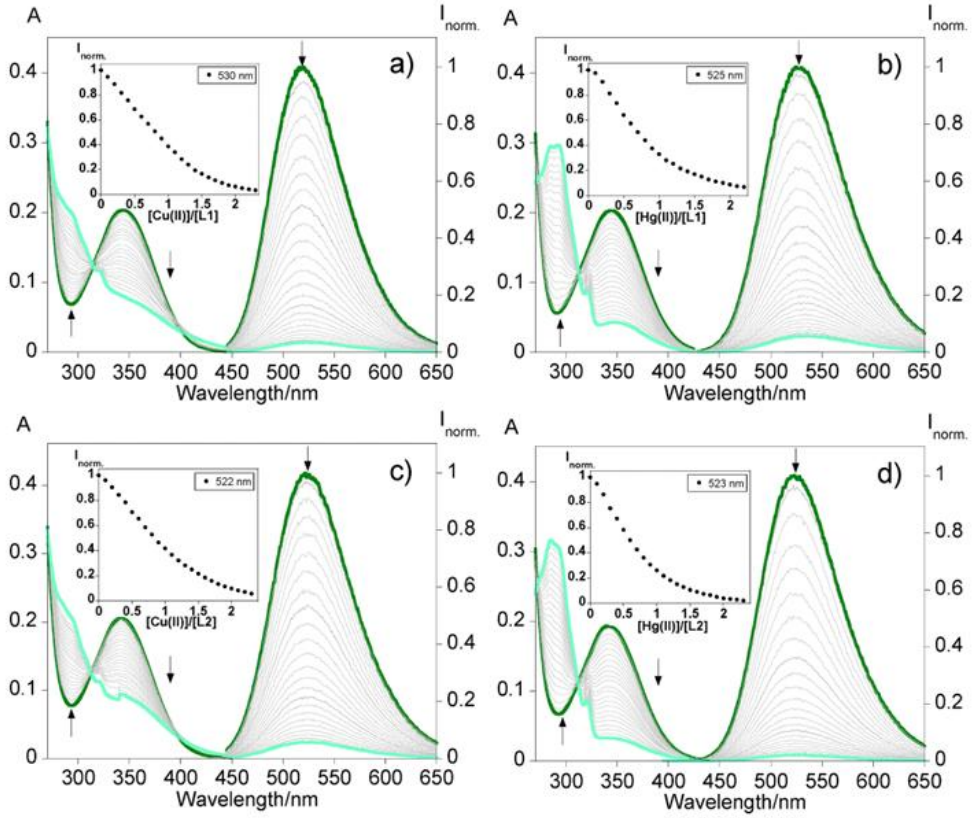


Fig. 5. Spectrophotometric and spectrofluorimetric titrations of compounds **L1** (a, b) and **L2** (c, d) with increased additions of Cu^{2+} (a, c), and Hg^{2+} (b, d) in CH_3CN. The inset represents the emission (a–d) as a function of $[Cu^{2+}]/[\mathbf{L1}]$ at 530 nm (a), of $[Cu^{2+}]/[\mathbf{L2}]$ at 525 nm (c), of $[Hg^{2+}]/[\mathbf{L1}]$ at 525 nm (b) and of $[Hg^{2+}]/[\mathbf{L2}]$ at 523 nm (d). $[\mathbf{L1}] = [\mathbf{L2}] = 5\ \mu M$, T = 298 K).

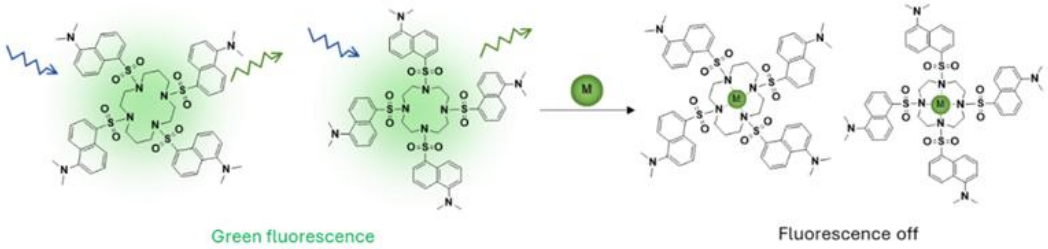


Fig. 6. General representation of the chelation enhanced quenching effect after complexation with Cu^{2+} and Hg^{2+} metal ions.

the next step is to modulate the emission of these ligands in solid-supported materials to develop molecular thermometers based on their emission properties. Initially, these compounds have been studied without the use of solid supports. To this end, the emission of each probe was recorded as the temperature increased in the solid state. Fig. 7 presents the emission spectra and the plot of I_{norm} versus temperature for compound both compounds. While heating, both compounds display a quenching in the fluorescence emission, linear at certain ranges, in the case of **L1**, with no visible shift with respect to the maxima band. Between ca. 40 °C–110 °C a linear behaviour is evident, therefore, within this range, this ligand can function as a probe in optical sensing due to its photochemical stability. However, around 120 °C, a sudden decrease in intensity was observed compromising the recovery of luminescence (only *ca.* 20 %, Fig. S7). The decrease in the fluorescence intensity with

Table 4
Association constants using HypSpec software for compounds **L1** and **L2** towards Hg^{2+} and Cu^{2+} ions with included stoichiometry in acetonitrile. Respective values for the detection limit (LOD) and quantification limit (LOQ) amounts (μM) were measured by the emission at 509 and 513 nm for **L1** and **L2**, respectively.

Compounds	Metal (M)	Association constants ($LogK_{ass.}$), L:M	LOD (μM)	LOQ (μM)
L1	Cu^{2+}	5.613 ± 0.002	2.9	3.4
	Hg^{2+}	5.104 ± 0.002	3.5	3.8
L2	Cu^{2+}	5.870 ± 0.003	2.8	4.4
	Hg^{2+}	5.047 ± 0.002	2.0	3.0

increasing temperature is caused by the loss of intermolecular interactions that leads to the melting point observed at 178 °C in the case of **L1**.

In another way, **L2** can maintain a steady emission and there is no observation of a sharp quenching on the fluorescence intensity until 200 °C due to the higher melting point observed for this compound at 227 °C, characteristic that provides the recovery of *ca.* 90 % of the emission (Fig. S7).

Building on previous findings, several doped polymer thin films have been developed to enhance sensing applications. Following the synthesis procedure of Fig. 1, compounds **L1** and **L2** were doped into Kurarity and TPU. Fig. 8 compares the emission spectra of these compounds in their solid state with their emission in the various polymer thin films.

In summary, polymer thin films were effectively created, and their emission characteristics were examined. Fig. 8 clearly shows that the Kurarity of the polymer matrix can adjust the final emission of the film by interacting with the probe, causing a blue shift in the emission to 480 nm for both compounds. On another hand, the Irogran films maintain the emission maximum wavelength observed in the solid state. Similar behaviours have been observed in a previous work demonstrating the modulation of the emission using polymer matrix of dansyl derivatives [1].

Considering the previous results, the polymer-doped films were studied under varying temperatures to determine if the constraints found in the solid state for **L1** and **L2** could be mitigated. Fig. 9 presents the temperature dependent emission spectra of **L1** doped in both Kurarity and Irogran polymer matrixes as a representative example. The emission spectra for polymer-doped films of **L2** can be found in Fig. S8.

An attenuation of the emission is observed in both polymer-doped films as the temperature increases, up to a maximum of 200 °C. Intriguingly, the behavior of **L1** in its solid state, as influenced by its melting point, does not have an impact on the emission profile in Kurarity. In this case, the polymer matrix functions as a medium to maintain emission at higher temperatures by offering adequate conductivity, thereby reducing the thermally activated non-radiative processes displayed by the compounds and prevent the melting. During the temperature variation cycle, it is possible to perceive linearity from 40 °C to 200 °C and a recovering to 80 % of the initial fluorescence is observed after cooling. Regarding the Irogran doped material, it exhibited the

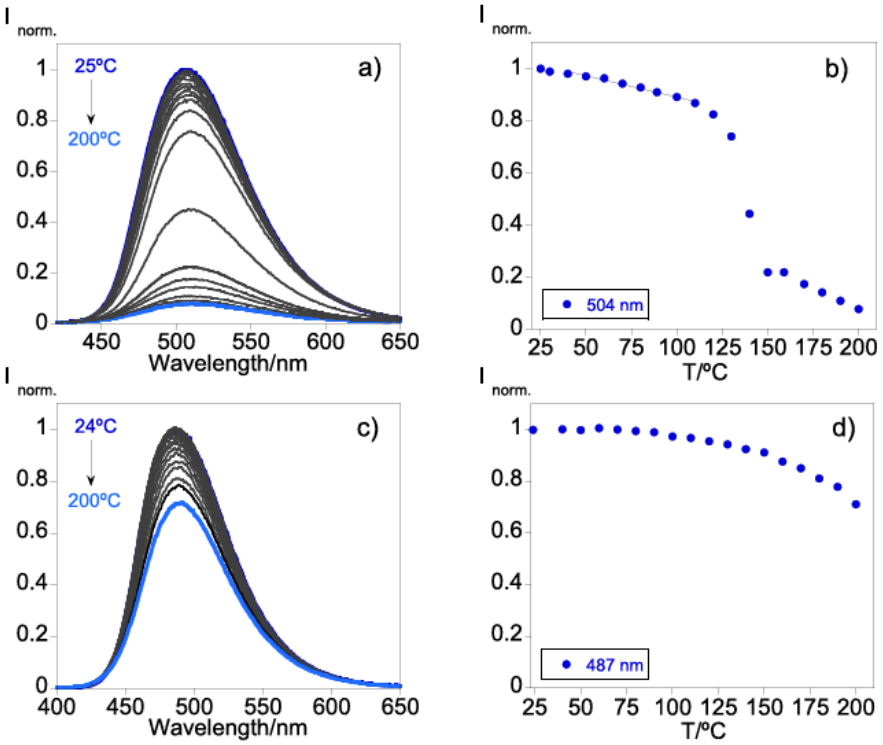


Fig. 7. Temperature-dependent emission spectra of **L1** in the solid state (a) collected through a warming cycle between 25 °C to 200 °C. $I_{norm.}$ vs. T plot recorded in the emission maximum at 504 nm upon heating (b) [40 to 110 °C (Y = 1.0529 - 0.0016231x), yielding R = 0.99139]. Temperature-dependent emission spectra of **L2** (d) collected through a warming cycle between 24 °C to 200 °C. $I_{norm.}$ vs. T plot recorded in the emission maximum at 487 nm upon heating (d).

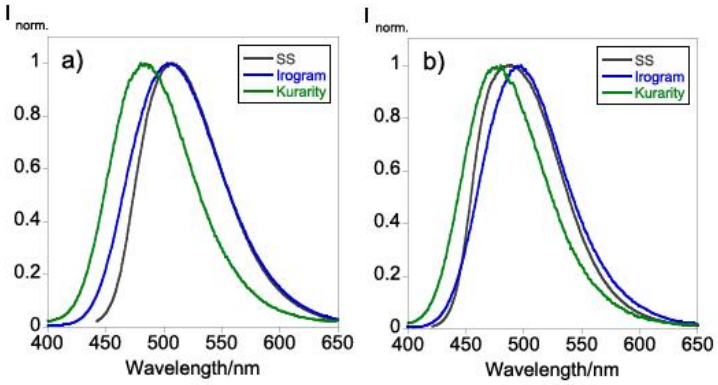


Fig. 8. Comparison between the emission spectra of the different polymer thin films doped with (a) L1 and (b) L2 and the respective emission spectrum in the solid state.

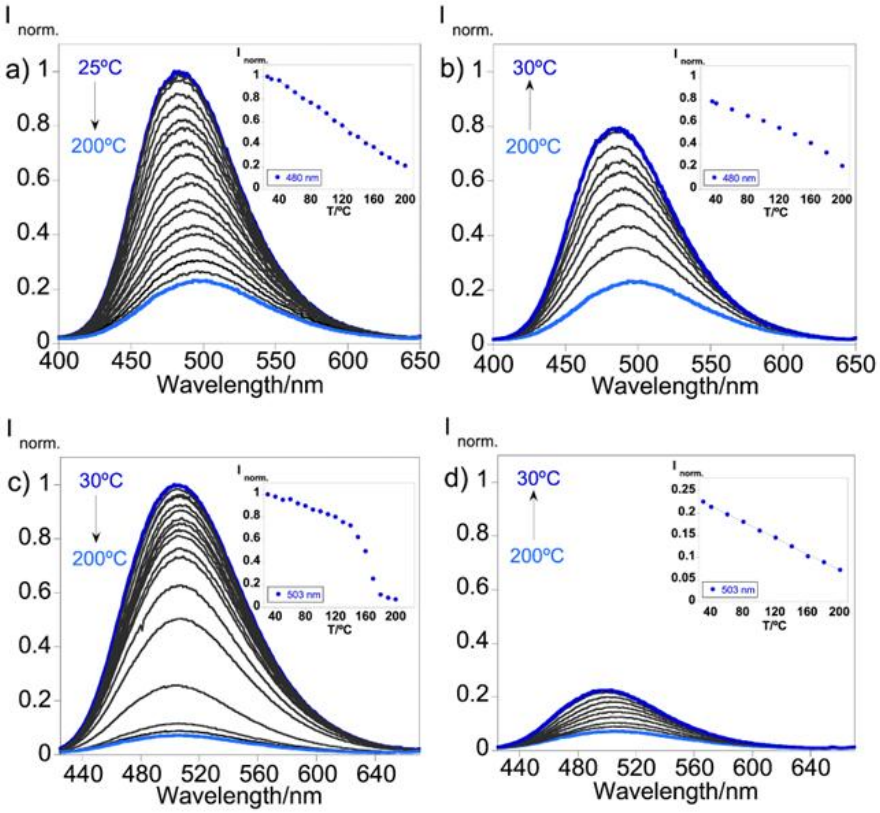


Fig. 9. Temperature-dependent emission spectra of **L1** doped in (a) Kurarity during heating cycle [Inset: $I_{norm.}$ vs. T plot at 480 nm upon heating: 40 to 200 °C (Y = 1.151 - 0.004844x), yielding R = 0.9975]; (b) Kurarity during cooling cycle [Inset: $I_{norm.}$ vs. T plot at 480 nm upon cooling]; (c) Irogran during heating cycle [Inset: $I_{norm.}$ vs. T plot at 503 nm upon heating: 60 to 120 °C (Y = 1.099 - 0.00251x), yielding R = 0.9916]; (d) Irogran during cooling cycle [Inset: $I_{norm.}$ vs. T plot at 503 nm upon cooling: 30 to 200 °C (Y = 0.2527 - 0.0009083x), yielding R = 0.9989].

same behavior as in its solid state, which hindered the restoration of the emission at the end of the cycle.

In the case of **L2** doped materials (Fig. S8) similar ranges of linearity have been found when doped in Kurarity with also almost complete recovery of the emission while for Irogran the fast quenching at 150 °C hampered the emission rise at 25 °C to reach past 25 %. These data show that by attaching the probe to a solid substrate, it can be used as a molecular thermometer without being limited by its physical properties.

4. Conclusions

Two fluorophores, based on tetradansylated cyclen and cyclam, were synthesized and their photoluminescent characteristics were investigated. Efforts were undertaken to study the photophysical features of dansyl compounds in various solvents to fully understand the impact of each solvent's intrinsic properties on the emission of the probes, considering that dansyl compounds commonly display solvatofluorochromism. Implementation of the Kamlet-Taft equation expressed in detail the solute-solvent interactions with a positive solvatofluorochromism behaviour is present for both compounds. Furthermore, the compounds were found to modulate their emission in the presence of water expressing aggregation induced emission at high water content that was confirmed by dynamic light scattering experiments with hydrodynamic sizes of 134 ± 3 nm (**L1**) and 98 ± 1 nm (**L2**). From an environmental remediation perspective, **L1** and **L2** were found to quench their emission in the presence of Hg^{2+} and Cu^{2+} ions. Mononuclear species were proposed with Cu^{2+} and Hg^{2+} and that **L2** has the highest association constant with Cu^{2+} (Log $K_{ass.}$ = 5.87) while the lowest LOD and LOQ was found for Hg^{2+} of 2 μM and 3 μM, respectively. Finally, the probes were characterized in the solid state and incorporated into solid supports to develop molecular thermometers. Polymers such as Kurarity and TPU were doped with the compounds, and their luminescence properties were studied. The polymer matrix Kurarity was discovered to regulate the emission maxima for both compounds. The probes demonstrated excellent linearity throughout the heating cycle, rendering them highly appropriate for utilization as temperature sensors in industrial applications.

Funding

This work received support from PT national funds (FCT/MCTES, *Fundação para a Ciência e Tecnologia* and *Ministério da Ciência, Tecnologia e Ensino Superior)* through the projects UIDB/50006/2020 and UIDP/50006/2020. This work received support from PROTEOMASS Scientific Society through the General Funding Grant 2022–2023, and the projects #PM001/2019 and #PM003/2016. This work is also developed and acknowledged by A.K. as part of contract №: BG-RRP-2.004-0002-C01, Laboratory of Organic Functional Materials (Project BiOrgaMCT), Procedure BG-RRP-2.004 „Establishing of a network of research higher education institutions in Bulgaria ", funded by BULGARIAN NATIONAL RECOVERY AND RESILIENCE PLAN".

CRediT authorship contribution statement

Inès Pereira-Gomes: Writing – review & editing, Validation, Software, Investigation, Formal analysis, Data curation. **Frederico Duarte:** Writing – review & editing, Writing – original draft, Visualization, Validation, Software, Methodology, Investigation, Formal analysis, Data curation. **Georgi M. Dobrikov:** Writing – review & editing, Visualization, Validation, Resources, Investigation, Funding acquisition, Data curation. **Ivaylo Slavchev:** Writing – review & editing, Validation, Investigation. **Atanas Kurutos:** Writing – review & editing, Visualization, Validation, Resources, Methodology, Funding acquisition, Formal analysis, Conceptualization. **Jose Luis Capelo-Martinez:** Writing – review & editing, Writing – original draft, Visualization, Resources, Funding acquisition. **Hugo M. Santos:** Writing – review & editing, Writing – original draft, Visualization, Validation, Resources, Investigation, Formal analysis, Data curation. **Carlos Lodeiro:** Writing – review & editing, Writing – original draft, Validation, Supervision, Resources, Project administration, Funding acquisition, Formal analysis, Conceptualization.

Declaration of competing interest

The authors declare that they have no known competing financial interests or personal relationships that could have appeared to influence the work reported in this paper.

Data availability

Data will be made available on request.

Acknowledgements

This work was supported by the Associate Laboratory for Green Chemistry LAQV which is financed by national funds from *Fundação para a Ciência e Tecnologia and Ministério da Ciência, Tecnologia e Ensino Superior* (FCT/MCTES) through the projects UIDB/50006/2020 and UIDP/50006/2020. PROTEOMASS Scientific Society (Portugal) is acknowledged by the funding provided through the General Funding Grant 2022–2023, and by the funding provided to the Laboratory for Biological Mass Spectrometry Isabel Moura (#PM001/2019 and #PM003/2016). F.D. thanks to FCT/MCTES (Portugal) for his doctoral grant 2021.05161.BD. H. M. S. acknowledges the Associate Laboratory for Green Chemistry LAQV (LA/P/0008/2020) funded by FCT/MCTES for his research contract. The financial support by the Bulgarian National Science Fund (BNSF) under grant – "Novel styryl and polymethine fluorophores as potential theranostic agents "contract № КП-06-M59/1 from November 15, 2021 is gratefully acknowledged by A.K. This work is also developed and acknowledged by A.K. as part of contract №: BG-RRP-2.004-0002-C01, Laboratory of Organic Functional Materials (Project BiOrgaMCT), Procedure BG-RRP-2.004 „Establishing of a network of research higher education institutions in Bulgaria", funded by BULGARIAN NATIONAL RECOVERY AND RESILIENCE PLAN".

G. D. thanks to the European Regional Development Fund within the Operational Programme Science and Education for Smart Growth 2014–2020 under the Project Center of Excellence: National center of mechatronics and clean technologies - BG05M2OP001-1.001-0008 for the financial support.

Appendix A. Supplementary data

Supplementary data to this article can be found online at https://doi.org/10.1016/j.dyepig.2024.112461.

References

[1] Duarte F, Dobrikov G, Kurutos A, Capelo-Martinez JL, Santos HM, Oliveira E, Lodeiro C. Development of fluorochromic polymer doped materials as platforms for temperature sensing using three dansyl derivatives bearing a sulfur bridge. J Photochem Photobiol Chem 2023;445:115033. https://doi.org/10.1016/j.jphotochem.2023.115033.

[2] Jiang H, Li Z, Kang Y, Ding L, Qiao S, Jia S, Luo W, Liu W. A two-photon fluorescent probe for Cu^{2+} based on dansyl moiety and its application in bioimaging. Sensor Actuator B Chem 2017;242:112–7. https://doi.org/10.1016/j.snb.2016.11.033.

[3] Pisagatti I, Crisafulli D, Pappalardo A, Trusso Sfrazzetto G, Notti A, Nastasi F, Parisi MF, Micali N, Gattuso G, Villari V. Photoinduced electron transfer in host-guest interactions of a viologen derivative with a didansyl-pillar[5]arene. Mater Today Chem 2022;24:100841. https://doi.org/10.1016/j.mtchem.2022.100841.

[4] Duarte F, Dobrikov G, Kurutos A, Santos HM, Fernández-Lodeiro J, Capelo-Martinez JL, Oliveira E, Lodeiro C. Enhancing water sensing via aggregation-induced emission (AIE) and solvatofluorochromic studies using two new dansyl derivatives containing a disulfide bound: pollutant metal ions detection and preparation of water-soluble fluorescent polymeric particles. Dyes Pigments 2023;218:111428. https://doi.org/10.1016/j.dyepig.2023.111428.

[5] Aliberti A, Vaiano P, Caporale A, Consales M, Ruvo M, Cusano A. Fluorescent chemosensors for Hg^{2+} detection in aqueous environment. Sensor Actuator B Chem 2017;247:727–35. https://doi.org/10.1016/j.snb.2017.03.026.

[6] Wei P, Xiao L, Gou Y, He F, Zhou D, Liu Y, Xu B, Wang P, Zhou Y. Fluorescent "on–off–on" probe based on copper peptide backbone for specific detection of Cu (II) and hydrogen sulfide and its applications in cell imaging, real water samples and test strips. Microchem J 2022;182:107848. https://doi.org/10.1016/j.microc.2022.107848.

[7] Srivastava P, Verma M, Sivakumar S, Patra AK. *Sens Actuators B Chem*, A smart FRET probe exhibiting a molecular keypad lock device based on rapid detection of nitric oxide mediated by Cu^{2+} ion, vol. 291; 2019. p. 478–84. https://doi.org/10.1016/j.snb.2019.04.093.

[8] Cai H, Liang Y, Huang L, Wang J. Relay detection of Cu^{2+} and bovine serum albumin by a dansyl derivative-based fluorescent probe. Spectrochim Acta Mol Biomol Spectrosc 2022;277:121281. https://doi.org/10.1016/j.saa.2022.121281.

[9] Wang Y, Zhou J, Zhao L, Xu B. A dual-responsive and highly sensitive fluorescent probe for Cu^{2+} and pH based on a dansyl derivative. Dyes Pigments 2020;180:108513. https://doi.org/10.1016/j.dyepig.2020.108513.

[10] Liu Y, Jiang B, Zhao L, Zhao L, Wang Q, Wang C, Xu B. A dansyl-based fluorescent probe for sensing Cu^{2+} in aqueous solution. Spectrochim Acta Mol Biomol Spectrosc 2021;261:120009. https://doi.org/10.1016/j.saa.2021.120009.

[11] Wang P, Zhou D, Chen B. High selective and sensitive detection of Zn(II) using tetrapeptide-based dansyl fluorescent chemosensor and its application in cell imaging. Spectrochim Acta Mol Biomol Spectrosc 2018;204:735–42. https://doi.org/10.1016/j.saa.2018.07.001.

[12] Wang P, Wu J. Highly selective and sensitive detection of Zn(II) and Cu(II) ions using a novel peptide fluorescent probe by two different mechanisms and its application in live cell imaging. Spectrochim Acta Mol Biomol Spectrosc 2019;208:140–9. https://doi.org/10.1016/j.saa.2018.09.054.

[13] Su P, Zhu Z, Wang J, Cheng B, Wu W, Iqbal K, Tang Y. A biomolecule-based fluorescence chemosensor for sequential detection of Ag^{+} and H_2S in 100% aqueous solution and living cells. Sensor Actuator B Chem 2018;273:93–100. https://doi.org/10.1016/j.snb.2018.06.037.

[14] Wang P, Zhou D, Chen B. A fluorescent dansyl-based peptide probe for highly selective and sensitive detect Cd^{2+} ions and its application in living cell imaging. Spectrochim Acta Mol Biomol Spectrosc 2019;207:276–83. https://doi.org/10.1016/j.saa.2018.09.029.

[15] Yu S, Gao L, Li R, Fu C, Meng W, Wang L, Li L. Ultrasensitive mercury ion and biothiol detection based on Dansyl-His-Pro-Gly-Asp-NH_2 fluorescent sensor. Spectrochim Acta Mol Biomol Spectrosc 2021;250:119246. https://doi.org/10.1016/j.saa.2020.119246.

[16] Li Y, Ren Z, Ge Y, Di C, Zhou J, Wu J, Jia L. A novel peptide fluorescent probe based on different fluorescence responses for detection of mercury species and hydrogen sulfide. Microchem J 2023;184:108160. https://doi.org/10.1016/j.microc.2022.108160.

[17] Pang X, Dong J, Gao L, Wang L, Yu S, Kong J, Li L. Dansyl-peptide dual-functional fluorescent chemosensor for Hg^{2+} and biothiols. Dyes Pigments 2020;173:107888. https://doi.org/10.1016/j.dyepig.2019.107888.

[18] Wang P, An Y, Wu J. Highly sensitive turn-on detection of mercury(II) in aqueous solutions and live cells with a chemosensor based on tyrosine. Spectrochim Acta Mol Biomol Spectrosc 2020;230:118004. https://doi.org/10.1016/j.saa.2019.118004.

[19] Li CL, hsuan Lu P, Lin SY, Wu AT. A turn-on dansyl-based fluorescent chemosensor for the recognition of Pb^{2+}. J Photochem Photobiol Chem 2019;385:112088. https://doi.org/10.1016/j.jphotochem.2019.112088.

[20] Tosato M, Asti M, Dalla Tiezza M, Orian L, Häussinger D, Vogel R, Köster U, Jensen M, Andrighetto A, Pastore P, Di Marco V. Highly stable silver(I) complexes with cyclen-based ligands bearing sulfide arms: a step toward silver-111 labeled radiopharmaceuticals. Inorg Chem 2020;59:10907–19. https://doi.org/10.1021/acs.inorgchem.0c01405.

[21] Wang ZF, Zhou XF, Wei QC, Qin QP, Li JX, Tan MX, Zhang SH. Novel bifluorescent Zn(II)–cryptolepine–cyclen complexes trigger apoptosis induced by nuclear and mitochondrial DNA damage in cisplatin-resistant lung tumor cells. Eur J Med Chem 2022;238:114418. https://doi.org/10.1016/j.ejmech.2022.114418.

[22] Blahut J, Bernášek K, Gálisová A, Herynek V, Císařová I, Kotek J, Lang J, Matějková S, Hermann P. Paramagnetic ^{19}F relaxation enhancement in nickel(II) complexes of N-trifluoroethyl cyclam derivatives and cell labeling for ^{19}F MRI. Inorg Chem 2017;56:13337–48.

[23] Cheung TL, Tam LKB, Tam WS, Zhang L, Kai HY, Thor W, Wu Y, Lam PL, Yeung YH, Xie C, Chau HF, Lo WS, Zhang T, Wong KL. Facile peptide macrocyclization and multifunctionalization via cyclen installation. Small Methods 2024:2400006. https://doi.org/10.1002/smtd.202400006.

[24] Surender EM, Comby S, Martyn S, Cavanagh B, Lee TC, Brougham DF, Gunnlaugsson T. Cyclen lanthanide-based micellar structures for application as luminescent [Eu(III)] and magnetic [Gd(III)] resonance imaging (MRI) contrast agents. Chem Commun 2016;52:10858–61. https://doi.org/10.1039/C6CC03092K.

[25] Naher M, Su C, Harmer JR, Williams CM, Bernhardt PV. Macrocyclic copper(II) complexes as catalysts for electrochemically mediated atom TransfeR. Inorg Chem 2024;63:6453–64. https://doi.org/10.1021/acs.inorgchem.4c00311.

[26] Annunziata A, Esposito R, Gatto G, Cucciolito ME, Tuzi A, Macchioni A, Ruffo F. Iron(III) complexes with cross-bridged cyclams: synthesis and use in alcohol and water oxidation catalysis. Eur J Inorg Chem 2018;2018:3304–11.

[27] Ollier C, Méndez-Ardoy A, Ortega-Caballero F, Jiménez-Blanco JL, Le Bris N, Tripier R. Extending the scope of the *C*-functionalization of cyclam via copper(I)-Catalyzed alkyne–azide cycloaddition to bifunctional chelators of interest. J Org Chem 2024;89:5988–99. https://doi.org/10.1021/acs.joc.3c02854.

[28] Yu Y, Tan P, Huang X, Tao J, Liu Y, Zeng RJ, Chen M, Zhou S. Homogeneous activation of peroxymonosulfate using a low-dosage cross bridged cyclam manganese(II) complex for organic pollutant degradation via a nonradical pathway. J Hazard Mater 2020;394:122560. https://doi.org/10.1016/j.jhazmat.2020.122560.

[29] Wong JKH, Todd MH, Rutledge PJ. Recent advances in macrocyclic fluorescent probes for ion sensing. Molecules 2017;22:200. https://doi.org/10.3390/molecules22020200.

[30] Ozay H, Gungor Z, Yilmaz B, Ilgin P, Ozay O. Dual use of colorimetric sensor and selective copper removal from aqueous media with novel p(HEMA-co-TACYC) hydrogels: cyclen derivative as both monomer and crosslinker. J Hazard Mater 2020;389:121848. https://doi.org/10.1016/j.jhazmat.2019.121848.

[31] Fang X, Wang S, Wang Q, Gong J, Li L, Lu H, Xue P, Ren Z, Wang X. A highly selective and sensitive fluorescence probe based on BODIPY-cyclen for hydrogen sulfide detection in living cells and serum. Talanta 2024;268:125339. https://doi.org/10.1016/j.talanta.2023.125339.

[32] Tomczyk MD, Matczak K, Skonieczna M, Chulkin P, Denel-Bobrowska M, Różycka D, Rykowski S, Olejniczak AB, Walczak K. Synthesis and in vitro cytotoxic activity of dye-linker-macrocycle conjugates with variable linker length and components. Bioorg Chem 2023;140:106782. https://doi.org/10.1016/j.bioorg.2023.106782.

[33] Aoki S, Kawatani H, Goto T, Kimura E, Shiro M. A double-functionalized cyclen with carbamoyl and dansyl groups (cyclen = 1,4,7,10-tetraazacyclododecane): a selective fluorescent probe for Y^{3+} and La^{3+}. J Am Chem Soc 2001;123:1123–32. https://doi.org/10.1021/ja0033786.

[34] Lowe MP, Parker D. pH Switched sensitisation of europium(III) by a dansyl group. Inorg Chim Acta 2001;317:163–73. https://doi.org/10.1016/S0020-1693(01)00346-2.

[35] Siters KE, Fountain MA, Morrow JR. Selective binding of Zn^{2+} complexes to human telomeric G-quadruplex DNA. Inorg Chem 2014;53:11540–51. https://doi.org/10.1021/ic501484p.

[36] Del Mundo IMA, Siters KE, Fountain MA, Morrow JR. Structural basis for bifunctional zinc(II) macrocyclic complex recognition of thymine bulges in DNA. Inorg Chem 2012;51:5444–57. https://doi.org/10.1021/ic3004245.

[37] Kim JY, Sarkar S, Bobba KN, Huynh PT, Bhise A, Yoo J. Development of dansyl based copper(ii) complex to detect hydrogen sulfide in hypoxia. Org Biomol Chem 2019;17:7088–94. https://doi.org/10.1039/C9OB00948E.

[38] O'neil LL, Wiest O, Selective A. Noncovalent assay for base flipping in DNA. J Am Chem Soc 2005;127:16800–1. https://doi.org/10.1021/ja056274+.

[39] Rivas C, Stasiuk GJ, Sae-Heng M, Long NJ. Towards understanding the design of dual-modal MR/fluorescent probes to sense zinc ions. Dalton Trans 2015;44:4976–85. https://doi.org/10.1039/C4DT02981J.

[40] Yang L, Zhao J, Wang J, Han G, Liu B, Zhang W, Fu Y, Han MY, Wang Z, Zhang Z. An azacyclo-localizing fluorescent probe for the specific labeling of lysosome and autolysosome. Talanta 2020;216:120941. https://doi.org/10.1016/j.talanta.2020.120941.

[41] Xue G, Bradshaw JS, Song H, Bronson RT, Savage PB, Krakowiak KE, Izatt RM, Prodi L, Montalti M, Zaccheroni N. A convenient synthesis and preliminary photophysical study of novel fluoroionophores: macrocyclic polyamines containing two dansylamidoethyl side arms. Tetrahedron 2001;57:87–91. https://doi.org/10.1016/S0040-4020(00)00999-6.

[42] Fabbrizzi L, Foti F, Licchelli M, Maccarini PM, Sacchi D, Zema M. Light-emitting molecular machines: pH-induced intramolecular motions in a fluorescent nickel(II) scorpionate complex. Chem Eur J 2002;8:4965–72. https://doi.org/10.1002/1521-3765(20021104)8:21<4965::AID-CHEM4965>3.0.CO;2-X.

[43] Bergamini G, Sottilotta A, Maestri M, Ceroni P, Vögtle F. Cyclam-cored dendrimers appended with four dendrons of two different types: intradendrimer energy transfer. Chem Asian J 2010;5:1884–95. https://doi.org/10.1002/asia.201000170.

[44] Pillai ZS, Ceroni P, Kubeil M, Heldt JM, Stephan H, Bergamini G. Dendrimers as Nd^{3+} ligands: effect of generation on the efficiency of the sensitized lanthanide emission. Chem Asian J 2013;8:771–7. https://doi.org/10.1002/asia.201201065.

[45] Branchi B, Ceroni P, Bergamini G, Balzani V, Maestri M, Van Heyst J, Lee SK, Luppertz F, Vögtle F. A cyclam core dendrimer containing dansyl and oligoethylene glycol chains in the branches: protonation and metal coordination. Chem Eur J 2016;12:8926–34. https://doi.org/10.1002/chem.200601129.

[46] Montalti M, Credi A, Prodi Mg L, Montalti M, Credi A, Prodi LGM. Handbook of photochemistry. third ed. Boca Raton: Taylor & Francis; 2006. BOCA.

[47] Macdougall D, Crummett WB. Guidelines for data acquisition and data quality evaluation in environmental chemistry. Anal Chem 1980;52:2242–9. https://doi.org/10.1021/ac50064a004.

[48] Long GL, Winefordner JD. Limit of detection A closer look at the iupac definition. Anal Chem 1983;55:713A–24A. https://doi.org/10.1021/ac00258a724.

[49] Mocanu S, Ionita G, Matei I. Solvatochromic characteristics of dansyl molecular probes bearing alkyl diamine chains. Spectrochim Acta Part A Mol Biomol Spectrosc 2020;237:118413. https://doi.org/10.1016/j.saa.2020.118413.

[50] Oliveira E, Baptista RMF, Costa SPG, Raposo MMM, Lodeiro C. Solvatochromic Effects of bis(indolyl)thienylaril derivatives as new Colored Materials. Photochem Photobiol Sci 2014;13:492–8. https://doi.org/10.1039/C3PP50352F.

[51] Alam P, Leung NLC, Zhang J, Kwok RTK, Lam JWY, Tang BZ. AIE-based luminescence probes for metal ion detection. Coord Chem Rev 2021;429:213693. https://doi.org/10.1016/j.ccr.2020.213693.

[52] Wang H, Zhao E, Lam JWY, Tang BZ. AIE luminogens: emission brightened by aggregation. Mater Today 2015;18:365–77. https://doi.org/10.1016/j.mattod.2015.03.004.
[53] Koucký F, Kotek J, Císařová I, Havlíčková J, Kubíček V, Hermann P. Transition metal complexes of cyclam with two 2,2,2-trifluoroethylphosphinate pendant arms as probes for ^{19}F magnetic resonance imaging. Dalton Trans 2023;52:12208–23. https://doi.org/10.1039/D3DT01420G.
[54] Le Roy MM, Héry S, Saffon-Merceron N, Platas-Iglesias C, Troadec T, Tripier R. A phosphine oxide-functionalized cyclam as a specific, copper(II) chelator. Inorg Chem 2023;62:8112–22. https://doi.org/10.1021/acs.inorgchem.3c00329.
[55] Naher M, Su C, Harmer JR, Williams CM, Bernhardt PV. Macrocyclic copper(II) complexes as catalysts for electrochemically mediated atom transfer. Inorg Chem 2024;63:6453–64. https://doi.org/10.1021/acs.inorgchem.4c00311.
[56] Li X, Pan L, Yang F, Yang L. Blue carbon dot-based portable smartphone platform for visualization of copper(II). ACS Appl Nano Mater 2022;5:9252–9. https://doi.org/10.1021/acsanm.2c01595.
[57] Lelong E, Suh JM, Kim G, Esteban-Gómez D, Cordier M, Lim MH, Delgado R, Royal G, Platas-Iglesias C, Bernard H, Tripier R. Inorg Chem 2021;60:10857–72.
[58] Brown AM, Butman JL, Lengacher R, Vargo NP, Martin KE, Koller A, Śmiłowicz D, Boros E, Robinson JR. *N,N*-Alkylation clarifies the role of *N*- and *O*-protonated intermediates in cyclen-based ^{64}Cu radiopharmaceuticals. Inorg Chem 2023;62:1362–76. https://doi.org/10.1021/acs.inorgchem.2c02907.
[59] Almada S, Maia LB, Waerenborgh JC, Vieira BJC, Mira NP, Silva ER, Cerqueira F, Pinto E, Alves LG. Cyclam-based iron(III) and copper(II) complexes: synthesis, characterization and application as antifungal agents. New J of Chem 2022;46:16764–70. https://doi.org/10.1039/D2NJ03161B.
[60] Zhang H, Song J, Wang S, Song Q, Guo H, Li Z. Recent progress in macrocyclic chemosensors for lead, cadmium and mercury heavy metal ions. Dyes Pigments 2023;216:111380. https://doi.org/10.1016/j.dyepig.2023.111380.
[61] Tosato M, Randhawa P, Asti M, Hemmingsen LBS, O'Shea CA, Thaveenrasingam P, Sauer SPA, Chen S, Graiff C, Menegazzo I, Baron M, Radchenko V, Ramogida CF, Di Marco V. Capturing mercury-197m/g for auger electron therapy and cancer theranostic with sulfur-containing cyclen-based macrocycles. Inorg Chem 2024;63:14241–55. https://doi.org/10.1021/acs.inorgchem.4c02418.
[62] Gans P, Sabatini A, Vacca A. Investigation of equilibria in solution. Determination of equilibrium constants with the HYPERQUAD suite of programs. Talanta 1996;43:1739–53. https://doi.org/10.1016/0039-9140(96)01958-3.

. .

G

Published Paper in Spectrochimica Acta Part A: Molecular and Biomolecular Spectroscopy- Corresponding to Chapter to Chapter 9

Spectrochimica Acta Part A: Molecular and Biomolecular Spectroscopy 349 (2026) 127285

Contents lists available at ScienceDirect

Spectrochimica Acta Part A:
Molecular and Biomolecular Spectroscopy

journal homepage: www.journals.elsevier.com/spectrochimica-acta-part-a-molecular-and-biomolecular-spectroscopy

Engineering multifunctional Cyclen fluorophores for metal ion sensing, self-assembly and Nanocolloid applications

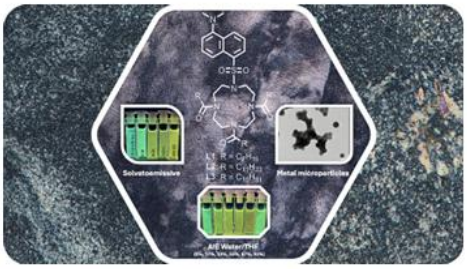
Frederico Duarte [a,f], Cristián Cuerva [b,*], Georgi M. Dobrikov [c,d], Atanas Kurutos [c,e,*], Nikolay G. Vassilev [c], Javier Fernández-Lodeiro [a,f], José Luis Capelo-Martinez [a,f], Hugo M. Santos [a,f], Carlos Lodeiro [a,f,g,*]

[a] BIOSCOPE Research Group, LAQV-REQUIMTE, Chemistry Department, NOVA School of Science and Technology, FCT NOVA, Universidade NOVA de Lisboa, 2829-516 Caparica, Portugal
[b] MatMoPol Research Group, Department of Inorganic Chemistry, Faculty of Chemical Sciences, Complutense University of Madrid, Ciudad Universitaria, 28040 Madrid, Spain
[c] Institute of Organic Chemistry with Centre of Phytochemistry, Bulgarian Academy of Sciences, Acad. G. Bonchev str., bl. 9, 1113 Sofia, Bulgaria
[d] National Centre of Excellence Mechatronics and Clean Technologies, Sofia, Bulgaria
[e] University of Chemical Technology and Metallurgy, 8 St. Kliment Ohridski blvd, 1756 Sofia, Bulgaria
[f] PROTEOMASS Scientific Society, Costa de Caparica, 2825-466, Portugal
[g] Canterbury Christ Church University, School of Human and Life Sciences, Life, Sciences Industry Liaison Lab, Sandwich, UK.

HIGHLIGHTS

- Three new monodansylated cyclen derivatives (L1–L3) were synthesized and fully characterized.
- The compounds exhibit strong solvatochromism and high fluorescence quantum yields up to 55% in chloroform.
- Variable alkyl chain length modulates aggregation-induced emission (AIE) behavior and self-assembly in THF–water mixtures.
- L1 selectively detects Cu^{2+} and Hg^{2+} ions with distinct Cu^{2+}/Cu^{+} and Hg^{2+}/Hg^{0} speciation capability (LOD = 2 μM for Cu^{2+}).
- L3 stabilizes spherical platinum nanoparticles with low polydispersity.

GRAPHICAL ABSTRACT



ARTICLE INFO

Keywords:
Dansyl fluorophores
Mesomorphism
Aggregation-induced emission (AIE)
Metal ion sensing
Platinum nanoparticles

ABSTRACT

We report the design, synthesis, and comprehensive characterization of three novel monodansylated cyclen derivatives (L1–L3), each bearing alkyl side chains of varying lengths (n = 8, 12, 16), developed as multifunctional fluorophores. Polarized optical microscopy (POM) and differential scanning calorimetry (DSC) were employed to evaluate mesomorphism, a property often associated with extended alkyl chains. These compounds exhibited pronounced solvatochromic behavior and high fluorescence quantum yields, reaching up to 55 % in chloroform. The influence of solvent polarity on their photophysical properties was quantitatively analyzed using the Kamlet–Taft equation. Self-assembly behavior in THF–water mixtures revealed aggregation-induced emission

* Corresponding authors.
E-mail addresses: c.cuerva@ucm.es (C. Cuerva), Atanas.Kurutos@orgchm.bas.bg (A. Kurutos), cle@fct.unl.pt (C. Lodeiro).

https://doi.org/10.1016/j.saa.2025.127285
Received 22 September 2025; Received in revised form 7 November 2025; Accepted 30 November 2025
Available online 1 December 2025
1386-1425/© 2025 The Authors. Published by Elsevier B.V. This is an open access article under the CC BY-NC-ND license (http://creativecommons.org/licenses/by-nc-nd/4.0/).

(AIE), with emission profiles varying according to alkyl chain length, as confirmed by dynamic light scattering (DLS) and fluorescence lifetime measurements. Selective detection of Cu^{2+} and Hg^{2+} ions by **L1** was demonstrated through significant fluorescence quenching, with detection limits of 2 μM and 40 μM, respectively. Speciation amount Cu^{2+}/Cu^{+} and Hg^{2+}/Hg^{+} was observed. Additionally, **L3** functioned effectively as a stabilizing agent in the colloidal synthesis of platinum nanoparticles, resulting in spherical nanostructures with low polydispersity, as confirmed by transmission electron microscopy (TEM) and DLS. These results highlight the versatile utility of alkylated dansyl–cyclen hybrids as fluorescent probes with self-assembly properties useful as nanomaterial stabilizers for advanced functional applications.

1. Introduction

The advancement of environmental monitoring, imaging, and medical diagnostics has been significantly influenced by the development of fluorescent probes and sensors. Dansyl (5-dimethylaminonaphthalene-1-sulfonyl) derivatives have endured as a fundamental class of fluorophores over time as a result of their well-established photophysical properties, which are present in the extensive collection of fluorescent dyes. These include large stokes shifts, high fluorescence quantum yields, and a strong modulation of emission characteristics on the surrounding microenvironment [1,2]. However, modern design of dansyl-derived fluorophores have shifted away from traditional single-function probes to advanced multiresponsive compounds towards pH, polarity, metal ions, with special focus towards the sensing of hg(II) and cu(II), and materials science [3–12]

In recent studies, several fluorophores have been functionalized with azamacrocycle groups to enhance their applications [13,14]. Dansyl-based azamacrocyclic compounds are no exception, with various examples being reported in the literature that combine the advantages of the dansyl fluorophore and azamacrocyclic scaffolds improving selectivity, sensitivity and biological compatibility [1,15–18]

Our previous studies on tetra-dansylated cyclen and cyclam derivatives have demonstrated pronounced emission modulation in response to solvent polarity reaching fluorescence quantum yields up to 41 % in chloroform. Dependence of the emission in the presence of higher fractions of water content in tetrahydrofuran (THF), demonstrated aggregation-induced emission (AIE) accompanied with the rise of the quantum yield. The formation of nanoaggregates was followed by dynamic light scattering (DLS) analysis, which achieved an average size of 134 ± 3 nm for the dansyl bearing a cyclen moiety. The application of these compounds towards metal ion remediation demonstrated the quenching of emission and the formation of mononuclear species with Hg^{2+} and Cu^{2+} reaching a limit of detection and quantification up to 2 μM and 3 μM, respectively [1]

Modification of the cyclen core with flexible alkyl side chains has recently emerged as an effective strategy to enhance its amphiphilic character [19,20]. The hydrophobic nature of the alkyl substituents not only improves solubility in nonpolar media but also promotes anisotropic molecular alignment. Liquid crystals (LCs) represent an intermediate state of matter that combines the fluidity of liquids with the structural order of crystalline solids, which is possible given their anisotropic molecular nature [21]. In turn, fluorescent liquid crystals (FLCs), a subclass of LCs, have attained increasing attention since they provide new platforms for the development of advanced materials in various research fields [22–27]. These structural adaptations open new opportunities for designing cyclen-based LC materials with tunable self-assembly behavior, metal coordination, and supramolecular material applications

Since their anisotropic and self-organizing nature, liquid crystals can intersect with nanoparticle synthesis serving as a stabilizing agent or template media, functioning similarly to surfactants in respect to guiding growth, controlling morphology and preventing aggregation. In particular, colloidal syntheses of platinum nanoparticles have gained wide adoption owing to their relative simplicity, controllable reaction parameters, and strong potential for scalable production which may benefit from such templating approaches [28]

Thus, we report the synthesis and characterization of three monodansylated cyclen compounds (L1−L3), each bearing a set of alkyl side chains of varying lengths on the remaining nitrogen atoms. The primary distinction being the length of these side chains. Polarized optical microscopy (POM) and differential scanning calorimetry (DSC) were employed to evaluate potential mesomorphic behavior. Additionally, their photophysical properties were investigated, and solvent–solute interactions were analyzed using the Kamlet–Taft equation. The effect of alkyl chain length on AIE behavior was examined in THF–water mixtures and monitored via DLS. Given the cyclen core's well-known ability to coordinate metal ions, the compounds were also evaluated for their potential in metal remediation. Finally, colloidal platinum nanoparticles were synthesized through an accessible route in which the cyclen compounds acted as stabilizing agents

2. Experimental section

2.1. Materials

All solvents used for the synthesis and purification including dichloromethane (DCM) and methyl-tert-butyl ether (MTBE) were of analytical grade (p.a.) and dried over molecular sieve (3 Å). The starting fine chemicals - cyclen (1,4,7,10-Tetraazacyclododecane), *N,N*-diisopropylethylamine (DIPEA), dansyl chloride, n-Octanoyl chloride, n-Dodecanoyl chloride, and n-Hexadecanoyl chloride used for the synthesis of the target fluorophores were purchased from Sigma Aldrich, Tokyo Chemical Industry Co. Ltd., and BLDPharm and utilized as received. Silica gel (high-purity grade, pore size 60 Å, 230–400 mesh particle size, 40–63 μm particle size, for flash chromatography) employed for the column chromatography was purchased from Sigma Aldrich.

Spectroscopy grade solvents, such as acetonitrile (CH_3CN), chloroform ($CHCl_3$), dimethyl sulfoxide (DMSO), ethanol (EtOH), and tetrahydrofuran (THF), were used for spectrophotometric and spectrofluorimetric measurements. Trifluoromethanesulfonate salts Ca$(OTf)_2$, Co$(OTf)_2$, Ni$(OTf)_2$, Cu$(OTf)_2$, Zn$(OTf)_2$, Ag(OTf) and Cd$(OTf)_2$, were provided from Solchemar, while Cu$(NCCH_3)_4$(OTf), Hg$(OTf)_2$, $HgCl_2$ and $Pb(ClO_4)\cdot 3H_2O$ were purchased from Sigma Aldrich.

2.2. Instrumentation

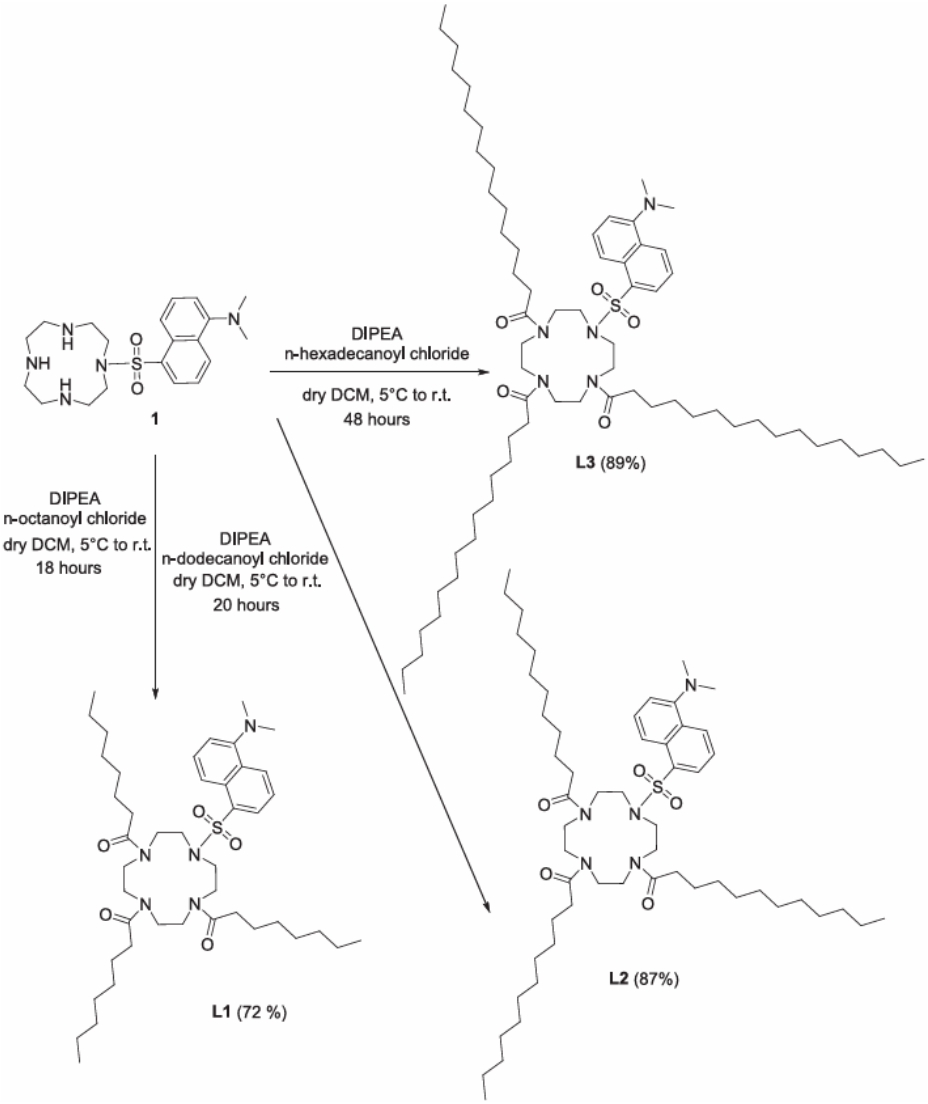
The chemical identities of all compounds were confirmed by a combination of ^{1}H NMR, ^{13}C NMR, 2D-COSY, 2D-HSQC, and 2D-HMBC spectroscopic techniques. Utilizing 5 mm tubes on a Bruker Avance II+ 600 spectrometer (Institute of Organic Chemistry with Centre of Phytochemistry-Bulgarian Academy of Sciences / NMR Centre), the ^{1}H NMR and ^{13}C NMR spectra were acquired in 1,1,2,2-Tetrachloroethane-d_2 (TCE), with spectrometer operating frequencies of 600.13 MHz and 150.92 MHz, respectively. The ^{1}H NMR and ^{13}C NMR spectra were standardized to the tetramethylsilane (TMS) signal at δ = 0.00 ppm. Chemical changes were quantified with a precision of 0.01 ppm (ppm). The coupling constants (J) were given with an accuracy of 0.1 Hz. The spin multiplicity in the ^{1}H NMR is represented by the following abbreviations: s = singlet, d = doublet, t = triplet, q = quartet,

dd = doublet of doublets, dt = doublet of triplets, td = triplet of doublets, and m = multiplet.

^{1}H spectra (0.05 M in 0.6 mL TCE) were recorded on a Bruker Avance Neo instrument (5 mm BBO CryoProbe Prodigy) at 600.18 MHz in steps of 10 K in the interval between 243 K and 393 K. The sample temperature was controlled by the temperature control system (BSVT) and BCU-II cooling unit. ^{1}H NMR spectra were acquired using a spectral width of 10 kHz, an acquisition time of 1.7 s and 32 scans, zerofilled to 64 k datapoints (0.15 Hz per point) and processed without apodization.

High-Resolution Mass Spectrometry analyses have been performed in the Laboratory for Biological Mass Spectrometry–Isabel Moura (PROTEOMASS Scientific Society Facility), using UHR ESI-Qq-TOF IMPACT HD (Bruker-Daltonics, Bremen, Germany). Samples of the corresponding compounds were prepared by dissolution in 50 % (*v*/v) Acetonitrile containing 0.1 % (v/v) aqueous formic acid to obtain a working solution of 0.1 μg/mL. Mass spectrometry analysis was carried out by the direct infusion of the compound solutions into the ESI source. MS data were acquired in positive polarity over the mass range of 80–1300 *m/z*. (Capillary voltage: 4500 *V*, End plate offset: −500 V, Charging voltage: 2000 V, Corona: 4000 nA, Nebulizer gas: 0.4 Bar, Dry Heater: 180 °C, Dry gas: 4.0 L/min).

Polarized optical microscopy (POM) observations were carried out



Scheme 1. Synthetic approach to the preparation of **L1-L3**.

by using an Olympus BX50 microscope equipped with a Linkam THMS 600 heating stage. The transition temperatures and their associated enthalpy data were determined with a PerkinElmer Pyris 1 differential scanning calorimeter. Samples were hermetically sealed in aluminum pans and measurements were carried out with heating and cooling rates of 10 K min^{-1}.

The UV–Vis absorption spectra were recorded using a JASCO V-650 spectrophotometer, while the fluorescence emission spectra were measured with a HORIBA Scientific FLUOROMAX-4 spectrofluorometer. Otherwise stated, all photophysical experiments were performed at 293 K using quartz cells with 10 mm optical path. Spectra of solid samples were collected using an optic fiber coupled to the spectrofluorometer by exciting the solid compounds at the appropriated wavelength. Fluorescence lifetime measurements were performed on TemPro, Deltahub Nanoled of Horiba Jobin-Yvon, using a 390 nm Nanoled. All instrumentation was provided by PROTEOMASS-BIOSCOPE facility.

Transmission electron microscopy (TEM) images were obtained using a JOEL JEM 1400 transmission electron microscope from the i3S, University of Porto (Portugal), operating at 80 kV. Samples were prepared by dropping 5 μL of the colloidal suspension on a copper grid coated with a continuous carbon film, and the solvent was allowed to evaporate.

Dynamic light scattering (DLS) data was obtained on a Malvern Zetasizer Nano series (Worcestershire, WR14 1XZ, UK) from PROTEOMASS Scientific Society-BIOSCOPE Facility Lab. The samples were analyzed at a scattering angle of 90° and at a temperature of 25 °C and 20 °C for water and ethanol, respectively, while supported in a glass cell. The z-potential measurement of microparticles was performed using a dip-cell.

2.3. Synthetic procedures

2.3.1. Synthesis of 1,1′,1″-(10-(5-(dimethylamino)naphthalen-1-ylsulfonyl)-1,4,7,10-tetraazacyclododecane-1,4,7-triyl)trioctan-1-one

Ds-cyclen **1** (0.36 mmol, 144 mg, 1 equiv.) and DIPEA (3.55 mmol, 0.62 mL, 10 equiv.) were dissolved in 25 mL of dry DCM resulting in the formation of a clear yellow solution, which was cooled down to 5 °C. n-Octanoyl chloride (2.13 mmol, 0.36 mL, 6 equiv.) was added dropwise at this temperature and the mixture was stirred for 30 min (Scheme 1). The colour changed to red, but the solution remains clear. Stirring was maintained for 18 h at r.t. The reaction mixture was worked up with DCM and consequently washed with conc. aq. citric acid, brine, aq. $NaHCO_3$ and water. The organic phase was dried over anhydr. Na_2SO_4 and the flask content was evaporated to dryness. The target product was subjected to purification by column chromatography on a silica gel employing DCM:MTBE = 10:1 *v*/v as a mobile phase to furnish 0.200 g (72 %) of a thick yellow oil.

2.3.2. Synthesis of 1,1′,1″-{10-[5-(dimethylamino)naphthalene-1-sulfonyl]-1,4,7,10-tetraazacyclododecane-1,4,7-triyl}tri(dodecan-1-one)

Ds-cyclen **1** (0.50 mmol, 201 mg, 1 equiv.) and DIPEA (4.96 mmol, 0.86 mL, 10 equiv.) were dissolved in 25 mL dry DCM resulting in the formation of a clear yellow solution, which was cooled down to 5 °C. n-Dodecanoyl chloride (2.48 mmol, 0.58 mL, 5 equiv.) was added dropwise at this temperature and the mixture was stirred for 30 min (Scheme 1). The colour changed to orange-red, but the solution remains clear. Stirring was maintained for 20 h at r.t. The reaction mixture was worked up with DCM and washed consequently with conc. aq. citric acid, brine, aq. $NaHCO_3$ and water. The organic phase was dried over anhydr. Na_2SO_4 and the flask content was evaporated to dryness. The target product was subjected to purification by column chromatography on a silica gel employing DCM:MTBE = 10:1 *v*/v as a mobile phase to furnish 0.411 g (87 %) of a thick yellow oil.

2.3.3. Synthesis of 1,1′,1″-{10-[5-(dimethylamino)naphthalene-1-sulfonyl]-1,4,7,10-tetraazacyclododecane-1,4,7-triyl}tri(hexadecan-1-one)

Ds-cyclen **1** (0.41 mmol, 168 mg, 1 equiv.) and DIPEA (4.14 mmol, 0.72 mL, 10 equiv.) were dissolved in 50 mL of dry DCM resulting in the formation of a clear yellow solution, which was cooled down to 5 °C. n-Hexadecanoyl chloride (2.07 mmol, 0.57 mL, 5 equiv.) was added dropwise at this temperature and the mixture was stirred for 30 min (Scheme 1). The colour changed to orange-red, but the solution remains clear. Stirring was maintained for 48 h at r.t. The reaction mixture was worked up by stirring with 1 % aq. NaOH for 2 h, followed by extraction with DCM (2 × 50 mL). The combined organic phase was consequently washed with conc. aq. citric acid, brine, aq. $NaHCO_3$ and water. The organic phase was dried over anhydr. Na_2SO_4 and the flask content was evaporated to dryness. The target product was subjected to purification by column chromatography on a silica gel employing DCM:MTBE = 20:1 *v*/v as a mobile phase to furnish 1.421 g (89 %) of a yellow solid.

2.4. Spectrophotometric and spectrofluorimetric measurements

2.4.1. Photophysical characterization and titrations

Stock solutions of each compound (ca. 1 mM) were prepared in various solvents (CH_3CN, DMSO, EtOH, $CHCl_3$, and THF), by dissolving the respective ligand in a 10 mL volumetric flask and diluting with the chosen solvent. Working solutions, ranging from 10 μM to 1 μM, were obtained by further dilution of the stock solutions.

Titration experiments with ligand L1 were conducted through the stepwise addition of microliter aliquots of standard metal ion solutions (Ca^{2+}, Co^{2+}, Ni^{2+}, Cu^{+}, Cu^{2+}, Zn^{2+}, Ag^{+}, Cd^{2+}, and Hg^{2+}) in acetonitrile. For Hg^{+} and Pb^{2+}, aqueous solutions were used. Absorbance corrections were applied where necessary.

To study the aggregation effects, mixtures with varying water fractions (f_w = 0 %, 17 %, 33 %, 55 %, 67 % and 83 %) were prepared in THF at a final concentration of 10 μM and characterized using absorption and emission spectroscopy.

2.4.2. Fluorescence quantum yield and lifetime

The relative photoluminescence quantum yields were evaluated using dansylamide dissolved in DMSO (φ_F = 0.61) as a reference standard for quantifying the QY of each compound across all tested solvents [29]. Fluorescence lifetime measurements were conducted using a Tempro Fluorescence Lifetime System equipped with a Horiba Jobin-Yvon NanoLed pulsed diode controller. All experiments were performed at 293 K.

2.5. Determination of the detection and quantification limits (LOD and LOQ)

The determination of the detection limit (LOD) and quantification limit (LOQ) began with ten independent measurements of a solution containing the selected probe, without the addition of any metal ions (y_{blank}). The LOD and LOQ were then calculated using the following equations. LOD = y_{dl} = y_{blank} + 3std and LOQ = y_{dl} = y_{blank} + 10std, where y_{dl} = signal detection limit and std. = standard deviation.

Finally, titrations with the ligands were carried out to determine the lowest concentrations of metal ions that could be reliably detected and quantified [30,31].

2.6. DFT calculations

All calculations were performed by means of quantum chemical calculations at the density functional theory (DFT) level using Gaussian16 program package [32]. The geometries of all compounds have been fully optimized and the corresponding transition states were localized using B3LYP [33] functional with 6–31 + G(d,p) basis set [34]. The nature of all critical points was confirmed by means of the vibrational analysis. The ΔH, ΔS and ΔG values were calculated at T =

298.15 K at the same level of theory including zero-point energy and vibrational, rotational and translational thermal energy corrections.

2.7. Colloidal synthesis of platinum nanoparticles

The synthesis of platinum nanoparticles began with the preparation of an aqueous solution of K_2PtCl_4 with a concentration of 2.72 mM. Compound **L3** was used as a stabilizing agent in different ratios of metal: **L3** (1:1, 1:2, 1:5, 1:7.5, 1:10). In a round-bottom flask, 10 mL of ethanol was added to the weighted compound **L3** (0.29 mM, 0.53 mM, 1.36 mM, 2.05 mM, 2.66 mM) and heated to 87 °C to allow solubilization. Then, 1 mL of the platinum solution was added, and the solution was allowed to run for ten minutes. The resulting solutions were centrifuged three times for thirty minutes at 6000 rpm in ethanol.

3. Results and discussion

3.1. Conformational analysis and molecular geometry

The NMR spectra of the obtained and purified compounds display signals indicating a mixture of conformers, with their exchange occurring slowly on the NMR time scale. Variable temperature ^{1}H NMR spectra of compounds **L1**-**L3** were measured in TCE in order to reach slow and fast exchange limits. As the temperature decreases, the separation of signals of rotamers increases. However at 243 K (Figs. S6, S12 and S18), the signals were still broad and we were not able to reach slow exchange regime. With increasing the temperatures to 393 K (Figs. S6, S12 and S18) the fast exchange regime was reached and we were able to measure ^{1}H, ^{13}C, 2D COSY, 2D HSQC and 2D HMBC NMR spectra allowing full structure elucidation of the new compounds.

To investigate the exchange behavior of the new compounds in solution, we performed DFT calculations on a model compound in which all long alkane chains were replaced with methyl. There are four possible conformations of the cyclen ring [35] depending on the *R* or *S* configurations of the chiral nitrogen atoms. In our case, the substitution of the amine protons with rather bulky substituents reduces the possible conformations to one with alternating up and down substituents. Reaction coordinate type calculations using variation of the dihedral angles around the S—N and S—C bonds estimate a barrier in the range 5–8 kcal/mol. However, reaction coordinate type calculations using variation of the dihedral angles of the three amide bonds estimate rotation barriers in the range 15–18 kcal/mol, revealing that these restricted rotations are responsible for the dynamic behavior of the NMR spectra of the **L1**-**L3** compound. Eight conformers with *syn* and *anti* conformations around the three amide bonds are possible (Fig. 1). The B3LYP/6–31 + G (d,p) calculated thermodynamic parameters of all eight GS stereoisomers at 298 K are presented in Table 2. The most preferable conformer is GS5 (*syn, syn, syn*). The exchange between the ground state structures GS1 (*syn, anti, anti*) and GS2 (*syn, anti, syn*) of the model compound together with the two transition states TS12 and TS21 are illustrated in Scheme 2. Further optimizations of transition state (TS) structures during the rotation around amide bonds allow localization of all TS geometries and estimation of rotational barriers (Table S2). The DFT calculations of the model cyclen elucidate the conformational behavior of the studied compounds in solution: the possible conformers, their populations in solution according to their energy, and the energy barriers of the rotational transformations between them. These calculations are consistent with the measured broad NMR signals at 243 K.

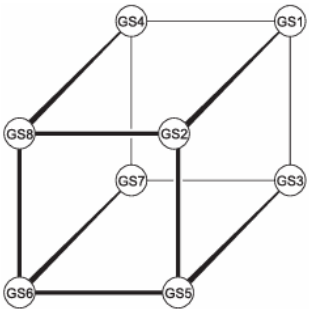


Fig. 1. Cube vertices representing the eight conformations of model compound and the edges mapping out the exchange pathways. The nomenclature of all conformations is presented in Table 2.

3.2. Mesomorphic behavior

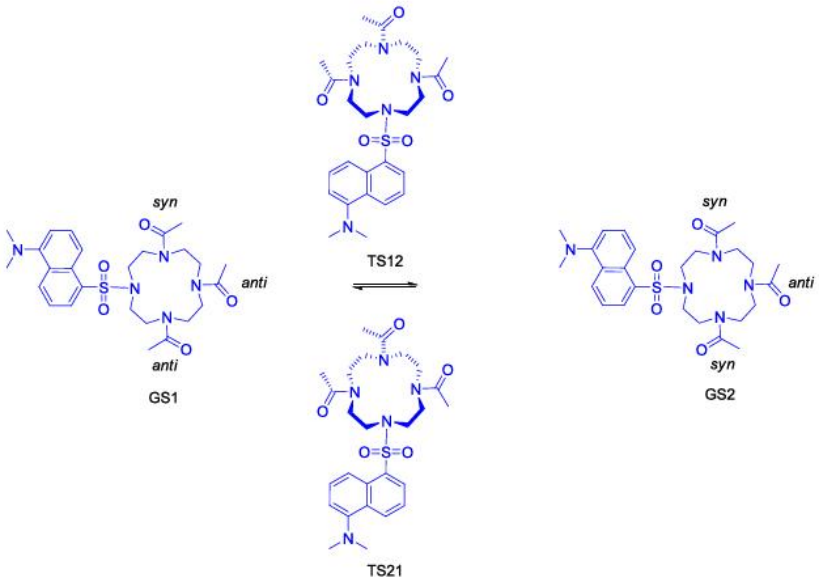
Polarized light optical microscopy (POM) and differential scanning calorimetry (DSC) studies were conducted to determine if the new compounds bearing terminal alkyl chains exhibit mesomorphism. The optical observations under polarized light show that compounds **L2** and **L3** form a fluidic and birefringent liquid-crystalline mesophase just before melting into the isotropic liquid, as demonstrated in Fig. 2. In accordance with the POM studies, the corresponding DSC thermograms displayed a unique and broad endothermic peak that involves both the solid-mesophase and the mesophase-isotrope phase transitions. The onset temperatures and the enthalpy values are gathered in Table 3. Note that no exothermic peaks appear in the thermograms upon cooling. In fact, the formation of the mesophase from the isotrope was not observed by POM at the expected temperature, neither the solidification process. This feature can only be understood if a hysteresis phenomenon [36] occurs during the heating and cooling cycles. To verify this behavior, samples were allowed to cool slowly, and solidification was finally observed after several hours at r.t.

Regarding the mesophase nature, it could be possible that the mesophases are columnar, based on the disc-like shape of these molecules (see Scheme 1). Regrettably, the narrow temperature range of just some degrees in which the mesophases are stable prevented analyzing their supramolecular organization by powder X-ray diffraction experiments, and the texture of the mesophases observed under polarized light did not allow their identification either.

3.3. Photophysical characterization

The monodansylated cyclen compounds bearing different alkyl side chains exhibit photophysical properties both in solution as well as in the solid state. The complete photophysical data are provided in Fig. 3, as well as Table 4 and in Figs. S22 to S24 of the supporting information. Special focus has been given to the investigation of **L1** in various solvents given the constraints associated with the increment in length of the alkyl side chains in terms of solubility for **L2** and **L3**.

Providing a closer look at the UV–Vis spectra, all compounds display a broad absorption band with a maximum centered between 341 and 350 nm depending on the employed solvent, associated with the π - π^* transition of dansyl chromophore promoting the absence of any colour in the visible region. As we consider each solvent used, the excitation of the solutions at the appropriate wavelength for **L1** results in a shift of the emission from 504 to 537 nm enabling the display of solvatochromism that it will be further explored and can be confirmed by Fig. 3, panel 3c. Although no confirmation of solvatochromism is possible for **L2** and **L3**, due to solubility limitations, no evidence has been found in chloroform or THF that could suggest any influence of the length of the alkyl side chains onto the photophysical properties given the similarities observed. Furthermore, large Stokes shifts, commonly found for dansyl derivatives, were observed ranging from 8730 to 10,113 cm^{-1}. On a relatable note, solid-state emission spectra were recorded for all compounds exhibiting an emission maximum between 486 and 498 nm that is blue-shifted in comparison to all the spectra recorded in solution.



Scheme 2. Exchange between GS1 (*syn, anti, anti*) and GS2 (*syn, anti, anti*) ground state structures of the model compound. The two transition states TS12 and TS21 are also presented.

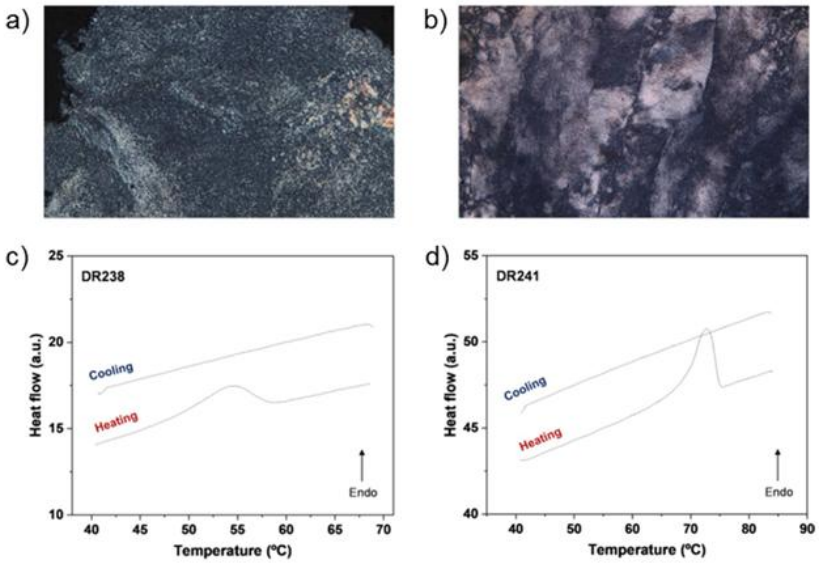


Fig. 2. (a,b) Textures of the mesophases observed by POM for (a) **L2** and (b) **L3**, at 43 and 68 °C, respectively, in the first heating cycle. (c,d) DSC thermograms registered in the first heating and cooling cycles.

Finally, elucidation in terms of fluorescence quantum yield efficiency and characterization of fluorescence lifetime decay were investigated and are summarized in Table 4. Once again, the solvent used was found to influence the quantum yield efficiency with lower values for more polar solvents starting from 26 % in ethanol and reaching a maximum of up to 55 % in chloroform as **L1** is considered. In turn, the time-resolved fluorescence decay curves give us insights into the double-digit nanosecond times sitting in the range of 12 to 14.98 ns with no relevant

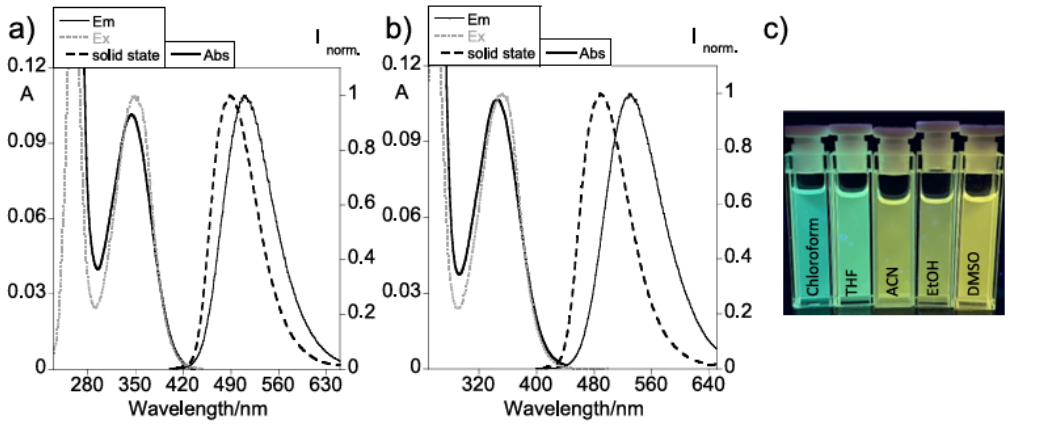


Fig. 3. Photoluminescent characterization of compound **L1** in THF (a) and acetonitrile (b). Image (c) under UV light (365 nm) of **L1** dissolved in various solvents.

association between this parameter and the solvent used.

As mentioned before, efforts were placed to investigate the solvatochromic behavior of these dansyl derivatives given the visual detection of a colour change under UV radiation from bluish green to yellow. This transition with the increase in solvent polarity relates to positive solvatochromism and has been characterized by their solvent-compound interactions through the multiparametric fitting of the Kamlet-Taft equation (Eq. 1).

$$\upsilon = \upsilon_0 + a\alpha + b\beta + p\pi^*\nu = \nu_0 + a\alpha + b\beta + p\pi^* \quad (1)$$

Where υ_0 represents the wavenumber value in a reference solvent; the solute dependent parameters a, b and p are obtained through multiple regression analysis that elucidate the susceptibility for the probes' photophysical behavior to be influenced by solvent polarity; α: hydrogen bond donor acidity (HBD); β: hydrogen bond acceptor basicity (HBA); π*: stabilization of a charge or dipole without a specific dielectric interaction (Table 1) [37,38].

Table 5 gathers the reference wavenumber value υ_0, the fitted parameters (a, b and p) along with the slopes and correlation coefficients obtained through the fitting of a linear plot of $\upsilon_{exp.}$ Versus υ_{calc}, by applying the Kamler-Taft model excluding acetonitrile.

The Kamlet-Taft analysis of the solvatochromic behavior reveals that the observed positive solvatochromism for **L1** is primarily driven by solvent polarity effects. The observed negative coefficients suggest that any increase of the solvent parameters leads to a bathochromic shift in the emission spectrum in accordance with what is observed experimentally. Among these values, the largest is associated with p parameter suggesting that dipolarity and polarizability of the solvent have the strongest influence on the spectral shifts. In turn, hydrogen bond basicity also plays a comparatively smaller role, while hydrogen bond acidity employs the least effect.

Table 1
Spectroscopic polarity parameters, physical properties of the different solvents. ε_r: relative permitivity; η: refractive index; α: the solvent's HBD acidity; β: the solvent's HBA basicity; π*: the solvent's dipolarity/polarizability.

Solvent	ε_r	α	β	π*	η
DMSO	47.24	0	0.76	1.00	1.47
EtOH	24.3	0.86	0.75	0.54	1.36
CH_3CN	35.94	0.19	0.40	0.66	1.34
THF	7.58	0	0.55	0.58	1.40
$CHCl_3$	4.89	0.20	0.10	0.69	1.44

Table 2
B3LYP/6–31 + G(d,p) calculated thermodynamic parameters for stereoisomers at 298 K.

Stereoisomer	Nomenclature	ΔH≠ (kcal/mol)	ΔS≠ (e.u.)	ΔG≠ (kcal/mol)	Populations (%)
GS1	syn,anti,anti	0	0	0	0.002
GS2	syn,anti,syn	−3.05	7.89	−5.41	22.1
GS3	syn,syn,anti	−4.34	2.76	−5.16	14.5
GS4	anti,anti,anti	−2.97	5.97	−4.74	7.2
GS5	syn,syn,syn	−3.32	7.62	−5.59	30.2
GS6	anti,syn,syn	−2.25	8.34	−4.73	7.1
GS7	anti,syn,anti	−3.21	6.92	−5.23	17.6
GS8	anti,anti,syn	−1.33	8.03	−3.72	1.3

Table 3
Phase behavior of **L2** and **L3** established by DSC.

Compound	Transition[a]	Onset temperature[b] (°C)	ΔH ($kJmol^{-1}$)
L2	Cr → M → I	47	47.8
L3	Cr → M → I	68	80.3

[a] Cr = solid, M = mesophase, I = isotrope. [b] Onset temperature determined by DSC.

3.4. Modulation of aggregation induced emission in water.

The assessment of the formation of aggregates, according to the implementation of different alkyl side chains in the compounds under investigation, was accomplished with different ratios of water in THF, and were followed by photophysical and dynamic light scattering techniques. Fig. 4 illustrates the absorption and the emission profile at increasing water fraction (f_w) whereas Table 6 summarizes the DLS data alongside the quantum yield and lifetime measurements of the high f_w samples of all compounds. As far as the emission and the absorption profiles are concerned, key changes can be perceived with increasing alkyl side chains. Figs. 4a-c demonstrate that the absorption profile suffers changes with the slight increase of the baseline at f_w = 83 % for all compounds and a larger increase at 67 % for the latter two compounds, without variation of the absorption maximum wavelength. These increases serve as evidence for the formation of aggregates at high water content ratios. DLS data help consolidate these findings with the identification of aggregates with an average size between 66.8 and

Table 4
Absorption maximum wavelength in solution (λ_{abs}), emission maximum wavelength in solution (λ_{em}), molar absorption coefficients (ε), Stokes shift ($\Delta\lambda$), emission maximum in the solid state (λ_{em}^{Solid}), fluorescence quantum yields (φ), fluorescence lifetimes (τ) for compounds **L1** to **L3** in different solvents.

Cpd.	Solv.	λ_{abs} [nm]	λ_{em} [nm]	ε [10^4 cm^{-1} M^{-1}]	Stokes shift [cm^{-1}]	λ_{em}^{Solid} [nm]	φ	τ[ns]
L1	DMSO	348	537	0.466	10,113	486	0.32	14.29
	EtOH	345	526	0.534	9974		0.26	12.04
	CH_3CN	345	531	0.557	10,153		0.40	12.56
	THF	341	508	0.497	9640		0.42	13.30
	$CHCl_3$	350	504	0.500	8730		0.55	14.98
L2	THF	340	509	0.494	9765	488	0.43	13.36
	$CHCl_3$	350	503	0.460	8691		0.57	14.98
L3	THF	341	508	0.507	9640	498	0.44	13.48
	$CHCl_3$	350	502	0.524	8651		0.54	15.03

Table 5
Independent fluorescence wavenumber ($\upsilon 0$), solvent polarity (p), HBD (a), HBA (b), slope and coefficient (R [2]) of the linear fitting plot $\upsilon_{exp.}$ Versus $\upsilon_{calc.}$

	υ_0	a	b	p	Slope	R^2
L1	21,440	−618	−1105	−1978	1.00	1.00

Table 6
Dynamic light scattering data, quantum yield and lifetime measurements of each compound in different mixtures of THF and water.

f_w(%)	Z-Average (nm)	PDI	ζ-Potential (mV)	φ	τ[ns]
L1 (83 %)	98.6 ± 4.2	0.19 ± 0.13	−24.6 ± 1.1	0.26	$\mathbf{T_1}$ = 1.4; $\mathbf{T_2}$ = 16.0
L2 (67 %)	322.1 ± 5.2	0.09 ± 0.03	−17.5 ± 0.4	0.16	$\mathbf{T_1}$ = 4.5; $\mathbf{T_2}$ = 14.0
L2 (83 %)	66.8 ± 0.5	0.16 ± 0.02	−18.7 ± 0.4	0.28	$\mathbf{T_1}$ = 4.8; $\mathbf{T_2}$ = 17.1
L3 (67 %)	298.5 ± 4.1	0.05 ± 0.01	−8.4 ± 0.9	0.20	$\mathbf{T_1}$ = 3.5; $\mathbf{T_2}$ = 15.3
L3 (83 %)	132.7 ± 0.7	0.06 ± 0.01	−25.1 ± 1.3	0.40	$\mathbf{T_1}$ = 8.4; $\mathbf{T_2}$ = 18.1

Table 7
Association constants and stoichiometry for compound **L1** in the sensing of Hg^{2+} and Cu^{2+} ions in acetonitrile, determined using HypSpec software. Detection limit (LOD) and quantification limit (LOQ) values (in μM) were calculated based on emission intensity at 530 nm.

Compounds	Metal (M)	Association constants (LogKass.), L:M	LOD (μM)	LOQ (μM)
L1	Cu^{2+}	4.73±0.01 (1:1)	2	6
	Hg^{2+}	3.10±0.01 (1:1)	40	60

Table 8
Dynamic light scattering data for the obtained particles.

Particles	Z-Average (nm)	PDI
Pt@1:1	194.1 ± 3.2	0.23 ± 0.01
Pt@1:2	157.5 ± 1.0	0.17 ± 0.02
Pt@1:5	187.0 ± 0.9	0.20 ± 0.03
Pt@1:7.5	229.7 ± 11.5	0.30 ± 0.05
Pt@1:10	225.4 ± 4.9	0.23 ± 0.01

106.8 nm considering the f_w = 83 %. Interestingly, larger aggregates were identified for the mixtures of f_w = 67 % but only for compounds **L2** and **L3** with an average size of 322.1 and 298.5 nm, respectively, suggesting that the formation of these aggregates can only be stabilized by the implementation of larger alkyl side chains.

The photoluminescent profile of these mixtures is characterized by a continuous quenching of the emission as the water content increases in tandem with a bathochromic shift of the fluorescence emission maximum, that can be visualized in Figs. 4d-f in combination with the images under UV light (Figs. 4g-i). Deviations from this are observed with the increase of the emission close to the original one for **L1** at f_w = 83 %. A similar behavior is addressed for **L2** with an additional regain of emission for f_w = 67 % whereas for **L3** the emission at f_w = 83 % was recorded past the original one. The aggregation induced emission was then characterized for its quantum yield, suggesting values from 16 % to 40 % and the identification of two fluorescence lifetimes for each mixture indicates the presence of different relaxation pathways. Being the contribution of $\mathbf{T_1}$ lower than $\mathbf{T_2}$ while the latter resembles in great length the ones found for the other solvents used.

3.5. Metal ion interaction

Given the established usefulness of dansyl derivatives for metal ion detection, **L1** has been evaluated for this application. Hence, acetonitrile solutions of several metal ions; namely Ca^{2+}, Co^{2+}, Ni^{2+}, Cu^{+}, Cu^{2+}, Zn^{2+}, Ag^{+}, Cd^{2+}, and Hg^{2+} were used, while Hg^{+} and Pb^{2+} were prepared in aqueous solution. These metal ions have been added to **L1** in proportions of 1, 5, and 10 equivalents, and their corresponding emission intensities are shown in Fig. 5. Clear modulation of the emission intensity was found in the presence of copper(II) ions due to the extensive quenching of the emission with only 1 equivalent followed by the total absence of emission in the case of 5 equivalents. It is also noteworthy to mention the much less pronounced effect of mercury(II) on the quenching of **L1**.

Despite the visible difference in magnitude, titrations of compound **L1** with Cu^{2+} and Hg^{2+} metal ions were carried out in acetonitrile. The absorption and luminescent behavior were recorded and are gathered in Fig. 5. The spectrophotometric and spectrofluorimetric titrations yielded results that were consistent for both metals.

For both cases the absorption spectral behavior is characterized by a decrease of the absorption band centered at 345 nm and an opposite move for the band found at 290 nm, additionally for Hg^{2+}, a substantial decrease at 250 nm was observed. Furthermore, both titrations evolve with the presence of one and two isosbestic points for Cu^{2+} and Hg^{2+}, respectively, assuring a complexation interaction among these species. Regarding the fluorescence emission spectra, a suppression was followed at 530 nm, showing this fluctuation of the emission intensity maxima of **L1** in both insets of Fig. 5b and c. The emission quenching observed with Hg^{2+} is presumably due to its nature as a heavy atom, which enhances spin-orbit coupling and facilitates non-radiative decay pathways that compete with fluorescence. As a result, chelation with Hg^{2+} leads to chelation-enhanced quenching (CHEQ). Likewise, Cu^{2+} is often detected via CHEQ, owing to its paramagnetic nature arising from unpaired electrons in its d-orbitals. This quenching occurs through various mechanisms such as either electron transfer or energy transfer. In contrast, the closed-shell configuration of Cu^{+} makes it incapable of quenching fluorescence. Thus, this system can effectively distinguish between Cu^{2+} and Cu^{+}, as well as Hg^{2+} and Hg^{+}, serving as a useful tool for metal ion speciation.

The complete assessment of the sensing profile for Cu^{2+} and Hg^{2+}

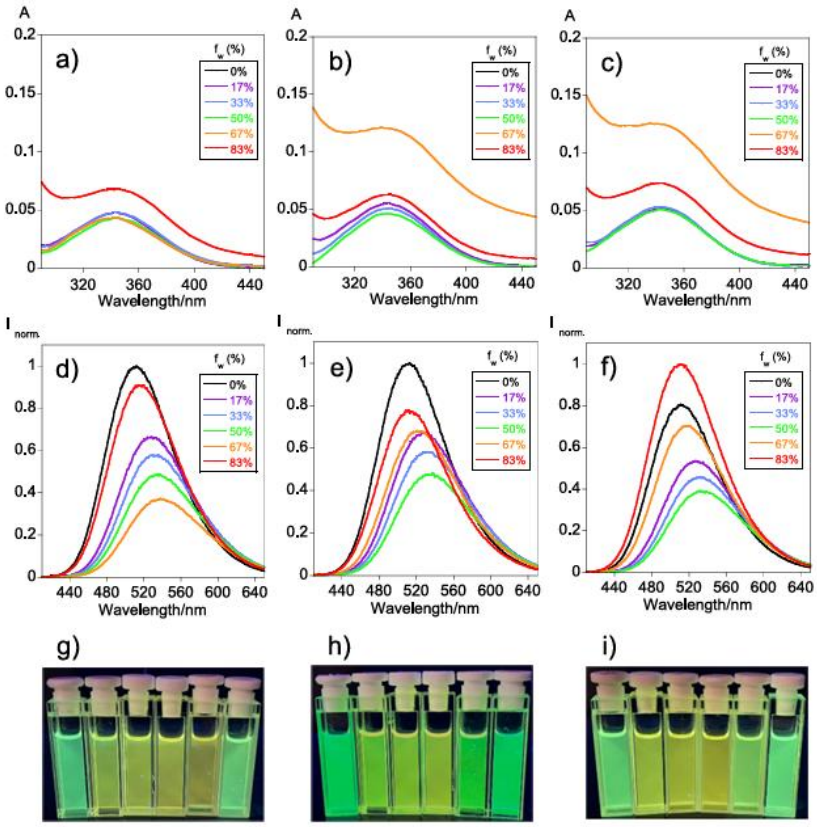


Fig. 4. Absorption (a-c) and emission (d-e) spectra of **L1** (a,d), **L2** (b,e) and **L3** (c,f) in different mixtures THF and water fractions f_w (0 %, 17 %, 33 %, 55 %, 67 %, 83 %). Images of **L1** (g), **L2** (h) and **L3** (i) with different water fractions under UV light (365 nm). The images are displayed in increasing water fraction order.

was accomplished with the use of the HypSpec software [39] to determine the interaction constants. Additionally, limits of detection (LOD) and quantification (LOQ) were evaluated. Table 7 presents the association constants along with the corresponding LOD and LOQ values.

The proposed interaction constants have in consideration the stoichiometric ratio of 1:1 (L:M) provided the well-defined cyclen core as the coordination site. Naturally, the highest association constant was found for Cu^{2+} with a value of $LogK_{ass.} = 4.73 \pm 0.01$. This large gap in the interaction constants between **L1** and both metal ions may be assigned to the imposed rigidity of the tertiary amides which hinder the most favorable conformation of the core. This effect allied with the larger size of the Hg^{2+} ion, translates to a more challenging sensing of this metal. In our previous work, where the tetra dansylation of cyclen core was accomplished, these hindrances were not evident, which in turn promoted a slightly higher constant in the case of Cu^{2+} that were in par with Hg^{2+} [1]. Furthermore, the lowest detectable amounts corresponded to Cu^{2+} (2 μM and 6 μM) indicating its potential suitability for applications such as environmental monitoring, where detecting and quantifying low levels of Cu^{2+} is essential. A comparison among dansyl derivatives reported in the literature that were employed for the detection of both metal ions can be seen in Table S1.

3.6. Colloidal synthesis of platinum nanoparticles

Considering the capacity of these compounds to self-assemble in solution, together with the mesomorphic properties conferred by the alkyl chains in the cyclen core, we redirected our focus to investigate these compounds in the colloidal production of platinum particles. Given the simplicity and vast literature surrounding the methodologies for the synthesis of these nanomaterials, our approach employs ethanol as a reducing agent and **L3** was used in order to explore it as stabilizing [28]. As expressed in the experimental section, several syntheses were accomplished by varying the ratio of the compound's concentration while maintaining the platinum salt's concentration constant. All the resulting colloidal solutions were followed by DLS while, from the selected Pt@1:5 AND Pt@1:10, TEM images were obtained. Overall, this synthesis method allows the intended formation of platinum particles, with **L3** acting as an effective stabilizing agent. Due to their non-plasmonic nature, no characteristic absorption bands have been found (Fig. S25). However, DLS data presented in Table 8 reveal variations in the average particle size, depending on the **L3** ratio used, ranging from 157.5 ± 1.0 to 229.7 ± 11.5 nm. The associated polydispersity index (PDI) values indicate a low degree of polydispersity across all samples. Complementary transmission electron microscopy (TEM) images (Figs. S26 and S27) further support the formation of spherical particles.

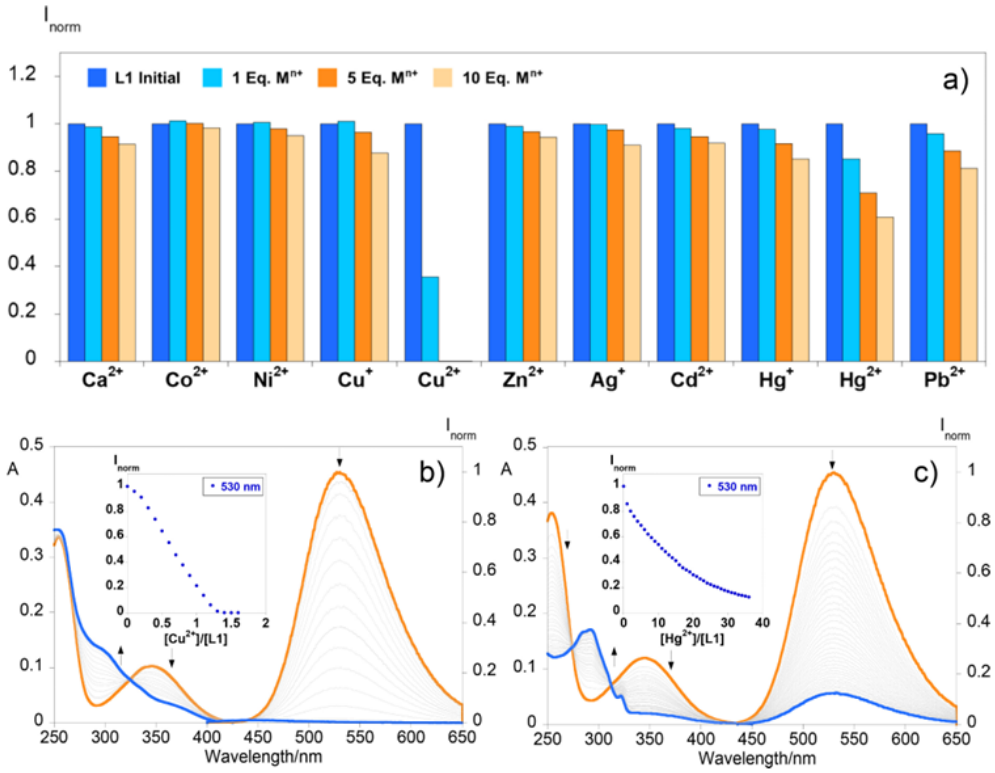


Fig. 5. Maximum emission intensities of **L1** in acetonitrile (a) after the addition of 1, 5, and 10 equivalents of Ca^{2+}, Co^{2+}, Ni^{2+}, Cu^{+}, Cu^{2+}, Zn^{2+}, Ag^{+}, Cd^{2+} and Hg^{2+} in acetonitrile while Hg^{+} and Pb^{2+} metal ions were in aqueous solution. Spectrophotometric and spectrofluorometric titrations of compound **L1** with increased additions of Cu^{2+} (b) and Hg^{2+} (c) in acetonitrile. The inset represents the emission as a function of $[Cu^{2+}]/[\mathbf{L1}]$ at 530 nm (b), of $[Hg^{2+}]/[\mathbf{L1}]$ at 530 nm (c). For clarity of the reader the orange spectra are refered to the start of the titration and the blue spectra at the endpoint. (For interpretation of the references to colour in this figure legend, the reader is referred to the web version of this article.)

These images reveal a clear contrast between the dense metal core and the surrounding **L3** layer, which serves to inhibit coalescence. These results open for consideration the use of new synthesizable molecules as stabilizing agents and as a method of functionalization broadening the range of applications.

4. Conclusion

In this study, three novel monodansylated cyclen derivatives (**L1**–**L3**), functionalized with alkyl chains of varying lengths, were successfully synthesized and characterized. POM experiments showed that **L2** and **L3** exhibit a fluidic and birefringent liquid-crystalline mesophase immediately before transitioning into the isotropic liquid. Meanwhile, thermograms revealed a distinct and broad endothermic peak corresponding to both the solid-to-mesophase and mesophase-to-isotropic phase transitions.

Photophysical studies were carried out in several solvents, revealing a positive solvatofluorochromism behavior, which was quantitatively analyzed using the Kamlet–Taft equation, providing relevant information regarding solute–solvent interactions. Different mixtures of aqueous environments promoted tunable photophysical properties through AIE, which was found to be dependent on the length of the alkyl chains. DLS provided the means to determine the size of the formed aggregates, which were also monitored by fluorescence decay lifetime measurements.

As a reference example, **L1** was used to establish the interaction potential towards metal ions, demonstrating efficient fluorescence quenching in the presence of Cu^{2+} and Hg^{2+} ions, reaching a detection limit of 2 μM for the former metal ion, with an association constant of $\log K_{ass} = 4.73$. Notably, the system was able to differentiate between Cu^{+}/Cu^{2+} and Hg^{+}/Hg^{2+}, offering added analytical value.

Given its embedded multifunctional design, **L3** served as an effective stabilizing agent in the colloidal synthesis of platinum nanoparticles. TEM images revealed spherical-shaped particles, while DLS data showed that the hydrodynamic diameters were centered between 157.5 ± 1.0 and 229.7 ± 11.5 nm, depending on the salt-to-ligand ratio used. This result illustrates the versatility of these macrocyclic fluorophores, not only as responsive sensors but also as functional components in nanomaterial synthesis.

CRediT authorship contribution statement.

Frederico Duarte: Formal analysis, Investigation, Writing - Original Draft, Writing - Review & Editing, Visualization.

Cristián Cuerva: Methodology, Validation, Formal Analysis, Investigation, Writing - Review & Editing, Resources, Visualization,

Supervision, Funding acquisition

Georgi Dobrikov: Methodology, Validation, Formal Analysis, Investigation, Writing - Original Draft, Writing - Review & Editing, Resources, Visualization.

Atanas Kurutos: Methodology, Validation, Formal Analysis, Investigation, Conceptualization Writing - Original Draft, Writing - Review & Editing, Resources, Visualization, Supervision, Funding acquisition.

Nikolay G. Vassilev: Investigation, Visualization, Writing - Original Draft.

Jose Luis Capelo-Martinez: Resources, Writing - Review & Editing, Funding acquisition.

Hugo M. Santos: Investigation, Resources, Validation, Writing - Review & Editing.

Carlos Lodeiro: Conceptualization, Methodology, Validation, Formal Analysis, Investigation, Resources, Writing - Review & Editing, Visualization, Supervision, Funding acquisition, Project administration.

Funding

This work received support from PT national funds (FCT/MCTES, *Fundação para a Ciência e Tecnologia* and *Ministério da Ciência, Tecnologia e Ensino Superior)* through the projects UIDB/50006/2020 and UIDP/50006/2020. This work received support from PROTEOMASS Scientific Society through the General Funding Grant 2022–2023, and the projects #PM001/2019 and #PM003/2016. This work is also developed and acknowledged by A.K. as part of contract №: BG-RRP-2.004-0002-C01, Laboratory of Organic Functional Materials (Project BiOrgaMCT), Procedure BG-RRP-2.004 „Establishing of a network of research higher education institutions in Bulgaria", funded by BULGARIAN NATIONAL RECOVERY AND RESILIENCE PLAN". Research equipment of Distributed Research Infrastructure INFRAMAT, part of the Bulgarian National Roadmap for Research Infrastructures, supported by the Bulgarian Ministry of Education and Science, was used in this investigation and acknowledged by N.G.V.

Declaration of competing interest

The authors declare that they have no known competing financial interests or personal relationships that could have appeared to influence the work reported in this paper.

Acknowledgements

This work was supported by the Associate Laboratory for Green Chemistry LAQV which is financed by national funds from Fundação para a Ciência e Tecnologia and Ministério da Ciência, Tecnologia e Ensino Superior (FCT/MCTES) through the the project UID/50006/2023 of the Associate Laboratory for Green Chemistry - LAQV REQUIMTE, details here: https://laqv.requimte.pt/a/74-funding. PROTEOMASS Scientific Society (Portugal) is acknowledged by the funding provided through the General Funding Grant 2024-2025, and by the funding provided to the Laboratory for Biological Mass Spectrometry Isabel Moura (#PM001/2019 and #PM003/2016). F.D. thanks to FCT/MCTES (Portugal) for his doctoral grant 2021.05161.BD. H. M. S. acknowledges the Associate Laboratory for Green Chemistry LAQV (LA/P/0008/2020) funded by FCT/MCTES for his research contract. This work was supported by the Associate Laboratory for Green Chemistry - LAQV (UIDB/50006/2020 (DOI: 10.54499/UIDB/50006/2020) and UIDP/50006/2020 (DOI: 10.54499/UIDP/50006/2020)), which are financed by national funds from Fundacão para a Ciência e a Tecnologia, MCTES (FCT/MCTES). C.L. and H. M.S thanks the Royal Society of Chemistry for the Sustainable Laboratory Grants 2023 reference L23- 8861107285.

The financial support by the Bulgarian National Science Fund (BNSF) under grant – "Novel styryl and polymethine fluorophores as potential theranostic agents "contract No KII-06-M59/1 from 15.11.2021 is gratefully acknowledged by A.K. This work is also developed and acknowledged by A.K. as part of contract №: BG-RRP-2.004-0002- C01, Laboratory of Organic Functional Materials (Project BiOrgaMCT), Procedure BG- RRP-2.004 „Establishing of a network of research higher education institutions in Bulgaria", funded by BULGARIAN NATIONAL RECOVERY AND RESILIENCE PLAN".

G. D. thanks to the European Regional Development Fund within the Operational Programme Science and Education for Smart Growth 2014 - 2020 under the Project Center of Excellence: National center of mechatronics and clean technologies - BG05M2OP001-1.001-0008 for the financial support. Research equipment of Distributed Research Infrastructure INFRAMAT, part of the Bulgarian National Roadmap for Research Infrastructures, supported by the Bulgarian Ministry of Education and Science, was used in this investigation and acknowledged by N.G.V.

Appendix A. Supplementary data

Supplementary data to this article can be found online at https://doi.org/10.1016/j.saa.2025.127285.

Data availability

Data will be made available on request.

References

[1] I. Pereira-Gomes, F. Duarte, G.M. Dobrikov, I. Slavchev, A. Kurutos, J.L. Capelo-Martinez, H.M. Santos, C. Lodeiro, Tetra dansylamides substituted cyclen and cyclam macrocycles as fluorescent sensing probes for metal ions and temperature-responsive materials in dopped polymers, Dyes Pigments 232 (2025) 112461, https://doi.org/10.1016/j.dyepig.2024.112461.

[2] Y. Wang, J. Zhou, L. Zhao, B. Xu, A dual-responsive and highly sensitive fluorescent probe for Cu^{2+} and pH based on a dansyl derivative, Dyes Pigments 180 (2020) 108513, https://doi.org/10.1016/j.dyepig.2020.108513.

[3] W. Deng, S. Li, M. Zhou, M. Zheng, P. Wang, Y. An, Ratiometric peptide-based fluorescent probe with large stokes shift for detection of Hg2+ and S2− and its applications in cells imaging and smartphone-assisted recognition, Spectrochim. Acta A Mol. Biomol. Spectrosc. 315 (2024) 124306, https://doi.org/10.1016/j.saa.2024.124306.

[4] L. Zhang, P. Zhao, S. Yu, J. Kong, L. Gao, L. Li, Dansyl-modified tryptophan fluorescence sensor for highly sensitive and selective detection of Hg^{2+} in aqueous solutions, Microchem. J. 200 (2024) 110520, https://doi.org/10.1016/j.microc.2024.110520.

[5] B. Uttam, S. Polepalli, S. Sinha, A. Majumder, C.P. Rao, Selective sensing and removal of mercury ions by encapsulating Dansyl appended calix[4]conjugate in a Zeolitic Imidazolate framework as an organic−inorganic hybrid nanomaterial, ACS Appl. Nano Mater. 5 (2022) 11371–11380, https://doi.org/10.1021/acsanm.2c02459.

[6] A. Aliberti, P. Vaiano, A. Caporale, M. Consales, M. Ruvo, A. Cusano, Fluorescent chemosensors for Hg^{2+} detection in aqueous environment, Sensors Actuators B Chem. 247 (2017) 727–735, https://doi.org/10.1016/j.snb.2017.03.026.

[7] P. Wang, Y. An, J. Wu, Highly sensitive turn-on detection of mercury(II) in aqueous solutions and live cells with a chemosensor based on tyrosine, Spectrochim. Acta A Mol. Biomol. Spectrosc. 230 (2020) 118004, https://doi.org/10.1016/j.saa.2019.118004.

[8] J.Y. Kim, S. Sarkar, K.N. Bobba, P.T. Huynh, A. Bhise, J. Yoo, Development of dansyl based copper(ii) complex to detect hydrogen sulfide in hypoxia, Org. Biomol. Chem. 17 (2019) 7088–7094, https://doi.org/10.1039/C9OB00948E.

[9] R. Nagarajan, H.I. Ryoo, B.D. Vanjare, N. Gyu Choi, K. Hwan Lee, Novel phenylalanine derivative-based turn-off fluorescent chemosensor for selective Cu^{2+} detection in physiological pH, J. Photochem. Photobiol. A Chem. 418 (2021) 113435, https://doi.org/10.1016/j.jphotochem.2021.113435.

[10] H. Jiang, Z. Li, Y. Kang, L. Ding, S. Qiao, S. Jia, W. Luo, W. Liu, A two-photon fluorescent probe for Cu^{2+} based on dansyl moiety and its application in bioimaging, Sensors Actuators B Chem. 242 (242) (2017) 112–117, https://doi.org/10.1016/j.snb.2016.11.033.

[11] Y. Liu, B. Jiang, L. Zhao, L. Zhao, Q. Wang, C. Wang, B. Xu, A dansyl-based fluorescent probe for sensing Cu^{2+} in aqueous solution, Spectrochim. Acta A Mol. Biomol. Spectrosc. 261 (2021) 120009, https://doi.org/10.1016/j.saa.2021.120009.

[12] G. Pedro, F. Duarte, G.M. Dobrikov, A. Kurutos, H.M. Santos, J.L. Capelo-Martínez, E. Oliveira, C. Lodeiro, Optical evaluation of dansyl derivatives and their implementation in low-cost and flexible dye-doped PMMA platforms for efficient detection of hazardous chemical vapours, Dyes Pigments 224 (2024) 112042, https://doi.org/10.1016/j.dyepig.2024.112042.

[13] X. Fang, S. Wang, Q. Wang, J. Gong, L. Li, H. Lu, P. Xue, Z. Ren, X. Wang, A highly selective and sensitive fluorescence probe based on BODIPY-cyclen for hydrogen

sulfide detection in living cells and serum, Talanta 268 (2024) 125339, https://doi.org/10.1016/j.talanta.2023.125339.
[14] M.D. Tomczyk, K. Matczak, M. Skonieczna, P. Chulkin, M. Denel-Bobrowska, D. Różycka, S. Rykowski, A.B. Olejniczak, K. Walczak, Synthesis and in vitro cytotoxic activity of dye-linker-macrocycle conjugates with variable linker length and components, Bioorg. Chem. 140 (2023) 106782, https://doi.org/10.1016/j.bioorg.2023.106782.
[15] K.E. Siters, M.A. Fountain, J.R. Morrow, Selective binding of Zn^{2+} complexes to human Telomeric G-Quadruplex DNA, Inorg. Chem. 53 (2014) 11540–11551, https://doi.org/10.1021/ic501484p.
[16] C. Rivas, G.J. Stasiuk, M. Sae-Heng, N.J. Long, Towards understanding the design of dual-modal MR/fluorescent probes to sense zinc ions, Dalton Trans. 44 (2015) 4976–4985, https://doi.org/10.1039/C4DT02981J.
[17] L. Yang, J. Zhao, J. Wang, G. Han, B. Liu, W. Zhang, Y. Fu, M.Y. Han, Z. Wang, Z. Zhang, An azacyclo-localizing fluorescent probe for the specific labeling of lysosome and autolysosome, Talanta 216 (2020) 120941, https://doi.org/10.1016/j.talanta.2020.120941.
[18] D. Paderni, D. Lopez, A. Ciavarella, M. Montanari, G. Panza, M. Voccia, M. Formica, B. Canonico, E. Macedi, S. Papa, V. Fusi, A new macrocyclic dansyl-cyclen fluorescent probe for the identification of mildly acidic intracellular compartments, Inorg. Chim. Acta 581 (2025) 122620, https://doi.org/10.1016/j.ica.2025.122620.
[19] M. Tosato, M. Asti, M. Dalla Tiezza, L. Orian, D. Häussinger, R. Vogel, U. Köster, M. Jensen, A. Andrighetto, P. Pastore and V. Di Marco, Highly Stable Silver(I) Complexes with Cyclen-based ligands bearing sulfide arms: a step toward Silver-111 labeled radiopharmaceuticals, Inorg. Chem. 59 (2020) 10907–10919. DOI: https://doi.org/10.1021/acs.inorgchem.0c01405.
[20] E.M. Surender, S. Comby, S. Martyn, B. Cavanagh, T.C. Lee, D.F. Brougham, T. Gunnlaugsson, Cyclen lanthanide-based micellar structures for application as luminescent [Eu(III)] and magnetic [Gd(III)] resonance imaging (MRI) contrast agents, Chem. Commun. 52 (2016) 10858–10861, https://doi.org/10.1039/C6CC03092K.
[21] S. Rani, S. Prasad Gupta, M. Gupta, S. Kumar Pal, Color-tunable photoluminescent discotic liquid crystal based on perylene – Pentaalkynylbenzene triad, J. Mol. Liq. 385 (2023) 122202, https://doi.org/10.1016/j.molliq.2023.122202.
[22] N. Wang, W. Bi, Y. Liu, S. Xu, K. Wang, S. Cao, Recent progress of fluorescent liquid crystals, J. Mol. Liq. 432 (2025) 127741, https://doi.org/10.1016/j.molliq.2025.127741.
[23] Q.Q. Xiong, J.Y. Wu, H.S. Zhang, J.F. Gao, S.Y. Ma, X.Z. He, Liquid crystal polymers with dual properties of fluorescence and selective reflection-design, synthesis and characterization, Liq. Cryst. 51 (2024) 696–710, https://doi.org/10.1080/02678292.2024.2321453.
[24] Y. Li, Y. Shen, K. Liu, Y. Quan, Y. Cheng, Tunable AI-CPL behavior by regulation of microstructure of AIE-active isomers through chiral emissive liquid crystals, Dyes Pigments 186 (2021) 109001, https://doi.org/10.1016/j.dyepig.2020.109001.
[25] F. Duarte, K. Morice, T. Ghanem, D. Puchán Sánchez, P. Blanchard, C.S.B. Gomes, S. Herrero, C. Cabanetos, C. Cuerva, J. Luis Capelo-Martinez, C. Lodeiro, Harnessing liquid crystal attributes of near-unit photoluminescent benzothioxanthene photosensitizers: Photophysical profiling in solution, solid state, and polymer matrix embedding, J. Mol. Liq. 409 (2024) 125424, https://doi.org/10.1016/j.molliq.2024.125424.
[26] A. Kumar, G. Singh, Recent advances and future perspectives of photoluminescent liquid crystals and their nanocomposites for emissive displays and other tunable photonic devices, J. Mol. Liq. 386 (2023) 122607, https://doi.org/10.1016/j.molliq.2023.122607.
[27] Y. Li, K. Yao, Y. Chen, Y. Quan, Y. Cheng, Full-color and white circularly polarized luminescence promoted by liquid crystal self-assembly containing chiral Naphthalimide dyes, Adv. Opt. Mater. 9 (2021) 2100961, https://doi.org/10.1002/adom.202100961.
[28] J. Quinson, K.M.Ø. Jensen, From platinum atoms in molecules to colloidal nanoparticles: a review on reduction, nucleation and growth mechanisms, Adv. Colloid Interf. Sci. 286 (2020) 102300, https://doi.org/10.1016/j.cis.2020.102300.
[29] M. Montalti, A. Credi, Prodi LMG, M. Montalti, A. Credi, Prodi LGM, Handbook of Photochemistry, 3rd Ed., BOCA, Taylor & Francis, Boca Raton, 2006.
[30] D. Macdougall, W.B. Crummett, Guidelines for data acquisition and data quality evaluation in environmental chemistry, Anal. Chem. 52 (1980) 2242–2249, https://doi.org/10.1021/ac50064a004.
[31] G.L. Long, J.D. Winefordner, Limit of detection a closer look at the IUPAC definition, Anal. Chem. 55 (1983) 713A–724A, https://doi.org/10.1021/ac00258a724.
[32] M.J. Frisch, G.W. Trucks, H.B. Schlegel, G.E. Scuseria, M.A. Robb, J.R. Cheeseman, G. Scalmani, V. Barone, G.A. Petersson, H. Nakatsuji, X. Li, M. Caricato, A. V. Marenich, J. Bloino, B.G. Janesko, R. Gomperts, B. Mennucci, H.P. Hratchian, J. V. Ortiz, A.F. Izmaylov, J.L. Sonnenberg, D. Williams-Young, F. Ding, F. Lipparini, F. Egidi, J. Goings, B. Peng, A. Petrone, T. Henderson, D. Ranasinghe, V. G. Zakrzewski, J. Gao, N. Rega, G. Zheng, W. Liang, M. Hada, M. Ehara, K. Toyota, R. Fukuda, J. Hasegawa, M. Ishida, T. Nakajima, Y. Honda, O. Kitao, H. Nakai, T. Vreven, K. Throssell, J.A. Montgomery Jr., J.E. Peralta, F. Ogliaro, M. J. Bearpark, J.J. Heyd, E.N. Brothers, K.N. Kudin, V.N. Staroverov, T.A. Keith, R. Kobayashi, J. Normand, K. Raghavachari, A.P. Rendell, J.C. Burant, S.S. Iyengar, J. Tomasi, M. Cossi, J.M. Millam, M. Klene, C. Adamo, R. Cammi, J.W. Ochterski, R.L. Martin, K. Morokuma, O. Farkas, J.B. Foresman, D.J. Fox, Gaussian 16, in: Revision C.01, Gaussian, Inc, Wallingford CT, 2016.
[33] A.D. Becke, Density-functional thermochemistry. III. The role of exact exchange, J. Chem. Phys. 58 (1993) 5648–5652, https://doi.org/10.1063/1.464913.
[34] P.C. Hariharan, J.A. Pople, The influence of polarization functions on molecular orbital hydrogenation energies, Theoret. Chim. Acta (Berl.) 28 (1993) 213–222, https://doi.org/10.1007/BF00533485.
[35] M. Meyer, V. Dahaoui-Gindrey, C. Lecomte, R. Guilard, Conformations and coordination schemes of carboxylate and carbamoyl derivatives of the tetraazamacrocycles cyclen and cyclam, and the relation to their protonation states, Coord. Chem. Rev. 178-180 (1998) 1313–1405, https://doi.org/10.1016/S0010-8545(98)00169-6.
[36] D. Lu, X. Xu, X. Zhang, W. Xie, Y. Gao, Study on influencing factors of phase transition hysteresis in the phase change energy storage, Materials 15 (2022) 2775, https://doi.org/10.3390/ma15082775.
[37] S. Mocanu, G. Ionita, I. Matei, Solvatochromic characteristics of dansyl molecular probes bearing alkyl diamine chains, Spectrochim. Acta A Mol. Biomol. Spectrosc. 237 (2020) 118413, https://doi.org/10.1016/j.saa.2020.118413.
[38] E. Oliveira, R.M.F. Baptista, S.P.G. Costa, M.M.M. Raposo, C. Lodeiro, Solvatochromic effects of bis(indolyl)thienylaril derivatives as new colored materials, Photochem. Photobiol. Sci. 13 (2014) 492–498, https://doi.org/10.1039/C3PP50352F.
[39] P. Gans, A. Sabatini, A. Vacca, Investigation of equilibria in solution. Determination of equilibrium constants with the HYPERQUAD suite of programs, Talanta 43 (1996) 1739–1753, https://doi.org/10.1016/0039-9140(96)01958-3.

.

FREDERICO GONÇALO DO VALE DUARTE

2026

ADVANCED WATER-SOLUBLE SOFT NANOMATERIALS ENCAPSULATING LUMINESCENT INORGANIC AND ORGANIC EMITTERS AND HYDROPHOBIC DRUGS AS NOVEL NANOCARRIERS: FROM BIOIMAGING TO DRUG DELIVERY AND ENVIRONMENTAL APPLICATIONS